GSI

GSI Report 2013-1
May 2013

SCIENTIFIC REPORT 2012

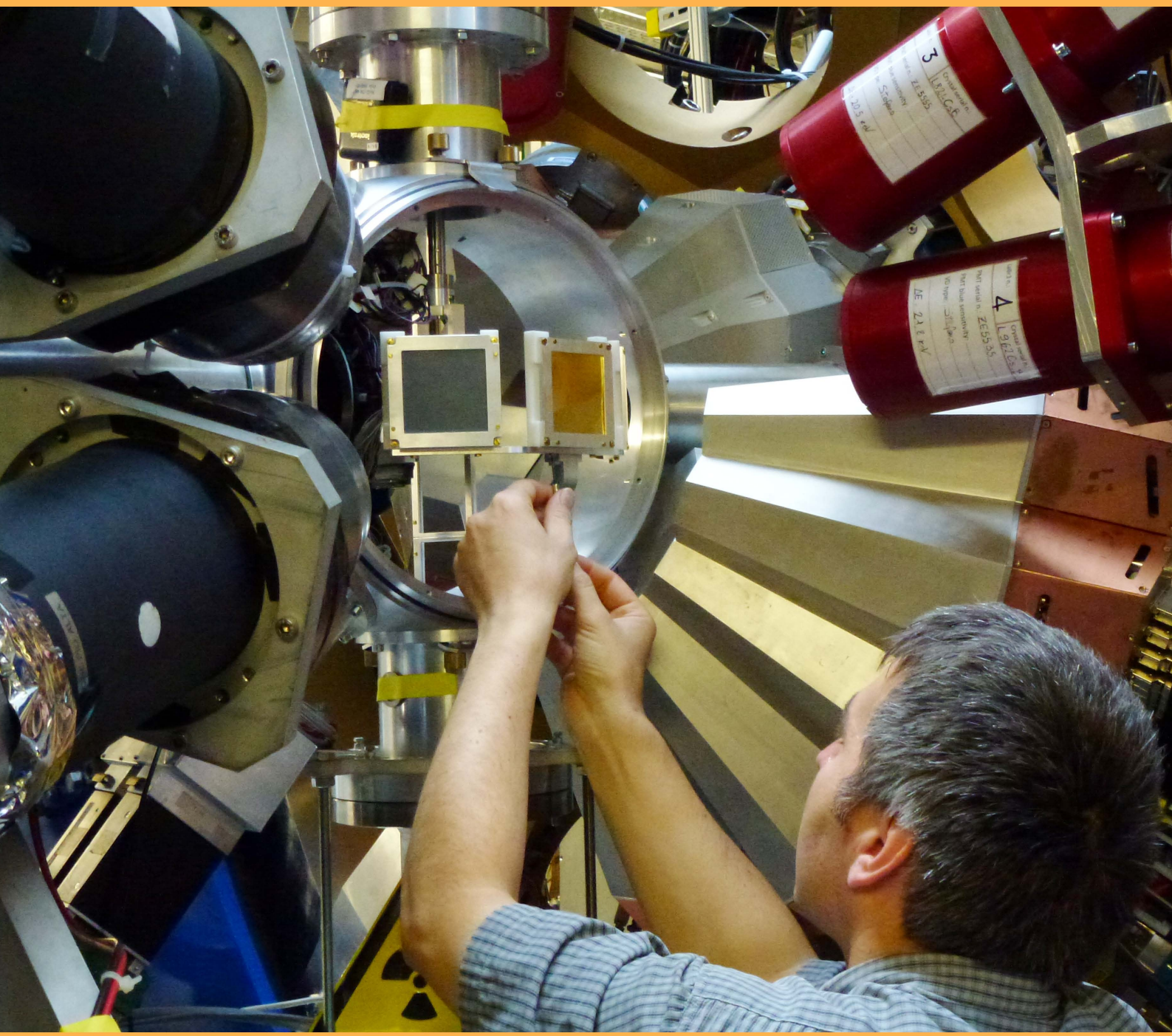

GSI Helmholtzzentrum für Schwerionenforschung GmbH
Member of the Helmholtz Association

Final target adjustment by Dr. Boutachkov from GSI's Gamma Spectroscopy Department before starting the PRESPEC-AGATA experiment campaign at the FRS at GSI. The set-up constitutes the first implementation of the FAIR/NUSTAR experiment HISPEC.
Photograph by Dr. H-J. Wollersheim/GSI

GSI Scientific Report 2012

GSI Report 2013-1
<http://www.gsi.de/library/GSI-Report-2013-1/>

ISSN: 0174-0814
and GSI Report 2013-1

Publisher: GSI Helmholtzzentrum für Schwerionenforschung GmbH,
Planckstr. 1, 64291 Darmstadt, Germany, <http://www.gsi.de>
GSI is a member of the Helmholtz association of national research centres <http://www.helmholtz.de>.
Open Access e-only edition at: <http://www.gsi.de/library/GSI-Report-2013-1/>

Editor: Katrin Große,
Contact: gsilibrary@gsi.de, phone: +496159 712610, fax: +496159 713049.
Cover photograph: Hans-Jürgen Wollersheim/GSI.
Publication date: May 2013
Technical team at GSI: I. Giese, K. Große, S. Hesselbach, V. Schaa and K. Schiebel.

For the production of this report templates and scripts of the JACoW collaboration (Joint Accelerator Conferences on Web <http://www.jacow.org>) were used.

Foreword

Last year – 2012 – has been exceptional. It certainly marks the crossroad from GSI with its world-leading facilities and science output towards FAIR, the Facility for Antiproton and Ion Research, which is the definite future for the fields of hadron and nuclear sciences as well as for many applications in atomic and biophysics and material research. Last year has witnessed, like in the many years before, a long and successful beamtime campaign, once again proving the ability of the GSI accelerator and detector equipment and, as important, of its personnel. However, 2012 also marks the last year of such an extensive campaign at GSI as now the switches have been put towards FAIR for which GSI, with its international partners, has agreed to built, besides important parts for the experimental detectors, the heart of the new facility: the SIS100 accelerator. To fulfill this task, the GSI organisation has been restructured. A new project division, FAIR@GSI, has been established under the leadership of Oliver Kester. It comprises besides the accelerator division also the scientific infrastructure departments and approximately 60 scientists and technical personnel from the four research divisions responsible for the GSI in-kind contributions to the large experiments. Although this procedure of internal staff redeployment has been quite extensive, it went very smoothly proving once again the firm commitment of the GSI personnel towards its project.

While now the GSI organigramm reflects our path towards FAIR, the scientific and technical developments have already been focussed on FAIR for several years. This trend was continuing in 2012 with many milestones reached. The HADES upgrade has been finished and was successfully exploited in an Au+Au beamtime. It includes a major data acquisition upgrade which enables data taking with a rate of 200 MB/s. This is a major step towards data acquisition systems required for the CBM experiment at FAIR. The Cryring, an ion synchrotron and storage ring with electron cooling successfully operated at the Manne Siegbahn Laboratory in Stockholm, has been delivered as a Swedish contribution to FAIR offering new scientific perspectives for the SPARC and NuSTAR collaborations. It will also be used as a machine test facility during the FAIR construction time. Like in the last years the continuous upgrade of the existing GSI accelerator facilities has led to another major milestone now delivering U-beams ($3.2 \cdot 10^{10}$ U^{28+}) with worldwide unprecedented intensities and quality. This progress could be used by the first campaign of the AGATA detector which will be

the heart piece of the HISPEC/DESPEC gamma spectrometer at FAIR. In close collaboration with our Russian partners the PRIOR setup has been completed which will serve as a proton radiography facility for plasma and biophysics and material research. In an experiment performed at CERN ground was broken towards the challenging goal at a precision measurement of the anti-proton's magnetic moment being planned at FLAIR by manipulating the spin of a single proton and determine its magnetic moment with this technique.

These milestones reflect the truly international collaborations and partnerships driving the construction and science of FAIR. However, from the GSI point of view the strong network of regional and national partners is a cornerstone on our pathway to FAIR: German universities focus their activities within the BMBF Verbundforschung towards GSI and FAIR science. The two Helmholtz Institutes in Jena and Mainz have grown into indispensable partners in atomic, plasma, hadron and accelerator physics and in particular in the research with super-heavy nuclei. The Helmholtz International Center for FAIR, founded within the Excellence Initiative Loewe of the Hessian state in collaboration of the universities of Darmstadt, Frankfurt and Giessen with the Frankfurt Institute of Advanced Studies FIAS and GSI, serves as a think tank to develop novel methods and models for the accelerators and experiments at FAIR. The Helmholtz Alliance EMMI, which combines GSI, the universities of Darmstadt and Frankfurt and FIAS with 9 other internationally leading scientific institutions, has clearly established itself as a respected institute which brings together researchers from atomic, nuclear, particle, plasma and astrophysics to perform interdisciplinary research on strongly correlated systems. A particularly important role in the network is being played by the Helmholtz Graduate School (HGS) "Hire for FAIR". Supported with funds from the Helmholtz Association the school comprises now nearly 300 students doing FAIR-related research under the supervision of about 100 professors at the partner universities in Darmstadt, Frankfurt, Giessen, Heidelberg, Jena and Mainz.

In times of limited beamtimes and complete focus on FAIR construction at GSI, the importance of the network is bound to grow. The collaboration and partnership with the universities provide not only synergy and expertise for the scientific and technical developments required for FAIR, but they also guarantee education of the next generations of researchers in the field of FAIR sciences to conserve the unique research expertise present in the GSI neighbourhood and so much needed once FAIR gets operational.

During the last months independent committees of international experts have evaluated the Helmholtz International Center for FAIR, the EMMI Alliance and the HGS Hire for Fair. In each case the vote was extraordinary. Convinced by the achievements of these three institutions and recognizing their essence for FAIR, their permanent continuation has been demanded by the international expert committees. It is now a task of paramount importance to develop a concept to reach this goal.

Like in every year GSI is also in 2012 looking back on many outstanding research highlights. Exploiting the worldwide unique high-intensity ^{50}Ti beam at GSI the TASCA collaboration has successfully detected element 117, confirming a result obtained 2010 in Dubna. Using a ^{249}Bk target provided by Oak Ridge National Laboratory and the ^{50}Ti beam a long-term experimental hunt, led by scientists from the Helmholtz Institut Mainz and GSI, has been performed for element 119. The sensitivity of the experiment reached a limiting cross section of $\sigma_{limit} = 60$ fb, which is an order of magnitude lower than the production cross section of element 118. First data of the successful Au-Au Hades run which has supplied di-lepton spectra and data on strangeness production are presented in this annual report. With the 60 new isotopes produced at the FRS/GSI and published in 2012, Hans Geissel has become the world record holder in isotope discoveries. The EXL collaboration studied for the first time nuclear reactions with stored radioactive ions. The ions have been produced by the FRS and have been investigated in the ESR. Building on their world-leading expertise in cancer treatment with ion beams, GSI biophysics and colleagues have bombarded cancer stem cells pathing a way towards the cure of cancer cells which are resistant against normal chemical and radiation treatments. A breakthrough has been achieved very recently during the investigation of the Lamb shift in the largely unexplored regime of extremely strong electric fields. In an experiment performed within the FOCAL project at the ESR the Lyman transitions of the H-like gold (Au^{78+}) ion have been measured by applying for the first time a high resolution transmission crystal-spectrometer system. GSI plays also an important role in the experiments and the evaluation of the data at the ALICE detector at the CERN Large Hadron Collider. Apart from p+p and Pb+Pb collisions data were taken for asymmetric p+Pb collisions. It could be shown that, in contrast to Pb+Pb, high momentum particles leave the collision zone in p+Pb essentially undisturbed. The production run for p+p collisions lasted nine months, the final reaction rate measured with the ALICE detector was 400.000 events/s. This is the highest reaction

rate at which a Time Projection Chamber was ever operated and its faultless functioning is an important step towards the next heavy ion runs at LHC in 2014.

The present Scientific Report gives again proof of the widespread and high-quality research activities performed at GSI. I wish you much pleasure at reading about achieved scientific milestones, but also about the plans and progress on our pathway to construct FAIR. However, there are now several years of restricted science at GSI ahead of us before we can start to exploit the unprecedented research opportunities offered by FAIR.

Karlheinz Langanke

Contents

GSI's Commitment for FAIR: Development and Implementation of the New Project Structure "FAIR@GSI"

O. Kester, U. Weinrich, G. Hickler, B. Schönfelder, M. Hinkelmann

GSI GmbH, Planckstraße 1, 64291 Darmstadt, Germany

History

In April 2012 the GSI supervisory board requested the GSI management to more consequently focus the company's activities on the realization of the FAIR project. This mainly addresses the requirements concerning the GSI in-Kind contributions to FAIR within the framework of the three subprojects accelerators, experiments, and civil construction. As a result, the GSI management realized this in form of a new project structure within GSI, called "FAIR@GSI". Over the year 2012 and under the overall project leadership of Prof Oliver Kester "FAIR@GSI" successively arose from the former accelerator division, some units from the technical infrastructure as well as from the science division. FAIR@GSI finally comprises 7 divisions, 6 technical ones and 1 newly installed "Project Coordination" [PC] under the leadership of Dr Udo Weinrich. The 6 technical divisions are: Common Systems [CS] with Dr Hartmut Reich-Sprenger, Engineering [EN] with Dr Ralf Fuchs, Primary Beams [PB] with Dr Peter Spiller, Stored Beams [SB] with Dr Markus Steck, Rare Isotope Beams [RB] with Dr Haik Simon and Linac&Operations [LO] with Dr Winfried Barth. Each division supersedes 2 - 7 departments (see Figure 1). The new division and department leaders then created their business plans with interface management and job descriptions, the latter mainly for acquiring new personnel but also for attracting GSI personnel to take over new tasks. Within seven workshops the division and project leads elaborated the following items:

- a list of major milestones for the FAIR accelerator without HESR
- a detailed work breakdown for FAIR@GSI for the full project period
- the matrix including all line and project responsibilities for the FAIR accelerators without HESR

These organizational changes will successively cause a personnel shift of at least 300 persons into new project and hierarchic units under FAIR@GSI. This was and is still a big challenge for the technical staff concerned as well as for GSI's administration.

Performance

As new hierarchical entity the "FAIR@GSI" organisation shall adapt and optimize the overall workflow for an adequate response of all in-Kind activities towards FAIR within the boundary conditions of granted project money, corresponding spending profiles and envisaged timelines.

With an engaging "major milestone list" FAIR@GSI will account for the fulfilment of all in-Kind obligations ("commissioning without beam") by the second quarter of the year 2019.

With "Link existing facilities", the Detector and Target Laboratories and the CBM, SPARC and PANDA Detector departments being part of FAIR@GSI, the new project structure serves all three subprojects (accelerators", experiments and civil construction) of FAIR. The staff is requested to focus their activities on main issues such as

- the construction of FAIR accelerators,
- activities concerning in-Kind contributions,
- activities concerning the FAIR campus development.

Since the allocation of a first badge of project funds for FAIR accelerator construction and experiments end of the year 2011 (50.2 Mio Euro from BMBF and 146 Mio Euro from the State of Hesse) GSI GmbH has been required to realize the corresponding deliveries in compliance with this framework.

Major tasks in this respect comprise e. g.:

- administrative activities such as a so-called "resource-loaded scheduling" (interaction and display at a glance of costs, timelines and human resource [HR] requirements of the FAIR in-Kind activities, see below),
- the generation of comprehensive technical documentation (e.g. specifications, service contracts)
- accelerator construction
- component testing (e. g. magnets)
- a professional execution of purchase processes for GSI in-Kind contributions (i. e. international call-for-tender procedures),
- design and realization of sensible and effective processes,
- creation and/or improvement of communication platforms and controlling issues.

All this has to be done for either own German in-Kind contributions or for contribution by the other partners or direct tendering via the FAIR GmbH.

In-Kind to FAIR Accelerators

The business of allocating accelerator in-Kind contributions to the applying national and international FAIR partners is done by recommendations through the international FAIR committees such as Machine Advisory Committee (MAC) and In-Kind Review Board (IKRB) and finally by decision in the FAIR Council.

So far, GSI GmbH has been assigned to at least contribute to:

- major long-lead items such as the SIS100 dipole modules, the Super-FRS superconducting multipletts, the CR Debuncher system and the SIS100 Bunch Compression system;
- the Accelerator Control system including its interface components within the different technical systems such as the Adaptive Control unit of the Power Converters, the Data Acquisition of the Beam Instrumentation and the low-level parts of the RF systems with cross-functional importance;
- major infrastructure for the accelerator such as the cryogenic plant

Other In-Kind-Related Activities

An important precondition to start in-Kind activities is the completion of specifications. They describe in detail design, technical and functional details of any in-Kind accelerator component. They are the basis for preparing corresponding service contracts with potential contractors.

Specifications and service contracts constitute the main documents to start out with the international procurement processes. In close collaboration with the purchase and legal departments of GSI GmbH “long-lead” items such as the CR Debuncher, the production of superconducting magnets or the diverse magnet testing activities are already subject to comprehensive Europe-wide call-for-tender processes and/or contract negotiations. Last but not least FAIR@GSI has to prepare the overall schedule for the assembly and commissioning without beam phases. All this requires a profound time scheduling for the call-for-tender process itself as well as for the production period, the testing and commissioning processes.

One key issue for steering the FAIR project in these respects is the “integrated project planning” (= resource loaded planning), which is performed in conjunction with the GSI administration. Different project data such as timelines and costs are laid down in different software tools (here MS Project Server 2010 and SAP). With implementing the new software module “SAP-PS” (= Project System) this project data will be linked, additionally together with HR requirements as third factor. This measure shall enable FAIR@GSI to interactively control the project and to amend the planning on one aspect with immediately being aware of related implications on the other two. By end of 2012 every division was involved in creating and or updating their time, cost and resource plans for the realization of dedicated machine components. Bringing these individual plans together into an overall integrated project plan via SAP-PS and taking advantage of the performance of this new software tool constitutes a considerable milestone to further optimize GSI’s in-Kind activities towards FAIR in time.

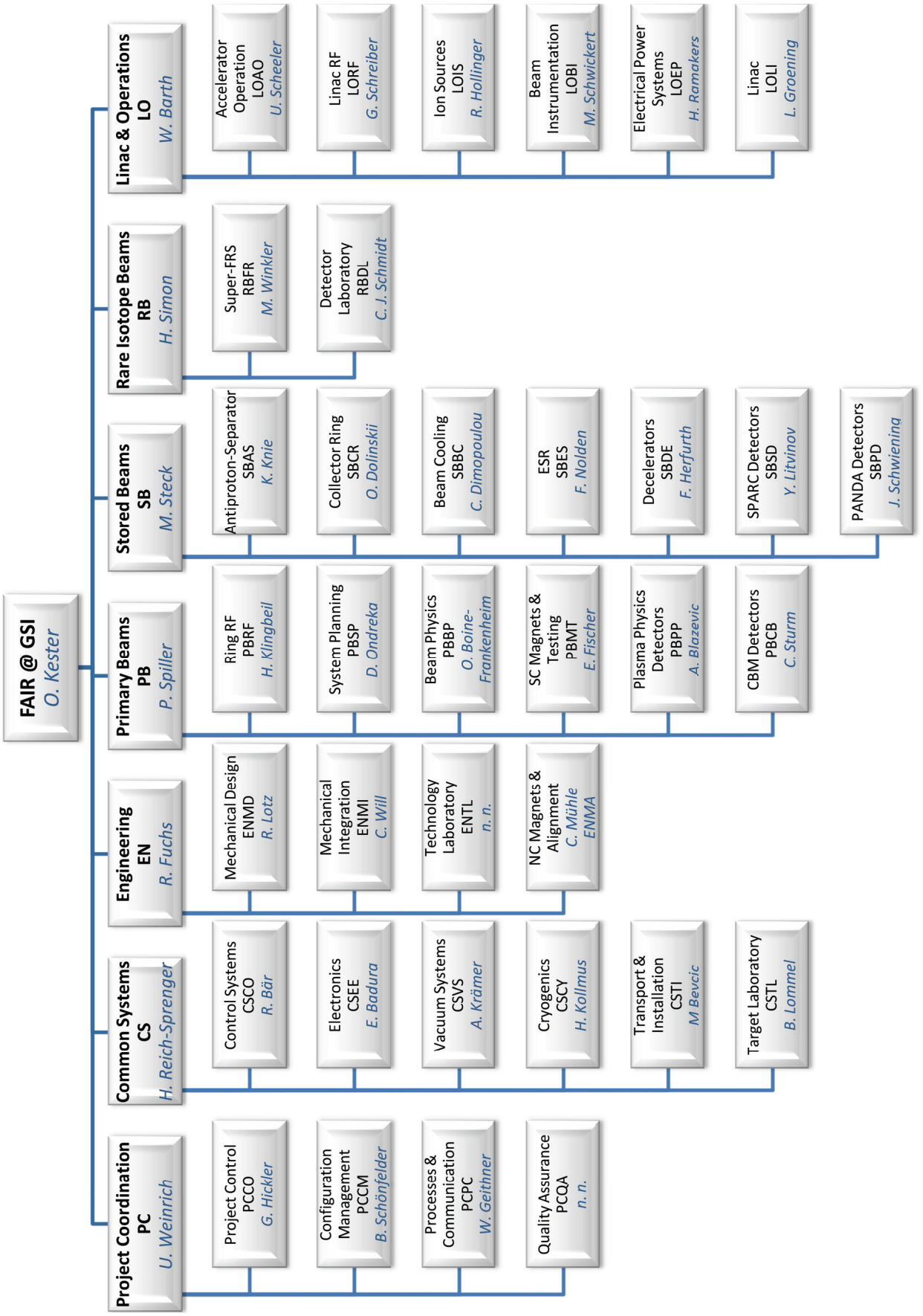

Figure 1: The FAIR@GSI organigram

The ExtreMe Matter Institute EMMI

P. Braun-Munzinger[1,2,3] *and C. Ewerz*[1,4]

[1]ExtreMe Matter Institute EMMI, GSI, Darmstadt, Germany; [2]Research Division, GSI, Darmstadt, Germany; [3]TU Darmstadt, Germany; [4]University of Heidelberg, Germany

Since 2008 the Helmholtz Alliance 'Cosmic Matter in the Laboratory' is funded in the framework of the Alliance program of the Helmholtz Association. The aim of the Alliance program is to strategically enhance the profiles of the participating Helmholtz Centres and to transfer successful developments into one of the Helmholtz Association's research programs. The research performed within the Helmholtz Alliances is collaborative and brings together universities, Helmholtz Centres and other non-university research institutions. In the case of the Alliance 'Cosmic Matter in the Laboratory' the funding contribution from the Helmholtz Association amounts to 18.745 Mio. Euro for six years.

A key step in the strategic positioning of the Helmholtz Alliance 'Cosmic matter in the Laboratory' was to establish a new, world-leading institute for research on matter at the extremes of density and temperature: the ExtreMe Matter Institute EMMI hosted by GSI. It was founded simultaneously with the start of the Alliance in April 2008.

The scientific aim of the ExtreMe Matter Institute is to perform forefront research in the area of matter under extreme conditions. This comprises in particular four key areas of the research field 'Structure of Matter' of the Helmholtz Association:

- quark-gluon plasma and the phase structure of strongly interacting matter
- neutron matter
- electromagnetic plasmas of high energy density
- cold quantum gases and extreme states in atomic physics.

The relevant science themes range from the quark-gluon plasma as it existed shortly after the Big Bang to ultracold quantum gases created in laboratory experiments, to the quantum dynamics of extreme fields, and from hot and highly compressed classical bulk plasmas to the astrophysically relevant dense medium of nucleons and neutrons that governs the properties of the evolution of supernovae and neutron stars. It hence comprises the study of the coldest, of the hottest, and of the densest known forms of matter in the Universe. The key idea is to conduct this research in an interdisciplinary framework, based upon common underlying concepts for the theoretical and phenomenological understanding of the physical phenomena in the four areas.

Under the lead management of the GSI Helmholtz Centre for Heavy Ion Research the Alliance links 13 German and international research centers and universities as partner institutions:

- GSI Helmholtzzentrum für Schwerionenforschung, Darmstadt, Germany
- Forschungszentrum Jülich, Germany
- Ruprecht-Karls-Universität Heidelberg, Germany
- Goethe Universität Frankfurt, Germany
- FIAS Frankfurt Institute for Advanced Studies, Germany
- Technische Universität Darmstadt, Germany
- Universität Münster, Germany
- Université VI, Paris, France
- Max-Planck-Institut für Kernphysik, Heidelberg, Germany
- Lawrence Berkeley National Laboratory, Berkeley, USA
- Joint Institute for Nuclear Astrophysics (JINA), USA
- RIKEN, Saitama, Japan
- University of Tokyo, Japan.

In addition, the Alliance benefits from the expertise of internationally renowned scientist who are closely linked to it as Associated Partners. Currently, the Alliance has 32 Associated Partners, among them two Nobel laureates. In total, more than 400 scientists contribute to the activities of EMMI.

The partner institutions have committed themselves to creating 18 senior positions, including full professorships and equivalent tenure-track and tenured positions, in the framework of the Alliance. By the end of 2012, 16 of these 18 positions are filled. Among these positions are four EMMI Fellow positions in experimental physics at GSI, one for each of the main research areas of EMMI. The EMMI fellows lead their own research groups and organize joint activities.

12 renowned experts have visited EMMI partner institutions for extended periods in 2012 as EMMI Visiting Professor, and have made progress in their collaborations with EMMI members.

EMMI is strongly committed to fostering the education and training of young researchers through a postdoctoral research program and training of graduate students. Structured PhD education for students within the Alliance is offered in close collaboration with the various Graduate Schools at the partner institutions, for example with the Helmholtz Graduate School for Hadron and Ion Research (HGS-HIRe), the Heidelberg Graduate School of Fundamental Physics (HGSFP) and the Helmholtz Research School Quark Matter Studies (H-QM). Many of the students in the Alliance have participated in various events (lecture weeks of HGS-HIRe, H-QM and HGSFP, graduate days of the HGSFP etc.) of these Graduate Schools in 2012.

An important activity of the ExtreMe Matter Institute EMMI is to organize and to host workshops and research

programs on topical and interdisciplinary subjects in the area of matter under extreme conditions. 7 EMMI Workshops and one four-week EMMI Program with strong international participation took place in 2012. In November 2012, the EMMI Physics Days were organized at GSI in which 174 EMMI members participated.

In addition, 29 'EMMI Seminars' were organized in 2012 in which external experts and guest scientists present their work on subjects related to EMMI. These seminars, mostly taking place in Darmstadt, form a nucleus for frequently attracting EMMI members from the nearby partner institutions.

Since 2012, EMMI provides the possibility to have talks at EMMI workshops recorded on video. The recorded talks are made available to all EMMI members and other interested scientists.

EMMI organized two masterclass events for high school students in 2012. In these masterclasses the students analyzed actual data from the ALICE experiment at the Large Hadron Collider at CERN. In total, 50 students participated in these masterclasses.

In 2012 the research within EMMI resulted in more than 300 publications in refereed journals. Many important results are described in various contributions to the GSI Scientific Report 2012.

A cooling system for the HADES pion tracker*

J. Wirth[2], M. Berger[2], L. Fabbietti[1,2], and R. Lalik[2]
[1]GSI, Darmstadt, Germany; [2]Physik Department TUM, E12, Munich, Germany

One of the next proposed experiments at the SIS18 with the HADES spectrometer plans the employment of a pion beam on nuclear and LH2 targets. The fact that the pion beam is a secondary beam leads to rather wide spread ($\sim 8\%$) of its momentum. Since the precise knowledge of the momentum is essential for exclusive measurements as planned by the HADES collaboration, the momentum for each pion has to be determined.
For this propose our group is developing a pion beam tracking system called CERBEROS. The system consists of two silicon detector, which are located directly along the pion beam chicane between the production target and the HADES spectrometer. Consequently, these detectors have to tolerate the high intensity of the pion beam, that close to the secondary beam production target reaches the value of 10^8 part./s. Cooling improves the radiation hardness and performance of the detectors, which is crucial for the measurement of MIPs like pions.

Since the detectors have to be located inside the beam pipe, we have developed a vacuum chamber which is compatible with the beam pipe structure. The vacuum chamber for each detector consists of two identical aluminium parts that are arranged face to face. Between them is a feed-through PCB for the electronic read out. One of the chamber parts has additional feed-throughs for the cooling and vacuum pump. In Fig. 1 one can see one half of the vacuum chamber.

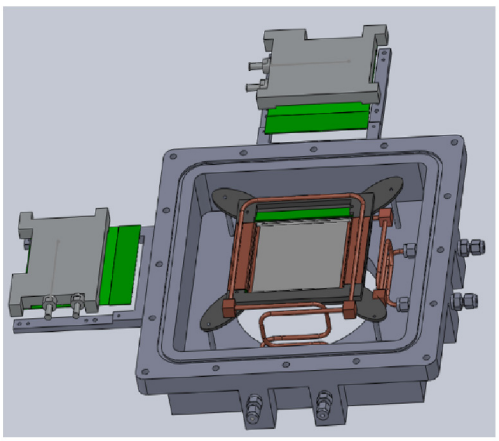

Figure 1: View of one half of the vacuum chamber. The detector and also the cooling is mounted in the center. The front-end electronic is located outside the chamber.

Development of a cooling system

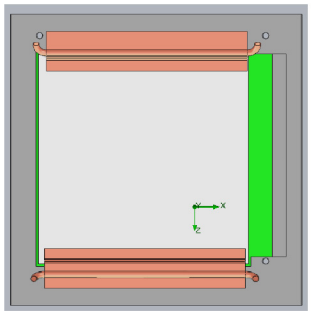

Figure 2: Technical drawing of detector with attached cooling device.[1]

The cooling system was developed relying on the results of thermal simulation that are based on the Finite Element Method.
In Fig. 2 one can see the technical drawing of the cooling device. It consists of two quadratic FR4 blocks, which surround the detector. Mounted on each block are two bent copper plates. The copper plates are connected to the silicon wafer through heat conduction pads that are included as a thermal resistance. These heat conduction pads isolate voltages and thus ensure that the copper plates introduce no short cuts on the silicon wafer . The copper plates are located parallel to the strips of the wafer. The silicon detector is located in a vacuum pipe. The outer side of the vacuum pipe is set to 20°C and Propane is used as cooling liquid at a temperature of -15°C. The glue between the silicon wafer and the PCB is included in the simulation as a thermal resistance . Moreover heat is exchanged through heat radiation between the elements.[1]

By cooling the detector on the four sides we achieved a quit homogeneous temperature distribution at temperature around -10°C. All in all only little losses are expected and a prototype has been already built and is currently under testing procedure.[1]

References

[1] J. Wirth, "Development of a cooling system for a silicon particle detector" (2012), http://www.e12.ph.tum.de/groups/kcluster/Documents/ Publications/bachelorthesis_joana_wirth.pdf.

* Work supported by VH-NG-330 and TMFABI1012.

A data-driven calibration procedure for the HADES electromagnetic calorimeter*

D. Mihaylov†[1], *L. Fabbietti*[1], *and K. Lapidus*[1]

[1]Excellence Cluster "Universe", TU München, Boltzmannstr. 2, 85748 Garching, Germany

In its present configuration the HADES detector system is not able to detect photons. The proposed lead-glass electromagnetic calorimeter (EMC) [1] will, besides improving the electron-pion separation, enable the identification of the neutral pseudoscalar mesons (π^0, η) via their decay into two photons and their Dalitz decay[1]. The exclusive reconstruction of π^0 and η is achieved by analyzing the invariant mass spectrum (IMS) of the detected photons. The interpretation of the signal from the EMC is a complex process, which involves multiple steps. An algorithm, capable of reconstructing the initial photons hitting the EMC, has been developed [1]. Mostly due to energy losses inside the EMC this algorithm delivers systematical errors to the reconstructed momenta of the photons. A calibration procedure able to eliminate these systematical effects is, therefore, required.

The analysis of simulated data has shown that for photons the inaccuracy in the energy reconstruction is much larger than the errors in the reconstruction of polar and azimuthal angles [2]. Thus it is sufficient to calibrate only the energies of the single photons, in a first step this can be achieved by applying a correction to the energy using the equation:

$$E_C = E \times f\,(E, \theta, \varphi)\,, \tag{1}$$

where E_C and E are the calibrated and reconstructed energies, respectively, and f is a calibration function. A convenient general form of the function f is [2-3]:

$$f(E, \theta, \varphi) = \exp\left(\sum_{i=0}^{n} A_i \ln^i E\right), \tag{2}$$

where A_i are calibration coefficients, which need to be determined. The summation limit n is usually set to 2 or 3 [2]. The coefficients A_i are determined using the likelihood function $\mathcal{L}$, which is defined as [3]:

$$\mathcal{L} = \sum_{j=1}^{N} \left[\ln M_{\gamma\gamma j} - \ln m_{\pi^0}\right]^2. \tag{3}$$

Here the summation is over all photon pairs in the data sample, $M_{\gamma\gamma j}$ is the invariant mass of the j-th photon pair and m_{π^0} is the reference mass value, which is the mass of π^0. If the summation is performed only over photon pairs with invariant masses $M_{\gamma\gamma}$ in the range $M_{\pi^0} \pm \sigma_{M_{\pi^0}}$, then the likelihood function $\mathcal{L}$ should converge towards zero. Thus the calibration coefficients A_i can be determined by minimizing $\mathcal{L}$ with respect to A_i. The minimization of $\mathcal{L}$ and calculation of the coefficients A_i is performed numerically. A distinctive feature of this approach is that no prior knowledge of the calorimeter response is required: the calibration is based solely on measured data. Figure 1 shows the performance of the calibration procedure on the IMS of a simulated data sample.

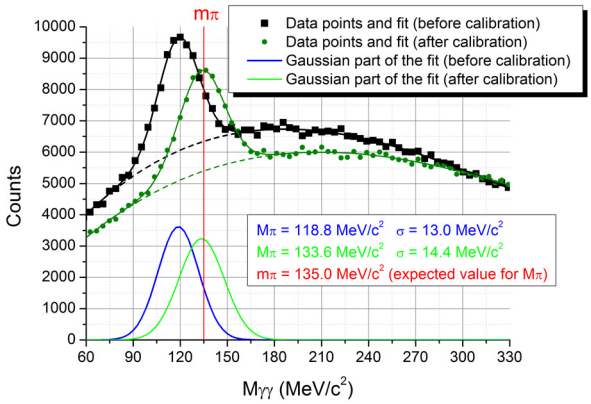

Figure 1: Two-photon invariant mass spectra showing π^0-peaks before and after calibration. The data are full-scale simulations of Ni+Ni collisions at 8 AGeV [2].

From Fig. 1 follows that the developed calibration procedure is accurate in the mass region of interest for the HADES experiment.

The calibration procedure was implemented in a standalone C++ program that uses only standard C++ and ROOT libraries [2] and can be, therefore, used for a broad class of electromagnetic calorimeters.

References

[1] W. Czyzycki *et al.*, "Electromagnetic Calorimeter for HADES", arXiv:1109.5550 [nucl-ex].

[2] D. Mihaylov, "Calibration Software for the HADES Electromagnetic Calorimeter", 2012, `http://www.e12.ph.tum.de/groups/kcluster/Documents/Publications/Dimitar_Thesis.pdf`.

[3] D. J. Tanner, "Energy calibration of the BaBar EMC using the π^0 invariant mass method", SLAC-R-850.

* Work supported by the BMBF grant 06MT9156

† dimitar.mihaylov@mytum.de

Status of the n-XYTER readout for the HADES Pion-Beam Tracker*

R. Lalik[1], *E. Epple*[1], *L. Fabbietti*[1], *L. Maier*[1], *R. Münzer*[1], *J. Siebenson*[1], *T. Schmitt*[1], *J. Wirth*[1], *and HADES collaboration*

[1]Excellence Cluster 'Universe', Technische Universität München, Germany

The n-XYTER chip is currently being employed to develop a fast read-out of the pion beam tracker (CERBEROS – **Cen**tr**a**l **Be**am **T**racker for Pi**ons**) for the HADES experiment. Indeed this self-triggering system should enable the on-line tracking of each particle in pion secondary beams at SIS18.

In order to perform exclusive measurements with the HADES spectrometer and a pion beam, due to the large momentum spread (≈ 8 %) of the secondary particle, fast tracking detectors along the pion chicane are necessary to measure on-line the beam momentum.

Differently to past approaches [1] based on scintillator detectors, in CERBEROS two large-area silicon detectors are employed to measure the pion momentum and and pion impact angle on target.

The detector system that has been developed so far, has been first tested in the laboratory with radioactive sources and then with deutron and Ni beams at 1.9 and 1.7 GeV kinetic energy respectively at GSI in November 2012. Two Pb targets corresponding to an interaction probability of 2% and 10% respectively were used. The primary beam intensity was varied between 10^6 and $3 \cdot 10^7$ part./s. This corresponds to a reaction rate of 10^2 and $5 \cdot 10^5$ part./s (dependently on projectile kind) on the scintillator detectors placed in front of the CERBEROS system, that have been used as triggers.

Fig. 1 presents the experimental setup consisted of two double sided silicon detectors of 10×10 cm^2 dimension and 128 channels on each side, readout by n-XYTER modules connected to SysCore readout boards. The trigger was provided by two scintillators placed one in front and the other after the silicons. Coincidence of both or each separately can be used as a trigger source.

Detectors have been located around 10 m upstream the target and 30 cm from the beam axis to avoid direct heavy fragments hits. The distance between the detectors was 7 cm.

* Supported by VH-NG-330 and TMFABI1012

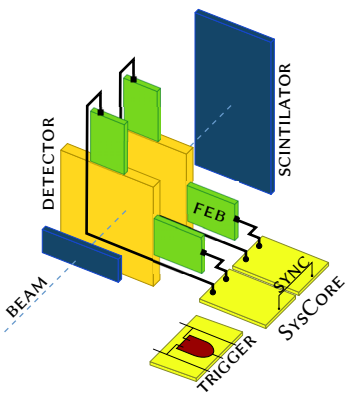

Figure 1: Experimental setup based on CBM readout.

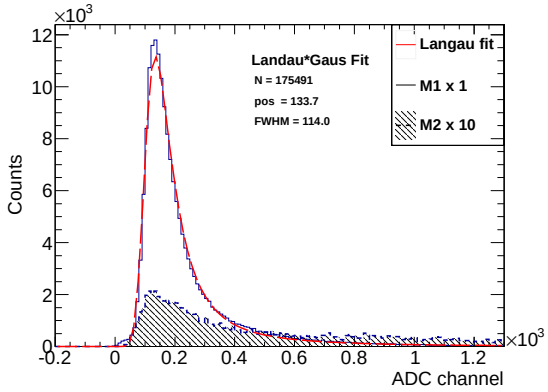

Figure 2: ADC spectrum of MIP signal (M1). Fitted is convolution of Gauss and Landau distribution to describe properly energy deposition in silicon.

Our goal was to the performance of the tracking system under realistic beam conditions, electronics stability and possibility of internal n-XYTER MIPs triggering.

Fig. 2 shows the ADC spectrum of measured signals after pedestal suppression and cluster reconstruction, integrated over all channels of one n-XYTER. The dominating part of the spectrum (M1) belongs to events with only one fired strip which corresponds to pure MIP signals without charge sharing. The average signal to background ratio obtained with a deuteron beam of 300 Hz intensity is ≈ 14 while the measured detector efficiency is higher than 95%.

We proved that with proper shielding of the detector and electronics together with careful settings of internal n-XYTER threshold it is possible to separate the MIP signal from the noise. The detector efficiency measured with the beam is consistent with laboratory tests. We are currently preparing the TRB3-based native HADES readout which will allow us to test the n-XYTER performance for high rate beams. The maximal data rate of n-XYTER is 32 MHz and average rate per channel is 160 kHz with 10% deadtime which will allow to cope with the maximal rate of 10^8 particle/sec expected along the pion chicane in the region close to the production target.

References

[1] J. Diaz et al. Design and commissioning of the GSI pion beam *Nuclear Instruments and Methods in Physics Research Section A: Accelerators, Spectrometers, Detectors and Associated Equipment, 478(3):511–526, 2002*

Constraining K^0 production channels in proton-proton collisions for transport models*

J.-C. Berger-Chen[1], *L. Fabbietti*[1], *K. Lapidus*[†1], *and the HADES Collaboration*
[1]Excellence Cluster "Universe", TU München, Boltzmannstr. 2, 85748 Garching, Germany

The HADES collaboration performed measurements of strangeness production in p+p and p+^{93}Nb collisions at a beam kinetic energy of 3.5 GeV. The analysis of the K^0-meson emission in p+Nb collisions aims to refine the knowledge of the kaon in-medium behaviour in terms of the repulsive potential and the in-medium kaon-nucleon scattering cross sections. The tool to extract these characteristics is a transport code incorporating kaon production mechanisms and kaon final state interactions with nuclear environment. The measurement of kaons in p+p collisions serves as an important reference, which allows to constrain production cross sections of the different final states in transport models.

Spectra of kaons produced in p+p collisions were compared with the GiBUU [1] simulations based on the resonance model by Tsushima et al. [2]. In this model, all hyperon-kaon pairs are products of the nucleon resonances decays, e.g. $N(1650) \rightarrow \Lambda + K$. The resonance model incorporates all possible channels of type $B + B \rightarrow B + Y + K$, where B can be either a nucleon or a $\Delta(1232)$-resonance, Y is a hyperon (Λ or Σ) and K stands for a positively charged or a neutral kaon. It was shown that for the case of inclusive K^0 production in p+p reactions the resonance model significantly overestimates the K^0 yield.

A systematical comparison of the various kaon production channels, implemented in the resonance model, with available published data shows that: i) the channel $p\pi^+\Lambda K^0$ is significantly overestimated by the resonance model; ii) the channel $p\Sigma^+K^0$ is slightly overestimated as well.

Besides overestimation of the major K^0 production channels, the resonance model [2] has other shortcomings. One of the main assumptions of the model is that all nucleon-nucleon reactions with the pion in the final state ($N + N \rightarrow N + \pi + Y + K$) proceed through an intermediate $\Delta(1232)$-resonance with its subsequent decay $\Delta(1232) \rightarrow N + \pi$. These final states can be, however, produced in a non-resonant way as well. An on-going analysis of the exclusive kaon production in the reaction $p + p \rightarrow p + \pi^+ + K^0 + Y$ allows to disentangle the two production mechanisms. The missing mass to the reconstructed $p\pi^+\pi^-\pi^+$ system after pre-selection of K^0 candidates (accessible via $K^0_S \rightarrow \pi^+\pi^-$ decays) is shown on Fig. 1. The three peaks correspond to the missed neutron (background reaction $p + p \rightarrow p + n + \pi^+ + \pi^+ + \pi^-$), $\Lambda(1116)$- and $\Sigma^0(1192)$-hyperon. A further inspection of the $p\pi^+$ invariant mass distribution will allow to separate two production mechanisms (with or without intermediate $\Delta(1232)^{++}$ state).

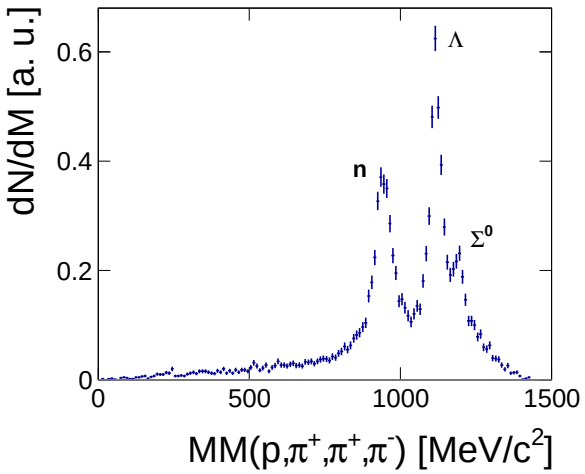

Figure 1: Distribution of the missing mass to $p\pi^+\pi^+\pi^-$-system. Peaks marked "n", "Λ" and "Σ^0" originate from reactions $p + p \rightarrow p + n + \pi^+ + \pi^+ + \pi^-$, $p + p \rightarrow p + \pi^+ + \Lambda + K^0$ and $p + p \rightarrow p + \pi^+ + \Sigma^0 + K^0$, respectively.

After taking into account the experimentally obtained constraints on the kaon production in elementary collisions, tuned transport models can be used to simulate proton-nucleus and nucleus-nucleus collisions. This will lead to the reliable determination of in-medium characteristics of kaon-nucleon interactions. Further information is expected from on-going investigations of other strange particles (Λ, $\phi(1020)$, $K^*(892)$) produced in p+p and p+Nb reactions.

References

[1] O. Buss *et al.*, "Transport-theoretical Description of Nuclear Reactions", Phys. Rept. **512** (2012) 1.

[2] K. Tsushima, A. Sibirtsev and A. W. Thomas, "Resonance model study of kaon production in baryon baryon reactions for heavy ion collisions", Phys. Rev. C **59** (1999) 369.

* Work supported by the grants BMBF (06MT9156) and VH-NG-330
† kirill.lapidus@ph.tum.de

Direct measurement of the proton magnetic moment

A. Mooser[1,2], *K. Blaum*[3,4], *S.A. Bräuninger*[3,4], *H. Kracke*[1,2], *C. Leiteritz*[1], *W. Quint*[4,5], *C.C. Rodegheri*[1,4], *S. Ulmer*[6], *and J. Walz*[1,2]

[1]Institut für Physik, Johannes Gutenberg-Universität Mainz, Germany; [2]Helmholtz Institut Mainz, Mainz, Germany; [3]Max-Planck-Institut für Kernphysik, Saupfercheckweg 1, Heidelberg, Germany; [4]Ruprecht Karls-Universität Heidelberg, Heidelberg, Germany; [5]GSI - Helmholtzzentrum für Schwerionenforschung, Darmstadt, Germany; [6]present address: RIKEN Advanced Science Institute, Hirosawa, Wako, Saitama, Japan

Up to now the magnetic moment of the proton has never been measured directly. The present most precise value for the magnetic moment comes from measurements of the hyperfine splitting in atomic hydrogen by Winkler *et al.* [1]. Several bound-state corrections have to be included to extract the magnetic moment of the free proton with a precision of 8.2 parts in 10^9 [2]. A direct and precise measurement with just one single isolated proton stored in a cryogenic Penning trap has the potential to improve this value by one order of magnitude without a need for theoretical corrections and opens the way for a corresponding measurement on the antiproton.

An ideal Penning trap is a superposition of a homogeneous magnetic field and an electrostatic quadrupole potential. In such a trap an ion has three independent eigenmotions: two radial modes, the modified cyclotron motion with frequency ω_+ and the magnetron motion with frequency ω_-, and an axial motion with frequency ω_z. The principle of a measurement of μ_p is the determination of two frequencies of the proton: the spin-precession frequency ω_L and the free cyclotron frequency ω_c. The frequency ratio yields the magnetic moment $\omega_L/\omega_c = \mu_p/\mu_N$ in units of the nuclear magneton μ_N.

The Larmor frequency is determined by measuring the spin transition probability as a function of the frequency of an external magnetic driving field. To this end an inhomogeneous magnetic field, a so-called *magnetic bottle*, is used to couple the spin magnetic moment to the axial motion of the proton. Using this *continuous Stern-Gerlach effect* a spin transition results in a frequency jump of the axial motion. In our magnetic bottle with $B_2 = 3 \cdot 10^5\,\mathrm{T/m^2}$ a spin transition results in an axial frequency jump of 171 mHz at 742 kHz.

However, the strong magnetic bottle also couples the magnetic moments of the radial modes to the axial mode. Thus the axial frequency is extremely sensitive to energy changes in the radial modes. This results in axial frequency fluctuations. As a measure for these fluctuations the standard deviation of the difference between two subsequent axial frequency measurements $\alpha = \nu_z(t) - \nu_z(t+\Delta t)$ can be defined, $\Xi = \left((N-1)^{-1}\sum(\alpha_i - \bar{\alpha})^2\right)^{1/2}$. The minimal fluctuation achieved is $\Xi_{opt} \approx 150\,\mathrm{mHz}$. This value is not sufficient to detect spin transitions directly. However, a series of spin transitions leads to an increase of the fluctuations $\Xi_{SF} \approx \sqrt{\Xi_{opt}^2 + P_{SF}\Delta\nu_{z,SF}^2}$. A measurement of Ξ_{SF} and Ξ_{opt} then allows a determination of the spin transition probability [3], thus the Larmor frequency.

The spin-flip resonance has been measured by tuning the spin transition drive over the Larmor frequency. The result is presented in Fig. 1. The line broadening is due to the coupling of the axial motion to the thermal bath of the detection system in the magnetic bottle. From this the Larmor frequency can be determined to 2 parts in 10^6, limited by the line broadening. Combined with a measurement of the free cyclotron frequency the *g*-factor was determined to $5.585696(50)$ [4].

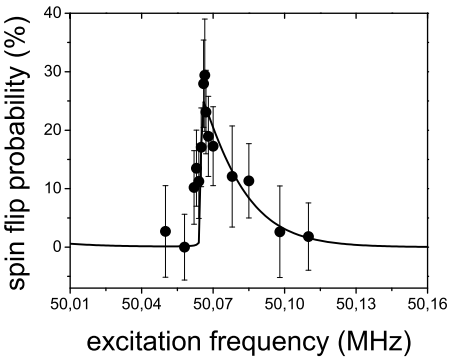

Figure 1: Larmor resonance of a single proton stored in the analysis trap. The broadening is due to the coupling of the axial motion to the thermal bath of the detection system in the inhomogeneous magnetic field.

Taking advantage of the so-called double Penning-trap setup, a narrower spin-flip resonance is expected, which allows for a measurement of the g-factor with even higher precision in the future. To this end spin transitions are driven in a Penning trap with a homogeneous magnetic field, where no additional line broadening occurs, and subsequently detected in a second Penning trap with a magnetic bottle. This will demand the direct detection of spin transitions, hence lower axial frequency fluctuations. In the future, we plan to measure the antiproton magnetic moment as a test of CPT invariance within the FLAIR Collaboration.

References

[1] P. F. Winkler *et al.*, Phys. Rev. **A 5**, 83 (1972).

[2] P. J. Mohr *et al.*, Rev. Mod. Phys. **80**, 633 (2008).

[3] S. Ulmer *et al.*, Phys. Rev. Lett. **106**, 253001 (2011) .

[4] C. C. Rodegheri *et al.*, New J. Phys. **14** 063011 (2012)

Distortion Studies for the FOPI GEM-TPC*

M. Berger† [1] *and the GEM-TPC Collaboration*[1,2,3,4,5]

[1]Technische Universität München, Germany; [2]GSI Helmholtzzentrum für Schwerionenforschung GmbH, Darmstadt, Germany; [3]Helmholtz-Institut für Strahlen- und Kernphysik, Bonn, Germany; [4]Universität Heidelberg, Heidelberg, Germany; [5]Stefan Meyer Institut für Subatomare Physik, Wien, Austria

A TPC (Time Projection Chamber) with a GEM readout was employed inside the FOPI [1] detector for several tests and a physics experiment with a pion beam. This TPC has an cylindrical fieldcage with with an driftlengh of 72.28 cm an outer diameter of 15 cm and an inner diameter of 5 cm. For field homogenization the fieldcage consists of more than 900 strips at the inner as well as on the outer fieldcage. The distance from the GEMs to the fieldcage strip with the lowest potential – the last strip – is 3.5 cm. The potential on this last strip can be set to define the voltage drop over the fieldcage and the field between the last strip and the GEMs. Since inhomogeneities in the occupancy suggested the presence of distortions and the estimated spatial resolution was worse than the expected value confirmed by [2], a detailed modeling of the drift field is necessary to reproduce quantitatively the distortion effects

Fieldcage Simulation

For this purpose a FEM simulation of the electric field inside the fieldcage was carried out. The first results of this simulation can be seen in Figure 1 where the radial electric field component and the component along the TPC symmetry axis is plotted. In this first simulation the setting for the field as they were used during the tests with the cosmic particles were implemented. These settings include a drift field of 309.6 V/cm and the potential of the last strip was set to 70 V. Furthermore the first strip after the cathode is on the same potential. To simplify the calculations azimuthal symmetry of the field was assumed. One can see from Figure 1 that the first as well as the last strip are sources of field distortions. A unwanted radial component of the drift field appears at the positions of these strips which leads to distorted electron drift paths.

Distortions

With the knowledge of the effective drift field and the magnetic field, the Langevin equation can be solved numerically in order to obtain a map of drift distortions as a function of the starting point of the drift [3]. For the magnetic field, the FOPI field map was used. Figure 2 shows the distortion of electrons as a function of the radius and the position along the drift. The distortion map will be used as an input for a Monte Carlo simulation to reproduce the

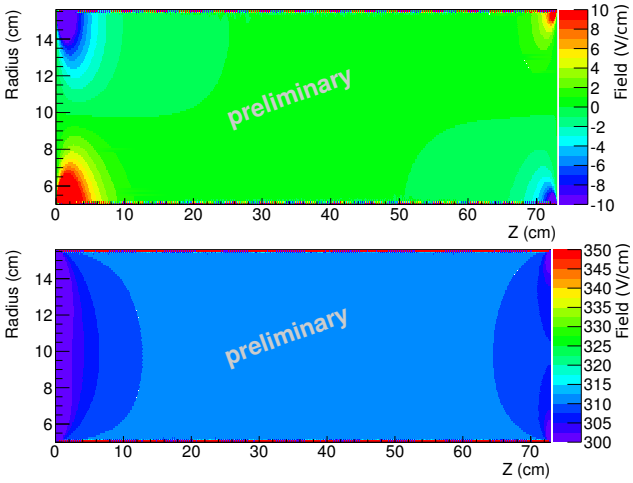

Figure 1: The electric field inside the TPC prototype for 309.6 V/cm drift field and 70 V potential at the last strip. The radial and along the beam axis component of the electric field inside the GEM-TPC is shown in the upper and lower panels respectively.

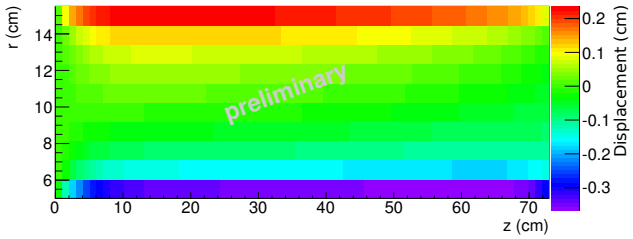

Figure 2: The displacement in radial direction in cm for an electron starting at a given position.

experimentally found inhomogeneities in the spacial resolution. A first evaluation of the experimental data agrees qualitatively with assumption that the distortions are linked to the last strip settings.

References

[1] K. Hildenbrand, GSI Nachr. **91-02**, 6 (1992)

[2] Q. Weitzel et al, *"Development of High-Rate GEM-based TPC for PANDA"*, IEEE NSS-MIC 2006 Conference Record, 1:227-233 (2007)

[3] F. Böhmer et al., *"Space-Charge Effects in an Ungated GEM-based TPC"*, eprint arXiv:1209.0482 (2012)

* Work supported by EU, BMBF, VH-NG-330

† mberger@ph.tum.de

Partial Wave Analysis of the Reaction $\mathrm{p} + \mathrm{p} \rightarrow \mathrm{p} + \mathrm{K}^+ + \Lambda^*$

E. Epple[1] and L. Fabbietti[1] for the HADES Collaboration

[1]Excellence Cluster Universe, Technische Universität München, Boltzmannstr. 2, D-85748, Garching, Germany

The ongoing discussion about anti-kaonic nuclear bound states is still far from being solved. Besides various theoretical models, predicting a range of possible width and masses, the experimental quest for this state has also delivered no clear picture up to now.
The HADES collaboration will search for this state in a measured p+p run at E_{kin} = 3.5 GeV. The predicted bound state would be produced in the following reaction:

$$p + p \rightarrow \bar{K}NN + K^+ \rightarrow p + \Lambda + K^+. \qquad (1)$$

Where $\bar{K}NN$ is the kaonic cluster, which is often also called ppK^-. Thus, we aim to reconstruct this bound state in the final state $p + \Lambda + K^+$. In order to understand, if a new state contributed to the reaction one has to understand how the $p\Lambda K^+$ final state is formed in $p + p$ reactions. In fact, it is well known that these three particles can also be produced via the decay of intermediate N^* resonances:

$$p + p \rightarrow N^* + p \rightarrow K^+ + \Lambda + p. \qquad (2)$$

To describe the measured data with help of a model one needs to know the contributing N^* resonances. Additionally their exact production properties, like angular distributions, have to be as well included correctly. In order to model the transition amplitudes from the $p + p$ initial state to the $pK^+\Lambda$ final state we choose the Bonn-Gatchina Partial Wave Analysis (PWA) [1].

To select a data sample, which contains mostly the final state $pK^+\Lambda$, a kinematic fit was applied to the data. The data were compared to an event hypothesis, which demanded that the three particles fulfill energy and momentum conservation. Additionally, the $p + \pi^-$ from the Λ decay had to have an invariant mass close to the nominal Λ mass of 1115.7 MeV/c^2. A measure for the agreement between the event and the hypothesis is the p-value, which is an output of the fit. The event hypothesis was fulfilled, if the p-value from the kinematic fit did exceed 0.01. In this way 13,000 events have been selected with a contamination by wrong events of $\approx 7\%$. This data set is the input for the PWA.

There are seven resonances listed in the PDG that can be possibly produced in our energy regime and have a known decay branching into $K^+ + \Lambda$. These are $N(1650)$, $N(1710)$, $N(1720)$, $N(1875)$, $N(1880)$, $N(1895)$ and $N(1900)$. Several solutions were tested in the PWA, which include different combinations of N^* resonances and non-resonant production of $pK^+\Lambda$. An example of a good solution is shown in Figures 1 and 2. Here, the invariant mass distribution of ΛK^+ and Λp is displayed. The PWA

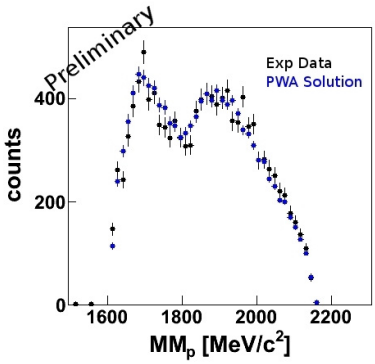

Figure 1: ΛK^+ inv. mass. Data with a PWA solution

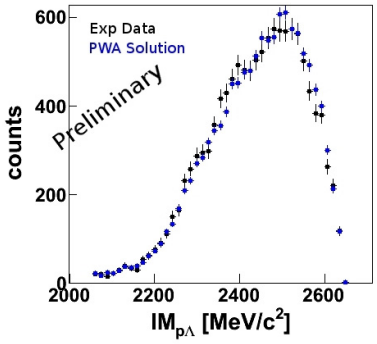

Figure 2: Invariant mass of Λp compared to a PWA solution

solution, that is overlaid to the data inside the acceptance of the HADES spectrometer, contained as input $N(1650)$, $N(1710)$, $N(1720)$, $N(1875)$, $N(1895)$ and several non-resonant waves of $pK^+\Lambda$ production. One can see that this particular solution yields an excellent description of the experimental distribution. The data show no significant yield exceeding the PWA solution. According to these results, the next step of this work is to include the ppK^- wave in the PWA fit and determine an upper limit for the production cross section of a kaonic cluster, produced in $p + p$ collisions at 3.5 GeV kinetic beam energy.

References

[1] A.V. Anisovich, V.V. Anisovich, E. Klempt, V.A. Nikonov and A.V. Sarantsev Eur. Phys. J. A 34, 129152 (2007).

*This research was supported by the DFG cluster of excellence 'Origin and Structure of the Universe'

Status of the pkΛ Analysis in pp Collisions with the FOPI Spectrometer*

R. Münzer[1], *L. Fabbietti*[1], *and M. Berger*[1] *for the FOPI Collaboration*

[1]TU München - Excellence Cluster Universe, 85748 Garching

The investigation of the kaon-nucleon interaction has been intensified in the last years due to new results on Λ(1405) and indications on the existence of the ppK^- bound state [1]. The possible creation of the ppK^- has been investigated with the FOPI spectrometer at GSI in proton-proton-collisions at 3.1 GeV beam kinetic energy. Indeed, according to some theoretical predictions, this reaction should favor the formation of the ppK^-[2].
Additionally to the FOPI spectrometer a silicon detector system placed close to the target has been constructed and employed to improve the vertex determination and used as an on-line trigger for the selection of Λ hyperons. This trigger system allows an enhancement of events containing a Λ-hyperon of a factor 8 [3]. About $70 \cdot 10^6$ events have been collected after the second level trigger selection.

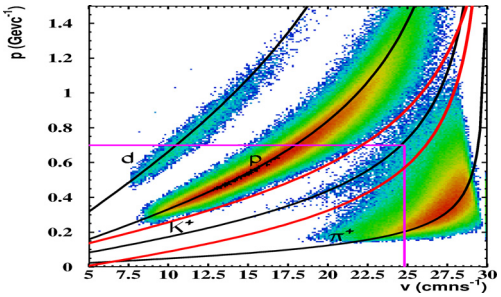

Figure 1: Momentum versus velocity of CDC-RPC tracks (desciption s. text)

These LVL2 events have been analyzed to reconstruct exclusively the final state of $p + K^+ + \Lambda[- > p + \pi^-]$. The selection is divided into two main steps. First events with K^+ candidates are chosen, which were identified by their velocity and momentum information. Figure 1 shows the particle momentum versus flight time. Different particle species, whose nominal $\beta\gamma$-curves are indicated by the black lines, are clearly separable - in case of K^+ up to a momentum of $0.7GeVc^{-1}$ (violett lines). Kaon candidates are selected within the red lines. In the second step events with three positive and one negative charged particles are selected under the condition $|MM(p,p,K^+) - m_{pi^-}| < 0.6GeVc^{-2}$.
From those events the invariant mass of $p - \pi^-$-pair was reconstructed and is shown in the upper plot of figure 2 (black line). The red line indicated the polynomial fit used to describe the background distribution below the Λ-signal. The lower picture shows the background subtracted signal, which includes about 7800 $pK^+\Lambda$ candidates. Since the

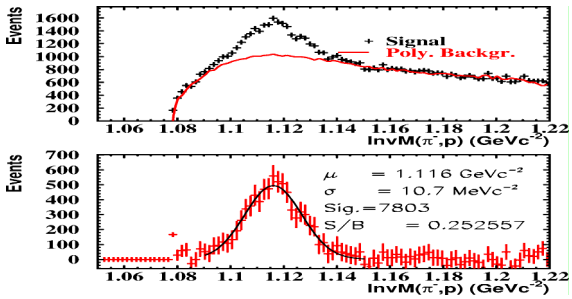

Figure 2: Invriant mass of p and π^- after K^+ and exclusivity selection (desciption s. text)

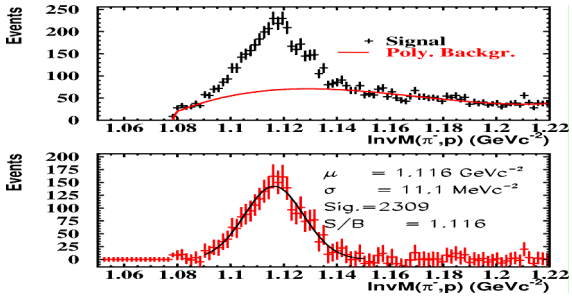

Figure 3: Λ spectrum after cutting on the Confidence Level of the kinematical Refit.

signal to background ratio of 0.25 is still quite low and for a exclusive analysis of the $pK^+\Lambda$ final state a low background contribution is required, it has to be reduced by further cuts. One possible method is the employement of a kinematical refit [4]. This tool iteratively varies the four-momenta of the four particles within their statistical errors in such way, that constraints like energy and momentum conservation are fulfilled. By cutting on the refit quality values like χ^2 and the confidence value, events, which could not fulfill the constraints can by rejected. Figure 3 shows the Λ spectrum after a cut on the refit quality. One can clearly see, the increased signal to background value of 1.116 with a remaining amount of $pK^+\Lambda$ candidates of 2300. A further tuning of the input parameter is still ongoing to increase the total statistics.

References

[1] G. Agakishiev et al.,arXiv:1208.0205

[2] Yamazaki and Akaishi, Phys.Rev.C 76(2007)045201

[3] SiΛViO - A Trigger for Λ-Hyperons - in print

[4] Diploma Thesis Dominik Pleiner `https://www.e12.ph.tum.de/groups/kcluster/Documents/Publications/Thesis_Pleiner.pdf`

* Work supported by VH-NG-330

Measurement of $\Lambda(1405)$ in p+p reactions at 3.5 GeV

J. Siebenson[1], *E. Epple*[1] , *and L. Fabbietti*[1] *for the HADES collaboration*

[1]Excellence Cluster "Universe", TU München, Boltzmannstr. 2, 85748 Garching, Germany

The $\Lambda(1405)$ resonance is known to be an exotic state, which can not be understood as a usual 3-quark baryon. In fact, it turns out that the attraction in the $\bar{K}-N$ channel with isospin I=0 is sufficient strong to generate a bound state below the $\bar{K}N$ threshold. This bound state is commonly identified with the $\Lambda(1405)$. Today, theory uses coupled channel calculations, based on the chiral unitary approach, to generate the $\Lambda(1405)$ dynamically as an interference between a $\bar{K}N$ quasi-bound state and a $\pi\Sigma$ resonance [1]. The properties of the $\Lambda(1405)$, especially its line shape, are therefore sensitive to the low energy $\bar{K}N$ dynamics.

As the data base on $\Lambda(1405)$ is rather scarce, we aimed to measure its properties in $p+p$ reactions at 3.5 GeV kinetic beam energy [2, 3]. In these reactions, the $\Lambda(1405)$ is mainly produced together with a proton and a K^+ ($p+p \rightarrow \Lambda(1405)+p+K^+$). We have performed an exclusive analysis of the charged decay channels ($\Lambda(1405) \rightarrow \Sigma^{\pm}\pi^{\mp}$). After identifying all final state particles, we were able to reconstruct the Σ^+ and the Σ^- hyperons. By selecting these intermediate state particles, we could finally investigate the missing mass to proton and K^+, where the $\Lambda(1405)$ signal appears. Figure 1 shows the obtained distributions for both decay channels. The experimental data (black points) are corrected for acceptance and efficiency. Compared to the data, are simulations of different reaction channels, contributing to the finally observed spectra. The contribution of $\Sigma(1385)^0$ ($p+p \rightarrow \Sigma(1385)^0+p+K^+$) in the violet histograms could not be determined independently in the analysis, as it shows the same decay channels as $\Lambda(1405)$. Its contribution could, however, be fixed by the neutral channel analysis, presented in [4]. The green histograms show the signals due to $\Lambda(1520)$ production ($p+p \rightarrow \Lambda(1520)+p+K^+$), giving rise to signals above 1500 MeV/c^2. The red, phase space like distributions, are attributed to the non-resonant production of $\Sigma\pi$ pairs (see [3] for details). Finally, the black histograms are simulations of $\Lambda(1405)$. The yields of all the simulations have been fixed by a simultaneous fit to different observables. The incoherent sum of the different contributions is shown in the gray histograms.

The most prominent feature of the obtained spectra is that the mass peak of $\Lambda(1405)$ is clearly located below its nominal mass value of 1400 MeV/c^2. Indeed, also the simulations of $\Lambda(1405)$ assume a Breit-Wigner mass of 1385 MeV/c^2 in order to fit the data reasonably. First theoretical interpretations on this observation have been proposed in [5], where a phenomenological approach is used to describe the $\Lambda(1405)$ as a pure $\bar{K}N$ quasi-bound state, with a binding energy of $\approx$ 30 MeV. The predictions from this model are in fairly well agreement with the measured mass spectra of Figure 1.

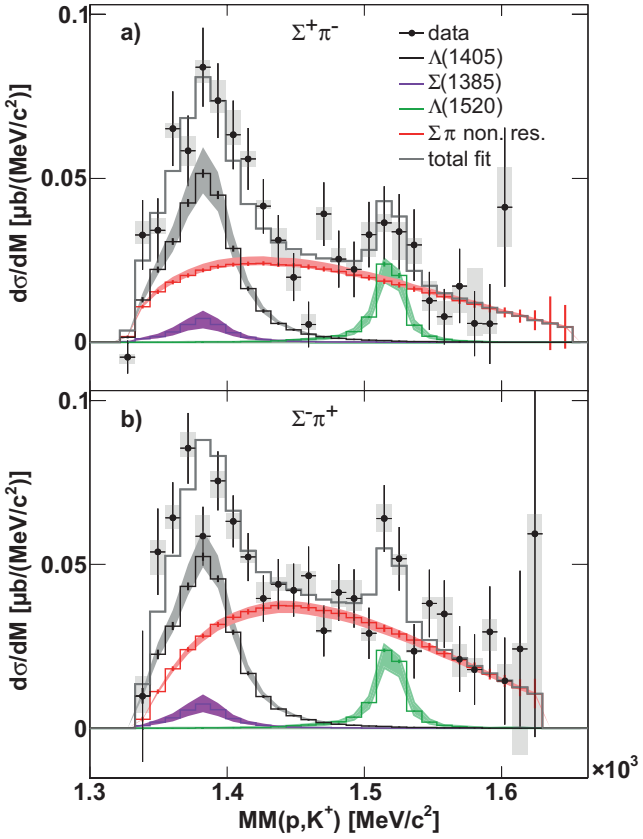

Figure 1: Missing mass to proton and K^+ for the two different decay channels of $\Lambda(1405)$. The histograms show the different contributions to the experimental data. The shaded bands and boxes indicate the extracted systematic errors on the experimental data and on the simulations.

The observed line shape of $\Lambda(1405)$ with its shift below 1400 MeV/c^2 has the potential to reveal further insight into the low energy $\bar{K}N$ dynamics. Therefore, the development of adequate theory models, which are able to handle the complex $p+p$ reaction mechanisms, is requested.

References

[1] T. Hyodo et al., Phys.Rev. C **77**, 035204 (2008).

[2] G. Agakishiev et al., arXiv:1208.0205, (2012).

[3] G. Agakishiev et al., Nucl.Phys. A **881**, 178-186 (2012).

[4] G. Agakishiev et al., arxiv:1202.0232 (2012).

[5] M. Hassanvand et al., arxiv:1210.7725 (2012).

Flex-PCB Pitch-Adapters for Silicon Micro-Strip Detectors*

R. Schnell†[1], *K.-Th. Brinkmann*[1], *and S. Krah*[2]

[1]II. Physikalisches Institut, Justus-Liebig-Universität Gießen, Heinrich-Buff-Ring 16, 35392 Gießen, Germany;
[2]Helmholtz-Institut für Strahlen- und Kernphysik, Universität Bonn, Nussallee 14-16, 53115 Bonn, Germany

Introduction

Silicon micro-strip sensors for tracking detectors with high spacial resolution feature a vast number of channels. A single detector can have up to one thousand channels per side to be read out. With a strip pitch in the order of tens of micrometers, a high interconnection density between the detector and the front-end chip is required. In most cases the read-out pitch of the sensor and the input pitch of the front-end chip do not match. Thus, an interconnection device between sensor and front-end is required to adapt for this. These pitch-adapters are often made by thin film technology on a glass or ceramic substrate. This report demonstrates the effort to use advanced flex-PCB technology as pitch-adapter. This development was carried out for the Micro-Vertex-Detector (MVD) of $\overline{\mathrm{P}}$ANDA [1].

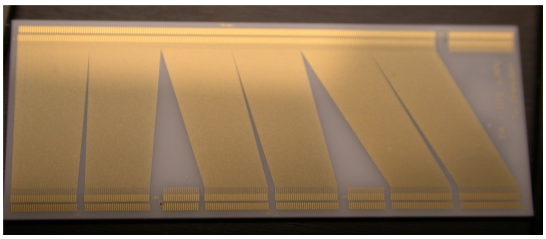

Figure 1: Photograph of the pitch-adapter design based on thin film technology [2].

Pitch-Adapter Design

Prototyping for silicon strip sensors was done with a pitch-adapter made by thin film technology with a wire structure of 2.0 µm thickness made from TiW with gold plating for wire bonding. The pitch is 44.0 µm on the front-end input side and 50.0 µm on the sensor side using two staggered rows of bond pads. A change of the sensor or the front-end would need a redesign with a new set of production masks. Therefore, the possibility to reach the same interconnection density employing standard PCB-technology was explored. In order to reach this aim, a two-layer design of flex-PCB was chosen. This was necessary since the trace width of 35 µm is larger than using thin film technology. The traces on the bottom layer are connected to the top bonding pads using laser-drilled microvias of 50 µm diameter [3].
The production with standard industrial methods will allow the pitch-adapter to be seamlessly integrated into the front-end hybrid circuit. In addition, the flexible material permits the realization of detector geometries not possible using rigid hybrid carriers.

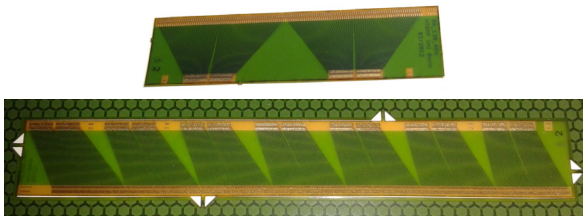

Figure 2: Photographs of two out of ten designs of flex-PCB pitch-adapters. Top: Design for two front-ends and 130 µm sensor strip pitch. Bottom: Design for seven front-ends and 65 µm sensor strip pitch.

Results

A double-sided prototype module based on $\overline{\mathrm{P}}$ANDA geometry sensors and flex-PCB pitch-adapters was produced and employed in a CERN test-beam. No changes in performance compared to thin film technology pitch-adapters were observed.
An electrical characterization measurement using an LCR-meter was performed to investigate the influence of the additional capacitance and resistivity introduced by the pitch-adapter. The results indicate an additional crosstalk up to 2% and an increase in noise of less than 0.5% [4]. Advantages in terms of material budget arise from the small thickness and the material composition of flex-PCB. The radiation length of polyimide is 28.6 cm compared to 7.4 cm for aluminum oxide [5]. Therefore, a pitch-adapter based on thin film technology made from aluminum oxide with a thickness of 0.38 mm yields 0.51 % of one radiation length. Whereas a pitch-adapter based on polyimide films with a total thickness of 50 µm (25 µm for core layer and coverlay respectively) exhibits 0.017 % of one radiation length.

References

[1] $\overline{\mathrm{P}}$ANDA Collaboration, arXiv:1207.6581v2 [physics.ins-det], November 2011

[2] RHe Microsystems GmbH

[3] GS Swiss PCB AG

[4] S. Krah: “Entwicklung von Testsystemen zur Charakterisierung von Silizium-Streifen-Detektoren”, Diploma Thesis, Bonn, November 2012

[5] PDG, Atomic and Nuclear Properties of Materials

* Work supported by BMBF [05P09RGFP6] and HIC4Fair.
† Robert.Schnell@exp2.physik.uni-giessen.de

Laval Nozzle Production for Internal Targets*

E. Köhler†[1], *D. Bonaventura*[1], *S. Grieser*[1], *A.-K. Hergemöller*[1], *H.-W. Ortjohann*[1], *A. Täschner*[1], *and A. Khoukaz*[1]

[1]Institut für Kernphysik, Westfälische Wilhelms-Universität Münster, Germany

A powerful type of target for internal fixed target experiments at storage rings is given by the cluster-jet target which allows for typical target thicknesses of 10^{12} to $10^{15}\,\mathrm{atoms/cm^2}$. Furthermore, this type of target provides a stream of particles which is homogeneous and constant in space and time. At the University of Münster several cluster-jet targets were already designed and constructed, e.g., for COSY-11, ANKE, and $\overline{\mathrm{P}}$ANDA, where the latter one is currently under construction. The target density can be easily adjusted by changing the temperature or pressure of the gaseous target material (e.g., hydrogen, deuterium) before the so-called Laval nozzle, the heart of a cluster source. The specific convergent-divergent shape of the Laval nozzle generates a supersonic flow of the target material. Supported by the adiabatic cooling the, e.g., hydrogen, molecules condensate to clusters (see Figure 1). The mean velocity and the velocity distribution of the extracted and shaped cluster-jet beams are strongly dependent on the operational parameters. In recent measurements mean velocities of 200 to 1000 m/s were observed when a $28\,\mu\mathrm{m}$ Laval nozzle was operated with hydrogen at 17 bar and a temperature between 20 and 50 K [1, 2]. This velocities could be described by numerical calculations [3]. Essential

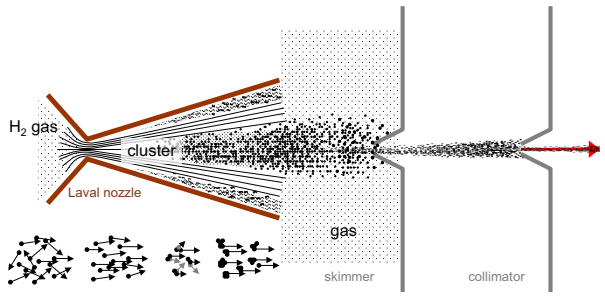

Figure 1: Cluster production process with a Laval nozzle. Skimmer and collimator are responsible for extracting and beam shaping [4].

for the performance of a cluster-jet target are the properties of the Laval nozzle which itself can be divided into an inlet and an outlet zone (see Figure 1). The short inlet zone converges to the narrowest point of the nozzle and merges into the divergent, long outlet zone. The production of a small inner diameter (e.g., $30\,\mu\mathrm{m}$) in combination with the long trumpet part with an opening angle of, e.g., $7\,^\circ$, represents a major technical challenge. In the past these fine Laval nozzles were produced at CERN but the manufacture was discontinued [5]. To ensure the production of these fine Laval nozzles for future internal targets and for further target optimisation studies an improved production process

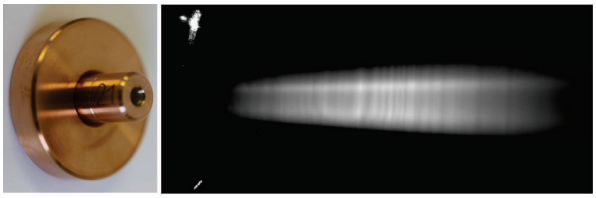

Figure 2: Left: Finished Laval nozzle of the first successfully produced set, Right: First cluster-jet beam of a new Laval nozzle (beam direction from left to right) installed at the $\overline{\mathrm{P}}$ANDA cluster-jet target prototype.

based on the initial CERN production was recently developed at the University of Münster. Due to several optimised production steps a minimal failure rate of the particularly fine Laval nozzles is ensured.

A first set of Laval nozzles was successfully produced and initial measurements with these new nozzles (see Figure 2 left) are running at the $\overline{\mathrm{P}}$ANDA cluster-jet target prototype. Figure 2 (right) presents the first cluster-jet beam of a new nozzle with the characteristic high intense core beam structures [6]. The part of the cluster beam directly after the Laval nozzle (left, not visible) is illuminated with a laser diode. The possibility to produce new micrometer nozzles opens the way for future investigations on the cluster production process with the modification of, e.g., length and aperture angle of the trumpet, with the objective to further optimise cluster-jet targets for storage rings.

References

[1] E. Köhler, Das Münsteraner Cluster-Jet Target MCT2, ein Prototyp für das $\overline{\mathrm{P}}$ANDA-Experiment, & die Analyse der Eigenschaften des Clusterstrahls, Diploma Thesis, University of Münster, 2010

[2] A. Täschner et al., Nucl. Instr. and Meth. A 660 (2011) 22-30, doi:10.1016/j.nima.2011.09.024

[3] A. Täschner, Entwicklung und Untersuchung von Cluster-Jet-Targets höchster Dichte, PhD Thesis, University of Münster, 2013

[4] A.-K. Hergemöller, Preparation of cluster beams and the construction of the final cluster source for the $\overline{\mathrm{P}}$ANDA experiment, Master Thesis, University of Münster, (in preparation) 2013

[5] R. Kopp, N. Mézin, Technical Note EST-MF 96-05, CERN, 1996

[6] E. Köhler, High Intense Hydrogen Cluster-Jet Beams for $\overline{\mathrm{P}}$ANDA, Annual Report GSI, 2011

* Work supported by EU (FP7), BMBF, and GSI.

† e_koeh02@uni-muenster.de

Cluster-Jet Beam Visualisation with Micro Channel Plates*

E. Köhler†[1], *D. Bonaventura*[1], *S. Grieser*[1], *A.-K. Hergemöller*[1], *H.-W. Ortjohann*[1], *A. Täschner*[1], *A. Zannotti*[1], *and A. Khoukaz*[1]

[1]Institut für Kernphysik, Westfälische Wilhelms-Universität Münster, Germany

A cluster-jet target will be the first installed internal target for the PANDA-Experiment at HESR/FAIR. To investigate the performance and characteristics of the future cluster-jet installation, a target station prototype in complete PANDA geometry was built up at the University of Münster. The target prototype is routinely operated with hydrogen and achieves target densities of more than $2 \times 10^{15}\,\mathrm{atoms/cm^2}$ at a distance of $2.1\,\mathrm{m}$ behind the nozzle. The target density is reproducible, constant in time, and can be varied over several orders of magnitude with the change of the temperature and pressure before the Laval nozzle [1]. Beside the absolute target density also the reduction of the residual gas background at the interaction point is of highest importance. For this purpose special sized orifices (collimators) are placed close to the nozzle, which define the cluster-jet beam size and shape at the interaction point [2]. The size and shape of the cluster beam can be visualised with a newly developed Micro Channel Plate detector system mounted inside the vacuum at the end of the target beam dump. This MCP system allows for a direct observation of an ionised cluster-jet beam [3]. It consists of an electrically grounded entrance grid

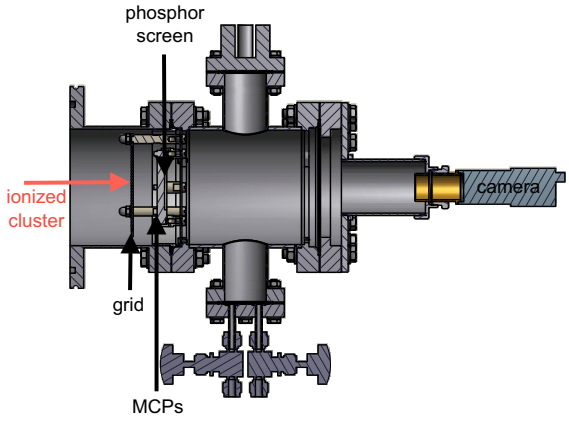

Figure 1: Sectional CAD view of the MCP detector system.

with $2.5\,\mathrm{mm}$ lattice spacing, two MCPs in chevron assembly with an effective diameter of $40\,\mathrm{mm}$ and a phosphor screen combined with a CCD camera (see Figure 1). The clusters in the cluster-jet beam are ionised by an electron beam close to the nozzle and the MCP signals, originating from positively charged clusters, can be observed directly (see MCP images: Figure 2, right). The clearly visible grid structure offers the possibility to estimate the cluster beam size at this position and the image intensity corresponds to the relative cluster beam density distribution. This system

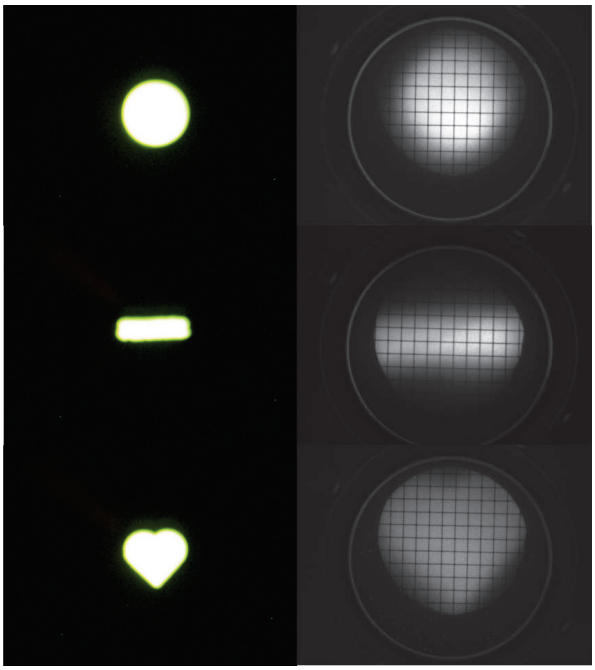

Figure 2: Microscopic view of collimators (left) with round ($\varnothing \approx 0.5\,\mathrm{mm}$), slit ($0.77 \times 0.19\,\mathrm{mm^2}$) and heart (max. width $\approx 0.76\,\mathrm{mm}$) shaped orifice and resulting MCP images (right) of the cluster-jet beam at a distance of approximately $4\,\mathrm{m}$ behind the nozzle.

opens a complete new opportunity to run target beam adjustment checks during target operation. In addition, with this device the visualisation of the interaction region between a cluster beam and an accelerator beam, was successfully demonstrated at ANKE/COSY allowing for new diagnostic tools for vertex point studies. These experimental results are presented in [4] in more detail.

References

[1] A. Täschner et al., Nucl. Instr. and Meth. A 660 (2011) 22-30, doi:10.1016/j.nima.2011.09.024

[2] A.-K. Hergemöller, Preparation of cluster beams and the construction of the final cluster source for the PANDA experiment, Master Thesis, University of Münster, (in preparation) 2013

[3] A. Zannotti, Implementation and test of fundamental production, adjustment, and detection components of PANDA cluster-jet target, Bachelor Thesis, University of Münster, 2012

[4] E. Köhler, Cluster Target Vertex Zone Visualisation at Storage Rings with MCPs, Annual Report GSI, 2012

* Work supported by EU (FP7), BMBF, and GSI.

† e_koeh02@uni-muenster.de

Cluster Target Vertex Zone Visualisation at Storage Rings with MCPs*

E. Köhler[†1], *D. Bonaventura*[1], *S. Grieser*[1], *A.-K. Hergemöller*[1], *H.-W. Ortjohann*[1], *A. Täschner*[1], *A. Zannotti*[1], *and A. Khoukaz*[1]

[1]Institut für Kernphysik, Westfälische Wilhelms-Universität Münster, Germany

For the future $\overline{\text{P}}$ANDA experiment at FAIR a novel technique to visualise the interaction zone of the cluster-jet target beam and the antiproton beam has been developed. For this purpose in recent tests at the COSY accelerator at FZ Jülich the interaction region of the passing COSY beam through the internal ANKE cluster-jet target was observed for the first time by using a Micro Channel Plate detection system. Initially the detector system was designed and constructed to run adjustment checks and to monitor the $\overline{\text{P}}$ANDA cluster-jet target during operation [1]. However, the installation at the end of the ANKE beam dump demonstrated a completely new possibility to visualise and monitor the interaction region of beam and target at internal target experiments. The passage of the COSY beam through the cluster-jet target ionises the uncharged clusters, which are detected with the MCPs (see Figure 1).

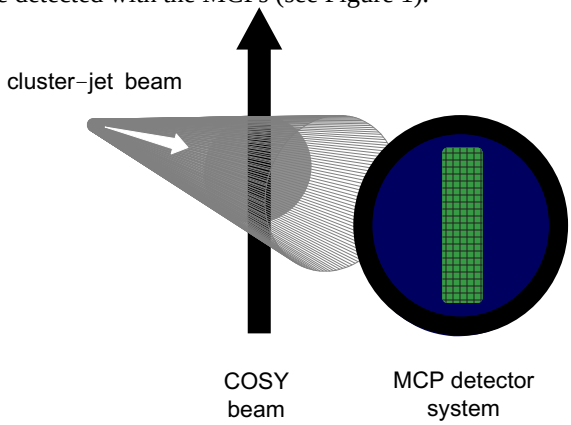

Figure 1: Schematical drawing of the passing COSY beam through the cluster-jet target. The thereby ionised clusters are subsequently detected with the MCPs.

A direct observation of the ionised cluster-jet beam is presented in the following Figures. The abscissa represents the horizontal spatial direction and the ordinate the COSY beam direction. Figure 2 depicts the projection of the interaction zone at COSY beam injection energies and Figure 3 the interaction zone after acceleration, where the influence of the adiabatic cooling is clearly visible (reduced phase space). The shift of the interaction zone induced by switching on a steerer magnet is shown in Figure 4. This new diagnostic tool is particularly suited for quantitative vertex point investigations at internal target experiments.

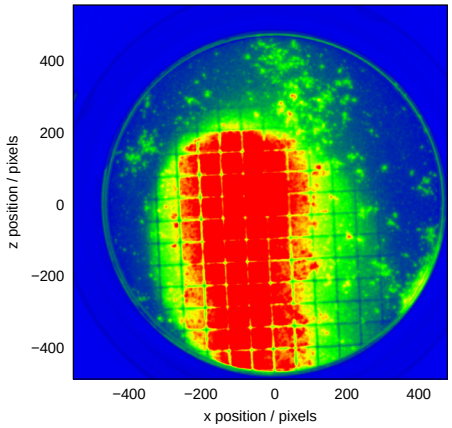

Figure 2: Interaction region at COSY beam injection energies.

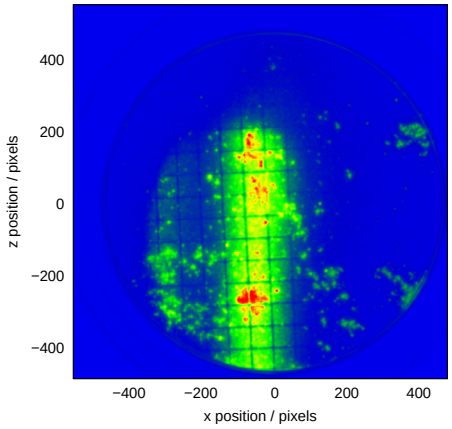

Figure 3: Interaction region after COSY beam acceleration.

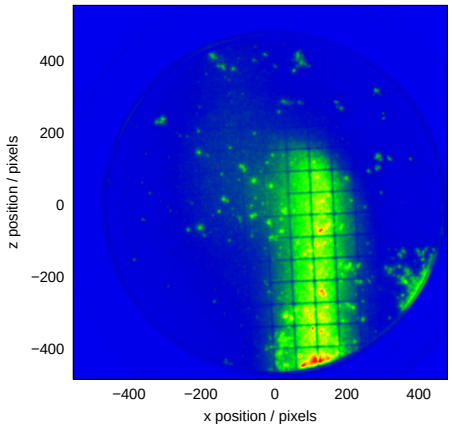

Figure 4: Shift of the interaction region caused by an active steerer magnet.

References

[1] E. Köhler, Cluster-Jet Beam Visualisation with Micro Channel Plates, Annual Report GSI, 2012

* Work supported by EU (FP7), BMBF, and GSI.

† e_koeh02@uni-muenster.de

Significantly improved lifetime of Microchannel Plate PMTs*

A. Britting[1], *W. Eyrich*[1], *A. Lehmann*[†1], *F. Uhlig*[1], *and PANDA Cherenkov group*

[1]Physikalisches Institut IV, Universität Erlangen-Nürnberg, Erwin-Rommel-Str. 1, D-91058 Erlangen

The main particle identification devices of the PANDA experiment will be two DIRCs placed around (barrel) and downstream (disc) of the target. The preferred photon sensor option are microchannel plate (MCP) PMTs because they can be operated inside the 2 Tesla magnetic field of the solenoid. Furthermore, these multi-anode sensors are rather compact and show a superior time resolution which is typically <50 ps.

Until recently the major drawbacks of MCP-PMTs were serious shortcomings with their rate capability and in particular with aging effects. The main cause of aging are rest-gas ions in the tube being accelerated towards the photo cathode (PC), whose surface gets damaged by their impact and the quantum efficiency (QE) suffers. Although the rate capability issue was resolved already a few years ago, the aging remained a serious problem [1, 2].

In the latest generation of MCP-PMTs important counter measures were taken to seriously tackle the aging problem. These include a higher vacuum inside the tube and electron scrubbing of the MCP surfaces (PHOTONIS, BINP), an Al_2O_3 protection layer between the 2 MCPs (Hamamatsu R10754X), an ALD coating of the whole MCP capillaries to prevent outgassing of the glass substrate (PHOTONIS XP85112), and even a modified photo cathode (BINP). For further details see Ref. [3].

At the design luminosity of PANDA the anticipated photon rates at the DIRC focal planes range from a few hundred kHz for the barrel DIRC to several MHz at the disc DIRC. Integrated over the envisaged 10 years operation period of the PANDA experiment these rates accumulate to anode charges of ≈5 C/cm^2 for the barrel DIRC and even more for the disc DIRC. Since about 18 months we are simultaneously and permanently illuminating the most recent MCP-PMTs to study their aging. The single photon rate at the PCs is chosen to be comparable to that expected in the PANDA environment. The accumulated anode charge is determined by a permanent monitoring of the pulse heights. Every few days a wavelength scan of the QE is done for all illuminated MCP-PMTs. In addition, every few months a QE scan as a function of the PC surface is performed to identify critical regions where the QE may start to drop.

Currently, >4 C/cm^2 of integrated anode charge are accumulated. In Fig. 1 the behaviour of the quantum efficiency at a wavelength of 400 nm is compared for several MCP-PMTs. While the QE of the older models (open dots) dropped to 5% after typically <300 mC/cm^2 the results for the most recent models (solid dots) is very different. In particular, the ALD coated PHOTONIS XP85112 shows no obvious QE loss even at 4 C/cm^2 which corresponds to 8 years operation of the PANDA barrel DIRC.

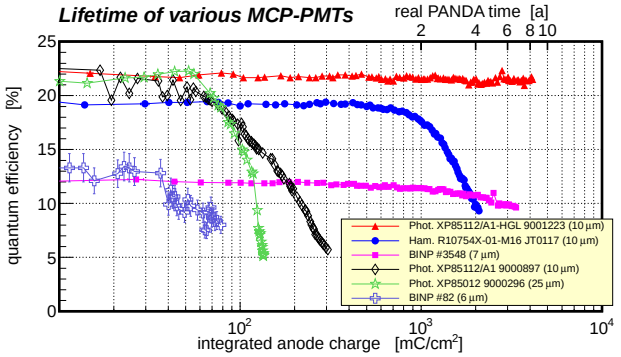

Figure 1: QE at 400 nm for old (open) and new generation (solid dots) MCP-PMTs as a function of the anode charge.

In Fig. 2 the QE is shown as a function of the PC surface. While the QE of all tubes was rather uniform across the PC at the beginning, it starts dropping from the corners and the rim of the PC after a long-term illumination. The figures show that after an integrated anode charge of ≈1.8 C/cm^2 for the Hamamatsu and of ≈3.4 C/cm^2 for the BINP MCP-PMT the PCs show clear signs of aging. The PHOTONIS XP85112 does not yet show such effects after >4 C/cm^2.

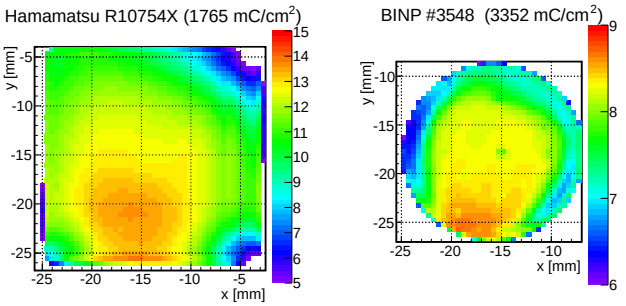

Figure 2: QE across the PC at 372 nm after long-term illumination. The plots scale with the actual dimensions of the PCs (22x22 mm^2 for R10754X [left] and 18 mm diameter for BINP #3548 [right]; the PHOTONIS XP85112 [not shown] has a much larger PC: 51x51 mm^2).

References

[1] A. Lehmann et al., GSI Scientific Report 2009, p. 7.

[2] A. Lehmann et al., GSI Scientific Report 2010, p. 106.

[3] A. Lehmann et al., Nucl. Instr. and Meth. A (2012), http://dx.doi.org/10.1016/j.nima.2012.11.109

* Work supported by BMBF and GSI

† lehmann@physik.uni-erlangen.de

Study of PANDA Barrel DIRC design options*

K. Götzen[1], *G. Kalicy*[1,2], *M. Patsyuk*[†1,2], *K. Peters*[1,2], *C. Schwarz*[1], *J. Schwiening*[1], *and M. Zühlsdorf*[‡1,2]

[1]GSI, Darmstadt, Germany; [2]Goethe Universität Frankfurt, Germany

A detector based on the DIRC (Detection of Internally Reflected Cherenkov light) principle [1] will be used in the target spectrometer of the PANDA experiment to distinguish between charged pions and kaons for momenta between 0.5 and 3.5 GeV/c. The design of the PANDA Barrel DIRC is based on the *BABAR* DIRC [2] (the first successful DIRC counter) with some important improvements, such as fast photon timing, focusing optics, and a compact expansion volume.

In the PANDA Barrel DIRC baseline design the barrel of 47.6 cm comprises 16 sections with 5 fused silica radiator bars (1.7 cm x 3.2 cm x 250 cm) each. Cherenkov photons, produced along the charged particle track in the bar, are guided inside the radiator via total internal reflection. A mirror is attached to the forward end of the bar to reflect photons towards the read out end, where they are focused with a lens and projected onto a flat photo detector plane behind the 30 cm-deep oil-filled expansion volume. An array of Micro-Channel Plate Photomultiplier Tubes (MCP-PMTs) is used to detect the photons and measure their arrival time with a precision of about 100 ps.

In order to meet the PANDA resolution requirement and reduce the detector cost, the influence of different parameters and geometry options on the detector performance are being studied. One of the design elements that influence the operation and performance of the detector is the material and shape of the expansion volume. A compact fused silica prism can be used as a photon camera in front of each bar box instead of the single volume filled with mineral oil. This option reduces the number of required pixels. Moreover, the prism has much better optical properties, which improves the photon yield. The thickness of the bars defines the number of Cherenkov photons produced per track and the amount of the material in front of the calorimeter, whereas the width influences the detector cost. The use of one wide plate per bar box significantly reduces the total detector production cost in comparison to the baseline design with 5 narrow bars in each bar box, as there are less pieces to be polished. Another important element is the focusing system. It can be a lens attached to the read out end or a focusing mirror on the forward end of the bar.

The detailed simulation of the baseline design and many design options, including different focusing systems, shapes of the expansion volume and bar dimensions, is implemented using Geant [4]. A design using wide plates and fused silica prisms is shown on the Fig. 1. A fast reconstruction method, similar to the approach used for the *BABAR*-DIRC, is utilized to evaluate the performance of each design. The single photon Cherenkov angle resolution and photon yield are determined for a wide range of particle angles using several simplified designs without focusing optics. The results are consistent with expectations and demonstrate that a focusing system is required to achieve the DIRC performance goals for PANDA. The evaluation of more advanced designs, both in simulation and detector prototypes, is currently ongoing.

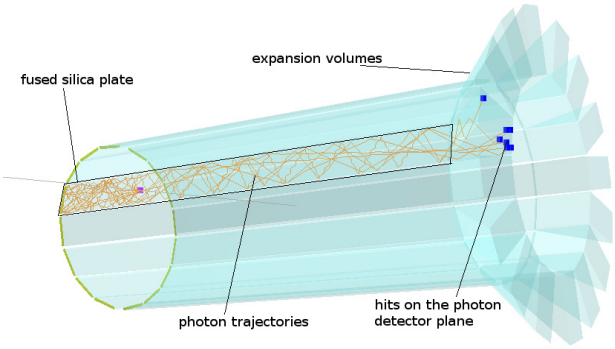

Figure 1: Geant-based simulation of the PANDA Barrel DIRC using radiator plates and compact expansion volumes.

References

[1] B. N. Ratcliff, SLAC-PUB-5946 (1992), SLAC-PUB-6047 (1993); P. Coyle et al., Nucl. Instr. and Meth. Phys. Res. Sect. A 343 (1994) 292.

[2] I. Adam et al., Nucl. Instr. and Meth. Phys. Res. Sect. A 538 (2005) 281.

[3] J. Schwiening, Nucl. Instr. and Meth. Phys. Res. Sect. A 639 (2011) 315.

[4] S. Agostinelly et al., Nucl. Instr. and Meth. Phys. Res. Sect. A 506 (2003) 250; J. Allison et al., Nuclear Science, IEEE Transactions **53** (2006) 270-278; S. Spataro, J. Phys. Conf. Ser. **119** (2008) 032035; M. Al-Turany and F. Uhlig, Proceedings of Science (ACAT08) 048.

*Work supported by HGS-HIRe, HIC for FAIR, EU FP6 grant #515873, and EU FP7 grant #227431.

† M.Patsyuk@gsi.de

‡ M.Zuehlsdorf@gsi.de

Test of a PANDA Barrel DIRC Prototype in a Particle Beam at CERN*

A. Gerhardt[1], *K. Götzen*[1], *G. Kalicy*[†1,2], *D. Lehmann*[1], *M. Patsyuk*[1,2], *K. Peters*[1,2], *G. Schepers*[1], *C. Schwarz*[1], *J. Schwiening*[1], *and M. Zühlsdorf*[1,2]

[1]GSI, Darmstadt, Germany; [2]Goethe Universität Frankfurt, Germany

Particle identification (PID) will play a crucial role in reaching the physics goals of the PANDA experiment at FAIR. The charged PID in the barrel region of the target spectrometer (polar angles between 22° and 140°) needs a thin detector operating in a 1 T magnetic field, capable of pion-kaon separation with more than three standard deviations for momenta between 0.5 and 3.5 GeV/c. A Ring Imaging Cherenkov detector using the DIRC (Detection of Internally Reflected Cherenkov light) principle is an excellent candidate to match to those requirements.

The PANDA Barrel DIRC design [1] is based on the successful *BABAR* DIRC [2] detector with several important improvements, such as focusing optics, fast timing, and a compact expansion region. Several key aspects of the current design were implemented in a prototype and tested in the summer of 2012 in a hadronic particle beam at CERN.

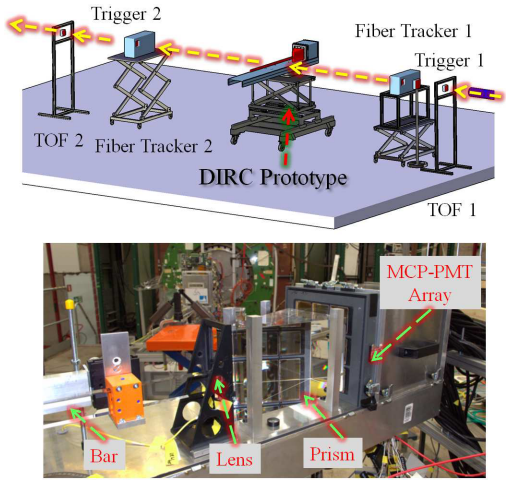

Figure 1: Schematic (top) and photo of the prototype setup.

A schematic of the setup and a photo of the prototype components are shown in Figure 1. Most of the measurements were performed with a synthetic fused silica bar ($17 \times 35 \times 1225$ mm^3) with a focusing lens attached to one end and a mirror attached to the other end, placed into a light-tight container. A large synthetic fused silica prism with a depth of 30 cm, located about 2 mm from the lens, served as expansion volume. An array of 9 Photonis XP85112 Micro-Channel Plate Photomultiplier Tubes (MCP-PMTs) was coupled with optical grease to the back surface of the prism. The data acquisition[1] for 896 detector channels was performed using the HADES trigger and readout board (TRB) [3] with the TOF add-on, combining the NINO chip and CERN HPTDC to provide timing with a resolution of 98 ps per count and pulse height information from charge-to-width.

The setup was placed into the mixed hadron beam at the T9 area of the CERN PS with momenta adjustable between 1.5 and 10 GeV/c. The trigger was provided by two scintillator counters. Two tracking stations using scintillating fibers measured the beam direction. A time-of-flight system provided pion/proton tagging up to 6 GeV/c momentum. A total of about 220M triggers were recorded in several configurations. Spherical and cylindrical focusing lenses with and without anti-reflective coating were tested in combination with bars produced from different manufacturers, including a bar made of acryllic glass and a 17 cm-wide radiator plate made from synthetic fused silica as a possible alternative to the narrow bar geometry. The polar angle between the particle beam and the bar was varied between 20° and 156° and the interception point between beam and bar was adjusted by some 80 cm along the long bar axis. Figure 2 shows the distribution of hits per MCP-PMT pixel for a 124° polar angle. The overlapping ring segments, corresponding to reflections from the top and bottom surfaces of the prism, are consistent with the expected Cherenkov ring image for 10 GeV/c pions, calculated from simulation (shown as points). Detailed analysis of the data set, including the determination of the Cherenkov angle resolution for each prototype and beam configuration, is ongoing.

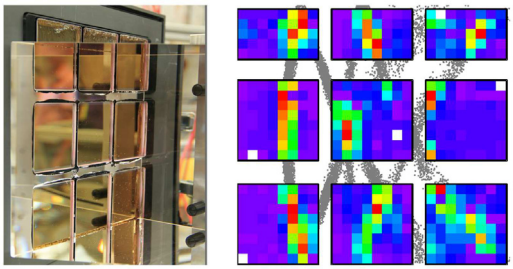

Figure 2: Photo of the prism and MCP-PMT array (left) and example of the observed Cherenkov hit pattern (right).

References

[1] J. Schwiening et al., Nucl. Instr. and Meth. Phys. Res. Sect. A 639 (2011) 315.

[2] I. Adam et al., Nucl. Instr. and Meth. Phys. Res. Sect. A 538 (2005) 281.

[3] I. Fröhlich, et al., IEEE Trans. Nucl. Sci. 55 59 (2008).

*Work supported by HGS-HIRe, HIC for FAIR, EU FP6 grant #515873, and EU FP7 grant #227431.

† G.Kalicy@gsi.de

[1]We would like to thank J .Michel, M. Palka, and M. Traxler for their help with the data acquisition system.

A new approach to chiral two-nucleon dynamics

A. M. Gasparyan[1,2]*, M.F.M. Lutz*[3]*, and E. Epelbaum*[1]
[1]Ruhr-Universität Bochum, Germany; [2]ITEP, Moscow, Russia; [3]GSI, Darmstadt, Germany

Chiral perturbation theory is a powerful tool for studying low-energy hadron dynamics. It is quite successful, for instance, in describing the $\pi\pi$ and πN scattering processes in the threshold region. On the other hand in the nucleon-nucleon sector a strictly perturbative treatment is impossible even close to threshold. Large S-wave scattering lengths and the deuteron bound state are obvious manifestations of this fact. One of the solutions of this problem within ChPT based on the ideas of Weinberg [1] is to implement a potential approach. In such a scheme, the scattering amplitude is generated by solving a dynamical equation in a non-perturbative manner with a potential calculated from the chiral Lagrangian [2].

We suggest an alternative approach [3] based on analytic properties of the scattering amplitude and the assumption that the interaction turns perturbative in some energy region below the two-nucleon threshold. The starting point of our approach is the nucleon-nucleon scattering amplitude calculated from the relativistic chiral Lagrangian using perturbation theory. We follow here the regular dimensional power counting that leads to the contributions up to the chiral order Q^3 as shown in Fig. 1.

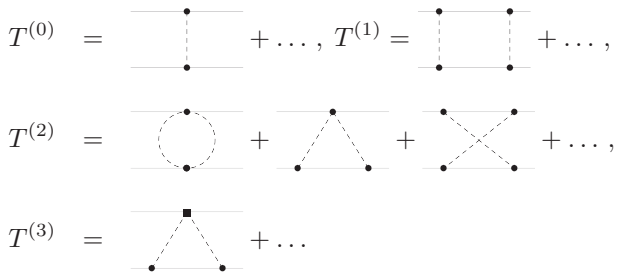

Figure 1: Feynman diagrams contributing to the NN scattering amplitude $T^{(i)}$ at order Q^i in the chiral expansion. While solid dots denote the lowest-order vertices from the chiral Lagrangian, the filled squares refer to subleading vertices. The ellipses denote diagrams leading to shorter-range contributions.

The next step consists in the analytic continuation of the subthreshold and perturbative partial-wave amplitudes into the physical and non-perturbative region taking into account the singularity structure of the amplitude in the complex s-plane. The partial-wave dispersion relation separates right- and left-hand singularities of the amplitude and reads

$$T(s) = U(s) + \int_{4m_N^2}^{\infty} \frac{ds'}{\pi} \frac{s-\mu_M^2}{s'-\mu_M^2} \frac{T(s)\,\rho(s')\,T^*(s')}{s'-s-i\epsilon}\,, \qquad (1)$$

where μ_M is the matching point where perturbation theory is assumed to converge most rapidly. The generalized potential $U(s)$ possesses only left-hand cuts and is calculated from the chiral Lagrangian using conformal expansion techniques [4]. Finally, one restores the amplitude above threshold by solving Eq. (1) with $U(s)$ as an input.

The free parameters, which are related to the low-energy constants of the chiral Lagrangian, were adjusted to the empirical nucleon-nucleon phase shifts. The obtained fits are in a reasonable agreement with the data. As an example the results for the coupled partial waves, where at oder Q^3 there are only four unknown counter terms available for the fit, are shown in Fig. 2. Similar results are available for the uncoupled partial waves. The quality of the fit at order

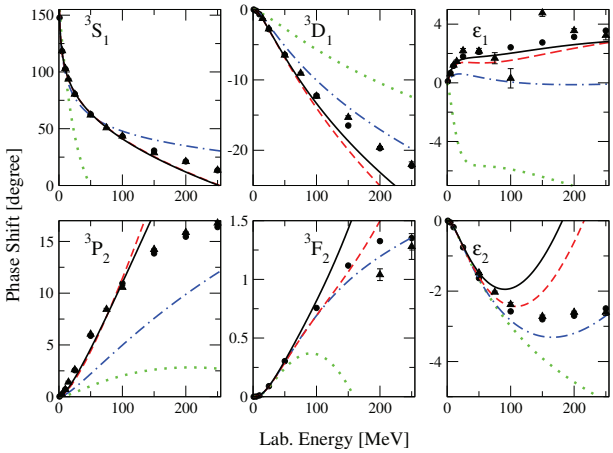

Figure 2: Phase shifts and mixing angles in the coupled $^3S_1$-$^3D_1$ and $^3P_2$-$^3F_2$ channels calculated at orders Q^0 (dotted lines), Q^1 (dash-dotted lines), Q^2 (dashed lines) and Q^3 (solid lines).

Q^3 is comparable with the one obtained in conventional approaches based on the chiral expansion of the NN potential. In all partial waves, the expansion for the phase shifts converges when going from the order Q^0 to Q^3. This supports our assumption of the validity of a perturbative expansion of the NN scattering amplitude in the subthreshold region.

References

[1] S. Weinberg, Phys. Lett. B **251**, 288 (1990).

[2] E. Epelbaum, W. Glockle and U. -G. Meißner, Nucl. Phys. A **747**, 362 (2005) [nucl-th/0405048].

[3] A. M. Gasparyan, M. F. M. Lutz and E. Epelbaum, arXiv:1212.3057 [nucl-th].

[4] A. Gasparyan and M. F. M. Lutz, Nucl. Phys. A **848**, 126 (2010) [arXiv:1003.3426 [hep-ph]].

Chiral extrapolations of baryon masses

M.F.M. Lutz and A. Semke, GSI, Darmstadt, Germany

We consider the chiral extrapolation of the baryon masses to unphysical quark masses assuming exact isospin symmetry. The dependence on the light quark masses may be traded against a dependence on the pion and kaon masses, where we assume a quark-mass dependence of the meson masses as predicted by χPT at the next-to-leading order with parameters as recalled in [2]. The 'physical' strange quark mass is determined such that at the physical pion mass the empirical kaon mass is reproduced. The baryon masses are computed at N^{3}LO where we use physical baryon and meson masses in the one-loop contributions to the baryon self energies and assume systematically large-N_c sum rules for the parameter set. Our approach is detailed in [1, 2]. Initially we adjusted the parameter set to the physical masses of the baryon octet and decuplet states and to the results for the pion-mass dependence of the nucleon and omega masses as predicted by the BMW group [2]. That initial parameter set was further slightly adjusted in [3] to achieve consistency with recent lattice results of the LHPC and PACS-CS groups. Insisting on a simultaneous description of the BMW and PACS-CS data we unambiguously recover the unfitted results of the HSC and QCDSF-UKQCD groups with an amazing accuracy [4]. We also explored the role of the axial coupling constants F and D, which we found to be accurately determined from a simultaneous fit of the lattice data [4]. In Fig. 1 we show the baryon masses for our favored parameter set as a function of the linear pion mass [3]. It is a striking phenomena that for pion masses larger than 300 MeV there appears to be an approximate linear dependence for all baryon masses. Note however, that given our approach the linear dependence is significantly and systematically altered at smaller pion masses. Our results are confronted against the lattice data from the HSC groups (open circles), which provide data for an almost physical strange quark mass. In order to provide a quantitative comparison, we compute the baryon masses for the pion and kaon masses as predicted by the HSC group. The grey filled circles show our results. The distance of the filled circles to the solid lines measures the importance of taking the precise physical strange quark mass in the computation of the baryon masses. In Fig. 1 we also confront our approach with the simulation data of the PACS-CS (open squares) and QCDSF-UKQCD (open diamonds) groups. Since the later groups use strange quark masses that are significantly off the physical value, the data points are typically quite distant from the solid line. Again our results, green squares and red diamonds, are quite close to their corresponding lattice points, open squares and diamonds. Note that all lattice points are shown with statistical errors only, where we assume the central values of the lattice spacing as provided by the various lattice groups.

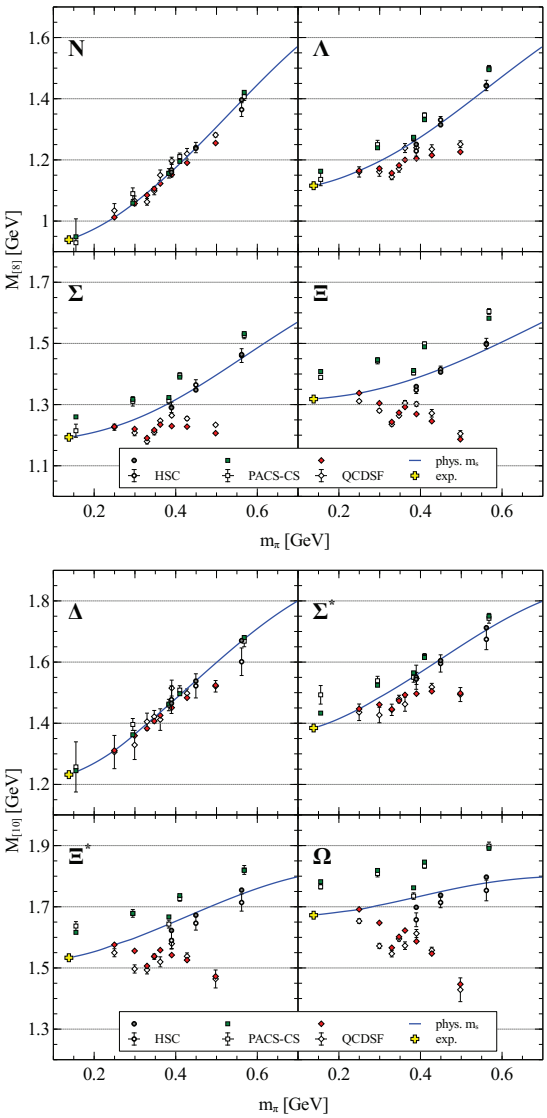

Figure 1: Baryon masses as a function of the pion mass as explained in the text.

References

[1] A. Semke, M. F. M. Lutz, Baryon self energies in the chiral loop expansion, Nucl. Phys. A778 (2006) 153.

[2] A. Semke, M. F. M. Lutz, Quark-mass dependence of the baryon ground-state masses, Phys. Rev. D85 (2012) 034001.

[3] A. Semke, M. F. M. Lutz, Strangeness in the baryon ground states, Phys. Lett. B717 (2012) 242.

[4] M. F. M. Lutz, A. Semke, On the consistency of recent QCD lattice data of the baryon ground-state masses, Phys. Rev. D86 (2012) 091502.

Photon-fusion reactions from chiral dynamics with vector fields

I. V. Danilkin[1,3], *M. F. M. Lutz*[1], *S. Leupold*[2], *and C. Terschlüsen*[2]
[1]GSI, Darmstadt, Germany; [2]Uppsala Universitet, Sweden; [3]ITEP, Moscow, Russia

Photon-fusion reactions $\gamma\gamma \to PP$ (with $PP = \pi^0\pi^0$, π^-, $K^0\bar{K}^0$, K^+K^-, $\eta\eta$ and $\pi^0\eta$) play an important role in our understanding of non-perturbative QCD. As a systematic approach chiral perturbation theory (χPT) is applied to describe these reactions at low energies [1]. An extension of χPT to the resonance region can be achieved by recently proposed novel scheme [2], which implements constraints from micro-causality and coupled-channel unitarity.

The cross sections of fusion processes are very sensitive to hadronic final-state interactions. Therefore, a crucial input is a proper description of the Goldstone boson scattering. This study has been performed in [3] within the novel unitarization scheme. The scalar resonances $f_0(980)$ and (980) are dynamically generated from coupled-channel $PP \leftrightarrow PP$ interactions. An important ingredient of these calculations is the chiral Lagrangian supplemented with light vector-meson degrees of freedom. The latter plays a crucial role in the hadrogenesis conjecture [4].

In the case of photo-fusion reactions, the chiral Lagrangian has five unknown parameters [5]. They parameterize the strength of interaction terms involving two vector meson fields. These parameters are fitted to $\gamma\gamma \to \pi^0\pi^0$, $\pi^-, \pi^0\eta$ data and to the decay $\eta \to \pi^0\gamma\gamma$, which is linked to $\gamma\gamma \to \pi^0\eta$ by crossing symmetry. For the decay amplitude we use the tree-level result, while for the reaction amplitudes we use the full rescattering formalism outlined in [2]. The results are depicted in Figs. 1 and 2.

The photon-fusion cross sections for the two-pion final states are in good agreement with the existing experimental data from threshold up to about 0.9 GeV. The $a_0(980)$ meson in the $\pi^0\eta$ channel is dynamically generated and an accurate reproduction of the $\gamma\gamma \to \pi^0\eta$ data is achieved up to 1.2 GeV. Based on our parameter sets we predict the $\gamma\gamma \to K^0\bar{K}^0$, K^+K^-, $\eta\,\eta$ cross sections (see Fig. 2).

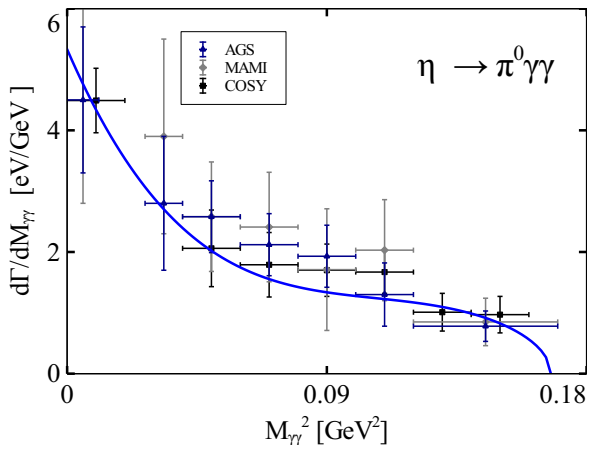

Figure 1: The single-differential invariant-mass distribution of the decay $\eta \to \pi^0\gamma\gamma$.

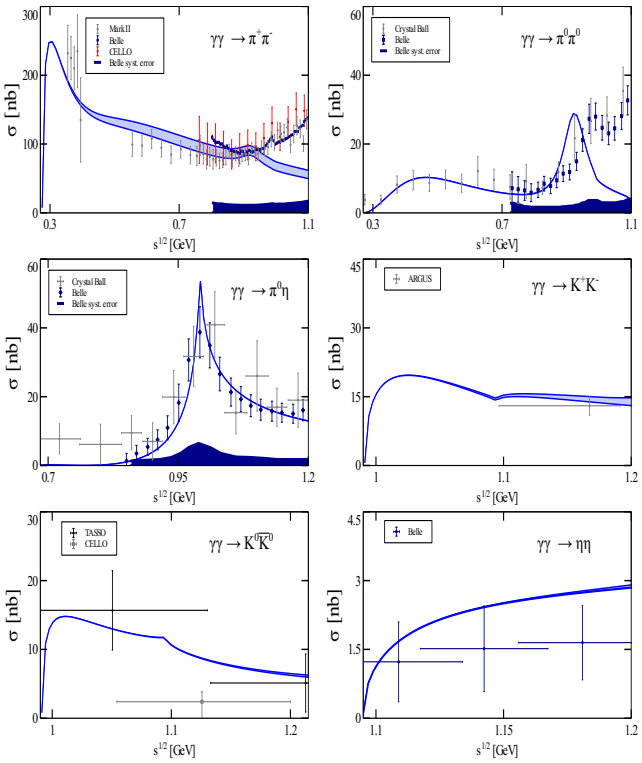

Figure 2: Total cross sections for the reactions $\gamma\gamma \to \pi^+\pi^-$, $\pi^0\pi^0$, $\pi^0\eta$, K^+K^-, $K^0\bar{K}^0$ and $\eta\eta$.

References

[1] J. Gasser, M. A. Ivanov and M. E. Sainio, Nucl. Phys. B **728** (2005) 31; Nucl. Phys. B **745** (2006) 84

[2] A. Gasparyan and M. F. M. Lutz, Nucl. Phys. A **848**, 126 (2010)

[3] I. V. Danilkin, L. I. R. Gil and M. F. M. Lutz, Phys. Lett. B **703** (2011) 504

[4] M. F. M. Lutz and E. E. Kolomeitsev, Nucl. Phys. A **730** (2004) 392; Nucl. Phys. A **700** (2002) 193

[5] I. V. Danilkin, M. F. M. Lutz, S. Leupold and C. Terschlusen, arXiv:1211.1503 [hep-ph].

Production of double-Λ hypernuclei at PANDA*

T. Gaitanos[1], *A.B. Larionov*[2,3], *H. Lenske*[1], *and U. Mosel*[1]

[1]Inst. für Theor. Physik, Universität Giessen, Germany; [2]bFrankfurt Inst. for Adv. Studies, J.W. Goethe-Universität, Frankfurt, Germany; [3]National Research Center "Kurchatov Institute", Moscow, Russia

Hypernuclear physics provides the challenge to investigate the hyperon-nucleon (YN) and the hyperon-hyperon (YY) interaction inside excited hadronic matter [1] at terrestrial laboratories, such as the FAIR facility at GSI, Darmstadt. Such studies are important for a better understanding of the still little known strangeness sector of the equation of state and also relevant for nuclear astrophysics, e.g., the properties of neutron stars [2]. The empirical situation on multi-strangeness hypernuclei has been rather scarce. However, with the high-intensity heavy-ion beams at GSI the hypernuclear ($S = -1$) production rate is considerably enhanced (HypHI project, [3]), while high luminosity antiproton beams at the future FAIR facility are expected to abundantly produce double-strangeness ($S = -2$) hypernuclei (part of the PANDA project, [4]).

The theoretical study of heavy-ion reactions has been carried out in Ref. [5] within a covariant kinetic theory, Giessen-BUU (GiBUU) approach [6], for the non-equilibrium reaction dynamics. Fragment formation appears at the final stage of reactions. It is modelled by a statistical decay model (SMM) [7]. The formation of hypernuclei is simulated by a coalescence prescription. Furthermore, the theoretical framework has been extended by including all necessary channels of double-strangeness hyperon production [5]. We have applied the GiBUU+SMM model in collisions induced by antiprotons at relativistic energies just above the Ξ-production threshold, using two targets, as proposed by the experiment of the PANDA collaboration. The cascade particles, which are emitted by the antiproton interaction with the first target, are used then as secondary beams for collisions with a second nuclear target. In the latter the formation of hypernuclei occurs.

The results are shown in Fig. 1 in terms of the double-Λ production cross section versus the Ξ-beam momentum (main panel). It turns out that the double-Λ hypernuclei yield strongly decreases with increasing beam energy. This is because of the quickly dropping $\Xi^- p \to \Lambda\Lambda$ elementary cross section as compared to the elastic one [8]. Therefore, in order to measure double-strange hypernuclei with very high cross section, the cascade particles produced in collisions between the antiproton beam with the primary target should have as low energy as possible. For the determination of the total production cross section of double-strange hypernuclei one needs the momentum distribution of the Ξ-particles emitted from the antiproton-reaction with the primary target. As one can see from the inserted panel in Fig. 1, the region around $P_\Xi \simeq 0.5 - 1.2$ GeV/c will contribute mostly to the total production cross section, for the considered $\bar{p} + {}^{64}\mathrm{Cu}@5$ GeV reaction. Thus, the effective

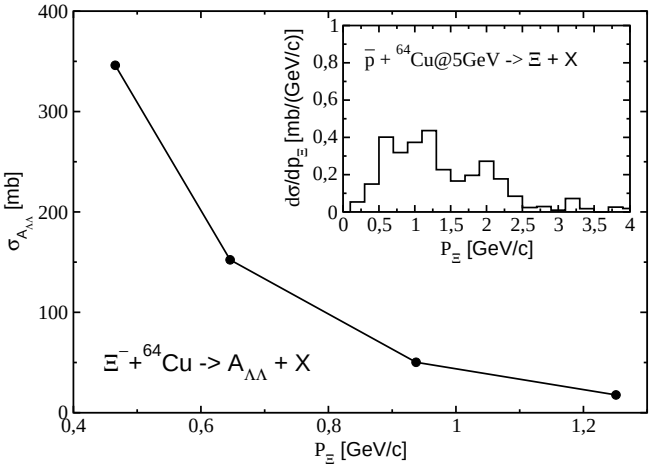

Figure 1: (Main panel) Production cross section for double-Λ hypernuclei as function of the Ξ-beam momentum. The inserted panel shows the Ξ-production cross section from $\bar{p}$-collisions on the first target, as indicated.

value of the total double-Λ hyperfragment cross section is estimated to be of the order of several mb.

In summary, we have studied the formation of hypernuclei in reactions relevant for the PANDA project at the new FAIR facility. We have investigated hypernuclear production in two steps, as suggested in the proposal of the PANDA experiment. We have estimated the production cross sections of double strange hypernuclei as function of the Ξ-hyperon energy by its capture with the secondary target. As an important result, double-Λ hypernuclear production at PANDA is possible with high probability, if low energy cascade-particle beams will be used. We emphasize the relevance of our theoretical results for the future activities at FAIR.

References

[1] A.D. Wroblewski, Acta Physica Polonica, B35 (2004) 901.

[2] J. Schaffner, I. Mishustin, Phys. Rev. C53 (1996) 1416.

[3] C. Rappold et al. (HypHI collaboration), Nucl. Phys. A622 (2010) 231.

[4] A.S. Lorente, A.S. Botvina, J. Pochodzalla, Phys. Lett. B 697 (2011) 222.

[5] T. Gaitanos, A.B. Larionov, H. Lenske, U. Mosel, Nucl. Phys. A881 (2012) 240.

[6] O. Buss, it et al., Phys. Rep. 512 (2012) 1.

[7] J.P. Bondorf et al., Phys. Rep. 257 (1995) 133.

[8] T.A. Rijken, Y. Yamamoto, nucl-th/0608074.

* Work supported by DFG

Strange and charm meson masses from twisted mass lattice QCD

Martin Kalinowski[*1] *and Marc Wagner*[1]

[1]Goethe-Universität Frankfurt am Main, Institut für Theoretische Physik Max-von-Laue-Straße 1, D-60438 Frankfurt am Main, Germany

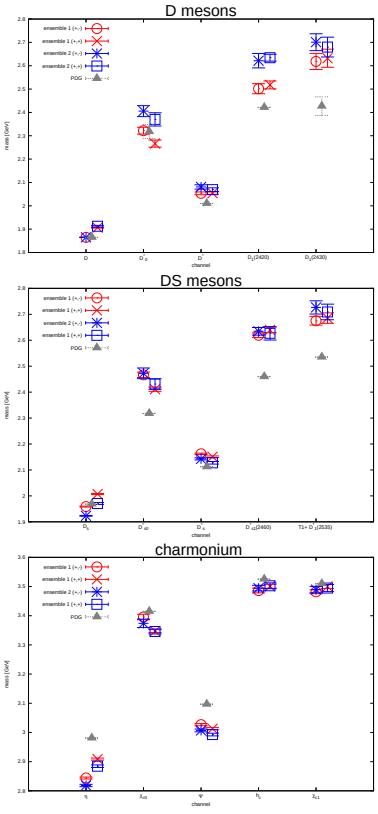

Figure 1: Calculated D, D_s meson and charmonium masses at the two ensembles. Grey data points represent experimental results.

Introduction

The recent discoveries of new open charm mesons at the BaBar, Belle and CLEO has attracted much interest both in the theoretical and experimental community, since the new states do not fit well into the quark model predictions for heavy-light systems in contrast to the previously known D states. Lattice QCD gives us a non-perturbative method to calculate numerically the spectrum of bound states consisting of quarks, antiquarks and gluons from first principles. We intend to extract part of the meson spectrum with focus to highly excited states, i.e. states with quantum numbers ($J^{PC} = 1^{-+}, 2^{+-}, ...$). For this we use $2+1+1$ lattice gauge configurations produced by the $ETMC$ (European Twisted Mass Collaboration).

Setup

Currently we have performed computations on $\approx$ 700 gauge field configurations from two ensembles.

For both the valence strange and charm quarks we use degenerate twisted mass doublets, i.e. a different discretization as for the corresponding sea quarks. We do this, to avoid mixing of strange and charm quarks [1], which inevitably takes place in a unitary setup, and which is particularly problematic for hadrons containing charm quarks.

For the computation of the corresponding correlation matrices we use spin diluted timeslice sources in combination with the "one-end trick". Meson masses are then determined from plateaux values of corresponding effective masses, which we obtain by "diagonalizing" the correlation matrices by solving generalized eigenvalue problems. For more details see [2] and references within.

Results

In fig.[1] we show results for our first two ensembles which differ in the pion mass. The red points correspond to the lower, more physical pion mass. At finite lattice spacing in the twisted mass formulation we get two numbers for every meson mass. These differences vanish in the continuum limes. From the shown differences we expect the discretization effects to be smaller than 5%.

Future plans include computations on further ensembles with various light quark masses and even finer lattice spacings. This will enable us, to extrapolate our theoretical results to physical quark masses and to the continuum, which in turn allows a direct meaningful comparison with experimental results as e.g. expected from the PANDA experiment at FAIR.

Acknowledgements

The authors acknowledge support by the Emmy Noether Programme of the DFG (German Research Foundation), grant WA 3000/1-1 and by Helmholtz Graduate School HGS-HIRe for FAIR. This work was supported in part by the Helmholtz International Center for FAIR within the framework of the LOEWE program launched by the State of Hesse.

References

[1] R. Baron *et al.* [ETM Collaboration], Comput. Phys. Commun. **182**, 299 (2011) [arXiv:1005.2042 [hep-lat]].

[2] M. Kalinowski and M. Wagner, [arXiv:1212.0403 [hep-lat]].

* kalinowm@th.physik.uni-frankfurt.de

Status of the AsyEOS S394 experiment: first preliminary results

A. Le Fèvre[1] *and the AsyEOS Collaboration*[2]

[1]Bucharest,Catania,Daresbury,Darmstadt,GANIL,GSI,Kraków, Liverpool, Messina, Milano, MSU, Munich, Napoli, RIKEN, Riyadh, Santiago, TAMU, Warsaw, Zagreb

The AsyEOS Collaboration aims at improving the knowledge of the asymmetry part of the nuclear equation of state. The purpose of the recent experiment S394, performed at GSI in May 2011, is to determine the behaviour of the asymmetry potential at supra-saturation density, using the ratio of the strengths of the elliptic flow of neutrons with respect to that of protons in heavy-ion reactions at relativistic energy. The method, the motivations and the experimental set-up have been described in [1, 2, 3, 4, 5].

For the first time, the FAIRRoot software framework – which is presently dedicated to the simulations of the future FAIR detectors – has been applied for the analysis of experimental data. The discriminating power of the method relies on the measurement accuracy of several observables. The first one is the centrality of the collisions. For this, we mainly use the information delivered by the ALADiN Time-Of-Flight Wall which collects the spectator residues at very forward angles. One of the observables giving a centrality scaling is the total charge of fragments with $Z > 1$, called Z_{bound}. Fig. 1 shows the evolution of the biggest fragment charge Z_{max} measured in an event as a function of Z_{bound}, very similar to the "universality" curve obtained in the past for the same system with the ALADiN set-up [6], although the acceptance for the projectile spectator is slightly smaller in S394.

Another key ingredient of the study of the elliptic flow is the precision of the reaction plane determination, done here by coupling the informations provided at various polar angles with the μ-Ball (backward), CHIMERA and ToF-Wall detector arrays (forward). Fig. 2 shows a preliminary example of the good agreement obtained for the azimuthal orientation of the reaction plane between these detectors.

The remaining crucial point for measuring the neutron and proton elliptic flows is the precise determination of their momenta with a high detection efficiency, provided by the LAND array at mid-forward angles. Fig. 3 shows the angular distributions of neutrons with respect to the reaction plane for two rapidity intervals, as obtained after subtracting the background contribution.

The preliminary results are promising. The data analysis is still on the way, towards the determination of accurate elliptic flow parameters with high statistics.

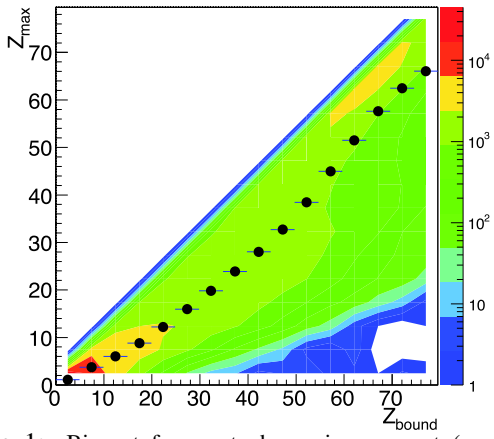

Figure 1: Biggest fragment charge in an event (symbols = mean values) as a function of Z_{bound} (see text) measured in the ToF-Wall and CHIMERA for the reaction $^{197}Au + ^{197}Au$ at 400 A.MeV incident energy.

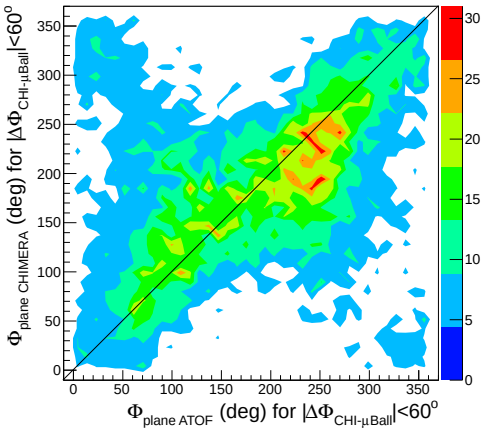

Figure 2: For the same reaction, bi-dimensionnal representations of azimuthal angles of the reaction plane as measured by CHIMERA and the ToF-Wall, under the condition of consistency between CHIMERA and μ-Ball.

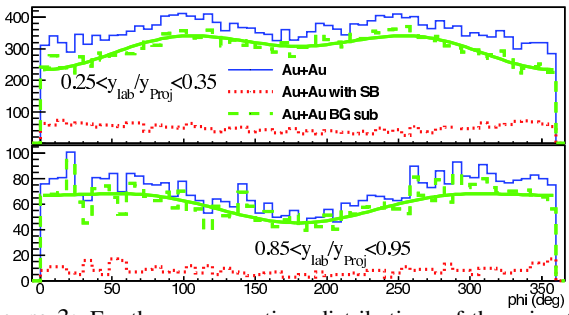

Figure 3: For the same reaction, distributions of the azimuthal angle of neutrons measured in LAND with respect to the reaction plane determined by CHIMERA, for different intervals of neutron rapidity. "SB" and "BG sub" mean respectively "shadow bar" and "background subtracted" (i.e. "no SB" minus "with SB"). The smooth curve is the Fourier decomposition of the elliptic flow.

References

[1] P. Russotto et al., GSI Scientific Report 2010, p.68.

[2] P. Russotto et al., Phys. Lett. B697 (2011) 471.

[3] P. Russotto et al., GSI Scientific Report 2012, p.90.

[4] J. Łukasik et al., GSI Scientific Report 2010, p. 69.

[5] J. Łukasik et al., GSI Scientific Report 2011, p. 91.

[6] A. Schüttauf et al., Nucl. Phys. A607 (1996) 457-486.

Pulse shape analysis for the KRATTA modules*

J. Łukasik[†1], *P. Pawłowski*[1], *A. Budzanowski*[‡1], *B. Czech*[1], *I. Skwirczyńska*[1], *J. Brzychczyk*[2], *M. Adamczyk*[2], *S. Kupny*[2], *P. Lasko*[2], *Z. Sosin*[2], *A. Wieloch*[2], *M. Kiš*[3], *Y. Leifels*[3], *and W. Trautmann*[3] *for the ASY-EOS Collaboration*

[1]IFJ-PAN, Kraków, Poland; [2]IF UJ, Kraków, Poland; [3]GSI, Darmstadt, Germany

The KRATTA, Kraków Triple Telescope Array [1], has been built to measure flow of midrapidity light charged particles in the ASY-EOS experiment [2] conducted at GSI in 2011. Modular design, portability, low thresholds (below 3 MeV/nucleon) and high maximum energy (∼260 MeV/nucleon for p and α) are its main characteristics.

The off-line pulse shape analysis applied to the data from KRATTA allowed to decompose the complex signals from the Single Chip Telescope, SCT [3], segment into their individual ionization and scintillation components and to obtain a satisfactory isotopic resolution with a single readout channel. The obtained, ballistic-deficit free, amplitudes were constrained to follow the trends of the range-energy tables, which allowed for easy identification and energy calibration.

The final agreement between the decomposed ionization and scintillation components and the calculated ATIMA [4] lines presented in Fig. 1, is a result of an iterative procedure of improving the calibration and searching for optimal values of the fixed parameters. This procedure finally converged into providing quite reasonable trends of the isotopic lines.

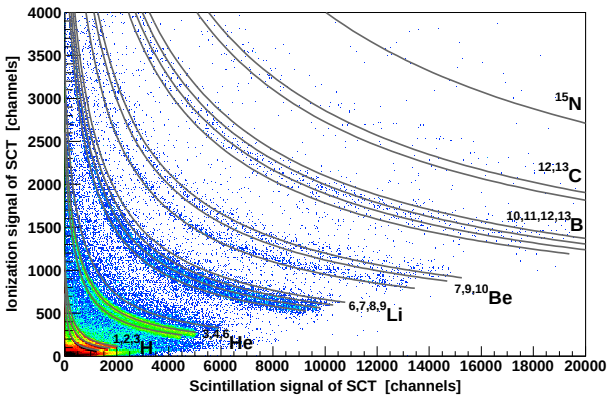

Figure 1: Decomposed SCT ΔE-E identification map (obtained with a single readout channel) with the superimposed ID lines calculated using the ATIMA tables.

The pulse shape analysis allows also to identify particles stopped in the first photodiode [1] and helps to isolate the secondary reactions and scatterings in the crystal as well as the punch-through hits, which leads to a substantial reduction of the background in the thick crystal of the KRATTA module. An example of a quite useful identification map, which profits from both, the ΔE-E and the Fast-Slow representations, is presented in Fig. 2.

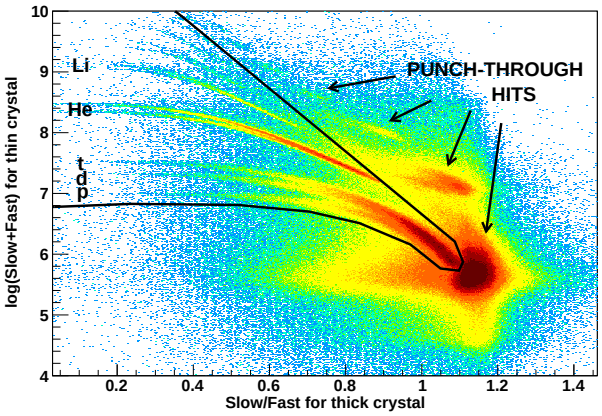

Figure 2: Logarithm of the total light in the thin crystal vs Slow over Fast component of light in the thick crystal. The line defines the border of the region of well identified particles (inside the cut).

In this representation the punch through segments as well as a substantial amount of secondary reactions and γ-ray hits can be isolated from the well defined hits of particles stopped in the thick crystal (located inside the cut). Since the ratio of the Slow over Fast amplitudes increases monotonically, and is well correlated, with the fall time of the CsI(Tl) fluorescence, the observed separation between the well identified and punching-through or scattered particles can be possibly interpreted by taking into account the relation between the effective fall time of the pulse and the ionization density [5] in the crystal. For particles escaping from the crystal, one can expect that the high ionization density part of the track (near the Bragg peak) contributes less to the fluorescence signal than in the case of stopped particles. Thus, the light signal is mainly due to the low ionization density part of the track which is characterized by a longer effective fall time and, consequently, by a larger Slow over Fast ratio.

References

[1] J. Łukasik et al., arXiv:1301.2127 [physics.ins-det], to be published in Nucl. Instr. Meth. A (2013); J. Łukasik et al., GSI Scientific Reports 2010, p. 69 and 2011, p. 91.
[2] P. Russotto et al., IWM 2011 Conf. Proc. Vol. 105, p. 91. P. Russotto et al., IWM 2009 Conf. Proc. Vol. 101, p. 22.
[3] G. Pasquali et al., Nucl. Instr. Meth. A 301 (1991) 101. J. Friese et al., Conf. Record of the 1992 IEEE, 1 (1992) 61.
[4] `http://www-linux.gsi.de/~weick/atima`
[5] T. Masuda et al., Nucl. Instr. Meth. A 322 (1992) 135.

* Work supported by Polish Ministry of Science and Higher Education under grant No. DPN/N108/GSI/2009 and by the Foundation for Polish Science - MPD program, co-financed by the European Union within the European Regional Development Fund.

† jerzy.lukasik@ifj.edu.pl
‡ deceased

Production of hypernuclei in Ni+Ni collisions at 1.91A GeV *

Y.P.Zhang[†1], *N.Herrmann*[1], *and FOPI collaboration*

[1]Physikalisches Institut, Universität Heidelberg, Germany

In non-central HICs at the SIS18 energies (1-2A GeV), the emission pattern of sideflow and elliptic flow vividly illustrates that the hot fireball matter strongly interacts with the cold spectator matter [1]. Mesons like π, K and baryons like Λ, Σ, produced in the fireball, could react with the cold spectator matter in the nuclear medium. Since the properties of hadrons may be modified by the nuclear medium, the cross sections and reaction rates of such reactions may be modified as well. Hypernuclei are the possible products of these processes. In such collisions, hypernuclei can also be formed by the coalescence process, i.e. the Λ hyperon may bind with the spectator-like cluster(s) [2]. In our previous contributions [3, 4], the method for reconstructing ${}^{3}_{\Lambda}$H from its two-body π^--decay channel, i.e. ${}^{3}_{\Lambda}\mathrm{H}\rightarrow\pi^- + {}^{3}\mathrm{He}$, the observed ${}^{3}_{\Lambda}$H signal and its mean lifetime were described. It has to be noted that the ${}^{3}_{\Lambda}$H signal was only observed in a limit phase space region, i.e. $0.2 < p_t/m_{{}^{3}_{\Lambda}\mathrm{H}} < 0.4$, $0.2 < y_{lab} < 0.4$ and $30^o < \theta_{{}^{3}\mathrm{He}} < 52^o$, where p_t and y_{lab} are the transverse momentum and the rapidity in the laboratory frame of ${}^{3}_{\Lambda}$H candidate, $m_{{}^{3}_{\Lambda}\mathrm{H}}$ is the nominal mass of ${}^{3}_{\Lambda}$H and $\theta_{{}^{3}\mathrm{He}}$ is the polar angle of ^{3}He. To obtain a significant signal, it is necessary to introduce in additional multiplicity cuts, i.e. $20 < T_{MUL} < 60$ and $50 < P_{MUL} < 45$, where T_{MUL} is the track multiplicity in the CDC, and P_{MUL} is the charged particle multiplicity in the forward plastic wall (PLW).

In this contribution, we show the identification of another hypernucleus, i.e. ${}^{4}_{\Lambda}$H, from its two-body π^--decay channel, i.e. ${}^{4}_{\Lambda}\mathrm{H}\rightarrow\pi^- + {}^{4}\mathrm{He}$. The procedure for identifying ${}^{4}_{\Lambda}$H from the considered channel is the same as the one for ${}^{3}_{\Lambda}$H reconstruction by replacing ^{3}He to ^{4}He. Similarly, a clear signal of ${}^{4}_{\Lambda}$H can only be observed in a limited phase space region, i.e. $0.15 < p_t/m_{{}^{4}_{\Lambda}\mathrm{H}} < 0.35$, $0.15 < y_{lab} < 0.4$ and $30^o < \theta_{{}^{4}\mathrm{He}} < 52^o$, when applying multiplicity cuts of $30 < T_{MUL} < 50$ and $10 < P_{MUL} < 35$. In Fig. 1(a), the invariant mass distribution of selected (π^-,^{4}He) pairs in the above phase space region is depicted by the open circles. The obtained mixed-event background spectrum is shown by the solid blue curve. After subtracting the background, the resulting spectrum is shown in Fig. 1(b). An excess in the spectrum near the nominal mass of ${}^{4}_{\Lambda}$H is attributed to the decay of ${}^{4}_{\Lambda}$H . The fit of a Gaussian distribution revels a mean value of 3922.6±1.0 MeV/c^2 and a width of 4.0±1.6 MeV/c^2, compatible with the nominal mass of ${}^{4}_{\Lambda}$H and the detector response. The significance of signal is calculated to be 4.2 in the interval, marked by two vertical dashed lines in Fig. 1(b). About 74±29(sta.) ${}^{4}_{\Lambda}$H were identified.

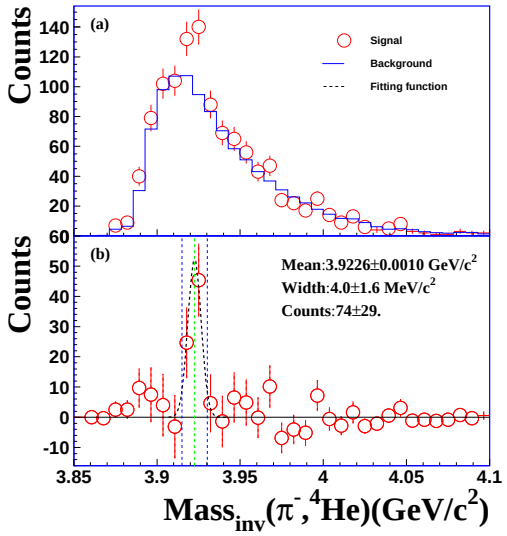

Figure 1: (a) Invariant mass spectrum of (π^-,^{4}He) pairs (open circles) and optimized mixed-event background (solid line); (b) Invariant mass spectrum after the background subtraction, the excess is fitted by a Gaussian function. For detailed desription see the text.

The reconstruction efficiency of ${}^{3}_{\Lambda}$H and ${}^{4}_{\Lambda}$H is studied by a full Geant simulation of the FOPI data analysis chain, and is found to be about 2% in the phase space regions where the signals were observed. After the efficiency correction, the yield of ${}^{3}_{\Lambda}$H and ${}^{4}_{\Lambda}$H is 7.7×10^{-4} and 1.3×10^{-4}, regarding to a total event number of 56×10^{6}, of which 51% (21%) passed the multiplicity selection for the ${}^{3}_{\Lambda}$H (${}^{4}_{\Lambda}$H) case. The mean lifetime of particle species can be extracted from their efficiency-corrected decay time spectrum, as described in [4]. The mean lifetime of ${}^{3}_{\Lambda}$H is further evaluated and it has a value of 263±64(sta.)±44(sys.) ps. In the same manner, the mean lifetime of ${}^{4}_{\Lambda}$H is found to be 196±75(sta.)±43(sys.) ps. The quoted systematic errors are the quadratic sum of the contribution of individual cuts, which is obtained by varying the cut in a range of 10-20% around its fixed value. Within errors, the observed lifetimes are consistent with the measured lifetimes from other experiments.

References

[1] A. Andronic, et al, Phy. Lett. B612, 173 (2005).

[2] A. K. Kerman and M. S.Weiss, Phys. Rev. C 8, 408 (1973).

[3] Y. P. Zhang, N. Herrmann, et al. GSI Sci. Rep. 2010, p67

[4] Y. P. Zhang, N. Herrmann, et al. GSI Sci. Rep. 2011, p80

* This work supported by BMBF 06HD7141I.

† ypzhang@physi.uni-heidelberg.de

Differences in population of the phase space for $K^{\pm}$-mesons produced in π-induced reactions with heavy and light targets. *

V. Zinyuk[†1], *N. Herrmann*[1,2], *for the FOPI Collaboration*[2], *and the GEM-TPC Collaboration*[2]

[1]Physikalisches Institut, Universität Heidelberg, Germany; [2]GSI, Darmstadt, Germany

Partial restoration of chiral symmetry in hot and dense environment is believed to influence the in-medium properties of hadrons. Various theoretical approaches agree qualitatively on the decrease(increase) of the effective $K^-(K^+)$ - mass with increasing nuclear matter density, resulting in the attraction(repulsion) of $K^-(K^+)$ toward nucleons[1].

The FOPI Collaboration in cooperation with the GEM-TPC Collaboration has performed an experiment bombarding heavy and light targets with an intense pion beam. About 4×10^6 events in ^{208}Pb-target and 3×10^6 events in ^{12}C-target were recorded. The beam momentum of 1.7 GeV/c was chosen such that the direct production of K^+K^--pairs is possible. Thereby the recorded sample of charged kaons, produced close to threshold, is highly sensitiv to the $KN(\bar{K}N)$-potential and allows to study in-medium effects at normal nuclear matter density.

In π-induced reactions with a heavy target K-mesons are produced on the surface of the nucleus and have to propagate through the nucleus to be detected. If the kaon is attracted(repelled) by the nuclear matter, its momentum distribution in the final state will be shifted to smaller(larger) momenta. These changes in the phase space distribution can be quantified by comparing the momentum spectra of kaons produced in a heavy target to a reference system provided by a light target.

First results, from the recent experiment, of such momentum ratios $R((dN/dp)_{Pb}/(dN/dp)_C)$ are presented in Fig. 1 for K^+-mesons (left panel) and K^--mesons (right panel). In case of K^+-mesons repulsion from nuclear matter due to strong interaction(the KN-potential), and an additional repulsion due to the Coulomb-interaction are expected. Therefore, the low momentum region of the phase space of K^+-mesons from the heavy target is populated weaker than the one from the reference system, i.e. light target. The ratio of the momentum distributions has small values and rises as the momentum increases. Particles with larger momentum leave the interaction region rapidly and therefore are not influenced by the repulsion. The phase space distributions in both systems are equal and the momentum ratio reaches a constant value. The discussed effects from the strong interaction has been observed before by the FOPI Collaboration for K^0_S [3] and the interplay of strong and Coulomb interactions for K^+-mesons by the ANKE collaboration [2]. Transport model calculations confirm the expectations for different attraction scenarios. K^+ and K^0_S were found a to be good probes for in-medium effects due to relatively long mean free path in nuclear matter at small momenta. Our new measurement is in qualitative agreement with the previous one. The momenta with the highest ratio and the region with a constant ratio are compatible to ANKE results, however the earlier observed strong decrease at smaller momenta could not be confirmed.

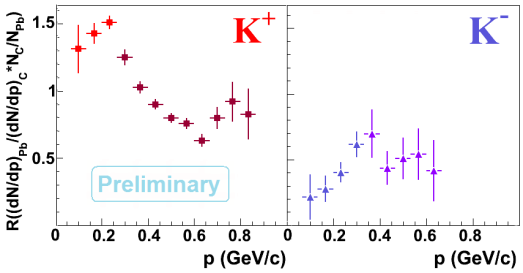

Figure 1: The ratio of $K^+(K^-)$ yields, per event, produced by pions on heavy and light targets as a function of the momentum in the lab system. Different colors indicate a separate analysis of different detector components.

In case of the attracted particles, like K^-, one would expect the largest value for the momentum ratio at smallest momentum and a continuous decrease with increasing momenta, as far as the $\bar{K}N$-potential is concerned. On the other hand, K^--mesons have a very short mean free path in nuclear matter of about 0.6 fm for $p_{K^-} = 0.1 GeV/c$ and therefore they are expected to suffer collisions in both heavy and light targets. Part of K^--mesons are absorbed in inelastic scattering processes another part exchanges momentum as a consequence of elastic scattering. Both processes influence the momentum distribution in the final state. Recent version of transport model calculations, taking into account scattering and the effect from repulsive $\bar{K}N$-potential, predict a steady decrease of the ratio with increasing momentum. Our recent measurement (Fig. 1, right) shows no sign of expected behavior.

To draw any quantitative conclusions on the influence from the $KN(\bar{K}N)$-potential on this observable detailed comparison to transport model calculations is necessary and will hopefully lead to a consistent description of especially K^- in nuclear matter.

References

[1] C. Fuchs, Prog. Part. Nuclear Phys. **56**, 1 (2006).

[2] M. Bueschner *et al.*, Eur. Phys. J. A **22**, 301 (2004).

[3] M. L. Benabderrahmane *et al.*, Phys. Rev. Lett. **102**, (2009) 182501.

* Work supported by BMBF 06HD7141I.

† v.zinyuk@gsi.de

Production of p, d and t in Ar+KCl at 1.76 AGeV*

[1]*H. Schuldes,* [1]*M. Lorenz,* [1]*C. Müntz and* [1]*J. Stroth for the HADES-Collaboration*

[1]Goethe-University Frankfurt

This contribution presents preliminary data on proton, deuteron and triton production in Ar+KCl reactions at 1.76 AGeV. The interpretation of HI collisions by means of theoretical models, often focusing on rare observables in this energy regime, such as strangeness or vector mesons, needs to be contrasted to global event characteristics, probing the dynamics of a HI collision. Rapidity distributions of protons and heavier fragments, such as d and t, comprise a direct view on the HI dynamics. At SIS energies valuable systematics have been collected and published by the FOPI collaboration in [1] mostly for central Au+Au collisions. Data of HADES on Ar+KCl at 1.76 AGeV extends this study to a system of medium size.

The protons, deuterons and tritons have been identified by means of three independent informations provided by different sub-systems of the spectrometer. The first selection has been performed with cuts on the energy loss of the particles in the Multiwire Drift Chambers (MDC) and Time of Flight detectors (TOF and TOFino). To improve on that particle identification, the time of flight information and momentum reconstruction is used by cutting on mass windows of the selected particle species in different phasespace regions. After background subtraction and corrections for acceptance and efficiency, one obtains the transverse mass spectra for different rapiditiy regions.

In order to extrapolate to unmeasured m_t-regions, the corrected transverse mass spectra are fitted simultaneously with Siemens-Rasmussen-functions [2]. The resulting parameters for the system are T = (72 $\pm$ 9) MeV and β = 0.40 $\pm$ 0.03, Which is in fair agreement with the chemical freezeout temperature T = 73 MeV of a statistical model fit to the yields and the radial flow velocity of β = 0.39 estimated from the inverse slope parameters of light particles [3].

Fig.1 shows the rapidity distributions of the particles after extrapolation from $0 \leq m_t \leq \infty$ (red), in comparison to the measured data in the HADES acceptance (blue). After integration of the extrapolated rapidity distributions, the multiplicities can be determined to (19.19 $\pm$ 0.92 $\pm$ 0.80) protons, (3.09 $\pm$ 0.03 $\pm$ 0.16) deuterons and (0.45 $\pm$ 0.01 $\pm$ 0.03) tritons (per event). The systematical errors have been estimated by varying the parameters of the extrapolation. The rapidity distributions show a clear two peak structure, not supporting the assumption of a thermal source at mid-rapidity.

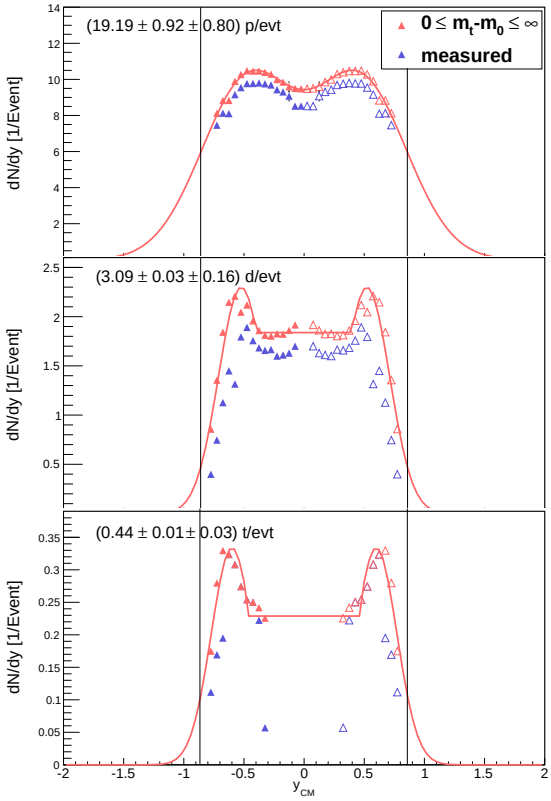

Figure 1: dN/dy-distributions of protons (top), deuterons (middle) and tritons (bottom) in the HADES acceptance (blue) and extrapolated with Siemens-Rasmussen fits from m_t-m_0=0 to m_t-m_0=∞ (red). Open triangles show reflected data around mid-rapidity. The lines at y=$\pm$0.86 represent projectile and target rapidity.

References

[1] W. Reisdorf *et al.* (FOPI Collaboration), Nucl. Phys. A **876** 1 (2012).

[2] Ekkard Schnedermann and Josef Sollfrank and Ulrich Heinz, "Thermal phenomenology of hadrons from 200 AGeV S+S collisions", PHYS.REV.C, 48, 2462, doi:10.1103/PhysRevC.48.2462, (1993).

[3] M. Lorenz, "Vector meson production in p+Nb reactions and statistical particle production in Ar+KCl collisions", PhD-Thesis, Goethe-Universität Frankfurt, (2012).

* Work supported by BMBF 06FY9100I 06FY7114, HIC for FAIR, HQM, HGS-Hire, EMMI and GSI.

Inclusive π^0 and η production in the 1.76 GeV/u Ar+KCl reaction*

R. Holzmann[1], *and M. Gumberidze*[2,3] *for the HADES collaboration*

[1]GSI, Darmstadt, Germany; [2]IPN, CNRS/IN2P3 – Université Paris Sud, Orsay, France; [3]TUD, Darmstadt, Germany

We have applied the method of 4-lepton invariant-mass reconstruction [1] to data taken with HADES in the reaction 1.756 GeV/u ^{40}Ar+KCl [2]. The aim was to investigate if π^0 and η production can be studied also in heavy-ion collisions with conversion-pair spectroscopy of the decays $\pi^0, \eta \rightarrow e^+e^-e^+e^-$. Indeed, as the Dalitz decays of these pseudoscalar mesons contribute strongly to the dilepton yield, their multiplicities need to be known sufficiently well in order to be able to disentangle the e^+e^- cocktail. The Ar+KCl system constitutes a convenient starting point for such studies as one can still expect only a moderate combinatorial background (CB). In addition, excitation functions of pion and eta production in light systems are available for comparison from earlier studies done with the TAPS photon calorimeter in the range of 1 – 2 GeV/u [3].

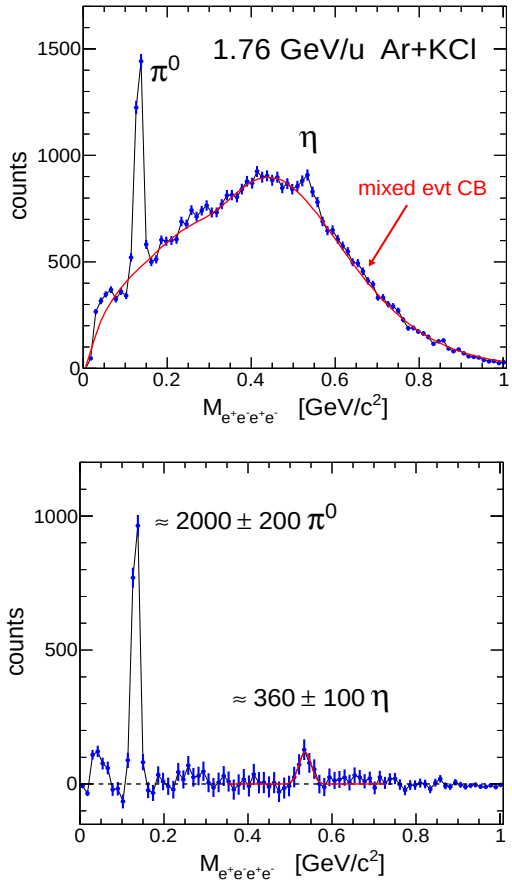

Figure 1: Invariant mass distribution of $e^+e^-e^+e^-$ events measured with HADES in the 1.756 GeV/u Ar+KCl reaction. The lower part shows the signal after CB subtraction together with a Gaus fit to the η peak.

Figure 1 shows the reconstructed $e^+e^-e^+e^-$ invariant mass spectrum together with its combinatorial background (CB) of uncorrelated lepton pairs as obtained from event mixing. Both, the π^0 and η peaks are clearly identifiable. While the pion statistics is sufficient for a differential analysis, the eta peak allows only for a direct integration, e.g. by Gaus fit, as indicated in Fig. 1. Correcting for conversion and reconstruction efficiencies, and rescaling for the mean A_{part} selected by the HADES LVL1 trigger [2] we obtained (preliminary) inclusive multiplicities of $M_{\pi^0} = 2.0 \pm 0.5$ and $M_\eta = 0.047 \pm 0.014$ in the 1.756 GeV/u Ar+KCl reaction.

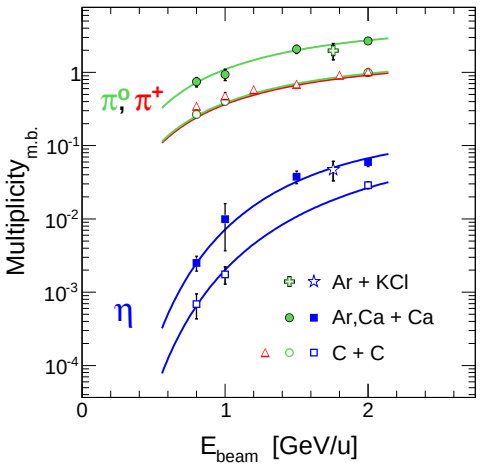

Figure 2: Comparison of the present results with excitation functions of inclusive pion and eta production in the light systems C+C and Ca+Ca. The π^0 and η data were obtained with TAPS [3], the π^+ data stem from KaoS [4]. Curves are log-log polynomial fits to the TAPS data.

Figure 2 shows our multiplicities in comparison with the systematics of data obtained by the TAPS [3] and KaoS [4] experiments in the C+C and Ca+Ca systems. The good agreement obtained gives hope that the 4-lepton channel can be exploited also in heavier reaction systems, in particular for Au+Au, where the available information on neutral meson production is still quite limited.

References

[1] M. Gumberidze *et al.*, contribution to GSI 2012 Annual Report (2013).

[2] G. Agakishiev *et al.*, Phys. Rev. C **84**, 014902 (2011).

[3] R. Averbeck *et al.*, Phys. Rev. C **67**, 024903 (2003).

[4] Ch. Sturm, doctoral thesis, TU Darmstadt (2001).

*Work supported by EMMI and the IN2P3/GSI agreement

Hypertriton reconstruction in Ar+KCl reactions at 1.756A GeV with HADES*

T. Scheib[1], M. Lorenz[1], R. Holzmann[2], J. Markert[2], J. Stroth[1,2], and the HADES Collaboration
[1]Goethe-Universität Frankfurt am Main; [2]GSI, Darmstadt, Germany

In September 2005 the collision system Ar+KCl at a kinetic beam energy of 1.756 GeV per nucleon was measured with HADES. Among other observables, in particular several hadron species carrying strangeness have been reconstructed. Due to the conservation of the strangeness quantum number its production is a highly correlated process. The relative distribution of strange and anti-strange quarks among the hadrons in the final state, including excited states and resonances, can provide important insight into the production and propagation of quarks [1].

In this contribution, we investigate the production of the hypertriton ${}^3_\Lambda H$, the lightest of the so-called hypernuclei. In addition to the nucleons - the proton and the neutron - these nuclei contain at least one hyperon, which is in the explicit case of the hypertriton a $\Lambda-$hyperon.

Hypertritons are most easily reconstructed through their bound decay into a negative pion and a ${}^3He$. The branching ratio for this decay is about 35% [2]. Hence, an important issue of the analysis is a good identification of the two final-state particles π^- and ${}^3He$ via the Time-of-Flight information in the TOF and TOFino walls and the energy loss in the Multiwire Drift Chambers (MDC) as well as in the TOF and TOFino walls.

In order to reduce the background stemming from uncorrelated pairs of negative pions and helium nuclei, secondary-vertex cuts are applied. The procedure is comparable to the $\Lambda \rightarrow \pi^- + p$ analysis in Ar+KCl, but since the mass of ${}^3_\Lambda$H is significantly higher than that of Λ, the cut on the mean flight distance has to be widened. For the optimization of the applied cuts, the hypertriton decay is simulated in order to observe their effects on the significance of the signal. After generating with Pluto [3] hypertritons produced either thermally or via coalescence processes, the detector response on the analyzed decay channel is simulated with HGeant [4]. The simulated signal is embedded into real data to get a realistic estimate of the uncorrelated background. Then, the distributions of the topology variables from simulations are compared to those of data.

Additionally, the acceptance and reconstruction efficiency of the hypertriton are determined via simulations to acc $\cdot$ eff$_{rec} = (0,1031 \pm 0,0054)\%$ for those produced by coalescence and acc $\cdot$ eff$_{rec} = (0,14 \pm 0,013)\%$ for those coming from thermal sources.

After subtracting the background, which is obtained via the mixed-event-method and delivers an invariant mass spectrum of uncorrelated π^--^{3}He pairs, from the invariant mass spectrum of the same event, there is no significant hypertriton signal visible.

However, an upper production limit can still be calculated. This can either be done by using the Feldman-Cousins method [5], which only takes underlying statistics of the invariant mass spectrum into account. Another way is to embed simulated hypertritons into the measured data at such a ratio, that a reconstruction becomes just possible. The multiplicities are calculated for the different methods to Mult$_{FC} = (7,493 \pm 3,371 \pm 0,465) \cdot 10^{-4}$ respectively Mult$_{embed} = (2,96 \pm 0,93 \pm 0,67) \cdot 10^{-4}$. The obtained values of the different methods are within errors in agreement with each other. Additionally, they agree well with results from former reconstructions on rare, strange particles in Ar+KCl collisions measured with HADES, namely the Ξ^-, which was observed significantly in this collision system [6]. Considering the upper production limit obtained via the second method, the production ratio of hypertritons to the successfully reconstructed Λ-hyperons could be calculated, which provides the limiting value of $N_{{}^3_\Lambda H}/N_\Lambda(embedded) = (7,24 \pm 3,94) \cdot 10^{-3}$.

* Supported by BMBF (06 FY 9100 I), HIC for FAIR, EMMI and GSI

References

[1] G. Agakishiev et al., "Hyperon Production in ArKCl collisions at 1.76A GeV", Eur. Phys. J. A 47 (2011) 21.

[2] H. Kamada, J. Golak, K. Miyagawa, H. Witala, W. Gloeckle, "Pi-mesonic decay of the hypertriton", arXiv:nucl-th/9709035v1

[3] PLUTO, Pluto++, A Monte Carlo Simulation Tool for Hadronic Physics, 2004. http://wwwhades.gsi.de/computing/pluto/html/PlutoIndex.html.

[4] GEANT. Detector Description and Simulation Tool, 2004. http://cont.cern.ch/writeup/geant/, Online User Guide.

[5] G. J. Feldman and R.D. Cousins, *Unified approach to the classical statistical analysis of small signals.* Phys. Rev. D57, 3873, 1998.

[6] G. Agakishiev et al. (HADES Collaboration), Phys. Rev. Lett. 103, 132301, 2009.

Inclusive pion and eta production in the 3.5 GeV p+^{93}Nb reaction*

M. Gumberidze[1,2], *R. Holzmann*[3], *and P. Tlusty*[4] *for the HADES collaboration*

[1]IPN, CNRS/IN2P3 – Université Paris Sud, Orsay, France; [2]TUD, Darmstadt, Germany; [3]GSI, Darmstadt, Germany; [4]Nuclear Physics Institute, Academy of Sciences of Czech Republic, Rez, Czech Republic

In recent years HADES has studied inclusive electron pair production in the proton-induced reactions p+p and p+Nb at 3.5 GeV [1, 2]. These data are interpreted with the help of transport models such as UrQMD [3], GiBUU [4], HSD [5], and IQMD [5]. We provide now further constraints from an analysis of 4-lepton events detected in HADES which yield information on the inclusive production of the π^0 and η mesons. Indeed, the electromagnetic decays of the latter, in particular the decays $\pi^0, \eta \rightarrow \gamma e^+e^-$ and $\pi^0, \eta \rightarrow \gamma\gamma$, combined with the external conversion of the decay photon(s) on material in the inner region of HADES, lead to events with a characteristic 4-lepton signature, namely $\pi^0, \eta \rightarrow e^+e^-e^+e^-$. The low conversion probability ($\simeq$4%) and the rather low lepton momenta lead to an overall acceptance for these final states on the order of $10^{-6} - 10^{-5}$ only. Nevertheless, in $9 \cdot 10^9$ triggered p+Nb events a sizeable statistics could be accumulated.

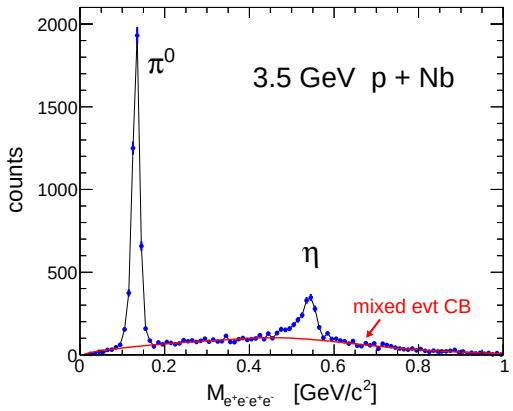

Figure 1: Invariant mass distribution of $e^+e^-e^+e^-$ events measured with HADES in the 3.5 GeV p+Nb reaction.

Figure 1 shows the reconstructed $e^+e^-e^+e^-$ invariant mass spectrum together with its combinatorial background (CB) of uncorrelated lepton pairs as obtained from event mixing. The π^0 and η peaks are prominently visible over the CB with a statistics of a few thousand counts each. Both mesons can easily be selected with appropriate mass cuts and, after having applied corrections for conversion and reconstruction efficiencies, their rapidity and transverse momentum distributions have been obtained. Of those the latter are displayed in Fig. 2. In addition to the π^0 and η distributions we show there the result obtained for negative pions [6]. As the acceptance of π^0 is limited to $p_\perp > 0.3$ we have used the π^- to extrapolate the neutral pion yield to low $p_\perp$ values. Extrapolating as well beyond the accepted rapidity range of $0.2 < y < 1.8$ we obtain (preliminary) inclusive multiplicities of $M_{\pi^-} = 0.62 \pm 0.15$ and $M_{\pi^0} = 0.60 \pm 0.20$ in 3.5 GeV p+Nb reactions.

In contrast to the pions, the eta coverage of HADES is complete in $p_\perp$, as visible in Fig. 2, and nearly so in y. Furthermore, the η phase space distribution seems to be well described by a Boltzmann fit. Integrating and extrapolating to full rapidity yields a (preliminary) multiplicity of $M_\eta = 0.032 \pm 0.005$ for inclusive eta production.

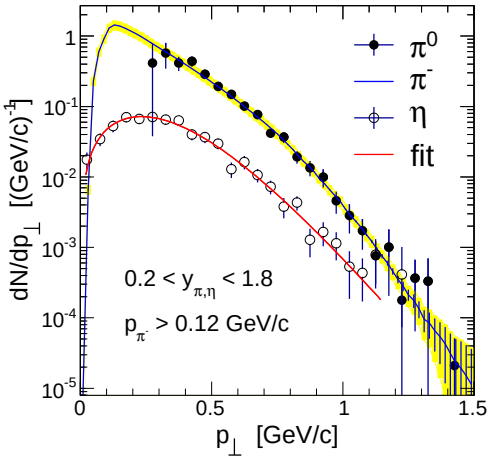

Figure 2: Reconstructed and efficiency-corrected π^0 (closed circles), π^- (blue line) and η (open circles) transverse momentum distributions $dN/dp_\perp$ within the HADES acceptance. Statistical errors are indicated by vertical bars and systematic uncertainties by the yellow shading. A Boltzmann fit (red line) to the η data yields the temperature $T = 84 \pm 3$ MeV.

Our *proof-of-principle* result demonstrates that 4-lepton final states can be reconstructed reliably with HADES and we believe that such data provide additional valuable input for the modeling of proton-nucleus and heavy-ion collisions in the few-GeV regime.

References

[1] G. Agakishiev *et al.*, Eur. Phys. J. A **48**, 64 (2012).

[2] G. Agakishiev *et al.*, Phys. Lett. B **715**, 304 (2012).

[3] K. Schmidt *et al.*, Phys. Rev. C **79**, 064908 (2009).

[4] J. Weil *et al.*, Eur. Phys. J. A **48**, 111 (2012).

[5] E. Bratkovskaya *et al.*, arXiv:1301.0786v1 [nucl-th].

[6] P. Tlusty *et al.*, PoS **Bormio2012**, 019 (2012).

*Work supported by EMMI and the IN2P3/GSI agreement

Development of the HADES Electromagnetic Calorimeter *

P. Tlustý[1], *A. Kugler*[1], *Y. Sobolev*[1], *O. Svoboda*[1], *B. Kardan*[2], *T. Galatyuk*[3], *A. Rost*[3], *J. Pietraszko*[4], *E. Bayer*[4], *P. Salabura*[5], *G. Korcyl*[5], *F. Guber*[6], *A. Reshetin*[6], *and A. Ivashkin*[6]

[1]Nuclear Physics Institute of ASCR, Rez, Czech Republic; [2]Goethe-Universität, Frankfurt; [3]TU Darmstadt, Darmstadt; [4]GSI, Darmstadt; [5]Smoluchowski Institute of Physics, Jagiellonian University of Kraków, Poland; [6]Institute for Nuclear Research, Russian Academy of Science, Moscow, Russia

The electromagnetic calorimeter (ECAL) for the HADES experiment is currently under design[1]. The ECAL will replace the Pre-Shower detector located at forward angles $18° < \theta < 45°$ and allows to measure neutral meson (π^0 and η) production, which is essential for the interpretation of dilepton data, but up to now unknown in heavy-ion reactions in the energy range of the planned FAIR experiments at SIS100. An additional advantage of such a upgrade would be the improvement of the electron/pion separation at large momenta ($p > 400$ MeV/c).

The ECAL will consist of 978 modules divided in six trapezoidal sectors. Each module will based on lead-glass modules (obtained on loan from the OPAL experiment at CERN) assembled with photomultiplier (PMT) and highvoltage-divider in a housing construction (see Fig. 1).

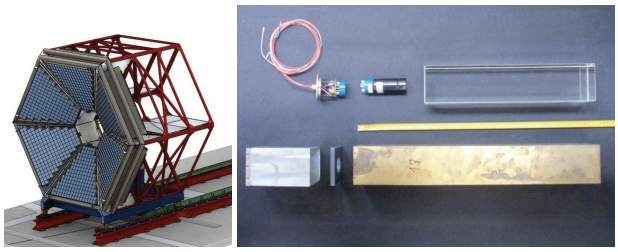

Figure 1: Schematic drawing of the ECAL detector (left) and construction parts of one module (right).

EMI 1.5inch PMT (9903KB) were tested with small scintillator and gamma source to sort out those with low gain or defect ones. Since there will be not enough EMI PMT, 130 Hamamatsu 3inch PMT (R6091) were ordered and 65 of them were already delivered. Performance of modules equipped with the two different types of PMTs are comparable (see Fig.2). Special housing for these photomultipliers were developed, manufactured and successfully tested. Own high voltage dividers were designed and mounted. First tests show that their properties are comparable with original Hamamatsu HV dividers.

For stability-monitoring a light distribution system based on common blue LED light source is foreseen. Totally 15 modules equipped with optical fiber were assembled and tested both with LED light and cosmic muons.

The readout of ECAL will be based on TRB3[2] boards and dedicated frontend-electronics (FEE). Prototype FEE were designed and manufactured at Jagiellonian University

* Supported by Czech MSMT (LG12007), GAAS (M100481202) and BMBF (06FY9100I and 06FY7114), HIC for FAIR, EMMI and GSI.

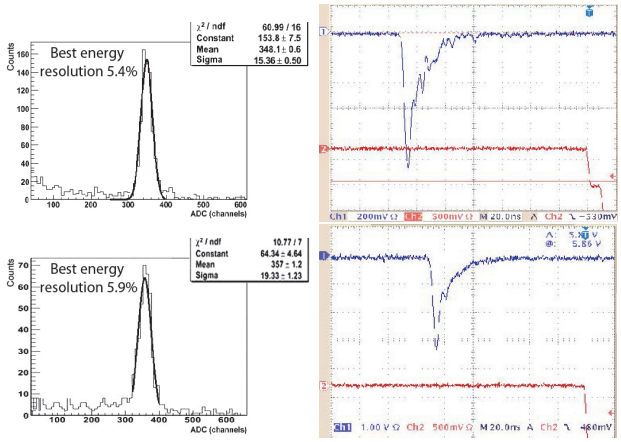

Figure 2: Best measured energy resolution with cosmic muons with EMI 1.5inch PMT 5.4% (top) and Hamamatsu 3inch PMT 5.9% (bottom). right: PMT signal (blue) and trigger signal (red).

of Cracow and intensively tested with a HADES-like DAQ based on TRB2 for time measurement (TDC) and Shower-Addon board for amplitude measurement (ADC). The trigger signal was processed in a central trigger system board (CTS) and distributed to the ADC and TDC boards. The current version of the FEE has eight input channels, separated outputs for time and amplitude and is powered by 5V. The threshold for time signal can be set separately for each of the eight channels. The FEE were tested in detail with pulser- and PMT-signals from LED-light and cosmic muons and modified at GSI Darmstadt to optimize the energy resolution.

New FEE are in developement based on the idea of charge digitisation in FPGAs[3]. The concept is to use a QDC by implementing a modified Wilkinson ADC. The width of the digital pulse is measured using a FPGA-TDC, delivering the time measurement of the leading edge as well as the charge encoded in the width of the pulse.

References

[1] W. Czyzycky et al.: Electromagnetic Calorimeter for HADES, arXiv:1109.5550

[2] C Ugur et al.: 2012 JINST 7 C02004, doi:10.1088/1748-0221/7/02/C02004

[3] C Ugur et al.: 2013 JINST 8 C01035, doi:10.1088/1748-0221/8/01/C01035

Status of the CBM Experiment at FAIR*

P. Senger and the CBM Collaboration
GSI, Darmstadt, Germany

The Compressed Baryonic Matter (CBM) experiment is designed to explore the QCD phase diagram in the region of high net-baryon densities using novel diagnostic probes. The layout of the CBM detectors is driven by the experimental requirements concerning reaction rates, radiation tolerance, particle densities, and selectivity. The experimental setup comprises the following components.

The superconducting dipole magnet
In 2012 the design of the CBM SC dipole magnet has been optimized. The magnet is of H-type with circular superconducting coils and with two cryostats (see figure 1). It has a large aperture (gap height 140 cm, gap width 260 cm) in order to host the Silicon Tracking System. The field integral is 1 Tm. The Technical Design Report has been submitted to FAIR in December 2012.

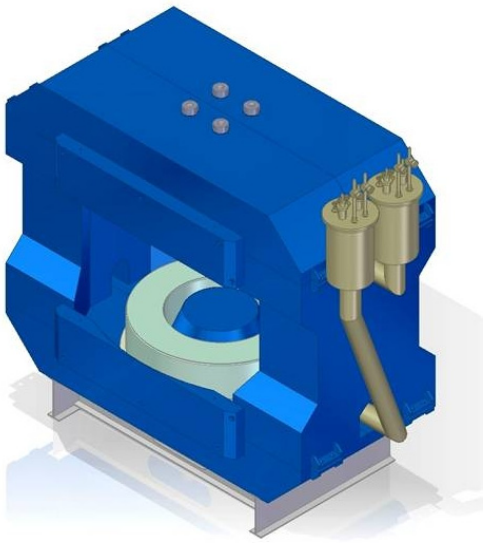

Fig.1: The CBM Superconducting Dipole Magnet.

The Micro-Vertex Detector
The precise determination of the secondary decay vertices of charmed particles requires a highly-granulated, fast, radiation-hard, and low-mass detector system. We will use silicon pixel stations which are based on ultra-thin "Monolithic Active Pixel Sensors" (MAPS). Sensors have been developed which exhibit a high signal-to-noise ratio even after an integrated neutron dose of 10^{13} n_{eq}/cm^2. Prototype detectors comprising sensors, a read-out-system, a cooling and support structure have been successfully tested with a 120 GeV pion beam at CERN.

The silicon tracking system
The CBM Silicon Tracking System (STS) is based on double-sided micro-strip sensor with outer dimensions of 6.2x2 cm^2, 6.2x4 cm^2, and 6.2x6.2 cm^2. The front side strips are inclined by a stereo angle of 7.5°. Short strips in the sensor corners will be interconnected to a strip in the opposite corner either via a second metallization layer, or via an additional micro-cable. Both options are under investigation. Each sensor (2048 strips) is read out via 16 low-mass micro cables (128 wires each) by 8 free-streaming ASICs (2 channels each). The cables will be tab-bonded at both ends. Several of these modules consisting of a sensor, the cables and the Front-End-Board carrying 8 ASICs will be mounted on a light-weight carbon ladder. Up to 16 of these ladders will be integrated into a detector station. The STS consists of 8 stations of increasing size and increasing granularity with increasing distance from the target (see figure 2). The STS will be operated in a thermal enclosure at about -10°. The Technical Design Report has been submitted to FAIR in December 2012.

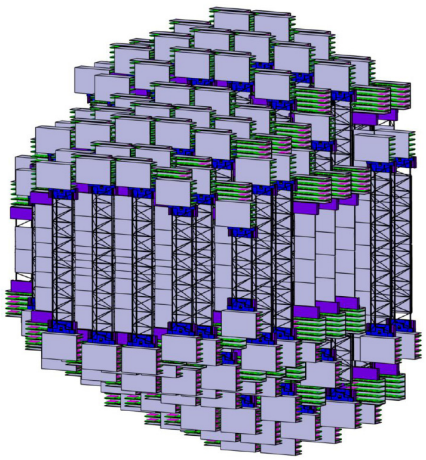

Fig.2: The CBM Silicon Tracking system

The Ring Imaging Cherenkov (RICH) detector
The RICH photo-detector exhibits an active area of 2.4 m^2 covered by multi-anode photomultipliers (MAPMTs).
Beam tests at GSI and CERN, and measurements with LEDs in the laboratory demonstrated that the Hamamatsu H8500 with 64 pixels is very well suited for the detection of single Cherenkov photons. Properties like the quantum efficiency (with and without wavelength shifting films), crosstalk and the performance of MAPMTs in the presence of magnetic fields have been successfully studied in 2010. The MAPMT signals were read-out with the self-triggered electronics using the nXYTER chip.

*Supported by the Hessian LOEWE initiative through the Helmholtz International Center for FAIR (HIC for FAIR), and by EU/FP7 Hadronphysics3

The Transition Radiation Detector
The CBM Transition Radiation detector (TRD) has to provide an electron/pion suppression factor of the order of 100 for momenta above 1 GeV/c at hit rates of 100 kHz/cm^2. A pion suppression factor of 100 (corresponding to a pion efficiency of 1 %), together with an electron efficiency of better that 90%, can only be achieved with 9 -12 layers of TRD chambers, resulting in an overall detector area of almost 1000 m^2. Several prototype detectors have been developed to fulfil the requirements. Prototype fast multi-wire chambers with and without drift section read-out by the self-triggered SPADIC chip have been developed. Moreover, a two-dimension position sensitive prototype TRD with diagonally split rectangular (i.e. triangular) read-out pads has been built. All prototype TRDs were successfully tested at CERN using a mixed beam of electrons and pions.

The Muon Detection System
In order to identify the soft muons from vector meson decays in a large combinatorial background the CBM we will use an instrumented hadron absorber. The detection system comprises 6 iron slabs of varying thickness from 20 cm to 100 cm, with detector triplets behind each iron absorber. The technology of the gaseous muon tracking detectors is matched to the hit density and rate: behind the first and second hadron absorber (particle density up to 500 kHz/cm^2) we will install Gas Electron Multiplier (GEM) Detectors. Prototype GEM detectors with single-mask foils have been successfully tested with particle beams at CERN. Further downstream, where the hit density is reduced, straw-tube detectors will be used. Full size prototype straw-tube detector modules have been built and tested.

Timing Multi-gap RPCs
An array of Multi-gap Resistive Plate Chambers (MRPCs) will be used for hadron identification via TOF measurements. The TOF wall covers an active area of about 120 m^2 and is located about 6 m downstream of the target for measurements at SIS100, and at 10 m at SIS300. The required time resolution is of the order of 80 ps. For 10 MHz minimum bias Au+Au collisions the innermost part of the detector has to work at rates up to 20 kHz/cm^2. Prototype MRPCs built with low-resistivity glass have been tested with a time resolution of σ = 40-60 ps at 20 kHz/cm^2. At small deflection angles the pad size is about 5 cm^2 corresponding to an occupancy of below 5% for central Au+Au collisions at 25 AGeV. In order to optimize the number of gaps, the pad layout, and the read-out electronics several prototype MRPCs have been tested with particle beams at CERN. At large polar emission angles, i.e. in most of the active area of the CBM ToF detector, the hit rate is of the order of 1 kHz/cm^2. At these low rates, a conventional MRPC in multi-strip configuration with thin standard float glass can be used. For this application, a fully differential prototype MRPC has been built and tested successfully at COSY with a proton beam.

Online Event selection
Measurements with high event rates require online event selection algorithms (and hardware) which reject the background events (which contain no signal) by a factor of 100 or more. The event selection system will be based on a fast on-line event reconstruction running on a high-performance computer farm equipped with many-core CPUs and graphics cards (GSI GreenIT cube).

Table 1: CBM subsystems, their status, and time of TDR submission

Subsystem	**Status**	**TDR**
Magnet	Design ready	Dec. 2012
Micro-Vertex Detector (MVD)	successful prototype tests with beams	2014
Silicon Tracking System (STS)	Design ready, successful prototyp tests with beams	Dec. 2012
Ring Imaging Cherenkov Detector	Design ready, successful prototyp tests with beams	Spring 2013
Time-of-Flight wall (Multi-gap RPCs)	Prototype MRPCs successfully tested with beams	2013
Transition Radiation Detector (TRD)	Prototype TRDs successfully tested with beams	2014
Muon Tracking Chambers (MUCH)	Prototype MUCH successfully tested with beams	End of 2013
Projectile Spectator Detector (PSD)	Design ready, established technology	Spring 2013
Electromagnetic Calorimeter (ECAL)	Design ready, established technology	2013/14
DAQ/FLES	Prototype tests with beams	2013 - 2016

Prototyping the CBM Micro-Vertex Detector (MVD).*

M.Koziel for the CBM-MVD collaboration
Institut für Kernphysik, Goethe-Universität, Frankfurt

This report will summarize the goals and achievements of the beam tests performed with the CBM-MVD CVD-diamond based, double-sided prototype.

The need for prototyping and characterizing the CBM-MVD motivated the construction of an ultra-low mass, high precision detector setup incorporating several prototype stations. Each station consists of a "core module", that is two 50-µm thick MIMOSA-26 CMOS pixel sensors [1] adhesive-bonded to a mechanical support ensuring heat evacuation and wire-bonded to the dedicated Flex Print Cable. Three mechanical supports were used: 1-mm thick aluminium with openings, a 200-µm thick CVD Diamond with and without (double-sided module) openings. The openings are 16.5×8.2 mm^2 in size and located in the middle of an active area of the MIMOSA-26 sensor. Modules with openings ensure stable mechanical support with minimum material budget of 0.05% X_0 (Si only) at the region of openings. The double-sided unit features a material budget of 0.3% X_0 (Si + adhesive + CVD).

Figure 1: CDV diamond support with openings to reduced the material budget.

The detector setup discussed here incorporates four single-sided reference stations and one double-sided station in the middle which is called a Device Under Test (DUT) and serves for both, a high-precision stand-alone tracking device as well as a test site for advanced integration concepts, with the focus on high-performance materials (e.g., CVD diamond). In addition, the full setup allows for validating the customized and scalable readout system design together with dedicated data analysis tools.

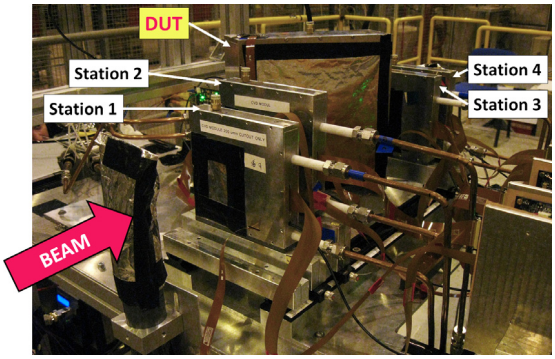

Figure 2: The IKF detector setup installed at CERN-SPS extraction (EHN1-North Area).

The beam test was ongoing for five days in November 2012 (at the CERN-SPS H6 extraction line) highlighting several aspects, as described in the following.

To validate our concepts regarding sensor integration and read-out the main focus was given at reproducing the test-beam results achieved with MIMOSA-26 sensors by the IPHC-Strasbourg: A detection efficiency of $>99.5\%$ and spatial resolution of about 3.5 µm (σ) were observed for an average fake hit rate[1] of about 10^{-5}, very well in accordance with the previously known sensor characteristics.

The precise knowledge about the sensor response to charged particles needed to address proper simulations of the CBM detector motivated the beam-test runs taken for different inclination angles (0°, 30°, 45°, 60°), beam energies (10, 80 and 120 GeV) as well at various DUT-heat-sink temperatures (-6°C, +6°C, +17°C) and threshold voltages of the pixel discriminators housed by the chip. This analysis is on-going, based on a precise alignment of the single-sided stations.

Since the double-sided CVD-diamond based prototype was designed to serve as a precise micro-tracking device, some test runs with a metal target in front of the DUT were addressed.

The MIMOSA sensors have never been tested at running condition imposing the high sensor occupancy. Since such conditions are expected at the CBM experiment, tests at high beam intensities were addressed. The average flux was expected to be at about 10 hits/frame but due to the beam non-uniformity about 300 hits/frame are expected for some frames.

Simultaneously to data taking, it was possible to monitor the data quality and stability of the readout system. A typical frame rate was 8.68 kHz corresponding to the data rate of 6 – 25 MB/s for the whole telescope (12 sensors running in parallel). The readout system was observed to be very stable for different data load generated by ten working in parallel MIMOSA-26 sensors. An absence of lost or corrupted frames was observed. Moreover, sensors were synchronized with precision of one signal clock.

The developed beam setup allowed studying different aspect related to sensor behavior needed for further simulations as well as proved the DAQ flexibility and mechanical stability. The results obtained for different detector setups and for various sensors parameters and running conditions are considered as very successful. The data analysis is in progress and announces gaining further insights in sensor operation and integration concepts.

[1] C. Hu-Guo et al.: http://dx.doi.org/10.1016/j.nima.2010.03.043

* Work supported by GSI, BMBF (06FY9099I), ULISI (EU-FP7), and HIC for FAIR.

[1] The fake hit rate is defined as the average number of fake hits per pixel per frame.

Mechanical Integration of the CBM MVD Prototype*

T. Tischler, S. Amar-Youcef, M. Deveaux, M. Koziel, C. Müntz, C. Schrader, and J. Stroth for the CBM-MVD Collaboration

Institut für Kernphysik, Goethe-Universität, Frankfurt

The need of prototyping and characterizing the CBM-Micro Vertex Detector (MVD) motivated the construction of an ultra-low mass, high precision detector setup comprising several stations. This setup aims at validating the detector concept (Figure 1 a) and selected technologies. The setup - one double-sided and four single-sided stations - was successfully tested at CERN SPS in November 2012.

Geometry

Served by a customized data acquisition for the sensor read-out, each station contains two (single-sided station) or four (double-sided station) 50 µm thick thinned CMOS sensors (MIMOSA-26 AHR [1]). The sensors are glued to 200 µm thin CVD diamond [2] carriers which provide at the same time a mechanical support and efficient heat evacuation. The setup allows for different distances between the single-sided stations, for different incident angles of the beam to the double-sided station, and for temperature cycling in a range between -20 ℃ and $+20$ ℃. The double-sided station - the ultra thin, stand alone tracking device with a material budget of $0.3\%X_0$ - represents the prototype and is closest to the MVD geometry. Its active sensor area covers $1/4$ of the active sensor area of the final detector. However, the relative position of the front- and back-side sensors focus on stand alone tracking (rather than on maximum acceptance). The four single-sided stations are serving as reference system also demonstrating the scalability of the read-out system. In contrast to the double-sided station, the CVD diamond carriers of the single-sided stations provide cut-outs in the major part of the active area of the sensors to achieve a minimum material budget for reference system of $0.053\%X_0$ per station.

Integration methods and tools

The integration of the 50 µm thick thinned sensors calls for dedicated customized pick-up and positioning tools. The mechanical and thermal connection between the sensors and their carriers is realized with a low viscosity glue E501 - from Epotency. The thickness of the deposited glue has been evaluated to be less than 50 µm. The electrical connectivity between a dedicated FlexPrint-Cable (based on copper-traces [3]) and the sensors is established via wire bonding. The wire bonds were encapsulated with Sylgard 186 - a soft, silicon-based elastomer - to be protected against mechanical damage while handling.

*Work supported by the GSI Helmholtzzentrum für Schwerionenforschung, BMBF (06FY9100I and 06FY7114I), HIC for FAIR, H-QM Helmholtz Research School.

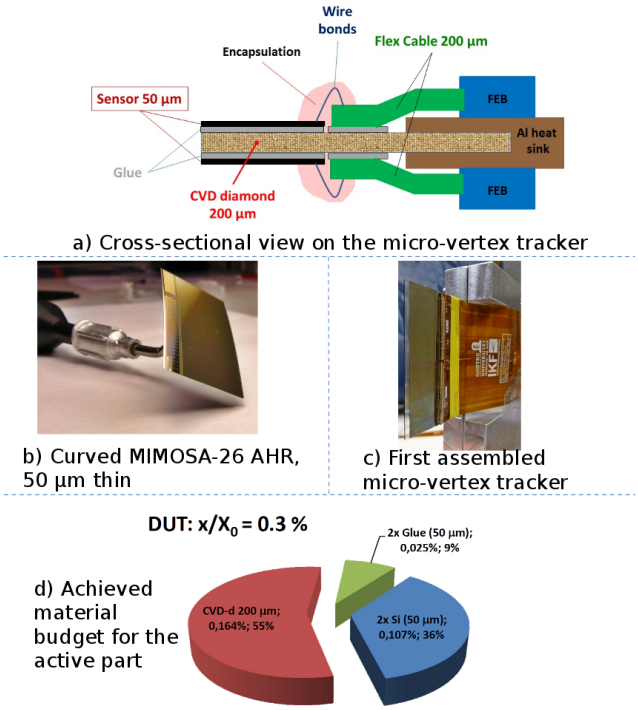

Figure 1: Mechanical integration - overview

Results

For the first time, a detector station in a **double-sided** arrangement was realized with two 50 µm thick thinned sensors glued on each side of a 200 µm thin CVD diamond carrier, see Figure 1 c). The active area of the sensors is chosen to be overlapping to allow for mirco-tracking with a fixed distance forming a double-sided, ultra thin tracking device with a thickness of $0.3\%X_0$, Figure 1 d).
The reference stations provide precision tracking with a minimum material budget of $0.053\%X_0$ per station.
The preliminary analysis of the recorded data results a spatial resolution of the double-sided station of < 4µm with a detection efficiency $> 99.8\%$.

References

[1] MIMOSA-26, DOI: 10.1016/j.nima.2010.03.043.

[2] T. Tischler et. al , GSI Scientific Report 2010.

[3] C. Schrader et. al , GSI Scientific Report 2011.

Beamtime Results of the MVD Prototype DAQ Network*

B. Milanović, B. Neumann, M. Wiebusch, S. Amar-Youcef, M. Koziel, T. Tischler, Q. Li, I. Fröhlich, M. Deveaux, C. Müntz, and J. Stroth

IKF, University Frankfurt, Germany

Recently, the MVD Prototype has been developed at the IKF in Frankfurt. The module contains one quarter of the first MVD station featuring 4 thinned MIMOSA-26AHR sensors on CVD support. The prototype has been tested at the CERN SPS accelerator in 2012.

The CBM Micro Vertex Detector (MVD) is based on Monolithic Active Pixel Sensors (MAPS). In order to prove its suitability for upcoming experiments, the MVD-Prototype has been developed and tested during a beamtime at the CERN SPS accelerator with high energetic pion beams of varying intensity. The prototype (Device Under Test, DUT) features four MIMOSA-26AHR MAPS sensors thinned down to 50 μm and glued back-to-back on the 200 μm thick CVD diamond support. It features therefore doublesided MAPS sensors with excellent heat conductivity, material budget and non-ionizing radiation hardness. The test setup intended to demonstrate tracking capabilities of the MVD. Therefore the DUT was placed between four reference detector planes (see Fig. 1, left) containing MIMOSA-26AHR sensors as well.

The sensors are operated via JTAG which is implemented on a central controller board called MVD Acquisition and Interaction Node (MAIN). The MAIN board is capable of controlling three independent JTAG chains with up to 6 MIMOSA sensors (tested). In total 12 sensors are used in the setup, 4 per chain. Specialized Front-End Electronics (FEEs), designed to sustain large radiation doses, were used to operate the sensors. Sensors are connected via short Flexprint Cables (FPCs) to the FEEs and the FEEs are all connected with RJ45 cables over patch panels either to the MAIN board or the Readout Controllers (ROCs) (see Fig. 1). The ROCs are responsible for the actual acquisition of data. Each ROC can process 4 sensors in parallel. Sensor data is checked online for errors and a status report containing all the errorbits is written with the data. For the implementation of the MAIN board and the ROCs a TRBv2 board [1] with a general purpose addon is used. Data is encoded using TrbNet [1] as a network protocol and transmitted via optical links.

One single MIMOSA-26AHR chip can produce up to 20 MB/s data at full occupancy. It can theoretically detect up to 342 particles per event at an event rate of 8,68 kHz and under the asumption that each hit activates an area of 3×3 pixels. However, the datarate throughout the beamtime was very low. Even after achieving maximum beam intensity of 33 kHz, the entire setup featuring 10 active sensors produced 25,1 MB/s on average, half of which was noise. Peak sensor occupancy was at 75 particles per event. After putting four sensors manually into saturation mode, the peak readout rate of 98 - 99 MB/s could be achieved. Under overload, the network synchronizes all frames by stopping the data buffers. New data is discarded until all buffers can take another event. Then, the data acquisition continues in a synchronous manner without errors. All sensors are synchronized within 10 ns due to a common clock and simultaneous *start* signal provided by the MAIN board.

All power supplies, FPGAs and sensors have been controlled and monitored actively. An automated PERL script acquired data from 244 TrbNet registers and stored them in a local ASCII file for error analysis. Throughout the beamtime, no errors have been observed. The system was running very stable at all times. Merely two FEE boards had to be replaced due to mechanical damage. In future, a new ROC based on TRBv3 will be implemented in order to support CBMNET and higher readout rates for the final MVD.

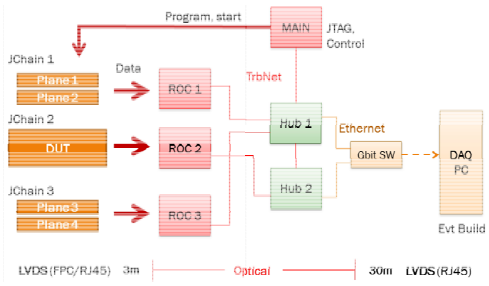

Figure 1: The prototype readout network

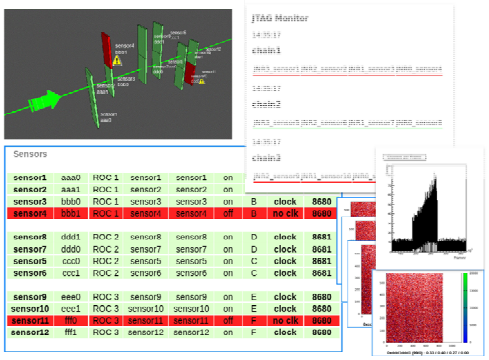

Figure 2: Beamtime DAQ monitoring tools

References

[1] J. Michel, "Development and Implementation of a New Trigger and Data Acquisition System for the HADES Detector", PhD Thesis, University Frankfurt, 2012.

* Supported by BMBF grants 06FY9099I and 06FY7113I

Online data processing with the CBM-MVD prototype*

Q. Li, S. Amar-Youcef, M. Deveaux, C. Müntz, and J. Stroth for the CBM-MVD Collaboration

Institut für Kernphysik, Goethe-Universität, Frankfurt, Germany

The CBM Micro Vertex Detector (MVD) will have to handle high data rates and occupancies, which calls for efficient data processing. We study the option to complement the on-chip zero suppression of the CMOS sensors by an online cluster finding and classification. The aim is to exploit the computing resources of the FPGAs controlling the sensors without increasing the network bandwidth needed for the consecutive data transport.

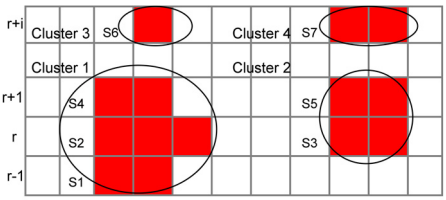

Figure 1: Clusters encoded in states

Our study relies on the MIMOSA-26AHR (M26) CMOS sensors [1] known from the MVD prototype. These sensors host digital circuits for data sparsification, which group up to four consecutive fired pixels in a line into a so-called state. This shape information is encoded together with the column number of the first pixel into a 16-bit word. Separate data words are needed to indicate the line number of the group. Fig. 1 shows an example of four hit clusters comprising seven states (S1-S7) and four states for line information (not shown). In the example, one requires 11 words of 16 bit to encode four clusters. In general, the precise number of states depends on the detector occupancy and the cluster shape.

Our strategy for data pre-processing is to perform an FPGA-based cluster finding and to fit each of the resulting clusters into a single 32-bit word. As 22-bits are needed for position information, 10-bits remain for encoding the cluster shape. This space is insufficient to encode the pixels bit-wise. Therefore, it was considered to attribute a unique shape code to a given cluster shape. Provided, the total number of different cluster shapes found in the MVD data remains below 1024, this concept allows for a lossless encoding of the experimental data.

To test this approach, the cluster finder was implemented in C++ and tested with data from CBMRoot simulations and experimental data obtained from the beam test of the MVD prototype in Nov. 2012 at the CERN-SPS. The six stations of the prototype allowed for a precise tracking of the traversing high energy pions and hence, for selecting high-purity tracks and clusters. Data on the shape of the clusters was recorded for various sensor temperatures, inclination angles, and discriminator thresholds. Fig. 2 presents preliminary results on the dependence of the mean number of fired pixels per cluster as a function of inclination angle for three different applied discriminator thresholds. In general, the number of pixels in a cluster is smaller than known from earlier studies (see for example [2]). This is due to the more efficient charge collection mechanism found in the partially depleted active volume [3] of the novel sensor. Fig. 3 shows the cluster shape distributions and the eight most frequent cluster shapes. Only substantially less than 0.01% of all measured clusters (the ones with ShapeCode=0) could not be encoded with the shape code algorithm proposed.

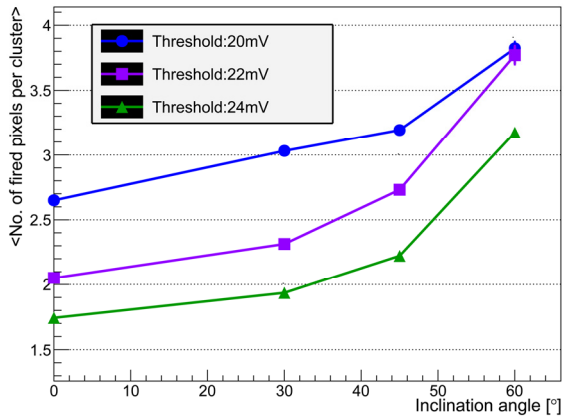

Figure 2: Mean cluster size

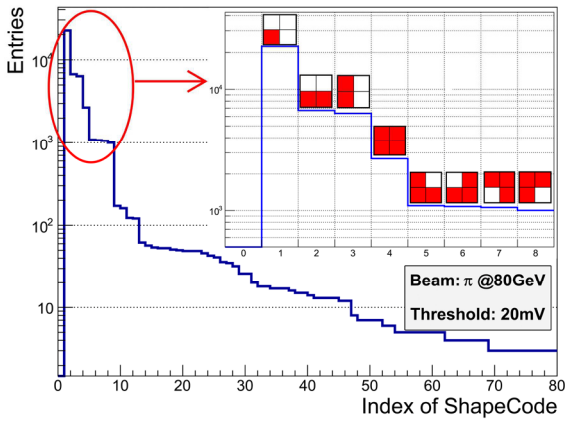

Figure 3: Cluster shape distribution

Both preliminary results are in favour of the strategy proposed. Still, the analysis of the experimental data remains to be completed and simulations are needed to confirm the conclusion for the higher occupancies of the real MVD. Hereafter, the algorithm will be encoded on FPGA.

*Work supported by GSI, BMBF (06FY9100I and 06FY7114I), HIC for FAIR, and H-QM Helmholtz Research School.

References

[1] C. Hu-Guo et al., NIM-A 623, P. 480-482 (2010)
[2] C. Dritsa et al., POS(BORMIO2010)015
[3] A. Dorokhov et al., NIM-A 624, P. 432-436 (2010)

Radiation tolerance of a CMOS Monolithic Active Pixel Sensor produced in an $0.18\mu m$ CMOS process*

D. Doering[1], *J. Baudot*[2], *M. Deveaux*[1], *M. Goffe*[2], *S. Senyukov*[2], *J. Stroth*[1], *and M. Winter*[2]
[1]Institut für Kernphysik, Goethe University Frankfurt, Germany; [2]IPHC Strasbourg, France

So far CMOS active pixel sensors (MAPS) matched the requirements of CBM in terms of spatial resolution and material budget. During several years, their radiation tolerance has been adapted to the needs of this experiment. In 2012, the radiation tolerance of a sensor, produced in an 0.18 μm CMOS process was tested. It could be demonstrated that this sensor provides the radiation tolerance required for CBM at SIS-100.

In a first step, the tolerance of MAPS to non-ionizing radiation was improved by more than one order of magnitude. This was reached by partially depleting the active volume of the sensors [2, 3]. Still, the tolerance of the sensors to ionizing radiation remained to be improved. This was done by migrating a simple imager sensor from the established 0.35 μm process to an 0.18 μm process. It was hoped that this would allow for exploiting the known higher intrinsic radiation tolerance of deep sub-micron CMOS processes. Besides providing benefits in terms of radiation tolerance, the 0.18 μm process comes with additional features which are expected to allow for a better time resolution of the device.

To explore the new technology, three different prototypes named MIMOSA-32 (V1-3) were designed by the PICSEL group of the IPHC and tested in the laboratory and at the CERN-SPS.

Each flavor of MIMOSA-32 is composed of arrays of 32 different pixels with various parameters, which were put to study selected pixel parameters in a systematic way. To perform radiation tolerance studies, some of the sensors were irradiated with combined non-ionizing and ionizing doses of $10^{13}\ n_{eq}/cm^2$ and 1 Mrad. Those radiation doses match the design requirements of CBM running at SIS-100[1].

After being irradiated, the sensors were tested by the PICSEL group at the CERN-SPS. Some results for the particularly unfavorable running conditions of $T > +15\ ^\circ\mathrm{C}$ and for relatively high pixel pitches of $20 \times 40\ \mu m^2$ are shown in figure 1. The non-irradiated sensor shows an excellent detection efficiency of $\gtrsim (99.78 \pm 0.08)\%$ independent of the operation temperature. The detection efficiency of the irradiated sensor keeps a very good detection efficiency of $(98 \pm 0.3)\%$ at even $T = +30\ ^\circ\mathrm{C}$. When operating the sensors with a slight cooling at $T = +15\ ^\circ\mathrm{C}$ this detection efficiency raises to $\gtrsim (99.5 \pm 0.3)\%$.

This work was complemented at IKF with studies exploring the properties of the sensor at higher ionizing doses of up to 10 Mrad. The gain shrinks slightly about 5% after 3 Mrad, while the noise of the sensor remains mostly constant. After a dose of 10 Mrad, the gain of the sensor is reduced by a factor of two and the noise raises by about 40%, which is not yet fully understood. The signal-to-noise ratio of this sensor was measured with a Sr-90-source and found to remain above 30 (Most Probable Value). This appears sufficient for obtaining a satisfactory detection efficiency for minimum ionizing particles.

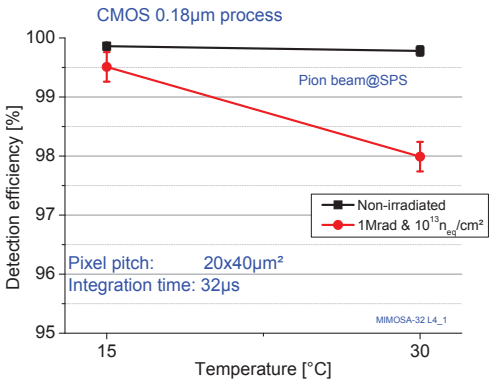

Figure 1: Detection efficiency of elongated pixels at a coolant temperature of $T = +15\ ^\circ\mathrm{C}$ and $T = +30\ ^\circ\mathrm{C}$ before and after irradiation ($1\ \mathrm{Mrad} + 10^{13}\ \mathrm{n_{eq}/cm^2}$).

We conclude MAPS manufactured in an 0.18 μm CMOS process combined with a high-resistivity epitaxial layer provide the radiation tolerance required by the micro-vertex-detector of CBM at SIS-100. Moreover, there are first evidences that the technology might also match the higher needs of CBM at SIS-300. While this conclusion appears robust for simple imagers, it remains to be confirmed for the more complex sensors with integrated data processing circuits.

References

[1] M. Deveaux. Status of the MVD - Getting prepared for SIS-100, 2011. CBM Collaboration Meeting Beijing.

[2] A. Dorokhov et al. Imp. rad. tol. of MAPS using a depleted epi layer. *NIM A* , 624(2):432–436, 2010.

[3] M. Deveaux et al. Rad. tol. of a column parallel cmos sensor with partially depleted sensitive volume. *NIM A* , 583(1):134 – 138, 2010.

*This work has been supported by the BMBF (06FY9099I and 06FY7113I), HGS-HIRe, HIC for FAIR and GSI.

Full-size silicon microstrip sensors for the CBM Silicon Tracking System*

J. M. Heuser[1], *C. J. Schmidt*[1], *J. Eschke*[1], *S. Chatterji*[1], *W. Niebur*[1], *W. F. J. Müller*[1], *P. Senger*[1], *C. Sturm*[1], *C. Simons*[1], *D. Soyk*[1], *T. Balog*[1,2], *A. Lymanets*[3,4], *I. Sorokin*[5,4], *M. Singla*[5], *P. Ghosh*[5], *Y. Murin*[6], *M. Merkin*[7], *V. M. Borshchov*[8], *M. Protsenko*[8], *and I. Tymchuk*[8]

[1]GSI, Darmstadt, Germany; [2]Comenius University, Bratislava, Slovakia; [3]Eberhard Karls University, Tübingen, Germany; [4]Kiev Institute for Nuclear Research, Kiev, Ukraine; [5]Goethe University, Frankfurt, Germany; [6]JINR, Dubna, Russia; [7]Moscow State University, Moscow, Russia; [8]SE SRTIIE, Kharkov, Ukraine

The layout of the CBM Silicon Tracking System foresees the application of double-sided microstrip sensors in three sizes. All sensors have the same width of 6.2 cm, matching the width of the detector ladders that build up the tracking stations, and are segmented into 1024 strips of 58 μm pitch. The sensor heights, essentially corresponding to the strip lengths, are 6.2, 4.2 and 2.2 cm, depending on the position of the sensors within the tracking stations. Sensors close to the beam line, which are exposed to the highest track densities, have the shortest strip length. Towards the periphery of the STS, sensors with longer strips, even daisy-chained sensors can be used still yielding small enough particle hit occupancies for efficient pattern recognition. A first series of silicon microstrip sensors in all three sizes has been designed in 2012. Their profiles are shown in Fig. 1. The projects, conducted in close cooperation of GSI (*CBM05, CBM05H4*) and JINR (*CBM05H2s*) complement the previous prototyping activities [1] in terms of design optimization towards the emerging silicon detector module structure, and high production yield. They will yield tested pre-series prototypes in 2013.

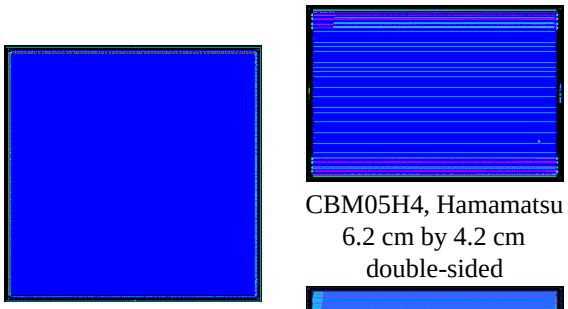

CBM05, CiS
6.2 cm by 6.2 cm
double-sided

CBM05H4, Hamamatsu
6.2 cm by 4.2 cm
double-sided

CBM05H2s, Hamamatsu
6.2 cm by 2.2 cm
single-sided

Figure 1: Prototype microstrip sensors, *CBM05* family.

Full-size prototype CBM05

The largest of the three sensors is currently in production at CiS [1]. It is a p-in-n type double-sided sensor of 300 μm thickness with a 7.5° stereo angle between front and back side strips. Strips of the corner regions of the stereo side are interconnected through lines on a second metal layer so that their full read-out can be achieved from one edge. The complex sensor structure was optimized based on the good results with a similar single-sided technology sensor *CBM03'* built in 2012.

Full-size prototype CBM05H4

The mid-size sensor is being realized in parallel with Hamamatsu Photonics. Since 2011, Hamamatsu offers again the fabrication of double-sided sensors. With *CBM05H4* we realize a double-sided sensor with double-metal interconnecting lines in the complementing dimensions 6.2 cm by 4.2 cm. The layout of the sensor is essentially identical to the *CBM05* layout, including a double metal layer on the p-side.

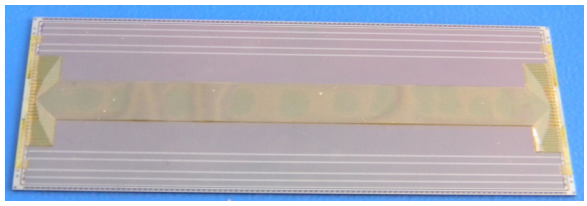

Figure 2: Microcable replacing the second metal layer mounted on a mockup of sensor *CBM05H2s*.

Full-size prototype CBM05H2s

The small prototype sensor is also developed in cooperation with Hamamatsu. The objective is to realize a sensor with minimum complexity to study an alternative for the double-metal interconnection layer. Its layout has no second metal layer but pads for the attachment of a separate microcable fulfilling the same function as the lines otherwise integrated into the sensor. The microcable is designed and produced at SE SRTIIE. A mock-up of the sensor fitted with its on-chip cable are shown in Fig. 2. The final sensor will be also produced as a double-sided structure.

References

[1] GSI Scientific Reports 2009 70, 2010 21 and 2011 34

[2] http://www.cismst.de

[3] http://www.hamamatsu.com

* Work supported by BMBF and EU-FP7 HadronPhysics3.

Design options for radiation tolerant microstrip sensors for the CBM Silicon Tracking System (STS)*

S. Chatterji[1], *M. Singla*[2], *W.F.J. Müller*[1], *and J.M. Heuser*[1]
[1]GSI, Darmstadt, Germany; [2]University of Frankfurt, Germany

The expected neutron fluence for the CBM STS is 1×10^{14} $n_{eq}cm^{-2}$, after which an upgrade of sensors is foreseen. The main impact of radiation damage is the loss in the charge collection efficiency (CCE) limited by the breakdown voltage V_{bd}. Also we aim to minimize the capacitive noise. The dominant contributor to the capacitive noise comes from the interstrip capacitance C_{int}. To summarize, we aim to develop microstrip detectors having low C_{int}, high V_{bd} and maximum CCE.

Fluence Profile

Table 1 shows the expected neutron fluence for five years of required CBM runtime. In this table, the initial resistivity of silicon has been taken to be 5.33 KΩ-cm,the lifetimes of electrons τ_e and holes τ_h have been calculated using Kramberger's model [1] assuming an operating temperature of -10^0C. One can observe a deterioration of carrier life time with fluence which will have an impact on the CCE, especially on the p-side since this side collects less mobile holes.

Table 1: Fluence profile of neutrons for the CBM STS.

Year	Fluence (n_{eq} cm^{-2})	N_{eff} (cm^{-3})	τ_e (ns)	τ_h (ns)	V_{fd} (V)
1	2×10^{13}	2.8×10^{11}	1140	1050	28
2	4×10^{13}	-1.54×10^{11}	570	527	20
3	6×10^{13}	-5.35×10^{11}	380	351	44
4	8×10^{13}	-8.84×10^{11}	285	263	75
5	1×10^{14}	-12.1×10^{11}	228	211	100

Strip Isolation

In order to investigate the life time of sensors, it is imperative to extract the CCE as a function of fluence for which one has to understand the strip isolation in particular on the ohmic side. Hence various isolation techniques have been explored both through prototyping as also through simulations, for example P-stop, P-Spray, Modulated P-spray (conventional isolation techniques) and also a new isolation technique, the Schottky barrier. Schottky barrier can be defined either through metal work function value or through barrier height which in turn depends on the substrate type and the metal used for Schottky contact. For Aluminum, the barrier height is 0.72 eV for n-type silicon while for p-type silicon, the barrier height is 0.58 eV [2]. A comparison of the conventional isolation techniques with Schottky barrier in terms of V_{bd}, C_{int} and CCE is shown in Table 2. One can infer that the Schottky barrier is the best choice in terms of V_{bd} and C_{int}. However in terms of CCE, the Schottky barrier gives the worst performance especially after type-inversion. Therefore, Schottky barrier has not been opted as a suitable isolation technique. Besides P-stop and P-spray, another isolation technique namely modulated P-spray has also been explored. An optimization of modulated P-spray has been performed. It has been found that using a moderate P-stop width of around 15 μm and very low P-spray concentration of around 1×10^{15} $n_{eq}cm^{-3}$ gives the best performance in terms of V_{bd} and C_{int}, referred to as Optimized Modulated P-spray in Table 3. Finally a comparison of P-stop, P-spray and Optimized Modulated P-spray after one year of operation and the maximum fluence expected at the end of five years of CBM run is shown in Table 3. One can notice from this table that using Optimized Modulated P-spray, the V_{bd} has increased by around 60% and C_{int} has reduced by 25% while maintaining the same CCE as with conventional isolation techniques. In Tables 2 and 3, V_{bd}, C_{int} and CCE are simulated values confirmed with measurements. Hence Optimized Modulated P-spray is the best choice for isolation technique in terms of V_{bd}, C_{int} and CCE.

Table 2: Comparison of conventional isolation techniques with Schottky barrier.

Isolation Technique	Fluence (n_{eq} cm^{-2})	V_{bd} (V)	C_{int} (pF cm^{-1})	CCE %
P-stop	3.93×10^{12}	1010	2.1	91.25
	20.60×10^{12}	890	2.29	86.25
P-spray	3.93×10^{12}	524	2.6	93
	20.60×10^{12}	450	2.7	86.25
Schottky	3.93×10^{12}	1450	2.05	79
Barrier	20.60×10^{12}	1350	1.80	77.5

Table 3: Comparison between p-stop, p-spray and optimized modulated p-spray at low and high fluence.

Isolation Technique	Fluence (n_{eq} cm^{-2})	V_{bd} (V)	C_{int} (pF cm^{-1})	CCE %
P-stop	2×10^{13}	980	2.02	93.15
	1×10^{14}	720	2.03	88.87
P-spray	2×10^{13}	513	2.56	93.17
	1×10^{14}	495	2.44	89
Opt. Mod.	2×10^{13}	1600	1.58	93.22
P-spray	1×10^{14}	1150	1.60	89

References

[1] V.Cindro et. al., *IEEE Trans. Nucl. Sci.* N09-2, pp.139-142, 2006.

[2] http://www.pfk.ff.vu.It/lectures/funkc_dariniai/diod/schottky.htm.

* Supported by EU-FP7 HadronPhysics3 and HICforFAIR

Quality assurance tests of silicon microstrip sensors for the Silicon Tracking System in the CBM experiment at FAIR

P. Larionov[1] *and P. Ghosh*[1]
[1]Goethe Universität, Frankfurt am Main, Germany

The Compressed Baryonic Matter (CBM) experiment aims to explore the QCD phase diagram in the region of high net baryonic densities and moderate temperatures. The core of the CBM experimental setup — the Silicon Tracking System — will consist of 8 stations based on double-sided silicon strip sensors and self-triggered read-out. It will have to cope with large track densities and event rates up to 10^7 s^{-1}, will have to enable high momentum resolution and detection efficiency as well as stand radiation doses up to 1×10^{14} n_{eq}/cm^2.

A large amount of sensors (about 1400) will be required to construct the STS. For the proper operation of the system, each sensor requires a number of procedures to ensure proper production and to verify the full accordance to the technical specifications. Local laboratory tests are as important as verification of the technical specifications provided by the manufacturer. These tests will ensure that the sensors will be suitable for the STS detector and will satisfy its requirements. Both these two procedures define Quality Assurance for the Silicon Tracking System, which includes visual inspection, bulk and interstrip parameters measurements, sensor efficiency and total signal to noise ratio tests, measurements of irradiated sensors, low temperature performance and current stability tests. In the following, we report on QA tests of STS prototype sensors with 256 strips per side, 300 μm thickness and 58 μm strip pitch [1].

Bulk measurements — current-voltage (I-V) and capacitance-voltage (C-V) characteristics (see Figure 1) — can serve as basic acceptance criteria. These measurements are a good instrument to assess the quality of the sensor, to verify the manufacturer data and to make sure there has been no damage during sensor manufacturing or handling.

Also, some passive electrical characteristics were measured for different strips of the sensor. These measurements aim to investigate the charge collection and the equivalent noise charge of the sensor. The value of coupling capacitance (Figure 2) allows to judge about the transmission of the signal. The ratio of coupling and interstrip capacitances affects the value of the signal transmitted to the read-out electronics. For these measurements the wafer prober Süss-PA300 was adapted in the clean room with temperature and humidity control.

Figure 3 indicates the variation of current-voltage curves for sensors that were irradiated with different fluences. As a part of QA, these measurements were carried out to investigate the sensor's behavior and perfomance after irradiation.

Future QA activities for STS include long-term stability tests, low temperature performance measurements and optimization of the measurement procedures via LabView software.

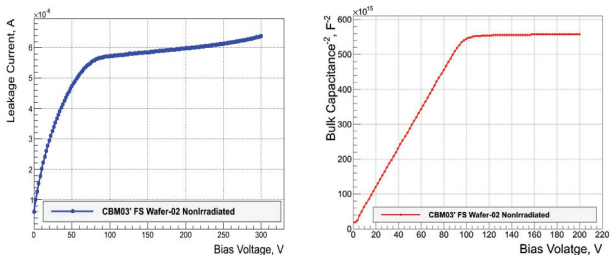

(a) (b)

Figure 1: Bulk measurements: a) current-voltage; b) capacitance-voltage.

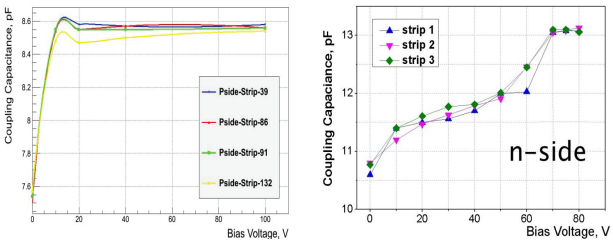

(a) (b)

Figure 2: Coupling capacitance measurements: a) p-side of the sensor; b) n-side of the sensor.

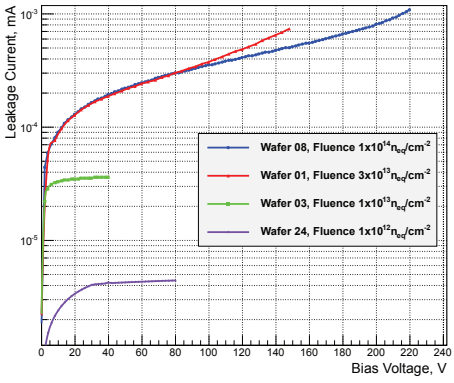

Figure 3: Current-Voltage curves for irradiated sensors.

References

[1] J. M. Heuser *et al.*, CBM Progress Report 2011, Darmstadt 2012, p.17

Characterization of double sided silicon micro-strip sensors with a pulsed infra-red laser system for the CBM experiment*

Pradeep Ghosh† [1,2] *and Jürgen Eschke*[2,3]

[1]Goethe-Universität, Frankfurt am Main, Germany; [2]GSI Darmstadt, Germany; [3]FAIR GmbH, Darmstadt, Germany

The Silicon Tracking System (STS) of the Compressed Baryonic Matter (CBM) experiment at FAIR is composed of 1292 double-sided silicon micro-strip sensors. For the development and the quality assurance of produced sensors a laser test system has been built up. The main aim of the sensor scans with the pulsed infra-red laser system is to determine the charge sharing between strips and to measure the uniformity of the sensor response over the whole active area. The prototype sensors CBM02 tested so far with the laser system have 256 strips with a pitch of 50 μm on each side [1]. They are read out by the self-triggering n-XYTER prototype read-out electronics.

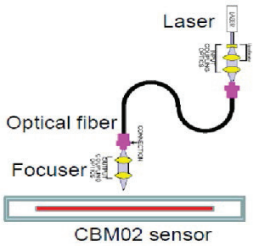

Figure 1: Schematic representation of the laser setup.

The laser system is intended to measure the sensor response in an automatized procedure at several thousand positions across the sensor with focused infra-red laser light ($\sigma_{spotsize} \approx 15$ μm). The duration ($\sim$5 ns) and power (few mW) of the laser pulses are selected such that the absorption of the laser light in the 300 μm thick silicon sensors produces about 24k electrons, which is similar to the charge created by minimum ionizing particles (MIP) there.

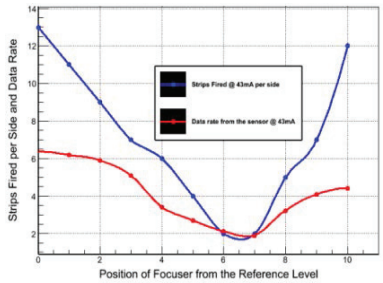

Figure 2: Dependence of number of fired strips on the distance to focuser from the sensor surface.

The wavelength of the laser was chosen to be 1060 nm because the absorption depth of infra-red light with this wavelength is of the order of the thickness of the silicon sensors [2]. Figure 1 shows the measurement setup in a schematic view. The laser light is transmitted through a 6 μm (inner diameter) thick optical fibre to a two-lens focusing system, which focuses the light to a spot size of about 15 μm diameter; working distance is about 10 mm. Figure 2 shows the dependence of the number of fired strips as a function of the distance of the laser to the sensor surface. The best focusing was obtained at position 7 w.r.t the reference level.

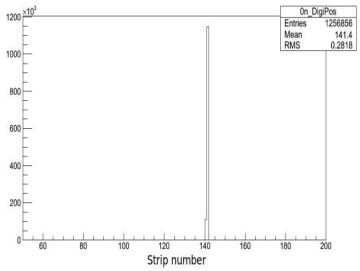

Figure 3: Distribution of hits per strips on n-side.

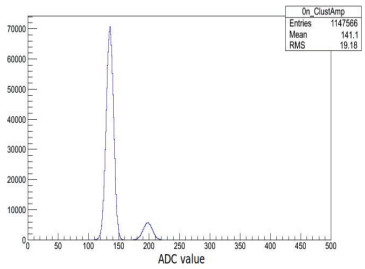

Figure 4: ADC amplitude distribution (n-side).

We have illuminated a prototype sensor with a focused pulsed laser and could achieve a spot size of a little more than one strip [See Figure 3]. The preliminary results demonstrate that we are successful in inducing charge similar to 1 MIP (24k electrons). Figure 4 shows that the number of single-strip clusters is about an order of magnitude higher than that of two-strip clusters. The next step of our work will be to investigate the charge sharing function between the strips.

References

[1] J.M. Heuser *et al.*, CBM Progress Report 2011, Darmstadt. 2012 p.17

[2] P.O'Connor *et al.*, Proc. of SPIE Vol. 6276 62761W-1, p.2

* Work supported by HGS-HIRe, H-QM and HIC-for-FAIR

† Pr.Ghosh@gsi.de, Tel. +49-6159-71-2586

Signal transmission in low-mass readout cables for the CBM Silicon Tracking System *

M. Singla[1,2], *S. Chatterji*[2], *W.F.J. Mueller*[2], *V. Kleipa*[2], *and J.M. Heuser*[2]
[1]Goethe University, Frankfurt; [2]GSI, Darmstadt, Germany

Readout cables will bridge the distance between the microstrip sensors and the electronics placed at the periphery of the tracking stations. Since the length of cables can reach up to 50 cm for the inner modules, it is very important to extract the expected transmission losses in the cables as this will be reflected in the signal/noise ratio. Mixed-mode simulations have been done to assess transmission loss in cables. The mixed-mode capability of Sentaurus Device (subpackage of SYNOPSYS) [1] allows for the simulation of a circuit that combines any number of Sentaurus devices of arbitrary dimensionality (1D, 2D, or 3D) with other devices based on compact models (SPICE).
To study the impact of input pulse frequency, square pulses are injected through the sensor and the output pulse is seen at the end of the cable. Figure 1 shows the impact of input pulse frequency on the output pulse. For higher frequencies, the signal amplitude decreases and the pulse broadens at the input of the front end electronics which may lead to charge loss depending on the RC time constant of the readout chip shaper. The decrease in signal amplitude may lead to lower threshold which could result in more noise again depending on the RC time constant of the integrator. Secondly, the pulse broadening may lead to the charge loss if we use fast electronics, i.e. a short shaping time of the preamplifier. One can notice pile up effect at higher frequencies. Pile-up effect is when the second pulse arrives relatively early and rides on the falling tail of the first pulse. Also a baseline shift can be observed for higher frequency pulse output. For example, in Figure 1(b) the baseline shift is around 18% of the input pulse amplitue (0.6×10^{-7}). In our calculations, baseline corrections have been taken into account.

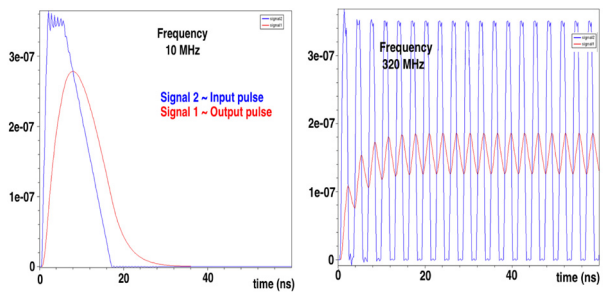

(a) (b)

Figure 1: Dependence of transmission losses on input pulse period using mixed-mode simulation: (a) 100 ns, (b) 3.13 ns.

For validation of the transmission (dB) loss determined using mixed-mode simulations, dB loss in a CBM prototype cable with aluminum traces has been measured using a Vector Network Analyser [2]. Figure 2(a) shows the comparison of measured values with simulations up to 240 MHz. The simulated data match with measurements withing 5% error thus validating the simulation approach. In simulations, continuous attenuation with frequency can be seen since the readout cable acts as a low pass filter. Figure 2(b) shows the dependence of transmission loss on the length of the cables. Simulation and measurements match well. A mathematical model for the dependence of transmission loss on the length of cables has been extracted.
The transmission losses increase with frequency and length of the cable. Also for the frequency range of interest for the present prototype front-end chip in the fast shaper mode (25 MHz), the transmission is expected to be around 85% for a 30 cm long cable.

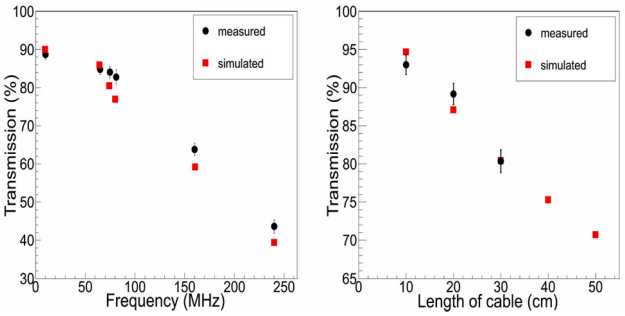

(a) (b)

Figure 2: (a) Comparison of measured transmission coefficient with simulations for a CBM prototype readout cable of length 30 cm; (b) dependence of transmission loss on the length of cables.

References

[1] http://www.synopsys.com/home.aspx.

[2] http://www2.rohde-schwarz.com/product/ZVA.html
Vector Network Analyzer. 10Hz/9KHz...4GHz . ZVRE

* Supported by EU-FP7 HadronPhysics3 and HICforFAIR

Transconductance calibration of n-XYTER 1.0*

I. Sorokin[1,2], *T. Balog*[3,4], *V. Krylov*[5], *and C.J. Schmidt*[4]

[1]Goethe University Frankfurt a.M., Germany; [2]KINR, Kiev, Ukraine; [3]Comenius University, Bratislava, Slovakia; [4]GSI, Darmstadt, Germany; [5]Kyiv University, Ukraine

Motivation

Since long, the n-XYTER 1.0 [1] has been used as a prototype readout chip for the Silicon Tracking System (STS), the muon and Cherenkov detectors of the CBM experiment. Transconductance calibration of the n-XYTER was already reported [2]. However, it was done with only one channel of one chip, only at one polarity and without thermal stabilization of the chip. An inconsistency between this calibration and results of measurements with various microstrip detectors done by the CBM-STS group [3] necessitated to repeat the calibration thoroughly.

Calibration setup

To generate reference charge pulses, voltage steps were applied to the n-XYTER input over a capacitor. The injected charge in this case is $C \cdot \Delta V$. The voltage steps were generated with an ordinary laboratory pulser and attenuated down to the millivolt level with passive attenuators. In order to minimize the systematic error the actual attenuation factors were measured with high precision, and also their independence of the freqency was checked. The capacitance (including parasitics) was also measured precisely (1.051±0.001 pF). As a cross-check, the calibration of one channel was repeated with a capacitor of a different type and value, and a good agreement was observed.

Finally, the independence of the n-XYTER response of the width of the injected pulse was checked (as expected, observed roughly up to 50 ns).

The n-XYTERs were operated on front-end boards rev. D, with thermal stabilization and in conjunction with a 12-bit ADC (AD9228, dynamic range –1..1 V).

Results

The calibration was done on 3 chips and 42 channels at negative polarity and 10 channels at positive. Within the same polarity the data from all channels were combined and fitted with a 4^{th} order polynomial (Fig. 1). The results are[1]:

$$Q_- = 0.2025 + 2.053 \cdot 10^{-2} \cdot A - 6.733 \cdot 10^{-6} \cdot A^2 + \\ +1.324 \cdot 10^{-8} \cdot A^3 - 3.566 \cdot 10^{-12} \cdot A^4$$

$$Q_+ = 0.3966 + 1.921 \cdot 10^{-2} \cdot A + 2.603 \cdot 10^{-6} \cdot A^2 - \\ -1.062 \cdot 10^{-8} \cdot A^3 + 1.227 \cdot 10^{-11} \cdot A^4$$

where $Q_\pm$ is the input charge in fC, and A is the n-XYTER output amplitude in ADC LSB (least significant bit).

A straight-line fit in the linear range (0–700 LSB) yields:

$$Q_- = 0.07757 + 0.02051 \cdot A = 0.07757 + 1.002 \cdot 10^{-2} \cdot U$$

$$Q_+ = 0.3718 + 0.01960 \cdot A = 0.3718 + 9.573 \cdot 10^{-3} \cdot U$$

Here U — is the n-XYTER output amplitude in mV.

The dominant contribution to the calibration uncertainty comes from the fact that a single calibration curve is applied to all channels, even though they have slightly different gains. This uncertainty was parametrized with a 2^{nd} order polynomial w.r.t. the amplitude and estimated by requiring that it compares to the dispersion of the data. Because of the small number of data points at positive polarity the uncertainty was assumed to be the same for both polarities (ΔQ in fC, A in ADC LSB):

$$\Delta Q = 0.1 - 4 \cdot 10^{-4} \cdot A + 1.4 \cdot 10^{-6} \cdot A^2$$

Cross-check with a Si-detector and a γ-source

As a cross-check against possible systematic errors a planar silicon detector was connected to one n-XYTER channel, and the amplitude corresponding to the 59.6 keV line of ^{241}Am was measured (114 ADC LSB). According to the calibration of the same channel, the amplitude corresponds to a charge of 2.57 fC, which is in a very good agreement with the expected value of 2.64 fC (2.7 % difference).

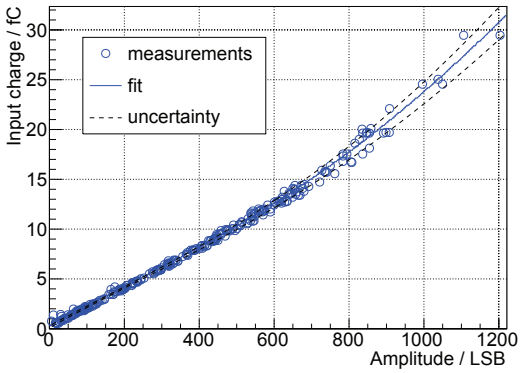

Figure 1: n-XYTER calibration at negative polarity.

References

[1] A.S. Brogna et al., Nuclear Instruments and Methods in Physics Research Section A 568 (2006) 301–308

[2] GSI Scientific Report 2009 84, Darmstadt 2010

[3] GSI Scientific report 2010 26, Darmstadt 2011

* Work supported by HIC for FAIR, HGS-HIRe and H-QM

[1]Parameter values were not rounded because their uncertainties were not calculated. Instead the total uncertainty will be specified below.

STS-XYTER a prototype silicon strip detector readout chip for the STS

P. Grybos[1], *K. Kasinski*[1], *R. Kleczek*[1], *P. Otfinowski*[1], *and R. Szczygiel*[*1]
[1]AGH-UST, Krakow, Poland

The STS-XYTER prototype readout ASIC for the CBM STS detector was designed in 2012. It is a full size prototype dedicated for signal detection from the double-sided microstrip sensors in the CBM environment. The self-triggering ASIC provides both timing and energy information for each incoming signal in its channels.

The chip includes 128 channels. The input current pulse from the detector is processed by the charge sensitive amplifier (CSA). The signal path is then split into a fast and a slow one (Fig. 1). The fast path includes a fast shaper with a typical shaping time of 30 ns, a discriminator and a timestamp latch. It is optimized to provide good timing resolution (<10 ns). The slow path consists of a slow shaper with the typical shaping time of 80 ns, a 5-bit flash ADC and a digital peak detecting logic. It is optimized for energy measurement and noise performance.

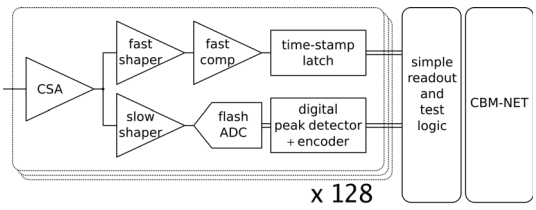

Figure 1: Block scheme of the STS-XYTER chip.

For a particle hit, each channel provides the timestamp and the ADC value corresponding to the deposited charge. Data from the channels are read out using a token-ring structure, controlled by a readout controller. The gathered data are sent out via up to four 500 Mbit/s LVDS serial data links. The data transfer to and from the chip is implemented according to the CBMnet protocol description. The HDL code of the CBMnet-related digital part was provided by ZITI, UNI-Heidelberg [1]. A simplified I2C interface allows to configure the chip without protocol overhead for test purposes. A summary of the most important parameters can be found in table 1.

The essential new feature compared to the n-XYTER architecture is an effective two level discriminator scheme. The discriminator in the fast signal lane triggers the latch of the timestamp at high timing resolution. Because of the higher bandwidth of the fast lane, the noise level and thus the noise related trigger rate is comparatively high in such a self-triggered system if the discriminator level is kept low. The noise-related trigger rate is determined by the Rice formula. If the discrimination level is kept below 3σ, noise-related hits would swamp data channels and create dead time, while if kept too high, the essential low level hits would remain undetected. The two level trigger scheme employed in the STS-XYTER adds a veto to the transmission of data in case the flash ADC has generated "zero". The discrimination level of the LSB is controlled by an internal register and effectively serves as a secondary discriminator that is exposed to the low bandwidth, low noise energy signal. This strategy makes the Rice formula applicable to the signal of the energy channel while keeping the high time resolution achieved from triggering on the fast timing channel.

Table 1: Design parameters of ASIC.

Number of channels	128 + 2 test
Pad / channel pitch	58 μm
Input signal polarity	Positive and negative
Accepted input leakage current	10 nA
ENC @ 30 pF det. capacitance	900 e-
Voltage gain in slow path	25 mV/fC
Voltage gain in fast path	71 mV/fC
ADC range	16 fC
Input clock frequency	250 MHz
Timestamp resolution	<10ns
Power consumption	<10 mV/channel
Operating temperature range	0 °C < T < 40°C
Digital interface standard	4x 500 Mbit/s LVDS

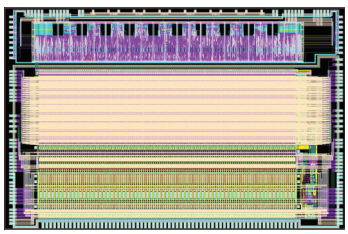

Figure 2: STS-XYTER ASIC layout.

The ASIC was designed using the UMC 180 nm process and was sent for manufacturing in October 2012. The die size is 6.5 mm x 10 mm (Fig. 2). A detector is to be connected via a Kapton cable attached to the ASIC using tab bonding. The power supply, biasing and digital interface pads are designed for wire-bonding. Particularly sensitive elements of the chip were made radiation hard.

References

[1] F. Lemke, D. Slogsnat, N. Burkhardt, U. Bruening, "A Unified DAQ Interconnection Network with Precise Time Synchronization", IEEE Transactions on Nuclear Science (TNS), Vol. 57, No. 2, 2010.

* robert.szczygiel@agh.edu.pl

An assembly concept for modules of the CBM Silicon Tracking System*

C. J. Schmidt[1], *J. M. Heuser*[1], *W. F. J. Müller*[1], *V. Kleipa*[1], *C. Simons*[1], *D. Soyk*[1], *U. Frankenfeld*[1], *V. M. Borshchov*[2], *M. Protsenko*[2], *I. Tymchuk*[2], *and H. R. Schmidt*[3]

[1]GSI, Darmstadt, Germany; [2]SE SRTIIE, Kharkov, Ukraine; [3]Eberhard Karls University, Tübingen, Germany

The functional building block in the layout of the CBM experiment's Silicon Tracking System (STS) is a detector module, definded as the assembly of a single double-sided silicon microstrip sensor or several daisy-chained sensors, micro cables and two front-end electronics boards, one for each sensor side. Various module types will be applied, differing in the sensor arrangement and the length of the read-out cables to the front-end electronics at the top and bottom periphery of the STS. A module is a non-reworkable unit, which in case of failure will need to be replaced as a whole. Due to the thin micro cables it is a very delicate device that can be mounted onto and dismounted from the ladder structure only by means of specialized assembly tools and procedures.

Components

The components of a module as shown in Fig. 1 are:

- Sensor: Double-sided silicon strip sensor with 7.5° stereo angle and 1024 strips of 58 μm pitch per side. One or several daisy-chained sensors of 6.2 cm width and either 6.2, 4.2 or 2.2 cm length are used.
- Microcables: Single-layer Aluminum cables on polyimide carrier, 64 leads at a pitch of 116 μm. Two staggered layers at twice the pitch will be used to connect all sensor channels. Eight doubly-layered cables read out the 1024 channels per sensor side. The total number of cable stacks per module is 16.
- Readout ASIC: The dedicated STS-XYTER chip comprises 128 readout channels.
- Front-end board: A FEB receives eight read-out ASICs and serves 1024 input channels. The digital data from the chips are channeled by the data aggregator HUB chip into four high-speed serial links. Two FEBs are applied per module.

Assembly

The following sequence of assembly steps has been worked out from an analysis of ladder manufacturing options taking into account risk and yield evaluation [1, 2]. The scheme aims to minimize the overall risk, to maximize complete assembly yield and to minimize production costs while avoiding the shift of crucial challenges to later assembly steps. Current work is focused on a detailed refinement of the technological steps and the demonstration of their feasibility.

1. FEB is fully populated with parts including the HUB chip. STS-XYTER chips not yet installed.
2. Tab bonding of first 64-channel micro cable onto the STS-XYTER chip in a dedicated tool followed by a connectivity test.
3. Tab bonding of second 64-channel micro cable onto the STS-XYTER chip; connectivity test.
4. Tab bonding of micro cables with attached read-out chips to the p-side of a sensor; connectivity test.
5. Tab bonding of micro cables with read-out chips to the n-side of a sensor; connectivity test.
6. Installation of first row of four chips to FEB.
7. Wedge-wedge wire bonding of chips to FEB; successive application of glob top.
8. Installation of second row of four chips to FEB.
9. Wedge-wedge wire bonding of chips to FEB; application of glob top.
10. Flipping upside down of module. Repetition of the installation of read-out chips into the second FEB.
11. Functional test of FEBs with connectivity test of the sensor through the micro cables.

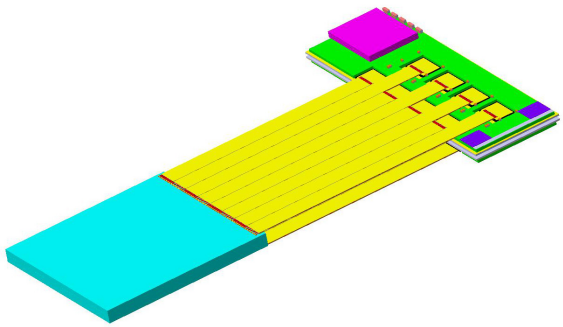

Figure 1: Schematical view of an assembled STS module.

References

[1] Workshop on quality assurance for the CBM Silicon Tracking System, Univ. Tübingen, 14-15 June 2012, `https://indico.gsi.de/conferenceDisplay.py?confId=1621`

[2] Workshop on Module Assembly for the CBM Silicon Tracking System, GSI Darmstadt, 3-7 December 2012, `https://indico.gsi.de/conferenceDisplay.py?confId=2021`

* Work supported by EU-FP7 HadronPhysics3.

Performance of a first prototype module for the CBM Silicon Tracking System*

T. Balog[1,2], *I. Sorokin*[3,4], *and J. M. Heuser*[1]

[1]GSI, Darmstadt, Germany; [2]Comenius University, Bratislava, Slovakia; [3]Goethe University Frankfurt a.M., Germany; [4]KINR, Kiev, Ukraine

The building block of the CBM Silicon Tracking System is a detector module, a functional unit of one or several daisy-chained double-sided silicon microstrip sensors, read-out cables and front-end electronics. Ten modules will be located on a detector ladder. Several ladders build up a STS tracking station [1].

A first prototype module comprises CBM01 double-sided sensor with 1024 channels on both sides. On every side 1/8 of the channels are read out via low-mass cables connected to two front-end boards each hosting one n-XYTER chip.

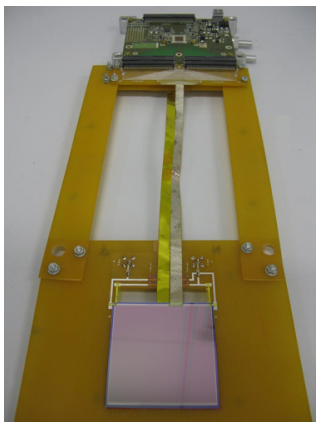

Figure 1: Photo of the prototype module.

Measurements

The noise performance of the system was determined using external triggers where baselines of the read-out electronics were triggered. Main noise source in the strip silicon detectors with cables is interstrip capacitance which was determined for all three prototypres (Table 1). In the analysis the gaussian fits of the baseline distributions were calculated and their standard deviations (σ) taken as a measure of the noise in the channels. According to the n-XYTER ADC calibration the noise is then expressed in equivalent noise charge (ENC) - amount of charge seen by the read-out electronics (Figure 2) [2].

Afterwards the charge collection efficiency for all three demonstrators was measured using a ^{241}Am source with Silicon detector. It's 59.5 keV gamma line corresponds to 114 ADC units. As seen in Figure 3 signal amplitude depends on the length of the cable connected to sensor. Within the measured prototypes the charge collection efficiency was above 85%.

*Work supported by EU-FP7 HadronPhysics3, Helmholtz International Center for FAIR and EU-FP7 MC-PAD.

Length of read-out cable [cm]	Interstrip capacitance [pF]
10 cm	16.5 pF
20 cm	22.1 pF
30 cm	26.8 pF

Table 1: Measured interstrip capacitances of prototypes.

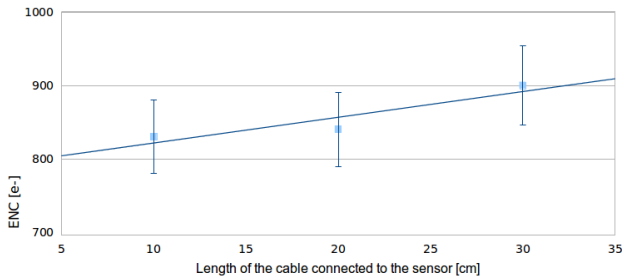

Figure 2: Noise performance of the prototype modules as a function of read-out cable length.

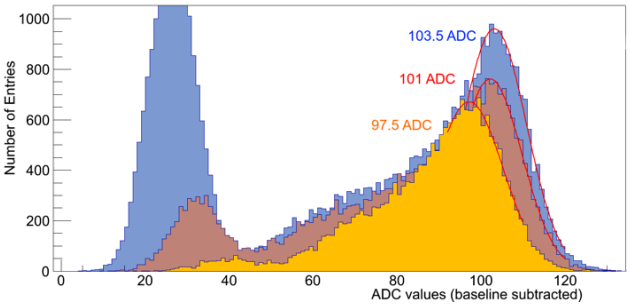

Figure 3: ^{241}Am spectra from the prototype modules.

Conclusion

For efficient track recontruction with the STS the noise of the read-out module is required to be below 4 ke$^-$. The measurements with the prototype module achieved a noise level well below 3 ke$^-$ (measure of 3σ).

According to the measured noise and the charge collection efficiency the expected signal-to-noise ratio for minimum ionizing particle in the prototype modules is above 20.

References

[1] GSI Scientific Report 2011, p.22

[2] I. Sorokin et al.: Transconductance calibration of n-XYTER 1.0, This report

TRACI-XL, the test cooling system for the CBM Silicon Tracking System*

J. Sánchez[1], *J. M. Heuser*[1], *C. J. Schmidt*[1], *P. Petagna*[2], *B. Verlaat*[2], *L. Zwalinski*[2], *and H. R. Schmidt*[3]
[1]GSI, Darmstadt, Germany; [2]CERN, Geneva, Switzerland; [3]Eberhard Karls University, Tübingen, Germany

An evaporative bi-phase cooling system based on CO_2 has been chosen as the best option to extract the heat produced by the read-out electronics in the CBM Silicon Tracking System. In the framework of the EU-FP7 project CRISP, the system TRACI (Transportable Refrigeration Apparatus for CO_2 Investigation), developed at NIKHEF/CERN to provide support to the ATLAS and LHCb experiments, is being upgraded at GSI from 100 W to 1 kW cooling power. This system TRACI-XL will be used as a testing device for the CBM application.

I-2PACL concept applied to TRACI-XL

The I-2PACL principle (Integrated 2 Phase Accumulator Controlled Loop) was created as simplification of the 2PACL systems by using the CO_2 line to condensate the gas inside the accumulator instead of using a branched line derived from the condensing unit. Therefore the control is reduced to one cartridge heater controlled by PLC Siemens Simatic S7-1200. The size of the control unit is decreased and it allows a wider range of possible operating temperatures from -30° C up to room temperature.

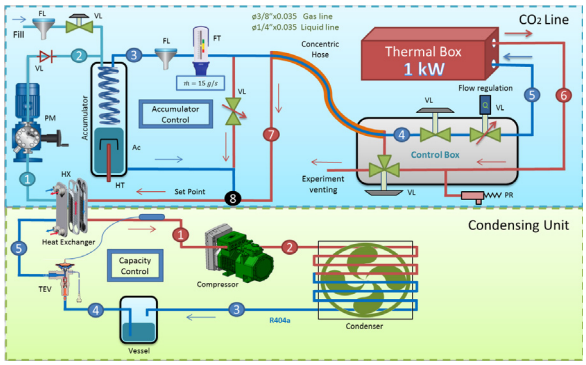

Figure 1: Process diagram of TRACI-XL.

This range is obtained due to the implementation of a condensing unit equipped with a Bitzer 2DC-3.F1Y Varispeed compressor and Swep heat exchanger with a system performance as follows:

- at 30 Hz; Q_0 = 0,55 kW, T_0 =-45° C, $T_{suction}$ = -30° C, T_c = +35° C, T_{sub} = 3 K, R404a.
- at 87 Hz; Q_0 = 1.59 kW, T_0 = -45° C, $T_{suction}$ = -30° C, T_c = +35° C, T_{sub} = 3 K, R404a.

System operation

A LEWA membrane pump with remote head design, as innovation to avoid the addition of residual heat in the coolant, transports sub-cooled CO_2 to the evaporator in the thermal box (1-2-3-4-5 in Fig. **??**). The CO_2 is heated up to the right evaporation temperature by a heat ex-change produced inside an inner hose with the returning CO_2 line (6-7). Due to the pulses generated by the metering pump the installation of a pulsation dampener is needed.

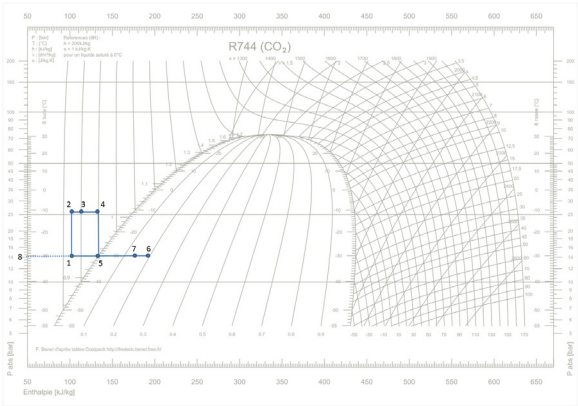

Figure 2: Cycle in Enthalpy-Pressure diagram for R744.

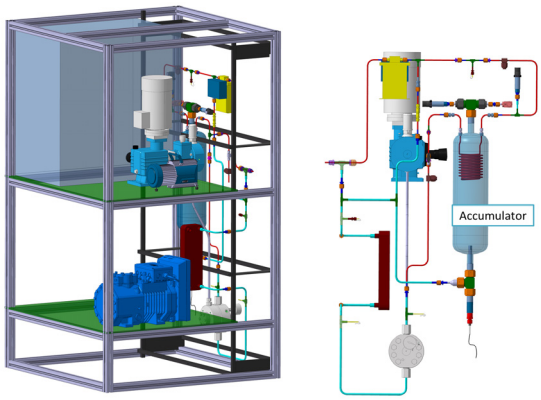

(a) Full model. (b) CO_2 Line.

Figure 3: CAD model with CO_2 line detail.

The heat generated in the read-out electronics is absorbed and extracted by the evaporator capillaries inside the thermal box (5-6). The return line (8-1) contains a bi-phase mixture which is liquefied by the condensing unit named previously below the operating temperature. By controlling the pressure inside an accumulator the evaporation temperature can be fixed. This vessel contains two-phase CO_2 in contact (see Fig. **??**).

References

[1] Verlaat, B., International Conference of Refrigeration 2007, Beijing, China, ICR07-B2-1565

* Supported by EU-FP7 CRISP.

System Integration of the CBM Silicon Tracking System*

U. Frankenfeld[1], *S. Belogurov*[2], *J. Eschke*[3,1], *J.M. Heuser*[1], *V. Kleipa*[1], *P. Koczon*[1], *N. Kolosova*[2], *J. Kunkel*[1], *W.F.J. Müller*[3,1], *J. Sanchez Rosado*[1], *C.J. Schmidt*[1], *H.R. Schmidt*[1,4], *P. Senger*[1,5], *C. Sturm*[1], *and D. Soyk*[1]

[1]GSI, Darmstadt, Germany; [2]ITEP, Moscow, Russia; [3]FAIR, Darmstadt, Germany; [4]Eberhard Karls University, Tübingen, Germany; [5]IKF, Frankfurt, Germany

For the system integration task, a top-down approach has been chosen, starting from the physics requirements of the CBM experiment: interaction rates, radiation environment, tracking aperture and detector segmentation. A functional plan of the STS and its surrounding structural components is being worked out from which the STS system shape is derived and the power need, cooling, the connector and cable space requirements, live span of components, and installation/ repair aspects etc. are determined.

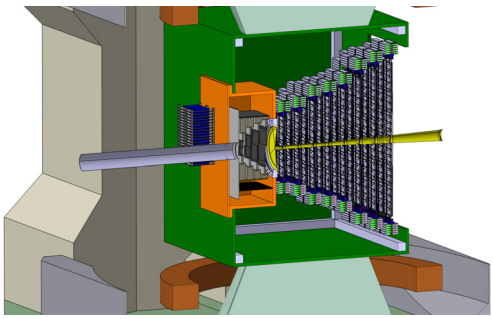

Figure 1: Detailed view of the STS in its envelope, MVD, beam pipe and target

Mechanics

The Silicon Tracking System (STS) of the CBM experiment will be installed into the superconducting dipole magnet, sharing the confined space with the target, the microvertex detector (MVD) and the beam pipe. The STS stations will be surrounded by a thermal enclosure to minimize radiation damage to the silicon sensors. This envelope is the supporting structure for the STS detector as well as for the MVD detector, which is located in its own vacuum vessel, the target and the beam pipe. The MVD vacuum chamber is mounted to the front side of the STS. The MVD detector itself is mounted on a flange, it can therefore be removed without opening the STS volume. The MVD flange also supports the target. Figure 1 shows a sectional view of the STS isolation envelop (green) with the eight half stations of the STS. The beam pipe (yellow) and the MVD vacuum vessel (orange) are integrated into the isolation volume.

The STS envelope will be installed into the magnet from the upstream beam side. It is mounted on rails with prolongations which allow the insertion into the magnet. The position of the rails and the maximum dimensions of the STS envelope are predetermined by the dimensions of the magnet. The dipole magnet is being designed by a separate workgroup. The so called H-type magnet allows STS envelope dimensions to be $1400 \times 2000 \times 1100\,\mathrm{mm}^3$.

Services

All Services like HV, LV, data and monitoring signals and cooling lines will be routed through the front panel into the STS envelope. This allows the dismounting of a half station through the open side panel of the STS box. The exact position will be optimized in order to minimize the interference between the MVD and the STS while dismantling one of the detectors for service work. The services have to be fed through the front panel such that its thermal isolation properties are preserved.

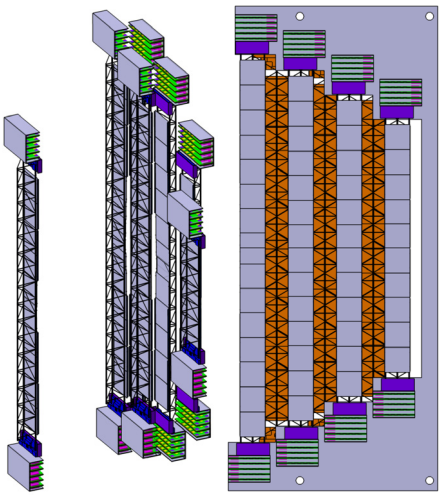

Figure 2: STS ladders assembled to a half station

Installation and maintenance

The installation procedure of the STS will consist of the assembly of ladders equipped with modules (sensors and front end electronic) to a half station (see Fig. 2). The half station will be installed into the STS box. After installation of the services the STS will be inserted into the magnet.

In the case of maintenance it is required to remove the STS, to get access to an arbitrary half station without dismantling the others and then to remove an arbitrary ladder leaving the other ladders in place.

* supported by BMBF, EU-FP7 HadronPhysics3 and CRISP

In-beam test of a prototype CBM Silicon Tracking System at COSY*

J. M. Heuser[1], *W. Niebur*[1], *J. Eschke*[1], *S. Chatterji*[1], *C. J. Schmidt*[1], *W. F. J. Müller*[1], *I. Vassiliev*[1], *V. Kleipa*[1], *C. Simons*[1], *T. Balog*[1,2], *S. Linev*[1], *J. Adamczewski-Musch*[1], *B. Kolb*[1], *P. Zumbruch*[1], *A. Lymanets*[3,4], *I. Sorokin*[5,4], *A. Kotynia*[5], *and H. Malygina*[5]

[1]GSI, Darmstadt, Germany; [2]Comenius University, Bratislava, Slovakia; [3]Eberhard Karls University, Tübingen, Germany; [4]Kiev Institute for Nuclear Research, Kiev, Ukraine; [5]Goethe University, Frankfurt, Germany

In January 2012, a prototype setup of the Silicon Tracking System (STS) for the CBM Experiment has been tested in a 2.4 GeV/c proton beam at the COSY synchrotron of Research Center Jülich, Germany. The experiment aimed at a full-sytem test of prototype detector stations, data acquisition system, detector controls and online monitoring. Hit and cluster finding algorithms were applied to evaluate the performance of neutron-irradiated prototype sensors. A simple track reconstruction algorithm was applied to the data acquired to determine the position resolution of the system.

Experimemtal set-up

The experiment in the JESSICA cave is shown in Fig. 1. It comprised three silicon detector stations and two scintillating fiber hodoscopes for beam monitoring. A further CBM prototype detector for the muon detection system was installed downstream of the silicon stations. All detectors were read out with self-triggering front-end electronics based on the n-XYTER1.0 ASIC that delivered time-stamped digitized analog data to the acquisition system. The two outer silicon stations, operated already in the 2010 beam test [1], included *CBM02* prototype sensors and were used as reference detectors. In the middle station, that could be rotated around the vertical axis to allow for different beam incidence angles, *CBM04* prototype sensors were under test irradiated with neutrons up to the maximum fluence 10^{14} n_{eq}/cm^2 expected in the CBM experiment. The sensors have been described in [2].

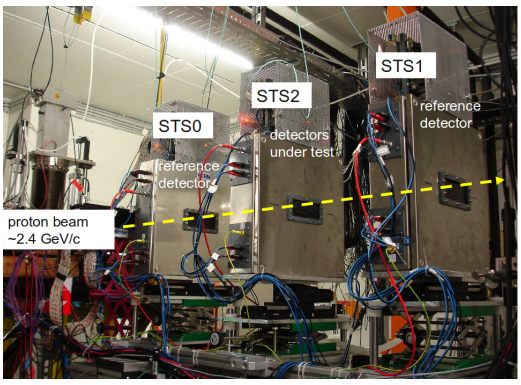

Figure 1: Beam test set-up of the prototype STS.

Results

The amplitude distributions of particle hits in the sensors demonstrated clear separation of the signal from the noise. An example of a strip hit pattern is shown in Fig. 2 (a). With increasing beam incidence angle, the charge spread over clusters of adjacent strips grows as expected, which is shown in Fig. 2 (b). After geometrical alignment of the system a simple track algorithm was applied to selected events with single particle hits, as depicted in Fig. 3. The spatial resolution obtained in both transverse coordinates was of the order of 35 μm for the reference stations, about a factor two worse that expected from the 58 μm strip pitch alone. The resolution of the irradiated sensors was slightly worse. It has to be further investigated how the increased currents with irradiated sensors and thus imposed higher thresholds, and other factors, impact on those results.

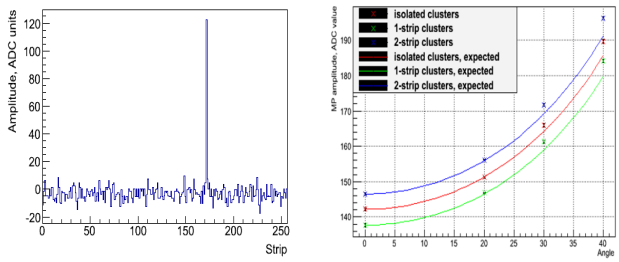

(a) (b)

Figure 2: (a) Example of a single strip fired by a passing proton in a test sensor with 256 strips. (b) Cluster charge as a function of the beam incidence angle.

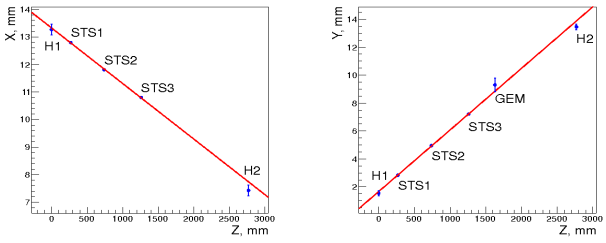

Figure 3: A reconstructed track shown in two projections.

References

[1] GSI Scientific Report 2010 26

[2] GSI Scientific Reports 2009 10 and 2011 34

* Work supported by EU-FP7 HadronPhysics3.

Performance simulations of the CBM-STS with realistic material budget*

V. Friese[1] *and A. Kotynia*[2]
[1]GSI, Darmstadt, Germany; [2]Goethe-Universität, Frankfurt, Germany

The task of the Silicon Tracking System (STS) of the CBM experiment is to reconstruct the trajectories of up to 600 charged particles created in nucleus-nucleus collisions. For the performance of the system, its material budget is a crucial issue since multiple scattering in the detector material will lead to a decrease in both track finding efficiency and momentum resolution. In order to assess these performance figures, a realistic implementation of active and passive materials in the simulations is required.

The system is composed of double-sided micro-strip sensors of 300 μm thickness, which was found to be the best balance between signal-to-noise ratio and material budget. In addition to these active sensors, cables transporting the analog signals from the inner sensors to the read-out at the top or bottom of the system add to the material in the acceptance. Lately, a detailed design of the analog cables was developed [1], which now allows to have a realistic description of the material budget as input to the simulations.

The signals will be transported by two staggered layers of Aluminum cables on polyimide carriers. Each module contributes two of these cable stacks, reading out the front and the back side, respectively. In the simulation geometry, these cables are represented by a single volume of 100 μm silicon (0.11 % X_0) as equivalent material budget. At the vertical periphery of a STS station, up to four of such cable volumes overlap. Consequently, the material budget within one station varies with the vertical distance from the beam; its maximal value is about 0.8 %. As an example, the material budget distribution of station 4 at z = 60 cm is shown in Figure 1.

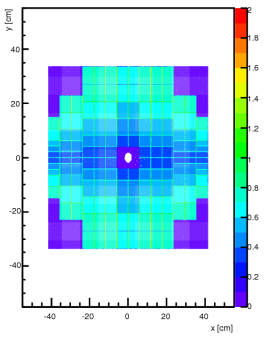

Figure 1: Distribution of material budget in tracking station 4

This model of the STS was implemented in the CBM software framework and subjected to simulations of Au+Au collisions in the CBM detector setup. A realistic detector response was applied as described previously [2]. The tracks were reconstructed by the Cellullar Automaton track finder algorithm; their parameters were determined by the Kalman Filter. The results of these simulations are shown in Fig. 2. The average efficiency for primary tracks above 1 GeV is 96 %, only 1 % less than obtained in previous simulations without the cable materials. Similarly, the efficiency for secondary tracks is hardly affected by the additional material. A more noticeable, but still moderate effect of the cable material is seen in the momentum resolution. Its average value is found to be 0.98 % (Gaussian σ), compared to 0.87 % without cables.

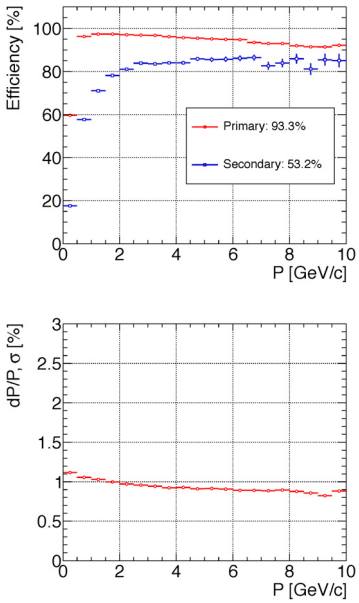

Figure 2: Track reconstruction efficiency (upper panel) and momentum resolution (lower panel) in the STS as a function of the momentum for all tracks in central Au+Au collisions at 25 AGeV projectile energy

In summary, the current simulations of the STS comprise a realistic material budget, including the analog read-out cables. The support structures made of carbon fibre are not yet included, but their contribution to the total material is minor. Within our simulations, we find the track reconstruction efficiency and the momentum resolution to match the CBM requirements. The module concept for the STS can thus be considered validated.

References

[1] C. J. Schmidt *et al.*, *An assembly concept for modules of the CBM Silicon Tracking System*, this report

[2] A. Kotynia and J. M. Heuser, GSI Scientific Report 2010, 22

* Supported by EU/FP7 HadronPhysics2 and Helmholtz International Center for FAIR

Neutron shielding for the CBM silicon tracker

A. Senger[1]

[1]GSI, Darmstadt, Germany

The CBM experiment is designed as a multi-purpose device which will be able to measure hadrons, electrons and muons in heavy-ion collisions. The core detector of the CBM setup is a Silicon Tracking System (STS) located in the gap of a superconducting dipole magnet. Electrons will be identified with a Ring-Imaging Cherenkov Detector (RICH), a Transition Radiation Detector (TRD), and a Time-of-Flight Detector (ToF). In order to measure muons the RICH will be replaced by Muon Tracking Chambers (MuCh). The MuCh consists of 6 hadron absorbers and tracking stations in between. The first 20 cm iron absorber is located 5 cm behind last silicon tracking station. FLUKA [1, 2] calculations predict an increased non-ionizing energy loss (NIEL) level in the STS with the muon setup.

The main reason for the increase of the NIEL level is back-scattered neutrons from the hadron absorber. This was studied with a simple model presented in Figure 1. It consists of the CBM target (250 µm Au foil), the magnet, and the beam pipe. The neutron flux at the position of the last STS station (see scoring plane in Fig. 1) was calculated with and without 20 cm iron absorber. The neutron distributions are shown on Figure 2 (blue and red lines). The number of neutrons increases up to 10 times if the hadron absorber was put in. In order to shield the neutrons from the absorber a borated polyethylene layer was placed between the scoring plane and the iron. The neutron distributions with 5 cm neutron shielding for different fractions of boron are presented in Figure 2 (light blue and green lines). The number of neutrons decreases up to 4 times if a 5 cm 5% borated polyethylene layer was put between the scoring plane and the iron. Figure 3 shows the NIEL distribution in the last STS layer for the electron setup (right), for the muon setup (left), and for the muon setup with the neutron shielding (middle). The NIEL level decreases substantially if the neutron shielding is used.

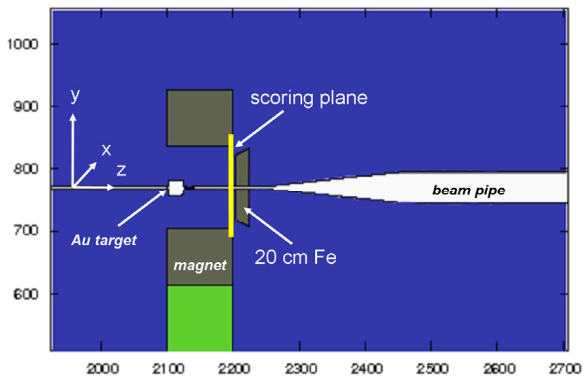

Figure 1: the FLUKA geometry for neutron shielding optimizations.

The FLUKA study demonstrated the possibility to shield neutrons from the iron absorber. The 5 cm 5% borated polyethylene layer allows to reduce the NIEL level in the last STS station by a factor of up to five.

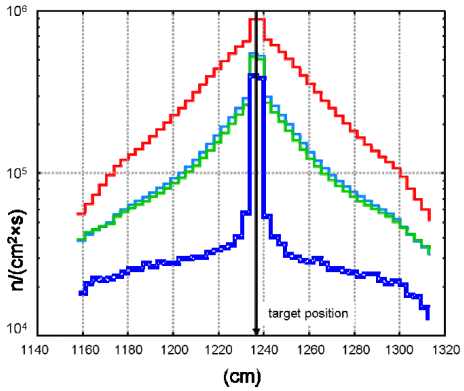

Figure 2: neutron distributions in the position of the last STS station calculated with FLUKA. Blue line – without 20 cm iron absorber, red – in front of the absorber without neutron shielding, light blue – with 5 cm 5% borated polyethylene layer, and green – with 5 cm 30% borated polyethylene.

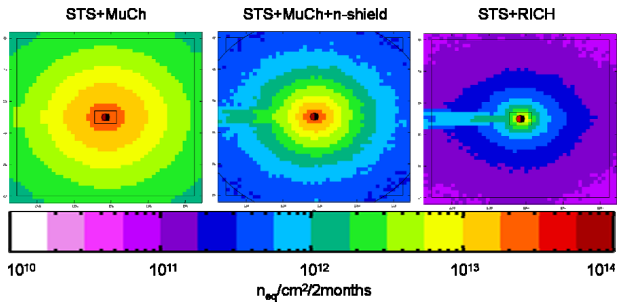

Figure 3: NIEL distributions in the last STS station for 35 GeV/u Au beam after 2 months of run with an intensity of 10^9 ions per second for the electron setup (right picture), for the muon setup with 5 cm neutron shielding (middle), and for the muon setup without shielding (left).

References

[1] "The FLUKA code: Description and benchmarking", G. Battistoni, S. Muraro, P.R. Sala, F. Cerutti, A. Ferrari, S. Roesler, A. Fasso`, J. Ranft, Proceedings of the Hadronic Shower Simulation Workshop 2006, Fermilab 6-8 September 2006, M. Albrow, R. Raja eds., AIP Conference Proceeding 896, 31-49, (2007)

[2] "FLUKA: a multi-particle transport code", A. Fasso`, A. Ferrari, J. Ranft, and P.R. Sala, CERN-2005-10 (2005), INFN/TC_05/11, SLAC-R-773

Crosstalk between neighbouring channels in multianode PMTs *

J. Kopfer[1], *K.-H. Becker*[1], *K.-H. Kampert*[1], *C. Pauly*[1], *J. Pouryamout*[1], *S. Querchfeld*[1], *J. Rautenberg*[1], *and S. Reinecke*[1]

[1]Bergische Universität Wuppertal, Germany

The photo-detector of the CBM-RICH detector is foreseen to be built from multinanode photomultiplier tubes (MAPMTs). The usage of MAPMTs has the advantage of good time and spatial resolution and a very low dark rate. Up to now, R&D was focussed on the Hamamatsu metal channel dynode type PMTs H8500 and R11265. The H8500 has 64 pixels of 5.8 x 5.8 mm^2 each. The R11265 has 16 pixels with the same pixel size. The suitability of the H8500 for single Cherenkov photon detection has been demonstrated in laboratory tests [1] and in beam tests [2, 3].

In a RICH detector the number of registered photons per Cherenkov ring is important for the efficiency of ring finding and the quality of the ring fitting. In order to evaluate the number of registered photons, crosstalk has to be taken into account. There are two different sources of crosstalk: firstly optical crosstalk from the incident light spread in the front window and from photo electrons travelling on a curved trajectory from photo cathode to first dynode and secondly electrical crosstalk from the splitting of the electron avalanche between the dynodes during secondary electron multiplication and on the segmented anodes. Optical crosstalk will mainly cause a smearing of position information and does not influence the number of registered photons whereas electrical crosstalk generates additional hits in the neighbouring pixels.

Crosstalk measurements for the H8500 have already been done by illuminating one pixel with a pulsed 350 nm LED/tungsten lamp with the help of an aperture mask or optical fibre [4, 5]. Here, we present measurements of additional hits caused by crosstalk on single photon level at a wavelength of 275 nm.

The measurement is based on a homogeneous single photon illumination of the MAPMT without usage of an aperture mask or light fibre which has the advantage that the photons hit the pixel not only at the central part but homogeneously distributed over the whole surface as it will be the case in the RICH detector. Single photons hitting the outer parts of a pixel will create more crosstalk than those hitting the centre. Data readout is done as described in [3]. In order to estimate the number of additional hits in neighbouring pixels due to crosstalk, the distribution of the geometrical distance of hits in events with exactly 2 hits per MAPMT (2-hit-events) is compared to a simulation without crosstalk (Fig. 1). The normalized excess of entries in the bin corresponding to direct and diagonal neighbours in the data compared to the simulation quantifies the crosstalk.

* supported in part by GSI project WKAMPE1012 and BMBF grant 06WU9195I

The crosstalk extracted by this method depends on the threshold applied to the ADC signal. Figure 2 shows the additional hit fraction (crosstalk) as function of MAPMT gain for 12 H8500 and 7 R11265. It can be seen that for a common threshold for all MAPMTs the crosstalk rises with gain. This is expected as for high-gain MAPMTs the relatively small ADC values of the crosstalk hits more likely pass the threshold. If, however, individual thresholds for every MAPMT at 10 % of the single photo electron peak are applied, the crosstalk is fairly constant. When averaging the values we see that for H8500 (6.8 ± 1.2) % additional crosstalk hits are found and (3.2 ± 0.7) % for R11265.

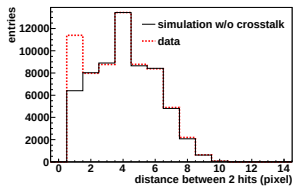

Figure 1: Geometrical distance of hits in 2-hit-events within one MAPMT in simulation (continuous) and data (dashed). Because of crosstalk, simulation and data differ in the second bin (”neighbour bin”).

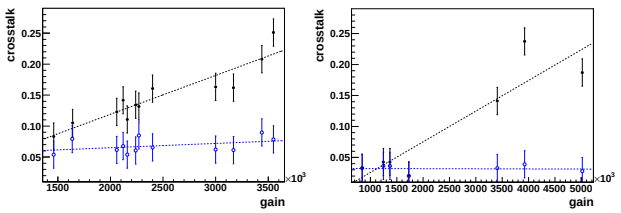

Figure 2: Crosstalk as function of gain for common threshold (filled black circles) and for threshold at 10 % of the single photon peak (open blue circles) for H8500 (left) and R11265 (right). Linear fits to the data are shown as dashed lines. Every data point corresponds to one MAPMT. HV of all MAPMTs was set to the same nominal value of 1000 V.

References

[1] C. Pauly et al., CBM Progress Report 2010, p. 26

[2] J. Eschke et al., CBM Progress Report 2010, p. 24

[3] J. Kopfer et al., CBM Progress Report 2011, p. 32

[4] J. Eschke et al., CBM Progress Report 2010, p. 28

[5] Hamamatsu Photonics K.K., Photomultiplier Tubes: Basics and Applications, Word Technical Writing Inc., 2007

Construction and simulations of full-size CBM-TRD prototypes without drift region*

E. Hellbär, H. Appelshäuser, A. Arend, C. Baumann, T. Bel, C. Blume, P. Dillenseger, K. Reuß, F. Roether, and M. Seidl

Institut für Kernphysik, Goethe-Universität, Frankfurt am Main, Germany

To provide a fast and efficient e/π separation and charged particle tracking for the Compressed Baryonic Matter (CBM) experiment a Transition Radiation Detector (TRD) based on a thin Multiwire Proportional Chamber (MWPC) without an additional drift region is considered [1].

Corresponding to this design two full-size prototypes have been developed and built with an anode-cathode spacing of 4 mm and 5 mm, respectively, resulting in amplification regions of 8 mm and 10 mm depth. The gold-plated tungsten wires with a diameter of 20 μm have a pitch of 2.5 mm. They are glued on distance ledges which are attached to the frame of the detector made out of aluminium with dimensions of 60 $\times$ 60 cm^2. The back side consists of a honeycomb structure supporting the pad plane. The common pad plane design features different pad sizes, where the read-out pads used during tests have a size of 7.125 $\times$ 75 mm^2. A second frame to seal the MWPC includes a thin aluminized mylar foil serving as the entrance window as well as an optional support structure. Figure 1 shows a technical drawing of the prototypes with the aforementioned components.

To avoid large changes of the gas gain due to its deformation the thin mylar foil has to be stretched uniformly and with appropriate tension. To achieve this requirement a method based on thermal expansion is being used [2]. The foil is fixed to a plexiglass frame which is heated up by heating coils resulting in the expansion of the frame and thus a mechanical stretching of the foil. To quantitatively analyse the bulge of the stretched foil caused by overpressure inside the chamber the deformation of the entrance window and the mechanical stress of the MWPC body are simulated with the Abaqus software package [3]. According to these simulations the entrance window stretched at a plexiglass temperature of 55°C gets deformed by 160 μm at an overpressure of 0.01 mbar which is verified by measurements. The resulting gain variation as a function of the modified distance between the entrance window and the anode wires is simulated with Garfield [4] and shown for three detector geometries without drift region in Figure 2. Keeping the deformation of the entrance window below than 120 μm leads to a gain variation of less than 10% and can be achieved by limiting the differential gas pressure variations to less than 0.01 mbar.

The full-size prototypes described in this article were tested along with several other considered prototype geometries with dedicated drift regions at the common test beam campaign at CERN-PS in October 2012 [5][6].

* Work supported by BMBF and HICforFAIR

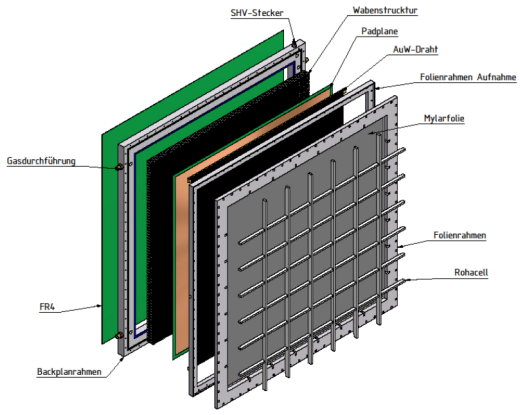

Figure 1: Technical drawing of a full-size TRD-prototype without drift region.

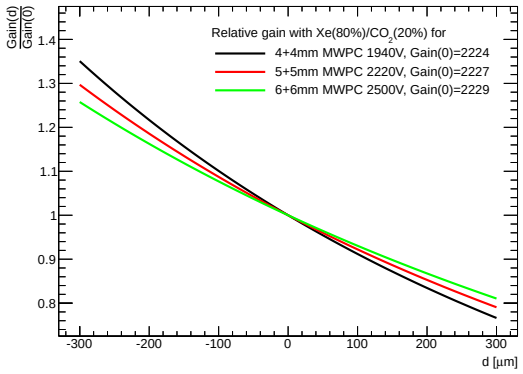

Figure 2: Relative gain depending on the displacement of the entrance window for three detector types without drift region.

References

[1] P. Reichelt, H. Appelshäuser, and M. Hartig, CBM Progress Report 2010, Darmstadt 2011, p. 39.

[2] Michael Staib *et al.*, RD51-Note-2011-004.

[3] http://www.3ds.com/de/products/simulia/portfolio/abaqus/overview/

[4] http://garfield.web.cern.ch/garfield/

[5] P. Dillenseger *et al.*, *In-beam performance studies of the first full-size CBM-TRD prototypes developed in Frankfurt*, this report.

[6] D. Emschermann *et al.*, *Common CBM beam test of the RICH, TRD and TOF subsystems at the CERN PS T9 beam line in 2012*, this report.

In-beam performance studies of the first full-size CBM-TRD prototypes developed in Frankfurt*

P. Dillenseger, H. Appelshäuser, A. Arend, C. Baumann, T. Bel, C. Blume, E. Hellbär, K. Reuß, F. Roether and M. Seidl

Institut für Kernphysik, Goethe-Universität, Frankfurt am Main, Germany

Introduction

For the Compressed Baryonic Matter (CBM) experiment at the Facility for Antiproton and Ion Research (FAIR) a Transition-Radiation Detector (TRD) is being developed. Its goal is to provide a good particle identification and tracking performance in the high particle-density environment of the experiment. The aim is to achieve 90 % electron efficiency with a pion miss-identification below 1%. For the test beam at the CERN-PS in October 2012 [1] full-size prototypes were build and used. Detailed information about the prototypes and their manufacturing can also be found in this report [2].

To match the challenge of the high-flux environment in the CBM experiment, we employ thin symmetric Multi-Wire Proportional Chambers (MWPC), with a single wire plane, 8 or 10 mm gas volume region, and a 20 μm thick aluminized mylar-foil as cathode plane and at the same time entrance window. In order to maximize electron-identification power, the optimization of the radiator performance is essential. During the test-runs in October 2012 several different types of radiators have been tested, including regular and irregular foil radiators, several foam radiators and fibre radiators. In addition to the radiator scan, the dependence of the gas-gain on the gas-pressure inside the chambers was measured, to investigate the deformation of the mylar-foil and its influence on the gas-gain.

Measurements

Two prototypes with dimensions of 60×60 cm^2, one with a 4+4 mm and the other one with a 5+5 mm gas gap [2], were used with a SPADIC rev 0.3 [3] readout-chain for the measurements at the CERN-PS. The radiator scan included 15 different radiators and was performed with a 3 GeV/c mixed electron-pion beam.

Results

Figure 1 displays the signal of electrons and pions averaged over one run. The dashed curve are electrons with FFM R002 (shown in Figure 2) as radiator, the signal below the dashed curve are electrons without a radiator and the filled area is the average pion signal. The used radiator is made out of polyethylene foam with a bubble-diameter of about 1 mm, which corresponds to approximately 260 surface boundaries for a total radiator thickness of 26 cm.

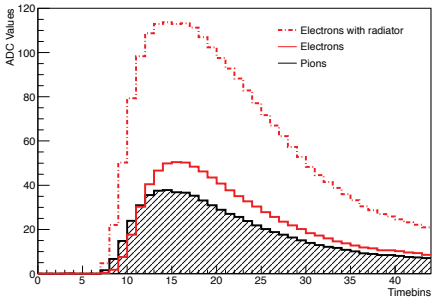

Figure 1: Average electron and pion signal of the 5 + 5 mm prototype without a radiator and with the FFM R002 radiator.

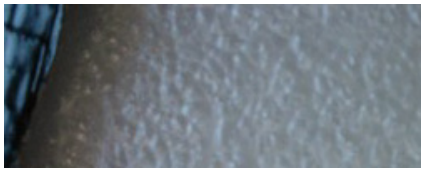

Figure 2: The radiator FFM R002. It consists of polyethylene foam with a bubble-diameter of about 1mm.

The measurement shows a difference of more than a factor two between the electron signal with and without the FFM R002 radiator. At the same time the FFM R002 is cost efficient and mechanically stable, which makes it an attractive choice for a radiator material.

Outlook

The next steps of the CBM-TRD development will be to investigate combinations of the thin entrance window and the stiff radiator, in order to minimize the deformation of the entrance window.

References

[1] D. Emschermann et. al., "Common CBM beam test of the RICH, TRD and TOF subsystems at the CERN PS T9 beam line in 2012", this report.

[2] E. Hellbär, et al., "Construction and simulations of full-size CBM-TRD prototypes without drift region", this report.

[3] T. Armbruster, et. al., "CBM-TRD readout with the SPADIC amplifier / digitizer chip", CBM Progress Report 2010, Damrstadt 2011, p. 44.

* Work supported by BMBF and HICforFAIR

Test of Münster CBM TRD prototypes at the CERN PS/T9 beam line *

C. Bergmann[1], *R. Berendes*[1], *D. Bonaventura*[1], *D. Emschermann*[1], *N. Heine*[1], *J. Hehner*[2], *B. Kolipost*[1], *W. Verhoeven*[1], *and J. P. Wessels*[1]

[1]Institut für Kernphysik, Münster, Germany; [2]GSI, Darmstadt, Germany

The Münster real-size CBM TRD prototypes [1] of 59×59 cm^2 shown in Fig. 1 are derived from the design of the ALICE TRD modules. An amplification region of 3.5+3.5 mm is combined with a 5 mm drift section leading an active gas volume thickness of 12 mm. Signals are induced on rectangular pads of 7.125 mm width, respectively, to allow for charge collection on 3 adjacent pads. This design corresponds to the smallest module size next to the beam-pipe, required for 12% of the total CBM TRD area, and is scalable to 1 m^2-size detector modules.

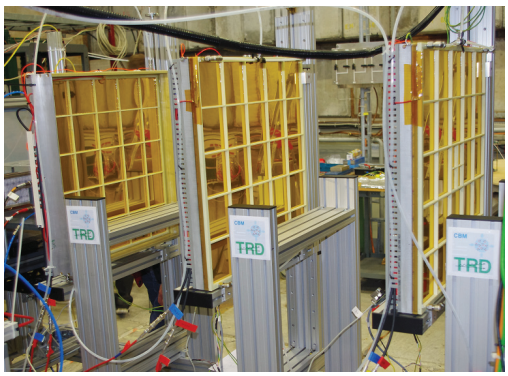

Figure 1: Münster TRD protoypes in the CBM beam test.

Various radiator types were investigated on these 3 TRD prototypes during the common CBM beam test [2] in 2012. The read-out was performed with the SPADIC v0.3 / Susibo [3], SPADICv1.0 [4] and FASP [5] front-ends. The setup was entirely EPICS controlled, allowing for online monitoring of the HV settings, gas flow and inclusion of these values in the DAQ stream. First results of the ongoing analysis are shown in Figure 2. One important aspect of radiator choice is to match of the TR-emission spectrum with respect to the absorption spectrum of the detector. For a detailed investigation, we have built different radiator types: regular foil and irregular foam, fiber and sandwiches. Ideally, a radiator should yield an optimal TR-performance, while keeping the material budget as low as possible. While this consideration favors regular foil radiators, they usually require a significant external support frame to keep the foils stretched and in position. This additional frame material is avoided in our first micro-structured self-supporting radiators (Kshort, K, K++). First results using self-supporting radiators type K (Fig. 3) are promising and comparable to the classical radiator type B with the same properties made from the identical material.

* Work supported by BMBF and the HadronPhysics3 project financed by EU-FP7.

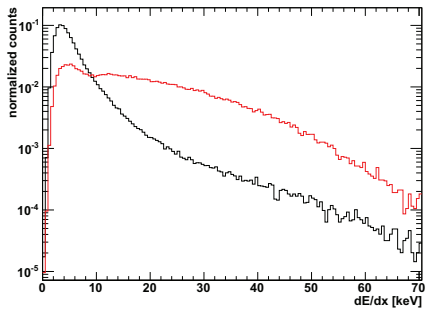

Figure 2: ADC spectra for π (black) and e (red), integrated and calibrated, on the 2nd TRD operated with Xe/CO_2 (80:20) gas in combination with 350 foil layer micro-structured self-supporting radiator (K++) at 3 GeV/c.

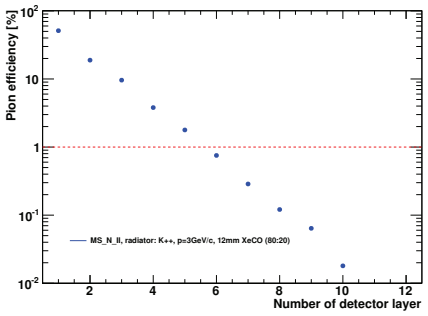

Figure 3: Extrapolated pion efficiency for a TRD consisting of up to 10 layers for micro-structured self-supporting radiator (K++). The dashed line indicates the design goal of 1% π efficiency, at 90% e efficiency which is reached in this configuration with 6 layers.

References

[1] D. Emschermann et al. “Development and CbmRoot implementation of the Münster CBM TRD prototypes 2012”, CBM Progress Report 2012

[2] D. Emschermann et al., “Common CBM beam test of the RICH, TRD and TOF subsystems at the CERN PS T9 beamline in 2012”, this report

[3] T. Armbruster et al.,“CBM-TRD readout with the SPADIC amplifier / digitizer chip”, CBM Progress Report 2010

[4] T. Armbruster et al.,“SPADIC 1.0 - a Self-triggered Amplifier/Digitizer ASIC for CBM-TRD”, this report

[5] V. Catanescu et al., “Front End Electronics for High Counting Rate TRD using a prototype ASIC”, CBM Progress Report 2009

Beamtest results of the CBM-TRD feature extraction using SPADIC v1.0*

C. Garcia[1], *C. Bergmann*[2], *D. Emschermann*[2], *M. Krieger*[3], *and U. Kebschull*[1]

[1]Infrastructure and Computer Systems for Data Processing (IRI), Frankfurt University, Frankfurt/Main, Germany;
[2]Institute für Kernphysik, Münster, Germany; [3]ZITI, Heidelberg University, Germany

The feature extraction is a data processing stage of the proposed data acquisition chain (DAQ) for the CBM/TRD experiment aiming to deliver event-filtered and bandwidth-reduced data to the First Level Event Selection (FLES). The feature extraction processing stage will be implemented at the Data Processing Board (DPB) located in the TRD-DAQ. A data rate of about 1TB/s and a high event rate of approximately 10 MHz is expected for the final experiment [1].

In October and November 2012 a common CBM subsystems (RICH/TRD/TOF) beam test was performed at the CERN Proton Synchrotron (PS) T9 accelerator beamline [2]. A full size (59×59 cm^2) TRD detector prototype from Münster [3], with an amplification/drift region of 7.0/5.0 mm was used for this experimentation. The readout and signal processing of the TRD module was performed by the Self-triggered Pulse Amplification and Digitization asIC (SPADIC) version 1.0 [4]. The SPADIC chip reads out 32 channels in self-triggered mode and, compared to the previous SPADIC v0.3 chip, it implements new features which are of importance for the feature extraction (e.g. neighbor channel-trigger readout).

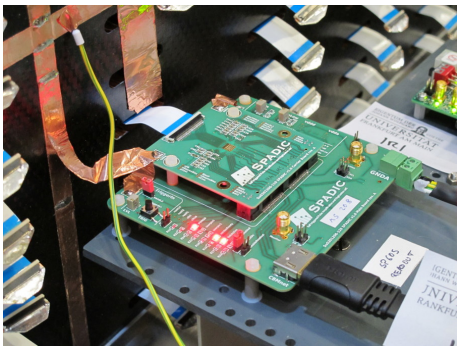

Figure 1: Full size TRD prototype and SPADIC v1.0 PCB. Experimental setup in the CERN PS/T9 in 2012.

In order to perform further developments for the feature extraction stage, obtaining real data samples from TRD full size prototypes by means of the new SPADIC v1.0 chip, was one of the main purposes during the beam test in the CERN PS T9. The experimental data acquisition setup was composed of the SPADIC v1.0 connected by a HDMI cable to a Readout Controller (ROC). The latter was interfaced with an optical connection to an Active Buffer Board (ABB) in a data acquisition computer. The communication protocol used was CBMnet 2.0 [5]. An effective area of 16 channels were read out in self-triggered mode, however, a total area of 8 channels were read out using the neighbor channel-trigger feature. A set of recorded data was acquired during the beam test, however, this data set lacks of synchronization to any other subsystem detector.

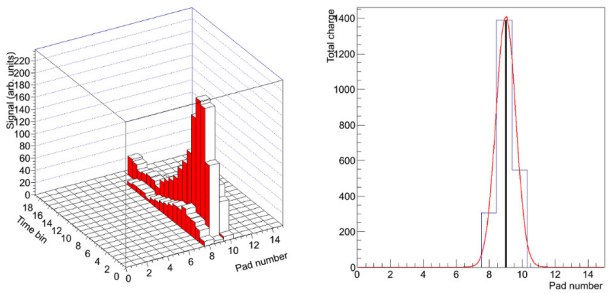

Figure 2: Left plot, reconstructed TRD cluster for a single particle. Right plot, hit position approximation by a fit on total charge deposition. The central fit line indicates the reconstructed hit position.

An online cluster reconstruction is currently being designed using beam test data. Even if it is not possible to reconstruct the whole physical event, it helps to simulate specific high particle rates scenarios in order to develop a DPB feature extraction module. As shown in Figure 2, a 3 pad cluster and its approximated position reconstruction were obtained using a clusterizer algorithm that is easily parallelizable. Furthermore, the firmware migration of the actual feature extraction processing board (Xilinx SP605 FPGA) into the new SysCore v3 [6] will be one of the main tasks in 2013.

References

[1] J. de Cuveland and V. Lindenstruth, J. Phys. Conf. Ser. 331 (2011) 022006

[2] D. Emschermann et al., “Common CBM beam test of the RICH, TRD and TOF subsystems at the CERN PS T9 beam line in 2012”, GSI Scientific Report 2012

[3] C. Bergmann et al., “Test of Münster CBM TRD prototypes at the CERN PS/T9 beam line”, GSI Scientific Report 2012

[4] T. Armbruster et al., “SPADIC 1.0 a Self-triggered Amplifier/Digitizer ASIC for CBM-TRD”, CBM Progress Report 2012

[5] F. Lemke et al., “Status of CBMnet integration and HUB design”, CBM Progress Report 2012

[6] J. Gebelein et al., “SysCore3 A universal Read Out Controller and Data Processing Board”, GSI Scientific Report 2012

* Work supported by BMBF (06HD9123I, 06FY7090)

Analysis of TRD beam test data 2011 in CBMROOT

A. Lebedev[1,3], *S. Lebedev*[2,3], *and G. Ososkov*[3]

[1]IKF Frankfurt University, Germany; [2]Giessen University, Germany; [3]LIT JINR, Dubna, Russia

Transition Radiation Detector (TRD) prototypes from Frankfurt [1] and Münster [2] groups were tested at CERN PS/T9 beam line in October 2011. In this report we present some results of data analysis employing electron identification algorithms developed in the CBMROOT framework.

An example of energy loss spectra for electrons and pions for the foam radiator is shown in Figure 1. The energy loss data for our study was generated from energy loss distribution histograms assuming that all TRD layers are identical with respect to energy loss measurements.

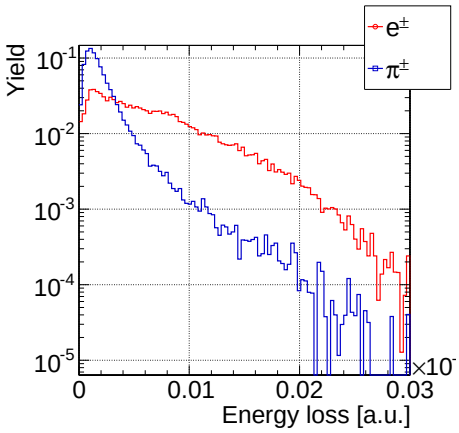

Figure 1: Energy loss spectra for electrons and pions.

Several electron identification algorithms were developed in CBMROOT including algorithm based on the artificial neural network (ANN) [3], algorithm based on boosted decision tree (BDT) [4], Likelihood method, threshold on the mean value, threshold on the median value.

Number of TRD layers required to achieve necessary pion suppression level is a crucial parameter for TRD. We studied the algorithms to evaluate required number of layers. Results are shown in Figure 2. Pion suppression efficiency is shown assuming 90% of electron identification efficiency. According to our results required pion suppression level can be achieved with 9-10 TRD layers for regular foiled radiator as well as for irregular foam radiators.

Different radiator types were investigated on the TRD prototypes. Here we present the results for selected radiators tested by Münster group (**B, F** - regular foil radiator, **H++** - irregular foam, **G30** - fiber) and by Frankfurt group (**5mm_fibre** - a fiber radiator as used in the ALICE TRD, **4mm_foam** - a polypropylene foam radiator, **4mm_f350** - regular foil radiator). The best results were achieved for regular foil type radiator (see Figure 3). Such radiators usually require a significant external support frame to keep

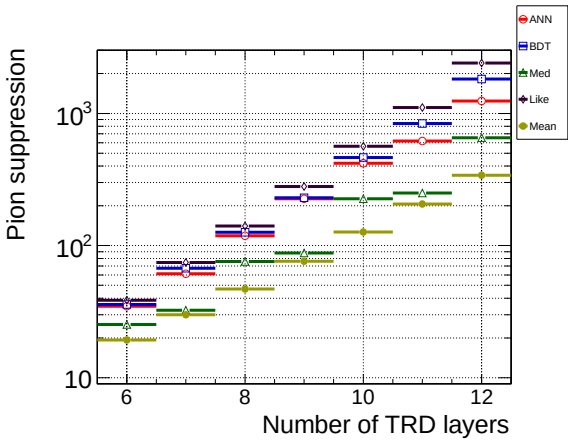

Figure 2: Pion suppression level in dependence on number of TRD layers for **4mm_foam** radiator from Frankfurt group.

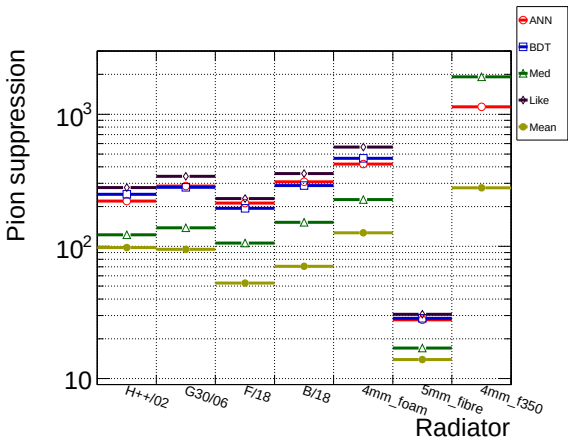

Figure 3: Pion suppression level for different radiator types.

the foils. But the reasonable pion suppression can also be achieved with irregular foam radiator. These radiators are self supporting and much cheaper than regular ones.

The best performance as expected showed three methods: Likelihood, ANN and BDT.

References

[1] A. Arend et al., GSI Progress Report 2011, p.48

[2] C. Bergmann et al., GSI Progress Report 2011, p.47

[3] E.P. Akishina et al., CBM Progress Report 2009, p.82

[4] S.Lebedev et al J. Phys.: Conf. Ser. **396** 022029, 2012

A CBM Time-of-Flight outer wall layout *

I. Deppner[†1], *N. Herrmann*[1], *P.-A. Loizeau*[1], *C. Simon*[1], *C. Xiang*[1,2], *M. Ciobanu*[3], *J. Frühauf*[3], *M. Kis*[3], *and the CBM-TOF working group*

[1]Physikalisches Institut Universität Heidelberg, Heidelberg, Germany; [2]Institute of Particle Physics, Central China Normal University, China; [3]GSI, Darmstadt, Germany

The key element providing hadron identification at incident energies between 2 and 10 AGeV is a Time-of-Flight (ToF) wall covering the polar angular range from $2.5\,^{\circ}$-25° and full azimuth [1]. The ToF-wall is subdivided into different regions covered by different counters arranged in super modules (SM). A possible layout of the outer wall is presented in this report.

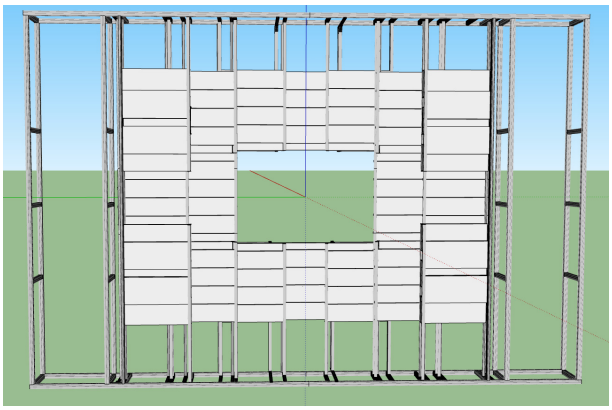

Figure 1: 3D drawing of the outer CBM ToF-wall as designed for the start version of CBM. For details see text.

Figure 1 shows a 3D drawing of the outer part of the ToF-wall, designed for the starting phase of CBM. In the start version of CBM it is planed to locate the wall 6 m downstream of the target. Upon completion of SIS 300 the wall will be extended and relocated to 10 m downstream from the interaction point demanding flexible positioning of the counter elements. The main frame (15 m $\times$ 10 m) is designed in such a way that it is usable for both positions which minimizes the cost for the upgrade substantially. The SMs are mounted on commercial bars made of aluminum profiles running in vertical direction which allow for shifting of the SM in this direction (see Fig. 1). The bars placed in front of the active detector material have a typical radiation length of about 6 %. The bars carrying most of the load are placed behind the active detector material. The outer wall is built from 2 types of super modules (SM) only:
1. small SM, size 1800 mm $\times$ 490 mm $\times$ 100 mm
2. big SM, size 1800 mm $\times$ 740 mm $\times$ 130 mm
Hence the cost for development and production is reduced. In addition the same size of the SM allows a better and more compact staggering in order to avoid holes in the acceptance. Both types of SM are constructed in the same way. The SM boxes are made out of aluminum. The counters mounted in the small chamber are staggered in two ways. For the central column of the wall the staggering of the RPC is done symmetrically in an alternative fashion. In the other columns the counters are tilted to the beam by an certain angle and overlapped like roof tiles. The preamplifier cards (see [2, 3]) carrying 2 PADI chips each are mounted inside the super modules directly to the readout electrode of the counter in order to improve shielding and thus stability. The discriminated signals are transmitted via twisted pair cable to a multilayer PCB acting as a feedthrough. The outer side of the PCB contains connectors where the TDC (GET4 or FPGA-TDC) can be plugged. A data collector board combining all TDCs is sending the data via glass fiber cable to a FPGA based pre-processing board. This solution decreases the amount of cables leaving the wall tremendously. The super modules are based on 2 types of counters only:
a) small RPC: 27 cm $\times$ 32 cm using low resistivity glass
b) large RPC: 53 cm $\times$ 52 cm using window glass
The dimensions of the active area of the counter modules are compatible with the production limitations of the respective glasses. In order to implement impedance matching with the FEE strip widths of about 7 - 8 mm, gap number between 8 and 9 and a gap width of 220 μm have to be used, fixing the strip number of the counters to 56 (32) for the large (small) modules, respectively. Some of the technical characteristics are summarized in Table 1. Further detailed information about the performance of the differential strip RPCs can be found in [4, 5]

Table 1: Technical characteristics of the super modules

	small SM	big SM
# of RPCs	5 small RPC	3 large RPC
# of strips	160	168
# of channels	320	336
# of FEE-cards	40	42
total active area	152 $\times$ 27 cm^2	152 $\times$ 53 cm^2
overlap to next SM	h.: 2 cm, v.: 2 cm	h.: 3 cm, v.: 2 cm

References

[1] I. Deppner et al, Nucl. Instrum. and Methods A, Volume 661, Supplement 1, 2012, Pages S121 - S124

[2] M. Ciobanu et al, PAD-6 and PADI-7, new prototypes for CBM ToF, this Report

[3] J. Frühauf et al, Hardware Developmant for CBM ToF, this Report

[4] I. Deppner et al, Journal of Instrumentation. 10/2012; 7(10). DOI:doi:10.1088/1748-0221/7/10/P10008

[5] C. Simon et al, RPC test with heavy-ion beams, this Report

* Work supported by BMBF 06HD7141I and EU/FP7 HadronPhysics3

† deppner@physi.uni-heidelberg.de

RPC test with heavy-ion beams*

C. Simon[1], *N. Herrmann*[1], *I. Deppner*[1], *P.-A. Loizeau*[1], *J. Frühauf*[2], *C. Xiang*[1,3], *M. Kiš*[2], *M. Petriş*[4], *M. Petrovici*[4], *and the CBM-TOF working group*

[1]Ruprecht-Karls-Universität, Heidelberg, Germany; [2]GSI, Darmstadt, Germany; [3]Central China Normal University, Wuhan, China; [4]NIPNE, Bucharest, Romania

The Time-of-Flight (ToF) wall of CBM, conceptualized on the basis of high-resolution timing Multi-gap Resistive Plate Chambers (MRPC), is intended to account for concise hadron identification at an unprecedented event rate of 10 MHz. For the layout of the outer wall, strip-MRPCs are foreseen [1]. To explore the performance and limitations of the current design, high-rate tests with GSI/SIS-18 heavy-ion beams irradiating the full surface of a $30 \times 30\,\mathrm{cm}^2$, fully differential multi-strip MRPC demonstrator [2] have been performed in the fall of 2012. In order to test the equipment under realistic conditions, data were taken from several heavy-ion reactions (Kr+Pb, Ni+Pb, D+Pb) at beam energies of 1-2 AGeV with particle fluxes on the detector surface between $50\,\mathrm{Hz/cm}^2$ and $20\,\mathrm{kHz/cm}^2$. In this report, we present preliminary results from the Ni+Pb beamtime in early November 2012, where the incident particle flux amounted to $\sim 50\,\mathrm{Hz/cm}^2$.

The testbeam setup (cf. Fig. 1) consisted - looking downstream - of a diamond start counter, the target, two plastic counters of size $2 \times 2\,\mathrm{cm}^2$ for cross checks, the MRPC demonstrator and a reference MRPC constructed by the Bucharest group [3], enabling us to determine the efficiency and timing resolution of the demonstrator against a substantial area ($85\,\mathrm{cm}^2$) of the reference counter. A

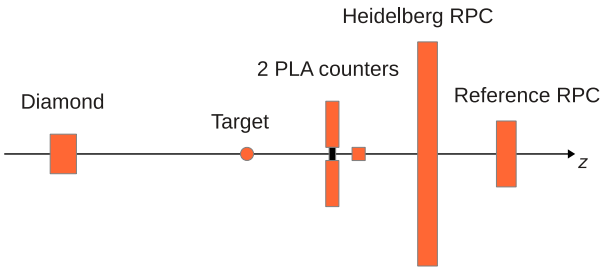

Figure 1: Testbeam setup in November 2012.

calibration scheme, based on ROOT and Go4, adjusted to the layout of the prototype is currently under development [4]. First, hits are built and clustered in both the demonstrator and the reference counter. Then a matching algorithm assigns the geometrically most suitable pendant in the demonstrator to clusters originating from one-cluster events in the reference counter. We find that our demonstrator is capable of dealing well with multi-hit exposure (cf. Fig. 2 left), facilitating the study of inter-hit dependencies. Furthermore, we studied the counter response in terms

* Work supported by EU/FP7 HadronPhysics3 and BMBF 06HD7141I.

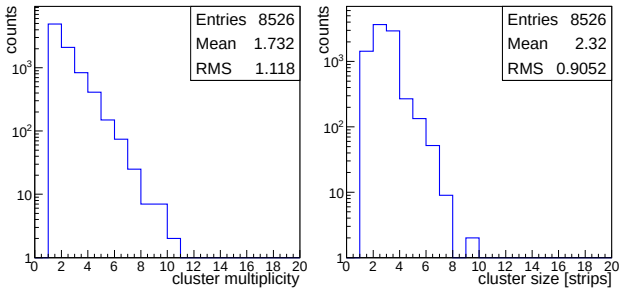

Figure 2: Cluster multiplicity (left) and cluster size (right) of the demonstrator.

of the cluster size (cf. Fig. 2 right), which averages at about 2.3 strips. On the strip level, we found the resolution of the cluster mean time difference to be 80 ps (cf. Fig. 3), which approximately translates into a single-counter timing resolution of 57 ps for our demonstrator. This promising result was achieved so far only for the small area ($4\,\mathrm{cm}^2$) covered by the plastic counters, that were requested to have clean conditions. The analysis of the efficiency as function of the hit rate on the counter surface, a task of utmost importance, is in progress.

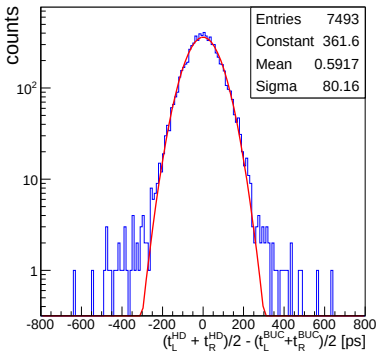

Figure 3: First hint at timing resolution on the strip level.

References

[1] I. Deppner et al., A CBM Time-of-Flight outer wall layout, this report

[2] I. Deppner et al., Performance of large area MMRPC prototype, 2011 report

[3] M. Petriş et al., Towards a real size RPC cell for CBM RPC-TOF, 2011 report

[4] P.-A. Loizeau et al., Status of the CBM TOF free streaming electronics chain, this report

ToF-ROC FPGA Irradiation Tests 2012*

S. Manz[1], *J. Gebelein*[1], *A. Oancea*[1], *H. Engel*[1], *and U. Kebschull*[1]

[1]Infrastruktur und Rechnersysteme in der Informationsverarbeitung (IRI), Frankfurt University, Frankfurt, Germany

Introduction

Ionizing radiation can severely disturb the operation of electronic devices, especially SRAM based electronics like *Field Programmable Gate Arrays* (FPGAs). The theory of radiation induced failures is well known and radiation mitigation techniques have been developed [1, 2]. However, when using commercial of-the-shelf electronics the internal details of electronic circuits are generally not known and the efficiency of the mitigation techniques need to be tested in experiments before the usage of those electronics can be approved. Here we show the result of a test carried out at the accelerator facility at the *FZ Jülich*, Germany, in August 2012. Contrary to previous tests, our intention was not to characterize the chip's internal logic cells using an academic test design. We evaluate the efficiency of the radiation mitigation technique *scrubbing* on logic of an actual firmware that is currently used for readout of the GET4 TDC [3]. For characterizing the efficiency we do not use the particle flux as reference but directly count the induced upset rate in the configuration memory of a second identical device in the beam. The firmware itself was running on a Xilinx Virtex-4 FPGA operating directly in a $2\,GeV$ proton beam at a particle rate in the order of $10^7 s^{-1} cm^{-2}$.

Results

Figure 1 shows a direct impression of the values recorded during the beam time. Both diagrams show the results of a three hours run, where scrubbing is disabled (figure 1(a)) and enabled (figure 1(b)). The in-beam tests showed very promising results when using the *scrubbing* technique on an operational detector read-out firmware. The dead time of the device could be reduced by almost a factor of 50 and corrupted data could be reduced by a factor of 200 while ressource utilization increased by less than a factor of two.

Outlook

With the great efficiency of the configuration scrubber, an FPGA based read-out controller for the CBM-ToF front-end electronics is absolutely feasible.

For the real CBM experiment the occurance of an SEU needs to be logged directly in the data stream for data analysis. A concept for doing so needs to be developed and experimentally approved, also considering new possibilities that emerge with the Xilinx series 7 FPGAs [4].

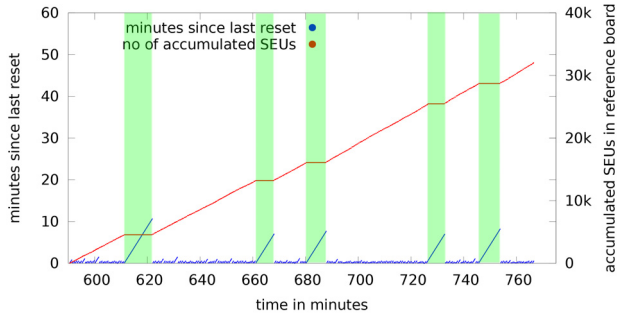

(a) Scrubbing is disabled. Full reset of the setup required in less than a minute. The setup is only stable when beam turned off.

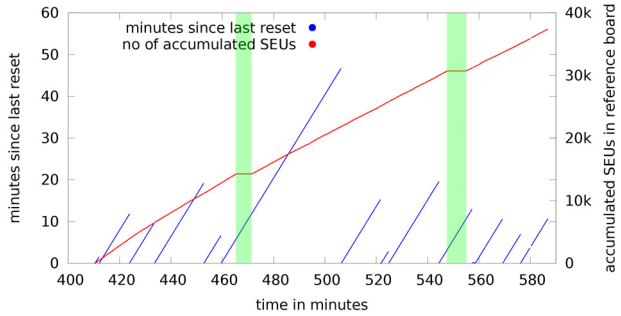

(b) Scrubbing is enabled. The setup runs stable for several minutes.

Figure 1: The red plot refers to the number of SEUs collected in the reference board while the blue plot shows the time since the last full reset of the setup, every return-to-zero of the blue plot refers to an unrecoverable failure of the setup caused by radiation. During the highlighted time slots the beam was shut down for technical reasons.

References

[1] H. Quinn *et al.*, "An Introduction to Radiation-Induced Failure Modes and Related Mitigation Methods For Xilinx SRAM FPGAs," *Proc. Engineering of Reconfigurable Systems and Algorithms*, 2008

[2] Mike Wirthlin, "FPGAs Operating in a Radiation Environment: Lessons Learned from FPGAs in Space," TWEPP 2012 Conf., 2012

[3] H. Flemming and H. Deppe, "The GSI event-driven TDC with 4 channels GET4," *Proc. IEEE Nucl. Sci. Symp. Conf. Rec.*, 2009

[4] *7 Series FPGAs Configuration User Guide, UG470 (v1.5)*, Xilinx Inc, 2012

* Work supported by BMBF No. 06HD9123I.

A reaction detector for CBM

P. Koczoń[1]
[1]GSI, Darmstadt, Germany

A detector placed around the target outside of the CBM acceptance (θ >25 deg) and registering reaction products of AuAu @ 10 AGeV and pC @ 30 GeV reactions was simulated. Equipped with a simple signal summing-up and threshold electronics such a reaction detector (RD) can distinquish between central, minimum bias and empty reactions in case of Au+Au and can deliver a "time zero" signal for TOF measurement even for p+C reactions.

Details of the simulation

A detector in form of a ring consisting of eight trapezoidal tails installed side by side (as depicted in Fig.1) covering polar angle of 30 to 60 deg and full azimuthal angle was investigated in the framework of the FAIR-ROOT [1] simulation system using Geant3 transport engine. Sensor material of 2 mm thickness and density of silicon has been assumed for the flat dies installed at 60 mm distance from the target center (0.25 Au or 1 mm C). This thickness corresponds to either ceramic RPC or to a MCP sensors - both posessing excellent timing properties and certain energy resolution. Standard URQMD AuAu @ 10 AGeV minimum bias and central events as well as pC @ 30 GeV have been used as input. FAIR-ROOT intrinsic "FairIonGenerator" method has been used to simulate "empty events" e.g. passage of heavy ion through the target material without any nuclear interaction, thus producing only delta electrons.

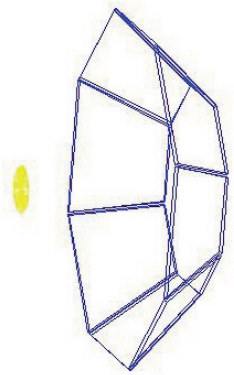

Figure 1: Reaction detector: ring of eight trapezoidal segments around the target (beam direction horizontally).

Simulations results

The sum of energy loss signals of all products from a nuclear collision in the reaction detector differs significantly for minimum bias or central events and "empty events" as presented in Fig.2. The lowest energy losses (below 10 MeV) and lowest multiplicities (8±2.5) are registered mainly for "empty events". Minimum bias events are characterized by the sum of energy loss in the reaction detector in the range up to 50 MeV. The highest energy loss (and at the same time highest particle multiplicity) is observed for central events. A simple threshold at 10 MeV of total energy loss per event would deliver a clear signature for nuclear reaction events (about 10 % of min bias events would be lost).

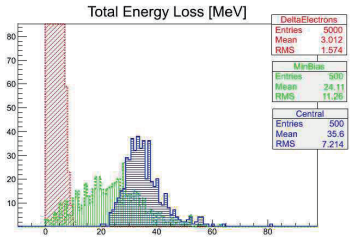

Figure 2: Total energy loss for central (hatched horizontally), minimum bias (hatched vertically) and empty events (inclined hatching).

Timing properties

The total energy loss signal can be used not only for nuclear reaction tagging but also as a "time zero" for TOF measurement. Due to the RD axial symmetry around the target the time spread of arriving particles is very narrow: RMS=10 ps. For 30 GeV protons on carbon target a similar time resolution is achieved as shown in Fig.3.

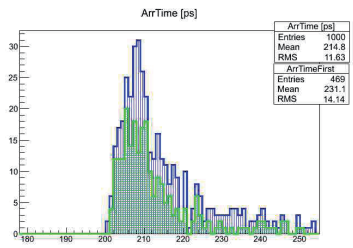

Figure 3: Time resolution for 30 GeV protons on carbon target. An additional requirement of at least a double hit in RD reduces the efficiency to 50%.

References

[1] http://fairroot.gsi.de/

Common CBM beam test of the RICH, TRD and TOF subsystems at the CERN PS T9 beam line in 2012 *

D. Emschermann[1], *J. Adamczewski-Musch*[2], *A. Arend*[3], *C. Bergmann*[1], *C. Garcia*[4], *N. Heine*[1], *S. Linev*[2], *T. Morhardt*[2], *C. Pauly*[5], *M. Petriş*[6], *M. Petrovici*[6], *W. Verhoeven*[1], *and J. P. Wessels*[1]

[1]Institut für Kernphysik, Münster, Germany; [2]GSI, Darmstadt, Germany; [3]Institut für Kernphysik, Frankfurt/M, Germany; [4]IRI, Frankfurt/M, Germany; [5]Bergische Universität Wuppertal, Germany; [6]NIPNE, Bucharest, Romania

A common beam test of the CBM Ring Imaging CHerenkov (RICH), Transition Radiation Detector (TRD) and Time Of Flight (TOF) subsystems was performed at the CERN Proton Synchrotron (PS) accelerator in October/November 2012. The measurements were carried out at the T9 beam line in a mixed beam of electrons and pions with momenta from 2 to 10 GeV/c. In addition to the above mentioned detectors, the setup consisted of: two Cherenkov detectors, two fiber-trackers, beam trigger scintillators and a lead-glass calorimeter. The first fiber-tracker was placed at the upstream end of the setup, followed by a large volume RICH prototype, 8 real-size TRD prototypes, 2 TOF detectors and finally the second fiber-tracker at the downstream end, see Figure 1.

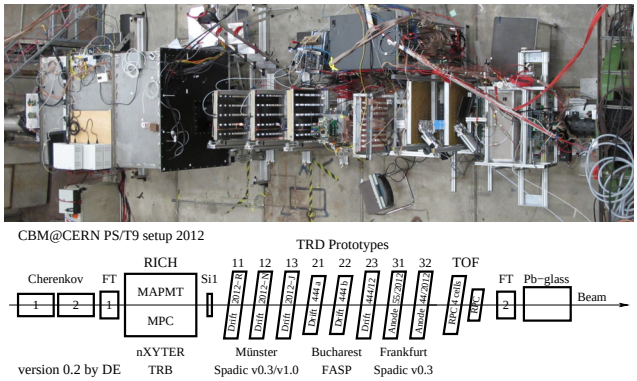

Figure 1: Setup of CBM in the PS/T9 beam line in 2012.

The RICH prototype [1] was based on a mirror focusing setup with CO_2 gas as radiator. The photon camera was composed of 4 micro channel plate (MCP) detectors plus 20 Hamamatsu multi-anode photo-multipliers (MAPMTs). Two concurrent approaches to readout the RICH camera were tested: the traditional trigger-less nXYTER front-end as well as a free streaming approach based on the HADES Trigger and Readout Board (TRB3).

The TRD laboratories in Münster [2], Bucharest [3],[4] and Frankfurt [6],[7] have built real-size (59×59 cm^2) detector modules based on MWPC technology with cathode pad readout. The large size of the TRDs has triggered innovative developments to stabilize the entrance window to the gas volume, while minimizing the loss of transition radiation between the radiator and the detection volume. The readout of the Bucharest prototypes was based on the Fast Analog Signal Processor (FASP) ASIC, either digitized in a VME-based MADC32, or using free streaming MAXIM [5] based converters. The signal processing on the TRD modules from Münster and Frankfurt was performed with the SPADIC v0.3 from 2011. A TRD prototype from Münster served as platform to compare the performance of the FASP, the SPADIC v0.3 and the recently developed SPADIC v1.0 [8],[9]. The latter reads out 32 channels in self-triggered mode and implements the CBMnet protocol on the ASIC. The TRD test program consisted of a systematic study of different radiator prototypes with a Xe(80%)+CO_2(20%) gas mixture in the detection volume, as well as beam momentum and high voltage scans.

Bucharest completed the setup with a segmented TOF prototype, consisting of 4 partially overlapping RPC cells, combined with a single RPC cell reference TOF prototype from 2011. These 2 TOF modules were again tested using a $C_2F_4H_2$(90%)+SF_6(5%)+iso-C_4H_{10}(5%) gas mixture allowing for fast signal generation.

All prototypes under test were read out in a common hybrid data acquisition system based on MBS and DABC.

* Work supported by BMBF, EU-FP7/HP3 Grant No. 283286 and NASR/CAPACITATI contract no.179

References

[1] S. Reinecke et al., “Overview RICH prototype beamtest 2012 at CERN-PS”, CBM Progress Report 2012

[2] C. Bergmann et al., “Test of Münster CBM TRD prototypes at the CERN PS/T9 beam line”, GSI Scientific Report 2012

[3] M. Petriş et al., “e/π identification and position resolution of high granularity TRD prototype based on MWPC”, GSI Scientific Report 2012

[4] M. Tarzila et al., “Two dimension position sensitive real size CBM-TRD protype”, GSI Scientific Report 2012

[5] F. Constantin et al., “FPGA Based Free Running Mode Acquisition for High Counting Rate TRD”, GSI Scientific Report 2012

[6] E. Hellbär et al., “Construction and simulations of full-size CBM-TRD prototypes without drift region”, GSI Scientific Report 2012

[7] P. Dillenseger et al., “In-beam performance studies of the first full-size CBM-TRD prototypes developed in Frankfurt”, GSI Scientific Report 2012

[8] T. Armbruster et al., “SPADIC 1.0 - a Self-triggered Amplifier/Digitizer ASIC for CBM-TRD”, CBM Progress Report 2012

[9] C. Garcia et al., “Beamtest results of the CBM TRD feature extraction using SPADIC v1.0”, GSI Scientific Report 2012

Design calculations for the superconducting dipole magnet for the Compressed Baryonic Matter (CBM) experiment at FAIR*

P. Akishin[1], A.Bychkov[1], E. Floch[2], Yu. Gusakov[1], V. Ivanov[1], P. Kurilkin[1], V. Ladygin[1], H. Leibrock[2], A. Malakhov[1], G. Moritz[2], C. Muehle[2], W.F.J. Müller[2], W. Niebur[2], I. Pschorn[2], P. Senger[2], A. Shabunov[1], P. Szwangruber[2], Y. Xiang[2], C. Will[2]
[1]JINR, Dubna, [2]GSI, Darmstadt

Calculations have been performed to design the coil case, the coil vessel, the support links and the quench protection scheme for the CBM superconducting dipole magnet. The general parameters of the magnet have been discussed in a separate contribution to this Scientific Report. The code TOSCA was used for calculating electromagnetic forces exerted on the coil, while the structural analysis was made by using the code ANSYS. The radial F_r and vertical F_y forces were calculated at 1.08 T with TOSCA as a function of the azimuthal angle of the coil. The radial force points toward the outer direction, while the vertical force attracts the coil toward the iron yoke. The integrated forces along the coil circumference are radially 60 tons and vertically 254 tons. The ANSYS calculation was based on the results of TOSCA.

Coil case

The coil case is designed considering two main functions: one is to protect the windings against magnetic forces during operation, and the other is to use the case as a container for liquid helium (LHe) to cool the winding. The volume of the LHe in the case is about 20 liters for one coil, including the LHe stored in the current leads box. The case is welded of stainless steel 316LN [1]. The minimal thickness of the case is 20 mm. The steel magnetic permeability is about 1.01 ~ 1.02. The cross section of the coil has the height of 236 mm and the width of 221 mm. The coil occupies only a part of the internal space of the case. The rest space is filled with the spacers made of NEMA G10 and an aluminum circular shim (AW6061 or AW3003). In addition, the shim provides good thermal conduction that allows to distribute the heat load caused by friction if the coil moves or cracks under the Lorentz forces. The large cross section is necessary to have a very rigid structure. The case should transmit huge vertical forces from the coil to the supports.

The case is supported by six main cylindrical supports and six tie rods. To reduce the heat flux to the helium system, the outer surface of the casing will be wrapped with 10 layers of a multi-layer insulation.

Thermal shield

The thermal shield must have good thermal conductivity, good rigidity to weight ratio, and it should be easy to fabricate and assemble. The thermal shield consists of two main pieces: the top shield and the cover. The shield has a radial cut for an electrical break. All pieces are made of copper sheets each 2 mm thick. The forced-flow cryogen for cooling the thermal shield is cold helium gas to intercept thermal radiation from the cryostat. The cooling pipes are made of a copper tube 1 mm thick having a rectangular shape with an outer dimension of 20 mm × 8 mm. To reduce the heat flux to the helium system, the outer surface of the thermal shield will be wrapped with insulation of 20 layers. The thermal shield is fixed to the main cylindrical supports.

Suspension

The cold mass is suspended from the room temperature (RT) vacuum vessel using 6 support struts and 6 tie rods. These support struts are described as "warm-to-cold" because the warm end is attached to the RT vacuum vessel and the cold end is attached to the cold mass. The suspension during the working cycle has two types of loading. When the magnet is switched off only the weight of the cold mass is applied to the suspension. In this case the vertical force is about 2000 kg. When the magnet is switched on, the vertical component of the Lorenz forces should be added to the weight of the cold mass. The maximum vertical force in this case is 254 tons. The lateral forces should not exceed a few hundred kilograms due to symmetry of the magnet. The support struts are typically compressed. Only the green parts require pre-compression while manufacturing the CBM dipole magnet. The tie rods will provide this pre-compression. The support struts have a nominal compression force of 42 tons [2]. The tie rods are tensed with the force of 500 kg.

The support strut consists of four composite tubes nested coaxially in each other and connected in series by three stainless steel tubes with Z-shaped cross section. The composite tubes are a polar wound tube with glass fibers and epoxy resin. The axial winding angle is ± 15º. Few layers have the winding angle of 90º to fix the main layers. The glass fiber composite has small thermal conductivity at low temperature. The Z-shape tubes are made of the SAE 304 stainless steel. Five layers of MLI are inserted in each gap between the tubes. The middle tube is connected with the thermo shield at the temperature of 80 K.

The tie rods are used to sustain the cold mass and preload the support struts. The tie rods, which are attached on one side to the vacuum vessel and on the other side to the coil case, are subjected to a thermal gradient from 4.5 K till room temperature. Titanium alloy Ti 5Al 2.5Sn has been chosen as tie rod material for its low thermal conductivity and high

*Supported by the BMBF, JINR Dubna, and by EU/FP7 Hadronphysics3

mechanical strength [3] The tie rods have spherical hinges on both sides. The hinge attached to the vacuum vessel is fixed with a key. The hinge on the other side has a thread for adjusting. On 1/3 of the length from the vacuum vessel it has a shoulder for a thermo bridge [4].

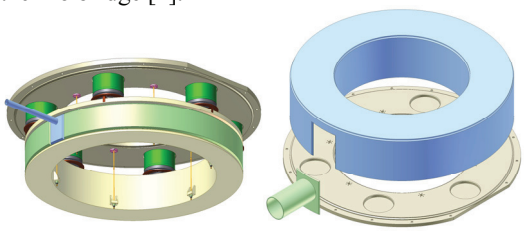

Figure 1: Suspension on the coil (left) and the vacuum vessel (right)

Vacuum vessel

The vacuum vessel seals the vacuum around the cold mass to allow the cooling system to reach the desired cryogenic temperature. The vacuum vessel consists of a support ring, a shell and a weldolet. The rest parts are made of stainless steel SAE 304 [1]. The thickness of the shell is 15-20 mm. The support ring is 48 mm thick. All parts of the vacuum vessel will be assembled by welding.

The space between the spacers is used for the liquid helium circulation. Over the spacers there is a tray made from thin G-10 Glass Epoxy laminate and covered by few layers of fiber glass fabric with epoxy resin with total thickness of 2 mm. The coil is wound inside this tray. Each layer is insulated with three layers of 0.1 mm fiber glass fabric with epoxy resin. Since the coils and conductor experience radial and axial forces of a high magnitude, the winding is required to be done at high tension of 20 kg and gaps between turns are needed to be filled with epoxy resin to restrict movement of the conductor. This impregnation should be done with a brush. The last layer should be wrapped with six layers of 0.1 mm fiber glass fabric with epoxy resin. Then aluminum banding is carried out around the coil at 200 kg tension for restricting the movement of the conductor and the coil while the magnet is energized. Aluminum banding gives more compressive stress to the coil at 4.5 K as compared to SS because of the higher thermal contraction coefficient. A special grade of Aluminum (5052 - H34) strip having high hardness and tensile strength of 267 MPa is used. The strip has a cross section of 2.5 mm x 5 mm.

Instantaneous quench

Figure 2 shows the instantaneous quench calculation results [5,6]. This calculation was done with a constant inductance of 21.9 H (L_w at 686 A). The average temperature is equal to 81 K. The resistance of quenched pole is equal to 2.6 Ohm and the maximum quench voltage is equal to 737 V. The quench detection and protection scheme is shown in figure 3.

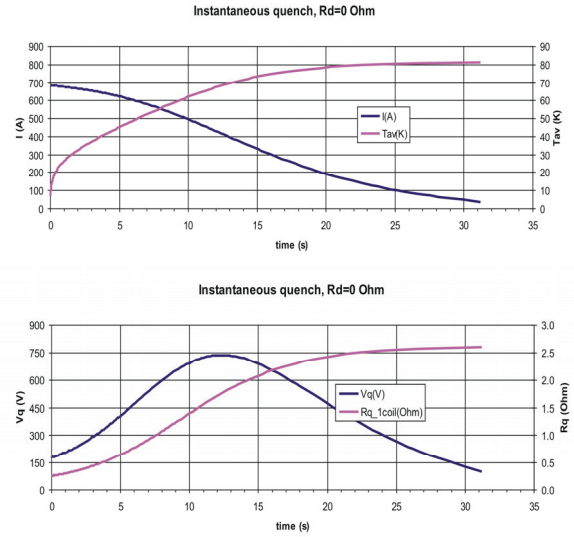

Figure 2: Instantaneous quench calculation of the CBM dipole: magnet current and average coil temperature (upper plot) and quench voltage and quench resistance (lower plot)

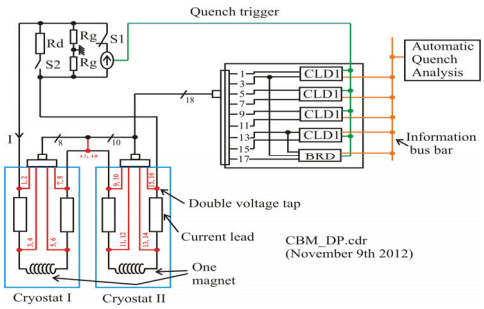

Figure 3: Quench detection and protection scheme (including voltage taps)

References:

[1] Cold work study on a 316LN modified alloy for the ITER TF coil conduit by R. Walsh et al., ADVANCES IN CRYOGENIC ENGINEERING: Transactions of the International Cryogenic Materials Conference - ICMC, Volume 58. AIP Conference Proceedings, Volume 1435, pp. 63-69 (2012).

[2] Toshiyuki Kabo, RIKEN, private communications.

[3] M. Reytier, F. Kircher, B. Levesy,
Adv. In Cryogenic Eng., submitted for publication.

[4] Cure, B. et al., IEEE Transactions on Applied Superconductivity, Date of Publication: Mar 2002, Volume: 12 , Issue: 1 Page(s): 1014 – 1017.

[5] P. Szwangruber et al., “Quench calculations and measurements on the FAIR Super-FRS dipole” Physics Proceedia 36 (2012) 872–877.

[6] E. Floch. “Magnet Inductance and quench computations” MT-INT-ErF-2009-010.

Design of the beam dump for HADES at SIS100

A. Senger[1]

[1]GSI, Darmstadt, Germany

HADES at SIS100 will be placed in front of the CBM experiment as sketched in Figure 1. The beam can be focused either on the target of HADES (left setup), or on the CBM target (right setup). The possibility to run the HADES experiment with the CBM experiment in place was studied using FLUKA [1, 2].

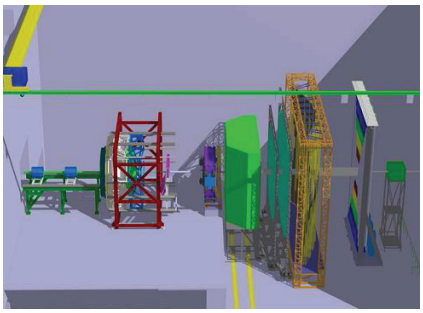

Figure 1: HADES (left setup) and CBM (right setup) experiments.

If the beam is focused on the HADES target, the beam size in the CBM Silicon Tracking Stations (STS) will be larger as a CBM beam pipe. FLUKA calculations have been performed to study the non-ionizing energy loss (NIEL) in the CBM cave for different scenarios. Figure 2 (left) illustrates the NIEL in the CBM cave for Ni+Ni collisions at 8 GeV/u with an intensity 10^7 ions per second at the HADES target. For comparison, in Figure 2 (right) the NIEL distribution during a CBM run of Au+Au collisions at 10 GeV/u with an intensity 10^7 ions per second is shown.

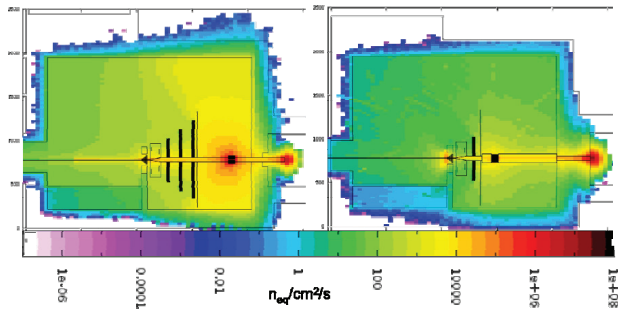

Figure 2: NIEL distributions in the CBM cave during the HADES experiment Ni+Ni at 8 GeV/u with an intensity 10^7 ions per second (left), and during the CBM run Au+Au at 10 GeV/u with an intensity 10^7 ions per second (right).

In order to protect CBM experiment during runs with HADES, a beam dump will be placed in front of the CBM magnet. In a first step, the thickness of an iron beam dump was determined with FLUKA. It was found, that a thickness of 1.5 m iron is sufficient to fully stop the beam. However, the radiation level outside the iron is too high (see Fig. 3 left). In order to reduce this radiation an additional concrete shielding was studied. It turns out, that the radiation level can be drastically reduced by 50 cm of concrete around the iron core, and 150 cm of concrete in front of the iron (see Fig. 3 right).

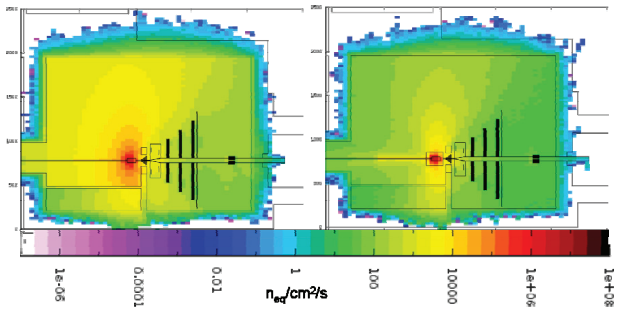

Figure 3: NIEL distributions in the CBM cave during the HADES experiment Ni+Ni at 8 GeV/u with an intensity 10^7 ions per second: with 1.5 m iron as beam dump (left), and with concrete around the iron (right).

References

[1] "The FLUKA code: Description and benchmarking", G. Battistoni, S. Muraro, P.R. Sala, F. Cerutti, A. Ferrari, S. Roesler, A. Fasso`, J. Ranft, Proceedings of the Hadronic Shower Simulation Workshop 2006, Fermilab 6-8 September 2006, M. Albrow, R. Raja eds., AIP Conference Proceeding 896, 31-49, (2007)

[2] "FLUKA: a multi-particle transport code", A. Fasso`, A. Ferrari, J. Ranft, and P.R. Sala, CERN-2005-10 (2005), INFN/TC_05/11, SLAC-R-773

Superconducting dipole magnet for the Compressed Baryonic Matter (CBM) experiment at FAIR*

P. Akishin[1], A.Bychkov[1], E. Floch[2], Yu. Gusakov[1], V. Ivanov[1], P. Kurilkin[1], V. Ladygin[1], H. Leibrock[2], A. Malakhov[1], G. Moritz[2], C. Muehle[2], W.F.J. Müller[2], W. Niebur[2], I. Pschorn[2], P. Senger[2], A. Shabunov[1], P. Szwangruber[2], Y. Xiang[2], C. Will[2]
[1]JINR, Dubna, [2]GSI, Darmstadt

The CBM superconducting dipole magnet is a central part of the detector system. The target station and the Silicon Tracking System are placed in the magnet gap. The magnet has to provide the vertical magnetic field with a bending power of 1 Tm on the length 1m from the target. A perspective view of the magnet is shown in figure 1.

The magnet gap has a height of 140 cm and a width of 250 cm in order to accommodate the STS with a polar angle acceptance of ± 25° and a horizontal acceptance of ± 30°. The magnet is of the H-type with a warm iron yoke/pole and cylindrical superconducting coils in two separate cryostats like the SAMURAI magnet at RIKEN [1, 2]. The potted coil has 1749 turns. The wire – similar to the CMS wire – has Nb-Ti filaments embedded in a copper matrix, and is soldered in a copper stabilizer with a total Cu/SC ratio of about 13 in the conductor. The operating current and the maximal magnetic field in the coils are 686 A and 3.25 T, respectively. The coil case made of stainless steel contains 20 liters of liquid helium for one coil. The vertical force in the coils is about 250 tons. The cold mass is suspended from the room temperature vacuum vessel by six suspension links. Six cylindrical support struts compensate the vertical forces.

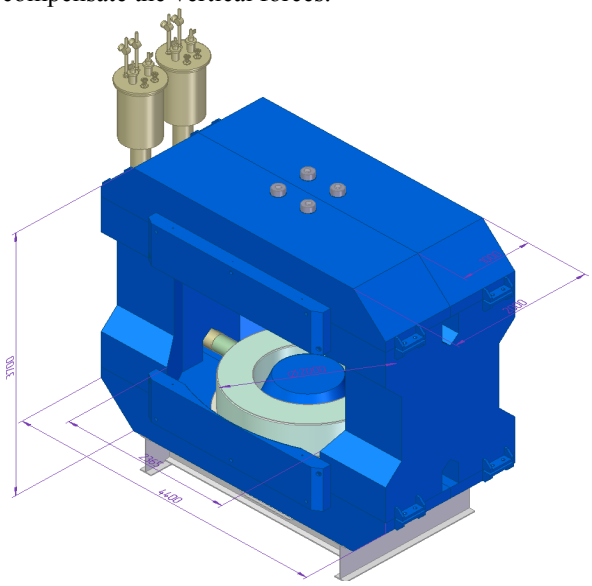

Fig.1: View of the CBM superconducting dipole magnet

The energy stored in the magnet is about 5 MJ. The magnet will be self-protecting. However, in order to limit the temperature rise to 100 K in case of a quench, the energy will be dumped in an external resistor. The parameters of the magnet are listed in table 1.

Table 1: Parameters of the magnet

Type	H-type, superconducting magnet
Number of turns	1749 turns/coil
Windings of coil	impregnated close coiling
Maximum current	686 A
Magnetomotive force	1.2 MA turns/coil
Current density	48 A/mm^2
Central field	1.08 T
Field integral at T m	1 Tm
Maximum field at coil	3.25 T
Inductance	396 – 150 H
Stored energy	5.15 MJ
Coil	
inner diameter	1.37 m (at 4 K)
outer diameter	1.82 m (at 4 K)
cross section	149.2 x168 mm ^{2}(at 4 K)
weight	1644 kg/coil
Pole	
shape	circular type
gap	1.4 m
diameter	2.0 m
height	0.5 m
Yoke	
width	4.4 m
depth	2.0 m
height	3,7 m
weight	250 tons

References

[1] H. Sato et al., "Design of large-gap superconducting dipole magnet for SAMURAI spectrometer" RIKEN Accel. Prog. Rep. 43, 180 (2010).
[2] H. Sato “Superconducting Dipole Magnet for SAMURAI” Proc of SAMURAI workshop 2011.

*Supported by the BMBF, JINR Dubna, and by EU/FP7 Hadronphysics3

SysCore3 – A universal Read Out Controller and Data Processing Board*

J. Gebelein[1], *D. Gottschalk*[2], *G. May*[3], *and U. Kebschull*[1]

[1]Infrastructure and Computer Systems for Data Processing (IRI), Frankfurt University, Frankfurt/Main, Germany; [2]Physikalisches Institut (PI), Heidelberg University, Heidelberg, Germany; [3]GSI, Darmstadt, Germany

The universal SysCore architecture was initially announced in 2007 to provide an optimum balance between fixed requirements and flexibility. The first instance of boards following this principle, acted as development platform for FEE (Front End Electronic), especially the nXYTER with ADC (Analog Digital Converter) and ROC (Read Out Controller). The second slightly modified instance of this board came into operation in several subdetector systems of the CBM experiment, especially as ToF (Time of Flight) ROC where it is used for years now. To extend the usability spectrum, whilst keeping the re-usability approach, a completely new and improved version 3 of the SysCore architecture board has been developed [1]. It allows the CBM collaboration not only to prototype FEE or to develop ROCs, but also to evaluate the DPB (Data Processing Board) capabilities for an optical readout in the CBM service building. In this specific context, the TRD (Transition Radiation Detector) feature extraction is currently an active field of research.

Considering all requirements, such as FMC HPC connectors for high performance connectivity, USB for programming and data transfer, DDR3 for fast memory access, Jitter Cleaner for clock distribution across several boards, optical SFP connectors for CBMnet integration [2] and not to forget an inexpensive central processing FPGA which can be operated in radiation environments, the PCB got a size of 230x230mm. It is made of 16 different layers with a track width/distance of 0,15-0,09mm (micro fine lines). Length compensation for the most critical components such as DDR3, FMC and SFP has been performed. Functional blocks such as power supply, scrubbing controlling or high performance data transfer have been locally combined to provide optimal results. The final board layout can be seen in figure 1.

Programming of the major components on the board can be performed in different ways: The Spartan-6 FPGA itself can be programmed either via USB (Cypress FX2) or JTAG programmer or by the onboard Microsemi ProASIC3 scrubbing controller from a nearby flash memory. The PROASIC3 can be programmed via the Spartan-6 FPGA or a JTAG programmer. This combination allows remote configuration of both FPGAs on the board. Furthermore, the ProASIC3 acts as scrubbing controller for the ToF ROC when it is operated in radiation susceptible environments [3, 4, 5]. This fault tolerance approach has always been a major component of the SysCore architecture and can only by achieved when all components go together. Therefore, the major processing FPGA has been selected to support the background scrubbing feature, the flash memory holding its configuration is a Micron SLC NAND memory with durable charge pumps [6] and the power supply utilizes Linear Technology POL (Point of Load) converters.

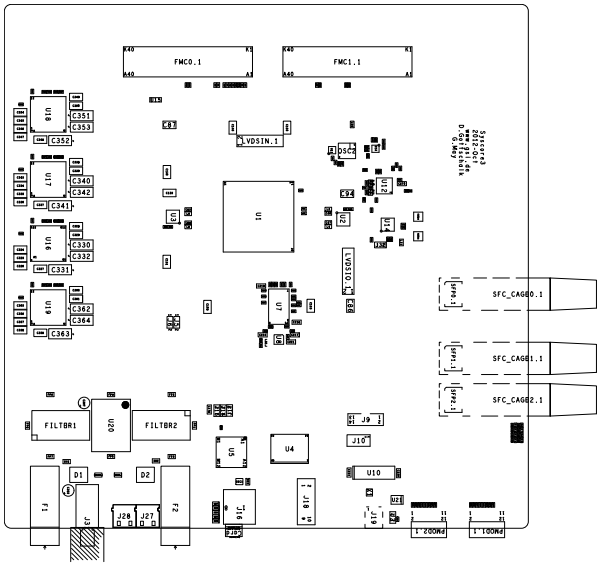

Figure 1: PCB top view of the SysCore3.

References

[1] N. Abel, C. Garcia, J. Gebelein, S. Manz, U. Kebschull, "SysCore3 – a new board for the Universal ROC", CBM Progress Report 2011, Darmstadt, Germany, ISBN 978-3-9811298-9-2

[2] F. Lemke, "Unified Synchronized Data Acquisition Networks", Dissertation, 2012, Mannheim, Germany

[3] N. Abel, H. Engel, J. Gebelein, D. Gottschalk, S. Manz, A. Oancea, U. Kebschull, "Radiation tolerance of the Universal Read Out Controller", CBM Progress Report 2010, Darmstadt, Germany, ISBN 978-3-9811298-8-5

[4] J. Gebelein, H. Engel, U. Kebschull, "FPGA fault tolerance in radiation susceptible environments", Proceedings on Radiation Effects on Components and Systems (RADECS) 2010, Austria

[5] J. Gebelein, U. Kebschull, "Investigation of SRAM FPGA based Hamming FSM encoding in beam test", Proceedings on Radiation Effects on Components and Systems (RADECS) 2012, France

[6] F. Irom, D. N. Nguyen, "Radiation Tests of Highly Scaled High Density Commercial Nonvolatile NAND Flash Memories", JPL TRS, 2011, USA

* Work supported by BMBF (06HD9123I, 06FY7090/05P12RFFCM)

ALICE C-RORC as CBM FLES Interface Board Prototype*

H. Engel and U. Kebschull
Goethe University Frankfurt, Germany

The ALICE Common ReadOut Receiver Card (C-RORC) is an FPGA-based PCIe readout card with high density parallel optical connectivity addressing the needs for the upcoming ALICE upgrade. This card is also considered as a prototype for the CBM First Level Event Selector Interface Board (FLIB) and CBM related requirements have already been integrated during development. First prototypes of this board have been produced and could be tested successfully.

FLES Interface Board

The FLES Interface Board serves as an interface between Data Processing Boards and the First Level Event Selector in the CBM readout chain. It is planned to be implemented as an FPGA-based PCI-Express plug-in card with optical interfaces at the FLES input nodes. Streaming data received on the optical interface from the front-end electronics via Read-Out Controllers and Data Processing Boards is received by the FLIB and provided the host machine using Direct Memory Access (DMA). Prototype boards are required as a test platform for FLES hardware and software development as well as for testbeam and lab setup readout. A more detailed description of the FLES developments can be found in [1].

The C-RORC is a Xilinx Virtex-6 based FPGA board developed by ALICE to replace existing readout boards and enable upgrades of the current readout architecture. The board comes with an eight lane PCI Express Gen2 interface to the host machine and 12 serial optical links up to 6.6 Gbps using three QSFP modules. The highly parallel optical connectivity, the DDR3 RAM and its interface to the host machine makes this board a suitable prototype for first FLIB firmware developments. Requirements for the usage as FLIB prototype have already been considered during the development of the card. The layout of this board was completed in 2012 and first prototypes have been produced. A picture of the board is shown in figure 1.

C-RORC Hardware Test Status

Several hardware tests have been performed to confirm the correct operation of the board and have been compared to previous firmware tests with commercially available evaluation boards. The throughput of the PCIe interface has been directly compared with a reference implementation on the HitechGlobal board and could be confirmed to be identical. All DMA tests have been performed with a custom device driver and DMA engine. A generic device driver, DMA library and software architecture is currently being developed. More details on this can be found in [2]. The onboard flash memories are accessible with both the PCIe interface and the programming cable. The FPGA gets automatically configured from these memories on power-on and the device is correctly detected on all tested host machines. The serial optical links have been tested with electrical and optical loopback adapters, optical QSFPs and active optical cables. A long term test of a full setup with two boards interconnected with QSFP transceivers and parallel fibers did not show any bit errors. First DDR3 tests with SO-DIMM modules operating with 800Mbps and 1066Mbps could also be concluded successfully. The onboard microcontroller for configuration monitoring and control could also be verified. The board is accessible from the I2C chain of the host machine, the configuration status and the board voltages can be read out with I2C and a reconfiguration of the FPGA from a selected flash partition can be triggered. There are no major PCB changes required for the next series of boards.

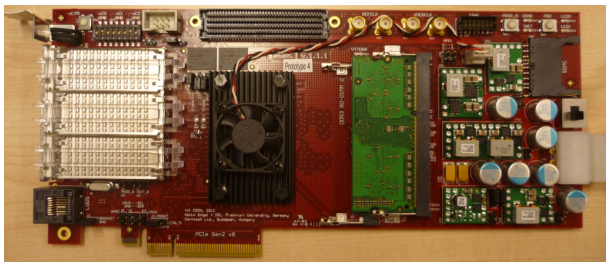

Figure 1: Photo of a C-RORC prototype with one DDR3 module.

Conclusion

All hardware tests that have been performed by now could be concluded successfully. All major interfaces have proved reliable behavior and there are only a few untested aspects of the board remaining. A larger number of boards is going to be produced in 2013 and will be provided to several working groups to investigate the hardware more deeply and continue the development of firmware and software.

References

[1] J. de Cuveland et al., “Status of CBM FLES Prototype Developments” , This report

[2] D. Eschweiler, V. Lindenstruth, “Microdrivers in High-Throughput and Real-Time Environments”, FIAS Scientific Report 2012 (to appear)

* Work supported by BMBF and HGS-HIRe

Status of CBM First-level Event Selector Prototype Developments*

J. de Cuveland[1], *D. Hutter*[1], *and V. Lindenstruth*[1]

[1]FIAS Frankfurt Institute for Advanced Studies, Goethe-Universität Frankfurt am Main, Germany

The First-level Event Selector (FLES) is the central event selection system in the CBM experiment. Its task is to select data for storage based on online analyses including a complete event reconstruction. To do so, the FLES timeslice building has to combine data from all input links to time intervals and distribute them via a high-performance network to the compute nodes. Data rates at this point are expected to exceeds 1 TByte/s. It has proven practical to use an InfiniBand network for data transfer between the FLES nodes. Even so, further investigations are needed to design the final system and develop the required software algorithms.

Micro-FLES Cluster

To provide a small scale, highly customizable platform for these studies, the *Micro-FLES* cluster was installed at GSI (see Fig. 1). Eight identical compute nodes provide a total of 192 logic cores and 512 GB memory. While consuming only 1 U of installation space, the nodes still provide PCIe 3.0 expansion slots for up to 2 FLES Interface Boards (FLIB) and 3 GPU cards. This allows additional tests of the full data transport chain and reconstruction algorithms in the future. In addition to the compute nodes, one head node provides infrastructure services such as storage and boot images. Although there is local storage in the compute nodes for test purposes, it is currently not used for operating the cluster.

For timeslice building the cluster is equipped with a state-of-the-art InfiniBand FDR network. Each node offers two 56 Gbit/s 4x FDR ports currently connected to one core switch. The availability of two ports per node easily allows the study of more complex network topologies.

Complementarily, the development of a timeslice-building test software based on InfiniBand Verbs has started. Especially questions regarding data structures, buffer management, and network scheduling are addressed. Preliminary tests using the same data structures as intended for the final setup have shown promising results.

FLES Interface Board (FLIB)

In the process of upgrading the CBMnet-based prototype read-out chain, a replacement for the currently used PC interface board (namely the ABB) is needed. For this purpose the FLIB prototype board derived from the ALICE C-RORC [1] has been chosen. Based on a Xilinx Virtex-6 FPGA, it features an eight-lane PCIe Gen 2 interface, up to 12 optical links and two DDR3 memory sockets.

* Work supported by BMBF (05P12RFFCP) and HIC for FAIR

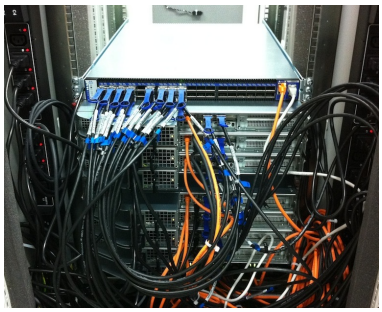

Figure 1: The *Micro-FLES* cluster installed at GSI

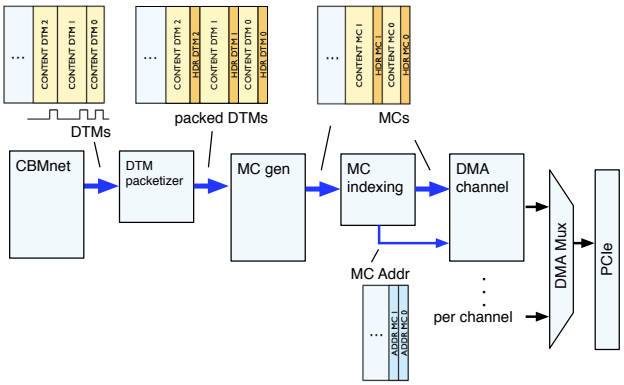

Figure 2: Schematic view of the FLIB read-out data path

In contrast to the final system, early prototype setups will not support the creation of microslice containers (MC) (as described in [2]). Hence, a firmware was developed that is capable of reading out raw CBMnet messages as delivered from the CBM front-end electronics.

The corresponding data path is shown in Figure 2. In the first step, incoming CBMnet messages are preprocessed in hardware to facilitate subsequent software processing. After preprocessing, a separate module packages the incoming data into simplified MCs, whose reduced data content requirements (in comparison to ordinary MCs) support not yet fully synchronized detector electronics. Finally, an address index table is created and MCs are written to the PC host memory via the PCIe interface. The chosen partitioning of the design and the creation of simplified MCs enables reuse of developed hardware and software components when migrating to a fully microslice-based read-out chain.

References

[1] H. Engel *et al*, "ALICE C-RORC as CBM FLES Interface Board Prototype", this report

[2] J. de Cuveland *et al*, "CBM First-level Event Selector Dataflow Architecture and Microslice Concept", GSI Sci. Report 2011, PHN-NQM-CBM-41, p 63.

FLES: Standalone First Level Event Selection Package for CBM*

V. Akishina[1,2,3], *I. Kisel*[1,2,4], *I. Kulakov*[1,2,4], *and M. Zyzak*[1,2,4]

[1]Uni-Frankfurt, Germany; [2]GSI, Darmstadt, Germany; [3]JINR, Dubna, Russia; [4]FIAS, Frankfurt, Germany

The main focus of the CBM experiment is the measurement of very rare probes, that requires interaction rates of up to 10 MHz. Together with the high multiplicity of charged particles (up to 1000) produced in heavy-ion collisions, this leads to huge data rates of up to 1 TB/s. Most trigger signatures are complex (short-lived particles, e.g. open charm decays) and require information from several detector sub-systems.

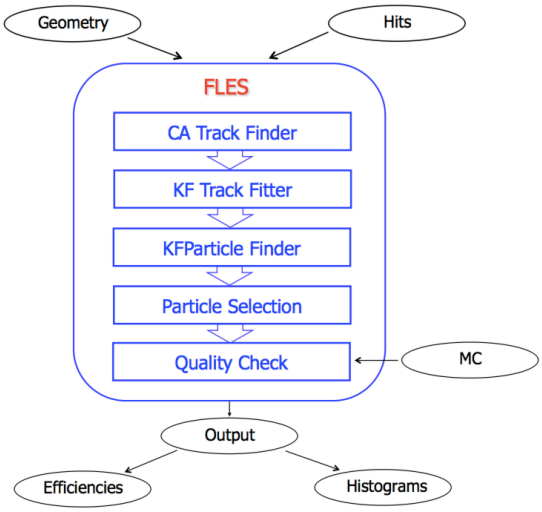

Figure 1: Block diagram of the FLES package.

The First Level Event Selection (FLES) package of the CBM experiment is intended to reconstruct the full event topology including tracks of charged long-lived particles and short-lived particles. The FLES package consists of several modules (see Figure 1): track finder, track fitter, particle finder and physics selection. As an input the FLES package receives the geometry of the tracking detectors and the measurements, which are created by the charged particles crossing the detectors — hits. Tracks of the charged particles are reconstructed by the Cellular Automaton track finder [1]. The Kalman filter based track fitter [2] is used for precise estimation of the track parameters. The KF Particle Finder [3] is used to find short-lived particles. In addition, a module for quality assurance is implemented, that allows to monitor the quality of the reconstruction at all stages.

The package provides the high reconstruction efficiency and the high signal to background (S/B) ratio for the reconstructed decays. For instance, for 240 000 minimum bias Au+Au UrQMD events at 25 AGeV the reconstruction efficiency (normalized on 4π) for the K_s^0 meson is 15.3% with the S/B ratio 3.5 and for the Λ hyperon — 17.2% and 5.1 respectively.

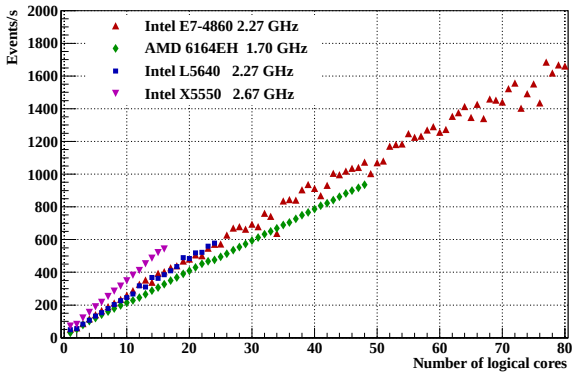

Figure 2: Scalability of the FLES package on many-core servers.

The first version of the FLES package is optimized with respect to speed, intrinsically local and parallel. The implemenation is based on the SIMD instructions and have been parallelized between cores using the Intel Threading Building Blocks package [4], that provides scalable event-level parallelism with respect to the number of hardware threads and CPU cores. Four servers with Intel Xeon and AMD processors have been used for the scalability tests. The most powerful server has 4 processors with 10 physical cores each, that gives 80 logical cores in total. Figure 2 shows a strong scalability for all many-core systems. The achieved reconstruction speed is 1700 events per second on the 80-cores server.

References

[1] I. Kisel, "Event reconstruction in the CBM experiment," *Nucl. Instr. and Meth.* A566 (2006) pp. 85–88.

[2] S. Gorbunov, U. Kebschull, I. Kisel, V. Lindenstruth, and W.F.J. Müller, "Fast SIMDized Kalman filter based track fit," *Comp. Phys. Comm.* 178 (2008) pp. 374–383.

[3] M. Zyzak et al., "The KF Particle Finder package for short-lived particles reconstruction for the CBM experiment", this report.

[4] *ITBB Reference Manual.* Available at: http://threadingbuildingblocks.org

*This work was supported by the Hessian LOEWE initiative through the Helmholtz International Center for FAIR (HIC for FAIR) and EU-FP7 HadronPhysics2. Das Projekt wird vom Hessischen Ministerium fuer Wissenschaft und Kunst gefoerdert.

The Cellular Automaton track finder at high track multiplicities for CBM*

V. Akishina[1,2,3], *I. Kisel*[1,2,4], *I. Kulakov*[1,2,4], *and M. Zyzak*[1,2,4]

[1]Uni-Frankfurt, Germany; [2]GSI, Darmstadt, Germany; [3]JINR, Dubna, Russia; [4]FIAS, Frankfurt am Main, Germany

The CBM experiment at FAIR is being designed to study heavy-ion collisions at extremely high interaction rates (up to 10 MHz) and high track multiplicities (up to 1000). Since the beam in the CBM experiment will have no bunch structure, but continuous, the groups of events may be close or overlapped in time. Measurements in this case will be 4D (x, y, z, t). Thus, the reconstruction of time slices rather than events will be needed. In addition to such high input rate and complicated event topology, the full event reconstruction and selection will be done at the First Level Even Selection (FLES) stage. In this respect, both the speed of the reconstruction algorithms and their efficiency are crucial.

The Cellular Automaton (CA) [1] track finder is fast and robust and thereby is used both for the online and offline track reconstruction in the CBM experiment. The algorithm creates short track segments in each three neighbouring stations, then combines them into track-candidates and selects the best tracks according to the maximum length and minimum χ^2 criteria. The algorithm was further optimized for the case of high track multiplicity with respect to time: additional sorting of found hits according to 2-dimensional (y, z) grid was introduced in order to speed up the search for the next hit. The standalone FLES package [2] was used to investigate the stability of the CA track reconstruction with respect to a track multiplicity per event. For the study 1000 of minimun bias Au+Au UrQMD events at 25 AGeV was simulated. As the first step towards 4D tracking a number of minimum bias events (up to 100) were packed into one group with no time measurement taken into account. The group was treated by the CA track finder as a single event and the regular reconstruction procedure was performed (Figure 1).

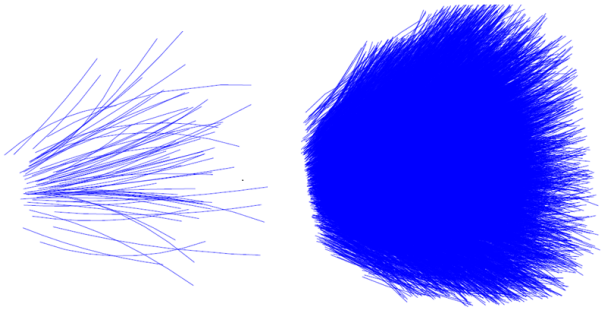

Figure 1: Reconstructed tracks in minimum bias event (left) and packed group of 100 minimum bias events (right), 109 and 10 340 tracks in average respectively.

The dependence of the track reconstruction efficiency on the track multiplicity is stable (Figure 2). In particular, the efficiency of the algorithm decreases only by 4% for 100 minimum bias events in one group, comparing to the case of a single minimum bias event. The efficiencies for the reference tracks ($p > 1$ GeV/c), which include tracks of particular physics interest, remains high for all range of track multiplicities. The efficiencies for extra (100 MeV/c $< p <$ 1 GeV/c) and secondary tracks are also stable. The level of ghost tracks is less than 10%. Thus, the study has shown that the CA track finder is stable with respect to the track multiplicity.

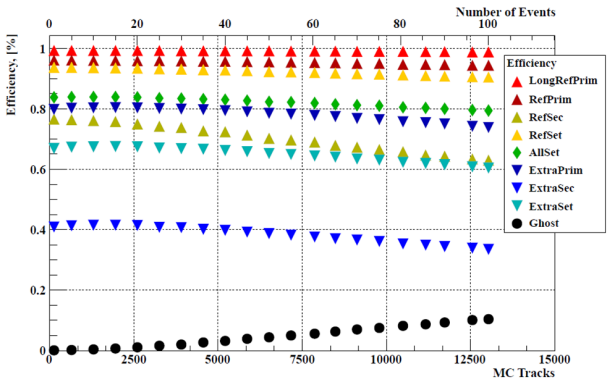

Figure 2: Track reconstruction efficiencies and ghost rate for different sets of tracks versus track multiplicity.

The speed of the algorithm was studied as a function of track multiplicity. The time, which algorithm needs to proceed a grouped event, behaves as a second order polynomial with respect to a number events in the group. Due to this fact, the CA track finder needs less than 2 seconds in order to reconstruct a grouped event combined of 100 minimum bias events, that corresponds to about 10 000 reconstructed tracks.

Summarizing, the CA track finder reconstruction algorithm shows high speed performance and stability with respect to the track multiplicities, up to the extreme case of about 10 000 reconstructed tracks per event.

References

[1] I. Kisel, Nucl. Instr. and Meth. A566 (2006) 85-88.

[2] V. Akishina, I. Kisel, I. Kulakov, M. Zyzak, *FLES: Standalone First Level Event Selection Package for the CBM experiment*, this report.

*This work was supported by the Hessian LOEWE initiative through the Helmholtz International Center for FAIR (HIC for FAIR) and EU-FP7 HadronPhysics2. Das Projekt wird vom Hessischen Ministerium fuer Wissenschaft und Kunst gefoerdert.

The KF Particle Finder package for short-lived particles reconstruction for CBM*

M. Zyzak[1,2,3], *I. Kisel*[1,2,3], *I. Kulakov*[1,2,3], *and I. Vassiliev*[1,3]

[1]Uni-Frankfurt, Germany; [2]FIAS, Frankfurt am Main, Germany; [3]GSI, Darmstadt, Germany

Today the most interesting physics is contained in the properties of short-lived particles which can not be registered by a detector system directly but only reconstructed through their decay products. Also, short-lived particles which have a very small production probability are of the particular interest. Thus, a statistically significant result can be obtained only in case of the operation with a high rate of collisions up to 10^7 Hz. This raises the problem of data processing and storage. Therefore only those events are selected for the further analysis that can potentially contain interesting particles. The CBM experiment requires the full reconstruction of events, including reconstruction of short-lived particles, already at the selection stage.

A fast and efficient algorithm based on the Kalman filter (KF) method for finding, reconstruction and selection of short-lived particles is developed. A search for about 50 particles (decay channels) has been implemented. At first all tracks are divided into two groups for a further analysis: secondary and primary. Secondary tracks are produced in a decay of short-lived particles that have sufficient lifetime to move away from the primary vertex. These particles are strange particles (K^0_s-mesons and Λ-hyperons), multi-strange hyperons (Ξ and Ω) and charmed particles (D^0, $D^{\pm}$, $D^{\pm}_s$ and Λ_c). Primary tracks are those, which are produced directly in the collision of a beam with a target. Tracks from the resonances decays (strange, multi-strange and charmed resonances, light vector mesons, charmonium) are also considered as primary since they are produced directly at the point of the primary vertex due to the extremely small lifetime.

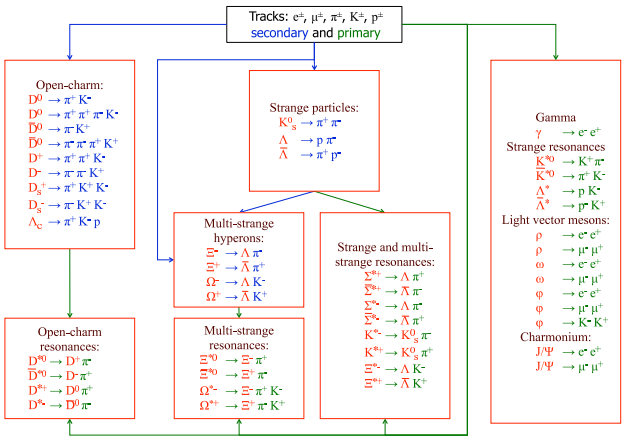

Figure 1: Block diagram of the KF Particle Finder algorithm.

Selected tracks are combined into particle-candidates according to the block diagram in Figure 1. The particles are reconstructed with the KFParticle package [1]. All particles are reconstructed in one go that makes the algorithm local with respect to the data and therefore very fast.

KF Particle Finder achieves a high efficiency of the particle reconstruction. For example, the efficiency of the strange particles reconstruction for 240 000 of minimum bias Au+Au collisions at 25 AGeV as well as a signal to background ratio is given in Table 1.

Particle	K^0_s	Λ	Ξ^-	Ω^-
Efficiency, %	15.3	17.8	5.0	2.5
S/B	3.5	5.1	42.2	4.3

Table 1: The efficiency and a signal to background ratio (S/B) for strange particles.

In order to utilize all possible resources of modern CPUs and to achieve the highest possible speed KF Particle Finder is based on the SIMD instructions. Also, the algorithm has been parallelized between cores of the modern CPUs and demonstrates a strong linear scalability on many-core servers with respect to the number of cores (see Figure 2).

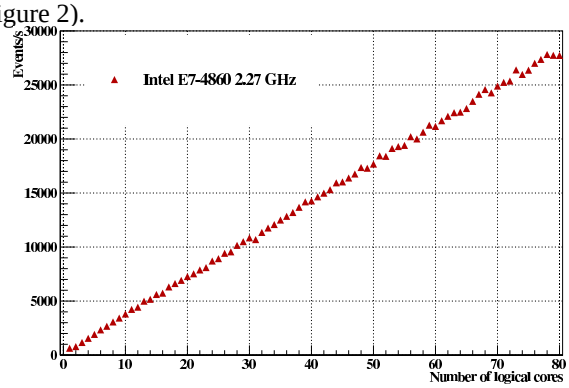

Figure 2: Scalability of the KF Particle Finder package with minimum bias Au+Au events at 25 AGeV on a many-core server lxir075 equipped with four Intel E7-4860 (2.27 GHz) CPUs.

Summarizing, the KF Particle Finder package reconstructs about 50 of the most important decay channels for the CBM experiment with a high efficiency and a high signal to background ratio achieving speed of 1.5 ms per Au+Au minimum bias collisions at 25 AGeV on a single core.

References

[1] S. Gorbunov and I. Kisel, Reconstruction of decayed particles based on the Kalman filter. CBM-SOFT-note-2007-003, 7 May 2007.

*This work was supported by the Hessian LOEWE initiative through the Helmholtz International Center for FAIR (HIC for FAIR) and EU-FP7 HadronPhysics2. Das Projekt wird vom Hessischen Ministerium fuer Wissenschaft und Kunst gefoerdert.

The KF Particle Finder package for short-lived particles reconstruction for CBM*

M. Zyzak[1,2,3], *I. Kisel*[1,2,3], *I. Kulakov*[1,2,3], *and I. Vassiliev*[1,3]

[1]Uni-Frankfurt, Germany; [2]FIAS, Frankfurt am Main, Germany; [3]GSI, Darmstadt, Germany

Today the most interesting physics is hidden in the properties of short-lived particles which can not be registered directly by a detector system but only reconstructed from their decay products. Also, short-lived particles which have a very small production probability are of the particular interest. Thus, a statistically significant result can be obtained only in case of the operation with a high rate of collisions up to 10^7 Hz. This raises the problem of data processing and storage. Therefore only those events are selected for the further analysis that can potentially contain interesting particles. The CBM experiment requires the full reconstruction of events, including reconstruction of short-lived particles, already at the selection stage.

A fast and efficient KF Particle Finder package for short-lived particles reconstruction and selection is developed for the CBM experiment. A search for about 50 decay channels has been currently implemented. At first, all tracks are divided into groups of secondary and primary tracks for further analysis. Primary tracks are those, which are produced directly in the collision of beam and target ions. Tracks from decays of resonances (strange, multi-strange and charmed resonances, light vector mesons, charmonium) are also considered as primaries since they are produced directly at the point of the primary vertex. Secondary tracks are produced by the short-lived particles, which decay not in the primary vertex point and can be well separated. These particles include strange particles (K^0_s and Λ), multi-strange hyperons (Ξ and Ω) and charmed particles (D^0, $D^\pm$, $D^\pm_s$ and Λ_c).

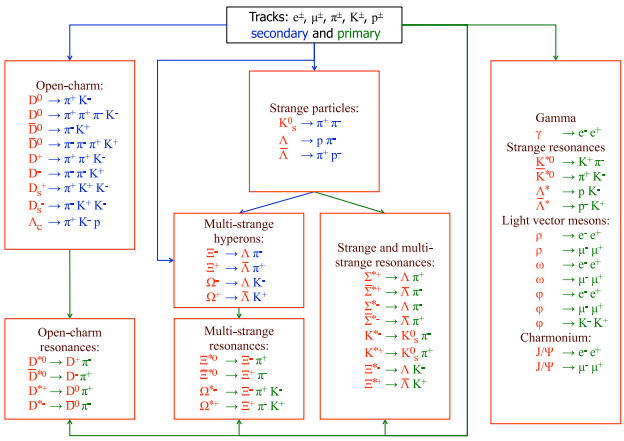

Figure 1: Block diagram of the KF Particle Finder algorithm.

Then tracks are combined according to the block diagram in Figure 1 and particle-candidates are produced from these combinations. The particles are reconstructed with the KF Particle package [1], which is based on the Kalman filter (KF) method and finds parameters of the particle, such as decay vertex, momentum, energy, mass, etc., together with their errors. All particles of the event are reconstructed at once that makes the algorithm local with respect to the data and therefore very fast.

KF Particle Finder achieves a high efficiency of the particle reconstruction. For example, efficiencies of K^0_s, Λ, Ξ^- and Ω^- reconstruction are 15.3%, 17.8%, 5.0% and 2.5% respectively for 240 000 of minimum bias Au+Au collisions at 25 AGeV. The corresponding signal to background ratios are 3.5, 5.1, 42.2 and 4.3.

In order to utilize all possible resources of modern CPUs and to achieve the highest possible speed KF Particle Finder is based on the SIMD instructions. Also, the algorithm has been parallelized between cores of the modern CPUs and demonstrates a strong linear scalability on many-core servers with respect to the number of cores (see Figure 2).

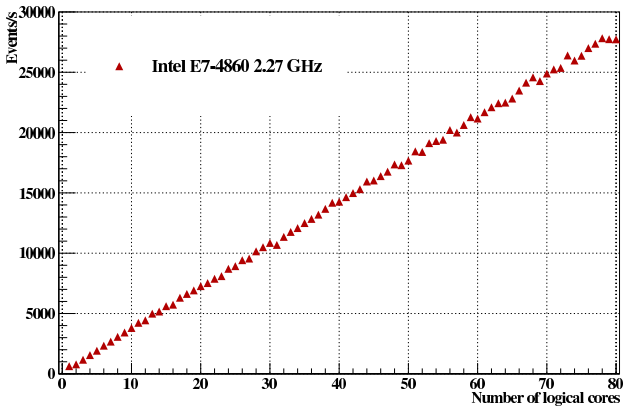

Figure 2: Scalability of the KF Particle Finder package with minimum bias Au+Au events at 25 AGeV on a many-core server lxir075 equipped with four Intel E7-4860 (2.27 GHz) CPUs.

Summarizing, the KF Particle Finder package reconstructs about 50 of the most important decay channels for the CBM experiment with a high efficiency and a high signal to background ratio achieving speed of 1.5 ms per Au+Au minimum bias collisions at 25 AGeV on a single core.

References

[1] S. Gorbunov and I. Kisel, Reconstruction of decayed particles based on the Kalman filter. CBM-SOFT-note-2007-003, 7 May 2007.

*This work was supported by the Hessian LOEWE initiative through the Helmholtz International Center for FAIR (HIC for FAIR) and EU-FP7 HadronPhysics2. Das Projekt wird vom Hessischen Ministerium fuer Wissenschaft und Kunst gefoerdert.

Antihyperon decay reconstruction in the CBM experiment

I. Vassiliev[1,2], *I. Kisel*[1,3], *I. Kulakov*[1,3], *M. Zyzak*[1,3], *and the CBM Collaboration*

[1]Goethe-Universität, Institut für Kernphysik, Frankfurt am Main; [2]GSI, Darmstadt; [3]FIAS. Frankfurt am Main

One of the most challenging tasks of the CBM experiment is to measure yields, excitation functions and flows of antihyperons. Antihyperons like Ω^+ and Ξ^+ will be measured in the CBM-detector by its decay into charged hadrons, which are detected in the Silicon Tracking System (STS) and in the Time-of-Flight detector (TOF). The key role of the TOF detector is antiproton selection in very dense negative pions and Kaons environment. On the Fig. 1 is shown calculated by TOF tracks m^2 vs particle momentum. Negative track with $\mid m^2 - m_p^2 \mid < 2\sigma$ and $\mid m^2 - m_K^2 \mid > 3\sigma$ and $\mid m^2 - m_\pi^2 \mid > 3\sigma$ was used as an antiproton candidate to reconstruct $\bar{\Lambda}$.

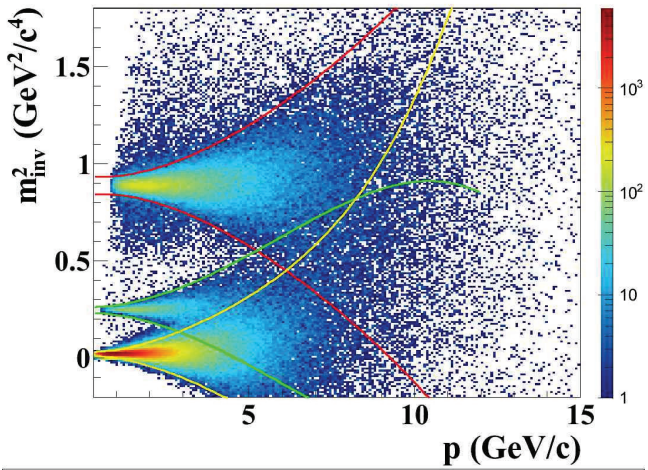

Figure 1: Tracks m^2 vs particle momentum calculated by TOF.

On the Fig. 2 is shown invariant mass distribution of $\bar{p}\,\pi^+$ pairs. Clear $\bar{\Lambda}$ peak is visible. $\bar{\Lambda}$ reconstruction efficiency is above 14% for 35 AGeV and achieve its maximum about 22% at 8 AGeV. One or two antiproton track-candidates per event allows significantly decrease the combinatorial background. Signal to background ratio is above 3.4 for central Au + Au collisions at 35 AGeV. KFParticle finder was used in order to reconstruct $\bar{\Lambda}$ combining secondary $\bar{p}$ and π^-.

Then, combining $\bar{\Lambda}$ with positive secondary Kaon or pion, the Ω^+ and Ξ^+ candidates were tested. The Ω^+ or Ξ^+ was accepted if it has good quality geometrical and topological detached vertex: ($\chi^2_{geo} < 3\sigma$, $\chi^2_{topo} < 3\sigma$) and z-vertex greater than 3 cm downstream the target plane.

To study the feasibility of multi-strange antihyperon decay reconstruction in the CBM experiment, a sets of 10^6 central Au+Au UrQMD events at 2, 4, 6, 8, 10, 15,

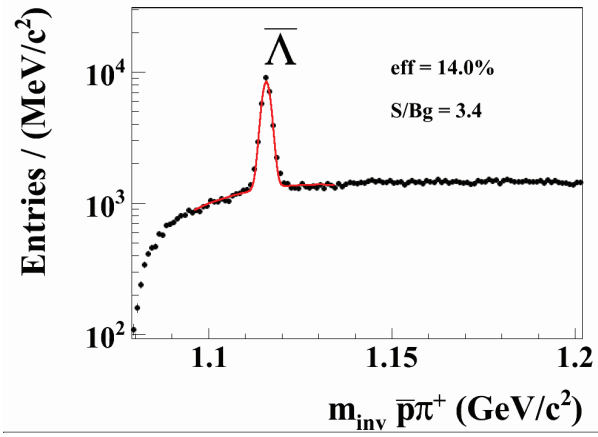

Figure 2: Reconstructed invariant mass distribution of $\bar{p}\,\pi^+$ pairs in central Au+Au collisions at 35 AGeV. Red line is polynomial background plus signal Gaussian fit.

20, 25, 30 and 35 *A*GeV were simulated. Typical invariant mass spectrum is shown in Fig. 3. The Ξ^+ reconstruction efficiency is about 3.1% for central Au + Au UrQMD events at 35 AGeV. The reconstructed mass value $1.321 \pm 0.003\ GeV/c^2$ is in a good agreement with the simulated PDG's data. Invariant mass resolution is 2.3 (MeV/c^2).

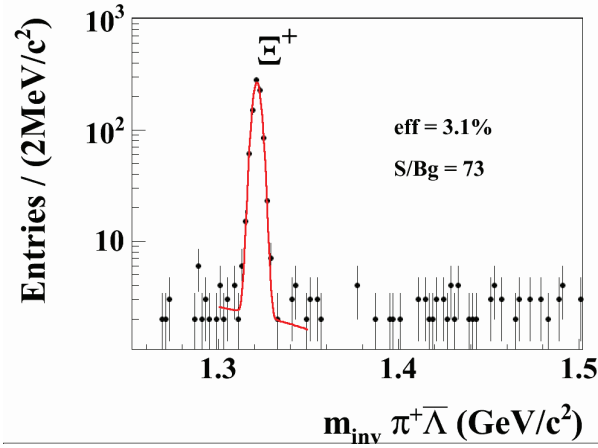

Figure 3: Reconstructed invariant mass distribution of $\bar{\Lambda}\,\pi^+$ pairs in central Au+Au collisions at 35 AGeV. Red line is polynomial background plus signal Gaussian fit.

Multi-strange baryon decay reconstruction in the CBM experiment

I. Vassiliev[1,2], *I. Kisel*[1,3], *I. Kulakov*[1,3], *A. Lebedev*[1,4], *M. Zyzak*[1,3], *and the CBM Collaboration*

[1]Goethe-Universität, Institut für Kernphysik, Frankfurt am Main; [2]GSI, Darmstadt; [3]FIAS. Frankfurt am Main; [4]JINR, Dubna

One of the predicted signatures of the phase transition from nuclear matter to deconfined quark gluon plasma is the enhanced production of multi-strange particles. Also the yield of particles carrying strange quarks is expected to be sensitive to the fireball evolution. The CBM detector will provide an unique opportunity to measure yields, direct and elliptic flows, excitation functions of multi-strange baryons at different energies and sizes of the colliding heavy ions. Ω^- baryon consists of 3 strange quarks, Ξ^- baryon contains 2 strange quarks and Λ — one strange quark. Multi-strange baryons will be measured in CBM by its decay into charged hadrons, which are detected in the Silicon Tracking System (STS) and in the Time-of-Flight detector (TOF).

To study the feasibility of multi-strange baryons decay reconstruction in the CBM experiment, a sets of 10^6 central Au+Au UrQMD events at 2, 4, 6, 8, 10, 15, 20, 25, 30 and 35 AGeV were simulated. High statistic allows to calculate even $\Omega^{\pm}$ reconstruction efficiency directly, avoiding signal embedding into the UrQMD events. Together with wide range of the beam energies, it allows to investigate systematic behavior of different physics observables like direct and elliptic flows, excitation functions, antibaryon to baryon ratios and many others. In Fig. 1 the reconstructed multi-strange antibaryon to baryon production ratios versus beam energy is shown. Strange quarks number hierarchy is clearly visible. Black points correspond to Ω^+ to Ω^- ratios (S = 3), red points are Ξ^+ to Ξ^- ratios (S = 2) and blue points are $\bar{\Lambda}$ to Λ ratios (S = 1).

The Ω^- decays into $\Lambda + K^-$ with branching ratio 67.8% and $c\tau$ = 2.46 cm., the Ξ^- decays to $\Lambda + \pi^-$ with branching ratio 99.89% and $c\tau$ = 4.92 cm decays of Λ happen most often in the STS detector. The STS geometry with 8 double-sided segmented strip detectors, cables and support frames were used for event reconstruction. Particle identification with TOF was applied. The KFParticle Finder package was used to reconstruct about 50 particles and resonances including $\Omega^{\pm}$, $\Xi^{\pm}$, Λ and $\bar{\Lambda}$. Typical invariant mass spectrum is shown in Fig. 2. The Ω^- reconstruction efficiency is about 1.8% for central UrQMD events. The reconstructed mass value $1.672 \pm 0.003\ GeV/c^2$ is in a good agreement with the simulated PDG's data. The Ω^- invariant mass resolution is 2.3 (MeV/c^2).

The $\Omega^{\pm}$ or $\Xi^{\pm}$ are accepted if they have good quality geometrical and topological detached vertex with $(\chi^2_{geo} < 3\sigma,\ \chi^2_{topo} < 3\sigma)$ and z-vertex farther than 3 cm downstream of the target plane.

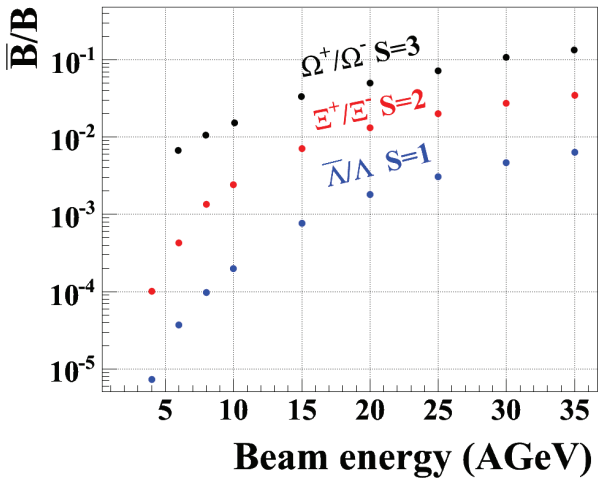

Figure 1: Recalculated ratios of anti-baryon to baryons yields versus beam energy

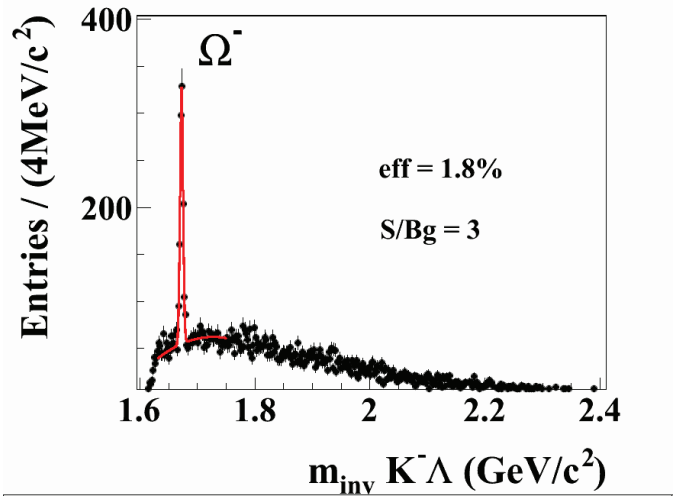

Figure 2: Reconstructed invariant mass distribution of $\Lambda\ K^-$ pairs in central Au+Au collisions at 35 AGeV. Red line is polynomial background plus signal Gaussian fit.

Σ^* decay reconstruction in the CBM experiment

I. Vassiliev[1,2], I. Kisel[1,3], I. Kulakov[1,3], M. Zyzak[1,3], and the CBM Collaboration

[1]Goethe-Universität, Institut für Kernphysik, Frankfurt am Main; [2]GSI, Darmstadt; [3]FIAS. Frankfurt am Main

The investigation of p+A up to 30 GeV and A+A from 4 to 11 AGeV beam energies is considered as part of the research program and will be performed in the first phase of FAIR with a start version of the CBM detector at the SIS-100 accelerator. This start version consists of two detector systems: the Silicon Tracking System (STS) placed in a magnetic field for the measurement of momenta and vertices; and a Time-Of-Flight (TOF) wall placed at 6-10 meter downstream of the target for hadron identification. $\Sigma^{*\pm}$ is the members of multi-strange hyperon family. Σ^{*+} consist of uus and Σ^{*-} of dds quarks correspondingly. Opposite to $\Omega^{\pm}$ and $\Xi^{\pm}$, $\Sigma^{*\pm}$ hyperon decay very fast inside the fireball carrying out information about fireball evolution.

To study the feasibility of $\Sigma^{*\pm}$ decay reconstruction in the CBM experiment, a sets of $6 \cdot 10^6$ central C+C UrQMD events at 10 AGeV were simulated. High statistic allows to calculate $\Sigma^{*\pm}$ reconstruction efficiency and signal to background ratio directly, avoiding signal embedding into the UrQMD event. $\Sigma^{*\pm}$ will be measured in the CBM-detector by its decay into charged hadrons, which are detected in the Silicon Tracking System (STS) and in the Time-of-Flight detector (TOF). The $\Sigma^{*\pm}$ decays to $\Lambda + \pi^{\pm}$ with branching ratio 87%, Λ decays most often happen in the STS detector. The STS geometry with 8 double-sided segmented strip detectors, cables and support frames were used for L1 tracking [1]. Particle identification with TOF was applied. KFParticle finder [2] was used to reconstruct about 50 particles and resonances including $\Sigma^{*\pm}$. In order to reconstruct Σ^* all primary pions were combined with all reconstructed primary lambdas.

The invariant mass spectrum of primary Λ and primary π^+ pairs is shown in Fig. 1 and primary Λ plus primary π^- pairs in Fig. 2 correspondingly. The reconstructed mass value $1.383 \pm 0.003\ GeV/c^2$ is in a good agreement with the simulated PDG's data.

The $\Sigma^{*\pm}$ was accepted if it has good quality geometrical and topological vertex: ($\chi^2_{geo} < 3\sigma$, $\chi^2_{topo} < 3\sigma$).

$\Sigma^{*\pm}$ peaks are clearly visible. Signal to background ratios are 0.16 and 0.24 correspondingly.

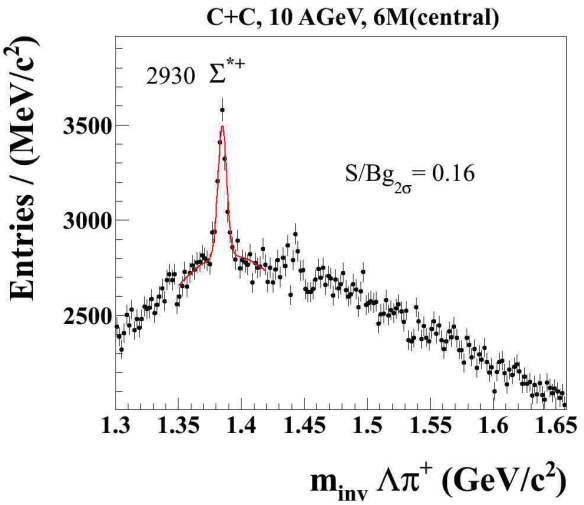

Figure 1: Reconstructed invariant mass distribution of primary π^+ and Λ pairs in central C+C collisions at 10 AGeV. Red line is polynomial background plus signal Gaussian fit.

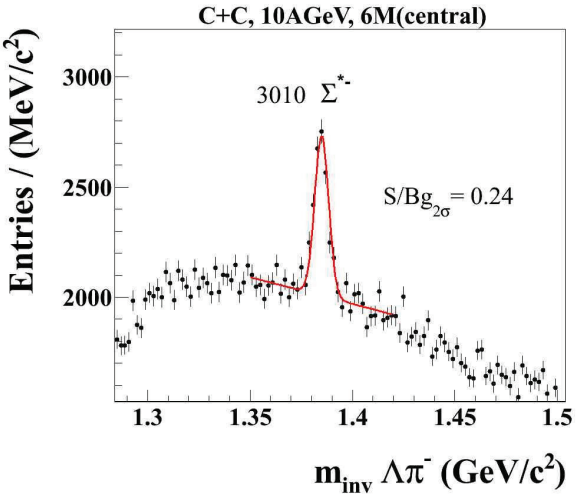

Figure 2: Reconstructed invariant mass distribution of primary π^- and Λ pairs in central C+C collisions at 10 AGeV. Red line is polynomial background plus signal Gaussian fit.

References

[1] I. Kisel, Nucl. Instr. and Meth. A566 (2006) 85-88.

[2] M.Zyzak, I.Kisel, Status of KFParticle and SIMD KF, 20. CBM Collaboration Meeting, September 24-28, 2012, Kolkata, India

Status of low-mass di-electron simulations in the CBM experiment *

E. Lebedeva[1] *and C. Höhne*[1]
[1]JLU Gießen University, Gießen, Germany

The reconstruction of low-mass vector mesons is one of the main goals of the CBM experiment at FAIR. The CBM experiment will be able to reconstruct low-mass vector mesons in di-electron and di-muon decay channels. The current status of low-mass di-electron simulations in central Au+Au collisions at 8 AGeV (SIS100) and 25 AGeV (SIS300) beam energy is presented in this report.

Results were obtained with the latest version of the CBMROOT software (January 2013) which includes realistic detector descriptions. The background was generated using the transport code UrQMD including di-electron pairs from γ-conversions, π^0- and η- Dalitz decays. Di-electron pairs from ρ, ω, ϕ, and ω-Dalitz decays were simulated by the PLUTO event generator and embedded into UrQMD events. The detector setup includes STS, RICH, TRD and TOF detectors. For 8 AGeV beam energy the TRD detector was excluded from simulations. A 25 μm thick gold target was used in order to avoid additional background from γ-conversions in the target.

An electron candidate has to be reconstructed and identified in all detectors, namely RICH, TRD and TOF. Since the TRD is not used for 8 AGeV beam energy simulations, an additional momentum cut at 5.5 GeV/c was implemented in order to reject large momentum pions.

The background rejection strategy includes several cuts. The first cut is based on the assumption that all pairs with $M_{ee} < 25\ MeV/c^2$ stem from γ-conversion and they are fully removed from further combinatorics. The aim of the next two cuts is to reject $e^{\pm}$ pairs where one partner is reconstructed only in the STS (segment track) or was fully reconstructed but not identified as electron. The last cut is a transverse momentum cut.

The dominant background source are random combinations of $e^{\pm}$ from π^0-Dalitz decays and γ-conversions. For 8 AGeV beam energy the main contributions to background pairs come from combinations of $e^{\pm}$ from π^0-Dalitz decays and other particles (35%), $e^{\pm}$ from π^0-Dalitz and γ-conversion (23%) and $e^{\pm}$ from different π^0-Dalitz decays (18%). For 25 AGeV beam energy the numbers are 23%, 31% and 29%, respectively.

The invariant mass spectra after applying all cuts are presented in the upper plot for 8 AGeV and in the lower plot for 25 AGeV beam energy in Figure 1.

The final S/B ratio and reconstruction efficiency for ρ^0, ω and ϕ mesons and for different invariant mass regions are presented in Table 1.

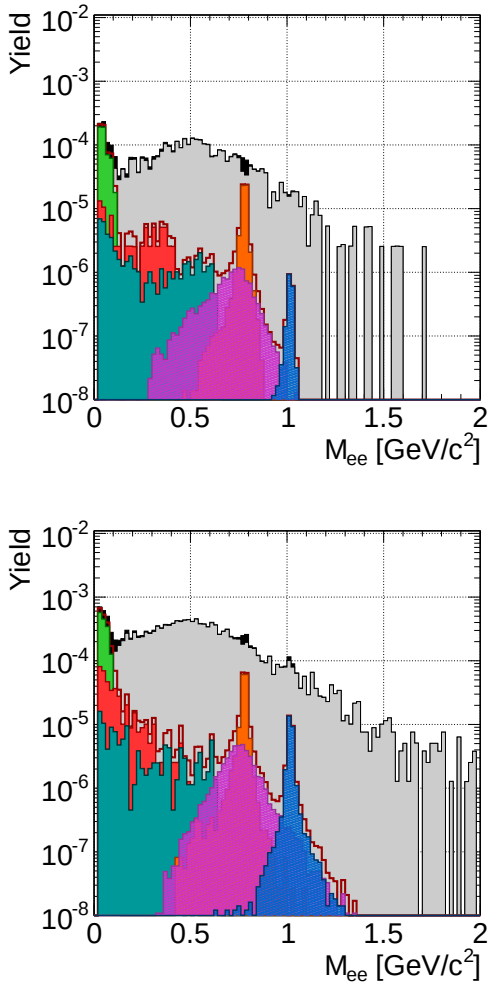

Figure 1: Invariant mass spectra after applying all cuts for central Au+Au collisions at 8 AGeV (above, 100k events) and 25 AGeV (below) beam energy.

Table 1: S/B ratio and reconstruction efficiency after applying all cuts.

	8AGeV		25AGeV	
	S/B	Eff.[%]	S/B	Eff.[%]
ρ	-	3.12	-	4.39
ω	0.64	4.11	0.31	5.53
ϕ	0.04	4.89	0.11	7.08
M_{ee}:0.0-0.2	1.94	-	1.44	-
M_{ee}:0.2-0.6	0.031	-	0.019	-
M_{ee}:0.6-1.2	0.067	-	0.053	-

* Work supported by BMBF and HIC for FAIR

Reaction plane reconstruction in the CBM experiment at SIS100

S. Seddiki[1]
[1]GSI, Darmstadt, Germany

The determination of the azimuthal orientation of the reaction plane in nucleus-nucleus collisions is crucial for anisotropic flow measurements. In the CBM experiment, the reaction plane can be measured from the sidewards deflection of spectator particles using a forward hadronic calorimeter, referred to as the Projectile Spectator Detector (PSD). The Silicon Tracking System (STS) of the experiment, designed to cover a different region of particle rapidity, can provide another independent and complementary measurement. This work consisted in investigating the capabilities of each of these detectors for reconstructing the reaction plane at SIS100 energies. Also, to improve the collision rate capability of the experiment [1], an alternative solution involving a forward Time Of Flight (TOF) wall instead of a PSD has been studied.

The simulations were carried for Au+Au collisions in the CBMroot environment, using the event generator SHIELD and the transport code GEANT, the latter being complemented with the hadronic interaction package GEISHA. A realistic model of the CBM detector was considered, including a 250 μm thick Au target, a STS consisting of 8 silicon stations located between 30 cm and 1 m from the target and embedded in a dipole magnet, and a PSD constituted transversally of 44 modules of 20 $\times$ 20 cm^2, each composed, along the beam axis, of 60 layers with combined Lead absorber and scintillator material. The optimum position of the latter detector along the beam axis was one the objects of this study. As for the forward TOF wall, it is modeled by a silicon circular plane with approximately the same transverse dimensions as for the PSD.

The azimuthal orientation of the reaction plane has be determined with the help of the so-called event plane method [2]. The latter uses the anisotropic flow of emitted particles. This flow can be exploited directly by measuring the momentum of charged particles in the STS, while it is reflected in the distribution of the energy deposited by projectile spectators in PSD modules. In this study, Monte Carlo tracks with at least 4 hits in STS stations have been used. In the case of the forward TOF wall, the distribution of the position of impact of charged particles was used, assuming an ideal granularity. As the elliptic flow of charged particles is very weak at SIS100 energies, the results are given using the directed flow of emitted particles (a selection of forward rapidity particles in the STS is performed). The reaction plane resolution is then defined as the Gaussian width (σ) of the distribution of the measured reaction plane (Ψ_1) around the true one (Ψ_R).

It has been found that the reaction plane resolution is optimum when the PSD is located no further than 10 m from the target, over the range of SIS100 beam energies (see Figure 1). The degradation observed going to higher distances

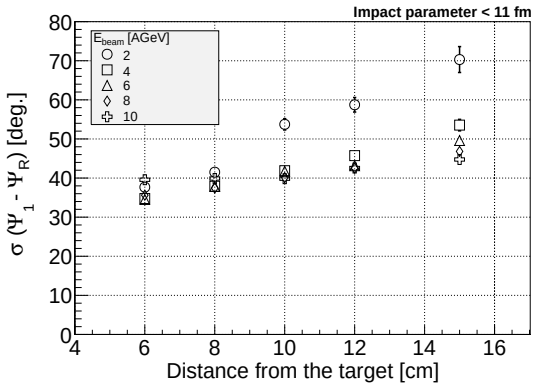

Figure 1: Reaction plane resolution achieved with the PSD as a function of the distance from the target.

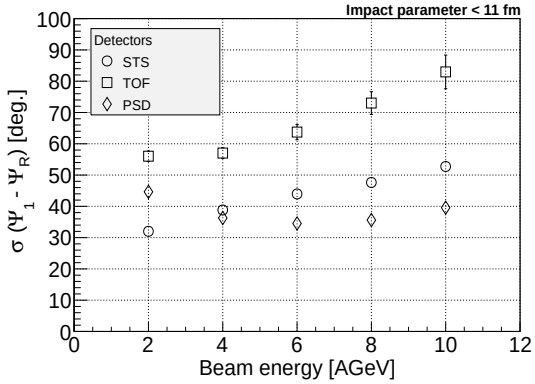

Figure 2: Reaction plane resolution as a function of beam energy. PSD and TOF are located at 6 m from the target.

is an acceptance effect. This effect is particularly strong at lower energies where the particle emission cone is wider due to a lower Lorentz boost. The resolutions obtained with the different detectors can be compared in Figure 2. The PSD shows significantly better resolutions with respect to the TOF ones, mostly as an effect of the loss of neutrons in the latter case. Both PSD and STS provides fairly good resolutions ($\sigma(\Psi_1 - \Psi_R) \in [30; 50]$ degrees). While the former gives better resolutions at higher energies due to the loss of forwardly emitted particles in the STS, the trend is opposite below 4 AGeV. These results show that STS and PSD can provide fairly precise, independent, and complementary reaction plane estimates in CBM at SIS100.

References

[1] A. Senger, this report

[2] A. M. Poskanzer et al., Phys. Rev. C 58, 1671-1678 (1998)

J/ψ production in pp collisions measured with ALICE at the LHC*

A. Andronic[1], *I.C. Arsene*[1], *C. Blume*[2], *P. Braun-Munzinger*[1,3], *A. Maire*[4], *J. Stachel*[4], *J. Wagner*[1], *J. Wiechula*[5], *M. Winn*[4] *for the ALICE Collaboration*

[1]EMMI & GSI Darmstadt; [2]Universität Frankfurt; [3]Technische Universität Darmstadt; [4]Universität Heidelberg; [5]Universität Tübingen

Charmonium production in elementary hadronic collisions remains a challenge to theoretical models. It also constitutes a reference for production in nucleus-nucleus collisions, where charmonium is a special observable for deconfinement [1] (and refs. therein). Measurements at the Large Hadron Collider (LHC) open up an energy regime never explored before.

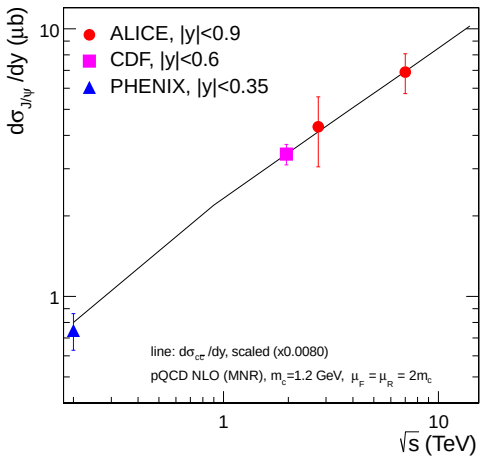

Figure 1: Collision energy ($\sqrt{\mathrm{s}}$) dependence of inclusive J/ψ production cross section dσ/dy at central rapidity in pp collisions for collider experiments.

The ALICE detector has the unique capability among the detectors at the LHC to measure charmonium production down to transverse momentum p_{T}=0. The ALICE measurements of the inclusive J/ψ production cross section in pp collisions at $\sqrt{\mathrm{s}} = 2.76$ TeV [4] and at $\sqrt{\mathrm{s}} = 7$ TeV [2] for central rapidity ($|y| < 0.9$) are shown in Fig. 1 together with measurements at lower energies. Calculations for the overall charm ($c\bar{c}$) production cross section, arbitrarily scaled, are also shown.

At $\sqrt{\mathrm{s}} = 7$ TeV it was possible to measure the fraction $\mathrm{f_B}$ of J/ψ from decays of hadrons carrying bottom quarks [3], shown in Fig. 2. The ALICE measurement at central rapidity is complementary to the other measurements at the LHC. The results of the p_{T}differential prompt J/ψ cross sections at mid-rapidity show that current next-to-leading order (NLO) non-relativistic QCD calculations agree very well with the measured data (see [3] and refs. therein).

Further studies have been performed with data at $\sqrt{\mathrm{s}} = 7$ TeV. Polarization was measured in the muon channel

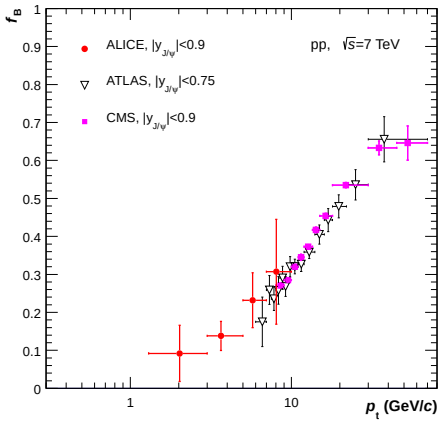

Figure 2: The fraction of J/ψ mesons from feed-down of hadrons with bottom quarks as a function of p_{T}. The error bars represent the quadratic sum of the statistical and systematic uncertainties.

($-4.0 < y < -2.5$) [5] and found to be small (compatible with zero). The production of J/ψ as a function of charged hadron multiplicity [6] show an interesting linear increase of J/ψ yield as a function of (relative) multiplicity, both at central and at forward rapidity. For the central rapidity region, feasibility studies for J/ψ polarization as well as for the J/ψ-hadron correlations were carried out.

Data in pp collisions at $\sqrt{\mathrm{s}} = 8$ TeV , acquired with a minimum bias as well as with a TRD trigger [7], will further contribute to such studies, while data in p-Pb collisions at $\sqrt{s_{\mathrm{NN}}} = 5.02$ TeV will allow to probe a new regime of quarkonium production.

References

[1] J. Wiechula et al., this Report.

[2] K. Aamodt *et al.* [ALICE Collaboration], Phys. Lett. B **704** (2011) 442 [Erratum-ibid. B **718** (2012) 692]

[3] B. Abelev *et al.* [ALICE Collab.], JHEP **1211** (2012) 065

[4] B. Abelev *et al.* [ALICE Collab.], Phys. Lett. B **718** (2012) 295

[5] B. Abelev *et al.* [ALICE Collab.], Phys. Rev. Lett. **108** (2012) 082001

[6] B. Abelev *et al.* [ALICE Collab.], Phys. Lett. B **712** (2012) 165

[7] J. Klein, arXiv:1112.5110; see also this Report.

* Work supported by GSI, BMBF, Helmholtz Alliance HA216/EMMI, HQM, and HGS-HIRe

J/ψ production in Pb–Pb collisions at $\sqrt{s_{\rm NN}} = 2.76$ TeV*

J. Wiechula[1], *A. Andronic*[2], *I. Arsene*[2], *C. Blume*[3], *J. Book*[3], *A. Maire*[4], *J. Stachel*[4], *M. Winn*[4] *for the ALICE Collaboration*

[1]Universität Tübingen; [2]GSI Darmstadt; [3]Universität Frankfurt; [4]Universität Heidelberg

J/ψ mesons are expected to provide essential information on the properties of high-energy heavy-ion collisions where a plasma of quarks and gluons (QGP) is formed. Due to colour screening, J/ψ production is expected to be suppressed in a QGP [1]. The level of suppression provides information on the temperature of the plasma. At LHC energies, charm is produced abundantly in central Pb–Pb collisions and scenarios where originally uncorrelated charm and anti-charm quarks (re)combine gain importance (e.g. [2, 3, 4]). Measuring J/ψ production at the LHC will help to disentangle between the different mechanisms.

ALICE [5] measures J/ψ production at mid- ($|y| < 0.9$) and forward ($2.5 < y < 4$) rapidity in the di-electron and di-muon decay channel, respectively. The analysed data from the 2011 Pb–Pb run at $\sqrt{s_{\rm NN}}$=2.76 TeV, correspond to an integrated luminosity of $15\,\mu{\rm b}^{-1}$ in case of the di-electron channel, for the di-muon analysis a dedicated trigger allowed for sampling $70\,\mu{\rm b}^{-1}$. Fig. 1 (top) shows the di-electron invariant mass spectrum for the 0-10% most central collisions (blue) and the combinatorial background (red) obtained from event mixing. The bottom panel shows the background subtracted spectrum together with the MC line shape. The raw yields, extracted from the di-lepton invariant mass spectra, were corrected for acceptance and efficiency based on Monte Carlo (MC) simulations and MC J/ψ embedded into real Pb–Pb events for the di-electron and di-muon analysis, respectively. The total acceptance times efficiency is $\approx 8\,\%$, in case of the di-electron and $\approx 14\,\%$ in case of the di-muon decay channel.

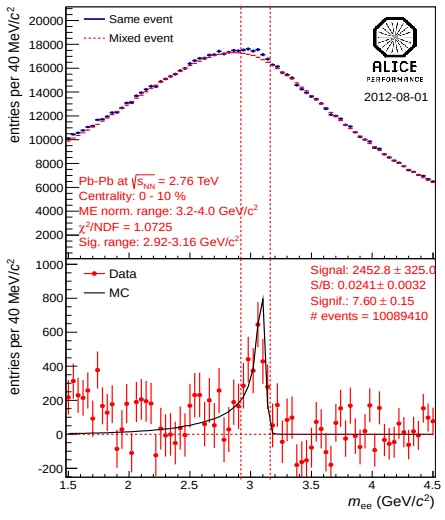

Figure 1: Invariant mass spectrum of e^+e^- pairs for 0-10% most central events. For details see text.

* Supported by GSI, BMBF and Helmholtz Alliance HA216/EMMI

The nuclear modification factor is given by $R_{\rm AA} = Y^{PbPb}_{J/\psi}/(T_{\rm AA} \cdot \sigma^{pp}_{J/\psi})$ where $Y^{PbPb}_{J/\psi}$ is the measured J/ψ yield, $T_{\rm AA}$ the nuclear overlap function, obtained from a Glauber MC, and $\sigma^{pp}_{J/\psi}$ the J/ψ production cross-section in pp collisions at the same $\sqrt{s_{\rm NN}}$ [6].

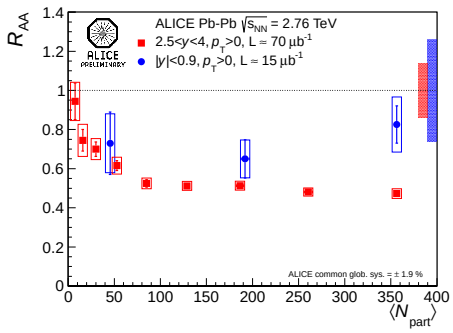

Figure 2: $R_{\rm AA}$ as a function of the average number of participant nucleons at mid- (blue) and forward (red) rapidity.

Fig. 2 shows the preliminary $R_{\rm AA}$ at mid- (red) and forward (blue) rapidity [7, 8] vs. the number of participants. Error bars correspond to statistical, open boxes to systematic uncertainties of the Pb–Pb measurement. Uncertainties of the pp references are visualised by coloured boxes (right side of the plot). At forward rapidity $R_{\rm AA}$ decreases with centrality from unity to about 0.5. For most central collisions there is a hint of a larger $R_{\rm AA}$ at mid- compared to forward rapidity. At forward rapidity also the transverse momentum ($p_{\rm T}$) dependence of $R_{\rm AA}$ was measured [8] which shows significantly larger values at low $p_{\rm T}$ compared to results at lower energy. In addition J/ψ shows a non vanishing elliptic flow at forward rapidity [9].

The results above hint at the presence of the (re)generation mechanism, contributing preferentially to the low $p_{\rm T}$ region, at the LHC.

References

[1] T. Matsui and H. Satz, Phys. Lett. B **178** (1986) 416.

[2] A. Andronic, P. Braun-Munzinger, K. Redlich and J. Stachel, J. Phys. G **38** (2011) 124081.

[3] X. Zhao and R. Rapp, Nucl. Phys. A **859** (2011) 114.

[4] Y.-p. Liu *et al* Phys. Lett. B **678** (2009) 72.

[5] K. Aamodt *et al.* [ALICE Coll.], JINST **3** (2008) S08002.

[6] B. Abelev *et al.* [ALICE Coll.], Phys. Lett. B**718** (2012) 295.

[7] I. -C. Arsene [ALICE Coll.], arXiv:1210.5818 [nucl-ex].

[8] C. Suire [ALICE Coll.], arXiv:1208.5601 [hep-ex].

[9] H. Yang [ALICE Coll.], arXiv:1211.0799 [nucl-ex].

Perspectives for charmonium measurements at the LHC with the ALICE upgrade program*

A. Andronic[1] *and the ALICE Collaboration*

[1]EMMI & GSI Darmstadt

Among the various suggested probes of deconfinement, charmonium plays a distinctive role. It is the first hadron for which a clear mechanism of suppression in deconfined matter (QGP) was proposed early on, based on the color analogue of Debye screening [1]. The idea of statistical hadronization of charm quarks in nucleus-nucleus collisions [2] has gained support from data, in particular that recently measured at the LHC [4]. An alternative mechanism of quarkonium production (and destruction), that during the entire lifetime of the QGP (realized in a transport approach, see [3] and refs. therein) is also able to reproduce the RHIC and LHC data. Based on these observations, the J/ψ production can be considered a probe of QGP as initially proposed [1], but may not be a "thermometer" of the medium. Discriminating the two pictures implies providing an answer to fundamental questions related to the fate of hadrons in a hot medium.

High-quality J/ψ data over broad ranges in $p_{\rm T}$ and y and a precision measurement of $\psi(2S)$ and χ_c charmonium states could allow this and is a major component of physics envisaged with the ALICE Upgrade Project [5]. The unique capability of the ALICE detector is to measure charmonium production down to $p_{\rm T}$ =0. This will be complemented by a challenging data taking at very high rate. In the following we present estimates of the performance of the ALICE measurement of J/ψ and $\psi(2S)$ in the Central Barrel ($|y|$ <0.9, measurement done in the e^+e^- channel). The measurement performance has been estimated for integrated luminosities of 1 nb^{-1} and 10 nb^{-1}, corresponding to the data sample expected for the baseline ALICE data taking and after the upgrade, respectively.

The expected absolute statistical error of the elliptic flow (v_2) measurement is shown in Figure 1 (a $v_2^{J/\psi}$ magnitude in the range 0.06-0.1 is expected around $p_{\rm T}$ =3 GeV/c [6]). The measurement of elliptic flow of J/ψ is only possible with the 10 nb^{-1} Pb-Pb data (10^{10} collisions) expected with the upgrade. A measurement with a good significance over a broad range in $p_{\rm T}$ (up to 5-6 GeV/c) can be achieved with the usage of the TRD electron identification. In this case, a direct measurement of elliptic flow of J/ψ from B hadrons could become also feasible.

In the dielectron channel the measurement of $\psi(2S)$ production is challenging and can be achieved with good significance only with the 10 nb^{-1} Pb-Pb data expected with the full upgrade, see Figure 2. Such a measurement will allow, together with the measurement in the dimuon channel, to disentangle between a statistical production at the phase boundary [2] and production during the QGP lifetime [3].

* Work supported by GSI, BMBF, Helmholtz Alliance HA216/EMMI

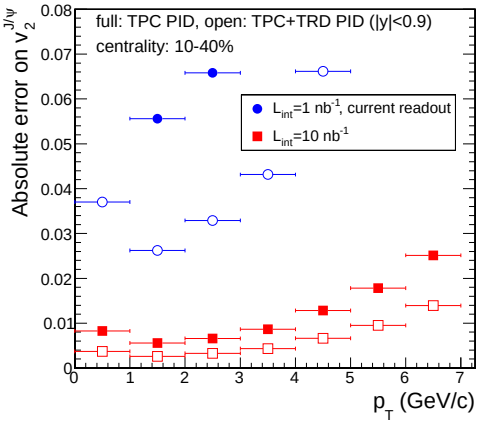

Figure 1: The absolute statistical error of the elliptic flow of J/ψ $v_2^{J/\psi}$ as a function of transverse momentum for the centrality range 10-40%.

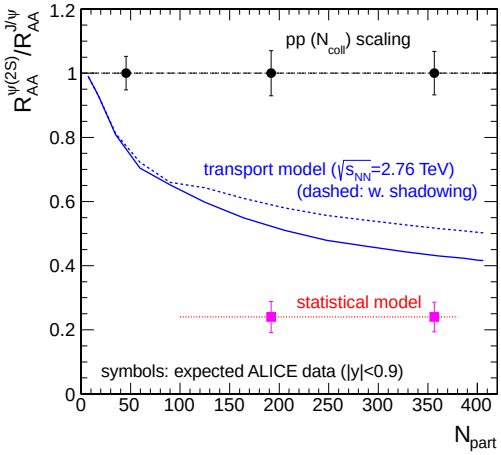

Figure 2: Centrality dependence of the expected statistical error of the $\psi(2S)$ measurement in the Central Barrel with 10 nb^{-1} Pb-Pb data in the hypothesis of pp scaling and of the statistical model production for the ratio of nuclear modification factors of $\psi(2S)$ and J/ψ.

References

[1] T. Matsui, H. Satz, Phys. Lett. B **178** (1986) 416.

[2] P. Braun-Munzinger, J. Stachel, Phys. Lett. B **490** (2000) 196; A. Andronic et al., this Report

[3] X. Zhao, R. Rapp, Nucl. Phys. A **859** (2011) 114,

[4] J. Wiechula et al., this Report.

[5] ALICE Collaboration, CERN-LHCC-2012-012.

[6] H. Yang [ALICE Collab.], arXiv:1211.0799.

Measurement of electrons from semi-leptonic heavy-flavour hadron decays with ALICE at the LHC*

R. Averbeck[1], R. Bailhache[2], M. Fasel[3], M. Heide[4], M. Kweon[3], Y. Pachmayer[3], T. Rascanu[2], S. Masciocchi[1], C. A. Schmidt[1], M. Völkl[3] for the ALICE Collaboration

[1]Research Division and ExtreMe Matter Institute, GSI Helmholtzzentrum für Schwerionenforschung GmbH, Darmstadt, Germany; [2]Institut für Kernphysik, Goethe-Universität Frankfurt/Main, Germany; [3]Physikalisches Institut, Ruprecht-Karls Universität Heidelberg, Germany; [4]Institut für Kernphysik, Westfälische Wilhelms-Universität Münster, Germany

The production of heavy quarks, i.e charm and beauty, in proton-proton (pp) collisions allows to test perturbative Quantum ChromoDynamics (pQCD) calculations. pQCD calculations in the framework of fixed-order plus next-to-leading-logarithm resummation (FONLL) [1, 2] are in good agreement with previous experiments at lower center-of-mass energies ($\sqrt{s}$). Furthermore, pp results serve as a reference for heavy-ion collisions. In such collisions, the study of heavy quarks can provide insight into partonic energy loss in the Quark Gluon Plasma (QGP) phase. In addition, the measurement of the elliptic flow, defined as the second harmonic component of the fourier expansion of the azimuthal particle distribution with respect to the reaction plane, carries information on the degree of thermalisation of heavy quarks at low p_{T}, as well as on the path length dependence of their energy loss in the QGP at high p_{T}.

ALICE [3] is well suited for the measurement of electrons at mid-rapidity. The measured specific energy deposition in the Time Projection Chamber (TPC), the main tracking detector in the central barrel, allows the identification of electrons up to a momentum of about 6 GeV/c. In addition, at low momentum (p <2 GeV/c), the velocity measurement provided by the Time Of Flight Detector (TOF) situated around the TPC can be employed to separate kaons and protons from electrons. At intermediate and higher p, where with the TPC pions can not be separated from electrons, the Transition Radiation Detector (TRD) and ElectroMagnetic Calorimeter (EMCal) are mandatory to prepare a pure sample of electrons. Both provide the possibility to trigger on electrons to enhance the statistics in the data sample. The results summarized here are from different analyses combining the particle identification capabilities of these detectors.

The sample of electrons contains background from various other sources, e.g. Dalitz decays or the conversion of real photons, which needs to be subtracted. The background can be estimated either using a cocktail based on the π^0 measurement [6] or by reconstructing the photonic background using an invariant mass technique. The background estimates from the two methods are in agreement.

In pp collisions at $\sqrt{s}$ = 7 TeV, the p_{T}-differential cross section of electrons from semi-leptonic heavy-flavour hadron decays was measured with ALICE at mid-rapidity ($|y| < 0.5$) for 0.5 GeV/c < p_{T} < 8 GeV/c [4]. This p_{T} range includes $\approx$ 50% of the charm and $\approx$ 90% of the beauty cross section at mid-rapidity. Fig. 1 shows that a FONLL calculation [5] is in good agreement with the data. The preliminary results at $\sqrt{s}$ = 2.76 TeV, the same center-of-mass energy as used in Pb-Pb collisions, show a similar agreement.

Using tracks with a large distance to the primary event vertex, the cross section of electrons from beauty hadron decays was extracted in pp collisions at $\sqrt{s}$ = 7 TeV [7] and at $\sqrt{s}$ = 2.76 TeV. Both measurements were performed at mid-rapidity in a p_{T} range from 1 to 8 GeV/c. Results were confirmed by an alternative method, using azimuthal electron-hadron correlations. Moreover, they are well described by FONLL calculations. The total beauty cross sec-

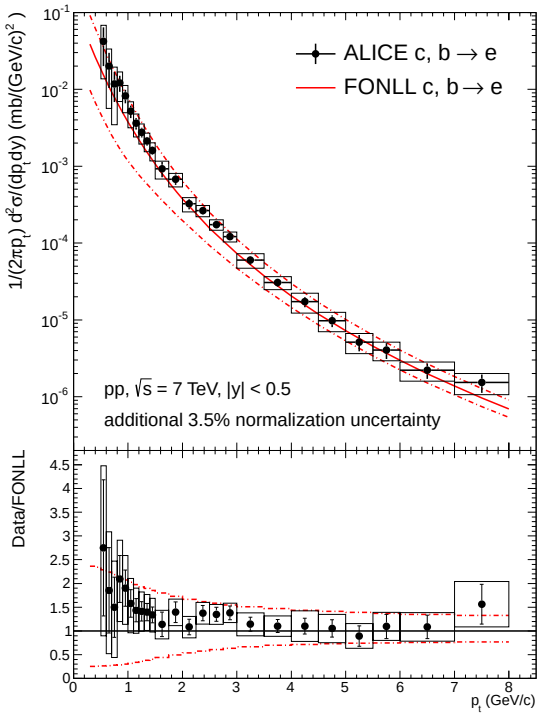

Figure 1: p_{T}-differential cross section of electrons from semi-leptonic heavy-flavour hadron-decays in pp-collisions at $\sqrt{s}$ = 7 TeV [4] in comparison with a FONLL pQCD calculation [5].

* Work supported by GSI, BMBF, HGS-HIRe, and Helmholtz Alliance HA216/EMMI

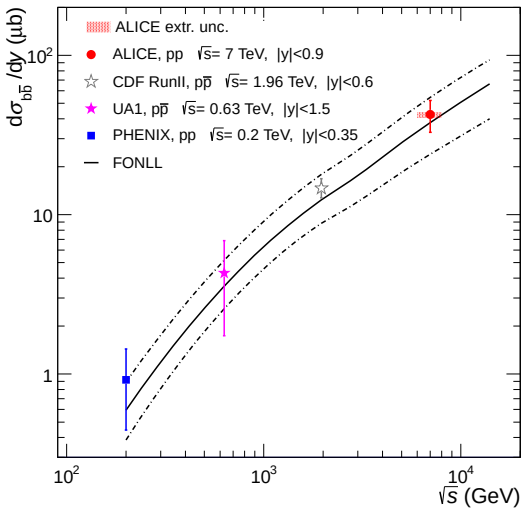

Figure 2: $\mathrm{d}\sigma_{\mathrm{b\bar{b}}}/\mathrm{d}y$ at mid-rapidity as a function of $\sqrt{s}$ in pp and p$\bar{\mathrm{p}}$ collisions [8]. The black solid (dashed) line indicates the FONLL calculation (uncertainty).

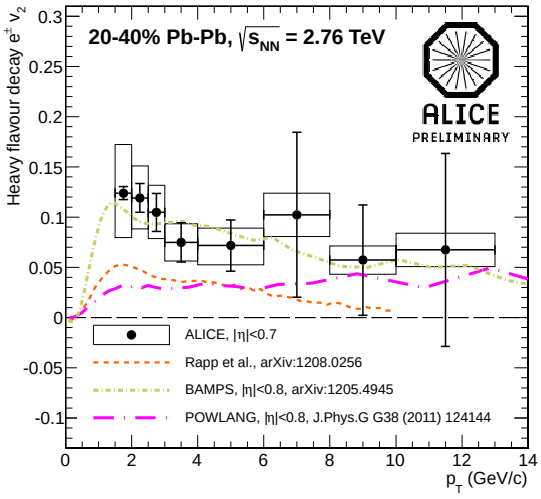

Figure 3: Elliptic flow v_2 of electrons from heavy-flavour hadron decays in 20-40% central Pb-Pb collisions, compared to different theoretical models [9].

tion per unit of rapidity is plotted in Fig. 2, together with measurements at lower $\sqrt{s}$ in pp and p$\bar{\mathrm{p}}$ collisions. The ALICE measurement is the weighted average of the results from the non-prompt J/ψ [8] and the beauty electron [7] analyses. A FONLL prediction is in good agreement with the various measurements.

In the 10% most central Pb-Pb collisions at $\sqrt{s_{\mathrm{NN}}} = 2.76$ TeV, a strong suppression of electrons from heavy-flavour hadron decays is observed in the p_{T} range from 3 to 18 GeV/c for $|y| < 0.5$ [9]. Since the yield is expected to be dominated by beauty hadron decays in the high-p_{T} region, this indicates that beauty quarks experience substantial energy loss. A similar suppression was observed for muons from heavy-flavour hadron decays at forward-rapidity, as well as for D mesons at mid-rapidity. The suppression increases from peripheral to central collisions [10]. In addition, the elliptic flow v_2 of electrons from heavy-flavour hadron decays was measured using the event-plane method in mid-central (20-40%) Pb-Pb collisions in the p_{T} range from 1.5 to 13 GeV/c at mid-rapidity. A non-zero v_2 is observed at low p_{T} (see Fig. 3), consistent with a non-zero v_2 of D mesons in 30-50% central Pb-Pb collisions [11]. Both results are compatible with measurements in Au-Au collisions at $\sqrt{s_{\mathrm{NN}}} = 0.2$ TeV [12]. In Fig. 3 various transport model calculations are compared with the experimental results. Current models are only partially successful in reproducing the measured suppression and v_2 of D mesons and of leptons from heavy-flavour hadron decays simultaneously.

In preparation for the p-Pb run taking place in the year 2013 at the LHC, an electron trigger using the Transition Radiation Detector (TRD) was commissioned with the 2012 pp data set at $\sqrt{s} = 8$ TeV. The trigger selects electron candidates with $p_{\mathrm{T}} > 3$ GeV/c using a likelihood method. The TRD triggered p-Pb data will provide an electron measurement at intermediate and high p_{T}.

References

[1] M. Cacciari, M. Greco, and P. Nason, JHEP, 9805:007, 1998.

[2] M. Cacciari, S. Frixione, and P. Nason, JHEP, 0103:006, 2001.

[3] K. Aamodt *et al.* (ALICE Collaboration), JINST, 3:S08002, 2008.

[4] B. Abelev *et al.* (ALICE Collaboration), Phys. Rev. D 86, 112007, 2012.

[5] M. Cacciari *et al.*,, JHEP, 1210:137, 2012.

[6] B. Abelev *et al.* (ALICE Collaboration), Phys. Lett. B 717, 162, 2012.

[7] B. Abelev *et al.* (ALICE Collaboration), arXiv:1208.1902.

[8] B. Abelev *et al.* (ALICE Collaboration), JHEP 1211:065, 2012.

[9] S. Sakai *et al.* (ALICE Collaboration), Proceedings, Quark Matter 2012.

[10] S. Masciocchi *et al.* (ALICE Collaboration), J. Phys. G: Nucl. Part. Phys. 38, 124069, 2011.

[11] G. Luparello *et al.* (ALICE Collaboration), Proceedings, Hot Quarks 2012.

[12] A. Adare *et al.* (PHENIX Collaboration), Phys. Rev. C 84, 044905, 2011.

Direct Photon Spectrum and Elliptic Flow in Pb-Pb Collisions with ALICE*

F. Bock[1], P. Braun-Munzinger[2], T. Dietel[3], P. Gonzalez[4], M. Heide[3], M. Ivanov[2], C. Klein-Bösing[2,3], P. Ladrón de Guevara[4], D. Lohner[1], A. Marín[2], A. Passfeld[3], K. Reygers[1], J. Stachel[1], J.P. Wessels[3], M. Wilde[3], and the ALICE Collaboration

[1]Physikalisches Institut, Ruprecht-Karls-Universität Heidelberg, Heidelberg, Germany; [2]ExtreMe Matter Institute EMMI, GSI Helmholtzzemtrum für Schwerionenforschung, Darmstadt, Germany; [3]Institut für Kernphysik, Westfälische Wilhems-Universität Münster, Münster, Germany; [4]Centro de Investigaciones Energeticas, Medioambientales y Tecnológicas (CIEMAT), Madrid, Spain

With the ALICE experiment, photon measurements with an excellent precision are available via external conversions. The reconstruction of the e^+e^- pairs is done with the Inner Tracking System and the Time Projection Chamber of the experiment. The conversion method provides the advantage of high tracking efficiency and excellent photon momentum resolution at low p_T ($p_T < 6\,\mathrm{GeV}/c$). The direct photons yield is obtained by subtracting a cocktail of hadronic decay photons, calculated from the measured π^0 spectrum, from the measured inclusive photons. The neutral mesons are extracted from the same set of photons via an invariant mass analysis of photon pairs.

At low and intermediate p_T, thermal photons from a QGP and from the hadronic phase are expected to contribute significantly to the total amount of direct photons. These photons are emitted over the whole system evolution time and do not interact with the strongly coupled medium. Despite the fact that the photons are blue-shifted, they carry information about the system at their production time.

In Fig. (1) the direct photon invariant yield for the 0-40% most central Pb-Pb collisions at $\sqrt{s_{NN}} = 2.76\,\mathrm{TeV}$ is presented. In addition, a NLO direct photon calculation for pp at $\sqrt{s} = 2.76\,\mathrm{TeV}$, scaled by the number of binary collisions and an exponential fit is shown. The inverse slope parameter of the fit ($0.8\,\mathrm{GeV}/c < p_T < 2.2\,\mathrm{GeV}/c$) is found to be $T_{\mathrm{LHC}} = 304 \pm 51^{syst+stat}\,\mathrm{MeV}$. In hydrodynamic models, in which the low p_T direct photons are dominated by thermal photons, this slope parameter reflects an effective temperature averaged over the time evolution of the system.

From the direct photon excess the azimuthal asymmetry of the photon production can be extracted. Fig. (2) shows a non-zero elliptic flow in the region where the pQCD calculations fail to describe the direct photons. The magnitude is similar to the elliptic flow of charged pions. This favors similar production times of light mesons and the measured photons. In contrast, the large value for T_{LHC} seems to point to earlier production times when the QGP is still present. This poses a challenge for the current theoretical modelling of the time evolution of ultra-relativistic heavy-ion collisions.

* Work supported by GSI, BMBF, HGS-HIRe, and Helmholtz Alliance HA216/EMMI.

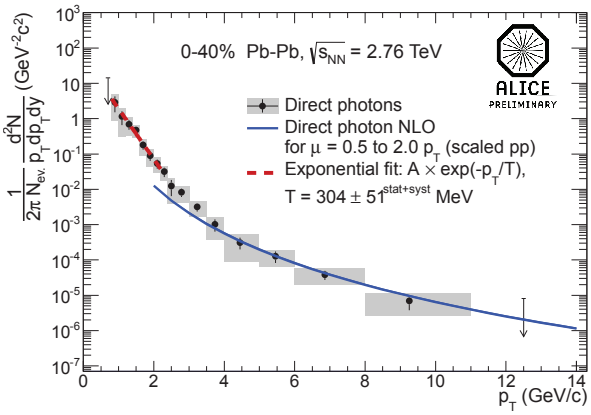

Figure 1: Direct photon invariant yield in Pb-Pb collisions at $\sqrt{s_{NN}} = 2.76\,\mathrm{TeV}$ for 0-40% centrality with pp NLO pQCD predictions scaled with the number of binary collisions and low p_T exponential fit. [1]

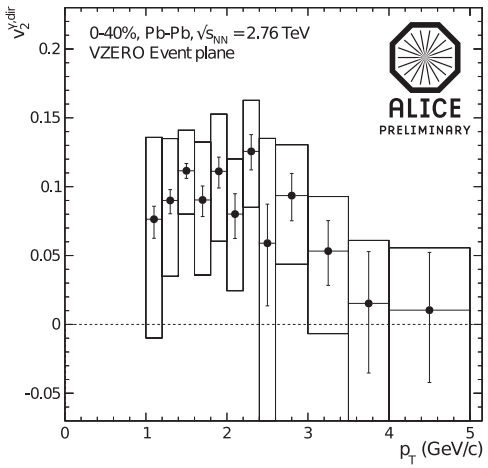

Figure 2: Direct photon elliptic flow (v_2) at $\sqrt{s_{NN}} = 2.76\,\mathrm{TeV}$ in 0-40% Pb-Pb collisions. [2]

References

[1] M. Wilde [ALICE Collaboration], Quark Matter 2012 Proceeding [arXiv:1210.5958 [hep-ex]].

[2] D. Lohner [ALICE Collaboration], Hot Quarks 2012 Proceeding [arXiv:1212.3995 [hep-ex]].

Measurement of low-mass dielectrons with ALICE in pp collisions at $\sqrt{s} = 7$ TeV*

Markus K. Köhler for the ALICE Collaboration
Research Division and ExtreMe Matter Institute EMMI, GSI Helmholtzzentrum für Schwerionenforschung, Darmstadt

Dileptons are an important probe for the medium, which is created in heavy-ion collisions. Electromagnetic probes do not interact strongly and carry the information from all collision stages to the detector. Modifications of the medium could have a measurable impact on the emission pattern, and proton-proton (pp) collisions provide a reference measurement of a medium free environment.
The ALICE detector system [1] at the CERN LHC has excellent capabilities for the tracking and electron identification in particular for low particle momenta. In the central barrel, low-momentun electrons can be identified via their specific energy-loss in the Inner Tracking System and the Time Projection Chamber (TPC) and via their specific velocity measured with the Time Of Flight detector (TOF). Electrons at higher transverse momentum can be identified with the Transition Radiation Detector or the electromagnetic calorimeter EMCal.
In this analysis, the dielectron production in pp collisions at $\sqrt{s} = 7$ TeV is measured. The analysis was performed over the full azimuth in the pseudo-rapidity range $|\eta^e| < 0.8$ and the transverse momentum $p_{\mathrm{T}}^e > 0.2$ GeV/c. Electrons were identified using the combined information from TPC and TOF. At $p_{\mathrm{T}}^e > 0.2$ GeV/c, TPC information was used to reject pions. In the momentum range $0.4 < p < 5$ GeV/c, kaons and protons can be separated from electrons using the TOF and were efficiently rejected. The hadronic contamination is below 1 %.
The measured unlike-sign spectrum is an overlay of the signal and combinatorial background pairs. The combinatorial background N_{+-}^{CB} was reconstructed with the same-event like-sign method. Under the assumption, that the signal consists only of unlike-sign pairs, the combinatorial background was calculated as $N_{+-}^{CB} = 2 \times \sqrt{N_{++}N_{--}}$, where N_{++} and N_{--} are the yields of like-sign pairs of positive and negative particles, respectively.
The expected mass spectrum of dielectrons in the range $0 < m_{ee} < 3.3$ GeV/c^2 was derived from p_{T} differential cross sections of π^0, η, ϕ and J/ψ measured with ALICE at mid-rapidity [2–4].
The shape of the mass distribution of dielectrons from correlated semi-leptonic decays of charmed mesons was calculated with PYTHIA, which was scaled to the measured charm cross section [5]. Other contributions, which were not measured, such as dielectrons from η' and the ρ, were calculated by assuming m_T scaling. The detector resolution was folded into the mass spectra.

* Work supported by GSI, BMBF, HGS-HIRe, and Helmholtz Alliance HA216/EMMI

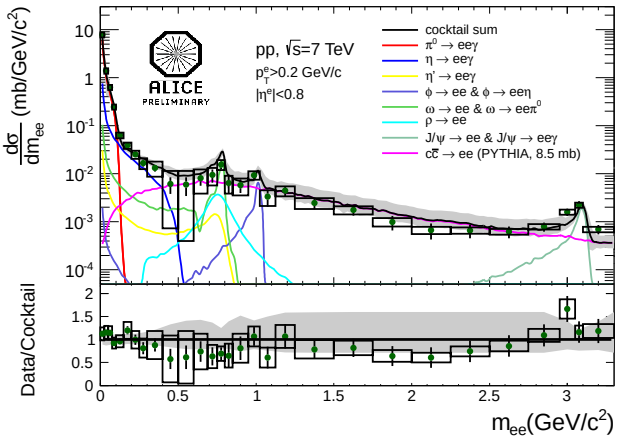

Figure 1: Background subtracted invariant mass distribution in terms of total cross section compared to the hadronic cocktail for pp collisions at $\sqrt{s} = 7$ TeV. The boxes indicate the systematic uncertainty of the measurement, the grey band shown the systematic uncertainty of the cocktail.

The systematic uncertainty is dominated by the combinatorial background subtraction over a wide mass range of the dielectron continuum. Systematic uncertainties due to track cuts and the efficiency correction contribute significantly only at very low and high masses, where the signal to background ratio is large.
Figure 1 shows the comparison of the measured dielectron continuum with the expected hadronic sources for pp collisions at $\sqrt{s} = 7$ TeV. The hadronic cocktail agrees with the data within statistical and systematic uncertainties.
The invariant mass analysis of dielectrons in Pb–Pb collisions at $\sqrt{s_{NN}} = 2.76$ TeV is currently ongoing.

References

[1] K. Aamodt et al. (ALICE Collaboration) *JINST 3 S08002* 2008.

[2] B. Abelev et al. (ALICE Collaboration) Phys. Lett. B 717, p. 162, 2012

[3] B. Abelev et al. (ALICE Collaboration) Phys. Lett. B 704, p. 442, 2011

[4] B. Abelev et al. (ALICE Collaboration) Preprint arXiv:1208.5717 [hep-ex], 2012

[5] B. Abelev et al. (ALICE Collaboration) Journal of High Energy Physics 1207, p. 116, 2012

Prospects of Low-Mass Dielectron Measurements in ALICE with an upgraded Central Barrel Detector*

P. Reichelt† [1] *and the ALICE Collaboration*
[1]IKF, Goethe-Universität Frankfurt, Germany

The measurement of electron-positron pairs in the low invariant mass region allows to study the vacuum and in-medium properties of light vector mesons. Dielectrons also probe the production of thermal photons in heavy-ion collisions. ALICE is well-suited to perform this measurement due to its excellent tracking and particle identification capabilities at very low momenta. However, Dalitz decays and photon conversions lead to a high combinatorial background. Additionally, coincident semi-leptonic decays of charm and anti-charm hadrons produce a continuum signal, which dominates over a thermal dielectron signal.
Both contributions can be reduced by an improved Inner Tracking System, to be installed during LHC's long shutdown 2 (2018). It will further improve the tracking efficiency at low p_{T} and provide excellent detection capabilities for electrons from secondary vertices like conversions and heavy-quark decays. Additionally, an upgrade of the TPC readout will substantially increase the data taking rate [1]. We present the expected impact on the low-mass dielectron measurement in Pb–Pb collisions at full LHC energy.

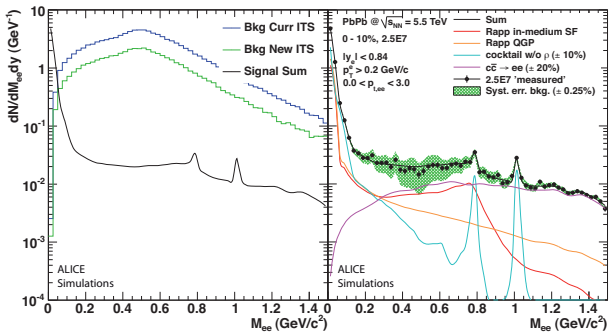

Figure 1: Left: modelled combinatorial background in central Pb–Pb collisions. Right: composition of the expected signal and sampled data points.

The electron selection is simulated using data-driven parameterizations of the TPC and TOF detectors. A reduced solenoid magnetic field of $B = 0.2$ T is assumed to increase the low-p_{T} acceptance. ITS standalone tracks are used to reject electrons from unwanted sources. The resulting combinatorial background (invariant mass distribution of like-sign pairs) is shown left in Figure 1 for both the current and planned ITS version. The right side shows the composition of the real signal, consisting of a hadronic cocktail, open charm decays, and a thermal radiation prediction [2]. Also included are 'data' points sampled according to the significance expected with the current ITS for 25M central Pb–Pb events and their systematic error.
The thermal excess spectrum is obtained by subtracting cocktail and charm and assigning estimated uncertainties as given in Figure 1. Figure 2, left panel, shows the resulting excess spectrum for the current ITS, which is dominated by systematic errors.
The planned ITS is expected to reduce the background and thus its error by a factor of about 2. Pairs from open charm decays can be suppressed by a factor of 5 using a vertex cut, at the cost of some statistics. This will be compensated with the additional TPC upgrade, as 100 times more data can be taken. The result of these improvements is seen in the right panel of Figure 2.

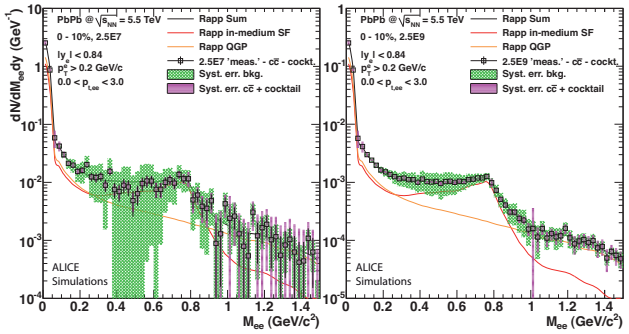

Figure 2: Left: thermal excess spectrum with current ITS for 25M events. Right: same with planned ITS for 2.5B events, using a vertex cut to reduce the error from charm.

Further implications of such a precise measurement of the thermal excess yield are the possibility to determine the QGP temperature by a fit to the mass region above $1\ \mathrm{GeV}/c^2$, and we find the uncertainties to be within about $10\ \%$. A more differential analysis even allows to determine the elliptic flow v_2 of dielectrons as function of mass or p_{T}, and the absolute uncertainty is expected to be of the order of $\sigma_{v_2} = 1\ \%$.
The variety of these measurements will give deeper insight into the early phase of the heavy ion collisions.

References

[1] ALICE Collaboration, *Upgrade of the ALICE Experiment Letter Of Intent*, CERN-LHCC-2012-012, (2012).

[2] R. Rapp and J. Wambach, Eur. Phys. J. A6 (1999) 415, and private communication.

* Work supported by BMBF, GSI, EMMI and HGS-HIRe
† preichelt@ikf.uni-frankfurt.de

Observation of the anti-nucleus $^4\overline{\mathrm{He}}$ with the ALICE apparatus at the LHC*

B. Dönigus†[1], *A. Kalweit*[2], *N. Martin*[1,3] *for the ALICE Collaboration*

[1]ExtreMe Matter Institute EMMI and Research Division, GSI Helmhotzzentrum für Schwerionenforschung, Darmstadt, Germany; [2]European Organization for Nuclear Research (CERN), Geneva, Switzerland; [3]Institut für Kernphysik, Technische Universität Darmstadt, Darmstadt, Germany

Heavy-ion collisions at the LHC give the opportunity to measure all known particles in higher abundances as it was possible before, like for example light (anti-)nuclei. These heavy particles are rarely produced, because the production probability decreases with increasing mass. But the energy regime reached at the LHC leads to large production probabilities even for these particles, as described for example by thermal models [1, 2]. So far, data of Pb–Pb collisions at $\sqrt{s_{\mathrm{NN}}} = 2.76\,\mathrm{TeV}$ per nucleon–nucleon pair was taken in the years 2010 and 2011.

Further, the unique particle identification capabilities of the ALICE detector [3] allow for the measurement of rarely produced states created in Pb–Pb collisions. Anti-matter studies have the advantage that the anti-particles suffer only from annihilation when detector material is crossed, whereas on the matter side a substantial background is created via knockout reactions within the detector material.

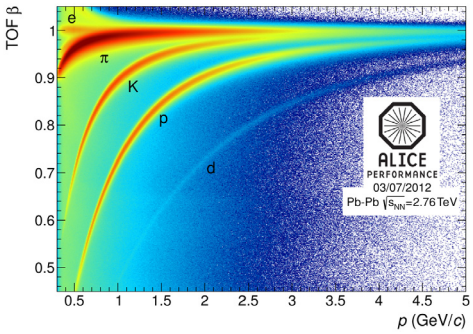

Figure 1: TOF β versus p, a clear seperation of hadrons is visible.

The excellent performance of the Time-Projection Chamber (TPC) [4] and the Time-Of-Flight detector (TOF) [3] allows for the clear identification of all stable particles over a wide range in rigidity $R = p/z$, where p is the track momentum and z is the charge number. In figure 1 the TOF performance is shown exemplarily. Here β measured with the TOF detector is plotted as function of p. Combining the specific energy loss ($\mathrm{d}E/\mathrm{d}x$) in the TPC and the TOF information, we identified 10 anti-alpha nuclei. Here we present results for 23 million Pb–Pb collisions at $\sqrt{s_{\mathrm{NN}}} = 2.76\,\mathrm{TeV}$ per nucleon–nucleon pair, recorded in the heavy-ion run of November 2011 where a trigger mix of minimum bias, semi-central and central events was applied.

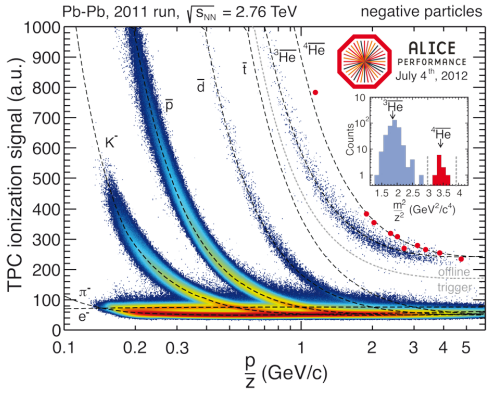

Figure 2: TPC $\mathrm{d}E/\mathrm{d}x$ spectrum, the inlet shows the m^2/z^2 distribution. The 10 anti-alphas clearly identified by TPC and TOF are indicated with larger markers.

We further apply an offline trigger selecting all $^3\overline{\mathrm{He}}$-nuclei or heavier candidates. Figure 2 shows the $\mathrm{d}E/\mathrm{d}x$ versus rigidity distribution for candidates after the offline selection for negative particles in the region where the bands of $^3\overline{\mathrm{He}}$ and $^4\overline{\mathrm{He}}$ are clearly visible. Below a rigidity of $p/z \approx 2\,\mathrm{GeV}/c$ three candidates are clearly identified based on the $\mathrm{d}E/\mathrm{d}x$ information only. At higher p/z the energy-loss information of the candidates is combined with mass determination performed with the TOF detector following $m^2/z^2 = R^2/(\gamma^2-1)$. The inlet in Fig. 2 shows the m^2/z^2 distribution for all tracks within a 2σ-band around the expected $\mathrm{d}E/\mathrm{d}x$ for $^4\overline{\mathrm{He}}$. The 10 identified anti-alphas are highlighted in both the m^2/z^2 and the $\mathrm{d}E/\mathrm{d}x$ versus rigidity plot. A similar analysis had been performed for the 2010 data, which led to four anti-alpha candidates [5]. The first anti-alphas were detected by the STAR collaboration at RHIC in Au–Au collisions [6]. The work on the extraction of the corrected particle yield is currently ongoing.

References

[1] A. Andronic *et al.*, Phys. Lett. B 697 (2011) 203

[2] J. Cleymans *et al.*, Phys. Rev. C 84 (2011) 054916

[3] K. Aamodt *et al.* (ALICE Collaboration), JINST 3 (2008) S08002

[4] J. Alme *et al.*, Nucl. Instr. Meth. A 622 (2010) 316

[5] A. Kalweit for the ALICE Collaboration, J. Phys. G: Nucl. Part. Phys. 38 (2011) 124073

[6] H. Agakishiev *et al.* (STAR Collaboration), Nature 473 (2011) 353

* Work supported by GSI, BMBF, Helmholtz Alliance HA216/EMMI, H-QM, and HGS-HIRe

† b.doenigus@gsi.de

Search for hyper-matter with ALICE at the LHC*

B. Dönigus[†1], *N. Martin*[‡1,2] *for the ALICE Collaboration*

[1]ExtreMe Matter Institute EMMI and Research Division, GSI Helmhotzzentrum für Schwerionenforschung, Darmstadt, Germany; [2]Institut für Kernphysik, Technische Universität Darmstadt, Darmstadt, Germany

The unique particle identification capabilities of the ALICE detector [1] allow for the measurement of rarely produced exotic states created in Pb–Pb collisions. This also gives the opportunity to search for hypothetical states like the Λn bound state and the H-Dibaryon, a six quark state ($uuddss$), which was already predicted in 1977 [2] using a bag model calculation.

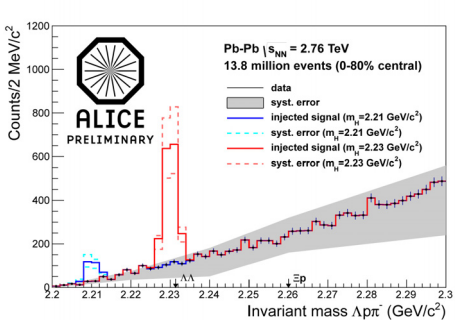

Figure 1: Invariant mass of $\Lambda + \mathrm{p} + \pi^-$.

Since current theoretical discussions favour a low binding energy - if bound at all - for the H-Dibaryon, we concentrate on the mass region of 2.2-2.3 GeV/c^2 in the decay channel Λpπ. In this channel a signal for a bound state would result in a peak in the invariant mass distribution or in a broad structure above the $\Lambda\Lambda$ threshold in case of a resonant state. In a similar way, we also study here the possible decay of a Λn bound state decaying into d+π^- which was observed at GSI by the HypHI collaboration [4] at a mass of 2.054 GeV/c^2.

The results shown here for the H-Dibaryon and the $\overline{\Lambda\mathrm{n}}$ bound state are based on the analysis of about 13.8 million Pb–Pb events in the centrality class of 0-80% taken with the ALICE apparatus in 2010. We focus here on the $\overline{\Lambda\mathrm{n}}$, since the experimental background is much lower compared to Λn. The reconstructed invariant mass distributions are shown in figure 1 and 2. No evidence for a signal, neither for the H-Dibaryon nor the $\overline{\Lambda\mathrm{n}}$ bound state was found. The figures 1 and 2 also show the expected signal for the H-Dibaryon for two assumed masses of 2.21 GeV/c^2 and 2.23 GeV/c^2 (corresponding to binding energies of 21 MeV and 1 MeV) and a possible $\overline{\Lambda\mathrm{n}}$ signal. The expected signal was computed estimating the acceptance $\times$ efficiency (from a Monte-Carlo simulation), the

* Work supported by GSI, BMBF, Helmholtz Alliance HA216/EMMI, H-QM, and HGS-HIRe

† b.doenigus@gsi.de

‡ n.martin@gsi.de

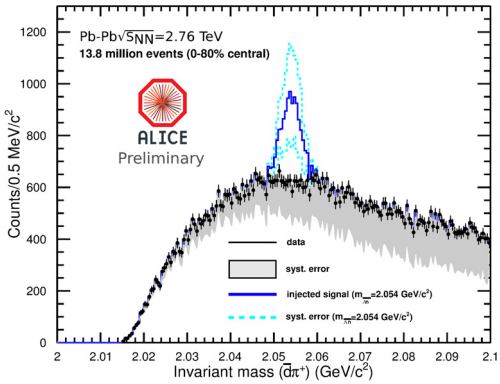

Figure 2: Invariant mass for $\overline{\mathrm{d}} + \pi^+$.

production rates as predicted by the thermal-model [5] and the predicted branching ratios [3, 6]. For the Monte-Carlo simulation, involving full decay kinematics and transport in the material utilizing GEANT3, the lifetime of the free Λ hyperon was assumed for both exotic states. We calculate upper limits for the production yields:

H-Dibaryon: $\mathrm{d}N/\mathrm{d}y\ (m_\mathrm{H} = 2.21\,GeV/c^2) \leq 8.4 \cdot 10^{-4}$

$\mathrm{d}N/\mathrm{d}y\ (m_\mathrm{H} = 2.23\,GeV/c^2) \leq 2 \cdot 10^{-4}$

$\overline{\Lambda\mathrm{n}}$ bound state: $\mathrm{d}N/\mathrm{d}y \leq 1.5 \cdot 10^{-3}$

The extracted limits are a factor of 10 lower than the thermal-model predictions [5] used to estimate the expected signal while these successfully describe the yields measured by STAR for the hypertriton [7] within uncertainties [8]. The results shown here are described in more details in [9].

References

[1] K. Aamodt *et al.* (ALICE Collaboration), JINST 3 (2008) S08002

[2] R. Jaffe, Phys. Rev. Lett. 38 (1977) 195, and erratum ibid 38 (1977) 617

[3] J. Schaffner-Bielich, R. Mattiello, H. Sorge, Phys. Rev. Lett. 84 (2000) 4305

[4] T. Saito *et al.* (HypHi Collaboration), invited talk presented at the NUFRA2011 conference, Frankfurt (2011)

[5] A. Andronic, private communication

[6] J. Schaffner-Bielich, private communication

[7] B. I. Abelev *et al.* (STAR Collaboration), Science 328 (2010) 58

[8] A. Andronic *et al.*, Phys. Lett. B 697 (2011) 203

[9] B. Dönigus, Dissertation, TU Darmstadt, in preparation

Azimuthal correlation measurements in a heavy-ion collisions*

M. Krzewicki[1,2], J. Onderwaater[1,2], and I. Selyuzhenkov[1,2] for the ALICE Collaboration

[1]ExtreMe Matter Institute EMMI and GSI Helmhotzzentrum für Schwerionenforschung, Darmstadt; [2]Frankfurt Institute for Advanced Studies (FIAS), Germany

Azimuthal anisotropic flow in heavy-ion collisions is recognized as a key observable used to infer information about the early time evolution of the nucleus-nucleus interaction. We report recent results by the ALICE Collaboration at the LHC on the identified particle elliptic flow v_2 measured in Pb-Pb collisions at $\sqrt{s_{\rm NN}} = 2.76$ TeV. ALICE experimental findings from the search for effects of local parity violation in the strong interaction using charge dependent azimuthal correlations with respect to the reaction plane are also discussed.

v_2 of identified particles at high $p_{\rm T}$

Identified particle anisotropic flow is sensitive to the particle production mechanism in different transverse momentum, $p_{\rm T}$, regions. For $p_{\rm T} < 2-3$ GeV/c, the particle type dependence of v_2 is qualitatively described by hydrodynamic model calculations. At intermediate $p_{\rm T}$, $3 < p_{\rm T} < 6$ GeV/c, the observed flow of the baryons is larger than that of the mesons. For $p_{\rm T} > 8$ GeV/c, the high-energy parton fragmentation due to initial hard scatterings is expected to play the dominant role. While traversing the hot and dense quark matter these partons experience collisional and radiative energy losses, which are strongly dependent on the thickness of the created medium. In azimuthally asymmetric system, the energy loss depends on the azimuthal emission angle of the parton, which leads to an azimuthal anisotropy in particle production at high $p_{\rm T}$. Figure 1 presents charged pion and proton $v_2(p_{\rm T})$ in

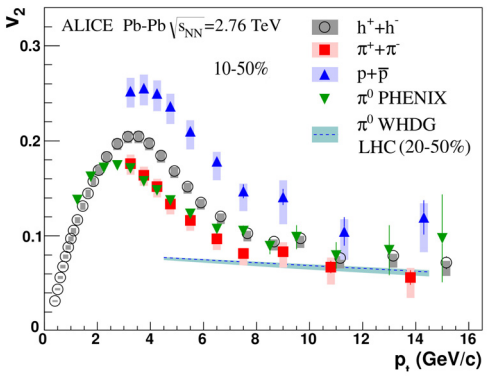

Figure 1: $v_2(p_{\rm T})$ of $\pi^{\pm}$ and $\bar{\rm p}/{\rm p}$ measured by ALICE compared to π^0 v_2 at RHIC and WHDG model calculations.

the 10-50% centrality range of Pb-Pb collisions. The proton v_2 is higher than that of pions up to $p_{\rm T} = 8$ GeV/c which is qualitatively consistent with a picture where particle production in this intermediate $p_{\rm T}$ region includes the interaction of jet fragments with bulk matter. The magnitude of the measured charged pion v_2 for $p_{\rm T} > 8$ GeV/c is compatible with that of unidentified charged particles, and the π^0 v_2 measured by PHENIX in Au-Au collisions at $\sqrt{s_{\rm NN}} = 0.2$ TeV. Results are reproduced by the WHDG model calculations for neutral pions.

Charge dependent correlations

The parity symmetry violation in strong interactions remains one of the open fundamental questions in quantum chromodynamics. It is argued that parity symmetry can be locally violated in a heavy-ion collision which will result in an experimentally observable separation of charges along the extreme magnetic field generated by the moving ions, the so called chiral magnetic effect (CME). As an experimental probe of the CME it was proposed to use the azimuthal correlations with respect to the collision reaction plane which is perpendicular to the magnetic field generated in the collision. ALICE observed a clear charge dependence of the two-particle correlation with respect to the reaction plane as shown in Fig. 2. The observed difference between the same- and opposite charge correlations may in part originate from effects of local parity violation. However, a number of other charge dependent effects which preserve parity symmetry can also contribute. At the moment none of the models is able to reproduce simultaneously the charge dependence and the charge insensitive baseline of the measured correlations.

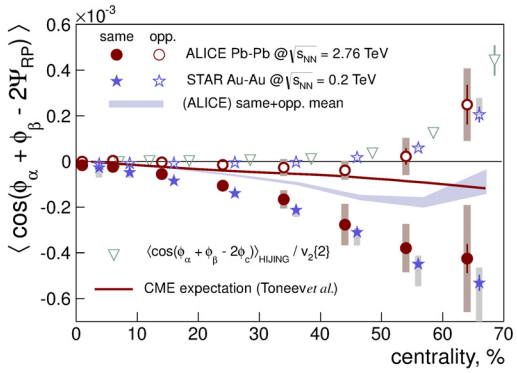

Figure 2: Centrality dependence of the 3-particle correlator measured with respect to the reaction plane.

References

[1] B. Abelev *et al.* [ALICE Coll.], Phys.Lett.B **719** (2013), 18.

[2] B. Abelev *et al.* [ALICE Coll.], Phys.Rev.Lett. **110** (2013) 012301.

*Supported by GSI, BMBF, HGS-HIRe, and Helmholtz Alliance HA216/EMMI

Monte Carlo studies on event-by-event mean p_{T} fluctuations and comparison with results from the ALICE experiment*

S. Heckel[1], *H. Appelshäuser*[1] *for the ALICE Collaboration*

[1]Institut für Kernphysik, Goethe-Universität, Frankfurt am Main, Germany

For the study of event-by-event fluctuations in heavy-ion collisions the understanding of effects seen in pp collisions is of major importance. They serve as a baseline for the interpretation of observations in heavy-ion collisions.

In this analysis, non-statistical event-by-event fluctuations of the mean transverse momentum $M(p_{\mathrm{T}})$ of charged particles are studied as a function of the event multiplicity. A detailed comparison of results for pp collisions at $\sqrt{s}$ = 7 TeV, obtained with the ALICE detector [1] at the LHC, with different Monte Carlo event generators is performed in $0.15 < p_{\mathrm{T}} < 2$ GeV/c and $|\eta| < 0.8$.

Full simulations including the implementation of the detector setup are computing expensive. To be able to compare the data to a larger set of generators and tunes, a fast simulation method based on a simple p_{T}-dependent efficiency filter is developed. The filter is shown for both pp and Pb–Pb collisions in figure 1.

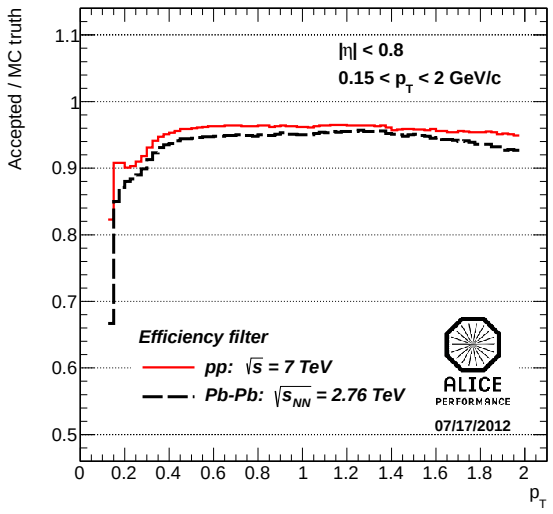

Figure 1: Efficiency filter as a function of p_{T} in pp collisions at $\sqrt{s}$ = 7 TeV (solid line) and Pb–Pb collisions at $\sqrt{s_{\mathrm{NN}}}$ = 2.76 TeV (dashed line).

As a measure of dynamical fluctuations the two-particle correlator $C = \langle \Delta p_{\mathrm{T},i}, \Delta p_{\mathrm{T},j} \rangle$ [2] is analysed, with

$$C = \frac{1}{N_{\mathrm{ev}}^{\mathrm{ps}}} \sum_{k=1}^{n_{\mathrm{ev}}} \sum_{i=1}^{N_k} \sum_{j=i+1}^{N_k} (p_{\mathrm{T},i} - M(p_{\mathrm{T}}))(p_{\mathrm{T},j} - M(p_{\mathrm{T}})),$$

where n_{ev} is the number of events, N_k the number of particles and N_k^{ps} the number of particle pairs in event k and $N_{\mathrm{ev}}^{\mathrm{ps}} = \sum_{k=1}^{n_{\mathrm{ev}}} N_k^{\mathrm{ps}}$. By construction, C equals zero in the presence of only statistical fluctuations. The correlator is calculated in bins of the event multiplicity N_{acc}, where N_{acc} is the number of tracks accepted by the analysis cuts.

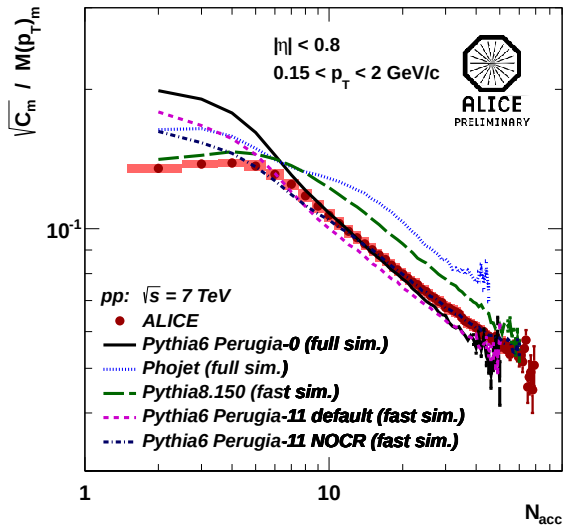

Figure 2: $\sqrt{C_m}/M(p_{\mathrm{T}})_m$ as a function of N_{acc} in pp collisions at $\sqrt{s}$ = 7 TeV and comparison to different Monte Carlo generators and tunes.

The results for pp collisions at $\sqrt{s}$ = 7 TeV are presented in figure 2 in terms of the relative fluctuations $\sqrt{C_m}/M(p_{\mathrm{T}})_m$, where m indicates the given multiplicity class. The Monte Carlo simulations PHOJET [3], PYTHIA6 (Perugia-0 and -11) [4] and PYTHIA8 are analysed. For Perugia-11, the default version is compared to one without color reconnections (NOCR), which is expected to show a steeper slope in figure 2. All PYTHIA6 tunes show a good description of the data, though, Perugia-11 slightly better than Perugia-0. The good agreement of Perugia-11 NOCR rules out color reconnections as the reason for the slope being different from a simple superposition expectation. PYTHIA8 also shows the correct slope, but overestimates the data by about 10–15%, while PHOJET shows only qualitative agreement.

References

[1] K. Aamodt *et al* [ALICE] 2008 *JINST* **3** S08002
[2] S.A. Voloshin *et al* 1999 *Phys. Rev.* C **60** 024901
[3] R. Engel *et al* 1995 *Phys. Rev.* D **52** 1459
[4] P.Z. Skands 2010 *Phys. Rev.* D **82** 074018

* Work supported by GSI, BMBF, HGS-HIRe, and Helmholtz Alliance HA216/EMMI.

Measurement of the Nuclear Modification Factor of Charged Particles in p–Pb Collisions at $\sqrt{s_{NN}} = 5.02$ TeV with ALICE at the LHC*

M. L. Knichel[1], *A. Andronic*[1], *P. Lüttig*[2] *and J. Otwinowski*[1] *for the ALICE Collaboration*

[1]GSI, Darmstadt, Germany; [2]Institut für Kernphysik, Goethe University, Frankfurt, Germany

In September 2012 the LHC at CERN provided p–Pb collisions for the first time at the center-of-mass energy of $\sqrt{s_{NN}} = 5.02$ TeV in a short run test run for the main p–Pb run in 2013. During a few hours of collisions the ALICE detector [1] collected data using a minimum bias trigger. For this analysis non-single-diffractive collisions have been selected with a trigger efficiency of 99.2%, leading to a 1.7×10^6 events, with negligible contributions from beam-gas background, single-diffractive and electromagnetic interactions. For tracking and determination of the transverse momentum the information from the large Time Projection Chamber (TPC) is combined with the hits in the Inner Tracking System (ITS).

The p_{T} spectra are measured for primary charged particles in the p_{T} range 0.5 GeV/c $< p_{\mathrm{T}} <$ 20 GeV/c and pseudorapidity $|\eta_{\mathrm{cms}}| < 0.3$. Primary charged particles are defined as all prompt particles produced in the collision, including decay products, except those from weak decays of strange hadrons. Details of the analysis can be found in [2].

The measured p_{T} distribution can be compared to that measured in proton-proton collisions in terms of the nuclear modification factor R_{pPb} which is defined as

$$R_{\mathrm{pPb}}(p_{\mathrm{T}}) = \frac{\mathrm{d}^2N/\mathrm{d}\eta\,\mathrm{d}p_{\mathrm{T}}}{\langle T_{\mathrm{pPb}}\rangle\,\mathrm{d}^2\sigma^{\mathrm{pp}}_{\mathrm{ch}}/\mathrm{d}\eta\,\mathrm{d}p_{\mathrm{T}}}$$

$\langle T_{\mathrm{pPb}}\rangle$ is the average nuclear overlap function calculated using Glauber MC, $\langle T_{\mathrm{pPb}}\rangle = 0.0983 \pm 0.035\,\mathrm{mb}^{-1}$.

As there is no measurement of $\sigma^{\mathrm{pp}}_{\mathrm{ch}}$ at $\sqrt{s} = 5.02$ TeV, the pp reference spectrum has been derived from the ALICE measurements at $\sqrt{s} = 2.76$ and 7 TeV. For the high-p_{T} part above 5 GeV/c, where pQCD is reliable, the measured differential cross section at 7 TeV was scaled with a factor obtained from NLO calculations. At lower and intermediate $p_{\mathrm{T}} < 5$ GeV/c, the measured cross sections at $\sqrt{s} = 2.76$ and 7 TeV have been interpolated in every p_{T} bin assuming a power law behaviour in $\sqrt{s}$.

In absence of any nuclear effects R_{pPb} equals unity under the assumption of binary collision scaling expected for high-p_{T} processes. In Figure 1, the measured R_{pPb} is compared to nuclear modification factors measured in Pb–Pb [3].

In our measurement of R_{pPb} there is almost no enhancement at intermediate p_{T}, known as Cronin effect, which was observed at RHIC. For $p_{\mathrm{T}} >$ 2 GeV/c the nuclear modification factor is consistent with unity, indicating only small contributions from cold nuclear matter effects in this p_{T} range. At low $p_{\mathrm{T}} < 2$ GeV/c production of charged particles is supressed in p–Pb compared to pp. Predictions from several models have been compared to the data, calculations based on the Color Glass Condensate (CGC) model are consistent with the measurement, see [2] for details including other models.

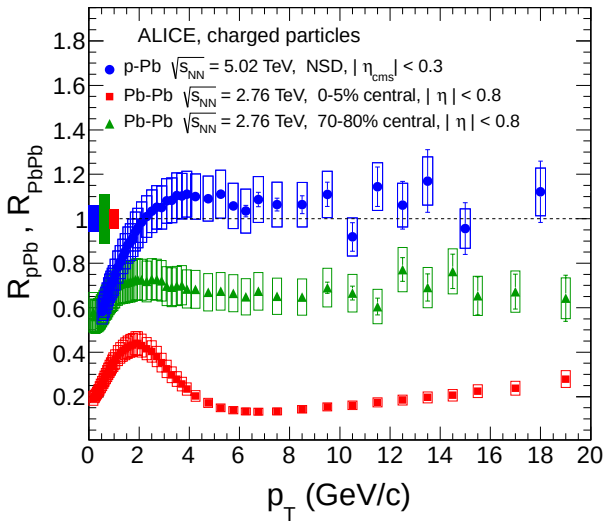

Figure 1: The nuclear modification factor of charged particles as a function of transverse momentum in NSD p–Pb collisions as $\sqrt{s_{NN}} = 5.02$ TeV compared to measurements in central (0-5%) and peripheral (70-80%) Pb–Pb collisions at $\sqrt{s_{NN}} = 2.76$ TeV. Systematic uncertainties are represented as boxes, the statistic uncertainties by lines around the data points. Normalization uncertainties are shown as filled boxes around unity.

In central Pb–Pb collisions a strong suppression of particle production at high p_{T} was observed, which remains substantial also for peripheral collisions. The measurement of p–Pb clearly shows that the suppression observed in Pb–Pb is not an initial state effect but due to the hot QCD medium.

References

[1] ALICE Collaboration, K. Aamodt *et al.*, JINST **3**, S08002 (2008), doi:10.1088/1748-0221/3/08/S08002.

[2] ALICE Collaboration, B. Abelev *et al.*, Phys.Rev.Lett, in press (2013), arXiv:1210.4520.

[3] ALICE Collaboration, B. Abelev *et al.*, Phys.Lett.B, in press (2013), arXiv:1208.2711.

* Work supported by GSI, BMBF, HGS-HIRe, and Helmholtz Alliance HA216/EMMI

Modification of Jets Reconstructed with Charged Particles in Pb–Pb Collisions at $\sqrt{s_{NN}}$ = 2.76 TeV with the ALICE-Experiment *

C. Klein-Bösing[†1,2], *J. Anielski*[1], *B. Bathen*[1], *O. Busch*[3], *L. Cunqueiro*[4], *T. Dietel*[1], *M. van Leeuwen*[5], *L. Feldkamp*[1], *M. Heide*[1], *A. Passfeld*[1], *H. Poppenborg*[1], *E. Sicking*[1], *M. Wilde*[1], *M. Verweij*[5], *J. P. Wessels*[1], *U. Westerhoff*[1], *and M. Zimmermann*[1] *for the ALICE Collaboration*

[1]Institut für Kernphysik, University of Münster, Germany; [2]ExtreMe Matter Institute EMMI, GSI Darmstadt, Germany; [3]Physikalisches Institut, University of Heidelberg, Germany; [4]INFN, Frascati, Italy; [5]Institute for Subatomic Physics, Utrecht University, Netherlands

The reconstruction of jets in elementary pp-collisions provides the most direct access to the properties of hard scattered (large momentum transfer Q^2) partons. In heavy-ion collisions the initial hard parton scattering occurs before the formation of a thermalized medium ($t \approx 1/Q \ll 1$ fm/c) and the modification of the subsequent jet fragmentation process compared to the QCD vacuum potentially allows to map out the properties of the QCD-medium. However, in nucleus-nucleus collisions the reconstruction of jets is complicated by the background from the underlying event and its fluctuations not associated with the hard scattering.

Jets have been reconstructed in Pb–Pb collisions with the sequential recombination algorithms k_{T} and anti-k_{T} based on charged particle tracks measured with the Inner Tracking System and the Time Projection Chamber of the ALICE-Experiment. The impact of the underlying event background on the reconstructed jet momentum depends strongly on the jet radius and the minimum p_{T} threshold ($p_{\mathrm{T}}^{\mathrm{min}}$) applied to the input particles of the jet finding process and has been determined in a data driven fashion as follows: The background momentum-density ρ is calculated on an event-by-event basis as the median of reconstructed p_{T} per area using all but the two leading reconstructed k_{T} clusters within one event [2]. Clusters reconstructed with the anti-k_{T} algorithm, the same $p_{\mathrm{T}}^{\mathrm{min}} = 0.15$ GeV/c, and $R = 0.2$ or 0.3 are used as basis for signal jets and corrected for the average background contribution via:

$$p_{\mathrm{T,jet}} = p_{\mathrm{T,jet}}^{\mathrm{rec}} - \rho \cdot A_{\mathrm{jet}}^{\mathrm{rec}}. \qquad (1)$$

The impact of region-to-region fluctuations of the underlying event background has been evaluated by probing measured heavy-ion events on the scale of a typical reconstructed jet, e.g. via embedding cones with radius R at a random position in the event and summing up the p_{T} of all reconstructed tracks [1]. The distribution of the residuals after correcting for the average momentum background density in each random cone with $A = \pi R^2$ following Equation 1 is used as the measured background response (smearing), i.e. the probability distribution for a change of the jet momentum by δp_{T} due to a local fluctuation of the event background. It is combined with the detector response matrix, which encodes the detector specific modification of the jet momentum scale mainly due to track finding efficiency and momentum resolution. The reconstructed jet spectra for various centrality selections are corrected for their respective background fluctuations and the detector effects on a statistical basis via a χ^2 unfolding technique [3].

The resulting, fully corrected spectra allow to study the modification of jet production when going from peripheral to central Pb–Pb collisions. This is shown in Figure 1 a) using the most peripheral bin (50-80%) as reference in R_{CP}, the ratio of invariant yields scaled by the appropriate number of binary collisions. An increasing suppression is observed for more central events. The comparison of the jet yield for different cone radii as shown Figure 1 b) exhibits no significant modification in central collisions compared to peripheral Pb–Pb and simulated pp reactions.

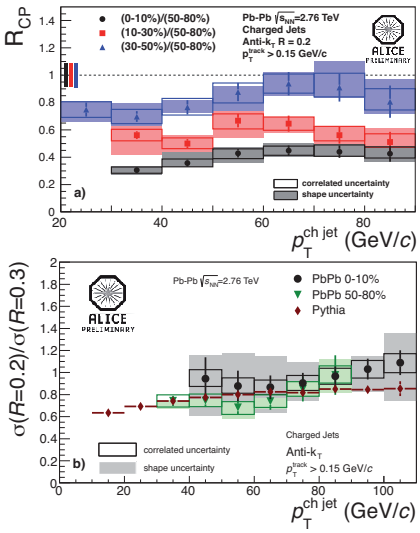

Figure 1: a) Nuclear modification factor R_{CP} for charged jets b) Ratio of charged jet cross sections for two radii.

References

[1] B. Abelev et al. (ALICE) *JHEP*, 1203:053, 2012.

[2] Cacciari and G. P. Salam. *Phys. Lett.*, B659:119–126, 2008.

[3] M. Verweij for the ALICE Collaboration, arxiv:1208.6169.

*Work supported by GSI, BMBF, and Helmholtz Alliance HA216/EMMI.

† Christian.Klein-Boesing@uni-muenster.de

Three-Particle Azimuthal Correlations with an Intermediate-p_{T} Trigger Particle in ALICE*

J.G. Ulery† *for the ALICE Collaboration*
Institut für Kernphysik, Goethe Universität, Frankfurt, Germany

Introduction

Lead ions are collided at energies up to 2.76 TeV per nucleon pair in the ALICE detectors at the Large Hadron Collider. These collisions produce hot and dense matter, possibly a deconfined state of quarks and gluons called a Quark Gluon Plasma. A method of studying this matter is by examining correlations of particles with a trigger particle. An intermediate p_{T} trigger particle is chosen to preferentially select jets. This can be used to study how jets and the produced medium interact. Three-particle correlations provide us with different insights and systematics than two-particle correlations and the technique was designed to look for conical emission in heavy-ion collisions[1], which could come from Mach Cones[2] or Čerenkov Gluon radiation[3].

Analysis

Correlations between the differences in azimuthal angle between a 3< $p_{\mathrm{T,Trigger}}$ <4 GeV/c and two 1< $p_{\mathrm{T,Associated}}$ <2 GeV/c associated particles are studied. Before background subtraction the three-particle correlations contains backgrounds from two-particle correlations and three-particle flow. To subtract the two-particle correlations one particle is taken from a mixed event while the other two are taken from the same event. To remove the three-particle flow background the measured flow values of orders v_2, v_3, and v_4 were used. An additional background exists from the correlation of the flow of the jet with the other particle. Background subtracted two-particle correlations and the measured flow values were used to subtract this background. Backgrounds were normalized assuming the background subtracted two- and three-particle correlations have Zero Yield At Minimum.

Results

Background subtracted three-particle correlations are shown for two different centrality selections in Fig. 1. Both associated particles in peak at $(\Delta\phi, \Delta\phi)$ =(0,0) are near the trigger particle. In the peak at (π, π) is from both are on the away side. This peak is elongated along the diagonal consistent with k_T broadening. The peaks at $(0, \pi)$ and $(\pi, 0)$ are from where one associated particle is near the trigger and the other is opposite in azimuth. In addition, there are peaks in central collisions at about $(\pi \pm 1.5, \pi \mp 1.5)$. These peaks are a non-dijet signal. In the projections, these peaks show up as the two side peaks and it can be seen that these peaks are significant in the 0-5% collisions but not in 40-50%. The dominant contributions to these systematic errors are the uncertainty in the measured flow values from different methods used to obtain them and from the jet flow cross term.

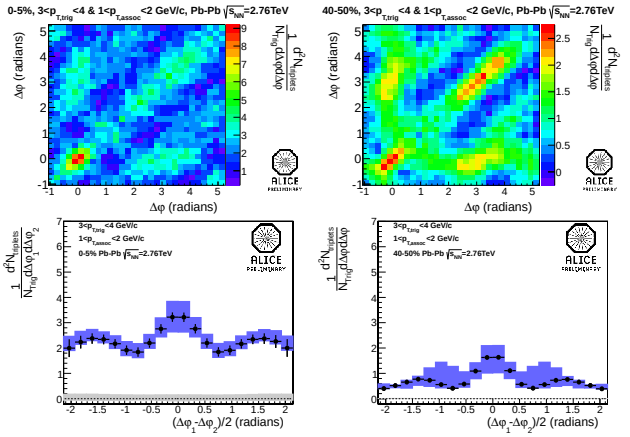

Figure 1: Three-particle correlation for $2.5 < p_{\mathrm{T,Trigger}} < 4$ GeV/c and $1 < p_{\mathrm{T,Associated}} < 2$ GeV/c in 0-5%, left, and 40-50%, right, most central Pb-Pb collisions at $\sqrt{s_{NN}} = 2.76$ TeV. Bottom panels show the away-side projection along the $\Delta\phi_1 + \Delta\phi_2 = 2\pi$ axis along with systematic errors. Uncorrelated systematic errors are shown in blue around the points and correlated systematic errors are shown in grey about 0.

Summary

In conclusion, significant off-diagonal peaks are seen in central Pb-Pb collisions at $\sqrt{s_{NN}} = 2.76$ TeV. These peaks are a non-dijet signal. Broadening consistent with k_T broadening is also seen along the diagonal.

References

[1] J.G. Ulery and F. Wang, *Analysis Method for Jet-Like Three-Particle Azimuthal Correlations*, *NIM* **A595** 502 (2008).

[2] J. Hofmann, H. Stöcker, U. Heinz, W. Scheid, and W. Greiner, *Possibility of Detecting Density Isomers in High Density Nuclear MACH Shock Waves*, *Phys. Rev. Lett.* **36** 88 (1976).

[3] I.M. Dremin, *Ring-like events: Cerenkov Gluons or Mach Waves?*, *Nucl. Phys.* **A767** 233 (2006).

* Supported by GSI, BMBF, and Helmholtz Alliance HA216/EMMI.
† ulery@ikf.uni-frankfurt.de

HBOM method for Event-Background Fluctuations in Pb-Pb Collisions at the LHC*

M. Zimmermann[1], *J. Anielski*[1], *B. Bathen*[1], *T. Dietel*[1], *S. Dyba*[1], *L. Feldkamp*[1], *M. Heide*[1], *C. Klein-Bösing*[1,2], *M. Kohn*[1], *A. Passfeld*[1], *E. Sicking*[1], *M. Tegeder*[1], *M. Wilde*[1], *J.P. Wessels*[1], *and U. Westerhoff*[1] *for the ALICE Collaboration*[1]

[1]Institut für Kernphysik, University of Münster, Germany; [2]ExtreMe Matter Institute EMMI, GSI Darmstadt, Germany

With the measurement of jets and their modification in heavy-ion collisions the quark-gluon plasma can be investigated tomographically. However, the determination of the jet momentum in Pb–Pb-collisions is complicated by the background of the underlying event and its fluctuations. The fluctuations of the jet momentum scale can be described by the distribution of residuals (δp_T) after background subtraction of the momentum in a cone placed randomly in φ and η in real Pb–Pb events. The standard deviation $\sigma(\delta p_{\mathrm{T}})$ of the resulting distribution is used to classify these fluctuations [1].

The measured fluctuations depend on the correlations within the heavy-ion event as well as on the detected particle number. The correlations in the event are a-priori unknown, which is the motivation for a data-driven correction of detector effects on the width of the fluctuations. This is done here with the so called Hit Backspace Once More (HBOM) method [2] for the 10% most central heavy ion events measured in Pb-Pb collisions at 2.76 TeV with ALICE. It is a model independent method to back-extrapolate the data to no detector effect (truth) [3].

The method works as follows. First the $\sigma(\delta p_{\mathrm{T}})$ is determined for the measured events as usual. Then the efficiency is applied again to all particles in the event by a Monte Carlo method that only accepts a particle, if a random number is lower than the p_T and φ dependent detection efficiency. Doing this once for all particles is called one detector hit. After the detector hit the $\sigma(\delta p_{\mathrm{T}})$ is determined again. This is done up to five times. The fit to 0–4 detector hits is back-extrapolated to -1 detector hits which corresponds to the efficiency-corrected value of the standard deviation [3].

The method has been validated in simulations that emulate the generic features of heavy-ion collisions such as the multiplicity, the p_T spectrum, and flow (v_2, v_3). In Fig. 1 the back-extrapolation is shown. Since the *truth* value is known in the simulation the number of fit points and its functional form can be optimized. With the best configuration, a corrected $\sigma(\delta p_{\mathrm{T}}) = (9.43 \pm 0.02(stat) \pm 0.05(syst))$ GeV/c is achieved and the *truth* value $\sigma(\delta p_{\mathrm{T}}) = (9.458 \pm 0.005)$ GeV/c is reproduced [3].

After the validation, the method has been applied to measurements of 2010 and 2011 Pb–Pb collisions as shown in Fig. 2 and a value of $\sigma(\delta p_{\mathrm{T}}) = (11.85 \pm 0.14)$ GeV/c is obtained consistently in both Pb–Pb data sets. A comparison with the simulated value is not meaningful because the simulation does not consider all correlations [3].

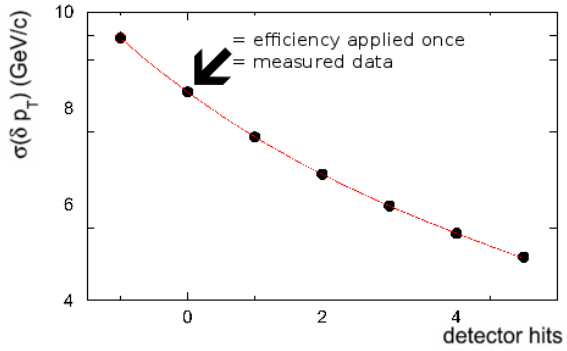

Figure 1: HBOM back-extrapolation for $\sigma(\delta p_{\mathrm{T}})$ in simulated Pb–Pb events. The point at zero detector hits corresponds to the measured spectrum [3].

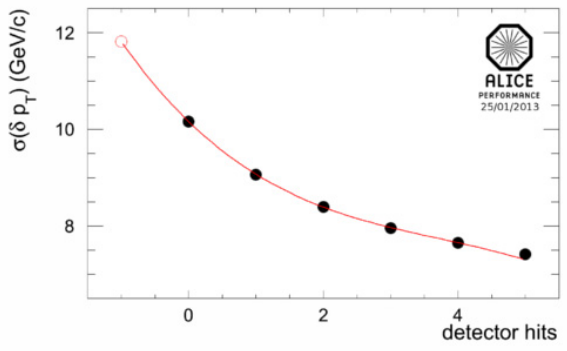

Figure 2: HBOM back-extrapolation for $\sigma(\delta p_{\mathrm{T}})$ in Pb–Pb collisions from 2010. The red point at minus one shows the corrected value [3].

References

[1] Abelev, Betty and others. *JHEP*, 1203:053, 2012.

[2] Monk, James W. and Oropeza-Barrera, Cristina. *Nucl.Instrum.Meth*, A701:17-24, 2011.

[3] M. Zimmermann. Master Thesis, Westfälische Wilhelms-Universität Münster, 2012.

*Work supported by BMBF and Helmholtz Alliance HA216/EMMI

Operation and performance of the ALICE Time Projection Chamber, a high-resolution detector for the highest particle multiplicities*

C. Lippmann[1] *and J. Thäder*[1] *for the ALICE Collaboration*

[1]ExtreMe Matter Institute EMMI and Research Division, GSI Helmhotzzentrum für Schwerionenforschung, Darmstadt, Germany

Introduction

The unique feature of ALICE [1], the general-purpose heavy-ion experiment at the LHC, is the optimization of the detector for the reconstruction and identification of particles over a broad momentum range and in an environment with the highest particle multiplicities. Using a large cylindrical Time Projection Chamber (TPC) [2] embedded in a solenoid magnet with a magnetic field of 0.5 T as the main element, ALICE is able to provide precision tracking and particle identification (PID) from 100 MeV/c to 50 GeV/c.

Running Conditions

During 2012 the LHC was performing outstandingly well. ALICE and the TPC were in continuous data taking mode, while the LHC delivered collisions of protons at high luminosity ($\sim 10^{31}\mathrm{cm}^{-2}\mathrm{s}^{-1}$). Compared to the other LHC experiments the luminosity in ALICE was limited by using special filling schemes, where some of the up to 1,368 main bunches per ring collide with the much less populated satellite bunches in the interaction region of ALICE. However, this scheme made the experiment quite sensitive to vacuum problems, which increase the rate of background events to a level that reached a significant fraction of the total event rate. Instabilities of the TPC readout chambers had already been an issue in the previous years (in particular in the 2011 Pb-Pb run) and were coped with by removing the high voltage capacitors from all TPC readout chambers in 2011 and by investing in higher performance high voltage power supplies in the beginning of 2012.

Performance

Fig. 1 shows the relative momentum resolution $\sigma(p_\mathrm{T})/p_\mathrm{T}$ as a function of the transverse momentum p_T. p_T is reconstructed from the track curvature, measured in the magnetic field, and combines the information from the TPC and from the silicon Inner Tracking System (ITS). At low momentum $\sigma(p_\mathrm{T})/p_\mathrm{T}$ is dominated by multiple scattering, but stays at only $\sim$1% at $p_\mathrm{T} \approx 1\,\mathrm{GeV/c}$, thanks to the small material budget (10% of a radiation length between the vertex and the outer wall of the TPC). At higher momenta the resolution increases linearly and reaches $\sim$10% at $p_\mathrm{T} = 50\,\mathrm{GeV/c}$ for the data sample used here.

Charged particles are identified in the TPC in a broad momentum range. The PID in the TPC is based on the measurement of the momentum and the specific energy loss per unit path length $\mathrm{d}E/\mathrm{d}x$. For a particle with a given momentum $\mathrm{d}E/\mathrm{d}x$ depends only on its charge and mass.

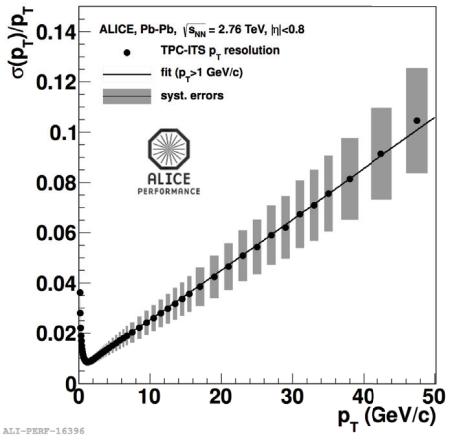

Figure 1: The relative p_T resolution $\sigma(p_\mathrm{T})/p_\mathrm{T}$ as a function of p_T for combined tracking in TPC and ITS.

The functional dependence of the specific energy loss on particle momenta is shown as lines together with data for negatively charged particles in Fig. 2. The particle separation capabilities are excellent; the method even allows for the observation of rare (with charge $|z| > 1$) anti-nuclei (these particles were enhanced in the data sample used for Fig. 2 by the use of an offline trigger).

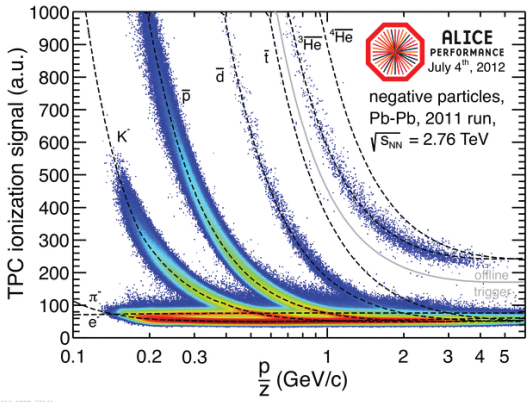

Figure 2: The TPC $\mathrm{d}E/\mathrm{d}x$ vs p/z in Pb–Pb collisions at $\sqrt{s_{\mathrm{NN}}} = 2.76$ TeV, highlighting the PID performance.

The TPC shows excellent performance. After the PbPb runs of November 2010 and 2011 the next highlight and milestone is the pPb run that is set to take place in January and February 2013. After the two-year LHC shutdown, where the LHC and the experiments will be consolidated, further Pb-Pb runs at nominal LHC energy are foreseen.

References

[1] K. Aamodt et al. (ALICE Collaboration), JINST 3 (2008) S08002.

[2] J. Alme et al., Nucl. Instr. Meth. A 622 (2010) 316.

*Work supported by GSI, BMBF, and Helmholtz Alliance HA216/EMMI.

Offline Signal Tail-Correction for the ALICE TPC*

M. Arslandok[1], *H. Appelshäuser*[1], *M. Ivanov*[2] *for the ALICE Collaboration*

[1]Institut für Kernphysik (IKF), Goethe-Universität, Frankfurt; [2]GSI, Darmstadt

The ALICE Time Projection Chamber (TPC) is the main tracking and particle identification (PID) detector of ALICE at the CERN-LHC [1]. It was designed for multiplicities of up to 20,000 primary and secondary charged particles emerging from a single central Pb-Pb collision. The PID in the TPC is calculated from the specific energy loss measurement (dE/dx), which is derived from the pulse height distribution of charged particle tracks measured along 159 read-out planes. The signals from the Multi Wire Proportional Chambers (MWPC) show a characteristic long undershoot after the signal, which is due to the long ion drift times in the MWPC amplification region. Such an ion tail may lead to a loss of signal amplitude for the following signals on the same readout pad. Eventually this results in a deterioration of the dE/dx resolution, in particular in the high multiplicity environment of Pb-Pb collisions. Therefore, it was aimed to improve the dE/dx resolution and thus the PID quality via an offline correction.

Signal-Tail Shape Studies

In order to investigate the raw signal shape, the TPC Laser System was used. It generates 336 straight laser tracks similar to ionising particle tracks, at known positions in the drift volume of the TPC.

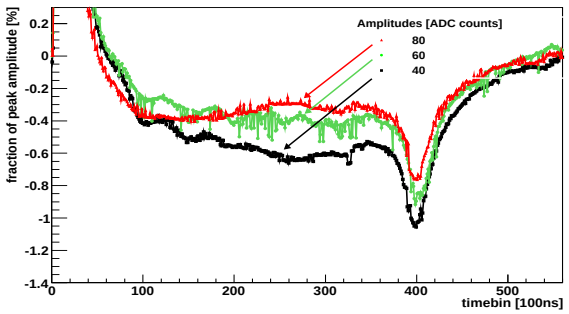

Figure 1: Side pad time response functions for different signal amplitudes.

Several dedicated laser runs with different anode voltage settings were taken. Analysis of these data allowed us to draw the following conclusions;

- The lower anode voltage settings lead to a slower drift of ions in the amplification region which results in a longer ion tail along the time direction.
- The shape of the time response function depends on the relative position of the pad with respect to the cluster position.
- The central pad of a cluster does not show a dependency of the shape on the signal amplitude, while neighbouring pads (side pads) do.

Fig.1 illustrates the amplitude dependence of the side pad time response function, where the x-axis is the length of the ion tail in units of timebins [100ns] and the y-axis shows the amplitude relative to the peak amplitude of the signal in percent.

Offline Signal Tail-Correction

The two readout planes of TPC are composed of 18 sectors each having 159 radial pad rows. For each row in a sector the signals are clusterized into matrices of 5×5 *pad*×*timebin*. The dE/dx calculation is based on either Q_{tot} or Q_{max} of the clusters, where Q_{tot} is defined as the sum of all charge and Q_{max} is the charge at the centre bin of a cluster. In the offline correction procedure it is tried to recover the loss in Q_{tot} and Q_{max} of the clusters later in time.

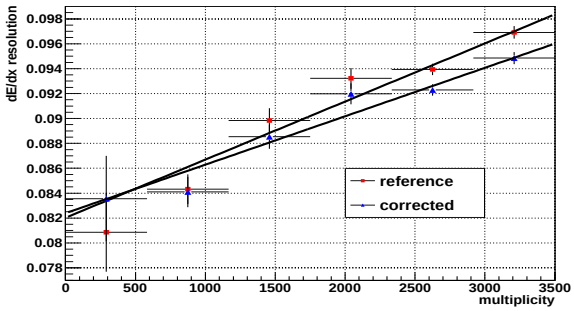

Figure 2: dE/dx resolution for different multiplicity bins.

For this, several pad time response functions were produced from laser tracks, in order to be used for different running conditions. A row by row algorithm was applied iteratively along the drift time from the earliest to the latest cluster read out. Fig.2 shows the first results (with relatively low statistics) of the improvement in the dE/dx resolution for different multiplicity bins. The method will be tested with higher statistics and applied to the Pb-Pb collision data sets taken in 2010 and 2011.

References

[1] ALICE TPC Collaboration, Nucl. Instr. Meth. A622, 316-367, (2010); arxiv.org/abs/1001.1950.

* Work supported by GSI, BMBF, HGS-HIRe, and Helmholtz Alliance HA216/EMMI

The electron identification performance of ALICE TRD*

A. Andronic[1], *M. Fasel*[1,2], *L. Feldkamp*[3], *D. Lohner*[2], *X.-G. Lu*[2], *Y. Pachmayer*[2] *for the ALICE Collaboration*

[1]EMMI & GSI Darmstadt; [2]Universität Heidelberg; [3]Universität Münster

The Transition Radiation Detector (TRD) is designed to enhance electron identification in the ALICE central barrel ($|\eta|$ <0.9) and to provide a level-1 hardware trigger (about 8μs after a hadron-hadron collision) on electrons with high transverse momenta and on jets [1]. The electron identification is achieved by the detection of the specific energy loss and transition radiation (TR). Transition radiation is produced when a relativistic charged particle ($\gamma \gtrsim 1000$) traverses many interfaces of two media of different dielectric constants composing a radiator [2]. On average, in the ALICE TRD, for each electron above 1 GeV/c momentum, one TR photon (of 1-30 keV) is absorbed in the high-Z gas mixture (Xe-C0$_2$ [85-15]) of the 3.7 cm thick detector.

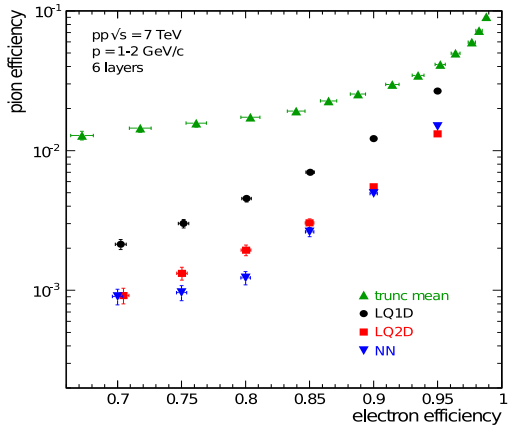

Figure 1: Pion efficiency as a function of electron efficiency for the momentum range 1-2 GeV/c for various methods (see text).

To quantify the TRD identification performance we use the data collected in proton-proton collisions at $\sqrt{s}$ = 7 TeV. Using topological cuts we select clean samples of electrons from γ conversions and pions from K^0_s decays and employ also TPC and TOF particle identification. We express the performance in terms of the pion efficiency, which is the fraction of pions wrongly identified as electrons. The pion suppression factor is the inverse of the pion efficiency. We employ the following methods: (i) truncated mean; (ii) one-dimensional likelihood on the total integrated charge (LQ1D); (iii) bidimensional likelihood on integrated charge in two intervals of drift time (LQ2D); and (iv) neural networks (NN) [4]. The results are compared in Fig. 1, where we show, for tracks with signals in all six layers of the TRD, the pion efficiency as a function of the electron efficiency. While the truncated mean and the LQ1D are the simplest and, consequently, more robust methods, the full exploitation of the TRD capability is reached taking advantage of the temporal pattern of the signal, utilized in the LQ2D and NN methods. Those bring a further pion suppression factor of about two compared to the LQ1D method. The present pion suppression factors obtained from collision data confirm the design value measured in testbeams with prototypes [3].

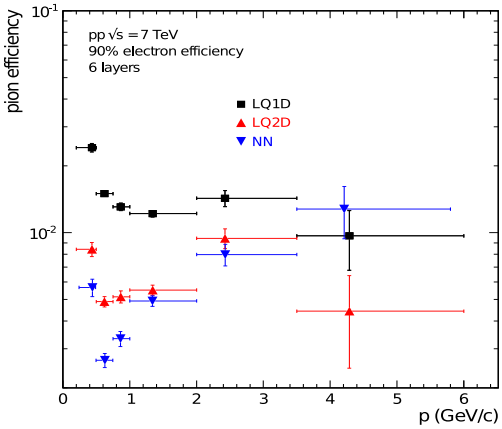

Figure 2: Momentum dependence of the pion efficiency for the LQ1D, LQ2D and NN methods. The results are for 90% electron efficiency.

The momentum dependence of the pion efficiency is shown in Fig. 2. The pion suppression improves with increasing momentum up to about 1 GeV/c as a consequence of the strong onset of TR production by electrons in this momentum range. Above 1 GeV/c TR production starts to saturate and the relativistic rise of the specific energy loss of pions leads to a reduction of the pion rejection factor.

The TRD particle identification is at present successfully used for the measurement of electrons from heavy-flavour decays [5] and for the study of J/ψ mesons.

References

[1] J. Klein, arXiv:1112.5110; see also this Report.

[2] A. Andronic, J.P. Wessels, Nucl. Instrum. Meth. A 666 (2012) 130.

[3] R. Bailhache and C. Lippmann [ALICE TRD Collab.], Nucl. Instrum. Meth. A **563** (2006) 310.

[4] C. Adler et al. [ALICE Collab.], Nucl. Instrum. Meth. A552, 364 (2005).

[5] B. Abelev et al. [ALICE Collab.], Phys. Rev. D **86** (2012) 112007.

* Work supported by GSI, BMBF, Helmholtz Alliance HA216/EMMI, HQM, and HGS-HIRe

Triggering with the ALICE TRD*

T. Dietel[1], *S. Kirsch*[3], *J. Klein*[2], *V. Lindenstruth*[3], *Y. Pachmayer*[2], *F. Rettig*[3], *J. Stachel*[2], *J. P. Wessels*[1], *U. Westerhoff*[1] *for the ALICE Collaboration*

[1]Institut für Kernphysik, Münster; [2]Physikalisches Institut, Heidelberg; [3]Frankfurt Institute for Advanced Studies

Introduction

The Transition Radiation Detector (TRD) in ALICE provides hardware triggers within 7 µs after an interaction, e.g. for electrons and jets. The TRD is azimuthally segmented into 18 supermodules, 13 of which are currently installed. Each supermodule consists of 30 individual tracking chambers, arranged in 6 layers with 5 chambers each. Besides the specific energy deposit, electrons can be identified by the additional detection of transition radiation produced in a fibre-foam radiator. The signals are used for both tracking and particle identification.

The front-end electronics digitizes the amplified and shaped signal. In a digital processing chain, a straight-line fit on cluster positions is calculated. The track segments are characterized by fit parameters and accumulated charge. The latter is translated into an electron likelihood by a tuned look-up table. These data are transferred to the Global Tracking Unit (GTU). Within 2 µs the track segments are combined into TRD global tracks by a 3-dimensional matching algorithm. For every track the transverse momentum with a resolution of 20 % down to 10 % in the $p_\perp$ range from 2 to 8 GeV/c and the electron probability (PID) are calculated. Based on this information, a variety of triggers can be implemented.

Electron Triggers

The TRD single electron triggers require at least one track exceeding configurable $p_\perp$ and PID thresholds. Only tracks with a contribution in the innermost TRD layer and at least four others are considered in order to maximize the rejection. Two combinations of $p_\perp$ and PID thresholds are provided to the central trigger processor. They have been in production since September 2012.

One trigger is optimized to select electrons from $\mathrm{J/\psi} \rightarrow \mathrm{e^+\,e^-}$. Due to the low mass of 3.1 GeV/c^2 of the J/ψ, this trigger has a low transverse momentum threshold of 2 GeV/c. A high electron threshold is chosen in order to keep the rejection sufficiently high, approximately 1500 in pp collisions at 8 TeV.

The second trigger extends the $p_\perp$ reach for electrons from semi-leptonic decays of heavy-flavor hadrons (open charm and beauty). The transverse momentum threshold of this trigger is set to 3 GeV/c. To achieve a comparable trigger rate, the threshold for the electron likelihood is lower allowing for a higher electron efficiency. Figure 1 shows the enhancement of electrons above the trigger threshold.

* Work supported by GSI, BMBF, HGS-HIRe, and Helmholtz Alliance HA216/EMMI

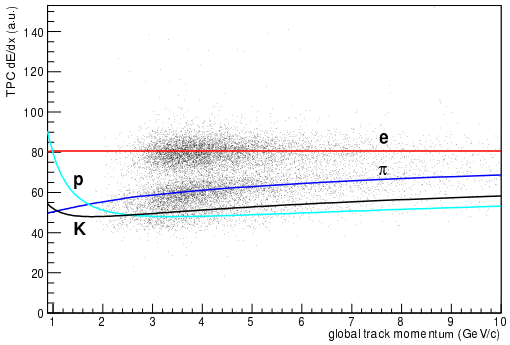

Figure 1: Ionization energy loss in the TPC as a function of momentum for tracks which fulfilled the TRD trigger condition

Jet Trigger

Jets are characterized by an increased local multiplicity. A typical jet area in $\eta - \phi$ used in jet finding, e.g. with anti-kt algorithm with $R = 0.4$, corresponds approximately to the area covered by a TRD stack. Thus, events containing 3 tracks with transverse momentum above 3 GeV/c within any TRD stack are triggered, see Figure 2. Despite being sensitive to charged tracks only, the trigger becomes fully efficient for jets of $\sim$ 100 GeV/c.

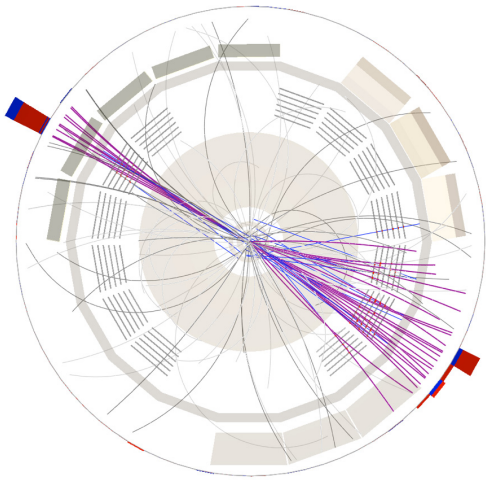

Figure 2: Event display of a di-jet event triggered by the TRD in pp collisions at 7 TeV

References

[1] J. Klein et al., Triggering with the ALICE TRD, NIM A, doi: 10.1016/j.nima.2012.05.011

The statistical model in Pb-Pb collisions at the LHC*

A. Andronic[1], *P. Braun-Munzinger*[1,2,3], *K. Redlich*[1,4], *and J. Stachel*[5]

[1]EMMI & GSI Darmstadt, Germany; [2]Technical University Darmstadt, Germany; [3]Frankfurt Institute for Advanced Studies, J.W Goethe University, Germany; [4]University of Wroclaw, Poland; [5]Physikalisches Institut der Universität Heidelberg, Germany

We investigate the production of hadrons in nuclear collisions within the framework of the thermal (or statistical hadronization) model. We discuss both the ligh-quark hadrons as well as charmonium and discuss the predictions for the LHC energy [1] in light of the recently released data from ALICE.

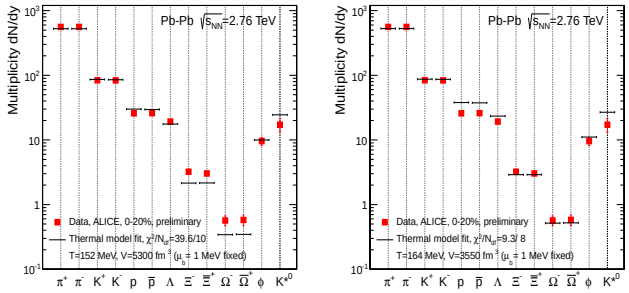

Figure 1: Thermal model fits to ALICE data on hadron production in central Pb–Pb collisions. The left panel shows the result of the fit to all available data, while protons and anti-protons are excluded from the fit in the right panel.

In Fig. 1 we show the results of thermal model fits to recently released ALICE data [2]. The left panel shows a fit to all currently available data. The unexpectedly low yields for protons and anti-protons drive the temperature of the fit to a rather low value ($T = 152$ MeV) while the yield of multi-strange baryons is significantly underpredicted. This is somewhat similar to the situation observed at RHIC. With the more than a factor of 2 smaller error bars of the ALICE data compared to results from the RHIC experiments the reduced χ^2 value approaches 4, and the temperature parameter is significantly lower than expected from the extrapolation from the data at lower energies. The right hand panel in Fig. 1 shows the result of excluding protons and anti-protons from the fit. This leads to a very good description of all remaining data, with excellent χ^2 parameter and a temperature value (164 MeV) completely in line with expectations. Naturally, the nucleon yields are now about a factor of 1.4 below the calculated values. This apparent proton anomaly could be due to annihilation in the hadronic phase near the phase boundary. Indeed, schematic model calculations indicate such an effect [3].

The centrality dependence of the nuclear modification factor $R_{AA}^{J/\psi}$ as measured recently by ALICE [4] is shown in Fig. 2, for central and forward rapidity, and compared to RHIC data from the PHENIX collaboration [5] as well

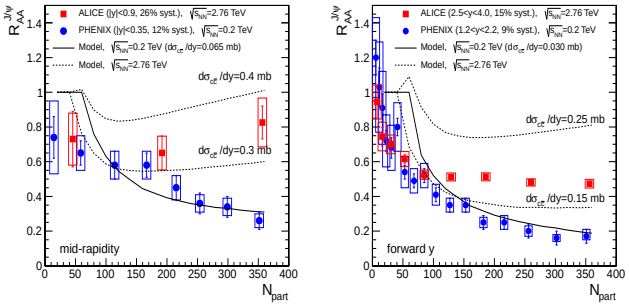

Figure 2: Centrality dependence of $R_{AA}^{J/\psi}$ for RHIC and LHC energies at mid-rapidity (left panel) and forward rapidity (right panel). The two curves shown for the LHC energy correspond to a range of expected shadowing.

as to predictions from the statistical hadronization model. We first note that, at LHC energy, much less suppression is observed compared to the RHIC results, both at forward- and at mid-rapidity. The model calculations reproduce this trend very well. In our model the larger $R_{AA}^{J/\psi}$ values at midrapidity are due to the enhanced generation of charmonium around mid-rapidity, determined by the rapidity dependence of the charm production cross section. Also the observed centrality dependence is correctly reproduced.

The successful description of the new ALICE data lends strong support to the interpretation that, at LHC energy, J/ψ mesons do not form or survive inside the QGP, implying strong color screening. Rather, the observations are consistent with the formation of charmonium bound states at hadronization of the QGP. Conceptually, this is very different from the mechanism of continuous formation and destruction of charmonia in the QGP, as employed in transport models. In our model, charmonium production is a direct signal for deconfinement of charm quarks: the charmonia are dominantly formed from initially uncorrelated c and $\bar{c}$ quarks.

References

[1] A. Andronic, P. Braun-Munzinger, K. Redlich, J. Stachel, J. Phys. G **38** (2011) 124081; arXiv:1210.7724.

[2] B. Abelev et al. [ALICE collab.], Phys. Rev. Lett. **109** (2012) 252301; D. Chinellato, arXiv:1211.7297

[3] J. Steinheimer, J. Aichelin and M. Bleicher, Phys. Rev. Lett. **110** (2013) 042501.

[4] I.C. Arsene, arXiv:1210.5818; R. Arnaldi, arXiv:1211.2578

[5] A. Adare et al. (PHENIX coll.), Phys. Rev. Lett. **98** (2007) 232301; arXiv:1103.6269.

* Work supported by GSI, BMBF, Helmholtz Alliance HA216/EMMI

Transport coefficients of $O(N)$ scalar field theories close to the critical point*

E. Nakano[1,2]*, V. Skokov*[3]*, and B. Friman*[3]

[1]Kochi University, Kochi, Japan; [2]EMMI, GSI, Darmstadt, Germany; [3]GSI, Darmstadt, Germany

In recent decades transport coefficients of quantum chromodynamics (QCD) have attracted much interest in the context of Relativistic Heavy Ion Collider (RHIC) experiment, which are aimed at creating and studying the quark-gluon plasma. One of the interesting experimental findings, the large elliptic flow v_2 observed in high energy non-central collisions, implies that the spatial anisotropy of the initial state is, during the expansion, very efficiently converted to a transverse momentum anisotropy of the observed hadrons. These experimental results are well described by ideal hydrodynamics with vanishing viscosity. Thus, the large elliptic flow observed in such collisions implies that the fireball created behaves as an almost perfect fluid.

Although the transport coefficients in viscous hydrodynamics are phenomenological parameters, they can in principle be computed from a microscopic starting point. Since the shear viscosity, one of transport coefficients, has a direct influence on the elliptic flow, the experimental results have triggered numerous theoretical efforts to unravel its behavior as a function of thermodynamic variables. By and large, these are performed in the framework of kinetic theory, e.g. using the Boltzmann equation, applied to effective theories of QCD and to perturbative QCD. Furthermore, some results on the temperature dependence of the transport coefficients have been obtained in lattice simulations.

The experimental results have motivated recent work on a field theoretical approach to evaluate transport coefficients. The $O(N)$ scalar field theory offers a testing ground for developing computational methods before facing the complications of a full QCD calculation. In the present work we discuss the critical behavior of the shear viscosity and other transport coefficients in the $O(N)$ scalar field theory. As demonstrated by Wilson using the renormalization group, there is a second-order phase transition in the $O(N)$ scalar field theory with a finite ultraviolet cutoff Λ. Kinetic approaches employed for computing the transport coefficients rely heavily on Boltzmann-like approximations, which take only the single particle distribution into account and neglect higher order correlations. Although these correlations, may be unimportant far from the critical point, they play a key role in the critical region.

In our study of the critical transport properties, we employ the dynamical renormalization group (DRG) combined with the epsilon expansion. This method was tested for model H developed by Hohenberg and Halperin [1]. Within this approach we examine the scale evolution of a stochastic equation of motion, which describes the critical dynamics of the slow modes. These include fluctuations of the order parameter and of conserved quantities. These are the relevant variables when addressing the long-wave length behavior of the system near the critical point.

In analogy to the static case, the flow equations for transport coefficients derived from the DRG admit non-trivial fixed points, from which the *dynamical critical exponent*, z, and the dynamical scaling relations can be deduced. The dynamical critical exponent, z, defines the characteristic frequency of the most relevant slow mode $\omega \sim k^z$. Using the DRG approach, one can also derive scaling relations for the transport coefficients, and deduce the singular behavior of the transport coefficients. Based on the universal behavior, i.e. on the dynamical critical exponents and scaling laws, one identifies each systems with a dynamical universality class. In contrast to the static case, the dynamical universality class is governed not only by the dimensionality, locality, and the symmetries of the system under consideration, but, in addition, by the properties of the relevant slow modes.

In this work [2], we determine the dynamical universality class of the $O(N)$ scalar field theory and show how the dynamical universality class depends on the number of components, N, and on the dimensionality, d. As demonstrated in Ref. [2], the dynamical universality class of the single component theory reduces to that of model C. The dynamical critical exponent is given by $z = 2+\alpha/\nu$, where α and ν are the static critical exponents of $O(N)$ model. On the other hand, for the multicomponent theory ($N > 1$), the critical dynamics is dominated by $O(N)$ charge fluctuations. This drives the critical exponent down to the value $z = d/2$ and the theory belongs to the dynamic universality class of model G. In both cases, $N = 1$ and $N > 1$, the shear viscosity remains finite at the critical point, while the bulk viscosity diverges for $N = 1$ with the dominant singular contribution proportional to $\zeta \sim \xi^{z-\alpha/\nu} \sim \xi^2$, and remains finite for $N > 1$. In QCD, the $O(4)$ chiral symmetry in the light quark sector is broken by the non-zero u and d quark masses. For high temperatures and small values of the chemical potential, the second-order phase transition is replaced by a crossover. Our results imply that the singular part of the shear and bulk viscosity remain finite also at the QCD phase transition.

References

[1] P. C. Hohenberg and B. I. Halperin, Rev. Mod. Phys. **49**, 435 (1977).

[2] E. Nakano, V. Skokov, B. Friman, Phys. Rev. D **85**, 096007 (2012)

* Work supported by EMMI

Non-perturbative dynamics and charge fluctuations in effective chiral models*

V. Skokov[1,2], *B. Friman*[1], *and K. Redlich*[3,4]

[1]GSI, Germany; [2]BNL, N.Y., U.S.A.; [3]University of Wroclaw, Poland; [4]EMMI, GSI, Germany

Lattice QCD (LQCD) results show that at finite temperatures, QCD exhibits restoration of chiral symmetry and deconfinement in a crossover transition. The LQCD equation of state indicates a clear separation between the confined hadronic phase and the deconfined quark–gluon plasma. The transition between the phases is accompanied by characteristic fluctuations of conserved charges [1].

At vanishing chemical potential the fourth order cumulants of both the net baryon number and the electric charge show peaked structures, while the sixth order cumulants are negative in a narrow temperature interval close to the transition region. These properties of the fluctuations for small masses of the up– and down–quarks can be attributed to the critical dynamics of the explicitly broken chiral symmetry, which is characterized by the O(4) universality class of two-flavor QCD [2].

The critical behavior of strongly interacting matter related with chiral dynamics should be common to all models which reproduce the underlying chiral symmetry of QCD and the pattern of spontaneous chiral symmetry breaking at finite temperature. In this work we explore the characteristic behavior of fluctuations of the electric charge near the chiral transition at vanishing chemical potential within the functional renormalization group (FRG) approach to the linear sigma and Polyakov-loop extended quark (PQM) models.

The fluctuations of the electric charge are characterized by the generalized susceptibilities,

$$\chi_n^Q(T) = \frac{\partial^n [p\,(T,\mu_Q)/T^4]}{\partial(\mu_Q/T)^n}. \qquad (1)$$

The charge fluctuations reflect the critical behavior of the fluctuations of the net baryon density. However, in contrast to the net baryon number, an important contribution to fluctuations of the electric charge is due to pions.

In the region of the crossover transition, the fluctuations of the electric charge should reflect the critical scaling of the underlying O(4) symmetry. A scaling analysis shows that at vanishing baryon chemical potential, the second and fourth order cumulants remain finite, while for $n \geq 6$ the cumulants χ_n^Q diverge at the O(4) transition [3]. It is expected that this critical behavior is reflected in the cumulants at the crossover transition for small explicit symmetry breaking, corresponding to the QCD transition at physical values of the light quark masses.

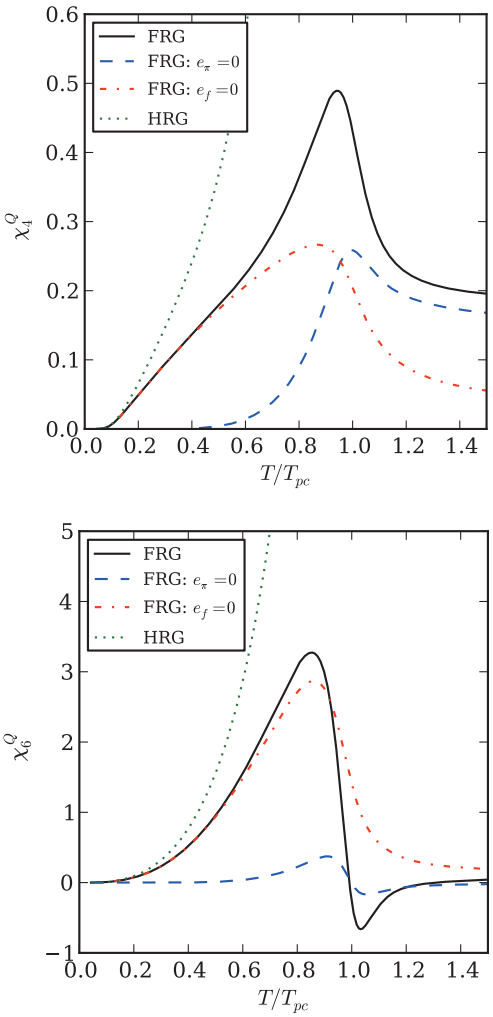

The figures show the cumulants (top $n = 4$, bottom $n = 6$) of the electric charge fluctuations in the Polyakov loop extended quark-meson model calculated within the functional renormalisation group approach (solid lines). The results are also shown for only charged quarks $e_\pi = 0$ and only charged pions $e_f = 0$. The hadron resonance gas contributions are shown by the dotted lines. We note that the χ_6^Q is negative close to the transition temperature, and thus reflects the characteristic critical behavior of the net baryon density in the O(4) universality class.

References

[1] S. Ejiri *et al.*, Nucl. Phys. Proc. Suppl. **140**, 505 (2005).

[2] B. Friman et al., Eur. Phys. J. **C71**, 1694 (2011).

[3] V. Skokov *et al.*, Phys. Lett. B **708**, 179 (2012)

* Work supported by EMMI

Net-charge probability distributions in heavy ion collisions at chemical freeze-out*

P. Braun-Munzinger[1,2,3,4], *B. Friman*[1], *F. Karsch*[5,6], *K. Redlich*[7,1,2], *and V. Skokov*[5]

[1]GSI, Darmstadt, Germany; [2]EMMI, GSI, Darmstadt, Germany; [3]TU Darmstadt, Germany; [4]FIAS, Frankfurt, Germany; [5]BNL, NY, USA; [6]Universität Bielefeld, Germany; [7]University of Wroclaw, Poland

The distributions for strangeness, electric charge and baryon number are explored in heavy ion collisions within the hadron resonance gas model. The proximity of the freeze-out curve to the phase boundary indicates that the QCD phase transition and its related critical properties should be observable in heavy ion collisions. However, an experimental verification of a phase change in a medium created in such collisions requires sensitive probes. In this context, a particular role is attributed to fluctuations of conserved charges [1].

Recently, it was argued that, at high energies, the history of the system, in particular the path through the QCD crossover transition from the deconfined and chirally symmetric phase to the hadronic one, may be reflected in fluctuations of conserved charges, specifically in their higher cumulants [2]. The characteristic signature, which is a consequence of the critical O(4) dynamics at the chiral phase transition, may thus be manifested in a deviation of higher cumulants of the charge distributions from the HRG results, if the freeze-out happens near or at the QCD phase boundary. At vanishing chemical potential, the sixth and higher order cumulants can be negative, also in the hadronic phase, in contrast to the HRG model, which yields only positive values. It is therefore useful to consider the HRG model results on moments of charge fluctuations as a theoretical baseline; any deviation from this could be an indication for critical phenomena at the time of hadronization [2].

In this work we explore the influence of multi-charged particles and of quantum statistics on fluctuations [3]. In the HRG model, the product of kurtosis and variance of the net baryon number, $\kappa\sigma^2$, which receives contributions from singly charged particles only, is always equal to unity. This result does not depend on the hadron mass spectrum nor on the thermal parameters. However, for fluctuations of the electric charge, the contribution of particles with charge two, Δ^{++} and $\bar{\Delta}^{--}$, leads to a non-trivial T and μ dependence of this quantity [1]. Furthermore, a straightforward calculation shows that in an ideal pion gas, $\kappa\sigma^2$ is temperature dependent and differs from unity, due to quantum statistics effects.

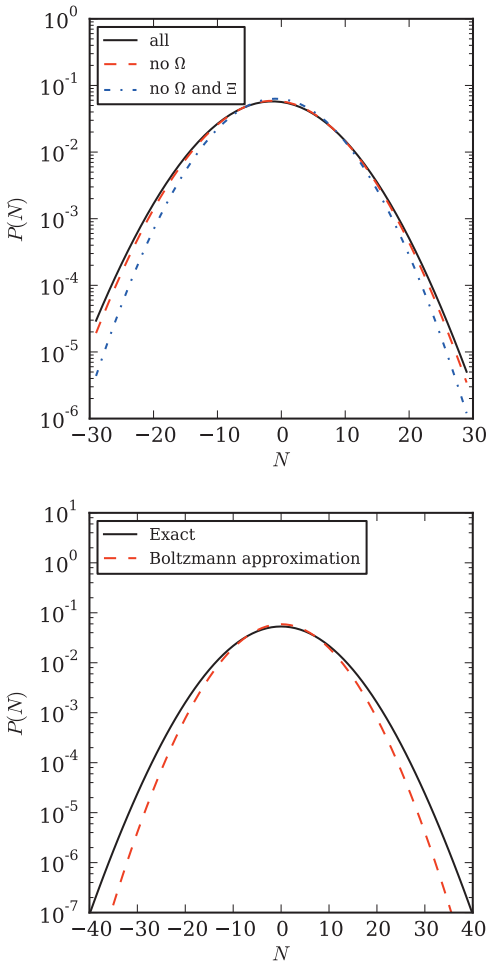

In the top figure, the probability distribution for net strangeness is shown. It is clear that the multi-strange states broadens the distribution. Similarly, as illustrated in the lower figure, the quantum corrections to the Bose-Einstein distribution of the pions lead to a broader probability distribution for net electric charge.

References

[1] S. Ejiri *et al.*, Nucl. Phys. Proc. Suppl. **140**, 505 (2005).

[2] B. Friman et al., Eur. Phys. J. **C71**, 1694 (2011).

[3] P. Braun-Munzinger, B. Friman, F. Karsch, K. Redlich and V. Skokov, Nucl. Phys. A **880**, 48 (2012) [arXiv:1111.5063 [hep-ph]].

* Work supported by EMMI

Heavy Quarks in Ultrarelativistic Heavy Ion Collisions *

J. Uphoff[1], *O. Fochler*[1], *Z. Xu*[2], *and C. Greiner*[1]

[1]Institut für theoretische Physik, Johann Wolfgang Goethe-Universität Frankfurt, Frankfurt am Main; [2]Physics Department, Tsinghua University, Beijing 100084, China

In ultra-relativistic heavy ion collisions a unique state of matter is produced, in which quarks and gluons form the relevant degrees of freedom. This quark gluon plasma (QGP) has exciting properties such as collective behavior like a nearly perfect liquid or the quenching of high energy particles. In particular heavy quarks (charm and bottom) provide an insightful way to learn more about the properties of this matter. Since they are heavy, their production time is at a very early stage of the heavy ion collision when enough energy is available [1].

In the last year we extended the partonic transport model Boltzmann Approach to MultiParton Scatterings (BAMPS) to study heavy quarks at the LHC [2] and also included interactions between light and heavy quarks. More specifically, we investigated the elliptic flow and nuclear modification factor of several heavy flavor particles, namely D mesons, non-prompt J/ψ, muons, and electrons. Using only elastic collisions of heavy quarks with medium particles with an improved Debye screening inspired by hard thermal loop calculations and a running coupling the RHIC heavy flavor electron data can only be reproduced with scaling the binary cross section with $K = 3.5$. With the same parameter we find a good agreement with the D meson and electron elliptic flow data at LHC (see Fig. 1). However, the R_{AA} of D mesons, non-prompt J/ψ, and

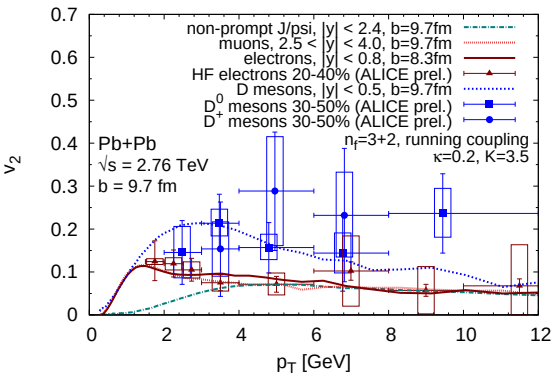

Figure 1: Elliptic flow v_2 of D mesons, non-prompt J/ψ, muons, and electrons at LHC together with available data.

muons are underestimated. Currently, we are implementing also the radiative processes [3] for heavy quarks in BAMPS. It will be highly interesting to see what impact these have on the results. As part of this work, we extensively compared the widely used Gunion-Bertsch approximation of the radiative matrix element to the exact one for both light and heavy partons [4]. Furthermore, we are working on implementing also the running coupling for light particles for both elastic and radiative processes.

Complimentary to the open heavy flavor particles are particles in which the flavor is hidden. That is, bound states of a heavy quark and an anti-heavy quark. They can survive in the QGP to some extent, but melt if the temperature of the medium is too high [5]. Therefore, they could be used as a thermometer. In addition to this melting they can also be regenerated by two heavy quarks which meet in the medium. The most prominent hidden heavy flavor particle is the J/ψ, which consists of a charm and an anti-charm quark.

First BAMPS results on the suppression of J/ψ mesons at RHIC were presented in Ref. [6]. With a J/ψ formation time of $\tau = 0.6\,\mathrm{fm}$ to prevent early melting when the temperature cannot be properly defined, the experimental data of the R_{AA} at mid-rapidity is well described. However, our results at forward rapidity underestimate the suppression for central and semi-central events. In recent calculations [2] we investigated the elliptic flow of prompt J/ψ and found a small v_2, even with regeneration of J/ψ, which is in good agreement with the experimental findings. BAMPS is an ideal framework to study this in more detail since it reproduces the D meson flow and also allows recombination of charm quarks to J/ψ. Currently, we are also studying the J/ψ suppression and elliptic flow at the LHC.

References

[1] J. Uphoff, O. Fochler, Z. Xu and C. Greiner, Phys. Rev. **C 82**, 044906 (2010).

[2] J. Uphoff, O. Fochler, Z. Xu and C. Greiner, Phys. Lett. **B 717**, 430 (2012).
J. Uphoff, O. Fochler, Z. Xu and C. Greiner, arXiv:1212.0358 [hep-ph].
J. Uphoff, O. Fochler, Z. Xu and C. Greiner, arXiv:1208.1970 [hep-ph].

[3] R. Abir, C. Greiner, M. Martinez, M. G. Mustafa and J. Uphoff, Phys. Rev. **D 85**, 054012 (2012).

[4] O. Fochler, J. Uphoff, Z. Xu and C. Greiner, "Gunion-Bertsch matrix element revisited," in preparation (2013).

[5] A. Mocsy and P. Petreczky, Phys. Rev. Lett. **99**, 211602 (2007).

[6] J. Uphoff, K. Zhou, O. Fochler, Z. Xu and C. Greiner, PoS BORMIO **2011**, 032 (2011) [arXiv:1104.2437 [hep-ph]].

* Work supported by the Helmholtz Research School for Quark Matter Studies (H-QM).

Complex Transport Simulations*

K. Gallmeister[1]

[1]Institut für Theoretische Physik, Johann Wolfgang Goethe - Universität Frankfurt, Max-von-Laue-Str. 1, D-60438 Frankfurt am Main, Germany

In order to understand and analyze current and future experiments in modern nuclear and hadron physics, a number of very complex computer programs based on transport theoretical models have been developed in the last years.

One prominent example is the program BAMPS[1], which is a important tool for the understanding of the dynamics of the hot and dense quark gluon phase in high energetic heavy ion collisions. This description is primarily relevant for the understanding of RHIC and LHC experiments. Here quarks and gluons are the relevant degrees of freedom. On the other side, hadronic models try to describe the same topic in terms of hadronic degrees of freedom, as, e.g. UrQMD[2, 3] or GiBUU[4].

Unfortunately, all these programs reside in different stages of programming techniques. The used programming languages range from Fortran 77 up to C++. Accordingly, the underlying program structures as modularity or object orientation differ drastically.

In addition, due to the different used languages, the use of standardized (and well tested) libraries is implemented in different levels. A very strong deficiency of these programs is the heterogeneous input/output strategy. It is not possible, to import immediately the results of one program into another in order to process them further.

Also the aspect of maintainability is diversified. A concept of version control is implemented at the moment only partially.

A very important aspect is the development of computer hardware during the last years. In order to cope with this, new programming techniques are necessary. Thus an adaption of the existing software and their development for multi and many-core architectures is very important.

At the moment we are using the program BAMPS as a test field for possible improvements.

It has shown up, that some cleaning up of the code, including restructuring of some of its elements was necessary to enhance the readability and maintainability. Especially, a clean implementation of the 4D vectors for position and momentum is essential. In addition, performing Lorentz transformations is one of the bottlenecks of all transport codes. Here an implementation in terms of SSE intrinsics has been proven to be very successful (cf. fig. 1). A speedup in the overall computation time up to 10% was achieved contrary to standard implementations, combined with a tremendous increase of readability of the code.

The transport codes mentioned above have some underlying structure, which contradicts in general some (naive) parallelization. Thus we are currently working to use the modern hardware architectures in the framework of GPGPU programming. Here first steps have been done, to parallelize the calculation of complex particle-particle cross sections for the BAMPS simulation in the framework of OpenCL [5].

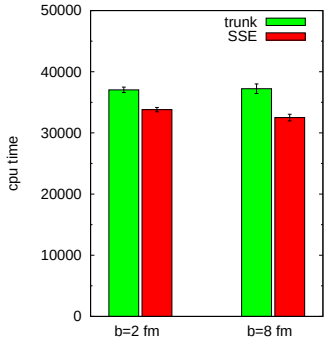

Figure 1: Comparison of the CPU time (with arbitrary normalization) of some sample configurations ($\mathrm{Pb}+\mathrm{Pb}$, RHIC conditions) for two impact parameter b for the original implementation ("trunk") and the new implementation using SSE3 instructions ("SSE") on the LOEWE CSC cluster.

While already some essential improvements have been reached, we are still in a learning phase to really figure out, where and how we can put the different codes on some common footing.

To summarize we state, that it is very important to bring the computer programs used by physicists in order to understand modern experiments to a stage, that corresponds modern programming knowledge and eliminate old coding techniques and languages. This will facilitate the use of the programs and allow their direct use by the experimentalist as a tool for planning, understanding and analyzing their experiments. We have started this effort successfully for the transport theoretical programs BAMPS, UrQMD and GiBUU.

References

[1] Z. Xu and C. Greiner, Phys. Rev. C **71**, 064901 (2005).

[2] S. A. Bass, M. Belkacem, M. Bleicher, M. Brandstetter, L. Bravina, C. Ernst, L. Gerland and M. Hofmann *et al.*, Prog. Part. Nucl. Phys. **41**, 255 (1998) [Prog. Part. Nucl. Phys. **41**, 225 (1998)].

[3] H. Petersen, J. Steinheimer, G. Burau, M. Bleicher and H. Stocker, Phys. Rev. C **78**, 044901 (2008).

[4] O. Buss, T. Gaitanos, K. Gallmeister, H. van Hees, M. Kaskulov, O. Lalakulich, A. B. Larionov, T. Leitner, J. Weil and U. Mosel, Phys. Rept. **512**, 1 (2012).

[5] http://www.khronos.org/opencl

* Work supported by GSI F&E.

Dynamical investigation of the chiral phase transition with a linear σ-model *

C. Wesp[1], *A. Meistrenko*[1], *H. van Hees*[1], *and C. Greiner*[1]
[1]Institut fr theoretische Physik, Goethe-Universitt Frankfurt, Germany

In this work we investigate effects of the chiral phase transition and the critical point in the phase diagram of nuclear matter. We use a linear sigma model with constituent quarks, numerical simulations are done to research the dynamical non-equilibrium behavior of this system.

The underlying Lagrangian of the linear σ-model [1],

$$\mathcal{L} = \bar{\psi}\left[\imath\partial - g\left(\sigma + \imath\gamma_5\vec{\pi}\cdot\vec{\tau}\right)\right]\psi + \frac{1}{2}\left[\partial_\mu\sigma\partial^\mu\sigma + \partial_\mu\vec{\pi}\partial^\mu\vec{\pi}\right) - U(\sigma,\vec{\pi}). \quad (1)$$

Constituent quarks acquire their mass dynamically via a coupling to the chiral fields,

$$m^2(\vec{x},t) = g^2\left(\sigma^2(\vec{x},t) + \vec{\pi}^2(\vec{x},t)\right). \quad (2)$$

The chiral potential $U(\sigma,\vec{\pi})$ includes the self-interaction of the fields and a term explicitly breaking the chiral symmetry, leading to a vacuum expectation of the chiral order parameter $\sigma_0 = 93$ MeV. To employ non-equilibrium scenarios, both the chiral fields and the quarks are treated fully dynamically. The chiral fields σ and $\vec{\pi}$ are treated as classical fields and are calculated on a real time 3+1D grid. Quarks are described as quasi-particles in a Vlasov equation, which allows to model arbitrary energy and momentum distributions,

$$\left(\partial_t + \frac{\vec{p}}{E}\vec{\nabla}_{\vec{r}} - \left(\vec{\nabla}_{\vec{r}}E\right)\cdot\vec{\nabla}_{\vec{p}}\right) f(\vec{x},\vec{p}) = 0. \quad (3)$$

Using Monte-Carlo techniques, quarks interact via a stochastic heat bath or via elastic collisions. Fields and quarks are coupled via a mean-field approach.

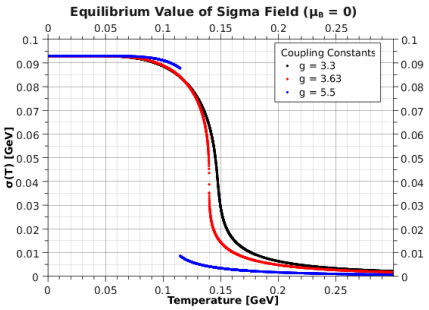

Figure 1: Equilibrium temperature dependence of the chiral order parameter σ

The equilibrium behavior of the linear sigma model is well known, see Fig 1 for a temperature dependence of the order parameter. Different scenarios and initial conditions are treated within the numerical simulation. Current scenarios are:

- thermal equilibrium
- quenched scenarios (sudden drop in temperature)
- temperature shifts by heat bath interaction
- fluctuations generated by interactions of the medium
- fluctuations by the canonical heat bath
- non-equilibrium expansions of exploding droplets

Fig 2 shows a snapshot of an exploding droplet of hot quark-matter. First results show that quark-interactions increase the fluctuations on the chiral fields, even though they are only coupled via mean-field interactions. While the chiral phase transition is a temperature driven phenomena, other results show the dynamics of the chiral order parameter σ is dominated by chemical processes rather than temperature dependent effects. Non-equilibrium effects of the barionic and quark-densities could have a large impact on the system dynamics.

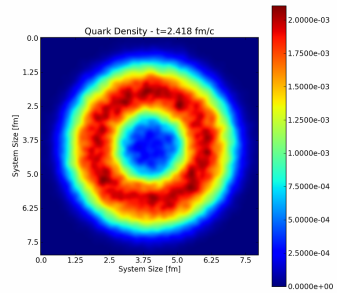

Figure 2: Example of an exploding drop of hot quark-matter.

For further investigation of non-equilibrium effects, critical slowing-down and correlations at the critical point, an extension of the current model is planned. Monte-Carlo interactions between the fields and the quarks will be included as well as chemical processes for the quarks. To model a gluonic background, a Polyakov-Loop motivated potential will be included.

References

[1] M. Gell-Mann, M. Levy, "The axial vector current in beta decay", Nuovo Cim. 16 (1960) 705.

[2] Scavenius, Mócsy, Mishustin, "Rischke, Chiral phase transition within effective models with constituent quarks", Phys. Rev. C (2001) 64

* Work supported by H-QM and HGS-HIRe.

Elliptic flow and nuclear modification factors of D-mesons at FAIR*

T. Lang[1], *H. van Hees*[1], *J. Steinheimer*[2], *and M. Bleicher*[1]

[1]FIAS, Frankfurt, Germany; [2]Lawrence Berkeley National Laboratory, Berkeley, CA 94720, USA

The CBM experiment at FAIR will provide new possibilities for D-meson observables in heavy-ion collisions at low collision energies and high baryon densities. To predict D-meson observables in this environment we apply a Langevin approach for the transport of charm quarks in the UrQMD hybrid model [1]. Due to the inclusion of event-by-event fluctuations [2] and a full (3+1) dimensional hydrodynamical evolution, the UrQMD hybrid approach provides a realistic evolution of the matter produced in heavy ion collisions. As drag and diffusion coefficients for the Langevin approach we use a resonance model for elastic heavy-quark scattering [3] and assume a decoupling temperature of the charm quarks from the hot medium of 130 MeV, which has already been successfully applied at RHIC and LHC energies [4]. The hadronization of charm quarks to D-mesons is included by a coalescence mechanism. To account for the high baryon chemical potential at FAIR-energies we use fugacity-factors in our calculation. Therefore we multiply the anti-charm drag- and diffusion-coefficients by $e^{\mu_B/T}$ and the charm coefficients by $e^{-\mu_B/T}$. Here μ_B is the baryon chemical potential of the surrounding quarks and T is the local temperature of the medium.

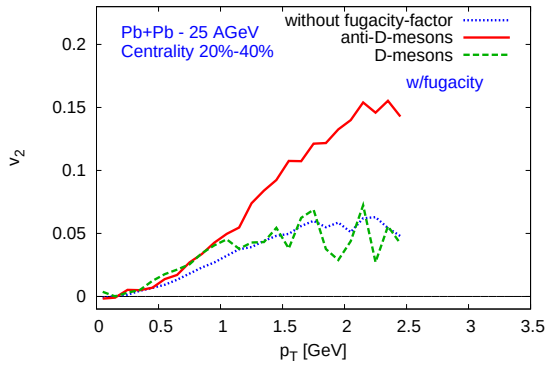

Figure 1: v_2, of D-mesons and $\bar{D}$-mesons in Pb+Pb collisions at 25 AGeV using fugacity-factors. We use a rapidity cut of $|y| < 0.35$.

Fig. 1 shows our results for the elliptic flow and Fig. 2 for the nuclear modification factor, both in Pb+Pb collisions at 25 AGeV Our calculation shows a strong difference between D-mesons and $\overline{\mathrm{D}}$-mesons. The elliptic flow of $\overline{\mathrm{D}}$-mesons reaches up to 15% and that for D-mesons

*Work supported by H-QM, HIC for FAIR, GSI Helmholtzzentrum, Office of Nuclear Physics in the US Department of Energy's Office of Science under Contract No. DE-AC02-05CH11231, Bundesministerium für Bildung und Forschung (BMBF) grant No. 06FY7083

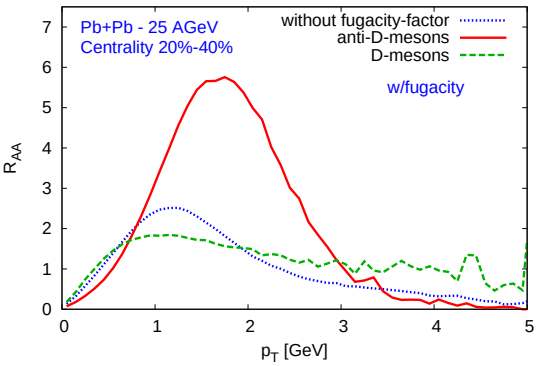

Figure 2: R_{AA} of D-mesons and $\bar{D}$-mesons in Pb+Pb collisions at 25 AGeV using fugacity-factors. We use a rapidity cut of $|y| < 0.35$.

about 5%. If we have a look on the difference between the D-mesons and the calculation neglecting fugacity-factors we realize that the difference is much smaller than for $\overline{\mathrm{D}}$-mesons. This small difference is not due to a small difference of the coefficients used, but to the role of the coalescence mechanism that accounts for the overwhelming fraction of the flow of D-mesons if the coefficients are small. The medium modification in our calculation is considerably stronger than at RHIC and LHC energies [4]. We relate this to the very soft initial momentum distribution of the charm-quarks and the slower bulk medium evolution at FAIR energies compared to RHIC and LHC energies. In the R_{AA} this results in a strong suppression at low p_T due to a "heating-up" of the charm quarks.

We should mention that the difference seen between D-mesons and $\overline{\mathrm{D}}$-mesons is sensitive to the model used to calculate the drag- and diffusion-coefficients. In case of the T-Matrix approach applied [5] this difference should not arise. Therefore D-meson measurements at FAIR can provide an excellent test for a confirmation or rejection of different heavy-quark-coupling mechanisms to the QGP.

References

[1] H. Petersen, J. Steinheimer, G. Burau, M. Bleicher and H. Stocker, Phys. Rev. C **78** (2008) 044901

[2] S. A. Bass, A. Dumitru, M. Bleicher, L. Bravina, E. Zabrodin, H. Stoecker and W. Greiner, Phys. Rev. C **60** (1999) 021902

[3] H. van Hees and R. Rapp, Phys. Rev. C **71** (2005) 034907

[4] T. Lang, H. van Hees, J. Steinheimer and M. Bleicher, arXiv:1211.6912 [hep-ph].

[5] H. van Hees, M. Mannarelli, V. Greco and R. Rapp, Phys. Rev. Lett. **100** (2008) 192301

Non-equilibrium Photon production in an external Yukawa field

H. van Hees[1,2], *F. Michler*[1], *D. D. Dietrich*[1], *S. Leupold*[3], *and C. Greiner*[1]

[1]Inst. für Theoretische Physik, Goethe-Universität Frankfurt, Frankfurt/Main, Germany; [2]Frankfurt Institute of Advanced Studies, Frankfurt/Main, Germany; [3]Inst. för fysik och astronomi, Uppsala Universitet, Uppsala, Sweden

Electromagnetic probes, i.e., direct photons and dileptons provide an interesting probe for the strongly interacting, hot and dense matter, created in high-energy heavy-ion collisions. Due to their penetrating nature the transverse-momentum spectra of photons and dileptons as well as the invariant-mass spectra of dileptons provide information from the entire fireball evolution and the hot central regions of the matter. This is of particular interest in the connection with the study of the QCD phase diagram and chiral-symmetry restoration.

On the other hand, in the past there have been claims that the photon emission caused by non-equilibrium processes in the very early pre-equilibrium phase of the fireball evolution outshine the yield of the photons emitted from the equilibrated thermal sources, where medium properties are well defined in terms of an equilibrium phase diagram [1, 2, 3]. On the other hand, these studies have been challenged due to problems concerning the proper renormalization procedure used in the non-equilibrium quantum-field-theory framework [4].

In our study we use a toy model to investigate the in detail the subtleties of non-equilibrium photon production within the Schwinger-Keldysh real-time formalism, coupling quark-Dirac fields to an external homogeneous time dependent scalar field. This allows us to mimic the expected chiral-symmetry restoration by switching the effective quark mass from its constituent value of around 350 MeV to its current-mass value of a few MeV within a hot QGP [5]. In this framework, the problem of the quark fields coupled to this external scalar field can be solved semi-analytically.

Here, the first fundamental problem arises in how to define quark and antiquark occupation numbers. It turns out that a consistently defined particle number observable is only available in the form of counting occupation numbers for asymptotically free Fock states. Using the vacuum as the initial state in the remote past ($t \to -\infty$) we have calculated the $q\bar{q}$-pair yield in the remote future ($t \to +\infty$), by determining the corresponding Bogolyubov transformation semi-analytically.

To evaluate the photon-production yield we employed the perturbative expansion with respect to α_e and calculated the photon self-energy. In contrast to the equivalent case in thermal equilibrium where the leading $\mathcal{O}(\alpha_e)$ one-loop polarization tensor of the photon vanishes on-shell due to the time-dependence of the non-equilibrium situation, leading-order processes like the production of a photon together with a $q\overline{q}$ pair as well as bremsstrahlung and pair-annihilation processes become available.

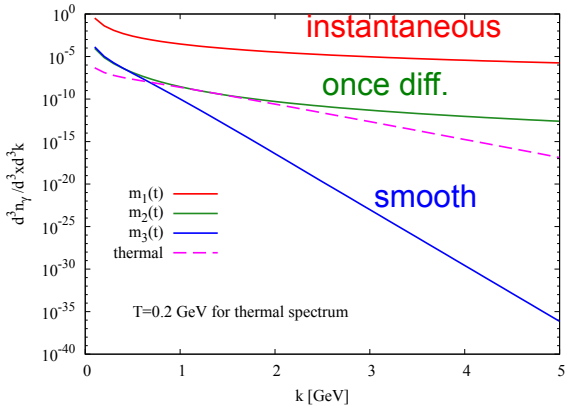

Figure 1: Photon production in a time-dependent scalar field coupled to a $q\bar{q}$ Dirac fermions. As the photon-spectral density for instantaneous mass switching is UV divergent, it has been regularized by a momentum cutoff of $\Lambda = 100$ GeV. The photon spectrum (red) is $\propto 1/k^3$ for large k. Thus the total photon number and energy density are both divergent. For a once-differentiable function the photon-spectral density is UV convergent. The results have been extrapolated to $\Lambda \to \infty$. The spectrum (green) behaves like $1/k^6$ for large momenta. So both the number and energy density are convergent. For a smooth switching function the spectrum (blue) falls off exponentially for large k and is subdominant compared to a typical thermal radiation spectrum from an equilibrated QGP (magenta).

The asymptotic photon-momentum spectra are sensitive to the choice of the mass switching function. While for instantaneous switching of the masses the photon-spectral density, $\mathrm{d}n_\gamma/\mathrm{d}^3\vec{x}\mathrm{d}^3\vec{k}$, is UV divergent, for an at least once differentiable switching function it is UV finite, and the vacuum contributions vanish when the correct Gell-Mann-Low adiabatic switching of the electromagnetic interaction is applied (for details, see Fig. 1).

References

[1] S.-Y. Wang and D. Boyanovsky, Phys. Rev. D **63**, 051702 (2001).

[2] D. Boyanovsky and H. de Vega, Phys. Rev. D **68**, 065018 (2003).

[3] D. Boyanovsky and H. J. de Vega, Nucl. Phys. A **747**, 564 (2005).

[4] E. Fraga, F. Gelis, and D. Schiff, Phys. Rev. D **71**, 085015 (2005).

[5] F. Michler, H. van Hees, D. D. Dietrich, S. Leupold, and C. Greiner (2012), `arXiv:1208.6565[nucl-th]`.

Transition from ideal to viscous Mach cones in a partonic transport model

I. Bouras[1], A. El[1], O. Fochler[1], H. Niemi[2], Z. Xu[3], and C. Greiner[1]

[1]Goethe-Universität Frankfurt, Germany; [2]University of Jyväskylä, Finland; [3]Tsinghua University, Beijing, China

In relativistic heavy-ion collisions (HIC) at RHIC and LHC a new state of matter, the Quark-Gluon Plasma (QGP), is supposed to be created. In such collisions highly energetic partons propagate through the hot and dense medium and rapidly lose their energy and momentum as the energy is deposited in the medium. Measurements of two- and three-particle correlations in heavy-ion collisions show a complete suppression of the away-side jet, whereas for lower p_T, a double peak structure is observed in the two-particle correlation function. In the last couple of years a promising origin of these structures was assumed to be the interaction of fast and high-energetic partons with the soft matter, which generates collective motion of the medium in form of Mach cones [1].

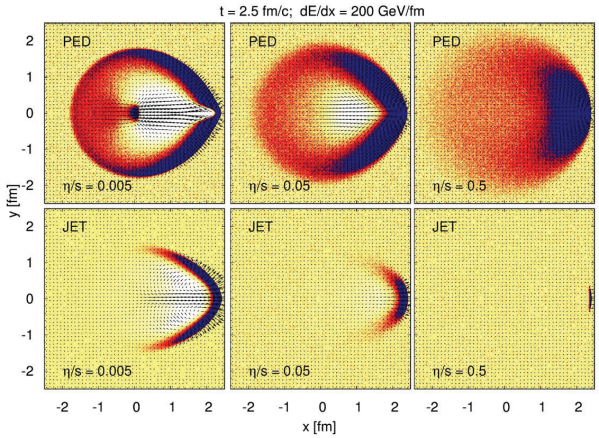

Figure 1: (Color online) Transition from ideal to viscous Mach cones for different shear viscosity over entropy density ratios.

For this purpose we investigate the propagation and formation of Mach cones [2] in the partonic transport model BAMPS (Boltzmann Approach of MultiParton Scatterings) [3] in the limit of vanishing mass and very small shear viscosity over entropy density ratio η/s of the matter. The Mach Cones studied here are induced by two different sources. The first of them we refer to as the pure energy deposition scenario (PED). This is simulated by a moving source depositing momentum end energy isotropically according to the thermal distribution $f(x,p) = \exp(-E/T)$. The second source we refer to as JET. This is simulated by a highly massless particle (jet) which has only momentum in x-direction, i.e. $p_{\mathrm{x}} = E_{\mathrm{jet}}$. After each time step the energy of the jet particle is reset to its initial value.

In Fig. 1 we show the numerical results with $\eta/s = 0.005$, 0.05 and 0.5 from left to right, respectively. We show a snapshot at $t = 2.5\,\mathrm{fm/c}$. The energy deposition rate is fixed to $dE/dx = 200$ GeV/fm. In both scenarios, PED and JET, for $\eta/s = 0.005$ (left panel), a conical structure is observed, but with obvious differences. The PED case with the isotropic energy deposition induces a spherical shock into back region; this structure is missing in the JET scenario because of the high forward peaked momentum deposition. Another difference is that in the JET scenario a clearly visible head shock appears. This in turn is missing in the PED scenario. Furthermore a (anti)-diffusion wake is induced by the JET (PED) scenario. However, with increasing viscosity over entropy density ratio the conical structure smears out. This is shown in the middle and left panel for 0.05 and 0.5, respectively.

However, the more interesting part is the issue, whether a double peak structure is created by the high energetic jets. In Fig. 2 we show the two-particle correlations extracted from BAMPS calculations of the Mach cones shown in Fig. 1. For the JET scenario (a) and sufficiently small $\eta/s = 0.005$ we observe only a peak in direction of the jet. The typical double peak structure, which has been proposed as a possible signature of the Mach cone in HIC, can only be observed for the PED scenario (b) and small η/s. However, the PED scenario has no correspondence in heavy-ion physics. For the JET scenario, which is a simplified model of jets depositing energy and momentum, a double peak structure never appears. This is due to the strong formation of a head shock and diffusion wake.

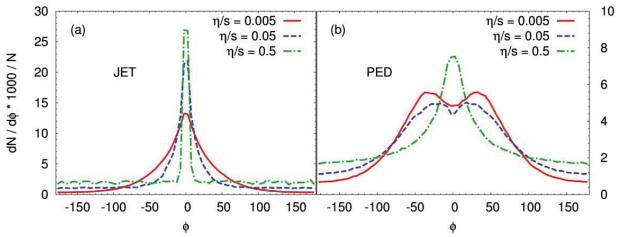

Figure 2: (Color online) Two-particle correlations $dN/(Nd\phi)$ for different viscosities extracted from calculations shown in Fig. 1. The results are shown in the for the JET (a) and PED (b) scenario.

References

[1] Horst Stoecker. *Nucl. Phys.*, A750:121–147, 2005.

[2] I. Bouras, A. El, O. Fochler, H. Niemi, Z. Xu, et al. *Phys.Lett.*, B710:641–646, 2012.

[3] Zhe Xu and Carsten Greiner. *Phys. Rev.*, C71:064901, 2005.

Studies of reconstructed jets within a partonic transport model*

F. Senzel[1], *O. Fochler*[1], *J. Uphoff*[1], *Z. Xu*[2], *and C. Greiner*[1]

[1]Institut für Theoretische Physik, Johann Wolfgang Goethe-Universität, Max-von-Laue-Str. 1, D-60438 Frankfurt am Main, Germany; [2]Department of Physics, Tsinghua University, Beijing 100084, China

One method for determining the energy loss of a high-p_t parton traversing a heavy-ion medium and thereby studying the properties of the created hot and dense matter is "jet reconstruction". Initial hard scattered back-to-back partons decrease their virtuality in splitting processes, which lead to particle showers with a broad angular and momentum distribution, which is enhanced by in-medium radiation processes. In order to develop a description of the energy loss of the partons, jet reconstruction algorithms are used that combine the single shower particles to a common "reconstructed jet" based on their distance in the $\eta - \phi$ plane.

When studying reconstructed jets in central $\sqrt{s_{NN}} = 2.76$ TeV Pb + Pb collisions, the experiments at the LHC [1, 2, 3, 4] have seen an enhancement of dijet events with asymmetric transverse momenta in comparison with p + p-collisions. This momentum asymmetry can be expressed by

$$A_J = \frac{p_{\mathrm{t;Leading}} - p_{\mathrm{t;Subleading}}}{p_{\mathrm{t;Leading}} + p_{\mathrm{t;Subleading}}}\,, \qquad (1)$$

where $p_{\mathrm{t;Leading}}$ ($p_{\mathrm{t;Subleading}}$) is the transverse momentum of the reconstructed jet with the highest (second highest) transverse momentum. The additional enhancement of asymmetric events in heavy-ion collisions is assumed to be caused by the different in-medium path lengths of the non-centrally produced initial parton pair and thereby different energy loss of the jets within the created bulk medium.

Here we want to show our result on this momentum imbalance A_J simulated within the partonic transport model BAMPS [5], which allows the simulation of multiple in-medium scattering processes and the 3+1D medium evolution in one common framework, while providing the configuration and phase space information of every particle at every timestep.

For the momentum spectra of the initial partons we use a distribution based on parton distribution functions. In order to properly reproduce the p + p data [2] we model the initial vacuum splitting processes by shower routines of the event generator PYTHIA. Because the medium modification of the parton showers is evaluated within the BAMPS framework it is necessary to terminate the vacuum splitting processes prematurely. The initial spatial production point of the parton pair is determined by a Glauber modeling based on a Woods-Saxon density profile.

The created parton showers are subsequently evolved within an offline recorded BAMPS background event, in which at every timestep the shower particles may interact with medium particles which then become shower particles themselves and may scatter further inside the medium. One difficulty which emerges while reconstructing jets in heavy-ion collisions is the subtraction of the underlying event contribution to the momenta of the reconstructed jets. For considering this, we sort the shower particles as well as an appropriately sampled background medium into "calorimeter cells" to obtain an calorimetric event comparable to experimental events. By doing this we can use common experimental background subtraction methods to remove the medium contribution in the reconstructed jets.

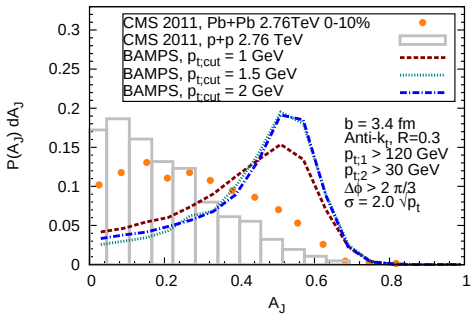

Figure 1: Momentum imbalance A_J in central Pb + Pb collisions at the LHC. The evolution of the shower particles is stopped when reaching $p_{t;cut}$. After background subtraction, the distribution is shown independent from $p_{t;cut}$.

Fig. 1 shows the calculated A_J distribution for central (0-10%) $\sqrt{s_{NN}} = 2.76$ TeV Pb + Pb collisions in comparison with experimental data[2]. For that comparison, trigger conditions as used by CMS are chosen. For an effective modeling of the detector response a Gaussian smearing of the reconstructed jet momenta based on the comparison between our initial shower and p + p data by CMS is used.

At present the calculated momentum imbalance of reconstructed jets within BAMPS is too strong which is in qualitative agreement with other energy loss studies within BAMPS, e.g. R_{AA} of gluons and light quarks[6, 7].

References

[1] ATLAS Collaboration, Phys. Rev. Lett. **105** (2010) 252303

[2] CMS Collaboration, Phys. Rev. C **84** (2011) 024906

[3] CMS Collaboration, Phys. Lett. B **712** (2012) 176

[4] ATLAS Collaboration, arXiv:1208.1967 [hep-ex].

[5] Xu, Z. and Greiner, C., Phys. Rev. C **71** (2005) 064901.

[6] Fochler, O. and Xu, Z. and Greiner, C., Phys. Rev. C **82** (2010) 024907.

[7] Fochler, O. and Uphoff, J. and Xu, Z. and Greiner, C., in preparation

* Work supported by F&E Frankfurt/GSI, H-QM and HGS-HIRe.

Rotating ultracold quantum gases *

A. Sedrakian and H. Warringa
Institut für Theoretische Physik, J. W. Goethe-Universität Frankfurt am Main, Germany

Rotating condensates of ultracold Bose or Fermi gases form vortex lattices above a critical rotation frequency. Such states were indeed observed in a number of experiments on superfluid bosonic and fermionic vapors confined to magnetic and/or optical traps. The measurements of the $l = 2$ modes are in good agreement with the theoretical predictions based on the coarse grained hydrodynamics. The studies of rotating condensates provide a useful testbed for exploring strongly correlated systems under rotation, due to the high experimental flexibility available in these systems. We anticipated insights from experiments for systems that are difficult or impossible to manipulate and/or observe. One such example are the rotating neutron stars containing strongly interacting condensates of nuclear and quark matter.

In our work [1] we use superfluid hydrodynamics to explore the rotational states and oscillations of *non-uniformly rotating* condensates. We concentrated on a special class of departures from rigid body rotation, which feature a constant condensate circulation in the frame rotating with the surface of the condensate. These states are supported by sufficiently dense mesh of quantum vortices, which guarantee the non-zero circulation in the laboratory frame. We have studied both the equilibrium structure of the condensates and their lowest order non-trivial $l = 2$ modes.

Within this set-up a new state of rotating, harmonically trapped, condensates of atomic clouds was found. The resulting equilibrium configurations are non-axisymmetric, and thus are a manifestation of the spontaneous symmetry breaking (SSB) in superfluid hydrodynamics (see Fig. 1). We have derived the complete set of $l = 2$ harmonic modes. Several experimental tests have been suggested, including the violation of the Feynman formula relating the rotation frequency to the number of quantized vortices, which can shed light on the structure and small amplitude oscillations of non-uniformly rotating clouds of Bose and Fermi condensates.

In Ref. [2] a two-component Fermi gas with attractive s-wave interactions, which forms a superfluid at low temperatures, was studied. When this gas is confined in a rotating trap, fermions can unpair at the edges of the gas and vortices can arise beyond certain critical rotation frequencies. We computed these critical rotation frequencies and constructed the phase diagram in the plane of scattering length and rotation frequency for different total numbers of particles. The calculations are performed in the Hartree-Fock-Bogoliubov approximation. We find that in the phase diagram three phases can be distinguished. For small rotation frequencies the entire gas forms a superfluid. At a certain critical frequency a second order transition occurs to a superfluid phase, which features unpaired fermions that are concentrated at the edges of the gas. At this critical rotation frequency the gas resides at a quantum critical point when the temperature vanishes. For even larger rotation frequencies vortices are formed via a first order transition.

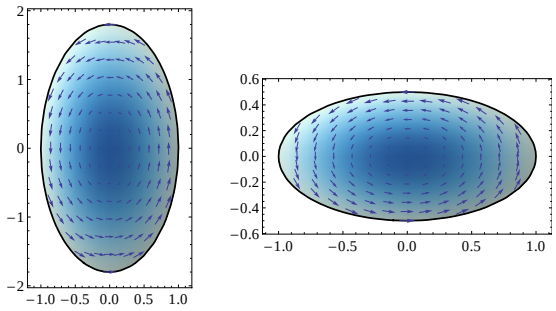

Figure 1: Illustration of the velocity vector field in the x-y plane for two possible solutions with SSB.The color coding reflects the Thomas-Fermi density distribution of the cloud.

The method of Ref. [2] was used in Ref. [3] to analyze numerically the phase diagram of a trapped, rotating, and weakly-interacting two-component Fermi gas including vortices. Detailed predictions were made for the conditions under which superfluidity with and without vortices is formed as a function of rotation frequency, scattering length, temperature, number of atoms and population imbalance. The phase diagram is quantitatively reliable and is in principle directly comparable to a possible future experimental determination. The analysis can be extended to more complicated systems, like Fermi gases with p-wave pairing, Fermi gases with more than two components, and Fermi gases in which the two components have unequal mass. This will be useful for the experimental search for superfluidity in such systems.

* Work supported by the GSI-GU R&D project and EMMI.

References

[1] A. Sedrakian, *Spontaneous symmetry breaking in rotating condensates of ultracold atoms.* Phys. Rev. A **86**, 051602(R) (2012).

[2] H. J. Warringa, A. Sedrakian, *Vortex formation in a rotating two-component Fermi gas.* Phys. Rev. A **84**, 023609 (2011).

[3] H. J. Warringa, *Location of the vortex phase in the phase diagram of a rotating two-component Fermi gas.* Phys. Rev. A **86**, 043615 (2012).

Phases of nuclear matter and electroweak interactions within SM and beyond *

A. Sedrakian, J. Keller, and M. Stein
Institut für Theoretische Physik, J. W. Goethe-Universität Frankfurt am Main, Germany

We have performed a comprehensive study of the phase structure of cold, dilute nuclear matter featuring a S-D condensate at non-zero isospin asymmetry, within wide ranges of temperatures and densities. We find a rich phase diagram comprising three superfluid phases, namely a Larkin-Ovchinnikov-Fulde-Ferrell phase, the ordinary BCS phase, and a heterogeneous, phase-separated BCS phase, with associated crossovers from the latter two phases to a homogeneous or phase-separated Bose-Einstein condensate of deuterons. The phase diagram contains two tricritical points (one a Lifshitz point), which may degenerate into a single tetracritical point for some degree of isospin asymmetry. The formation of such isospin-asymmetric condensates is relevant to the astrophysical type-II supernovae and dilute tails of the heavy neutron-rich nuclei. Our model solves the Nozières–Schmitt-Rink equations for asymmetrical nuclear matter with a phase-shift equivalent (so-called realistic) interactions [1]. These results are shown in Fig. 1

Electroweak dynamics of baryons in dense matter has been studied within a formalism based on the re-summation of particle-hole ladders in bulk nuclear matter. As an application, the pair-breaking neutrino bremsstrahlung – an important process contributing to the neutrino cooling of a compact star – was computed. The vertex corrections substantially suppress the emission via vector currents, while they leave the axial vector emission unaffected. Neutrino emission rate from baryonic matter in neutron stars via weak neutral vector interaction was computed up to order $O(v_F^6)$, where v_F is the Fermi velocity in units of speed of light. The neutrino emissivity is enhanced compared to the result at $O(v_F^4)$ order up to 10% for values $v_F \leq 0.4$ characteristic to baryons in compact stars [2]. Although the next-to-leading correction is small, it provides a proof that the series expansion converges quickly and the leading order result is accurate to order 10%.

Once formed in a supernova explosion, a neutron star cools rapidly via neutrino emission during the first 10^4-10^5 yr of its life-time. Some extensions of the standard model (SM) invoke axions to solve several problems, including the strong CP problem of QCD and the nature of dark matter. We have computed the axion emission rate from baryonic components of a neutron star at temperatures below their respective critical temperatures T_c for normal-superfluid phase transition [3]. The axion production is driven by a charge neutral weak process, associated with Cooper pair breaking and recombination. The requirement that the axion cooling does not overshadow the neutrino cooling puts a lower bound on the axion decay constant $f_a > 6 \times 10^9\, T_{c\,9}^{-1}$ GeV, with $T_{c\,9} = T_c/10^9$ K. This translates into a upper bound on the axion mass $m_a < 10^{-3}\, T_{c\,9}$ eV.

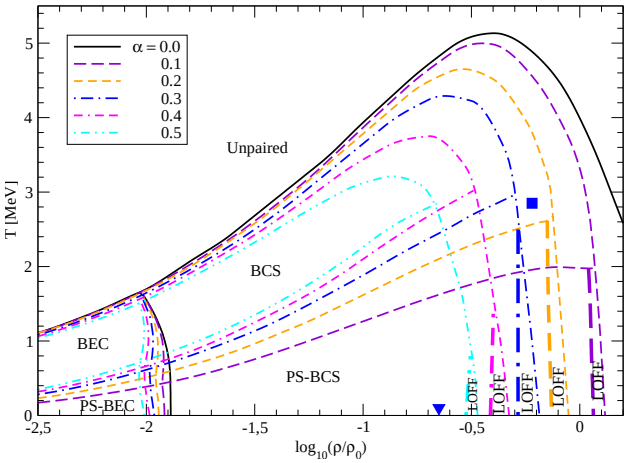

Figure 1: Phase diagram of dilute nuclear matter in the temperature-density plane for isospin asymmetries $\alpha = 0$ (solid, black online), 0.1 (dashed), 0.2 (short-dashed), 0.3 (dash-dotted), 0.4 (double-dash-dotted), and 0.5 (dash-double-dotted). Included are four phases: unpaired, BCS (BEC), LOFF, and PS-BCS (PS-BEC). For each asymmetry there are two tri-critical points, one of which is always a Lifshitz point. For special values of asymmetry these two points degenerate into a single tetracritical point at $\log_{10}(\rho/\rho_0) = -0.22$ and $T = 2.85$ MeV (shown by a square dot) for $\alpha_4 = 0.255$. The LOFF phase disappears at the point $\log_{10}(\rho/\rho_0) = -0.65$ and $T = 0$ (shown by a triangle) for $\alpha = 0.62$. The density-temperature strips where the LOFF phase is the ground state are marked, for each asymmetry, by "LOFF".

References

[1] M. Stein, X. -G. Huang, A. Sedrakian and J. W. Clark, *Phase diagram of dilute nuclear matter: Unconventional pairing and the BCS-BEC crossover.* Phys. Rev. C **86**, 062801(R) (2012).

[2] A. Sedrakian, *Vertex renormalization of weak interactions in compact stars: beyond leading order*. Phys. Rev. C **86**, 025803 (2012).

[3] J. Keller and A. Sedrakian, *Axions from cooling compact stars: pair-breaking processes.* Nuclear Physics A **897**, 62 (2013).

* Work supported by the GSI-GU R&D project and HGS-HIRe.

Hypernuclear and strange quark matter in compact stars *

A. Sedrakian, M. Sinha, and G. Colucci
Institut für Theoretische Physik, J. W. Goethe-Universität Frankfurt am Main, Germany

We have performed several studies of dense hypernuclear matter under conditions relevant to neutron stars within density dependent relativistic mean fields models [1]. Our models include the full baryon octet. One study was aimed at solving the so-called "hyperon puzzle", i.e., the fact that the observation of two solar mass neutron star virtually excludes all the models of hypernuclear matter proposed prior to this observation. We have studied the sensitivity of the equation of state on the interaction between the baryon octet and the scalar mesons. The allowed values of the hyperon-hyperon coupling via the scalar sigma meson was varied within a range admissible by the symmetries and QCD sum rules. We have demonstrated that the equation of state of hypernuclear matter can be stiffer in a certain range of parameters. This observation is a possible solution of the puzzle mentioned above. The finite temperature equation of state was studied under conditions when the neutrinos are trapped. It has been shown that the neutrino trapping stiffens the equation of state.

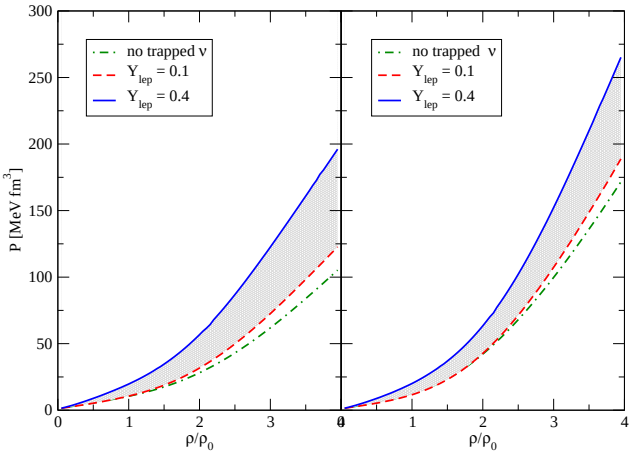

Figure 1: Equation of state in the DD-ME2 parametrization in presence of hyperons. Left panel: we fix the coupling constant $g_{\Lambda\Lambda\sigma} = 0.58 g_{NN\,\sigma}$ from NSC89 potential and we vary the couplings for the Σ and Ξ hyperons. The dashed area shows the variation of the EoS with the variation of the coupling constants of the remaining hyperons with the scalar meson. Right panel: the same as the left panel, but for a fixed coupling constant $g_{\Sigma\Sigma\sigma} = 0.448 g_{NN\sigma}$.

Compact stars with strong magnetic fields (magnetars) have been observationally determined to have surface magnetic fields of order of $10^{14} - 10^{15}$ G, the implied internal field strength being several orders larger. We have studied the equation of state and composition of dense hypernuclear matter in strong magnetic fields in a range expected in the interiors of magnetars [2]. We use the same model as above, but with density independent coupling constants. One advantage of our study is that we have implemented realistic density profiles of magnetic fields, which assume that the field decreases from the center of the star and reaches asymptotically its value at the surface $\sim 10^{15}$ G characteristic for magnetars. Thus, we have extended the previous studies of hypernuclear matter to realistic situation of density dependent field profiles and conducted a study of parameter space that defines the shape of the field profile. It should be noted that the previous studies overestimated the effects of magnetic field on the matter at low densities, simply because of the constant field Ansatz.

We have found that for sufficiently large fields $B_c \geq 10^{18}$ G the matter becomes unstable. The instability is associated with the negative contribution of the field pressure to the baryonic and leptonic pressures in the direction parallel to the magnetic field, which renders the total pressure of the system anisotropic. We have found that the onset of instability depends on the magnetic field profile (parameterized in terms of two parameters) as well as on the central field value B_c. The instability sets in always for critical central field values $B_{\rm cr} \approx 10^{19}$ G for any values of the parameters. This gives a natural bound for the central magnetic field of neutron stars with *homogeneously distributed magnetic field*. We have shown also that the abundances of baryons are weakly affected by the magnetic field, whereas those for the light leptons show de-Haas—van Alfven type oscillations as a function of the magnetic field.

Finally, we are conducting a study of strange quark matter in strange stars which is exposed to large magnetic fields [3]. The confinement feature is included via the phenomenological Richardson potential, which corresponds to static gluon exchange among the quarks. The model is compared to the MIT model and differences between these two confining models are discussed.

References

[1] G. Colucci and A. Sedrakian, *Equation of state of hypernuclear matter: impact of hyperon-scalar meson couplings.* in preparation.

[2] M. Sinha, B. Mukhopadhyay, and A. Sedrakian, *Hypernuclear matter in strong magnetic field*, Nuclear Physics A **898**, 43 (2013).

[3] M. Sinha, X.-G. Huang, and A. Sedrakian *Strange quark matter within a confining model*. in preparation.

* Work supported by the GSI-GU R&D project, HGS-HIRe and the Alexander von Humboldt Foundation.

Triangular Flow as a Measure of Initial State Granularity*

H. Petersen [†1] *and S. A. Bass*[2]

[1]Frankfurt Institute for Advanced Studies, Germany; [2]Department of Physics, Duke University, Durham, NC, USA

Introduction

Higher order flow coefficients have recently been recognized as new observables to gain information about the creation of the quark gluon plasma in relativistic heavy ion reactions and its properties [1]. Pressure gradients translate the initial state coordinate space eccentricity to the final state momentum space ellipticity and this connection is affected by the viscosity and the equation of state [2]. The higher odd anisotropic flow coefficients require the treatment of event-by-event fluctuations, since for smooth initial conditions they vanish by symmetry constraints. The ultimate goal is to understand the initial energy deposition which is related to the distributions of the nucleons/partons in the incoming nuclei and the interactions they are undergoing [3].

Anisotropic Flow Coefficients

By using a hybrid transport approach that is based on the Ultra-relativistic Quantum Molecular Dynamics including an (3+1) dimensional ideal hydrodynamic expansion, we demonstrate that triangular flow is directly related to the amount of fluctuations in the initial state.

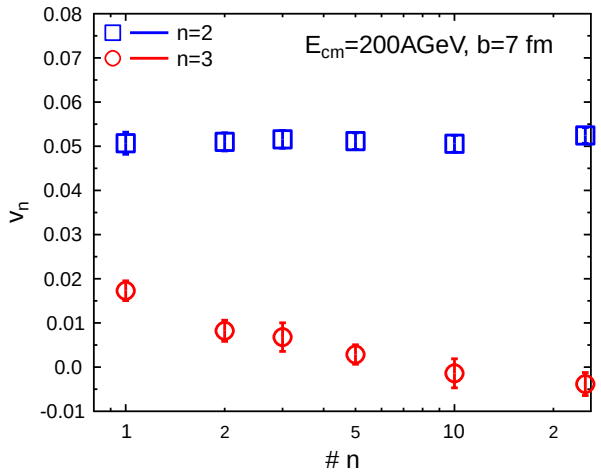

Figure 1: Anisotropic flow for different granularities in mid-central ($b = 7$ fm) Au+Au collisions at $\sqrt{s_{\rm NN}} = 200$ GeV.

In Fig. 1 below results for the averaged $v_{2,3}$ coefficients for charged particles calculated for different granularities ($n = 1, ..., 25$) via the event plane method are presented. The clear dependency of the mean values of triangular flow in non-central collisions on the number of events over which the initial average has been performed proves that one can constrain the granularity of the initial state by comparing flow coefficients of calculations to experimental data. The average elliptic flow stays constant since it is related to the overall geometry of the event.

Constraints on Granularity

To get a first impression on the amount of fluctuations that is consistent with the PHENIX data on triangular flow, the transverse momentum dependence of triangular flow of charged particles has been calculated in the hybrid approach (see Fig. 2).

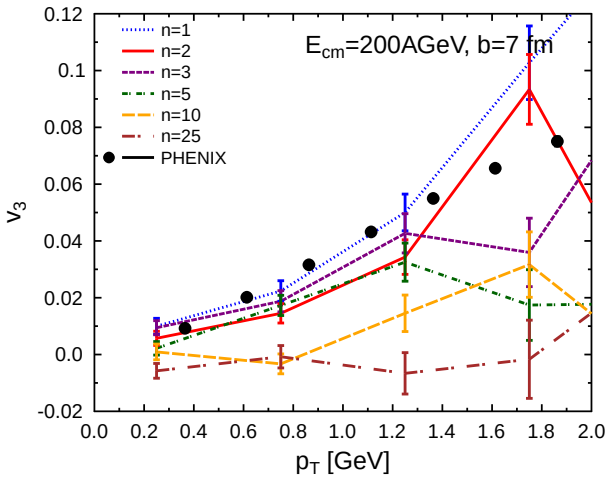

Figure 2: Triangular flow versus transverse momentum for different granularities mid-central ($b = 7$ fm) Au+Au collisions at $\sqrt{s_{\rm NN}} = 200$ GeV compared to PHENIX data.

This first comparison to data indicates that the full single-event configuration is close to the amount of initial state fluctuations that is necessary. That indicates that a hadron-based initial state description with a particle size of the order of 1 fm generates the least amount of fluctuations that is needed. Since additional viscosity during the hydrodynamic evolution would dilute fluctuations faster this is a lower bound on the initial state granularity.

References

[1] H. Petersen, R. La Placa, S. A. Bass, J. Phys. G 39, 055102 (2012)

[2] H. Petersen, arXiv:1211.5526, to be published in JPG

[3] A. Adare, M. Luzum and H. Petersen, arXiv:1212.5388

*Work supported by Helmholtz Association, Young Investigator Group VH-NG-822.

† petersen@fias.uni-frankfurt.de

Centrality dependence of the emission of thermal photons from fluctuating initial conditions*

H. Holopainen[1], *R. Chatterjee*[2], *T. Renk*[2,3], *and K. J. Eskola*[2,3]

[1]FIAS, Frankfurt, Germany; [2]University of Jyväskylä, Jyväskylä, Finland; [3]Helsinki Institute of Physics, Helsinki, Finland

Event-by-event fluctuations in the initial density profile in the hydrodynamical modeling of ultrarelativistic heavy ion collisions have been shown to enhance the production of thermal photons compared to a smooth initial profiles [1]. This enhancement is originating from the fact that hot spots in the fluctuating initial conditions produce much more photons with transverse momenta $p_T > 1$ GeV due to strong temperature dependence of the photon emission rates.

In this work the event-by-event fluctuating initial states are obtained from Monte Carlo Glauber model and density is distributed around the positions of the wounded nucleons using 2-dimensional Gaussians with width σ. These initial states are then evolved with (2+1)-dimensional ideal hydrodynamics [2] and thermal photon emission is obtained by integrating over the whole medium using thermal emission rates [3, 4]. The switch from plasma emission rate to hadron gas emission rate is assumed to happen instantaneously at temperature $T_s = 170$ MeV.

In the figure 1 we have plotted the p_T-spectra of thermal photons in Au+Au collisions at $\sqrt{s_{NN}} = 200$ GeV for different centralities. We can see from the figure that the enhancement is more prominent in the peripheral collisions: the exponential slope of the spectra in the region $2 < p_T < 4$ GeV is 10%, 12% and 16% flatter for fluctuating initial conditions at 0–20%, 20–40% and 40–60% centrality bins respectively [5]. This shows that the relative importance of the hot spots increases towards peripheral collisions, where the number of sources, *i.e.* the number of participants, is smaller.

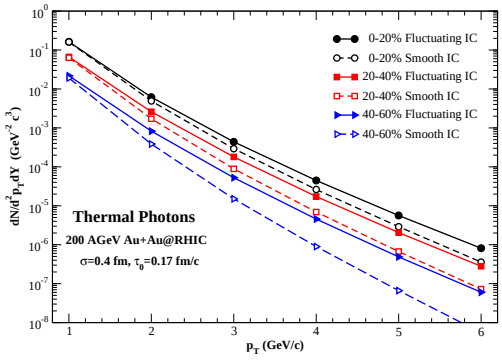

Figure 1: Transverse momentum spectra of thermal photons from smooth and fluctuating initial conditions at RHIC for different collision centralities.

The initial time τ_0 used in these calculations should also vary as a function of centrality – it should be larger for more peripheral collisions. This was studied at LHC energies and we found out that the larger initial times in more peripheral collisions lead to smaller photon yield at large transverse momenta. However, the net effect from density fluctuations and initial time centrality dependence is positive, i.e. the photon production is enhanced relative to the simpler smooth initial state calculation [5].

In figure 2 is plotted the ratio of thermal photons from smooth and fluctuating initial conditions in 0–20% central collisions. Here we have compared the calculations at RHIC and LHC energies and we found out that the enhancement is larger at smaller energies. This suggests that photon measurements at even lower energies than $\sqrt{s_{NN}} = 200$ GeV could be more sensitive to the initial state density fluctuations.

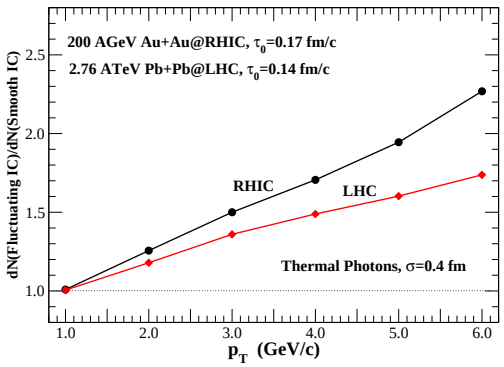

Figure 2: The ratio of thermal photon spectra with fluctuating and smooth initial conditions for 0–20% centrality bin in Au+Au collisions at $\sqrt{s_{NN}} = 200$ GeV and in Pb+Pb collisions at $\sqrt{s_{NN}} = 2.76$ TeV.

References

[1] R. Chatterjee, H. Holopainen, T. Renk and K. J. Eskola, Phys. Rev. C **83** (2011) 054908.

[2] H. Holopainen, H. Niemi and K. J. Eskola, Phys. Rev. C **83** (2011) 034901.

[3] P. B. Arnold, G. D. Moore and L. G. Yaffe, JHEP **0112** (2001) 009.

[4] S. Turbide, R. Rapp and C. Gale, Phys. Rev. C **69** (2004) 014903.

[5] R. Chatterjee, H. Holopainen, T. Renk and K. J. Eskola, Phys. Rev. C **85** (2012) 064910.

* Work supported by Extreme Matter Institute (EMMI).

Linking Fluctuations and Correlations in Relativistic Heavy Ion Collisions *

G. Moschelli[1] *and S. Gavin*[2]

[1]FIAS, Frankfurt am Main, Germany; [2]Wayne State University, Detroit, MI, USA

We investigate the connection between previously unassociated multiplicity, transverse momentum, and flow correlation and fluctuation observables in relativistic heavy ion collisions [1, 2, 3]. Multiplicity fluctuations can provide a means to test theories of the initial production of partons, while transverse momentum fluctuations are used to study the degree of equilibration of the matter in the following system. Flow studies generally focus on relating a deterministic transverse expansion of that matter to the initial geometrical shape of the partonic distribution with the expectation that event-by-event fluctuations in this shape explain fluctuations in flow measurements. In all cases the measured observables rely on two or more particle correlation methods. We show that these three observables probe the same correlation function and therefore require a common explanation. We further argue that the common correlation is the result of an inhomogeneous initial parton density in conjunction with anisotropic transverse expansion. Finally, we take the origin of the initial state inhomogeneities to be the result of particle production from Color Glass Condensate (CGC)-Glasma flux tube sources and calculate the collision centrality and beam energy dependence of these observables in a common framework.

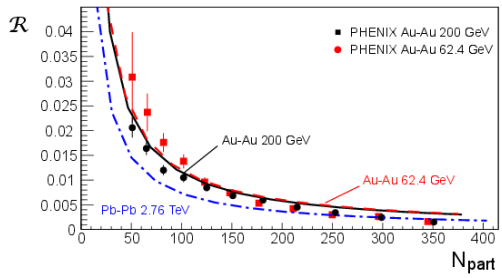

Figure 1: Multiplicity fluctuations $\mathcal{R}$. PHENIX data [4].

Multiplicity fluctuations $\mathcal{R}$ quantify the deviation of the pair momentum distribution of hadrons from that of the singles squared. In the absence of correlations, the pair distribution factorizes and $\mathcal{R}$ vanishes. We calculate $\mathcal{R}$ in a CGC-Glasma framework where coherent flux tube parton sources are randomly distributed at distances determined by the gluon saturation scale Q_s with multiplicities proportional to $\alpha_s^{-1}(Q_s)$. Figure 1 shows our comparison to PHENIX data for RHIC energies with a prediction for Pb-Pb collisions at 2.76 TeV.

We take correlated particles to be those emerging from the same source. Anisotropic flow modifies these correlations such that the final transverse momenta of partons depends on their initial location and partons with common origins are modified in the same way. From this, we calculate transverse momentum fluctuations in Fig. 2 and elliptic flow fluctuations in Fig. 3 noting the change in collision energy is due primarily to Q_s. Importantly, if global equilibrium of the medium is achieved or flow fluctuations arose solely from fluctuations in geometrical shape then transverse momentum fluctuations should vanish. Our results and positive values of momentum fluctuations suggest that flow fluctuations (as they are measured) probe the two-particle correlation function rather than the fluctuation in geometrical shape of the collision volume.

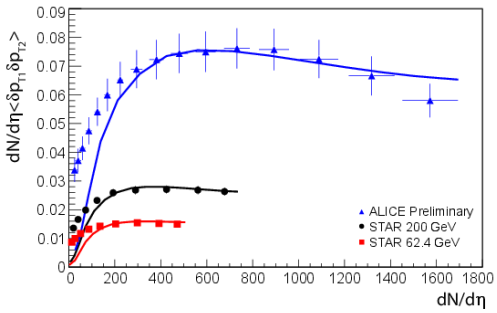

Figure 2: Transverse momentum fluctuations. Data: [5, 6].

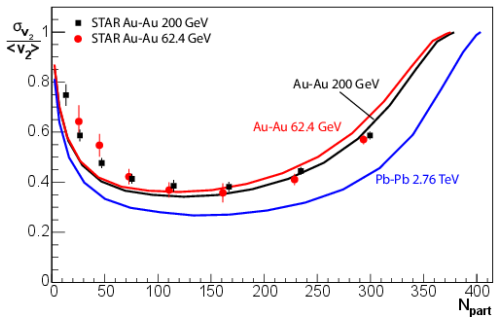

Figure 3: Elliptic flow fluctuations. STAR data [7].

References

[1] S. Gavin and G. Moschelli, Phys.Rev. C85 (2012) 014905.

[2] S. Gavin and G. Moschelli, Phys.Rev. C86 (2012) 034902.

[3] S. Gavin and G. Moschelli, J.Phys.Conf.Ser. 389 (2012) 012038.

[4] A. Adare et al. (PHENIX), Phys. Rev. C78 (2008) 044902.

[5] J. Adams et al. (STAR), Phys. Rev. C72 (2005) 044902.

[6] S. Heckel (ALICE), J.Phys. G38 (2011) 124095.

[7] G. Agakishiev et al. (STAR), Phys.Rev. C86 (2012) 014904.

* Work supported by EMMI (GM) and U.S. NSF grant PHY-0855369 (SG)

QCD phase transitions in Polyakov-chiral fluid dynamics*

C. Herold† [1,2] *and M. Bleicher*[1,2]

[1]Institut für theoretische Physik, Goethe Universität Frankfurt; [2]Frankfurt Institute for Advanced Studies

Introduction

The possibility of a critical point (CP) in QCD is under intensive theoretical and experimental investigation. For thermalized systems, fluctuations of conserved quantities may serve as a probe for the CP. However, it is not yet clear if and how these signals can survive the impact of nonequilibrium effects, which may become dominant in heavy ion collisions. On the other hand, for the same reason, effects at a first-order (FO) phase transition are enhanced. Here phenomena like nucleation or spinodal decomposition may lead to characteristic signals like the formation of disoriented chiral condensates or non-monotonic hadron multiplicity fluctuations.

Polyakov-chiral fluid dynamics

With the use of the Polyakov loop extended chiral fluid dynamics model (PχFD) we study these effects for a FO and a CP scenario at vanishing baryochemical potential. A heat bath of quarks and antiquarks provides the fluid dynamically expanding background on which the relevant order parameters are propagated. These are the sigma field for the chiral and the Polyakov loop for the deconfinement phase transition. For the latter one we deploy its explicit propagation via a relaxation equation including stochastic noise [1,2].

Main results

If we allow the system to thermalize we observe critical slowing down and an enhancement of soft modes at the CP compared with the FO scenario [2]. During the expansion of a hot plasma, supercooling and reheating significantly delay the relaxation process in the FO scenario [1,2]. Correlating the stochastic fluctuations over spatial areas of volume $(1/m_\sigma)^3$ gives us the possibility to study qualitative differences in the two transition processes. While through the CP it proceeds smooth and homogeneous, we observe coexisting domains of the high- and low-temperature phases near the FO transition temperature, cf. Fig. 1. We expect this behavior to create clusters of high baryon density in systems of finite chemical potential, an excellent probe for the QCD phase transition in upcoming experiments at FAIR.

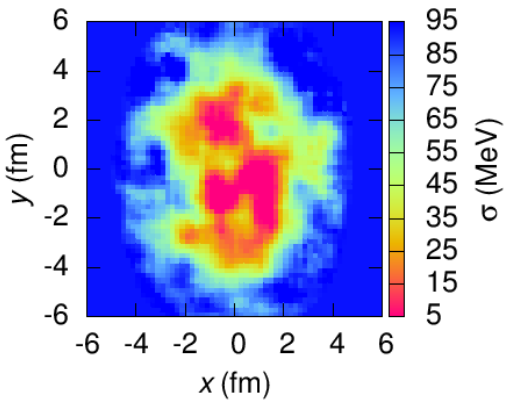

(a)

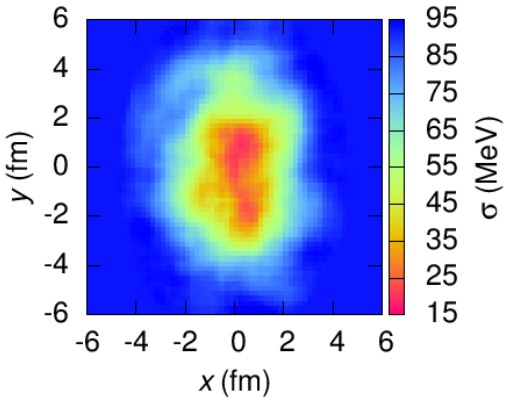

(b)

Figure 1: (a) Sigma field for $z = 0$ at $t = 4$ fm at the FO phase transition. Domain formation creates coexisting bubbles of the chirally broken and restored phase. (b) Sigma field for $z = 0$ at $t = 3.2$ fm near the CP. Here the ellipsoidal shape is preserved. Figures from [2].

References

[1] C. Herold, M. Bleicher and M. Nahrgang, "Fluctuations and correlations in Polyakov loop extended chiral fluid dynamics", Acta Phys. Polon. Supp. **5**, 529 (2012).

[2] C. Herold, M. Nahrgang, I. Mishustin and M. Bleicher, "Chiral fluid dynamics with explicit propagation of the Polyakov loop", Phys. Rev. C **87**, 014907 (2013).

* This work was supported by GSI and the Hessian LOEWE initiative Helmholtz International Center for FAIR.

† herold@fias.uni-frankfurt.de

Radial oscillations of hybrid stars in general relativity

A. Brillante[1,2] *and I. Mishustin*[1,3]

[1]FIAS, Frankfurt am Main, Germany; [2]Goethe University, Frankfurt am Main, Germany; [3]Kurchatov Institute, Russian Research Center, Moscow, Russia

We review the equations governing adiabatic, small radial oscillations of compact stars within the framework of general relativity. We apply these equations to modern realistic equations of state and compute oscillation frequencies for hadronic stars and hybrid stars. The results indicate that the 'static stability criterion' or 'turning point criterion' [1] for dynamical stability is not applicable to hybrid stars.

General relativistic framework

We start with the spherically symmetric line element $ds^2 = -e^{2\Phi}dt^2 + e^{2\Lambda}dr^2 + r^2(d\theta^2 + sin^2\theta d\phi^2)$ and the energy-momentum tensor for a perfect fluid $T^{\mu\nu} = (\rho + P)u^\mu u^\nu + Pg^{\mu\nu}$. To derive the oscillation equation Einstein's equation $G^{\mu\nu} = 8\pi T^{\mu\nu}$ is perturbed in such a way, as to preserve spherical symmetry. This is done by expressing all time tependent quantities as a sum of a time independent part and a time dependent perturbation. Omitting all nonlinear terms in the velocity one can derive the oscillation equation [2][4].

$$0 = \frac{d}{dr}\left[P\frac{d\zeta}{dr}\right] + \left[Q + \omega^2 W\right]\zeta$$

with

$$r^2 W = (\rho + P)\, e^{3\Lambda+\Phi}$$
$$r^2 P = \gamma p e^{\Lambda+3\Phi}$$
$$r^2 Q = e^{\Lambda+3\Phi}\,(\rho + P)\left(\Phi'^2 + 4\frac{\Phi'}{r} - 8\pi e^{2\Lambda} p\right)$$

Here ζ denotes the renormalized Lagrangian displacement of a fluid element due to the oscillation. All perturbed quantities are assumed to have a harmonic time dependence.

Model for dense matter

For the hadronic matter we employ the relativistic mean field model with the parameter set TM1, which is fitted to the properties of heavy nuclei [7]. The quark matter phase is modelled using an effective MIT bag like model [6].

Results

We compare purely hadronic stars with hybrid stars containg a quark core. In Figure 1 the density discontinuity at the center of hybrid stars is shown. The softening of the matter associated with the phase transition to deconfined quark matter leads to an initial decrease in the gravitational mass. According to the turning point criterion this leads to instability with respect to small perturbations. Our calculation of the eigenmode frequencies is shown in Figure 2. We conclude that the turning point criterion is inapplicable to stars with a sharp internal density discontinuity.

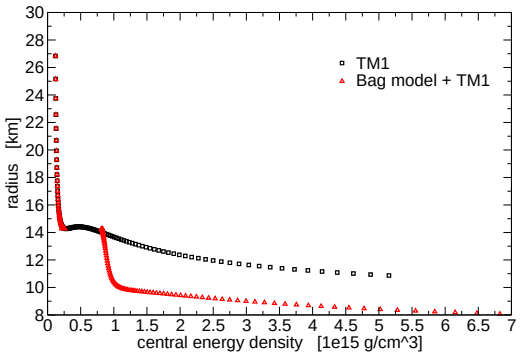

Figure 1: Radius as function of central energy density

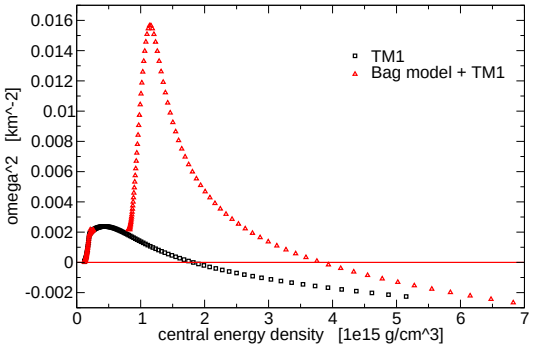

Figure 2: Squared oscillation frequency of fundamental mode as function of central energy density

References

[1] Harrison, Thorne, Wakano, Wheeler "Gravitation Theory and Gravitational collapse", 1965, University of Chikago Press

[2] Chandrasekhar, S. 1964, ApJ, 140, 417

[3] Chanmugan, G. 1977, ApJ, 217, 799

[4] Bardeen, J. M., Thorne, K. S., Meltzer, D. W. 1966, ApJ, 145, 505

[5] Kokkotas, K. D., Ruoff, J. 2001, A&A 366, 565-572 (2001)

[6] Alford, M. G., Reddy, S. 2003, Physical Review D 67,074024 (2003)

[7] Sugahara, Y., Toki, H. 1994, Nucl Phys A 579, 557-572

Initial conditions, transport and hadronization in heavy-ion collisions*

R. Marty[1], *E. Bratkovskaya*[1], *W. Cassing*[2], *and J. Aichelin*[3]
[1]FIAS, Frankfurt, Germany; [2]ITP, Giessen, Germany; [3]Subatech, Nantes, France

Introduction

The study of the properties of the Quark-Gluon Plasma (QGP) –formed in heavy-ion collisons– requires to understand how initially nuclei convert to quarks and gluons and how the partonic matter hadronizes again.

Initial conditions

We have developed a relativistic molecular dynamics approach based on the Nambu–Jona-Lasinio (NJL) Lagrangian [1] for the light u, d, s quarks in order to study the hadronization from an initial state of quarks and antiquarks while in NJL the gluonic degrees of freedom are integrated out and not considered explicitly but contained in an effective coupling constant for the interaction of quarks/antiquarks. As initial condition we use the energy density profile (Fig. 1) from an actual heavy-ion collision calculated within the Parton-Hadron-String-Dynamics (PHSD) transport approach [2].

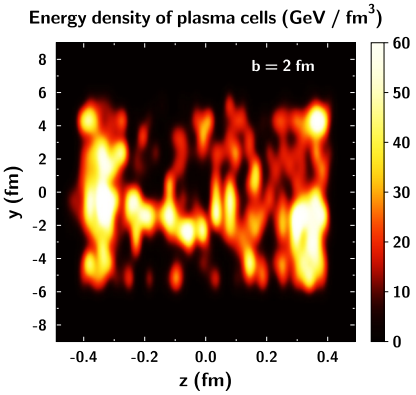

Figure 1: Initial energy density for cells in the local rest frame in the $y - z$ plane of the heavy ion collision.

Relativicstic Molecular Dynamics

In Fig. 1 we show the slice of plasma during the beginning of a Au+Au collision at $\sqrt{s} = 200$ GeV in terms of the energy density in the local cells. In Fig. 2 we show an example of initial conditions using the PHSD energy density converted to NJL partons with the help of the NJL equation of state. Fluctuations in the energy density are clearly visible in the initial parton density. The microscopic study of the expansion and the hadronization through a cross over transition is possible within our transport model.

* Work supported by the HIC for FAIR framework of the LOEWE program and the LOEWE-CSC for computational resources.

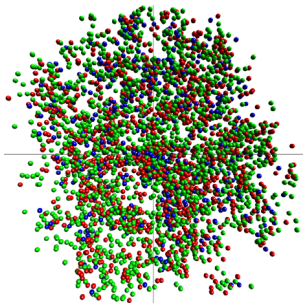

Figure 2: Initial geometry profile of quarks and antiquarks in the $x - y$ plane of the heavy ion collision.

Hadronization

The hadronization volume can be extracted from the r.h.s of Fig. 3 where we show the position in space and time of the inelastic collisions $q\bar{q} \rightarrow MM$ that lead to hadron production in the NJL. Since the full microscopic information is available we can also extract a variety of observables from such simulations as the transverse flow, the p_T-spectra and also study of the influence of the initial condition fluctuations on the final observables.

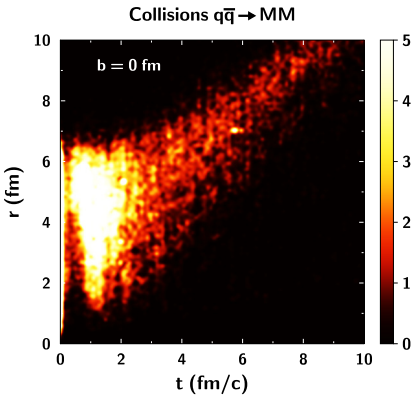

Figure 3: Distribution of inelastic collisions $q\bar{q} \rightarrow MM$ in space $\vec{r}$ (distance from the center of the plasma) and time t from the molecular dynamics calculations.

References

[1] R. Marty, J. Aichelin, *Molecular dynamics description of an expanding $q/\bar{q}$ plasma with the Nambu-Jona-Lasinio model and applications to heavy ion collisions at RHIC and LHC energies*, arXiv:1210.3476 [hep-ph]

[2] V. P. Konchakovski, E. L. Bratkovskaya, W. Cassing, V. D. Toneev, S. A. Voloshin, and V. Voronyuk, *Azimuthal anisotropies for Au+Au collisions in the parton-hadron transient energy range*, Phys. Rev. C **85** (2012) 044922, arXiv:1201.3320 [nucl-th]

Heavy quark dynamics in vacuum and in the quark gluon plasma (QGP)*

H. Berrehrah[1], *E. Bratkovskaya*[1], *W. Cassing*[2], *P.B Gossiaux*[3], *and J. Aichelin*[3]
[1]FIAS, Frankfurt, Germany; [2]ITP, Giessen, Germany; [3]Subatech, Nantes, France

Introduction

Heavy quarks (Q) are produced in hard binary initial collisions between the incoming nucleons in relativistic heavy-ion reactions. They provide an important independent observable that can probe some proprieties of the quark-gluon plasma (QGP) produced in these collisions. To this aim, we study the heavy quarks dynamics from their production until hadronization and freeze-out.

Heavy quark scattering

Our study of the heavy quark propagation is realized within the microscopic Parton-Hadron-String-Dynamics (PHSD) transport approach [1, 2], where hadronic and partonic interactions and the dynamics of heavy flavours degrees-of-freedom are included. The scattering of heavy quarks with the QGP particles represents the first step of this study. Therefore, we have determined the elastic scattering cross section (σ^Q_{elas}) of heavy quarks in vacuum and in the QGP medium. Indeed, the calculation of σ^Q_{elas} at finite temperature in the strongly interacting medium is considered for the first time.

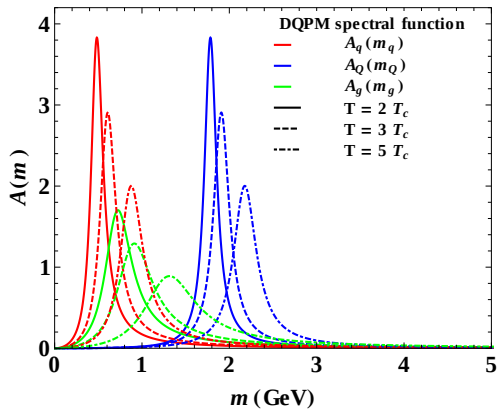

Figure 1: DQPM spectral functions of the gluon ($A_g(m_g)$), light ($A_q(m_q)$) and heavy quarks ($A_Q(m_Q)$) for T = 2; 3; 5 Tc.

Our determination of σ^Q_{elas} at finite temperature couples pQCD calculation with the dynamical Quasi-Particle Model (DQPM). The partons are considered as off-shell quasi-particles, their masses are described by DQPM spectral functions for different temperatures of the medium. Figure 1 shows the gluon, light and heavy quark DQPM spectral functions at different temperatures. In Fig. 2 we show the elastic scattering cross section of heavy quark on a light quark as a function of $\sqrt{s}$, the energy in the c.m of the collision for different temperatures. This figure shows clearly the effect of finite parton masses and widths on the perturbative elastic cross section, [3].

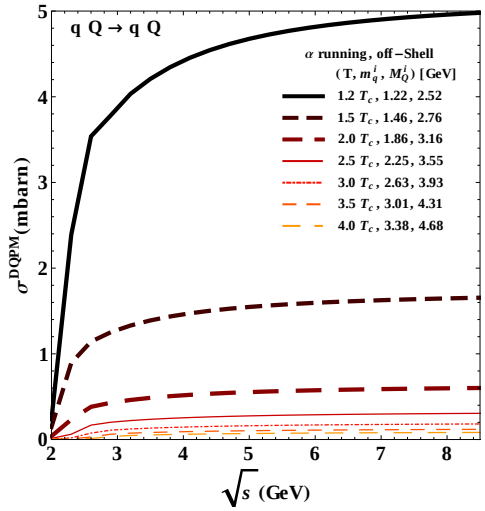

Figure 2: Elastic scattering cross section of heavy quark on light quarks ($qQ \to qQ$) as a function of $\sqrt{s}$, the energy in the c.m of the collision for different temperatures.

Heavy quark dynamics

The knowledge of elastic and inelastic scattering cross sections of heavy quarks in a finite temperature medium leads to the relevant evaluation of several physical quantities, the dynamical collisional and radiative energy loss of heavy quarks, their interaction rates, diffusion coefficients, viscosity, etc. Ultimately, the explicit microscopic dynamics of heavy flavours in the QGP and the hadronic phase can be performed within PHSD.

References

[1] W. Cassing, and E. L. Bratkovskaya, "Parton-Hadron-String Dynamics: an off-shell transport approach for relativistic energies", Nucl.Phys. A831 (2009) 215-242.

[2] V. P. Konchakovski, E. L. Bratkovskaya, W. Cassing, V. D. Toneev, S. A. Voloshin, and V. Voronyuk, "Azimuthal anisotropies for Au+Au collisions in the parton-hadron transient energy range", Phys. Rev. C 85 (2012) 044922.

[3] H. Berrehrah, P.B. Gossiaux, J. Aichelin, E. Bratkovskaya, W. Cassing and M. Bleicher, "Collisional and radiative processes of heavy quarks in vaccum and in the QGP medium", in preparation.

* Work supported by the HIC for FAIR framework of the LOEWE program and the LOEWE-CSC for computational resources.

Lattice QCD based on OpenCL

M. Bach[*1,2], *V. Lindenstruth*[1,2], *O. Philipsen*[3], *and C. Pinke*[†3]

[1]Frankfurt Institute for Advanced Studies, Frankfurt, Germany; [2]Institut für Informatik, Goethe-Universität Frankfurt, Germany; [3]Institut für theoretische Physik, Goethe-Universität Frankfurt, Germany

Introduction

Quantum Chromodynamics (QCD) is the theory of the strong interactions between elementary particles. Since an analytical treatment is not possible, it is well established to study QCD in numerical simulations via a discretized version, Lattice QCD (LQCD). State-of-the-art lattice simulations require high-performance computing and constitute one of the most compute intensive problems in science. Graphics Processing Units (GPUs) have become an interesting alternative to classical CPUs as they offer fast computing facilities at a very attractive price-per-flop ratio. So far, however, most applications in this field have been based on NVIDIA CUDA, locking the software to run on hardware by the single vendor NVIDIA. As a rather new alternative, OpenCL offers a vendor independent developement platform, and, in addition, allows for executing the code also on classical CPUs. We have developed the first LQCD application based on OpenCL for Wilson fermions, in particular concentrating on so-called twisted Mass Wilson fermions [1].

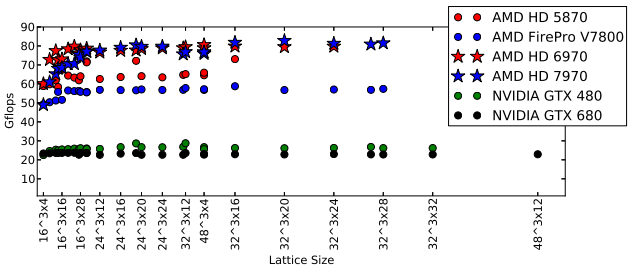

Figure 1: $\not{D}$ performance in Gflops for different lattice sizes on a variety of GPUs.

Performance results

LQCD simulations are always memory bound, meaning they have a low numerical density. Hence, the most compute intensive part, the application of the $\not{D}$ operator, benefits most strongly from an optimal usage of memory bandwidth. We were able to utilize more than 70 % of the available memory bandwidth for all lattice sizes on a variety of AMD GPUs, outperforming published performances of CUDA based codes (Figure 1). The code also works on NVIDIA GPUs, although with reduced performance, as no optimization has been performed for that hardware.

A full LQCD application is the so-called Hybrid Monte-Carlo (HMC) algorithm, which is used to generate ensembles of gauge configurations. Our HMC implementation for twisted-mass Wilson fermions shows a speedup factor of four running on an AMD FirePro V7800 compared to a CPU based reference code running on a single AMD Opteron 6172 socket with 12 cores (Figure 2). In addtion we could show an additional performance increase on the newer generations of AMD GPUs, AMD RADEON HD 6970, substituting the overall good picture of performance and applicability of our code.

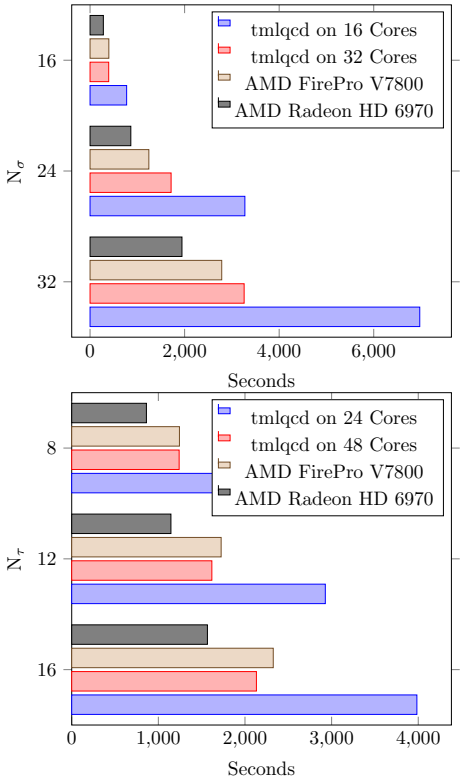

Figure 2: HMC runtimes in seconds using $\mu = 0.1$, $m_\pi = 520$, $\beta = 3.9$ and $\kappa = \kappa_c = 0.160856$ for fixed $N_\sigma = 8$ and $N_\sigma = 24$, respectively, compared to reference code "tmlqcd".

Acknowledgements

The authors were supported by the Helmholtz International Center for FAIR.

References

[1] M. Bach, V. Lindenstruth, O. Philipsen, C. Pinke, "Lattice QCD based on OpenCL", arXiv:1209.5942 [hep-lat]

* bach@compeng.uni-frankfurt.de
† pinke@th.physik.uni-frankfurt.de

Dilepton production at SIS energies with the GiBUU transport model*

J. Weil† *and U. Mosel*
Institut für Theoretische Physik, Universität Giessen, Germany

The HADES collaboration has recently measured dilepton spectra from pp, pA and AA reactions (see e.g. [1, 2]) in order to investigate in-medium properties of vector mesons and solve the long-standing "DLS puzzle" (for a review see [3]).

We simulate the corresponding reactions with the GiBUU transport model, which provides a unified framework for various types of elementary reactions on nuclei as well as heavy-ion collisions [4]. This model takes care of the correct transport-theoretical description of the hadronic degrees of freedom in nuclear reactions, including the propagation, collisions and decays of particles.

While a string-model approach may still be applicable at the highest HADES energies [5], a resonance-model description of the elementary NN collisions is surely more appropriate below $\sqrt{s} \approx 3\,\mathrm{GeV}$. We have recently extended the GiBUU resonance model, which is based on the Teis analysis [6], to higher energies, in order to have one consistent model for the whole energy regime probed by HADES [7].

Fig. 1 shows a comparison plot of a resonance model simulation to HADES data for p+p collisions at 3.5 GeV. The simulation results have been corrected for the HADES detector acceptance and resolution and provide an excellent description of the data over the complete spectrum.

The ρ contribution to the dilepton spectrum deserves particular attention, since its shape is strongly influenced by the ρ meson's production mechanism via baryonic resonances. In particular the $D_{13}(1520)$ contributes significantly to the low-mass part of the ρ spectral function. Together with the contributions from other resonances (only a few of which are shown in the figure), this results in a rather flat shape of the ρ channel, which dominates the intermediate-mass region of the dilepton spectrum around 600 MeV.

After fixing the cocktail contributions in the elementary reactions, the next step is to investigate heavy-ion collisions. Fig. 2 shows the GiBUU spectrum for Ar+KCl at 1.76 GeV [8] in comparison to the HADES data [1]. The simulation shown here relies on vacuum spectral functions and yields a reasonable agreement with the data in the vector-meson mass region as well as the pion region. In the mass region of 200 - 500 MeV, however, the data are underestimated significantly, and it remains to be seen whether this discrepancy can be resolved by e.g. including in-medium spectral functions or other effects. Even larger medium effects than in ArKCl are expected in the heavier Au+Au system, which we plan to investigate in the future.

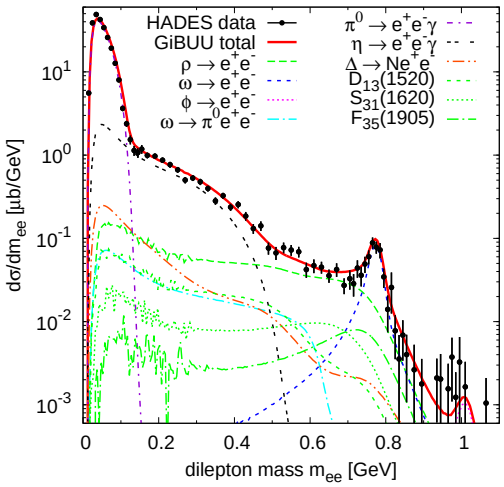

Figure 1: Dilepton spectrum for p+p@3.5GeV compared to HADES data [2].

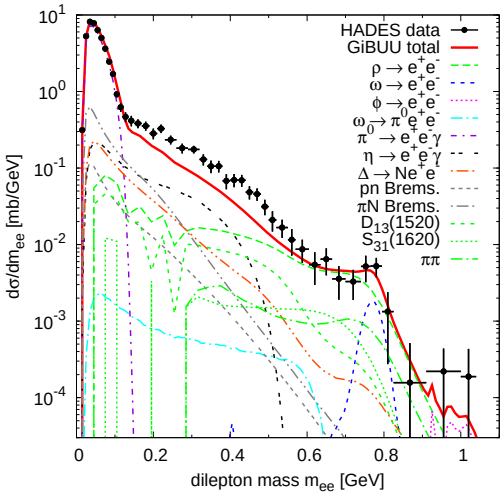

Figure 2: Dilepton spectrum for Ar+KCl@1.76GeV: GiBUU transport simulation compared to HADES data [1].

References

[1] G. Agakishiev et al., Phys. Rev. C 84 (2011) 014902.
[2] G. Agakishiev et al., Eur. Phys. J. A 48 (2012) 64.
[3] S. Leupold, V. Metag, U. Mosel, Int. J. Mod. Phys. E 19 (2010) 147-224.
[4] O. Buss et al., Phys. Rep. 512 (2012) 1.
[5] J. Weil et al., arXiv:1105.0314v1 [nucl-th].
[6] S. Teis et al., Z. Phys. A 356 (1997) 421.
[7] J. Weil et al., Eur. Phys. J. A 48 (2012) 111.
[8] J. Weil et al., arXiv:1211.3761 [nucl-th].

* Work supported by HGS-HIRe and BMBF.
† janus.weil@theo.physik.uni-giessen.de

Propagators and phase structure of $N_f = 2$ and $N_f = 2 + 1$ QCD

Christian S. Fischer[1,2] *and Jan Luecker*[1]

[1]Institut für Theoretische Physik, Justus-Liebig-Universität Gießen; [2]GSI Helmholtzzentrum für Schwerionenforschung GmbH

We study quantum chromodynamics (QCD) at finite temperature T and chemical potential μ by solving the Dyson-Schwinger equations (DSEs) for the quark and gluon propagators.

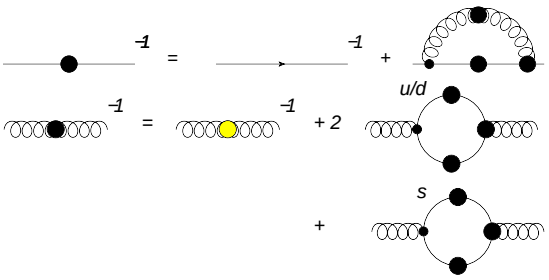

Figure 1: The coupled system of Dyson-Schwinger equations for the quark (upper line) and gluon (lower line).

This set of equations is shown in Fig. 1, where we show the quark DSE in the upper line and the gluon DSE in the lower line. For the gluon we use an approximation where the Yang-Mills part of the equation is substituted by quenched gluon propagators obtained from lattice simulations [1]. To account for unquenching effects, we add the quark loop as it appears in the gluon DSE. This truncation has been introduced in Ref. [2] with bare quarks in the quark loop, and with fully dressed light and strange quarks in Ref. [3]. This is the first $N_f = 2 + 1$ calculation in the Dyson-Schwinger framework of QCD.

From solutions of the DSEs we can extract the quark condensate and the dressed Polyakov loop order parameters for chiral symmetry breaking and confinement. The chiral condensate, shown in Fig. 2 at $\mu = 0$ is in good agreement with lattice data [4] for $2 + 1$ flavours. This is only possible when the back-reaction of quarks and gluons is carefully taken into account, since this leads to a steeper crossover compared to simpler truncations. From the condensate we identify the (pseudo-)critical temperature as a function of μ_q. At $\mu_q \approx 190$ MeV we find a critical end-point. The position of this point is again strongly affected by the back-reaction of quarks and gluons.

From the dual condensate we extract a pseudo-critical temperature for the deconfinement transition. This transition always stays close to the chiral transition, with almost equal transition temperatures above $\mu_q \approx 125$ MeV. Our findings are summarised in the phase diagram shown in Fig. 3. We also show results for two flavours. The impact of strange quarks is evidently a reduction of T_c by almost 50 MeV, while the relative position of the critical end-point is hardly affected.

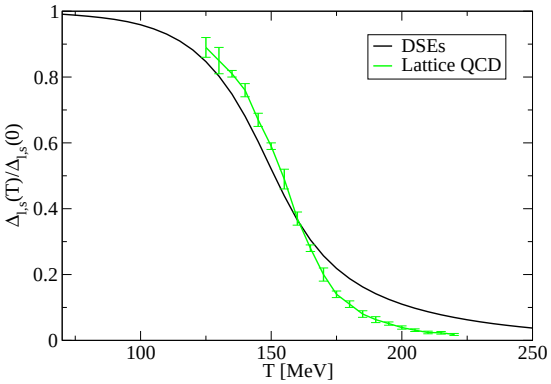

Figure 2: The condensate compared to lattice data.

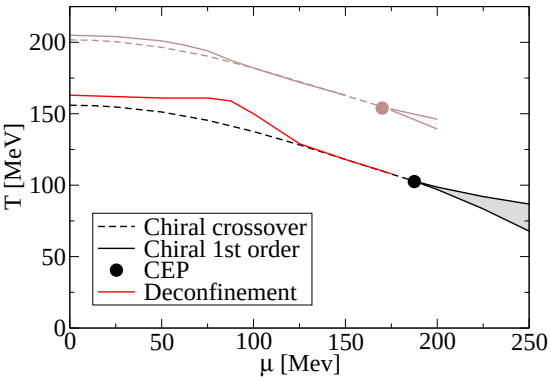

Figure 3: The resulting phase diagram for $N_f = 2 + 1$ and $N_f = 2$ (lighter colours).

References

[1] C. S. Fischer, A. Maas and J. A. Muller, EPJC **68**, 165 (2010)

[2] C. S. Fischer, J. Luecker and J. A. Mueller, PLB **702** (2011) 438

[3] C. S. Fischer and J. Luecker, PLB **718** (2013) 1036

[4] S. Borsanyi *et al.* JHEP **1009** (2010) 073

Shear and bulk viscosities of strongly interacting parton-hadron matter*

V. Ozvenchuk[1], *O. Linnyk*[2], *M. I. Gorenstein*[1,3], *E. L. Bratkovskaya*[1,4], *and W. Cassing*[2]
[1]FIAS, Frankfurt, Germany; [2]ITP, Giessen, Germany; [3]ITP, Kiev, Ukraine; [4]ITP, Frankfurt, Germany

Introduction

We study the shear and bulk viscosities of "infinite" partonic and hadronic matter as functions of temperature T within the parton-hadron-string dynamics (PHSD) off-shell transport approach [1]. The PHSD transport model, which is based on a lattice QCD (lQCD) equation of state [2] and accordingly well describes the entropy density $s(T)$, the energy density $\varepsilon(T)$ as well as the pressure $p(T)$ in comparison to lQCD results.

The "infinite" matter is simulated within a cubic box with periodic boundary conditions initialized at various values for baryon density (or chemical potential) and energy density. The size of box is fixed to 9^3 fm^3. The initialization is done by populating the box with light (u, d) and strange (s) quarks, antiquarks and gluons with random space positions. If the energy density in the system is below the critical energy density ($\varepsilon_c \approx 0.5$GeV/fm^3), the evolution proceeds through the dynamical phase transition and ends up in an ensemble of hadrons. The system initially is close to the thermal equilibrium with thermal distribution for the momenta of partons and far out from the chemical equilibrium due to the strangeness suppression by factor of 3 in comparison to the light quarks and antiquarks. The system approaches kinetic and chemical equilibrium at all energies densities during it's evolution within PHSD. After equilibration, the properties of the system at given temperature can be studied. For more details we refer thre reader to Ref. [3], where the particle abundances, spectra, fluctuations and spectral functions were studied.

Shear and bulk viscosities

The ratio of the shear viscosity to entropy density $\eta(T)/s(T)$ extracted from the PHSD simulations in the box, which is presented in Fig. 1, shows a minimum (with a value of about 0.1) close to the critical temperature T_c, while it approaches the perturbative QCD (pQCD) limit at higher temperatures. For $T < T_c$, i.e. in the hadronic phase, the ratio η/s rises fast with decreasing temperature due to a lower interaction rate of the hadronic system and a significantly smaller number of degrees of freedom. We obtain practically the same results in the Kubo formalism and in the relaxation time approximation. Our results are also in almost quantitative agreement with the ratio $\eta(T)/s(T)$ from the virial expansion approach as well as with lQCD data for the pure gauge sector.

The bulk viscosity $\zeta(T)$ evaluated in the relaxation time approach, which is shown in Fig. 2, is found to strongly depend on the effects of mean fields (or potentials) in the partonic phase. We find a significant rise of the ratio $\zeta(T)/s(T)$ in the vicinity of the critical temperature T_c, when consistently including the scalar mean-field from PHSD, which is also in agreement with that from lQCD calculations.

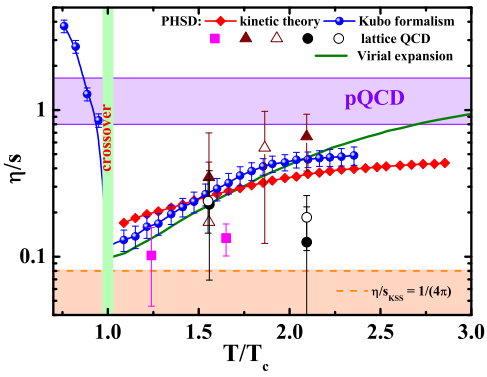

Figure 1: The specific shear viscosity η/s as a function of T/T_c extracted from PHSD simulations in the box.

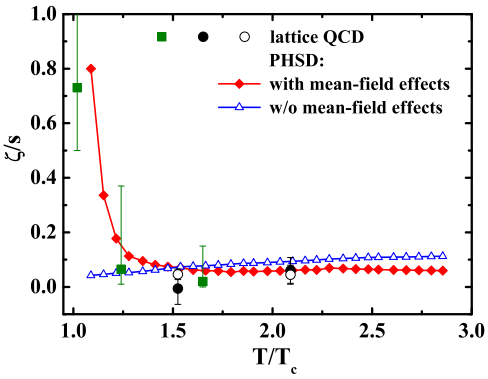

Figure 2: The specific bulk viscosity ζ/s as a function of T/T_c extracted from PHSD simulations in the box.

References

[1] V. Ozvenchuk, O. Linnyk, M. I. Gorenstein, E. L. Bratkovskaya, W. Cassing, arXiv:1212.5393 [nucl-th]

[2] S. Borsanyi *et al.*, J. High Energy Phys. **09** (2010) 073; **11** (2010) 077.

[3] V. Ozvenchuk, O. Linnyk, M. I. Gorenstein, E. L. Bratkovskaya, and W. Cassing, arXiv:1203.4734 [nucl-th]

* Work supported by the HIC for FAIR framework of the LOEWE program and the Helmholtz Research School for Quark Matter Studies in Heavy Ion Collisions.

The Superheavy Element Search Campaigns at TASCA

J. Khuyagbaatar[1,2], A. Yakushev[1], Ch.E. Düllmann[1,2,3], H. Nitsche[4], J. Roberto[5], D. Ackermann[1], L.-L. Andersson[2], M. Asai[6], H. Brand[1], M. Block[1], D.M. Cox[7], M. Dasgupta[8], X. Derkx[2,3], A. Di Nitto[3], J. Dvorak[2], K. Eberhardt[2,3], P.A. Ellison[4], N.E. Esker[4], J. Even[2,3], M. Evers[8], C. Fahlander[9], U. Forsberg[9], J.M. Gates[4], N. Gharibyan[10], K.E. Gregorich[4], P. Golubev[9], O. Gothe[4], J.H. Hamilton[11], D.J. Hinde[8], W. Hartmann[1], R.-D. Herzberg[7], F.P. Heßberger[1,2], J. Hoffmann[1], R. Hollinger[1], A. Hübner[1], E. Jäger[1], J. Jeppsson[9], B. Kindler[1], S. Klein[3], I. Kojouharov[1], J.V. Kratz[3], J. Krier[1], N. Kurz[1], S. Lahiri[12], B. Lommel[1], M. Maiti[12], K. Miernik[5], S. Minami[1], A. Mistry[7], C. Mokry[2,3], J.P. Omtvedt[13], G.K. Pang[4], P. Papadakis[7], I. Pysmenetska[1], D. Renisch[3], D. Rudolph[9], J. Runke[1], K. Rykaczewski[5], L.G. Sarmiento[9], M. Schädel[1,6], B. Schausten[1], D.A. Shaughnessy[10], A. Semchenkov[13], J. Steiner[1], P. Steinegger[14], P. Thörle-Pospiech[2,3], E.E. Tereshatov[10], T. Torres De Heidenreich[1], N. Trautmann[3], A. Türler[14], J. Uusitalo[15], D. Ward[9], N. Wiehl[2,3], M. Wegrzecki[16], V. Yakusheva[2]

[1]GSI, Darmstadt, Germany, [2]HIM, Mainz, Germany, [3]U. Mainz, Germany, [4]LBNL+UC Berkeley, CA, USA, [5]ORNL / UT Knoxville, USA, [6]JAEA Tokai, Japan, [7]U. Liverpool, UK, [8]ANU, Canberra, Australia, [9]Lund U. Sweden, [10]LLNL, USA, [11]Vanderbilt U, USA, [12]SINP, Kolkata, India, [13]U. Oslo, Norway, [14]U. Bern+PSI Villigen, Switzerland, [15]U. Jyväskylä, Finland, [16]ITE Warsaw, Poland

Successful experiments on the synthesis of elements with Z=114-118 in ^{48}Ca-induced reactions with actinide targets were first performed at the DGFRS in Dubna [1]. Results for Z=114 (Fl) and Z=116 (Lv) nuclei have been later on confirmed by other groups [2-4].

Using doubly-magic ^{48}Ca for the synthesis of yet heavier elements is not possible due to the lack of sufficient amounts of target materials for elements beyond Cf. Thus, several attempts to produce element 120 in reactions with projectiles beyond ^{48}Ca have been carried out at DGFRS and SHIP [5-7]. The separator TASCA and its detection systems were significantly upgraded since the experiment on ^{288,289}Fl [3] was performed [8]. In the past two years, two experiments on the synthesis of elements beyond Z=118 have been undertaken at TASCA using the reactions ^{50}Ti + ^{249}Bk $\rightarrow$ ^{299}119* and ^{50}Ti + ^{249}Cf $\rightarrow$ ^{299}120*. To verify the performance of the setup, element 117 was also synthesized.

The first attempt to form element 120 at TASCA was performed in August-October 2011. The search for element 119 was performed in two series from April to September 2012. The beam energies from the UNILAC, average initial target thicknesses (*d*) [9], and accumulated beam doses for each reaction are given in Table 1. These values are **preliminary**. Beam doses were deduced from beam current measurements in front of the target. 85% of the beam doses were estimated to be on the target.

Subsequent to the months-long experiments on elements 119 and 120, an experiment on the synthesis of element 117 in reaction ^{48}Ca + ^{249}Bk $\rightarrow$ ^{297}117* was successfully performed. In about one month of experiment time, the Bk target was bombarded by ^{48}Ca ions at three different beam energies. The final data analyses of all these experiments are currently ongoing.

We are grateful for support by the GSI directorate, ion source, accelerator, and experiment electronics staff.

References

[1] Y. Oganessian, Radiochim. Acta 99, 429 (2011)
[2] L. Stavsetra *et al.*, PRL. 103, 132502 (2009)
[3] Ch.E. Düllmann *et al.*, PRL. 104, 252701 (2010)
[4] S. Hofmann *et al.*, EPJ. A 48, 62 (2012)
[5] S. Hofmann *et al.*, GSI Scientific Report-2007, 131 (2008)
[6] Yu.Ts. Oganessian *et al.*, PRC. 79, 024603 (2009)
[7] S. Hofmann *et al.*, GSI Scientific Report-2011, 205 (2012)
[8] see GSI Scientific Report-2011, pages-206, 212, 217, 218, 251-253 (2012)
[9] J. Runke *et al.*, J. Radioanal. Nucl. Chem. (accepted)

Table. 1. The parameters of the experiments. For details, see text.

Beam	Target	CN	Date	E_{lab} (MeV)	*d* (μg/cm^2)	Beam dose	Beam dose on target
^{50}Ti	^{249}Cf	^{299}120	25.08-12.10.2011	306	515	1.1·10^{19}	0.9·10^{19}
	^{249}Bk	^{299}119	13.04-03.07.2012 23.07-03.09.2012	300	440	4.2·10^{19}	3.6·10^{19}
^{48}Ca		^{297}117	26.09-09.10.2012	270		0.6·10^{19}	0.5·10^{19}
			09.10-22.10.2012	274		0.5·10^{19}	0.4·10^{19}
			22.10-29.10.2012	268		0.3·10^{19}	0.2·10^{19}

Superheavy Element Flerovium is the Heaviest Volatile Metal

A. Yakushev[1], J.M. Gates[1,2†], A. Gorshkov[1], R. Graeger[1], A. Türler[1‡], D. Ackermann[2], M. Block[2], W. Brüchle[2], Ch.E. Düllmann[2,3], H.G. Essel[2], F.P. Heßberger[2,3], A. Hübner[2], E. Jäger[2], J. Khuyagbaatar[2,3], B. Kindler[2], J. Krier[2], N. Kurz[2], B. Lommel[2], M. Schädel[2], B. Schausten[2], E. Schimpf[2], K. Eberhardt[4], M. Eibach[4], J. Even[4], D. Hild[4], J.V. Kratz[4], L.J. Niewisch[4], J. Runke[4], P. Thörle-Pospiech[4], N. Wiehl[3,4], J. Dvorak[5,6], H. Nitsche[5,6], J.P Omtvedt[7], A. Semchenkov[7], U. Forsberg[8], D. Rudolph[8], J. Uusitalo[9], L.-L. Andersson[10], R.-D. Herzberg[10], E. Parr[10], Z. Qin[11], M. Wegrzecki[12]*

[1]TUM, Garching, Germany; [2]GSI, Darmstadt, Germany; [3]HI Mainz, Germany; [4]University of Mainz, Germany; [5]LBNL, Berkeley, USA; [6]University of California, Berkeley, USA.; [7]University of Oslo, Norway; [8]Lund University, Sweden; [9]University of Jyväskylä, Finland; [10]University of Liverpool, UK; [11]IMP, Lanzhou, P.R. China, [12]ITE, Warsaw, Poland

Electron shells of superheavy elements (SHE), i.e., elements with atomic numbers $Z \geq 104$, are influenced by strong relativistic effects caused by the high value of Z. Early atomic calculations for element 112 (copernicium, Cn) and element 114 (flerovium, Fl) predicted them to have closed and quasi-closed electron shell configurations, respectively, and to be noble gas-like due to very strong relativistic effects [1]. Recent fully relativistic calculations studying Cn and Fl in different environments suggest them to be less reactive compared to their lighter homologues in the groups, but still exhibiting metallic character (see, e.g., [2]). Experimental gas-chromatography studies on Cn have, indeed, revealed a metal-metal bond formation with gold [3]. In contrast to this, for Fl, the formation of a weak physisorption bond with gold was inferred from first experiments [4].

A gas chromatography experiment on Fl at TASCA was conducted subsequently to the study of the reaction ^{244}Pu(^{48}Ca; 3,4n)^{289,288}Fl [5]. The coupling of chemistry setups to a recoil separator promises extremely high sensitivity due to strong suppression of background from unwanted species. TASCA was operated in the Small Image Mode, focusing the products into a Recoil Transfer Chamber (RTC) of 29 cm^3, from where they were flushed within 0.8 s to a detection setup (Fig. 1). Two COMPACT detectors [6] connected in series were used; each detector consisted of 32 pairs of 1x1 cm^2 PIN diodes covered with a 35 nm gold layer. The first detector was connected directly to the RTC exit and kept at room temperature.

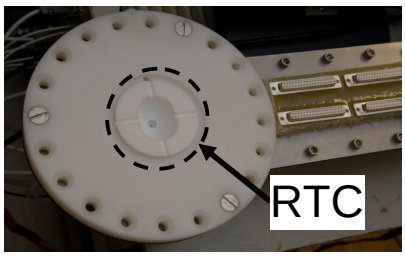

Fig.1: First COMPACT with the attached RTC.

A negative temperature gradient from +20 to −162 °C (Fig. 2, panel a) was applied in the second detector channel placed downstream to the first one. The use of two detectors in series allowed the detection of species in a wide volatility range – from the non-volatile Pb, the nearest homolog of Fl in the group, to the noble gas Rn. Two decay chains, one from ^{288}Fl and one ^{289}Fl were detected. Both decays from Fl isotopes occurred in the first detector channel at room temperature. The positions of decay chain members are shown in Fig. 2 (e) together with the Monte Carlo simulated deposition peak for ^{285}Cn (dashed line). Distributions of Pb, Hg, and Rn (Fig. 2, b-d) are also shown for comparison. The observed behavior of Fl in the chromatography column is indicative of Fl being less reactive than Pb. The evaluated lower limit of the adsorption enthalpy on gold reveals formation of a metal-metal bond with Au, which is at least as strong as that of Cn, and thus demonstrates the metallic character of Fl.

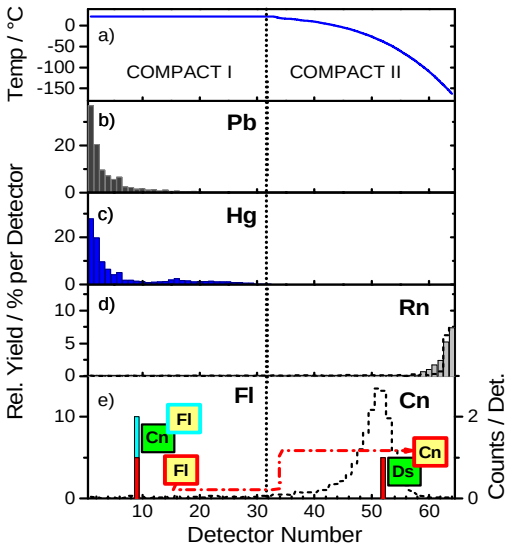

Fig. 2: The observed gas-chromatography behavior of Fl and Cn in COMPACT compared to those of Pb, Hg and Rn.

[1] K.S. Pitzer. *J. Chem. Phys.* **63**, 1032 (1975).
[2] V. Pershina *et al. J. Chem. Phys.* **131**, 084713 (2009).
[3] R. Eichler *et al. Nature* **447**, 72-75 (2007).
[4] R. Eichler *et al. Radiochim. Acta* **98**, 133-139 (2010).
[5] Ch.E. Düllmann *et al.* PRL **104**, 252701 (2010).
[6] J. Dvorak *et al.* PRL **97**, 242501 (2006).

* Current address: GSI Darmstadt, Germany
† Current address: LBNL, Berkeley, USA
‡ Current address: PSI, Villigen & Uni Bern, Switzerland

The reactions ^{50}Ti+^{206,208}Pb studied at TASCA

J. Khuyagbaatar[1,2], A. Yakushev[1], D. Ackermann[1], L.-L. Andersson[2], M. Block[1], Ch.E. Düllmann[1,2,3], J. Even[2,3], F.P. Heßberger[1,2], A. Hübner[1], E. Jäger[1], B. Kindler[1], J.V. Kratz[3], J. Krier[1], N. Kurz[1], B. Lommel[1], J.P. Omtvedt[4], J. Runke[1], M. Schädel[1,5], B. Schausten[1], J. Steiner[1], A. Türler[6], J. Uusitalo[7], N. Wiehl[2,3], V. Yakusheva[2]

[1]GSI, Darmstadt, Germany, [2]HIM, Mainz, Germany, [3]U. Mainz, Germany, [4]U. Oslo, Norway, [5]JAEA Tokai, Japan, [6]U. Bern+PSI Villigen, Switzerland, [7]U. Jyväskylä, Finland

Cross sections of the 1n and 2n evaporation channels of the complete fusion reactions ^{50}Ti + ^{206,208}Pb were measured. Selected beam energies correspond to the known or expected maxima of the 1n and 2n excitation functions. Evaporation residues (ER) were separated from the primary beam by TASCA [1] and implanted into a stop detector consisting of two double-sided silicon-strip detectors (DSSD). Two signals from the DSSD were read out and processed in analog (front strips) and digital electronics (back strips) as described in [2].

Rf isotopes were identified in a correlation analysis between the ER implantation signal and the subsequent radioactive decay (alpha emission or/and spontaneous fission (SF)).

Half-lives were deduced from the measured time distributions (see Fig. 1) and agree well with literature values [3]. Time distributions of the correlated alpha or/and SF decays of these isotopes are shown in Fig. 1 together with fits of the universal time distribution function [4].

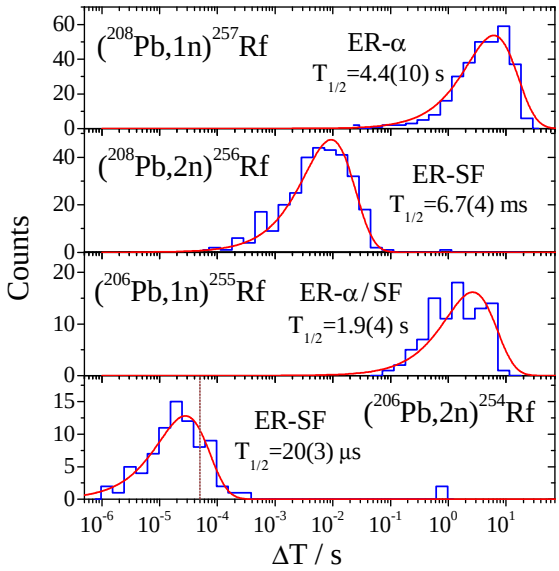

Fig 1: Time distribution of α/SF decays of $^{254-257}$Rf. The dotted line indicates the minimum readout time of the combined DAQ system.

Both analog and digital data were evaluated for the identification of short-lived ^{254}Rf.

The analog energy *vs.* correlation time plot for ER-SF correlations is shown in Fig. 2a. This energy is the uncorrected pulse height recorded in the stop detector, applying a calibration with an external α-source. Traces of two SF events (circled in Fig. 2a) are shown in Fig. 2b as illustrative examples. The energies recorded by the analog electronics were 94 and 150 MeV. In the digital part both traces saturate due to the pre-amplified SF signals, which are higher than the input voltages of the sampling ADC. However, the saturation time, T_{sat}, can be related to the SF energy. A typical trace of an ER correlated with a short-lived SF is shown in Fig. 2c. Such digital data were exploited in the analysis of ^{254}Rf data given in Fig. 1. Note that such events result in a single ER event in the analog electronics and fast decays of ^{254}Rf would be lost.

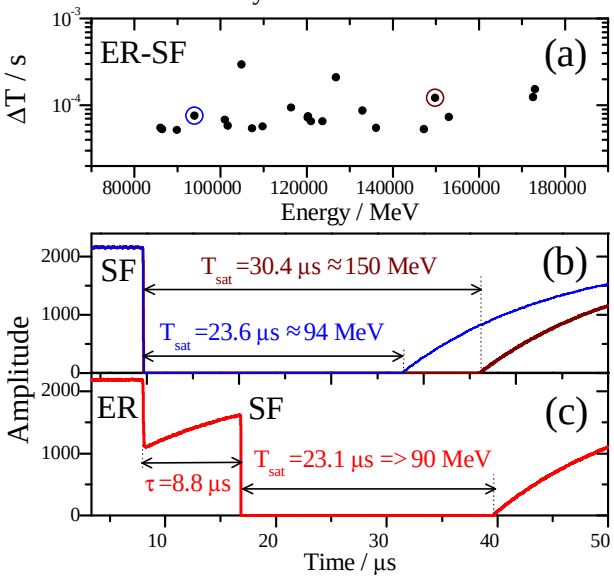

Fig 2: (a) Energy *vs.* correlation time plot. (b) Two traces of SF events selected from the analog ER-SF correlations. (c) Trace of an ER followed by a short-lived SF.

The cross section values for ^{50}Ti(^{208}Pb,1-2n)^{256,257}Rf and ^{50}Ti(^{206}Pb,2n)^{254}Rf were in agreement with the values measured at SHIP [5]. The cross section around the expected maximum for the ^{50}Ti(^{206}Pb,1n)^{255}Rf excitation function was measured for the first time. The data are currently under final analysis.

References

[1] A. Semchenkov *et al.*, NIM. B 266, 4153 (2008)
[2] J. Khuyagbaatar *et al.*, GSI Scientific report (2012)
[3] http://www.nndc.bnl.gov/ensdf/
[4] K.H. Schmidt *et al.*, Z. Phys. A 316, 19 (1984)
[5] F. P. Heßberger *et al.*, Z. Phys. A 359, 415 (1997)

Alpha Decay of $^{197-199}$Fr*

Z. Kalaninová[†1], *A.N. Andreyev*[2,3,4], *S. Antalic*[1], *F.P. Heßberger*[5,6], *D. Ackermann*[5], *B. Andel*[1], *M.C. Drummond*[7], *S. Hofmann*[5], *M. Huyse*[8], *B. Kindler*[5], *J.F.W. Lane*[2], *V. Liberati*[2], *B. Lommel*[5], *R.D. Page*[7], *E. Rapisarda*[8], *K. Sandhu*[2], *Š. Šáro*[1], *A. Thornthwaite*[7], *and P. Van Duppen*[8]

[1]Comenius University, Bratislava, Slovakia; [2]University of the West of Scotland, Paisley, UK; [3]University of York, York, UK; [4]ASRC, JAEA, Ibaraki, Japan; [5]GSI, Darmstadt, Germany; [6]Helmholtz Institut Mainz, Mainz, Germany; [7]University of Liverpool, Liverpool, UK; [8]K.U. Leuven, Leuven, Belgium

In order to optimize and test theoretical nuclear-structure models, experimental data is needed for isotopes far from the line of β stability. Especially regions near closed shells provide a possibility to study unique phenomena. In this work we report on a study of nuclei in the vicinity of the $Z = 82$ shell closure.

We produced very neutron-deficient francium isotopes at the velocity filter SHIP (GSI, Darmstadt) using the fusion-evaporation reaction ^{60}Ni + ^{141}Pr $\rightarrow$ ^{201}Fr*. The irradiations were performed at several beam energies from 262 to 300 MeV. After separation from the primary beam, the evaporation residues were implanted into a position-sensitive silicon detector (PSSD) surrounded by six silicon detectors used to detect α particles escaped from the PSSD.

Prior to this work, the lightest identified francium isotopes were ^{199,198}Fr. The ^{199}Fr isotope was produced using the fusion-evaporation reaction ^{36}Ar + ^{169}Tm $\rightarrow$ ^{205}Fr* at the GARIS separator (RIKEN). Five α-decay chains were reported yielding E_α = 7655(40) keV and $T_{1/2} = 12^{+10}_{-4}$ ms [1]. The isotope ^{198}Fr was produced at the RITU separator (JYFL) [2], but no results were published so far.

In our study we detected $\sim$ 60 and $\sim$ 70 α-decay chains of ^{199}Fr and ^{198}Fr, respectively. These isotopes have similar half-lives and overlapping α-decay energies. However, a careful measurement of excitation functions for both isotopes enabled us the unambiguous distinction between them. We registered a single peak at 7675(6) keV for ^{199}Fr in contrast to the wide range of α-decay energies from 7470 to 7930 keV for ^{198}Fr (see Fig. 1).

In ^{195}At, the α-decay daughter of ^{199}Fr, two α-decaying states with different spins and parities are known. We observed the decay of both of these states correlated to the α decay of ^{199}Fr. We present two scenarios for this observation. The first possibility is that in ^{199}Fr exists one α-decaying state with E_α = 7675(6) keV, $T_{1/2} = 6.0^{+1.0}_{-0.7}$ ms populating ^{195m}At [see Fig. 2(a)]. This state decays with 88(5)-% probability by α decay and with 12(5)-% probability by an E3 IT transition to ^{195g}At. The second possibility is the presence of two α-decaying states in ^{199}Fr with similar decay properties: the decay with E_α = 7676(6) keV, $T_{1/2} = 6.2^{+1.1}_{-0.8}$ ms populating ^{195m}At and the decay with E_α = 7664(11) keV, $T_{1/2} = 4.5^{+3.1}_{-1.3}$ ms populating ^{195g}At [see Fig. 2(b)]. Within the limited statistics, we cannot favour either of the proposed decay patterns.

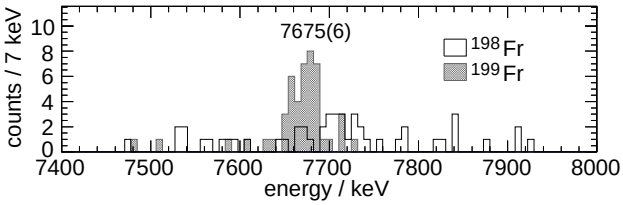

Figure 1: The α-decay energy spectra of ^{199}Fr (shaded region) and ^{198}Fr (black solid line). The isotopes were distinguished using the different beam energies for their production: $(262 - 272)$ MeV for ^{199}Fr and $(282 - 300)$ MeV for ^{198}Fr.

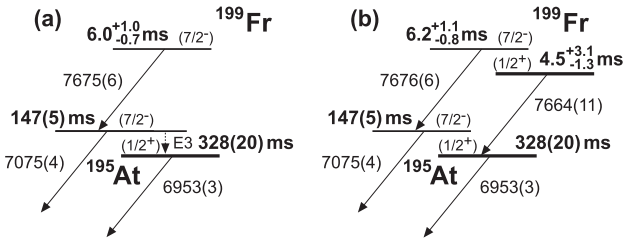

Figure 2: Proposed α-decay schemes for ^{199}Fr. The values for ^{195}At are from [3]. Alpha-decay energies are in keV.

For the α decay of ^{198}Fr we identified two components: a shorter-lived one with $T_{1/2}$ = 1.1(7) ms and α-decay energy from 7580 to 7930 keV and a longer-lived one with $T_{1/2}$ = 15(3) ms and α-decay energy from 7470 to 7920 keV. The existence of two α-decaying states in ^{198}Fr was confirmed by the correlated decay of ^{190}Bi; we observed decays of ^{190m1}Bi correlated with the 15(3)-ms state in ^{198}Fr and decays of ^{190m2}Bi correlated with the 1.1(7)-ms state in ^{198}Fr.

At the highest beam energy we detected one triple-α decay chain attributed to the decay of the new isotope ^{197}Fr. The identification was based on the correlations of the parent α decay with the known decays of daughter nuclei ^{193}At and ^{189}Bi.

References

[1] Y. Tagaya *et al.*, EPJ A **5**, 123 (1999).

[2] J. Uusitalo, private communication (2012).

[3] H. Kettunen *et al.*, EPJ A **16**, 457 (2003).

* Supported by FWO-Vlaanderen (Belgium), UK Science and Technology Facilities Council, Slovak Research and Development Agency

† Zdenka.Kalaninova@fmph.uniba.sk

Fission Hindrance in Odd-Mass Transuranium Nuclei*

F.P. Heßberger[1,2]

[1]GSI, Darmstadt, Germany; [2]HIM, Mainz, Germany

It had been realized already in early studies of nuclear fission, that partial fission half-lives of nuclei having odd proton and/or neutron numbers were considerably longer than those of even-even nuclei [1]. In this sense spontaneous fission of odd-mass and odd-odd nuclei was regarded as 'hindered'.

This phenomenom has been explained as the consequence of spin and parity conservation (see e.g. [2,3]). While in case of nucleon pairs at level crossings the nucleons may change from one orbital to another, in case of odd-Z or odd-N nuclei the unpaired nucleon has to 'keep' its level at deformation and thus the energetic most favourable fission path may be forbidden, leading to an increase of the fission barrier, often denoted as 'specialzation' energy. The influence on the fission half-life depends on the change of the energies of the regarded single particle levels at deformation, in other words, on the nuclear structure. Quantitatively it is usually expressed by a hindrance factor HF, defined as HF = T_{sf} / T_{sf}(unh). T_{sf} denotes the partial fission half-life, simply expressed as $T_{sf} = T_{1/2}/b_{sf}$, with $T_{1/2}$ being the half-life and b_{sf} the fission branching. T_{sf}(unh) is the 'unhindered' fission half-life, defined as the geometrical mean of the fission half-lives of the neighbouring even-even nuclei, e.g., in the case of odd-N nuclei $T_{sf}(Z,N)\,(unh) = (T_{sf}(Z,N-1) \times T_{sf}(Z,N+1)^{1/2}$ [4].

In fig. 1 hindrance factors are plotted for those odd-mass nuclei for which spin and parity of the fissioning state are assigned beyond reasonable doubt, and the fission branching as well as the fission half-lives of the neighbouring even-even nuclei have been determined experimentally.

Evidently there is no correlation between spin / parity and the hindrance factor. Also hindrance factors for fission from the same Nilsson level are quite different in different nuclei. Eye-catching in even-Z, odd-N nuclei, however, are the higher hindrance factors for the lower-Z nuclei for Nilsson levels with spin-up (↑) projections and the lower hindrance factors for the lower-Z nuclei for Nilsson levels with spin-down (↓) projections. With respect of the low number of cases it is, however, presently too speculative to ascribe it to a nuclear structure effect, it still might be accidential.

In fig. 2 the hindrance factors are plotted versus the fissility parameter Z^2/A of the fissioning nuclei. The black squares denote the nuclei regarded in fig. 1, the coloured ones the nuclei for which spin and parity of the fissioning state is not known or uncertain and /or fission half-lives of at least one even-even neighbour has been taken from theory [5,6]. The magenta squares finally show as a subgroup the values of sf-activities being end products of α-decay chains observed in hot fusion reactions ^{48}Ca + actinide targets and ascribed to the decay of superheavy nuclei with Z > 112 (see e.g. [7]).

Despite the strong straggling of the data a trend towards lower hindrance factors at increasing Z^2/A is indicated, suggesting a lower influence of the odd nucleon on the fission life-times in the region of superheavy nuclei than for the actinides.

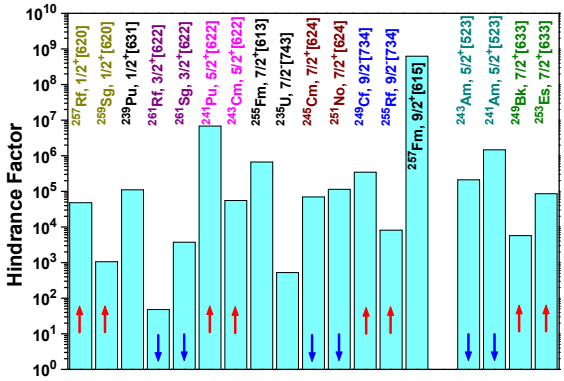

Fig. 1: Experimental sf hindrance factors of odd-mass nuclei

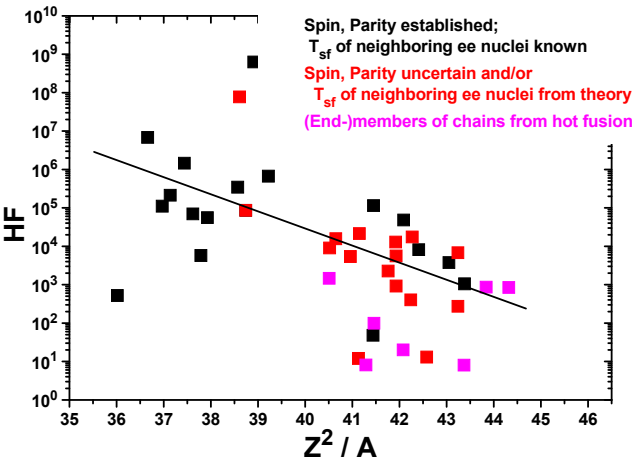

Fig. 2: sf hindrance factors of odd-mass nuclei plotted versus the fissility parameter Z^2/A

References

[1] G.T. Seaborg Phys. Rev. 85, 157 (1952)
[2] S.A.E. Johansson Nucl. Phys. 12, 449 (1959)
[3] J. Randrup et al. Nucl. Phys. A 217, 221 (1973)
[4] D.C. Hoffman et al. Nucl. Phys. A502, 21c (1989)
[5] R. Smolanczuk et al. Phys. Rev. C 52, 1871 (1995)
[6] R. Smolanczuk Phys. Rev. C 56, 812 (1997)
[7] Yu.Ts. Oganessian J. Phys. G: Nucl. Part. Phys. 34, R165 (2007)

* **supported by HI Mainz**

Spontaneous Fission Properties of ^{259}Sg and ^{255}Rf*

F.P. Heßberger[1,2], S. Antalic[3], D. Ackermann[1], M. Block[1,2], S. Heinz[1], S. Hofmann[1,4], Z. Kalaninová[3], I. Kojouharov[1], J. Khuyagbaatar[2,1], B. Kindler[1], B. Lommel[1], R. Mann[1]

[1]GSI, Darmstadt, Germany; [2]HIM, Mainz, Germany, [3]Comenius University, Bratislava, Slovakia, [4]Goethe Universität, Frankfurt a. Main, Germany

In a recent study decay properties of ^{259}Sg, produced in the reaction ^{206}Pb(^{54}Cr,n)^{259}Sg, were investigated at SHIP [1]. Alpha decay from two nuclear states in this isotope was observed: a) the ground state having a half-life of 411 ms and attributed to the Nilsson level 11/2$^-$[725]; b) an isomeric state located at $E^* \approx 92$ keV with a half-life of 254 ms, assigned as 1/2$^+$[620]. Search for spontaneous fission branches was rendered more difficult by the fact that the α-decay daughter ^{255}Rf has a fission branch of 52% and a half-life of 1.64 s [2]. Thus we searched for spontaneous fission events following the implantation of an evaporation residue (ER) within 10 s and not being preceded by an α-decay neither with full energy release nor with partial energy release in the focal plane detector. A probability $p_w < 0.05$ that a preceding α decay could have been missed and thus an sf event of ^{255}Rf wrongly assigned as an sf event of ^{259}Sg was estimated from the number of correlations α(^{259}Sg) – α(^{255}Rf) – α(^{251}No), α(^{259}Sg) – α(^{251}No) (without observation of α's of ^{255}Rf), and an ≈20% probability to observe only the escaping α-particle as obtained from α – γ - measurements.

Altogether 24 sf events not preceded by an α-decay were observed. Their time distribution (Δt(ER-sf)) is shown in fig. 1. A half-life $T_{1/2}$ = 235 +62/-41 ms was obtained. As the half-life is in-line with that of the α activity attributed to the decay of the 1/2$^+$[620] level, the sf activity is also assigned to it. From the number of α decays and spontaneous fission events a branching ratio b_{sf} = 0.06±0.015 was obtained, resulting in a partial half-life of $T_{sf} \approx 3.9$ s. Our branching ratio is in-line with $b_{sf} \approx 0.11$, obtained from each one α-sf – correlation in decay studies of ^{263}Hs [3,4].

A hindrance of fission in nuclei having odd proton and/ or neutron numbers compared to neigbouring even-even nuclei is well known. The degree of hindrance can be expressed by a hindrance factor HF defined as HF = T_{sf}/T_{sf}(unh), with the partial fission half-life T_{sf} and the hypothetical 'unhindered' fission half-life T_{sf}(unh), usually obtained as the geometric mean of the fission half-lives of the neighbouring even-even nuclei [5]. Using the known values for the neighbours ^{258}Sg (2.6 ms) [6] and ^{260}Sg (7.0 ms) [7] we obtain T_{sf}(unh)(^{259}Sg) = 4.3 ms, and thus HF ≈ 907, which is about an order of magnitude lower than the value for the daughter ^{255}Rf.

Striking differences have also been observed for the measured 'fission energies', which are displayed in fig. 2. It should be noted, that the probability to stop both fission fragments in the focal plane detector is only 30%. So in most of the cases the observed 'fission energy' represents the sum of the kinetic energy of one fragment and the energy loss of the other fragment. We observed for ^{259}Sg an about 10% higher mean energy value and a narrower distribution of the fission energies than for ^{255}Rf. This is presently regarded as sign of two components in the mass distribution of the fission fragments of ^{255}Rf, but only one component in that of ^{259}Sg, i.e. a transition from asymmetric fission of ^{255}Rf to symmetric fission of ^{259}Sg.

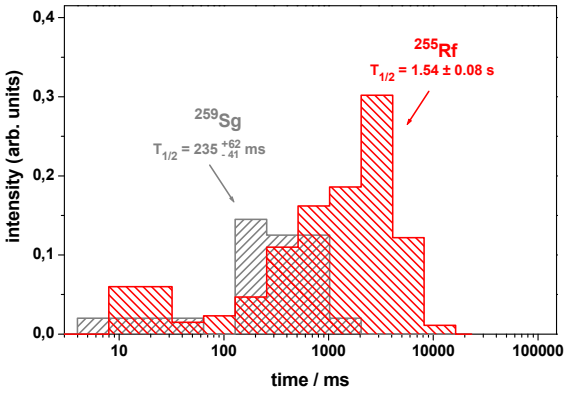

Figure 1: Time distributions Δt(ER-sf) of fission events not preceded by an α decay (^{259}Sg) and Δt(α-sf) of fission events preceded by an α decay (^{255}Rf)..

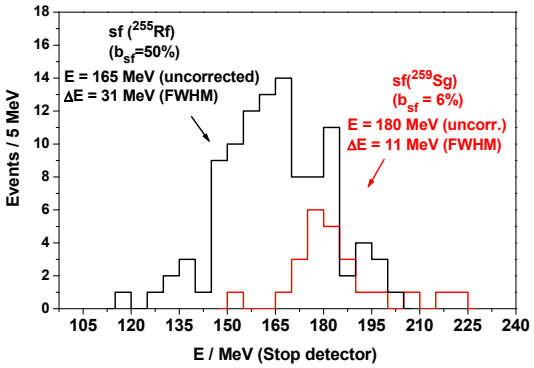

Figure 2: Energy distributions of fission events assigned to ^{255}Rf and ^{259}Sg. Given energy values are not corrected for pulse height defect.

References

[1] F.P. Heßberger et al. GSI Scientific Report 2011
[2] F.P. Heßberger et al. EPJ A 12, 57 (2001)
[3] I.Dragojevic et al. Phys.Rev.C79, 011602(R) (2008)
[4] D. Kaji et al. J. Phys. Soc. Japan 78, 035003 (2009)
[5] D.C. Hoffman Nucl. Phys. A 502, 21c (1989)
[6] F.P. Heßberger et al. Z. Phys. A 359, 415 (1997)
[7] F.P. Heßberger et al. EPJ A 41, 145 (2009)

*** supported by HI Mainz**

Identification of the Proton $2p_{1/2} \rightarrow 2p_{3/2}$ M1 Spin-Flip Transition in ^{87}Rb*

C. Stahl[1], J. Leske[1], N. Pietralla[1], P. R. John[2], G. Rainovski[3], J. Gerl[4], I. Kojouharov[4], and H. Schaffner[4]

[1]IKP, TU Darmstadt, Germany; [2]Univ. degli Studi di Padova and INFN Sezione di Padova, Padova, Italy; [3]Faculty of Physics, St. Kliment Ohridski Univ. of Sofia, Sofia, Bulgaria; [4]GSI, Darmstadt, Germany

M1 transitions between two spin-orbit partner orbitals with $j_> = l + 1/2$ and $j_< = l - 1/2$, so-called spin-flip transitions, with transition rates on the order of $B(M1) \approx 1\mu_N^2$ represent some of the strongest M1 transition rates observed in nuclei. In the semi-magic N=50 nucleus ^{87}Rb, the nuclear properties are governed by the proton $1f_{5/2}$, $2p_{3/2}$ and $2p_{1/2}$ orbitals. The Fermi surface is located between the $2p_{3/2}$ and $2p_{1/2}$ orbitals, which is reflected in the $J^\pi = 3/2^-$ ground state of ^{87}Rb. Shell model calculations indicate that the second excited state of ^{87}Rb at 845.4 keV is dominated by the $2p_{1/2}$ orbital and thus is the spin-orbit partner of the $2p_{3/2}$-dominated ground state [1]. The experimental proof for this assumption is still pending, since the spin of the 845.4-keV state could so far not unambiguously be determined although the orbital quantum number $l = 1$ of this state is already known from (^{3}He, d) [2] and (d,^{3}He) measurements [3, 4]. Since the transition strength for the 845-keV M1 transition to the ground state of ^{87}Rb is already known to be sufficiently large [1], a determination of the spin of the 845-keV state will decide whether the respective transition really is the dominant part of the proton $2p_{1/2} \rightarrow 2p_{3/2}$ spin-flip transition.

This spin assignment was achieved [5] by measuring the lifetime of the 845-keV state and comparing the resulting transition strength for the deexcitation, $B(M1)\downarrow$, to the transition strength for the excitation of this state, $B(M1)\uparrow$, which is known from a (γ, γ') measurement [1]:

$$J_2 = \frac{1}{2}\left[(2J_1+1)\frac{B(M1)\uparrow}{B(M1)\downarrow} - 1\right] = 0.56(19) \qquad (1)$$

Here, J_2 denotes the spin quantum number of the excited 845-keV state and $J_1 = \frac{3}{2}$ the spin of the groundstate of ^{87}Rb. The level lifetime of the 845-keV state was measured using the Doppler-shift attenuation method (DSAM) after the proton-transfer reaction ^{12}C(^{86}Kr,^{11}B)^{87}Rb, which was observed in experiment U246 performed at the X7 experimental station at GSI in Oktober 2011. In this experiment, an isotopically pure beam of ^{86}Kr with an energy of 2.85 MeV/u provided by the UNILAC accelerator impinged on a multi-layered target consisting of 0.33 mg/cm^2 $^{\rm nat}$C followed $^{\rm nat}$Gd, $^{\rm nat}$Ta and $^{\rm nat}$Cu. The original aim of the experiment was to populate low-lying states in ^{86}Kr and ^{90}Sr by Coulomb excitation and an α-transfer reaction, respectively, for the measurement of g-factors by the transient field technique. However, also deexcitation γ-rays from the excited ^{87}Rb nuclei were detected in coincidence with the target-like reaction recoils by four EUROBALL cluster HPGe detectors. The γ-events were sorted into 6 groups of identical polar angle of γ-ray detection with respect to the beam axis. A fit of calculated lineshapes to the experimentally observed spectra was performed using the computer code APCAD [6]. A mean lifetime of $\tau = 146(\pm 10)_{stat}(^{+8}_{-12})_{sys}$ fs for the 845-keV state could be extracted from the data, where the systematic error stems from uncertainties of the ion stopping powers that were assumed in the analysis process. The corresponding M1 transition strength for the deexcitation is $B(M1)\downarrow = 0.644^{+0.075}_{-0.053}\mu_N^2 = 0.36^{+0.04}_{-0.03}$ $W.u.$ With this information, the spin of the excited state at 845 keV could be pinned down to be $\frac{1}{2}$ (see Fig. 1), comfirming the dominant proton $2p_{1/2} \rightarrow 2p_{3/2}$ M1 spin-flip character of the 845-keV transition.

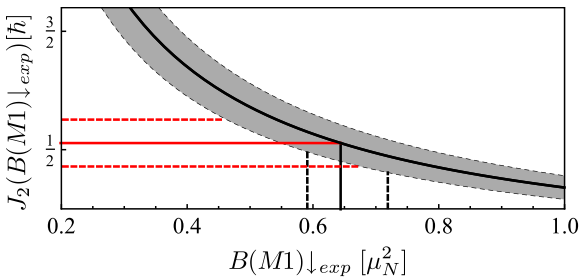

Figure 1: Determination of the spin of the 845-keV state of ^{87}Rb using eq. 1, the value of $B(M1)\uparrow$ determined in a (γ, γ') experiment [1] and the value of $B(M1)\downarrow$ determined in this work. The gray band depicts the functional dependance of the derived spin from the measured value of $B(M1)\downarrow$, accounting for the experimental uncertainties of $B(M1)\uparrow$. The horizontal lines mark the spin of the 845 keV state of ^{87}Rb resulting from the value of $B(M1)\downarrow$ measured in this work (vertical lines).

*This work was supported by the BMBF under grant 05P12RDFN8, by the German-Bulgarian exchange program under Grant Nos. PPP 50751591 and DNTS/01/2/2011 and resources of the European gammapool.

References

[1] L. Käubler *et al.*, Phys. Rev. C **65** (2002) 054315

[2] L. R. Medsker *et al.*, Phys. Rev. C **12** (1975) 1516-1523

[3] J. F. Harrison *et al.*, Nucl. Phys. A **185** (1972) 385-402

[4] J. R. Comfort *et al.*, Phys. Rev. C **8** (1973) 1354-1362

[5] C. Stahl *et al.*, to be published

[6] C. Stahl, Master thesis, TU Darmstadt (2011)

Carbonyl Complex Formation of Short-Lived Ir and Re Isotopes*

J. Even[1#], A. Yakushev[2], Ch.E. Düllmann[1,2,3], J. Dvorak[1], R. Eichler[4], O. Gothe[5], D.Hild[3], E. Jäger[2], J. Khuyagbaatar[1,2], J.V. Kratz[3], J Krier[2], L. Niewisch[3], H. Nitsche[5], I. Pysmenetska[3], M. Schädel[2,7], B. Schausten[2], A. Türler[4,6], N. Wiehl[1,3], D. Wittwer[4,6]

[1]HIM, Mainz, Germany, [2]GSI, Darmstadt, Germany; [3]University Mainz, Mainz, Germany; [4]PSI, Villigen, Switzerland, [5]LBNL, Berkeley, CA, USA; [6]University of Bern, Bern, Switzerland; [7]JAEA, Tokai, Japan

We recently reported on the in-situ carbonyl complex formation of short-lived group 6 and group 8 elements [1]. These elements are well known to form mononuclear, volatile carbonyl complexes. However, no mononuclear, binary complexes of group 7 and 9 elements are known from literature (see e.g. [2]). We studied the transport of short-lived Ir and Re isotopes in a He-CO atmosphere, which gives a hint at the formation of volatile carbonyl complexes of these elements.

In first experiments at the TRIGA reactor in Mainz, the transport of fission products of the neutron induced fission of ^{249}Cf in a CO containing gas-stream was studied. The transported isotopes were collected on a charcoal filter and measured with a γ detector. Volatile fission products as well as short-lived isotopes of the refractory elements Mo, Tc, Ru and Rh were identified. However, precursor effects prevent a clear assignment to the transported element. To get a better understanding, the homologs Re and Ir were produced in ^{24}Mg-induced fusion reactions with ^{nat}Eu and ^{nat}Tb targets at the gas-filled separator TASCA. The recoiling isotopes were separated from the primary beam and transfer products in TASCA and thermalized in the recoil transfer chamber in a He-CO atmosphere. The volatile species were transported in the gas stream through a 10-m long capillary to a charcoal filter which was monitored by a γ detector. This way the transport of $^{178\text{-}179}$Ir and $^{170\text{-}172/172m}$Re was observed. Both, Re and Ir, apparently form volatile complexes with CO under these experimental conditions.

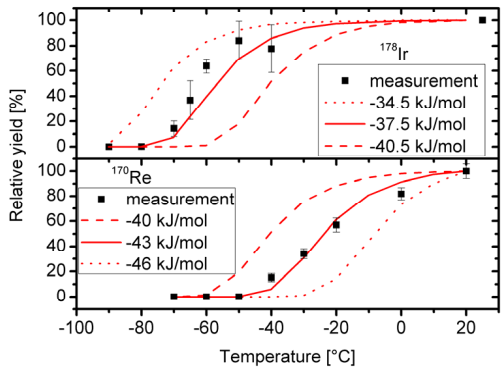

Figure 1: Transport yield of Re and Ir depending on the temperature of the isothermal chromatography column. The lines show results of Monte Carlo Simulations.

* Work supported by the Helmholtz Institute Mainz, the Research Center Elementary Forces and Mathematical Foundations (EMG), the BMBF under contract No. 06MZ223I, and the Swiss National Science Foundation under contract No. 200020 126639 #j.even@gsi.de

In further investigations the adsorption and decomposition of these complexes were studied. In the adsorption-studies on a quartz surface, the gas-stream was guided through an isothermal quartz column. The temperature was varied from measurement to measurement and the transport yield through the column was determined for each temperature. These measurements were modeled with Monte Carlo Simulations, which yield values for the adsorption enthalpy of these complexes on the quartz surface. For the Re complexes the adsorption enthalpy was determined to be (−43 ± 3) kJ/mol, and for the Ir ones (−37.5 ± 3.0) kJ/mol. Figure 1 shows the breakthrough curves and the results of the Monte Carlo Simulations. The thermal stabilities of these compounds were studied by passing the gas stream through a quartz wool plug heated by an oven before reaching the charcoal filter. The transport yields were determined for various temperatures. (see Figure 2) The complexes start to decompose at temperatures around 300°C.

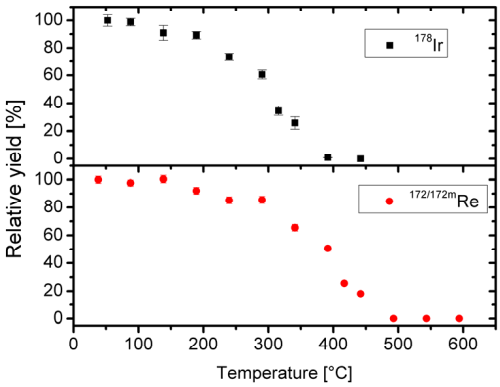

Figure 2: Transport yield of Re and Ir vs. the temperature of the quartz wool plug in the decomposition setup.

The experimental observation of the transport of Re and Ir in a CO-containing gas stream gives a hint on the formation of volatile complexes in CO. Further studies are planned to elucidate the nature of these complexes, which might open the door for bohrium and meitnerium chemistry experiments.

References

[1] J. Even et al., Inorg. Chem. **51**, 6431-6433 (2012).
[2] H. Werner, Angew. Chem. Int. Ed. **29**, 1077-1089 (1990).

Chemistry for Isobar Separation behind SHIP*

J. Even[1#], D. Ackermann[2], M. Block[2], H. Brand[2], Ch.E. Düllmann[1,2,3], E. Jäger[2]; J. Khuyagbaatar[1,2], B. Kindler[2], J.V. Kratz[3], J. Krier[2], B. Lommel[2], F.P. Heßberger[1,2], J. Maurer[2]; J. Steiner[2], Th. Traut[3], N. Wiehl[1,3] and A. Yakushev[2]

[1]Helmholtz-Institut Mainz; Germany; [2]GSI, Darmstadt, Germany; [3]Johannes Gutenberg-Universität Mainz, Germany.

Recoil separators are powerful instruments for the isoltation of desired nuclear reaction products. However, separation of ions of similar masses and isobaric nuclides is not possible at such a device without additional separation stages. One possibility for a second separation step is provided by chemistry. Two recoil separators at GSI are dedicated to superheavy element research – the velocity filter SHIP and the gas-filled separator TASCA. At gas-filled separators like TASCA, the coupling with chemistry setups is established[1]. In contrast, no vacuum separator has been used as a preseparator for chemical investigations so far. We have demonstrated that SHIP also can be combined with chemistry setups. Recently the in-situ formation of volatile metal carbonyl complexes was studied at TASCA [2,3]. Recoiling W, Re, Os, and Ir isotopes were thermalized in a CO containing atmosphere and formed volatile complexes. These complexes were transported in a gas jet over several meters to detection setups.

Short-lived Ta isotopes as well as Re and W isotopes were produced in the complete fusion reaction of ^{48}Ca projectiles with a ^{133}Cs^{127}I target at SHIP, in order to investigate the behaviour of Ta under comparable conditions. The Recoil Transfer Chamber (RTC), which was originally built for experiments at TASCA in the small image mode, was attached to SHIP. The chamber was separated from the high vacuum of SHIP by a 5.8-µm thick Mylar window supported by a honeycomb grid. The size of the RTC window was 3 cm × 4 cm. The chamber was cylindrical with an inner diameter of 3 cm. The depth of the RTC was 3 cm.

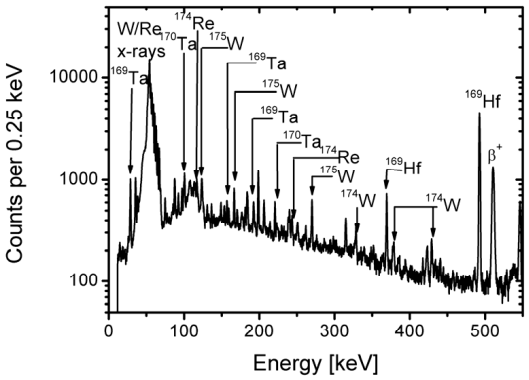

Figure 1: γ-spectrum of fusion products stopped in Al-foil behind SHIP.

In the first part of the experiment, an aluminium catcher foil was placed 5 mm behind the RTC window, where the recoiling ions were collected for 30 min. Within 2 min the foil was taken out of the RTC, placed in front of a γ detector, and measured for 10 min. Figure 1 shows a typical spectrum. γ-lines of ^{170,169}Ta produced in the reaction ^{127}I(^{48}Ca, 5-6n) and ^{174}Re produced in the reaction ^{133}Cs(^{48}Ca,7n) were observed. Furthermore ^{174,175}W and ^{169,170}Hf were identified. These are either produced in the (^{48}Ca,p xn)- reactions, or are decay products of the Re and Ta isotopes. In the second part of the experiment the catcher foils were removed, and the RTC was flushed with either a He/CO mixture or pure CO. The gases were purified by passing oxysorb and hydrosorb cartidges. The pressure in the RTC was kept at 600 hPa. The recoiling ions were thermalized in the RTC and all volatile compounds were transported in the gas stream out of the RTC through a 566 cm long capillary to a filter of activated charcoal. The volatile compounds adsorbed on the charcoal filter, which was monitored with the γ detector. Figure 2 shows a spectrum of the charcoal trap. Only W and Re isotopes were identified. No Ta and Hf isotopes were observed in the spectra.

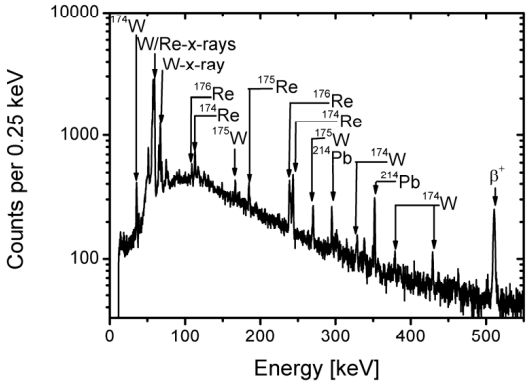

Figure 2: γ-spectrum of the charcoal filter. Pb γ-lines originate from the natural background.

This confirms former results that W and Re form volatile complexes in a CO atmosphere. However, Ta and Hf were not transported so that the formation of volatile complexes with CO was excluded. Gas phase carbonyl chemistry is therefore an appropriate tool to separate group 4 and 5 elements from group 6 and 7 elements and can thus be used for isobar separation.

References

[1] Ch.E. Düllmann et al., Radiochim. Acta **99** (2011), 515.
[2] J. Even et al., Inorg.Chem. **51**, (2012) 6431-6433.
[3] J. Even et al., this report.

* Work supported by the Helmholtz Institute Mainz, and the BMBF under contract No. 06MZ7165I,
#j.even@gsi.de

Towards Radiation Detected Resonance Ionization Spectroscopy of Nobelium*

F. Lautenschlaeger[1], *M. Laatiaoui*[2,3], *M. Block*[2,3], *W.Lauth*[4], *H.Backe*[4], *F.P. Hessberger*[2,3], *Th. Walther*[1], *and P. Kunz*[5]

[1]TU Darmstadt; [2]GSI, Darmstadt; [3]HIM Mainz; [4]JGU Mainz; [5]TRIUMF, Vancouver, Canada

Relativistic effects are responsible for the change in the atomic structure and thus the order of the periodic table of the heaviest elements. In addition correlations between the many electrons in the shells are crucial. Nowadays, these relativistic effects can be described by using modern Multi-Configuration-Dirac-Fock (MCDF)[2] and Relativistic Coupled-Cluster (RCC)[3] calculations. A comparison of the predicted and the measured atomic properties is needed for benchmarking these theoretical predictions. At present, no data are available on the atomic level schemes of transfermium elements as they can be experimentally investigated solely online at low production rates. Thus, the study of the atomic structure of transfermium elements, e.g. nobelium (No) and lawrencium (Lr) via Radiation Detected Resonance Ionization Spectroscopy (RADRIS)[1] belongs to one of the most fascinating and challenging problems of modern atomic physics.

Based on RADRIS, it is possible to investigate the atomic properties of these elements. After separation from the primary beam by the velocity filter SHIP [4], the fusion products enter a buffer gas cell, where they are stopped in 50 mbar argon and collected on a tantalum filament. The next step is to re-evaporate the atoms and to ionize them with tunable lasers in a two-step photoionization process. In case of resonance ionization, the such created ions are transferred to a Si-detector with which they are identified by their characteristic α-decay. An optical buffer-gas cell for this method has been commissioned during a beamtime in 2006 with the radionuclide ^{155}Yb, a chemical homologue of nobelium. During this experiment, an overall efficiency of about 0.8% was obtained [1].

Meanwhile, this buffer-gas cell has been installed permanently at GSI, including a dedicated laser cabin. Extensive off-line measurements concerning the impact of critical parameters like buffer gas pressure, filament temperature, filament geometry, laser power, and laser repetition rates on the laser resonance ionization efficiency have been performed with nat. ytterbium. Among others, the position of the atomic cloud above the filament was mapped by the RIS ion signal for different filament temperatures and buffer-gas pressures. Due to convection phenomena above the filament, the atoms of interest diffuse out of the laser beam interaction volume resulting in a decrease of the resonance ionization efficiency.

Such problems require an on-line monitoring of the RIS efficiency during envisaged RADRIS experiments on the element nobelium, which can be produced at SHIP via the reaction ^{208}Pb(^{48}Ca,2n)^{254}No at a rate of 17/s. For that purpose and for the commissioning of a new data acqusition and several digital laser control systems we have performed an online experiment on ^{155}Yb in 2012. The radio nuclide ^{155}Yb has been produced in the reaction ^{112}Sn(^{48}Ca,5n)^{155}Yb at a typical particle beam intensity of I_p= 50 nA$_P$ (3 Hz parasitic) and an estimated incoming rate of about $R \approx 180\frac{1}{s}$ in front of the entrance window. In this experiments the efficiency of the gas cell has been measured. An evaporation and RIS efficiency of $\epsilon_{Evap} \cdot \epsilon_{RIS} \approx 15\%$ was determined, similar to that obtained in Ref. [1]. From this value, the overall efficiency of the gas cell could be determined as $\epsilon^{tot} \approx 0.8\%$. Based on this performance, we are ready to search for atomic states in nobelium in future on-line experiments.

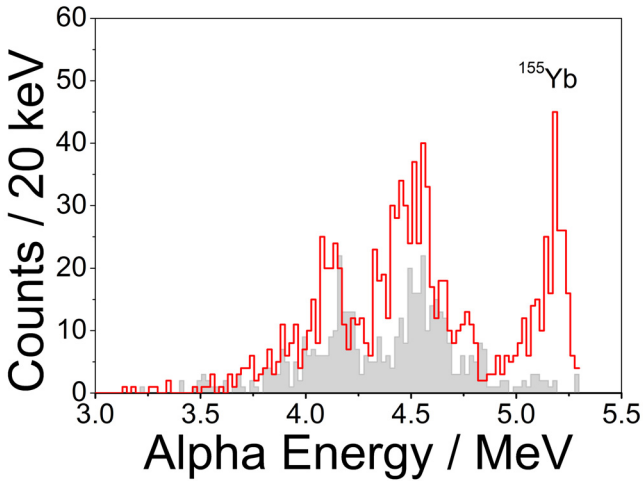

Figure 1: Two-step resonant laser ionization of ^{155}Yb. Alpha spectrum with laser on (red line) and off (black line). The measurement was performed for a buffer-gas pressure p= 60.4 mbar, filament current I_{fil} = 2.6 A, laser excitation energy equivalents ν_1 = 25068.3 cm^{-1}, ν_2 = 25026.2 cm^{-1}, laser pulse energy P(λ_1)= 133 μJ, P(λ_2)= 242 μJ, laser repetition rate L_{rep} = 100 Hz, and laser beam diameter d_{laser} = 40 mm.

References

[1] H. Backe et al., *Eur. Phys.* J. D **45**, 99-106 (2007).

[2] S. Fritzsche, *Eur. Phys.* J. D **33**, 15 (2005)

[3] Borschevsky et al., *Phys. Rev.* A **75**, 042514 (2007)

[4] G. Muenzenberg et al., *Nucl. Instr. and Meth.* **161**, 65-82 (1979).

* Work supported by the BMBF (FAIR NuSTAR 06DA70471 9, FAIR NuSTAR 05P12RDFN8) and the Helmholtz-Institut Mainz.

First Extraction Measurements with the Cryogenic Gas Stopping Cell at SHIPTRAP*

C. Droese[1], *K. Blaum*[2], *M. Block*[3], *S. Eliseev*[2], *F. Herfurth*[3], *M. Laatiaoui*[4], *F. Lautenschläger*[5], *G. Marx*[1], *E. Minaya Ramirez*[4], *L. Schweikhard*[1], *and P. G. Thirolf*[6]

[1]Ernst-Moritz-Arndt-Universität Greifswald; [2]Max-Planck-Institut für Kernphysik Heidelberg; [3]GSI Darmstadt; [4]Helmholtz-Institut Mainz; [5]Technische Universität Darmstadt; [6]Ludwig-Maximilians-Universität München

One of the open questions in modern nuclear physics is the existence and the exact location of the so called 'Island of Stability' of superheavy elements. The evolution of the nuclear binding energy close to the region of the superheavy elements, an indicator of nuclear stability, can be obtained by high-precision mass measurements. Recently, the masses of $^{252-255}$No [1] and ^{255,256}Lr [2] were directly measured for the first time with the Penning-trap mass spectrometer SHIPTRAP. From the results the strength of the deformed shell closure at neutron number N = 152 has been determined experimentally.

To extend the reach of SHIPTRAP towards superheavy elements it is crucial to increase the overall efficiency of the setup. The bottleneck is the deceleration of the fusion-evaporation reaction products from SHIP from a kinetic energy of MeV down to meV in a gas stopping cell. Thus, a second generation gas stopping cell (CryoCell) operating at cryogenic temperatures was built as described in detail in [3]. An increase of the overall efficiency by at least a factor of 5 [4] is anticipated.

In August 2012 the first measurement of the extraction efficiency was performed with a ^{223}Ra (half-life 11.43 days) recoil ion source. Figure 1 shows the alpha spectrum obtained in vacuum to determine the initial activity of ^{223}Ra. Afterwards, the source was placed axial symmetrically in front of the largest ring electrode of the RF-Funnel inside the CryoCell. From there, the recoil ions, *i.e.* ^{219}Rn$^+$ (half-life 3.96 s), are extracted. The number of extracted ^{219}Rn$^+$ ions was determined with a silicon detector placed behind the extraction radio-frequency quadrupole (RFQ). The ^{219}Rn recoils were accumulated on an aluminium foil with a thickness of 0.8 μm at -1400 V positioned in front of the detector. Direct implantation of the ^{219}Rn$^+$ ions would corrupt the result. Due to its noble gas configuration a major fraction of the extracted ions would diffuse out of the silicon detector before the decay occurs. The resulting alpha spectrum looks similar to that shown in Fig. 1 however without the lines of the ^{223}Ra decay. The number of ^{219}Rn$^+$ ions detected behind the Extraction RFQ is compared to the number of ^{219}Rn$^+$ recoil ions emitted by the ^{223}Ra source that can be derived from the initial activity. Taking into account the exponential decay of the initially determined activity of ^{223}Ra and the solid angle covered by the silicon detector the extraction efficiency was calculated. The measurement was performed at room temperature and at 40 K. A similar buffer-gas flow (1 mbar·l·s^{-1}) of ultra pure helium (purity 99.9999 %) was used which corresponds to a pressure of 60 mbar at 300 K and 21 mbar at 40 K, respectively. DC-gradients of 7 V/cm at the DC-Cage, 2 V/cm at the RF-Funnel and 0.2 V/cm at the Extraction RFQ were applied. RF amplitudes of 160 V at the RF-Funnel for a frequency f = 1014 kHz and 240 V at the Extraction RFQ (f = 907 kHz) were used. At room temperature a maximum extraction efficiency of 37(3) % was obtained. The extraction efficiency increased to 64(3) % as the system was cooled to 40 K. The operation at cryogenic temperatures, *e.g.* the increased buffer-gas cleanliness, result in a relative gain in transmission efficiency of 75 % compared to the operation at room temperatures. An experiment with a radioactive ion beam, directly delivered by SHIP, will be performed soon to confirm this promising result that will pave the way towards high-precision mass measurements of superheavy elements at SHIPTRAP.

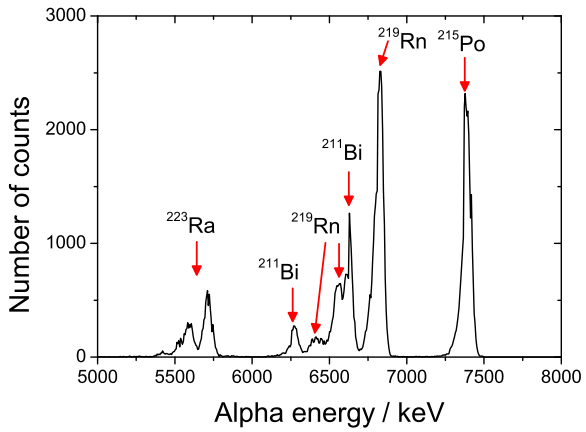

Figure 1: Alpha-decay spectrum obtained in 3600 s with a ^{223}Ra recoil ion source.

*We acknowledge the support of the German BMBF (Grants 05P09HGFN5, 05P12HGFN5, 06ML9148), GSI (Grants LMTHIR1012 and GFMARX1012) and the Max-Planck Society.

References

[1] M. Block et al., Nature 463 (2010) 785

[2] E. Minaya Ramirez et al., Science 337 (2012) 1207

[3] C. Droese et al., GSI Scientific Report 2012

[4] S. Eliseev et al., Nucl. Instr. Meth. B 266 (2008) 4475

Preparation of ^{249}Bk targets

J. Runke[1], R.A. Boll[2], Ch.E. Düllmann[1,3,4], K. Eberhardt[3,4], B. Kindler[1], B. Lommel[1], C. Mokry[3], J.B. Roberto[2], K.P. Rykaczewski[2], P. Thörle-Pospiech[3], N. Trautmann[3], A. Yakushev[1]

[1]GSI Helmholtzzentrum für Schwerionenforschung GmbH, Darmstadt, Germany; [2]Oak Ridge National Laboratory, Oak Ridge, TN, USA; [3]Johannes Gutenberg-Universität Mainz, Germany; [4]Helmholtz-Institut Mainz, Germany

In the year 2012 two long experiments to synthesize the elements 119 and 117 have been performed at the gas-filled recoil separator TASCA at GSI. In both experiments ^{249}Bk was used as the target material, which was bombarded with ^{48}Ca for the synthesis of element 117 and ^{50}Ti to search for the new element 119.

For this, a ^{249}Bk target-wheel was used [1]. 12.7 mg ^{249}Bk in form of the nitrate were provided by Oak Ridge National Laboratory. The target segments were produced by Molecular Plating (MP) with high deposition yields at the Institute for Nuclear Chemistry at the University of Mainz [2,3].

The total amount of ^{249}Bk was delivered in four quartz vials covered with a Teflon septum. This septum was penetrated with a syringe containing 100 µl 0.1 M HNO_3 to dissolve the ^{249}Bk nitrate prior to the MP. After complete dissolution, the solution was transferred into the electrochemical deposition cell (EDC). The quartz vial was washed with 1 ml isopropanol and this solution was also transferred to the EDC. Finally 51 ml isobutanol were added.

The EDC [3,4] is made from polyether-etherketone (PEEK). On one side of the EDC, the target backing - a thin (~2 µm) Ti-foil produced by cold rolling and glued on an Al frame at the GSI Target Laboratory - was mounted and acted as the cathode. As an anode, a Pd-foil in the same geometry as the target frame was used. The EDC was clamped between two water cooled Ti blocks. For the mixing of the ^{249}Bk solution, an ultrasonic stirrer was applied. The deposition parameters for ^{249}Bk were similar to those for ^{249}Cf targets produced in 2011 [5], i.e., a current density of 0.3 mA/cm^2 was applied, resulting in voltages of 300 to 600 V. After deposition times of 3 to 4 hours target thicknesses of 354±18 – 508±25 µg/cm^2 with deposition yields exceeding 90 % were obtained.

The deposition yield and kinetics were determined by α-particle and γ-ray spectroscopy. Prior to the start of the deposition and then in one hour steps during the deposition, 10 µl aliquots of the supernatant solution were evaporated to dryness and measured by α-particle spectroscopy. Due to the rather short half-life of ^{249}Bk, its daughter, ^{249}Cf, is also present in the solution. Because both isotopes have α branches with significantly different α-particle energies, the deposition of both elements can be followed simultaneously in this way. The deposition kinetics of ^{249}Bk and ^{249}Cf are very similar. This allows the determination of the ^{249}Bk target thickness also via the γ-rays from ^{249}Cf, which is not possible for ^{249}Bk directly due to the absence of suitable γ-lines. For the determination of the deposition yield by γ-ray spectroscopy, a thin ^{249}Bk target was used as reference sample. The results of the yield determination by α-particle and γ-ray spectroscopy are in good agreement with each other. The average thickness of the target on the day of production was 463±23 µg/cm^2. The target segments were delivered to GSI and mounted on a target-wheel as shown in Fig. 1. The produced ^{249}Bk targets were able to resist a high total beam dose with beam intensities of over 4 particles microAmp for a long time.

Figure 1: ^{249}Bk target-wheel

Acknowledgments:
We are very thankful to the Oak Ridge National Laboratory for providing ^{249}Bk. The authors thank the Target Laboratory at GSI for providing the Ti-backing foils and the Mechanical Workshop of the Institute for Nuclear Chemistry in Mainz for the construction of the plating cells. This work was supported by the Helmholtz Institute Mainz.

References

[1] Jäger E, et al. (2012) submitted to J. Radioanal. Nucl. Chem.
[2] Eberhardt K, et al. (2008) Nucl. Instrum. Meth. Phys. Res. A 590:134-140
[3] Runke J, et al. (2012) submitted to J. Radioanal. Nucl. Chem.
[4] Haba H, et al. (2006) RIKEN Accel. Prog. Rep. 39:109
[5] Düllmann ChE, et al., GSI Sci. Rep. 2011 (2012), p. 206, PHN-NUSTAR-SHE-02

High Intensity TASCA Target Wheel Control System and Target Monitoring

E. Jäger[1], H. Brand[1], Ch.E. Düllmann[1,2,3], J. Khuyagbaatar[1,3], J.Krier[1], M. Schädel[1], T. Torres[1], A. Yakushev[1]

[1]GSI Helmholtzzentrum für Schwerionenforschung GmbH, Darmstadt, Germany; [2]Johannes Gutenberg-Universität Mainz, Mainz, Germany; [3]Helmholtz-Institut Mainz, Mainz, Germany

The gas-filled recoil separator TASCA [1], optimized for actinide-target based hot fusion reactions, was recently used for studies of superheavy elements with Z = 115,117 and for the search for new elements [3,4]. These experiments require transuranium targets made from isotopes that are produced in high-flux nuclear reactors and are available only in very limited amounts [5-7]. At the GSI Darmstadt, the UNILAC provides intense beams, delivered with a 25% duty cycle (5 ms pulse length, 50 Hz repetition rate). Due to small cross sections for the production of the heaviest elements, maximum beam intensities are applied, which in turn put a large heat load onto the target.

At TASCA, a new target wheel has recently been developed [8], which was optimized for maximum applicable beam intensities, respecting the available amounts of target material, the desired areal density of 0.5 mg/cm^2, the maximum permissible beam spot size of 8 mm diameter, and the beam macrostructure. This new target wheel rotates at 2250 rpm and consists of four individual target segments with 6 cm^2 area each, necessitating about 12 mg of target material (Figure 1). Each beam pulse illuminates one single target, which subsequently cools during 75 ms before being hit by the next pulse. The target wheel is placed inside a target cassette. Upstream of the target wheel, a second wheel can be mounted, e.g., containing carbon stripper foils to increase the charge state of the beam.

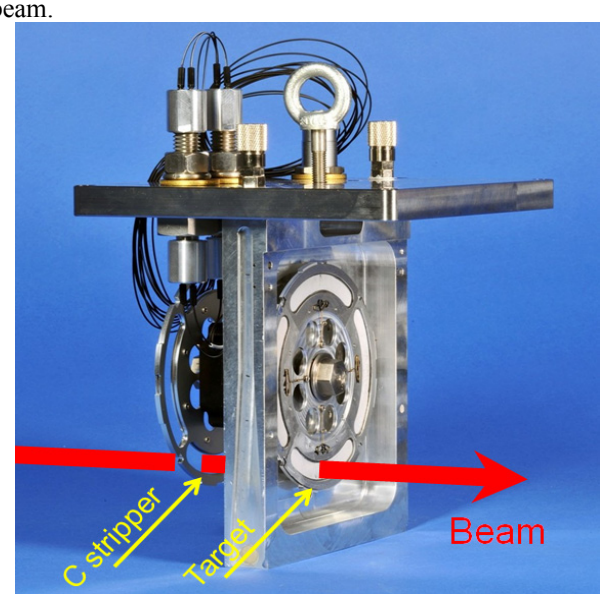

Figure 1. Photograph of the new TASCA target wheel.

The wheels are driven by a stepper motor (Nanotec). The wheel position control is provided by a microcontroller SPS and an industrial PC, which use signals from 2 photodiodes outside the target chamber connected to the target cassette through light fibers. This allows synchronizing the wheel rotation with the beam macrostructure such that each individual macro pulse illuminates a single target segment.

To insure target integrity, several on-line as well as off-line monitoring possibilities are exploited. The on-line control is a part of the "TASCA Control System" (Figure 2) and is based on a beam current measurement and a contact-free temperature measurement of the beam-spot area with a pyrometer. Upon violation of user-defined thresholds, or asynchronous rotation, the beam is switched off within 1 µs. Off-line capabilities include the monitoring of the target and the carbon stripper foil wheel with two endoscopes, which allows obtaining sets of 36 pictures covering all four segments. If the target isotope has a significant α branch, the α particles can be guided to the focal plane detector in TASCA, where the rate of incoming α particles and the energy spectra yield information on the target thickness and status of the layer.

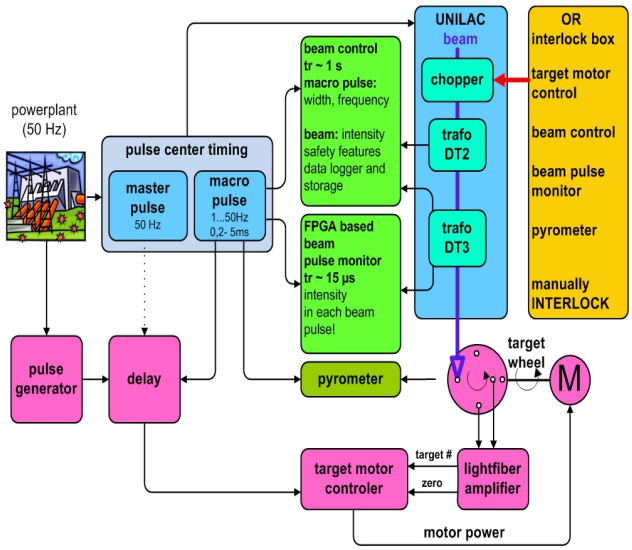

Figure 2. Scheme of on-line target monitoring system.

[1] A. Semchenkov et al., NIMB 266 (2008) 4153
[2] J.M. Gates et al., PRC 83 (2011) 054618
[3] J. Khuyagbaatar et al., This GSI Annual Report.
[4] U. Forsberg, Acta Phys. Pol. B 43 (2012) 305.
[5] J.E. Bigelow et al., ACS Symp. Ser. **161**, 3-18 (1981).
[6] K. Eberhardt et al., NIMA 590, 134-140(2008).
[7] J. Runke et al., J. Radioanal. Nucl. Chem. (in print).
[8] E. Jäger et al., J. Radioanal. Nucl. Chem. (in print)

^{50}Ti for a High-Intensity Heavy-Ion Beam

Bettina Lommel[1], Andreas Beusch[1], Willi Hartmann[1], Annett Hübner[1], Birgit Kindler[1], Jutta Steiner[1], Vera Yakusheva[2,1]

[1]GSI, Darmstadt, Germany; [2] Helmholtz-Institut Mainz, 55099 Mainz, Germany

The semi-magic ^{50}Ti has a closed neutron shell with N = 28 and is the most neutron rich of the stable Ti-isotopes. This makes the isotope especially interesting as a beam projectile for heavy-element synthesis. For the production of a high intensity ion beam over long time periods, the metallic form of the enriched isotope is preferable for both, ECR and PIG ion sources.

Highly enriched ^{50}Ti is delivered either as the dioxide or as the tetrachloride. The task was to establish a process to reduce the compound to the metal with a high efficiency and a high chemical purity.

Process

For the reduction process we preferred the solid TiO_2 to the liquid $TiCl_4$ since handling gaseous $TiCl_4$ at higher temperatures needed for the reduction process involves a higher risk of losing material. For the TiO_2 there are in principle two common routes for reducing it to the metal either with metallic Ca or with CaH_2 as reducing agent [1]. Since for the affectivity of the reduction the purity of the Ca is crucial we decided to use the CaH_2 in the process. The Ca vapours are generated within the mixture via thermal decomposition of the hydride and can react immediately with the adjacent TiO_2.

The process chosen [2] is described by the following chemical equation:

$$TiO_2 + 2\ CaH_2 \rightarrow Ti + 2\ CaO + 2\ H_2 \uparrow \qquad (1)$$

For the reduction we prepared a mixture of the two components in an agate mortar with a 40% access of CaH_2 to the stoichiometric composition described by the reaction equation (1) and pressed to tablets with a hydraulic press. The tablets are heated in a molybdenum boat inside a stainless steel tube at 950°C for an hour in a constant flow of dry argon. After the reduction the tablets now containing Ti-metal, CaO and rest of Ca are cooled down to room temperature, dissolved in diluted acetic acid; then the precipitate is washed and dried, obtaining a fine powder of metallic Ti.

Analysis

At first the setup and the process were tested with different batches of natural TiO_2 where a yield of 95 % was achieved. For the application in the ion sources ten different batches of $^{50}TiO_2$ from three different producers were reduced. The starting material obviously differed in colour, in grain size and in softness leading to quite different behaviour by pressing tablets for the reduction and by melting metallic Ti, as well as a significantly variation in yield during reduction.

To get an understanding of the impurities in the starting material and their behaviour during the reduction process, energy-dispersive x-ray analysis (EDX) of all batches before and after the reduction was applied. In the natural material no impurities were detectable before the reduction, after the reduction a Ca-content of ~ 0.3 – 0.6 % was observed. Several batches of the enriched $^{50}TiO_2$ showed no impurities before and only the expected amount of calcium after the reduction. But a number of batches had impurities of Cl, Si or Sn or a combination of those. All impurities were in in the range of 1.5 % up to 5 %. The Cl vanished completely after the reduction, whereas the Si and the Sn stayed in the same amount.

The different impurities caused different behaviour in the further processing especially by melting tablet of Ti powder to beads.

Results

With the new setup we are able convert between 0.5 g up to several grams of highly enriched ^{50}Ti in one run with yields between 90 % and 98 %. Different impurities in the starting material influence the melting behaviour and therefore the final yield significantly. We obtain enriched metallic titanium for application in the ion source or as a starting material for target production. The reduced material was used at UNILAC for production of ^{50}Ti-beam with intensities of about 1 particleμA at a target for experiments which lasted several month in 2011 and 2012 [3,4,5].

References

[1] Handbuch der präparativen anorganischen Chemie (ed. G. Brauer) Ferdinand Enke Verlag, Stuttgart 1978, vol. 2

[2] W. Freundlich, M. Bichara, Comptes rendus hebdomadaires des séances de l'Académie des sciences / publiés par MM. les secrétaires perpétuels T238 (1954) p. 1324.

[3] K. Tinschert et al., this report.

[4] R. Hollinger, this report.

[5] B. Lommel, A. Beusch, W. Hartmann, A. Hübner, B. Kindler, J. Steiner, V. Yakusheva, J. Radioanal. Nucl. Chem. to be published.

β-decay of very neutron-rich Rh, Pd, Ag nuclei

K. Smith[1,2,3], *J. Agramunt-Ros*[4], *A. Algora*[4], *J. Benlliure*[5], *R. Caballero-Folch*[6], *D. Cano-Ott*[7], *T. Davidson*[8], *I. Dillmann*[3,9], *C. Domingo-Pardo*[4], *A. Estrade*[3,10], *A. Evdokimov*[9], *T. Faestermann*[11], *D. Galaviz-Redondo*[12], *A. García-Rios*[7], *H. Geissel*[3,9], *R. Gernhäuser*[11], *M.B. Gómez-Hornillos*[6], *M. Heil*[3], *C. Hinke*[11], *R. Knöbel*[3], *J. Kurcewicz*[3], *Y. Litvinov*[3], *G. Lorusso*[13], *L. Maier*[11], *J. Marganiec*[3], *M. Marta*[3,9], *F. Montes*[2,14], *I. Mukha*[3], *C. Nociforo*[3], *A. Parikh*[6,15], *G. Perdikakis*[2,14], *S. Pietri*[3], *A. Prochazka*[3], *S. Rice*[16], *B. Rubio*[4], *H. Schatz*[2,14,17], *C. Scheidenberger*[3,9], *K. Steiger*[11], *B. Sun*[3], *J.L. Taín*[4], *M. Takechi*[3], *H. Weick*[3], *J.S. Winfield*[3], *R. Wood*[16], *and P. Woods*[8]

[1]Department of Physics, University of Notre Dame; [2]Joint Institute for Nuclear Astrophysics (JINA); [3]GSI Helmholtzzentrum für Schwerionenforschung GmbH; [4]Instituto de Física Corpuscular, CSIC-Universitat de Valencia; [5]Universidad de Santiago de Compostela; [6]Departament de Física i Enginyeria Nuclear, Universitat Politecnica de Catalunya; [7]CIEMAT; [8]School of Physics and Astronomy, University of Edinburgh; [9]II. Physikalisches Institut, Justus-Liebig Universität Giessen; [10]St. Mary's University; [11]Department of Physics E12, Technische Universität München; [12]Centro de Física Nuclear da Universidade de Lisboa; [13]RIKEN Nishina Center; [14]National Superconducting Cyclotron Laboratory, Michigan State University; [15]Institut d'Estudis Espacials de Catalunya; [16]Department of Physics, University of Surrey; [17]Department of Physics and Astronomy, Michigan State University

The astrophysical origin of about half of the elements heavier than iron have been attributed to the rapid neutron capture process (r-process). Reliable nuclear physics is needed to link theoretical models with astronomical observations. The region around the $N = 82$ shell closure is of particular interest as it is responsible for the $A = 130$ peak in the solar abundance pattern. The peak is the result of the longer β-decay timescale compared to the neutron capture timescale when the r-process path reaches the shell closure [1] [2] [3].

An experiment to investigate half-lives and β-delayed neutron emission branching ratios of neutron-rich nuclei was performed at the GSI projectile FRagment Separator (FRS) [4]. A 900 MeV/u, ^{238}U beam delivered by the SIS-18 synchrotron impinged upon a 2480 $\mathrm{mg/cm^2}$ thick beryllium target placed at the FRS entrance. Produced fission fragments were selected in flight via the $B\rho - \Delta E - B\rho$ method. The ions were then implanted at the final focal plane of the FRS into the Silicon IMplantation detector and Beta Absorber (SIMBA) [5]. SIMBA detected implants as well as subsequent β-decays which can be correlated in time and position to its respective implant. The silicon arrays were surrounded with the BEta deLayEd Neutron detector (BELEN-30) [6]. BELEN-30 consisting of 30 ^{3}He tubes embedded in a polyethylene matrix which thermalized and detected β-delayed neutrons emission with an efficiency of about 40%.

Several $B\rho$ settings of the FRS were used during the experiment to yield optimum secondary beam intensities of the ions of interest. Preliminary analysis has identified neutron-rich Rh, Pd, Ag, and Cd isotopes in the region close to the $N = 82$ shell closure. The identification of the ions implanted into SIMBA has been completed. Figure 1 shows the separation between different species in the particle identification. Some species identified have no previous measurement of half-life and/or β-delayed neutron emission branching ratio. The determination of the implanted ion's half-lives and branching ratios is currently underway.

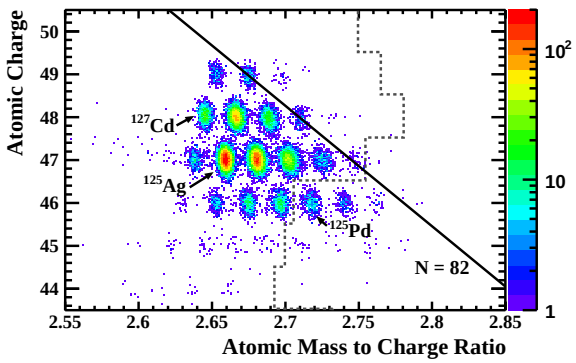

Figure 1: Cumulative Implanted Particle IDentification (PID). Isotopes left of the dashed jagged line have known half-lives. Isotopes along the solid line have $N = 82$.

References

[1] E. M. Burbidge, *et al.*, Rev. Mod. Phys. **29**, 547 (1957)

[2] J. J. Cowan, *et al.*, Phys. Rep. **208**, 267 (1991)

[3] M. Arnould, *et al.*, Phys. Rep. **450**, 97 (2007)

[4] H. Geissel, *et al.*, Nucl. Intr. and Meth. B, 70 (1992) 286

[5] C. Hinke, PhD Dissertation, Technische Universität München (2010); GSI-Diss. 2010-15.

[6] M. B. Gómez-Hornillos, *et al.*, contribution to GSI Scientific Report 2011

Measurement of β-delayed Neutrons Around the Third r-process Peak*

J. Agramunt[1], *A. Algora*[1], *F. Ameil*[2], *Y. Ayyad*[3], *J. Benlliure*[3], *M. Bowry*[4], *R. Caballero-Folch*[5], *F. Calviño*[5], *D. Cano-Ott*[6], *T. Davinson*[7], *I. Dillmann*[8,2], *C. Domingo-Pardo*[1], *A. Estrade*[2], *A. Evdokimov*[8,2], *F. Farinon*[2], *D. Galaviz-Redondo*[9], *A. García-Rios*[6], *H. Geissel*[2], *W. Gelletly*[4], *R. Gernhuser*[10], *M.B. Gómez-Hornillos*[5], *C. Guerrero*[11], *M. Heil*[2], *C. Hinke*[10], *R. Knöbel*[2], *I. Kojouharov*[2], *J. Kurcewicz*[2], *N. Kurz*[2], *Y. Litvinov*[2], *L. Maier*[10], *J. Marganiec*[2], *M. Marta*[2,8], *T. Martinez*[6], *F. Montes*[12], *I. Mukha*[2], *D.R. Napoli*[13], *C. Nociforo*[2], *C. Paradela*[3], *S. Pietri*[2], *A. Prochazka*[2], *S. Rice*[4], *A. Riego*[5], *B. Rubio*[1], *H. Schaffner*[2], *C. Scheidenberger*[8,2], *K. Smith*[14,15,2], *E. Sokol*[16], *K. Steiger*[10], *B. Sun*[2], *J.L. Taín*[1], *M. Takechi*[2], *D. Testov*[17,16], *H. Weick*[2], *E. Wilson*[4], *J. Winfield*[2], *R. Wood*[4], *and P. Woods*[7]

[1]IFIC, Valencia, Spain; [2]GSI, Darmstadt, Germany; [3]Univ. de Santiago de Compostela, Spain; [4]Univ. of Surrey, UK; [5]Universitat Politecnica de Catalunya, Barcelona, Spain; [6]CIEMAT, Madrid, Spain; [7]Univ. of Edinburgh, UK; [8]Justus-Liebig Univ. Giessen, Germany; [9]CFNUL, Centro de Fisica Nuclear da Universidade de Lisboa, Portugal; [10]Technische Universität München, Germany; [11]CERN, Geneva, Switzerland; [12]NSCL, Michigan State University, Michigan, USA; [13]Laboratory Nazionali di Legnaro, INFN, Italy; [14]Department of Physics, Univ. of Notre Dame, Indiana, USA; [15]JINA, Indiana, USA; [16]Joint Institute for Nuclear Research, Dubna, Russia; [17]IPN Orsay, France

Half of the observed solar abundances for the elements heavier than iron is produced by the so-called r process during neutron star mergers or Core Collapse Super Novae. In such scenario a very large neutron flux is present, which produces a wide range of very neutron-rich species on a timescale of few seconds. When the neutron flux ceases these radioactive nuclei decay β^-, in some cases including β-delayed neutrons. These decays deviate the reaction flow back to stability and produce additional neutrons which affect the neutron-to-seed ratio at later phases of the r-process. Calculations [1, 2] of half-lives and βdn-emission probabilities ($P_{\rm n}$ values) show differences of a up to a factor of 10 for regions where no experimental data are available for constraining the models, e.g. at the N=126 shell closure. Therefore new results in this mass region are strongly desired.

The S410 experiment aimed at measuring half-lives and β-delayed neutron branchings of nuclei with A>200 and N>126. A primary beam of ^{238}U and 1 GeV/u from the SIS impinged on a thick Be target and the produced fragments were in-flight selected via the $B\rho-\Delta E-B\rho$ method in the FRagment Separator (FRS) [3]. The nuclei of interest were slowed down and implanted in the Silicon array detector SIMBA (Silicon IMplantation detector and Beta Absorber) [4], that was used for measuring both implants and β-decays. A surrounding polyethylene matrix with 30 ^{3}He proportional counters embedded (BELEN-30 [5]) detected the emitted β-delayed neutrons with $\approx$ 40% efficiency.

Two different production settings were used, one centred on ^{215}Tl and the other on ^{211}Hg. The standard FRS detectors and data acquisition system allowed to identify event-by-event the isotopes arriving at the final focal plane. Fig. 1 shows the cumulative statistics of species implanted in SIMBA during the whole campaign. These data will provide neutron branchings $P_{\rm n}$ and decay half-lives $t_{1/2}$ in the following phases of the ongoing analysis.

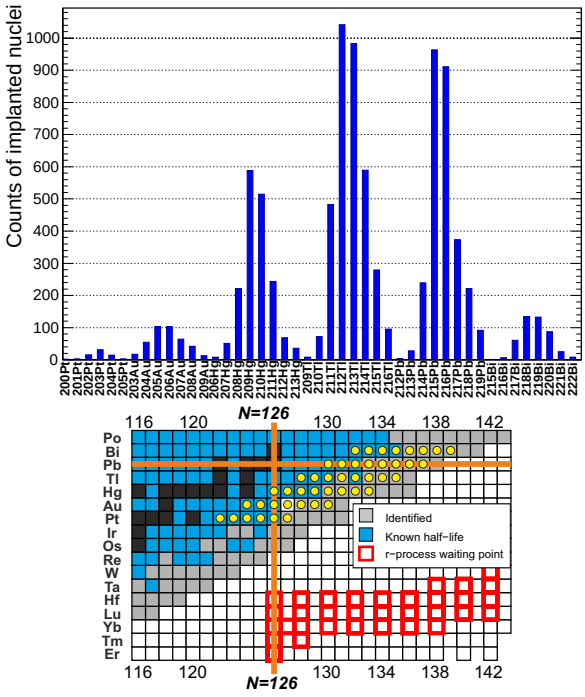

Figure 1: Implanted species during the S410 experiment.

References

[1] I. Borzov, Physics of Atomic Nuclei, 74 (2011) 1435-1444.

[2] P. Möller et al., Phys. Rev. C 67, 055802 (2003).

[3] H. Geissel et al., NIM B70 (1992) 286-297.

[4] C. Hinke, PhD thesis, TU München.

[5] M.B. Gómez-Hornillos et al., contribution to GSI Scientific Report 2011

*This work is supported by the Helmholtz association via the Young Investigators Group VH-NG-627.

Observation of Beta-delayed Three-proton Emission from ^{31}Ar with the Optical Time Projection Chamber at the FRS*

M. Pfützner[1,3,#], W. Dominik[1], A. Fomichev[2], H. Geissel[3], Z. Janas[1], G. Kamiński[2], S. Krupko[2], M. Kuich[4], A. Lis[1], C. Mazzocchi[1], I. Mukha[3], C. Nociforo[3], M. Pomorski[1], R. Slepnev[2], H. Weick[3], and the S388 Collaboration

[1]Faculty of Physics, University of Warsaw, Warsaw, Poland, [2]JINR, Dubna, Russia, [3]GSI, Darmstadt, Germany, [4]Faculty of Physics, Warsaw University of Technology, Warsaw, Poland

A characteristic feature of exotic nuclei at the proton drip-line is the large energy released in beta decay. As a consequence, highly excited, and unbound, states in the daughter nucleus can be populated in the decay. Thus, beta decay can be followed by emission of protons. Since the first observation of delayed proton emission almost 50 years ago, followed by the discovery of beta-delayed two-proton emission in 1983, such decays have provided a wealth of information on structure of neutron-deficient nuclei far from stability, allowing tests of nuclear models and yielding data needed for the understanding of the astrophysical *rp* process [1,2].

The first unambiguous observation of the beta-delayed three-proton emission (β3p) was succeeded only in 2007 when a new type of gaseous time projection chamber with optical readout (OTPC) was applied to study nuclei in vicinity of ^{45}Fe [3,4]. This novel type of detector, developed at University of Warsaw (Poland), records tracks of particles emitted in the decay and can provide a direct and unambiguous evidence on the decay mode even if only one event is recorded. In the experiment carried out at NSCL/MSU laboratory (East Lansing, USA) the β3p emission was identified in the beta decays of ^{45}Fe and ^{43}Cr [5,6].

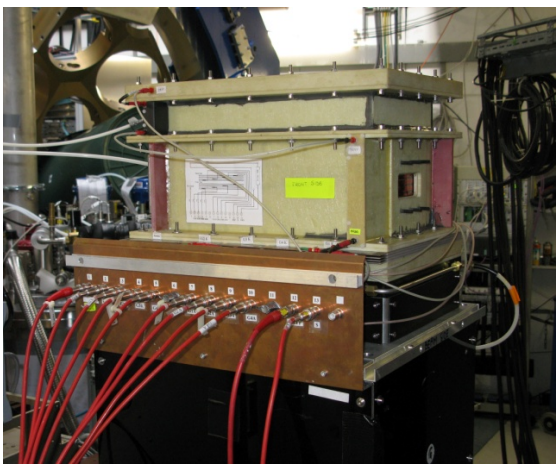

Figure 1. The Optical Time Projection Chamber mounted at the final focal plane of the FRS. Ions enter the active gas volume through a window seen on the right. The CCD camera is mounted inside the black support box below the chamber.

In August 2012 in an experiment at the GSI Fragment Separator (S388) the OTPC chamber was used to investigate the beta decay of ^{31}Ar. A photo of the detector installed at the final (F4) FRS focus is shown in Figure 1. The ions of ^{31}Ar ($T_{1/2}$=15 ms) were produced by the fragmentation of a ^{36}Ar primary beam at 880 MeV/nucleon impinging on a 8 g/cm^2 beryllium target. During about five days of data taking, a few tens of thousands of ^{31}Ar ions were implanted into the chamber and their decays with emission of protons were recorded. Among these decays a few events showing the simultaneous emission of three protons were clearly observed. An example event is shown in Figure 2. The probability of this decay branch and other spectroscopic features will follow from the analysis which is going on. The observation of the third case of this exotic decay branch – the emission of 3 protons following beta decay – was possible due to extreme sensitivity of the OTPC detector and the separation power of the FRS.

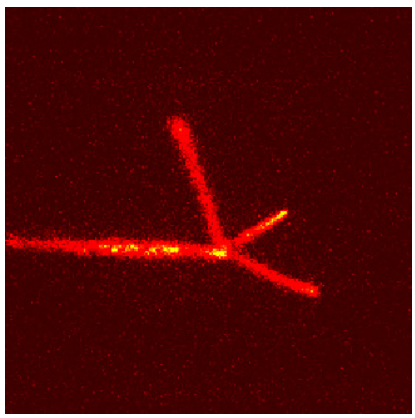

Figure 2. An example image, taken by the CCD camera, showing a β3p decay event. An ion of ^{31}Ar entered the chamber horizontally from left and stopped in the gas. Several milliseconds later three protons were emitted simultaneously from the same point where the ion was stopped.

References

[1] B. Blank and M. J. G. Borge, Prog. Part. Nucl. Phys. 60 (2008) 403.
[2] M. Pfützner, M. Karny, L. Grigorenko, K. Riisager Rev. Mod. Phys. 84 (2012) 567.
[3] K. Miernik *et al.*, Nucl. Instrum. Methods A 581 (2007) 194.
[4] K. Miernik *et al.*, Eur. Phys. J. A 42, 431 (2009).
[5] K. Miernik *et al.*, Phys. Rev. C 76 (2007) 041304(R).
[6] M. Pomorski *et al.*, Phys. Rev. C 83 (2011) 014306.

* This work is supported by the BMBF grant GSI-JINR.
# pfutzner@fuw.edu.pl

PreSPEC-AGATA Experiments at the Frontier of Nuclear Structure

P. Boutachkov[*1], *N. Pietralla*[1], *J. Gerl*[2] *for the PreSPEC-AGATA collaboration*

[1]TU, Darmstadt, Germany; [2]GSI, Darmstadt, Germany

In 2012, Coulomb excitation and secondary fragmentation experiments using radioactive ion beams at relativistic energies have been performed for the first time with the new PreSPEC-AGATA setup.

PreSPEC-AGATA is a unique combination of the FRagment Separator(FRS) [1], used for providing and selecting specific radioactive ion beams, the Lund-York-Cologne CAlorimeter (LYCCA) [2], which discriminates heavy ions produced in nuclear reactions taking place at the secondary target, the HECTOR [3] array and 10 $LaBr_3$ detectors used for detection of high-energy γ-rays and the Advanced Gamma Tracking Array (AGATA) [4] , for the precise measurement of γ-ray energies. PreSPEC-AGATA is based on the very successful RISING campaign [5]. The major improvements are the ability of LYCCA to determine the mass of the reaction products and the accurate determination of the first γ-ray interaction point in the AGATA array. The latter leads to a higher γ-efficiency ($\sim$ 10%) keeping the γ-ray energy resolution at about 1%, after Doppler correction, as AGATA can be positioned closer to the PreSPEC-AGATA target. These improvements together with the higher beam intensity provided by the SIS-UNILAC accelerators, yield a factor of 10 higher sensitivity compared to RISING. A picture of the setup is shown in Figure 1.

In 2012, four experiments were performed with the new setup. They investigated how the collectivity is build-up from single particle excitations and how it evolves away from magic nuclei.

Excitation probabilities of the first excited states in nuclei south-west of ^{208}Pb were measured, including heavy Pb, Hg and Pt isotopes. The level scheme of the ^{52}Fe nucleus which is only two valence proton and neutron holes away from the doubly magic ^{56}Ni, shows rotational behavior for the low spin states. In the primary FRS production target ^{52}Fe nuclei were not only populated in their ground state but also in the 12^+ isomeric state, which was Coulomb excited using a gold target at the PreSPEC-AGATA setup. For ^{64}Fe the Pygmy dipole resonance was studied, which probes the properties of neutron skin. Finally, neutron rich Zr isotopes were excited to determine their shape evolution.

A γ-spectrum taken during the commissioning is shown in Figure 2. The fragments identification with LYCCA is discussed in Reference [6], while the trigger configuration used for the experiments is described in Reference [7].

In 2013, the PreSPEC-AGATA experiments will be extended to life-time measurements as well as scattering on a liquid hydrogen target.

*This work was supported by NAVI, Helmholtz Association Nuclear Astrophysics Virtual Institute.

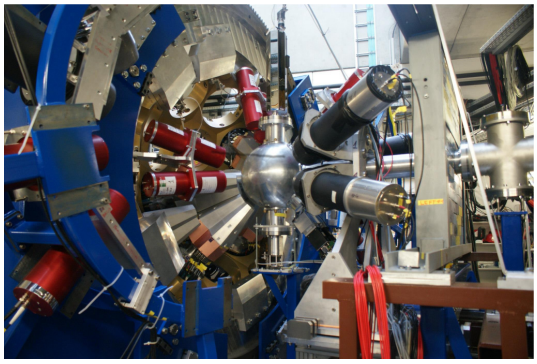

Figure 1: A photograph of the PreSPEC-AGATA setup. The beam from the FRS comes from the right. HECTOR detectors in black, chamber with target manipulators, $LaBr_3$ detectors in red, the AGATA detectors are mounted on the large metal ring, a beam tube connects the target chamber to the LYCCA array.

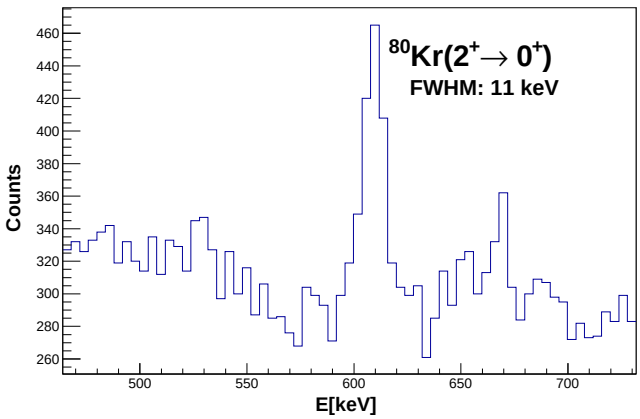

Figure 2: γ-ray spectrum from Coulomb excitation of ^{80}Kr on a gold target at the PreSPEC-AGATA setup. The γ-transition from the first 2^+ excited state to the ground state of ^{80}Kr is marked.

References

[1] H. Geissel *et al.*,Nucl. Instr. and Meth. B**70** (1992) 286.

[2] `http://www.nuclear.lu.se/english/research/basic_nuclear_physics/nustar/lycca/`

[3] A. Maj *et al.*,Nucl. Phys. A**571** (1994) 185.

[4] S. Akkoyun *et al.*,Nucl. Phys. A**668** (2012) 26.

[5] H.J. Wollersheim *et al.*,Nucl. Phys. A**537** (2005) 637.

[6] P.P. Singh *et al.*,"LYCCA Performance During the PreSPEC-AGATA Campaign", GSI Scientific Report 2012.

[7] D. Ralet *et al.*,"Trigger Configuration for the PreSPEC-AGATA Campaign at GSI", GSI Scientific Report 2012.

High-Precision Measurement of Total Fission Cross Sections in Spallation Reactions of ^{208}Pb and ^{238}U*

K.-H. Schmidt[1], B. Jurado[2], R. Pleskač[1], M. V. Ricciardi[1], J. Benlliure[3], A. Boudard[4], E. Casarejos[3], T. Enqvist[5], F. Farget[6], A. Bacquias[1], M. Fernandez[3], L. Giot[1], V. Henzl[1], D. Henzlova[1], A. Kelić-Heil[1,#], T. Kurtukian[2], S. Leray[4], S. Lukić[1], Son Nguyen Ngoc[1], P. Nadtochy[1], D. Perez[3], C. Schmitt[6]

[1]GSI, Darmstadt, Germany ; [2]CENBG, Bordeaux, France ; [3]USC, Santiago de Compostela, Spain; [4]CEA, Gif-sur-Ivette, France; [5]University of Oulu, Oulu, Finland; [6]GANIL, Caen, France

Since the accelerator-driven system (ADS) is considered as an option for the incineration of radioactive waste, intense effort has been made in providing experimental data on interactions of intermediate-energy protons and neutrons with the neutron-production target, with construction material, and with materials that undergo transmutation in the ADS. In last two decades, the experimental knowledge on the production of individual nuclides in spallation reactions has improved substantially also thanks to the results of an experimental campaign executed at GSI [1] with a high-resolution magnetic spectrometer. Also improved codes, e.g. [2, 3] have been developed on the basis of this new generation of experimental results.

The situation has not so much improved, however, concerning total fission cross sections. Experimental uncertainties are often rather large, and the results of different experiments severely contradict each other in many cases, as discussed in Ref. [4]. In the present work, we report on the first results of a new generation of high-precision measurements of total fission cross sections in spallation reactions of ^{208}Pb and ^{238}U at energies between 0.5 and 1 *A* GeV. The experiments were performed with a novel experimental approach in inverse kinematics using a full-acceptance detection system. This technique has decisive advantages and copes with several problems of most conventional direct-kinematics experiments performed up to now: The most important feature is that, due to the inverse kinematics, all fission fragments (FFs) leave the target with high energy in a narrow cone in forward direction. In addition, the individual projectiles are registered and identified with the same detectors which also register the FFs. The angular range where FFs are emitted is fully covered. Further on, both FFs are registered and identified simultaneously, and their velocity vectors are determined. Finally, the multiplicity of the reaction products is accessible. All these features are crucial for obtaining total fission cross section with high precision.

The fission set-up used in the present work was developed at the GSI experimental facility and was situated behind the fragment separator (FRS), see Fig.1 Details on the experimental setup and data analysis can be found in ref. [5].

The total fission cross sections measured in the present work are shown in Table 1.

* Work supported by EU, EURATOM contract no. 012985 and EUTRANS contract no. 516520-FI6W

#a.kelic@gsi.de

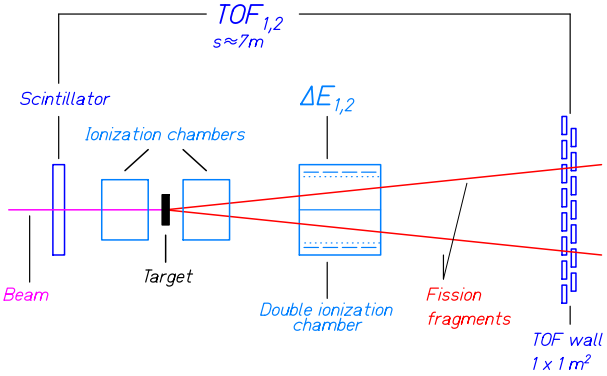

Figure 1: Side view of the fission set-up mounted behind the FRS at GSI Darmstadt. Two ionization chambers (MUSIC1 and MUSIC2) with the target mounted in-between form an active target. A double ionization chamber (TWIN) and a TOF wall detect the two fission fragments.

Table 1: Measured total fission cross sections.

Reaction	σ_{tot} / mb
^{208}Pb(500 *A* MeV)+ ^{1}H	(146 ± 7)
^{208}Pb (500 *A* MeV) + ^{2}H	(203 ± 9)
^{238}U (545 *A* MeV) + ^{1}H	(1.49 ± 0.10) ·1E+3
^{238}U (935 *A* MeV) + ^{1}H	(1.55 ± 0.10) ·1E+3

High precision between 5% and 7% could be achieved due to the fact that the experimental set-up detects the FFs with efficiency close to 100% and that fission events are unambiguously identified and distinguished from other reactions by the dedicated high-resolution detection system. In addition, the projectiles are individually counted using the same detectors. More details can be found in [5].

References

[1] http://www.gsi.de/charms
[2] A. Boudard, J. Cugnon, S. Leray, and C. Volant, Phys. Rev. C **66,** 044615 (2002).
[3] A. Kelić et al, arXiv:0906.4193 [nucl-th]
[4] A. V. Prokofiev, Nucl. Inst.. Meth. A 463 (2001) 557
[5] K.-H. Schmidt et al, *accepted in* Phys. Rev. C; see also arXiv:1208.6115 [nucl-ex]

Fission Dynamics at High Excitation Energy in Complete Kinematic Measurements of the Reaction ^{208}Pb+p at 500 A MeV

J.L. Rodríguez-Sánchez[1], J. Benlliure[1], J. Taieb[2], A. Kelić-Heil[3], C. Paradela[1], H. Álvarez-Pol[1], Y. Ayyad[1], E. Casarejos[4], D. Cortina-Gil[1], B. Pietras[1], D. Ramos[1], J. Vargas[1], G. Boutoux[2], A. Chatillon[2], T. Gorbinet[2], B. Laurent[2], C. Rodríguez-Tajes[5], L. Audouin[6], and A. Heinz[7]

[1]USC, Santiago de Compostela, Spain; [2]CEA/DAM, Paris, France; [3]GSI, Darmstadt, Germany; [4]Univ. de Vigo, Vigo, Spain; [5]GANIL, Caen, France; [6]IPNO, Paris, France; [7]Univ. of Chalmers, Gothenburg, Sweden

Fission is an extremely complex mechanism that requires a dynamical approach to describe the evolution of the process in terms of intrinsic and collective excitations of the nuclear constituents. The first to consider the dynamics of nuclear fission was Kramers [1], who proposed an interpretation of fission as a diffusion process, where a particle moves in a heat bath. In this process appears two terms, a diffusion term and a friction term that transfers the energy between the collective degrees of freedom and the heat bath, this effect is known as dissipation and is characterized by the dissipation coefficient β. The quantitative determination of this coefficient and possible temperature and deformation dependencies are still under debate [2].

The ideal scenario for studying this process requires high excitation energies (E^* >100 MeV), where the dissipation coefficient depends strongly on the temporal evolution of the fissioning system [3], low angular momentum and small deformation [4]. Moreover, one needs observables such as the evolution of the fission probability with the violence of the reaction or the particles emitted by the hot fissioning nuclei before or after scission. All these requirements were met in an experiment recently performed at the ALADIN-LAND cave at GSI.

In this experiment we investigated proton induced fission on lead at relativistic energies using inverse kinematics. This reaction mechanism guarantees that fission reactions take place at large values of excitation energy and low values of angular momentum and deformation. Moreover, we use a complex experimental setup [5] providing for the first time, an almost complete kinematic measurement of these kind of reactions.

A high-resolution twin-ionisation chamber provides an unambiguous determination of the atomic number of both fission fragments. Accurate tracking measurements using multi-wire chambers and the drift time in the ionisation chamber, together with an extremely accurate time-of-fight measurement and the bending of the fragments flying through the ALADIN magnet will make possible to determine the mass number of both fission fragments. Moreover, a segmented plastic-scintillator wall and the neutron detector LAND were used to detect and identify light-charge particles (LCP) and neutrons emitted during the fission process.

In Fig. 1 we show some preliminary results. In this figure we report the sum of the atomic numbers of the two fission fragments obtained from their energy loss in the twin ionisation chamber for different multiplicities of light-charged particles determined with the segmented plastic-scintillator wall. As can be seen in the figure, the average charge of the fissioning nucleus (Z_1+Z_2) clearly scales with the multiplicity of light-charged particles and then with the violence of the reaction.

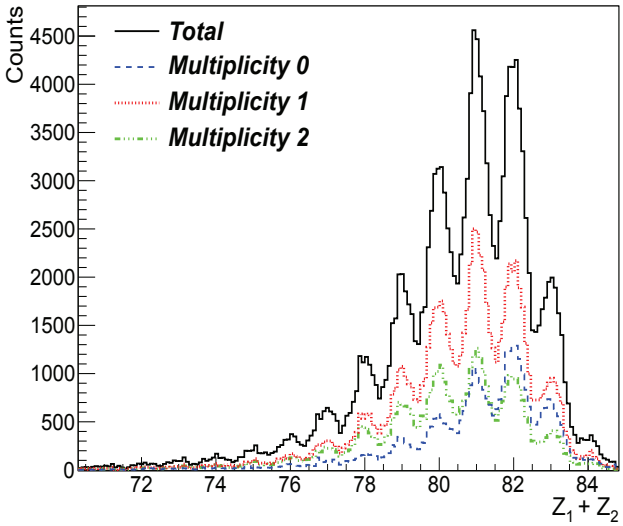

Figure 1: Charge distribution of the fissioning system (Z_1+Z_2) as a function of the LCP multiplicity.

References

[1] H.A. Kramers, Physika VII (1940) 284.

[2] D. Jacquet and M. Morjean, Prog. Part. Nucl. Phys. 63 (2009) 155.

[3] K.H. Bhatt, Phys. Rev. C 33, (1986) 954.

[4] B. Jurado et al Phys. Rev. Lett. 93 (2004) 072501.

[5] A. Bail et al, "Next generation Fission experiments at GSI: short and long term perspectives" in Proceedings of Seminar on Fission, Het Pand, Ghent, Belgium, May 2010.

A New Method for Measuring Neutron-skin Thickness by Exciting the Anti-analog Giant Dipole Resonance *

A. Krasznahorkay[1], *T. Aumann*[2,3], *A. Algora*[1], *M. Csatlós*[1], *J. Gulyás*[1], *N. Kalantar-Nayestanaki*[4], *L. Stuhl*[1], *and J. Tímár for the R3B and EXL collaborations*[1]

[1]Inst. for Nucl. Res., Hung. Acad. of Sci. (MTA Atomki), Debrecen, Hungary; [2]Technische Universität Darmstadt, Germany; [3]GSI, Darmstadt, Germany; [4]KVI, Univ. of Groningen, The Netherlands

A new method, based on the excitation of the anti-analog giant dipole resonance (AGDR) in (p,n) reaction, for measuring the neutron skin thickness has been tested. The γ-decay of the AGDR to the isobaric analog state (IAS) has been measured. The difference in excitation energy of the AGDR and IAS was calculated. By comparing the theoretical results with the measured one, the ΔR_{pn} value for ^{124}Sn was deduced to be 0.21$\pm$0.07 fm. The present method provides a new possibility for measuring neutron skin thickness of very exotic nuclei.

The experiments, aiming at studying the neutron-skin thickness of ^{124}Sn, were performed at GSI using 600 MeV/nucleon ^{124}Sn relativistic heavy-ion beams on CH_2 and C targets. This allowed us to subtract the contribution of the C to the yield measured from the CH_2 target during the analysis. The ejected neutrons were detected by a low-energy neutron-array (LENA) ToF spectrometer, which was developed in Debrecen [1].

The energy of de-exciting γ-transitions was measured in coincidence with slow neutrons by six large cylindrical ($\Phi = 3.5''$, $L = 8''$) state-of-the-art $LaBr_3$ γ-detectors. The Doppler shift was taken into account in the analysis. The precise energy and efficiency calibrations of the detectors were performed after the experiments by using different radioactive sources and (p,γ) reactions on different targets. The γ-ray energy spectrum measured in coincidence with the low-energy neutrons is shown in Fig. 1.

The direct γ-branching ratio of the AGDR to the IAS is expected to be similar to that of the GDR to the g.s. in the parent nucleus, which can be calculated from the parameters of the GDR [2]. In contrast, in the investigation of the electromagnetic decay properties of the spin dipole resonance (SDR) by Rodin and Dieperink [3] the γ-decay branching ratio was in the range of 10^{-4}. Therefore, the coincidence measurements deliver a precise energy for the AGDR.

The theoretical analysis is performed using the fully self-consistent relativistic proton-neutron quasiparticle random-phase approximation based on the relativistic Hartree-Bogoliubov model (RHB) [4] as described previously in Ref. [5].

By comparing the experimental result for E(AGDR) - E(IAS) to the theoretical energy differences, we deduce the value of the neutron-skin thickness in ^{124}Sn: $\Delta R_{np} =$ 0.21 ± 0.07 fm (including theoretical uncertainties). The very good agreement with previously determined values [5] reinforces the expected reliability of the proposed method.

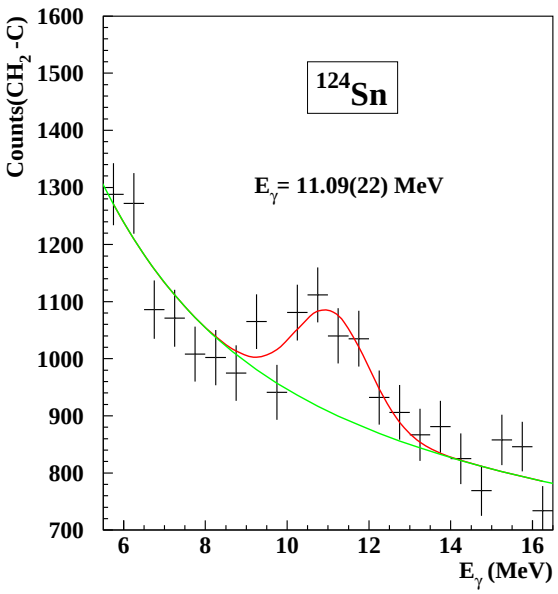

Figure 1: The γ-ray energy spectrum measured in coincidence with the low-energy neutrons that fulfill the conditions of $1.0 \leq E_n \leq 3.5$ MeV and $67^\circ \leq \Theta^n_{LAB} \leq 70^\circ$, which corresponds to the exciation of the AGDR in inverse kinematics. The calibrated energy scale was corrected already for the Doppler effect. The solid line shows the result of the fit using Gaussian line shape and a third order polinomial background.

References

[1] C. Langer et al., Nucl. Instr. Meth. Phys. Res. **A659** (2011) 411.

[2] A. Krasznahorkay et al., Nucl. Phys. **A567** (1994) 521.

[3] V. A. Rodin and A. E. L. Dieperink, Phys. Lett. **B 541** (2002) 7.

[4] D. Vretenar, A. V. Afanasjev, G. A. Lalazissis, and P. Ring, Phys. Rep. **409** (2005) 101.

[5] A. Krasznahorkay et al., AIP Conf. Proc. 1491 (2012) 190; in print in Phys. Lett. B, Acta Phys. Pol. B, Phys. Scripta.

* Work supported by EU, ENSAR, No. 262010, and HIC for FAIR.

Measurement of the Direct Neutron Decay of ^{68}Ni*

D. M. Rossi[1,2], *P. Adrich*[1], *F. Aksouh*[1], *H. Alvarez-Pol*[3], *T. Aumann*[4,1], *J. Benlliure*[3], *M. Böhmer*[5], *K. Boretzky*[1], *E. Casarejos*[6], *M. Chartier*[7], *A. Chatillon*[1], *D. Cortina-Gil*[3], *U. Datta Pramanik*[8], *H. Emling*[1], *O. Ershova*[9], *B. Fernandez-Dominguez*[3,7], *H. Geissel*[1], *M. Gorska*[1], *M. Heil*[1], *H. Johansson*[10,1], *A. Junghans*[11], *O. Kiselev*[1,2], *A. Klimkiewicz*[1,12], *J. V. Kratz*[2], *N. Kurz*[1], *M. Labiche*[13], *T. Le Bleis*[1,9,14], *R. Lemmon*[15], *Yu. A. Litvinov*[1], *K. Mahata*[1,16], *P. Maierbeck*[5], *A. Movsesyan*[4], *T. Nilsson*[10], *C. Nociforo*[1], *R. Palit*[17], *S. Paschalis*[4,7], *R. Plag*[9,1], *R. Reifarth*[9,1], *H. Simon*[1], *K. Sümmerer*[1], *A. Wagner*[11], *W. Walus*[12], *H. Weick*[1], *M. Winkler*[1], *and the R^{3}B collaboration*

[1]GSI, Darmstadt, Germany; [2]Univ. of Mainz, Germany; [3]Univ. of Santiago de Compostela, Spain; [4]TU Darmstadt, Germany; [5]TU München, Germany; [6]Univ. of Vigo, Spain; [7]Univ. of Liverpool, United Kingdom; [8]SINP, Kolkata, India; [9]Univ. of Frankfurt, Germany; [10]Chalmers Univ. of Technology, Göteborg, Sweden; [11]HZDR, Dresden, Germany; [12]Jagiellonian Univ., Krakow, Poland; [13]Univ. of the West of Scotland, Paisley, United Kingdom; [14]IPHC, Strasbourg, France; [15]STFC Daresbury Laboratory, United Kingdom; [16]BARC, Mumbai, India; [17]TIFR, Mumbai, India

The investigation of low-lying dipole strength in atomic nuclei is of great interest due to its connections to fundamental nuclear properties, such as neutron-skin thicknesses or the symmetry energy of the equation-of-state of nuclear matter. The experimental data presented here was obtained using the R^{3}B-LAND setup at GSI in Darmstadt, offering a possibility to study collective excitations in radioactive nuclei using Coulomb excitation. One of the goals of the present experiment was to study the E1 strength in neutron-rich Ni isotopes, such as ^{68}Ni which is discussed here.

In the present experiment, the measured E1 strength is limited to excitation energies above the neutron threshold. The energy range of interest, covering the low-lying E1 strength and the Giant Dipole Resonance regions, involves mainly the (γ^*,n) and (γ^*,2n) reaction channels in ^{68}Ni. The quantitative description of the experimental data relies on the precise understanding of the response of the various detector systems of the setup. A trial input is convoluted with this response and compared to the measured data, as is shown for the neutron kinetic-energy distributions in Fig. 1. As an example for the various observables, the neutron kinetic-energy differential cross section for the 1n channel is presented in the upper and those for the 2n channel in the lower panel. The former shows the experimental data (open black dots) and the corresponding convoluted differential cross section related to the E1 strength input distribution (solid black line). The latter can be divided into a statistical-decay contribution (dashed blue line) and into a direct-decay contribution (dotted red line), where the excited nucleus decays to the ground state by emitting a single neutron. The lower panel presents the kinetic-energy differential cross section of both detected neutrons (solid black dots), as well as the sum of the kinetic energies of both neutrons (open red boxes). The corresponding convoluted differential cross sections for the E1 strength input are shown as solid black and dashed red lines, respectively. While the trial E1 strength input is adjusted to describe the

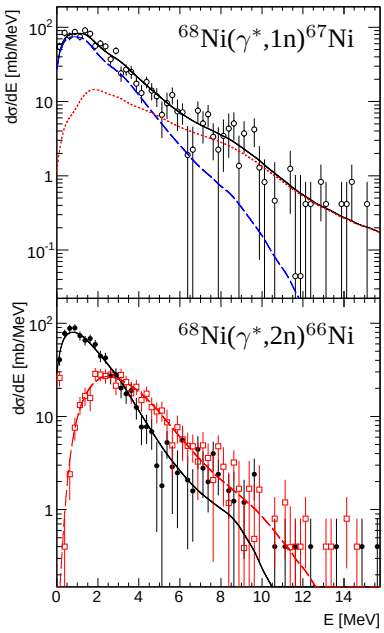

Figure 1: Neutron kinetic-energy differential cross sections. See text for description.

1n and 2n data shown in Fig. 1, the branching ratio for the direct neutron decay can also be obtained by using this quantity as a free parameter during the fitting procedure. A direct-decay contribution of 25(2)% was obtained, which is in good agreement with estimation values of ∼30% for the A=60 mass region [1].

References

[1] M. N. Harakeh and A. van der Woude, "Giant Resonances", 2001 (Clarendon Press, Oxford).

* This work has been supported by HIC for FAIR and EMMI.

Study of the Ground State Properties of Neutron-rich ^{29,30,31}Na Isotopes through Coulomb Breakup

A. Rahaman[1], U. Datta Pramanik[1], T. Aumann,[2,5], G. De Angelis[3] , S. Beceiro[4], T. Le Bleis[5], K. Boretzky[2], D. Cotrina-Gil[4], C. Caesar[2], S. Chakraborty[1], M. Chariter[6], W. N. Catford[7], D. Gonzalez-Diaz[2], H. Emling[2], P. Diaz-Fernandez[4], Y. Dimitry[8], L. M. Fraile[9], O. Ershova[2], H. Geissel[2], M. Heil[2], M. Heine[2], B. Jonson[10], A. Kelic[2], H. Johansson[10], R. Krucken[11], T. Kroll[5], C. Langer[2], Y. Leiffel[2], G. Munzenberg[2], J. Marganice[2], C. Nociforo[2], A. Najafi[12], V. Panin[2], R. Plag[2], H. A. Pol[4], S. Paschalis[13], R. Reifarth[2], V.M. Ricciardi[2], D. Rossi[2], H. Simon[2], C. Scheidenberger[2], S. Typel[2], J. Taylor[6], Y. Togano[14], V. Volkov[2], H. Weick[2], A.Wagner[8], F. Wamers[2], J. Winfield[2], M. Zoric[2] for S306 collaboration.*

[1]Saha Institute of Nuclear Physics (SINP) Kolkata; [2]GSI, Darmstadt; [3] INFN LNL, legnaro; [4]Univ. of Santiago de Compostela; [5]Technical Unin. Darmstadt; [6] Department of Physics; University of Liverpool; [7]University of Surrey, Guildford; [8] Forschungszentrum Dresden-Rossendorf (FZD), Dresden; [9] *Universidad Complutense, Madrid;* [10] Fundamental Fysik, Chalmers Tekniska Högskola, Göteborg; [11]Technical Unin. Munich; [12]Kernfysisch Versneller Instituut; [13]Lawrence Berkeley National Laboratory; [14]The Institute of Physical and Chemical Research (RIKEN)

For several decades the "*island of inversion*" around N~20 has been the subject of interest of many experimental and theoretical investigations. In 1975, Thibault *et al.* [1] through a classic experiment, established that the ground state of ^{31}Na (N=20) is deformed. This deformation cannot be explained by occupation of valence nucleon in normal *sd shell* and it is necessary to consider the valance nucleon occupation from next *pf* shell. Recent experimental result for ^{30}Na (with N=19) by V. Tripathi et. al. [2] has reported the intruder effect from next *pf* shell in the ground state. Coulomb excitation of ^{30}Na [3] by S. Ettenauer et. al. has suggested the ground state as 2^+ but inconclusive. Coulomb break up is a direct probe to explore the ground state configuration of loosely bound nuclei [4,5]. This probe is highly sensitive to the tail part of the wave function of the valence nucleon. Aim of this experiment (S306) is to probe the ground state configuration of ^{29,30,31}Na through Coulomb break up. Experiment S306 was performed on September, 2010 using LAND-FRS set up at GSI, Darmstadt. After fragmentation of ^{40}Ar beam with energy 530 MeV/u, delivered by SIS-18 on 8 gm/cm^2 thick ^{9}Be primary target, several exotic nuclei were populated. Na isotopes with A/Z ratio 2.60 -2.85 were separated at FRS and transferred to Cave C where complete kinematic measurements were performed after Coulomb break-up using secondary target ^{208}Pb (2gm/cm^2). The cocktail incoming beam of the exotic nuclei is shown in figure 1. The reaction run for secondary target ^{12}C (935 mg/cm^2) was also taken to subtract the nuclear contribution in ^{208}Pb target.

After the secondary target the reaction product(s) and fragment(s) were tracked using the tracker programme developed at SINP. Fig. 2 shows the outgoing mass distribution after secondary reaction target for incoming ^{29}Na beam. Four momentums of all the decay product(s) were measured using the LAND, SST, GFI, TFW and Crystal Ball detectors. After measuring all these, the excitation energy of the projectile is reconstructed from invariant mass analysis method.

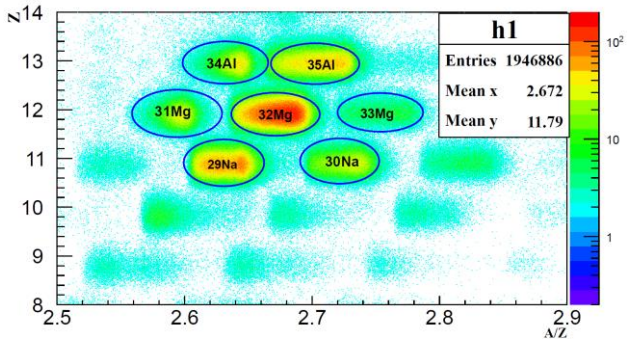

Fig 1: Cocktail incoming PID plot

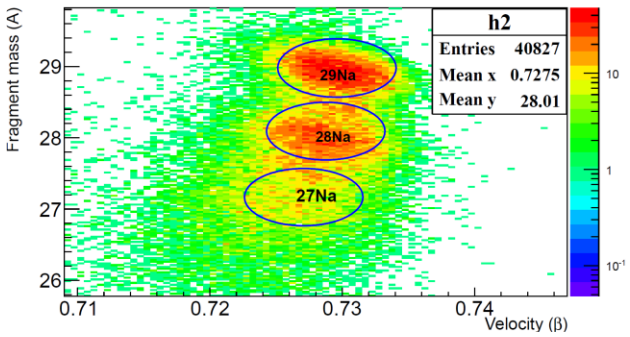

Fig 2: Outgoing mass distribution for incoming ^{29}Na

From the shape differential Coulomb dissociation cross-section with excitation energy and considering the effect of core excitation, it is expected that the valence nucleon of ^{30}Na (gr. state) majorly occupies the low '*l*' orbital. The detailed investigation is going on to understand the ground state configurations of these exotic nuclei.

References

[1] C. Thibault et al., PRC 12 (1975) 644.
[2] Vandana Tripathi et al.PRC **76**, (R) (2007), 021301
[3] S.Ettenauer et. al. PRC 78, (2008), 017302
[4] U. DattaPramanik et al., PLB 551 (2003) 63
[5] T. Nakamura et. al. ; PRL. 83, (1999), 1112

*Supported by Alexander von Humboldt (AvH) foundation. /ushasi.dattapramanik@saha.ac.in

^{25}O - Beyond the Neutron Dripline *

C. Caesar[1,2], T. Aumann[1,2], K. Boretzky[2], M. Heil[2], M. Heine[1,2], M. Holl[1,2], R. Plag[3], D. Rossi[2], H. Scheit[1], H. Simon[2], and the R^{3}B Collaboration

[1]IKP, TU Darmstadt, Germany; [2]GSI, Darmstadt, Germany; [3]Goethe Universität, Frankfurt a.M., Germany

The R3B-collaboration has studied proton knock-out reactions from the very neutron-rich isotope ^{26}F populating neutron-unbound states in ^{25}O [1, 2]. The incoming ^{26}F ions have been identified on a event-by-event basis. For the outgoing reaction products the four-momenta ($P_i = (E_i/c, \vec{p}_i)$) have been measured and those have been combined to reconstruct the invariant mass.

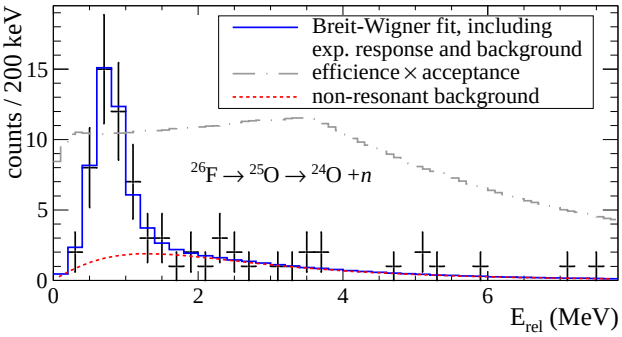

Figure 1: Relative-energy spectrum of the ^{24}O+n system. The blue solid line shows a Breit-Wigner fit to the data, which includes the experimental response and a non resonant background (red dotted curve). The grey dashed-dotted histogram indicates the experimental response to a white spectrum.

The resulting ^{24}O+n relative-energy spectrum as shown in Fig. 1 exhibits a peak at around 700 keV. This peak corresponds to the ground-state of ^{25}O. The resonance position E_r and width Γ were determined in the following way. A Breit-Wigner line shape in the one-level approximation as given in [3] has been used:

$$f(E; E_r, \Gamma) = \frac{\Gamma}{(E_r + \Delta - E)^2 + 1/4 \cdot \Gamma^2} \ . \qquad (1)$$

The resonance shift Δ has been set to zero, the width Γ is given by the reduced width γ and the penetration factor P_l; $\Gamma = 2P_l(E; R) \cdot \gamma^2$. For the angular momentum $l = 2$ is used, since the additional neutron of ^{25}O compared to ^{24}O is most likely in the $0d_{3/2}$ - shell. A channel radius R of 4 fm has been choosen.

This distribution has been convoluted with the experimental response as shown in Fig. 2. A non-resonant background has been modeled with:

$$f(E) = a \times \mathrm{erf}(b \cdot E) \times e^{c \cdot E} \ , \qquad (2)$$

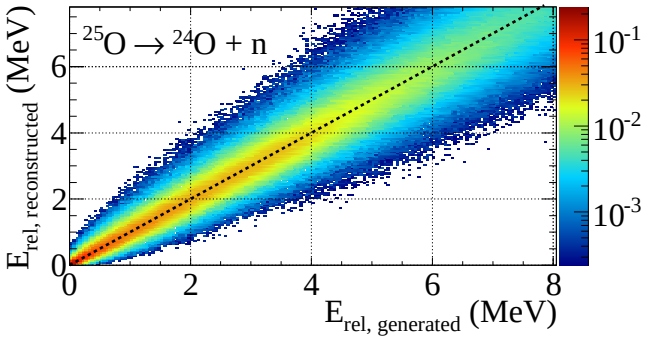

Figure 2: Simulated experimental response for detection of a ^{24}O+n decay from the (unbound) isotope ^{25}O. The x-axis depicts the relative energy used as input for the simulation while the y-axis shows the reconstructed relative energy E_{rel} reflecting the measured values.

where 'erf' is the error-function and the paramters a, b and c have been varied freely. The sum of convoluted Breit Wigner and background was used to fit the experimental data. The χ^2 minimization was done using a χ^2 based on the Poisson likelihood [4]. The results are as follows:

$E_r = 725^{+54}_{-29}$ keV,

$\Gamma = 20^{+60}_{-20}$ keV.

The result on the resonance position (width) is in agreement with the result from [5] within 1-σ (2-σ). Our result is within (1-σ) in agreement with a single-particle width calculated for a pure d-state character ($\Gamma_{s.p.} \approx 65$) keV.

References

[1] T. Aumann *et al.*, GSI Scientific Report (2010) PHN-NUSTAR-NR-04.

[2] C. Caesar *et al.*, GSI Scientific Report (2011) PHN-NUSTAR-NR-12.

[3] A. M. Lane and R. G. Thomas, Rev. Mod. Phys. **30** (1958) 257.

[4] S. Baker and R.D. Cousins, NIM A **221** (1984) 437.

[5] C.R. Hoffman *et al.*, Phys. Rev. Lett. **100** (2008) 152502.

*This work was supported by HIC for FAIR, BMBF (06DA70471), and through the GSI-TU Darmstadt Cooperation.

Direct Reactions with Light Neutron-Rich Nuclei*

L. Atar[1,2], T. Aumann[1,2], J. Enders[1], H. Scheit[1,2], S. Paschalis[1], F. Wamers[1,2], V. Panin[1,2], C. Caesar[1,2], M. Heine[1,2], and the R^{3}B Collaboration

[1]TU Darmstadt, Germany; [2]GSI Darmstadt,Germany

Quasi free (p,2p) and (p,pn) knockout reactions with radioactive beams in inverse kinematics allow us to obtain spectroscopic information about valence and deeply bound single-particle states and to study their evolution over a large variation in isospin. Recent studies have shown that the occupancies of loosely bound valence nucleons in neutron- or proton-rich nuclei have a spectroscopic factor close to unity, whereas single-particle strength for deeply bound nucleons is suppressed in isospin asymmetric systems compared to the predictions of the many-body shell model [1]. Further experimental and theoretical studies are needed for a qualitative and quantitative understanding.

For this aim a series of measurements have been performed on the complete oxygen isotopic chain using the existing experimental setup LAND/R3B at GSI (Cave C). In the experiment S393 the primary beam ^{40}Ar with an energy of 600 AMeV is fragmented into the exotic ions on a beryllium target using the Fragment Separator FRS.

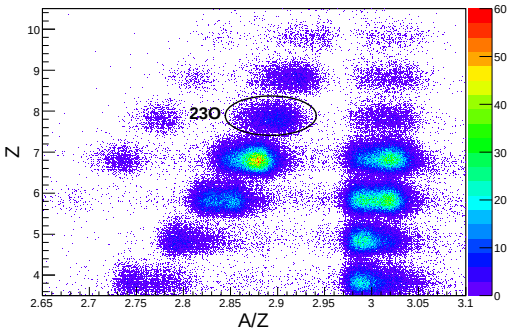

Figure 1: Identification plot of the incoming ions with the graphical cut around the ^{23}O.

The charge Z and mass A of the projectiles hitting the target in Cave C are determined from energy-loss and time-of-flight measurements using silicon PIN diodes and plastic scintillators before the target. Figure 1 depicts charge of ions versus A/Z ratio for a run optimized for transportation of ions with $\sim$ A/Z=3. One can identify here the isotopes from helium up to fluorine.

In order to reconstruct the reaction channel of interest the outgoing fragments are detected and tracked by using silicon strip detectors (SSD), the dipole magnet ALADIN, fibre detectors and Time of Flight Wall detector (TFW), which are located downstream of the target. Two SSDs are located after the target and offer a good charge resolution.

Figure 2 shows the reconstructed fragment-mass distribution for the incoming beam ^{23}O on the target CH_2 by applying a cut on outgoing Oxygen ions (Z=8). Additionally it is required that the cyrstal ball detector (XB), which surrounds the target area and consists of 162 NaI(Tl) crystals, detects at least one high energetic nucleon (neutron).

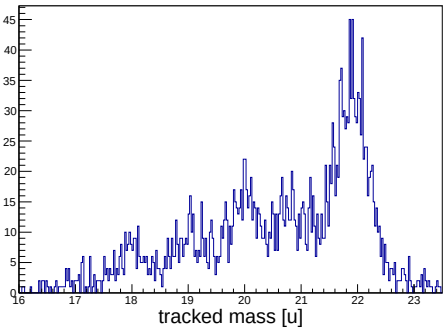

Figure 2: Tracked mass of the outgoing Oxygen fragments after one neutron removing from the projectile ^{23}O.

An indication of the quasi free knockout reactions is the angular correlation between the knocked-out nucleon from the projectile and the protons from the CH_2 target. Figure 3 presents the polar (left) and the azimuthal (right) correlation of proton and neutron of the investigated reaction channel ^{23}O(p,pn)^{22}O. Due to the momentum conservation proton and neutron show opposite azimuthal angels, while they are scattered within a polar angle $0° < \theta < 90°$ by sharing the beam energie of $\sim$ 500 MeV. Background, including reactions induced by the carbon in the target, have been subtracted using measurements with empty and carbon target.

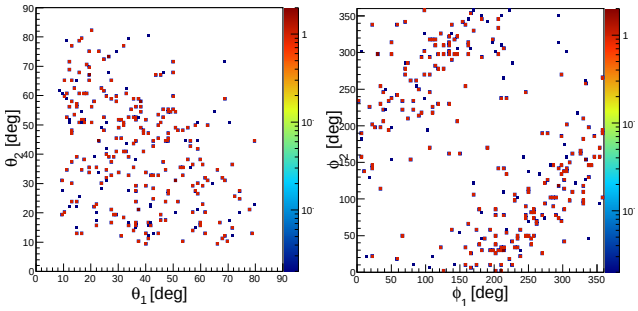

Figure 3: Angular correlations of protons from the CH_2 target and neutrons from the projectile ^{23}O. Left: polar-angle correlations; right: azimuthal-angle correlations.

References

[1] A. Gade et al., Phys. Rev. C77 (2008) 044306.

*Supported by GSI F&E and HIC for FAIR. Work is part of HGS-HIRe.

Study of the Ground-state Configuration of Neutron-rich Aluminium Isotopes through Coulomb Breakup

S. Chakraborty[1], U. Datta Pramanik[1#], T. Aumann[2,3], G. De Angelis[4], S. Beceiro[5], T. Le Bleis[2], K. Boretzky[2], D. Cotrina-Gil[5], C. Caesar[2], M. Chariter[6], W. N. Catford[7], D. Gonzalez-Diaz[2], H. Emling[2], P. Diaz-Fernandez[5], L. M. Fraile[9], O. Ershova[2], H. Geissel[2], M. Heil[2], M. Heine[2], B. Jonson[10], A. Kelic[2], H. T. Johansson[10], R. Krucken[11], T. Kroll[3], C. Langer[2], Y. Leiffel[2], G. Munzenberg[2], J. Marganiec[15], C. Nociforo[2], M. A. Najafi[12], V. Panin[2], R. Plag[2], H. A. Pol[5], S. Paschalis[13], A. Rahaman[1], R. Reifarth[2], D. Rossi[2], H. Simon[2], C. Scheidenberger[2], S. Typel[2], J. Taylor[6], Y. Togano[14], V. Volkov[2], H. Weick[2], A. Wagner[8], F. Wamers[2], J. Winfield[2], M. Zoric[2] and the S306 collaboration.

[1]Saha Institute of Nuclear Physics, Kolkata, India; [2]GSI, Darmstadt, Germany; [3]TU, Dramstadt; [4]INFN, legnaro, Italy; [5]Univ. of Santiago de Compostela, Spain; Germany; [6]University of Liverpool, UK; [7]University of Surrey, UK; [8]HZDR Dresden-Rossendorf, Germany; [9]UCM, Madrid, Spain; [10]Chalmers University of Technology, Sweden; [11]TU, Munich, Germany; [12]KVI Groningen, Netherland; [13]LBNL, Berkeley, USA; [14]RIKEN, Japan; [15]EMMI, GSI, Darmstadt, Germany;

In 1949 Mayer and Jensen successfully explained the magic number in the nuclei using the spin-orbit interaction. This theory explained a vast amount of reachable experimental data in the next three decades until the ground breaking experiment by Thibault et. al.[1] in 1975 on neutron rich nuclei near the neutron magic number N ~ 20. In this region of nuclei, the ground states are dominated by intruder configurations from upper *pf* orbits [2]. Hence, this region of nuclear chart is called "*island of inversion*". Nuclei like $^{34, 35}$Al are lying close to this *island of inversion*. Little experimental information on ground state configuration of those isotopes are available in literature [3,4] regarding their intruder *pf-shell* contribution. Coulomb excitation is a direct probe for studying the ground state configuration of loosely bound nuclei [5,6]. Experiment S306 was performed using the existing RIB facility at GSI, Dramstadt to study the properties of the nuclei in and around the N~20 *island of inversion* through electromagnetic excitation. Short-lived radioactive nuclei were produced by the fragmentation of ^{40}Ar beam (at 531 MeV/u) on Be (8 gm/cm^2) production target at fragment separator (FRS). Secondary beam from FRS, containing ^{34,35}Al were allowed to fall on various targets [Pb for electromagnetic excitation, Carbon for nuclear excitation and without target for reactions induced by detector materials] at Cave C with the exclusive set-up for kinematically complete measurement, the FRS -LAND set-up.

The incoming beam was identified uniquely by energy loss and ToF measurements before the reaction target along with the known magnetic rigidities of FRS. Neutrons and γ-rays from the de-exciting projectile or projectile like fragments were detected by the LAND and the 4π-Crystal Ball spectrometer, respectively. Reaction fragments were tracked via the Silicon Strip Trackers and GFI detectors placed before and after the magnetic spectrometer (ALADIN), respectively. Finally, mass of the outgoing fragments were identified by reconstructing the magnetic rigidities inside ALADIN event by event using the tracker programme developed at SINP. Fig. 1 shows the γ-sum spectra of ^{33}Al obtained after Coulomb breakup of ^{34}Al. The spectrum was obtained in coincidence with ^{33}Al fragments and one neutron. These observed γ-lines are in agreement with the characteristic γ-rays of ^{33}Al reported in the literature [7]. Comparison of the measured Coulomb breakup differential cross-sections with the theoretically calculated cross-sections will help us to pin down the ground state configuration and shell inversion in these neutron-rich nuclei.

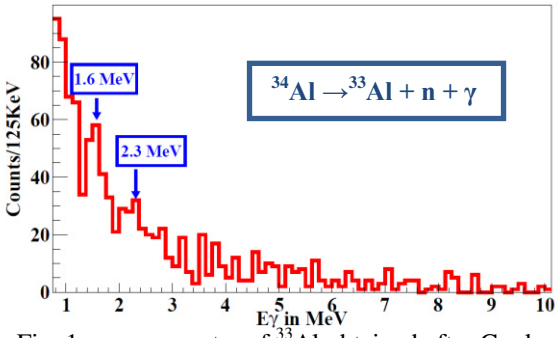

Fig. 1: γ-sum spectra of ^{33}Al obtained after Coulomb breakup of ^{34}Al in lead target.

References

[1] C. Thibault, et al., Phys. Rev. C 12 (1975) 644.
[2] T. Motobayashi, et al., Phys. Lett. B 346 (1995) 9.
[3] P. Himpe, et al., Phys. Lett. B 643 (2006) 257.
[4] C. Nociforo, et. al. Phys. Rev. C 85 (2012) 044312.
[5] T. Nakamura, et. al. Phys. Rev. Lett. 83, (1999) 1112.
[6] U. DattaPramanik, et al., Phys. Lett. B 551 (2003) 63.
[7] www.nndc.bnl.gov/

*Supported by Alexander von Humboldt (AvH) foundation.
#ushasi.dattapramanik@saha.ac.in

Fully Exclusive Measurements of Quasi-Free Knockout Reactions With ^{12}C *

V. Panin[1,2], J. Taylor[3], T. Aumann[1,2], M. Chartier[3], L. Chulkov[1], R. Lemmon[4], R. Plag[1], F. Wamers[1,2], and the R^{3}B collaboration

[1]Institut für Kernphysik, TU Darmstadt, Germany; [2]Kernreaktionen und Nukleare Astrophysik, GSI Darmstadt, Germany; [3]Physics Department, University of Liverpool, UK; [4]STFC Daresbury Laboratory, UK

A novel experimental method of measuring quasi-free knockout reactions in inverse and complete kinematics is being developed as an ideal way to study single-particle structure of exotic nuclei. First results from the observation of (p,2p) reactions with a benchmark ^{12}C beam at 400MeV/u were reported previously [1, 2]. The reaction manifests itself in a strong spatial correlation of the emerging nucleon pair and the residual nuclear system carries the information about the single-particle states involved in the reaction. In particular, the internal momentum of the knocked-out proton can be extracted by measuring the recoil momentum of the (A-1) fragment. The same information can be obtained redundantly from the kinematics of the outgoing proton pair. Figure 1 illustrates the correlation between these two methods applied to the case of a proton knockout from the valence p-shell in ^{12}C.

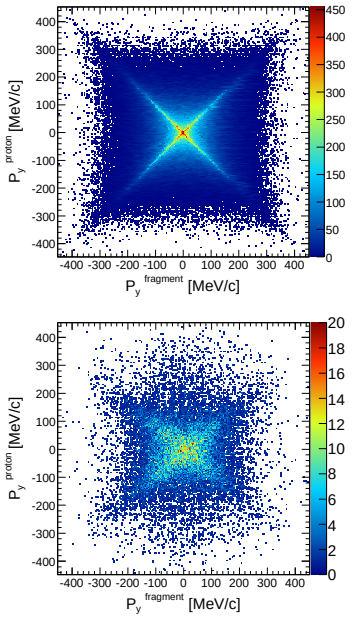

Figure 1: Correlation between the internal momentum component reconstructed via outgoing proton pair and the recoil momentum component of ^{11}B fragment from the same reaction. Top figure shows the kinematical simulation and the bottom figure is the experimental data. The cross-like shape is due to uncertainty of which one of the two protons is knocked out.

*Supported by GSI - TU Darmstadt cooperation, HIC for FAIR and BMBF (05P12RDFN8, 06DA7047I)

A detailed simulation of the experimental response has been developed based on Geant3 and FAIRroot/R3Broot software packages [3]. The improved geometrical description includes aluminum casing of NaI crystals in the Crystal Ball detector, which is aimed at the detection of outgoing protons. Additionally, copper holding structure for the silicon trackers, target-wheel motor and other materials surrounding the reaction target have been introduced into the simulation. An event generator for quasi-free scattering reactions with the proper kinematics has been implemented in the simulation code. The results of the simulation are compared to the experimental data as shown in Figure 2. The absolute efficiency for the simultaneous detection of two protons in the Crystal Ball is found to be 62$\pm$2 %.

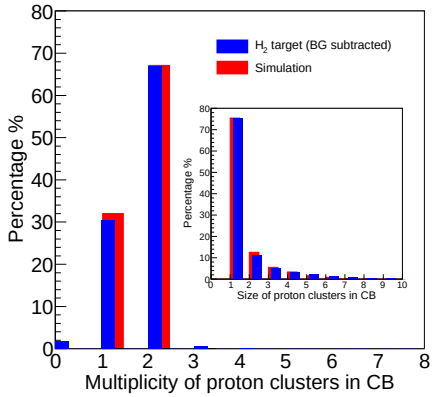

Figure 2: Simulated and experimental multiplicity distributions of high-energy proton hits (clusters) in the Crystal Ball under the condition to observe at least one non-zero signal in any crystal. The inset figure illustrates the number of crystals forming individual clusters in the case of two-proton hits.

Further development of the simulations will concern the response of the detector with respect to γ-rays accompanying the reactions. Theoretical calculations of the reaction cross sections and the momentum distributions are also under development.

References

[1] V. Panin *et al*, GSI Scientific Report 2010.

[2] V. Panin *et al*, GSI Scientific Report 2011.

[3] http://fairroot.gsi.de/

Quasi-Free Scattering of Relativistic Neutron-Deficient Carbon Isotopes*

M. Holl[1] *and the R*^{3}*B Collaboration*

[1]Institut für Kernphysik, Technische Universität Darmstadt, Germany

Single-nucleon knockout reactions and quasi-free scattering are valuable tools to determine single-particle properties of nuclei. The R^{3}B-collaboration conducted an experiment studying such reactions for light nuclei in a wide A/Q range in August 2010 [1]. Among others, the neutron-deficient carbon isotopes ^{10}C and ^{11}C were measured. The study was aimed at a quantitative understanding of absolute spectroscopic factors that appear to be quenched for deeply bound nucleons [2].

A ^{40}Ar primary beam was incident on a production target, and the selected reaction residues were then transported through the fragment separator FRS to the R^{3}B-LAND setup in Cave C. The incoming beam was identified using the time-of-flight between two scintillators, one at focus S8 of the FRS and one at the entrance of Cave C, and the energy loss in a PIN diode. The incoming angle of the beam was determined from the position on two silicon strip detectors in front of the target.

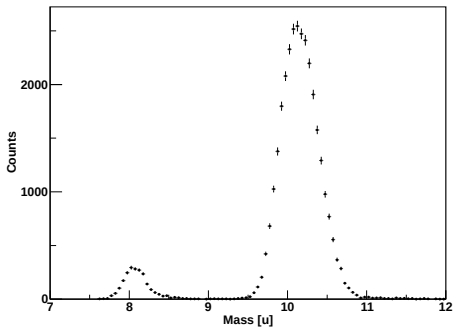

(a) Boron, $Z = 5$

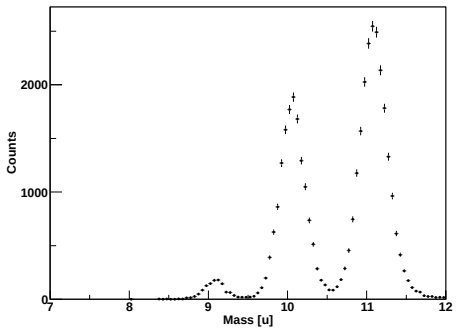

(b) Carbon, $Z = 6$

Figure 1: Tracked masses of fragments coincident with a proton in the NaI array. The charge of the fragments was determined using the energy loss in the silicon strip detectors behind the target and in the time-of-flight wall.

The target area was surrounded by a NaI array used for γ and proton detection and a box consisting of four silicon strip detectors. After passing through the ALADIN magnet, the outgoing fragments were identified and tracked using the position and energy information given by two additional silicon strip detectors, two fibre detectors, and a time-of-flight wall.

Figure 1 shows the result of this tracking. Plotted is the mass spectrum of the fragments in coincidence with a detected proton in the NaI array. By selecting $A = 10$ and requiring two proton hits in the NaI array, a preliminary cross section of 14(2) mb could be determined for the ^{11}C(p,2p)^{10}B reaction at 340 MeV/nucl. incident energy.

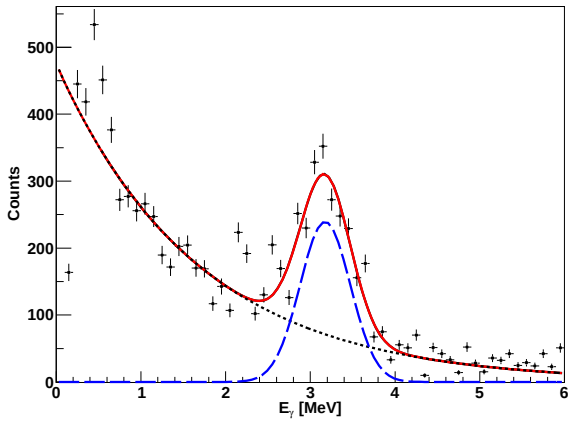

Figure 2: Gamma Spectrum measured in coincidence with the ^{11}C(p,2p)^{10}B reaction. The fitted curve is a combination of a Gaussian and an exponential background.

In Figure 2 the γ-spectrum as measured in coincidence with the ^{11}C(p,pn)^{10}C reaction is shown. To obtain this spectrum, the spectrum measured by the NaI array with a carbon target was subtracted from the spectrum measured with a CH_2 target. The spectrum is fitted by a combination of a Gaussian and an exponential background. The single bound excited state of ^{10}C can be identified very well. In the case of ^{10}B several excited states contribute to the spectrum which makes the disentanglement of the γ-ray spectrum more difficult. This analysis is still in progress.

References

[1] 'Direct Reactions of light exotic beams measured in complete kinematics at R3B', GSI Scientific Report 2010, p.166,

[2] A. Gade et al., Phys. Rev. C 77 (2008)

*Supported by the state of Hesse through the LOEWE center HIC for FAIR, and through the GSI-TU Darmstadt cooperation contract.

Simulation of the R^{3}B-LAND Response for Proton Channels using R3BROOT

F. Wamers[1,2], T. Aumann[1,2], D. Bertini[3], M. Heil[2], D. Kresan[2,3], J. Marganiec[5], R. Plag[2,6], H. Simon[2], and the R^{3}B Collaboration

[1]Institut für Kernphysik, TU Darmstadt, Darmstadt, Germany; [2]Kernreaktionen und Nukleare Astrophysik, GSI, Darmstadt, Germany; [3]IT Dept. Scientific Computing, GSI, Darmstadt, Germany; [5]ExtreMe Matter Institute, GSI, Darmstadt, Germany; [6]Goethe Universität, Frankfurt, Germany

In order to conclude the analysis presented in [1, 2] we have set up an R3BROOT-based simulation to determine the *response* of the experimental setup, in particular the *relative-energy* dependent *acceptance* and *resolution*. The presented work is based on several upgrades of the definition of the R^{3}B-LAND setup within R3BROOT, including, e.g., the reaction targets, the helium filling of the Aladin magnet, and the proton drift chambers. We have developed the following procedure to determine the setup's response:
1) Simulation of a c.o.m. phase-space decay of the fragment+proton (f+p) system at a given relative energy.
2) Lorentz boost of the f+p system into the lab system. The experimental ^{17}Ne *beam profile* and *reaction vertex* are randomised. Spatial and momentum components of fragment and proton are stored in an event-based text file.
3) Input of the text-based events to R3BROOT and corresponding MC transport via Geant3. *Energy loss* and *straggling* may be activated or not.
4) Digitisation of the Monte-Carlo data to an experiment-identical "h509" HIT-level tree, with detector-internal data in terms of PID, position, time, and energy loss.
5) Experiment-identical *tracking* of the simulated HIT data. Particle trajectories are determined, and physics observables such as masses, momenta, and also the f+p relative energy are reconstructed.
Fig. 1 shows the relative-energy resolution of the R^{3}B-LAND setup for the decay of ^{15}O+p produced via 1p-knockout from ^{17}Ne at 500 AMeV. The major contributions to the resolution are straggling and the detector resolution. The total resolution varies from about 50 keV at 100 keV to about 400 keV at 5 MeV. A first test of the performance of this simulation framework in a comparison to experimental data is shown in Fig. 2. The black data points show the relative energy of ^{15}O+p (= ^{16}F) stemming from ^{17}Ne breakup on the carbon target. The response of the first ten ^{16}F resonances is represented in the six dashed-line histograms, where the two high-lying ones combine two and four states, respectively. These response spectra have been fitted to the data in a linear superposition, shown as the red solid line. The fit does not describe the data very well. For the low-energy peak (0-2 MeV), supposed to be populated via knockout of halo-protons from ^{17}Ne [3], the tails are under-produced, while the central region is overproduced. The valley region (2-3 MeV) is not reproduced at all, and the high-energy bump (3-6 MeV) slightly overshot. Therefore, further contributions to the observed experimental spectrum, such as non-resonant background and mis-identified ^{15}O+2p events, will be added the fit.

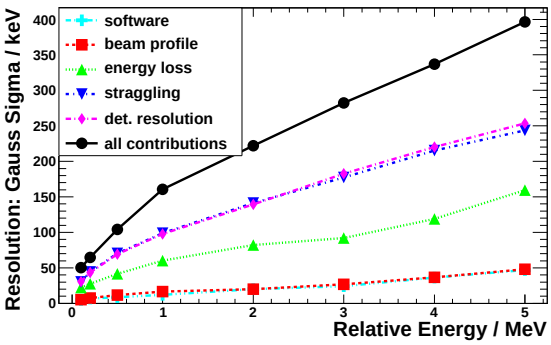

Fig. 1: Relative-energy resolution for ^{15}O+p decay at about 500 AMeV beam energy. Shown are different contributions to the resolution: software and tracking (light-blue), beam profile (red), energy loss (green), straggling (blue), detector resolution (pink), total resolution (black).

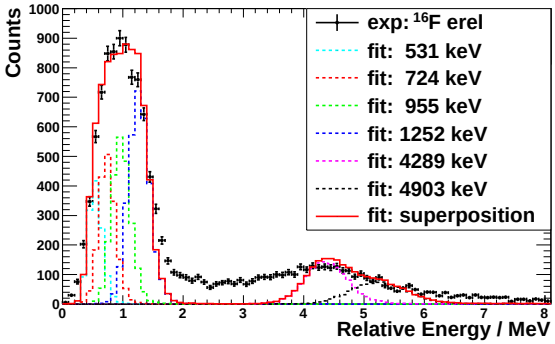

Fig. 2: Carbon-target experimental ^{16}F relative energy (black markers) compared to the simulated response for the four low-lying and six (2+4) high-lying ^{16}F resonances (dashed lines). The first two (pink) and last four (black) high-lying resonances have been merged into one response each. The six components have been linearly combined to fit (red solid line) the experimental data.

References

[1] Felix Wamers, GSI Scientific Report 2010.
[2] Felix Wamers, GSI Scientific Report 2011.
[3] L. V. Grigorenko et al., Phys. Rev. C **71** (2005) 051604.

Proton-Muon Energy Correlation in the Crystal Ball

S. Lindberg[1], *R. Thies*[*1], *T. Axelsson*[1], *V. Babic*[1], *K. Boretzky*[2], *A. Charpy*[1], *E. Fiori*[3], *I. Gasparic*[4], *P.M. Hansson*[1], *A. Heinz*[1], *H.T. Johansson*[1], *J.L. Håkansson*[1], *N.S. Kudelkin*[1], *M. Mårtensson*[1], *T. Nilsson*[1], *R. Plag*[5], *N. Rosholm*[1], *D. Rossi*[2], *H. Simon*[2], *F. Strannerdahl*[1], *and the R*^{3}*B-collab.*[2]

[1]Chalmers Univ. of Technology, Göteborg, Sweden; [2]GSI, Darmstadt, Germany; [3]EMMI, GSI Darmstadt, Germany; [4]TU Darmstadt, Germany; [5]University Frankfurt, Germany

Measurements of the response of a NaI crystal to protons and muons have been performed, and a nontrivial energy dependence has been observed.

The Darmstadt-Heidelberg Crystal Ball [1], recently upgraded to detect also protons at large scattering angles [2], is the key detector for (p,2p) reaction tagging in experiments with the LAND/R^{3}B setup at Cave C. Measurements of the proton energies are based on calibrations performed with tracked cosmic muons. This is the only readily-available method, but requires a hitherto unknown correlation between the muon and proton energy deposit. Protons at several energies from break-up of the deuteron beam during the S406 calibration experiment for NeuLAND were available, thus a dedicated test setup [3] using one crystal from the Crystal Ball was installed in order to find this correlation.

The test setup was designed to mimic the surrounding Crystal Ball in order to tag muons passing through the crystal in a similar manner as if it was sitting inside the Crystal Ball. Plastic scintillators were used in order to realise this, arranged as shown in Fig. 1. The setup was placed behind the proton arm time-of-flight detector.

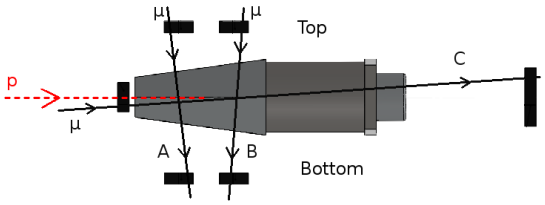

Figure 1: Detector setup. The NaI crystal is 20 cm long and surrounded by 6 plastic scintillators, five of which have an area of 5x5 cm^2 and one an area of 10x10 cm^2, all being 2 cm thick. The solid lines show different muon tracks used for calibration, c.f. Fig. 2.

Both proton and muon energy deposits were measured in the NaI crystal. The muon energy deposits for different pathlenghts, used for calibration by comparison to GEANT3 [4] simulations, are displayed in Fig. 2. The measured proton energy deposits for different beam energies are shown in Fig. 3. While we see the punch-through peak approximately at its expected position (276 MeV), the overall gain is clearly lower for protons compared to muons. An open question is the nonlinear response below punch-through, which is in contradiction to expected behaviour [5]. For details of the analysis see [6].

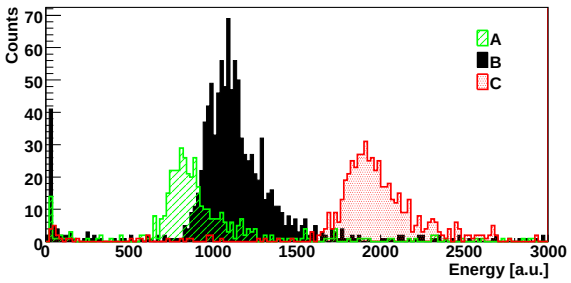

Figure 2: Energy deposited by muons for different paths (A, B, C) through the crystal, as indicated in Fig. 1.

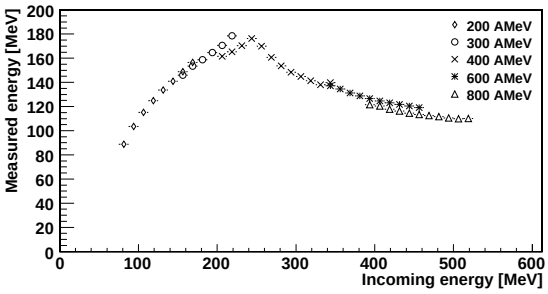

Figure 3: The y-axis, calibrated by muons, shows the proton energy deposit in the crystal. The x-axis displays the energy of the proton derived from its time of flight between the (main experiment) start detector and the scintillator in front of the crystal. The symbols indicate nominal deuteron beam energies.

References

[1] V. Metag *et al.*, "Physics with 4π-γ-detectors", Nucl. Phys. A 409, 1983, p. 331.

[2] F. Wamers, "Quasifree Scattering with Relativistic 17Ne Beams in Inverse Kinematics", GSI Sci. Rep. 2008, p. 156.

[3] T. Axelsson *et al.*, "Calibration Detector for Crystal Ball", Chalmers, Göteborg, 2012.

[4] GEANT, CERN Program Library Long Write-up W5013, CERN Geneva, 1993.

[5] K. Anami *et al.*, NIM A 404, 1998, p. 327.

[6] S. Lindberg, "Optimised use of detector systems for relativistic radioactive beams", Chalmers, Göteborg, 2013.

* ronja.thies@chalmers.se

Multivariate Analysis of the Phase 0 Experiment Data with TMVA

C.Rappold[*1,2], *O. Borodina*[1,3], *V. Bozkurt*[1], *E. Kim*[1], *F. Maas*[1,4], *and T.R. Saito*[1,2,4]

[1]GSI, Darmstadt, Germany; [2]JLU Giessen, Germany; [3]Johannes Gutenberg-Universität, Mainz, Germany; [4]The Helmholtz Institute Mainz, Mainz, Germany

The first experiment of the HypHI collaboration aimed to demonstrate the feasibility of the hypernuclear spectroscopy by means of heavy ion beam induced reactions. The phase 0 experiment was performed with a ^{6}Li beam at 2AGeV impinged on a stable ^{12}C target material. The main goal of the experiment was to produce, reconstruct and identify decay vertexes of Λ particle and $^{3}_{\Lambda}$H, $^{4}_{\Lambda}$H and $^{5}_{\Lambda}$He hypernuclei [1]. With the finalized data analysis of Phase 0 experiment, the first results show that the experimental method is viable for the study of hypernuclei.

The current analysis method involved series of rectangle cut over several geometrical observables in order to increase the signal-to-background ratio of the hypernuclear signal over the combinatorial and physical background. The hypernuclear events are reconstructed by the invariant mass of the mother system which had decayed into 2- or 3-body daughter particles and fragments. The invariant mass distribution is the principal observable used to determine the significance of the hypernuclear signal proportion.

The TMVA package included inside the ROOT framework allows multivariate analysis of the data sets [2, 3]. Those analysis methods have been employed to improve the quality and purity of the hypernuclear data sets from the experimental data of the Phase 0 experiment. For each species of interest, Λ, $^{3}_{\Lambda}$H and $^{4}_{\Lambda}$H, a set of input observables were selected for the discrimination of the signal and background component of the invariant mass distribution. The signal data set used for the training of the different classifiers was characterized to be in the mass interval $\bar{m} \pm 3\ \sigma_m$, where $\bar{m}$ and σ_m were obtained from the signal+background global fit of the invariant mass. The background data set is then characterized by the side bands of the peak region ($[\bar{m}-6\sigma_m, \bar{m}-3\sigma_m]$ and $[\bar{m}+3\sigma_m, \bar{m}+6\sigma_m]$). After the training of the classifiers of interest over a partial sample of the experimental data, those classifiers are tested to estimate their background rejection power and signal efficiency. The top panel of Fig. 1 shows the results of several multivariate classifiers over the $^{3}_{\Lambda}$H data set. The used classifiers were based on the Projective Likelihood method (*LikelihoodPCA*, *LikelihoodKDE*), the Linear Discriminant method (*LD*) and Artificial Neural Network methods (*MLP*, *MLPBNN*). In the case of the named *MLPBNN* classifier, its output is shown in the bottom panel of Fig. 1. An output value close to 0 means that the event is considered as part of the background, while a value close to 1 would mean a $^{3}_{\Lambda}$H event. A threshold cut can be applied in order to select the most probable $^{3}_{\Lambda}$H events. Thanks to the classification of the events, the background contribution inside of the signal region $\bar{m} \pm 3\ \sigma_m$ can be identified and thus rejected. By using the best classifier from the multivariate analysis, one can obtain a data set of most probable hypernuclear events which can then be used for extracting diverse physical observables with good statistics.

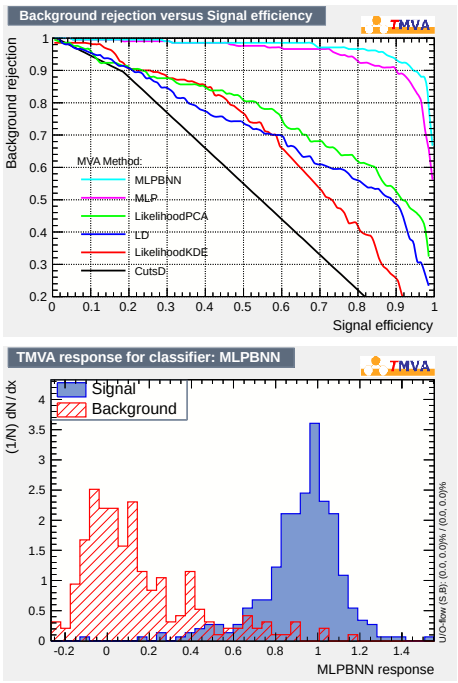

Figure 1: Top panel : the Reciever Operating Characteristics"ROC" curve of the multivariate analysis of experimental data for the $^{3}_{\Lambda}$H hypernucleus. It represents background rejection power as function of the signal efficiency obtained for each classifier used for different multivariate analysis. Bottom panel : Output of the Multilayer perceptron (artificial neural network) classifier used to discriminate the signal of $^{3}_{\Lambda}$H hypernucleus (blue distribution) to the background component (red distribution).

References

[1] Proposal of the HypHI Phase 0 experiment, the HypHI collaboration.

[2] A. Hoecker, et al. (2007) arXiv preprint physics/0703039.

[3] P. Speckmayer, et al., Journal of Physics: Conference Series **219** (2010) 032057.

* c.rappold@gsi.de

First Mass Measurements of Projectile Fragments with a Multiple-Reflection Time-of-Flight Mass Spectrometer at the FRS Ion Catcher*

J. Ebert[1], *T. Dickel*[1,2], *W. R. Plaß*[1,2], *S. Ayet*[2], *P. Dendooven*[3], *M. Diwisch*[1], *A. Estrade*[2], *F. Farinon*[2], *H. Geissel*[1,2], *F. Greiner*[1], *E. Haettner*[1,2], *C. Jesch*[1], *N. Kalantar-Nayestanaki*[3], *R. Knöbel*[1,2], *J. Kurcewicz*[2], *J. Lang*[1], *I. Moore*[4], *I. Mukha*[2], *C. Nociforo*[2], *M. Petrick*[1], *M. Pfutzner*[2], *S. Pietri*[2], *A. Prochazka*[2], *S. Purushothaman*[2], *M. P. Reiter*[1], *A.-K. Rink*[1], *C. Scheidenberger*[1,2], *M. Takechi*[2], *H. Weick*[2], *J. S. Winfield*[2], *and M. I. Yavor*[5]

[1]Justus-Liebig-Universität, Gießen, Germany; [2]GSI, Darmstadt, Germany; [3]KVI, University of Groningen, The Netherlands; [4]University of Jyväskylä, Finland; [5]Institute for Analytical Instrumentation, St. Petersburg, Russia

The FRS Ion Catcher [1] is a test facility for the Low Energy Branch (LEB) of the Super-FRS at FAIR. It includes a novel cryogenic stopping cell (CSC) [2] and a multiple-reflection time-of-flight mass spectrometer (MR-TOF-MS) [3, 4] for mass measurements, isobar separation and broad-band mass spectrometry for ion identification and diagnostics purposes.

In an online experiment in July and August 2012 at the FRS Ion Catcher the performance characteristics of the cryogenic stopping cell [5] have been investigated and first direct mass measurements of ^{238}U projectile fragments have been performed with a MR-TOF-MS. For three of the nuclides, ^{211}Po, ^{211}Rn and ^{213}Rn, the mass was measured directly for the first time (Fig.1, Fig.2). The successful measurement of the noble gas isotope ^{213}Rn with a half life of only 20 ms and 25 detected ions demonstrates that very short-lived nuclides can be stopped and extracted from the CSC and measurements can be performed quickly, efficiently and with high sensitivity.

Usually, in MR-TOF-MS only ions are considered, which have performed the same number of turns inside the mass analyzer, otherwise ions with different masses and turn numbers could make the mass spectrum ambiguous. At a high resolving power and a large number of turns of the ions in the analyzer, only isobars are hence available as calibrants. For measurements of nuclides with $A = 211$ isobaric ions from an internal ion source could be used as calibrants. However, for nuclides with $A = 213$, no such isobaric calibrants were available. Therefore a novel analysis method was developed, that allows calibration of a time-of-flight (TOF) spectrum without isobaric calibrants, making use of ions that have undergone a different number of turns.

Similar instruments have been developed for use as isobar separator at the TITAN facility at TRIUMF (Canada) and as a mobile high-resolution mass spectrometer in analytical mass spectrometry [6].

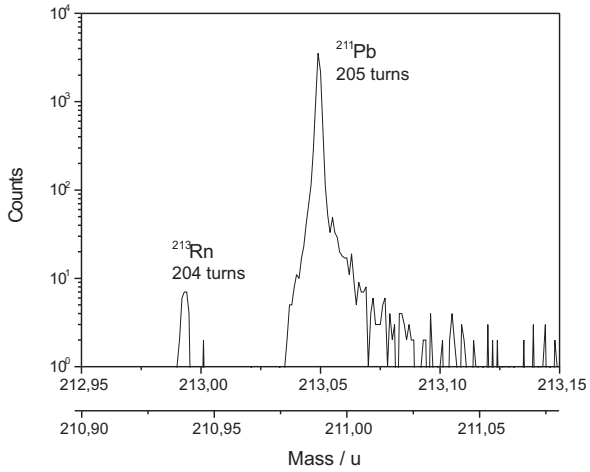

Figure 1: Mass spectrum of ^{213}Rn ions together with ^{211}Pb calibrant ions from an internal ion source.

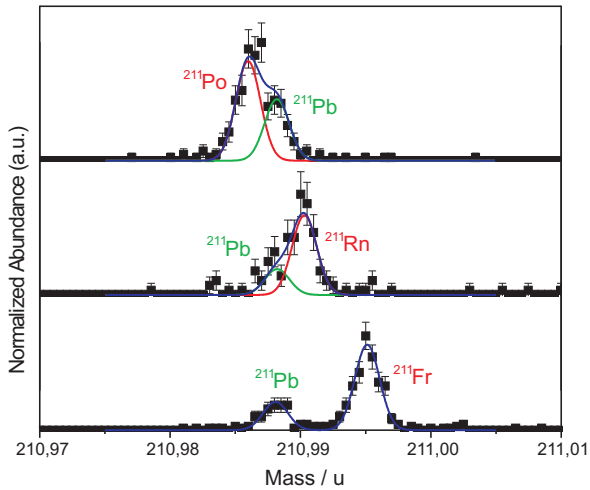

Figure 2: Mass spectrum of the mass 211 isotopes Fr, Po and Rn.

References

[1] T. Dickel et al., this volume.

[2] M. Ranjan et al., Eur. Phys. Lett. 96 (2011) 52001.

[3] W.R. Plaß et al., Nucl. Instrum. Methods B 266 (2008) 4560.

[4] T. Dickel, Doctoral Thesis, 2010, JLU Gießen.

[5] M. P. Reiter et al., this volume.

[6] J. Lang et al., this volume.

*This work was supported by the BMBF under contracts no. 06GI9114I and 05P12RGFN8 and by the state of Hesse (LOEWE-Schwepunkt AmbiProbe)

Design and Commissioning of a Mobile Multiple-Reflection Time-of-Flight Mass Spectrometer for In-situ Analytical Mass Spectrometry*

J. Lang[1], W.R. Plaß[1,2], T. Dickel[1,2], J. Ebert[1], H. Geissel[1,2], E. Haettner[1], W. Lippert[1], M. Petrick[1], A. Pikhtelev[3], C. Scheidenberger[1,2], and M. Yavor[4]

[1]Justus-Liebig-Universität, Giessen, Germany; [2]GSI, Darmstadt, Germany; [3]Institute for Energy Problems of Chemical Physics, Chernogolovka, Russia; [4]Institute for Analytical Instrumentation, RAS, St. Petersburg, Russia

The goal of the LOEWE-Schwerpunkt AmbiProbe [1] is the development of new mass spectrometric tools and methods for in-situ analytics applied to the fields of health, security, and environmental and climate research. In-situ analytics require direct and reliable sampling of ions from the environment and mobile mass spectrometers with minimum infrastructural requirements. Developments within AmbiProbe allow for innovative and hitherto inaccessible applications.

One of these developments is a mobile high-resolution multiple-reflection time-of-flight mass spectrometer (MR-TOF-MS). For the first time, this MR-TOF-MS allows for high-resolution ($m/\Delta m > 10^5$) and highly accurate ($\delta m/m < 10^{-6}$) mass analysis in a mobile device. Strong synergy effects exist with the previously developed MR-TOF-MS [2] for applications in nuclear physics in combination with the cyogenic stopping cell (CSC) at the FRS and Super-FRS [3].

The system consists of several components (Fig. 1): An atmospheric pressure interface (API) with an inlet capillary, differential pumping stages and RF ion guide, to introduce ions from different kinds of atmospheric ion sources. An RF mass filter to suppress contaminents, an RF cooler quadrupole and a subsequent RF ion trap for thermalization and bunching of the ions. This beam preparation system allows for a duty cycle close to 100% for the continously produced atmospheric ions and injects the short ion bunch (< 8 ns) into the coaxial multiple-reflection time-of-flight analyzer. This is traversed many times by the ions to increase the total flight path and thus increase the mass resolving power. The flight time is determined by an MCP detector. The system is placed in a differentially pumped recipient and mounted with all components required for its operation, such as vacuum pumps, power supplies, electronics and data acquisition system in a mobile frame with a total volume of only 0.8 m^3 (Fig. 2). Compared to other high resolution mass spectromteres the setup is small and light and therefore ideally suited for in-situ meassurements.

The MR-TOF-MS has been designed, built and commissioned. A preliminary mass resolving power of $m/\Delta m \approx 100000$ has been achieved and further work is underway to increase the resolving power to several 10^5. Transmission with mass range of a factor 4 (i.e. with a maximum mass that is 4 times larger than the minimum transmitted mass) with constant mass resolving power has been demonstrated. A repetition rate up to 2 kHz features measurements of time-dependent processes such as LC and GC. The mobile MR-TOF-MS offers two different operation modes; a pass-through mode with broad mass range and a multiple-turn mode for high resolution. Further, an ion beam camera has been built for diagnostic purposes and developments of a DAQ, analysis and control software have been done and are ongoing.

The unique combination of high resolution and mobility is of great advantage for various in-situ messurements. Envisaged applications for 2013 are realtime tissue recognition during electro-surgery, in-situ determination of the composition and structure of biomolecules as well as the investigation of soil and water samples. Further developments in automation, ion optics, mass range extension and calibration methods will again provide benificial synergy effects with MR-TOF-MS application in other fields.

*This work was supported by the state of Hesse (LOEWE-Schwerpunkt AmbiProbe)

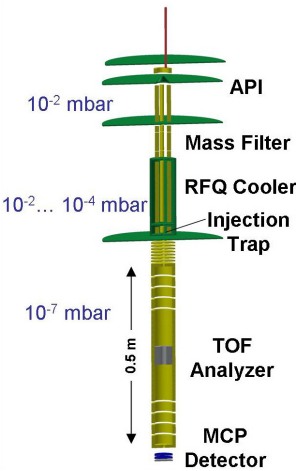

Figure 1: Schematic view of the mobile MR-TOF-MS

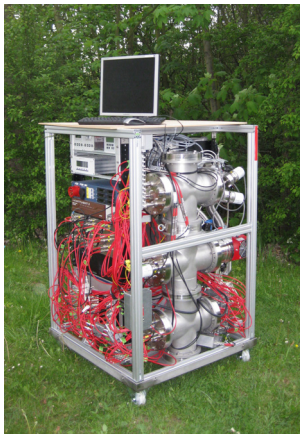

Figure 2: Photograph of the instrument

References

[1] B. Spengler et al., Spiegel der Forschung - Wissenschaftsmagazin der JLU Gießen 27 (2010) 64-69.

[2] W.R. Plaß et al., Nucl. Instrum. Methods B, 266 (2008) 4560.

[3] J. Ebert et al., this volume.

Experimental and Theoretical Studies of Cherenkov Radiation Angular Distributions from Relativistic Au Beam at SIS-18 GSI*

E. Fiks[1], Yu. Pivovarov[1#], O. Bogdanov[2], H. Geissel[3], C. Scheidenberger[3], J. Ruzicka[4]

[1]National Research Tomsk Polytechnic University, Tomsk, Russia; [2]INFN Laboratori Nazionali di Frascati, Frascati (RM), Italy; [3]GSI, Darmstadt, Germany; [4]Faculty of Mathematics, Physics and Informatics, Comenius University, Bratislava, Slovakia.

Several experiments [1-3] on detection of the Cherenkov radiation (ChR) from ~0.9 GeV/u Au relativistic heavy ions (RHI) were performed during 1996-2001 at SIS-18 heavy ion accelerator, GSI.

An unusual relation between ChR angular distribution width and radiator thickness was observed in [2]. Unusual means, that the width of the standard Tamm-Frank angular distribution of ChR should decrease with increase of the radiator thickness, while the experiment showed larger broadening of the ChR ring width in the case of the thicker radiator compared to the thinner one (Fig. 1, top). Both ChR images on the photographic films were recorded under the same conditions but for different radiator thicknesses. Therefore, the difference in widths of both rings may be only due to different energy loss in the radiators L_1 and L_2, i.e. due to different exit velocities of RHI. At that time, obtained experimental data were explained only qualitatively, as the influence of RHI slowing-down in a radiator, but both quantitative theory and numerical calculations have not been developed.

In our work [4] the analysis of these experiments is performed and the experimental data are compared with numerical calculations which take into account the RHI slowing-down in a radiator [4]. Our calculations are based on the theory developed in [5-6] except that RHI mean ionization energy loss is calculated now using the computer code ATIMA [7].

Our numerical calculations (Fig. 1, bottom) are performed with the same parameters of RHI beam and radiator as in [2]. To take into the fact that ChR was detected in a definite wave length range (photographic film), we summed up the ChR intensities over optical wave length range. Besides, we took into account the initial energy spread of Au beam. The black curve in the Figure 1 (bottom) is calculated using the Bethe-Bloch formula for RHI ionization energy loss, while the red one is calculated using ATIMA. The Bethe-Bloch formula gives lower values of ionization energy loss (for the RHI energy ~ 1 GeV/u) – that is why the ChR intensity is greater and angular distribution is broader in the case of red (ATIMA) curve.

Our numerical calculations are in quantitative agreement with experiment, especially if the calculated ChR angular width is recalculated to obtain the experimentally observed ChR spatial distribution, using the fitting function from [2]. So, for several GeV/u RHI, an unusual relation between ChR angular distribution width and radiator thickness is now explained quantitatively as an effect of RHI slowing down in radiator.

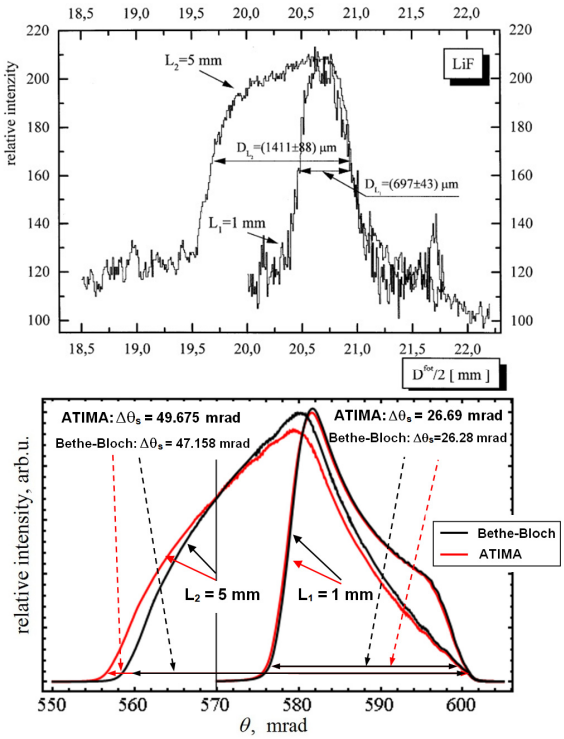

Figure 1: Experimentally recorded [2] ChR spatial distribution on a photographic film (top) and calculated [4] ChR angular distribution (bottom) for 2 different radiator thicknesses.

References

[1] J. Ruzicka et al., Nuclear Instruments and Methods in Physics Research. A. 369 (1996) 23.

[2] J. Ruzicka et al., Nuclear Instruments and Methods in Physics Research. A. 431 (1999) 148.

[3] J. Ruzicka et al., Vacuum. V. 63 (2001) 591.

[4] O. V. Bogdanov, E. I. Fiks, Yu. L. Pivovarov, H.Geissel, C. Scheidenberger, J. Ruzicka, submitted to Nucl. Instr. and Meth. B (2013).

[5] O.V. Bogdanov, E.I. Fiks and Yu.L. Pivovarov, Journal of Physics. V. 357 (2012) 1.

[6] O.V. Bogdanov, E.I. Fiks and Yu.L. Pivovarov, Journal of Experimental and Theoretical Physics. Vol. 115 No. 3 (2012) 391.

[7] http://www-linux.gsi.de/~weick/atima/.

* Work supported by "Russian Foundation for Basic Research" contract No. 12-02-01314-a, by the Grant from President of Russian contract No. MK 2059.2011.2, by "HIC for FAIR" program, Giessen Universitat, Germany.

#pivovarov@tpu.ru

Slowing-Down in the Radiator and Cherenkov Radiation Angular Distributions from Relativistic Heavy Ions at FAIR, SPS and LHC energies*

E. Fiks[1#], Yu. Pivovarov[1], O. Bogdanov[2], H. Geissel[3], C. Scheidenberger[3]

[1]National Research Tomsk Polytechnic University, Tomsk, Russia;
[2]INFN Laboratori Nazionali di Frascati, Frascati (RM), Italy; [3]GSI, Darmstadt, Germany.

As shown earlier in Ref. [1-3], at relativistic heavy ion (RHI) energies of order of 1 GeV/u the slowing-down in a radiator leads to a significant broadening of the Cherenkov ring and forming a specific diffraction-like structure of the Cherenkov radiation (ChR) angular distribution, which is different compared with standard Tamm-Frank distribution (see, in Fig. 1, top). The ChR angular distribution width becomes dependent on: the energy, charge and mass of an ion; Cherenkov photon wave length and corresponding refractive index; stopping power of radiator and its thickness. The results of calculation show that only at higher RHI energies (> 30 GeV/u) (FAIR, SPS and LHC), the ChR angular distribution (at the reasonable radiator thickness) becomes very close to the Tamm-Frank distribution and practically does not depend on the RHI slowing-down in a radiator (Fig.1, bottom), if only ionization energy loss is taken into account [4].

Our calculations are based on the theory developed in [2-3] except that RHI mean ionization energy loss (stopping power) is calculated now using the computer code ATIMA [5] valid for RHI energies < 450 GeV/u. For higher RHI energies we used Lindhard and Sorensen theory of ionization energy loss [6], valid for ultra-relativistic case. Based on our calculations, we can distinguish three different RHI energy regions:

1. The first region (~ 1 GeV/u) - may be the most interesting, here the ionization energy loss is significant and ChR emission angle essentially decreases following the decrease of velocity during RHI penetration through a radiator. A complicated diffraction-like structure of the ChR angular distribution appears, and it probably can be used for Z- and A- identification of RHI.
2. The second region (> ~5 GeV/u < ~ 100 GeV/u): ChR emission angle depends on the RHI initial velocity, therefore the angular distribution of ChR is shifted towards greater ChR emission angles (compared to region 1), but ChR emission angle almost does not change during RHI penetration through a radiator of reasonable thickness and the structure of ChR angular distribution is similar to the Tamm-Frank distribution (calculated for RHI constant velocity).
3. The third region (> ~100 GeV/u): ChR radiation angle practically does not depend on the RHI initial energy and does not change during RHI penetration through a radiator of reasonable thickness and ChR angular distribution also remains similar to the Tamm-Frank distribution.

The RHI threshold energy for each of three regions is different for different ions species and radiators.

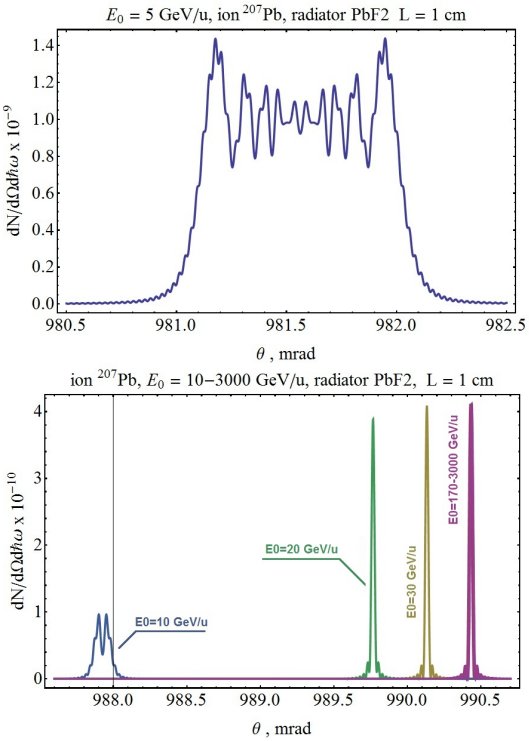

Figure 1: ChR angular distribution from 5 GeV/u (top) and 10-3000 GeV/u (bottom) ^{207}Pb beam in a PbF_2 radiator, thickness L = 1cm. The ChR photon wavelength is 0.39 nm, the corresponding refractive index = 1.82.

References

[1] V.R. Altapova, O.V. Bogdanov and Yu.L. Pivovarov, Nucl. Instr. and Meth. B. 256 (2009) 109.
[2] O.V. Bogdanov, E.I. Fiks and Yu.L. Pivovarov, Journal of Physics. V. 357 (2012) 1.
[3] O.V. Bogdanov, E.I. Fiks and Yu.L. Pivovarov, Journal of Experimental and Theoretical Physics. Vol. 115 No. 3 (2012) 391.
[4] O. V. Bogdanov, E. I. Fiks, Yu. L. Pivovarov, H.Geissel, C. Scheidenberger, Nucl. Instr. and Meth. B (2013), accepted for publication.
[5] http://www-linux.gsi.de/~weick/atima/.
[6] J. Lindhard and A.H. Sorensen, Phys. Rev. V. 53, N.4 (1996) 2443.

* Work supported by "Russian Foundation for Basic Research" contract No. 12-02-01314-a, by the Grant from President of the Russian Federation contract No. MK 2059.2011.2, by "HIC for FAIR" program, Giessen Universitat, Germany.

#elenafiks@gmail.com

Improved Empirical Parametrization of Fragmentation Cross Sections

K. Sümmerer[1]
[1]GSI, Darmstadt, Germany

A useful tool to predict production cross sections of exotic nuclei in high-energy fragmentation reactions is a universal analytical formula called EPAX [1, 2]. This formula allows to calculate the yields from fragmenting all non-fissile projectiles in the range of projectile masses between about 40 to 209. The cross sections are assumed to be energy-independent and appear to be reliable at incident energies above $\approx 100\,A$ MeV. The EPAX parametrization aims at reproducing the bulk of the measured cross sections within a factor of about two for fragment masses down to about half the projectile mass.

The previous version of the formula, EPAX 2 [2], has proven to give rather realistic estimates of many production cross sections of exotic nuclei, for some neutron-deficient fragments even down to the sub-nanobarn regime [2]. However, large discrepancies with measured data were found for extremely neutron-rich nuclei like, e.g., fragment yields from 1 A GeV ^{136}Xe+^{9}Be, which were overestimated by EPAX by up to two orders of magnitude.

A new version of the EPAX formula has therefore been proposed which maintains the relatively good agreement with measured data on the neutron-deficient side and improves the agreement on the neutron-rich side of the line of β-stability. A detailed description of this version (EPAX 3) and its differences with respect to the previous one has been given in a recent publication [3]; coded versions in FORTRAN [4] and C [5] language can be downloaded from the GSI Document Server.

An example of the improvement provided by EPAX 3 for neutron-rich fragments is given in Fig. 1. It plots the measured cross sections for proton-loss channels in the reaction 1 A GeV ^{136}Xe+^{9}Be [6] for a loss of up to 6 protons, covering about nine orders of magnitude in cross section. The full curve in this figure denotes the predictions of the new formula, EPAX 3, whereas the dashed one results from the previous version. The slope of the new curve fits much better to the measured data. The agreement is also comparable to the quality of a physical model, the "cold fragmentation" model, COFRA, by Benlliure *et al.* [7].

Figure 2 shows that the good agreement with experimental data for neutron-deficient fragments has been maintained. This figure also shows that the empirical scaling factor with target mass (Eq.(3) in Ref. [3]) is appropriate.

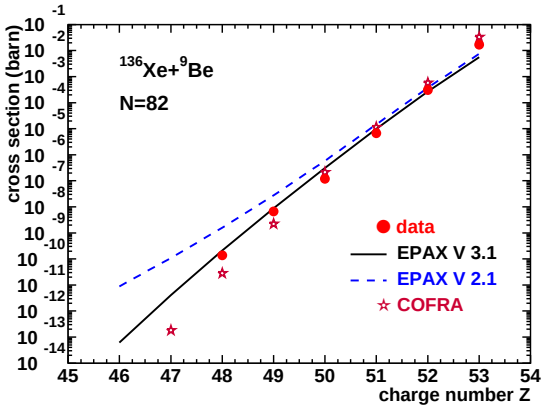

Figure 1: Experimental cross sections of proton-loss channels for the reaction of 1 A GeV ^{136}Xe on ^{9}Be (dots, Ref. [6]) in comparison with EPAX 3 (full line), EPAX 2 (dashed curve) and with the physical "cold fragmentation" model COFRA [7] (stars).

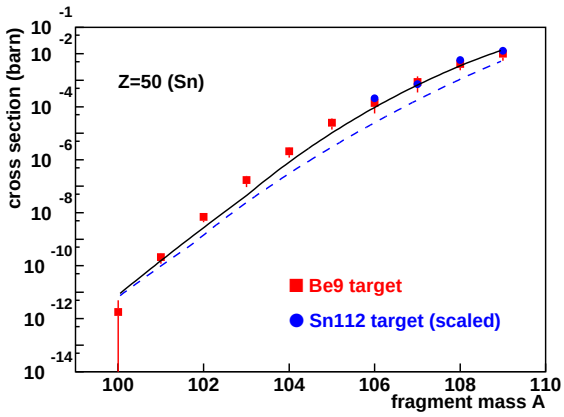

Figure 2: Experimental Sn fragment cross sections from the reaction of 1 A GeV ^{112}Sn on ^{9}Be (squares, Ref. [8]) and ^{112}Sn (dots, Ref. [9]) targets in comparison with EPAX 3 (full line) and EPAX 2 (dashed curve). The Sn-target data points have been scaled by a factor of 0.65.

References

[1] K. Sümmerer *et al.* Phys. Rev. C **42**, 2546 (1990).

[2] K. Sümmerer and B. Blank, Phys. Rev. C **61**, 034607 (2000).

[3] K. Sümmerer, Phys. Rev. C **86**, 014601 (2012). Errors in Eqs.(5), (6), and (19) of that article have been corrected in an Erratum (Phys. Rev. C, to be published).

[4] http://www.gsi.de/documents/FRS-reference-2012-001.html.

[5] http://www.gsi.de/documents/FRS-reference-2012-002.html.

[6] J. Benlliure *et al.*, Phys. Rev. C **78**, 054605 (2008).

[7] J. Benlliure *et al.*, Nucl. Phys. **A660**, 87 (1999).

[8] A. Stolz *et al.*, Phys. Rev. C **65**, 064603 (2002).

[9] V. Föhr *et al.*, Phys. Rev. C **84**, 054605 (2011).

Contributions to Reference Data Libraries *

B. Pfeiffer[1,2], *I. Dillmann*[1,2], *and C. Scheidenberger*[2,1]
[1]II. Physik. Institut, Justus-Liebig-Universität, Gießen, Germany; [2]GSI, Darmstadt, Germany

Introduction

In 2008, European nuclear physics research institutions instigated an effort to intensify their participation in the international task of establishing "Reference Data Libraries for Nuclear Applications" [1]. Researchers at the II. Physikalisches Institut at Gießen and GSI are participating in these tasks with their expertise.

Masses

The systematic screening of all relevant literature for experimental results on nuclear masses, half-lives, β-delayed proton and neutron emission probabilities, spins, parities and isomeric states has been continued. The values collected since 2003 have been entered into the data bases underlying two new compilations / evaluations:

A. The Atomic Mass Compilation AMC2012

In collaboration with Prof. Venkataramaniah from Sri Sathya Sai Institute for Higher Learning all new experimental results on nuclear masses have been combined with the older data included in AME03 [3] in the *Atomic Mass Compilation – AMC2012* [2].

B. The Atomic Mass Evaluation AME2012

Updated versions of the 2003 Atomic Mass Evaluations [3] have been prepared by an international collaboration including GSI / Gießen and been published in December 2012 [4, 5, 6].

Beta-delayed neutrons

The β-delayed neutron emission probabilities P_n and the energy spectra for fission products are important input data for the calculation of nuclear reactors, decay heat, and nuclear safeguard applications, requiring evaluated data sets. The latest compilations / evaluations date to around the year 2000 [7] and are limited to the fission product region. With the advent of radioactive beam facilities, the production of very neutron-rich nuclei is now possible for a wider range of elements. The decay of these nuclei is studied at GSI applying a variety of detection methods. One technique detects the β-delayed neutrons emitted by very neutron-rich isotopes. Such experiments will be an important research program at the future SUPER-FRS.
As a basis for these studies a new evaluation encompassing **all** known delayed-neutron emitting isotopes has to be undertaken. Given the experience of the IAEA in Vienna with these evaluations, the Nuclear Data Group was contacted to establish an IAEA coordinated research program. In October 2011 an *IAEA Consultant's Meeting on Beta-Delayed Neutron Emission Evaluation* [8] was held as a first step. The proposal for a Coordinated Research Program (CRP) on *Beta-Delayed Neutron Emission Evaluation* [9] has now been accepted by the IAEA: "The overall CRP objective is to enhance Member States knowledge and calculational capabilities in the fields of nuclear energy, safeguards, used fuel and waste management and nuclear sciences by creating a Reference Database for Beta-Delayed Neutron Emission that contains both a compilation of existing data and recommended data, which will be made readily available to the user community. The project is due to start in 2013 and is envisioned to have a length of five years" [10].

* Work supported by the Strategic Cooperation Contract between GSI and Justus-Liebig-Universität Gießen

References

[1] "Reference Data Libraries for Nuclear Applications – ENSDF"; Report of Technical Meeting of IAEA Nuclear Data Section INDC(NDS)-0543, November 2008, Vienna http://www-nds.iaea.org/publications/indc/indc-nds-0543.pdf

[2] B. Pfeiffer, K. Venkataramaniah, U. Czok, C. Scheidenberger, submitted to ADNDT.

[3] Nuclear Physics A729 (2003).

[4] G. Audi, F.G. Kondev, M. Wang, B. Pfeiffer, X. Sun, J. Blachot and M. MacCormick, Chinese Physics C36 (2012) 1157.

[5] G. Audi, M. Wang, A.H. Wapstra, F.G. Kondev, M. MacCormick, X. Xu and B. Pfeiffer, Chinese Physics C36 (2012) 1287.

[6] M. Wang, G. Audi, A.H. Wapstra, F.G. Kondev, M. MacCormick, X. Xu and B. Pfeiffer, Chinese Physics C36 (2012) 1603.

[7] G. Rudstam et al., ADNDT 53, 1 (1993); B. Pfeiffer et al., Prog.Nucl.Energy 41, 39 (2002), and refrences therein.

[8] Summary report of *The IAEA Consultant's Meeting on Beta-Delayed Neutron Emission Evaluation*, IAEA, Vienna, Austria, 10-12 October 2011
IAEA Report INDC(NDS)-0599 http://www-nds.iaea.org/publications/indc/indc-nds-0599.pdf

[9] http://www-nds.iaea.org/beta-delayed-neutron/

[10] IAEA - Nuclear Data Newsletter, No. 54, November 2012, p. 10
http://www-pub.iaea.org/MTCD/Publications/PDF/Newsletters/ND-NL-54.pdf

Super-FRS Design Status Report

M. Winkler[1,#], F. Amjad[1], K.-H. Behr[1], C. Betz[1], T. Blatz[1], A. Breidert[1], A. Brünle[1], F. Garcia[2], H. Geissel[1,3], M. Gleim[1], C. Karagiannis[1], B. Kindler[1], O. Kiselev[1], K. Kopp[1], E. Kozlova[1], A. Krämer[1], A. Kratz[1], H. Leibrock[1], B. Lommel[1], H. Müller[1], C. Mühle[1], G. Münzenberg[1], I. Mukha[1], C. Nociforo[1], L. Orona[1], S. Pietri[1], A. Prochazka[1], C. Scheidenberger[1,3] C. Schlör[1], B. Sitar[4], H. Simon[1], M. Tomut[1,5], H. Weick[1], A. Wiest[1], C. Will[1], J.S. Winfield[1] and Y. Xiang[1]

[1]GSI, Darmstadt, Germany; [2]HIP Helsinki, Finland; [3]JLU Giessen, Germany; [4]CUB Bratislava, Slovakia; [5]NIMP, Bucharest, Romania.

System and building design

A modular design of vacuum chambers for beam detectors at the focal planes of the Super-FRS has been developed. Such a design allows adapting the Super-FRS operation either to a separator or to a spectrometer mode.

Various modifications of the NUSTAR buildings occurred during the execution planning phase, mainly due to fire protection or radiation safety requirements. In particular the access as well as emergency exit schemes needed replanning. An important milestone was achieved in October 2012 when we got the construction permit for the target building including the hot cell complex.

In view of the optimization of the building size and the opportunities for the future research program, the layout and design of the Energy-Buncher Spectrometer of the Low-Energy Branch of the Super-FRS has been revisited. In this investigation a dispersion-matched operation has been added to the energy bunching and large acceptance operation. A new layout possibility for the Energy Buncher with the first dipole bending to the right is under investigation. With this "S-shaped" configuration and an additional intermediate x-focus between the dipole magnets, it is possible to reduce significantly the dispersion and the general horizontal beam envelope while still maintaining the required resolving power of 600.

Detector development

The GEM-TPC is considered as next generation particle tracking detector at Super-FRS. Two prototypes with single-strip and integrated digital GEMEX electronics readout were built with two different pad plane configurations in collaboration with HIP Helsinki, Finland and CUB Bratislava, Slovakia. Both prototypes were successfully tested during a S417 beam time at the FRS [1].

Si strip detectors are possible candidates for Time-of-Flight measurements at the Super-FRS. Two dedicated beam tests with several single Si samples (active area ≈ 25 mm^2) provided by PTI, St. Petersburg, demonstrated that it is possible to achieve a time resolution of 20-40 ps for Au (E = 600 MeV/u) and U ions (E = 350 MeV/u). The signals have been digitized by using a fast oscilloscope. No deterioration of timing properties was found after irradiating the detectors up to 1kGy (equivalent 1-3 weeks running at Super-FRS).

* Work supported by EU, CRISP contract No. 283745.

m.winkler@gsi.de

Remote handling

The development of large size (1200x200 mm^2) pillow seals is underway. These are inflatable seals and will be used in the target area where no direct human access is possible. These pillow seals are essential to guarantee the sealing between the large area dipole magnet chambers and beam catcher chambers.

A hot cell test stand was planned and will be build up in 2013. It will basically consist of a simple frame and two master-slave manipulators. It is of importance to have such a tool available in a very early project phase not only to start training on remote handling but especially to test the designs of RH components under realistic conditions.

Magnets

At the FAIR Council meeting in December 2012 it was decided that the superferric dipole magnets shall be purchased via a FAIR call for tender. The necessary specifications are under preparation and shall be ready until summer 2013.

The superferric multiplets are already assigned as German (GSI) In-Kind contribution to the FAIR-Project. The specifications for the various individual magnets, as well as the integrated modules (Fig. 1) are finished and the call for tender is in preparation. It is planned to have a signed contract for the first pre-series modules in mid 2013.

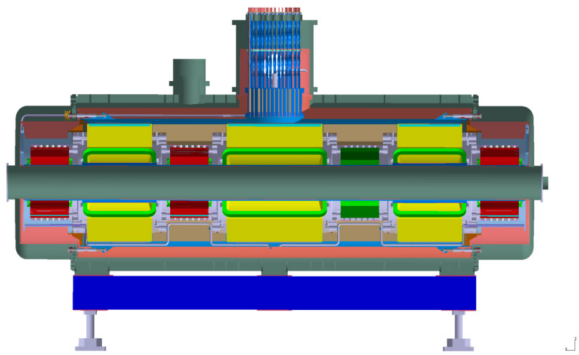

Figure 1: Design of the SC multiplet. Overall length: ≈7m; Total weight: ≈50 ton.

References

[1] F. Garcias *et al*., this report.

Unique Experiments at the Frontiers of Nuclear Physics: the Experimental Program for the Super-FRS

C. Scheidenberger[1,2], S. Gales[3], H. Geissel[1,2], C. Nociforo[1], H. Simon[1], I. Tanihata[4,5], H. Weick[1], M. Winkler[1]
for the Super-FRS Collaboration

[1] GSI Helmholtzzentrum für Schwerionenforschung GmbH, 64291 Darmstadt, Germany; [2] Justus-Liebig-Universität Gießen, 35392 Gießen, Germany; [3] IPN Orsay/IN2P3-CNRS and University Paris XI, 91406 Orsay Cedex, France; [4] Research Center for Nuclear Physics, Osaka University, Osaka 567-0037, Japan; [5] School of Physics and Nuclear Energy Engineering, Beihang University, Beijing, China

The superconducting fragment separator (Super-FRS) is the magnetic high-resolution spectrometer, which is coupled to the heavy-ion synchrotron complex at FAIR. It is the central device of the NuSTAR collaboration and will provide relativistic beams of exotic nuclei ranging from hydrogen to uranium. With intense primary beams in the range of 1000 A MeV, universal isotope production mechanisms (fragmentation, fission, spallation) and in-flight separation at a maximum magnetic rigidity of 20 Tm, high momentum resolution capability up to $p/\Delta p \sim 20.000$ in the dispersion-matched mode, strong background suppression (due to a multiple-stage separation scheme) and specialized detector systems, the Super-FRS [1] will allow for a variety of unprecedented nuclear physics experiments, which are not possible elsewhere in the world. In year 2012, the Super-FRS collaboration has identified its main goals:

- experiments along the lines described here
- construction of the Super-FRS, including R&D and commissioning, based on the FAIR partners by in-kind and additional contributions from collaboration partners
- operation for and together with all other NuSTAR sub-collaborations.

The experimental program will take advantage of the specific strengths mentioned above and will be complementary to other NuSTAR experiments. Key examples are for instance the production and study of exotic hypernuclei (i.e.: nuclei far-off stability containing hyperons) [2], the production and study of mesic atoms (i.e.: atoms containing bound mesons, like pions or eta mesons) [3], direct measurements of in-medium mass shifts [4], the discovery of new neutron-rich isotopes [5], the search for new phenomena in weakly bound or dilute nuclear systems, and the search for neutron radioactivity [6], an elementary radioactive decay mode which was not discovered so far. These experimental goals are intimately connected with the development of dedicated separation schemes and novel detection concepts, and it is the challenging goal of the Super-FRS collaboration to prepare and carry out these unique experiments. The existing FRS is the platform for developments and tests and will be used for pilot experiments in the coming years.

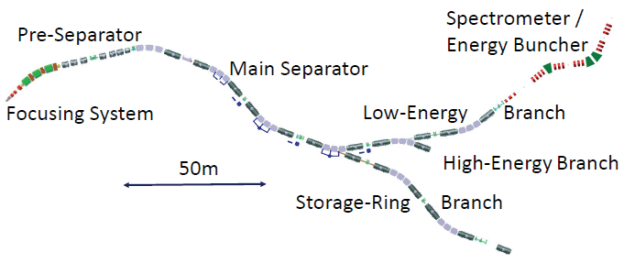

Figure 1. Schematic view of the Super-FRS and its branches. When the spectrometer/energy buncher at the Low-Energy Branch is operated in a dispersion-matched mode, secondary-reaction and charge-exchange experiments become possible with a momentum resolution down to $\delta p/p \sim 5 \cdot 10^{-5}$. An experimental program, specific for high energies and complementary to other existing or planned high-resolution spectrometers is presently under development.

References

[1] H. Geissel et al., Nucl. Phys. A701 (2002) 259c, H. Geissel et al., Nucl. Instr. Meth. B204 (2003) 71.
[2] C. Rappold et al., Nucl. Phys. A881 (2012) 218, C. Rappold et al., contribution to this report.
[3] T. Yamazaki et al., Z. Phys. A355 (1996) 219.
[4] K. Itahashi et al., Prog. Theor. Phys. 128 (2012) 601, and K.Itahashi et al., contribution to this report.
[5] J. Kurcewicz et al., Phys. Lett. B717, (2012) 371.
[6] L. Grigorenko et al., Phys. Rev. C84 (2011) 021303, and I. Mukha et al., contribution to this report.

Status of the Shielding Design for the Super-FRS

E. Kozlova[1], G. Fehrenbacher[1], T. Radon[1], H. Weick[1] and M. Winkler[1]

[1]GSI, Darmstadt, Germany

Introduction

The first calculations of the shielding thickness for the Super-FRS [1-3] in most cases were done without including of channels for the supplies, cryo-lines, ventilation ducts and etc. To make the shielding design more realistic it is obligatory to perform some detailed calculations. In this paper a short overview of such calculations is presented. All calculations were done with the Monte Carlo code FLUKA [4].

Prompt dose rates

The first investigated case is the prompt dose in the pre-separator area including a ventilation duct. The results are shown in Fig.1, where the selected ^{131}Pd interacts with the aluminium degrader at FPF2. The dose rate above the duct is in agreement with the design goal (0.5 µSv/h).

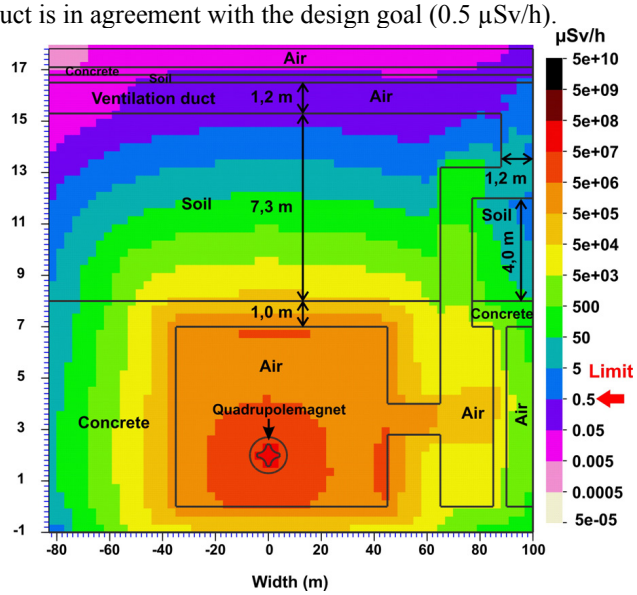

Fig. 1: Front view of the prompt dose rate distributions in the pre-separator area of Tunnel 103. The Pd beam (1.3 GeV/u, 3E10/s) interacts with the Al degrader (10 g/cm^2).

The next case is the detailed simulation of the labyrinth from Tunnel 103 to the Building 006a (Fig. 2). The results of this calculation helped to define the position of the cryo-line. The labyrinth connects to the branch area of the Super-FRS, where several beam losses appear: at the degrader, at the slits and the dipoles. For the dose rates calculations the most conservative case was taken. It is a beam loss at the high-energy branch (FHF1). The best position for the cryo-line exit is marked in Fig. 2.

In Fig. 3 also the branch area is presented, but the losses take place at the second degrader (FMF2). It is shown how the dose rates are distributed between the Tunnel 103 and Building 17.2. The channels for cryo-line and supplies are included in the shielding design. The calculations demonstrate that the dose rates in Building 17.2 are below 0.5 µSv/h.

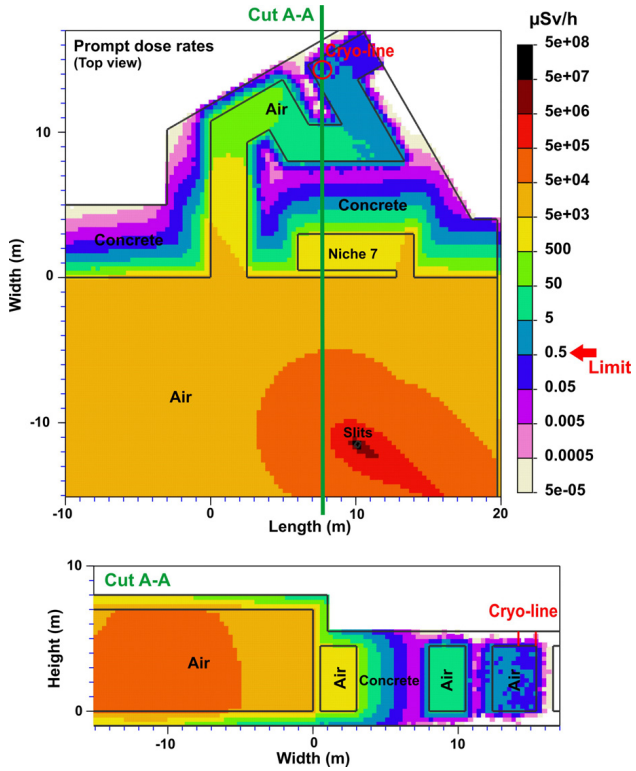

Fig.2: Horizontal and front views of the prompt dose rate distributions in the labyrinth from Tunnel 103 to the Building 006a. 50% of the uranium beam (1GeV/u, 1E9/s) is stopped at the slits.

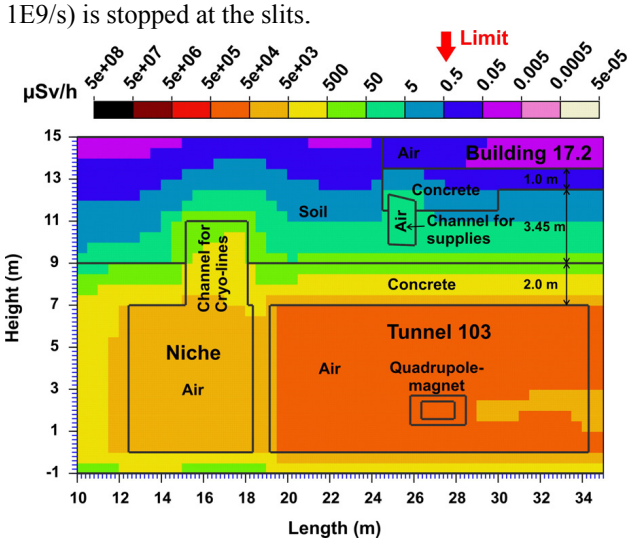

Fig. 3: Side view of the prompt dose rate distributions at the branch area of the Super-FRS. The antimony beam (1GeV/u, 8E9/s) interacts with the aluminium degrader (10 g/cm^2).

References

[1] E. Kozlova et al. GSI-Report 2008-1 (2008), p 247.
[2] A. Plotnikov et al. GSI-Report 2011-1 (2011), p 322.
[3] E. Kozlova et al. GSI-Report 2012-1 (2012), p 356.
[4] www. fluka.org

Beam Loss Distribution and Maintenance in Super-FRS*

H. Weick [1], F. Amjad[1], L. Orona[1], K.-H. Behr[1], C. Karagiannis[1], M. Winkler [1]

[1]GSI, Darmstadt, Germany

For radiation protection and maintenance planning the beam losses in different sections of the Super-FRS must be estimated carefully for prediction of prompt dose as well as for activation. As it is the purpose to select only few ions out of up to 10^{12}/s the losses and where they will occur exactly can also be predicted well. However, with many different settings for less and more rare isotopes the intensities in the main separator vary a lot.

To illustrate the situation two examples are shown: Selection of ^{132}Sn produced by fission of a ^{238}U beam and ^{100}Sn from projectile fragmentation of ^{124}Xe. ^{132}Sn and many other fission fragments with similar mass and atomic number can be produced in high quantity and are difficult to separate due to the larger momentum spread of the fragments behind the target. Contrary ^{100}Sn and its neighbors on the chart of nuclides are produced much less and at higher energies they are also easier to separate.

In simulations with the Monte-Carlo code MOCADI [1] for ion transport in beamlines including matter we collected the losses for all relevant nuclides produced as a function of position along the Super-FRS (around 1000 different nuclides for ^{132}Sn and 490 for ^{100}Sn).

For prediction of levels of activation of beamline components the number of ions only is not a good criterion, the energy of the ion and mass and atomic number are also important. This was considered by comparing the number of emitted neutrons for each ion derived from a simplified scaling rule [2]. So the number of ions lost shown in Figure 1 actually refers to ^{114}Pd ions at 1300 MeV/u an ion roughly in the middle of the mass and energy distributions of all ions in the different sections of the Super-FRS. This allows defining a loss number for inserts like the target or the degraders through which ions fly through without being absorbed but lose kinetic energy.

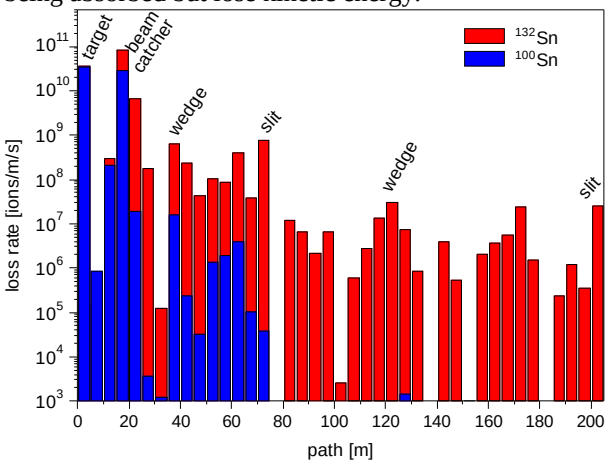

Figure 1: Number of ions lost along the path of the Super-FRS beamline per meter and second, for ^{132}Sn and ^{100}Sn settings with an initial energy of 1.5 GeV/u and an intensity of 3.3x10^{11} ions/s of ^{238}U or ^{124}Xe, respectively.

As one can see main loss points are the target and the beam catchers but also later in the system local maxima occur like the degraders or at the exit slits where a large part of the separation happens. Some ions drop out even earlier before the slits for example in the dipole regions. At the exit slit the difference between the two cases is huge. So far it cannot be foreseen how often which case will be used during operation. However, it is clear that the high intensity case is only one out of many and will therefore not run the whole operation time, but only a small fraction of it with correspondingly lower activation.

The highest activation will arise directly on the beam catchers which were already described and activation calculated in detail [3]. With the beam losses activation can now be predicted better in all parts of Super-FRS. Based on this, the frequency of planned maintenance and the likelihood of failure, four remote handling (RH) classes were defined:

- RH class 1 = components requiring regular planned replacement
- RH class 2 = components that are likely to require repair or replacement
- RH class 3 = components that are not expected to require maintenance or replacement during the lifetime of the facility but would need to be replaced remotely in case they fail
- RH class 4 = components that do not require remote handling

Classification of different parts:

Component	**RH class**
Target wheel	1
Beam catcher graphite	1
Drives for target and catcher	2
Pillow seals	2, 3
Wedge degrader	2, 4
Magnets near target	3
Alignment base	3
Target and catcher chambers	3
Shielding plugs	3
Devices on working platform	4
Slits	2, 4
Detectors in main separator	4

References

[1] N. Iwasa et al., NIM B 269 (2011) 752.
[2] E. Mustafin et al., NIM A 501 (2003) 553.
[3] E. Kozlova et al., NIM B 266 (2008) 4275.

* Work supported by EU, PURESAFE-ITN contract No. 264336.

Si detectors for Time of Flight measurements at the Super-FRS

O. Kiselev[1], V. Eremin[2], N. Egorov[3], I. Eremin[2], C. Karagiannis[1], S. Golubkov[3], C. Nociforo[1], Y. Tubolysev[2] and E. Verbitskaya[2]

[1]GSI, Darmstadt, Germany; [2]Ioffe Physical – Technical Institute RAS (PTI), St. Petersburg, Russia; [3]Research Institute of Material Science and Technology (RIMST), Zelenograd, Russia.

The beam diagnostics of the Super-FRS consists of several stations located along the pre- and main-separator [1]. In case of experiments with slow extracted-beams, it has to provide unambiguous fragment identification on event-by-event basis. Thus, position, energy-loss and Time of Fligth (ToF) measurements are mandatory. The ToF detector at the mid-focal plane should cover an active area of about 380 x 50 mm^2 and stand relativistic heavy ion rates up to 10^7 per spill over the whole area. Two ToF detectors located at the end of the Low- and High-Energy Branches of the Super-FRS should have an active area about 200 x 50 mm^2 and stand a rate of up to 10^6 ions per spill. The required time resolution of the ToF detectors is below 50 ps. Radiation-hard material (e.g. diamond) was considered to be a proper choice for the ToF systems of the Super-FRS. Recently, it turned out that the technology of producing large diamond detectors is not yet well established and the material price is very high. Radiation-hard planar Si detectors have been suggested to be an alternative solution.

Few Si detectors with different thickness (100, 300 and 600 µm) and different topology have been tested. Their arrangement is shown on Fig. 1. The active size (~25 mm^2) has been selected in order to have the same capacity of a single strip of a full-size Si-strip detector.

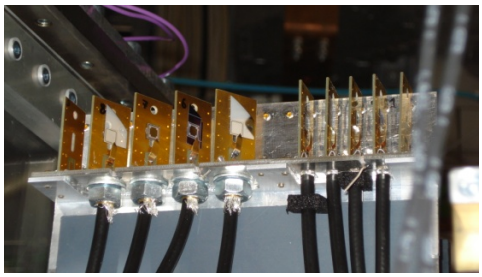

Figure 1: Si detector setup.

Beam test results

Two beam tests using ^{197}Au at 750 MeV/u and ^{238}U at 370 MeV/u have been performed at the FRS and HTD beam lines, respectively. The not amplified energy loss signals have been digitised using an oscilloscope with 4 GHz bandwith and sampling of 5 GS/s. The waveforms have been analyzed offline. A typical signal shape is shown in Fig. 2 for the 300 µm sample. The rise time of the 600, 300 and 100 µm thick detectors was ~700, 500 and 400 ps, respectively. The time jitter, calculated using a method similar to the one implemented in a leading edge discriminators with amplitude corrections, was found to be 20-40 ps (see Fig. 3). The measured energy resolution was close to few percent. The large dynamic range foreseen at the Super-FRS might be covered using amplifiers with moderate gain. After a high dose irradiation using ^{238}U ions, corresponding to 1kGy (1-3 weeks running at the Super-FRS), no deterioration of the timing properties has been observed.

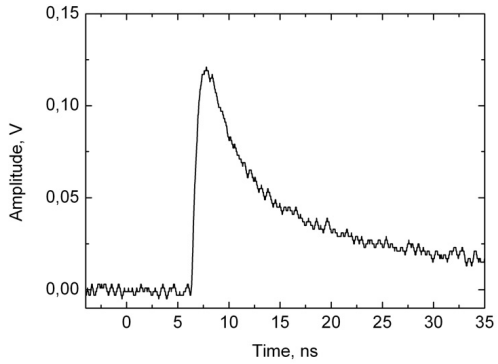

Figure 2: Typical shape of the signal of 300 µm Si detector irradiated by ^{197}Au ions.

Additionally, Si strip detectors can provide a position resolution comparable to the tracking detectors of the Super-FRS.

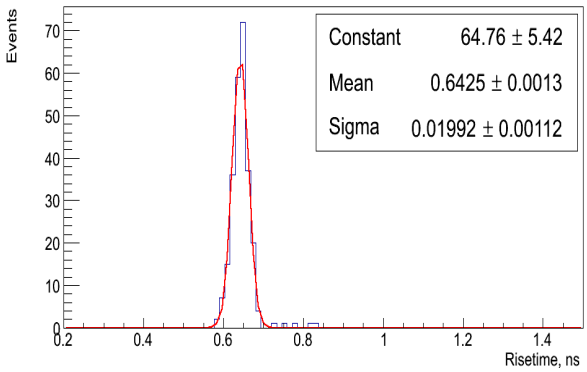

Figure 3: Time jitter of the 300 µm Si detector.

The data obtained in these two tests will help in developing a new prototype with a larger size (~40 cm^2). This prototype is planned to be tested in 2013-2014 together with a broad-band amplifiers (PADI, TAQUILA) and a TDC with resolution below 25 ps. An alternative electronics could be a fast sampling ADC with FPGA data processing on board.

References

[1] M. Winkler et al., Super-FRS Desing Status Report, GSI Annual Report 2010, p. 133.

The SuperFRS GEM-TPC Prototype Development

F. García[*1], *B. Voss*[3], *J. Hoffmann*[4], *R. Janik*[u2], *V. Kleipa*[3], *J. Kunkel*[3], *N. Kurz*[4], *R. Turpeinen*[1], *S. Minami*[4], *M. Pikna*[2], *A. Prochazka*[3], *I. Rusanov*[4], *B. Sitar*[2], *P. Strmen*[2], *E. Tuominen*[1], *R. Lauhakangas*[1]

[1]Helsinki Institute of Physics, University of Helsinki, 00014 Helsinki, Finland; [2]FMFI Bratislava, Comenius University, Bratislava, Slovakia; [3]Detector Laboratory, GSI Helmholtzzentrum, Darmstadt 64291, Germany; [4]Experimental Electronics Department, GSI Helmholtzzentrum, Darmstadt 64291, Germany.

Introduction

The FAIR facility at GSI will provide a variety of beams from protons and antiprotons to ions up to uranium with highest intensities and excellent beam quality in the longitudinal as well as transverse phase space. The NuSTAR experiments will be dedicated to the study of Nuclear Structure, Astrophysics and Reactions, in particular with the use of high energy spatially separated monoisotopic beams of radioactive species separated and identified by the Superconducting Fragment Recoil Separator (Super-FRS) [1]. The main task of the detection system [2] installed within the Super-FRS is threefold:

- it can be used to set up and adjust the separator,
- it provides the necessary measures for machine safety and monitoring,
- it allows for an event-by-event particle identification, tracking and characterization of the produced rare ion species.

The requirements for such detectors are:

- no interference with the beam
- large dynamic range
- coping with particle intensities up to 100 kHz

In order to satisfy these needs a further evolution of the existing GEM-TPC [3,4] system was required, now equipped with GEMEX [5] readout cards, each employing two n-XYTER [6] ASICs. The readout geometry was chosen to cope with the expected high particle rates at the FRS.

Results from test beam at the FRS

The S417 campaign gave us the possibility to test prototypes of these detectors. One of the tasks was to study the performance of the GEMEX readout integrated in GEM-based detectors. The ^{197}Au primary-beam particles of 750 MeV/u energy and intensities around 10^7 ions per 8-10 s spill was swept horizontally over the whole active area. In addition to that the beam was focused and defocused.

Fig. 3 shows the correlations between the 'front' and 'back' readout structures of the same detector. It can be stated that both parts of the detector perform identically. The center-position of the primary beam can be seen clearly.

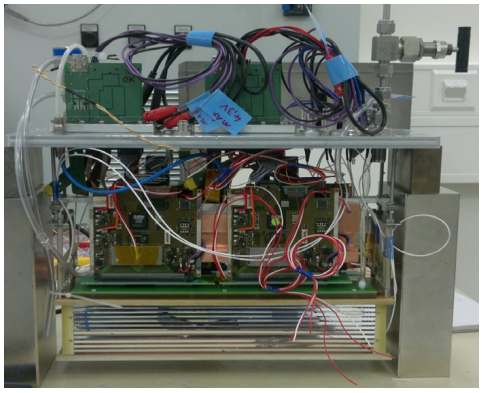

Figure 1: SuperFRS GEM-TPC prototype, equipped with four GEMEX readout cards.

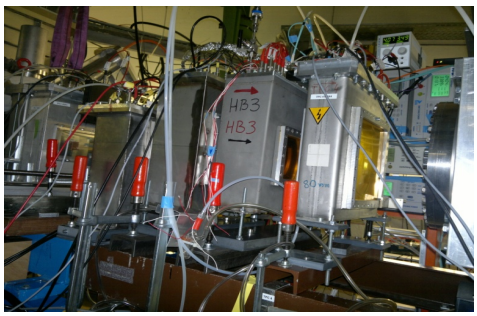

Figure 2: SuperFRS GEM-TPC prototype installed between two conventional TPCs at the focal plane S2 of the FRS/GSI.

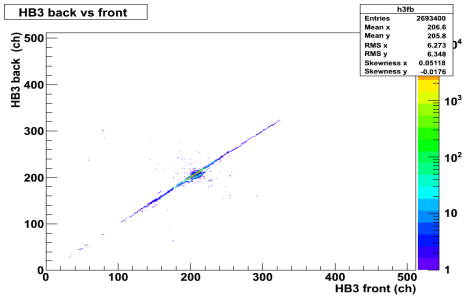

Figure 3: Correlations of hits between front and back readout.

References

[1] H. Geissel et al., Nucl. Instr. and Meth. B 204 (2003) 71-85.
[2] H. Geissel et al., Nucl. Instr. and Meth. B 70 (1992) 247.
[3] F. Garcia et al., 2009 IEEE Nuclear Science Symposium conference record, ISSN: 1095-7863, pp. 269-272.
[4] F. Garcia et al., 2011 IEEE Nuclear Science Symposium conference record, ISSN: 1082-3654, pp. 1788-1792.
[5] B. Voss et al., GSI Scientific Report 2011 (2012) 147.
[6] C. J. Schmidt et al., The n-XYTER Reference Manual. Version 1.0

Efficiency simulation of TPC detectors

A. Prochazka[1], *C. Nociforo*[1], *and B. Sitar*[2]
[1]GSI, Darmstadt, Germany; [2]Comenius University, Bratislava, Slovakia

Introduction

The Time Projection Chamber (TPC) are the standard high-resolution position measurement detectors used at the Fragment Separator FRS [1]. As gas detectors, they have the advantage to be very robust and cover a a wide dynamic range simply by HV tuning operation. On the other hand they can work up to $3 \cdot 10^4$ ion/s with an efficiency close to 100%. To improve the ion capability of these detectors, based on conventional delay lines, the use of a single channel digital readout electronics have been assumed. The advantage of the single-strip readout is the reduced time needed to collect the signals from the whole area of the detector. The efficiency at different ion rates for different readouts has been simulated using a Monte-Carlo method.

Simulation and Results

Time Projection Chamber type detectors with GEM foil amplification[2] have been proposed as tracking detectors for slow-extracted beams at the Super-FRS facility[3]. At the focal planes of the main separator of the Super-FRS a beam rate of several MHz is expected. There, ion tacking based on event-by-event analysis is needed for having the required separation and identification in mass and charge of the produced radioactive beams. To simulate the ion rate capability of a Super-FRS tracking detector we have assumed a gas chamber with active size of $38x8cm^2$. The drift velocity of the gas was $5cm/\mu s$, which corresponds to the drift velocity of the P10 gas at normal pressure and temperature at 400 V/cm electric field. The number of ions were generated according to the Poisson distribution around a fixed rate. For the x-coordinate a rectangular distribution over the whole chamber was used. The y-coordinates were generated according to a Gaussian distribution centered in the middle of the chamber with a sigma equal to $1cm$. The results shown here do not consider losses due to noise, delta electrons, recombination etc. The delay line configuration was like described in [1]. By using the delay-line readout we have the possibility to reject the noise because time measurement from delay line(t_L, t_R) and drift times(t_D) are correlated by relation $t_{CS} = t_L + t_R - 2t_D$ [1], where t_{CS} is constant. This method is no longer available in the case of single-strip readout. In other words, whenever two or more signals arrive within the same collection time, the two arrival times are mixed together with their y-coordinates. The collection time (time window) for 8cm drift corresponds to $1.6\mu s$. The results of the simulations are shown in the Fig. 1. The red and black points represents the efficiency curves of the delay line and single-strip readouts, respectively. The

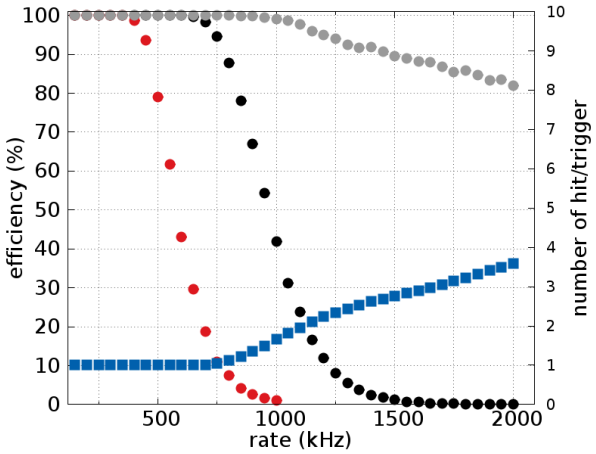

Figure 1: Rate dependence of the simulated efficiency of a TPC detector with P10 gas with different readouts. The red points correspond to the delay-line readout, black points correspond to the single strip readout and blue squares are the average detected particles in the $1.6\mu s$ time window (right y axis). The gray points correspond to the efficiency of a "twin" detector.

results of the simulations show that using a delay line readout the efficiency starts to decrease at beam intensities of 300kHz. Shortening the readout time by single-strip readout, a GEM-TPC design with the assumed gas could stand a rate up to 700kHz. At 700kHz the probability to have 2 or more hits in the same trigger window starts to increase, as shown in Fig. 1 by the blue points. To further increase the efficiency at even higher rates two solutions are possible. Introducing a control sum in the y-coordinate, by using a "twin" design, could further improve the efficiency by a factor of 2, as shown in Fig. 1 by the gray points. Additionally with a faster gas a higher efficiency can be achieved at several MHz.

References

[1] R. Janik et al., "Time Projection Chambers with C-pads for heavy ion tracking", NIM(2011)

[2] F. Garcia et al., "Prototype development of a GEM-TPC for the Super-FRS of the FAIR facility ", Proc. of the IEEE Nucl. Sc. Symp. Conf. 2011

[3] M. Winkler et al., "Super-FRS Design Status Report", GSI Scientific Report 2010-2012

First Operation of the GADAST, GAmma-ray Detector around a Secondary Target at the Middle FRS: Measurements of Inelastic Scattering of ^{17}Ne*

I. Mukha[1, #], A. Fomichev[2], V. Dunin[2], S. Krupko[2], C. Nociforo[1], S. Baraeva[2], H. Geissel[1], C. Scheidenberger[1], H. Simon[1], A. Gorshkov[2], R. Slepnev[2] and the S388 Collaboration

[1]GSI, Darmstadt, Germany; [2]JINR, Dubna, Russia

A pilot experiment with the GADAST demonstrator, an array of 16 γ-ray scintillation detectors with CsI(Tl) crystals installed near the secondary target position F2 of the fragment separator FRS has been performed (see Fig.1). Such array allows the detection of γ-rays emitted from the exited fragments produced in nuclear reactions with radioactive beams and will be used in addition to the other standard detectors of the Super-FRS [1].

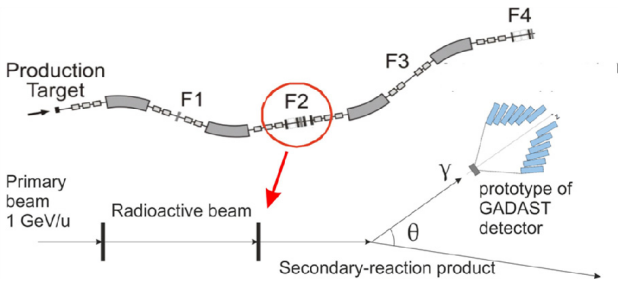

Figure 1. Position of the new gamma detector GADAST at the mid-focus F2 of the fragment separator FRS.

Each 3x6x15 cm^3 CsI(Tl) scintillating crystal produced by Amcrys (www.amcrys-h.com) was coupled to a 7 stage photo-multiplier tube ET-9106SB with green-light sensitive photocathode. The 8-crystal cluster is shown in Fig. 2 together with the corresponding optical guides, PMT and front-end electronics. The inset shows an in-board high-voltage generator coupled to the PMT socket and a board with the pre-amplifier of the anode signals.

Figure 2. A cluster of 8 CsI(Tl) scintillating crystals, constituting one half of the tested GADAST demonstrator.

The signals from the pre-amplifiers of all detectors were processed by a 16-channel board with electric filters, discriminators and shaper amplifiers. The board was developed at JINR. The produced timing logic and analog spectroscopic signals were directed to a standard VME digital electronics. The detectors can be operated in a broad energy range from ~0.04 to 40 MeV and have a low sensitivity to magnetic fields.

The γ-ray de-excitations of the ^{17}Ne isotopes produced at FRS at energy of 450 *A*·MeV were studied with the GADAST demonstrator during the S388 experiment "Two-proton decay of ^{30}Ar". In particular, an 1.288(7) MeV γ-ray emitted from the first excited state 1/2$^-$ of the ^{17}Ne in a inelastic scattering reaction has been measured in coincidence with ^{17}Ne ions identified by the standard FRS method. The measured Doppler-corrected γ-ray spectrum is shown in Fig. 3. The peak width of 0.10(2) MeV slightly exceeds the known 0.094 MeV width of this state, which provides an estimate of the GADAST energy resolution of 5(2)% .

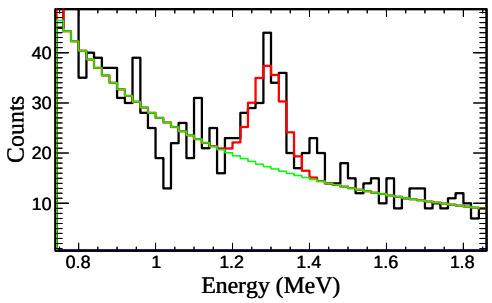

Figure 3. The Doppler-corrected γ-ray spectrum measured in the inelastic scattering of ^{17}Ne isotopes (the black histogram). The peak is fitted by a Gauss distribution. The continuum spectrum is approximated by a polynomial; their sum is the red-color curve. The measured energy of the ^{17}Ne excited state is 1.294(8) MeV matching the literature value of 1.288(7) MeV [2].

In conclusion, the performance of the GADAST demonstrator paves a way for a full-scale GADAST detector which will consist of 64 modules based on the tested CsI(Tl) crystals. Some planned experiments combine the use of GADAST with the unique features of the fragment separator Super-FRS: an identification of the heavy secondary fragments at energies up to 1.5 GeV/u, high transmissions of exotic nuclei produced via fission of U projectiles, and precise measurements of the ion momentum distributions by applying a dispersion-matched mode of the Super-FRS.

References

[1] I. Mukha *et al.,* Letter of Intent 49 to G-PAC GSI (2010), unpublished.

[2] Brookhaven National Nuclear Data Center, http://www.nndc.bnl.gov .

* This work is supported by the BMBF grant GSI-JINR N 4.8 NuSTAR.

I.Mukha@gsi.de

Simulation Study of the Production of Exotic Hypernuclei at the Super-FRS

C.Rappold[*1,2], *T.R. Saito*[1,3,4], *and C. Scheidenberger*[1,2]

[1]GSI, Darmstadt, Germany; [2]JLU Giessen, Germany; [3]Johannes Gutenberg-Universität, Mainz, Germany; [4]The Helmholtz Institute Mainz, Mainz, Germany

The first experiment of the HypHI collaboration aimed to demonstrate the feasibility of the hypernuclear spectroscopy by means of heavy ion beam induced reactions. The Phase 0 experiment was performed with a ^{6}Li beam at 2AGeV impinged on a stable ^{12}C target material. The main goal of the experiment was to produce, reconstruct and identify decay vertexes of Λ particle and ${}^{3}_{\Lambda}$H, ${}^{4}_{\Lambda}$H and ${}^{5}_{\Lambda}$He hypernuclei [1]. With the finalized data analysis of Phase 0 experiment, the final results show that the experimental method is viable for the study of hypernuclei. The future phases of the project focus on the study of exotic hypernuclei which can not be produced in typical missing mass experiments involved at JPARC or JLab and MamiC [2]. The study of exotic hypernuclei toward the proton- and neutron-drip line necessarily involves the use of rare-isotope beams. One of the main goals of the HypHI project is to extend the hypernuclear chart to the proton drip line up to ΛSi hypernuclei and neutron drip line up to ΛLi hypernuclei. A larger charge symmetric breaking effect may be expected in very proton/neutron rich hypernuclei. It may cause a change in the difference between Λ-proton and Λ-neutron interactions which may induce a shift of the drip-line positions.

The Super-FRS is crucial to the future phases of the HypHI project at FAIR. A feasibility study of the Super-FRS capability toward high energy of several GeV had to be achieved. This study was to determine which couple of primary beam and target isotopes have to be chosen to obtain the exotic beam of interest at 2 A GeV for the study of the subsequent exotic hypernuclei produced in the induced reaction of this secondary beam and the production target. A systematic study using EPAX [3] have performed to determine the production cross section of secondary beam isotopes between a large couple of beam and target isotopes (all combination up to ^{40}Ca + ^{40}Ca). Then MOCADI Monte Carlo simulations [4] was employed for calculating the transmittance of the secondary beam of interest and the possible other contaminating isotopes, also produced at the same time, up to the last stage of the High Energy Branch (HEB) of the SuperFRS. Once again a systematic study of all the possible couple of (Beam,Target) with several target thicknesses was performed in order to find the best possible parameters to obtain the highest intensity of the secondary beam of interest at the last stage of the HEB of the SuperFRS. Fig. 1 shows a summary of case study of ^{9}C secondary beam in which only the most predominant couple (Beam,Target) is represented. The calculation shows the reaction between (C,N) beam isotopes and (Li,Be,B,C) target isotopes gives the highest ^{9}C beam intensity up to $\sim 3 \cdot 10^{6}$ beam per second. More intensive simulations which aim to minimized the contamination of the other isotopes is on-going.

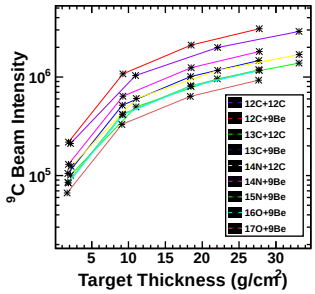

Figure 1: Intensity of secondary beam ^{9}C at the exit of the HEB of the SuperFRS as function of the target density, the primary beam and target isotope, which were used as variable inputs in MOCADI simulations. The intensity of the primary beam was set to 10^{10} per second which should be available at the SuperFRS.

The study of the production of the exotic hypernuclei with the secondary beam of interest is achieved thanks to the following theoretical model [5]. This is an hybrid model between the transport model "Dubna cascade model" (DCM), which simulates the collision between the beam and the target, and a statistical approach for the Fermi break up model to describe the deexictation of spectators. The first estimation of production cross section of some unknown proton-rich hypernuclei is listed in the table below. Further investigations are on-going about a future experimental setup.

${}^{4}_{\Lambda}$He	${}^{5}_{\Lambda}$Li	${}^{5}_{\Lambda}$Be	${}^{6}_{\Lambda}$Be	${}^{8}_{\Lambda}$B	${}^{8}_{\Lambda}$C
3.6 μb	1.2 μb	0.4 μb	1.6 μb	0.6 μb	0.2 μb

References

[1] T.R. Saito et al., Proposal of the HypHI Phase 0 experiment

[2] T.R. Saito et al., Letter Of Intent of HypHI project.

[3] K. Sümmerer, B. Blank, Nucl. Phys. A 701 (2002) 161.

[4] N. Iwasa et al., Nucl. Instr. Meth. B, **126** (1997) 284.

[5] A.S. Botvina, I. N. Mishustin, J. Pochodzalla Phys. Rev. C. **86** (2012) 011601.

* c.rappold@gsi.de

Development of a High Refractive Index Aerogel Cherenkov Detector for the Spectroscopy of η' Mesic Nuclei

Y.K. Tanaka[1], S. Friedrich[2], H. Fujioka[3], H. Geissel[4], R.S. Hayano[1], K. Itahashi[5], S. Itoh[1], V. Metag[2], M. Nanova[2], T. Nishi[1], K. Okochi[1], H. Outa[5], K. Suzuki[6], T. Suzuki[1], M. Tabata[7,8], Y.N. Watanabe[1], and H. Weick[4]

[1]The University of Tokyo, Tokyo, Japan; [2]Universität Gießen, Gießen, Germany; [3]Kyoto University, Kyoto, Japan; [4]GSI, Darmstadt, Germany; [5]RIKEN, Saitama, Japan; [6]SMI, Wien, Austria; [7]JAXA, Kanagawa, Japan; [8]Chiba University, Chiba, Japan

We have developed a Cherenkov counter using a high-refractive-index aerogel [1] for the hardware particle identification in the spectroscopy experiment of η' mesic nuclei with the (p,d) reaction [2, 3, 4]. In this experiment, we employ a 2.5 GeV proton beam of SIS-18 or SIS-100. Using the (Super-) FRS as a spectrometer, we measure the missing masses of the (p,d) reaction on ^{12}C target by momentum-measurement of ejectile deuterons. The expected rates at the focal planes are 0.5 kHz for the signal deuteron and 50 kHz for the background protons. Thus, we decided to develop a Cherenkov counter to provide hardware background rejection at a level of 1/500 based on the velocity difference of the signal (0.82 – 0.85) and the background (0.94 – 0.96) particles.

The structure of the developed detector is shown in Fig.1. As a radiator, we used a 2 cm-thick silica aerogel with a refractive index of 1.18 [5]. In the back of the radiator, a box consisting of mirror planes was placed to guide the Cherenkov photons to the eight PMTs attached to this box.

In November 2012, we have conducted a performance test of this detector using deuteron beams at GSI. We simulated the signals and backgrounds in our main experiment by using deuteron beams at two velocities $\beta = 0.843$ and 0.944, respectively.

We observed a sufficient number of photoelectrons to provide an anti-coincidence with the higher-velocity deuterons (background-like). The solid line in Fig.2 is the histogram of the total number of photoelectrons for this velocity. Analyzing the histogram, we obtain the mean number of photoelectrons to be 30.8, which gives an efficiency higher than 99.9 % setting the threshold at 9 photoelectrons. This is quite sufficient for the background rejection in the main experiment.

The observed histogram with the lower-velocity deuterons (signal-like) is shown by the dashed line in Fig.2. Although a peak was seen at the pedestal position, as expected, also a long tail up to more than 10 photoelectrons was observed. This can be caused by Cherenkov radiation in the ultraviolet region and/or Cherenkov photons emitted by delta rays produced in the aerogel. This tail will lead to a few percent overkill of the signal deuterons (e.g., 3 % at a 9-photoelectron threshold) in the main experiment.

The test experiment demonstrated that this Cherenkov detector can be used for the hardware background rejection in the spectroscopy experiment of η' mesic nuclei. As a near-future work, we will consider a possible improvement to reduce the expected signal overkill by testing a lower-refractive index radiator.

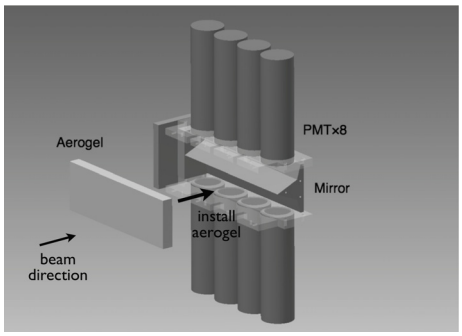

Figure 1: The structure of the aerogel Cherenkov detector. The radiator can be installed from the upstream side.

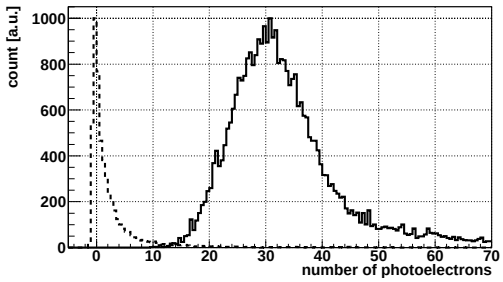

Figure 2: Histograms of the total number of photoelectrons. The solid line is for the higher velocity, $\beta = 0.944$. The dashed line is for the lower velocity, $\beta = 0.843$.

References

[1] Y.K. Tanaka *et al.* : RIKEN Accel. Prog. Rep. **45**, 172 (2012).
[2] K. Itahashi *et al.* : Letter of Intent for GSI-SIS (2011).
[3] K. Itahashi *et al.* : Prog. Theor. Phys. **128**, 601 (2012).
[4] D. Jido *et al.* : Phys. Rev. C **85**, 032201(R) (2012).
[5] M. Tabata *et al.* : Nucl. Instrum. Methods A **623**, 339 (2010).

A Framework for PreSPEC-AGATA Data Analysis*

M. Reese[1], *N. Pietralla*[1] *for the PreSPEC-AGATA-collaboration*
[1]Technische Universität Darmstadt, Germany

Introduction

The PreSPEC-AGATA experiment [1] at GSI investigates the structure of radioactive nuclei by means of in-flight γ-spectroscopy. This report describes a new software framework, which is a supportive tool to create data analysis programs for complex experiments like this. In order to reduce the workload of the user, the framework facilitates repetitive tasks, such as visualizing data in histograms, defining conditions and gates, and passing data to different stages of the analysis process. The user has only to write the actual data processing algorithms in C++, where a strict interface for data input and output ensures the re-usability of the analysis components. Examples of such algorithms are e.g. analysis of a specific detector or Doppler-correction of detected γ-rays.

The Framework

Every data analysis program is passing information through different stages of a data reduction process, until the final, high-level data is available. The layout of the information flow can be described as *directed graph*. The internal design of the described framework follows this graph structure as closely as possible. A user of the framework has to provide the description of the graph by means of two concepts:

1. Node types: Graph nodes process data. The definition of the node's algorithm, such as unpacking raw data or performing higher-level analysis tasks, is done in terms of C++ classes. These classes implement abstract interfaces: Processor and Unpacker. Every Processor implementation has to specify what output it provides and what input it requires. This is done in a way that strongly decouples the actual processing of data from passing it between different processing nodes. There are special nodes in the graph that are composed of Unpackers. These nodes are called Crates and get raw data, unpack it, and inject it into the graph.

2. The graph layout: A set of nodes and their connections define the graph. This information is provided by the user in a configuration script that is written in terms of a simple and specialized graph description language. It allows a compact description with loops and array assignments. Every node has a name and a type, where the type refers to an implementation of a Processor class. The node is internally represented as an instance of that Processor class. It has parameter and calibration files associated with its name, i.e. there is a unique place for every parameter.

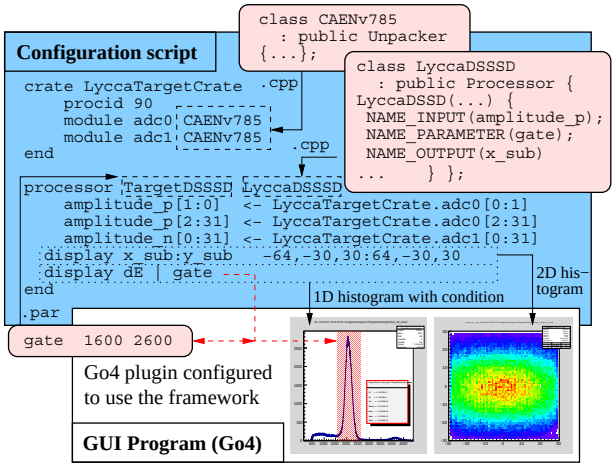

Figure 1: Complete analysis of the hitpattern of a DSSSD: A configuration script (big box) defines the graph structure. Dashed boxes indicate the use of a parameter file or Processor class (rounded boxes). Statements in dotted boxes create graphical representations in the GUI program (white box). The graphical cut (red area in the 1D-histogram) is defined by the parameter `gate`.

A simple example of the interplay between the components is shown in Fig. 1. The configuration script defines the graph (with 2 nodes) and provides, together with the parameter and calibration files, a complete description of the analysis for a given raw-event. The user can specify data or graphical cuts to be visualized during the analysis. All changes inside the configuration script have immediate effect after restarting the analysis, reducing development and debug time significantly.

The analysis framework is a C++ library, using STL and Boost. It does not provide any data-replay or visualization capability, but needs to be used by a host program that accesses the raw data and provides a graphical user interface. Inside the host program, the raw event data is passed to the analysis framework. Afterwards, the host program can read high level information from the framework and, for example, write it into a ROOT tree. Go4 (`http://go4.gsi.de`) is an example of such a host program, but any program capable of data replay and visualization can be adapted to use the framework. It is not restricted to the PreSPEC-AGATA setup but could as well be used for future experiments, like HISPEC/DESPEC at the FAIR facility.

References

[1] P. Boutachkov *et al.*, this report.

*Work supported by BMBF NuSTAR.DA - TP 6, FKZ: BMBF 05P12RDFN8 (TP 6)

Fast Pulse Shape Analysis for AGATA

T. Habermann[1,2], J. Gerl[2], and J. Maruhn[1]

[1]Goethe Universität Frankfurt, Germany; [2]GSI, Darmstadt, Germany

Introduction

The Advanced Gamma Tracking Array (AGATA) [1] will be used for nuclear structure experiments at the future FAIR facility as part of the NUSTAR program. Already in 2012 the PRESPEC-AGATA collaboration performed experiments with AGATA placed at the S4 area behind the FRS [2]. In its full configuration, the array consists of 60 high purity germanium crystals, each 36-fold electronically segmented to enable the identification of the gamma-interaction position inside the detector. For experiments with relativistic beam energies, it is a major issue to know the angle of the emitted gamma for calculating the energy in the rest frame and to produce a Doppler-corrected spectrum.

Pulse Shape Comparison

Pulse shape analysis (PSA) is applied to each of the recorded pulses of the detector to determine the interaction position. Due to a complicated geometrical shape of the AGATA crystals, there exists no simple algorithm to get the position from the pulse shape directly. However, it is possible to determine the position by comparing a recorded pulse with those from a database that contains pulse shapes for a huge number of interaction positions. As this procedure is rather time-consuming, the PSA is the rate-limiting part of the AGATA online analysis and requires optimization to make use of higher beam intensities. The algorithm that is currently used to find the best fit from the database is the Adaptive Grid Search Algorithm [3]. The basic ingredient for this algorithm is a χ^2-comparison of the recorded signal with the signals from the database. Without going into details, the next section will explain one feature of this algorithm, that is relevant for the present work.

Pulse Shape Comparison with threshold

A brute force algorithm would compare the full recorded signal with all signals from the database. Apart from selecting the part of the signal that is most sensitive to the interaction position, there is another way to make the search for the best fit more efficient. The comparison of two pulse shapes can be aborted, once the χ^2 value is higher than the best χ^2 value that has been calculated so far. On the other hand, if the χ^2 value is lower than any previous one, this one can be used as the new threshold. The top panel of Figure 1 shows the number of signals from the database that can be considered as candidates for the best fit depending on the number of samples that have been compared already (i.e. the number of database signals whose χ^2 value is below the threshold). The red curve shows the situation for the brute force algorithm without applying any threshold. The area under the curves can be considered as the required computing time to find the best fit, as it represents the total number of samples that have to be compared. It is obvious that the number of samples to be compared can be reduced by more than half by applying the threshold.

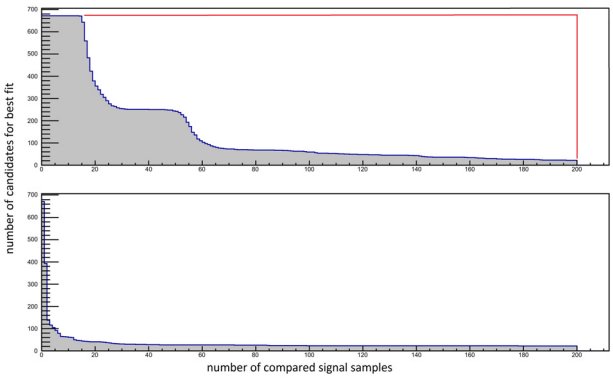

Figure 1: The red box corresponds to the computing time of a brute force algorithm. The grey area corresponds to the computing time when a threshold is applied (see text for details).

Fast Pulse Shape Comparison

The number of significant samples that have to be compared to find the best fit from the database can be reduced even further by applying a transformation to all the pulses before comparing them. By considering only orthogonal transformations it is ensured that the result of any comparison is unchanged. One can choose the transformation such that in the transformed signals, the relevant information is concentrated in only few signal components. The best result is achieved, when the signals are expanded in terms of their principal components. These are obtained by applying a singular value decomposition to the matrix whose columns are the pulse shapes from the signal database. The bottom panel of Figure 1 again shows the number of best fit candidates when the threshold is applied after each sample depending on the number of samples that have been compared. There is a clear advantage to the case when the signals are not transformed (cf. top panel of Figure 1). Compared to the brute force approach, the computation time can be reduced by a factor of roughly 20 (compared to ~6 for the original algorithm).

References

[1] the AGATA collaboration, NIM A668 (2012), 26
[2] C. Domingo-Pardo et al., NIM A694 (2012), 297
[3] R. Venturelli, D. Bazzacco, LNL Annual Report 2004, INFN-LNL, Italy, 220

Trigger Configuration for the PreSPEC-AGATA Campaign at GSI *

D. Ralet[1,2], N. Pietralla[1], S. Pietri[2] for the PreSPEC-AGATA collaboration

[1]Technische Universität, Darmstadt, Germany; [2]Helmoltzzentrum für Schwerionenforschung GmbH, Darmstadt, Germany

An online γ-ray spectroscopy campaign, PRESPEC-AGATA, was performed in 2012 using radioactive ions beam produced by the FRagment Separator (FRS [1]) and impinging on a target placed at the final focal plane (S4) of the FRS. The target was surrounded by segmented High Purity Germanium (HPGe) detectors called AGATA (Advanced GAmma Tracking Array [2]), and by the HECTOR+ detectors (LaBr3 and BaF2) in order to detect γ-ray transition. The reaction products were identified after the target with the Lund York Cologne CAlorimeter (LYCCA [3]).

γ-ray spectroscopy requires to record γ-rays emitted in coincidence with a nucleus identified in both FRS and LYCCA. The particle trigger request was given by the signal coming from a scintillator plastic, SC41, placed before the target. An AGATA detector consist of one core and 36 segments. In order to provide a γ-trigger request, the gain-matched core signals were cabled to a Constant Fraction Discriminator (CFD). A logic *OR* of all the signals was then sent to our trigger logic module. Previous experiments done with the PRESPEC setup showed that around 50% of the events were not properly identified in LYCCA. In order to increase this ratio, we included in our trigger a coincidence with LYCCA consisting in the coincidence of the Time of Flight start plastic scintillator with the DSSD wall. For details concerning the LYCCA setup, please refer to [3].

The trigger scheme consisted of 12 different triggers fired only when the acquisition is not in dead time. Each trigger was associated with an event configuration. Trigger 12 was a *spill on* trigger fired at the beginning of the beam pulse and trigger 13, a *spill off* trigger, fired at the end of the beam pulse. Trigger 10 was a particle trigger, i.e. a trigger generated for each SC41 trigger request. It was used with a reduction factor as a normalisation, and also for the isomer tagging configuration. Physics triggers (6-9) required a coincidence with a particle (SC41 signal), a LYCCA signal and with a γ-ray detected in AGATA (T9) or in HECTOR(T8). The trigger 7 was generated with the coincidence of a particle and a γ-ray detected by AGATA. Trigger 6 was obtained with a coincidence between a particle and a γ-ray from HECTOR detectors. Trigger 5 was a generic FRS trigger. It was used during the setting up of the FRS, and can be switched to any FRS detector trigger. Triggers from 2 to 4 are calibration triggers used for the calibration of HECTOR (T4), AGATA (T3),and LYCCA (T2). Trigger 1 was a scaler readout trigger. It ran at $10Hz$, and was always validated (no dead time rejection, it was pending until the dead time was released).

The priority in the trigger was set to the inverse of the trigger number, e.g. trigger 10 has a higher priority than trigger 9, which assured a good normalisation trigger 10, with no missed events. The trigger scheme was implemented on a Field Programmable Gate Array (FPGA) based module developed at GSI, the VULOM4, with the help of the *TRLO* firmware developed by Hakan T. Johansson [4].

This system (FRS+LYCCA+HECTOR) was running under the Multi Branch System (MBS) data acquisition system and triggered as previously explained. The AGATA Germanium detectors came with their own data acquisition system (see AGATA reference paper [2] for details). Its trigger is the Global Trigger and Synchronisation (GTS) system. The latter is built as a tree, where each Germanium detector is considered as a leaf. In the tree philosophy, each leaf can send a trigger request to the trigger processor unit, the root of the tree, which takes a decision and sends it back to the leaves. Each time a γ-ray is detected in one detector (i.e. above the AGATA electronic threshold), it sends a request to the trigger processor which will either accept the event (record the event via the AGATA data acquisition system), or reject it. In our case, the trigger processor was divided in two partitions. One consisted in all the leaves from the Germanium detectors, the other one was the MBS data acquisition system. In this way, for each trigger from the FPGA based module, a signal was sent to the trigger processor which validated each Germanium leaf with a request in coincidence with it. The GTS system assured the time-stamping of the data which was used for the merging of an MBS event with AGATA data.

With this system, 5 experiments were performed in 2012. It allowed in-flight γ-ray spectroscopy, and also isomer tagging for a confirmation of the identification with the FRS. In the case of trigger 9 more than 99% of the events were validated by the GTS system, which verifies the satisfactory behavior of the coupled system.

References

[1] H. Geissel, "The GSI Projectile Fragment Separator" NIM B70

[2] "AGATA-Advanced GAmma Tracking Array", NIM A668, 2012

[3] D. Rudolph, "LYCCA, Technical Design Report", June 2008

[4] Hakan T. Johansson, LAD TRLO II, TRLO Manual, 2010

*Work supported by the BMBF under Nos. 05P09RDFN4, 05P12RDFN8, and by the LOEWE center HIC for FAIR

Study of Hybrid Detector Sensitivity by Coincidence Scanning Technique

T. Arici[1,2]*, I. Kojouharov*[1]*, and J. Gerl*[1]
[1]GSI, Darmstadt, Germany; [2]Istanbul University, Turkey

Gamma-ray spectrometry with Ge and scintillation detectors is a well-established tool applied in many fields of investigation. The task is achieving the lowest detection limit in shortest measurement time, higher efficiency is supported by the technological progress in manufacturing new detection systems for a wide spread use of nuclear experiments [1].

The latest generation of Ge detectors, e.g. AGATA, have position sensitivity in order to enhance their capability of Doppler shift correction, background reduction and eventually tracking, thus improving the efficiency and the sensitivity. Due to the enormous complexity of such a system, the search for alternatives has led to the idea of a hybrid detector made out of a non-segmented HPGe detector and a position sensitive element. This element can be either another small segmented HPGe detector or a suitable position sensitive scintillator and will realize a system possessing position sensitivity for the first photon interaction, high efficiency typical for the large volume HPGe detectors and at the same time being simple, slim and less expensive. The hybrid system is based on photon scattering in a scattering detector and absorption in a large volume absorber detector. Useful events are selected as the sum of the energy deposited in the two detectors. Since the energy resolution of the system is the mean of scatterer and absorber detectors energy resolution, besides the HPGe detector, it is needed a new generation scintillation crystal which has respectively good energy resolution,e.g. $LaBr_3$.

A Geant4 simulation has been used to optimize the geometry of the assembly. There are a number of factors that influence the performance of a hybrid system which contribute to the sensitivity of the device.The major factors are thickness of the crystals, and the distance between the detectors. The results of the simulations have shown that the optimum configuration is a 15 mm thick scatter detector coupled to the absorber detector with 1 mm distance.

Triple Coincidence Measurement

An initial experiment with a ^{22}Na source was carried out using the coincidence scanning technique at the GSI scanning table[2]. Since the self-activity of employed LYSO scintillator results in peaks in the gamma spectrum due to random coincidences, the measurements were done by using an external p-type HPGe detector in coincidence with the system, as shown Fig. 1, to trigger the acquisition only when the both 511 keV photons of the source are observed.

Coincidence events appear in the central distribution of

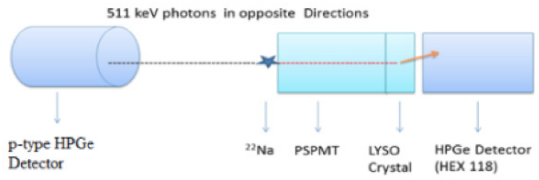

Figure 1: Geometry of the coincidence measurement using a p-type HPGe detector.

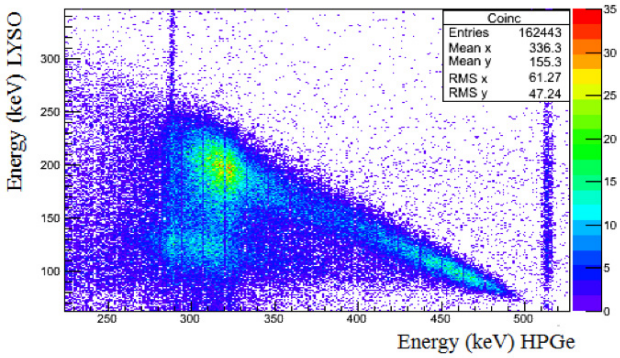

Figure 2: Coincidence energy matrix of energy deposition in LYSO scintillation detector and HPGe (Hex 118) detector.

the 45 degree line, as shown in Fig. 2. The sum of each event around this distribution gives the total energy of 511 keV corresponding to different scattering angles from the LYSO crystal. The vertical lines in the matrix which are originating on the HPGE axis indicates the events which trigger in random coincidence, owing to self-activity of the LYSO crystal and the background which is absorbed by the HPGe detector.

The hybrid detector can be used with superior energy and position resolution and large efficiency. Replacing the HPGe with a segmented planar HPGe one or it can be used for tracking and imagining.

References

[1] J.Gerl, W.Korten (Eds.) AGATA Technical Proposal, GSI Report, Darmstadt, 2001

[2] N.Goel, C.Domingo-Pardo, T.Engert, J.Gerl, I.Kojouharov, H.Schaffner, NIM A652 (2011) 591-594

A plunger for high energy beams to be used at HISPEC/ PRESPEC

C. Fransen[1], *T. Braunroth*[1], *A. Dewald*[1], *E. Ellinger*[1], *J. Litzinger*[1], *and D. Wölk*[1]
[1]IKP, Cologne, Germany

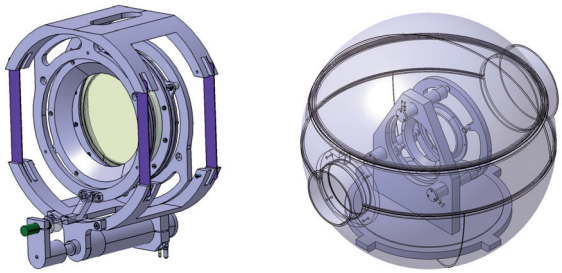

Figure 1: Left: Plunger device with flat springs. Right: Plunger device with three motors.

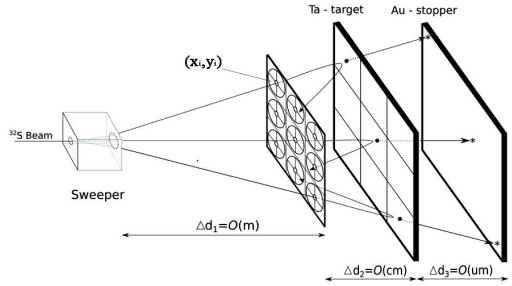

Figure 2: Experimental setup for measuments for RDDS experiments with extremly large beam diameters.

Development of a plunger for high energy beams to be used at HISPEC/ PRESPEC

A plunger for high energy beams to be used at the HISPEC/ PRESPEC set-up at GSI Helmholtzzentrum für Schwerionenforschung is under construction in Cologne.
There are special challenges for plunger measurements with relativistic beams.

- The distances between the target and the degrader foils have to be variable in a range from mechanical contact up to a few centimeters because of the high recoil velocities of the order of v/c = 50%.

- The target and degrader foils need to be large enough for a typical beam diameter up to 8 cm and the structure has to be sufficiently stable to allow an accurate and parallel mounting of target and degrader foils with thicknesses in the range of a few μm for foils up to more than 1 mm.

These are different dimensions compared to a standard plunger device for fusion evaporation reactions, where the foils have thicknesses in the order of micrometers and the beam diameter is typically around one millimeter.
Two different types of devices have been constructed and tested in Cologne, as described in the following passages.

A plunger with flat springs

For the exact movement of such extremly large and heavy target foils another plunger concept than usual is necessary. A plunger device with flat springs allow for a parallel movement of target and degrader with respect to each other. A prototype for testing was built (see Figure 1). It has a maximum driving range of 30 mm, limited by the piezo motor, and a precision of 0.1 mm. Thus this is a construction for experiments where a rather low precision is needed.

A plunger with three motors

A precision of 0.1 mm is not sufficient for all plunger measurements with low energetic beams. Therefore, the construction of a second plunger device with three piezo motors is in progress. A prototype for testing was built (see Figure 1 right-hand side). We proved that by using a new software developed at IKP, Cologne three Piezo motors can be operated parallel in a way to achieve a highly precise parallelism of target and degrader foil. It has been found, that this plunger fulfills all requirements of a future experiment to be performed at the HISPEC/ DESPEC/ AGATA experimental set-up. It is also possible to construct this plunger in a three foil version.

Experimental setup to test RDDS experiments with extremly large target and stopper/ degrader foils

A setup to test RDDS experiments with extremly large target and degrader/stopper foils is shown in Fig. 2. It is intended to excite levels in Ta via Coulomb excitation where lifetimes are very well known [1]. By this method it will be possible to measure absolute target to stopper seperations at different locations on the target. Separate sets of photodiodes will be used to measure backscattered projectiles at the specific target locations (x_i, y_i) to fix the kinematics of the coulomb excitations. This experiment will be performed at the Cologne FN tandem accelerator.

References

[1] T. Klug, A. Dewald, V. Werner, P. von Brentano, R.F. Casten, Phys. Lett. B 495 (2000) 55.

Fast Timing with DSSSD Detectors

P. Boutachkov[*1], *E. Gregor*[1,2], *N. Pietralla*[1], *I. Kojouharov*[2], *W. Koenig*[2], *M. Pfeiffer*[3], *M. Cappellazzo*[3], *C. Müller-Gatermann*[3], *and J. Jolie*[3]

[1]TU Darmstadt, Germany; [2]GSI Darmstadt, Germany; [3]IKP, University of Cologne, Germany

The NuSTAR HISPEC slowed down beams project at FAIR aims to produce rare isotopes with energies of 10 MeV/u and less. The setup requires Time of Flight (ToF) information to determine the ion velocity, energy loss for Z identification and beam tracking for scattering angle reconstruction [1]. A timing resolution of ΔT$\sim$100 ps, position resolution of the order of a mm and energy resolution of ΔE/E$\sim$1% is required [1]. Due to the low beam energy, the number of detectors should be kept to a minimum. Thin Double Sided Silicon Strip Detectors (DSSSD) provide energy loss and position information, while their use as fast timing detectors was not extensively studied. A combination of commercially available DSSSDs and a new 16ch fast pre-amplifier developed at GSI was investigated. The system was cooled to -17°C in order to reduce the detector noise, improving the time resolution.

A 5x5 cm^2, 40 μm DSSSD model W1(DS)-40 9G produced by Micron was glued on a copper frame. The DSSSD has 16$\times$16 x-y strips. They are bonded on one side only. A 16ch low power pre-amplifier based on BGA2712 amplifiers by NXP Semiconductors was attached to the DSSSD [2]. The detector and the pre-amplifier were cooled with a refrigerating machine and a two-stage Peltier cooler. A picture of the detector and the fast pre-amplifier mounted in the cooling frame is shown in Figure 1.

The detector performance was studied with a 48 MeV ^{12}C beam produced at the Cologne FN-Tandem Accelerator [3], where the DSSSD time resolution was measured relative to a transmission Micro-Channel Plate detector (MCP) [4]. The energy of 48 MeV was sufficient for the ^{12}C beam to punch through the thin DSSSD.

As mentioned above, the detector was cooled to -17°C. The signal amplitude and rise time varied along the length of the detector strips. The fastest rise times (10% - 90%) of order of 2 ns were measured for the pixels close to the strip readout contact. Such a signal is shown in Figure 2. The RMS noise after the fast pre-amplifier was in the order of 0.3 mV. The signal rise time and noise level indicate that a resolution better than 100 ps can be reached.

For timing measurements, the fast pre-amplifier was connected to a 16ch leading-edge discriminator, while the other side of the DSSSD was read out with a Mesytec MPR-32 charge sensitive pre-amplifier. A CAEN 1290A TDC with 25ps LSB was used to measure the ToF between the MCP and the DSSSD detector. A FWHM$\sim$0.4 ns was obtained for the DSSSD time resolution after subtracting the contribution from the MCP.

The difference between the expected and the measured time resolution was attributed to the variation of the signal rise time along the detector strips and high discriminator thresholds. The latter was due to a technical limitation of the fast discriminator used in the measurement.

Improvement of the cooling system in order to reach lower temperatures, will lead to rise times below 2 ns. The faster rise times and a readout from both sides of the detector strips should lead to resolutions better than 100 ps.

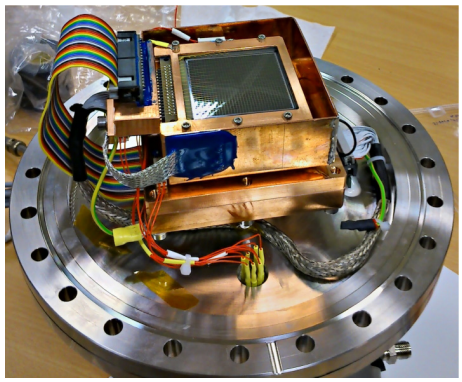

Figure 1: An assembly of the 40 μm DSSSD and the 16ch pre-amplifier mounted on the cooling frame.

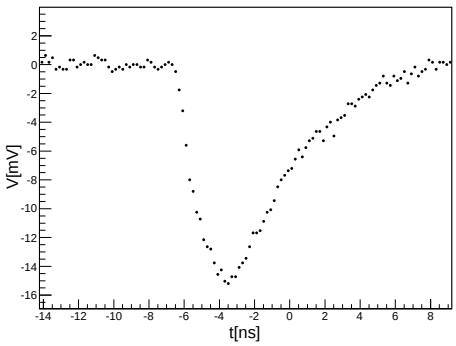

Figure 2: A fast pre-amplifier signal from a pixels close to the strip readout contact.

References

[1] P. Boutachkov *et al.*, GSI Scientific Rep. (2007) 215.

[2] W. Koenig and J. Pietraszko, GSI Scientific Rep. (2008) 218.

[3] M. Pfeiffer *et al.*,"A new Detector Testbed for future FAIR based Slowed Down Beam Setups at the Cologne FN-Tandem Accelerator Facility", GSI Scientific Rep. (2012).

[4] P. Boutachkov *et al.*, GSI Scientific Rep. (2008) 236.

*This work was supported by NAVI, Helmholtz Association Nuclear Astrophysics Virtual Institute.

LYCCA Performance During the PreSPEC-AGATA Campaign

Pushpendra P. Singh[1,], P. Golubev[2], D. Rudolph[2], for the PreSPEC-AGATA Collaboration*

[1]Technische Universität Darmstadt, Germany; [2]Lund University, Sweden

The PreSPEC-AGATA project at GSI aims at nuclear structure studies of exotic nuclear species produced in Coulomb excitation and secondary fragmentation reactions using radioactive isotope beams at relativistic energies. This pan-European campaign is the precursor of the HIgh-resolution in-beam SPECtroscopy (HISPEC) experiment of the NUSTAR collaboration within FAIR [1]. The high-resolution γ-ray spectroscopy employs state-of-the-art detection systems, e.g., the FRagment Separator (FRS) for selecting specific radioactive ion beams, the European Advanced Gamma Tracking Array (AGATA) for the measurement of precise γ-ray energies, and the Lund-York-Cologne CAlorimeter (LYCCA) to discriminate heavy-ions produced in nuclear reactions at the secondary target. To enable event-by-event correlations of the γ rays with the reaction residues, the LYCCA array has the central role of determining both *Z* and *A* of final reaction products by itself or in conjunction with FRS. Here, we report some results of LYCCA performance numbers achieved during commissioning experiments.

The various detector components of LYCCA are: a double-sided-Silicon-strip detector (DSSSD) at the secondary target, the LYCCA wall consisting of 16 Δ*E*-*E* telescopes, and three ToF detectors [2]. Each telescope comprises a DSSSD to measure energy loss (Δ*E*) as well as the position (*x*,*y*) of the heavy ions followed by an array of nine Cesium Iodide (CsI) detectors for the residual energy (*E*). The energy loss and residual energy signals provide the *Z*-identification of the reaction products. From the target DSSSD and those of the downstream LYCCA wall the precise (*x*,*y*)-tracking of the heavy ions can be obtained which allows the impact parameter determination especially needed for Coulomb excitation experiments. Time-of-flight (ToF, Δt << 50ps) information is obtained by ultrafast plastic scintillators (BC-422Q, BC-420) in conjunction with 12 or 32 small ultrafast PMT readout. The ToF-target detector is mounted close to the secondary target, while the ToF-stop detector is situated ~3.5m downstream just in front of the LYCCA telescopes. Mass resolution for reaction products up to A ≤ 100 is anticipated. For further details see Ref. [3].

In-beam commissioning experiments for PRESPEC-AGATA were conducted in the second half of 2012. An ^{80}Kr beam at 150MeV/u was impinging on a 0.4 g/cm^2 ^{197}Au foil for Coulomb excitation and on a 0.7 g /cm^2 ^{9}Be target for a fragmentation reaction. For the ^{80}Kr+^{197}Au reaction, Fig.1 shows the correlation of the *x*-*y* position of particles hitting the target DSSSD (left), DSSSD-Wall (center), and CsI-Wall (right), respectively. It illustrates the elastic scattering distribution and three angular regions (10,20,30 mrad). This indicates that the most relevant inelastic scattering events up to the grazing angle of typically some 26 mrad can be studied.

*Email: p.p.singh@gsi.de

Fig.2 (left) shows the Δ*E*-*E* correlation of the ^{80}Kr+^{9}Be reaction at 150 MeV/u. The different nuclear charges (*Z*) are clearly separated. From the diagonal projection of the Δ*E*-*E* correlation, the *Z*-distribution on the right hand side of Fig. 2 can be extracted.

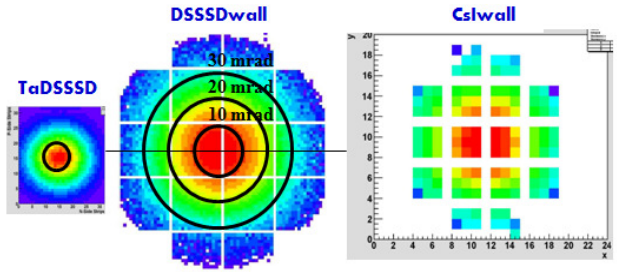

Figure 1: Correlation of the x-y position of particles hitting the target DSSSD (left), DSSSD-Wall (center), and CsI-Wall (right), respectively.

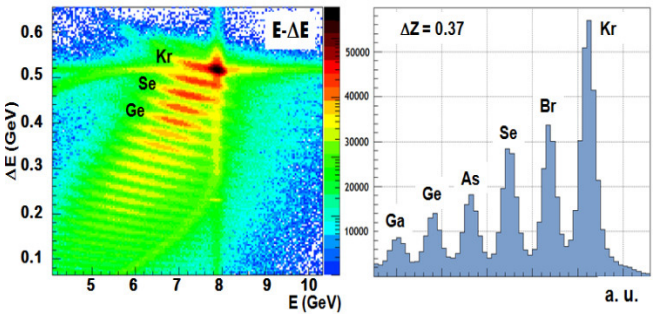

Figure 2: Δ*E*-*E* correlation measured with DSSSD-Wall and CsI-Wall (left). *Z*-distribution obtained from the diagonal projection of the Δ*E*-*E* correlation (right).

The resulting *Z*-resolution is determined to Δ*Z*/*Z* = 0.37% (an average of six peaks). This is almost identical with the value measured by the MUSIC detector of the FRS. The mass determination from the ToF measurement is described in some detail in Ref. [3], which continued optimization procedures being worked upon towards future experiments at HISPEC [4].

In the framework of the presently ongoing PreSPEC-AGATA campaign at GSI, we can show that LYCCA is able to discriminate relativistic heavy ion reaction products at typical energies of 100 – 300 MeV/u.

References

[1] PreSPEC. http://web-docs.gsi.de/~wolle/PreSPEC/
[2] LYCCA Technical Design Report (2008).
[3] P. Golubev *et al.*, submitted to Nucl. Instr. Meth.
[4] M. Reese *et al.*, this report.

Position Sensitivity of LYCCA Time-of-Flight Detectors*

M. Reese[1], *N. Pietralla*[1], *P. Golubev*[2], *D. Rudolph*[2] *for the PreSPEC-AGATA-collaboration*
[1]Technische Universität Darmstadt, Germany; [2]Lund University, Sweden

Introduction

The Lund York Cologne CAlorimeter (LYCCA) [1, 2] is an essential system of the PreSPEC-AGATA setup [3] located at GSI. Its main purpose is the identification (Z,A) and tracking ($\vec{v}$) of reaction products from the secondary target. The Z identification is done with a large $\Delta E - E$ telescope, consisting of Double-sided Silicon Strip Detectors (DSSSD) for the energy loss as well as position measurements, and CsI scintillation detectors to measure the residual particle energy. An additional time of flight (ToF) measurement is used to determine the particle mass. Thin, circular-shaped plastic scintillation detectors, read out with 12 or 32 photomultiplier tubes (PMTs), are used as to achieve the required timing precision [1, 4]. The large diameter of 27 cm of the ToF-Start and ToF-Stop membranes necessitates a correction for the path length of the photons inside the membrane. Therefore, the ion position inside the membrane has to be known and is usually determined with additional tracking detectors. This report describes a method of determining the particle position, based only on the 32 time signals from the large membrane's PMTs.

Method and Results

The position information is implicitly given as the minimum of the log-likelihood function $\log L(\vec{r}_p)$ of the particle hit position $\vec{r}_p$ on the membrane. Given the $N = 32$ PMT time signals, t_i, it can be written as

$$\log L(\vec{r}_p) = \frac{1}{N}\sum_{i=1}^{N} t_{c,i}^2(\vec{r}_p) - \left(\frac{1}{N}\sum_{i=1}^{N} t_{c,i}(\vec{r}_p)\right)^2 \quad (1)$$

where the measured time signals, corrected for the photon path length, are defined by $t_{c,i}(\vec{r}_p) = t_i - t_{i,\mathrm{prop}}(d_i)$. The propagation time, $t_{i,\mathrm{prop}}(d_i)$, is the time a photon needs to travel from the particle hit position in the membrane $\vec{r}_p$ to position $\vec{r}_i$ of the i-th PMT. It is assumed to be a linear function of the photon travel distance $d_i(\vec{r}_p) = |\vec{r}_i - \vec{r}_p|$. The two linear coefficients can be determined beforehand by a calibration procedure, using known particle positions measured with the DSSSD tracking and plotting the known distance d_i versus $t_i - \langle t_c\rangle$, as shown in fig. 1. The average $\langle t_c\rangle = \sum_i t_{c,i}$ is the best estimate of the time when the particle passes the membrane. The minimum of (1) is determined numerically by an iterative procedure, starting at the center of the membrane. As a final step, additional empirical corrections for small offsets and shearing effects are applied.

*Work supported by BMBF NuSTAR.DA - TP 6, FKZ: BMBF 05P12RDFN8 (TP 6)

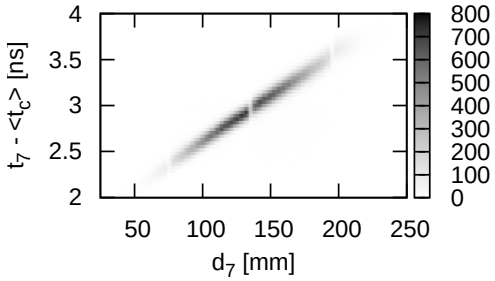

Figure 1: Linear correlation between $t_{c,7}(\vec{r}_p)$ and $d_7(\vec{r}_p)$ for the 7-th PMT.

The spatial resolution can be deduced from the differences between the positions given by DSSSD detectors and the result from the membrane detector. The resulting distribution is shown in fig. 2 and has 7.6 mm FWHM along the x and 6.8 mm along the y-direction, respectively. Taking into account the 3.6 mm wide DSSSD strips, the resulting position resolution for the membrane detector is 6.7 mm and 5.1 mm FWHM in x and y-direction, respectively. The reason for the difference in x and y is not yet understood. The analysis procedure was done using a new analysis framework for PreSPEC-AGATA data analysis [5] and data from a ^{132}Sn fragmentation setting. Upgrades of the LYCCA ToF system foresee the digitization of PMT signal heights, which should further improve the membranes' intrinsic position resolution.

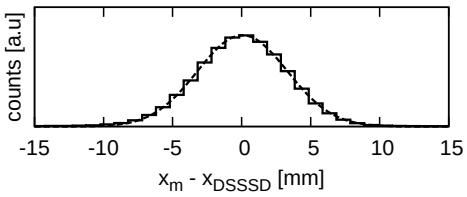

Figure 2: Histogram (solid line) of x-position difference from membrane (x_{m}) and DSSSD tracking (x_{DSSSD}). The dashed line is a Gaussian fit ($\mathrm{FWHM} = 7.6\,\mathrm{mm}$).

References

[1] D. Rudolph *et al.*, LYCCA Technical Design Report (2008); P. Golubev *et al.*, submitted to Nucl. Instr. Meth. A.

[2] A. Wendt *et al.*, GSI Sci. Rep. 2010, PHN-NUSTAR-FRS-03.

[3] P. Boutachkov *et al.*, this report.

[4] R. Hoischen *et al.*, Nucl. Instr. and Meth. A 654 (2011) 354.

[5] M. Reese *et al.*, this report.

Study of Neutron Damaged Germanium Detectors with Pulse Shape Comparison

M. L. Cortes[1,2], *T. Habermann*[3,2], *N.Goel*[2], *I. Kojouharov*[2], *J.Gerl*[2], *and N. Pietralla*[1]

[1]Technische Universität Darmstadt, Darmstadt, Germany; [2]GSI, Darmstadt, Germany; [3]Goethe Universität Frankfurt, Frankfurt, Germany

Neutron damage of Germanium detectors is very frequent in nuclear physics experiments. It decreases the energy resolution of the detector and it is necessary to anneal it or to characterize its damage to recover its performance. The neutron damage of an EUROBALL crystal was studied using a 511 keV source and the pulse shape comparison technique.

Experimental Set-up

A neutron-damaged EUROBALL crystal was studied using a coincidences scanning approach at the scanning table of GSI [1]. In this set-up a ^{22}Na source is placed between a position sensitive detector (PSD) and the Germanium detector to be scanned. The PSD is a LYSO scintillator glued to a Hamamtsu R2486 position sensitive photomultiplier and the source is surrounded by a Tungsten shielding with conical opening. Two 511 keV γ rays are emitted in opposite directions by the source. One going to the Ge detector and the other one to the PSD, allowing a 2D image of the Ge detector to be generated. With the setup it is possible to obtain an image from the front and an image from the side of the detector. Event by event the pulse shape from the Ge detector is recorded as well as the energy deposited in it. By using a novel analysis technique, the images can be used to select particular interaction positions inside the detector and to study the signals coming from that position.

Results

Fig. 1 shows the FWHM of the photopeak as a function of the radial distance in the detector. Near the surface of the detector the width of the peak is smaller, indicating a higher resolution. In the central part of the detector the photopeak becomes wider.

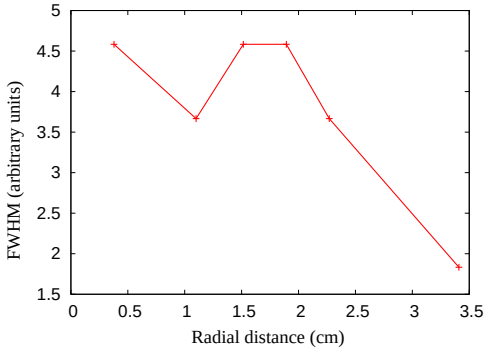

Figure 1: FWHM of the 511 keV photopeak as a function of the radial position.

For a coaxial Ge detector is expected that the rise time of the signals increase with the radial distance. For the EUROBALL crystal two cases were studied: Events dominated by full charge collection, in the central part of the photopeak and events with incomplete charge collection, recorded in the low energy tail. In both cases the behavior was as expected and no clear difference between the cases was found.

Signals associated with the same position in the detector were compared by pairs and the χ^2 value of this comparison was calculated. The distribution obtained is shown in Fig. 2. A comparison with the result obtained for an AGATA crystal is shown. Differences in the shape of the distributions, may be related to an effect of neutron damage, nevertheless a comparison with a non-damaged EUROBALL crystal is necessary.

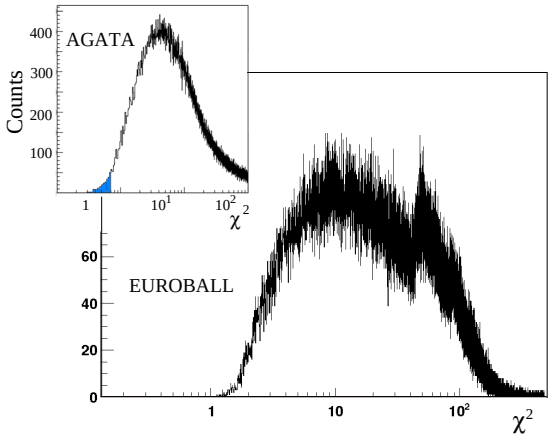

Figure 2: χ^2 distribution in the EUROBALL crystal compared to the distribution in an AGATA crystal

Conclusions

The neutron damaged EUROBALL crystal shows a radial dependence of the neutron damage. The shape of the χ^2 distribution suggest the possibility to quantify the neutron damage, but a comparison with a non-damage detector is needed to make a final conclusion.

References

[1] C. Domingo-Pardo, *et. al.*. NIM A643 (2011) 79-88

The R^{3}B Experiment*

H. Scheit[1] *and the R^{3}B Collaboration*
[1]Institut für Kernphysik, TU-Darmstadt, Germany

The experiment Reactions with Relativistic Radioactive Beams (R^{3}B) at the high-energy branch of the FAIR facility will allow for kinematically complete nuclear reaction studies with short-lived radioactive ion beams in inverse kinematics, utilizing a wide beam energy range from about 100–1000 MeV/u covering the full mass range up to uranium. Experimental programs will address fundamental questions in nuclear structure and reaction physics, as well as nuclear astrophysics.

The planned physics program requires a high resolution and high efficiency for all detection systems. This is reflected in the proposed experimental setup, which has been or will be designed and constructed by the R^{3}B collaboration based on many years of experience with the ALADIN/LAND setup at GSI.

Each part of the former LAND setup has its improved counter part in the proposed R^{3}B setup, adapted to reach much higher resolutions, to deal with the high-rigidity beams available at FAIR, and to deal with the large variety of reaction types to be studied. Several milestones toward the realization of the R^{3}B experiment have been reached this year: the technical design reports (TDR) for two core components of the R^{3}B setup, the NeuLAND high-resolution neutron time-of-flight spectrometer and the CALIFA Barrel detector, which serves as a γ-ray spectrometer, calorimeter and, together with the Si-tracker, as a target-recoil detector, have been accepted by FAIR following the recommendation by the expert committee experiments (ECE).

The NeuLAND detector is a next-generation neutron time-of-flight spectrometer featuring high detection efficiency, high resolution and an excellent multi-neutron hit resolving power. This is achieved by a high granularity—the detector consists of 3000 sub-modules with dimension of $5 \times 5 \times 250$ cm^3—and a fully active detector volume with good calorimetric properties. At the high-acceptance position 15.5 m downstream from the target the detector face covers the full acceptance of the R^{3}B-GLAD magnet of ± 80 mrad, corresponding to 100% acceptance for neutrons with a decay energy of up to 5 MeV for $E_{\mathrm{beam}} = 600$ MeV/u. The position and time resolutions of 1.5 cm and 150 ps, respectively, result in a decay energy resolution of 60 keV for a neutron with a decay energy of 1 MeV. At the furthest distance in the high-energy cave of FAIR the NeuLAND detector is 35 m downstream of the target. In this case the geometric acceptance is reduced to 35 mrad, but the decay energy resolution is less than 20 keV at 100 keV decay energy. Another major step forward is the improved multi-neutron hit recognition capability. For instance, a 4 neutron hit can be identified as such with an efficiency of 60% and the decay energy resolution is still 42 keV for a decay energy of 100 keV.

In order to benchmark the NeuLAND design under experimental conditions the experiment S406 was carried out. A dedicated setup was constructed consisting 150 NeuLAND modules (bars) mounted in an array of 15 layers. This array was the irradiated with nearly mono-energetic neutrons stemming from quasi-free breakup of deuterons with energies ranging from 200 to 1500 MeV/u. The data are currently under analysis.

The CALIFA calorimeter will surround the R^{3}B target position. The detector is sub-divided into a forward endcap and barrel section covering laboratory angles up to 43 $^\circ$ and 43–140°, respectively. Very high demands are placed on this detector by the planned physics program. It should not only detect γ-rays with energies from 100 keV up to several tens of MeV energy, but also highly energetic light charged particles, mainly protons, with energies reaching hundreds of MeV. The barrel section of the detector will consist of almost 2000 individual detector CsI crystals, which will be read out by avalanche photo diodes. This results, for instance, in an energy resolution of 5.5% and a full-energy peak efficiency of over 50% is achieved for 2 MeV photons emitted into the direction of the barrel section of CALIFA from a 700 MeV/u projectile.

The construction of another core component of the R^{3}B-setup, the superconducting large-acceptance large-gap dipole magnet R^{3}B-GLAD, is underway with an expected delivery at GSI in the fall of 2013.

Furthermore, the design and construction of the R^{3}B Si-tracker, which is already fully funded, is progressing well. Together with the CALIFA detector it will comprise the R^{3}B target recoil detector to accurately determine the momentum vectors of light charged particles after e.g. a (p,2p) reaction.

In addition a new thin and high-resolution fiber detector was commissioned with heavy ions and various new hard- and software components for the coupling of several DAQ systems were tested and evaluated.

First commissioning and physics experiments at GSI with R^{3}B-GLAD and 20%-versions of NeuLAND and the CALIFA Barrel will be carried out in 2014. Until 2016 the setup will be largely completed at GSI, used for commissioning and physics runs and moved to the new high-energy cave at FAIR in 2017/18.

* Support by HIC for FAIR, BMBF (06DA70471), and through GSI-TU Darmstadt Cooperation is thankfully acknowledged.

Status of the R3B GLAD Magnet Cryosystem

Christine Betz, Thomas Hackler, Eugen Momper, Claus Schroeder, and Haik Simon[1]

[1]GSI, Darmstadt, Germany

The superconducting GLAD magnet will be one of the major components of the R³B experiment to be installed at FAIR at the experimental area. Within the year 2013 we expect the full magnet, as described elsewhere in this report, to arrive at GSI in Cave C for field measurements and first commissioning experiments. To install and run the magnet in Cave C the magnet has to be provided with liquid Helium and therefore a new cryogenic system has to be installed at GSI target hall.

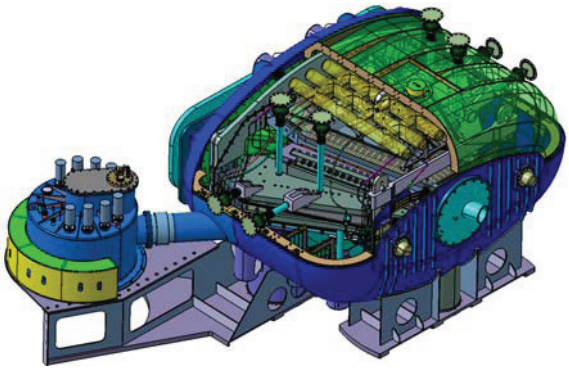

Figure 1: R3B Glad magnet with cold mass inside cryostat [1].

The GLAD magnet will be provided with Helium by a used TCF 50 Helium liquefier (year of manufacture 1986) which was used before for cooling magnets at DESY. The Cryoplant was moved to Darmstadt in June 2012.

The liquefier is currently refurbished and upgraded in collaboration with the Linde Kryotechnik company. These activities comprise, that the liquefier will be equipped with a new compressor, valves, temperature sensors, oil removal system, gas management panel, helium buffer, transfer lines, and control system.

The compressor will be installed outside the target hall on the west side in a 20 feet container. The coldbox and the oil removal system will be located in the target hall next to the Helium liquefier of former FOPI experiment (see figure 2).

Another part of this project is the relocation of the Helium buffers of the FOPI and HADES cryogenic systems and their connection to the R³B Helium Buffer. This is necessary in order to free the space needed to access the construction area, where FAIR site preparations for the HESR will be initiated soon, at the east site of the target hall.

After the successful disassembly and transportation from Hamburg to Darmstadt, oil contaminations stemming from the compressor were detected inside the coldbox. These contaminations resulted in the necessity to perform an extensive cleaning process of the coldbox as small amounts of hydrocarbons on the ppm level are sufficient to cause damages or a drop of cooling power in the system.

To remove the oil, 700 litre of acetone where pumped through different pathways in the coldbox using a special membrane pump at enhanced safety measures. Thus, the oil could be dissolved and eventually removed from the pipes.

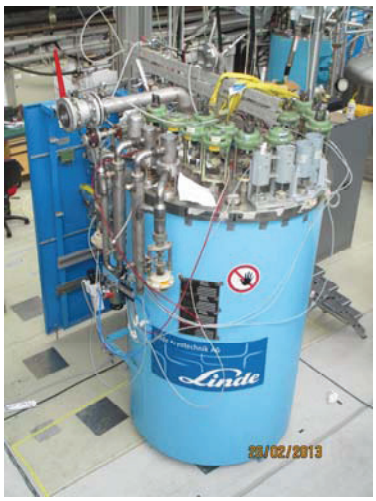

Figure 2: Linde TCF 50 Coldbox.

The full cryogenic system for the GLAD magnet will be equipped with a novel automation. In the course of the refurbishing and upgrade process, sensors and actors will be exchanged. The CERN build Framework „UNICOS“ is being used for the new control and data acquisition system. This can be seen as preparatory work for novel control systems to be established for the FAIR systems. We will use this to gather experience for this Control System, which will serve as basis for FAIR Automation. The GLAD Magnet cryogenic system will be the first system at GSI which will be controlled by UNICOS. The refurbishing will be used to test sensor and actor types for later use in other FAIR cryogenic systems.

Outlook

The delivery of the compressor container is expected for May 2013 and the delivery of the magnet for October 2013.

References

[1] P. Graffin et al., 22th International Conference on Magnet Technology, September 12th - September 16th 2011, Marseille

Cryogenic Test of the R3B-GLAD Magnet and Status of its Cryostat Production

C. Mayri, B. Gastineau, W. Abdel Maksoud, P. Charon, A. Donati, L. Genini, P. Graffin, Y. Queinec, and R. Vallcorba

IRFU, CEA Saclay, 91191 Gif-sur-Yvette, France.

Cryogenic test of the R3B-GLAD magnet

After the production of the coils and their mounting inside their casing [1] in 2010, the cold mass was built at Saclay in 2011. In addition to the assembly of the casing together with the cold mass structure, an important work was done on the electrical joints between the double pancakes of the coils. The all 27 joints were copper-stabilized then brazed with the challenge to obtain a joint resistance lower than few nano-ohms on each one. After modification of the feet swivels and production of new pieces the cold mass was ready at the spring 2012 to go inside one of the cryostats of the W7X test facility for the cryogenic test.

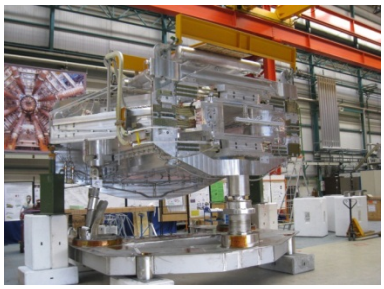

Figure 1: Cold mass on its three feet.

The cryogenic test needed a lot of improvements on the test facility which was not designed for a such big magnet. Unfortunately the first checks showed a small leak which was very difficult to localize and correct. At the present time, the cold mass is at 4.5 K. During the one month cooling down we already validated the behaviour of the feet which support the 22 tons of the cold mass and which have to accommodate the thermal shrinkage of the cold mass. At the end of the cool down, the start of the thermosiphon loops (26 lines in parallel) was also a success [2].

After final checks on the safety system the magnet will be energized soon up to the nominal current of 3584 A. Then we will check the behaviour of the magnet during the current ramping, the fast discharge and a steady state run during which the magnetic field on the axis will be measured.

Cryostat production

After its test, the magnet will be integrated inside its cryostat [3] in 2013. The cryostat production was divided in three parts and ordered at the end of 2011.

The transportation stops were designed to limit the stresses on the magnet feet during the magnet transport from Saclay to Darmstadt. They were delivered to Saclay in 2012 and will be mounted during the integration of the magnet.

The thermal shield surrounds the cold mass to decrease the thermal losses on the 4.5 K level. The panels are in stainless steel and are shared in few parts to limit the eddy current loops. The shield panels are equipped with brazed pipes in which helium gas at 50 K will flow.

The main part of the cryostat is the vacuum vessel which is under construction. This part represents more than the half of the 56 tons of the magnet weight. The shape of the vessel is rather complex and the construction implements specific technologies: electron beam welding or plate shaping by explosion.

Figure 2: Vacuum vessel and thermal shield panel under construction

The superinsulation blankets which surround the thermal shield are ordered and their final design is in progress. The parts dedicated to the satellite have been already delivered at Saclay. Then the integration of the valves and the current leads will start soon.

Figure 3: Magnet satellite

References

[1] G. Disset et al., “R3B-Glad magnet cold mass manufacture: coils and casings fabrication and integration”, MT 22, Marseille, September 2011.

[2] B. Gastineau et al., “R3B-Glad magnet R&D test program: Thermosiphon loop with horizontal section, superconducting cable joints at 3600 A, and reduced scale “coils in its casing” mock-up”, MT 22, Marseille, September 2011.

[3] P. Graffin et al., “The Cryostat design of the R3B-Glad Magnet”, MT 22, Marseille, September 2011.

Construction and Test of a Large NeuLAND Prototype Array*

K. Boretzky[1], B. Agrawal[3], G.D. Alkhazov[11], S. Altstadt[9], H. Alvarez Pol[17], V.A. Andreev[11], L. Atar[2], T. Aumann[2,1], P. Basu[3], D. Bemmerer[4], M. Bendel[14], D. Bertini[1], P. Bhattacharya[3], S. Bhattacharya[3], A. Blanco[5], J. Bonilla[9], C. Caesar[2], L. Cartegni[7], S. Chakraborty[3], A. Charpy[13], S. Chatterjee[3], M. Cherciu[6], L. Chulkov[12], M. Ciobanu[6], T. Cowan[4,10], U. Datta Pramanik[3], Z. Elekes[4], J. Endres[8], A.A. Fetisov[11], E. Fiori[15], P. Fonte[5], D. Galaviz[7], I. Gasparic[2], J. Gerbig[9], R. Gernhäuser[14], K. Göbel[9], V.L. Golotsov[11], M. Haiduc[6], T. Heftrich[9], J. Hehner[1], M. Heil[1], M. Heine[2], A. Heinz[13], A. Hennig[8], A. Henriques[7], M. Holl[2], A. Ignatov[2], G. Ickert[1], J. Isaak[15], E.A. Ivanov[11], S. Jährling[2], J. Johansen[2], H. Johansson[13], A. Kelic-Heil[1], O. Kiselev[1], D. Körper[1], D. Kresan[2], A.G. Krivshich[11], P. Kumar Das[3], T. LeBleis[14], C. Lederer[9], Y. Leifels[1], S. Lindberg[13], L. Lopes[5], B. Löher[15], J. Machado[7], J. Marganiec[15], L. Netterdon[8], T. Nilsson[13], V. Panin[2], J. Panja[3], S. Paschalis[2], A. Perea[16], B. Pietras[17], R. Plag[9], M. Pohl[9], M. Potlog[6], A. Rahaman[3], G. Rastrepina[9], A. Ray[3], R. Reifarth[9], T. Reinhardt[10], G. Ribeiro[16], M. Röder[10], D. Rossi[1], J. Sánchez del Rio[16], A. Sauerwein[8], D. Savran[15], H. Scheit[2], S. Schmidt[9], P. Schrock[2], J. Silva[15], H. Simon[1], T. Sinha[3], M. Sobiella[4], K. Sonnabend[9], D. Stach[4], E. Stan[6], O. Tengblad[16], P. Teubig[7], R. Thies[13], L.N. Uvarov[11], P. Velho[7], V.V. Vikhrov[11], S.S. Volkov[11], V. Volkov[2,12], A. Wagner[4], F. Wamers[2], M. Weigand[9], M. Winkel[14], J. Wüstenfeld[4], D. Yakorev[4], A.A. Zhdanov[11], A. Zilges[8], K. Zuber[10], and the R[3]B collaboration

[1]GSI, Darmstadt, Germany; [2]TU Darmstadt, Germany; [3]SINP Kolkata, India; [4]HZDR, Dresden-Rossendorf, Germany; [5]LIP, Coimbra, Portugal; [6]ISS, Bucharest, Romania; [7]Univ. Lisbon, Portugal; [8]Univ. of Cologne, Germany; [9]Univ. Frankfurt, Germany; [10]TU Dresden, Germany; [11]PNPI St. Petersburg, Russia; [12]Kurchatow Institute Moscow, Russia; [13]Chalmers Univ. of Technology, Göteborg, Sweden; [14]TU München, Germany; [15]EMMI, GSI Darmstadt, Germany; [16]CSIC Madrid, Spain; [17]U Santiago de Compostela, Spain

NeuLAND (new Large-Area Neutron Detector) is the next-generation neutron detector integrated into the R3B experiment, and is a key instrument for a major part of the physics program. NeuLAND features a high detection efficiency, a high resolution, and a large multi-neutron-hit resolving power, achieved by a highly granular design with a total of 3000 plastic scintillator bars [1]. In January 2013 the Technical Design Report [2] has been approved by FAIR, following the recommendation by the Expert Committee Experiments (ECE) at its first meeting in November 2012.

Here we report about the progress of the NeuLAND project, which was dominated in 2012 by the transition from prototypes to mass production. During the previous year 200 NeuLAND modules and their readout were purchased and brought into operation.

A number of the final size NeuLAND bars have been available for in-beam tests at the ELBE accelerator. There, bunches of 30 MeV electrons with a time definition of better than 20 ps impinged on the detectors to be tested. The number of electrons per bunch was reduced to one, enabling sensitive timing measurements with the accelerator RF signal as time reference [3]. As single 30 MeV electrons are close to minimum ionizing particles, this method gives an upper limit for the time resolution to be expected in NeuLAND, where the signal will mainly stem from protons.

Several NeuLAND bars of the final geometry have been tested at ELBE, using the recommended one inch photomultipliers, in several cases Tacquila electronics, and in others commercial electronics with 25 ps time-to-digital converters. The ELBE data show a time resolution of $\sigma = 130$ ps when a cut on a narrow slice of the charge / time over threshold signal is applied, consistent with the data from earlier proton experiments. When the whole charge distribution without any cuts is used instead and a walk correction is applied, the resolution worsens somewhat, to $\sigma = 170$ ps. This upper limit is very close to the required value of 150 ps. For some initial NeuLAND bars with deficient polishing, time resolutions of $\sigma > 200$ ps and a significantly suppressed charge spectrum were found at ELBE. The latter point was subsequently also observed in tests with radioactive sources and with LED's.

As consequence from the systematic ELBE data, a detailed quality check procedure was developed to verify a satisfactory light output, which turned out to be closely related to the surface treatment of the NeuLAND bars. The quality-control procedure for each bar contains, besides an optical inspection, a measurement of the light output, which is then related to the light output of a reference bar with a proven very good performance. For this relative measurement light emitted by an LED is illuminating the bar on one readout side. On the opposite readout side the

* Work supported by BMBF (06DA7047I, 06FY71051, 06KY71593,06DR134I, NupNET NEDENSAA 05P09CRFN5), by ENSAR, by GSI via the GSI-TU Darmstadt cooperation contract, by GSI F&E (DR-ZUBE) and by HIC for FAIR.

light is detected by using a photomultiplier (PM) of the same type as foreseen for the final assembly.

In late autumn the experiment S406 in Cave C was carried out using deuteron beams for calibration and benchmarking of both the existing LAND detector [4] and NeuLAND prototypes. For the latter 150 NeuLAND bars were mounted in a special array with 15 layers of ten vertical bars each. The bars in the array have been tested using cosmic rays, and in the best cases a time resolution of $\sigma_t^{Cosm.} = 130$ ps has been reached. The photographs in figure 1 detail the assembly and transport to Cave C prior to the beam time.

Figure 1: NeuLAND test array: after insertion of 100 scintillator bars (left) and transport of the assembly including 150 bars and its readout electronics to Cave C (right).

During the beam time the NeuLAND array was exposed to fast "mono-energetic" neutrons originating from quasi-free breakup reactions of deuterons impinging on a CH_2 target at six different beam energies. The collected data sets for neutrons at 200, 300, 500, 800, 1000 and 1500 MeV will serve to determine the efficiency of the NeuLAND test array as a function of neutron energy and thus be an important cross-check for the simulations carried out during the NeuLAND design phase [2, 5]. Another crucial parameter for NeuLAND is the time resolution. The measurement at 1500 AMeV was carried out at two different distances from the breakup target. At this high beam energy the time of flight variation due to the intrinsic momentum distribution of the knocked-out proton in the deuteron is rather small with ($\sigma_t^{int.} \approx 100$ ps) at 5 m distance. The measurement at 5 and 10 m distance therefore allow to disentangle the contribution from the ToF resolution of the detector and the width related to the wave function of the deuteron. While the results on neutron response demand a careful off-line analysis, on which we will report later, the online analysis of primary deuterons hitting the NeuLAND array results in a promising time resolution of $\sigma_t^D = 115$ ps.

Together with the NeuLAND test array two different large-size MRPCs (Multigap Resistive Plate Chambers) [6, 7], which were developed during the design phase of NeuLAND, were exposed to the neutron flux, allowing a characterization of these detectors.

In the same experiment, after removal of NeuLAND from the setup, LAND was calibrated using 200 to 1500 MeV neutrons as well. For the lower energy settings several parasitic experiments were carried out using the fast protons stemming from the break-up process. Behind ALADIN a ToF-Wall served for proton detection and various CsI and NaJ detectors were mounted for investigations of proton detection with the future R3B calorimeter CALIFA and with the existing Crystal Ball.

Approaching the step of mass production of NeuLAND double-planes an adaption of the HV supply and a redesign for the readout board of TacQuila electronics is underway. A cost-effective possibility for the HV supply of the 6000 PM's of NeuLAND has been developed by PNPI. It foresees one master HV supply per 3000 PM's providing 1.5-2 kV. Via distributor boards with adjustable attenuators for 50 PMs each, the supply voltage can be regulated downwards for the individual channels. A slow control via an FPGA based control board is provided via ethernet from a host computer. The design has been completed, and we are about to order the first demonstrator devices. An adaptation of the voltage divider stage of the PM with respect to a reduction of power-consumption was already realized by the provider. For the readout electronics we will move from the TAC27-ASIC based time measurement to an FPGA TDC measurement, which is much more flexible, and has been proven to be technologically feasible by GSI. This will enable a measurement of time over threshold, thus providing an additional independent energy measurement and will feature multi-hit capability. The design can be based on building blocks available for the FEBEX readout series, which also allows to avoid specialized VME boards, that became in the mean time more difficult to acquire. The FEBEX readout chain is set up via fibre optics so that grounding problems will be minimized.

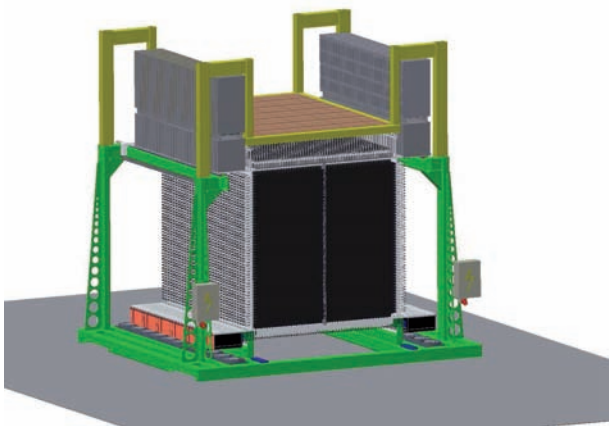

Figure 2: Technical drawings of the NeuLAND base frame together with its 30 double-planes and adjacent boxes for read-out electronics and HV-supply.

After construction and realization of the support structure for the NeuLAND test array the detailed design of the

holding structure for the planes and the base frame of NeuLAND has been reinvestigated. As detailed in the NeuLAND TDR, we foresee to arrange the 3000 scintillator bars in double-planes with 50 vertical and 50 horizontal bars, respectively. Fig. 2 shows the technical drawings for the frame loaded with all planned 30 double-planes.

It was decided to adapt also the read-out electronics, HV distribution and monitoring system to this modular design of the double-planes. This allows the collaborators to build individual and fully functional double-planes which can be tested separately and immediately used once mounted in the base frame. Fig. 3 displays a front view of one double-plane. The boxes on top, left and right contain the read-out electronics and will be connected via a read-out bus. The boxes at the bottom comprise the HV distribution system.

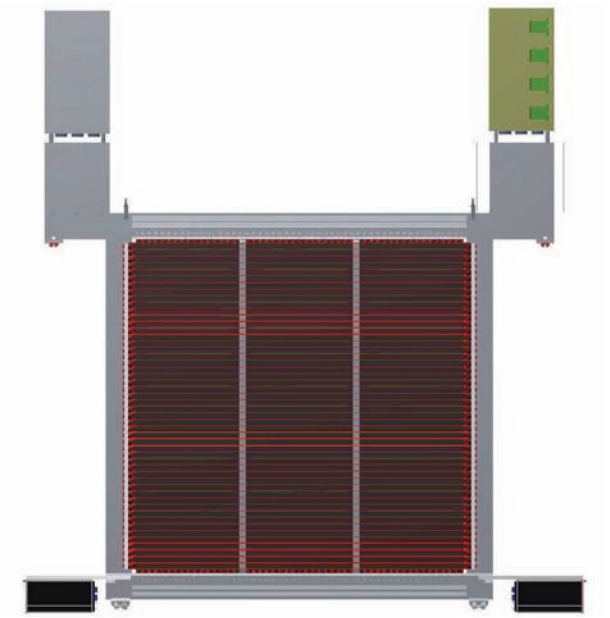

Figure 3: Technical drawings of one NeuLAND double-plane.

The next step is the assembly of NeuLAND double-planes and its inclusion into the detector frame. During 2013 a 20% NeuLAND demonstrator shall be accomplished and exposed to beams at GSI in beginning of 2014.

References

[1] K. Boretzky et al., GSI Scientific Report 2011, http://www-alt.gsi.de/informationen/wti/library/scientificreport2011/PAPERS/PHN-NUSTAR-NR-02.pdf

[2] NeuLAND@R3B: A Fully-Active Detector for Time-of-Flight and Calorimetry of Fast Neutrons, NeuLAND Technical Design Report, http://www.fair-center.de/fileadmin/fair/experiments/NUSTAR/Pdf/TDRs/NeuLAND-TDR-Web.pdf

[3] D. Yakorev et al., NIM **A654**(2011) 79.

[4] T.Blaich et al., NIM **A314** (1992) 136.

[5] D. Kresan et al., GSI Scientific Report 2011, http://www-alt.gsi.de/informationen/wti/library/scientificreport2011/PAPERS/PHN-NUSTAR-NR-03.pdf

[6] Z. Elekes et al., NIM **A701** (2013) 86.

[7] J. Machado et al., GSI Scientific Report 2012

R&D for NeuLAND development for R3B, FAIR at SINP, Kolkata

U. Datta Pramanik[1#], T. Aumann[2], K. Boretzky[2], P. Basu[1], J.Basu[1], S. Bhattachaya[1], D. Bemmerer[3], S. Chakraborty[1], S. Chatterjee[1], P.K.Das[1], Z. Elekes[3], D.Gonzalez-Diaz[2], M.Kempe[3], J.Panja[1], A. Rahaman[1], J.Ray[1], H.Simon[2], M.Sobiella[3], D.Stach[3], A.Wagner[3], D.Yakorev[3] for R3B collaboration

[1]*Saha Institute of Nuclear Physics, Kolkata, India;* [2]*GSI, Darmstadt, Germany;* [3] HZDR *Dresden-Rossendorf, Germany*

In the upcoming R3B-FAIR facility, to achieve the design goal for high resolution neutron time-of-flight [1,2], various types of prototypes have been explored at several places [3,4,5,6]. The possible candidates for active material of such a spectrometer can be either Multi-gap Resistive Plate Chamber (MRPC) or conventional plastic scintillators. At initial stage of NeuLAND development, at Saha Institute of Nuclear Physics, Kolkata, MRPC design feasibility was studied extensively[3,5].

Multi-strip Multi-gap Resistive Plate Chambers (MMRPC) has been built at SINP, Kolkata using local infrastructure (SINP workshop, dedicated laboratory, etc.) and major local raw materials [3]. The design of the detector elements is as followed: double stack MRPC with glass resistive plates and two gas gaps of 0.3 mm, each[3]. The Anode plate was segmented with 2cm wide strip. The detector was first tested in the laboratory using cosmic muons and gamma rays in coincidence with cerium doped $LaBr_3$ detector. Fig. 1 shows the experimental setup for testing MMRPC in coincidence with $LaBr_3$:Ce detector. Timing response corresponding to cosmic muons was observed to be around 150±30ps without slew correction.

The electron response of our developed detector was studied using the electron linac ELBE at Helmholtz-Zentrum Dresden-Rossendorf. The electron energy was chosen to 29 MeV with pulse width less than 10 ps. To find the optimum operational condition of the prototype, the detector was scanned with beam focused on a single strip of MMRPC. Measurements were also performed with the beam spot focused on each of the other individual strips of MMRPC. The absolute efficiency of the detector was measured to be more than 90% with cathode voltage above -7KV. Fig. 2(a) shows the 2-D plot for slew corrected ToF of developed MMRPC against deposited charge on a single strip. Measured time resolution (σ_t) after slew correction was 98.0±2.7 ps (Fig. 2(b)). Position information was extracted from the difference in time from either end of a strip. Position resolution along the strip (σ_x) was found to be 1.9±0.7 cm.

Recently, an extensive test and characterization of Plastic scintillators have been started at our laboratory at SINP, Kolkata. In laboratory, various types of plastic scintillator (BC408, BC422q etc) of several dimension coupled with PMTs at both ends have been procured.

*Supported by Dept. of Atomic Energy, Govt. of India
#ushasi.dattapramanik@saha.ac.in

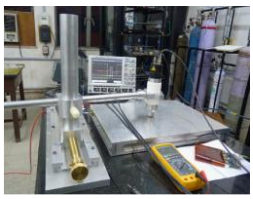

Fig: 1

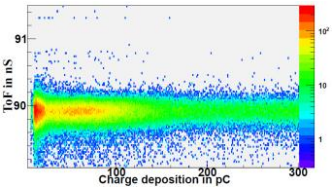

Fig: 2 (a)

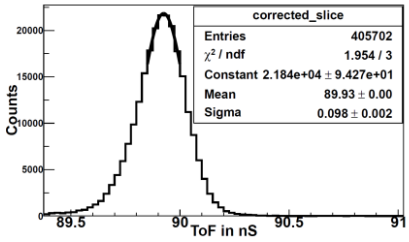

Fig: 2 (b)

Fig. 1: Testing of MMRPC in coincidence with $LaBr_3$:Ce detector at SINP laboratory; Fig 2(a) Slew corrected time vs charge deposition for electron at ELBE; Fig 2(b) Slew corrected ToF spectrum of MMRPC

Detector specification (PMT type)	Bias Voltage (V)	Rise time (ns)	Decay time (ns)	Pulse Height (mV)
HPK H3164-10	-1200	0.8-1.2	~80	200-300
HPK H6533	-2000	1.2-2	~80	200-320

Table - I: Properties of the various plastic scintillator tested at SINP Laboratory.

Response of these detectors to gamma and charge particle has been studied using available radioactive source ^{60}Co, ^{152}Eu, ^{22}Na, ^{241}Am etc. Timing responses are comparable with MMRPC. More extensive studies are going on.

References

[1] R3B Technical report.
[2]NeuLand@R3B: A Fully-Active Detector for TOF of fast neuron:http: //www.faircentre.de/fileadmin/fair/ experiments/NUSTAR/Pdf?TDRs/NeuLand-TDR-Web.pdf
[3] U. DattaPramanik et al., NIM A 661 (2012) S149.
[4] K.Boretzky et al, "Neuland@R3B- A Progress report", GSI scientific report 2012.
[5]U.Datta Pramanik et al, DAE, http://sympnp.org/proceedings/56/G12.pdf
[6]Z.Elekes et al, NIMA 701 (2013) 86.

Tests of Silicon Photomultipliers for NeuLAND *

T. Reinhardt[1], *D. Bemmerer*[2], *T. Cowan*[1,2], *K. Heidel*[2], *M. Kempe*[1,2], *M. Röder*[1], *D. Stach*[2], *A. Wagner*[2], *K. Zuber*[1], *and the R*^{3}*B collaboration*

[1]TU Dresden, Germany; [2]HZDR, Dresden, Germany

NeuLAND, the successor of the LAND time-of-flight neutron spectrometer is planned to be constructed of $5 \times 5 \times 250\,\mathrm{cm}^3$ scintillator bars of RP-408 [1] or equivalent. Light readout will be performed by $1''$ photomultiplier tubes (PMTs). A demonstration prototype of the detector concept was recently tested at GSI [2]. During the operation of the complete detector with 6,000 channels a significant number of photomultiplier tubes may have to be replaced each year. Recent developments in the field of semiconductor based photon readout systems [2, e.g.] raise the possibility of using Silicon Photomultipliers (SiPMs) for this task.

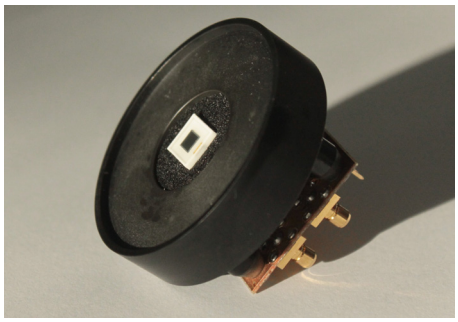

Figure 1: Setup to fix a $3 \times 3\,\mathrm{mm}^2$ SiPM on the $1''$ diameter side of a NeuLAND bar, mechanical support structure and preamplification board.

A cylindrical scintillator of EJ-200 (equivalent to RP-408) with a length of 15 mm and a diameter of 10 mm is instrumented subsequently with $3 \times 3\,\mathrm{mm}^2$ silicon photomultipliers of various manufacturers (fig. 1). For the supply of the high voltage and the preamplification of the signal, a dedicated electronic board was developed at HZDR. A collimated $^{90}\mathrm{Sr}/^{90}\mathrm{Y}$ β-source was used for measurements in self-triggering mode with one SiPM time-determining. It was found that a mean time resolution of $\sigma_t = 210\,\mathrm{ps}$ can be achieved assuming symmetric contributions of both KETEK PM3360 SiPM (figs. 2 and 3).

Coincidence timing resolution measurements on the scale of $\sigma = 100\,\mathrm{ps}$ are challenging, because they require a reference detector with similar time resolution. In contrast, the ELBE facility at HZDR provides electrons of 30 MeV in bunches of 5 ps length and a reference clock signal of better than 20 ps resolution. This allows testing of fast detectors with minimum ionizing particles.

First tests with a NeuLAND type scintillation bar instrumented with Hamamatsu R2059 PMT and $3 \times 3\,\mathrm{mm}^2$ SiPM

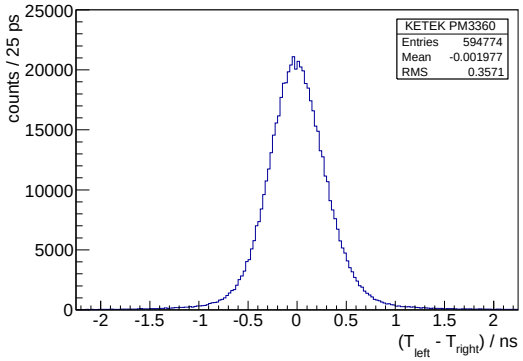

Figure 2: Averaged time from right and left side of setup with a small EJ-200 scintillator, a KETEK PM3360 SiPM and a collimated $^{90}\mathrm{Sr}/^{90}\mathrm{Y}$ β-source.

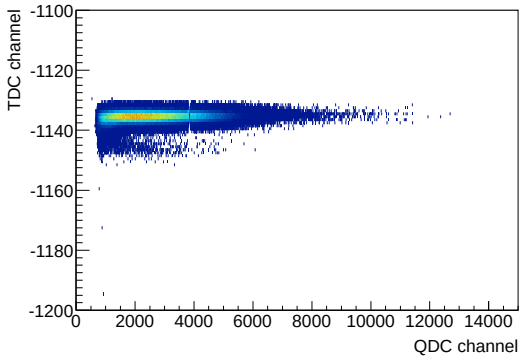

Figure 3: Charge versus time spectra for one KETEK PM3360 SiPM measured with $^{90}\mathrm{Sr}/^{90}\mathrm{Y}$ β-source.

in a hybrid setup and also with one SiPM on each side have been performed at ELBE. Light collection and dark count rate were identified as main issues for achieving the timing as well as efficiency requirements on large scale. Work is ongoing with SiPMs of $3 - 6$ mm side length from various manufacturers.

References

[1] NeuLAND@R3B: A Fully-Active Detector for Time-of-Flight and Calorimetry of Fast Neutrons, NeuLAND Technical Design Report, http://www.fair-center.de/fileadmin/fair/experiments/NUSTAR/Pdf/TDRs/NeuLAND-TDR-Web.pdf

[2] K. Boretzky *et al.*: NeuLAND@R3B. A Progress Report. GSI Annual Report 2012.

[3] T. Szczesniak *et al.*, Nucl. Inst. Meth. A 702, 91 (2013)

* Supported by NupNET NEDENSAA (05 P 09 CRFN5), GSI F&E (DR-ZUBE), and BMBF (06 DR 9058 I)

Testing Timing of Resistive Plate Chambers with Relativistic Neutrons at Experiment S406*

J. Machado[1], J. Adamczewski-Musch[2], A. Blanco[3], K. Boretzky[2], L. Cartegni[1], R. Ferreira Marques[3], P. Fonte[3], J. Fruehauf[2], D. Galaviz[1], M. Heil[2], A. Henriques[1], G. Ickert[2], D. Koerper[2], L. Lopes[3], M. Palka[4], A. Pereira[3], D. Rossi[2], H. Simon[2], P. Teubig[1], M. Traxler[2], P. Velho[1], and the R^{3}B collaboration

[1]Univ. Lisbon, Portugal; [2]GSI, Darmstadt, Germany; [3]LIP, Coimbra, Portugal; [4]Jagiellonian University, Cracow, Poland

Last Autumn 2012, quasi-monoenergetic neutrons were produced from a deuterium beam in experiment S406 to calibrate the neutron detector LAND and to study the performance of the NeuLAND prototype, the new neutron detector of the R^{3}B experiment [1]. During this experiment, prototypes based on the alternative detector concept considered during the R&D phase of the NeuLAND detector, which were based on timing Resistive Plate Chambers (tRPCs) [2], were also exposed to neutron beams of various energies (from 200 MeV to 1.5 GeV). More details on experiment S406 can be found in [3]. In this report we depict the characteristics of one of the two different approaches considered for the RPC concept, which was based on distinct converter materials for the detection and characterization of relativistic neutrons. Both prototypes were placed behind the NeuLAND prototype. The configuration during the experiment can be seen in Fig. 1.

The prototype described in this work, developed and constructed by a Portuguese collaboration involving the LIP laboratory in Coimbra and the Nuclear Physics Centre of the University of Lisbon, consisted in 4 tRPC layers. The particular aspect of this concept is that the glass electrodes that make up the gas gaps within the RPC act also simultaneously as converter material to detect the relativistic neutrons. The thickness of the adopted glass plates was approximately 3 mm [4]. This detector configuration was previously simulated, obtaining very satisfactory efficiency and momentum resolution results that motivated its construction and test at GSI [4].

Each RPC layer, with an active area of about 2000 x 500 mm^2, is made of 2 modules containing the active gaps. Half of the layers are built from modules with 2 gaps, while the rest are built with 5 gaps, all in multigap construction [5]. Each module consists in a plastic tight case enclosing the active gaps built entirely from 2.85 mm thick float glass[1] electrodes and defined by 300 μm nylon mono-filaments. The HV is applied to the outer glasses through a resistive surface layer applied on the glass surface with airbrush techniques. The readout of the signals is made by a pick-up electrode located in between two identical modules equipped with 15 copper strips 30 mm wide. The prototype is operated with a non-flammable gas mixture composed of 90 % $C_2H_2F_4$ and 10 % SF_6 under a continuous gas flow of 120 cm^3/min at a pressure slightly under atmospheric pressure to define correctly the gap width. The prototype was mounted in a vertical configuration, as it can be seen in Fig. 1.

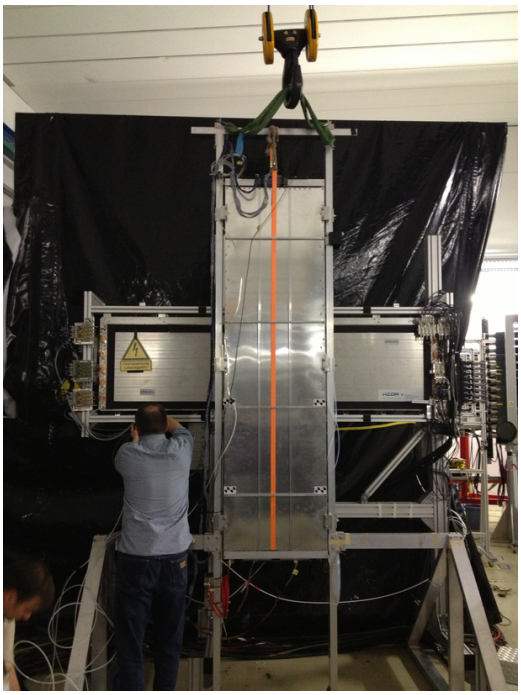

Figure 1: tRPCs mounted during experiment S406. The prototype described in this work was mounted on a vertical configuration.

The readout of the entire prototype comprises 120 Front End Electronics (FEE) channels [6]. These, together with the corresponding Low Voltage Power Supply (LVPS) and service boards [7, 8], were borrowed from the RPC-TOF Wall [9] of the HADES collaboration [10]. The Data Acquisition System (DAQ) consists basically in a TRB (Trigger Readout Board, [11]) while data gathering is performed by standard HADES eventbuilder software on a compact ARM based "dreamPlug" computer [12] able to write 12 kEvents/s to the disk. This all together forms a

*Work supported by the European Community FP7 Capacities, contract ENSAR no. 262010, and Portuguese FCT project PTDC/FIS/114876/2009

[1]Bulk resistivity of approximately 6.10^{12} Ωcm at 25^{o}C.

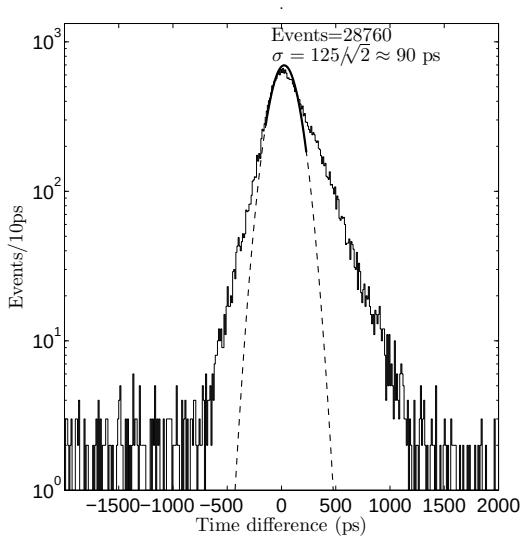

Figure 2: Time difference for two layers of the Portuguese prototype showing a time resolution for the entire chain (RPC + FEE +DAQ) of $\sigma \approx 90$ ps per layer.

very compact and portable DAQ, which is ideal for testing proposes. Additionally, the RPC DAQ has been synchronized with the MBS-based (Multi Branch System, [13]) LAND DAQ by means of a synchronization message from a VOLUM4 [14] module to the TRB. This allows an off-line synchronization of both data streams for later data analysis.

This prototype has been tested and calibrated previously with cosmic rays showing a time resolution better than 90 ps (See Fig. 2)

The second RPC prototype present at the measurements had been developed by HZDR [15].

The prototype has been exposed to relativistic neutrons during S406 experiment in order to characterize the response of tRPCs to this type of particles. The data analysis is ongoing.

References

[1] NeuLAND@R3B: A Fully-Active Detector for Time-of-Flight and Calorimetry of Fast Neutrons, NeuLAND Technical Design Report, http://www.fair-center.de/fileadmin/fair/experiments/NUSTAR/Pdf/TDRs/NeuLAND-TDR-Web.pdf

[2] P. Fonte *et al.*, "A new high-resolution TOF technology". Nuclear Instruments and Methods A443, 201 (2000)

[3] K. Boreztly *et al.*, "Construction and Test of a Large NeuLAND Prototype Array". GSI Scientific Report 2012.

[4] J. Machado *et al.* "Simulations of an innovative ToF detector for high energy neutrons based on iron-less RPCs", PoS(RPC2012) 039 (2012)

[5] E. Cerron-Zeballos *et al.* "A new type of resistive plate chamber: The multigap RPC", Nucl. Instr. Meth. A 374, 132 (1996)

[6] D. Belver *et al.*, "Performance of the Low-Jitter High-Gain/Bandwidth Front-End", IEEE TNS 57, 2848 (2010)

[7] A. Gilet *et al.*, "Distributed Low-Voltage System for the Front End of the HADES Timing RPC Wall", IEEE TNS 56, 382 (2009)

[8] A. Gil *et al.*, "The slow control system of the HADES RPC wall", Nucl. Instr. Meth. A 661, S118 (2012)

[9] D. Belver *et al.*, "The HADES RPC inner TOF wall", Nucl. Instr. Meth. A 602, 687 (2009)

[10] P. Salabura *et al.*, "The High-Acceptance Dielectron Spectrometer HADES", Eur. Phys. J. A 41, 243 (2009)

[11] J. Michel *et al.*, "The HADES DAQ System: Trigger and Readout Board Network", IEEETNS 58, 1745 (2011)

[12] dreamPlug at http://www.globalscaletechnologies.com

[13] http://daq.gsi.de

[14] J. Hoffmann, https://www.gsi.de/de/C/work/organisation/wissenschaftlich_technologische_abteilungen/experiment_elektronik/digitalelektronik/digitalelektronik/module/vme/vulom/vulom4.htm

[15] Z. Elekes *et al.*, Nucl. Inst. Meth. A 701, 86 (2013)

Recent Developments in NeuLAND Simulations

D. Kresan[1], *T. Aumann*[2], *K. Boretzky*[1], *D. Bertini*[1], *M. Heil*[1], *D. Rossi*[1], *and H. Simon*[1]
[1]GSI, Darmstadt, Germany; [2]TU, Darmstadt, Germany

The New Large Area Neutron Detector (NeuLAND) will be used in the R3B experiment at FAIR for high-precision multi-neutron recognition and measurement. It has a fully active large detector volume, constructed out of plastic crossed scintillator bars, read out from both ends with photomultipliers [1]. Detailed simulations of the performance in different measurement scenarios are strongly required. Such feasibility studies were done within the R3BRoot simulation and data analysis framework [2]. The description of the neutron tracking and reconstruction algorithm in NeuLAND can be found here [3].

Geometry interface

One of the major improvements in the R3BRoot framework is the support of flexible geometry description in the TGeo format (see ROOT home page for details [4]). This need is set by the large amount of the detector subsystems in R3B, each having several versions of geometry. This holds also for the LAND/ALADIN experiments.
Using this interface, provided by base classes of the FairRoot framework, one sets the geometry to be used in the simulation from the steering ROOT macro, which does not require recompilation of the code. In addition, it is also possible to describe the geometry of the complex detectors with very high granularity.

Improvements in multi-neutron tracking

The multi-neutron tracking in the NeuLAND consists out of two major steps: determination of the number of incident neutrons (based on the values of total energy deposit and number of clusters) and finding the first interaction of each incoming neutron.
As discussed in [3], very important step in the finding of neutrons first interaction is the elimination of secondary hits after the elastic scattering. This requires the measurement of the angle of the cluster, which becomes impossible if the cluster consists out of only one hit (fired bar). Thus, the clusters with the size smaller than 2 are skipped in the analysis of elastic scattering patterns. This modification results in the increase of the fraction of properly reconstructed tetra-neutrons from 58 to 63% (see Fig. 1).

Simulations for prototype test experiment

The first full-size NeuLAND prototype was tested in the deuteron beam in S406 experiment at GSI in October - November 2012. The goals of this beam time were to check the time resolution of the scintillator bars, compare total deposited energy versus simulation results and estimate the total neutron detection efficiency. The prototype was built out of 150 bars, organized in 15 planes, all in vertical direction.
Prior to the experiment, the required simulations were performed, including the calculations of:

- expected geometrical acceptance at different positions and beam energies;
- total neutron efficiency as a function of beam energy and detector thickness;
- trigger rate from the background (deuteron break-up in the start counter and beam straggling).

Analysis of the NeuLAND data from S406 experiment is ongoing and in future it should shed the light onto question of disagreement between total energy deposit when comparing Monte Carlo simulations versus real data.

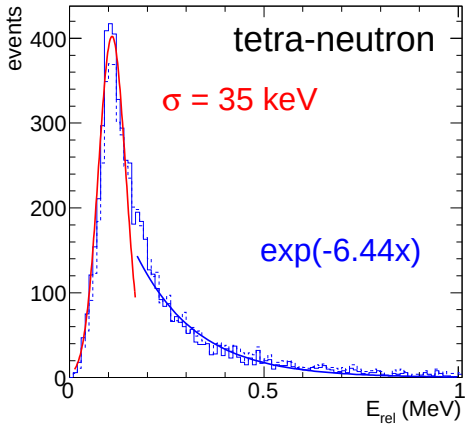

Figure 1: Simulated relative energy spectra of four-neutron events reconstruction at 600 AMeV beam energy. Dotted histogram - previous result, solid histogram - spectrum after improvement in the tracking algorithm. The absolute increase in the total efficiency of the order of 5% is observed. The fits with Gaussian and exponential tail are shown.

References

[1] K. Boretzky et al., this report
[2] http://fairroot.gsi.de
[3] D. Kresan et al., GSI Scientific Report 2011, p. 175
[4] http://root.cern.ch

Status of the CALIFA/R^{3}B calorimeter*

D. Cortina-Gil †[1], H. Álvarez-Pol[1], T. Aumann[2,5], V. Avdeichikov[3], M. Bendel[4], J. Benlliure[1], D. Bertini[5], A. Bezbakh[6], T. Bloch[2], M. Böhmer[4], M.J.G. Borge[7], J.A. Briz[7], P. Cabanelas[1], E. Casarejos[8], M. Carmona Gallardo[7], J. Cederkäll[3], L. Chulkov[9], M. Dierigl[4], D. Di Julio[3], I. Durán[1], E. Fiori[10], A. Fomichev[6], D. Galaviz[11], M. Gascón[1], R. Gernhäuser[4], J. Gerl[5], P. Golubev[3], M. Golovkov[6], D. González[1], A. Gorshkov[6], A. Heinz[12], M. Heil[5], W. Henning[4], G. Ickert[5], A. Ignatov[2], B. Jakobsson[3], H.T. Johansson[12], Th. Kröll[2], R. Krücken ‡[4], S. Krupko[6], F. Kurz[4], T. Le Bleis[4], B. Löher[10], N. Montes[1], E. Nacher[7], T. Nilsson[12], C. Parrilla[8], A. Perea[7], N. Pietralla[2], B. Pietras[1], R. Reifarth[13], J. Sanchez del Rio[7], D. Savran[10], S. Sidorchuk[6], H. Simon[5], L. Schnorrenberger[2], O. Tengblad[7], P. Teubig[11], R. Thies[12], J.A. Vilán[8], M. von Schmid[2], M. Winkel[4], S. Winkler[4], F. Wamers[2], and P. Yañez[8]

[1]Universidad de Santiago de Compostela; [2]Technische Universität Darmstadt; [3]Lund University; [4]Technische Universität München; [5]Helmholtzzentrum für Schwerionenforschung, Darmstadt; [6]Joint Institute for Nuclear Research, Dubna; [7]Instituto Estructura de la Materia, CSIC Madrid; [8]Universidad de Vigo; [9]National Research Centre, Kurchatov Institute Moscow; [10]Extreme Matter Institute and Research Division, GSI; [11]Centro de Física Nuclear da Universidade de Lisboa; [12]Chalmers University of Technology, Göteborg; [13]Goethe University Frankfurt am Main

CALIFA (the CALorimeter for In Flight detection of γ rays and light charged pArticles) is one of the key detectors of the R^{3}B experiment. It surrounds the reaction target and is optimised according to the exacting requirements given by the ambitious physics program proposed for the R^{3}B facility [1]. CALIFA is a versatile detector and will be used in a wide spectrum of experiments. In certain spectroscopy experiments, high γ-ray energy resolution (5% at 1 MeV) as well as multiplicity determination is required. In other experiments the goal is to attain calorimetric response with high efficiency. Part of the complexity arises from the reaction kinematics which leads to large Lorentz boosts and broadening of the detected γ rays peaks, i.e. effects that the detector should be able to account for. Charged particles of moderate energy, e.g. protons up to 300 MeV, should also be identified with an energy resolution better than 1%.

In order to meet these targets the detector is divided into two sections, a "Forward EndCap" covering polar angles between 7-43.2^o and a cylindrical "Barrel" section that provides angular coverage up to 140.3^o. The Technical Design Report (TDR) [2] of the Barrel section was recently approved (January 2013) by FAIR, following the recommendation of the Expert Committee for Experiments (ECE)[1]. The adopted technical solution consists of 1952 CsI(Tl) crystals, readout by Large Area Avalanche Photodiodes (LAAPDs), and a very compact geometry (internal radius 30 cm) in order to maximise the calorimetric properties. To optimize the detector efficiency and to minimize energy straggling for inter-crystal proton scattering, the passive material must be kept at an absolute minimum. These demands have lead to an in-depth investigation of the best crystal housing, support structures and overall mechanical design.

The coupling of LAAPDs to CsI crystals was found to fulfil many of the R^{3}B programme's most challenging demands. Their ability to meet the energy resolution requirement has been proven via an extensive R&D program using standard radioactive sources. The performance over a wide dynamic range has been investigated via irradiation of smaller size prototypes with proton beams at 25 (MLL, 2011), 180 (TSL, 2009), 200 and 400 MeV (GSI, 2012). Readout support for the photosensors is provided by Mesytec MPC-16B preamplifiers, which feature an online temperature-gain correction. A custom digital FEBEX electronic support system, envisaged for use in the final CALIFA setup is currently undergoing tests. In addition to the compact, high performance design, this approach takes advantage of the different CsI decay times for pulse shape analysis for particle identification. The FEBEX setup is highly flexible and allows for easy reprogramming of the FPGA online processing to suit individual experimental requirements [3].

Detailed simulations of the response of the CALIFA Barrel have been performed within the R3BROOT analysis framework in order to guide the progression through each stage of the development process. These simulations have been validated by comparison to experimental data for a number of smaller scale prototypes for both γ-ray and proton irradiation over a wide range in energy.

The next milestone as described in the TDR is the construction of the CALIFA Demonstrator. The Demonstrator will have a modular configuration of 8 petals each comprising 20 alveoli. The Demonstrator will cover a polar range of 32.5 – 65°, with 4 types of alveoli/crystals and 3 segments of 2 alveoli in the azimuthal direction and 10 alveoli in

* Work performed in the CALIFA/R^{3}B Working group and supported by the Helmholtz International Centre for FAIR

† Convener of the CALIFA Working group

‡ Also affiliated to TRIUMF

[1]Decision adopted in the ECE first meeting in November 2012

polar direction. The design provides a significant section of the final calorimeter and will ultimately be incorporated into CALIFA [4]. In addition to detector characterisation, the Demonstrator is intended for use in a real experimental campaign. In Figure 1 an artistic view of the CALIFA Demonstrator is shown.

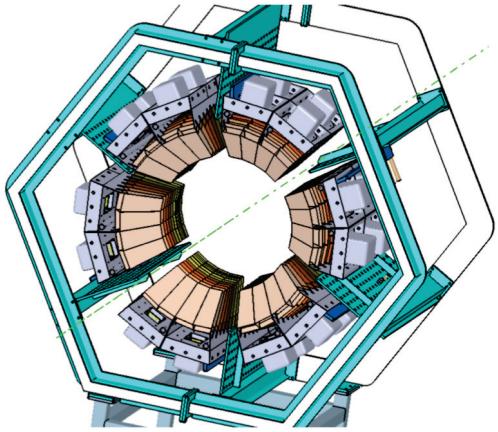

Figure 1: An artistic impression of the CALIFA Demonstrator.

We are in parallel working on the R&D towards an optimal solution for the "Forward EndCap" section. This polar region will be subject to high energy charged particles in addition to γ rays boosted to several times their energy in the projectile rest frame. The long CsI(Tl) crystals employed for the CALIFA Barrel section would fulfil the R^3B physics requirements for the EndCap section, however this option would suffer from incident charged particles undergoing a large number of inelastic reactions, significantly reducing the full energy peak efficiency. This restriction may be overcome by the use of a phoswich concept with two, relatively short, high performance scintillator layers which provide two ΔE measurements as charged particles pass through them. From these measurements the particle's incident energy can be determined. This approach reduces the detector volume significantly and several phoswich options are currently under investigation.
One such concept proposes a combination of two novel scintillation materials: 4 cm of $LaBr_3$(Ce) followed by 6 cm $LaCl_3$(Ce). This configuration works as a telescope, the first section ($LaBr_3$(Ce)) provides a ΔE measurement whereas the total E is obtained by the two consecutive energy loss measurements (ΔE $LaBr_3$+ΔE $LaCl_3$). An initial small size prototype consisting of an array of 2x2 phoswich $LaBr_3$+$LaCl_3$ elements, formed by rectangular crystals, was recently irradiated with high energy protons (GSI, 200-1000 MeV). Data analysis is currently under way.

We have also progressed towards the final design of the segmentation of the Forward EndCap. The large segmentation present in the Barrel must be preserved in order to retain the spectrometric capabilities. A dedicated design

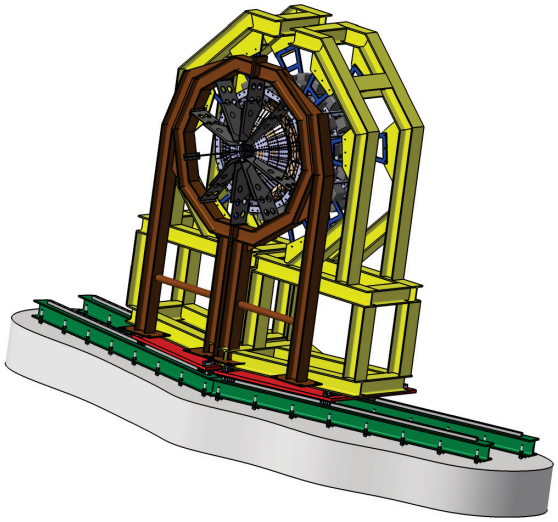

Figure 2: An artistic representation of the complete CALIFA calorimeter.

places frustum shaped crystals into 10 branches, each one containing 5 alveoli. The alveoli are sub-divided into 15 sectors holding individual crystals which results in a total of 750 crystals. The performance of this system has been studied by means of Monte Carlo simulations [5].
Figure 2 shows an artistic conception of CALIFA where both sections: Barrel and Forward EndCap, are mounted on a common platform. CALIFA is currently entering a very exciting period, with the full implementation and commissioning of the CALIFA Demonstrator expected in the first quarter of 2014. The submission of the TDR for the forward section is foreseen by the end of 2014. According to our plans the complete CALIFA should be installed and operational in the R^3B cave by the end of 2016.

This work was supported by Mineco (FPA2009-14604-C02-01, FPA2009-14604-C02-02, FPA2009-07387), HIC /FAIR, BMBF (06DA9040I, 05P12RDFN8, 06MT9156, 05P12WOFNF), DFG (EXC153), GSI-TU Darmstadt cooperationn and the EraNet NupNet GANAS.

References

[1] T. Aumann et al., Technical Proposal for the design, construction, commissioning and operation of R^3B, A universal setup for kinematical complete measurements of Reactions with Relativistic Radioactive Beams (2005).

[2] T. Aumann et al., Technical report for the Design, Construction and Commissioning of the CALIFA Barrel: The R^3B CALorimeter for In Flight detection of γ-rays and high energy charged particles (2011)

[3] T. le Bleis et al., Test of Integration of CALIFA into R3B, GSI SCIENTIFIC REPORT 2012

[4] E. Casarejos et al., Mechanics of CALIFA Barrel, GSI SCIENTIFIC REPORT 2012

[5] J. Sanchez del Rio et al., CEPA: A LaBr3(Ce)/LaCl3(Ce) phoswich array for detection of high energy protons and gamma radiation, GSI SCIENTIFIC REPORT 2012

The mechanical design of the BARREL section of the detector CALIFA*

J.A. Vilán[1], *E. Casarejos*[†1], *P. Izquierdo*[1], *P. Yañez*[1], *H. Alvarez-Pol*[2], *and I. Durán*[2]
[1]Dpt. of Mechanical Engineering, Univ. of Vigo, E-36310, Spain; [2]Univ. of Santiago de Compostela E-15782, Spain

The detector CALIFA (CALorimeter for the In Flight detection of gamma-rays and light charged pArticles) is one of the key detectors of the R3B experiment of FAIR. CALIFA will feature a high photon detection efficiency and good energy resolution even for beam energies approaching 1 AGeV, as well as the required calorimetric properties for detection of multiple gamma-ray cascades. For the detection of protons in coincidence, both the crystal length and the passive materials must be optimized.

CALIFA consists of two sections, a Forward EndCap and a cylindrical Barrel. The optimum cost-effective solution for the BARREL, covering an angular range from 43 to 140 degrees, is based on CsI(Tl) crystals. The BARREL will consist of almost 2000 crystals providing the angular resolution necessary to correct for the Doppler shift of the gammas emitted in-flight by the reaction products. The engineering design was aided with mechanical calculations using finite elements analysis with ANSYS and physics simulations with GEANT4. The design optimization was focused in the segmentation of crystals (increasing the segmentation helps for the energy resolution, but limits the calorimetric properties), and the amount of structural materials (with the motto 'the less, the better' to minimize the proton energy losses in the passive material).

The engineering design solution proposed for the core of the BARREL is based in a honeycomb-like structure made of epoxy based **carbon fiber composites**. The calculations performed confirm that such structure would conform the active region demands for physics, as well as the structural needs to support and tightly hold the many crystal units. The amount of passive (structural) material is **less than 0.7%** of the total mass of the whole active region.

The overall design conditions imposed by the project for the active core include: i/ a robust and safe structure; ii/ a minimum of structural material; and iii/ a tight definition of the static positioning and orientation of the active elements.

The CsI(Tl) crystals must be kept in a dry atmosphere. Moreover, the response of the crystal + photosensor (APD) is temperature dependent. To cope with the resolution requirements the active volume will be filled with nitrogen renewed in a closed loop at controlled temperature. That will be accomplished by means of a modular cover of the BARREL which is a key part of the external structure of the detector, that holds too the electronic front-end modules.

The standing structure, based in a gantry-like solution with moving platforms, must support the active core, allowing for the partition of the system in two autonomous symmetric halves, and the possibility to make a longitudinal shift between the halves to allow for a clearance of the forward angles, as well as helping in the setup of the Forward EndCap.

The TDR was approved by the end of 2012. The construction of the BARREL will start in 2013, with the so called DEMONSTRATOR, a structure based in CALIFA mechanical design solutions, covering 20% of the detector active elements, and ready for physics experiments in 2014 at GSI.

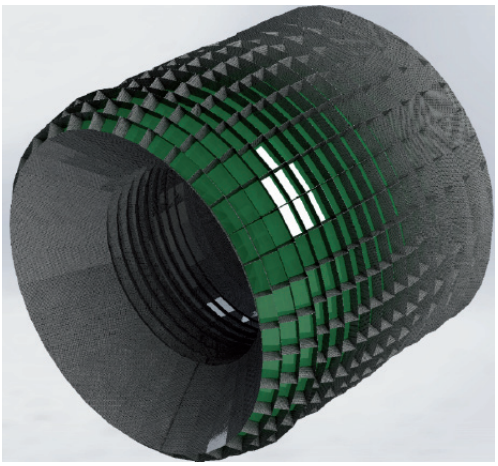

Figure 1: View of the active region of the BARREL. With almost 2000 crystals tightened by a honeycomb-like structure made of CF composites, it contributes to less than 0.7% of the mass.

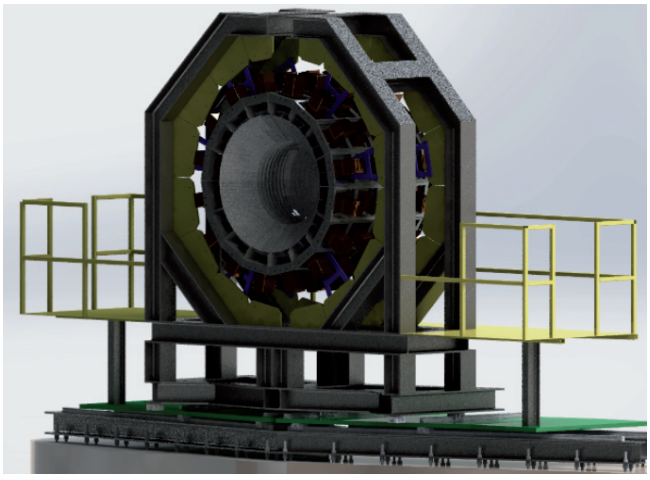

Figure 2: View of the external structure which allows for the splitting and longitudinal shifting of the active region. It also supports all the associated electronic modules.

* Work supported by Spanish Min. of Science, projects FPA2009-14604-C02-01 and -02, and Industry, project IDC-20101158
† e.casarejos@uvigo.es

Test of Integration of CALIFA into R3B*

T. Le Bleis[1], M. Bendel[1], R. Gernhäuser[1], J. Hoffmann[2], H.T. Johansson[3], N. Kurz[2], I. Lazarus[4], H. Simon[2], M. Winkel[1], and the R^{3}B-CALIFA Collaboration[2]

[1]E12, Physik-Department, Technische Universität München, Garching bei München, Germany; [2]GSI Helmholtzzentrum für Schwerionenforschung GmbH, Darmstadt, Germany; [3]Chalmers University of Technology, Göteborg, Sweden; [4]Sci. Tech. Daresbury, Daresbury, UK

CALIFA [1] is the γ-ray and large-angle high-energy particle detector for the R^{3}B setup at FAIR. Due to the physics requirements, CALIFA is composed of two pieces: a barrel that surrounds the beam axis and an end cap that closes the barrel in the forward direction. The barrel is composed of 1952 long CsI crystals connected to APDs.

The signals from the APDs are preamplified using Mesytec MPRB-16 with the differential output directly connected to FEBEX3 boards [2], developed at GSI, which host a 50 MHz, 14 bit fast sampling ADC per channel and a Lattice LFE3-150 FPGA where the pulse shape is analysed to determine the energy of the detected particle and its identity. Each FEBEX3 can analyse up to 16 channels and is located in a specially designed PCIe crate. Using the GOSIP protocol on optical fibres, and a minimum set of cables, data are collected on a PC.

Detector Triggers

Currently, the LAND setup in Cave C is fully based on MBS [3]. Each branch is equipped with a processor and a GSI-TRIVA trigger module, which guarantees a fully synchronous trigger and read-out. The triggers from different detectors are collected into a single GSI-VULOM module, whose firmware performs different logic for event and calibration trigger generation [4]. Through a long copper-based trigger bus, trigger and dead-time information is distributed between the master system and all slaves. It was observed during the 2012 experiments that signal integrity of the trigger bus constrains the size of the system.

R^{3}B at FAIR will be composed of larger systems (e.g. NeuLAND, recoil tracker and CALIFA), which due to high granularity, can accept a much higher event rate, and hence trigger rate (e.g. CALIFA could produce triggers and record data in the range of 2.5–35 kHz[1]). However, increased detector segmentation creates difficulties for the trigger logic, when based on simple combinations of an increasing number of channels. The validity of the selected events will reduce as the rate of the noise triggers increase. In order to keep reasonable event triggers, more advanced logic has to be applied at the detector level to reduce the background rate as early as possible. E.g. a local trigger connection between CALIFA and the recoil tracker is planned in order to reject very high rate of background from the delta electron hits in the R^{3}B Recoil Tracker based on fast ($\approx$1 μs) indication of proton detection in CALIFA.

* Work supported by BMBF(06MT9156) and DFG (EXC153).

[1] Depending on the reccording mode.

R^{3}B Setup Integration

The aim is that at the time of running at FAIR, the systems either include an interface to the BuTiS [5], called White Rabbit [6], or be able to handle the corresponding protocol. That way, some systems can be integrated in the master dead-time domain of the setup, while others are synchronised by an exchange of triggers and/or timing signals. Development for the White Rabbit has been launched and first tests are planned with detector demonstrators in 2014.

In a first step, intermediate solutions are developed, that allow integration of relatively different systems, based on event- and time-stamping [7, 8]. Two implentations of those concepts have been tested in Nov. 2012 during the S406 experiment. Some prototypes of CALIFA were synchronised using event tags generated by a VULOM in the LAND setup. The trigger signal, a trigger counter and a clock were received by the CALIFA electronic. This allowed a post-acquisition synchronisation, even for systems running different acquisition protocols (e.g. different MBS version, MBS and TRB).

Another protocol based on time stamping, originally developed to synchronise detectors located at the S2 position of the FRS, was also used during the S406 experiment for other detectors located in Cave C. Here, a serial protocol, which uses only one line for the transmission, allows additional systems to have a comparable time marking of the event as the master system. The synchronisation message is sent every 80 μs with a precision of 20 ns. The time between the synchronisation words can be used, to send some auxillary information, e.g. calibration triggers.

References

[1] CALIFA Collaboration, "Technical Design Report for the CALIFA Barrel.", November 2011.

[2] J. Hoffmann *et al.*, "New TASCA Data Acquisition Hardware Development for the Search of Element 119 and 120", GSI Scientific Report 2011, p. 253.

[3] H.G. Essel and N. Kurz, "The general purpose data acquisition system MBS", IEEE TNS Vol.47 No.2 (2000) p. 337.

[4] H.T. Johansson et al., GSI Scientific Report 2010, p231.

[5] P. Moritz and B. Zipfel, GSI Scientific Report 2011, p. 478.

[6] J. Serrano *et al.*, "The White Rabbit Project", Int. Conf. on Accelerator and Large Experimental Physics Control System, October 2009.

[7] E.S. Paul *et al.*, Physical Review C Vol 51 No.1 (1995) p. 78.

[8] J. Hoffmann and N. Kurz GSI Scientific Report 2002, p. 224.

Position-Sensitive Si Detectors for In-Beam Tracking at the R^{3}B Setup*

S. Paschalis[1], T. Aumann[1,2], J. Gronefeld[1], M. Heine[1], M. Holl[1], A. Ignatov[1], O. Kiselev[2], M. Patrizio[1], M. Petri[1], H. Scheit[1], F. Schindler[1], H. Simon[2], I. Syndikus[1], and the R^{3}B collaboration

[1]TU Darmstadt, Germany; [2]GSI, Darmstadt, Germany

An effective way for accessing the most rare and short-lived isotopes is to produce them via fragmentation of a high-energy primary beam on a thick reaction target and consequently separate the fragments to select the ions of interest. The separation is obtained using a fragment separator consisting of magnetic multipole elements. The resulting secondary beam is typically a cocktail beam of various isotopes which often have a large momentum spread. Several diagnostic tools along the beam line are necessary to identify the isotopes of interest and measure their momenta. These detector tools need to be as precise as possible, but with minimum material so that they do not introduce further spread in the ions' momenta. The possible near-target in-beam tracking detectors for the R^{3}B setup at GSI constitute an active area of research and development within the collaboration. We present here the status of such investigations regarding position-sensitive Si detectors.

For most experiments in the R^{3}B setup it is necessary to know the incoming and outgoing angles of the ions (to and from the target) with a resolution better than 1 mrad. In addition, a precise charge identification before and after the target is essential. In the past decade we have successfully used for simultaneous charge and position measurements a set of three 2-D position-sensitive Si detectors [1] of 300 μm thickness and with an active area of 4.5 x 4.5 cm^2 (two before and one after the target and before the magnet).

However, during this time we have also identified some limitations of the particular detector type, which become more prominent considering the new possibilities offered by the new superconducting magnet to be used in the setup in the near future. Namely these limitations are: 1) their rate capabilities are limited to few tens of kHz, 2) their thickness introduces an angular straggling which in most cases dominates the position resolution of the detector, 3) the size of the detector after the target is limiting the acceptance of the outgoing fragments.

In a recent 2012 experiment we have replaced these detectors with thinner and larger (6.3 x 6.3 cm^2) 2-D position-sensitive Si detectors [2] in order to minimize the latter two limitations. In particular we have replaced the two detectors before the target with 200 μm thick detectors and the one between the target and the magnet with a 100 μm thick detector. The results and a comparison with the older detector type are summarized in Table 1. From these results it is clear that although we gain in angular straggling and coverage we obtain worse performance for the larger and thinner detectors. This is attributed to the smaller energy loss and the larger capacitance of these detectors. Furthermore the rate limitation is still present and in the face of the more intense beams delivered by the FAIR facility this is an important drawback that needs to be addressed.

Table 1: The main characteristics (active area (a.a.), thickness (d)) and the performance (charge resolution (δZ/Z) and position resolution (δx) in σ values) are shown for the different types of position-sensitive Si detectors. The results were obtained using a ^{136}Xe beam at $\sim$500 MeV/A. The last lines present results calculated with ATIMA for the angular straggling (a.s.) and energy straggling (e.s.) divided by energy loss (e.l.). The measured charge resolution is limited by the energy straggling.

	Hamamatsu S5378	Micron TL63-200	Micron TL63-100
a.a. [cm^2]	4.5 x 4.5	6.3 x 6.3	6.3 x 6.3
d [μm]	$\sim$300	$\sim$200	$\sim$100
δZ/Z [%]	0.6	0.8	1.1
δx [μm]	100	150	350
a.s. [mrad]	0.4	0.33	0.23
e.s./e.l.[%]	1.3	1.6	2.3

We are currently exploring different Si detector types such as microstrip detectors and position sensitive strip detectors to be used instead of the 2-D position sensitive Si detectors. One of the obvious advantages of strip detectors is that the total beam rate is shared between the strips enabling overall higher-rate capabilities. At the same time the capacitance is smaller and the signal to noise ratio is expected to improve. In the microstrip detectors the position is reconstructed from the strip that "fired". In the resistive strip type detector, one (or both) sides of the detector is divided into resistive strips of about 1–2 mm wide and the position along the strip is determined through the charge division measured at the two ends. The position reconstruction is one dimensional minimizing the non-linearities observed from the 2-D position sensitive Si detector and simplifying the position dependency of the total energy. The size of such detectors can reach an active area of 10 x 10 cm^2, which should suffice our needs for acceptance, and their thickness can be as low as 100 – 150 μm.

References

[1] T.Yanagimachi *et al.*, NIM **A275** (1989) 307.

[2] A.Banu *et al.*, NIM **A593** (2008) 399.

*Work supported by BMBF (06DA7047I), by GSI via the GSI-TU Darmstadt cooperation contract and by HIC for FAIR.

Development of a Thin Large-Area Fiber Detector for Radioactive-Beam Experiments*

P. Schrock†[1], *T. Aumann*[1], *H. Scheit*[1], *H. Simon*[2], *and the R*^{3}*B Collaboration*
[1]TU Darmstadt, Darmstadt, Germany; [2]GSI, Darmstadt, Germany

The R^{3}B setup at FAIR will allow kinematically complete measurements in order to study various astrophysical and nuclear structure questions. For the identification of beamlike particles their mass number A is determined from the deflection of the beam in a magnetic field B which follows the relation $B\rho \propto A/Z$. To calculate the radius ρ of the trajectories in the magnetic field the position of the particles need to be measured at various positions. To achieve an adequate mass resolution a new fiber detector for tracking of heavy fragments has been designed and tested during several experiments.

The detector is built of 1024 scintillating optical fibers, each with a width of 250 μm plus 30 μm optical cladding. All individual fibers are read out separately. The needed 1024 electronic channels are realized by using four 16×16 multianode position sensitive photomultiplier tubes [1] and NXYTER (neutron-X-Y-time-energy read-out) chips [2]. The NXYTER is a self-triggered ASIC with 128 independent channels which buffer charge and time information for each hit in each fiber. It is included in the triggered R^{3}B-LAND setup by using Gemex front-end boards [3]. Two variants of Gemex were in use: original boards with a switched power supply and modified versions with linear regulators.
The noise level and baseline position of the NXYTER signals are highly temperature dependent. So, special attention to the cooling is required, especially if the detector is used in vacuum.

In the s415 experiment (Pb at 500 AMeV) one unmodified Gemex and a modified one were used in parallel. Example energy spectra of the signals produced by the beam are shown in Fig. 1. It can be seen that the modified variant provides under the given experimental conditions a much better energy resolution. Both versions can be used for tracking since the signals can be distinguished from the intrinsic noise of the detector. (Note: The ADC produces inverse spectra, i. e. the noise is supposed to be between channel 2000 and 2500, but in these cases it was cut via NXYTER slow control.)

During the s412 experiment (Sn at 300 to 600 AMeV) the detector was used with unmodified Gemex boards. Fig. 2 shows the position correlation between the new fiber detector and an old one being located around 2.7 m and 12 m after the center of the magnetic field, respectively. A clear correlation is visible. The gaps stem from a not working connector at one PMT.

* Work supported by HIC for FAIR, NAVI, GSI - TU Darmstadt Cooperation, HGS-HIRe and the BMBF project 06DA7047I.
† P.Schrock@gsi.de

For the future work the missing channels have to be recovered in order to get a complete spatial coverage. All Gemex boards will be modified to linear regulated power supply.

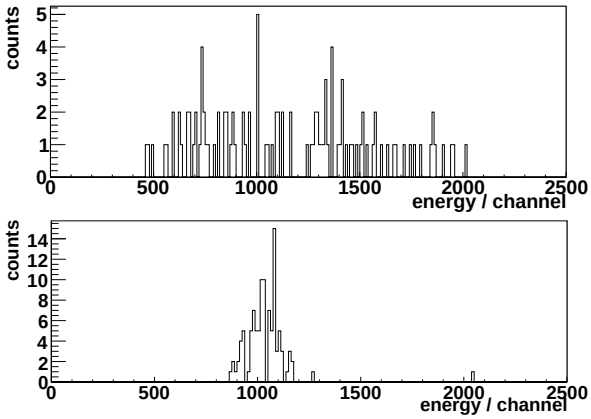

Figure 1: Shown are two examples of energy spectra. The upper and lower panel show one NXYTER channel from an unmodified and a modified Gemex board, respectively. Both spectra were recorded at the same time and stem from the same beam.

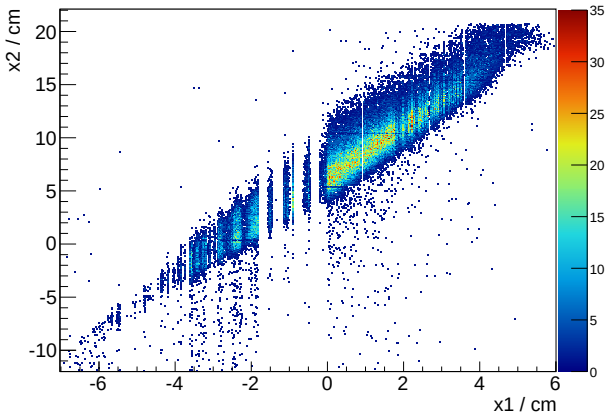

Figure 2: Position correlation of the new fiber detector (x1) and an other tracking detector (x2).

References

[1] http://sales.hamamatsu.com/assets/pdf/parts_H/H9500.pdf
[2] A.S. Brogna et al., NIMA 568 (2006) 301
[3] B. Voss et al., GSI Scientific report 2011, p. 247

Results from the SOFIA/ANDES TwinMUSIC

B. Voss for the SOFIA / ANDES-collaboration

GSI, Darmstadt, Germany.

Experimental aim, Setup

After commissioning of the detectors in parasitic test beam times in 2011/2012 physics runs addressing questions from both, SOFIA [1] and ANDES [2] were performed in August / September 2012 at CaveC / ALADIN@GSI.

An overview of the experimental setup and conditions leading to the production of the secondary beams is given in [3-6] together with the design of the TwinMUSIC detector employed to determine the nuclear charges and positions of fission fragments produced by coulomb excitation.

Results

Secondary and primary beams of various actinides ^{200}Ra, ^{202}Rn, ^{209}Ra, ^{217}Ac, ^{222}Th, ^{226}Th, ^{230}Th, ^{236}U, ^{238}U, ^{238}Np with energies of 700 AMeV to 950 AMeV and primary rates of several 10^5 particles/second over spill durations of 5s -10s were impinging on a set of foils of 2x 600 µm thick depleted Uranium (0.2% enrichment, 11.50 mg/cm^2) plus 1x 125 µm thick Lead (1.413 mg/cm^2) in the active target.

A charge-separation power of $\Delta Z/Z \approx 1.5\%$ - 2.4% for the TwinMUSIC has been achieved for (fission) fragments in the range of {30,60}. The respective spectra are shown in Fig. 1 and 2.

At the same time a spatial resolution of 60-80µm (FWHM) for single anodes was obtained from the drift in horizontal direction for the detector gases P25 and Ne/CO_2/CF_4/N_2 in use. This value is only slightly varying with the anode positions in in-beam direction.

Outlook

The still ongoing analysis is aiming for a refinement of the results obtained. Nevertheless already now it can be stated that the current concept of the SOFIA TwinMUSIC system will serve as a frame of reference for the R&D towards a modern energy-loss measurement device for the Super-FRS@FAIR. Here a detector system is required to work in transmission mode with an as low as possible material budget with respect to its active volume, providing excellent energy and spatial resolution for particles ranging from Protons up to Uranium impinging with high-rates of up to 10 MHz.

A compact detector setup and dedicated readout electronics coping with these needs are currently under development.

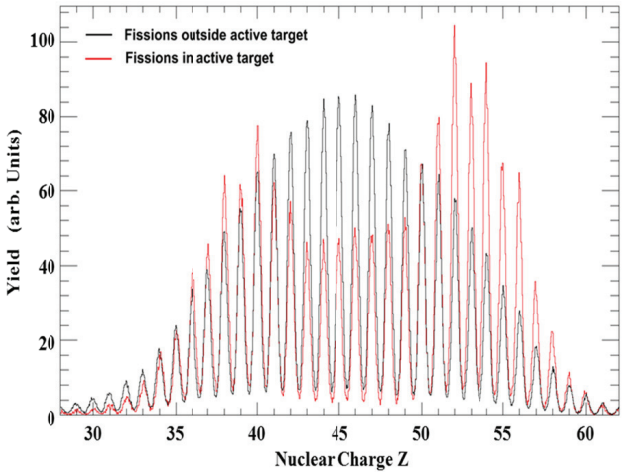

Figure 1: Charge distribution for light fragments emerging from fission inside (red) and outside (black) the active target as determined by the TwinMUSIC.

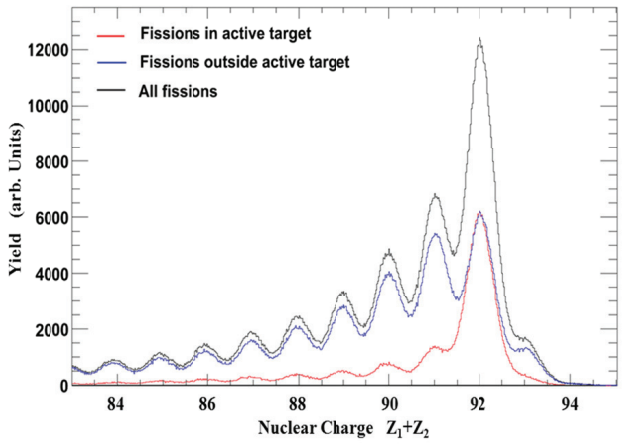

Figure 2: Charge distribution for the sum of fragments emerging from fission inside (red) and outside (black) the active target as determined by the TwinMUSIC.

References

[1] J. Taieb et al., Int. J. Mod. Phys. E 18 (2009) 767-772.
[2] http://www.andes-nd.eu
[3] K.-H. Schmidt et al., NPA 665 (2000) 221.
[4] B. Voss et al., GSI Scientific Report 2010, GSI Report 2011-1, 2011, p.223.
[5] B. Voss et al., Proceedings of the IEEE Nuclear Science Symposium, Medical Imaging Conference 2011, 2011, Valencia, Spain
[6] B. Voss et al., GSI Scientific Report 2011, GSI Report 2012-1, 2012, p.184-186.

R3BRoot: a FAIRRoot-based development for the analysis and simulation of the R^{3}B experiment*

H. Alvarez-Pol[1], M. Al-Turany[2], D. Bertini[2] and D. Kresan[2] for the R^{3}B collaboration

[1]Departamento de Física de Partículas, Santiago de Compostela, Spain; [2]GSI, Darmstadt, Germany

R3BRoot is the simulation tool for the R3B and LAND/ALADIN setup [1]. It inherits most of the behaviour from the FAIRRoot framework [2], a ROOT-based development for the simulation and data analysis developed at GSI for the analysis of the future FAIR experiments.

The framework delivers base classes which enable the users to construct their detectors and derive simulation and analysis tasks in a simple way. It also supplies some general functionality like track visualization, database support, event structure and persistency tools (binary ROOT files), and the full mathematical, histogramming and advance analysis machinery contained in the ROOT classes. As a data-analysis tool, R3BRoot allows an event-by-event based analysis, from the unpacking and basic calibration to the final processing of the combined physics observables, following a set of succesive tasks, ruled by user-friendly macros. As a simulation tool, R3BRoot supports Geant3 and Geant4 transport engines, interfacing with their geometry constructors.

R3BRoot features a complete description of the LAND/ALADIN setup detectors, including their basic response to the particle interaction and digitization and event generators for several reactions of interest, including QFS, spectroscopic decays, … The ALADIN magnet field map is included (as an interpolated value based on field-map measurements), as well as the design value of the future GLAD magnet. The user can switch between the two arrangements by a simple setup selection in the configuration macros, mixing of any kind of non-overlaping detectors.

Calibration and digitization parameters, geometry elements of detectors and other parameters are stored in a runtime database supporting different input/output methods, including Ascii, ROOT binary format and several available databases using SQL lenguage. The runtime database supports per-run parameter evolution (different level of analysis, evolution in the detector definition, …) in a multidimensional scheme. Different parameter tables has been already implemented for evaluation.

R3BRoot has been intensely employed during the design phase of the main R3B detectors, and along the evaluation of their characteristics performed during the redaction of the corresponding TDRs of the CALIFA Barrel [3] and NeuLAND [4], recently approved. Advanced reconstruction algorithms have been developed from both detectors, using this environment.

An important endeavor to expand the R3BRoot functionality to the analysis of the present and future data is ongoing, allowing the realization of the analysis and simulation under the same platform; the benefits of these aproach include the evaluation of the geometrical efficiencies and other systematical uncertainties under the same platform in a coherent process.

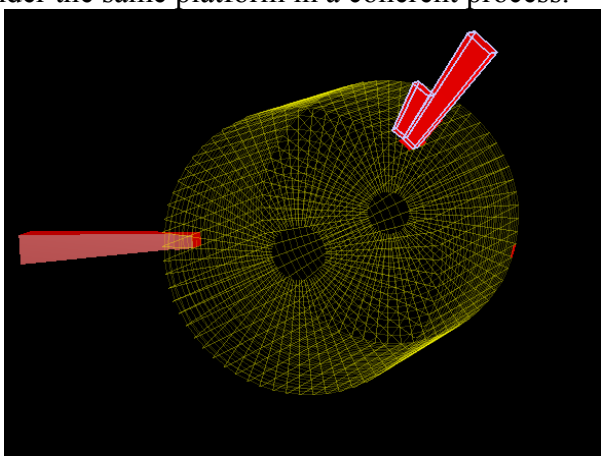

Figure 1: EVE event and hit finder outcome visualization for the CALIFA BARREL.

References

[1] FAIRRoot, http://fairroot.gsi.de/

[2] R3BRoot instalation instructions and repository, http://fairroot.gsi.de/?q=node/11

[3] D. Cortina *et al*., "The R3B CALIFA Barrel design" in this annual report.

[4] D. Boretzky *et al*., "NeuLAND@R3B - A Progress Report" in this annual report.

FRS Ion Catcher: A Test Facility for the LEB of the Super-FRS*

T. Dickel[1,2], W. R. Plaß[1,2], S. Ayet[2], P. Dendooven[3], J. Ebert[1], H. Geissel[1,2], F. Greiner[1], E. Haettner[1,2], C. Jesch[1], N. Kalantar-Nayestanaki[3], R. Knöbel[1,2], J. Lang[1], I. Moore[4], C. Nociforo[2], M. Petrick[1], S. Pietri[2], A. Prochazka[2], S. Purushothaman[2], M. P. Reiter[1], A.-K. Rink[1], C. Scheidenberger[1,2], H. Weick[2], J. S. Winfield[2], and M. I. Yavor[5]

[1]Justus-Liebig-University, Gießen, Germany; [2]GSI, Darmstadt, Germany; [3]KVI, University of Groningen, Netherlands; [4]University of Jyväskylä, Finland; [5]Institute for Analytical Instrumentation, St. Petersburg, Russia

The FRS Ion Catcher experiment consists of three main parts, (i) the FRS, (ii) a cryogenic gas filled stopping cell (CSC) [1] and (iii) the multiple-reflection time-of-flight mass spectrometer (MR-TOF-MS) [2]. The exotic nuclei are separated and energy-bunched in the FRS, stopped and thermalized in the CSC and transported in an RFQ beamline to the MR-TOF-MS, which allows for diagnosis and monitoring of the extracted beam, for accurate mass measurements and for isobar separation. The FRS Ion Catcher is an ideal test facility for the LEB of the SuperFRS, as it provides a complete system for the stopping, thermalization, fast extraction, diagnostics, beam preparation, isobar separation, and mass measurement of very short-lived nuclei produced by projectile fission or fragmentation.

The system was successfully commissioned in online experiments in October 2011 and July/August 2012 (Fig. 1) [3, 4]. The stopping and extraction efficiency of the CSC has been measured to be 12% for ^{223}Th. The extraction time of the gas cell, measured with ^{221}Ac (half-life: 52ms), is 24 ms [3]. Also, a first mass measurement with the MR-TOF-MS has been performed using the heavy, short-lived ^{213}Rn (half-life: 20ms) ions [4].

After the first beam time, the cooling of the CSC was changed from LN_2 to cold He provided by a cryocooler-based cooling system. This has the advantage that temperatures as low as 50 K can be achieved and that continuous operation of the system with less user interaction is possible. The CSC has been equipped with a laser ablation ion source, providing the system with an additional offline capability for investigating the performance of the system over a wide mass range, moreover the ion source delivers calibrants for accurate mass measurements.

As part of the FRS Ion Catcher a new detector (alpha tagger) for the FRS has been set up. It comprises a Double-sided Silicon Strip Detector (DSSD) in a vacuum chamber that can be moved in and out of the beam directly in front of the CSC. The ions are implanted in the DSSD and their position, decay energy and decay time are measured. These data are linked to the standard FRS data acquisition. Nuclei can thereby be identified by the energy and life time of their alpha decay offering a fast and efficient way of ensuring that the ion of interest is transmitted to the CSC.

As next steps, the stopping efficiency of the CSC will be doubled. This is possible because at the moment the limitation of the stopping gas density is the pumping speed in the beamline downstream of the CSC. This has recently been improved by more than a factor of 2 due to new turbo pumps. The mass resolving power of the MR-TOF-MS will be further increased by temperature stabilization of the most crucial electronics.

References

[1] M. Ranjan et al., Eur. Phys. Lett. 96 (2011) 52001.

[2] W.R. Plaß et al., Nucl. Instrum. Methods B 266 (2008) 4560.

[3] M. P. Reiter et al., this volume

[4] J. Ebert et al., this volume

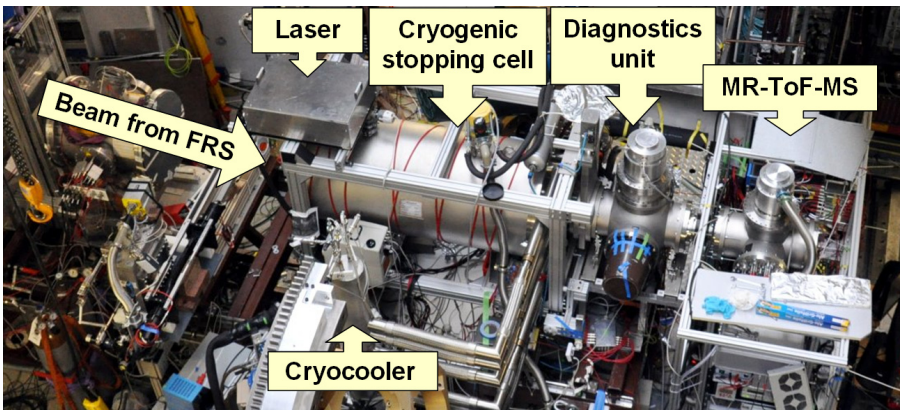

Figure 1: The FRS Ion Catcher at the final focal plane of the FRS during the beamtime in summer 2012.

* This work was supported by the BMBF under contracts no. 06GI9114I and 05P12RGFN8.

First EXL Experiment with Radioactive Beam: Proton Scattering on ^{56}Ni*

M. von Schmid[1], S. Bagchi[2], S. Bönig[1], M. Csatlós[3], I. Dillmann[4], C. Dimopoulou[4], P. Egelhof[4], V. Eremin[5], H. Geissel[4], R. Gernhäuser[6], M.N. Harakeh[2], A.-L. Hartig[1], S. Ilieva[1], N. Kalantar-Nayestanaki[2], O. Kiselev[4], H. Kollmus[4], C. Kozhuharov[4], A. Krasznahorkay[3], T. Kröll[1], M. Kuilman[2], S. Litvinov[4], Yu.A. Litvinov[4], M. Mahjour-Shafiei[2], M. Mutterer[4], D. Nagae[8], M.A. Najafi[2], C. Nociforo[4], F. Nolden[4], U. Popp[4], C. Rigollet[2], S. Roy[2], C. Scheidenberger[4], M. Steck[4], B. Streicher[2,4], L. Stuhl[3], M. Takechi[4], M. Thürauf[4], T. Uesaka[9], H. Weick[4], J.S. Winfield[4], D. Winters[4], P.J. Woods[10], T. Yamaguchi[11], K. Yue[4,7], J.C. Zamora[1], and J. Zenihiro[9]

[1]IKP, TU Darmstadt; [2]KVI, Groningen; [3]Atomki, Debrecen; [4]GSI, Darmstadt; [5]PTI, St. Petersburg; [6]TU München; [7]IMP, Lanzhou; [8]University of Tsukuba; [9]RIKEN, Tokio; [10]University of Edinburgh; [11]Saitama University

EXL (**EX**otic nuclei studied in **L**ight-ion induced reactions at the NESR storage ring) is a project within NUSTAR at FAIR. The nuclear structure will be probed with direct reactions in inverse kinematics. One of the key interests of EXL is the investigation of reactions at very low momentum transfer where, for example, the nuclear matter distribution, giant monopole resonances or Gamow-Teller transitions can be studied [1].

The existing storage ring ESR at GSI, together with its internal gas-jet target, provides a unique opportunity to perform this kind of experiments on a smaller scale already. In autumn of 2012, we successfully performed an experiment (E105) with stable ^{58}Ni as well as radioactive ^{56}Ni beams interacting with H_2 and ^{4}He targets. The main goal was the investigation of the reaction ^{56}Ni(p,p)^{56}Ni at 400 MeV/u in order to measure the differential cross section for elastic proton scattering and deduce the nuclear matter distribution of ^{56}Ni. The experiment was the first of its kind and represents an essential milestone towards the realization of the EXL project.

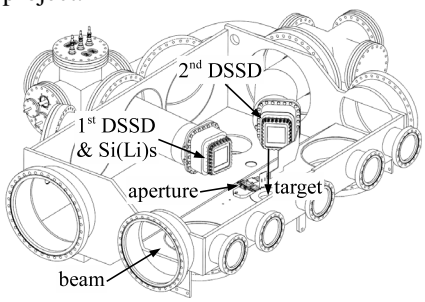

Figure 1: Schematic drawing of the EXL setup at the ESR.

In the last years we have developed a UHV compatible detector setup mainly based on DSSDs (**D**ouble-sided **S**ilicon-**S**trip **D**etector) for the target-like recoils [2]. Here, the DSSDs act as active windows separating the UHV from an auxiliary vacuum where non-bakeable components can be placed. In this way, additional dead layers are avoided and a low energy-threshold is maintained. Figure 1 shows a schematic drawing of the setup around the gas-jet target of the ESR. The two DSSDs have an active area of (6×6) cm^2 each and are divided into 128×64 strips. The first detector close to 90° is set up as a telescope of one DSSD and two 6.5 mm thick Si(Li) detectors placed in the auxiliary vacuum. During bake-out of the ESR and during the experiment the Si(Li)s were actively cooled. To reach the necessary angular resolution a remotely moveable aperture with two motors operated inside the UHV was placed in front of the extended target. Not shown is a detection system for the projectile-like heavy ions further downstream of the target. It features an array of six silicon PIN-diodes directly facing the UHV. Furthermore, a SSD was used in a vacuum pocket for the same purpose. To investigate the conditions for the detection of neutrons and gammas we utilized ELENS (**E**uropean **L**ow **E**nergy **N**eutron **S**pectrometer) and a CsI detector placed outside the vacuum chamber.

Figure 2 shows a preliminary 2-dimensional plot of the reconstructed energy of the recoiling protons as function of laboratory scattering angle measured by the detector telescope close to 90°. The kinematical lines for both elastic and inelastic scattering are nicely separated and clearly visible. The data analysis is currently in progress.

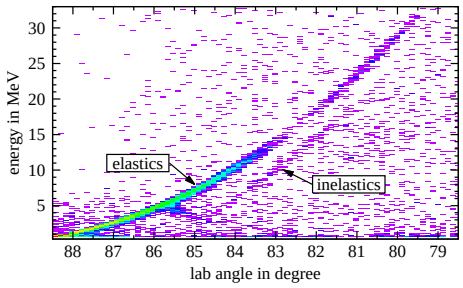

Figure 2: Reconstructed energy vs. angle of recoil protons for ^{56}Ni(p,p)^{56}Ni and ^{56}Ni(p,p')^{56}Ni* reactions.

After this successful experiment, an upgraded detector setup covering a substantially larger solid angle is envisioned to be implemented for further reaction experiments at the ESR.

References

[1] H.H. Gutbrod et al. (Eds.), FAIR Baseline Technical Report, ISBN-3-9811298-0-6, Nov. 2006

[2] B. Streicher et al., Nucl. Instr. and Meth. A 654 (2011) 604.

*Work supported by BMBF (06DA9040I and 05P12RDFN8) and HIC for FAIR.

A new Detector Testbed for future FAIR based Slowed Down Beam Setups at the Cologne FN-Tandem Accelerator Facility

M. Pfeiffer[*1], *M. Cappellazzo*[1], *E. Gregor*[2], *P. Boutachkov*[2], *G. Pascovici*[1], *S. Thiel*[1], *N. Warr*[1], *and J. Jolie*[1]

[1]Institut für Kernphysik, Universität zu Köln, Germany; [2]GSI, Darmstadt, Germany

At the new FAIR facility one will have the unique opportunity to slow down relativistic, highly exotic nuclei being produced by the SuperFRS to energies of about $5 - 10\mathrm{MeV/u}$ [1]. Thus a complete new field of research will become available. The major problem will be the creation of secondary fragments, spatial straggling and energy straggling. In order to maintain acceptable statistics for the desired nuclear reaction channels, one is in need of highly reliable and efficient auxiliary detectors.

Such detectors, not only for slowed down beams but experimental setups with SuperFRS beams in general, are under development within the NUSTAR collaboration. Since beamtime at most large research centers is very sparse, it is not easy for them to provide beamtime for basic detector tests. In addition, one is in need of a well defined, known beam for such basic tests. These conditions can be delivered at the Cologne FN-Tandem accelerator, where a dedicated beamline is being set up. First measurements have already been performed.

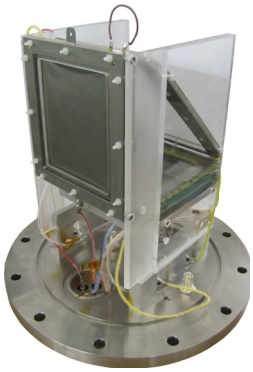

Figure 1: Single unit of the improved beam profile monitor / time of flight detector. Two successive units mounted in ISO 200 parts form the entire detector (as seen in figure 2).

The beamline is equipped with a variety of slits and ion optical lenses to form various kinds of beam spots. One major feature is an electrostatical sweeper to steer the beam over a large area. The beam currents of the many available stable ion beams being delivered by the $10\mathrm{MV}$ Tandem accelerator vary from $< 1\mathrm{pA}$ to several $10^1\mathrm{mA}$. A second feature of the beamline is an improved, highly transparent beam profile monitor (BPM) with integrated time of flight (ToF) measurements on an event by event basis, as seen in figure 1. Its spatial resolution is in the order of few millimeters and its timing resolution is roughly $200\mathrm{ps}$ [2, 3].

* pfeiffer@ikp.uni-koeln.de

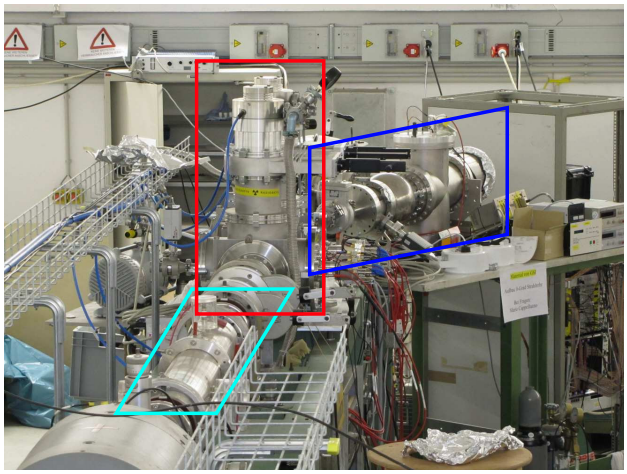

Figure 2: Picture of the cooled DSSSD preamplifier test at the new Cologne testbed. Framed in light blue one can see the electrostatic steerer, in red the highly transparent beam profile / time of flight detector and in blue the GSI testchamber mounted at 20° after a scattering chamber.

Afterwards a large ($\approx 60 \cdot 40 \cdot 40\mathrm{cm}^3$) vacuum chamber with an aligned optical bench and various feedthroughs is going to be mounted as major testbed. More specialised chambers might be used, as well.

Together with the ion optics and the BPM/ToF system this setup will give a unique opportunity to perform realistic tests of FAIR/SuperFRS based auxiliary detectors for future slowed down beams. A first test has been done with improved, GSI developed preamplifiers [4] in combination with a cooling frame and a $40\mu\mathrm{m}$ DSSSD. In this setup a scattering target was used and the detector was mounted at 20° with respect to the beam axis, as seen in picture 2. Future test experiments aim at an improvement of wide beam plunger measurements, as already being performed in a fast beam setup at GSI-FRS [5]. Work supported by F & E project KJOLIE1012.

References

[1] F. Naqvi et al, Acta Physica Polonica B (2011), Vol. 42, p. 725

[2] M. Pfeiffer et al, GSI SciRep 2011 (2012), No. 1, p. 172

[3] M. Pfeiffer et al, GSI SciRep 2010 (2011), No. 1, p. 136

[4] P. Boutachkov et al, GSI SciRep 2009 (2010), No. 1, p. 31

[5] M. Hackstein et al, GSI SciRep 2011 (2012), No. 1, p. 154

Mass measurement by track reconstruction with the LEB spectrometer

J.S. Winfield[*1], *H. Geissel*[1,2], *D. Ackermann*[1], *C. Nociforo*[1], *H. Weick*[1], *M. Winkler*[1], *and M.I. Yavor*[3]
[1]GSI, Darmstadt, Germany; [2]JLU, Giessen, Germany; [3]RAS, St. Petersburg, Russia

The large-acceptance spectrometer in the LEB cave will be used for experiments with intermediate or low energy radioactive beams from the Super-FRS. Gamma and charged-particle spectroscopy will be performed around a typically low-mass secondary target. Forward-focussed fragments are transported to the spectrometer's focal plane, where they are identified or "tagged" to complete the reaction analysis. The large beam emittance at the target means that event-by-event tracking is essential (position, angle, time-of-flight as well as the magnetic rigidity in the Super-FRS).

The simulations discussed here involve fragments in the mass 200 region, which are assumed to come from reactions at about 180 MeV/u. The goal is to resolve the different neighbouring-mass isotopes.

The Monte Carlo program MOCADI [1] was used for the simulations in which the secondary beam starts from the end focal plane of the Super-FRS. The secondary reaction target is a 500 mg/cm^2 beryllium foil, followed by a $300\ \mu m$ silicon double-sided strip detector (DSSD, P2) for the beam spot correction and a 1-mm thick plastic scintillator. A TPC tracking detector P1, is located 0.5 m before the target. P1 and P2 would be used to correct the fragment angle during the data analysis. However, only the uncorrected angle is needed for the mass reconstruction. This is obtained event-by-event from P2 and P3, another position detector 30 cm downstream from the target

The Lund-York-Cologne calorimeter LYCCA [2] is used for the measurements at the focal plane. This consists of a 2-mm thick plastic (stop ToF), a 0.3-mm Si DSSD ($\Delta E, x, y$: P4) and a 2.5-cm CsI(Tl) crystal (E_{res}).The achieved resolutions during the commissioning of Pre-SPEC [3] are $\sigma_x, \sigma_y = 0.5$ mm, $\Delta Z = 1/100$, $\Delta E = 1/100$ and ToF = 27 ps.

The following reconstruction equations are used:

- δ is calculated from

$$\delta = [x_f - \mathrm{R}_{11}x_i - \mathrm{R}_{12}a_i]/\mathrm{R}_{16}. \qquad (1)$$

  where x_i is taken from P2, a_i is calculated from P2 and P3, and x_f is taken from P4.

- The corrected $B\rho$ is calculated as $B\rho_n = B\rho_0(1+\delta)$, where $B\rho_0$ is the magnetic rigidity of the reference particle, ^{201}Pt^{78+}, before the spectrometer.

- The path length of the reference particle is corrected for the initial coordinates by

$$l_n = l_0 + \mathrm{R}_{51}x_i + \mathrm{R}_{52}a_i + \mathrm{R}_{56}\delta$$

  where the subscript 5 is the length parameter.

- β is calculated from the corrected path length:

$$\beta = l_n/c(t_2 - t_1)$$

- Finally, the mass A divided by charge Q is:

$$\frac{A}{Q} = \frac{B\rho_n}{\gamma\beta}\frac{c}{m_u} \qquad (2)$$

  where m_u = 931.494061 MeV/c^2.

A similar reconstruction scheme is made at BigRIPS [4]. The exact matrix elements are known from the ion-optics, but rather than putting these back into the equations, "empirical" first order matrix elements are used from a simulated test experiment with a well-focused primary beam. As seen in the cross-hatched peak for ^{201}Pt in Fig. 1, one

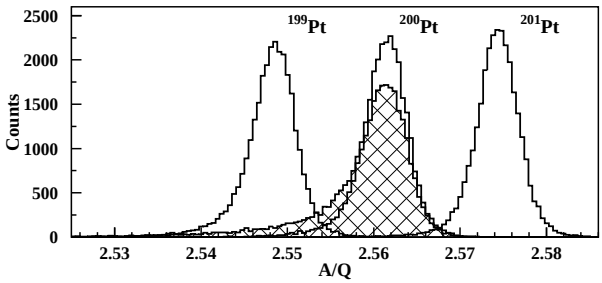

Figure 1: Simulated mass reconstruction for $A \sim 200$. Cross-hatched histogram is for 1^{st}-order matrix elements only. The finite resolution of the detectors is included.

could obtain reasonably resolved masses up to $A \sim 200$; however, there is a tail on the peak at the low A/Q side. The resolution can be improved by the inclusion of selected 2^{nd} and 3^{rd} order matrix elements, with appropriate modification of Eq. (1). Following the procedure used at BigRIPS, the Newton-Raphson iterative method is used to solve for delta. There is a clear improvement in the shape and width of the (unshaded) peaks of of Fig. 1 compared with the 1^{st}-order calculation. The FWHM of the ^{201}Pt peak corresponds to 0.53 mass units.

References

[1] N. Iwasa et al., Nucl. Instr. Meth. B 126 (1997) 284.

[2] http://www.nuclear.lu.se/english/research/basic-nuclear-physics/nustar/lycca D. Rudolf, Lund Univ., Sweden.

[3] H.J. Wollersheim, Acta Phys. Pol. B 42 (2011) 705.

[4] N. Fukuda, talk at Expert Meeting on In-flight Separators and Related Issues, Dec. 2010, GSI.

* j.winfield@gsi.de

FRS Experiment: Performance of the Cryogenic Stopping Cell for the Low-Energy Branch of the Super-FRS*

M. P. Reiter[1], *T. Dickel*[1,2], *S. Purushothaman*[2], *P. Dendooven*[3], *J. Ebert*[1], *H. Geissel*[1,2], *E. Haettner*[1,2], *C. Jesch*[1], *M. Ranjan*[3], *W. R. Plaß*[1,2], *H. Weick*[2], *F. Amjad*[2], *S. Ayet*[2], *M. Diwisch*[1], *A. Estrade*[2], *F. Farinon*[2], *F. Greiner*[1], *N. Kalantar-Nayestanaki*[3], *R. Knoebel*[1,2], *J. Kurcewicz*[2], *J. Lang*[1], *I. Moore*[4], *I. Mukha*[2], *C. Nociforo*[2], *M. Petrick*[1], *M. Pfutzner*[2], *S. Pietri*[2], *A. Prochazka*[2], *A-K. Rink*[1], *S. Rinta-Antila*[4], *C. Scheidenberger*[1,2], *M. Takechi*[2], *Y. Tanaka*[2], *J. S. Winfield*[2], *and M. I. Yavor*[5]

[1]Justus-Liebig-Universität, Giessen, Germany; [2]GSI, Darmstadt, Germany; [3]KVI, University of Groningen, Netherlands; [4]University of Jyväskylä, Finland; [5]Institut for Analytic Instrumentation, St. Petersburg, Russia

At the Low-Energy Branch [1] of the Super-FRS at FAIR projectile and fission fragments will be produced at relativistic energies, separated in-flight, range-bunched, slowed down and thermalized in a cryogenic stopping cell (CSC) [2], extracted and delivered to precision experiments at MATS and LaSpec.

The CSC consists of a double-walled vacuum vessel. The outer chamber provides the thermal insulation vacuum for the inner cold chamber, which is filled with typically 100 mbar of ultra pure He at cryogenic temperatures (70-100 K). The ions are thermalized in the He and transported by an electric DC field to the extraction side of the CSC. At this side an RF carpet produces a pseudopotential barrier, to keep the ions from hitting the electrodes, and transports them to an extraction nozzle, from which they are injected in to an low-energy RFQ beam line.

In October 2011 and July/August 2012, the CSC and the MR-TOF-MS [3] were commissioned on-line with the FRS [4] at GSI. For the first time, a stopping cell for exotic nuclei was operated on-line at cryogenic temperatures. Using a gas density almost two times higher than ever reached before for a stopping cell with RF ion repelling structures, various projectile fragments were thermalized and extracted with high efficiencies and short extraction times. In the first experiment, the areal density of the helium gas of the CSC amounted to 5 mg/cm^2 He. The range distribution of a 500 Mev/u ^{223}Th beam in the stopping cell (Fig. 1) was measured by varying the Al degrader in front of the cell and determining the ratio of the number of injected and extracted ^{223}Th. From this measurement a stopping efficiency of $(27 \pm 3)\%$ can be caluclated. The total efficiency for stopping, ion survival and extraction amounted to $(12 \pm 2\%)$, resulting in an extraction and survival efficiency of $(43 \pm 9)\%$.

The extraction time of the stopping cell was measured using short ^{221}Ac ion bunches (4 ms). Fig. 2 shows the ^{221}Ac count rate on the silicon detector behind the stopping cell as a function of the time after injection of each ion bunch. After 48 ms the last ^{221}Ac ions are extracted from the cell, giving an extraction time of only 24 ms for ions stopped in the center of the CSC. This measurement agrees well with the offline result of 25 ms obtained with a pulsed ^{223}Ra source and the expectations from mobility theory of 27.5 ms. With this unique combination of high efficiency and short extraction times the CSC is perfectly suited for new studies of projectile and fission fragments.

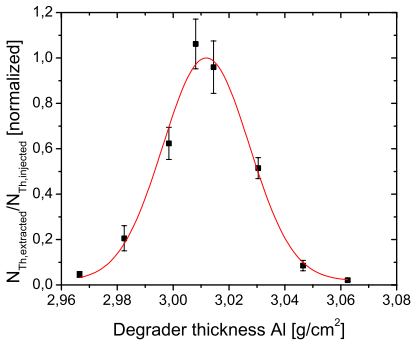

Figure 1: Ratio of the number of injected to extracted ^{223}Th ions of the CSC as a function of the Al degrader in front of the CSC. Note that the ratio has been normalized to unity.

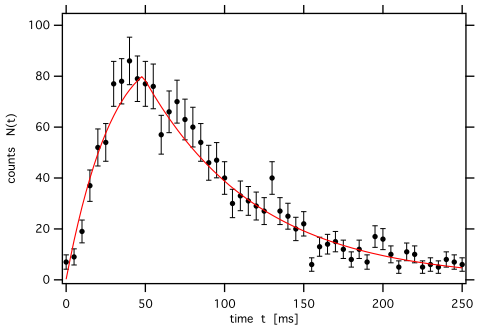

Figure 2: Decay spectra of the α-emitter ^{221}Ac (half life 52 ms) as a function of the time after injection of each ion bunch in the CSC.

References

[1] J.S. Winfield et al., NIM A 704 (2013) 76-83.

[2] M. Ranjan et al., Eur. Phys. Lett. 96 (2011) 52001.

[3] J. Ebert et al., this volume.

[4] T. Dickel et al., this volume.

*Work supported by BMBF under contracts no. 066I9114I and 05P12RGFN8

Isochronicity Correction for Mass Measurements in CR

H. Weick[1], S. Litvinov[1], D. Toprek[2], A. Dolinskii[1]

[1]GSI, Darmstadt, Germany ; [2] VINCA Belgrade, Serbia

Isochronous mass measurements in the CR by the ILIMA collaboration are a part of the initial experimental programme of FAIR. With higher primary beam intensities and higher acceptance of the Super-FRS also the CR in isochronous mode aims at acceptances of 100 mm mrad in vertical and horizontal plane combined with a momentum acceptance of δ= ±0.5%. This is about a factor 500 higher than the acceptance of the present ESR. The sufficient isochronicity to obtain the needed mass resolution of about $\Delta m/m=10^{-6}$ requires a dedicated correction scheme.

Past studies have shown that path length differences, which are described by the first order coefficients of the transfer matrix of the ring system, are easily compensated by having an overall achromatic system. However, for large emittance the 2nd order contributions already become so huge that the goal in Δm/m or acceptance would be far away [1]. Still in an overall bend system with help of symmetric imaging a higher order correction is possible. However, this would violate the stability criteria of non-zero phase advance for a storage ring [2]. As a way out we have found a partial correction. For this time aberrations are divided into contributions with varying size but fixed amplitude and others with increasing absolute sum over many turns. Only the growing contributions need to be corrected as the others will become small in relative time deviation (Δt/t) over many turns.

With the help of symplectic relations [2] we could show that in a 2nd order transfer matrix all quadratic contributions to Δt/t converge to zero with a sextupole correction that corresponds to the well-known chromaticity correction of the tune. In a mirror symmetric ring this requires only two sextupole families for each horizontal and vertical plane. A third independent sextupole is required for shaping the dispersion curve in the arc to provide the proper detour for faster ions to compensate the velocity dependence in 2nd order. The resulting sextupole strengths are well within the present specifications. A fourth sextupole could correct higher order mismatch of dispersion.

Figure1 shows a Monte-Carlo simulation with the MOCADI code [3] for the full acceptance of the CR. With a correction by three or four sextupole families a fast convergence to a low limit in Δt/t is given. This limit corresponds to higher orders of chromaticity. In principal this could also be corrected with octupoles.

In addition the influence of fringe fields and field inhomogeneities was studied. Based on realistic field calculations one can see that extended fringe fields cause a smaller shift in the tunes and lead to larger higher order geometrical time aberrations. Dipole inhomogeneities are very critical. At maximum field strength of 1.6T the CR dipole will have a field deviation of,

$$\Delta B/B(x) = 1.15\,(x/\rho)^2 + 0.2\,(x/\rho)^3 + 568\,(x/\rho)^4$$

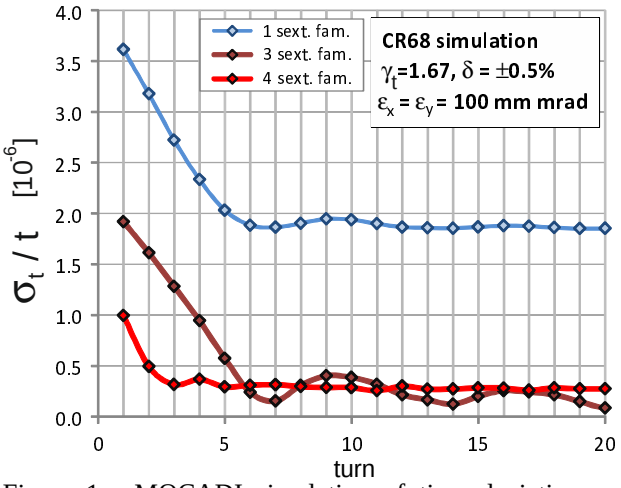

Figure 1: MOCADI simulation of time deviations as function of turns for the full CR acceptance, for corrections with different number of sextupole families.

with (x) being the distance from the optical axis (x_{max}=19cm) and ρ the radius of curvature (ρ=81.25cm).

The large sextupole component requires a completely different adjustment of the other explicit sextupoles in the ring, yet it is possible. Then the remaining 4th order contribution dominates the time deviations.

The calculation in Figure 2 shows a direct correspondence between the time deviations and the field distribution after correction of lower order terms. For further correction one decapole magnet at maximum dispersion would be required.

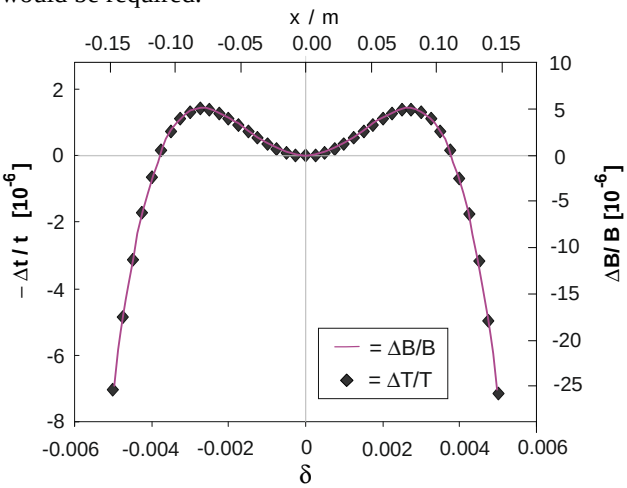

Figure 2: Direct correspondence between time deviations as function of relative momentum deviation (δ) and field shape as function of position (x).

References

[1] A. Dolinskii et al., NIM A 574 (2007) 207.
[2] H. Wollnik, NIM A 298 (1990) 156.
[3] N. Iwasa et al., NIM B 269 (2011) 752.

Design of the Dual TOF Detector System for Isochronous Mass Spectrometry in the CR at FAIR*

N. Kuzminchuk-Feuerstein[1,2], *M. Diwisch*[1], *T. Dickel*[1,2], *H. Geissel*[1,2], *C. Hornung*[1], *R. Knöbel*[1,2], *S.Litvinov*[2], *S. Nazarenko*[1], *W. R. Plaß*[1,2], *C. Scheidenberger*[1,2], *B. Sun*[1,2], *and H. Weick*[2]

[1]Justus-Liebig Universität, Gießen; [2]GSI, Darmstadt, Germany.

Isochronous Mass Spectrometry (IMS) was successfully performed for mass measurements of short-lived exotic nuclei at the FRS-ESR facility [1]. With the Super-FRS at FAIR a whole new range of exotic nuclei far away from stability will be accessible [2]. For direct mass measurements of these very short-lived nuclei using IMS, a new dual Time-of-Flight (TOF) detector system will be installed in the Collector Ring (CR).

Phase Space and Isochronicity in the CR

In order to exploit the full potential of IMS it is important to use the whole phase space volume of the beam provided by the Super-FRS with the detector system at the CR with improved time resolution. The maximum acceptance of the CR in isochronous mode is about 100 mm mrad [3]. The surviving phase space of the beam and the time resolution were simulated with the Monte-Carlo code MOCADI using an isochronous setting of the CR with γ_t=1.67. In the calculations 10^4 ions of one species (m/q=3.14) were circulated for 100 turns in the CR. At each turn the ions pass through the two TOF detectors, which were included in the simulations as two round apertures with a carbon foil of 24 μg/cm^2. Figure 1 indicates the phase space for the case of full emittance (+) and after inserting foils with Ø80 mm after 1 ($\times$) and 100 turns ($\star$), as well as for Ø40 mm foils after 100 turns ($\circ$).

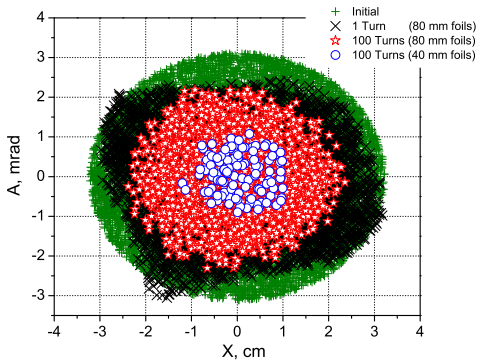

Figure 1: Beam emittance after 100 turns circulation with both TOF detectors in the CR.

These results show that the currently used foil diameter of 40 mm in the ESR TOF detector is too small to store enough ions in the CR for several turns and that larger foil diameters are needed. The time resolution for this emittance was investigated in the simulations as well. With corrections it can reach dT/T $\sim 4{\cdot}10^{-7}$ over 100 turns for this m/q.

Dual TOF Detector System Design

According to the results from the CR simulations a first design of a dual TOF detector system has been developed, which has an active area that is 4 times larger than in the TOF detector used in the ESR (Fig. 2). The increase of the aperture diameter leads to a larger total detector geometry. In the new design of the detector the electrodes which provide the electric field were optimized in extensive simulations to yield an even better detection efficiency from currently 78% up to 98%. Larger timing uncertainties due to longer path lengths for the secondary electrons can be compensated by increasing the transport energy of the secondary electrons from the foil to the MCP detectors [4]. With this compensation the simulated timing accuracy for the presently used ESR detector and the new design is approximately 40 ps.

Timing investigations of a new anode design for the MCP detectors have also been performed and further improvements for the new design are underway.

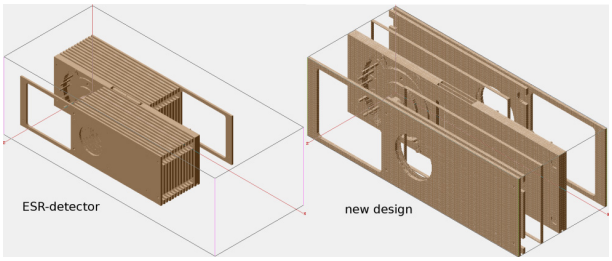

Figure 2: Comparison between the dimensions of the ESR-detector (left) and the new design (right). For the new IMS detector in the CR at FAIR a larger acceptance of the detector is needed and therefore the diameter of the carbon foil in the center of the detector will be increased.

References

[1] B. Sun et. al., Nucl. Phys. A 812,(2008) p. 1-12

[2] H. Geissel et. al., NIM B204,(2003) p. 71-85

[3] S. Litvinov et. al., PoS(STORI11)026, Frascati, Italy,(2011)

[4] M. Diwisch, Master thesis, JLU Giessen,(2011) p. 56-58

*Work supported by the BMBF under contract No.06GI9115I, by the HGF (NAVI) and by GSI (strategic university cooperation GSI-JLU-FAIR)

Large Area Continuous Position Sensitive Diamond Detector: First Tests

M. Ciobanu[1], *M. Pomorski*[2], *E. Berdermann*[3], *H. Comisel*[1], *V. Constantinescu*[1], *M. Kiš*[3], *O. Marghitu*[1], *and M. Träger*[3]

[1]ISS, Bucharest, Romania; [2]CEA, Saclay, France; [3]GSI, Darmstadt, Germany

Based on a polycrystalline chemical vapor deposition (pcCVD) diamond plate, a Large Area Continuous Position Sensitive Detector (LACPSD) of 30 mm×30 mm sensing area was fabricated and tested in Cave B. The beam used was ^{54}Ni of 1.7 AGeV and the beam intensities varied from a few kHz up to 10^7 particles/s.

The LACPSD is designed in parallel-plate geometry. A thin resistive layer of diamond like carbon (DLC) is deposited on the pcCVD diamond growth surface serving as the sensing electrode [1]. The surface resistance of the DLC layer amounts to $R_{\square} \sim 10$ kΩ. The 2D position information is obtained by the simultaneous measurement of the signal charge divided between four collecting pads, which are located at the corners of the DLC sensing electrode (Figure 1 left).

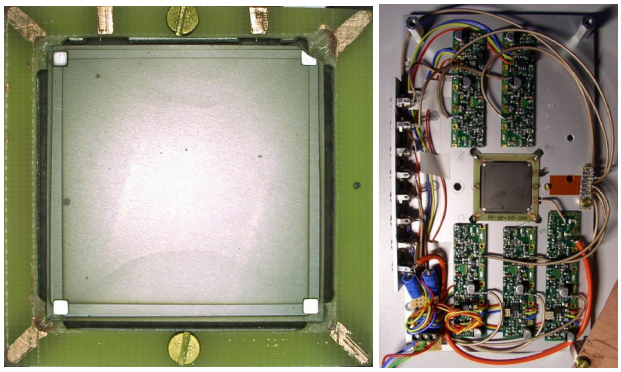

Figure 1: Left: top view of the LACPSD. At each border of the main DLC layer are DLC strips added which are placed between the four charge-collecting pads. This layout is intended to decrease the cushion error. Right: the LACPSD mounted at the centre of the board, which caries the five amplifier cards. This first test assembly has been tested with the diamond in air.

We have used four charge sensitive amplifiers (CSAs [2]) to measure the charge collected at each corner and one CSA for the back electrode to measure the total charge generated by each particle (Figure 1 right). The resistive electrode guides the particle-induced charge generated at the impact position towards the collecting contacts. From the charge q_i measured at each of the four contacts we can estimate the position of the particle impact. By assuming a uniformly resistive quadratic layer of surface L^2 the relative position is given by:

$$x = \frac{(q_2+q_3)-(q_1+q_4)}{q_1+q_2+q_3+q_4}\frac{L}{2}, y = \frac{(q_1+q_2)-(q_3+q_4)}{q_1+q_2+q_3+q_4}\frac{L}{2}.$$

A significant increase of the base line instability was observed when the detector was connected to the CSAs. We attributed this fact to the high total detector capacitance of $C_{DET} = 133$ pF and to the resistance distribution of the DLC layer with a total value of $R_{\square} \sim 10$ kΩ. In order to minimize this instability we have applied a lower feedback resistance and a higher feedback capacitance compared to the original CSA design. However, this action was at the expense of decreasing charge responsivity and increasing noise level. The lumped equivalent scheme of the next detector prototype will consist of a resistor and a capacitor of values, which have to be less than those used in this experiment.

The obtained results confirm the detectors good rate capability. Figure 2 shows the reconstructed profile of the traversing nickel beam. It has to be noticed that due to experimental constrains given by the main experiment, the diamond sensor was placed at the very end of the FOPI spectrometer with all other detectors placed in beam direction in front of it. An additional contamination of the nickel data is assumed due to ionization of the air near the detector electrodes.

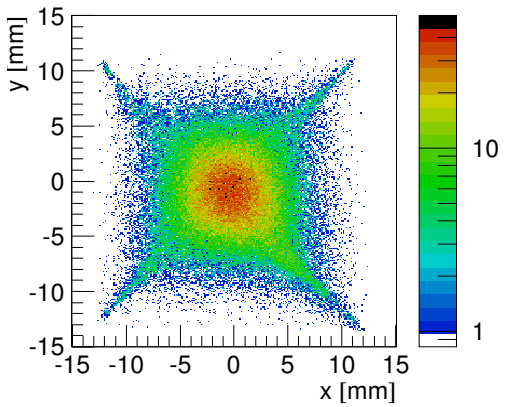

Figure 2: Reconstructed beam position and profile obtained from all unfiltered events recorded. The total range in x and y corresponds to the total sensing area (±15 mm) shown in a bin size of 10 μm/ch. The data (log-scale) are only corrected for gain differences between CSAs.

For the next test we are preparing an assembly with a FEE capable of decreasing base line instabilities and cross talk and where the LACPSD is isolated from the surrounding air. The final goal of this study is the development of LACPSD sensors using Diamond-on-Iridium(DOI) plates.

References

[1] M. Pomorski et al., Phys. Stat. Sol. A, 206, pp. 2109-2114, (2009).

[2] M. Ciobanu et al., IEEE NSS Conf. Rec., N30-20, pp. 2028-2032, (2008).

Growth of Heteroepitaxial CVD Diamond Films on Ir/YSZ/Si(001) for Detector Applications: Detection and Reduction of Crystal Defects*

C. Stehl[1], M. Fischer[1], M. Schreck[1,#], and E. Berdermann[2] for the ADAMAS collaboration

[1]Universität Augsburg, Augsburg, Germany; [2]GSI, Darmstadt, Germany

In the framework of the ADAMAS collaboration, which executed work package 16 of the EU FP7 HadronPhysics3 project, the diamond group at the University of Augsburg was responsible for the development and growth of heteroepitaxial diamond films, on which future tracking and timing detectors for heavy ions and minimum ionising particles shall be based. This work was a direct continuation of the activities within the former CARAT collaboration [1, 2].

Motivation

During the CARAT collaboration period, several heteroepitaxial diamond (called DoI = Diamond on Iridium, for the sake of simplicity) samples of different sizes had been grown in Augsburg and tested at GSI. During the α-particle and heavy ion beam tests, a large variation of detector performance among the samples, esp. in terms of charge collection efficiency (CCE) and polarisation effects, had been observed, leading to the need for getting a better understanding of the correlation between crystal lattice defect structure and detector performance of DoI samples. The newly gained insights are supposed to improve the growth process in order to minimise the defect density in the crystals, improving absolute detector performance and reducing relative spread among different samples. This will be crucial for the long-term targeted fabrication of DoI detector prototypes.

Detection of Dislocations

The dominating lattice defect type in DoI crystals is assumed to be the so-called threading dislocation. This one-dimensional irregularity originates from small angle grain boundaries which are formed during the earliest stages of DoI growth. The grain boundary network coarsens and finally dissolves during growth, leaving behind bands of agglomerated dislocations [3]. This process had been studied before by TEM investigations for a DoI film thickness up to ca. 34 µm. For thicker crystals in the range of several 100 µm, like the detector samples, data were not available up to now.

The newly applied method for the detection of dislocations in thick DoI crystals relies on the preferential etching of the crystal surface at defect sites, i.e. at points where dislocation lines intersect the surface. There, so-called etch-pits are formed, as shown in Fig. 1. Assuming a one-to-one correlation of dislocations and etch-pits, the areal dislocation density can be measured and the pattern of dislocation agglomerates revealed. This was done for differently thick DoI crystals in order to trace the changes during growth, as discussed in the next section.

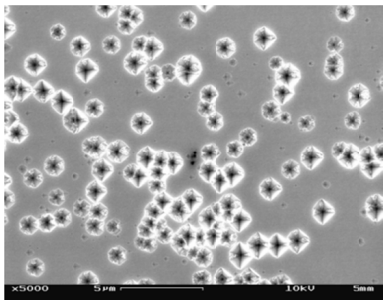

Figure 1: SEM image of etch-pits.

Reduction of Dislocation Density

The results of preliminary thickness dependent dislocation density measurements are shown in Fig. 2. The defect density is reduced with increasing crystal thickness, which quantitatively supports the previously taken route of using the upper parts of thick crystals for potential particle detectors. The dashed line indicates a $1/d$ behaviour as commonly observed for other heteroepitaxial material systems. The solid line represents a $1/\sqrt{d}$ behaviour, which seems to closer fit the experimental data. Further data are currently acquired to substantiate the behaviour and explore the mechanisms of dislocation reduction during film growth.

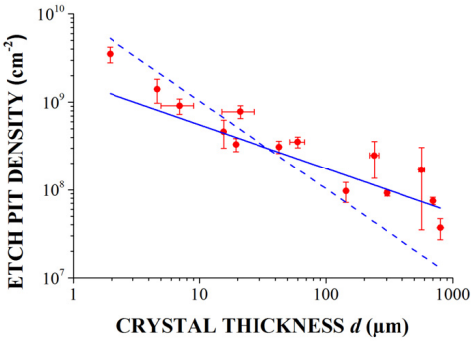

Figure 2: Areal density of etch-pits revealing dislocation density in DoI crystals of increasing thickness (The data are preliminary).

References

[1] C. Stehl et al., GSI Scientific Reports 2010, 2011.
[2] E. Berdermann et al., GSI Scientific Reports 2010, 2011.
[3] M.Schreck et al., Applied Physics Letters 78 (2001) 192.

* Work supported by EU, HadronPhysics3 project No. 283286.

#matthias.schreck@physik.uni-augsburg.de

Short-range correlations studied with unitarily transformed operators*

T. Neff[1], *H. Feldmeier*[1], *and D. Weber*[1,2]

[1]GSI, Darmstadt, Germany; [2]ExtreMe Matter Institute EMMI, GSI, Darmstadt, Germany

Introduction

Short-range correlations in nuclei are of great interest for the theoretical understanding of nuclear matter at high densities. Experimental investigations for example in $(e, e'pp)$ and $(e, e'pn)$ reactions at large momentum transfer [1] illustrate that the momentum distributions for momenta larger than the Fermi momentum are dominated by tensor correlations. In a previous study [2] we investigated short-range correlations and momentum distributions in $A = 2, 3, 4$ nuclei using exact few-body wave functions. For heavier nuclei this is no longer feasible and one has to use other many-body approaches like the no-core shell model. It is however not possible to obtain converged results with bare interactions. One therefore employs unitary transformations to soften the Hamiltonian. Typical approaches are the unitary correlation operator method (UCOM) [3] or the similarity renormalization group (SRG).

Similarity Renormalization Group

In the SRG approach one solves the flow equation

$$\frac{d\hat{H}_\alpha}{d\alpha} = (2\mu)^2 \left[\left[\hat{T}_{\rm int}, \hat{H}_\alpha\right], \hat{H}_\alpha\right] \qquad (1)$$

with $\hat{H}_{\alpha=0} = \hat{H}$ to obtain an effective Hamiltonian $\hat{H}_\alpha$. With increasing flow parameter α the effective interaction becomes softer and the eigenstates $|\Psi_\alpha\rangle$ of the evolved Hamiltonian

$$\hat{H}_\alpha |\Psi_\alpha\rangle = E_\alpha |\Psi_\alpha\rangle \qquad (2)$$

contain less and less high-momentum components than the eigenstates $|\Psi\rangle$ of the bare Hamiltonian. To recover the high-momentum components one has to use effective density operators that are obtained using the same unitary transformation as for the Hamiltonian. For computational reasons the flow equation (1) is solved in two-body approximation which induces a dependence on the flow parameter for observables like the energies E_α and also the two-body densities. This dependence on α can be used to study the importance of the omitted higher body contributions.

Results

In Fig. 1 we show the two-body densities of the ^{4}He nucleus in momentum space obtained in no-core shell model calculations using SRG transformed Hamiltonians and bare density operators (top) and SRG transformed density operators (bottom). With the bare interaction the two-body densities contain high-momentum components caused by the short-range repulsion in the Argonne interaction. The significantly larger high momentum components in the S=1, T=0 channel are caused by the tensor force. With increasing α the high-momentum components in the wave function get smaller. By using the transformed density operators the high-momentum components can be recovered. Comparing the two channels we observe a striking difference in the momentum region between 1.5 and 3.0 fm^{-1}. Whereas the two-body densities in the S=1, T=0 channel are almost independent from α, the two-body densities in the S=0, T=1 channel show a significant α-dependence. This reflects many-body correlations in the wave function induced by the tensor force.

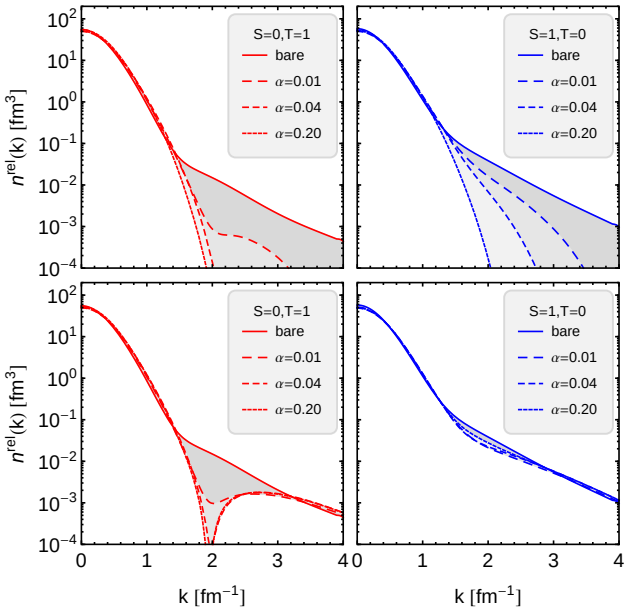

Figure 1: Two-body densities in momentum space for the S=0, T=1 and S=1, T=0 channels calculated with the eigenstates of SRG transformed AV8' Hamiltonians for flow parameters α of 0.01 fm^4, 0.04 fm^4 and 0.20 fm^4 using bare density operators (top) and effective density operators (bottom).

References

[1] R. Subedi *et al.*, Science **320**, 1476 (2008).

[2] H. Feldmeier, W. Horiuchi, T. Neff, Y. Suzuki, Phys. Rev. C **84**, 054003 (2011).

[3] R. Roth, T. Neff, H. Feldmeier, Prog. Part. Nucl. Phys. **65**, 50 (2010).

[4] T. Neff, H. Feldmeier, D. Weber, *in preparation*

* supported by Helmholtz Alliance EMMI

Operator representation for the SRG transformed Argonne potential*

D. Weber[1], *H. Feldmeier*[1], *and T. Neff*[1]

[1]ExtreMe Matter Institute EMMI and GSI Helmholtzzentrum für Schwerionenforschung, Darmstadt, Germany

Realistic nucleon-nucleon potentials are an essential ingredient of modern microscopic many-body calculations. These potentials can be either defined in operator representation by a set of quantum mechanical operators or in matrix element representation in a given basis. Many modern potentials are constructed directly in matrix element representation. However, some methods to solve the nuclear many-body problem, such as "Fermionic Molecular Dynamics" [1], require explicitly the operator representation of the potential, as they do not work in a fixed many-body basis. Therefore it is desirable to derive an operator representation also for interactions that are given only by matrix elements.

In this work we present an operator representation for the realistic "Argonne V18" potential [2] transformed by means of the "Similarity Renormalization Group" (SRG) [3]. The SRG transformation is performed in matrix element representation, so that the operator representation of the potential is not known.

To derive an operator representation from the matrix elements of the potential, we use the ansatz

$$\begin{aligned} \mathbf{V}^{\mathrm{SRG}}_{\mathrm{Operator}} &= \sum_{ST} \mathcal{V}^{C}_{ST}(\vec{\mathbf{r}}^{\,2},\vec{\mathbf{p}}^{\,2})\,\mathbf{\Pi}_{ST} \\ &+ \sum_{ST} \mathcal{V}^{L2}_{ST}(\vec{\mathbf{r}}^{\,2},\vec{\mathbf{p}}^{\,2})\vec{\mathbf{L}}^{\,2}\,\mathbf{\Pi}_{ST} \\ &+ \sum_{T} \mathcal{V}^{LS}_{1T}(\vec{\mathbf{r}}^{\,2},\vec{\mathbf{p}}^{\,2})(\vec{\mathbf{L}}\cdot\vec{\mathbf{S}})\,\mathbf{\Pi}_{1T} \\ &+ \sum_{T} \mathcal{V}^{T}_{1T}(\vec{\mathbf{r}}^{\,2},\vec{\mathbf{p}}^{\,2},\mathbf{S}_{12})\,\mathbf{\Pi}_{1T} \\ &+ \sum_{T} \mathcal{V}^{Tll}_{1T}(\vec{\mathbf{r}}^{\,2},\vec{\mathbf{p}}^{\,2})S_{12}(\vec{\mathbf{L}},\vec{\mathbf{L}})\,\mathbf{\Pi}_{1T}. \quad (1) \end{aligned}$$

It contains the operators present in the initial Argonne potential and additionally features nonlocal radial functions $\mathcal{V}^{P}_{ST}(\vec{\mathbf{r}}^{\,2},\vec{\mathbf{p}}^{\,2})$, which do not only depend on the absolute value of the relative distance operator $\vec{\mathbf{r}}$, but also on the relative momentum operator $\vec{\mathbf{p}}$. A parameterization with purely local radial functions or a simple quadratic momentum dependence fails to reproduce the SRG matrix elements. This indicates that the SRG transformation induces complicated momentum dependences that require a flexible nonlocal ansatz for the radial functions. Thus, we use the following parameterization:

$$\mathcal{V}^{P}_{ST}(\vec{\mathbf{r}}^{\,2},\vec{\mathbf{p}}^{\,2}) = \sum_{\kappa,\lambda} \gamma^{P}_{ST,\kappa\lambda} e^{-\frac{\lambda}{4}\vec{\mathbf{p}}^{\,2}}\, e^{-\frac{1}{2\kappa}\vec{\mathbf{r}}^{\,2}}\, e^{-\frac{\lambda}{4}\vec{\mathbf{p}}^{\,2}}. \quad (2)$$

The parameters in Eq. (2) are determined from a fit of the ansatz Eq. (1) to the matrix elements of the SRG transformed Argonne potential. The obtained operator representation succeeds in describing properties of few-nucleon systems like two-nucleon scattering phase shifts (Fig. 1) or binding energies of light nuclei (Tab. 1) with almost the same accuracy as the exact SRG transformed Argonne potential and thus provides a good description of this realistic interaction.

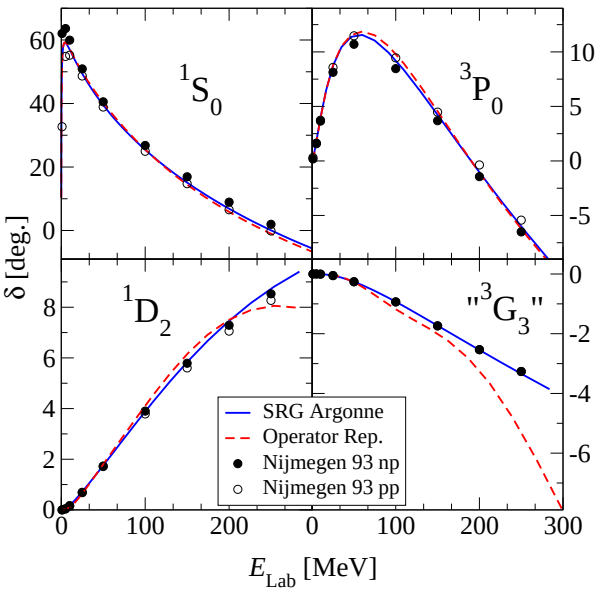

Figure 1: Nucleon-nucleon phase shifts calculated with the exact SRG transformed Argonne matrix elements (blue solid lines) and the operator representation Eq. (1) (red dashed lines). The dots indicate the results of the 1993 Nijmegen partial wave analysis [4].

	^{3}H	^{3}He	^{4}He	^{6}Li
SRG Argonne	8.35	7.62	28.38	31.8
Operator Rep.	8.33	7.61	28.41	31.9
Experiment	8.482	7.718	28.296	31.995

Table 1: Binding energies (in MeV) of some light nuclei calculated in the "No Core Shell Model".

References

[1] H. Feldmeier and J. Schnack, Rev. Mod. Phys., 72, 655, 2000

[2] R. B. Wiringa, V. G. J. Stoks and R. Schiavilla, Phys. Rev. C, 51, 38-51, 1995

[3] S. K. Bogner, R. J. Furnstahl and R. J. Perry, Phys. Rev. C, 75, 061001, 2007

[4] V. G. J. Stoks, R. A. M. Klomp, M. C. M. Rentmeester and J. J. de Swart, Phys. Rev. C, 48, 792-815, 1993

* supported by Helmholtz Alliance EMMI

Towards an effective relativistic density functional for dense matter*

S. Typel[1] *and M. D. Voskresenskaya*[1]
[1]GSI, Darmstadt, Germany

Simulations of astrophysical phenomena require the knowledge of the equation of state (EoS) of dense matter in a large range of density, temperature and isospin asymmetry. It is a great challenge to develop theoretical models for dense matter that cover the relevant parameter space in a single approach considering that many important features are governed by different many-body correlations. They can be taken into account in theoretical models by combining various methods in a global effective description.

There is a fundamental distinction between nuclear matter and stellar matter. The former is a theoretical model of strongly interacting particles. It neglects effects of the electromagnetic interaction. At temperatures below approx. 15 MeV, such a system is characterized by a "non-congruent" first-order liquid-gas phase transition in the thermodynamic limit due to the isospin degree of freedom.

The phase diagram of stellar matter displays a very different structure as compared to nuclear matter. Here, the strong interaction and the electromagnetic interaction have to be taken into account with hadrons and leptons as constituent particles. In addition, global charge neutrality is required. The competition of the interactions leads to the formation of finite-size structures such as nuclei and the appearance of a solid, crystalline phase at low temperatures, which occurs in the crust of neutron stars.

By generalizing a relativistic mean-field approach for nuclei and nuclear matter with density-dependent meson-nucleon couplings, a model for dense matter with light nuclei (mass number $A \leq 4$) was developed recently using a density functional formulation [1]. All constituent particles are considered as quasiparticles with medium-dependent properties. In particular, the mass of a cluster, regarded as a many-nucleon correlation, is shifted in the medium. This effect leads to the expected dissolution of nuclei at high-densities. Thus the model successfully exhibits the Mott effect. Different aspects of the formation and dissolution of light nuclei in warm, dilute matter were investigated experimentally and the validity of the theoretical approach was observed [3, 4, 5]. An important aspect is the modification of the symmetry energy of matter at low densities showing an increase as compared to conventional mean-field models without clusterization.

In order to reproduce the virial EoS, which is the correct model benchmark at low densities, it was necessary to incorporate nucleon-nucleon scattering correlations explicitly in the model [2]. They are represented by effective medium-dependent resonance states that appear as new degrees of freedom. A comparison of fugacity expansions leads to consistency relations that connect the strength of the meson-nucleon couplings with experimental scattering phase shifts. The relations require the introduction of effective degeneracy factors for the effective continuum states. Since a part of the many-body correlations is already accounted for in the self-energies of the quasiparticles, the strength of the residual continuum correlations is reduced [6]. The fugacity expansion also indicates relativistic corrections to the standard virial equation of state.

The model is presently extended further by adding heavy nuclei beyond ^{4}He using the same theoretical concept as for light nuclei. The shift of cluster masses in the medium is extracted from extensive calculations using the original relativistic density functional with nucleons in an extended Thomas-Fermi approximation in spherical Wigner-Seitz cells with electrons to achieve charge neutrality. Another extension of the model concerns the appearance of mesons (pions, kaons, ...) and heavier hadrons such as hyperons at high densities and temperatures. In the effective density functional the quantum statistics of particles is correctly taken into account with the possibility of boson condensation or nucleon-nucleon pairing. Antiparticles also appear naturally in the relativistic formulation.

The electromagnetic potential appears explicitly only in systems with a spatially inhomogeneous charge density distribution. The effective relativistic density functional approach assumes uniform matter. Hence effects of the Coulomb interaction are considered in an effective description using parametrized results from Monte Carlo simulations of classical one-component plasmas that are generalized to multi-component systems assuming a linear mixing rule. In the solid phase with heavy nuclei placed on lattice sites, the excitation of phonons is described with a Einstein-Debye model adjusted to reproduce known properties of Coulomb crystals. The gas/liquid $\leftrightarrow$ solid phase transition and thermodynamic properties of the crystal can be modeled within such an approach. These effects are presently not included in global EoS tables for astrophysical applications.

References

[1] S. Typel et al., Phys. Rev. C 81 (2010) 015803.
[2] K. Hagel et al. Phys. Rev. Lett. 108 (2012) 062702.
[3] L. Qin et al. Phys. Rev. Lett. 108 (2012) 172701.
[4] R. Wada et al., Phys. Rev. C 85 (2012) 064618.
[5] M.D. Voskresenskaya and S. Typel, Nucl. Phys. A 887 (2012) 42.
[6] G. Röpke et al., Nucl. Phys. A 897 (2013) 70.

*This research was supported by the Helmholtz Association (HGF) through the Nuclear Astrophysics Virtual Institute (VH-VI-417), EMMI, HGS-HIRe, HIC for FAIR and CompStar, a Research Networking Programme of the European Science Foundation.

Shell model half-lives for r-process nuclei*

Q. Zhi[1,2,3], *E. Caurier*[4], *J. Cuenca-García*[1], *G. Martínez-Pinedo*[2,1], *K. Langanke*[1,2,5], *and K. Sieja*[4]

[1]GSI-Helmholtzzentrum für Schwerionenforschung, Darmstadt, Germany; [2]Institut für Kernphysik (Theoriezentrum), Technische Universität Darmstadt, Darmstadt, Germany; [3]School of Physics and Electronic Science, Guizhou Normal University, PR China; [4]Université de Strasbourg, IPHC, Strasbourg, France; [5]Frankfurt Institute of Advanced Studies, Frankfurt, Germany

The astrophysical r-process produces about half of the heavy elements in the Universe by a sequence of the fast neutron-capture reactions interrupted by photodissociations and followed by beta decays, running through extremely neutron-rich nuclei. The beta decays of the waiting-points, associated with nuclei with the magic neutron numbers $N = 50, 82, 126$, play a crucial role for the r-process dynamics and elemental abundance distributions. Unfortunately only few data are known experimentally for the waiting point nuclei at $N = 50, 82$, while for $N = 126$ the astrophysical models rely fully on theoretical predictions. In addition to the Gamow-Teller (GT) transitions, the calculations of half-lives in this region have to account for first-forbidden (FF) contributions, as the neutron and proton Fermi levels of neutron-rich nuclei may be located in shells of different parities. A first attempt to estimate such forbidden contributions has been taken within the gross theory [1]. More recently, Borzov extended the QRPA studies based on the Fayans energy functional to a consistent treatment of allowed and first-forbidden contributions to r-process half-lives [2]. While these calculations find that forbidden contributions give only a small correction to the half-lives of the $N = 50$ and $N = 82$ waiting point nuclei, they result in a significant reduction of the $N = 126$ half-lives. This important finding has been our motivation to extend our shell model calculations of waiting point half-lives to include also FF transitions. We have thus developed the shell model code NATHAN [3, 4] to compute such transitions and studied their influence on the half-lives of r-process nuclei at $N = 50, 82$ and 126. Meanwhile similar shell model calculations became available for $N = 126$ isotones [5], however in a restricted valence space and applying different quenching factors for transition operators. The model spaces and interactions used in our shell model calculations are described in detail in Ref. [6]. Also the results for $N = 50$ and $N = 82$ nuclei are presented there, showing an overall good agreement with the half-lives known experimentally. The role of FF contributions in $N = 50, 82$ isotones appear to be minor in our SM calculations, as anticipated in [2]. For the $N = 126$ r-process nuclei, the calculations have been done in a large configuration space including ($d_{5/2,3/2}$, $s_{1/2}$, $g_{7/2}$, $h_{11/2}$) orbits for protons and ($h_{9/2}$, $f_{7/2,5/2}$, $i_{13/2}$, $p_{3/2,1/2}$) for neutrons and employing effective interaction from [7]. Seniority truncation scheme (up to 4 broken pairs) has been chosen to provide a realistic description of correlations within this valence space. In Fig. 1 we show the half-lives of $N = 126$ isotones obtained in our work and compared to other available theoretical models. The SM half-lives are noticeably faster than those predicted by global models, i.e. QRPA on top on the FRDM approach and do not exhibit any staggering. In spite of different model spaces and interactions employed, our results are very close to those from Ref. [5]. We confirm that the FF contributions to the total half-life are significant for all $N = 126$ isotones and start to dominate over the GT for nuclei with $Z \geq 70$.

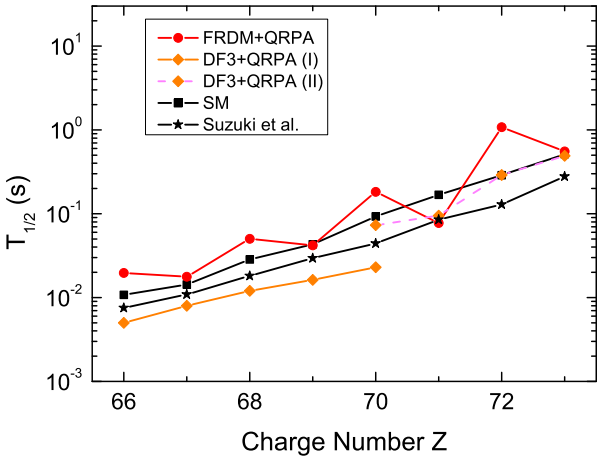

Figure 1: Half-lives of $N = 126$ r-process nuclei in different theoretical models. See text for more details.

References

[1] P. Möller, J. R. Nix, and K.-L. Kratz, Phys. Rev. C **67**, 055802 (2003).

[2] I. Borzov, Nucl. Phys. A **777**, 645 (2006).

[3] E. Caurier, G. G. Martinez-Pinedo, F. Nowacki, A. Poves, A. P. Zuker, Rev. Mod. Phys. **77**, 427 (2005).

[4] E. Caurier anf F. Nowacki, 1999, Acta Phys. Pol. B **30** 705 (1999).

[5] T. Suzuki, T. Yoshida, T. Kajino, T. Otsuka, Phys. Rev. C **85**, 015802 (2012).

[6] Q. Zhi, E. Caurier, J. Cuenca-Garcia, K. Langanke, G. Martinez-Pinedo and K. Sieja, to appear in Phys. Rev. C (2013).

[7] E. K. Warburton, Phys. Rev. C **44**, 233 (1991).

* Work supported by the IN2P3-GSI collaboration agreement (10-63)

Calculation of Q_α in heavy and superheavy nuclei*

Tomás R. Rodríguez[1,2]

[1]Technische Universität Darmstadt, Darmstadt, Germany

The study of alpha decay of heavy and superheavy nuclei is of key relevance to traceback the synthesis of new elements in the laboratory. In addition, this process plays an important role in the late stages of r-process nucleosynthesis calculations. However, a limited experimental information is available nowadays and reliable theoretical descriptions are already required. Energy density functional methods are currently the only theoretical approach to calculate microscopically properties of heavy and superheavy nuclei [1]. These methods are based on self-consistent mean field (MF) approximations such as the Hartree-Fock-Bogoliubov (HFB) one [2]. In spite of its simplicity, the HFB approach has proved to be successful in describing bulk properties of the atomic nuclei. However, some important correlations related to the symmetry restorations and quantum fluctuations cannot be accounted by the HFB approximation and one has to go beyond mean field (BMF) to get a better description of the system [1]. In this contribution we discuss an example of MF and BMF calculations of the Q_α-value in the plutonium isotopic chain using the Gogny D1M parametrization [3]. This quantity is defined as $Q_\alpha(A) = B.E.(^4\mathrm{He}) + B.E.(^{A-4}\mathrm{U}) - B.E.(^A\mathrm{Pu})$, where A and $B.E.$ are the mass number and the nuclear binding energy respectively.

We first analyze the convergence of the HFB calculations with the size of the spherical harmonic oscillator basis in which the HFB states are expanded [2]. In Fig. 1(a) the Q_α-values obtained for different number of major oscillator shells, $N_{h.o.}$, included in the MF calculation are represented. We observe the curves approaching each other with increasing $N_{h.o.}$ showing a nice convergence pattern. However, the fully converged HFB result is not able to reproduce the experimental data. In addition, the calculations are not fully converged for the lighter nuclei $N \in (138-146)$ using $N_{h.o.} = 12$, having Q_α differences up to 0.5 MeV with respect to the values obtained with $N_{h.o.} = 18$.

We can also explore at the MF level the role of octupole deformations (β_3) in the Q_α-values. In Fig. 1(b) the results of the calculations including or not this degree of freedom are represented. We see differences only in the three lightest nuclei and, surprisingly, the theoretical results with $\beta_3 = 0$ are in better agreement with the experiment. However, this is an artifact either from the interaction and/or from the lack of parity projection that must be further investigated.

Finally, we analyze the effect of including angular momentum and particle number restoration, plus axial quadrupole shape mixing (GCM method) in the Q_α-values calculated here. In this case, we have two additional important limitations: 1) only parity conserved HFB wave functions ($\beta_3 = 0$) are included, and, 2) we have used $N_{h.o.} = 12$ due to the large computational cost, although we have already discussed that the results are not fully converged. Nevertheless, it is important to study which are the changes introduced by these correlations in this particular example. Most of the nuclei calculated here are deformed and superfluid. Hence, both angular momentum and particle number restoration provide $\sim$ 4 MeV and configuration mixing gives $\sim$ 1 MeV of extra binding energy. However, this energy gain is not completely constant along the isotopic chain and depends on the underlying subshell structure of each nuclei. In Fig. 1(c) we show that the results are indeed quite sensitive to BMF effects, particularly from $N = 138-148$. However, artificial jumps in $N = 138$ and $N = 148$ are obtained and must be further investigated.

In summary, we have shown the Q_α-value calculation for plutonium isotopic chain using energy density functional methods with the Gogny D1M parametrization. We have observed that the results are very sensitive (up to $\sim$ 1 MeV) to the convergence of the method, the inclusion of collective degrees of freedom such as octupole deformation, and beyond mean field effects. These uncertainties require further analysis and work is in progress to provide reliable theoretical results in the near future.

*Work supported by BMBF-Verbundforschungsprojekt number 06DA7047I and HIC4FAIR.

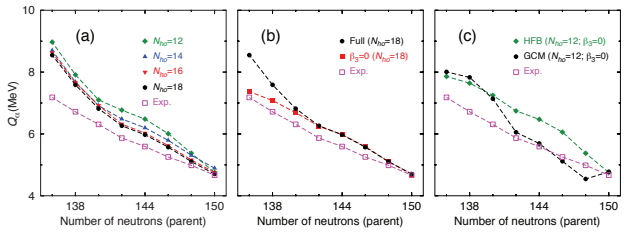

Figure 1: Q_α for the Pu chain calculated with the Gogny D1M interaction: (a) for different values of the oscillator shells included in the HFB calculation, (b) allowing octupole deformations (bullets) or not (filled squares) in the HFB states ($N_{ho} = 18$), (c) with plain HFB (bullets) or including BMF effects (filled squares) ($N_{ho} = 12$, $\beta_3 = 0$). Open squares are the experimental values.

References

[1] M. Bender, P.-H. Heenen, and P.-G. Reinhard, Rev. Mod. Phys. 75, 121 (2003).

[2] P. Ring, and P. Schuck, The Nuclear Many-Body Problem, Springer, New York (1980).

[3] S. Goriely, S. Hilaire, M. Girod, and S. Péru, Phys. Rev. Lett. 102, 242501 (2009).

Response Functions for Charge-Changing Weak Interactions*

A. Fedoseew[†1] *and H. Lenske*[1,2]

[1]Justus Liebig Universitaet, Giessen; [2]GSI, Darmstadt, Germany

We calculate the response of charge changing hadronic interactions by solving the extended RPA problem including nucleonic ph-states and Δh-configurations. The response of a nucleon to a spin-isospin sensitive probe is of major interest for the study of charge changing excitations as they typically occur in β-decay processes and quasielastic neutrino scattering experiments. Despite the large N-Δ energy gap, the Δ-components affect considerably the nucleonic ph-sector. Hence, quenching effects due to Δh-coupling are reasonably accounted for.

In our approach nuclear density functional theory is used for the description of the nuclear matter ground state and excitations. The residual p-h interaction is then derived self-consistently by applying Landaus Fermi-Liquid theory. As a result, our response function calculations are free of additional adjustable model parameters. The response functions to an external probe entering into cross sections are related to the imaginary part of the polarization tensor, which is calculated by solving the Dyson equation, $\hat{\Pi} = \hat{\Pi}^0 + \hat{\Pi}^0 \hat{V} \hat{\Pi}$, where $\hat{\Pi}^0 = \hat{\Pi_{ph}} + \hat{\Pi}_{\Delta h}$ is the in-medium polarization propagator including p-h and Δ-h states. The mixing between these states is embodied in the residual interaction $\hat{V}$ and leads to a quenching of the quasi-elastic peak. In our work $\hat{V}$ is calculated from the second order variation of the energy density functional with respect to the corresponding spin-isospin densities. With this approach our interaction exhibits a more genuine density and isospin dependence. This functional dependence is not considered in many other RPA calculations. However, our results show that it effects the strength and shape of the nuclear matter response. To properly account for nucleonic excitations in the spin-isospin channel as well as charge asymmetric ground states we extend $\hat{\Pi}^0$ to include density and isospin dependent self-energies in the neutron, proton and Δ propagators [1]. For the Δ self-energies we use a many-body approach which includes higher order quasielastic corrections in terms of two- and three-body absorptions [2]. The response functions for a finite nucleus are calculated in the local density approximation. For our calculations we use HFB proton and neutron ground state densities, which in case of quasi-elastic electron scattering provide a satisfactory description of the data as shown in Fig. 1.

Our results are in good agreement with other calculations in the considered energy-momentum region [3]. Furthermore, our approach provides a better understanding of the fundamental spin-isospin in-medium interactions. The higher order effects included in the residual interaction mostly affect the shape and strength of the quasielastic peak, where the self-energy insertions adjust the position as well as the width of the quasielastic peak. Fig. 2 shows typical quasielastic neutrino scattering results for some nuclei.

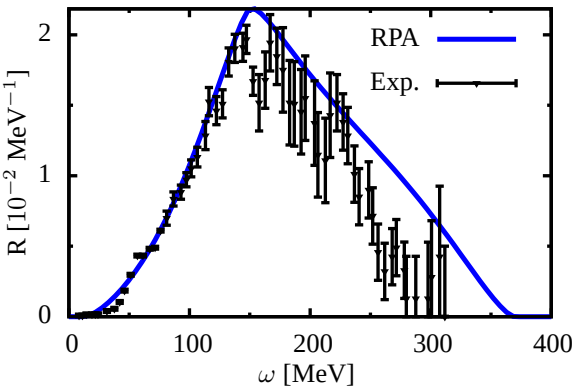

Figure 1: Quasielastic peak of the longitudinal electron scatterning response for fixed $\vec{q} = 550$.

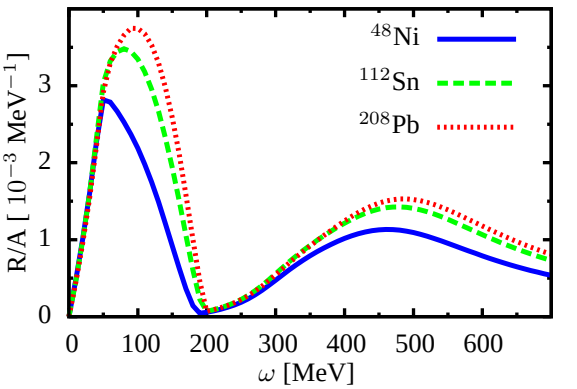

Figure 2: Longitudinal response per nucleon for neutrino scattering on different targets at $\vec{q} = 300$ MeV

References

[1] E. Chabanat et al., Nucl. Phys. A, 627:710746, 1997

[2] E. Oset, L.L. Salcedo, Nucl. Phys. A, 1987, vol. 468 pp. 631

[3] Martini et al., Phys. Rev. C (2009) vol. 80 (6) pp. 065501

* Work supported by HGS-HIRe.

† andreas.fedoseew@theo.physik.uni-giessen.de

Low-energy limit of the radiative dipole strength in nuclei

Elena Litvinova[1,2]

[1]ExtreMe Matter Institute EMMI and Research Division, GSI; [2]National Superconducting Cyclotron Laboratory, Michigan State University, East Lansing, MI 48824-1321, USA

We explain the upbend phenomenon, which was first reported in Ref. [1], later observed systematically in the γ-ray strength functions below neutron threshold of various light and medium-mass nuclei and probed by different experimental techniques [2]. Studies of Ref. [3] have revealed that this phenomenon, occuring in various astrophysical sites, can have a significant impact on their elemental abundances.

Phenomenological approaches approximate the γ-strength in this energy region by the tail of the giant dipole resonance with a temperature-dependent width. This is, however, absolutely not justified, because the low-lying γ-strength originates from underlying physics which is completely different from the giant vibrational motion. In addition, such approaches fail to reproduce the low-energy anomaly which is observed in medium-mass nuclei.

We propose a microscopic approach for the radiative strength function which is based on the statistical description of an excited compound nucleus. In is shown [4] that the thermal mean field model provides a very reasonable approach to the compound nucleus. At the same time, it is simple enough to allow a straightforward generalization of very complicated microscopic approaches to nuclear response for the case of a compound nucleus, in terms of finite temperature corresponding to the nuclear excitation energy. To describe transitions from a thermally excited state, in the first approximation we employ the finite-temperature continuum QRPA developed in [5]. Variation $\delta\mathcal{R}$ of the density matrix $\mathcal{R}$ in the external field P obeys the following integral equation:

$$\delta\mathcal{R}(x;\omega,T) = \int dx' \mathcal{A}(x,x';\omega,T) \times \Big(P(x') + \int dx'' F(x',x'')\delta\mathcal{R}(x'';\omega,T)\Big), \quad (1)$$

where $x = \{\mathbf{r}, s, \tau\}$, and $F(x,x')$ is the effective nucleon-nucleon interaction. The two-quasiparticle propagator $\mathcal{A}(x,x';\omega,T)$ is calculated in terms of the Matsubara temperature Green functions in the coordinate space [5]. Its continuum part is responsible for transitions from the thermally unblocked discrete spectrum states to the continuum (see Fig. 1). The radiative dipole strength function is determined as:

$$f_{E1}(E_\gamma,T) = -\frac{16e^2}{27(\hbar c)^3} Im \int dx \delta\mathcal{R}_{E1}(x;\omega,T) P_{E1}(x), \quad (2)$$

$\omega = E_\gamma + i\Delta$. Fig. 2 displays f_{E1} in ^{94}Mo at the excitation energy around its neutron separation energy S_n, that represents the case of radiative thermal neutron capture,

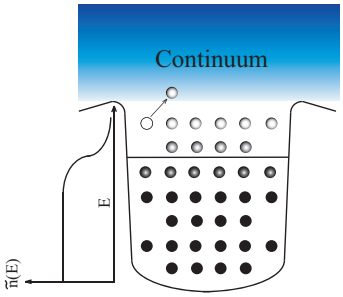

Figure 1: Schematic picture of the lowest-energy single-quasiparticle transitions from the thermally unblocked states with effective occupation probabilties $\tilde{n}(E)$ to the continuum.

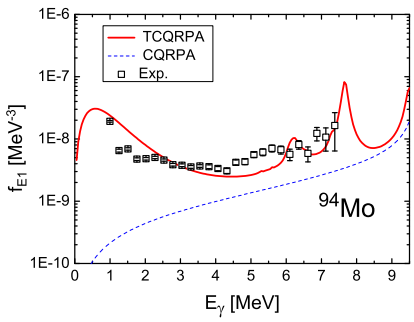

Figure 2: The E1 γ-strength for the thermally excited state of ^{94}Mo near S_n (solid), compared to the strength for the ground state (dashed) and to Oslo data.

compared to f_{E1} in the ground state. The upbend of the strength due to the transitions illustrated schematically in Fig. 1 appears as a typical feature of γ-strength in medium mass nuclei while in heavy nuclei f_{E1} comes out rather flat at $E_\gamma \to 0$.

In conclusion, we explain the systematic low-energy enhancement of the γ-strength on the microscopic level and show that the approaches to r-process nucleosynthesis, involving Brink hypothesis, may need to be revised.

Support from Helmholtz Alliance EMMI is gratefully acknowledged.

References

[1] A. Voinov *et al.*, Phys. Rev. Lett. 93, 142504.

[2] M. Wiedeking *et al.*, Phys. Rev. Lett. 108, 162503.

[3] A.C. Larsen, S. Gorieli, Phys. Rev. C 82, 014318 (2010).

[4] E. Litvinova, N. Belov, to be published.

[5] E.V. Litvinova, S.P. Kamerdzhiev, V.I. Tselyaev, Yad. Fiz. 66, 584 (2003); Phys. Atomic Nuclei 66, 558 (2003).

Ab initio Studies of Atomic Properties and Experimental Behavior of element 119 and Its Lighter Homologs

A. Borschevsky[1], V. Pershina[2], E. Eliav[3], and U. Kaldor[3]
[1]Helmholtz Institute Mainz, Mainz D-55128, Germany; [2]GSI, Darmstadt, Germany; [3] Tel Aviv University, Israel

We performed relativistic benchmark calculations of the polarizabilities (α) of element 119 and its lighter homologs, Cs and Ra, and their cations. Besides being of theoretical interest in the context of atomic studies of heavy and superheavy elements, these properties are also important for prediction of adsorption enthalpy (ΔH_{ads}) of the atoms on inert surfaces, which is required to guarantee the transport of the newly produced element from the target chamber to the chemistry set up.

The polarizabilities were calculated using the finite field approach [1]. The energy calculations were performed within the Dirac-Coulomb (DC) Hamiltonian,

$$H_{\mathrm{DC}} = \sum_i h_D(i) + \sum_{i<j} 1/r_{ij}.$$

Here, h_D is the one electron Dirac Hamiltonian,

$$h_D(i) = c\boldsymbol{\alpha}_i \cdot \mathbf{p}_i + c^2\beta_i + V_{nuc}(i),$$

where α and β are the four dimensional Dirac matrices. The nuclear potential V_{nuc} takes into account the finite size of the nucleus, modelled by a Gaussian distribution.

Electron correlation was taken into account at the relativistic coupled cluster level, including single, double, and perturbative triple excitations (RCCSD(T)). The uncontracted Faegri basis set [2] was used for the three atoms and extended to convergence with respect to the calculated polarizabilities. The final basis sets were 26*s*23*p*16*d*8*f*4*g* for Cs, 26*s*23*p*18*d*13*f*6*g*2*h* for Fr, and 29*s*26*p*20*d*15*f*6*g*2*h* for element 119. All the calculations were performed using the DIRAC08 computational package [3].

Based on the calculated polarizabilities and other atomic properties and using a physisorption model given by Eq. (6) of Ref. 4, we estimate the ΔH_{ads} of group-1 elements on a Teflon surface. The van der Walls radii (R_{vdW}) were determined from a linear correlation between the known R_{vdW} in Group 1 [5] and the radii of the maximal charge density (R_{max}) of the valence *ns* orbitals [6].

Table 1.Polarizabilities of neutral (α(M)) and singly charged ($\alpha(M^+)$) group-1 elements (a.u.), and their R_{vdW} (Å) and ΔH_{ads} (kJ/mol) on Telfon. All the values were calculated here, unless reference otherwise.

	Na	K	Rb	Cs	Fr	119
α(M)	162.7[a]	290.6[a]	318.8[a]	399.0	311.5	169.7
$\alpha(M^+)$	1.0[b]	5.5[b]	9.1[b]	15.5	20.1	31.6
R_{vdW}	2.27[c]	2.75[c]	2.90	3.16	3.09	2.78
$-\Delta H_{ads}$	32.7	29.3	26.6	24.6	21.2	17.6

[a] Exp., Ref. [7]; [b] Theor., Ref. [8]; [c] Exp., Ref. [5]

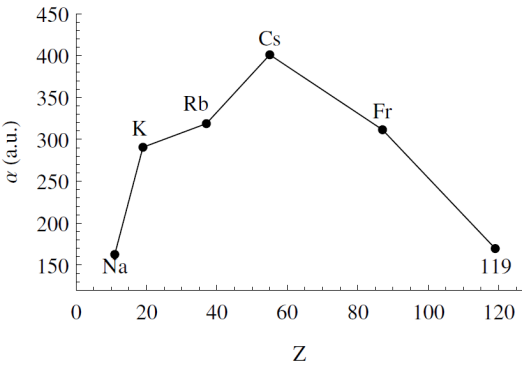

Figure 1. Polarizabilities of group-1 elements

The calculated α, R_{max}, and ΔH_{ads} of group-1 elements are presented in Table I. The obtained α of Cs is in excellent agreement with the experimental value (401.0±0.6 [9]); similar accuracy can be expected from our predictions for Fr and element 119. For the neutral atoms, α (Fig. 1) and R_{vdW} increase from Na to Cs and then decrease towards element 119, which can be explained by the strong relativistic contraction of the valence *ns* orbital in the heavier atoms in the group. In fact, the same trend reversal at Cs is also observed for the ionization potentials and electron affinities of group-1 atoms, discussed in Ref. 10. In case of the cations, a different trend in the polarizability is observed, defined by the outer $(n\text{-}1)p_{3/2}$ orbital, which expands in the group with the increase in the atomic number. Thus, 119^+ will have the highest polarizability of group-1 cations. The $-\Delta H_{ads}$ in the group decrease with the increase in the atomic number, and the predicted $-\Delta H_{ads}$ of element 119 on Teflon is the lowest among the atoms considered here, as is the case with its $-\Delta H_{ads}$ on noble metals [10] . The low value of 17.6 kJ/mol indicates that this atom should be easily transported through the Teflon capillaries to the chemistry set up.

References

[1] U. Kaldor, J. Phys. B **6**, 71 (1973)
[2] K. Faegri, Theor. Chim. Acta **105**, 252 (2001)
[3] DIRAC08, written by H. J. Ja. Jensen *et al*. (2008)
[4] V. Pershina and T. Bastug, Chem. Phys. **311**, 139 (2005)
[5] A. Bondi, J. Phys. Chem. **68**, 441 (1964)
[6] J. Desclaux, At. Data Nucl. Data Tables **12**, 311 (1973)
[7] V. Holmgen *et al.*, Phys. Rev. A **89** 053607 (2010)
[8] I.S. Lim *et al.*, J. Chem. Phys. **116**, 172 (2002)
[9] J. M. Amini and H. Gould, Phys. Rev. Lett. **91**, 153001 (2003)
[10] V. Pershina *et al.*, Chem. Phys. **395**, 87 (2012)

Theoretical Predictions of Properties and Gas-Phase Behaviour of Carbonyl Complexes of Group-6 Elements Cr, Mo, W, and Element 106, Sg

V. Pershina[1] and J. Anton[2]
[1]GSI, Darmstadt, Germany; [2]Institut für Elektrochemie, Universität Ulm, Germany.

Up to now, experimental gas-phase chemical studies were performed for elements 104 (Rf) through 108 (Hs), 112 (Cn) and 114 (Fl) [1]. A search for a new class of volatile species suitable for gas-phase chromatography studies resulted in the idea to synthesize carbonyl complexes of the heaviest elements. Accordingly, carbonyl complexes of Mo, W and Os, homologs of Sg and Hs, respectively, were synthesized and studied on their volatility by using both the isothermal (IC) and thermochromatography (TC) techniques [2].

Theoretical predictions of gas-phase properties and chromatography behaviour of the heaviest elements and their homologs has been a subject of our long-term research [3]. In the present work, we predict properties of group-6 $M(CO)_6$ (M = Cr, Mo, W, and Sg) and their adsorption behaviour on quartz for future gas-phase chromatography experiments. For calculations, we used our 4-component, fully relativistic, Density Functional Theory method developed within the non-collinear spin-polarized formalism [4]. For calculations of the adsorption energy of the molecules on a neutral (quartz) surface, the following model for a molecule-slab interaction was used [5]:

$$E(x) = -\Delta H_{ads} = -\frac{3}{16}\left(\frac{\varepsilon - 1}{\varepsilon + 2}\right)\frac{\alpha_{mol}}{\left(\frac{1}{IP_{slab}} + \frac{1}{IP_{mol}}\right)x^3}$$

Here, ε is the dielectric constant of the surface material, IP_{mol} and IP_{slab} are ionization potentials of the molecule and surface material, respectively, α_{mol} is molecular polarizability and x is the molecule - surface interaction distance estimated using molecular bond lengths.

Results of the calculations of molecular properties (also in comparison with other calculations [6]) needed for predictions of adsorption are given in Tables 1 and 2.

Table 1. Calculated and experimental bond lengths, R_e (in Å), of $M(CO)_6$ (M = Cr, Mo, W, and Sg)

	Method	R_e(M-C)	R_e(C-O)
$Cr(CO)_6$	4*c*-DFT	1.913	1.152
	exp.	1.918	1.141
$Mo(CO)_6$	4*c*-DFT	2.067	1.152
	RECP CCSD(T)[a]	2.076	1.147
	exp.	2.063	1.145
$W(CO)_6$	4*c*-DFT	2.062	1.153
	RECP CCSD(T)[a]	2.065	1.148
	exp.	2.058	1.148
$Sg(CO)_6$	4*c*-DFT	2.123	1.154
	RECP CCSD(T)[a]	2.112	1.150

[a] Ref. [6].

Table 2. Ionization potentials, IP (in eV), average polarizabilities, α (in a.u.), molecule-surface adsorption distances, x (in Å), and adsorption enthalpies, $-\Delta H_{ads}$ (in kJ/mol), of $M(CO)_6$ (M = Cr, Mo, W, and Sg) on quartz

	IP	<α>	x	$-\Delta H_{ads}$
$Cr(CO)_6$	9.07	133.24	2.695	45.4 ± 2.5
$Mo(CO)_6$	9.003	156.41	2.784	48.1 ± 2.5
				42.5 ± 2.5[a]
$W(CO)_6$	8.925	151.54	2.781	46.5 ± 2.5[b]
$Sg(CO)_6$	8.631	159.43	2.82	46.2 ± 2.5

[a] IC experiment [2]; [b] TC experiment [2].

The data show that the electronic structure of $Sg(CO)_6$ is very similar to those of the Mo and W homologs. Accordingly, its volatility should also be very similar to those of the lighter homologs (Table 2). Fig. 1 shows that, indeed, all the homologs will have similar, within the error bars, ΔH_{ads}(M) on quartz.

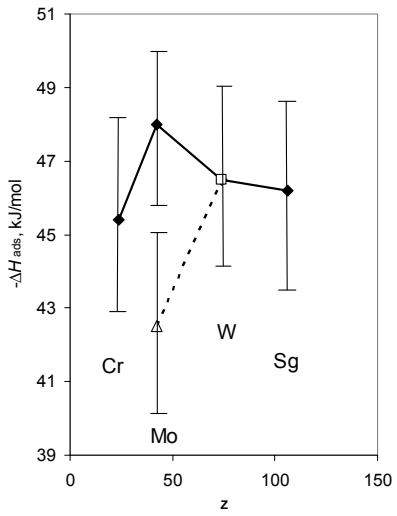

Fig. 1. Predicted (solid line) and measured (dashed line: the open rhomboid is the IC measurements; the open square is the TC ones [2]) adsorption enthalpies of $M(CO)_6$ (M = Cr, Mo, W, and Sg) on quartz.

References

[1] A. Türler and V. Pershina, Chem. Rev., in print
[2] J. Even, et al. Inorg. Chem. **51**, 6431 (2012).
[3] V. Pershina, Radiochim. Acta **99**, 459 (2011).
[4] J. Anton, et al., Phys. Rev. A **69**, 012505 (2004).
[5] V. Pershina and T. Bastug, Chem. Phys. **311**, 139 (2005)
[6] C. N. Nash, B. E. Bursten, J. Am. Chem. Soc., **121**, 10830 (1999).

Theoretical Predictions of Properties of Element 120 and its Adsorption on Noble Metal Surfaces

V. Pershina[1], A. Borschevsky[2] and J. Anton[3]
[1]GSI, Darmstadt, Germany; [2]HIM, Mainz, Germany; [3]Institut für Elektrochemie, Universität Ulm, Germany.

In the present work, we predict chemical properties and adsorption behaviour of element 120 whose production was attempted recently at the GSI, Darmstadt [1]. The most promising nuclear reaction appears to be ^{50}Ti + ^{249}Cf giving the ^{295}120 and ^{296}120 isotopes in the 4*n* and 3*n* evaporation channel, respectively [2]. Expected lifetime, of the order of μs, is too short for study of chemical properties of this element using current gas-phase chromatography techniques. However, development of vacuum chromatography could open new prospects in this field.

An analysis of atomic properties, calculated within the Dirac-Coulomb-Breit approach [3], shows that the relativistic stabilization and contraction of the valence ns AO in group 2 results in the inversion of trends beyond Ba, so that element 120 will be more electronegative than Ca. In this work, chemical reactivity of element 120 in comparison with its lighter homologs Ca through Ra was studied on the example of the M_2 and MAu dimers. Knowledge of properties of these compounds is indispensable for estimating quantities measured in the chromatography studies, i.e., sublimation, ΔH_{sub}, and adsorption enthalpies, ΔH_{ads}, on gold.

Molecular calculations were performed with the use of our fully relativistic, 4-component, Density Functional Theory method in the non-collinear spin-polarized approximation [4]. Results for M_2 and MAu are given in Tables 1 and 2, respectively.

Table 1. Spectroscopic properties of M_2 (M = K through element 120): bond lengths, R_e (in Å), dissociation energies, D_e (in eV) and vibrational frequencies, ω_e (in cm^{-1})[a]

Mol.	R_e	D_e	ω_e
Ca_2	4.236	0.141	66
	4.277	*0.137*	*65*
Sr_2	4.493	0.133	44
	4.498	*0.137*	*40*
Ba_2	4.831	0.226	43
Ra_2	5.193	0.106	25
$(120)_2$	5.646	0.018	9

[a] Values in italics are experimental.

The data of Table 1 show that $D_e(M_2)$ have a reversal of the trend beyond Ba. Thus, $(120)_2$ should be most weakly bound in the row of homologs, due to the 8s(120) AO contraction and van der Waals nature of bonding in M_2.

D_e(MAu) (Table 2) have also a reversal of the trend beyond Ba, so that 120Au should be the most weakly bound in the row of homologs due to the 8s(120) AO stabilization. ΔH_{sub} of the 120 metal and ΔH_{ads}(120) on gold were obtained via a correlation with the binding energies of the corresponding dimes in the group. According to the results, ΔH_{sub}(120) and -ΔH_{ads}(120) on Au (also on Pt and Ag) should be the smallest among the homologs.

Table 2. Properties of MAu (M = Ca through element 120): bond lengths, R_e (in Å), dissociation energies, D_e (in eV) and vibrational frequencies, ω_e (in cm^{-1})[a]

Mol.	R_e	D_e	ω_e
CaAu	2.627	2.706	221
	2.67	*2.545*	*221*
SrAu	2.808	2.629	159
BaAu	2.869	3.006	145
RaAu	2.995	2.564	105
120Au	3.050	1.902	97

[a] Values in italics are experimental.

Predicted trends in the adsorption of group-2 elements on noble metals are shown in Fig 1. The moderate values of ΔH_{ads}(120) are indicative of the feasibility of the chromatography chemical studies on this element.

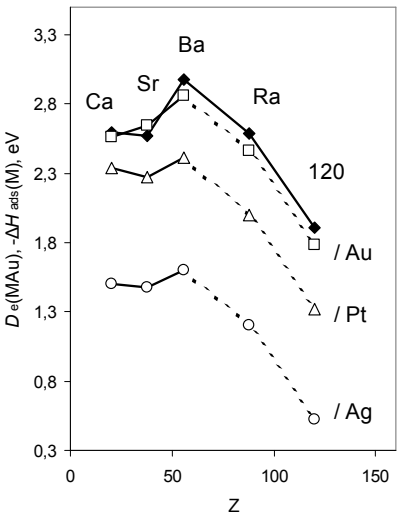

Fig. 1. Calculated D_e(MAu) (filled symbols) and -ΔH_{ads}(M) (open symbols), where M = Ca through element 120, on Au, Pt and Ag.

References

[1] Ch. E. Düllmann, et al., GSI Annual Report 2011.
[2] V. Zagrebaev and W. Greiner, Phys. Rev. C **78**, 034610 (2008).
[3] A. Borschevsky, et al. Phys. Rev. A, in print.
[4] J. Anton, et al., Phys. Rev. A **69**, 012505 (2004).

Status of the proton injector for FAIR

R. Berezov[1], A. Adonin[1], N. Chauvin[2], J. Fils1, R. Hollinger[1], J. Pfister[1]

[1]GSI, Darmstadt, Germany; [2]CEA, Saclay, France

The microwave ion source and low energy beam transport (LEBT) for the injection into the proton linac have to deliver a 100 mA proton beam with an energy of 95 keV at the entrance of the RFQ within an acceptance of 0.3π mm mrad (normalized rms). The source SILHI (high intensity light ion source) at CEA/Saclay meets these requirements. It operates with a frequency of 3 GHz and allows high brightness ion beams with energies up to 100 keV and full beam currents of 130 mA [1].

The proton injector for the FAIR facility is presented in Fig.1. The microwave ion source runs in a pulsed mode by pulsing the rf generator. The RF power is produced by a magnetron and injected into the source via standard rectangular wave guides. The duty cycle is 4 Hz with a pulse length of 0.2 ms. The minimum pulse duration is 300 µs with a 100 µs rise and fall time. The source is able to run with a long time of operation (several months) with good performance as noise to beam fluctuation ≤5 % and pulse-to-pulse repetition ≤2.5 %.

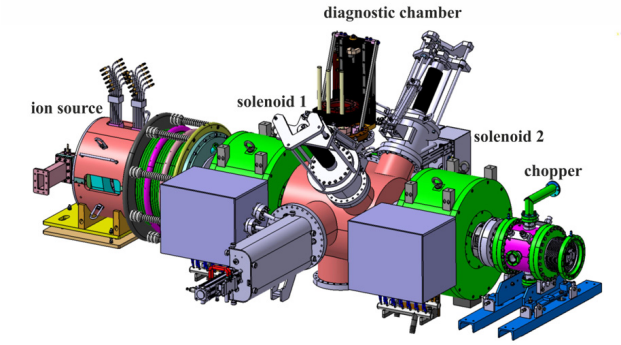

Figure 1: The proton injector for the FAIR (microwave ion source and LEBT)

The LEBT consists of two solenoids with a maximum magnetic field of 260 mT and two magnetic steerers to adjust the horizontal and vertical beam position [2]. The diagnostic chamber between both solenoids includes Iris (beam diaphragm), Allison scanner (emittance measurement), Secondary Emission (SEM)-Grid (beam profiler), beam stopper and a Wien filter (mass separator). The Iris is required for transverse beam limitation. The Wien filter composed of a 0.2 Tesla window frame and two electrodes inside with adjustable voltage allows the detection of different ion species (H^+, H_2^+, H_3^+) as a check of beam composition. For measuring ion beam intensity behind the pentode extraction system and at the end of the beam line a beam current transformer (ACCT) is installed. An electrostatic chopper right in front of the RFQ will shorten the beam pulse current to 36 µs [3].

The beam dynamics simulation in the proton injector is presented in Fig.2. The calculations were performed with TraceWin [3]. The simulations start at the plasma electrode of the ion source and ended at the entrance of RFQ. To simplify the calculations, the space charge compensation degree is considered constant in all the beam line and its value has been assumed to be 80 %. The compensation in the source extraction region and in the region between chopper and RFQ is less than 80 %. The estimated emittance and twiss parameters according to calculations are ε=0.18π mm mrad, α=0.48 and β=0.04 mm/mrad.

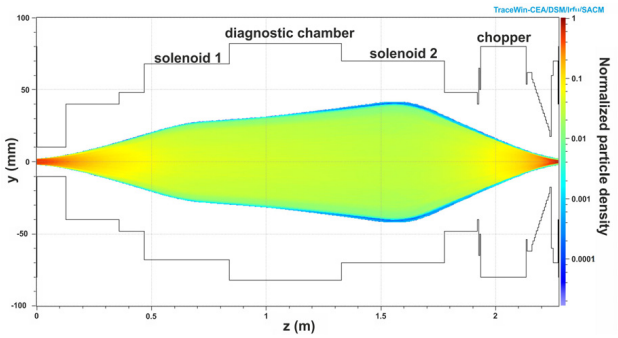

Figure 2: The beam particle distribution in the FAIR p-injector (performed by N. Chauvin)

At the end of 2013 it is planned to start the commissioning at CEA/Saclay, to perform the emittance measurements, space charge compensation measurements with a 4-grid-analyzer, current measurements and determination of the beam fractions as well as check for the reliability. The emittance measurements will be performed with a mobile emittance scanner [5] from GSI (MobEmi) that consists of two vacuum chambers including diagnostic components. The MobEmi will be installed at the end of the LEBT close to the later entrance of the RFQ.

After the commissioning the microwave ion source and LEBT will be transported to GSI for the commissioning and later operation of the proton linac. The installation into the tunnel is planned in the beginning of 2017.

References

[1] R. Hollinger, W. Barth et al., "High current proton beam investigations at the SILHI-LEBT at CEA/Saclay", Linac06 (2006) 232.

[2] R. Gobin et al., "Status of the Light Ion Source developments at CEA/Saclay", RSI, Vol.75, No. 5 (2004) 1414.

[3] L. Groening et al., "Technical report on the Design and construction of the proton linac of FAIR", FAIR-TAC (2010).

[4] http://irfu.cea.fr/Sacm/logiciels/index.php

[5] A. Reiter, Mobile emittance test bench, GSI internal documentation, (2012).

Status of the FAIR Proton Linac

G. Clemente[1*], W. Barth[1], R. Brodhage[2], N. Chauvin[3], S. Damjanovic[4], O. Delferrière[3], P. Forck[1], L.Groening[1], H.Podlech[2], V. Ivanova[4], M.S. Kaiser[1], P. Kowina[1], B. Launé[5], C. Mühle[1], U. Ratzinger[2], G. Schreiber[1], C. Simon[3], W. Vinzenz[1], C. Will[1]

[1]GSI, Darmstadt, Germany; [2]IAP, University of Frankfurt a.M., Germany; [3]CEA/Saclay, Gif-sur-Yvette, France; [4]CERN, Geneva, Switzerland; [5]CNRS/Orsay, Orsay, France

Introduction

The 70 MeV FAIR Proton Linac [1] has to provide the primary beam for the production of antiprotons. It will deliver from 35 to 70 mA protons for the injection into the SIS18 with a repetition rate of 4 Hz. The accelerator will be located north of the existing UNILAC complex. Its conceptual layout is shown in Fig. 1 and its main beam parameters are listed in Tab. 1.

Tab. 1: Main parameters of the proton linac for FAIR.

Final energy	70 MeV
Pulse current	70 mA
Protons per pulse	$7 \cdot 10^{12}$
Repetition rate	4 Hz
Trans. beam emittance	4.2 µm (tot. norm.)
Rf-frequency	325.224 MHz

In-Kind Contributions

The design of the LEBT has started and the production of the focusing solenoids was completed. The mechanical integration of the chopper is currently under discussion. Beam dynamics simulations have been performed for different integration scenarios. The kickoff even for the production of the klystrons took place in January 2013, while several components of the RF test bench have been already delivered and installed at GSI. The magnets located in the transfer channel are already at GSI as well.

A timetable for the production of the CH cavities was proposed by CNRS in collaboration with CEA. The contract concerning the production of those cavities will be signed soon.

Concerning the RFQ structure, currently R&D activities are ongoing at the Frankfurt University. Alternative solutions to the 4-rods option are presently under investigations. The contract with IAP is under preparation.

Civil Construction

The general design of the building including shielding and location of the RF system has been completed. Addional shielding material had to be located close to the transfer channel to reduce the radiation level coming from the SIS18 during operation.

Cavities

The prototype cavity (Fig. 2) [2] has been tested at the Frankfurt University. The desired resonance frequency and field distribution were achieved during the bead pull measurements campaign. The stainless steel stems and drift tubes were produced at IAP and later polished at GSI. The welding of those components into the outer cylinder will start in February 2013. Copper-plating is planned for summer followed by high power-rf testing at the dedicated cavity test stand.

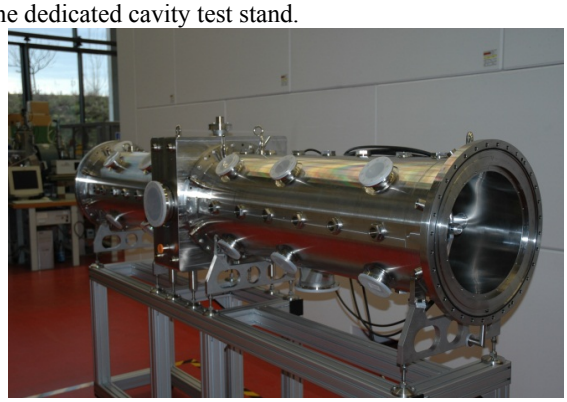

Figure 2: Prototype CCH-cavity (2.7 m)

Currently, the design of high power coupling loop is performed at GSI. RF simulations of the other cavities are ongoing. Within September all the specifications for the production of the technical drawings will be completed. A collaboration contract within GSI and the University of Frankfurt will be prepared shortly.

BPM / Phase Probes

RF simulations were performed to reduce the noise coming from the RF level and to compare that noise with the signal generated by the beam. Those simulations were performed for different energies and for different beam currents. The final design of the BPM has to be completed as soon as possible.

References

[1] *Technical Report "Proton Linac"*, https://edms.cern.ch/document/994418/1

[2] G. Clemente et al., PRST-AB **14**, 110101, (2011)

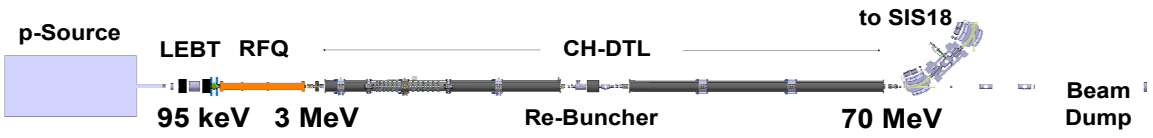

Figure 1: Conceptual layout of the FAIR proton Linac.

* g.clemente@gsi.de

Test of Digital Electronics for the p-LINAC BPMs at UNILAC

M. Almalki[1], P. Forck[1], W. Kaufmann[1], P. Kowina[1], R.Singh[1], C. Krüger[1], B. Baricevic[2], M. Znidarcic[2], R. Hrovatin[2]

[1]GSI, Darmstadt, Germany; [2]I-Tech, Solkan, Slovenia

Introduction

For the planned proton-LINAC at the FAIR facility [1], Beam Position Monitors (BPM) will be installed at 14 locations along the LINAC [2]. The digital signal processing to derive the transverse beam position and the beam velocity via time-of-flight determination could be implemented by so called Libera SPH (**Libera S**ingle **P**ass **H** **H**adron) electronic from company I-Tech [2,3]. The specification for position measurement is 0.1 mm spatial resolution averaged over one 30 ms long macro pulse. For time-of-flight beam velocity determination an accuracy of 10 ps is required corresponding to a phase of 1° with respect to 325 MHz acceleration frequency. A beam-based test was conducted at UNILAC to test the performance of Libera SPH electronics. For the same beam settings time-domain analogue signals were recorded with a 20 GSa/s oscilloscope for comparison. These time-domain data were Fourier-transformed and compared to the frequency-domain data from the Libera SPH.

Experimental Setup and First Results

The beam-based test was performed at UNILAC with a Ca^{10+} beam at 1.4 MeV/u and a beam current of ~ 80 µA. Using a buncher cavity for longitudinal focusing, several bunch shapes with different amplitudes and width were generated. A single BPM was used as a Bunch Arrival Monitor to further characterize the dependence of beam arrival time on bunch shape. The arrival time in time-domain was determined using zero crossing points with respect to a reference shape as depicted in Fig.1.

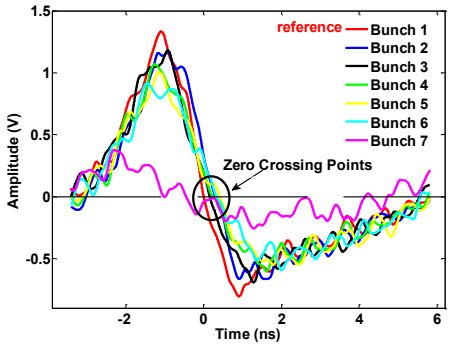

Figure 1: Time-domain recording of single bunches for different buncher cavity amplitudes are depicted to determine the individual zero crossing points.

The signals from a four plate BPM were sampled at 117.440 MSa/s with 16-bit ADC and digitally processed by Libera SPH unit to produce I and Q data stream for amplitude determination and phase calculation with respect to the 108.4 MHz acceleration frequecy. The RF analogue front-end of Libera SPH unit was customized for UNILAC parameters to perform the frequency-domain evaluation at the first two harmonics (108.4 MHz & 216.8 MHz). Using an amplification of 44 dB, the input peak voltages for seven bunch shapes recorded by Libera SPH were in the range of 0.57 V to 1.05 V.

As depicted in Fig. 2 the evaluated results showed some agreement between the Libera SPH phase readings and the time-domain measurements. Furthermore, Libera SPH processed the larger amplitude signals with a resolution of less than 1°. However, the FFT calculations of the single bunch data and the bunch stream are better matched to the time-domain evaluation.

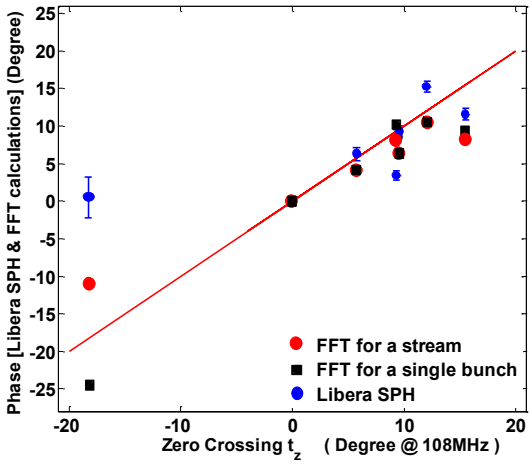

Figure 2: Time-domain data versus Libera SPH and FFT calculations for a single bunch and a stream of 30000 bunches.

Summary and Outlook

The tested Libera SPH digital electronics is suited for beam position determination but for phase detection it does not fulfil the requirements yet. However, modifications might lead to the desired accuracy. Therefore, further investigations are planned to improve the performance based on a comprehensive modelling of the digital signal processing algorithm.

References

[1] L. Groening et al., "FAIR Technical Design Report for Proton LINAC", March 2009. https://edms.cern.ch/document/994418/1

[2] P. Forck et al., "Design of the BPM System for the FAIR Proton-LINAC", GSI scientific report 2010.

[3] www.i-tech.si

New method for reducing the contribution of the beam position in the quadrupole signal *

Joel Alain Tsemo Kamga[1], *Wolfgang F.O. Müller*[1], *and Thomas Weiland*[1]

[1]Technische Universtät Darmstadt, Institut für Theorie Elektromagnetischer Felder (TEMF), Schlogartenstrasse 8, 64289 Darmstadt, Germany

Introduction

Quadrupole pickups are of particular importance in the accelerator physics because they allow the measurement of some parameters like the transverse extent of the beam, that can be obtained by measuring the quadrupole moment of the beam. However, this quadrupole moment is not only dependent on the r.m.s beam dimensions $(\sigma_x^2 - \sigma_y^2)$, which is the information we need, but also on the beam position $(\overline{x}^2 - \overline{y}^2)$ [1]. Therefore, the beam dimensions cannot be obtained directly from a traditional pickup, but by extracting from the quadrupole signal the contribution of the beam position. However a reasonable accuracy can be obtained only if the beam displacement from the center is small compared to the beam size. The goal of this work consists in developing a new method for calculating the quadrupole signal that will be much less sensitive to the beam position.

Methods to pickup $\sigma_x^2 - \sigma_y^2$

Known methods

The design used in this work is an electrostatic pickup with four plates as shown in Fig. (2a). The main goal of this work described in the introduction can be achieved by starting from the so called *Log-ratio method*, because this method compared for instance to the *difference/sum method* provides a quadrupole signal that is less sensitive to the beam position [2].

New method

The proposed method is described in Fig. (1). For more details about the *Log-ratio method*, see [2]. The quadrupole signal coming from the new structure is given by:

$$\Xi = \frac{160}{\ln(10)} \frac{\sin(\alpha)}{\alpha} \left[\left(1 - (1+2c)^2 \frac{\tan(\alpha/2)}{\alpha} \right) \cdot \frac{\overline{x}^2 - \overline{y}^2}{b^2} + \frac{\sigma_x^2 - \sigma_y^2}{b^2} \right] + O\left(\frac{1}{b^4}\right)$$

where α and b stand for the angular width of each electrode and the pickup radius, respectively. From the above Equation, while omit 4^{rd} order, an appropriate factor c can be found to eliminate the square term of the beam position.

* Work supported by GSI.

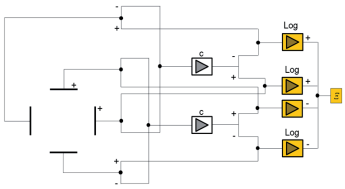

Figure 1: Pickup design for the new method

Simulation results

CST Particle Studio (PIC Solver) was used for the simulation. The transverse beam extent σ_x, σ_y was assumed to be less than $0.2b$ and the normalized beam velocity β was 0.5.

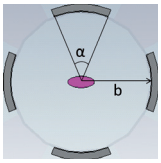

(a) Pickup design

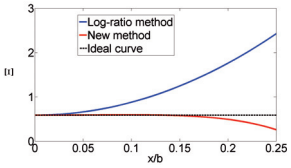

(b) Analytical results

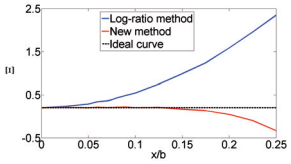

(c) Simulation results at 50 MHz

Figure 2: Quadrupole signal when $\overline{y} = 0$, $\alpha = 45^o$, $b = 50$ mm, σ_x/b = 0.1, σ_y/b = 0.025

Conclusions

In this work we have presented a new method to considerably reduce the effect of the beam position on the quadrupole signal. Looking at Fig. (2b) and (2c), we can see a good agreement between the analytical results and the simulations. The future work consists in testing the method to the other pickup types.

References

[1] A. Jansson, D.J. Williams "A new optimised quadrupole pick-up design using magnet coupling".

[2] P. Li, B. G. Sun, Q. Luo, X. H. Wang, H. L. Xu "New Methods of measuring Emittance Using Beam Position Monitors".

[3] CST GmbH, "CST PARTICLE STUDIO".

Engineering Study of the SIS100 Radiation Resistant Quadrupole Magnet Environment

N. Pyka[1], A. Kalimov[2], U. Kopf[3], and C. Mühle[1]

[1]GSI, Darmstadt, Germany, [2]State Polytechnic University, St. Petersburg, Russia; [3]PROCAD GmbH, Kleinheubach, Germany

A part of the extraction area of SIS100 is exposed to unavoidable particle loss during beam operation [1, 2]. The origin may be due to ion beam halo or due to ion beam losses during slow extraction. These losses will mainly be deposited into a dedicated radiation resistant quadrupole magnet doublet [3]. These magnets will be highly activated. Hence, maintenance will be extremely difficult if not impossible. A particular challenge would be the handling of heating devices to re-establish the necessary XHV conditions inside the beam pipe after a vacuum break. For this reason an automatic device has been designed to drive apart the magnet and position a heater box around the vacuum chamber. After the heating process has been finished, the heater box will be removed and the magnets are automatically repositioned properly. This special quadrupole doublet is located in cell-2 of sector-5 of SIS100.

Adjustment and moving device

The adjustment and moving device for these quadrupole magnets is rather challenging. It has to be very stable since each side of the magnet weights several tons. High rigidity is demanded since neither deformation nor torque is acceptable in order to assure reproducible movements and to withstand magnetic forces during operation. Lastly, in the final phase of closure the iron yoke and the coils have to match into the fits. Beyond that, the available space for this device is restricted to all sides by other installed equipment.

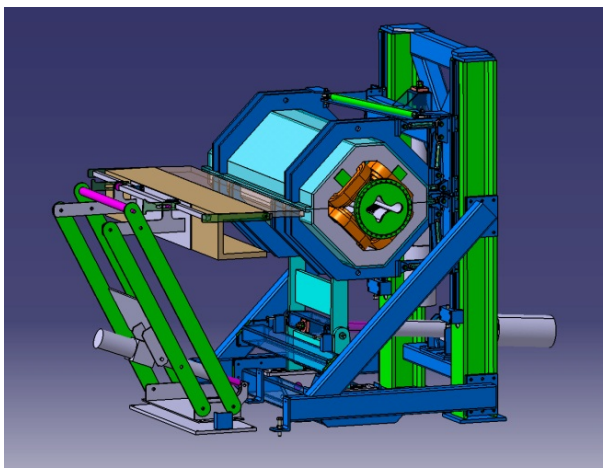

Figure 1: One radiation resistant quadrupole magnet in normal position hold by its adjustment and moving device; heater box on the left hand side in standby position. The vacuum chamber -beam pipe- is located between the coils.

The quadrupole magnet is symmetrically divided into an upper and lower part with a support structure around to absorb the forces during operation at high current. Each coil has to be installed separately in advance into one quarter of the iron yoke. The coil is mechanically fixed inside the mould of the yoke. Afterwards, two quarter of yoke and coil are mounted together via a thick sheet plate which itself is stabilized and hold by reinforcement stirrups. The latter are connected with the main holding structure via suspension bars.

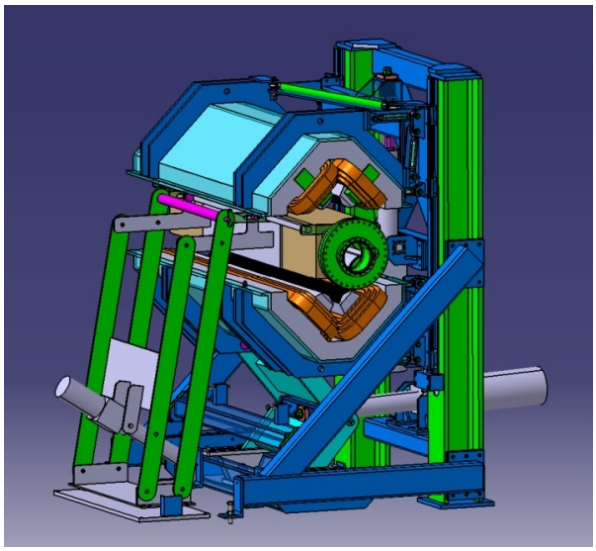

Figure 2: The quadrupole magnet opened with the beam pipe heater box in heating position.

On the basis of the existing design, the final construction and building of the adjustment and moving device can be placed. A careful adjustment and test phase of the whole assembly including the magnet has to follow the delivery before a fully automated routine operation can start.

References

[1] N. Pyka, et al., GSI Scientific Report 2009, Darmstadt, 2010, p. 98.

[2] A. Sokolov, et al., GSI Scientific Report 2011, Darmstadt, May 2012, p. 354.

[3] A. Kalimov, Radiation Resistant Quadrupol for SIS100, GSI Internal Report (2012).

TFS for SIS 18/SIS100

M. Alhumaidi[2], *U. Blell*[1], *J. Florenkowski*[1], *and V. Kornilov*[1]
[1]GSI, Darmstadt, Germany; [2]TU Darmstadt, Darmstadt, Germany

This short report gives an overview of the work on the project Transverse Feedback System (TFS) for the SIS 18, which will be commissioned later on at the SIS 100 of FAIR project, upon its completion.

The TFS is planned mainly for the SIS 100. However, experiments will be done this year 2013 after commissioning it at the SIS 18 for testing its functionality on stabilizing a real beam.

A new concept for using multiple pickups for estimating the feedback correction signal (beam angle at the kicker position) in order to minimize noise power. Furthermore, a system design for the existing SIS 18 facility has been developed.

Noise Minimization Using Multiple Pickups

A new concept for using multiple pickups for estimating beam angle at the kicker position has been addressed. The estimated signal should be the driving feedback signal of the kicker.

The signals from the different pickups are delayed, such that they correspond to the same bunch. Consequently a weighted sum of the delayed signals is suggested as an estimator of the beam angle at the kicker. The weighting coefficients are calculated such that the estimator is unbiased, i. e. the output corresponds to the actual beam angle at the kicker for non-noisy pickup signals. Furthermore, the estimator must give the minimal noise power at the output among all linear unbiased estimators. This is the so called Minimum-variance unbiased estimator (MVUE).

Simulation Results

The results are depicted in Figure 1 for horizontal direction of doublet mode. As a reference we take the noise power for using the closest two PUs to the kicker, which are the currently used PUs for the TFS in the SIS 18. Two curves are depicted, i.e. the noise power reduction by using increasing number of closest PUs to the kicker and the noise power reduction by using the best combinations of increasing number of PUs.

System Design

An overview of the main TFS design is depiction in Figure 2. The System is to be implemented on a Virtex 6 FPGA kit from the company Xilinx. The position data from the PUs are sampled and preprocessed at the Libera kits from the company intrumentation technology. The data are then sent from the Liberas to the TFS board via Aurora multi-Gigabit communication cores each.

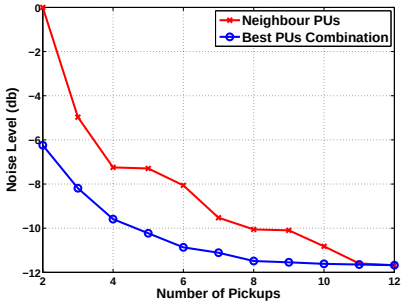

Figure 1: Noise power reduction.

In order to feedback head-tail oscillations, which become dangerous for high beam intensities, three positions are measured for every bunch, i.e., two for the ends and one for the middle.

In the case of coasting beam, three bunch positions per rf period are enough. Therefore, a generic data packet containing postion data and time stamps can be sent from each Libera to the TFS.

Providing feedback parameters, e.g., revolution frequency and linear combination factors, and system configuration are done by an external computer via ethernet connection. Implementation is planned to be finalized by October, where commissioning phase on the SIS18 will start.

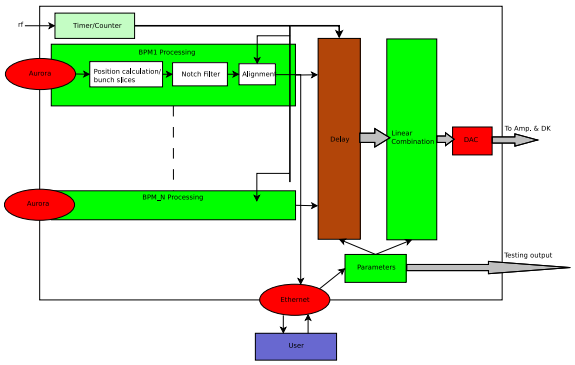

Figure 2: TFS design.

References

[1] M. Alhumaidi and A.M. Zoubir, “A TRANSVERSE FEEDBACK SYSTEM USING MULTIPLE PICKUPS FOR NOISE MINIMIZATION”, IPAC’11, September 2011, San Sebastin, Spain.

[2] M. Alhumaidi and A.M. Zoubir, “A ROBUST TRANSVERSE FEEDBACK SYSTEM”, IPAC’12, May 2012, New Orleans, USA.

FAIR HEBT System – Design and Status Report

F. Hagenbuck, S. Ratschow and P. Spiller

GSI, Darmstadt, Germany

The main goal of the last year was to complete the detailed specifications of the magnets including vacuum chambers and supports of the High Energy Beam Transport (HEBT) system [1] needed in module 0-3 of FAIR [2]. With starting the procurement of the first batch of magnets the realization phase of the HEBT system has started. Nevertheless optimisations in the ion optical layout (IOL) were required and carried out in parallel.

Ion Optical layout

All changes since the March 2011 IOL could be done without modifying the requirements for the building planning. By the end of the year a new official IOL was released, which includes the following larger modifications:

- A conflict with a crane runway in building G004 could be solved by repositioning four dipoles in T3F1 (module 6). The original height of the building could thus be kept while in the last part of the vertical transfer section the vertical distance from T3F1 to T1X2 was reduced.
- In TXL2 all quadrupoles were shifted to reduce unused free spaces. Thereby the remaining drift spaces got longer and were equipped with diagnostics, steerers, etc.
- In T1X1 the quadrupoles had to be moved as well to provide space for the installation of diagnostics.
- The Super-FRS ring branch is not in line with the end of the Antiproton separator. This offset, which was introduced when the HESR was moved to the west, was thought to be effected by double use of two dipoles at two different bending angles. This turned out to be impractical as their good field region would have to be made much wider. Meanwhile two additional dipoles are foreseen. As TFC1 is running in this region in between two other beam lines (whose magnets largely dictated the geometry of the newly laid out part) even this change in footprint of the accelerator had no influence on the building requirements.
- The CBM/HADES focusing system is planned to be made from normal conducting quadrupoles. Originally the quadrupoles were planned to be constructed from 750mm long modules each separately connected to the cooling water. Now it is foreseen to use 2250mm long quadrupoles instead, which will minimise the influence of the quadrupole fringe fields.
- Currently the usage of the SIS100 machine setup beam dump for emergency extraction of light ions from SIS100 is considered. From the beam transport point of view all magnets in between the SIS100 and the dump would need to be ramped at the same speed as the accelerator ring. This concept is under discussion and not yet finalized.

Technical Systems Design

The major part of the HEBT magnets (338 of 356) needed in module 0-3 is split into three batches. Next to batch1 (51 dipoles) also batch2 (17 dipoles, 102 quadrupoles, 80 steerers) and batch3 (5 dipoles, 71 quadrupoles, 12 steerers) were assigned, after a visit of GSI experts at the manufacturer, by the in-kind review board to the Efremov institute, St. Petersburg, Russia (magnets including supports). The corresponding vacuum chambers will be built by the Budker institute (BINP), Novosibirsk, Russia, in close contact with the Efremov institute. The detailed specifications – comprising magnets, supports and vacuum chambers – for batch1 were completed and handed over to the FAIR company in July 2012, the contract between FAIR and BINP was signed in January 2013, the contract between FAIR and Efremov is supposed to be signed in the beginning of 2013 as well. The detailed specifications for batch2 will be available in the mid of March 2013, the specifications for batch3 in the mid of May 2013. However, the production order of the components has to follow the classification of the HEBT system into beam lines for primary and secondary beams which is not reflected in the split-up into batch1-3.

The magnets not covered by Efremov – 2 CR equivalent dipoles and 5 CR wide type quadrupoles as well as 9 Super-FRS quadrupoles – should be procured together with the magnets of the corresponding machines.

The 3D (CATIA) modelling of the HEBT system was further worked out in close collaboration between the department of mechanical integration (ENMI) and an external engineering company with the main focus on preparing 3D models and drawings for the detailed specifications of batch1-3.

A first draft concept of assembly-, alignment- and disassembly processes for the beam lines in the central transfer building G004 was worked out in an advanced design project between ENMI and the department of computer integrated design of the TU Darmstadt.

Major efforts were taken to deliver further detailed input for the building planning. E.g. 3D models of the terraced ramps for the SIS100 injection and extraction beam line as well as for the SIS100 injection beam dump were prepared. Supply units on the HEBT supply area in G017.1 were completely rearranged to optimise false floor height and provide mandatory escape routes. Positions to cross below/over beam lines as well as for firewalls were fixed. In close collaboration with the radiation protection department several mobile radiation protection labyrinths were defined, e.g. for G004A, T113 and T112.

References

[1] FAIR Technical Design Report (TDR) – High Energy Beam Transport, GSI, December 2008

[2] FAIR Green Paper – The Modularized Start Version, GSI, October 2009

FAIR SIS100 Status Report

P. Spiller, O. Boine-Frankenheim, U. Blell, L. Bozyk, G. Franchetti, E. Fischer, E. Floch, F. Hagenbuck, M. Kauschke, A. Krämer, P. Kowina, H.G. Koenig, H. Klingbeil, M. Kirk, U. Laier,. P. Meier, C. Mühle, C. Omet, D. Ondreka, N. Pyka, H. Ramakers, S. Sorge, J. Stadlmann, S. Wilfert

GSI, Darmstadt, Germany

SYSTEM DESIGN

The system design has been further detailed. In order to prepare the specification of the extractions system components, special attention has been directed onto the completion of the design of the extraction straight. In this context, the design of the radiation hard normal conducting quadrupole magnets downstream the electrostatic septa has been developed. A special lifting device is required to open the two heavy yoke halfs for the bake-out system of the vaccum chamber. The special vacuum chambers of the normal conducting magnets consist of a main chamber for the revolving beam and an attached anti-chamber which hosts an impact plate for stripped beam ions and NEG panels for the removal desorped molecules.

New beam dynamics studies for the Proton operation have indicated potential beam loss by an insufficient bucket area. Therefore, the original concept of avoiding a gamma-T jump by means of a dedicated optics setting requires further verifications. However, it has been decided to keep a fast transition energy crossing as fall back-option. Therefore, positions for fast s.c. jump-quadruples has been defined and the feasibility of appropriate s.c. magnets is being studied. The application of the correction multipole systems situated at the ends of the six arcs has been studied for various beam dynamics issues. The main resonances in the neighbourhood of the heavy ion working point have been identified and the decision has been taken to build all quadrupoles as normal magnets, all sextupole magnets as skew magnets and all octupole magnets as normal magnets.

SUPERCONDUCTING MAGNETS

The design of the SIS100 dipole module has been completed by the manufacturer BNG. All major design reviews have been passed and the production of major parts of the magnet has been started. The special superconducting wire based on a Copper-Manganese matrix has been delivered from VNIINM (Bochvar) and the cable for the first of series dipole magnet could be produced without major difficulties or wire ruptures. The winding technique for the production of the single layer coil has been developed by means of a copper dummy cable. After initial difficulties, the small radius of curvatures of the coil ends could be realized with sufficiently small tolerances. However, it turned out that the production of the single layer coil is more challenging than of the two layer coil.

A major quadrupole module of the arc center has been selected as first of series module. The production ready design of this module and all its subcomponents (steerer magnet, sextupole magnet, BPM, cryocatcher, vacuum system, girder, cryostat etc.) has been completed by the GSI design department. I parallel, the tendering process for the completion of the engineering design of all remaining modules was launched. For the layout of the cryostat safety system, which shall cover major damages of the He system, simulations on the hydraulic shock propagations are performed at ILK Dresden.

RF SYSTEMS

The specifications for the acceleration and bunch compression systems and all appendices have been completed. The procurement of the ferrit loaded cavities of the acceleration system is in the responsibility of the FAIR GmbH, while the bunch compression cavities will be procured as German inkind contribution by GSI. The procurement of the supply units, the low level Rf systems and gap periphery will be excecuted in a separate processes. All tendering processes are in preparation.

INJECTION/EXTRACTION SYSTEMS

Further tests have been performed with the model setup of the bipolar kicker pulse power generator. Alternatively, a new circuit layout has been proposed which seem to provide more safety with respect to the cross talk among the two main thyratron switches. The new circuit layout makes use of two PFN systems instead of the originally foreseen one PFN system, but does not require a main pulse transformer.

LOCAL CRYOGENICS

A major change in the design of the SIS100 local cryogenics system has been proposed. All HTS current lead boxes, originally situated in the second floor of the supply tunnel, have been moved into the niches on the level of the accelerator. Thereby, two cold links could be removed completely. The challenge of the remaining cold link in niche 5 has been reduced to the supply the reference magnet system instead of the supply of the accelerator.

Two major specifications for local cryogenics components which will be part of the string test have been completed. In parallel, Wroclaw University continued working on the design of the bypass lines. The layout of the interconnections at the ends of the accelerator arcs are under design.

Effect of beam loss on long-term beam survival in SIS100

G. Franchetti, S. Sorge
GSI, Darmstadt, Germany

We present here results of beam loss during the injection of U^{+28} for an improved modeling of the nonlinear lattice of SIS100 as previous simulations reported in Ref. [1] where lacking of the effect of gradient errors. In Fig. 1a is shown for a possible model of the SIS100 the resonance web, which is formed by integer, half integer, third and fourth order normal and skew resonances. These resonances are found via tune scans of the short-term dynamic aperture (1000 turns). Beam survival (first bunch) for several intensities during one second storage are shown in Fig. 1b. The maximum intensity injected is of 0.625×10^{11} ions/bunch, which creates a large tune-shift represented schematically in the picture. The space charge tune-spread overlaps with 4 resonances hence several macro-particles will cross one or more lattice resonances, therefore periodic resonance crossing will affect the particle dynamics. The resulting first bunch survival is distinctively intensity dependent as shown by the black curve (0.125×10^{11} ion/bunch) in which beam survival is much better with almost no beam loss (Fig. 1b). Note that for the maximum intensity bunches, beam loss is more than 90% conflicting with the requirement of "low beam loss" needed for applying frozen model algorithms. Regardless the issue of self-consistency, the reduction of beam loss will certainly make the prediction with frozen algorithms more reliable. In Fig. 1c is shown again the working diagram with now the effect of an "ad hoc" activated compensation system, using also skew sextupoles located in the actual position of those foreseen in SIS100. The corresponding beam survival is comforting (Fig. 1d) as the beam loss appears significantly mitigated, validating also the computational algorithm for space charge. We also estimate the effect of the self-consistency on large beam loss scenario where the main complexity arises from the multiple resonance crossing. To assess the effect of large beam loss, as first approach we re-update in the algorithm only the intensity leaving the bunch sizes unchanged (hence noise is avoided). The results are shown in Fig. 2. The two black curves show the beam survival for 0.250×10^{11}, and 0.625×10^{11} ions/bunch, correspondent to the green and red curves in Fig. 1b. This improved procedure causes the black curves of beam survival to shift upward to the corresponding red curves as indicated by the blue arrows. The reason of this improved beam survival cannot be explained easier, but it appears that for SIS100 there is a beneficial effect. The green curves in Fig. 2 show results from an attempt of modeling the algorithm (Markovian mapping Ref. [2]) via a semi-analytic approach. These results are, however, conflicting with experimental findings in which beam loss (naturally self-consistent) are found larger than those predicted by simulations [3]. Further studies will be dedicated to this topic.

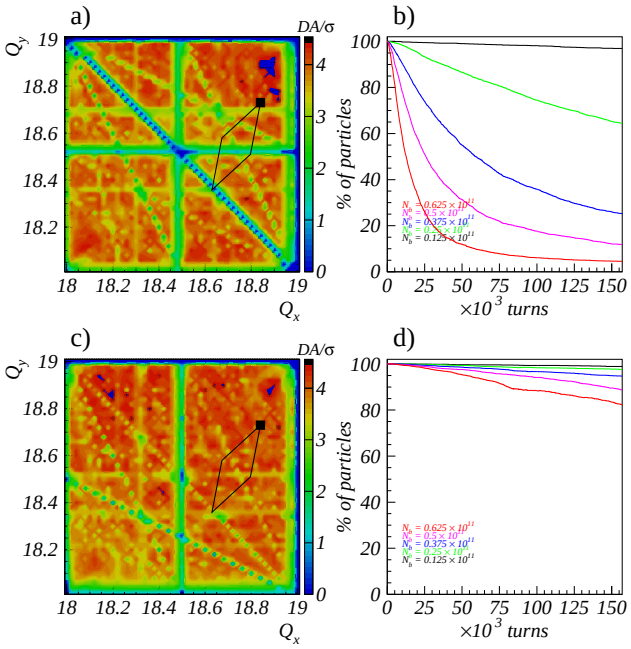

Figure 1: Resonance diagram and beam survival for uncorrected system (top). The same simulation when resonance overlapping the space charge tune-spread are compensated.

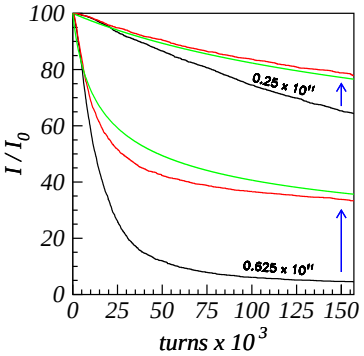

Figure 2: Comparison of the frozen space charge improved simulations (red curves) with a Markovian mapping approach (green curves). In black are shown the frozen space charge simulation results.

References

[1] G. Franchetti and S. Sorge, IPAC 2011, MOPS002. p. 589.
[2] G. Franchetti, Proc. HB2012, to be published on JACoW.
[3] G. Franchetti *et al.*, Phys. Rev. ST Accel. Beams **13**, 114203 (2010); G. Franchetti *et el.*, Phys. Rev. ST Accel. Beams **6**, 124201 (2003).

Influence of chromaticity correction on beam loss during SIS-100 proton operation

S. Sorge[*]*, GSI, Darmstadt, Germany*

In this report, results of multi-particle tracking simulations performed with MAD-X in order to estimate particle loss during SIS-100 proton operation are presented. The proton cycle requires the usage of beam optics which provide $\gamma_{tr} = 45.5$ in order to achieve the extraction energy $E = 29$ GeV without transition crossing. At this stage, a lattice consisting of magnets without errors and a single harmonic rf cavity to simulate synchrotron oscillations was used, where a scenario without acceleration was considered. The working point was $(Q_x, Q_y) = (21.8, 17.7)$ because it fits well in the mesh of resonance lines so that resonance excitation can be minimised.

The large-γ_{tr} lattice causes some difficulties. Besides horizontal beta and dispersion functions with large maxima, one finds the horizontal chromaticity $\xi_x = -2.44$. Assuming the maximum relative momentum deviation $\delta_{max} \equiv \Delta p_{max}/p = \mp 0.0043$ [1], the resulting maximum chromatic tune deviation is

$$\Delta Q_{x,max} = \xi_x Q_x \delta_{max} = \pm 0.23. \qquad (1)$$

Hence, the full tune spread is only a little less than 0.5 and, in any case, particles with large momentum deviations will approach an integer or half-integer tune. As a result, beam loss of about $9\ \%$ was found in multi-particle tracking simulations, about $1\ \%$ is considered as acceptable.

To investigate the generation of particle loss in more detail, single particles were tracked along the closed orbit deviation arising from their momentum deviations δ. In doing so, trajectories in the longitudinal phase space plane were found which are strongly non-symmetric with respect to the sign of δ, see Fig. 1, which is caused by a strong δ dependence of the phase slip factor, $\eta(\delta) = \eta_0 + \eta_1 \delta$. The result is the formation of the fixed point in longitudinal phase space, $(-ct, \delta) = (0, \delta_{FP})$, where $\eta(\delta_{FP}) = 0$, so that particles reach large positive momentum deviations, cross the half-integer resonance at $Q_{x,res} = 21.5$, and become lost. In order to avoid that, the chromaticities were partially corrected using all main sextupoles to reduce the maximum chromatic tune deviations to $\Delta Q_{x,max} = \Delta Q_{y,max} = \pm 0.1$. Correcting two chromaticities, ξ_x, ξ_y with 56 sextupoles allows to apply additional constraints. In order to minimise the non-linear influence of the sextupoles on the beam behaviour, three constraints were applied:

$$\sum_{i=1}^{n_{sext}} (k_2 L)_i^2 \rightarrow \text{min.} \qquad (2)$$

$$\sum_{i=1}^{n_{sext}} (k_2 L \beta_x)_i^2 \rightarrow \text{min.} \qquad (3)$$

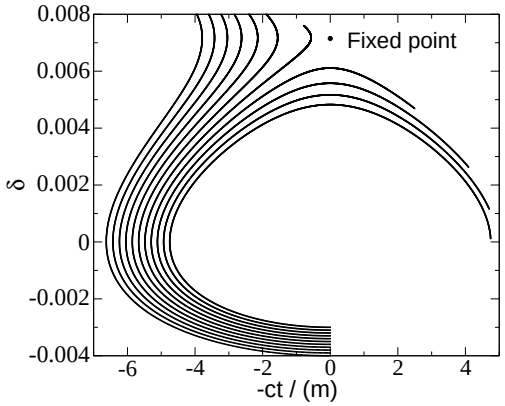

Figure 1: Trajectories in longitudinal phase space of 11 particles started at equidistant δ, $-ct = 0$, and transverse positions of the resulting closed orbit deviation $(x_{co}, x'_{co}) = (D_x, D'_x)\delta$. The chromaticities were not corrected. A fixed point appears at approximately $\delta_{FP} = 0.0071$.

Table 1: δ_{FP} from single-particle simulations, see caption of Fig. 1, and particle loss from multi-particle simulations.

Chromaticity correction	δ_{FP}	P_{loss}
none	0.0071	$8.8\ \%$
constraint of Eq. (2)	0.0079	$3.4\ \%$
constraint of Eq. (3)	0.0101	$0.04\ \%$
constraint of Eq. (4)	0.0101	$0.02\ \%$

$$\sum_{i=1}^{n_{sext}} (k_2 L)_i^2 \left(\beta_{x,i}^2 - D_{x,i}^2\right) \rightarrow \text{min.}, \qquad (4)$$

where in the 2nd and 3rd constraints the influence of horizontal beta and / or dispersion functions at the locations of the sextupoles were regarded. In doing so, more symmetric longitudinal particle trajectories and larger δ_{FP} could be achieved, see central column of Table 1.

The resulting particle losses, estimated by multi-particle tracking simulations, were found to be strongly reduced due to chromaticity correction, see right column of Table 1. However, the shifts of δ_{FP} obtained with the present settings for the sextupoles were found by chance what is somewhat unsatisfactory. Hence, the study will be continued by searching for a systematic way to set the sextupoles in order to shift δ_{FP} and by the inclusion of systematic and random multipolar errors in dipoles and quadrupoles.

References

[1] O. Chorniy, private communication.

[*] S.Sorge@gsi.de

Bench measurements of beam coupling impedances for SIS100 components

L. Eidam [*1], *U. Niedermayer*[1,2], *and O. Boine-Frankenheim*[1,2]
[1]GSI, Darmstadt, Germany; [2]TEMF, TU-Darmstadt, Germany

Introduction

Coupling impedance describes the force acting back on the beam due to the electromagnetic properties of the accelerator environment. The development of the high intensity Synchrotron SIS100 requires a detailed knowledge of the impedance contribution of individual components to prevent beam instabilities and additional heat load. Besides analytic calculations, which are only possible for simplified structures, numerical calculations are in progress. Bench measurements are required to cross-check simulations and their input parameters.

Measurement system

Measurements are performed by adding a central conductor on the beam axis to a DUT (Device Under Test) and connecting this formed transmission line to a VNA (Vector Network Analyzer). Describing this transmission line by an equivalent circuit the DUT adds a serial impedance to the equivalent line of a reference beam pipe. This additional impedance causes a variation of the wave number, which can be determined by changes of the scattering matrix. Assuming a successful matching of the transmission line to the VNA, the reflections vanish and the correlation for the longitudinal coupling impedance is [1]:

$$Z_{\parallel} = Z_0 \cdot \ln\left(\frac{S_{21}^R}{S_{21}^D}\right) \cdot \left(1 + \frac{\ln(S_{21}^D)}{\ln(S_{21}^R)}\right) \qquad (1)$$

where S_{21}^R / S_{21}^D describes the transmission component of the scattering matrix for the reference/DUT. To determine the transverse coupling impedance two anti-parallel driven wires are needed [2]:

$$Z_{\perp} = \frac{cZ}{\omega\Delta^2} \qquad (2)$$

where Δ is the displacement of the wires and Z comes from Eq. 1.
For low frequencies the accuracy can be increased by using a multiturn coil instead of two anti-parallel driven wires and measuring directly impedance variations by a LCR-meter. The sensitivity increases by number of turns squared:

$$Z_{\perp} = \frac{c \cdot (Z_{DUT} - Z_{Ref})}{\omega\Delta^2 N^2} \qquad (3)$$

As example the low frequency transverse impedance of a circular pipe will be discussed. The coupling impedance has been determined by several numerical and analytical calculations [3, 4]. A very good agreement between measurements and calculations has been achieved as seen in Fig. (1). The drawback of using coils with many turns is the lower resonance frequency. Nearby the resonance measurements are not possible, so this method is limited up to several MHz. To achieve good results in a broad frequency range two different coils were produced. One for high accuracy at low frequencies and one for measurements up to 2 MHz.

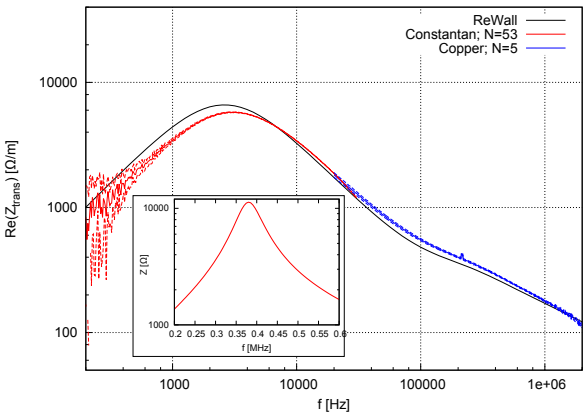

Figure 1: Measurement of the real part of the coupling impedance for a circular beam pipe compared to analytical results made by Rewall [4], the small picture shows the first resonance of the coil with 53 turns.

Conclusion and Outlook

The experimental setup for measuring coupling impedances in the low frequency regime has been build sucessfully. The measurement results for a reference beam pipe structure were compared to analytic calculations. The experimental setup for measurements above 2 MHz is presently under construction. The first planed device under test will be a kicker magnet module, where the ferrite and also the supply network cause to large impedances. The results of both measurement methods will be compared with numerical calculations of the measurement setup using CST MWS [5].

References

[1] V.G. Vaccaro, Coupling Impedance Measurements: An Improved Wire Method, INFN/TC-94/023

[2] G. Nassibian, F. Sacherer, NIM 159 (1979)

[3] U. Niedermayer, NIM A687, 2012

[4] N. Mounet, B. Salvant, E. Mètral, "ReWall", www.cern.ch/imp, 2010

[5] CST Studio Suite 2012®, www.cst.com

* l.eidam@gsi.de

TESTS ON SUPERCONDUCTING DIPOLE MODULES: DISPLACEMENT AND DEFORMATION

I. Pschorn[#], T. Miertsch[+], GSI, Darmstadt, Germany

Introduction

The Survey & Alignment Group within the department NC-Magnets and Alignment is involved in the organization and development of measuring concepts and techniques for the future FAIR project. These tasks are based on the knowledge and the experiences obtained by works at the existing machine at the GSI. The measurements for the coming facility contain tests both for normal conducting and superconducting magnets. The following passage gives an overview about a test at a superconducting dipole from the Budker Institute of Nuclear Physics (BINP) in Novosibirsk in order to detect displacements and deformations of the cold mass versus the cryostat.

Two prototypes of the dedicated dipole were extensively tested during the last years. Concerning alignment aspects, one of the questions to be answered was the behavior of the dipole yoke with respect to its surrounding cryostat during pumping processes, thermal cycles and after transport.

Magnet movement and yoke deformation

For financial reasons there was for a start no explicit development of a totally new measuring system for monitoring the displacement of a (in operative phases) non-accessible magnet at temperatures of 4 K. In fact, an existing KERN E2 theodolite combined with a FARO SI.2 laser tracker and supplemented by suitable tools for lighting and sighting together with an appropriate measuring methodology were chosen in order to be able to detect movements and deformations of the magnet yoke at least in vertical and longitudinal direction as well as its roll and tilt angle.

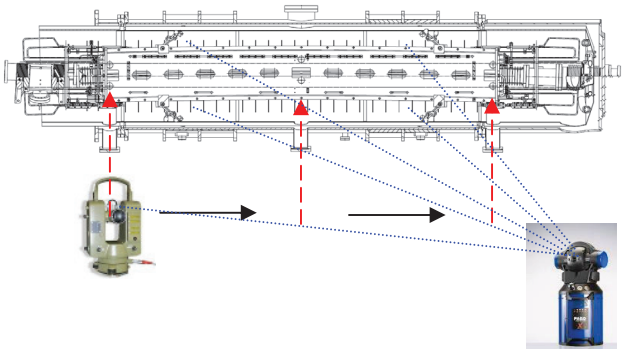

Figure 1: Measurement setup in front of cryostat and enclosed superconducting dipole with fit bores (top view)

The theodolite is placed rectangular to the magnets beam axis, each in front of the three cryostat windows in order to observe the 6 inside targets which are located next to the edges and at the center of the upper yoke half (fig. 1). Observations are possible in evacuated, cold condition of the superconducting dipole module as well as when the magnet has room temperature and the vacuum vessel is ventilated. Correction values for the glass window and the lighting unit with its semitransparent mirror are considered. The positions and orientation of the theodolite itself in relation to the outer cryostat fiducials are precisely determined by the laser tracker. As a result of fiducialisation measurements the relation between the magnets fit bores and the cryostat fiducials in warm condition with an opened cryostat is precisely known.

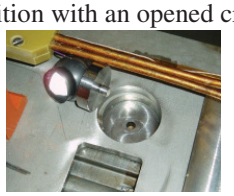

Figure 2 left: Fit bore in dipole yoke, right: Customized targets

This measuring procedure was performed at the same prototype in a total of 22 rounds during a period of 12 months, whereas 9 measurements - including fiducialisation - were carried out at warm (~297 K), 5 runs at cold (~10 K) and 8 runs at graded yoke temperatures from 18 K to 265 K. In doing so the tests were executed at very different condition of the module like opened (ventilated) and closed cryostat (under vacuum), with and without vacuum chamber and other mechanical fittings, after quenches.

Even after a number of thermal cycles the positions of the fiducial points that are placed on the surface of the upper magnet yoke are highly reproducible with mean standard deviations of ±0.06 mm. The data of the fiducial positions must not be seen as absolute displacements of the yoke but need to be corrected by appropriate material correction values in order to get real information about the movement of the magnet center axis. Doing this it can be stated that this investigated dipole remains at the edges in its axial position both in warm and cold condition within ±0.1 mm. An exception is the yoke center which shows a non-explicable bulge of +0.25 mm at almost operative temperature.

References

[1] A. Schnegg, “Bestimmung der geometrischer Veränderungen des BINP SIS100 Dipol“ (measurement report), 25.10.2011

[2] T. Miertsch, “Stabilitätskontrolle“ (measurement report), 16.03.2011 / 24.02.2012

[#] i.pschorn@gsi.de
[+] t.miertsch@gsi.de

FAIR Realisation – Superconducting Magnets Production Start

E. Fischer[*], *A. Bleile, E. Floch, W. Freisleben, V. Maroussov, F. Marzouki, H. Müller, J. P. Meier, A. Mierau, H. Raach, P. Schnizer, A. Stafiniak, K. Sugita, S. Y. Shim, P. Szwangruber, and D. Theuerkauf*

GSI, Darmstadt, Germany

Introduction

The realisation phase of the pilot project of FAIR - the SIS100 synchrotron was started in January 2012, when the manufacturing contract for the dipole series was signed with Babcock Noell. In parallel to the preparation for manufacturing the first dipole, urgent designed work was done for the quadrupole and corrector magnets as well as planning the cryogenic test facilities at GSI. The same work was concentrated on the Super Fragment Separator. In addition significant success was achieved in collaboration work by manufacturing and testing a first SIS300 dipole model magnet.

Superconducting Magnets

Rapidly-Cycling Magnets for SIS100

Dipoles The design phase of a First of Series magnet (FoS) finished with the FDR in October 2012 and the production of the magnet has started with the manufacturing of the most critical component: the superconducting single layer coil (see Fig. 1). It will be ready for testing in spring 2013. After a successful test of this first dipole the series production will start.

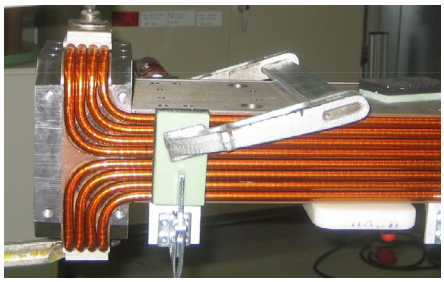

Figure 1: Winding of a copper dummy-coil of the SIS100 FoS dipole

Quadrupole Modules The SIS100 Quadrupole module contains two superconducting quadrupole magnets, corrector magnets and other devices such as BPM in the common quadrupole module cryostat [1, 2]. In the SIS100 accelerator ring, 9 standard types and 3 special types (at the injection, extraction and high radiation area), 84 modules in total will be installed.

The production of the module will be conducted as the German-Russian In-Kind contribution to FAIR. GSI will provide the superconducting wires and the all devices except the magnets. The AC-losses and the hydraulic resistances were recalculated based on the final design of the magnet components [3, 4]. The mechanical stability of the QP-doublet modules versus thermal and mechanical load was investigated. The assembly of the components, its mounting and operation procedure were analysed with FE models. The component stability during mounting was investigating, together with the cold mass suspension and its stability at 4 K (see also Fig. 2). A first series doublet will be build next, tested at JINR/Dubna and to be operated at GSIs prototype test facility, and at a test string setup (dipole and quadrupole doublet module as minimum). The final design of all different series SIS100 quadrupole doublet module types is actually under preparation. A tender for preparing CAD models to production plans is running, which will be based on the development results of the first doublet (type 3-F2).

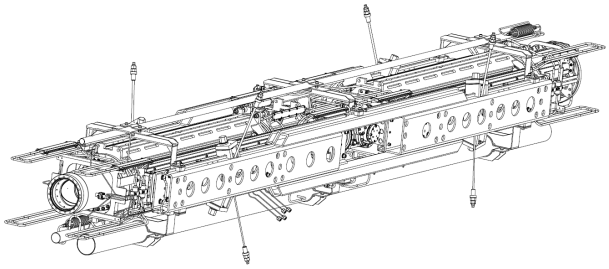

Figure 2: CAD Model of the cold mass of the SIS100 quadrupole doublet module, type 3-F2, including suspension system.

Rapidly-Cycling Magnets for SIS300

The first prototype of a SIS300 curved dipole has been tested at INFN-LASA in Milan, Italy [7, 8]. At the moment a second enhanced collared coil is built in frame of the European CRISP project. At IHEP in Protvino, Russia, a second SIS300 prototype quadrupole with enhanced low loss cable is built and tested. (We acknowledge the support of the European Community-Research Infrastructure Activity under the FP7 program CRISP [Grant agreement no: 283745] Work Package 5). A first prototype of the steering dipole is ready to be tested (see Fig. 3).

Magnets for the Super-FRS

Superferric dipole The superferric dipoles are no longer an In-Kind contribution from FAIR collaboration

[*] e.fischer@gsi.de

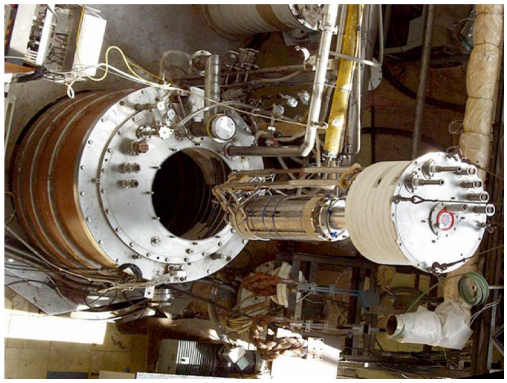

Figure 3: Insertion of the SIS300 prototype quadrupole into the test cryostat

partners, but will be purchased via a FAIR call for tender. The necessary specifications are under preparation and shall be ready until summer 2013.

Superconducting multiplets The superferric multiplets are a GSI In-Kind contribution to the FAIR-Project. The specifications for the different magnets, as well as the integrated modules are nearly finished and the call for tender is in preparation and will start in early 2013.

Planning for Testing

The general testing strategy was defined this year: SIS100 dipoles will be tested in the now currently erected series test facility at GSI, SIS100 quadrupole units are foreseen to be tested in collaboration with JINR and the Super-FRS magnet will be tested at CERN.

Prototype Test Facility Activities

The first SIS100 dipole magnet will be tested at the prototype test facility this year. So all required upgrade activities were started last year in particular: a new power converter has been procured and new HTS current leads were ordered with their production already started.

Series Test Facility Activities

The SIS100 series test facility will be constructed in SH2/SH3 at GSI. In the hall, 3 test benches for the series production SIS100 dipole magnets and the string test facility, which demonstrates the SIS100 accelerator construction and the system operation, will be installed. For the infrastructures such as power converters and cryo-plant, an utilitly building (SH5) will be errected. Necessary preparations are ongoing with the commissioning of the facility foreseen in the middle of 2014. Full scale tests will be start 2014 and continue until 2017.

Testing Super-FRS Magnets at CERN

The site of test was identified (building 180) and the infrastructure is refurbished. The collaboration committee will guide this process.

Electrical Systems and Magnet Protection

The coil design and 3D quench calculations were continued; both machines (SIS100 and SuperFRS) will use dump resistors as protection devices with their preliminary values defined. Bridge detectors for FAIR were successfully tested on a SIS100 dipole, and now the series is being tendered. For the SIS100 correctors special mutual inductance detectors are foreseen and will be tested on the SIS100 sextupole magnet currently fabricated at JINR.

The electrical safety systems for measuring insulation parameters for the SIS100 magnets are projected and shall be developed together with collaboration partners. Paschen tests were performed on the SIS100 prototype dipole performed in the range of 10^{-4} to 10^{-1} mBar. As the machine is not Paschen tight, appropriate interlocks are foreseen for the cryostat vacuum system.

Conclusion

In 2012 we achieved important results in preparing manufacturing and testing of the first fast ramped superconducting magnets of the SIS100, the Super-FRS and the SIS300 - core components of the FAIR project.

References

[1] E. Fischer et al.. “Superconducting Quadrupole Module System for the SIS100 Synchrotron”, RuPAC’12, St. Petersburg, September 2012, p. 143-145

[2] E. Fischer et al. “Sc Magnet Development for SIS100 at FAIR”, IPAC’13, New Orleans, June 2012, p. 3545-35478
%vspace.9ex

[3] E. Fischer et al. “Status of the SC Magnets for the SIS100 Synchrotron and the NICA Project” IEEE Journal Appl. Supercon. to be published

[4] P. Schnizer et al.“SIS100 Dipole Magnet Optimisation and Local Toroidal Multipoles”, IEEE Journal Appl. Supercon. to be published

[5] P. Schnizer et al. “Some comments to magnetic field representation for beam dynamic calculations”, IPAC’13, New Orleans, June 2012, p. 262-264

[6] Khodzhibagiyan, H.G. and Fischer, E. and Kovalenko, A.D., “New Design for the SIS100/300 Magnet Cooling” IEEE T. Appl. Supercon., 2006, vol. 16 p. 411 - 414

[7] P. Fabbricatore et al., “The curved fast ramped superconducting dipoles for FAIR SIS300 synchrotron: from first model to future developments”, IEEE Journal Appl. Supercon., to be published

[8] M. Sorbi et al.“The functional test of the SIS300 model dipole at INFN-LASA”, IEEE Journal Appl. Supercon. to be published

[9] G. Sobiegraj “The capacitor discharge setup for testing the turn-to-turn insulation of a superconducting magnet coil” Book of Reports, GSI Summer Student Program 2012

Status of the Integration of Technical Subsystems of the SIS100 Extraction Straight Section

N. Pyka[1], U. Blell[1], L. Bozyk[1], M. Kauschke[1], M. Konradt[1], U. Kopf[2], P. Kowina[1], A. Krämer[1], J.P. Meier[1], P. Moritz[1], C. Mühle[1], D. Ondreka[1], P. Spiller[1], S. Wilfert[1], and C. Will[1]

[1]GSI, Darmstadt, Germany; [2]PROCAD GmbH, Kleinheubach, Germany.

The integration of all technical subsystems of the extraction straight section, sector 5 of SIS100, by means of a 3D (CATIA) modelling has been continued [1, 2]. The following devices have been added and integrated successfully to complete all necessary components for beam operation: the knock-out-exciter, the BTF-exciter, the ion beam halo-scraper, the radiation resistant quadrupole doublet, and the internal emergency beam dump. In addition, each of the technical subsystems was improved until a state to be used for the call for tender of the corresponding component. Three out of four cells in the straight section have almost been finished with respect to integration.

Integration of components

The extraction straight comprises many different components. Figure 1 shows a part of cell 3 as example. Nearly all of them needed to be revised to meet the requirements in position, in size, to allow for alignment purposes, for the connections inside and outside of the vacuum chamber, and to compensate the elongation during the bake-out of the vacuum chamber in order to achieve the necessary XHV conditions.

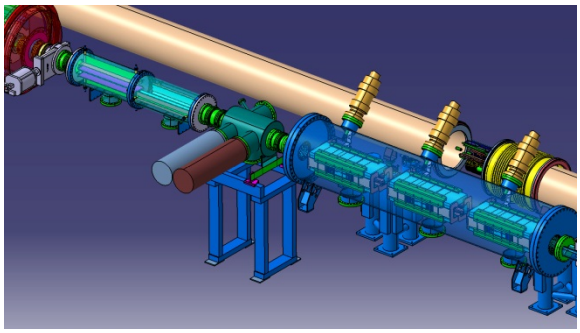

Figure 1: From left to right (part of cell 3): BTF-exciter, SEM grid and beam stopper, and triple kicker group. In the background the He-Bypass line can be seen.

Realistic solutions were implemented for all components at least up to a design stage which represents all technical requirements properly and therefore allows the final construction in a direct way.

Magnet extraction septum 3 has been equipped with a challenging but feasible solution for the guidance and connection of the complex coil system, figure 2. The main coils, blue, for the vertical deflection field, the steering coils for the horizontal deflection in case of the slow extraction mode of operation, and the correction coils, beige, are all guided in the necessary compact and independent way, maintaining the cooling water flow in the different coil sections.

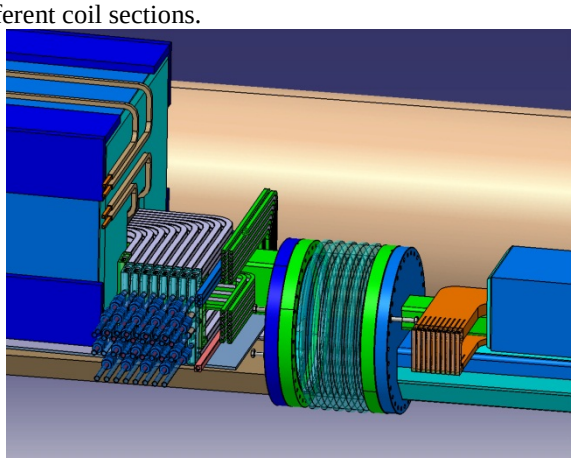

Figure 2: Detail of the crossover section between magnetic extraction septum-2 (right) and -3 (left). The bellow in the middle serves to compensate the elongation during the bake-out of the vacuum chamber and to adjust the septa in transverse direction.

The internal beam dump has been implemented by modifying the entrance section of the extractor cryostat and magnetic septum 3, figure 3. A huge gate valve allows for the passage of the circulating and the extracted beam independently.

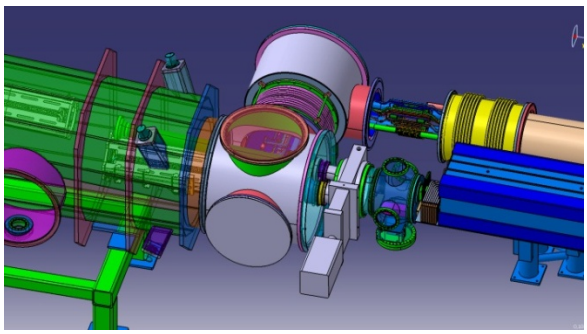

Figure 3: Crossover from MS-3 (right), via the internal beam dump, and the vacuum gate valve into the feed-in-box (grey with flanges) of the extractor cryostat (left)

References

[1] N. Pyka, et al., GSI Scientific Report 2010, Darmstadt, 2011, p. 289.

[2] P. Spiller, et al., GSI Scientific Report 2010, Darmstadt, 2011, p. 287.

BTF of bunches influenced by an electron lens

P. Görgen[1], *O. Boine-Frankenheim*[1], *and W. Fischer*[2]

[1]TEMF, TU-Darmstadt; [2]Brookhaven National Laboratory (BNL), Upton, NY, USA

The transverse Beam Transfer Function (BTF) represents an important diagnostic tool for the tune spread and and damping rates in synchrotrons and storage rings. Here we investigate the BTF for bunches interacting with a localized electron lens. The investigation takes place in collaboration with BNL and focuses on BTF of relativistic bunches affected by the beam-beam interaction and an electron lens. The electron lens should compensate the beam-beam tune spread. We investigate the BTF using a threefold approach:

Firstly we use measurements taken at the Relativistic Heavy Ion Collider (RHIC) [1]. Similar bunch parameters are expected in the SIS100 during proton operation. We focus on RHIC measurements of beams under so-called split-tune conditions. In RHIC, the beam-beam interaction can couple the bunches in the two rings coherently. This coherent coupling is strong when the fractional tunes of the two beams lie close to each other. Under split tune conditions the difference in fractional tunes is chosen large to reduce the amplitude of the coherent modes and move them away from or into the incoherent spectrum. Apart from the coherent coupling, the amplitude dependent fields of the beams result in an amplitude dependent kick on the particles of the other beam in the machine. This leads to an incoherent amplitude dependent tune shift of the particles.

Secondly we use a particle tracking code wherein we built a simplified model of RHIC: We use the one-turn-map to translate particles around the lattice of the two rings of RHIC. For each collision point the interaction of the beams is taken into account by computing the two-dimensional transverse fields of the beams, exchanging them and kicking the particles of the other beam accordingly. The BTF is modeled as a sinusoidal signal modifying the trasverse momentum of the particles. The excitation is swept in frequency and the BTF are computed in post-processing as the fraction of the complex response amplitude and the excitation amplitude. The model of the BTF is directly applicable for modeling FAIR machines.

Thirdly we obtain the BTF analytically using the dispersion function in the integral representation provided in [2]. We include the electron lens and the beam-beam interaction as external tune shifts. The integral is solved numerically and the results are compared with the simulation in fig. 1. After the successful validation of the simulation code against analytic models [3] we focused on the scenario including an electron lens. Such a device is presently being installed at RHIC. The BTF should be used to analyze its performance. In an electron lens an electron beam with a Gaussian profile acts as a nonlinear lens compensating the beam-beam interaction. For a bunch interacting with an electron lens the aforementioned analytic BTF should

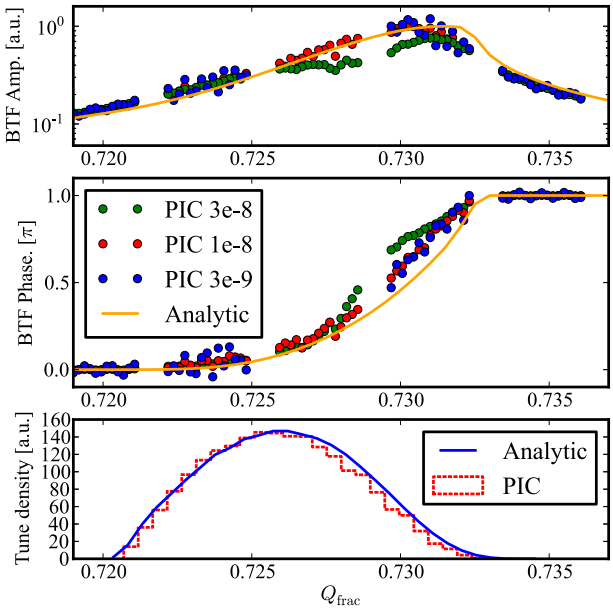

Figure 1: Horizontal BTF, particle tune density, comparison of simulation (PIC) for split tunes ($Q_h = 28.691$ and 28.735 in the two rings) and analytic results. Note the deviation for higher BTF excitation amplitudes in the simulations (at 3e-8). The observed agreement between simulation and analytic results holds for a range of beam currents. Higher currents give broader peaks shifted towards lower tunes.

hold. At split tune conditions the beam-beam should produce BTF comparable to an electron lens provided that the conditions are such that no coherent beam-beam modes lie near the incoherent spectrum. The double peak structure observed in some measured BTFs from beams under split tune conditions was reproduced in the simulations and found to be present only at high BTF excitation amplitude. At low excitation amplitude the analytic model reproduces the simulations of BTF both under e-lens and split tune conditions well. This allows to recover the strength of the observed interaction from the BTF of a beam interacting with an e-lens or a split-tune beam-beam interaction. We are confident we can now apply our method to SIS100 proton operation, where instead of beam-beam and e-lens we will encounter space charge and octupoles for Landau damping.

References

[1] S. White et al., Proc. of IPAC 2012, pp. 195ff

[2] V. Kornilov et al. doi:10.1103/PhysRevSTAB.11.014201

[3] P. Goergen et al. WEAAC2, Proc. of ICAP 2012

Development of cryosorption pumps for the SIS100 cryogenic beam vacuum system

St. Wilfert, T. Hackler, M. Wengenroth

GSI, Darmstadt, Germany

Abstract

We report on the development of a cryosorption pump type for the use in the cryogenic beam vacuum system of SIS100 and present some results on its pumping performance.

Introduction

The planned high beam energies and intensities in SIS 100 require stable vacuum pressures in the low UHV range. In order to reach and maintain such low vacuum levels even under dynamic machine operation, approximately 82% of the beam vacuum system will be operated at cryogenic temperatures. At temperatures between 5K…15K, the chamber walls become a very effective cryopump with high linear pumping speed and high pumping capacity for all condensable gases species. However, hydrogen and helium are exceptions as they can not be pumped by cryocondensation, but only by cryosorption. Since the cold chamber walls have a strongly limited cryosorption capacity for these both gas species, supplementary lumped pumps are required in order to provide additional pumping speed for H_2 and He. For that reason, the use of auxiliary cryosorption pumps in the cryogenic beam line sections is foreseen.

Within the framework of planning and designing the cryogenic SIS100 vacuum system, a prototype of a cryosorption pump has been developed and experimentally investigated.

Prototype and Experimental Results

Cryosorption pumps are passive pumping elements which typically contain highly porous materials (charcoal, molecular sieves or metal sponges) as cryosorbent. Cooled down to LHe temperatures, they are able to pump significant amounts of hardly condensable gas species by physical adsorption (i.e. cryosorption). Their property to be perfect gas sinks make their use particular in cryogenic vacuum systems indispensable, where the cryosorption capacity of bare tube walls is strongly limited. For SIS100, sixty cryosorption pumps distributed in 13m intervals between each SIS100 dipole doublet are foreseen.

The cryosorption pump to be developed had to meet three important key requirements: (i) a simple and cost-effective pump structure, (ii) the cryosorbent must be cooled uniformly down to LHe temperatures, and (iii) a high pumping speed as well as a high pumping capacity for He and H_2 are needed. The demands require a pump design as shown in Figure 1. The cryosorption pump developed is mounted on a conventional DN100CF flange and consists of six round cryopanels screwed on an axial running LHe cooling tube. Both, the LHe supply and the return line are embedded in the common central cooling tube. The cryopanels are copper disks coated with a well-tested charcoal as cryosorbent, denoted by SCII, produced by Chemviron Carbon Corp. The charcoal provided by KIT (Karlsruhe Institute of Technology, Germany) exhibits good pumping performance for H_2 and He at cryogenic temperatures [1,2]. In total, 25g charcoal are distributed over all six cryopanels.

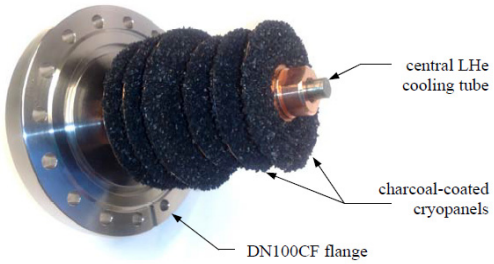

Figure 1: Prototype of a cryosorption pump for SIS100 cryogenic beam vacuum system

The pumping speed for H_2 and He was measured using a standardized PNEUROP vacuum dome [3]. The results are given in Figures 2. For H_2 at room temperature, the pumping speed is about 500ℓ/s, and for He approx. 250ℓ/s. The total pumping capacity of the pump is estimated theoretically to about 200mbar·ℓ at 5K.

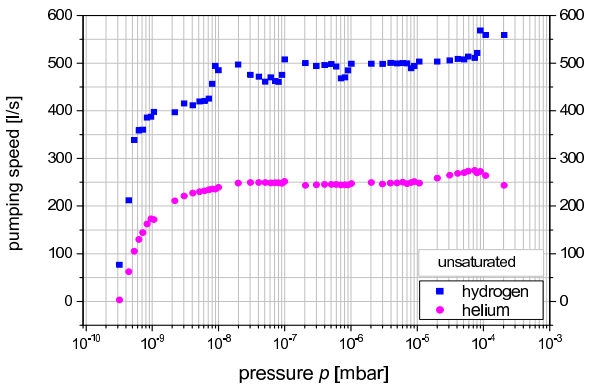

Figure 2: Measured pumping speed for H_2 and He

Summary

The pump prototype developed is characterized by a high pumping speed and high pumping capacity for both H_2 and He. Since the pump fulfils all requirements specified above, the pump design has been proved to be suitable for use in the future SIS100 machine.

References

[1] C. Day, Colloids and Surfaces A: Physicochemical and Engineering Aspects 187–188 (2001), 187–206

[2] M. Wengenroth, Diploma thesis, FH Wiesbaden (2008)

[3] DIN 28428, Deutsches Institut für Normung (1978)

Investigation of Thin-Sheet Approaches to Simulate Beam Tube Losses.*

J. Trommler[1], *S. Koch*[1], *and T. Weiland*[1]
[1]TU Darmstadt, Germany

Introduction

The beam tube in acceleration facilities is often made of very thin metal. During the switch-on or switch-off process of the dipole magnets, the fast changes in the magnetic field lead to eddy currents in the conductive beam tube. Consequently, electric losses emerge and the magnetic field inside the tube is perturbed. Both effects can be of importance. The purpose of this study is to accurately simulate the eddy current losses and their influence on the magnetic field by using the finite element method (FEM). Thin-sheet

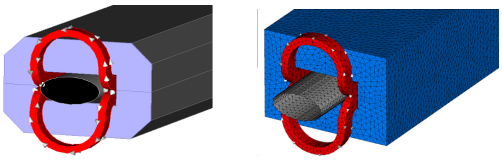

Figure 1: Model and reduced mesh of dipole magnet.

approaches are applied to avoid the high computational costs when the FEM is used with very small sheets like the beam tube. In a first step, different approaches from the literature are compared to a new method developed by the authors for a small test case. The focus of the comparison is put on the condition number of the final system matrix.

Thin-Sheet Approaches

Two main difficulties arise from very thin objects in the calculation domain. Automatic meshing often fails or ends up in inappropriate meshes. But even with a mesh found, the resulting system matrix is ill-conditioned and, consequently, hard to solve with iterative methods. The common idea of thin-sheet approaches is to replace the sheet volume by an interface and applying impedance transmission conditions (ITCs) between the two sides of the interface in order to reproduce the physical properties of the original sheet volume.

Many ITCs are given in the literature. The easiest way is to replace the interface by a perfect electric conductor which is a good approximation when the skin depth δ_{skin} is very small compared to the sheet thickness δ. Another possibility is the assumption that the field do not vary across the sheet [1]. These special elements (SE) are very easy to implement but only valid if the skin depth is large compared to the sheet thickness. For all other cases, higher order approximations are required, like ITCs using hyperbolic functions in thickness direction [2] (ITC-MB) or ITCs derived from prismatic elements where a polynomial of arbitrary order is considered in thickness direction (thin-sheet bases, TSB-<Order>). In taking the condition number of the system matrix into account, a new method [3] was derived by the authors that combines the advantages of [1] and [2]. In the new approach (MBF), the basis functions of the finite elements that are connected to the interface are modified in order to account for the variation in thickness direction.

Comparison

A 1D domain (μ_0, $\sigma = 0$) of 1m length including a sheet (μ_0, $\sigma = 10^7\,\mathrm{Sm}^{-1}$, $\delta = 1\mathrm{mm}$) is exited by a surface current $J_s = \pm 1000\mathrm{A/m}$ at the two boundaries. The condition number of the resulting system matrix is compared for all the thin sheet approaches with respect to the ratio $\delta_{\mathrm{skin}}/\delta$. All approaches are in some ranges advantageous, in some

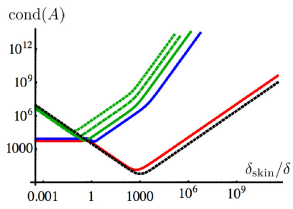

Method	rel. error $\mathrm{Re}\{E_z(-\frac{\delta}{2})\}$
SE	1
MBF	exact
TSB-2 (–)	0.18
TSB-4 (--)	0.0019
TSB-6 (···)	0.000003
ITC-MB	exact

Figure 2: Comparison of the condition number and the relative field error at the sheet boundary.

not, but it is obvious that the new method (MBF) combines the advantages of SE and ITC-MB: It is as accurate as the ITC-MB but also as good in the conditioning as SE.

Summary

Different thin-sheet approaches are compared with respect to the conditioning of the final system of equations. From the findings, a new method was developed that performs better according to this measure.

References

[1] Nakata, T. and Takahashi, N. and Fujiwara, K. and Shiraki, Y., “3-D magnetic field analysis using special elements”, IEEE Trans. Magn. 1990, vol. 26, no. 5, p. 2379–2381

[2] Mayergoyz, I.D. and Bedrosian, G., “On calculation of 3-D eddy currents in conducting and magnetic shells”, IEEE Trans. Magn. 1995, vol. 31, no. 3, p. 1319–1324

[3] Trommler, J. and Koch, S. and Weiland, T., “A finite-element approach in order to avoid ill-conditioning in thin-sheet problems in frequency domain - Application to magneto-quasistatics”, JCAM 2012, vol. 236, no. 18, p. 4671–4680

*Work supported by Kooperationsvertrag GSI - TU Darmstadt

Status report of the Collector Ring (CR)

A. Dolinskii, U. Blell, F. Becker, O. Chorniy, C. Dimopoulou , O. Gorda, U. Laier , H. Leibrock, S. Litvinov, J. Kurdal, I. Schurig, M. Steck, H. Welker

GSI, Darmstadt, Germany

System Design

In the frame of the progressing building and civil construction planning, a number of modifications in the CR system were implemented. For the civil construction planning, major assumptions have been made for the transportation, installation and maintenance of the CR components. The cross sections of the routes for transportation, the major transportation equipment and cranes were specified and summarized in a CR building specification document. The design of the CR layout accounting for all major ring components as simplified 3D CATIA models has been continued and completed for all ring sections. Major collisions have been identified and removed in an interactive process between the engineering- and ion optical designers.

In the context of the completion of the dipole, quadrupole and sextupole magnet designs the overall lattice cell has been further optimized. Cable lists, including cable types, numbers and start and end points have been established. Detailed requests for the supply room conditions were specified and information for component properties were handed over to the building planners.

Radiation of the CR system

The beam of 3 GeV negative particles ($\Delta p/p=6\%$) is injected from the p-bar separator into the CR. The ratio of pions to antiprotons is 100. These pions all decay in the CR. The detailed particle tracking in the ring in a combination with FLUKA simulations shows that the maximal radiation load for all CR system will be about 2.4 Gy/day if the CR operates 100% in the antiproton regime with a cycle time of 10 s.

Beam dynamics

The multipurpose operation of the CR requires that the orbit of the particle trajectories must be as smooth as possible in order to avoid the ring acceptance reduction at injection. Systematic studies of the Closed Orbit Distortion (COD) for all CR optics have been performed to define requirements for the corrector magnets, which were considered to be integrated either in the dipole or in the sextupole magnets. In calculations the random misalignments, roll and longitudinal placements of the dipoles, quadrupoles and Beam Position Monitor (BPM) in both horizontal and vertical planes have been introduced. Table 1 summarizes the results of these calculations, where the rms and maximum corrector strength required ("kick angle" in the table) to correct the closed orbit error in each case is given. In determining the maximum corrector strength we have considered the envelope of maximum corrector strength ignoring a few which lie outside this envelope. In the worst case considered, where the sigma of the magnet misalignment is 0.5 mm and magnets have a roll with a sigma of 0.5 mrad, the envelope of the maximum corrector strength required about ±3 mrad. If we can achieve this level of alignment tolerance, we will be operating the correctors with a maximum strength of 3 mrad giving us enough strength to correct for any unforeseen problem.

Table 1. Calculated Closed Orbit Distortion (COD) before and after correction in the horizontal (H) and vertical planes (V). 12(dip) means 12 correctors integrated in the dipole magnet. 6(h/v) - 6 horizontal/vertical combined corrector magnets in the long straight sections

	correctors	COD rms/max (mm)		rms/max (mrad)
		Before cor	After cor	Kick angle
H	12(dip)+6(h/v)	7.8 / 18	0.9 / 4.1	0.7 /2.4
V	12(dip)+6(h/v)	4.1 / 11.2	1.5 / 5.2	0.9 /3.1
V	24(sex)+6(h/v)	4.1 / 11.2	1.3 / 3.3	1.2 / 4.7

Different isochronous settings have been calculated [1], which give the possibility to measure masses of very exotic nuclei with mass-to-charge ratio up to A/q=4.1. The influence of the various field imperfections has been investigated and a proper sextupole-octupole correction scheme has been found. The required strength of octupole correctors should be within 100-600 G. Due to this correction the necessary mass accuracy $\Delta m/m=10^{-6}$ can be achieved for $\Delta p/p= \pm 0.2\%$. More details about the isochronous mode of the CR can be found in ref. [1].

Magnets

With the goal to procure the CR dipole magnets in 2013 the design of the dipole magnet has been slightly modified and completed. The detailed CR dipole specifications have been prepared at the end of 2012.

The CR optics of the injection scheme requires that the septum magnet deflects the incoming beam by 125 mrad onto the injection orbit. This requires a bending strength of 1.7 Tm. Initially a dc septum magnet was considered but quickly abandoned for the present pulsed magnet design. This decision was taken because of both the cooling problems anticipated with a calculated 398 kW power dissipation and the high running costs. To have a moderate power converter solution, the full-sine 600 ms (rise/fall time of 150 ms and flat top time of 5 ms) driving pulse is proposed. This gives the ramping rate of about 6.1 T/s. According to an ANSYS calculation, due to eddy currents the power dissipation in the injection septum chamber during the pulse is 1 kW. At the nominal operating conditions the mean power dissipation is about 79 kW for the cycle time of 1.5 s.

Power Converters

The concept of the power converter for the injection septum magnet has been reconsidered. To reduce losses due to eddy currents in the magnet and the vacuum chamber, the ramp up time was increased from 20 ms to 150 ms. The extraction septum power converter will be fast pulsed. The pulse power will be supplied by a capacitor of 90 mF capacitance; the required charging voltage is 850 V at the nominal peak current of 6.5 kA. The converters, both for the bending magnets and for the quadrupoles, form complicated networks with interlaced main and trimming supplies. The high stability requirements for the dipole power converter to handle the mass measurements (10^{-6}) are an additional challenge. In addition to a short time stability better than 10 ppm, the accuracy of the power converter is required to be 50 ppm.

RF system

The detailed specification have been established, proved and accepted by the FAIR company. A technical concept developed by GSI is considered as basis for further CR debuncher development. The main parameters of all subcomponents have been worked. A main contractor "Research Instruments" (RI) has been found and the technical design of the CR debuncher system is currently developed together with RI. The acquisition of the power supply units will start after the technical design has been established in Q3/2013. A variety of other subcomponents like the driver amplifier or the LLRF system is currently developed in house or in collaboration with different companies. The preseries RF station will be integrated by RI at GSI in Q4/2014.

Injection/extraction

The full aperture kicker magnet will be able to produce a field of 50 mT with a rise/fall time of 200 nsec in a magnet aperture of 290 x 160 mm^2 and over a total magnetic length of 1.35 m. For proper beam injection and extraction, 4 individual vacuum chambers are required, each is equipped with 3 kicker modules. The 3D field of the kicker magnets consisting of 3 modules is calculated. The particle tracking through this field has been done to define acceptable field performance on the flat top. Because of the field inhomogenity over the horizontal aperture the acceptance of the CR is predicted to be less by about 3% compared to the ideal linear optics. The kick variation in the median plane is required to be less than 2%. The preliminary design of the full aperture kicker magnets is still under study.

Beam diagnostics

The beam position monitor (BPM) is a prioritized component of the CR beam diagnostic. Beam position measurement with an accuracy better 5 mm for first turn diagnostics and an accuracy better 1 mm for the closed orbit measurement are specified. At the present stage the BPM electrodes are considered to be based on the spiral shape geometry. The disadvantage of such a geometry is a strong coupling between orthogonal electrodes. Therefore, the correlation between the electrode voltages and beam positions is not straightforward as, for example, in "shoe-box" type BPM. A realistic BPM model is used in numerical simulations in order to optimize the position calculation algorithm. This work is ongoing. Since the BPMs will be installed inside the wide aperture quadrupole magnets, their additional constraints to the BPM vacuum chamber are defined. The preliminary design of the spiral shaped electrodes and vacuum chamber, which must be of star-like shape, are shown in Fig.1. The Detailed Specification, which serves as an entry point for third parties, is in the final stage of preparation.

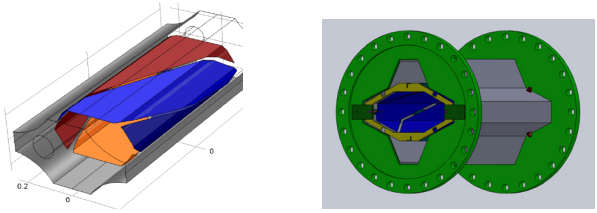

Fig1. Schematic drawing of the spiral-shape BPM electrodes inside the vacuum chamber (left) and preliminary vacuum chamber design (right).

Vacuum system

To reach the required beam lifetime, a vacuum pressure in the range of 10^{-9} mbar is needed. Therefore calculations of the pressure profile along the ring, where performed for various pumping speeds and pump positions to find the optimum positions [2]. Due to the required large aperture in the beam pipe (up to 480 mm horizontally) a new DN500CF was developed and tested. More details on this can be found in ref. [3]. In addition the first detailed specification of some vacuum chambers has been established. They describe in detail the required material properties, production and cleaning procedures.

Stochastic cooling

The CR serves mainly for fast stochastic cooling (SC) of antiproton and rare isotope beams, which have different velocities and requirements. The RF-block diagram of the SC system has been laid out; the technical specification of the 1-2 GHz power amplifiers has been written. The pickup slotline electrodes were further optimized, the first ceramic electrode plates have been delivered. Simulations of the Faltin electrodes for the Palmer pickup tank are underway. Two novel linear motor drive units were constructed; their synchronous operation will be tested at the GSI prototype pickup tank. A numerical code for solution of the 2D Fokker-Plank equation has been written. For more details see ref. [4].

References

[1] H. Weick et al., "Isochronicity Correction for Mass Measurements in CR", GSI Scientific Report 2012.
[2] J. Kurdal et al., "Vacuum Calculations of the FAIR Collector Ring", GSI Scientific Report 2012.
[3] L. Urban et al., "Analysis of ad DN500CF flange for the Collector Ring at FAIR", GSI Scientific Report 2012.
[4] C. Dimopoulou et.al,. "Developments for the CR stochastic cooling system", GSI Scientific Report 2012.

Analysis of a DN500CF flange for the Collector Ring of FAIR

L. Urban, A. Krämer, C. Will and I. Schurig

GSI, Darmstadt, Germany

Abstract

The Collector Ring (CR) is a storage ring of the accelerator complex of the Facility for Antiproton and Ion research (FAIR). Its purpose is the stochastic precooling of rare isotope and antiproton beams and the measure of the nuclear masses in an isochronous mode. Therefore large apertures of the beam pipe are needed in the ring. Due to this the use of flanges up to a size of DN500 are foreseen in some parts. The required vacuum pressure is in the range of 10^{-9} mbar, but due to radiation only metal sealed flanges can be used. An additional problem in the CR is a lack of space in longitudinal direction. In the technical specification ISO/TS 3669-2 CF flanges are only specified up to DN400CF [1]. Commercially available COF flanges have the drawback that their thickness of 43 mm for DN500 per flange is pretty large. Therefore, a 500CF knife-edge flange was designed and constructed, which has a thickness of only 28 mm per flange and which is still bake-able. Due to a smaller thickness one gains about 1.5 m additional space over the whole circumference of the CR.

Measurements

In order to perform leak tests of a DN500CF flange a setup was designed and commissioned at GSI, which consists of an extractor gauge, a residual gas analyzer and a pumping station. As gaskets we used OFHC flat copper gaskets with a thickness of 2 mm. The flange was mounted in vertical position and tightened with different torques (see figure 1). The final pressure and the leak rate were measured and the corresponding mass spectrum was recorded. Through further measurements, the behavior and the tightness of the flange were detected also during the bake-out.

For the measurements the flange was mounted at the setup and the screws were tightened. Then we measured the final pressure after 24h of pumping, determined the leak rate and recorded a mass spectrum. The torque was raised in steps of 5 Nm from 15 Nm up to 50 Nm (screws: DIN 933 M10x80-A4-80).

Table 1: torque, final pressure and leak rate

Torque [Nm]	Pressure [mbar]	Leak rate [mbarl/s]
15	$7x10^{-9}$	$1x10^{-10}$
20	$3.3x10^{-9}$	$1x10^{-10}$
25	$2.1x10^{-9}$	$1x10^{-10}$
30	$1.3x10^{-10}$	$1x10^{-10}$
35	$9x10^{-10}$	$1x10^{-10}$
40	$8x10^{-10}$	$1x10^{-10}$
45	$8x10^{-10}$	$1x10^{-10}$
50	$7x10^{-10}$	$1x10^{-10}$

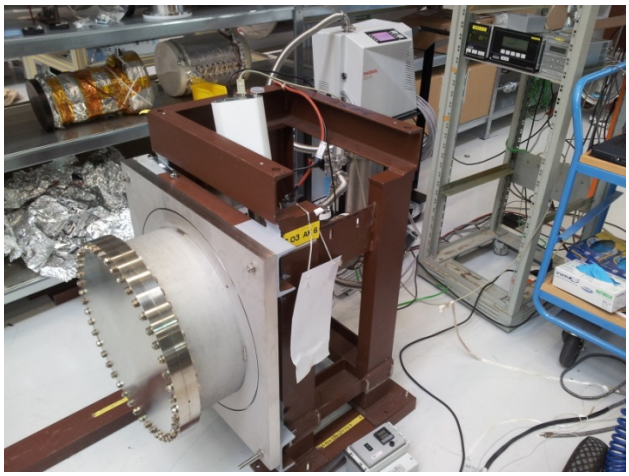

Figure 1: Test setup for the DN500CF flange.

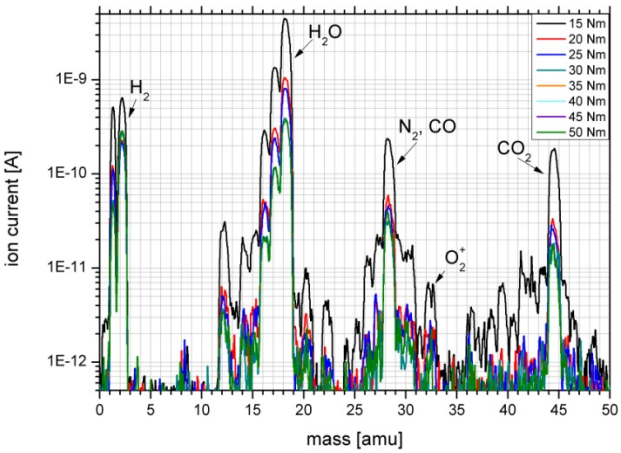

Figure 2: Comparison of RGA spectra for various torques.

Conclusion

First results of the measurement with the newly designed DN500CF knife-edge flanges were very promising. The ultimate pressure in the setup was $p=7x10^{-10}$ mbar and the leak rate was $L\leq1x10^{-10}$ mbar l/s. During the measurements we saw, that with a torque of more than 15 Nm there was no more space between the flanges. Looking into this, we figured out that the inner side of the flange on the recipient had a distortion of 0.2 mm most probably due to the welding. So the cutting edge of the flange cannot cut deep enough in the copper seal. With the help of a groove and/or a thicker gasket this problem could be overcome.

References

[1] Technical Specification ISO/TS 3669-2:2007(E)

Developments for the CR stochastic cooling system

C. Dimopoulou[1], D. Barker[1], R. Böhm[1], M. Dolinska[2], R. Hettrich[1], W. Maier[1], F. Nolden[1], C. Peschke[1], P. Petri[1], M. Steck[1], L. Thorndahl[3]

[1]GSI, Darmstadt, Germany; [2]Frankfurt University; [3]CERN, Geneva, Switzerland.

The Collector Ring (CR) serves mainly the fast 3D stochastic cooling (SC) of antiproton and rare isotope beams, which have different requirements. The SC system operates in the frequency bandwidth 1-2 GHz. The main challenges are the antiproton cooling by means of cryogenic movable pick-up electrodes and the fast two-stage cooling (Palmer method, followed by notch filter method) of the hot rare isotopes.

The FAIR Council has allocated this system to GSI as an in kind contribution. A detailed specification document describing the complete system and listing its main components has been prepared. The in-house engineering and design activities on various system components and their integration in the CR building have been intensified.

Electrodes and pick-up tanks

The prototype pick-up tank has been modified in the mechanical workshop in order to accommodate the two novel water-cooled linear motor drive units (Fig. 1) which were designed and manufactured in 2012; their synchronous operation remains to be tested. The cryogenic movable pick-up slotline electrodes were further optimized, the first ceramic electrode plates have been delivered. The pick-up electrodes will be cooled by helium cryoheads to about 20-30 K in order to enhance the signal to noise ratio. The intermediate cryoshield at 80 K inside the pick-up tank has been designed and ordered. It consists of 4 half-shells, each 1 m long and bears holes for the motor drives and openings for assembly purposes, it is made of oxygen-free copper and has to be gilded galvanically so as to reach very low thermal emissivity.

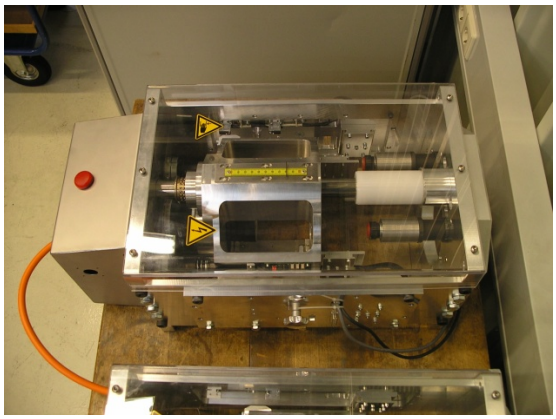

Figure 1: New linear motor drive unit.

Dedicated electromagnetic simulations with the HFSS code have been started in 2012 in order to design the electrodes (of Faltin type) of the Palmer pick-up.

RF signal processing and its components

A flexible RF signal processing scheme (RF block diagram) of the complete SC system has been laid out. It covers the transverse (horizontal, vertical) cooling branches as well as the longitudinal cooling using the notch filter, the time of flight (TOF) or the Palmer method.

The technical specification of the 1-2 GHz power amplifiers has been written, so that the procurement of this critical component can start in 2013. Because of the very demanding antiproton cooling a total cw microwave power of 8 kW is required, in combination with stringent requirements on amplitude flatness and phase linearity. Besides that, the short path between Palmer pick-up and kickers in the CR further restricts the allowed electrical length of the power amplifiers.

The experience gained from the successful tests of the prototype notch filter with beam in the ESR [1] is being used to optimize the set-up in view of the CR. In particular, the 180^0 hybrid which limited the filter performance will be replaced by a 180^0 power splitter.

Simulations of the system performance

The momentum cooling performance in the CR with the notch filter and TOF methods has been investigated theoretically using a Fokker-Planck approach (CERN code). The results confirm the necessity of a high-quality notch filter for efficient cooling; nevertheless, the TOF option is useful for pre-cooling of beam tails or in case of moderate cooling requirements [2].

In parallel, at CERN, a novel approach for simulating the cooling process in the time domain based on an ab initio calculation of the cooling and diffusion coefficients has been developed and applied to the CR case [3].

A numerical algorithm solving the 2D Fokker-Plank equation has been written at GSI [4]. This is a first effort towards a powerful treatment of the Palmer stochastic cooling of ions where, typically, the longitudinal and transverse phase space planes are strongly coupled.

References

[1] F. Nolden et al., ”ESR Operation and Development”, this report.

[2] C. Dimopoulou et al., IPAC’12, New Orleans, USA, May 2012, MOPPD005, http://www.jacow.org.

[3] L. Thorndahl et al., COOL’13, Mürren, Switzerland, http://www.jacow.org (to be published).

[4] M. Dolinska et al., IPAC’13, Shanghai, China, http://www.jacow.org (to be published).

Vacuum Calculations of the FAIR Collector Ring

J.Kurdal, J.Cavaco, I.Schurig

GSI, Darmstadt, Germany

Abstract

The Collector Ring (CR) of FAIR is characterised by a circumference of 225m and large beam pipe apertures in the order of 400mm. The CR is a storage ring; its design governed by the stochastic precooling of secondary particles, rare isotopes or antiprotons.

To reach the required beam life time, a pressure in the range of 10^{-9} mbar is needed. Therefore an in-situ bake-out of the ring is not required. Due to space constrains there is no possibility to mount large ion getter pumps, therefore new pumping solutions were studied.

The pumping concept is now based on NEG cartridge/ion getter combination pumps. To define the required pumping speed and positions of the pumps vacuum calculations of the CR were carried out by means of two different programs. The analysis of pressure profile of the whole ring was performed with VAKTRAK [1] (a transfer matrices program), which allowed us to optimise the position of the pumps. The conductance of each chamber was simulated with Molflow+ [2], a Monte Carlo Simulation program. The results obtained in these calculations for one arc will be presented and discussed.

Conductance Simulations

A Monte Carlo Simulation (Molflow+) was carried out, to determine the conductance for all different kinds of chambers mounted in one arc of the ring. To obtain the correct simulation data the CATIAV5® drawings have to be exported in stl. format. After an additional file modification required by Molflow+, the conductance for a specific gas is calculated by the following equation:

$$C = \frac{A_{Des} \cdot 11.77 \cdot \sqrt{\frac{28}{M_x}} \cdot A_i}{\sum_{Des} Part} \quad , \qquad (1)$$

where A_{Des} is the desorption area and 11.77 a factor given by the kinetic theory for N_2, A_i is the number of molecules absorbed on facet number i for the analysed part, M_x is the molecular mass of the specific gas, the $\sum_{Des} Part$ is the sum of all molecules generated, and C the conductance in [l/s].

Pressure Profile Calculations

For the pressure profile calculations VAKTRAK was used. The program required for every part an ICODE (a number to identify the part), length, conductance, pumping speed, outgassing, and 'Label' of the part. In conductance limited systems the longitudinal (equilibrium) pressure profile P is given by:

$$c \cdot \frac{d^2 P}{dz^2} - s \cdot P = -q \, , \qquad (2)$$

here is c the specific molecular conductance in [m·l/s], z the longitudinal position, s the linear pumping speed, and q the specific outgassing rate. The result for one arc of the CR is shown in Figure 1. The conductance was simulated with Molflow+ as explained before, the pumping speed of each pump was assumed to be 1000l/s for H_2 and the arc is around 75m long.

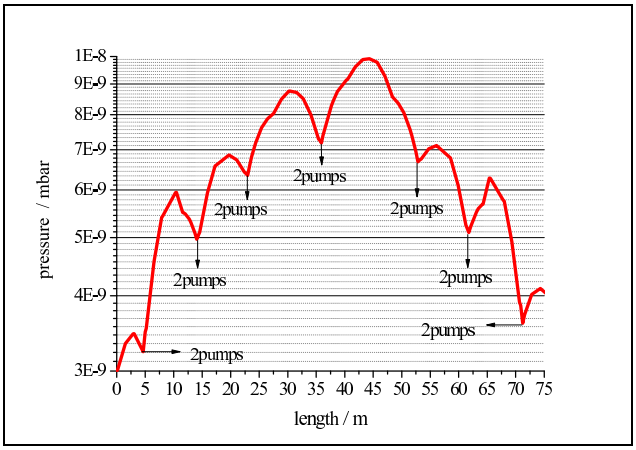

Figure 1: Pressure Profile for one arc of the CR.

The pressure is H_2 equivalent, and the considered outgassing rate is $1 \cdot 10^{-10}$mbar l/s cm^2.

Conclusion

A maximum pressure of $1 \cdot 10^{-8}$mbar was calculated at 45m from the beginning of the arc. This can be optimised by choosing more suitable pump positions.

References

[1] Volker Ziemann, "VAKTRAK", http://www.anst.uu.se/volkziemann/vaktrak2/

[2] Roberto Kersevan and Marton Szakacs, "Molflow+" http://test-molflow.web.cern.ch/

e/π identification and position resolution of high granularity TRD prototype based on MWPC *

M. Petriş[1], *M. Târzilă*[1], *M. Petrovici*[1], *V. Simion*[1], *V. Aprodu*[1], *D. Bartoş*[1], *A. Bercuci*[1], *G. Caragheorgheopol*[1], *V. Cătănescu*[1], *F. Constantin*[1], *L. Prodan*[1], *A. Radu*[1], *J. Adamczewski-Musch*[2], *and S. Linev*[2]

[1]NIPNE, Bucharest, Romania; [2]GSI, Darmstadt, Germany

The high granularity TRD prototype was designed and built as a single multi-wire proportional chamber with 2x4 mm amplification region coupled with a 4 mm drift zone. The readout electrode has triangular shaped pads of 2.7 cm height and 0.7 cm width with a readout cell area of 1 cm^2 corresponding to the requirements of the most inner zone of the first CBM-TRD station. Details on the architecture of this type of TRD prototype were already reported [1]. The present contribution is focused on the e/π discrimination and position resolution.

The in-beam tests were performed using a mixture of electrons and pions of 2-8 GeV/c momentum at T9 beam line of PS accelerator at CERN. The electrons and pions were selected using the information from a Cherenkov and a Pb glass calorimeter positioned in front and in the end of the beam line, respectivily. The detectors were flushed with a 80%Xe+20%CO_2 gas mixture. The triangular pads were readout by FASP front-end electronics [2, 3] selecting a shaping time of 40 ns. The measured pulse height

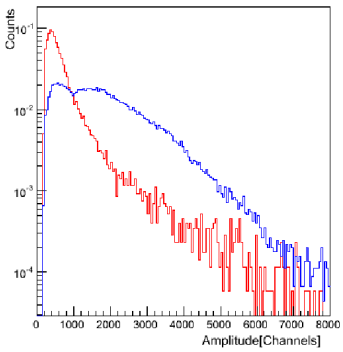

Figure 1: Pulse height distributions for pions (red line) and electrons (blue line)

distributions for electrons and pions at 3 GeV/c are shown in Fig.1 for an applied 2000 V anode voltage and 800 V drift voltage. The pion misidentification probability as a function of number of TRD layers (Fig.2) was obtained by Monte Carlo simulation based on the pulse height spectra presented in Fig.1. A pion misidentification probability of 1.25% for a 6 layer configuration was obtained using a regular foil radiator of 220 foils of 20 μm thickness and 250 μm air spacing. A 1% pion misidentification probability is obtained for a seven layer TRD configuration using a fibre radiator. The position across the pads is determined by the charge shared among consecutive rectangular pads:

* Work supported by EU-FP7/HP3 Grant No 283286 and Romanian NASR/CAPACITATI-Modul III contract nr. 179EU and NASR/NUCLEU Project

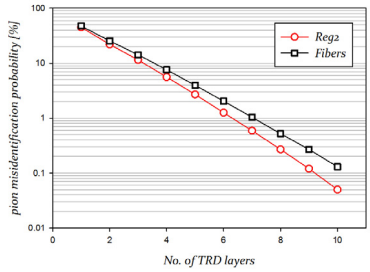

Figure 2: Pion misidentification as a function of number of TRD layers for 90% electron efficiency

the pad with maximum signal (pad i) and its left (pad $i-1$)/ right (pad $i+1$) neighbours. For the position reconstruction along the pads the algorithm described in [4] was used. The finite digitization of the signal, (i.e. three pads) obviously introduces systematic errors. For this reason corrections based on Monte Carlo simulations for the finite digitization and amplitude fluctuations are applied to the reconstructed position. The position resolution was obtained from the standard deviation of a Gauss function fitted to the difference between the reconstructed position with two identical detectors. A position resolution of 493 μm across the pads was obtained considering equal contribution of both chambers (Fig.3 left side). The beam profile obtained from the

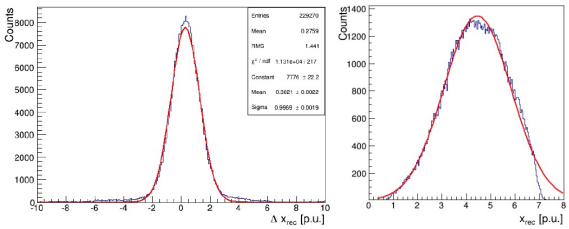

Figure 3: The difference between the reconstructed position across the pads with two identical detectors, fitted with a Gauss function (left side) and reconstructed beam profile (right side)

position information shows no discontinuities due to the reconstruction procedure (Fig.3 right side).

References

[1] M.Petriş et al., CBM Progress Report 2011, p. 47

[2] V. Cătănescu et al., CBM Progress Report 2009, p.47

[3] A.Caragheorgheopol et al., GSI Report 2010, p. 35

[4] M.Petriş et al. CBM Progress Report 2011, p. 48

CEPA: A $LaBr_3(Ce)/LaCl_3(Ce)$ phoswich array for detection of high energy protons and gamma radiation

J. Sánchez del Río[1], M.J.G. Borge[1], J.A. Briz[1], M. Carmona-Gallardo[1], A. Charpy[2], E. *Casarejos[3], D. Cortina-Gil[4], J. Benlliure[4], H.T. Johansson[2], E. Nácher[1], H. Álvarez-Pol[4], T. Nilsson[2], A. Perea[1], B. Pietras[4], G. Ribeiro[1], J. Sánchez[1] and O. Tengblad[1]*

[1]Instituto de Estructura de la Materia, CSIC Madrid; [2] Chalmers Univ. Technology, Göteborg, [3]Universidad de Vigo, [4]Universidad de Santiago de Compostela

The 'Forward EndCap' of CALIFA [1] should cover the polar angle region between the beam pipe i.e. 6^O to 43^O, where the CALIFA barrel takes over the detection. This region concentrates 58.3% of the total γ rays emitted by a source moving at the nominal value of 0.82c and where Doppler shift boosts the energy to 1.5 – 2.5 times its value in the Centre of Mass frame.

Working towards a final design an endcap (CEPA) is proposed that should satisfy these requirements. To be able to compensate for the mentioned Lorenz boost, a high segmentation is needed and an energy resolution due to this effect of $\Delta E/E=3.75$ % has been used as a design effort. The CEPA is divided into 10 branches of 5 alveoli, each alveoli is sub-divided into 15 slots to hold the individual crystals. In total the CEPA amount to 750 individual crystals of truncated pyramidal shape. The active detection coverage of the CEPA detector for the mention solid angle is more than 80%.

As the detector is to detect high energy protons up to 400 MeV as well as gamma radiation up to 30 MeV, a phoswich configuration of 4 cm $LaBr_3(Ce)$ + 6 cm $LaCl_3(Ce)$ long crystals was decided. This configuration makes the CEPA work as a telescope detector ΔE_{LaBr3}-E_{Tot} for protons up to 200 MeV or as a double energy loss detector $\Delta E_{LaBr3}+\Delta E_{LaCl3}$ for protons of higher energies.

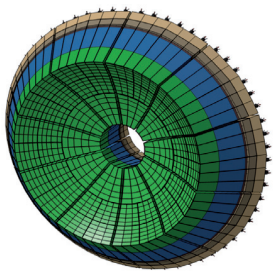

Figure 1: CEPA design.

For the design efforts, Montecarlo simulations were performed to especially study the efficiency for high energy protons, gamma resolutions, and to optimize the crystal length. The optimal phoswich crystal length of 10 cm (4+6 cm) was determined as a compromise between high gamma absorption efficiency (calorimeter) and proton spectroscopy up to the very high proton energies (400 MeV) [2]. By the use of the phoswich configuration, an analytical method that consists in representing the energy deposited in the $LaBr_3$ crystals vs the energy deposited in the whole calorimeter allows to resolve high energy protons. In these 2D histograms one can clearly distinguish the protons that are stopped in the first crystal, the ones that continue and stop in the second crystal and the ones that punch through even the second crystal. These results are shown in Fig. 2, that display the 2D spectrum resulting from the simulated $^{12}C(p,2p)^{11}B$ reaction at 400 MeV of initial kinetical energy when detecting coincident pairs of protons.

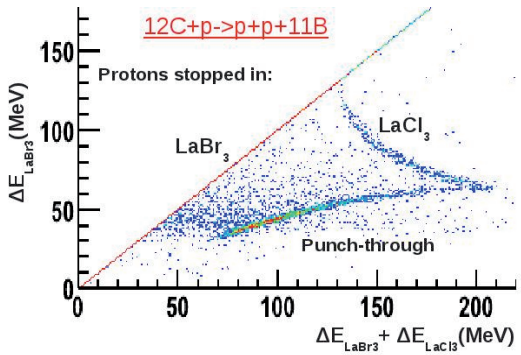

Figure 2: 2D spectrum of the protons from simulation of $^{12}C(p,2p)^{11}B$ reaction at 400 MeV/u.

Experimental tests for high energy protons (200 - 1000 MeV) were performed during the S406 experiment (Characterization of NEUland prototypes, described elswhere in this scientific report) in November using a prototype module consisting of 2x2 phoswich $LaBr_3(Ce)/LaCl_3(Ce)$ rectangular crystals array, placed at 18º from the beam. The geometrical dimensions of this 10 cm long array is 4 cm of $LaBr_3$ coupled with 6 cm of $LaCl_3$. The analysis of these data is ongoing.

References

[1] D. Cortina-Gil et al., GSI SCIENTIFIC REPORT 2011.

[2] O. Tengblad et al., Nucl. Inst. and Meth. in Phys. A704 (2013) 19-26.

* The Spanish ministry with the project FPA2009-07387 and the ERANET NupNET GANAS PRI-PIMNUP-2011-1333 has supported this work.

FPGA Based Free Running Mode Acquisition for High Counting Rate TRD *

F. Constantin[1]

[1]"Horia Hulubei" National Institute for Physics and Nuclear Engineering, Romania.

A new acquisition system, Free Running Mode for in-beam tests of the TRD prototypes, was developed; it is based on the Virtex®-6 FPGA ML605 Evaluation Kit. (see figure 1). This activity is a continuation of the one presented in the previous [1], aiming for a secure synchronization with MBS DAQ system.

The signal from the TRD amplified by a FEE based on FASP ASIC [2] are transported via twisted pair cable to a fast ADC, MAX1434 a 10-bit analog-to-digital converter which features fully differential inputs, a pipelined architecture, and digital error correction incorporating a fully differential signal path. The MAX1434 offers a maximum sample rate of 50Msps [3].

The main tasks of ML605 [4] are:

- clock generation
- de serialization of data delivered by MAX 1434
- reading the synchronization signal generated by MBS
- Ethernet communication

The VHDL language was used in order to perform the required tasks; 16 analog channels, corresponding to 16 TRD pads, were processed.

The sync signal from MBS was used in order to correlate the information delivered by the Max data with the other Read Out Controllers (mainly with the QDC operated in the VME crate used for lead glass and Cherenkov detectors). The information from ML605 was directed also to the general acquisition system and the data was made available in the Go4 environment, thus being used to monitor the whole system during data taking.

The figure 2 shows the electron / pion separation using a fibre radiator and one of the TRD prototypes of Bucharest group based on MWPC architecture with 2x4mm amplification zone and 4mm drift region [5]. Electrons and pions were selected using the information from Cherenkov detector and lead glass calorimeter [6]. Although quite preliminary, the results show that the information delivered by high counting rate prototypes developed for CBM and amplified by FASP could be processed by the free running mode architecture, conserving their performance. The activities along a higher integration of the present solution are in progress.

* Work supported by EU-FP7/HP3, Grant No 283286 and Romanian NASR/CAPACITATI-Modul III contract no. 196 and NASR/NUCLEU Project

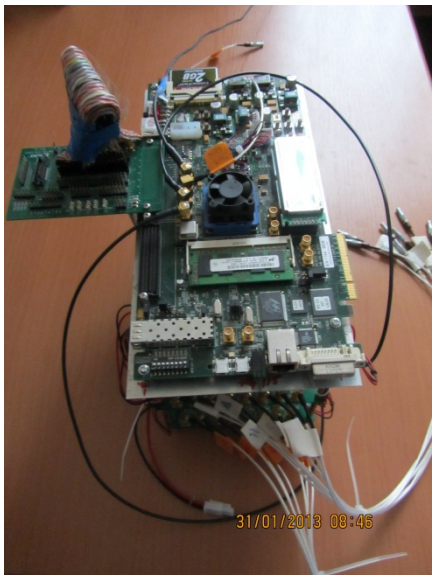

Figure 1. General view of the acquisition system

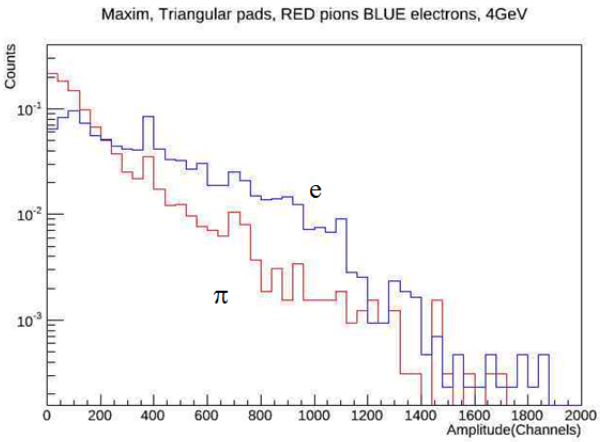

Figure 2: Electron/pion separation

References

[1] F. Constantin, M. Petcu PHN-NOM-CBM-27 GSI Scientific Report 2011

[2] V.Catanescu, CBM 10th Colaboration Meeting, Sept. 25-28,2007, Dresden

[3] http://www.maxim-ic.com/datasheet/index.mvp/id/4906

[4] http://www.xilinx.com/products/boards-and-kits/EK-V6-ML605-G.htm

[5] M. Petris et al, this report

[6] D. Emschermann et al, this report

#

Measurements on the 325 MHz Superconducting CH Cavity*

M. Busch†[1], *H. Podlech*[1], *U. Ratzinger*[1], *W. Barth*[2,3], *and M. Amberg*[3,4]

[1]Institut für Angewandte Physik, Goethe Universität, Frankfurt, Germany; [2]GSI, Darmstadt, Germany; [3]HIM, Mainz; [4]Johannes Gutenberg Universität, Mainz

Abstract

At the Institute for Applied Physics (IAP), Frankfurt University, a superconducting 325 MHz CH-Cavity has been designed and built. This 7-cell cavity has a geometrical β of 0.16 corresponding to a beam energy of 11.4 AMeV. The design gradient is 5 MV/m. Novel features of this resonator are a compact design, low peak fields, easy surface processing and power coupling. Furthermore a new tuning system based on bellow tuners inside the resonator will control the frequency during operation. First tests on the cavity have been performed including a cold test achieving a gradient of up to 2.3 MV/m.

Measurements

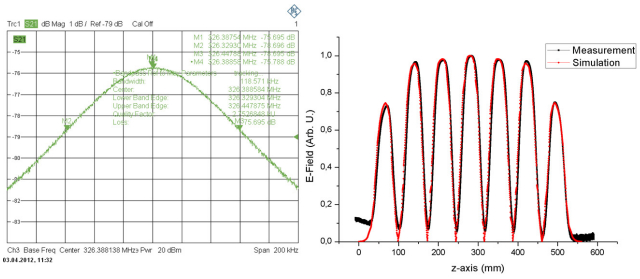

Figure 1: Left: Frequency of Mode 1. Right: Bead pull measurement and simulation.

Prior to the final fabrication steps of the cavity first measurements have been done at Research Instruments ensuring the envisaged design goals [1].

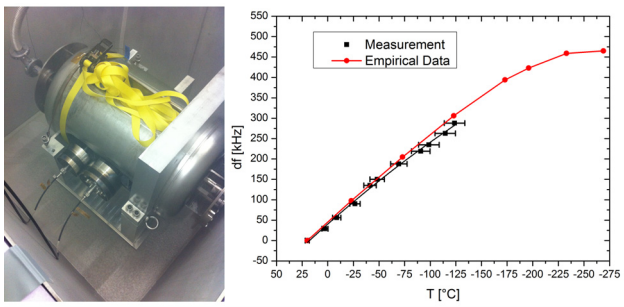

Figure 2: Cold test setup (left), temperature vs. frequency shift (right).

First the frequency and the electric field on axis have been measured with affixed end caps and without static tuners (see fig. 1). Determining the frequency shift of the static tuners by the use of provisional dummy tuners the final niobium tuners were welded into the cavity step-by-step. After welding of the end caps and three of the four static tuners into the cavity a preliminary cold test was set up to investigate the thermal response of the CH-Cavity (see fig. 2).

Subsequently the effect of the dynamic bellow tuners on the frequency as well as the mechanical rigidity of the cavity under evacuation have been studied (see fig. 3).

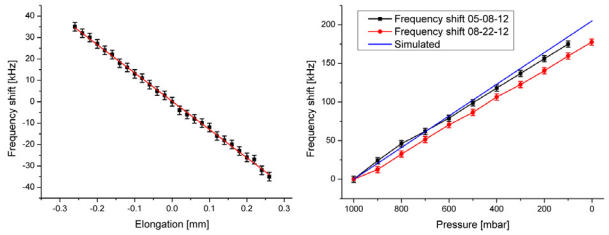

Figure 3: Bellow tuner elongation vs. frequency shift (left), pressure vs. frequency shift (right).

Finally the last static tuner has been fixed, a buffered chemical polishing treatment was performed and the cavity was delivered to IAP for a first test under LHe conditions. After experiencing multipacting barriers the achieved field gradient yielded $\approx 2.3\ MV/m$ (see fig. 4) limited by field emission due to a moderate surface purity of the cavity.

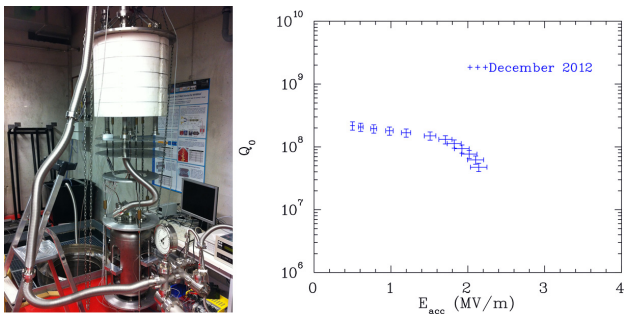

Figure 4: Measurement at IAP @4 K (left), E vs. Q curve (right).

References

[1] M. Busch, F. Dziuba, H. Podlech, U. Ratzinger, W. Barth, S. Mickat, M.Amberg, M. Pekeler, "First Measurements on the 325 MHz Superconducting CH Cavity", Linac 2012, Tel-Aviv, Israel.

* Work supported by GSI, BMBF Contr. No. 06FY7102, 06FY9089I

† busch@iap.uni-frankfurt.de

Status of the superconducting cw LINAC Demonstrator

M. Amberg[3], K. Aulenbacher[4], W. Barth[1], F. Dziuba[2], V. Gettmann[3], S. Jacke[3], S. Mickat[1], A. Orzhekovskaya[3], H. Podlech[2], U. Ratzinger[2]

[1]GSI, Darmstadt, Germany; [2]IAP, Frankfurt, Germany, [3]HIM, Mainz, Germany, [4]KPH, Mainz, Germany

Setup at GSI HLI

The Demonstrator should be mounted in straightforward direction to the existing GSI High Charge Injector (HLI), aiming at full performance tests of the key component, i.e. the superconducting (sc) CH-Cavity [1]. The setup at the GSI HLI is in progress: The radiation protection cave was mounted in July 2012 and the beam transport line is almost completed (fig.1).

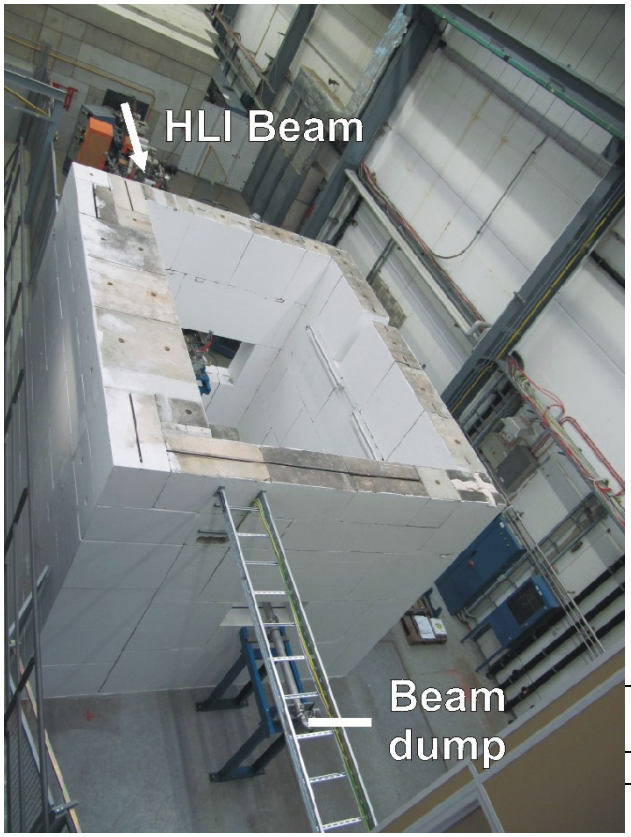

Figure 1: Photograph of the cw Demonstrator setup from July 2012 showing the radiation protection cave and the beam dump.

Emittance Measurements

In parallel to the beamline assembling the beam characteristics at the exit of the HLI were measured with a temporary emittance meter setup (fig.2). The analysis of the measurements allows detailed beam dynamic investigations with respect to a realistic input particle distribution [2]. The aims are matching the beam to the Demonstrator, and the adaption of the conceptual layout of the whole cw LINAC to realistic boundary conditions.

Scheduling

The commissioning of the Demonstrator at GSI depends on the delivery of the main components: The fabrication of the sc CH-cavity has started after the drawings were approved in June 2012 [3]. The delivery is expected in September 2013. The order for the cryostat and the solenoids was placed at Cryogenic, London, UK in late April 2012. Currently the final design is worked out. The final drawings are expected in spring 2013. The delivery of the cryostat and the solenoids is expected one year later in 2014.

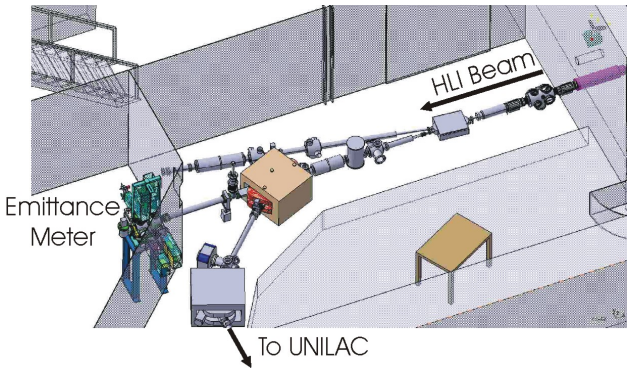

Figure 2: Intermediate setup comprising an emittance meter to measure the transverse beam characteristics at the exit of the HLI.

2013	1st half	• Setup at GSI HLI is completed • Fabrication of the cryostat and the solenoids starts
	2nd half	• Delivery of the cavity • rf-tests at IAP
2014	1st half	• Delivery of the cryostat and the solenoids
	2nd half	• Commissioning of the Demonstrator at GSI HLI with beam

Table 1: Project Schedule.

References

[1] S. Mickat et al., GSI Scientific Report 2011.
[2] A. Orzhekovskaya et al., HIM Scientific Report 2012.
[3] F. Dziuba et al., HIM Scientific Report 2012

Shielding wall optimization for FAIR

A. Senger[1], G. Fehrenbacher[1], and T. Radon [1]

[1]GSI, Darmstadt, Germany

FLUKA [1, 2] calculations have been carried out for the construction permission of the FAIR buildings and tunnels, in particular for the optimization of shielding walls between tunnels and caves. Free access to a certain cave while beam operations including regular beam losses take place in a neighbouring cave or tunnel can only be granted if the dose rate does not exceed 0.5 µSv/h. Moreover, often shielding walls have to be designed as a labyrinth in order to have access to the beam line components.

The planned concrete shielding wall between tunnel T113 and cave G050 is shown in Figure 1, blue line. Concerning radiation protection the wall is thick enough to reduce the dose rate in the cave down to 0.5 µSv/h in case of a beam loss in the tunnel, but the access to the beam line magnets is difficult.

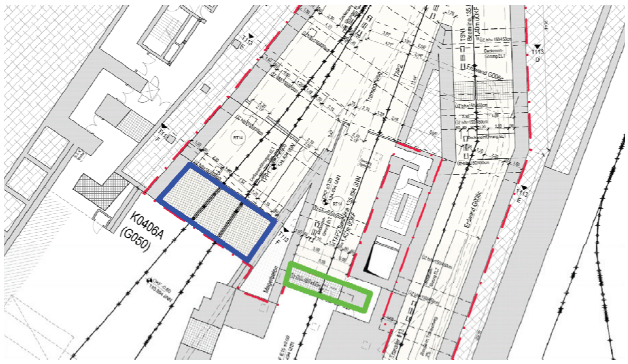

Figure 1: Architect plan of tunnel T113. Blue line – planned shielding wall for G050, green line – for G006c.

The new labyrinth was designed using FLUKA calculations. The dose rate in tunnel T113 and in cave G050 in case of a 2% beam loss of a proton beam at 29 GeV energy with an intensity 5×10^{11} p/s is shown in Figure 2. The black cross indicates the assumed point of beam loss. This scenario is possible during experiments in G006c.

Another scenario is the beam loss while G050 experiments are performed. The shielding wall for G006c was not optimized for such a situation (see green line in Figure 1). The FLUKA calculations allowed optimizing the thickness and structure of the concrete shielding wall for G006c. The dose rate in tunnel T113 and in cave G050 in case of a 3% beam loss of uranium beam at 2 GeV/u energy with an intensity 10^{10} particles per second is shown in Figure 3. The black cross indicates the point of beam loss. The level of 0.5 µSv/h will be reached with a total concrete thickness of 5 m. The labyrinth structure of the shielding wall allows the access to the beam line magnets.

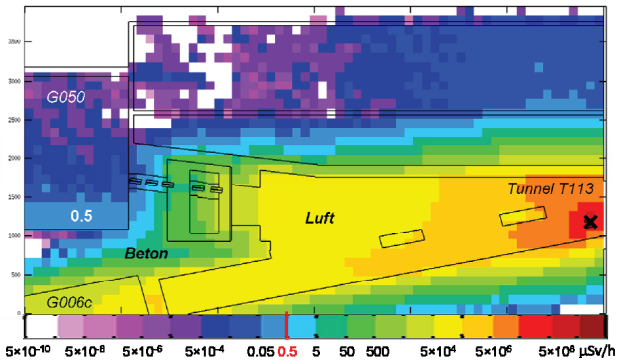

Figure 2: Dose rate in tunnel T113 and cave G050 for a 2% beam loss of proton beams at 29 GeV energy with intensities of 5×10^{11} p/s. The black cross indicates the beam loss position.

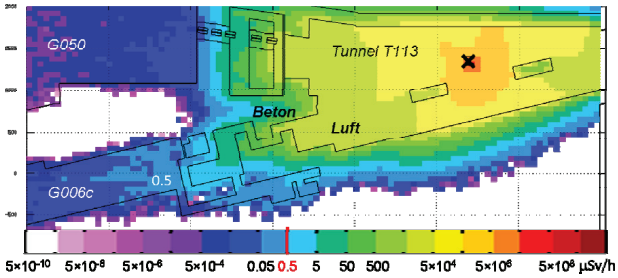

Figure 3: Dose rate in tunnel T113 and cave G006c for a 3% beam loss of uranium beam at 2 GeV/u energy with intensities of 10^{10} particles per second . The black cross indicates the beam loss position.

The final design of the concrete shielding walls between tunnel T113 and caves G050 and G006c together with FLUKA results will be included into the application for the construction permission of the tunnel and both caves.

References

[1] "The FLUKA code: Description and benchmarking", G. Battistoni, S. Muraro, P.R. Sala, F. Cerutti, A. Ferrari, S. Roesler, A. Fasso`, J. Ranft, Proceedings of the Hadronic Shower Simulation Workshop 2006, Fermilab 6-8 September 2006, M. Albrow, R. Raja eds., AIP Conference Proceeding 896, 31-49, (2007)

[2] "FLUKA: a multi-particle transport code", A. Fasso`, A. Ferrari, J. Ranft, and P.R. Sala, CERN-2005-10 (2005), INFN/TC_05/11, SLAC-R-773

Project Status of the New Setting Generation System for GSI and FAIR

D. Ondreka[1], *J. Fitzek*[1], *R. Hellmich*[1], *H. Liebermann*[1], *R. Müller*[1], *S. Reimann*[1], *B. R. Schlei*[1], *and J. Struckmeier*[1]

[1]GSI, Darmstadt, Germany

Introduction

Since 2008, a project group at GSI is developing a setting generation system for the accelerators of GSI and FAIR using the CERN LSA (LHC Software Architecture) framework [1]. This report summarizes the development progress during the year 2012.

LSA Framework

There were no major changes to the LSA framework. However, a strategy was devised within the LSA collaboration for the design and implementation of the pattern concept required for modeling the parallel operation modes of the FAIR facility. It was agreed that the implementation of this eminently important extension will take place during the long shutdown of the LHC this year.

Also, a first step was made towards a better separation of the FAIR specific resources and the common LSA framework. While the latter will remain hosted at CERN, all FAIR specific resources are now located in a repository of the GSI controls group.

Machine Modeling

The generic synchrotron model was adapted to make use of the recently implemented LSA support for flexible cycle lengths. The models for SIS18 and SIS100 were revised and improved.

The SIS18 machine model was used to perform machine experiments with and without beam for the planned booster operation mode. One experiment was devoted to the dual harmonic operation. Dual harmonic buckets could be successfully established at injection level. Acceleration was, however, not possible due to an insufficient phase calibration of the acceleration cavities.

A second experiment was performed to test a new parametrization of the optics change from triplet to doublet during the ramp. At the ramping speed of $10\,\mathrm{T/s}$ for the booster operation, the voltage of the triplet power supply would exceed its limit by fifty per cent. The booster parametrization escapes this limit by reducing the triplet strength faster (see figure 1). However, this scheme implies larger beam radii during the ramp, potentially leading to beam loss. Therefore, the number of particles as a function of time was measured with a U^{28+} beam of high intensity at $3\,\mathrm{T/s}$, for both the standard and the booster parametrization. No excess beam loss was observed, proving the feasibility of the booster parametrization (see figure 2).

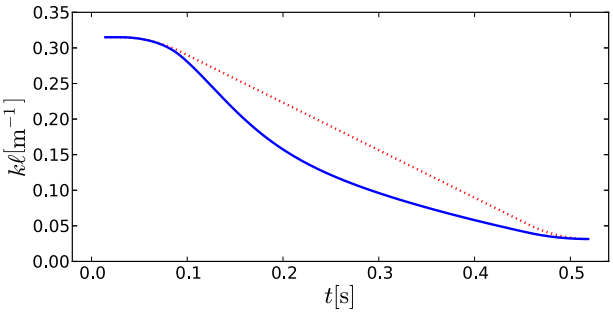

Figure 1: Triplet strength for the standard (dotted line) and booster (solid line) parametrization.

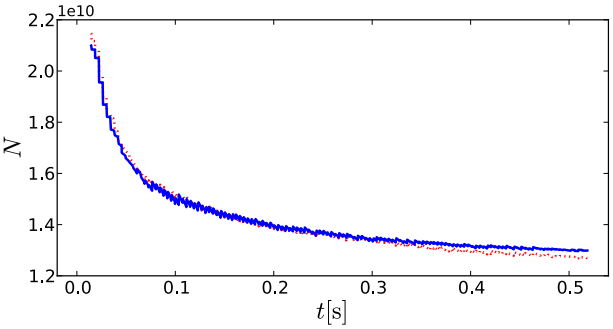

Figure 2: Normalized number of particles for the standard (dotted line) and booster (solid line) parametrization.

An experiment without beam was concerned with the capabilities of the power supplies at $10\,\mathrm{T/s}$. As a result, the supplies for the triplet and for the bump at the magnetic septum will be upgraded to sustain the booster operation.

Besides the work for SIS18, a minimal model of the ESR ring (without cooler yet) was implemented and the first settings have been generated.

Apart from the machine models, applications were further developed. The first one, ParamModi, was used extensively during the machine experiments for controlling SIS18. The second one, a Java version of the ion optics program MIRKO, was successfully converted into an application interacting with the LSA system.

In 2013, the main focus will be on the extension of LSA to support the pattern concept for parallel operation.

References

[1] G. Kruk et. al, “LHC Software Architecture LSA – Evolution Toward LHC Beam Commissioning”, ICALEPCS’07.

Accelerator Operation Report

W. Bayer, U. Scheeler*, P. Schuett

GSI, Darmstadt, Germany

This report describes the operation statistics of the GSI accelerator facility in the year 2012. The presented information is based on the data of the GSI electronic operation logbook OLOG [1] which allows for a detailed evaluation of operation statistics especially for the time-sharing operation mode of the accelerators.

General Overview

From March till November three beam time blocks were scheduled. This led to an increase in operation time compared to 2011. In total, the SIS has been operated for 5032 hours and the UNILAC for 5880 hours. 552 hours are included for the commissioning of the accelerators after shutdown.

The first shutdown period lasted from January the 1st till March the 25th. This shutdown was used for a careful and detailed maintenance of the second Alvarez section. The vacuum pressure in the SIS injection section was improved and the reinjection septum was replaced by a NEG coated vacuum chamber with a bigger aperture. Both measures improved the life time of low charged heavy ions. Leaks in the northern arc of the ESR were also repaired. The other long shutdown started on December the 1st. It will last until the second half of the year 2013.

Table 1: Overall beam time of the accelerator facility

	2012	2011
Integral target time for all experiments	**12105 h**	8809 h
Time for retuning	**103 h**	96 h
Time of interruption	**3680 h**	3518 h
Total beam time	**15888 h**	12432 h

In Table 1 the overall beam time of the whole facility is shown. In total 12105 hours of beam-on-target-time were successfully delivered to the different physics experiments, about 3296 hours more than in 2011. The category *retuning* includes the time necessary to improve the beam performance during the running experiment. The *time of interruption* covers the categories *accelerator setup* (1436 h), *ion source service* (553 h) and *unscheduled down time* (1690 h). These are all events which lead to a break of the running beam for the corresponding experiment. Altogether these times add up to the *total beam time*. Due to time sharing operation this amount is higher than the sum of the operation hours. Compared to 2011 the ratio between target time and total beam time (availability of the facility) increased by 5 percentage points to 76%. Less time for set up was needed and the unscheduled down time for SIS/ESR decreased as well.

Experimental Operation

Figure 1 gives an overview of target time for different experimental areas with the fraction of the 4 beam branches of the UNILAC on the right side, the ESR below and the different experimental caves behind the SIS on the left side. Details corresponding to the different experimental programs are given in [2].

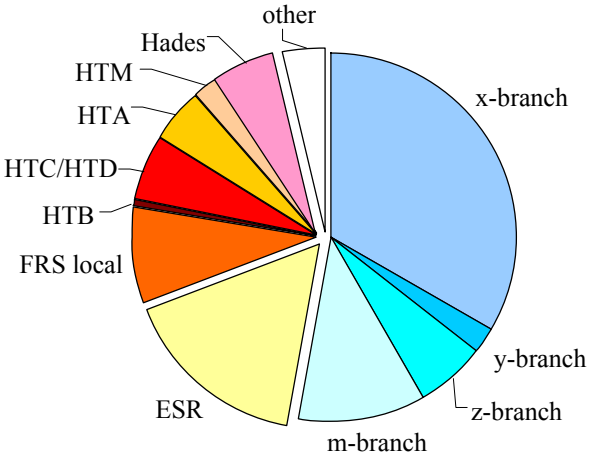

Figure 1: Distribution of target time with respect to the different experimental areas.

UNILAC Experiments

Details of the beam time for UNILAC experiments are shown in Table 2. Over the year 13 different experiments were performed at the UNILAC. In total 6501 hours of target time for physics experiments have been achieved. The main user was the TASCA experiment (3600 hours). Furthermore the beam was used by Material Science (1426 hours) and for biological experiments (277h). The fraction of target time remained constant compared to last year. We observed a decrease of time for accelerator setup and an increase of unscheduled down time.

Table 2: Beam delivered to UNILAC experiments

	Time	Fraction
Target time for experiments	6501 h	76,7%
Time for retuning	49 h	0,6%
Accelerator setup	743 h	8,8%
Ion source service	420 h	5,0%
Unscheduled down time	766 h	9,0%
Total beam time	**8478 h**	**100%**

* u.scheeler@gsi.de

SIS/ESR Experiments

The heavy ion synchrotron delivered beams to 23 fixed target experiments and to 9 experiments at the ESR. In total 5604 hours of target time have been achieved. A more detailed overview is given in Table 3.

Table 3: Beam delivered to SIS/ESR experiments

	Time	Ratio
Target time for experiments	5604 h	75,6%
Time for retuning	54 h	0,7%
Accelerator setup	948 h	12,8%
Ion source service	133 h	1,8%
Unscheduled down time	670 h	9,0%
Total beam time	**7410 h**	**100%**

In 2012 the target time for the ESR (direct beam and beam via FRS) increased to 1983 hours, 224 hours for HITRAP commissioning is included in this amount. For about 1005 hours beam was used at the local experiment of the FRS. 684 hours of beam time were delivered to HAD, which also was a main user at the SIS. Altogether 394 hours beam were delivered for biological experiments to HTA and HTM.

Accelerator Operation

In Table 4 all unscheduled down time events are shown in more detail. In 2012 the total amount of down time decreased about 96 hours although there were two major vacuum leaks, one in the second Alvarez section and the other at the entrance to the X-branch. Furthermore many interruptions due to leaks in cooling pipes of different accelerator components occurred. This led to an increase in down time for vacuum and structures compared to 2011.

Table 4: Statistics of all unscheduled down time events

	Down time	No. of events
Power supplies	256 h	279
Vacuum and structures	309 h	95
Beam diagnostics	29 h	13
Operation	6 h	11
Safety-/ Interlock system	110 h	25
Ion Sources	80 h	92
RF system	331 h	368
Controls	63 h	48
Infrastructure	59 h	15
Others / ambiguous	103 h	56
Total of unscheduled down time	**1346 h**	**1002**

Mainly problems with the control of interlock devices caused break downs of the interlock system. On the other hand the down time of ion sources was very low compared to the last years. The down time for the RF system decreased as well.

Over the year 16 different isotopes have been accelerated. Figure 2 shows the operation time for each isotope. The rare isotopes ^{48}Ca and ^{48}Ni were produced by the ECR ion source, which in total has been operated for 2723 h. The Penning ion source was mainly operated with ^{50}Ti and ^{197}Au (in total 4870 hours of operation). The high-current ion source was used for 4281 hours. Especially ^{136}Xe, ^{84}Kr and $^{6}D^{3}$ beams were delivered from the MUCIS ion source, ^{238}U was accelerated from the MEVVA ion source for 1472 hours. ^{197}Au and ^{208}Pb was provided for the first time for high current operation and it ran very stable and successful.

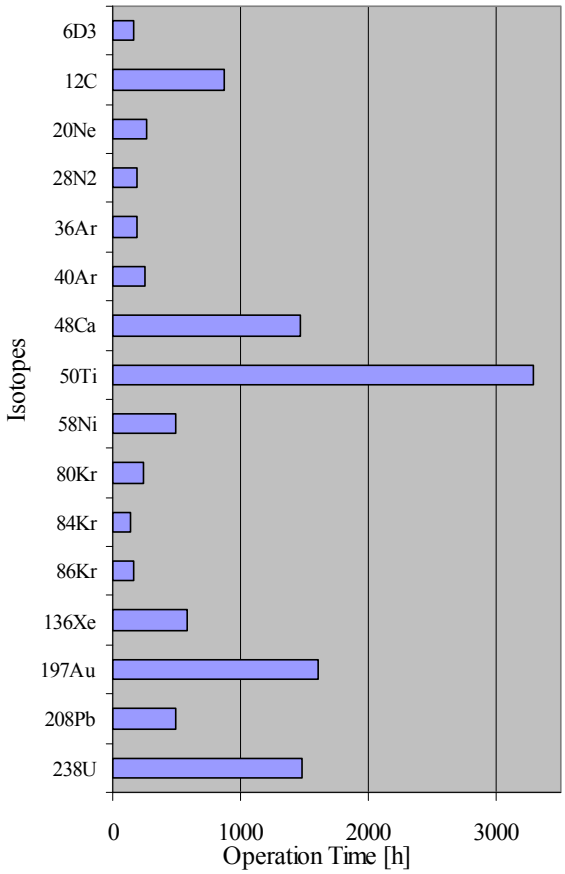

Figure 2: Total beam time for different ion species

For accelerator experiments at the UNILAC 195 hours, at SIS 317 hours and at ESR 101 hours beam were delivered, which is an increase for UNILAC and SIS. But for the ESR it is a decrease by a factor of three compared to last year.

References

[1] P.Schuett, the GSI Operation Logbook OLog, WAO2010 (http://wao10.komac.re.kr/PDF/O-17.pdf)
[2] Report of beam time coordinator, this report

Ion Source Operation at the GSI Accelerator Facility

R. Hollinger, K. Tinschert*, J. Pfister*, A. Adonin, R. Berezov, M. Brühl, B. Gutermuth, F. Heymach, R. Lang, J. Mäder, F. Maimone, K. Ochs, J. Roßbach, P. Schäffer, S. Schäffer, M. Stork, C. Vierheller, A. Wesp, S. Zulauf*

GSI, Darmstadt, Germany

High Current Ion Sources

In 2012 ion sources from Terminal North (MUCIS, CHORDIS, VARIS, MEVVA) and Terminal South (PIG ion sources) were supplying the GSI accelerator with various types of ions. The following Table 1 gives an overview of the ion species, which were delivered for physics and accelerator development experiments. A good representative value for delivered intensity to the linear accelerator UNILAC is the analysed current in the accelerator section *UH1* in front of the RFQ.

Table 1: Ion beams generated with high current ion sources in 2012. Filament driven volume type ion sources: MUCIS and CHORDIS; Vacuum arc ion sources: VARIS and MEVVA; Penning type ion sources PIG

Ion species	Duration (days)	Ion source	Beam for experiment	Analyzed intensity (emA)
$^{6}D_3^+$	6	MUCIS	UNI	2-3
$^{14}N_2^+$	7	MUCIS	SIS	4
$^{12}C^{2+}$	7	PIG	UNI	0.06…0.08
$^{20}Ne^{+}$	7	PIG	ESR	0.1
$^{36}Ar^{+}$	6	CHORDIS	SIS	8
$^{40}Ar^{2+}$	14	PIG	UNI	0.2…0.4
$^{50}Ti^{2+}$	137	PIG	UNI/ESR	0.04…0.07
$^{58}Ni^{2+}$	20	VARIS	SIS/ESR	5
$^{84}Kr^{2+}$	9	MUCIS	SIS	3-4
$^{86}Kr^{2+}$	9	MUCIS	SIS	4
$^{136}Xe^{3+}$	15	MUCIS	UNI/SIS	2
$^{197}Au^{4+}$	39	VARIS	UNI/SIS/ESR	3-6
$^{197}Au^{8+}$	28	PIG	UNI	0.06…0.1
$^{208}Pb^{4+}$	11	VARIS	UNI/SIS	6-8
$^{208}Pb^{8+}$	10	PIG	UNI/SIS	0.1
$^{238}U^{4+}$	58	VARIS	UNI/SIS/ESR	8-12

Ion beams generated in the high current sources can be distinguished into standard elements and non-standard, which are much more challenging to produce and the ion source being operated. In 2011 and especially in 2012 standard titanium-50 operation from the PIG source was established completely with more than one ion source exchange per day.

Another element, which was established in 2012 from the VARIS high current ion source, is the four-fold gold beam, which was not available from this kind of ion source before. The same approach as for $^{209}Bi^{4+}$-ions [1] was taken and a proper mixture of elements was found. Same as for the gold beam production the creation of high current four-fold led beam from the VARIS was established upon experimentalists request.

From Table 1 it can be deducted that the most requested ion beams in 2012 were titanium, gold and uranium. It is also shown that most time of the year both terminals were operated at the same time with mostly different ion species.

With a view to the super heavy element experiment TASCA with the need of high amounts of particles the possibility of production of the titanium-50 sputtering electrodes inside GSI was developed. Melting and machining was done in the melting oven of the ion source department as well as the ion source mechanical workshop.

An average particle current of 0.75pμA at the experiment was reached with an uptime of the ion source of 95%. In front of the accelerator an ion beam of $^{50}Ti^{2+}$ with an intensity of 40-70eμA was reached.

Refurbishment of the PIG sources started in spring of 2012. These sources have been in operation at GSI since the first days of the UNILAC. The goal of this action is a better performance of these high-duty-cycle ion sources.

Furthermore it was finally possible to built up the new PIG service area, where the service of the source can be done under “cleanroom conditions”

For the establishment of the high current gold beam different mixtures of gold and other elements were checked in order to change the physical properties of the element and having the maximum of the charge state distribution in the four-fold peak. Admixtures of elements like Pd, Cr, Zr, Ti and Ta were tested. Best results were reached with mixtures of 50% gold with 50% of chromium. The ion beam current of $^{197}Au^{4+}$ in front of the RFQ was 6mA.

On led beam the same procedure was undertaken as for gold and bismuth before and it was possible to provide for the first time ever an intensity of up to 8mA of $^{208}Pb^{4+}$ was measured in front of the high current injector RFQ.

High Charge State Injector HLI

For the operation of the GSI accelerator the CAPRICE ECR ion source (ECRIS) at the High Charge State Injector (HLI) delivered the ion species listed in table 2 for various physics experiments in the regular beam time schedule as well as for accelerator development.

* Corresponding authors

Two beam time periods in 2012 dedicated to biophysics experiments at the SIS under therapy conditions and to biophysics experiments at the UNILAC were provided with $^{12}C^{2+}$ ion beams.

Table 2: Ion beams delivered from the HLI in 2012.

Ion species	Auxiliary gas	Duration (days)	Analyzed intensity (eμA)
D_2^{1+}	-	3	270
$^{12}C^{2+}$	O_2	12	100
$^{12}C^{3+}$	-	9	150
$^{20}Ne^{4+}$	He	4	270
$^{40}Ar^{7+}$	He	2	90
$^{48}Ca^{10+}$	He	55	120
$^{80}Kr^{13+}$	He	10	60
$^{136}Xe^{19+}$	O_2	11	30

Ion beams of $^{20}Ne^{4+}$ and of $^{40}Ar^{7+}$ were exclusively used for machine investigations at the HLI in different periods. This was dedicated to the preparation of forthcoming experiments with a module of a new type of superconducting linear accelerator, the sc cw-LINAC-Demonstrator [3].

After investigations on the feasibility of producing a $^{12}C^{3+}$-beam from pure CH_4 in 2011 the corresponding dedicated physics experiment was performed at the ESR in the present reporting period. Due to the experiment conditions the $^{12}C^{3+}$-beam had to be extracted from the ECRIS and had to be accelerated and transported to the injection of the synchrotron (SIS) without passing through a further stripping target. As the only mass-to-charge separation of the ion beam is performed in the analyzing dipole directly behind the ion source, different ion species of the same mass-to-charge ratio - like $^{12}C^{3+}$ and $^{16}O^{4+}$ in this case - cannot be separated. The amount of beam contamination with O^{4+} from the residual gas can only be derived indirectly from the mass-to-charge spectrum. It was estimated in the test run to be in the order of 8% oxygen as background contamination. The oxygen contamination is expected to be mostly related to residual gas and surface layers. Therefore an operating period of 3 days for precleaning the plasma chamber of the ECRIS was performed before the dedicated beam time. In fact the amount of oxygen contamination at the mass/charge ratio of 4 ($^{12}C^{3+}$, $^{16}O^{4+}$) could be decreased from 11% to 4%.

All other ion beams delivered from the ECRIS were produced from highly enriched isotopic materials upon experimental request for rare isotope ion beams. Ion beams of $^{136}Xe^{19+}$ were routinely delivered to experiments behind the SIS. A gamma spectroscopy experiment requested for the first time an ion beam from the rare isotope ^{80}Kr. $^{80}Kr^{13+}$ from the ECRIS had to be selected. As the isotopic enrichment of the sample material was limited to 51.4% it had to be confirmed that a proper separation of the desired isotope peak in the mass-to-charge spectrum can be achieved. As Figure 1 demonstrates a correct setting of the ion beam optics of the low energy beam transport line fulfils this demand. A minor contamination of this peak with $^{86}Kr^{14+}$ cannot be avoided, but only amounts to less than 0.7%.

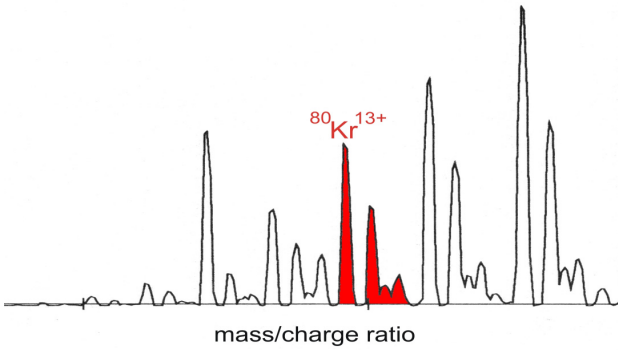

Figure 1: Separation of $^{80}Kr^{13+}$ in the mass/charge spectrum; Kr^{13+}-isotopes in red (mass 80, 82, 83, 84).

As last beam time in 2012 a long run with $^{48}Ca^{10+}$ was dedicated to experiments of the Super Heavy Element (SHE) programme at TASCA. This run was characterized by a very stable long time behaviour of the ion beam at high intensity. The mass/charge spectrum in figure 2 exhibits the very effective optimization on the desired charge state which also leads to a very high efficiency of material processing with an average material consumption of less than 200 μg/h.

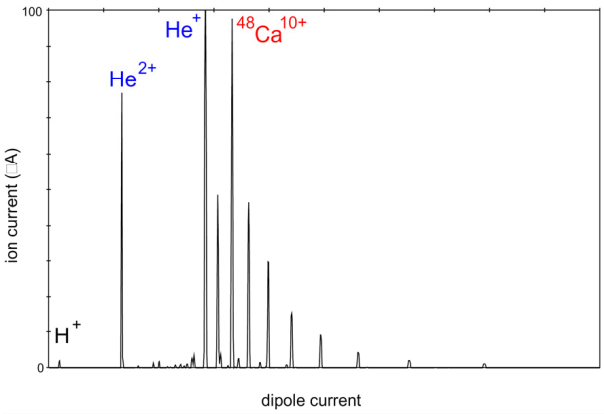

Figure 2: Mass/charge spectrum of ^{48}Ca.

References

[1] K. Tinschert, R. Hollinger et al., GSI Scientific Report 2011, GSI Report 2012-1, p.283

[2] A. Adonin, R. Hollinger, Challenges of Production of High Current four-fold Bi and Au Beams from Vacuum Arc Ion Sources at GSI Accelerator Facility, Proceedings of ISDEIV12

[3] S. Mickat et al., GSI Scientific Report 2011, GSI Report 2012-1, p. 292.

UNILAC Status and Development*

L. Groening, G. Clemente L. Dahl, P. Gerhard, M.S. Kaiser, M. Maier, S. Mickat, A. Orzhekhovskaya, B. Schlitt, H. Vormann, S. Yaramyshev

GSI, Darmstadt, Germany

Operation

Commissioning started in March with ^{40}Ar-beam from the PIG source. Operation of the PIG-branch was dominated by serving the TASCA experiment for a total of five months with $^{50}Ti^{2+}$ beam stripped to 12+ and further accelerated to 6.0 MeV/u. A beam current of more than 40 eμA at the experiment was achieved exceeding the expectations. SHIP was provided with the same beam through the month of June. $^{50}Ti^{12+}$ was delivered to the SIS18 for 11 days as well as $^{208}Pb^{26+}$ beam. Additionally, the PIG provided beams of $^{197}Au^{25+}$, with $^{20}Ne^{7+}$ beam, and $^{12}C^{6+}$.

The HLI with its ECR source also served TASCA with $^{48}Ca^{10+}$ for six weeks in fall. For two weeks $^{138}Xe^{54+}$ beam was taken by the SIS18. Finally, the HLI provided also $^{12}C^{6+}$ for the SIS18.

The MEVVA source was used during the full month of April to provide high current of $^{197}Au^{25+}$ for the SIS18. Another three weeks $^{58}Ni^{26+}$ was delivered to the same destination. Various experiments in the experimental hall and behind SIS18 were served with intense ^{238}U beams. Notably, dedicated SIS18 beam experiments used a stable $^{238}U^{28+}$ beam of 2 emA for dedicated beam experiments resulting in a new intensity record [1].

Operating the high current source terminal with the MUCIS ion source an intense $^{138}Xe^{54+}$ beam could be delivered to the SIS18 for two weeks and for ten days to the M-branch. Another eleven days saw $^{86}Kr^{33+}$ beam provided to the SIS18. Shorter beam times served the ions of $^{14}N^{7+}$ and the rare isotope of $^{36}Ar^{10+}$. Finally, a beam of singly charged D_3 molecules was provided in preparation of the novel beam experiment EMTEX [2]. The UNILAC provided 6501 hours of beam on target and 766 hours of scheduled beam time were not served due to failures [3].

The operation of the HLI RFQ was affected by presumably mechanical oscillations of the rods. The amplitude of the latter depends on the rf-pulse length and repetition rate and is subject to on-going investigations [4]. In June the rf-coupling loop of the cavity A2a needed to be replaced causing a downtime of 2.5 days. During the last week of June an internal HSI-IH quadrupole lense needed to be switched off due to a water leak. As a consequence the beam transmissions dropped by about 40% in this period, triggering the anticipation of the consecutive shutdown by one week.

Shutdown Activities

The first shutdown started with a general maintenance of the cavities A2a&b including a full revision of one of the inter-tank quadrupoles. New diagnostic chambers were installed into the LEBT of the HSI. The eigen-frequency control of the poststripper cavities was updated. Finally, the first shutdown was used for follow-up of the HLI-RFQ investigations [4]. Repair of the internal HSI-quadrupole was finished as scheduled during the second shutdown. A new rf-data-acquisition system was put into operation for cavity A3.

Machine Experiments

The mayor part of machine experiments was dedicated to experiments on stripping uranium ions to charge stated of about 40+ at energies of 1.4 and 3.6 MeV/u. The latter energy was used to irradiate foils mounted on a rotating wheel in the SHIP cave. Long pulses of low intensity U-beams did not reveal any damage of the foils. In contrast, high current pulses of less than 100 μs in length at 1.4 MeV/u at the HSI exit, impacting on fixed foils did destroy some foils. These experiments were done with different foils that underwent different production procedures. The damages revealed holes of few mm in diameter but some foils were fully ripped after seeing few pulses. Evaluation w.r.t. systematics in the damage pattern is on-going and partially reported in [5]. Apart from these findings, long-resisting (some 1000 pulses) foils were investigated w.r.t. long-term drifts in the beam parameters after the foil as transmission, charge spectrum, energy, and transverse emittance.

Alternative gaseous stripping media (H and CH_4) were tested behind the HSI [7], since results reported in [6] suggested significant increase of the medium charge state. Our experiments suffered from gas pressure limitations for safety reasons and did not confirm the findings of [6] so far.

References

[1] Y.A. El-Hayek et al. (this report).
[2] C. Xiao et al., ArXiv:1212.2034 [physics.acc-ph].
[3] W. Bayer et al. (this report).
[4] P. Gerhard and H. Vormann (this report).
[5] H. Vormann et al. (this report)
[6] H. Okuno, Proc. OINTDS Workshop, Mainz, Germany, 2012.
[7] B. Schlitt et al. (this report).

Dose Mesurements in SIS18 and in the experimental halls TR, EX,TH

T. Radon[1], K. Beverung[1], G. Fehrenbacher[1], C. Pöppe[1], and J. Sauer[1]

[1]GSI, Darmstadt, Germany

Dose Measurements in the SIS tunnel

During the accelerator development beam time in June 2012 dose measurements were performed in the SIS tunnel. The aim of the measurements was to get information about beam losses around the ring during fast and slow extraction of 14-N beams at energies of 1.9 GeV/u. About three hours of dose collection time was taken for each scenario. The intensities of the beams were 1.1E10 and 1.2E10 particles per second for the fast and slow extraction mode respectively. A thermo-luminescence detectors system [1] was placed on the floor approximately 3 meters away from the beam line.

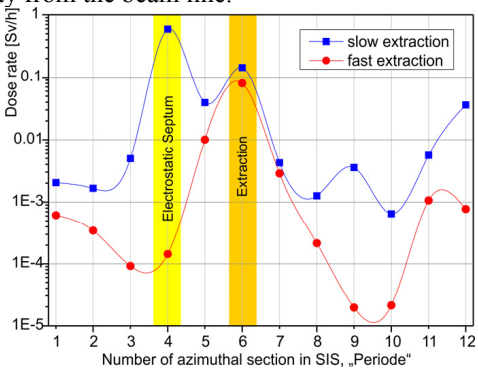

Figure 1: Neutron dose rate as a function of the azimuthal section in the SIS tunnel for slow and fast extraction.

The absolute maximum of the dose rates for fast extraction is clearly located at the extraction section of the SIS. However for the slow extraction mode the beam losses are even higher and have their absolute maximum at the electrostatic septum. The ratio of the dose rates at this position is nearly 4 orders of magnitude clearly demonstrating the different beam loss scenario.

Comparison of the annual doses outside the shielding with previous years

Due to the longer shut down periods and thus less beam time compared to 2011 the integral annual doses in 2012 are much lower than in the previous years, see ref. [2]. In particular the missing high current experiments for the pion production lead to considerably lower doses in the NE5 area. Also the area around the extraction from SIS, the target area of the fragment separator and the HHD beam dump usually being the hot spot in the dose chart reveals doses which are a more than factor of 5 lower compared to previous years.

References

[1] F. Gutermuth, T. Radon, G. Fehrenbacher, and J.G. Festag, Kerntechnik (2003), 68, 4, pp. 172-179

[2] T. Radon, et al. GSI-Report 2011-1 (2011) p. 352.

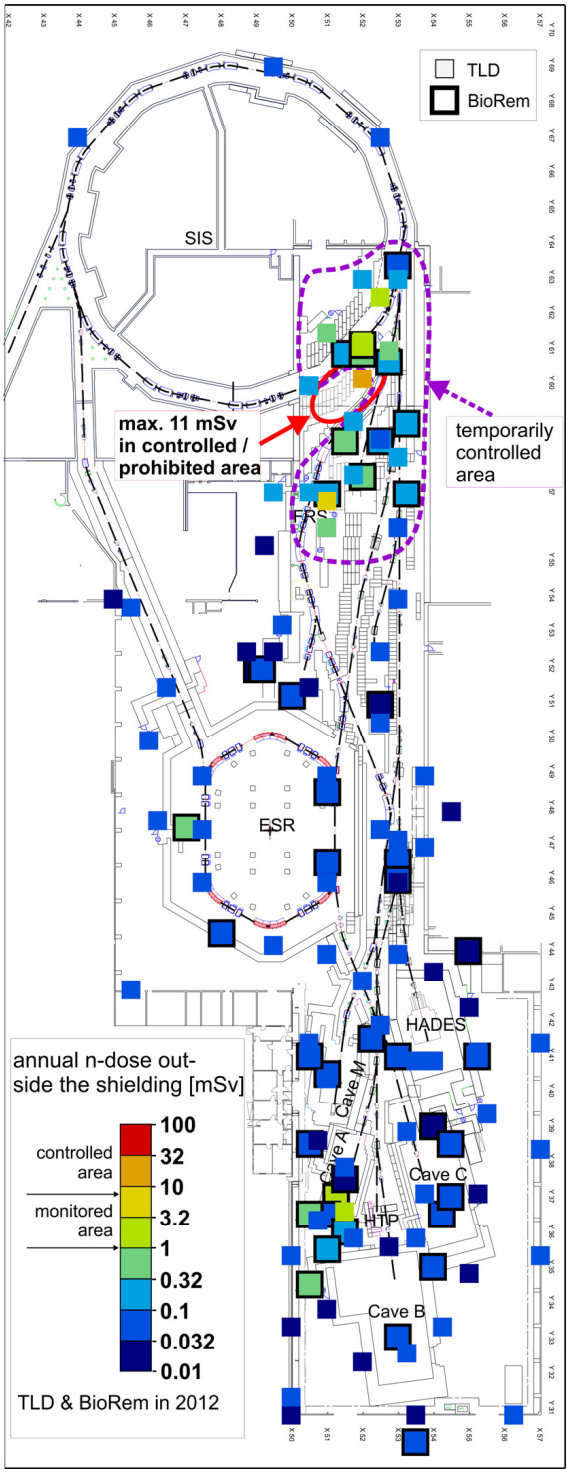

Figure 2: Map of the experimental areas fed by SIS. Measurement positions are shown with doses recorded by active dosimeters [2] (larger squares with frame) and passive detectors [2] (smaller squares).

Measurement of the behavior of residual gas particles on cryogenic surfaces to improve the simulation of dynamic vacuum effects

F. Chill[1,2], L. Bozyk[2], O. Kester[1,2], and P. Spiller[2]

[1]Goethe-Universität, Frankfurt, Germany; [2]GSI, Darmstadt, Germany

Introduction

The dynamic vacuum refers to pressure rises occurring during beam operation in particle accelerators. It is caused by charge exchange of beam ions and the stimulated desorption of gas particles from the walls and has to be compensated by the pumps as fast as possible.

The StrahlSim code, which is developed in the synchrotron department at GSI [1], can simulate the evolution of the residual gas pressure, its composition, and its interactions with the ion beam during a realistic synchrotron cycle. The code calculates for each timestep the amount and position of beamlosses and the resulting desorption. Locally elevated pressure values lead to higher beamlosses by charge exchange in corresponding areas during the next timestep, worsening the pressure even more. This self-amplifying effect is a limiting factor for the maximum beam intensity in circular accelerators.

To lift this intensity limit, the cryogenic vacuum chambers of the SIS100 will act as surface pumps. They are able to pump gases according to their vapor pressure curves which is sufficiently low for most gases. This is called *cryocondensation*. An important exception is hydrogen. Its saturated vapor pressure at 4.2 K (temperature of liquid helium) is 6E-7 mbar, which is too high for a stable operation with high intensity ion beams.

Fortunately hydrogen can be pumped to lower pressures by so called *cryosorption* if the surface coverage of the cold walls is sufficiently low [2]. This effect can be characterized by two parameters: The *sticking coefficient* describes the probability of a gas particle impacting on the surface to be bound. It is directly linked to the pumping speed provided by the cryogenic walls. The *mean sojourn time* describes how long a particle remains bound to a surface. Both parameters together determine the equilibrium pressure.

Measurement of the parameters

The planning and setup of an UHV experiment (Figure 1) to determine these parameters have begun. The cold surface that will be tested is provided in the form of a small chamber which is cooled by a cold head. The target temperature range is 5 to 20 K. The measurement will be divided in two phases: Firstly the pumping speed of the chamber is quantified at different temperatures and surface coverages to get the sticking coefficient. In the second phase, the corresponding equilibrium pressure is evaluated which yields the sojourn time.

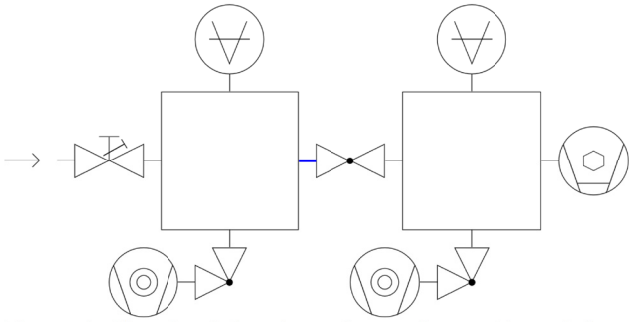

Figure 1: Sketch of the planned experiment. From left to right: Gas inlet, first recipient with extractor gauge and turbo pump, defined conductance (blue), valve to be closed for phase two, second recipient with cold-warm-transition to the cold chamber.

To link the pressure values measured by the gauges to the desired parameters, the simulation code Molflow+ [3] is used. It tracks gas particles through a system from a gas source to surfaces with non zero sticking by usage of a Monte Carlo based algorithm (Figure 2).

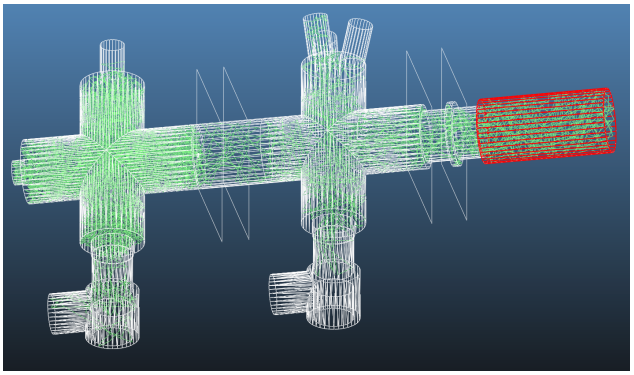

Figure 2: The Molflow+ model that is used to determine the properties of the experimental stand. The cold chamber (red) has a sticking assigned. This leads to a measurable pressure difference between the recipients.

The results will finally be integrated into StrahlSim to improve the quality of simulation for superconducting synchrotrons with cold surfaces.

References

[1] P. Puppel, PhD Thesis, 2012
[2] E. Wallén, J. Vac. Sci. Technol., A 14, 1996, p. 2916
[3] R. Kersevan, http://test-molflow.web.cern.ch

Potential-well distortion correction in a dual-harmonic RF system*

M. Mehler[1,2], *O. Boine-Frankenheim*[2,3], *and O. Chorniy*[2]
[1]IAP, Frankfurt, Germany; [2]GSI, Darmstadt, Germany; [3]TUD, Darmstadt, Germany

Introduction

In a synchrotron the sum of all impedances over n (see equation (1)) is responsible for the losses leading to phase shift and bunch form deformation by potential-well distortion (PWD) both in single- and dual-harmonic RF systems [1]. These can be described by the Haissinski equation for Gaussian longitudinal ion distributions. The phase shift of an ion beam distribution excited by a single harmonic RF system with the frequency $f_1 = h_1 f_{rev}$ (f_{rev}: revolution frequency) can be corrected by giving the RF voltage a synchronous phase Φ_{S1} (see equation (2)) as during acceleration. The beam distribution deformation cannot be corrected. It increases because of the accelerating bucket form [2]. For correcting the ion beam distribution deformation a second higher harmonic of the RF voltage with the frequency $f_2 = h_2 f_{rev}$ is necessary. This second harmonic defines the modified bucket- and therefore the bunch form. By varying the relationship $\alpha = \frac{V_2}{V_1}$ (see equation (2)) of the voltage amplitudes given for the second- (V_2) and main harmonic (V_1) and by varying the phase difference between the second- and main harmonic $\Delta\Phi$ the bunch form deformations can be corrected over all quality factors Q [3] leading to an increasing loss of bucket height with intensity. As the relationship for the frequencies of the dual-harmonic RF system $\frac{h_2}{h_1} = 2$ has been used for these numerical investigations.

$$Z_{Sh,n||} = \frac{R_{Sh,n}}{1 + iQ_n(\frac{\omega}{\omega_{RF,n}} - \frac{\omega_{RF,n}}{\omega})}$$
$$Z_{Sum||} = \sum_n (Z_{Sh,n||} - iX_{SC,n}) \quad (1)$$

Here n is the harmonic number of the shunt impedance $Z_{Sh||}$ and the space charge impedance X_{SC}. ω_{RF} is its resonance frequency.

$$V_{RF} = V_1(sin\Phi - sin\Phi_{S1} - \alpha(sin(\Phi_{S2} + \frac{h_2}{h_1}(\Phi - \Phi_{S1}) + \Delta\Phi) - sin\Phi_{S2})) \quad (2)$$
$$\Delta\Phi = \Phi_2 - \Phi_{S2} - \frac{h_2}{h_1}(\Phi - \Phi_S)$$

Simulation Results

With increasing intensity of U^{28+} the bunch form deformation and the phase shift caused by PWD is increasing too as can be seen in Figure (1). This leads to increasing requirements for its correction.

It has been found that with constant $\alpha = 0.5$ the necessary phase difference $\Delta\Phi$ to correct for PWD is higher than for addional variation of α between 0.5 and 1.0. For high quality factors Q (smallband impedances) the correcting α increases from 0.5 for low intensities up to 1.0 for high intensities. Only for broadband impedances with $Q \leq 0.1$ α stays constant, as can be seen in Figure (2), at the usually for dual-harmonic RF systems used value of $\alpha = 0.5$.

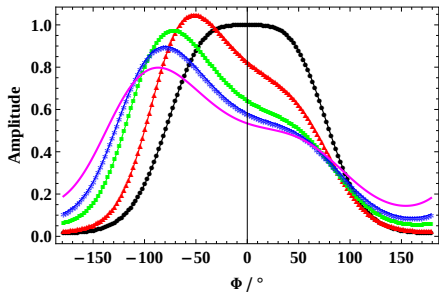

Figure 1: U^{28+} bunched beam distribution deformation and phase shift by PWD. The quality factor Q = 0.1. Black points: no PWD, red triangles: $N_b = 4 \cdot 10^{10}$, green squares: $N_b = 9 \cdot 10^{10}$, blue stars: $N_b = 13 \cdot 10^{10}$ and pink line: $N_b = 20 \cdot 10^{10}$ in SIS-100.

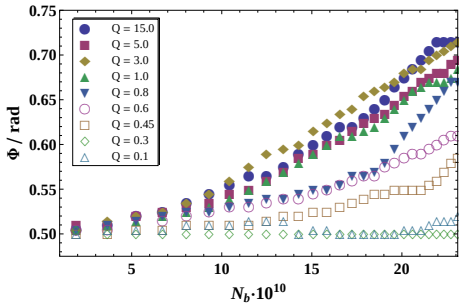

Figure 2: Development of $\alpha = \frac{V_2}{V_1}$ over the U^{28+} intensity with $X_{SC} \neq 0$.

References

[1] K. Y. Ng, "Physics of Intensity Dependent Beam Instabilities", (World Scientific, Singapore, 2006)

[2] M. Mehler et al., "Longitudinal dynamics of intense heavy-ion bunches in SIS-100", Proc. of IPAC2012, New Orleans, Louisiana, USA, p. 2937

[3] M. Mehler et al., "Intense heavy-ion bunches in dual-harmonic RF systems", Proc. of HB2012, Beijing, China, (to be published)

* Work supported by HGS-HIRe for FAIR

Development of a field emitter-based extractor gauge for pressure measurement in cryogenic vacuum systems

M. Lotz[1,2], St. Wilfert[1], A. Krämer[1], and O. Kester[1,2]

[1]GSI, Darmstadt, Germany, [2]Goethe University of Frankfurt, Germany

Motivation

In SIS100, stable beam operation with the planned high beam intensities and energies is ensured only if beam dynamic effects do not lead to pressure bumps exceeding the critical value of ~$5 \cdot 10^{-12}$ mbar (hydrogen equivalent at 10 K) in the cryogenic beam vacuum sections. In order to monitor this vacuum condition the use of pressure measuring devices has to be taken into account. Such low vacuum pressures can be measured commonly only by ion gauges of extractor type. Commercially available extractor gauges, however, use hot filament cathodes whose operation would generate an immense and non-tolerable heat load to the cryogenic system. To avoid this problem we developed an extractor gauge whose thermionic cathode was replaced by a field emitter (FE) cathode. Although the idea of field emitter-based ion gauges is not a new one [1], according to our knowledge, no one before has ever used a FE-based ion gauge for pressure measurement in a cryogenic vacuum system.

Gauge structure and experimental results

For our studies we modified a conventional extractor gauge of IE 514 type (Leybold). A CNT (carbon nanotube) cathode was used as 'cold' electron emitter. One possible gauge structure is shown in Figure 1.

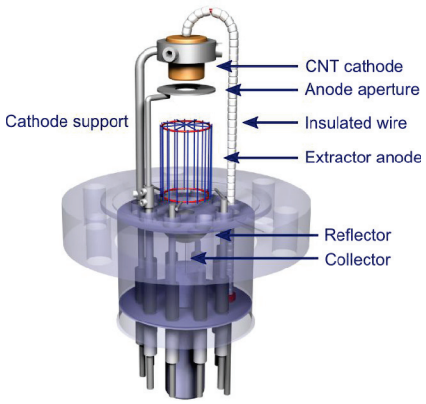

Figure 1: Possible layout of a CNT emitter-based extractor gauge

The gauge structure used in our experiments, however, deviated slightly from the one shown above. Instead of supporting wires, the CNT cathode and the deceleration electrode were mounted on a precision positioning manipulator with separate electrical feedthroughs in order to adjust an optimum distance between cathode and extractor anode.

First basic investigations have been carried out in order to study the long-term emission stability of the CNT cathode at cryogenic gas temperatures. Unfortunately, the long-term stability was only given for an anode current of 55 µA, which is a factor of ~30 lower than the anode current of an unmodified extractor gauge. At a higher value a sudden decrease in the emission current was observed, probably caused by a partial destruction of the CNT layer.

Following development work was focused on experimental studies for determination of an optimum working point of the gauge and measurement of basic gauge characteristics for different gas species. The experimental results at room temperature show, as expected, a perfect linear relationship between ion current and pressure in the vacuum range between $5 \cdot 10^{-9}$ and 10^{-5} mbar. Finally, the operability of the modified gauge was tested in a LHe-cooled vacuum chamber. For that purpose we recorded the gauge response against the pressure reading of an extractor gauge with thermionic cathode while the cooled chamber was moderately heated-up from 9 to 25 K. The thermal-triggered pressure rise inside the chamber caused by hydrogen desorption was used for gauge calibration. In Figure 2 the pressure-dependent ion current is given, indicating the strongly linear measuring behavior.

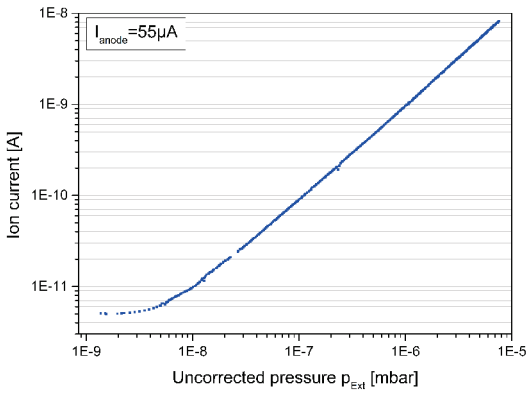

Figure 2: Ion current vs. pressure characteristic for H_2 at 9..25 K

Conclusion

We could clearly demonstrate that a FE-based extractor gauge works reliably under cryogenic vacuum conditions and provides meaningful pressure reading. However, the relative low emission current of the field cathode still restricts significantly the original measuring range of extractor gauge which is typically $1 \cdot 10^{-12}$ mbar (at RT).

References

[1] Wilfert, St., Edelmann, Chr.; Vacuum 86 (2012), 556

UNILAC Machine Experiments in 2012

H. Vormann[1], W. Barth[1], G. Clemente[1], L. Dahl[1], P. Gerhard[1], V. Gettmann[2], L. Groening[1], M. S. Kaiser[1], M. Maier[1], S. Mickat[1], A. Orzhekovskaya[2], B. Schlitt[1], and S. Yaramyshev[1]

[1]GSI, Darmstadt, Germany, [2]Helmholtz Institut Mainz, Germany

In the UNILAC machine experiments 2012 investigations on carbon foils and methane and hydrogen gas for stripping in future UNILAC scenarios have been performed as well as optimisations of the UNILAC.

Stripping experiments

Thin carbon foils from the GSI target laboratory (20 resp. 30 µg/cm^2) have been tested in March in the experimental areas at TASCA (X8) and SHIP (Y7) on rotating target wheels. At X8 a low current Au^{25+} beam (4 eµA, 3.6 MeV/u, 3 ms, 50 Hz) has been applied 24 hours on 4 foils, at Y7 a U^{28+} beam (2.5 emA, 3.6 MeV/u, 100µs, 2 Hz) has been applied to 8 foils 48 hours. While the long beam pulses at X8 were evenly distributed on the moving foils (by 5 cm) [Fig. 1], the beam spot of the short 100 µs pulses at Y7 was scanned over the foil by the rotary motion of the wheel by shifting the phase of the target wheel. In both setups the foils showed typical characteristics of the irradiation, without any damages.

Fig. 1: TASCA target wheel after irradiation.

In November a set of thin carbon foils has been tested with a 5 emA U^{4+} beam at 1.4 MeV/u (100 µs, 2 Hz). Ten standard carbon foils (20 µg/cm^2), all from the same material but prepared under different conditions, mounted on a fixed carrier, have been irradiated approximately four hours each. Although some of them seemed to be unharmed after irradiation (camera in the stripping chamber), only two were actually undamaged after venting and dismantling from the vacuum chamber [Fig. 2]. This confirms the experiments from October 2011, when similar foils had been damaged after irradiation with comparable dissipated energies (about 4 kWs/cm^2) [Fig. 3]. Emittance measurements behind the stripper showed no significant variation during irradiation. The energy loss through the foils was typically 24 keV/u at the beginning and 22 keV/u after irradiation. Two foils from an external provider have been tested too, but broke within few pulses of beam. Further carbon foils were irradiated in the M-Branch for materials research investigations.

Fig. 2: Carbon foils after irradiation (5 emA U^{4+}, 1.4 MeV/u).

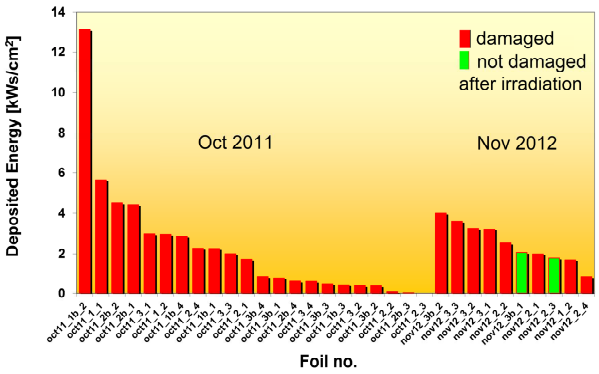

Fig. 3: Statistics of the irradiated foils (20 µg/cm^2).

In addition experiments with methane and hydrogen as stripping gas in the existing UNILAC gas stripper were performed (high current U^{4+}, 1.4 MeV/u). Charge state spectra, beam currents, and emittances behind the stripper were measured for various methane flow rates [1].

UNILAC Optimisations

Investigations of the HSI transmission showed that the small aperture of the quadrupole quartet in front of the RFQ restricts the matching, therefore the ongoing upgrade of the quartet (larger aperture) is essential. Beam attenuation by increasing instead of reducing the field strength in the quartet was proved, so the power supplies for the new quartet do not need to cover the full current range below the light-ion operation (5% of max. filed) down to zero with high accuracy.

To provide heavy ions with higher charge states than e.g. U^{73+} for the SIS, thicker stripping foils in the transfer channel (11.4 MeV/u) were tested (1000 µg/cm^2). The spectra revealed a slight increase of the U^{74+} charge state, but a worse separation.

Additionally the beam diagnostics department performed tests of a prototype signal processor for position and phase measurement, the bunch shape monitor in the transfer channel, SEM grids, scintillator targets, and fluorescent screens.

References

[1] B. Schlitt, "Beam Measurements CH4 and H-gas strippers", (this report).

R&D Projects with High Current Ion Sources

A. Adonin and R. Hollinger

GSI, Darmstadt, Germany.

Development of high current Au and Pb beams for experiments on SIS

As was reported previously [1,2], to enlarge the number of elements for acceleration and to fulfill the requests of several research projects at GSI the program of developing of further heavy elements for acceleration has been established. In the frame of this program the development of three additional elements: ^{197}Au, ^{208}Pb and ^{209}Bi for operation with the VARIS ion source was foreseen.

Challenges and Solution

Due to the requirements of HSI RFQ (the mass-over-charge ratio should not exceed 65) the requested charge state of ions for considered heavy elements is 4^+. It is challenging to produce a sufficient amount of four-fold ions in the plasma generated by vacuum arc discharge in the VARIS ion source, because of the physical properties of these elements. Rapidly increased flux of neutrals from a cathode surface during the discharge pulse shifts the charge state distribution of ions in the plasma to lower charge states (maximum at 1^+, 2^+) for the time of about 50 µs after ignition of the vacuum arc. As was confirmed experimentally [3], due to this effect it is not possible to provide stable high current operation of Au, Pb and Bi beams using the cathode made of pure materials. But the situation can be dramatically improved by using composite materials in cathodes with admixing of certain amount of more refractory metals.

Investigation of various Au-alloys

Proceed from the phase diagrams of different Au-Metal binary systems, the following metals were chosen for admixing to Au: Pd, Cr, Zr, Ti and Ta. First cathode sets were manufactured containing small amount of admixed material (between 5 % and 20 % wt.) After the first experiments the most promising results were achieved with Au-Cr (20 %) and Au-Zr (20 %) cathodes.

The composite cathodes required quite long conditioning time (more than 10 hours of operation with 1 Hz) before they could provide high current stable beam of Au^{4+}. The investigation of the surface and the material structure of the Au-Cr cathodes using optical and electron microscopes has shown appreciably higher concentration of Cr on the working surfaces of good conditioned cathodes (Fig.1). Considering this fact next tests (in February 2012) were performed with Au-Cr (50 % wt.) and Au-Cr (75 % wt.) cathodes. Manufacturing of Au-Zr cathodes with higher Zr percentage was not successful due to particular chemical properties of Zr. The cathodes from Au-Cr (50 %) material showed much better performance than others. After short (10-20 min) conditioning time they provided stable beam of Au^{4+} ions with beam currents up to 6 mA in front of the RFQ, proper beam pulse shape and good pulse-to-pulse repetition. The typical duty cycle was 1 Hz with 300 µs pulse length. The charge state distribution of Au ions was: 14 % of 2^+, 44 % of 3^+, 38 % of 4^+ and about 4 % of 5^+. The Cr-fraction in the ion spectrum was more than 50 % with maximum at 3^+. Since Au^{4+} and Cr^{1+} ions stay by ***A/Q*** ratio relatively close to each other, a variable slit behind the dipole magnet was used to cut Cr^{1+} ions. The high current ^{197}Au-beam was successfully provided for HADES experiment in April-May 2012 (5 weeks of beamtime).

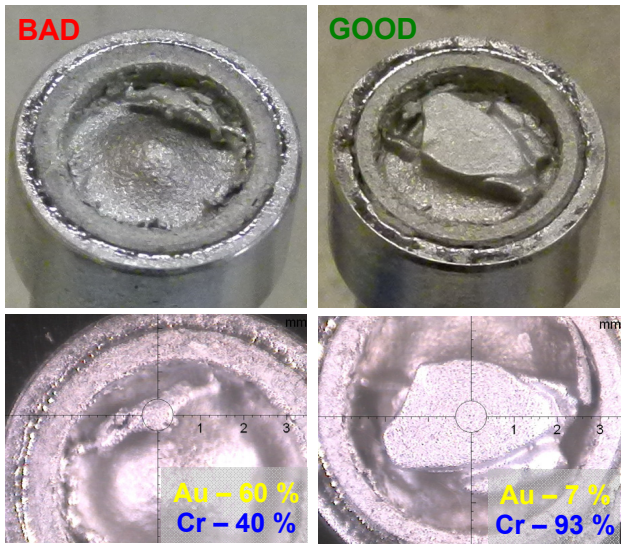

Figure 1: Au-Cr (20 % wt.) cathodes after 1 day of operation: bad performance (*left*) and good performance (*right*).

Investigation of Pb-Cu alloys

The first tests with Pb were performed in June 2012 using composite Pb-Cu cathodes with various amounts of Cu admixed (40 % and 60 %) and different manufacturing techniques (powder metallurgical and infiltration). The best performance has been shown by Pb-Cu (40 % wt.) infiltrated cathodes. They provided stable operation with good pulse-to-pulse repetition and beam currents up to 6 mA in front of the RFQ. However all cathodes required relatively long conditioning time (more than 3 hours with 1 Hz operation). The charge state distribution of Pb-ions was: 30 % of 3^+, 63 % of 4^+ and 7 % of 5^+. The ^{208}Pb-beam was successfully provided for FRS experiments in September-October 2012 (2 weeks of beamtime).

References

[1] A. Adonin et al., GSI Scientific Report 2010.
[2] K. Tinschert et al., GSI Scientific Report 2011.
[3] A. Adonin and R. Hollinger, Proceedings of the 25th ISDEIV, Vol.2, p.630, Tomsk, Russia, Sep. 2012.

Research and Development on ECR Ion Sources

K. Tinschert, R. Lang, J. Mäder, F. Maimone, J. Roßbach, P. Spädtke

GSI, Darmstadt, Germany

Microwave tuning for metal ion production

It has been demonstrated that frequency tuning of the microwave injected into an ECR ion source (ECRIS) using a travelling wave tube amplifier (TWTA) can provide a considerable increase of the ion beam intensity of highly charged gas ions [1]. Investigations on the application of this technique on the production of metal ion beams have been performed with the CAPRICE ECRIS at the ECR injector test setup (EIS).

The standard Klystron microwave generator working at 14.5057 GHz has been replaced by a TWTA driven by a variable frequency synthesizer initially adjusted to the same frequency and operated at a forward power of 250 W. The ECRIS was operated with natural Ti evaporated from the high temperature oven (HTO) at a heating power of 230 W. After optimization of the ECRIS for stable ion beam conditions of Ti^{8+} the microwave frequency was swept in the frequency range from 12.5 to 16.5 GHz exhibiting a pronounced intensity variation of Ti^{8+} and Ti^{11+}, respectively, as shown in figure 1 for the ion current of Ti^{11+}. During the sweep some frequencies were identified at which this ion current was considerably enhanced. E. g. compared to the initial frequency of 14.5057 GHz which corresponds to an ion current of 13 µA of Ti^{11+} at 13.725 GHz an increase of the intensity level by a factor of 3 could be observed. Moreover the long time stability of the ion beam properties could be demonstrated in a 12 hours run. Only the oven heating had to be slightly adjusted in order to compensate for the reduction of sample material by the evaporation process.

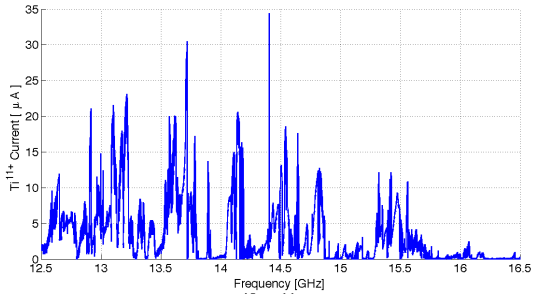

Figure 1: Variation of the $^{48}Ti^{11+}$ current as function of the microwave frequency.

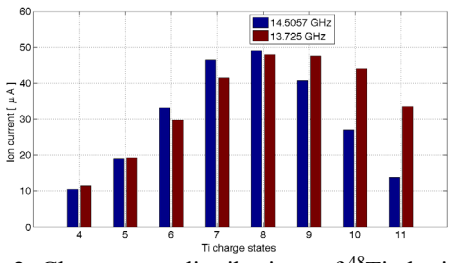

Figure 2: Charge state distributions of ^{48}Ti obtained for two microwave frequencies.

Figure 2 shows a comparison of the mass/charge spectra at these two selected frequencies. These spectra are obtained with identical source settings and oven heating. The shift of the charge state distribution, leading to a considerable intensity gain for the higher charge states, demonstrates that frequency tuning can be a versatile method to optimize for a suitable charge state distribution for the production of metal ion beams [2].

Pepper Pot emittance scanner devices

In the framework of a collaboration between the Kernfysisch Versneller Instituut (KVI) and GSI pepper pot emittance measurement devices have been designed and commissioned at KVI before installation at the EIS test setup at GSI. Such device utilizes a matrix of holes (10 µm diameter each) in a pepper plate which cuts beamlets out of the incoming ion beam. The local distribution of ion trajectories from the beamlets is collected and visualized by a sandwich MCP/phosphor screen. The image of the phosphor is recorded by a CCD camera and transformed into x−y coordinates. From the image data and from the original positions of the holes in the pepper plate the distribution of charged particle beams in the 4D transversal phase space can be evaluated. The evaluation method of such kind of device can account for the complex inhomogeneous structure of an ion beam originating from an ECRIS which is not possible with devices integrating over one space coordinate [3,4]. First tests were carried out with He and Ar beams. An optimization of the evaluation software is in progress.

Acknowledgements

The support of the European Union Seventh Framework Programme FP7/2007-2013 under Grant Agreement n° 262010 - ENSAR is acknowledged. The EC is not liable for any use that can be made on the information contained herein.

References

[1] F. Maimone, K. Tinschert, L. Celona, R. Lang, J. Mäder, J. Roßbach, and P. Spädtke, Rev. Sci. Instrum. 83, 02A304 (2012).

[2] K. Tinschert, R. Lang, J. Mäder, F. Maimone, J. Rossbach, Proc. of the 20th Workshop on ECR Ion Sources, Sydney, Australia, 25-28 Sept 2012.

[3] H. R. Kremers, J.P.M. Beijers, S. Brandenburg, Proc. of DIPAC 2007,Venice, Italy, p. 195.

[4] P. Spädtke, R. Lang, J. Mäder, F. Maimone, J. Roßbach, K. Tinschert, J.W. Stetson, Proc. of IPAC10, Kyoto, Japan, 2010, p. 4029

Prototype Testing of the Frankfurt Gabor Lens at HOSTI

K. Schulte[1], A. Adonin[2], R. Berezov[2], M. Droba[1], R. Hollinger[2], J. Pfister[2], O. Meusel[1], and U. Ratzinger[1]

[1]Goethe University, Frankfurt, Germany; [2]GSI, Darmstadt Germany

At the Institute for Applied Physics (IAP Frankfurt) the application of Gabor space charge lenses as a focusing device for low energy ion beams has already been studied for several decades with limitations to low currents. In mid-2012 the performance of a prototype lens has successfully been tested at the GSI High Current Test Injector (HOSTI).

GSI and IAP are currently investigating the possible application of such a device for the uranium operation at the new Terminal West for FAIR.

Prototype Gabor Lens

The prototype Gabor lens had been designed for focusing a $^{238}U^{4+}$ beam with an energy of 2.2 keV/u and a maximum beam radius of r_B=50 mm. In this context, emphasis was put on the homogeneity of the confined electron density distribution and connected to this the linearity of the electric space-charge field within the beam region to ensure transport free of aberrations [1].

Beam Transport Experiments at HOSTI

The beam transport measurements had been divided into two parts: low current measurements to study the quality of ion optics and high current measurements. In case of the low current measurements the focusing performance of the lens transporting a He^+ beam with currents up to 5 mA and beam energies of 12.6 keV/u was investigated. For the high current measurements an Ar^+ beam of currents up to 35 mA with beam energy of 3.1 keV/u was generated. In both cases the MUCIS ion source was operated in pulsed mode with a pulse length of 1.25 ms and a rep rate of 1 Hz [2]. Figure 1 shows a picture of the experimental setup at HOSTI.

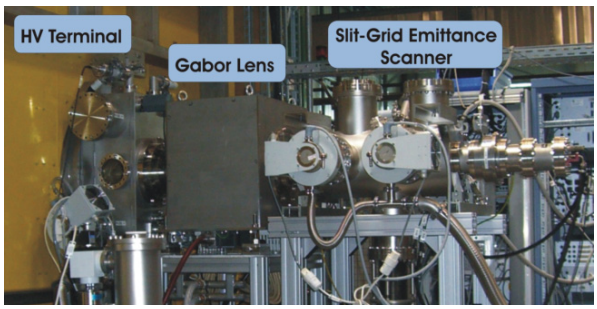

Figure 1: Picture of the experimental setup.

The low current measurements clearly show the influence of electron density distribution on the emittance figure (see Figure 2). In the illustrated beam transport simulations a compensation degree of 95 % was assumed.

The high current measurements demonstrate that this kind of Gabor lens is suitable for the transport of high current ion beams without reasonable emittance growth (see Figure 3).

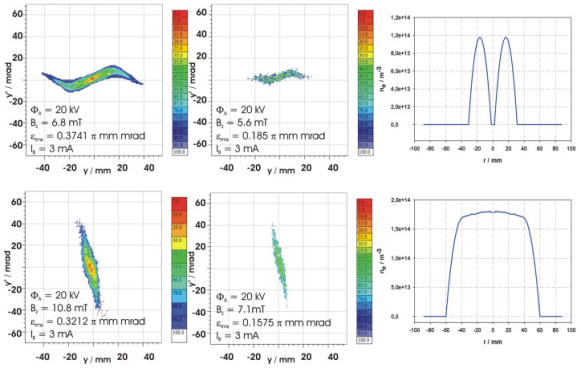

Figure 2: Comparison of measurement (left) and simulation of the transported He^+ beam (centre) as well as simulated electron density distribution (right).

A parallel beam is attained with lens parameters of Φ_A=9.8 kV and B_z=10.8 mT. One has to remark that the high current measurements were performed with an iris of 50 mm at the entrance of the lens to protect the insulator from the beam.

Improvements in the lens design concerning the magnetic field and the insulator of the electrode system are currently under discussion.

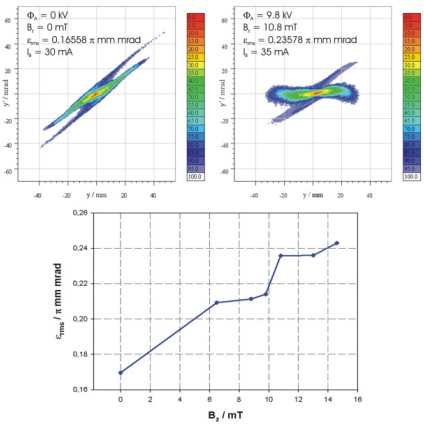

Figure 3: Phase space distribution of the drifted (left) and of the transported Ar^+ beam (right), emittance growth as a function of the confining magnetic field (bottom).

References

[1] K. Schulte, “Space Charge Lens for Focusing Heavy Ion beams”, GSI Scientific Report, 2010.

[2] A. Adonin et al., “Measurements of Transverse Ion Beam Emittance Generated by High Current Ion Sources at the GSI Test Injector Facility HOSTI”, Rev. Sci. Instrum. 81, 02B707(2010).

Preparation of an emittance transfer experiment in the UNILAC*

C. Xiao†[1], *L. Groening*[2], *O. Kester*[1,2], *H. Leibrock*[2], *and M. Maier*[2]
[1]IAP, Frankfurt am Main, Germany; [2]GSI, Darmstadt, Germany

Introduction

Flat hadron beams could facilitate the process of multi-turn injection into circular machines, which imposes different requirements on the horizontal and vertical emittance of the incoming beam. From first principles beams are created round without any coupling among planes. Their rms emittances as well as their eigen-emittances are equal in the two transverse planes. Thus, any transverse round-to-flat transformation requires a change of the beam eigen-emittances by a non-symplectic transformation. Such a transformation can be performed by placing a charge state stripper inside an axial magnetic field region as proposed in [1, 2]. Inside such a solenoid stripper, transverse inter-plane correlations are created non-symplectically. Afterwards they are removed symplectically by a decoupling section including skew quadrupoles.

Experimental Set-up

The new EMTEX (emittance transfer experiment) beam line for the demonstration of transverse emittance transfer is shown in Fig. 1.

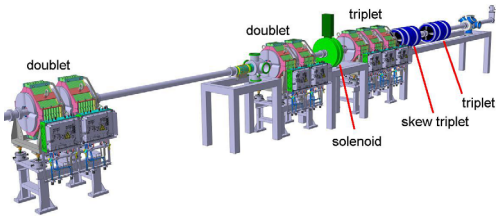

Figure 1: The layout of the EMTEX section at GSI.

The transverse emittance transfer beam line comprises two quadrupole doublets, a solenoid with stripper foil inside, a quadrupole triplet, a skew quadrupole triplet, another quadrupole triplet, a current transformer, and a transverse emittance measurement unit. Its total length is about 12.8 m.

Beam Dynamics Simulation

Fig. 2 illustrates the transverse emittance transfer. In the first step we assume that we turn off the power supplies of the solenoid and the skew quadrupole triplet. This process is an ordinary stripping process and the eigen-emittances are equal to the rms emittances at the exit of this section. Due to the stripping, growth of eigen-emittances and rms emittances is unavoidable. It is the reference scenario to which the emittance transfer scenario is to be compared. In the latter the solenoid field and the decoupling skew quads are turned on. The eigen-emittances diverge inside the solenoid but they are preserved afterwards. Along the decoupling skew quadrupole triplet the rms emittances are made equal to the diverged eigen-emittances. Compared to the reference scenario, the final horizontal rms emittance is reduced significantly by a factor two. The beam rms sizes along the total beam line are shown in Fig. 3 (solenoid and skew quads on).

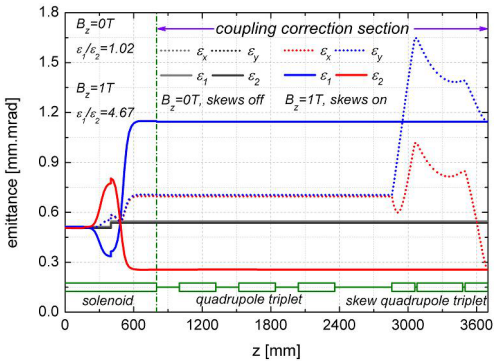

Figure 2: Evolution of rms emittances and eigen-emittances along the longitudinal magnetic field and the decoupling section for two scenarios: solenoid and skew quads off (reference, green and dark green lines); solenoid and skew quads on (emittance transfer), B_z=1.00 T.

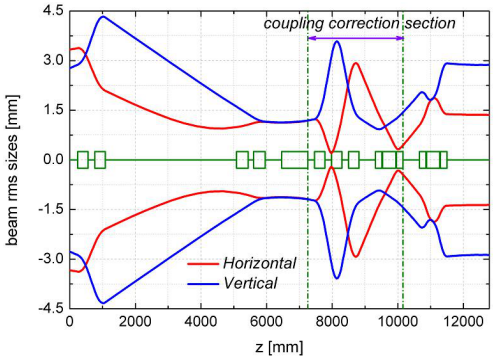

Figure 3: Horizontal and vertical beam rms sizes along the proposed transverse emittance transfer section.

References

[1] L. Groening, Phys. Rev. ST Accel. Beams **14**, 064201 (2011).
[2] C. Xiao et al, "JACoW, Preparation of an emittance transfer experiment", http://arxiv.org/abs/1212.2034.

*Work supported by the HIC for FAIR and the BMBF
†C.Xiao@gsi.de

Beam Measurements with CH4 an H2 Gas Strippers at the UNILAC

B. Schlitt, H. Vormann, L. Dahl, L. Groening, M. Maier, and S. Mickat

GSI, Darmstadt, Germany

The existing UNILAC gas stripper was operated with methane and hydrogen stripper gases to study the impact of low-Z gases on stripping of high current (up to 4 emA) U^{4+} ion beams at 1.4 MeV/u (100 µs, 2 Hz beam pulses). Since electron capture cross sections are considerably suppressed for low-Z gases, in particular hydrogen is promising higher equilibrium charge states compared to nitrogen [1–3]. As hydrogen gas has a very low density, hydrocarbons like methane or propane provide for higher hydrogen concentrations and may be better suited for gas stripper applications.

Gas Stripper Operation

To avoid explosive gas mixtures, nitrogen gas was injected as inert gas into the vacuum exhaust pipe of the gas stripper setup and of the neighbouring vacuum sections to provide for methane and hydrogen concentrations in the exhaust air below 2.2 % and 2 %, respectively – a factor of two below the lower explosion limits. The nitrogen gas was provided by the central GSI nitrogen gas distribution system fed by a LN2 tank and by additional bundles of N2 gas cylinders. An interlock system was installed to monitor the nitrogen gas flow, the pressure inside the vacuum exhaust pipe, and the vacuum pressure inside the gas stripper setup. The modified gas stripper was operated successfully for various ion beam measurements.

Beam Measurements

For increasing methane mass flow rates between 12 g/min and 23 g/min – corresponding to methane gas pressures between 2.4 bar and 4.5 bar at the gas inlet – the mean uranium charge states measured behind the stripper increased from about 23+/24+ to 25+/26+ (Fig. 1). For standard nitrogen operation of the stripper, higher mass flow rates around 26 g/min are routinely achieved at a gas pressure of roughly 4 bar resulting in mean charge states around 27+ (Fig. 1). A beam energy loss of 13 keV/u was measured for U^{28+} within the range of the methane flow rates given above, compared to 15 keV/u for the nitrogen gas stripper. Measured U^{28+} beam emittances were slightly increasing for increasing methane flow rates and were comparable to the values measured for the nitrogen gas stripper. The highest attainable methane flow rates were limited by the maximum pumping speed of the turbo pumps mounted at the gas stripper chamber.

For hydrogen stripper gas, a maximum mass flow rate of only about 1.4 g/min could be reached due to the low mass density of the hydrogen gas and because of the steeply rising vacuum pressures inside the stripper chamber and in the neighbouring vacuum sections, since hydrogen is only very poorly pumped by the vacuum pumps. Due to the low mass density of the hydrogen gas jet, the highest charge state which could be transported along the bending magnet installed behind the stripper was about U^{21+} (Fig. 2). The maximum of the charge state spectrum could not be measured due to the limited field strength of the bending magnet.

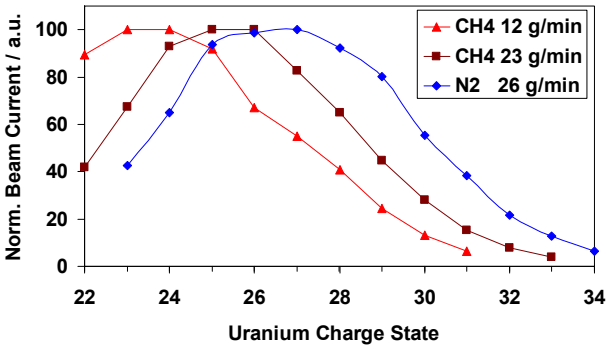

Figure 1: Uranium charge state distributions after stripping at different stripper gases and mass flow rates.

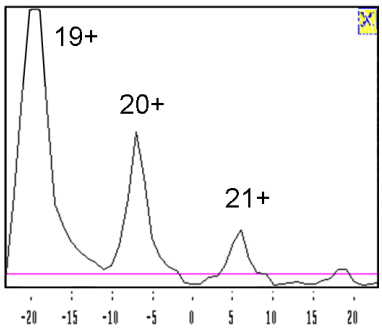

Figure 2: Measured uranium ion beam profiles behind the bending magnet with opened analyzing slits at the maximum attainable hydrogen stripper gas flow rate of about 1.4 g/min.

Finally, the experiments showed that currently neither methane nor hydrogen are serious alternatives to nitrogen for the existing UNILAC gas stripper since the highest uranium charge states and the highest U^{28+} beam currents were achieved with the nitrogen gas jet so far. To investigate higher mass densities for methane and hydrogen, substantial technical modifications of the gas stripper setup would be necessary (in particular for hydrogen).

We would like to thank P. Horn and B. Mai and several further colleagues at GSI for their support concerning the modifications of the gas stripper setup and its operation with explosive gases.

References

[1] H. Okuno et al., in: Proc. HIAT2012, p. 199.
[2] H. Okuno et al., PRST-AB **14**, 033503 (2011).
[3] V.P. Shevelko et al., NIM **B 218** (2012) 63.

Status of the High-Energy Linac Project at GSI

B. Schlitt, G. Clemente, W. Barth, and W. Vinzenz

GSI, Darmstadt, Germany

To assure reliable operation for FAIR, a new high-intensity heavy-ion injector linac for SIS18 (high-energy (HE) linac) was proposed as replacement for the existing post-stripper linac at the GSI UNILAC. A linac for short beam pulses, low repetition rate, and fixed end energy is under investigation. The first proposal [1, 2] included to extend the pre-stripper to 3 MeV/u to achieve higher charge states around U^{38+} behind the gas-stripper and the linac end energy was boosted to 22 MeV/u. Recently, a less ambitious solution was favoured without an extension of the pre-stripper linac and keeping U^{28+} for acceleration along the new HE linac and in SIS18 (Fig. 1, Table 1). Six 108 MHz IH-type drift-tube linac cavities within a total length of about 24 m accelerate the ions up to 11.4 MeV/u as provided by the existing linac. Fast pulsed quadrupole triplet lenses suitable for multi-beam operation are used for transverse focusing in between the IH cavities (Fig. 2). Quadrupole magnets inside the cavities should be avoided. This new HE linac solution is less expensive as the previous one and the existing gas-stripper section does not need to be shifted to a new location. The new solution leaves plenty of space within the existing UNILAC tunnel available for future linac energy upgrades (Fig. 1). In addition, alternative solutions to the present nitrogen gas stripper, like carbon foil strippers [3], a plasma stripper [4], and the use of low-Z gases like hydrogen at the gas stripper [5] are being investigated in order to generate higher charge states.

RF Systems

A preliminary study for 108 MHz, 1.8 MW high-power amplifiers for short-pulse low duty cycle operation was performed in collaboration with industrial partners. It is based on a TH558SC tetrode from THALES Electron Devices which is widely used worldwide for broadcast as well as for scientific applications. Thus, there is no known risk concerning the long-term availability of this tube for the coming decades. Pilot studies concerning solid-state driver amplifiers and amplifier supply units based on state-of-the-art technologies as well as for a modern digital low-level RF (LLRF) system were started.

Outlook

Design and construction of a prototype IH cavity as well as of a prototype RF amplifier are planned for 2013 – 15, followed by high-power RF tests and beam tests at GSI. Tests of a digital LLRF system on loan from an industrial partner are planned at GSI for 2013.

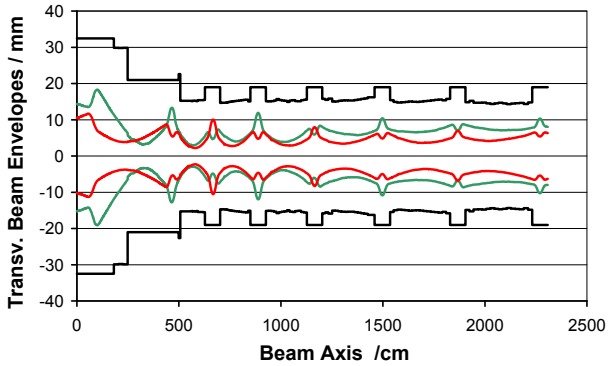

Figure 2: Hor. (red) and vert. (green) 99 % beam envelopes for a 20 mA U^{28+} beam along the HE linac.

Table 1: Main design parameters of the proposed linac

Design ion species	$^{238}U^{28+}$	
Design beam current (pulse)	15	mA
Max. mass / charge ratio	8.5	
Input beam energy	1.4	MeV/u
Output beam energy	11.4	MeV/u
Total acceleration voltage	85	MV
Linac length	ca. 24	m
RF frequency	108.4	MHz
Beam pulse length	≤ 100	µs
Beam repetition rate	≤ 4	Hz
RF duty factor	≤ 1	%
No. of IH-DTL cavities	6	
Cavity length	1.6 – 3.5	m
Max. RF power / cavity (incl. beam loading)	1300	kW

References

[1] B. Schlitt, G. Clemente, W. Barth, and W. Vinzenz, in: GSI Scientific Rep. 2011, p. 296.
[2] B. Schlitt et al., in: Proc. HIAT2012, p. 191.
[3] H. Vormann et al., this report.
[4] C. Teske, Y. Liu, S. Blaes, and J. Jacoby, Physics of Plasmas **19**, 033505 (2012).
[5] B. Schlitt, H. Vormann et al., this report.

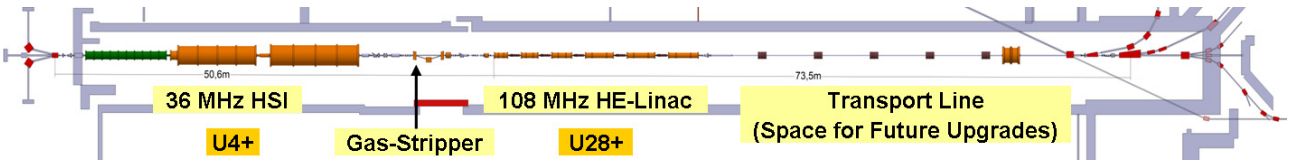

Figure 1: The proposed new 108 MHz high-energy (HE) linac within the existing UNILAC tunnel at GSI.

Experimental Investigation of the HLI-RFQ

P. Gerhard[*1] *and H. Vormann*[1]
[1]GSI, Darmstadt, Germany

Introduction

In 2010 the 4-rod Radio Frequency Quadrupole RFQ of the High Charge State Injector HLI at the UNILAC was replaced [1]. After solving serious thermal problems, the new RFQ was commissioned and operated successfully [2]. Yet there are still issues related to the thermal and mechanical stability, which have to be solved in order to reach full (design) performance.

Thermal Stability

Although all relevant parts of the structure are directly water cooled, the structure reacts rapidly to even small changes of the thermal load. The frequency changes by approx. 200 kHz from low to 50% design rf power. This has severe impact on the frequency controller, which acts on two plungers. During tuning of the machine, the average power $\bar{P} = P_{\mathrm{rf}} \cdot t_{\mathrm{pulse}} \cdot f_{\mathrm{rep.}}$ can only be changed in small steps to allow the controller to follow. For stable operation, all parameters have to be fixed. After rf breakdowns (sparking), the RFQ immediately loses resonance and has to be restarted from 'cold' position at low rf amplitude.

Estimates of the power loss and the cooling efficiency indicate a temperature change of 10–20 K. In order to verify this, parts of the structure were heated with warm water and the frequency change was monitored. The results agree well with the estimates. Further tests and simulations of the cooling, the power loss and resulting temperature distributions, and the frequency response are necessary to specify upgrade measures.

Mechanical Stability

The rf power reflected by the RFQ shows a modulation (Fig. 1), which is a feature already known from similar 4-rod RFQs. Here the magnitude of the modulation severely affects the frequency controller and limits the rf amplitude, while a nice flattop can still be provided. This modulation has a frequency of about 520 Hz, and most probably originates from mechanical vibrations of the electrode rods and/or the coupling loop. These are excited when the electric field is switched either on *or* off. First mechanical simulations of the rods agree well with the observations.

From routine operation at a pulse repetition rate of 50 Hz (Fig. 1 left), it was known that the modulation strongly depends on the pulse length, and operation with high rf amplitudes is only possible at certain values. By exchanging low level rf components, the RFQ could be operated at a pulse repetition rate of only 1 Hz (Fig. 1 right) [3]. With this, the modulation does not depend on the pulse length.

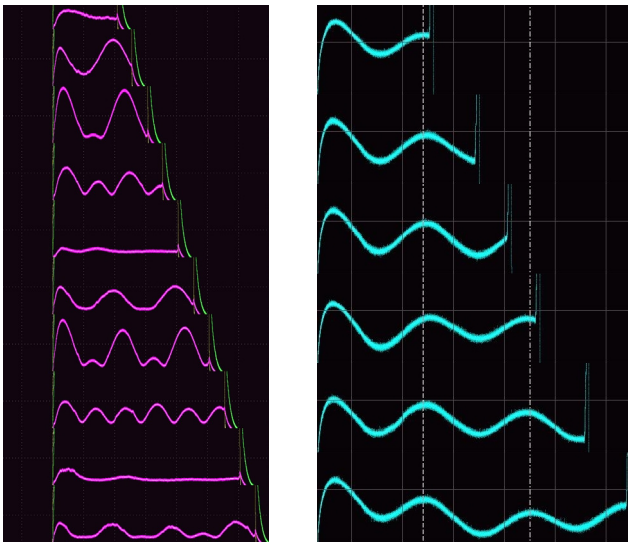

Figure 1: Rf modulation at $f_{\mathrm{rep.}}$=50 Hz (left) and 1 Hz (right) and t_{pulse} ≈2–6 ms.

At 50 Hz consecutive pulses interfere. By changing the pulse length, the relative phase between the interfering vibrations and hence the modulation is changed. A more detailed analysis of the rf signals revealed that the modulation is damped with a time constant between 6 and 10 ms. At 1 Hz the vibration is damped completely between two pulses, which are then uncorrelated, and the modulation does not depend on the pulse length.

Efforts were made to confine the region of the structure where the vibrations are excited. The RFQ was operated with clamps on the rods, but no influence could be observed. Only the damping time was slightly reduced [3].

Outlook

Further investigations are necessary before upgrade measures can be tackled. Emphasis will be on mechanical simulations, while tests on the vibrational behavior of the coupling loop are already in preparation.

References

[1] P. Gerhard, GSI-UPGRADE-ACC-03, p. 148, GSI SCIENTIFIC REPORT 2009

[2] P. Gerhard *et al.*, PHN-ACC-RD-05, p. 262, GSI SCIENTIFIC REPORT 2010

[3] P. Gerhard *et al.*, LINAC'12, September 2012, Tel Aviv, THPB035

* p.gerhard@gsi.de

Offline commissioning of the old and new HITRAP RFQ

M.Maier[1], K.Dermati[1], F.Herfurth[1], E.Kammer[1], M.König[2], N.Kotovskiy[1], M.Müller[1], D.Neidherr[1], R.Repnow[2], E.Scheurich[2], M.Trebis[2], H.Vormann[1], G.Vorobjev[1], P.Werle[2] and S.Yaramyshev[1]

[1]GSI, Darmstadt, Germany; [2]MPIK , Heidelberg, Germany

Introduction

The HITRAP facility is built to decelerate highly charged ions almost to rest and to provide them to experiments [1]. Until now the transition from the first deceleration step, an IH, to the second, a RFQ, was hampered by an energy mismatch as concluded from refined calculations [2]. An offline test at the MPI-K in Heidelberg has been set up to experimentally verify the calculated energy mismatch and to test the newly designed RFQ structure [2], built in-house [3].

The electrostatic accelerator at MPI-K [4] delivers a monochromatic H_2^+ ion beam variable in the required energy range around 500 keV/nucleon. A dedicated setup (Figure 1) was installed and used to measure deceleration for both, the old and the new, electrode structures. The incoming ion beam was chopped, verified on a first diagnostic system, decelerated and energetically selective detected. A wide range detector was used to optimize the working point before the resulting energy spectrum was analysed in detail.

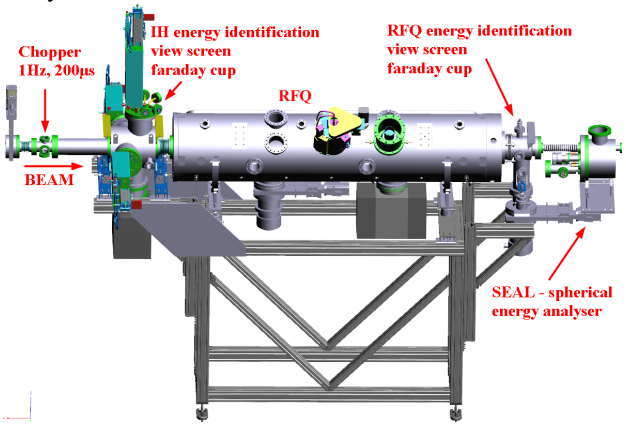

Figure 1: RFQ setup used at MPIK in Heidelberg.

Experimental results

There have been three goals to be achieved with the new design. Most important was to correct the input energy acceptance to match the output distribution of the IH. For the old design the measured energy acceptance shown in Figure 2 was centred at 525 ± 5 keV/nucleon and therefore too high and too narrow to allow for efficient capture. The new design has been tailored to the measured IH output distribution around 490 keV/nucleon, while simultaneously increasing the accepted phase and energy spread. For both RFQ's the energy acceptance has been measured and the rf working point has been found as shown in Figure 2. The accepted energy regime has successfully been corrected to centre on the IH output energy and its width has been increased by approximately 100%.

Indeed the deceleration efficiency for a small energy and rf-band of the old RFQ has been higher as seen in Figure 2, yet the upgraded RFQ will slow down a much larger fraction of the particle distribution as provided by the IH.

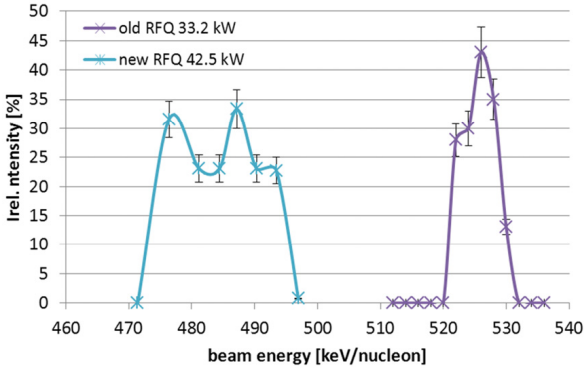

Figure 2: Comparison of the RFQ energy acceptances at their according rf-working points.

As different input energies require different rf-power it was desirable to decrease the touchiness of the RFQ for rf settings around the working point. As shown in Figure 3 the working area for the new RFQ is much less dependent on the rf power. For this reason it should become easier to achieve deceleration also on-line at the HITRAP setup.

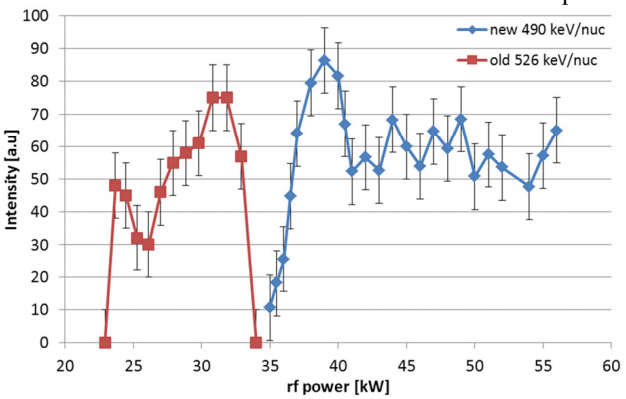

Figure 3: Decelerated beam intensity at the optimum input beam energy for both RFQ's varying the rf-power.

Outlook

The next step, scheduled for autumn 2013, is to achieve deceleration to 6 keV/nucleon on-line at GSI.

References

[1] H.-J. Kluge et al., Adv. Quant. Chem. **53** (2008) 83
[2] S. Yaramyshev, this annual report
[3] K. Dermati, this annual report
[4] „Der 3UH-Pelletron-Beschleuniger" MPIK (1989) 5

Manufacturing and assembly of the upgraded HITRAP RFQ decelerator

K. Dermati[1], *J. Borkowski*[1], *M. Buenger*[1], *R. Erlenbach*[1], *R. Fuchs*[1], *F. Herfurth*[1], *E. Kammer*[1], *C. Klammert*[1], *M. Maier*[1], *M. Müller*[1], *F. Persichella*[2], *E. Renz*[1], *M. Romig*[1], *W. Sturm*[1], *S. Teich*[1], *M. Uhlig*[1], *H. Vormann*[1], *D. Volz*[1], *O. Zurkan*[1] *and S. Yaramyshev*[1]

[1]GSI, Darmstadt, Germany; [2] Institute and Department for Material Science (IfW), TU Darmstadt, Germany

Introduction

A new HITRAP RFQ structure was designed and built at GSI according to the requirements and specifications of the accelerator physicists [1], [2]. There have been three goals to be achieved with the new construction. First an exact modulation of the electrodes, second an exact and repeatable mounting structure that needs not to be aligned and thirdly an ultra-high vacuum compatible construction.

Manufacturing

In the new design the stems as well as the electrodes were manufactured out of one peace. The electrodes were screwed on to the stems using a fit as shown in Figure 1. No brazing and alignment was needed for the fitting of the electrodes. The stems were additionally equipped with a base that was fitted into grooves on the revised ground plate. In order to match the ultra-high vacuum requirements ($< 10^{-8}$ *mbar*) no thread inserts were used anymore.

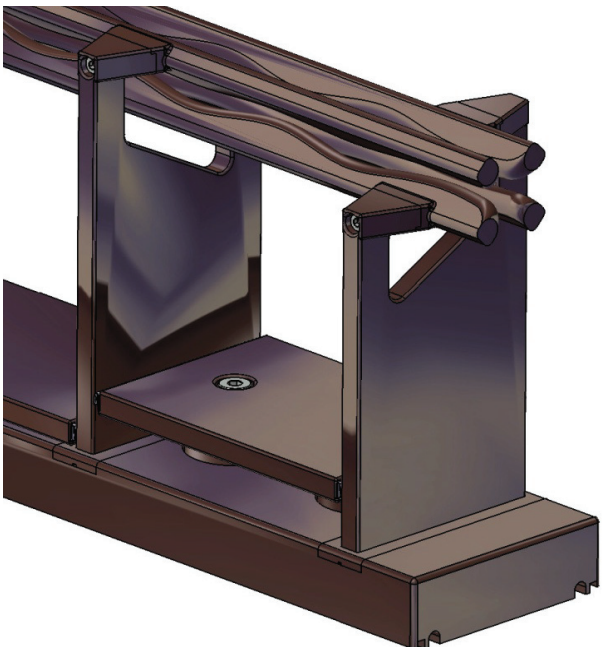

Figure 1: The new RFQ design.

All parts of the structure were made of oxygen free copper and manufactured in the workshop of GSI. A special treatment was carried out on the copper bars which were used for the RFQ electrodes. To relieve the residual stresses the bars were annealed under vacuum at 600°*C*. Additionally the bars were strain hardened through stretching of 1%. The stretch treatment took place at the Department for Material Science of the Technical University of Darmstadt. Due to this treatment residual stresses were reduced so that the deformations that appear during milling are reduced. An important issue, the vibrations during milling of the one meter long copper bars, were reduced by optimizing the feed rate and rotation speed of the milling tools. For the milling of the electrode modulation the design data of the code DESRFQ [2] was interpolated and a 3D surface for the milling machine has been created.

Assembly

Each produced part was directly measured and refinished after. The ground plate of the structure was mounted on a milling machine to simulate the mounting in the tank. Every stem was individually machined and aligned to the ground plate. After this step, the electrodes were mounted and final retouching applied. Finally the whole structure was placed and reassembled inside the tank, Figure 2.

Figure 2: Final assembly inside the RFQ tank.

Result

The new RFQ was commissioned with the expected performance. The sophisticated design of the stems and the electrodes was approved and an overall accuracy of better than ±0.15 *mm* referring to the beam axis has been achieved. To increase the performance for future projects is intended to reach an accuracy of better than ±0.05 *mm* referring to the beam axis. The fabrication procedure, measurement protocols and the gained experience might be used for upcoming accelerator projects.

References

[1] M. Maier, this anrep
[2] S. Yaramyshev, this anrep

A new Design of the RFQ-Decelerator for HITRAP

S. Yaramyshev, W. Barth, G. Clemente, F. Herfurth, M. Maier, H. Vormann

GSI, Darmstadt, Germany

Introduction

The HITRAP linear decelerator at GSI is designed to slow down heavy ions for experiments with ion traps [1]. During experimental campaigns the deceleration from 4 MeV/u to approx. 500 keV/u (design value) with an IH-DTL structure was demonstrated, while behind the HITRAP-RFQ no particles with design energy of 6 keV/u were observed.

Dedicated beam dynamics simulations with DYNAMION code for the old HITRAP-RFQ, based on 3D-fotometrie of the fabricated RFQ electrodes, demonstrated a significantly higher required input beam energy around 525 keV/u instead of the design value of 500 keV/u. The energy offset was experimentally confirmed at the test stand at MPI-K (Heidelberg). The mismatch of the RFQ acceptance to the design energy is the most probable explanation for not observing deceleration of the beam to energy of 6 keV/u at HITRAP facility [2].

The new RFQ decelerating-focusing channel was designed to reach the following main goals:

- correct RFQ input energy;
- increased longitudinal acceptance;
- low cost by use of the existing tank;
- improved alignment of electrodes using new mechanical design [3].

The new RFQ decelerating-focusing channel was designed with the interactive object-oriented code DESRFQ [4]. Dedicated features of the code provide for a detailed cell-by-cell design. A screenshot, which illustrates the final stage of a design process, is shown in Fig.1. A cross-check of the beam dynamics was made with DYNAMION package, which also comprises the built-in routines for reliable calculation of external electrical field on the base of real geometry of the electrodes and tank.

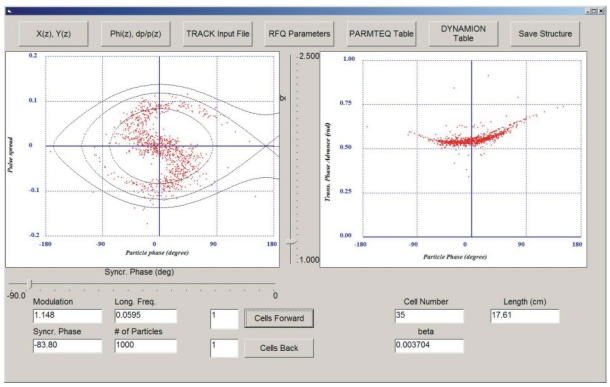

Figure 1: Typical screenshot from the code DESRFQ: beam portrait on longitudinal phase space (left) and stability diagram (right).

The new RFQ electrodes were designed with the same length as the old ones. New laws of modulation and synchronous phase provide for the correct input energy as well as for almost constant electrical field strength on the electrode surface, significantly lower than for the old RFQ, even in spite of 15% higher RFQ voltage between adjacent electrodes. This allows for higher focusing as well as for lower modulation (enlarged aperture). Both effects improve a transverse acceptance of an RFQ.

Improved longitudinal RFQ acceptance

Calculations of the old and new channel acceptances were performed with wide distribution of input particles in 6D phase space. The particles decelerated below 7 keV/u and filling the acceptance at the RFQ entrance, are shown on Fig. 2. The longitudinal acceptance for the new channel is about twice as high as the old one. The transverse acceptance is some percent lower due to the strong coupling between transverse and longitudinal properties of the RFQ. Nevertheless the total 6D acceptance for the new design is significantly higher.

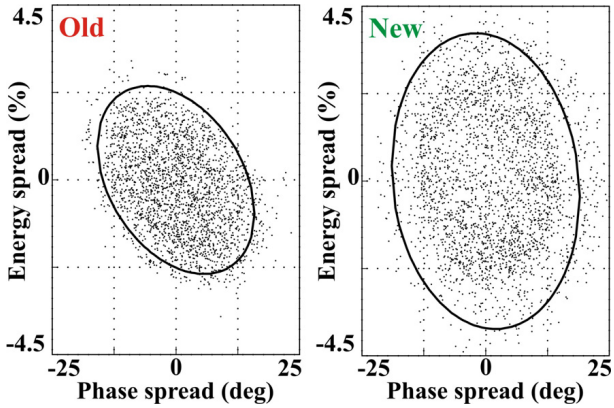

Figure 2: Particle distribution representing the longitudinal RFQ acceptance for old (left) and new (right) designs. The ellipses describe 90% of the particles.

Conclusion and outlook

The new HITRAP-RFQ has been designed, fabricated and assembled at GSI and successfully commissioned off-site at MPI-K [5]. Main goals of the design - correct input energy and about twice higher longitudinal acceptance - have been reached. Commissioning of the GSI HITRAP facility with the new RFQ is planned for 2013.

References

[1] F. Herfurth et al., HIAT-12, Chicago, 2012
[2] S. Yaramyshev et al., LINAC-12, Tel-Aviv, 2012
[3] K. Dermati et al., this Annual Report
[4] S. Yaramyshev, HB-10, Morschach, 2010
[5] M. Maier et al., this Annual Report

Non-invasive Bunch Shape Monitoring for high current LINACs*

B. Zwicker[1, 2], *P. Forck* [1], *P. Kowina*[1], *O. Kester* [1, 2]

[1]GSI, Darmstadt, Germany; [2]Goethe Universität Frankfurt, Germany

Introduction

Within the FAIR-Project a proton LINAC is scheduled as a new injector for the SIS18 synchrotron at GSI. The p-LINAC is proposed to achieve a high design value of 70 MeV and 70 mA current in addition to a compact construction. A new designed detector for the longitudinal ion distribution with a phase resolution up to 1° of 353 MHz is foreseen for efficient longitudinal matching of the accelerating structure.

Operating Principle

Several tests have been performed with an already existing **Bunch Shape Monitor BSM** at the UNILAC. The BSM prototype is schematically shown in Fig. 1. It is a non-invasive device based on detection of secondary electrons, which are liberated by the interaction of the beam ions with the residual gas. These electrons are accelerated towards an aperture by an external electrostatic field of 3 kV / cm. An electrostatic energy analyser together with an rf-deflector restrict the secondary electrons in transversal and longitudinal direction leading to a spatial distribution. By resolving the spatial distribution a direct image of the bunch shape is obtained.

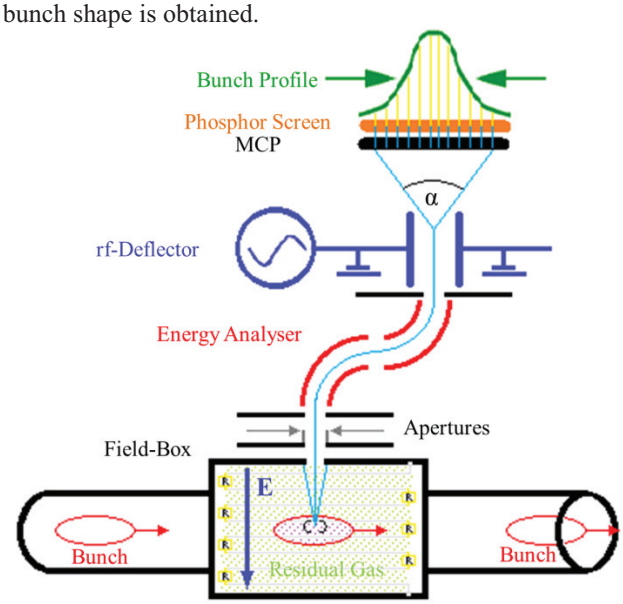

Figure 1: Schematic illustration of the BSM [1].

Results

Successful bunch shape measurements have been obtained with this monitor in 2012. With the BSM it was possible to measure different longitudinal profiles with a width ranging from 440 ps up to 1200 ps as shown in Fig. 2 and Fig. 3. These profiles were taken at identical beam parameters except for the bunch length, which was manipulated by a bunching cavity in order to test the BSM. The general functionality of this detection scheme is clearly demonstrated, but an unexpected high background was observed, which calls for further investigations. Due to this background and low signal level a bunch shape measurement with typical statistics as of Fig. 2 or Fig. 3 need 128 beam pulses which takes 20 minutes.

The experimentally confirmed phase resolution of the BSM is about 2° at 108 MHz, which corresponds to 51 ps. This level is sufficient to enable reliable bunch shape determination. Intense particle tracking simulations are ongoing to understand and improve the limitations of the actual design and further beam-based tests are planned for 2013 in the UNILAC.

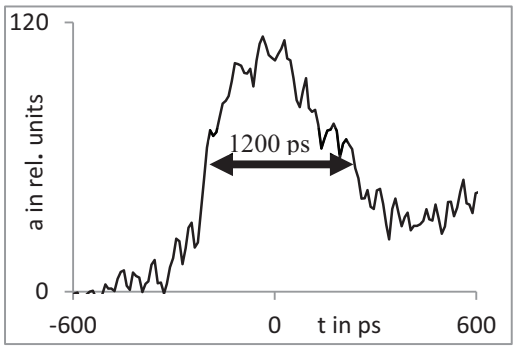

Figure 2: Focused bunch profile [2]. The beam parameters are: U^{28+}, I = 100 µA, t_{pulse} = 180 µs, P = $5 \cdot 10^{-6}$ mbar

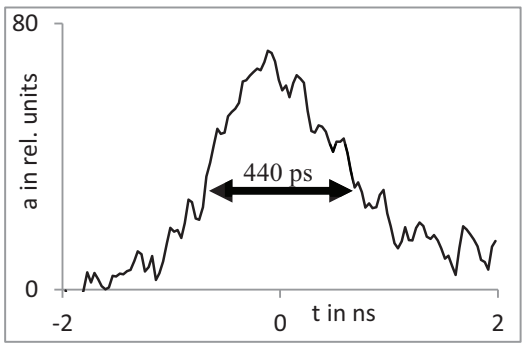

Figure 3: Stretched bunch profile [2]. The beam parameters are: U^{28+}, I = 100 µA, t_{pulse} = 180 µs, P = $5 \cdot 10^{-6}$ mbar

References

[1] P. Forck, “A non-intercepting Bunch Shape Monitor at GSI-UNILAC”, ABI Workshop, Kreuznach, Germany December 2008.

[2] B. Zwicker and P. Forck, “A Bunch Shape Monitor for high current LINACs”, Bunch Shape Monitor Workshop, Lund, Sweden, February 2013

*Supported by EU-Project CRISP, WP3 T1 Non-intercepting bunch shape monitors.

OPTICAL TRANSITION RADIATION FOR NON-RELATIVISTIC ION BEAMS

B. Walasek-Höhne[1], C. Andre[1], F. Becker[1], C. Dorn[1], R. Fischer[1], P. Forck[1], H. Graf[1], S. Güttler[1], R. Haseitl[1], A. Lumpkin[2], B. Lommel[1], A. Reiter[1], M. Schwickert[1], H. Reeg[1], J. Steiner[1], K. Steiner[1]

[1]GSI, Darmstadt, Germany, [2]Fermi National Accelerator Laboratory, U.S.A.

In this contribution, the results of applying the Optical Transition Radiation (OTR) beam profile monitor technique to a non-relativistic ion beam are presented. Usually beam profiles are measured with Secondary Electron eMission Grids (SEM-Grid), scintillating screens or Beam Induced Fluorescence (BIF) monitors [1]. As an alternative, OTR has been investigated [2] using an 11.4 MeV/u ($\beta = 0.16$) Uranium beam at the GSI UNIversal Linear ACcelerator (UNILAC). OTR is a classical electrodynamic process where the emitted photon number depends on the square of the ion charge state. Usage of a carbon stripping foil (570 µg/cm^2) to increase the mean charge state of ions, compensated the low beam energy and allowed imaging the ion beam. Various experiments, using a non-relativistic beam, have been performed to estimate signal strength and evaluate the working regime of the OTR technique.

RESULTS

Measurements were performed with 11.4 MeV/u Uranium beams of intensities up to $1 \cdot 10^{10}$ particles per pulse (ppp) and 300 µs pulse length for two target types: stainless steel disc and aluminized polyimide foil. The light was observed by an Image Intensified CCD camera (ICCD).
As transition radiation is instantaneously formed, we could measure the signal strength as a function of time to exclude long emission from any background sources.

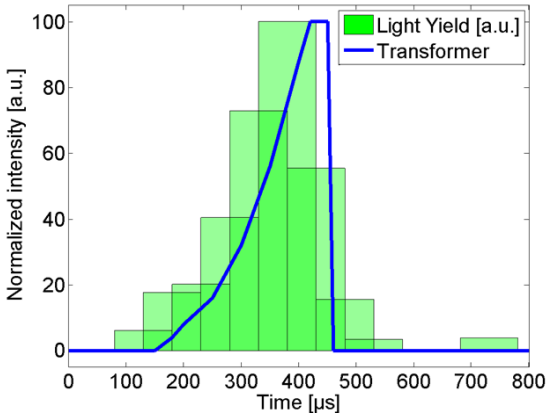

Figure 1: Time response of OTR (green) and beam current transformer signal (blue) of an $U^{\sim 73+}$ ion beam with 300 µs pulse duration. Each bar shows the OTR signal strength in a shifted 100 µs time window.

The ICCD was gated with 100 µs time window and shifted along the whole macro-pulse. The measured signal proves that only prompt emission was acquired as expected for the OTR effect (Figure 1).

In comparison to scintillating screens, OTR has the advantage of perfect linearity to the number of incident particles without risk of saturation. In our UNILAC studies the OTR signal shows linear behaviour with respect to the incident particle number.
To determine the imaging qualities of the OTR method, additional profile measurements with a SEM-Grid have been applied. In Figure 2, profiles show good agreement, but the origin of the observed shoulder in the OTR profile is not yet clear.

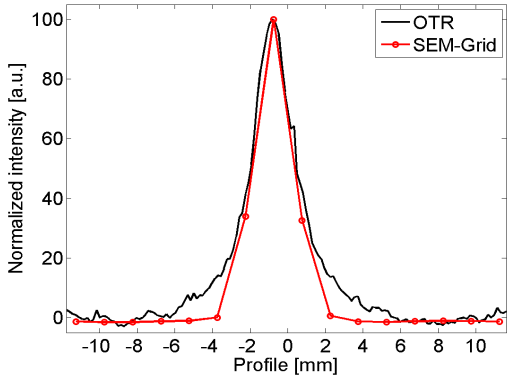

Figure 2: Comparison of the beam profile for OTR (black) and SEM-Grid (red). Beam parameters: $U^{\sim 73+}$, 11.4 MeV/u, $2.6 \cdot 10^8$ ppp in 300 µs.

Usability of the OTR method to obtain profiles of non-relativistic ion beams in the UNILAC was successfully demonstrated. Measurements indicate that observed signal levels are sufficient to allow imaging at particle intensities as low as $2 \cdot 10^7$ ppp. We observed that the signal has a linear dependency to the incident particle number. Secondly, beam profiles of SEM-Grid and OTR are in reasonable agreement. Moreover, OTR has the advantage to directly display the two dimensional beam shape. By spectroscopic studies a significant contribution of blackbody radiation could be ruled out.

ACKNOWLEDGMENTS

It is a pleasure to acknowledge members of the GSI operating team, beam diagnostic department, target and detector laboratories and mechanical workshop for their support and help before and during the experiment.

REFERENCES

[1] P. Forck, "Lecture notes on Beam Instrumentation and Diagnostics", Joint Universities Accelerator School (JUAS 2010), http://www-bd.gsi.de
[2] A. Lumpkin, "Feasibility of OTR imaging of non-relativistic ions at GSI", http://www-bd.gsi.de/ssabd

Simulations of the Position Sensitivity for the SIS18 Capacitive BPM with a Nonstandard Geometry

J.Latzko[1,2], P.Kowina[1], [1]GSI Darmstadt, [2]TU Darmstadt

Methods and Results

Standard SIS18 Beam Position Monitors (BPM) installed in 12 locations distributed over the SIS18 circumference have typical diagonal-cut geometry [1]. Such geometry allows for position determination with high linearity that, in addition, is independent from the transversal beam shape and homogeneity of the charge distribution. On the contrary, a BPM with a nonstandard geometry, as shown in Fig. 1, shows non-linear readout and is sensitive to higher order moments of the transversal charge distribution. Last feature was intended because this detector, installed in the straight section of sector S04, was initially foreseen for measurements of the quadrupolar Beam Transfer Function [2]. Since this detector is presently used for a Base-Band-tune determination (BBQ-method) [3] a simulation of its position sensitivity was of importance especially for a proper error estimation of the BBQ method.

The simulation was carried out using CST Microwave Studio, with a Time Domain Solver in the frequency range of D$C \leq f \leq 200MHz$. The beam was modeled by a stretched wire, whereas a signal propagation was considered as a TEM wave. This approximation is valid also for non-relativistic beams as long as the bunches are much longer than BPM itself. The frequency dependence of the position sensitivity, shown in Fig. 2, was extracted from the scattering parameters as described in [4]. The BPM constants $K_{x,y}$ and electrical offsets in respect to the geometrical center $\delta_{x,y}$ were obtained by a least square fit of the delta-over-sum function [4]. The mean values are:

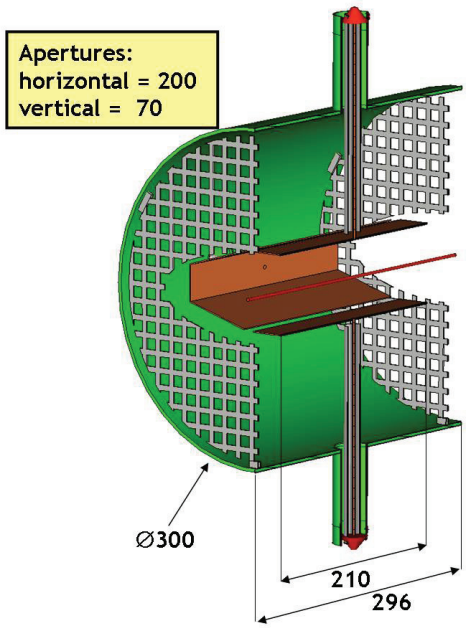

Figure 1: SIS18 BPM with a nonstandard geometry.

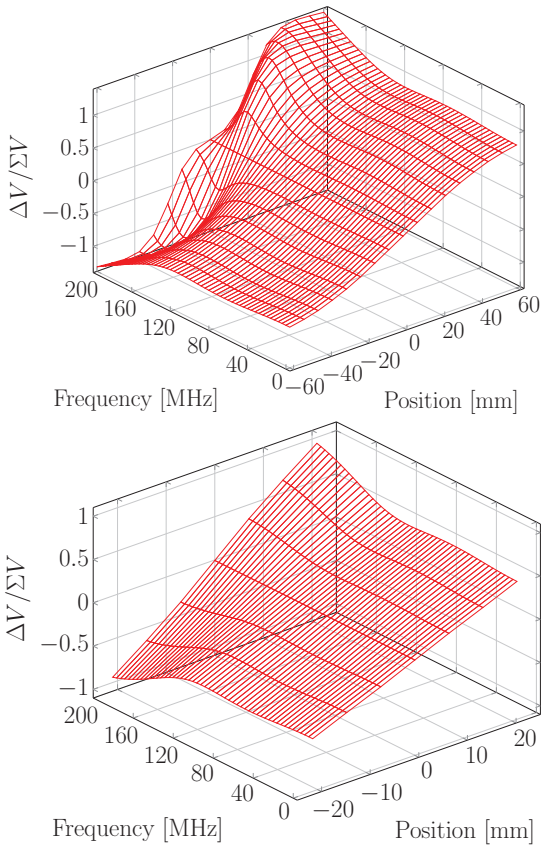

Figure 2: Position sensitivity as a function of frequency for horizontal (top) and vertical beam displacement (bottom).

$\hat{K}_x = 65$mm, $\hat{\delta}_x = -9 \cdot 10^{-8}$mm, $\hat{K}_y = 40$mm, $\hat{\delta}_y = 5 \cdot 10^{-5}$mm for horizontal and vertical plane, respectively.

Conclusions

The linearity of the position sensitivity is sufficient for measurements methods like BBQ [3] that base on the spectrum analysis in frequency domain: Within the beam displacement range of nearly 60% of the overall aperture the maximal deviation is in the order of 2.5% for frequencies below 100 MHz. Only at higher frequencies the position sensitivity is strongly effected by resonances which is mostly pronounced for the horizontal plane, see Fig. 2 (top). This, however, is irrelevant for the BBQ method, where interesting frequencies do not exceed 1 MHz.

References

[1] P. Kowina et al., Proc. DIPAC'05, Lyon (2005) p.114

[2] R. Bär, PhD Thesis, Universität Frankfurt, Germany (2000)

[3] R. Singh et al., Proc. of BIW2012, Newport (2012) p.1

[4] P. Kowina et al., Proc. EPAC'06, Edinburgh (2006) p.1022

Verification of the RF System Calibration by Means of a Debunching Experiment in SIS18

U. Hartel[*1], *J. Grieser*[1], *D. Lens*[1], *A. Klaus*[2], *H. Klingbeil*[1,2], *U. Laier*[2], *K.-P. Ningel*[2], *S. Schäfer*[2], *and B. Zipfel*[2]

[1]Technische Universität Darmstadt, Germany; [2]GSI, Darmstadt, Germany

Summary

For the FAIR synchrotrons and the upgrade of the GSI synchrotron SIS18, a completely new Low-Level RF system architecture has been realized [1]. Closed-loop control systems stabilize the amplitude and the phase of the RF gap voltages. Due to the non-ideal frequency response of several components, this stabilization is not perfect. The deviations are -10% to $+30\%$ for the amplitudes of the two SIS18 cavities, $-3°$ to $+10°$ for the phase of cavity BE1, and $-8°$ to $+1°$ for the phase of cavity BE2. The required accuracy is $\pm 6\,\%$ for the amplitude and $\pm 3\,°$ for the phase, which has been shown by previous machine experiments and theoretical investigations. In order to fulfil the requirements a dedicated programmable calibration electronics module was developed. Calibration curves can be measured and programmed offline without the beam, but nevertheless, the desired beam behaviour has to be verified by experiments. For this purpose a debunching scenario was realized as a SIS18 beam experiment [2] that proved to be very sensitive to inaccuracies. The results of the experiment show for the first time at GSI, by a beam observation, that the predefined calibration curves meet the accuracy requirements.

Debunching Experiment

A $^{238}\mathrm{U}^{73+}$ beam of about $1 \cdot 10^9$ particles with the kinetic energy $11.2\,\mathrm{MeV/u}$ was injected and accelerated up to $120\,\mathrm{MeV/u}$ or $600\,\mathrm{MeV/u}$. The central control system (CCS) provided the standard ramps for the cavities BE1 and BE2, which both operated at $h = 4$. At a fixed energy, a constant control voltage for the amplitudes for both cavities, which corresponds to about $4\,\mathrm{kV}$ amplitude per cavity, was generated by a combination of CCS ramps and manual setups. By synchronizing the cavities with opposite phase, i.e. $+90\,°$ for the cavity BE1 and $-90\,°$ for the cavity BE2, no residual gap voltage should be present. These phases were realized by a control voltage of about $4.5\,\mathrm{V}$ and $-4.5\,\mathrm{V}$ respectively. Thus, the experiment scenario allowed to check the debunching quality at injection energy or at extraction energy. In a two-step optimization process the bunching was minimized by adapting the control voltage of the BE1 target phase first and by adjusting the control voltage for the BE1 target amplitude afterwards.

Results

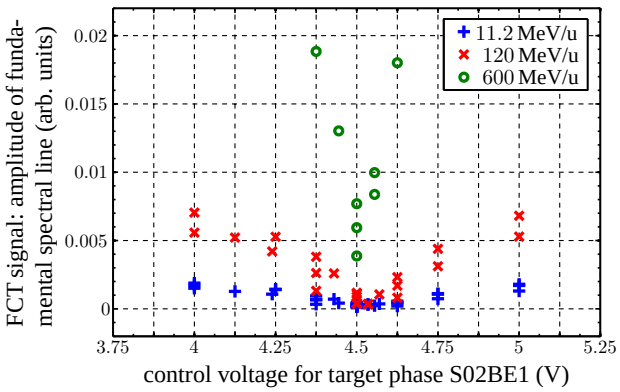

Figure 1: Phase optimization for the cavity BE1

Figure 1 shows the results for the first optimization step of the phase. The beam signal, measured by an FCT (Fast Current Transformer), is evaluated by a discrete Fourier transformation with respect to the control voltage at different energies. An optimum is achieved for a control voltage between $4.375\,\mathrm{V}$ and $4.625\,\mathrm{V}$, which corresponds to a target phase between $87.5\,°$ and $92.5\,°$. Therefore, optimum results for the beam with deviations of less than $\pm 2.5\,°$ from the theoretical value are reached by means of the calibration. In addition, the results of the amplitude optimization clearly show that the best results are obtained within deviations of less than $\pm 5\,\%$ from the theoretical value. The experiment successfully proved that the calibration fulfils the requirements and that the target values lead to the desired beam behavior.

References

[1] H. Klingbeil, U. Laier, K.-P. Ningel, S. Schäfer, C. Thielmann, B. Zipfel: "New digital low-level rf system for heavy-ion synchrotrons", Phys. Rev. ST Accel. Beams, Vol. 14, Issue 10, 2011, DOI 10.1103/PhysRevSTAB.14.102802, APS.

[2] H. Klingbeil, U. Hartel, B. Zipfel: "Beam experiment: Verification of phase and amplitude calibration by means of a debunching experiment in SIS18", GSI internal note 29112012, November 2012.

[*] supported by the Helmholtz Graduate School for Hadron and Ion Research and the Graduate School of Computational Engineering at Technische Universität Darmstadt

Radiation Damage in Alumina irradiated with heavy Ions of high Fluences*

S. Lederer[1,2], *E. Gütlich*[3], *P. Forck*[1], *B. Walasek-Höhne*[1], *and W. Ensinger*[2]

[1]GSI, Darmstadt, Germany; [2]Technische Universität Darmstadt, Germany; [3]Goethe-Universität Frankfurt, Germany

Scintillating screens are used at accelerator facilities for ion beam diagnostics with very high ion fluences. However, during irradiation of the material, formation of color centers occurs. This results in a degradation of light yield, which is one of the main problems using the screens as an appropriate tool for imaging the beam [1]. Due to its radiation hardness, alumina is an interesting material for scintillation applications [2]. Another advantage of using Al_2O_3 is that the understanding of its luminescence behavior is at an advanced stage [3].

High purity (99.9 %) alumina samples were irradiated with different ion species and different fluences (see table 1). The given value for the dose is integrated over the ion range, although the energy dissipation is a function of ion velocity [1, 4].

Table 1: Parameters for irradiation of the alumina samples. The range values are calculated with SRIM-2013 code.

Ion species	Energy [MeV]	Range [μm]	Dose [MGy]	Fluence [ions/cm^2]
^{12}C	136.8	169	0.09	$2.8{\cdot}10^{11}$
^{12}C	136.8	169	1.36	$4.1{\cdot}10^{12}$
^{50}Ti	570	78.6	0.30	$1.0{\cdot}10^{11}$
^{50}Ti	570	78.6	3.87	$1.3{\cdot}10^{12}$
^{197}Au	1162.3	37.3	0.64	$5.0{\cdot}10^{10}$
^{197}Au	1162.3	37.3	1.28	$1.0{\cdot}10^{11}$
^{197}Au	1162.3	37.3	6.39	$5.0{\cdot}10^{11}$
^{197}Au	1162.3	37.3	12.78	$1.0{\cdot}10^{12}$

After irradiation, absorption measurements were performed. F- and F_2-color centers are observed due to strong absorption bands in the range from 200 nm to 450 nm (figure 1).

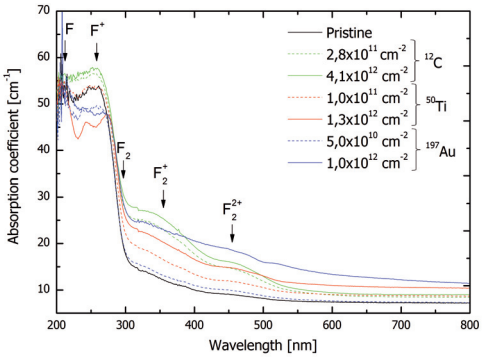

Figure 1: Absorption spectra of alumina samples irradiated with different ion species of given fluences.

To calculate the color center concentration the Smakula-Dexter formula was used (equation 1, [5]).

$$N_{[1/cm^2]} = 6.55 \cdot 10^{15} \cdot \frac{1}{f} \cdot FWHM_{[eV]} \cdot A, \qquad (1)$$

where A is the absorbance at peak maximum, *FWHM* is the full width at half maximum of the absorption peak and f is the oscillator strength ($f_F = 1.3$ respective $f_{F^+} = 0.6$). The volume concentration of F-centers as a function of the applied dose is shown in figure 2. The formation of color centers centers in alumina depends mainly on the ion species and on the applied dose. The fitting of data obeys an exponential law:

$$N_F = N_0 \left(1 - exp\left(\sigma_D \cdot D\right)\right) \qquad (2)$$

For low energy doses, color center formation complies with exponential growth. For higher doses of around 6 MGy, saturation in the concentration of color centers can be determined.

Further measurements will are planned to investigate color center formation for high energy ion doses.

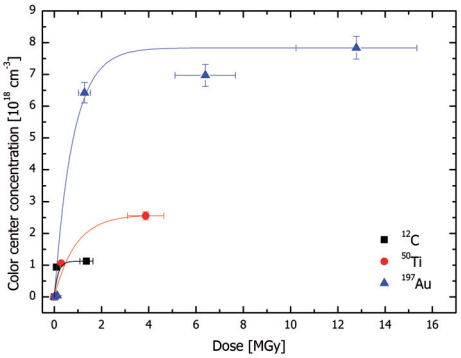

Figure 2: Volume concentration of color centers as a function of the applied dose. Solid line: fit with exponential growth function (2).

References

[1] E. Gütlich, P. Forck, B. Walasek-Höhne and W. Ensinger, IEEE T. Nucl. Sci 59 (2012) pp 2354-2359.

[2] N. Khalfaoui, J.P. Stoquert, F. Haas, C. Trautmann, A. Meftah and M. Toulemonde, Nucl. Instrum. Methods Phys. Res., Sect. B 146 (2012), pp 247-253.

[3] B.D. Evans, J. Nucl. Mater. 219 (1995), pp 202-223.

[4] P.A. Rodnyi, *Physical Progress in inorganic scintillators*, (CRC Press, New York, 1997)

[5] D. Curie, *Luminescence in crystals*, (Methuen&Co Ltd, London, 1963).

* Work supported by BMBF, project No. 06DA7026.

Status - SIS-18 Slow Extraction

M. Kirk, D. Ondreka, and P. J. Spiller

GSI, Darmstadt, Germany

We report here recent investigations with the aim to reduce the ripple in the spill coming out of SIS-18.

Tracking studies were undertaken in which the RF Knock-Out modulation was switched from the existing BPSK based method to the dual FM method. Instead of the conventional BPSK carrying a pseudo-random bit train from a 16-bit Linear Feedback Shift Register, the dual FM consists of two anti-phased saw-tooth FM signals [1]. In both cases the excitation spectrum is at the lowest frequency betatron sideband. Similar techniques have been evaluated by simulation for single FM as well as for band-limited white noise [2] however without the aim to assess the spill's microstructure.

Dual FM requires a larger peak voltage; however improvement to the microstructure has been demonstrated. Figure 1 shows a few ms of spill at 10 µs resolution with the Hardt condition set. The Hardt condition [3] is particularly important for high current operation. It remains to be seen if it would be simpler to increase the bandwidth and peak voltage of the BPSK modulation while observing that the voltage is limited by the size of the deflection angle of the ions from the RF exciter which should be small enough to maintain the beam's diffusion. The increased smoothness is also evident from figure 2 for the same spill at ms resolution for which the smoother curve results from dual FM. The BPSK's peak voltage was adjusted to closely match the curves for valid comparison.

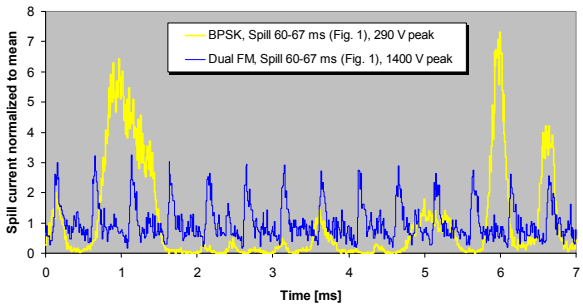

Figure 1: Simulated spills from a DC circulating beam.

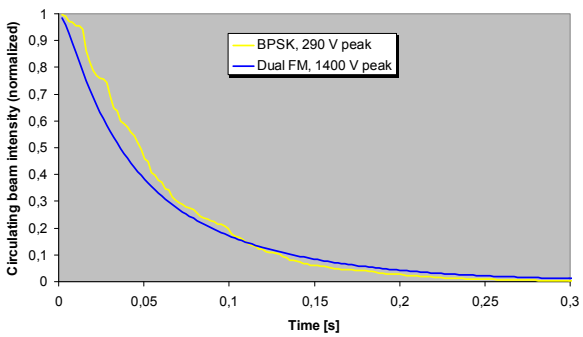

Figure 2: Simulated circulating beam intensity.

Experimental confirmation of the above prediction requires the Hardt condition to be fulfilled through a lowering of the horizontal chromaticity from its natural value. Accurate determination of chromaticity is necessary as the chromaticities are known to differ a lot from their set values according to analysis of head tail oscillations [4]. The histogram in figure 3 demonstrates the marginal improvement in spill quality by increasing the bandwidth of the BPSK excitation defined as the full width of the center lobe (i.e. twice the bit-train's frequency) in the spectral power density, normalized here to the revolution frequency. The spill quality factor (abscissa) is the spill current normalized to its local moving average in a window 100 bins wide. Each bin is as usual, 10 µs in size. As before, the circulating DC beam intensity curves were made to coincide by adjusting the peak voltage.

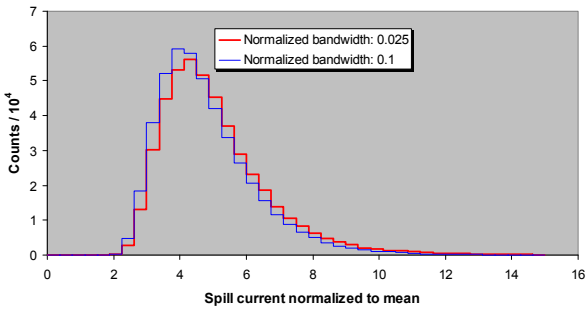

Figure 3: Spill quality measured for BPSK knock-out.

Dual FM is foreseen as a temporary solution; Demonstrated in [1], a third mono-frequency may serve to extract the ions close to the separatrix while the dual FM diffuses ions towards this region. Diode white noise is yet another alternative. It should be noted that power supply ripple to magnets, neglected in these simulations, may considerably add to the spill ripple making experimental confirmation more difficult but not impossible.

References

[1] K. Noda et al., "Advanced RF-KO slow-extraction method for the reduction of spill ripple", NIM A 492, (2002) p. 253.

[2] V. Nagaslaev et al., IPAC'11, "Third Integer Resonance Slow Extraction Using RFKO at High Space Charge", San Sebastián, September 2011, p. 3559.

[3] W. Hardt, "Ultraslow Extraction out of Lear", CERN/PS/DL/LEAR, Note 81-6.

[4] R. Singh, "Chromaticity Measurements using the Head-Tail modes at SIS-18", GSI 2012-Report.

New Data Acquisition for Beam Transformers in SIS18 and Transfer Lines

O. Chorniy, H. Bräuning, T. Hoffmann, H. Reeg, A. Reiter, M. Witthaus
GSI, Darmstadt, Germany

This contribution presents the development of new data acquisition system for fast beam current transformers (FCT) for SIS18 and HTP beam line. These systems serve as prototypes for the diagnostics in SIS100 and high-energy beam transfer lines of the FAIR facility.

Longitudinal Bunch Diagnostics in SIS18

Recently, the longitudinal diagnostics capabilities in SIS18 were upgraded by installation of a wide-band FCT [1] and a dedicated VME data acquisition (DAQ) system. A FESA [2] class on the front-end CPU controls the FCT amplifier stage and records the signal by a 500 MSa/s and 12 bit resolution ADC module [3].

Since the time scale for longitudinal motion is 100-1000 times longer than the revolution period T_r, sampling of the entire SIS18 machine cycle would result in an unnecessarily large amount of data. The DAQ system merely needs to acquire a sequence of single-turn data blocks at intervals larger than T_r, provided that these data blocks are synchronized to the radio-frequency (RF) signal. This data reduction is achieved by triggering the DAQ system on a rate divider output to which the RF master oscillator is connected. A complete sequence of data blocks is presented in Fig. 1 (top) together with the derived bunch length (bottom) of the central bunch. The measurements were done along the acceleration ramp at harmonic number $h = 4$.

A graphical user interface is under development. It will provide enhanced online features such as trending plots of bunch length or bunch center within the machine cycle.

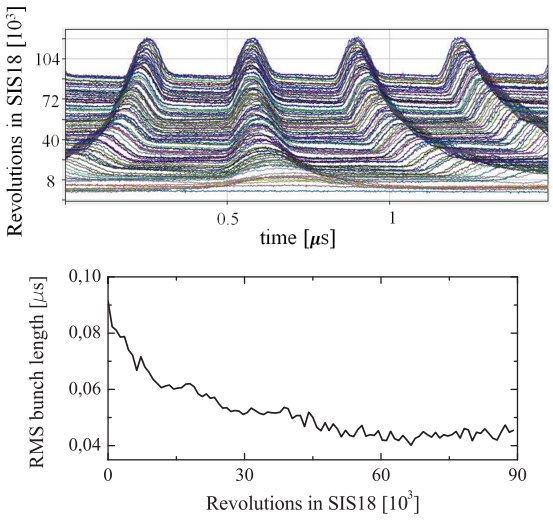

Figure 1: Online waterfall plot of bunch evolution (top) and RMS length evolution (bottom) of the central bunch.

Transformers in high-energy Beam Lines

Monitoring of beam transmission is an important task for an acceleration facility with several accelerators and experimental areas. Presently, two detectors for intensity measurements are installed at HTP: a GSI-made FCT and a charge-sensitive Resonant Transformer (RT). A new VME DAQ system has been tested with two FESA classes, one for FCT readout with a 5 GSa/s ADC (CAEN V1742) and one for RT readout with a 100 MSa/s ADC [3]. The FCT output is fed to a remote-controlled precision attenuator followed by a fixed-gain, inverting amplifier. The raw data of Fig. 2, taken at a rate of 1 GSa/s, presents the FCT response to a single bunch ($h = 1$) of 350 MeV/u U^{73+} ions. The observed ringing effects come from the FCT winding itself due to incomplete matching to 50 Ω geometry.

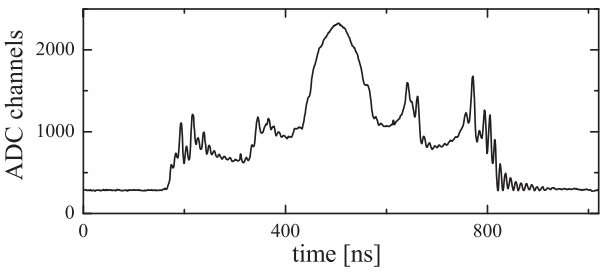

Figure 2: Bunch profile from FCT recorded at 1GSa/s.

Currently, only the RT is foreseen as charge monitor for FAIR. Considering the large bandwidth and dynamic range, the FCT may in principle also be used to measure bunch charges in transfer lines. Thereby, the offset-corrected and normalized FCT integral is multiplied by its calibration factor to derive the bunch charge. The comparison with the RT is under evaluation. Due to the uncertainty introduced by the unwanted ringing of the GSI-type FCT, this investigation will be continued with data of a new prototype FCT/RT transformer combination which is planned to be ready for tests in autumn 2013. This device will be equipped with a commercial FCT [1], similar to the one installed in the SIS18. A key component for the future transmission monitoring system will be a precision calibration circuit which must be developed in order to achieve a resolution in the percent region.

References

[1] http://www.bergoz.com/

[2] T. Hoffmann, M. Schwickert, G. Jansa, FESA at FAIR - the front-end software architecture, PCaPAC 2008 proceedings

[3] http://www.struck.de/

Determination of coherent and incoherent tune shifts at SIS-18*

R. Singh[1,2], O. Boine-Frankenheim[1,2], O. Chorniy[1], P. Forck[1], R. Haseitl[1], P. Kowina[1], W. Kaufmann[1], K. Lang[1], and T. Weiland[2]

[1]GSI, Darmstadt, Germany; [2]TEMF, TU Darmstadt, Germany

Introduction

Currently two systems for tune measurements are under operation in SIS-18 i.e. TOPOS and BBQ [1]. We present the measurement of coherent and incoherent tune shifts by evaluating relative spectral positions of various head tail modes in the tune spectra as a function of beam intensity.

Experiments and Results

At high beam intensities, the transverse space charge force together with the coherent force caused by the beam pipe impedance affects the motion of the beam particles and modifies the tune spectrum. The space charge force induces an incoherent tune shift ΔQ_{sc} which can be expressed for a symmetric beam profile of homogeneous density as

$$\Delta Q_{sc} = \frac{qI_pR}{4\pi\epsilon_0 cE_0{\gamma_0}^2\beta_0^3\varepsilon_x} \qquad (1)$$

. Here I_p is the peak bunch current, q the particle charge and $E_0 = \gamma_0 mc^2$ the total energy. The relativistic parameters are γ_0 and β_0, the ring radius is R and the emittance of the rms equivalent K-V distribution is ε_x. The image currents and image charges induced in the beam pipe, assumed here to be perfectly conducting, cause a real coherent tune shift

$$\Delta Q_c = -i\frac{qI_pR^2Z_x}{2Q_{x0}\beta_0E_0} \qquad (2)$$

where Z_x is the purely imaginary horizontal impedance. For the vertical plane the procedure is the same, with x replaced by y in Eq. 1 and Eq. 2. In the presence of incoherent space charge, given by ΔQ_{sc}, or pipe effects, given by ΔQ_c, the shift of the synchrotron satellites in bunches can be reproduced rather well by [2],

$$\Delta Q_k = -\frac{\Delta Q_{sc}+\Delta Q_c}{2} \pm \sqrt{(\Delta Q_{sc}-\Delta Q_c)^2/4 + (kQ_s)^2} \qquad (3)$$

where Q_s is the snychrotron tune and k is the mode number.

Experiments were conducted to understand the effects of high beam intensity on tune spectra at injection plateau of 11.4 MeV/u with U^{73+} and N^{7+} bunched ion beams up to $2\cdot10^9$ and $1.5\cdot10^{10}$ particles, respectively. Fig. 1 shows the tune spectrum obtained in horizontal plane at three different intensities with the same machine settings. The shift of head tail modes ΔQ_k with respect to beam intensity when fitted in the analytical predictions of Eq. 3 gives a direct measurement of incoherent tune shifts ΔQ_{sc}. The coherent tune shift ΔQ_c can be obtained by measuring shift of the $k = 0$ line as a function of the peak bunch current as shown in Fig. 2. The transverse impedance is thus obtained by a linear regression fit of the measured shifts in both planes to Eq. 2, i.e. $Z_x \approx -i(0.23 \pm 0.04)$ MΩ/m^2 and $Z_y \approx -i(1.78 \pm 0.04)$ MΩ/m^2. These values corresponds to the average beam pipe radii of the SIS-18 of 104 ± 6.5 mm and 37 ± 0.9 mm which closely match with expected values.

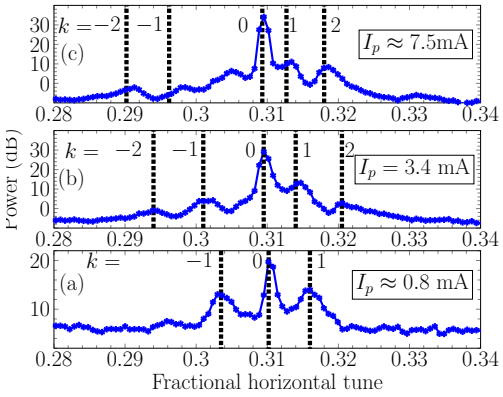

Figure 1: Horizontal tune spectra for U^{73+} ions (see text). The dashed lines indicate the head-tail tune shifts from Eq. 3.

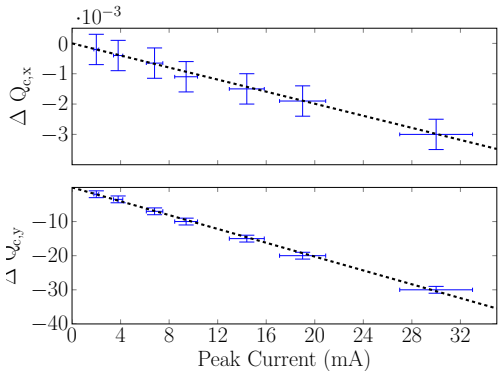

Figure 2: Coherent tune shift obtained from the measurement for the horizontal and for the vertical planes as a function of the peak beam current.

References

[1] R. Singh et al., "Interpretation of transverse tune spectra in a heavy-ion synchrotron at high intensities", Accepted for publication in Phys. Rev. ST Accel. Beams, Feb. 2012.

[2] O. Boine-Frankenheim et al., Phys. Rev. ST Accel. Beams, **12**, 114201 (2009)

* This work is supported by DITANET (novel DIagnostic Techniques for future particle Accelerators: A Marie Curie Initial Training NETwork),Project Number ITN-2008-215080

RESPONSE OF SCINTILLATING SCREENS TO FAST AND SLOW EXTRACTED BEAMS*

A. Lieberwirth[1,2], B. Walasek-Höhne[1], P. Forck[1] and W. Ensinger[2]

[1]TU Darmstadt, Darmstadt, Germany; [2]GSI, Darmstadt, Germany.

During the last years a significant increase of interest for inorganic scintillators in beam diagnostics applications has occurred [1]. To fulfil the challenging requirements for FAIR concerning precise beam profile measurement (linearity of response over a large dynamic range, harsh radiation environment), experiments were conducted at SIS18. Furthermore, the stability of various scintillator materials has been studied to identify radiation hard scintillators.

Results

Experiments were performed at GSI to characterize the inorganic scintillator response to slow (within 200 ms, SE) and fast (within 1 µs, FE) extracted 350 MeV/u Uranium beams from SIS18. The extracted particle number was varied between 10^5 and 10^9 particles per pulse (ppp) for the irradiation of 7 different scintillators, mainly a number of YAG-crystals with different qualities as well as pure and Cr-doped alumina-ceramics and two phosphor powders – P43 and P46.

A detailed description of the chosen experimental setup can be found in [2]. To increase the dynamical range of the DAQ system a second CCD camera of the same type with 5% transmission filter was mounted in parallel. With this system the emitted light of the scintillating area in 45° backwards direction to the beam (light output) was observed.

With a dedicated code written in Python the images were analysed concerning region-of-interest cutting, background subtraction and scaling of the optical parameters. As an example for the various materials under investigation, the light output of the P43 phosphor screen is displayed in Figure 1 as function of ppp. For each individual beam setting 30 images were taken.

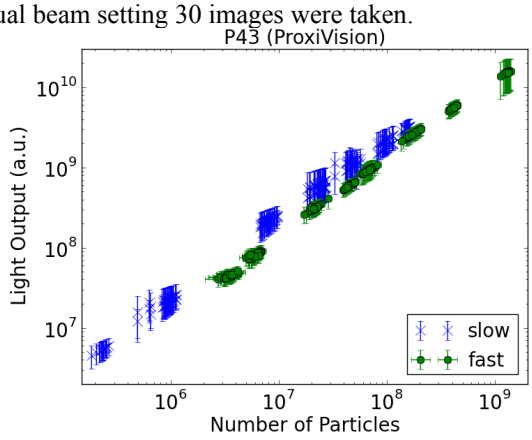

Figure 1: Comparison of P43 phosphor screen light output for SE and FE Uranium beam vs. particle number. Beam parameters: 350 MeV/u Uranium beam, pulse lengths 200 ms for SE (green circles) and 1 µs for FE (blue crosses).

The data show a linear response over a large range of ion intensity. No significant difference between SE and FE beams has been observed. The displayed trend is characteristic for all investigated scintillators.

Radiation hardness tests for all phosphor screens and the Cr-doped alumina screen were performed by irradiation with more than 700 pulses of ≈10^9 ions each. Figure 2 shows the light output of P43 phosphor screen measured with the FE beam as function of accumulated number of ions. Its linearity seems to be different from previous observations on SE beams [2] with comparable beam parameters. An explanation of this unexpected behaviour needs further beam-based investigations.

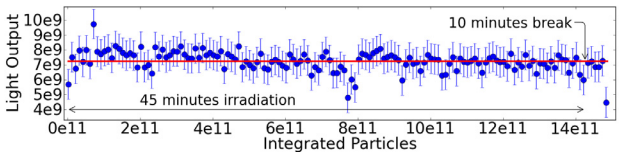

Figure 2: Radiation hardness test for FE Uranium beam on P43 target. Light output is approximately constant even after 45 minutes of permanent irradiation; its average is represented by the straight line. No discontinuity after 10 minutes beam pause could be observed. Beam parameters: 350 MeV/u Uranium beam, pulse length of 1 µs, 0.25 Hz repetition rate and 10^9 ppp.

Among the investigated materials different light outputs were recorded as expected from previous experiments [1-3]. For the given beam intensities no significant decrease of the light output caused by radiation induced material modifications was observed for all investigated materials. The sensitivity of P43 proves stable during continuous irradiation. Further investigations and material characterizations are necessary to understand the ion beam induced radiation changes in scintillating screens. The performed studies help to choose appropriate scintillator materials for the FAIR facility, which will deliver about a factor of 100 higher beam intensities as presently available. Therefore long term stability and performance during fast extraction of intense beams is a critical issue.

References

[1] B. Walasek-Höhne, et.al. "Scintillating Screen Applications in Accelerator Beam Diagnostics", IEEE Trans. on Nucl. Sci., Vol. 59 (2012), No. 5, p. 2307-2312

[2] K. Renuka, et.al. "Imaging Properties of Scintillation Screens for High Energetic Ion Beams", IEEE Trans. Nucl Sci, Vol. 59 (2012), No. 5, 2301-2306

[3] K. Renuka, et.al. "Transverse Beam Profile Monitoring using Scintillation Screens for High Energy Ion Beams", BIW2012 Proceedings, Virginia, USA

* Work supported by the German Ministry of Science (BMBF) under contract number 06DA7026

Chromaticity measurements at SIS-18 using the head-tail modes*

R. Singh[1,2], *O. Boine-Frankenheim*[1,2], *P. Forck*[1], *P. Kowina*[1], *and T. Weiland*[2]
[1]GSI, Darmstadt, Germany; [2]TEMF, TU Darmstadt, Germany

Introduction

Chromaticity measurements in a synchrotron are routinely performed for understanding and optimization of the machine model. The typical measurement method involves a systematic beam momentum offset, and measurement of the corresponding tune for each offset. However, this requires several machine cycles and is a dedicated experiment in itself. Here we present a fast method based on temporal excitation of the transverse center of mass of head-tail modes [1] using frequency sweep. Chromaticity is extracted by fitting transverse offset of the resulting modes with an analytical expression.

Experiments and Results

The head-tail eigenmodes for an airbag bunch distribution in a barrier potential [1] with the eigenfunctions

$$\bar{x}_k(\phi) = \cos(k\pi\phi/\phi_b)\exp(-i\chi\phi/\phi_b) \qquad (1)$$

where $\bar{x}_k$ is the local transverse bunch offset, $\chi = \xi\phi_b/\eta_0$ is the chromatic phase, ϕ_b is the full bunch length and η_0 is slip factor.

Experiments were conducted on the injection plateau of 11.4 MeV/u with a bunched N^{7+} ion beam with $5.0 \cdot 10^9$ particles. The frequency sweep excitation is used to excite each mode individually which allows to resolve the different head-tail modes both spectrally and temporally. The measured bunch offset of each excited mode is fitted to the analytical expression for the head-tail eigenfunction given in Eq. 1, with the chromaticity ξ as the fit parameter.

The fitting method is shown in Eq. 2; the head-tail eigenfunction from Eq. 1 is multiplied with the beam charge profile $\hat{Q}(t)$ and corrected for the beam offset (orbit distortion) Δx at the BPM where the signal is measured.

$$F(\phi, \xi, A) = \Delta x \cdot \hat{Q}(t) \cdot (1 + A \cdot \bar{x}(\phi)) \qquad (2)$$
$$E(\xi, A) = (M(\phi) - F(\phi, \xi))^2$$

The fit error $E(\xi, A)$ is minimized as a function of independent variables, chromaticity ξ and head-tail mode amplitude A. Typical measured curves and the fitted eigenfunctions are shown in Fig. 1 for $k = 0, 1$ and 2. The measured chromaticity is independent of the order of head-tail eigenfunction. The fit error is used to determine the error bars on measured chromaticity. Figure 2 shows the measured vertical chromaticity for various set values of chromaticity

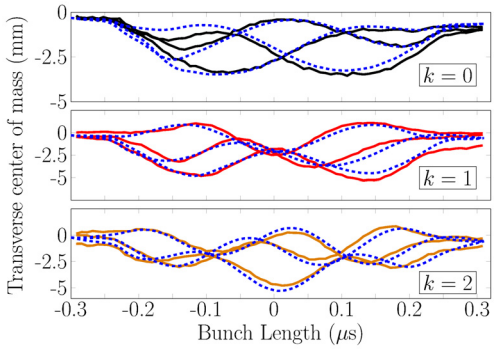

Figure 1: Analytical curves from Eq. 1 (dotted) are fitted to the local transverse offset for the $k = 0, 1$ and 2 modes with the chromaticity as the fit parameter.

using sextupolar settings. The measured tune values have a dependence on the value of chromaticity. It is important to note that this method works only with sweep excitation and requires high signal-to-noise ratio in time domain, which amounts to higher beam current or high excitation power. More details of the experimental set-up can be found in [2].

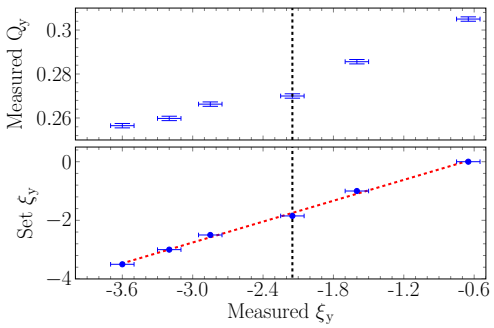

Figure 2: Vertical chromaticity measurement using the mentioned method. The black dashed line marks the measured natural vertical chromaticity of SIS-18.

References

[1] M. Blaskiewicz, Phys. Rev. ST Accel. Beams **1**, 044201 (1998)

[2] R. Singh et al., "Interpretation of transverse tune spectra in a heavy-ion synchrotron at high intensities", Accepted for publication in Phys. Rev. ST Accel. Beams, Feb. 2012.

* This work is supported by DITANET (novel DIagnostic Techniques for future particle Accelerators: A Marie Curie Initial Training NETwork),Project Number ITN-2008-215080

Eigenmode Computation for Biased Ferrite-Loaded Cavity Resonators*

K. Klopfer†[1], *W. Ackermann*[1], *and T. Weiland*[1]

[1]Technische Universität Darmstadt, Institut für Theorie Elektromagnetischer Felder (TEMF), Schlossgartenstraße 8, 64289 Darmstadt, Germany

Introduction

In the heavy-ion synchrotron SIS 18 two ferrite-loaded cavity resonators are operated for the further acceleration of charged particles. Since the speed of the heavy ions still increases significantly during the phase of acceleration, the operating frequency of the resonator has to be adjusted to the revolution frequency of the particles. To this end, dedicated biased ferrite-ring cores are installed together with the necessary current windings. Modifying the bias current results in an altered differential permeability of the ferrite material and finally enables to adjust the resonance frequency. The current study aims at the numerical computation of the lowest eigenmodes for biased ferrite-loaded cavity resonators.

Computational Approach

The fundamental relations relevant for the calculation of eigenmodes of biased ferrite cavities as well as the used computational model are discussed in [1]. To sum up the most important aspects briefly, the eigenfrequencies strongly depend on the magnetic properties of the ferrite material and particularly on its differential permeability at a given bias magnetic field. Hence, to determine the eigenmodes the bias field is calculated in a first step by means of a nonlinear magnetostatic solver. After linearizing the constitutive equation at this working point, the actual eigenmodes are computed by the subsequent solver (cf. fig. 1). Due to the frequency dependence of the permeability tensor, the eigenvalue problem is nonlinear. Additionally, the system matrix is non-Hermitian if magnetic losses are taken into account. Besides of that, the newly developed solver is designed for an efficient computation on distributed memory machines.

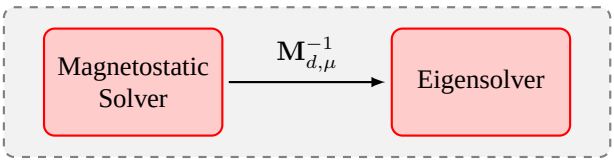

Figure 1: Subcomponents of the solver. Due to the dependence of the differential permeability $\mathbf{M}_{d,\mu}$ on the bias magnetic field, the magnetostatic field problem has to be solved before computing the actual eigenmodes.

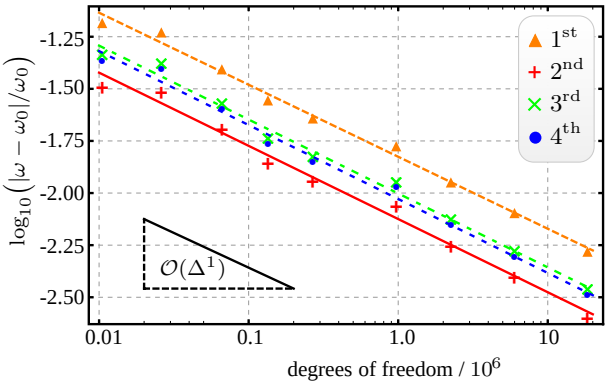

Figure 2: Relative deviation of the numerically obtained value ω to the semi-analytical result ω_0 as a function of the degrees of freedom for the four lowest eigenfrequencies for a lossless, ferrite-filled cylindrical cavity resonator (radius $= 1$ m, length $= 2$ m, $\mu_r = 7$, $H_{\text{bias}} = 2750$ A/m) [1].

Numerical Example

To verify the nonlinear eigensolver, a lossless, ferrite-filled cylindrical cavity resonator longitudinally biased by a homogeneous static magnetic field is considered, for which the solutions can be found semi-analytically [2, 3]. Performing convergence studies with different numbers of degrees of freedom, ensures a proper implementation of the underlying algorithms while good accordance of numerically obtained results with the reference values is observed (cf. fig. 2).

Summary and Outlook

A new solver for the determination of eigenmodes of biased ferrite-loaded cavity resonators is developed. Whereas promising results for simplified lossless resonators have been presented, the support of lossy material is currently in progress. Future work will also include the reliable implementation of the magnetic properties of the ferrite material installed in the SIS 18 cavities.

References

[1] K. Klopfer, W. Ackermann and T. Weiland, Proc. of 3rd Int. Particle Accelerator Conf. - IPAC 2012, MOPPC058, 2012.

[2] M. L. Kales, J. Appl. Phys. 24, 604, 1953.

[3] G. C. Chinn, L. W. Epp and G. M. Wilkins, IEEE Transactions on Microwave Theory Techniques, 43, May 1995.

* Work supported by GSI

† klopfer@temf.tu-darmstadt.de

n-XYTER 2.0 Operative and Tested

D. Dementyev[3], V. Krylov[2], S. Löchner[1], C.J. Schmidt[1] and I. Sorokin[1,4]

[1]GSI, Darmstadt, Germany; [2]Kyiv University, Kiev, Ukraine, [3]JINR, Dubna, Russia. [4]KINR, Kiev, Ukraine

n-XYTER is a self-triggered multi-channel charge sensitive detector readout chip, originally developed for the signal readout of thermal neutron detectors [1] and similar to FSSR2 [2]. It is being employed in many detector prototyping activities for the FAIR experiments and others [3], [4], as it is the only front-end chip available which realizes a self-triggered architecture, is applicable for both polarity signals and finally has sufficiently high gain for the detection of MIP size signals in Silicon.

The first prototype version 1.0 has been extensively tested and turned out to show a severe temperature coefficient in the DC-signal levels of about 4%/K, which made its employment very tedious and difficult, as the slightest temperature variations resulted in enormous pedestal drifts.

With the aim to repair the temperature coefficient, the chip underwent a redesign, which primarily focussed upon the supply of several biasing potentials from outside the chip, the correction of various layout deficiencies and finally the introduction of a switch that would change the gain by about a factor of 4 and thus extend the dynamic range by the same factor.

The submission of n-XYTER 2.0 was realized as an engineering run, which served to supply a sufficient number of dies for the use in FAIR detector prototyping activities as well as thermal neutron detector developments targeted at the Physikalisches Institut Heidelberg. The design was submitted in the AMS 0.35µm process, twelve wafers were produced in total. For risk mitigation purposes one out of four locations on the reticle was filled with the original design of n-XYTER 1.0, the other three locations realized n-XYTER 2.0.

Chip Testing

The chip was taken into operation on a pcb previously employed for n-XYTER 1.0 through the use of a little fudge board, which carried the four adjustable external bias sources that need to be supplied with this version of the chip.

The strategy for setting these biases turned out comparatively simple: the bias for the pre-amp is to be set such that the DC output of the pre-amp is identical to the input potential. Further, the three dc-bias voltages for the fast shaper circuit as well as the two successive slow shaper circuits can easily be set with the target of setting the output DC levels to adequate values.

The temperature coefficient was measured for every channel on a chip and found at a level of 0.12 mV/K or ~ 2 10^{-4}/K, an improvement by a factor of 200 as compared to n-XYTER 1.0.

Then the internal charge injection circuit was tested and calibrated for two individual chips by comparison to the response of a very well calibrated external charge injection circuit. Variations were found on the level of +- 5%, which may be attributed to variations of the effective input coupling capacitance of the internal test circuits.

Likewise the gain of every channel was individually determined. Fig. 2 shows the histograms of the channel gain of one chip for pos. and neg. signal polarities.

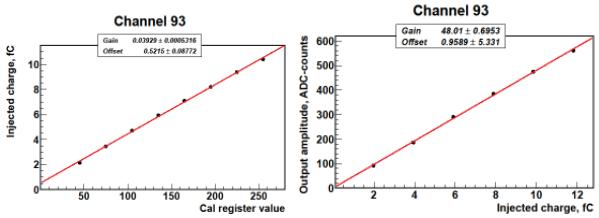

Figure 1: Calibration of the test pulse circuit, using a highly accurate external injection circuit (right) and comparing the signal response to the signals generated by the internal circuit (left)

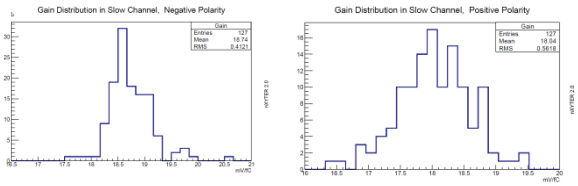

Figure 2: Histograms of measured gain for positive (right) and negative (left) input signals.

The newly introduced feature, the swichable dynamic range through swichable gain did result disappointing. Gain may indeed be changed by about a factor of 2.5. The dynamic range however resulted to remain the same, as the analogue output operating window is in effect reduced by the same factor. In conclusion, this feature may only be realized with much more sophisticated changes in the circuitry, which for this submission was omitted to minimize risk of failure.

Conclusion

n-XYTER 2.0 is functional. The temperature coefficient has been abolished. By now, the full set of tools for an automated serial test has been set up and may now be employed for a wafer-scale test campaign to characterize this batch of chips.

References

[1] A. Brogna et al., Nucl. Instr. Meth. Phys. Res. A568 (2006) 301-308
[2] Re et al, 2005 IEEE Nucl Sci Symp Conf Rec, N16-1
[3] GSI Scientific Report 2008, FAIR-Experiments 10
[4] GSI Scientific Report 2009 71

Ten Years of ASIC Design at GSI

H. Flemming[1]
[1]GSI, Darmstadt, Germany

Introduction

In May 2002 the author started to build up an ASIC design group as part of the DVEE department at GSI. Now 10 years later the ASIC design is well established at GSI and has an important role in electronics development for FAIR.

History

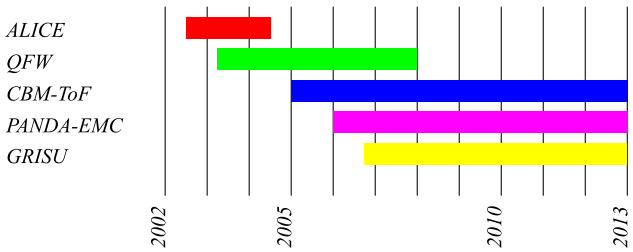

Figure 1: ASIC design projects at GSI since 2002.

The first years have been dominated by setting up the infrastructure and a support of colleagues at the Kirchoff institute of the university of Heidelberg developing readout ASICs for ALICE. As depicted in the time line in figure 1 the first GSI ASIC development started in 2003: the charge to frequency converter QFW[1] which plays now a major role in the beam diagnostics for FAIR.
In 2005 and 2006 the ASIC design group became active in developments for FAIR experiments. The GSI ASIC design started to develop a TDC ASIC for CBM-ToF[3] and a preamplifier and Shaper for PANDA[2]. In 2006 also a program to investigate radiation effects on CMOS semiconductors have been launched[4]. A special test ASIC named GRISU was designed and irradiated in several beam time campaigns.

These projects led into a large number of ASIC tape outs since 2002 as shown in figure 2. The number of designs in UMC 180 nm technology not only contains ASICs designed at GSI but also designs from other collaborators who participate on multi project wafer (MPW) productions financed by GSI. Especially from 2005 to 2008 a lot of developments for the FAIR experiments started which led into a large number of design submissions.
After that a design phase came up with less need of a big number of test structures but a smaller number of large prototype ASICs. In 2012 again a large number of different designs have been taped out.

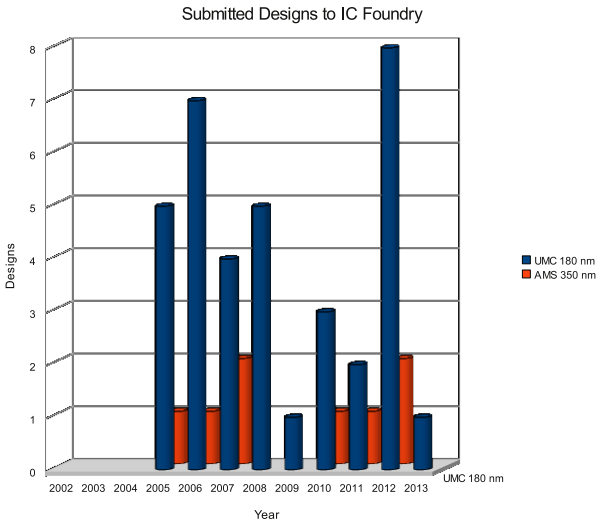

Figure 2: ASIC tape outs since 2002.

Status

The ASIC design group is now a very efficient working group of four designers and one technician. As part of the electronics department there is support from pcb layout and assembly and access to a very well equipped electronics laboratory. For the handling of ASICs the most important equipment like die bonder, wire bonder and prober is available under clean room conditions.
The importance of ASIC design is pointed by the number of ASICs which have to be processed at GSI. Whereas a few years ago only a few prototypes have to be processed for testing in the last years the number increased as more and larger detector modules have to be equipped with ASICs for readout. For 2013 it is expected that more than 1000 ASICs have to be handled at GSI.

References

[1] H. Flemming, E. Badura, “A high dynamic charge to frequency converter ASIC”, GSI Scientific report 2004

[2] P. Wieczorek, H. Flemming, “Low noise preamplifier ASIC for the PANDA EMC”, GSI Scientific report 2006

[3] H. Flemming, H. Deppe, “Development of High Resolution TDC ASICs at GSI”, 2007 IEEE Nuclear Science Symposium Conference Record

[4] S. Löchner, “Radiation Studies on the UMC 180 nm CMOS Process”, GSI Scientific report 2009

Control Software for the Ionization Profile Monitor of ESR@GSI

T. Giacomini, P. Forck
GSI, Darmstadt, Germany

After installation and successful commissioning of the new ESR@GSI Ionization Profile Monitor (IPM) [1,2] a capable control and readout software was required to support experiments like [3,4]. Due to the distributed system architecture several software tools and graphical user interfaces were developed for image-data network-storage, MCP calibration, defect pixel correction, high voltage control, user action logging, graphical user interfaces, digital IO configurtaion, etc.

Basic principle of IPM: The heavy ion beam ionizes the residual gas along the beam path. The ionized gas particles are accelerated transverse to the beam direction onto a phosphor screen. Before the residual gas particles hit the phosphor they are multiplied by a MCP in chevron configuration. The impacting particles create light spots on the phosphor screen which are viewed by a digital CCD camera from outside the vacuum. The phosphor screen has a rectangular shape of approximately 100 mm by 50 mm. On the phosphor screen the impacting residual gas particles create a luminous path in beam direction whose width corresponds to the width of the ion beam. These 2 dimensional images of the beam path are recorded by digital CCD cameras. Afterwards the images are integrated in beam direction to gather the beam profiles. To consider the defect pixel of the CCD a correction table is created at times. The number of beam profiles is equivalent to the cameras frame rate.

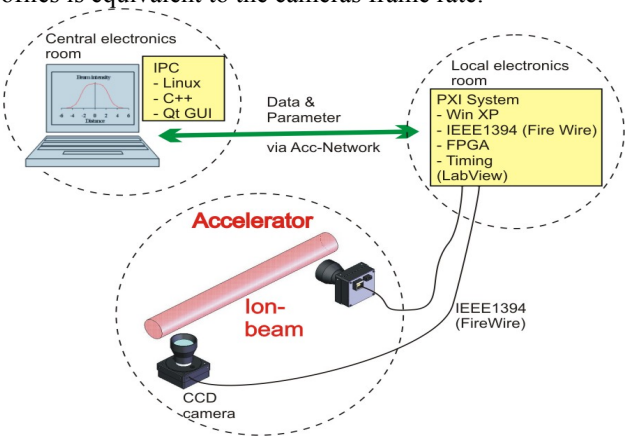

Figure 1: IPM DAQ system overview.

The data readout and analysis system consists of a DAQ (data acquisition) frontend system located in a local ESR electronics room and a DAN (data analysis) system located in the central electronic room. Both systems (DAQ and DAN) communicate with xml command strings sent via the GSI accelerator network. The splitting is necessary because of the strong deterministic timing requirements of the beam profile measurement.

The DAQ system consists of a PXI Crate with a 2.2 GHz pentium mobile controller with 1 GByte Ram and a 40 GByte hard disc drive to store the beam profile images during the measurement. The commercial frontend software is LabView® running on a XP® operating system. The two digital CCD cameras are connected to a PXI FireWire card. A PXI FPGA Module controls the external triggering of the cameras and the UV lamp calibration of the in-vacuum detector. Furthermore the FPGA includes several scaler channels. The frontend system is directly controlled by the new control software.

IPM Control Software

The control software is written in C++ with the Qt GUI framework. The main features of the software concern the readout of the two digital CCD cameras, the control of the IPMs high voltage system, the access to the digital IO ports, the data processing and display of measurement data.

When a start trigger occurs from machine timing or manually by an operator, the PXI system starts triggering the CCD cameras with a deterministic frame rate. Each time a beam image is measured all scaler channel are readout by the FPGA module. The scaler data represent amongst others the qualitative signals of the beams dc current, the dipole excitation and the rf signal. After the end-trigger the DAQ system waits until all measured data are downloaded to the DAN system. Then the DAQ system is initialized for the next start trigger.

Additionally, a new MCP-PH-Holder was developed providing much better performance at reduced risk for flashovers. This device was CAD designed and tested under vacuum conditions with an UV light calibration lamp of 120 nm wavelength.

Outlook

The new developed software will also be used for the new IPM@SIS18. The ipmproved MCP-PH-Module will be installed in the IPM@SIS18.

References

[1] M. Schwickert et al., “Beam Diagnostic developments for FAIR”, Proc. DIPAC09, Basel (2009).
[2] T.Giacomini at al., “IONIZATION PROFILE MONITORS - IPM @ GSI” Proc. DIPAC11, Hamburg, Germany, (2011), TUPD51419.
[3] M. Bussmann, D.F.A. Winters, et al., COOL09 Proceedings, IMPCAS Lanzhou, Atomic Energy Press, 22 (2009).
[4] D.F.A. Winters, “Laser cooling of stored relativistic C^{3+} ions at the ESR”, GSI scientific report 2013.

The GSI Event driven TDC GET4 V1

H. Flemming[1] *and H. Deppe*[1]
[1]GSI, Darmstadt, Germany

Introduction

In 2009 results of a first test design of the GET4 TDC ASIC have been obtained[1]. In the meantime additional analysis of the behavior of this ASIC in beamtimes as well as the submission of two test chips to improve the linearity of the TDC core have been done. Based on these activities in march 2012 the first fully equipped GET4 V1 was submitted to the IC foundry.

The GET4 ASIC

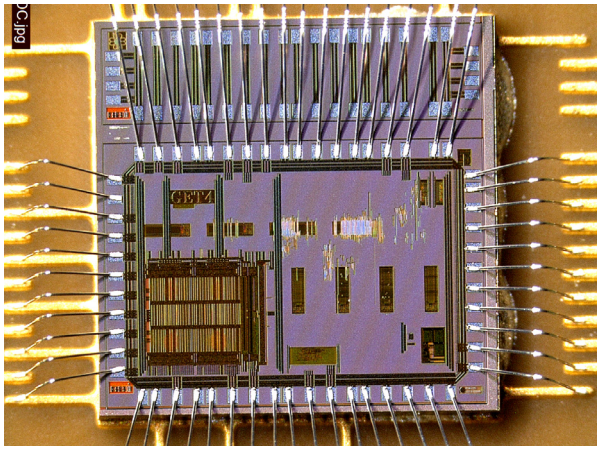

Figure 1: Die Picture of the GET4 ASIC.

The full custom designed TDC core of the GET4 V1 is based on the same architecture as the one of the first GET4 ASIC but is improved in many details. The TDC core is visible on the lower left side of the die picture in figure 1. The readout logic of the GET4V1 is completely new developed and automatically synthesised from a vhdl code. It contains a 24 bit readout mode that is compatible to the old GET4 ASIC and a new 32 bit mode that can cope with higher event rates. The 32 bit mode provides an internal time over threshold calculation and more slow control information. More information about internal structure, programming and data format can be found in the ASIC documentation[2].

Results

The tests and measurements of the GET4 V1 could confirm the good results of previous test chips. Figure 2 shows a pulse width spectrum and a time difference spectrum of a test signal generated with an internal test pattern generator. The width of the time difference peak is 27.9 ps rms. After division by $\sqrt{2}$ one gets an uncorrelated time resolution

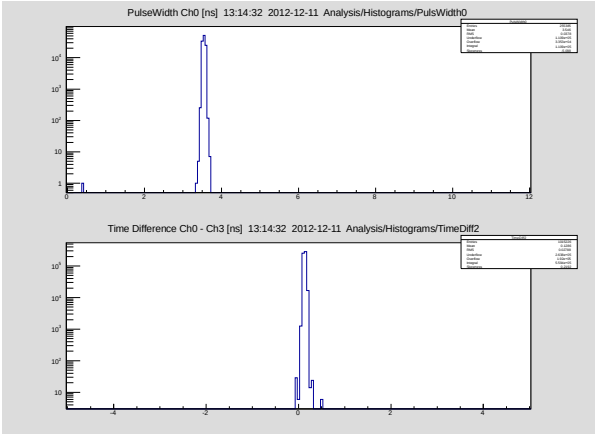

Figure 2: Pulse width and time resolution spectra.

of 19.7 ps for time differences. As the pulse width measurement contains the jitter of the internal ring oscillator as additional error contribution the result is slightly worse than the resolution for the time difference.

Outlook

Beside the very good TDC performance during tests also a few bugs have been found[3]. These bugs have been corrected in the design and on February 11th, 2013 a second iteration of this ASIC has been submitted to the foundry. This chip is expected to be produced in May. So for a new beam test campaign end of 2013 a bug fixed GET4 V1.2 will be available. In parallel the development of a programmable readout controller[4] will be continued with the second prototype that now fits to the 32 bit readout mode of the GET4 V1, delivered in February 2013. Tests will start in spring 2013.

References

[1] H. Deppe, H. Flemming, “A Wide Applicable TDC with Event-Driven Readout”, GSI Scientific report 2009

[2] H. Deppe, H. Flemming, “The GSI Event driven TDC with 4 Channels GET4 Version 1.20”, http://wiki.gsi.de/pub/EE/GeT4/get4.pdf

[3] H. Flemming, “Results of GET4 Tests, Known Bugs and Performance”,Talk in EE-meeting, http://wiki.gsi.de/pub/EE/EEMeetVortragArch/GET4V1.10Bugs.pdf

[4] H. Flemming, J. Frühauf, “A CPU Controlled SEU Hardened Readout Controller for the GET4 TDC Readout”, GSI Scientific report 2011, PHN-IS-EE-04

Single Event Effect and Beam Diagnostic Studies at the CBM Proton Test Beam

S. Löchner[*1], *H. Graf*[2], *and B. Walasek-Höhne*[2]

[1]GSI Darmstadt, Electronics (CSEE); [2]GSI Darmstadt, Beam Instrumentation (LOBI)

Introduction

Radiation damages to electronic components are an important issue for FAIR accelerator, FAIR experiments and the used equipment there. For the experiments one of the preferred technology for Application Specific Integrated Circuit (ASIC) developments is the 180 nm UMC CMOS process. In this regard the ASIC design group of the GSI Electronics department (CSEE) has been launched a research project, including the development of the *GRISU* ASIC with the main goal to characterise the Single Event Effects (SEE) on this process [1].

Within the CBM collaboration a SEE test with 2 GeV protons was realised in August 2012 at the particle accelerator COSY at Jülich [2]. Two aspects were tested: mobile beam diagnostic devices and the SEE characterisation itself.

Beam Diagnostic Devices

For the SEE cross section measurement it is essential to know the intensity and the position of the particle beam. The number of proton particles is measured via an ionising chamber [3], read out with a Charge to Frequency Converter ASIC (QFW) [4]. An online measurement of the proton beam position is done with a YAG:Ce scintillating screen and an attached CCD camera [5]. The entire setup is mounted on a moveable XY-table and alignment is done with the feedback from the online beam profile measurement. Once the system is aligned the scintillating screen is pneumatically moved out of the proton beam. In addition, the beam position has been approved by a self-developing dosimetry film [6]. A photography of the GSI test system at COSY is shown in Figure 1 as well as a typical corresponding measured beam profile.

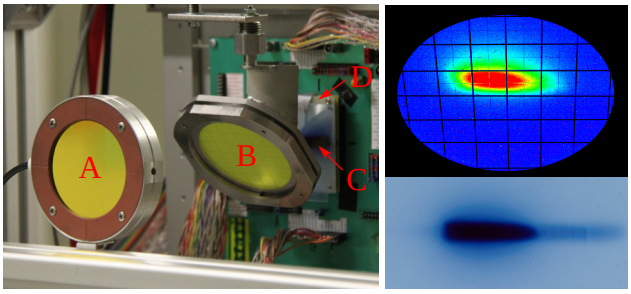

Figure 1: Left: SEE beam test system. A) ionising chamber, B) scintillating screen, C) dosimetry film, D) device under test. Right: beam position and dosimetry film.

Single Event Effects induced by Protons

Single Event Effects (SEE) is the main generic term for immediate effects in semiconductor devices triggered by the impact of particles. Of great interest are the so-called Single Event Upset (SEU) and Single Event Transient (SET) effects. These effects were studied in detail with heavy ions at the *GRISU* ASIC between 2008 and 2011 [1].

For proton radiation the SEE mechanism is different. Within the 2012 CBM proton test beam campaign at COSY the SEE cross sections of all *GRISU* circuits are tested. At a proton energy of 2.0 GeV and a fluence of $4.9 \cdot 10^{12}$ p/cm^2 in total 456 SEE are measured. Figure 2 shows exemplary the SET cross section data as well as its corresponding Weibull fit of a minimum sized inverter obtained from measurements with heavy ions. In the same diagram the saturated SET cross section region for proton radiation is drawn. This results for this inverter device in a ratio of maximum cross section between heavy ion and proton radiation of $\sigma_{\mathrm{sat,hi}} / \sigma_{\mathrm{sat,p}} \approx 4500$.

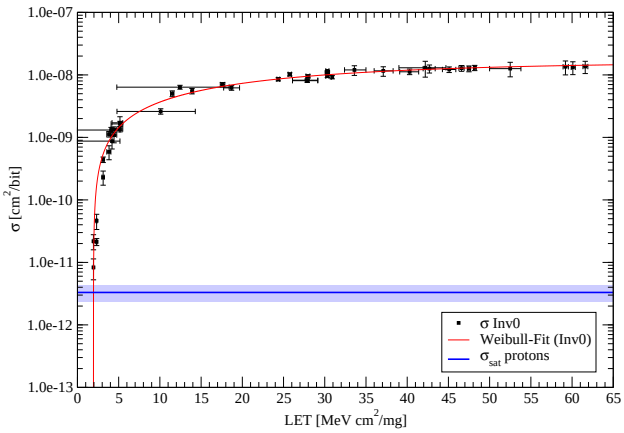

Figure 2: SET cross section for a minimum sized inverter.

References

[1] S. Löchner, "Radiation Studies on the UMC 180 nm CMOS Process", GSI Scientific Report 2009

[2] Forschungszentrum Jülich, Institut für Kernphysik (IKP), Cooler Synchrotron (COSY), http://www.fz-juelich.de

[3] GSI Detector Laboratory department (RBDL)

[4] H. Flemming, E. Badura, "A High Dynamic Charge to Frequency Converter ASIC", GSI Scientific Report 2004

[5] GSI Beam Instrumentation department (LOBI)

[6] GAFCHROMIC EBT self-developing dosimetry film, Sensitive dose range from about 1 cGy to 800 cGy

* s.loechner@gsi.de

PADI-6 and PADI-7, new ASIC prototypes for CBM ToF

M.Ciobanu[1], N.Herrmann[2], K.D.Hildenbrand[3], M.Kiš[3], A.Schüttauf[3], H.Flemming[3], H.Deppe[3], J.Frühauf[3], I.Deppner[2], P.A.Loizeau[2], M.Traeger[3]

[1]ISS, Bucharest, Romania; [2]Physikalisches Institut, Universität Heidelberg, Germany; [3]GSI, Darmstadt, Germany

We designed a general purpose PreAmplifier-DIscriminator (PADI) ASIC which can be used as a Front-End-Electronics for Resistive Plates Chambers in future CBM at FAIR. The low power PADI-chip can be used for different flavors of RPC's, with strip / pad like anode structures. These timing devises have signal rise times t_R<300 ps and primary charges in the range of 10 to 500 fC, which needs a preamplifier-discriminator stage with an intrinsic electronic resolution of σ_{tE} <15 ps. We developed and tested different 4 channels prototypes in CMOS 0.18 µm technology [1,2] with the following design key parameters: fully differential using a 50 Ω input impedance at a preamplifier gain of G_p> 100 with a bandwidth of BW_p > 300 MHz having a peaking time for the signal of t_{pk}< 1ns and a noise related to input of $V_{N\text{-}IN}$ < 25 μV_{RMS}. We use a DC feedback loop for offset and threshold stabilization; the threshold range between +/- 500 mV. As auxiliary functions PADI offers an OR-out. For the last prototypes, the increase of the charge responsivity and the decrease of the DC offsets where the main tasks. The Monte Carlo simulation shows that the preamplifier schematics must be drastically changed (Fig.1).

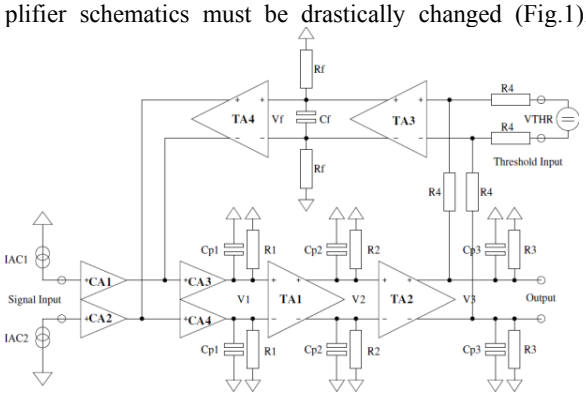

Figure 1: The simplified ac schematic of the preamplifier. The feedback path is now unique for signals and threshold voltage. The whole schematic can be evaluated like a full differential operational transconductance amplifier (OTA), having two inputs (VTHR and Signal) and one output. The resistive feedback realized with 4 identical resistors (R4) assure a linear DC transfer function. Except Rf, all resistors in schematic are physical resistors like in PADI-1. This solution achieves a maximum preamplifier bandwidth with good Monte Carlo results in matching of components or taking into account the technological dispersions. The threshold voltage is obtained from a DC bridge realized by 6 resistors R. This bridge is supplied from VDD and can be controlled internally by two 10 bits DACs (PADI-6) or externally (PADI-6 and PADI-7), by a potentiometer connected between VREF+ and VREF- pads and having the cursor at ground potential. These pads are common for all channels and one potentiometer can control all channels. The two DACs (PADI-6) are complementary commanded and the common mode voltage is not affected by the DAC code value. We have changed the type of the interface from I2C to the very often used SPI (Serial Protocol Interface) which is more simple and robust [3]. The SPI interface is currently used in many types of microcontrollers (e.g. the PIC family) and the implementation of PADI test equipment will be easier.

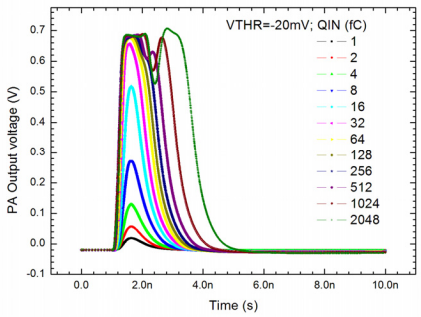

Figure 2 Simulation: PADI-6,-7 charge responsivity.

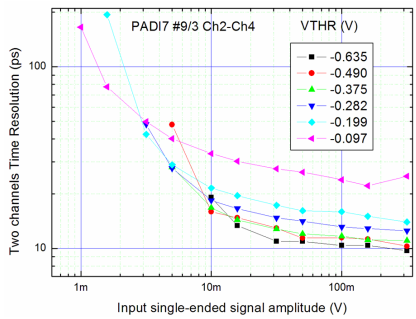

Figure 3 Measurement: Two channels time resolution versus input signal amplitude dependence to VTHR.

References

[1] M. Ciobanu, N. Herrmann, K.D. Hildenbrand, M. Kiš, A. Schüttauf, "PADI, a fast Preamplifier – Discriminator for Time-of-Flight Measurements", *IEEE NSS*, Conf. Rec., N30-18, 2018-2024, 2008.

[2] M. Ciobanu, N. Herrmann, K. D. Hildenbrand, M. Kiš, A. Schüttauf, PADI-2,-3 and -4: "The second iteration of the Fast Preamplifier – Discriminator ASIC for Time-of-Flight Measurements at CBM", *IEEE NSS*, Conf. Rec., N13-44, 401-406, 2009.

[3] J. Frühauf, N. Herrmann, M. Ciobanu, H. Flemming, H. Deppe, I. Deppner, P.A. Loizeau," Hardware Development for CBM ToF", this report.

Hardware Development for CBM ToF

J. Frühauf[1], N. Herrmann[2], M. Ciobanu[3], H. Flemming[1], H. Deppe[1], I. Deppner[2], P.-A. Loizeau[2]

[1]GSI, Darmstadt, Germany; [2]Physikalisches Institut, Universität Heidelberg, Germany; [3]ISS, Bucharest, Romania

The CBM-ToF-Readout-Chain is based on preamplifier and discriminator ASICs (PADI) [1] and event-driven TDC ASICs (GET4) [2] as front-end electronic. These ASICs are specially developed for the CBM-ToF detector.

Hardware: PADI-6 and PADI-7

For the preamplifier it is necessary to go nearby to the RPC to reach the best performance. Therefore it is decided to go even inside of the RPC-GAS-Box with the preamplifiers for the outer part of the ToF-Wall. Here we have a direct connection from the RPC to the FEE. The PCB layout was done in a way that there is one baseboard for power distribution, SPI-DAC-interface and connector for the output signals and "OR" signals from PADI. Each add-on PCB is equipped with two PADI-ASICs and the connector for the RPC.

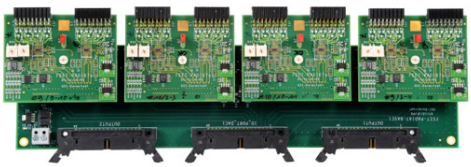

Figure 1: PADI-FEE (32 Channel)

Pulser Test: PADI-7

Two single ended pulses are injected into two input channels of PADI. The measurement was done for different signal amplitude as well as the threshold level of PADI was modified. The LVDS output signal was measured with an oscilloscope (Tektronix TDS6154C). The results of this measurement are shown in figure 2.

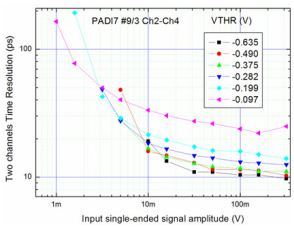

Figure 2: Resolution between two channels

The resolution between two channels for input signal amplitudes between 10mV and 100mV at different threshold values is below 20ps, which fulfils the CBM-ToF requirements.

Hardware: GET4 1.0

The test PCB for the GET4 1.0 ASIC is shown in the following picture. The main goal of this design is to test on board clock and power distribution, different supply voltages (5V; 12V and 48V) as well to test the new ASIC. One baseboard (Figure 3) can be equipped with four add-on PCBs, where each of them is equipped with four GET4 ASICs.

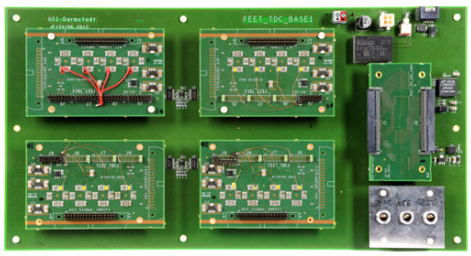

Figure 3: GET4-FEE (64 Channel)

On the left side of the picture the four add-on PCBs are seen. In the upper right corner the different power injections and in the lower right corner the two clock inputs as well as the sync signal input send out by CLOSY[3] are placed. In between, although as add-on PCB, the connector for the readout controller is placed.

Pulser Test: GET4 1.0

The result of a pulser test in the laboratory is depicted in figure 4.

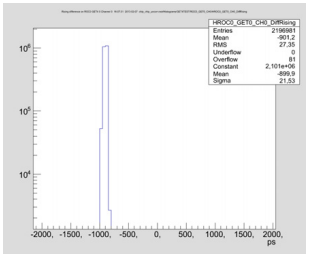

Figure 2: Resolution between two channels

The same LVDS signal is injected into two channels of two GET4 ASICs to mark each rising and falling edge with a time-stamp. The resolution between two channels is ~ 27ps.

Outlook

New frontend cards with specific layouts for each detector as well as test pcbs for the upcoming version of PADI and GET4 will be developed.

References

[1] M. Ciobanu et al., "PADI-6 and PADI-7, new prototypes for CBM ToF", this report
[2] H. Flemming et al., "GET4 1.0", this report
[3] K. Koch:"CLOSY", GSI Scientific Report 2009, p82

Status of the CBM TOF free streaming electronics chain*

P.-A. Loizeau[1], *N. Herrmann*[1], *I. Deppner*[1], *C. Simon*[1], *C. Xiang*[1,2], *M. Ciobanu*[3], *H. Deppe*[3], *H. Flemming*[3], *J. Frühauf*[3], *M. Kiš*[3], *K. Koch*[3], *S. Linev*[3], *S. Manz*[4], *and the CBM ToF working group*

[1]Physikalisches Institut, Universität Heidelberg, Germany; [2]Institute of Particle Physics, Central China Normal University, China; [3]GSI, Darmstadt, Germany; [4]IRI Goethe Universität, Frankfurt, Germany

The CBM experiment will have a data acquisition system operating in free-streaming mode for most of its detectors. In the case of the CBM Time-of-Flight (ToF) wall electronics chain, this new readout mode applies first to the Time to Digital Converter (TDC) and then to one or more FPGA based boards acting as Readout Controller (ROC) and Pre-Processor [1], until the input of the computer farm.

A first prototype of this readout chain consisting of the PADI3 and GET4 prototype ASICS and of the Syscore v2 ROC was assembled and tested in beam with Resistive Plate Chamber (RPC) prototypes[2]. Results of these test helped for the development of the GET4 v1.0 chip [3] and new versions of the PCB boards [4].

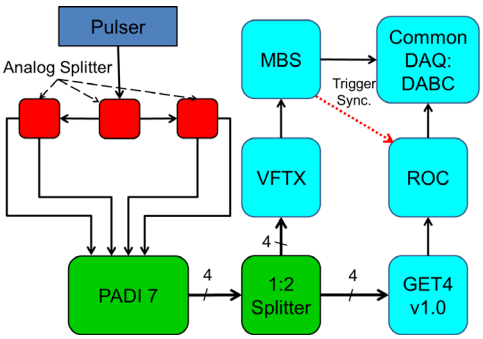

Figure 1: Sketch of the setup used to take pulser data with GET4 and VFTX in parallel.

These new developments were tested in beam with heavy ions at GSI in November 2012 and later in the laboratory with pulser signals. During the beam test, an RPC detector was equipped with PADI6 discriminators and two Plastic scintillators readout by Photo-multipliers (PMT) were equipped with PADI7 discriminators. The signals from the PADI boards were then splitted. On one side they were readout in a MBS/VME based triggered system using VFTX boards [5] as digitizer. On the other side the GET4 v1.0 based free-streaming system was used. Additionaly, a signal from the trigger board of the VME system is inserted in the data stream of the free-streaming system. This provides synchronization points between both systems. This also allows a comparison in the free streaming part between an event reconstruction based on using data themselves to detect events and a "triggered-like" event reconstruction. The pulser test is performed by replacing the 4 PMT signals with a single analog splitted pulser signal. A sketch of this setup is shown in figure 1.

The analysis software composed of an unpacker based on the GO4 framework and ROOT macros is now the same for the triggered and free streaming systems. A class for the VFTX unpacking and calibration and a class for the GET4 v1.0 unpacking and event building are feeding the same classes describing the detectors hits and clusters. The data taken in parallel can also be merged in a single output event using the event index sent from the triggered system to the free-streaming system. This allows direct comparison of the results, in particular time difference distibutions, obtained with the two systems.

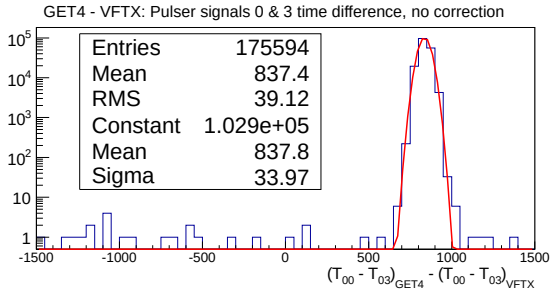

Figure 2: Example of a VFTX to GET4 comparison with pulser signals.

In the pulser test, the time differences between each pair of signals in each system are fitted with gaussian distributions. The difference between the time differences obtained in each system is also computed and fitted with a gaussian. Figure 2 shows an example of timing performances comparison between VFTX and GET4 based systems for the pulser test in the laboratory. Table 1 presents the mean sigma of the 6 possible signal combinations for each TDC and for their comparison.

Table 1: Mean sigma of the Gaus fit for each distibution in the pulser test for a 20mV pulse and a 150mV threshold.

	σ[ps]
PADI7 + VFTX	17.5
PADI7 + GET4	27.5
GET4 - VFTX	34.5

References

[1] C. Xiang et al., "The online data pre-processing for CBM-TOF", this report

[2] P.-A. Loizeau et al., "CBM Progress report 2011", Darmstadt 2012, p.59

[3] H. Flemming et al., "GET4 1.0", this report

[4] J. Frühauf et al., "Hardware Development for CBM ToF", this report

[5] J. Frühauf et al., "VFTX (VME-FPGA-TDC 10ps)", this report

*Work supported by EU/FP7 I3 Hadron Physik 3 and BMBF 06HD7141I

Two dimension position sensitive real size CBM-TRD prototype*

M. Târzilă[1], M. Petriş[1], M. Petrovici [1],V. Simion[1], V. Aprodu[1], D. Bartoş[1], G. Caragheorgheopol[1], V. Cătănescu[1], F. Constantin[1], L. Prodan[1], A. Radu[1], J. Adamczewsky-Musch[2], S. Linev[2]

[1]NIPNE, Bucharest, Romania; [2]GSI, Darmstadt, Germany

For the planned Compressed Baryonic Matter (CBM) experiment we have constructed and tested a real size CBM-TRD prototype (539.8 x 557.8 mm^2) with an architecture based on a MWPC coupled with a drift zone. The chamber design concept was retained from a previous small prototype [1]: a 2x4 mm amplification region and a drift zone of 4 mm, an anode pitch of 3 mm and a cathode pitch of 1.5 mm.

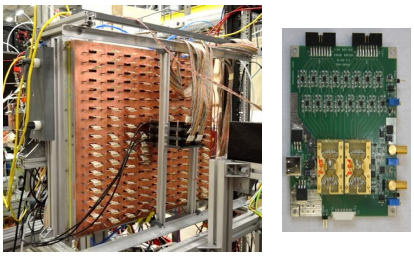

a) b)

Figure 1: a)The back side of the detector with signal flat cables; b) associated 16 channel FEE based on two FASP chips

The drift electrode, made from a 9 mm thick honeycomb plate placed between two Rohacell plates of 3 mm thickness, each one coated on the outer side with an aluminized kapton foil of 25 µm thickness, closes one side of the gaseous chamber. The other side is closed by the read out electrode made from a 300 µm thick PCB glued on a 2 cm honeycomb plate sandwiched by two layers of 100 µm carbon fiber. It has a structure of 9 columns and 20 triangular pad rows with 144 triangular pads per row, each triangular pad, with an area of ~1 cm^2, is readout individually. Signals delivered by pads are routed in groups of 16 to the flat cables as can be followed in Fig.1a, and processed by FASP [2] FEE (see Fig.1b).

The TRD prototype was tested with a mixed beam of electrons and pions, with particle momenta between 2 and 8 GeV/c, made available at T9 beam line by CERN Proton Synchrotron [3]. The chamber was flushed with a 80%Xe+20%CO_2 gas mixture and was operated at 2000 V anode voltage and 800 V drift voltage.

The electron and pion events are identified and selected using the correlation between signals provided by a Cherenkov detector and a lead-glass calorimeter positioned in front and at the end of the beam line, respectively.

*Work supported by BMBF, the HadronPhysics3 project financed by EU-FP7/HP3 Grant No. 283286 and NASR/Capacitati – Modul III contract no. 179

The obtained pulse height distributions for electrons and pions at 3 GeV/c are presented in Fig.2. The detector was operated with a regular foil radiator of 20/250/220 (20 µm foil thickness, 250 µm gap, 220 foils).

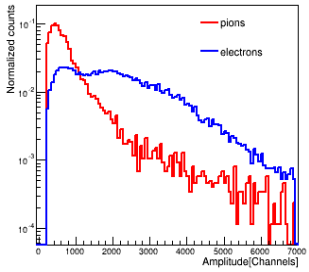

Figure 2: Pulse height distributions for pions (red line) and electrons (blue line)

The distributions obtained with one layer (Fig. 2) allow us to simulate the electron identification capability of a TRD as a function of the number of layers. The results are shown in Fig. 3a for a particle momenta of 3 GeV/c and for three types of radiators.

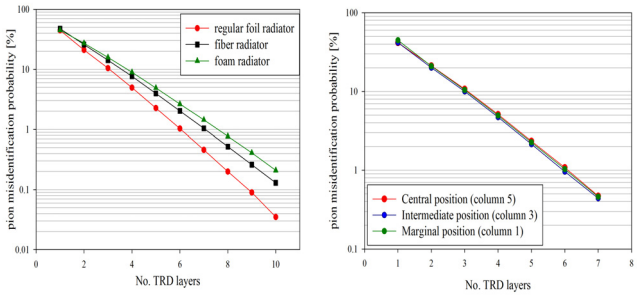

a) b)

Figure 3: Extrapolated electron/pion identification performance as a function of a) number of layers; b)operated area across the detector's surface

The best performance of ~ 1% was estimated for a configuration of six layers with the regular foil radiator.

Fig. 3.b shows that the electron/pion identification performance is not dependent on the position across the detector's surface, proving that the deformation of the drift readout electrode due to the slight overpressure of the circulated gas mixture is negligible.

References

[1] M. Petriş et al., CBM Progress Report 2011, p.47
[2] V. Cătanescu et al., CMB Progress Report 2009, p.47
[3] D. Emschermann et al., this report

The online data pre-processing for CBM-TOF

C. Xiang[*1,2], *N. Herrmann*[2], *P.-A Loizeau*[2], *I. Deppner*[2], *S. Manz*[3], *J. Frühauf*[4], *and S. Linev*[4]

[1]Key Laboratory of Quark and Lepton Physics (MOE) and Institute of Particle Physics, Central China Normal University, China; [2]Physikalisches Institut, Universität Heidelberg, Germany; [3]Kirchhoff-Institut für Physik, Heidelberg, Germany; [4]GSI, Darmstadt, Germany

The Compressed Baryonic Matter (CBM) experiment will operate a free streaming data acquisition system. In order to optimize the data bandwidth and to achieve high performance, a data pre-processing is designed in the readout chain in ROC firmware [1] for the CBM-TOF detector. It consists of three modules, data pre-processing module, monitor module and control module [2]. The data pre-processing module (DPM) which is the main part has two functions, hit building and cluster building, which are designed in two steps. See Fig. 1.

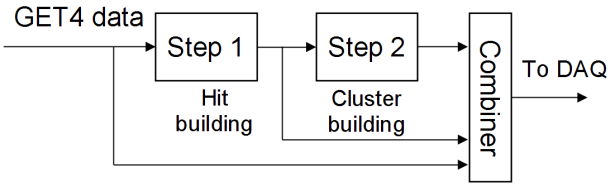

Figure 1: Structure of data pre-processing module

In the figure, the hit in the first step is built from rising edge and matched falling edge of GET4 data [3]. It has time information which is the rising edge time stamp and Time-Over-Threshold (TOT) information which is the time difference of rising edge and falling edge. The cluster in step 2 is a group of hit from 8 channels of two GET4 chips which connect to the two side of 4 neighbour Resistive Plate Chamber (RPC) strips. The time of the hits in the same cluster belongs to a certain time slice. All the data are combined together and sent to DAQ for cross checking.

Table 1: Data with/without DPM

	RAW data	**DPM data**	
Number of data	2.28E+08	1.39E+06	99.4%
Number of hits	967749	967604	0.015%
Number of events	237856	237848	0.003%

The ROC firmware with 1st step was tested at COSY with a proton beam in November 2011 with MMRPC detector[4]. A possible reduction of the data volume by means of online pre-processing with 1st step DPM is demonstrated, see Tab. 1. In the table, the 2nd column *Raw data* is the result from offline analysis on GET4 data, and the 3rd column *DPM data* is the result of online analysis from the 1st step data pre-processing on GET4 data. The last column show the result difference between offline analysis and online analysis. The final reduction of the output volume of the data depends on the hit rate, because most of the reduction is due to the rejection of the epoch data. In the case of hit rates in the order of 50 Hz per channel, as encountered during the test beam-time, about 99.4% reduction was achieved. As shown in table 1, during the test which run more than 49 minutes, the DPM lost only 145 hits (0.015%) , and only 8 events (0.003%).

The ROC firmware in which cluster building was implemented was test at lab in July 2012. The input signal of these two channels were from a splitter with input connect to signal generator. The result is illustrated in table 2. In principle, the number of *Raw data* from GET4 chip on these two channel should have same value. But in reality, they are different, see the 2nd row of the table. After the 2nd step of data pre-processing, the number of two channels are the same. This shows a single hit in a time slice will be rejected as the single hit is meaningless from detector physical point of view.

Table 2: Number of obtained hits from different data pre-processing level

	Chn. 1	Chn. 6
Raw data	2507905	2507991
1st step DPM data	2507243	2507217
Hit lost	0.0264%	0.0309 %
2nd step DPM data	2506236	2506236
Hit lost	0.07%	0.07%

These two test shows the data pre-processing module was fully functional and demonstrated the potential of implementing an on-line inspection of the data. Further features, like threshold self-adjusting can also be done in the readout chain.

References

[1] Manz, S., et al. ”An universal read-out controller.” Journal of Instrumentation 5.11 (2010): C11017.

[2] C.Xiang, FPGA based control and monitor for CBM-TOF - readout, CBM Progress Report 2011

[3] H. Flemming and H. Deppe, ”The GSI event-driven TDC with 4 channels GET4”,IEEE NSS, Orlando, FL, (2009) 1082-3654

[4] Deppner, I., et al. ”A glass type Multistrip-MRPC prototype for the low rate region of the CBM Time-of-Flight wall.” Journal of Instrumentation 7.10 (2012): P10008.

* chxiang@physi.uni-heidelberg.de. Work supported by China Scholarship Council and BMBF 06HD9121I and EU/FP7 I3 Hadron Physics 2.

Toward a RPC basic structure for the inner zone of CBM RPC-TOF wall *

M. Petriş[1], *M. Petrovici*[1], *V. Simion*[1], *V. Aprodu*[1], *D. Bartoş*[1], *A. Bălaceanu*[1], *G. Caragheorgheopol*[1], *F. Constantin*[1], *V. Duţă*[1], *L. Prodan*[1], *A. Radu*[1], *L. Rădulescu*[1], *I. Deppner*[2], *N. Herrmann*[2], *P. Loizeau*[2], *and M.C.S. Williams*[3]

[1]NIPNE, Bucharest, Romania; [2]Physikalisches Institut der Universitaet Heidelberg, Germany; [3]INFN, Bologna, Italy

For the inner zone of the CBM-TOF wall (polar angles between 50 mrad and 220 mrad) we proposed as basic unit a completely differential Multi-strip Multi-gap Resistive Plate Chamber (MSMGRPC) with a new geometry for the readout electrode of 7.1 mm strip pitch (5.6 mm strip width) and 96 mm strip length [1, 2]. With this value of the pitch size, the number of readout channels is reduced to one third of the estimated values of readout channels for the case of considering as basic unit the MGMSRPC with 2.5 mm strip pitch. High counting rate tests performed at COSY-Jülich with a proton beam of 2.5 GeV/c showed that even at 100,000 particles/cm^2·sec, the time resolution is better than 70 ps and the efficiency higher than 90% [2]. Constrained by the available dimensions of low resistivity glass ($\sim 10^{10}$ Ωcm) [3], the solutions foreseen for the present design is based on glass electrodes of 300 mm x 96 mm size. A modular structure divided in eight

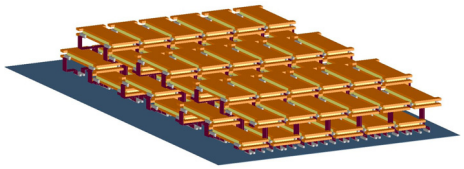

Figure 1: 3D image of RPC cells inside a supermodule

supermodules (SM) is proposed for the inner region of the CBM-TOF. A continuous coverage of the active area requires a staggered arrangement of RPC cells inside a supermodules and of supermodules, one relative to the other, as can be followed in Fig.1 and Fig.2, respectively. A demon-

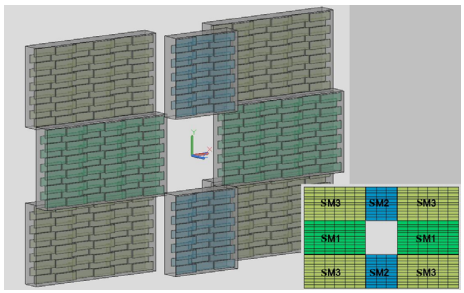

Figure 2: The 8 SM covering the inner wall active area

strator for the basic architecture of a supermodule contains four identical chambers staggered along (16.5 mm overlap) and across (17.5 mm overlap) the readout strips inside a gas tight box as it is illustrated in Fig3. The RPC cell structure is identical with the one reported in [1, 2]. The

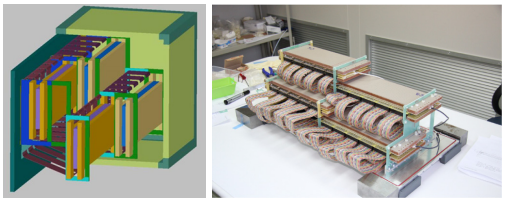

Figure 3: Sketch (left side) and photo (right side) of a basic architecture proposed for the inner zone of the CBM-TOF

lateral and front walls of the tight gas box are constructed from honeycomb sheets of 10 mm, sandwiched between two stesalit layers of 0.4 mm plated on the inner side by a pcb of 0.13 mm. The back plate, made from aluminum of 12 mm thickness supports the RPC cells. On rectangular openings machined on the plate are glued pcb plates with the connectors, for signal transmission from RPC cells to the front-end electronics.

The in beam test was performed at T9 beam line of CERN PS accelerator with a mixed electron and pion beam of 2 - 8 GeV/c momenta. Figure 4 left side shows the

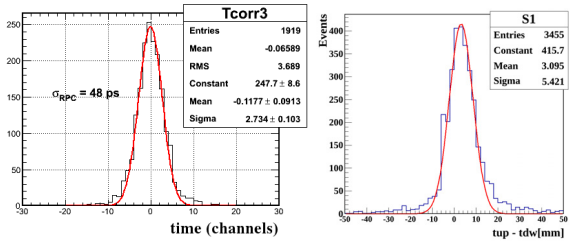

Figure 4: The TOF spectrum (left side); calibrated difference of the times measured at both strip ends (right side)

obtained time resolution of 48 ps measured for the overlapping zone along the strips of two MGMSRPC cells, after walk correction, including the electronics contributions. The 5.4 mm position resolution along the strip shown in Fig.4 right side was obtained from the calibrated time difference measured at both strip ends using position information from narrow strip reference RPC [2].

References

[1] M.Petriş et al. , CBM Progress Report 2011, p.56

[2] M. Petrovici et al., Journal of Instrumentation Volume 7, 2012 (JINST 7 P11003)

[3] Yi Wang et al., CBM Progress Report 2010, p.50

[4] M.Petriş et al. , CBM Progress Report 2011, p.55

* Work supported by EU-FP7/HP3 Grant No 283286 and Romanian NASR/CAPACITATI-Modul III contract nr. 179EU and NASR/NUCLEU Project

HADES trbnet data formats for DABC and Go4

J. Adamczewski-Musch[1], S. Linev[1], E.Ovcharenko[2], and C.Ugur[1]

[1]Common Systems/Electronics, GSI, Darmstadt, Germany, [2]ITEP, Moscow, Russia

Introduction

The *hadaq* data format via the *trbnet* transport protocol is used for many years to take data of the HADES experiment. The new TRB3 generation of read-out hardware is investigated for application with several FAIR experiments, e.g. PANDA and CBM. To support such developments, plug-in software has been implemented for the data acquisition framework DABC and the online/offline analysis framework Go4.

Plug-in for DABC

The *hadaq* plug-in defines an additional software library with the DABC framework. It provides classes to receive *trbnet* packets from the front-end boards via multiple UDP/Ethernet data streams and to align different message streams with respect to the "readout id" of the central trigger system (CTS). The resulting events may be stored in the standard HADES list mode data (*hld*) format. This re-implements the basic functionality of the current HADES production event builder software (Fig.1). The existing HADES event builder control system may even control the DABC event builders, since the export of the required parameters via shared memory to EPICS is completely emulated here.

A special DABC software module ("*MbsTransmitter*") allows wrapping the original *hadaq* data format into generic data packets of the MBS framework. As a consequence, data from *trbnet* frontends can be combined with data from other sources with MBS-type format by means of the generic MBS combiner module of DABC. Additionally, the *trbnet* data can be stored in MBS listmode (*lmd*) format or can be delivered to online monitoring clients like Go4 via standard MBS streamserver or eventserver protocols. As the *hadaq* plug-in can read *hld* files, also a conversion between *hld* and *lmd* files is possible.

Implementations for Go4

Generic unpacker code for *trbnet* data has been implemented as Go4 "processor" class. This expects the *hadaq* events to be wrapped into MBS event containers, as it is delivered by the DABC *hadaq* plug-in. Besides a special Go4 "user event source" class allows to read data directly from *hld* files and to wrap them into MBS containers as input for the processor. So the Go4 online analysis can either directly connect to the DABC application for quality monitoring or it can replay recorded data both from *hld* or *lmd* formatted list-mode files.

On top of this generic scheme, dedicated analysis codes for the TRB3 FPGA-TDC frontends [1] have been implemented in Go4. They can evaluate the TDC frontend format with up to 65 channels of time stamped messages. Each hit message contains a coarse time and a fine time counter value and leading/trailing edge property. A calibration procedure for the fine time counters allows correcting FPGA variations to improve individual channel resolution to 10 ps. An absolute timestamp range of 45 minutes is achieved by evaluating intermediate "epoch counter" messages. The time difference of each hit against a reference channel can be used in Go4 for hit selection with a time cut.

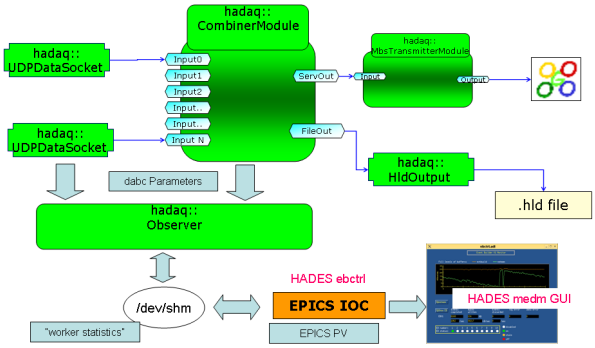

Figure 1: DABC components configured for HADES event building: Combined data channels can be saved as *hld* or *lmd* files. Go4 online monitoring may connect to MBS *streamserver* socket. The existing HADES eventbuilder control system with EPICS is fully supported.

Applications

At a test beam of CBM detector prototypes at CERN PS in November 2012, the DABC *hadaq* plug-in performed self triggered data readout from parts of the CBM-RICH prototype. The TRB3-TDC analysis had been integrated to the Go4 based CBM test beam framework [2] and was here running in the online monitoring.

A first version of the Go4 *hadaq* analysis was used for test beams of PANDA-DIRC collaboration at MAMI facility in February 2012. Most recent tests at COSY facility did benefit from applying the CBM improved analysis.

References

[1] C. Ugur, W Koenig, J. Michel, M. Palka, and M. Traxler, "Field Programmable Gate Array Based Data Digitisation with Commercial Elements", TWEPP-12, Oxford, September 2012, (JINST, accepted for publication)

[2] J. Adamczewski-Musch, N. Kurz, S. Linev, and P. Zumbruch, "Data acquisition and online monitoring software for CBM test beams", CHEP 2012, NY, May 2012 (J. Phys.: Conf. Ser. **396** 01 2001)

Further Development of the APFEL - ASIC for the PANDA Calorimeter *

P. Wieczorek[1] *and H. Flemming*[1]
[1]GSI, Darmstadt, Germany

Introduction

In 2012 the PANDA collaboration started to develop a first prototype for the barrel part of the PANDA electromagnetic calorimeter. The prototype consists of 120 PWO crystals which are equipped with 2 avalanche photo diodes (APD). These APDs are read out with the further development of the APFEL- ASIC (ASIC for PANDA Front-End ELectronics) which is developed at GSI. The APFEL-ASIC architecture is described in [1].

Readout Electronics

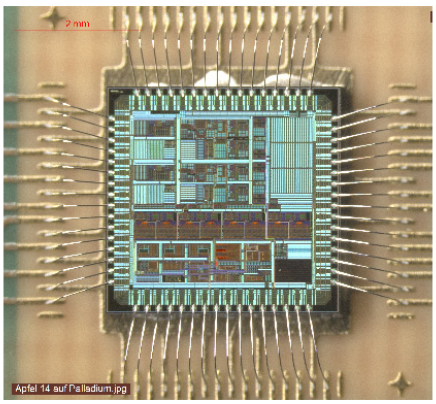

Figure 1: Photograph of the APFEL 1.4 - ASIC

A picture of the present APFEL - ASIC is shown in figure 1. On a chip area of 3.5 x 3.6 mm ^{2} two equivalent analogue channels and a digital part is implemented. Each analogue channel consists of a charge sensitive amplifier, a shaper stage and differential output drivers. After the first integrator stage the signal path is split into two sub paths. One of these sub paths has a programmable amplification of 16 or 32 in comparison to the other to get larger output signals in the low energy range. A schematic overview of the ASIC is presented in figure 2.

The further development of the APFEL - ASIC includes a decoupling of the first shaper stage of the two readout channels. Therefore a fourth DAC is implemented which was necessary to correct now all temperature and process variations for both channels individually. An essential design change is the programmable amplification. Therefore the second shaper feedback in the high amplification part is switchable. Using the serial receiver the amplification can be programmed. The present ASIC iteration also includes a new test pulser concept. For each channel four different charge injection capacitors are available so by combination in total 15 different pulse hights per channel are programmable.

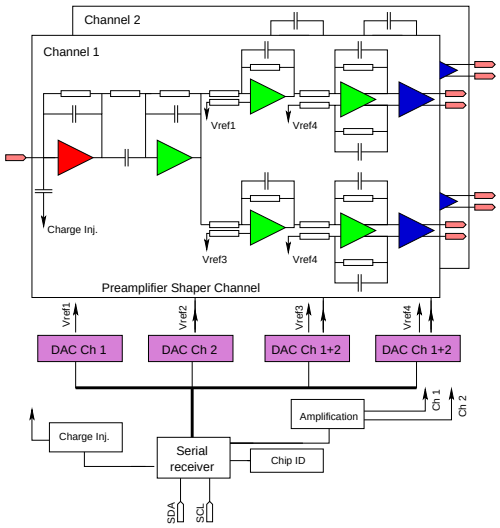

Figure 2: Overview of the ASIC architecture

Measured Results

The characterisation of the latest ASIC iteration at a temperature of T = $-25\,^{\circ}$C and a detector capacitance of 280 pF results in an equivalent noise charge of ENC=(4999$\pm$71) e$^-$ (or 0.78 fC) and a maximum input charge of 8.5 pC. Therefore a dynamic range of over 10 000 follows. The peaking time of the shaped signal was measured to τ_p=(248$\pm$3) ns. The event rate independent power consumption of one channel is P=(59$\pm$0.5) mW.

Summary and Outlook

The current design of the APFEL - ASIC is optimised for the effective conditions of the PANDA experiment and will be used for the barrel prototype 120. Therefore 120 flex cable PCB are designed and produced where the ASICs will be assembled. In spring 2013 the prototype 120 will be mounted and prepared for the beam time end of 2013.

References

[1] P. Wieczorek and H. Flemming, “Low Noise Preamplifier ASIC for the PANDA EMC”, IEEE Nuclear Science Symposium 2010, Knoxville, USA, NSS-N47-74, Published in NSS/MIC, 2010 IEEE DOI: 10.1109/NSSMIC 2010.5873982 Page 1319 - 1322

* Work supported by EU

Field-Programmable-Gate-Array Based Signal Discrimination and Time Digitisation*

C. Ugur†[1], *J. Michel*[2], *and M. Traxler*[1]
[1]GSI, Darmstadt, Germany; [2]Göthe-Universität Frankfurt, Frankfurt, Germany

The research about FPGA based Time-to-Digital Converter described in [1] is pushed further and tested with different boards using different FPGAs. As the results generated with Lattice FPGAs were promising, new boards with Lattice FPGAs have also been developed for experimental applications.

The TDC design is implemented with 16 channels on the EXPLODER1 and FEBEX 2 boards with ECP2M FPGAs. The precision of the TDC is improved to 11 ps in the single clock cycle measurement range by using the Wave-Union method [2]. For excess data suppression trigger window functionality is implemented.

For FPGA based time digitisation applications a new board, TRB3, has been developed. The board has 5 large and cost effective Lattice ECP3-150EA FPGAs with 150K LUTs, 4 of which are used for the TDC applications and the central one is used for the connectivity. The central FPGA can be configured to deliver the data through direct GbE-links or optical links running the mature TrbNet protocol also used in the HADES experiment. The TDC design is adapted to the ECP3 family architecture and each TDC-FPGA is equipped with 64 TDC channels for the time measurements and 1 reference channel for the synchronisation of the whole system with a total of 260 channels. The achieved time precision is similar with the ECP2M architecture ($\sim$11 ps) for single clock cycle time intervals. The board can cope with a hit rate of 50 MHz (in a burst) and a data readout trigger rate of 300 KHz. With the included epoch counter the measurement range of the TDC is increased to $\sim$45 minutes. The board is designed to be used in large systems using the TrbNet as well as a stand alone system with only a 48 V power supply and the GbE implementation in the central FPGA in order to send data out to a PC. The TRB3 is suitable for Time-of-Flight (ToF) and Time-over-Threshold (ToT) measurements, where the time information is encoded in the discriminated detector signals.

One of the applications for the TRB3 is the time digitisation and the readout of the photo-multiplier tubes (PMTs) and the micro-channel plate detectors (MCPs). The analogue signal from the detector is first amplified and then discriminated with the front-end electronics developed at the University of Mainz. The rising edge of the discriminated pulse carries the timing information, whereas the pulse width carries the time-over threshold (ToT) information. The discriminated pulse is then converted to a fast LVDS signal and delivered to the TRB3 for the time measurements. With this setup the readout of the PANDA Barrel-DIRC prototype was successfully carried out in the July 2012 beam time at MAMI.

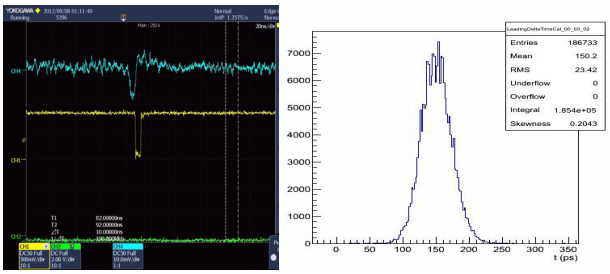

Figure 1: (a) The analogue signal is discriminated at the LVDS receivers of the FPGA and sent out for time measurements as a digital LVDS signal. (b) The precision of the whole system - discriminator board and TRB3 - is measured as $\sim$23 ps.

Another development is the discrimination of the detector signals using the LVDS buffers of an FPGA. The developed FEE board has MMICs at the amplification stage. The amplified signal is discriminated against the reference voltage at an LVDS input buffer. The time information of the leading edge and the ToT of the detector signal are encoded in the digital pulse in the FPGA. This digital pulse is sent out to the TRB3 as a differential signal via an LVDS output buffer for time measurements (Figure 1(a)). In order to set the threshold at the LVDS receiver the FPGA is used as a DAC via a Pulse Width Modulator (PWM) and low pass filter. The discrimination board is connected directly to the detector outputs. In the laboratory the time precision is measured as $\sim$23 ps RMS (Figure 1(b)). This development has been tested successfully during the PANDA-DIRC detector test beam time (@COSY) with 2400 channels in November 2012.

Further implementation of the FPGA based TDC design is carried out with FEBEX 3 boards and a prototype with 100-200 channels is foreseen.

References

[1] C. Ugur et.al, GSI Scientific Report 2010, p.237.

[2] J. Wu and Z. Shir, *The 10-ps wave union TDC: Improving FPGA TDC resolution beyond its cell delay*, Nuclear Science Symposium Conference Record, 2008 IEEE.

*This project is supported by the "Helmholtz Platform for Detector Technologies and Systems".

† c.ugur@gsi.de

VFTX (VME-FPGA-TDC 10ps)

J. Frühauf[1], J. Hoffmann[1], E. Bayer[1] and N. Kurz[1]

[1]GSI, Darmstadt, Germany

For high accuracy timing measurements the VME-Module VFTX (Figure 1) has been developed at GSI Experiment Electronic Department. It has an FPGA based TDC design using the tapped delay line method [1].

Figure 1: VFTX Module

The VFTX can handle up to 32 LVDS input signals or with a different add-on pcb 16 NIM signals. Available programs are:

- 16 Channel ~7ps (leading edge)
- 32 Channel ~10ps (leading edge)
- 28 Channel ~10ps with time over threshold information (leading edge and trailing edge)

An external clock input allows having more than one module running on the same clock. An external reset Input and a reset command via VME command assures that the modules clock counter are reset at the same time. Due to that there is no need of a reference signal in each TDC and no loss of √2 in resolution. The readout of this module is trigger based and the used data acquisition is MBS (Multi Branch System).

Laboratory Test Setup

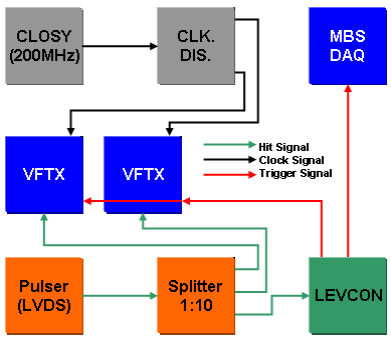

Figure 2: Block diagram Pulser Test

Figure 2 shows a simplified block diagram of the test setup in the laboratory. In grey the clock generator CLOSY [2] with the clock distribution can be seen. In orange the signal generator with the signals splitter, to have 10 times the same input pulse available. The blue blocks are the VME modules VFTX and the necessary modules for MBS readout. The LEVCON (Level-Converter) is used for sending out the trigger in different levels.

Results

The result of this measurment are despicted in Figure 3. On the left side of the picture the time resolution for a 28 channel (TOT) design with 9.5ps and on the right hand side the time resolution for a 16 channel design with 6.6ps time resolution are shown. These two results are measured both on the same VFTX module.

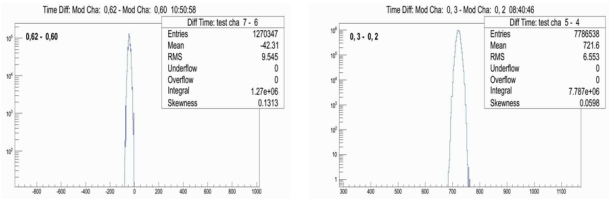

Figure 3: Time resolution between two channels.

Measurements between two VFTX modules have a resolution of ~12ps for a 10ps design and ~9ps for a 7ps design between two channels. This loss of 2ps is due to the clock splitter, which provides the master 200MHz clock for the different modules.

Conclusion & Outlook

The VFTX Module shows nice result in the laboratory tests and was already used successfully in beam by the SOFIA Collaboration for PMT readout and by the CBM–TOF Group for RPC readout.

The second iteration with small bug fixes will be available beginning March 2013.

References

[1] E. Bayer, M. Traxler: Development of a High-Resolution (< 10 ps RMS) 32-channel TDC in a Field-Programmable-Gate-Array, GSI Scientific Report 2009, p.325

[2] K. Koch: CLOSY: A very Precise Clock Generation for Timing Measurements and Synchronization of the CBM ToF Wall, GSI Scientific Report 2009, p.82

Panda GEM Tracker software status

R. Karabowicz[1]
[1]GSI, Darmstadt, Germany

PANDA experiment's forward tracking will be achieved using 3 stations of the GEM tracker. The stations in the form of circular planes perpendicular to and centered around the Z axis are placed 117, 153 and 188 cm in the downstream direction away from the interaction vertex. The detector covers polar angles from 3° to 20°. The detector geometry, simulation and reconstruction software are part of the PandaRoot framework [1].

Status

The GEM Tracker geometry description in PandaRoot consists of 3 stations. Several planes for each station simulate detector windows, cathodes, GEM foils and sensitive pad planes. The total thickness of one station is 5.255cm, including 5.212cm of gas, 0.0378cm of kapton, 0.0004cm of aluminium and 0.0048cm of copper. The material simulating readout electronics or support structure is not yet implemented.

Each of the pad planes, located in the centers of all GEM stations, will be double-sided coated with readout pads, grouped on each side in two perpendicular views. Thus, each station provides strip information about crossing particles in four directions: radial and circular (stations' front), horizontal and vertical (stations' back).

The digitization of the GEM Tracker has recently been updated to describe the detector response in more realistic way. In comparison to the first implementation, now the charge spread (of about 1mm) over several strips is taken into account, as seen in Figure 1. As a spin-off effect of this work also proper time information is attached to stimulated strips.

The first step in the data reconstruction is the cluster finder, which groups close lying strips and calculates mean strip value. These mean strips are subsequently input to the hit finder, which reconstructs the positions of tracks crossing the station.

The track reconstruction, performed by the GEM standalone track finder (described in [2]) has been only slightly modified as its performance was satisfactory.

Time based simulation

Since PANDA experiment is going to be read off continuously and all the data analysis like clusterization, hit finding, track reconstruction and event recognition are to be done online in order to select interesting events, PandaRoot packages are quickly being reorganized to adapt to this scenario [3].

In order to check the effect of this change on the GEM reconstruction, simple analysis has been performed, as seen in Figure 2. Digis belonging to different events are usually well separated and are coming at very similar times. One can observe (see times around 1790ns in Fig. 2) that for very close events they will be indistinguishable using the time information. The only solution is to separate them using vertex position. One can also see (see times around 1870ns in Fig. 2) signals from slow secondary particles coming even after few events. Detailed tracking is crucial in assigning them to proper events.

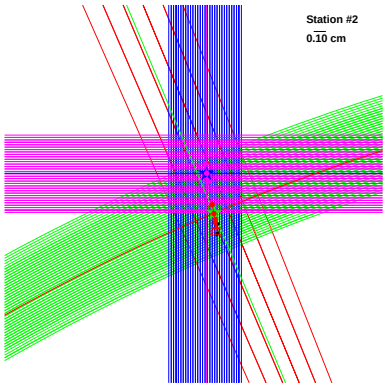

Figure 1: Fired strips on pad plane. Front (red and green) and back (pink and blue) views are plotted. The reconstructed clusters' mean values are also plotted, as green, red, blue and pink lines respectively. The star markers show the reconstructed hits. Red (pink) groups of 3 points and a line mark the particle trajectory in the detectors' front (back) drift volumes.

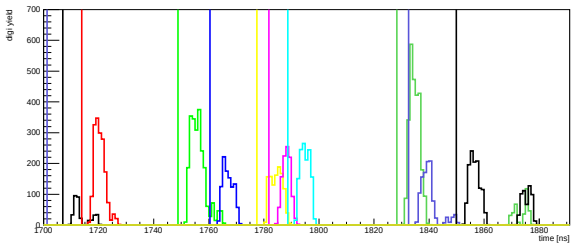

Figure 2: Digis time stamps. Different colors represent different events. The vertical lines mark the corresponding event time. Particularly event crowded time interval was chosen.

References

[1] Status of the FairRoot framework, M. Al-Turany *et al*, this report.

[2] Standalone track finding for the GEM-Tracker of the PANDA Experiment, R. Karabowicz *et al*, GSI Scientific Report 2010.

[3] FairRoot: Time-based simulation and reconstruction, M. Al-Turany, T. Stockmanns, GSI Scientific Report 2011.

Specific Energy Loss Performance of the GEM-TPC in FOPI*

M Ball†[1] *and the GEM-TPC Collaboration*[1,2,3,4,5]

[1]Technische Universität München, Germany; [2]GSI Helmholtzzentrum für Schwerionenforschung GmbH, Darmstadt, Germany; [3]Helmholtz-Institut für Strahlen- und Kernphysik, Bonn, Germany; [4]Universität Heidelberg, Heidelberg, Germany; [5]Stefan Meyer Institut für Subatomare Physik, Wien, Austria

A GEM TPC in Ungated Operation

Time Projection Chambers (TPCs) are usually equipped with a gating structure to prevent the migration of avalanche ions created during gas amplification – traditionally realized with Multi Wire Proportional Chambers (MWPCs) – in order to maintain drift field homogeneity. This, however, limits the application of TPCs to experiments with trigger rates smaller than $\mathcal{O}(10^3\,\mathrm{Hz})$. To overcome this important limitation introduced by gating techniques, one has to find other means of ion suppression. To test the capabilities of an ungated TPC equipped with Gas Electron Multiplier (GEM) [1] instead of MWPC we have built the largest GEM-TPC so far [2, 3].

The GEM-TPC in the FOPI Spectrometer

The GEM-TPC was installed inside the FOPI [4] spectrometer at GSI (Darmstadt, Germany). The FOPI spectrometer delivers a vertex resolution of few millimeters in the $x-y$ plane and a resolution along the beam axis of around 5 cm. The momentum resolution for particles in FOPI reaches 4-10 %. The main motivation to include a GEM-TPC in FOPI was to improve substantially the vertex and secondary vertex resolutions by an additional tracking detector. The performance of the prototype matches the expectations in terms of improving the momentum resolution of the existing spectrometer by 30 %. Furthermore the GEM TPC improve the track reconstruction in the forward region of phase space due to its large acceptance.

Measurement of the Specific Energy Loss

One of the key features of a TPC is the measurement of the specific energy loss as a function of the momentum. This allows identification of charged particles. The TPC was operated within FOPI measuring the reactions of a pion beam of $1.7\ \mathrm{GeV}/c$ hitting a carbon target. A gas mixture of Ar/CO_2 in the ratio 90/10 with a drift field of 235 V/cm has been used. The GEM amplification system produced a gain of about 1500. In Figure 1 the measured dE/dx distribution as a function of the particle momentum is shown. The particle momentum was reconstructed from a combined fit of the TPC together with the Central Drift Chamber (CDC) of FOPI. The energy loss was determined by the GEM-TPC alone. To minimize the influence of δ-electrons 40 % of the higher energetic samples have been truncated. The mean number of of samples is 21 with a sample length of 5 mm, which corresponds to an average track length of 10.5 cm. Cuts were made on the minimal number of samples ($N_{Sample} > 12$), on the scattering angle θ in the laboratory system ($0.4 < \theta < 2.4$) to match the acceptance of the CDC and on the χ^2_r of the track fit ($\chi^2_r < 5$). In Figure 1 one can see that pions, protons and also deuterons can be clearly separated. The band of kaons due to their much lower statistics is less pronounced, but also visible.

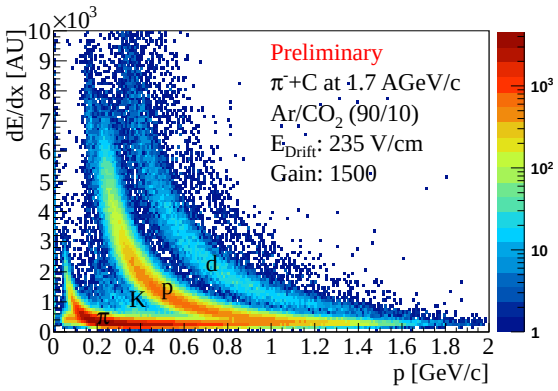

Figure 1: Specific energy loss (dE/dx) in the GEM-TPC. The the π-, proton- and deuteron-bands as function of the momentum can be clearly distinguished.

References

[1] F. Sauli, *"GEM: A new concept for electron amplification in gas detectors"*, Nucl. Instr. and Meth. A, 386 (1997), p. 531

[2] L. Fabbietti et al., *"The PANDA GEM-based TPC prototype"*, Nucl. Instr. and Meth. A, 628 (2011), pp. 204-208

[3] H. Angerer et al., *"First test of a prototype GEM-TPC for PANDA"*, GSI Scientific Report (2010)

[4] K. Hildenbrand, GSI Nachr. **91-02**, 6 (1992)

* Work supported by EU, BMBF, GSI

† markus.ball@tum.de

Annual neutron doses in the UNILAC experimental hall

C. Pöppe[1], T. Radon[1]
GSI, Darmstadt, Germany

Annual doses in 2011 and 2012

Figure 1 shows the downstream part of the UNILAC, a part of the TK and the experimental areas with the positions of the neutron detectors. The detectors are placed on the roof of the caves. The actual dose rates are listed in Tab.1. The measured values are in the range of 0.05 mSv/a up to 4.73 mSv/a. The highest dose values in 2012 were observed at X8.
The dose values are comparable to recent years [1] and are within the limits imposed by the radiation protection ordinance i.e. the annual doses are below 6 mSv/a.
An experiment carried out at X8 has been the reason for the increase of the accumulated dose in comparison to 2011. Additional shielding has been placed on several places, as mentioned later.

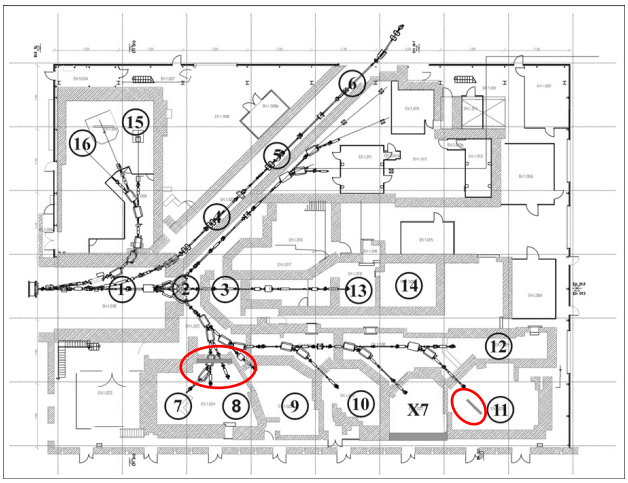

Figure 1: Measurement positions of the neutron doses in the UNILAC experimental hall outside the shielding.

Table 1: Measured Neutron doses in the UNILAC experimental hall outside the shielding, the positions are shown in Fig. 1

		Neutron - Dose H*(10) [mSv]	
Position	**Area**	**2011**	**2012**
1	end of UNILAC	0,08	0,22
2	end of UNILAC	0,12	0,25
3	end of UNILAC	0,11	0,28
4	TK	0,09	0,17
5	TK	0,09	0,15
6	TK	0,05	0,05
7	X 1	0,05	0,12
8	X 2,3	0,06	0,18
9	X 4	0,14	0,31
10	X 6	0,17	0,48
11	X 8	0,83	4,73
12	X 0	0,11	0,21
13	Y7 target	8,07	0,37
14	Y 7 Ship	0,12	0,21
15	M 1	0,07	0,09
16	M 3	0,07	0,10

Beamtime at X8

The beam time in X8 for the search of element 120 took almost 6 months in 2012. During the experiment it was necessary to declare certain areas around the cave and the beamline as temporarily controlled areas. This has been done due to dose rates higher than 3 µSv/h which represent the low limit value for controlled areas. Therefore based on the experience of the past year, the shielding was reinforced at two points before the experiment. This applies to the experimental cave X1 (fig. 1, position 7/8). Increased beam losses within the deflection of the beam coming from the UNILAC entering the X branch is producing additional neutrons, raising the local dose rates. The separating wall was reinforced by 0.5 m of concrete to reduce dose rates in X1. The reduction achieved by a factor of 10 was sufficient to leave X1 accessible during the beam time. Also a local shielding with Polyethylene was placed in the target area of X8 (fig. 1, position 11). As a result, the dose rates in X7 were reduced. However, due to higher beam losses along the X branch near X8, area X7 was declared a controlled area.

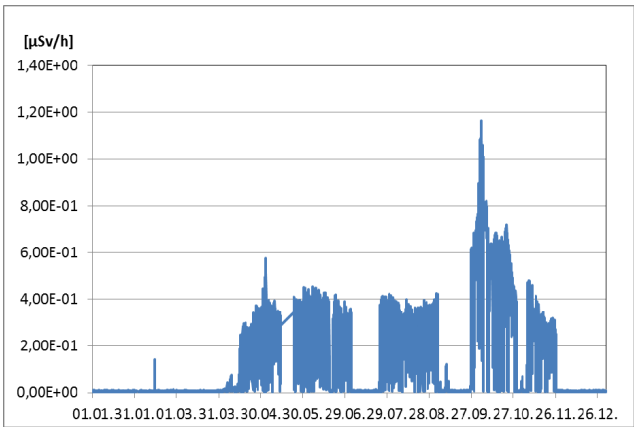

Figure 2: Measured neutron dose rate near X8 by ambient surveillance monitor in 2012. An accumulated dose of 1.33 mSv was observed for the operational year.

References

[1] C. Pöppe, P. Kewes, GSI annual report 2011

Cost calculation procedure for normal conducting magnets

C. Will, C. Mühle

GSI, Darmstadt, Germany

Previous procedure

In the past cost calculations for normal conducting magnets were usually done by using "cost per kilogram" assumptions. This method based upon a tight observation of production prices over the years.

During the process of ongoing planning for the production of components for the FAIR-Project a detailed price estimation became necessary.

Especially for normal conducting magnets as one of the biggest systems of the project cost estimations and production time estimations have been asked.

Figure 1 shows the distribution for costs per kilogram for dipole magnets, quadrupole magnets and steering magnets of the HICAT project [1].

This fast method of generating a cost estimation cannot consider the amount of magnets in one production cycle. In addition a reliable forecast about production duration is not possible.

Only in a double logarithmic representation the overall dependence is visible. If one examines magnets with similar weights a factor of 2 or more can be easily observed.

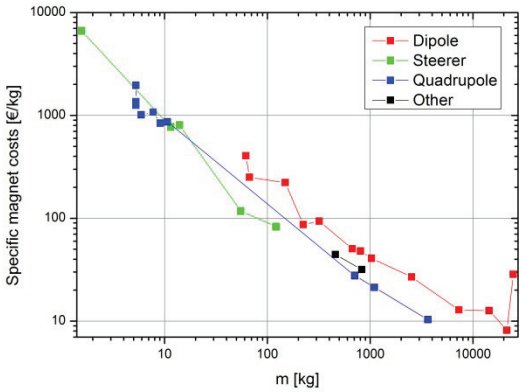

Figure 1: Specific costs (€/kg) for magnets built for HICAT [1].

New calculation procedure

Ambitions of a new procedure for calculation for normal conducting magnets were:

- Cost calculation on the basis of parameter tables given by magnetic calculation
- Consideration of the amount of magnets which have to be produced
- Generation of a pattern for time scheduling considering the amount of possible production lines
- Generation of an error analysis on basis of the calculated items

Parts of the calculations are mechanical design, tools for production, production of components for the magnets, assembly, mechanical, electrical and magnetic acceptance.

The method was developed for dipole magnets and quadrupole magnets. By using indicators the dipole calculation schema can be adopted for steering magnets, as well as the quadrupole schema for sextupoles.

Following the new method it is possible to generate price estimations with better accuracy in combination with a time table for the production of the magnets.

In addition a "design to cost" procedure is possible. The influence of magnetic and mechanical design options on the price of the components can be checked.

Additional factors for risk based on the error analysis and common commercial factors [2] also are included.

Analysis of deviances between offers by suppliers and calculated costs show that the error of calculation is higher for magnets with less weight.

This finding can be proven by separating the costs for materials and design. Table 1 shows the influence of the total magnet weight on the portions of costs for materials (steel, copper) and design for different magnet sizes and types calculated with the new schema. The error of material costs can be minimized by observing market prices. So the influence of uncertain information about working time decreases with increasing weight of the component. All calculations listed in table 1 were done for the production of a single magnet. The influence of the costs for design and for tooling decreases with increasing quantity of magnets.

Table 1: Portion of costs in reference to the weight of the component

Magnet	Weight	portion of costs		
	[kg]	% Steel	% Copper	% Design
Dipole	4331	4,44	6,91	13,16
Dipole	5907	6,02	8,18	9,64
Dipole	8612	5,98	7,12	6,47
Dipole	42468	15,36	12,45	5,31
Quadrupole	1262	2,14	4,39	26,19
Quadrupole	1944	2,25	8,34	24,45

References

[1] C. Muehle, B. Langenbeck, A. Kalimov, F. Klos, G. Moritz, B. Schlitt; Magnets for the Heavy-Ion Cancer Therapy Accelerator Facility (HICAT) for the Clinic in Heidelberg; IEEE Trans. on Appl. Supercon., vol. 14, no. 2, pp. 461-464, June 2004

[2] U. Fischer et al., Tabellenbuch Metall, Verlag Europa Lehrmittel, Haan-Gruiten, 2006

Annual Report of the ENMA Department

F. Klos, T. Knapp, H. Leibrock, C. Mühle, P. Rottländer, and M. Weipert

GSI, Darmstadt, Germany.

Introduction

This report summarizes the development and tests on normal conducting magnets at the ENMA department.

FAIR Magnets

Magnets for HEBT

The purchasing of the normal conducting magnets of the High Energy Beam Transport system (HEBT) is separated in three batches. All specifications of batch one, including all dipoles for the HEBT, has been finished. The corresponding contract is ready for signature. The specifications of the two other batches are close to finalization.

Solenoid development

Various Solenoids must be developed for different machines of the FAIR-Project. A solenoid design environment (SDE) has been developed to reduce expenditure of design time and work. The design environment is based on an Opera-2D-comi file. Most significant physical and technical parameters of a solenoid are considered. Due to the rotational symmetry a two-dimensional solenoid model describes well the main characteristics of a real magnet.

The first application of the SDE was the designing of a solenoid for an emittance transfer experiment (EMTEX) at GSI. The 35 cm long magnet creates a flux density of 1 Tesla at the center. The coil system of the solenoid is separated in two halves to allow placing of a movable stripping foil on the beam axis. Still, the magnet design avoids a local flux minimum in the center, since it might act as a trap for electrons.

Figure 1: EMTEX-Solenoid. The stripping foil is placed at the center of the magnet.

The additional man power for the development of a SDE is expected to pay-off soon, as it will help to decrease development time significantly in the future.

Magnet system of an Ion Position Monitor (IPM) for SIS18

The magnetic system of a new Beam Diagnostic (BD) component for the SIS18 section has been designed. It consists of two steering and two diagnostic magnets, which allow to measures the transverse profile of an ion beam both vertically and horizontally. The sextupole harmonic was significantly reduced by a special arrangement of the coils.

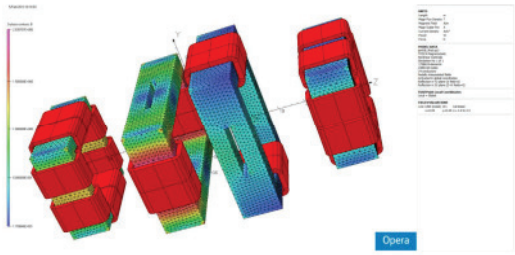

Figure 2: Opera-model of the magnet system of the IPM.

NC-Magnet Test Group

Magnetic measurements

The field distribution and quality of following magnets have been measured in the year 2012:

- 1 Electron spectrometer-quadrupole-triplet
- 1 Electron spectrometer-dipole
- 3 Quadrupole-triplets for the University of Frankfurt
- 1 LINAC-quadrupole-doublet

Other projects

- Development of a flexible research coil for dipole measurements. Several preliminary models have been designed and optimized. First parts of the mechanical integration have been designed.
- Optimization of the alignment device of the multipole measuring unit. An enlargement of the rotating coil system is in preparation.
- A procedure for demagnetizing of the mapper system was successfully developed and used.
- Installation of a ramping generator with corresponding software development and used.
- Handover of the stretched-wire--facility to the PBMT-department with training.
- Temperature measurements on a SIS18 quadrupole for reducing cooling water consumption with a new experimental water distribution system. A software for simulation of different operation modes has been developed.

Calibration method for the activity measurements in the 200-l barrels

E. Kozlova[1], A. Sokolov[1], J. Riemer[1], K. Vogt[1], K. Beverung[1], C. Fischer[1], T. Lehmann[1], V. Porwol[1], M. Wengenroth[1] and G. Fehrenbacher[1]

[1]GSI, Darmstadt, Germany

Motivation

At GSI in the near future some reconstructions of controlled areas and renovations of laboratory facilities as a preparation for the FAIR facility have to be performed. According to the German Radiation Protection Ordinance all objects and equipment from such areas must be inspected before a removal. To reduce time and keep the costs of the necessary measurements to a minimum the items can be analyzed directly in 200-l barrels, after sorting in disposal groups (e.g. „flammable“or „non flammable“).

For the activity estimation of the items situated in the barrels an ORTEC High Purity Germanium (HPGe) detector is used. Such measurement method requires efficiency calibrations, which is discussed in this paper.

Measurements and simulations

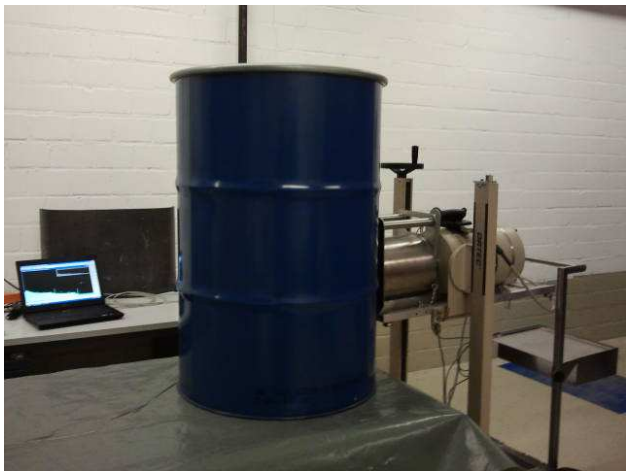

Fig. 1: 200-l barrel with the diameter 64.2 cm and height 92.3 cm. The weight of the empty barrel is 55 kg.

First measurements were done with an empty barrel. In Fig. 1 the barrel and detector are shown. For the calibration ^{241}Am, ^{22}Na, ^{137}Cs, ^{60}Co, ^{133}Ba and ^{152}Eu point sources were used. The sources were situated behind the empty barrel and the detector was in front. The results of the measurements are presented in Fig. 2. The energy range for the measured efficiency curve is between 59 keV and 1408 keV. The measured results were compared with simulations, which were done with the Monte Carlo code FLUKA [1]. The comparison is shown in Fig. 2. The results have 85 % agreement. The energy range of the simulated efficiency was extended up to 2500 keV, because in the activated waste can be a lot of nuclides with gamma lines above 1408 keV.

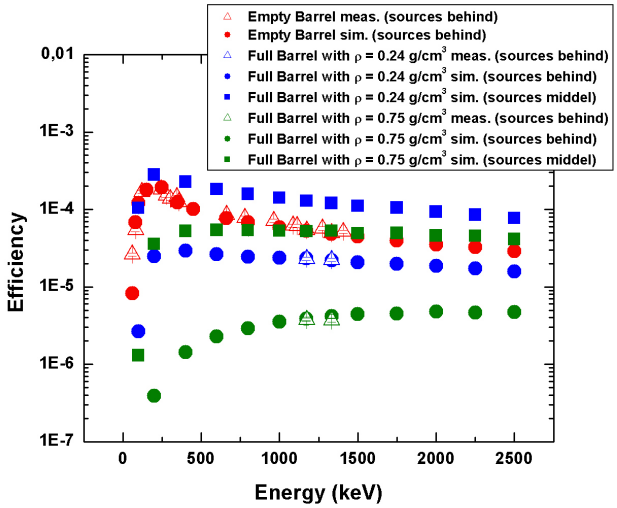

Fig.2: Detectors measured and simulated efficiency curves.

The next step was the calculation of the efficiency calibration for the full barrels. For these measurements a strong point source ^{60}Co was taken. It was situated behind the full barrel and the detector was in front. With the results of this measurement the density of the full barrel was defined. The defined density was taken for the simulations of the efficiency curve. The typical content of the barrel is a mixture of metal, glass, plastic and minor contributions of other materials. A mixture of steel and glass was taken for the simulations. The results for the barrels with a density of 0.24 g/cm^3 and 0.75 g/cm^3 are presented in Fig. 2. In most cases the waste in the barrels is distributed all over the barrel. Therefore calculating the activity by using the efficiency calibrations for the sources behind the barrels is too conservative and can lead to large overestimations of the waste activity (e. g. for the nuclides with gamma lines below 100 keV is a factor of 400, ρ = 0.24 g/cm^3). The most realistic estimation of the activity is achieved by applying the efficiency calibrations for the sources situated in the middle of the barrel. The efficiency curves for the sources in the middle of the full barrels were computed using FLUKA code. The results for the barrels with a density of 0.24 g/cm^3 and 0.75 g/cm^3 are shown in Fig. 2.

Conclusion

The developed calibration method for the activity measurements in the 200-l barrels can be applied for the safe routine radioactive waste management.

References

[1] www. fluka.org

Development of a Dosimeter for High Energy Photon Radiation

G. Fehrenbacher[1], A. Sokolov[1], T. Radon[1]

[1]GSI, Darmstadt, Germany

At high energy accelerators purpose-built dosimeters are necessary for the radiation survey in accelerator specific radiation fields. In recent years effort was dared to develop neutron dosimeters with an improved response to high energy neutron radiation. In this work a dosimeter is developed for the angular independent measurement of photon radiation in a wide energy range from about 100 keV up to 10 GeV or even higher energies. Basis of the dosimeter is a detection system using TL (**T**hermo**L**uminescence) and a design which is suitable to measure photon radiation in a conventional energy range (100 keV to some MeV) as well as for the high energy region. While for the conventional energy range only a PE scattering body around the TL cards can be used, for the high energy photons a metallic core has to be applied. The metallic core causes electromagnetic showers from the impinging high energy photons within the dosimeter and further energy deposition events in the TL elements occur. Figure 1 shows a picture of the dosimeter design. The dosimeter comprises 3 TL cards arranged as a triangle with 4 TL chips per card. In the center of the dosimeter a metallic core is mounted, consisting of 3 iron plates.

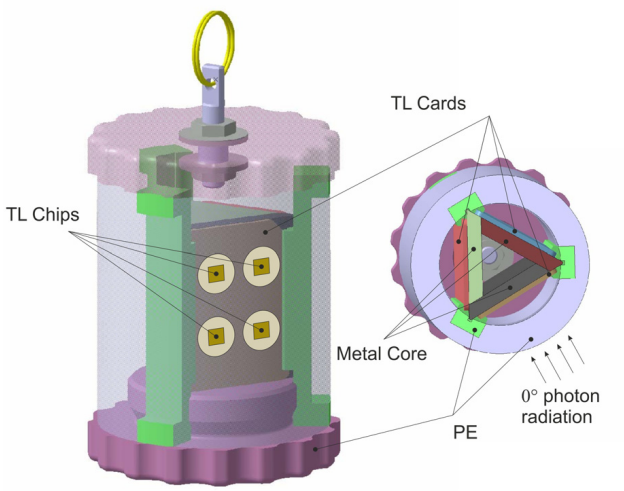

Figure 1: Design of the high energy photon dosimeter with a PE body, 3 TL-cards each with 4 chips and a metal core inside the dosimeter.

Response of the Dosimeter

The dosimeter is constructed for an optimized dose reading for high photon energies. Nevertheless the design of the dosimeter is appropriate to give a sufficient dose estimation in the lower photon energy region except for the energy range around 50 keV. The official dose quantity for area monitoring is the ambient dose equivalent H*(10). H*(10) is defined for the energy range from 10 keV to 10 MeV. For high energy accelerators photon energies higher than 10 MeV can occur and a conservative estimation of the effective dose is necessary. Therefore the effective dose for the isotropic irradiation was chosen as reference quantity. For the calculation of the dosimeter response a geometrical model was developed for FLUKA simulation calculations [1]. In figure 2 the response of the dosimeter irradiated along 0° direction (see fig. 1). For the predominant energy range from 10 keV to 10 GeV the dosimeter reading in isotropic irradiation geometry gives a conservative dose assessment either for the ambient dose equivalent or for the effective dose. The recommended energy range for application in photon fields is from 100 keV to 10 GeV or higher energies.

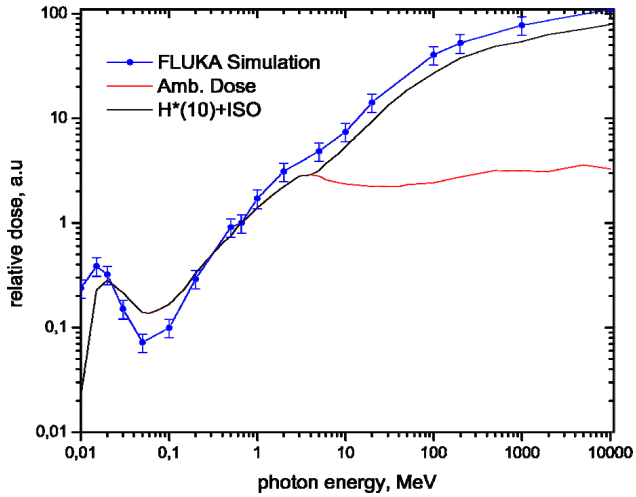

Figure 2: Calculated dosimeter response for the design of fig. 1 with 0° photon radiation incidence from 10 keV to 10 GeV.

Summary

A passive dosimeter using TL elements (3 cards with 4 TL chips per card) was developed for the high energy photon radiation. By means of metal layers inside the dosimeter the response to energetic photons is substantially improved. In the predominant energy range the dosimeter gives a conservative dose estimation with respect to the quantities H*(10) and the effective dose (ISO). The name of the dosimeter is *'**GA**mma dosimeter for **LIN**ear and Synchrotron **A**ccelerators (**GALINA**)'*.

References

[1] www.fluka.org

The *g* Factor of Lithiumlike Silicon $^{28}Si^{11+}$*

A. Wagner†[1], *S. Sturm*[1,3], *F. Köhler*[1,2], *W. Quint*[2], *G. Werth*[3], *and K. Blaum*[1]

[1]MPI für Kernphysik, D-69117 Heidelberg; [3]Institut für Physik, Johannes Gutenberg-Universität, D-55099 Mainz;
[2]GSI, D-64291 Darmstadt

The relativistic electron-electron interaction can be stringently tested by high-precision measurements of the gyromagnetic factor (*g* factor) of the valence electron bound in many-electron systems. Especially three-electron ions allow for a highly-sensitive test since they can be theoretically predicted to a high accuracy. To this end the *g* factor of the 2*s* valence electron bound in lithiumlike silicon $^{28}Si^{11+}$ has been determined with an uncertainty of $\delta g/g = 1.1 \cdot 10^{-9}$ [1], which is the most precise *g* factor measurement of a three electron system to date.

The *g* factor measurement

For the *g* factor measurement a single ion was stored in a cryogenic triple Penning trap setup for several months [2]. To determine the *g* factor via

$$g = 2\frac{\nu_L}{\nu_c}\frac{q}{M_{ion}}\frac{m_e}{e} \qquad (1)$$

the Larmor frequency ν_L and the free cyclotron frequency ν_c of the ion have to be measured, while the mass of electron m_e and ion M_{ion} are known from other high-precision experiments. The free cyclotron frequency can be determined by measuring the three eigenfrequencies of the ion in a first Penning trap. Simultaneously, microwaves close to the expected Larmor frequency are irradiated into the trap to induce spin flips. To determine the spin orientation with the continuous Stern-Gerlach effect, the ion is transported to a second Penning trap, where a magnetic inhomogeneity couples the spin orientation to the axial motion. Comparing the spin orientation to the orientation determined in the last cycle reveals if a spin flip was successfully induced. After several hundred cycles the spin flip probability as a function of the measured frequency ratio $\Gamma = \nu_L/\nu_c$ yields a *g* factor resonance as shown in Fig. 1.

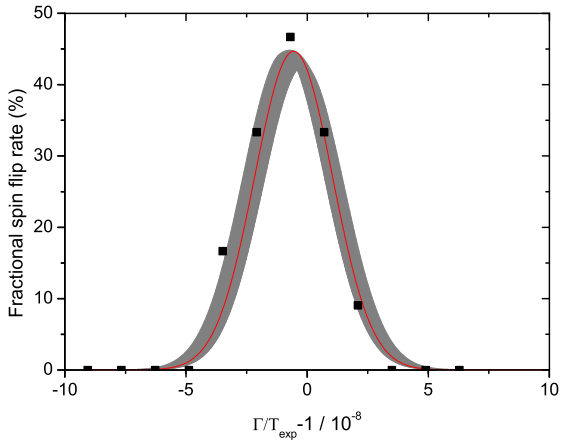

Figure 1: *g*-factor resonance of a single $^{28}Si^{11+}$-ion.

We have recorded three resonances with different microwave powers to check for related systematic shifts. The experimental result g_{exp}=2.000 889 889 9(21) is in excellent agreement with the theoretical value g_{exp}=2.000 889 909(51). The comparison between experimental and theoretical *g* factor confirms the many-electron contribution on the level of 10^{-4}, which is the most stringent test of relativistic many-electron calculations to date. Since the experimental value is by more than one order of magnitude more precise than the theoretical value, any improvement of the theoretical *g* factor will immediately improve this test.

Outlook

For highly sensitive tests of quantum electrodynamics with heavy ions the achievable theoretical precision is limited by unknown nuclear parameters. A measurement of both lithium- and hydrogenlike ions allows to cancel the contributions of the nuclear parameters to a large extent, hereby significantly increasing the stringency of the test [3]. Moreover, if combined with a measurement of the boronlike charge state, the fine structure constant α can be determined with a comparable uncertainty as the current value [4].

Having finished the *g* factor measurement of lithiumlike silicon, a *g* factor measurement of hydrogenlike carbon was started, aiming for an improvement of the precision of the electron mass by one order of magnitude.

References

[1] A. Wagner *et al.*, Phys. Rev. Lett. **110**, 033003 (2013)

[2] B. Schabinger *et al.*, Eur. Phys. J. D **66**, 71 (2012)

[3] V.M. Shabaev *et al.*, Phys. Rev. A **65**, 062104 (2002)

[4] V.M. Shabaev *et al.*, Phys. Rev. Lett. **96**, 253002 (2006)

*Work supported by Helmholtz Alliance HA216/EMMI, Max Planck Society and EU (ERC Grant No. 290870-MEFUCO).

† ankewag@uni-mainz.de

FOCAL – X-RAY SPECTROSCOPY FOR QED IN STRONG FIELDS *

H.F. Beyer[1], *D. Banaś*[2], *K.-H. Blumenhagen*[1], *F. Bosch*[1], *C. Brandau*[1], *W. Chen*[1], *Chr. Dimopoulou*[1], *E. Förster*[3,8], *T. Gaßner*[1], *A. Gumberidze*[4], *S. Hagmann*[1,5], *R. Heß*[4], *P.-M. Hillenbrand*[1], *P. Indelicato*[6], *P. Jagodzinski*[2], *T. Kämpfer*[8], *Chr. Kozhuharov*[1], *M. Lestinsky*[1], *D. Liesen*[1], *Yu.A. Litvinov*[1], *R. Loetzsch*[8], *B. Manil*[7], *R. Märtin*[8], *F. Nolden*[1], *N. Petridis*[4,5], *M.S. Sanjari*[1], *K.S. Schulze*[8], *M. Schwemlein*[1], *A. Simionovici*[10], *U. Spillmann*[1], *M. Steck*[1], *Th. Stöhlker*[1,8,c], *C.I. Szabo*[6], *M. Trassinelli*[10], *S. Trotsenko*[8], *I. Uschmann*[3,8], *G. Weber*[8], *O. Wehrhan*[3,8], *N. Winckler*[1], *D. Winters*[1], *N. Winters*[1], *and E. Ziegler*[11]

[1]GSI Helmholtzzentrum, Darmstadt, Germany; [2]Institute of Physics, Swietokrzyska Academy, Kielce, Poland; [3]Inst. für Optik und Quantenelektronik, F. Schiller-Universität, Jena, Germany; [4]Extreme Matter Institute, EMMI, GSI Helmholtzzentrum, Darmstadt, Germany; [5]Institut für Kernphysik, Goethe-Universität, Frankfurt am Main, Germany; [6]Lab. Kastler Brossel, Université P. et M. Curie, Paris, France; [7]Laboratoire de Physique des Lasers (LPL) UMR 7538 CNRS - Université Paris 13, Villetaneuse, France; [8]Helmholtz-Institut Jena, Jena, Germany; [9]LGIT, Observatoire des Sciences de l'Univers de Grenoble, Grenoble, France; [10]Institut des Nanosciences de Paris, Université Pierre et Marie Curie-Paris 6 and CNRS-UMR 7588, Paris, France; [11]ESRF, Grenoble, France

The goal of the present experiment is to access the quantum-electrodynamic (QED) contributions to the 1s binding energy in a heavy one-electron system in order to provide an accurate comparison with the most advanced QED calculations taking into account also two-photon exchange.

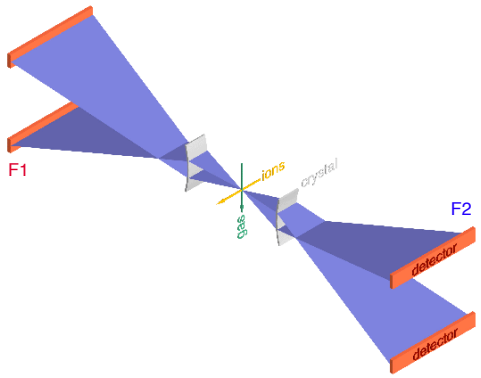

Figure 1: The Bi-FOCAL crystal-spectrometer arrangement at the ESR gas jet.

For this purpose the twin crystal-spectrometer assembly, Bi-FOCAL, operated in the FOcusing Compensated Asymmetric Laue geometry has been arranged for accurate x-ray spectroscopy at the ESR gas jet as schematically depicted in figure 1 [1]. Each spectrometer was equipped with one 2D position-sensitive Ge strip detector, F1 and F2. In May 2012, a major production run (E039) was conducted and the Lyman-α transitions of hydrogen-like Au^{78+} were measured in high resolution via spectroscopy of the corresponding x rays located near 63 keV in the laboratory system. Bare gold ions were stored in the ESR at a velocity corresponding to $\beta \approx 0.47$ and the x rays were measured in coincidence with ions undergoing single-electron capture in the argon gas target and being deflected into a particle detector by the bending magnet dowstream the gas jet. It could be demonstrated that the newly developed crystal optics in concert with the position sensitive detector can cope with the low count-rate situation encountered. Background could be effectively reduced, by proper shielding facilitated by the existence of a polychromatic focus and by making use of the time and energy resolving capabilities of our detectors.

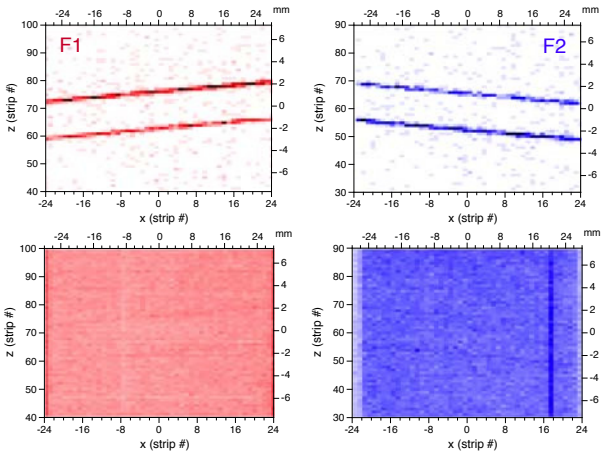

Figure 2: Lyman-α doublet of Au^{78+} recorded with the two 2D Ge strip detectors: *Bottom* – without, *top* – with energy and time discrimination in effect.

Figure 2 shows two-dimensional images of the Lyman-$\alpha_{1,2}$ doublet of hydrogen like Au^{78+} impressively revealing the low background when energy and time discrimination is in effect. The slanted lines observed are consonant with the underlying x-ray-optical design. This way spectral resolving power can be retained also for fast moving sources. Coming in pairs the x-ray optics provide Doppler cancellation capabilities. Data analysis is still in progress.

We thank the Institut für Kernchemie of the Johannes Gutenberg-Universität, Mainz, for the preparation of our calibration sources.

[1] H.F. Beyer *al.*, Spectrochim.Acta Part B **64** (2009) 736.

* Work supported by EU and EURONS contract No. 506065. D. Banas acknowledges the support by the Polish Ministry of Science and Higher Education under Grant No. N N202 46353.

Electron-impact Excitation of Hydrogenlike Uranium Ions*

A. Gumberidze[1,2], *D. B. Thorn*[1,2], *C.J. Fontes*[3], *B. Najjari*[4], *H.L. Zhang*[3], *A. Surzhykov*[†5,6], *A. Voitkiv*[4], *S. Fritzsche*[2,5,7], *D. Banaś*[8], *H. Beyer*[5,9], *W. Chen*[5], *R. D. DuBois*[1,10], *S. Geyer*[5,11], *R. Grisenti*[‡5,11], *S. Hagmann*[5,11], *M. Hegewald*[5,11], *S. Hess*[5,11], *C. Kozhuharov*[5], *R. Märtin*[5,9], *I. Orban*[12], *N. Petridis*[1,5,11], *R. Reuschl*[1,2,13], *A. Simon*[§14], *U. Spillmann*[5], *M. Trassinelli*[13], *S. Trotsenko*[5,9], *G. Weber*[5,9], *D. F. A. Winters*[5,6], *N. Winters*[5,6], *D. Yu*[5,15], *and Th. Stöhlker*[5,9,16]

[1]ExtreMe Matter Institute EMMI and Research Division, GSI, Darmstadt, Germany; [2]FIAS Frankfurt Institute for Advanced Studies, Frankfurt am Main, Germany; [3]Computational Physics Division, Los Alamos National Laboratory, Los Alamos, USA; [4]MPIK, Heidelberg, Germany; [5]GSI, Darmstadt, Germany; [6]Ruprecht-Karls-Universität Heidelberg, Heidelberg, Germany; [7]Department of Physics, University of Oulu, Finland; [8]Institute of Physics, Jan Kochanowski University, Kielce, Poland; [9]Helmholtz-Institut Jena, Jena, Germany; [10]Missouri University of Science and Technology, Rolla, USA; [11]Universität Frankfurt, Frankfurt am Main, Germany; [12]Department of Physics, Atomic Physics, Stockholm University, Stockholm, Sweden; [13]Inst. des NanoSciences de Paris, CNRS UMR7588 and UMPC-Paris 6, Paris, France; [14]Institute of Physics, Jagiellonian University, Krakow, Poland; [15]Institute of Modern Physics, Lanzhou, China; [16]IOQ, Friedrich-Schiller-Universität Jena, Jena, Germany

Electron-impact excitation (EIE) of bound electrons is one of the most fundamental processes and leads to the specific formation of spectral lines. In particular, it is responsible for the vast majority of x-ray radiation produced in various kinds of plasmas, in high energy density physics experiments and at laboratory fusion devices. Relativistic and retardation effects are known to affect the EIE process through the generalized Breit interaction (GBI) [1, 2].

Up to now, electron beam ion traps (EBITs) have been the preferred tool for studying the EIE [3]. Due to the small electron-impact ionization and excitation cross sections for heavy highly-charged ions, the focus of most of these EBIT studies has been confined to relatively low-Z systems.

In this contribution, we present an experimental and theoretical study of the electron-impact excitation effects in hydrogen-like uranium in relativistic collisions with different gaseous targets. The experiment was conducted at the experimental storage ring ESR. Recent developments, such as the anti-coincidence mode [4] and new micro-droplet target development [5], have rendered such studies feasible. By performing measurements with different targets as well as with different collision energies, we were able to gain access to both; proton (nucleus) impact excitation (PIE) and electron impact excitation (EIE) processes in the relativistic collisions. The large fine-structure splitting in H-like uranium allowed us to unambiguously resolve excitation to different L-shell levels. By looking at the intensity ratios of (Lyα_1/Lyα_2) of the subsequent decay photons, we were able to clearly identify and study the effect of the electron-impact excitation in H-like uranium (see Fig. 1). Combined calculations which treat both processes, PIE and EIE, provide a good agreement with the experimental data. Moreover, our experimental results clearly demonstrate the importance of including the effect of the GBI in the EIE calculations.

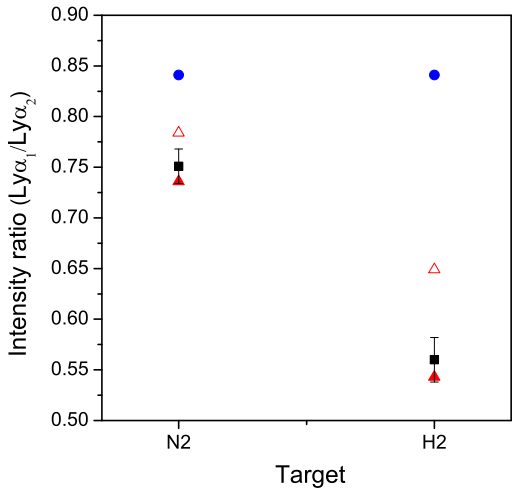

Figure 1: Experimental results (solid black squares) in comparison with theoretical predictions for Lyα_1/Lyα_2 ratios for the K-shell excitation of U^{91+} in collisions with N_2 and H_2 targets at 212.9 MeV/u. Solid blue circles show PIE results. Solid red triangles depict combined (PIE+EIE) calculations. In addition, the combined calculations are presented without inclusion of the GBI, by empty red triangles.

References

[1] C.J. Fontes, D.H. Sampson, and H.L. Zhang. Phys. Rev. A **51**, R12 (1995).

[2] D. L. Moores and K. J. Reed, Phys. Rev. A **51**, R9 (1995).

[3] H. Chen and P. Beiersdorfer, Can. J. Phys. **86**, 55-71 (2008).

[4] A. Gumberidze et al, Phys. Rev. A **82**, 052712 (2010).

[5] M. Kühnel et al, Nucl. Instrum. Meth. A **602**, 311 (2009).

* Work supported by Helmholtz Alliance EMMI.
† Work supported by the Helmholtz Association (VH-NG-421).
‡ Work supported by the Helmholtz Association (VH-NG-331).
§ Present address: NSCL Michigan State University, East Lansing, MI, 48223, USA

Experimental Investigation of Double Coherent Resonance of Li-like Ar in Si-crystal

A. Ananyeva[1,2], T. Azuma[3,4], A. Braeuning-Demian[2], H. Braeuning[2], Y. Kanai[4], K. Komaki[5] Y. Nakano[3,4], T. Masunaga[4] and Y. Yamazaki[4]

[1]GSI, Darmstadt, Germany; [2]Goethe-Universität, Frankfurt am Main, Germany; [3]Tokyo Metropolitan University, Japan; [4]RIKEN Advanced Science Institute, Japan; [5]University of Tokyo, Japan;

Introduction

We report on the experimental investigation of double resonant coherent excitation of Li-like Ar ions in traversing a Si crystal. The experiment was performed at the HIMAC accelerator at the National Institute of Radiological Science in Chiba, Japan.

Single and double excitation of incoming Argon ions were detected by measuring the change in the yield of different charge states of the projectile after passing through a Si crystal of 10 micron thickness. The measurements have been performed for different crystal orientations by using a two–dimensional position sensitive Si-detector.

Experiment

By passing a target with a regular structure, ions can be excited when the frequency the of the field created by the atoms of the ordered structure matches the frequency of an electronic transition into the ion. The excited state will de-excite via ionization and photon emission. By measuring the charge state distribution, electron and x-ray spectra from the ions after traversing the target, different excitations modes can be identified with large precision. In the present experiment single and double excitations in Li-like ions were measured.

The typical resonance spectrum is shown in the fig. 1 where the 2s to 3p transition is identified.

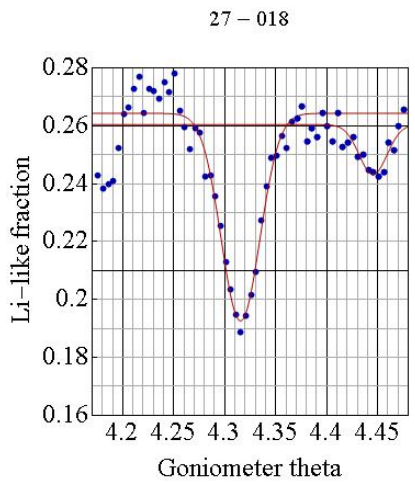

Fig. 1: 2s-3p transition in Li-like Argon single excited in Si crstal.

References

[1] C. Petit-Jean-Genaz and J. Poole, “JACoW, A Service to the Accelerator Community”, EPAC’04, Lucerne, July 2004, p. 249, http://www.jacow.org.

[2] A. Name and D. Person, Modern Editor’s Journal 25 (1997) 56.

[3] A.N. Other, “A Very Interesting Paper”, EPAC’96, Sitges, June 1996, p. 7984.

Laser cooling of stored relativistic C^{3+} ions at the ESR

D. Winters[1], *C. Clark*[1], *C. Dimopoulou*[1], *T. Giacomini*[1], *C. Kozhuharov*[1], *Th. Kühl*[1,2,3], *Yu. Litvinov*[1], *M. Lochmann*[1,2], *W. Nörtershäuser*[*1,2,4], *F. Nolden*[1], *R. Sanchez*[1,2], *S. Sanjari*[1], *M. Steck*[1], *Th. Stöhlker*[1,3,5], *J. Ullmann*[1,2], *T. Beck*[4], *G. Birkl*[*4], *B. Rein*[4], *S. Tichelmann*[4], *Th. Walther*[*4], *X. Ma*[†6], *W. Wen*[†‡6], *J. Yang*[†6], *D. Zhang*[†6], *U. Schramm*[7], *M. Seltmann*[7], *M. Siebold*[7], *and M. Bussmann*[7]

[1]GSI Darmstadt; [2]Uni Mainz; [3]HI Jena; [4]TU Darmstadt; [5]Uni Jena; [6]IMP CAS Lanzhou, China; [7]HZDR Dresden

After several years of planning [1], development [2], and tests [3], in August 2012 a new laser cooling experiment (E089) has been performed at the ESR. One essential goal of this beamtime was to demonstrate that the initially 'hot' ions can be collected inside the rf-bucket using just the laser, *i.e.* without changing the bucket frequency and without electron cooling. This scheme can namely be used to cool relativistic ion beams in future storage rings and synchrotrons, such as the HESR and SIS-100 at FAIR. A second goal was to demonstrate *in vacuo* optical detection of the UV-light (ca. 155 nm) emitted from the laser excited ions. Finally, we wanted to perform a systematic study of several relevant parameters [4]. This also required collecting data from many different recently installed ESR diagnostic systems, such as the resonant Schottky pick-up [5], the ionization profile monitor [6], and UV-photochanneltrons [3].

Laser cooling of relativistic ions in a storage ring can be performed using only one anti-collinear laser beam and a bunched ion beam. We wanted to demonstrate two cooling schemes: In the first scheme, the CW laser frequency is rapidly scanned over a large range, cooling all ions inside the bucket. The group of Th. Walther at the TU Darmstadt has therefore developed a fast scanning narrowband CW laser system, based on a seeded fiber amplifier (1028 nm) with two frequency doubling stages (514 and 257 nm) [7]. In the second scheme, a powerful pulsed laser system (broadband) is used to cool many velocity classes in one shot. Here, a sufficiently high repetition rate is important, since the laser pulses must hit the ion bunches, which have a revolution frequency of about 1 MHz, often enough. Such a laser system, based on a fs-oscillator, a fiber-coupled diodelaser, an Yb:YAG amplifier medium (1028 nm), and two frequency doubling stages to reach 257 nm, has been developed by the group of U. Schramm from HZDR in Dresden [8].

As in the two previous ESR laser cooling experiments (2004 and 2006), we have used $^{12}C^{3+}$ ions[1] with $2s \rightarrow 2p$ cooling transitions and a kinetic energy of 122 MeV/u. Typically, about 10^8 ions were stored in the ESR for about 5 minutes. During the 8 days of beamtime, we were able to have a fully functional laser cooling setup. From the Schottky spectrum in figure 1 it can *e.g.* be seen that the CW laser slows down the ions (*i.e.* they obtain a lower frequency) as it is scanning through its range. Fluorescence from the laser excited ions has been recorded with the UV-photochanneltron detectors, made possible by the support from the group of G. Birkl at the TU Darmstadt. We have also observed that the laser cooling scheme can change the velocity of the stored carbon ions, even when electron cooling is trying to keep the ions at a fixed velocity. This clearly demonstrates the power of the method. Detailed analysis of the large amount of data is currently being carried out by the collaboration.

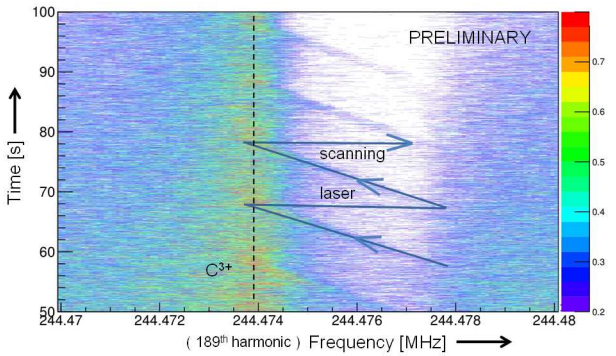

Figure 1: Schottky spectrum (time vs. frequency) of a stored C^{3+} beam in the ESR. The electron cooler is off, the ion beam is not bunched, and the CW laser scans through 12 GHz in 10 s. (All lines drawn are to guide the eye.)

In parallel to studies at the ESR, similar studies will be started at the CSRe storage ring in Lanzhou, China. The group of X. Ma in Lanzhou has also intensively contributed to the success of the recent ESR beamtime. The laser and detector systems will soon be shipped to Lanzhou.

References

[1] GSI scientific report 2009 ATOMIC-PHYSICS-34 384.

[2] GSI scientific report 2010 PNI-AP-13 339.

[3] GSI scientific report 2011 PNI-AP-14 373.

[4] M. Bussmann *et al.*, COOL09 Proceedings, IMPCAS Lanzhou, Atomic Energy Press, 22 (2009).

[5] F. Nolden *et al.*, Nucl. Instr. Meth. Phys. Res. A **659**, 69 (2011).

[6] T. Giacomini *et al.*, DIPAC2011 Proceedings, Hamburg, TUPD51 419.

[7] T. Beck *et al.*, GSI scientific report 2012 PNI-IONS-EXP.

[8] M. Siebold *et al.*, Opt. Expr. **20** 21992 (2012).

[*] Work supported by BMBF.

[†] Work supported by BMBF-WTZ.

[‡] Work supported by DAAD.

[1]With ca. 10% of $^{16}O^{4+}$ contamination from the ECR ion source.

An all-solid-state based laser system for laser cooling of relativistic ion beams*

Tobias Beck[1], *Benjamin Rein*[1], *and Thomas Walther*[†1]
[1]Institute of Applied Physics, TU Darmstadt, Germany

In 2004 and 2006 laser cooling experiments of relativistic C^{3+} beams were performed at GSI using frequency doubled Argon-ion lasers [1]. The results of these experiments were promising, but were limited by the large linewidth and the severely limited tunability of the Ar-ion lasers. While Ar-ion lasers are still quite common with applications in areas such as spectroscopy, laser pumping, medical care and even light shows, they have a relatively low efficiency and high maintenance costs [2].

Within this research project, we successfully developed an alternative laser system far superior to the existing Ar-ion laser: it is a rugged, efficient all-solid-state based system with output wavelengths of $1028\ \mathrm{nm}$, $514\ \mathrm{nm}$ and $257\ \mathrm{nm}$. It provides high output power, narrow linewidth, wide and fast tunability and a near perfect Gaussian beam profile.

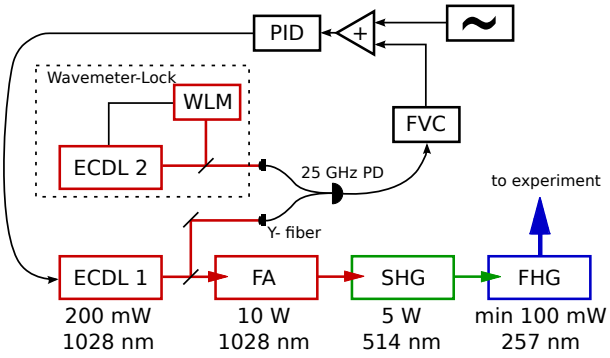

Figure 1: Schematic diagram of the system. ECDL: external cavity diode laser, FA: fiber amplifier, SHG: second harmonic generation, FHG: fourth harmonic generation, WLM: wavelength meter, FVC: frequency to voltage converter, PD: photo detector, PID: proportional-integral-derivative controller, +: signal adder, ∼: function generator

A schematic overview of our system is shown in Fig. 1. It mainly consists of a fiber amplifier seeded by an external cavity diode laser (ECDL). The output of this amplifier is frequency doubled and quadrupled in bow-tie built-up cavities using LBO and BBO crystals, respectively. The fiber amplifier delivers up to $15.3\ \mathrm{W}$ of optical power at 1028 nm. In Fig. 2 the output of the first cavity is plotted over the input power. We achieved nearly $5\ \mathrm{W}$ with a conversion efficiency of $57\ \%$ at 514 nm. The second cavity delivered up to $180\ \mathrm{mW}$ of UV light with a conversion efficiency of $12\ \%$.

The system is stabilized to an absolute frequency using an offset lock on another identical ECDL (master), which

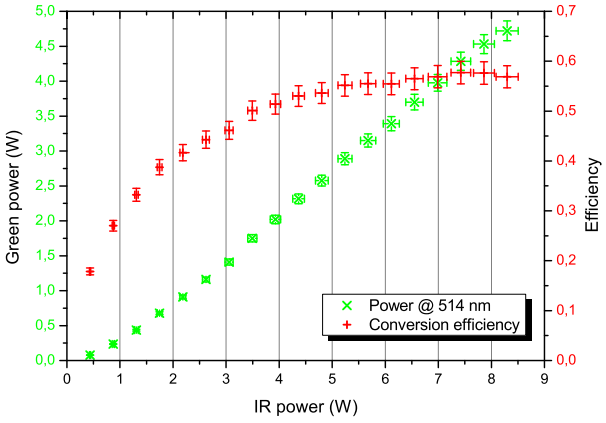

Figure 2: Optical power at $514\ \mathrm{nm}$ and conversion efficiency over infrared power in the first build-up cavity. The error bars result from the uncertainties of the detectors.

itself is locked to a high-precision wavelength meter. By adding an arbitrary ramp from the function generator to the error signal of the offset lock, the seed ECDL of the fiber amplifier can be scanned with respect to the master ECDL. In the UV it was possible to scan $12\ \mathrm{GHz}$ in $10\ \mathrm{ms}$. Mode hops were suppressed by a novel locking scheme developed in our group [3]. The offset lock is achieved by mixing small amounts of light of both ECDLs in a Y-fiber and observing the resulting beat signal with a fast photo detector. The beat frequency is divided by a factor of 1000 and fed into a frequency to voltage converter whose output serves as the error signal. By observing the beat signal of the two identical ECDLs, their linewidth was determined to $890\ \mathrm{kHz}$ in a $60\ \mathrm{s}$ time interval. This corresponds to $\frac{\Delta f}{f} \approx 3 * 10^{-06}$.

In conclusion, we were able to replace the Argon-ion laser with a more versatile light source. During a beam time in August 2012 stable long term operation was successfully demonstrated. Another beam time in Lanzhou (China) is planned in 2013 and further experiments at FAIR are possible.

References

[1] M. Bussmann et al., "All-optical ion beam cooling and online diagnostics at relativistic energies", Cool 2009, Lanzhou, http://cool09.impcas.ac.cn/.

[2] M. H. Dunn and J. N. Ross, "The Argon ion laser," Progr. Quant. Electr. **4,** 233–269 (1976).

[3] T. Führer, D. Stang and T. Walther, "Actively controlled tuning of an external cavity diode laser by polarization spectroscopy," Opt. Expr. **17,** 4991–4996 (2009).

* Work supported by BMBF Grant Nr. 06DA9045I and 06DA7053I
† thomas.walther@physik.tu-darmstadt.de

In vacuo detection of XUV photons at the ESR using a movable cathode system*

V.M. Hannen†[1], *H.-W. Ortjohann*[1], *J. Vollbrecht*[1], *D.F.A. Winters*[2], *and C. Weinheimer*[1]

[1]WWU Münster, Institut für Kernphysik, Wilhelm-Klemm-Str. 9, 48161 Münster; [2]GSI Helmholtzzentrum für Schwerionenforschung GmbH, Planckstr. 1, 64291 Darmstadt

The Institut für Kernphysik in Münster is currently developing a system for in-vacuum detection of XUV photons in the wavelength range from < 10 nm up to about 250 nm. The system will be installed at the ESR and consists of a movable cathode plate with a central slit that can be positioned around the ion beam axis to catch photons emitted in the forward direction during the de-excitation of stored highly-charged ions. Secondary electrons emitted from the cathode will be guided by a system of ring electrodes to a multi-channelplate (MCP) detector placed inside the vacuum. A similar detection system for optical photons making use of a movable parabolic copper mirror and a photomultiplier outside the vacuum, has successfully been applied in the detection of the HFS transition in lithium-like bismuth in the LIBELLE experiment two years ago [1, 2]. There it was demonstrated, that the introduction of a suitable optical system at the beam position does not disturb the stored ions apart from a small loss in beam current during the movement of the system.

Figure 1 displays the result of a tracking simulation produced with the SIMION [3] package. Five ring electrodes are placed between the cathode plate and the MCP, with the first electrode parallel to the cathode. The CF200 port into which the system can be retracted during injection of ions into the ESR actually acts as an additional sixth electrode on ground potential, but has been omitted from the figure for clarity. In the simulation, more than 75% of the secondary electrons emitted from the cathode plate are collected by the MCP.

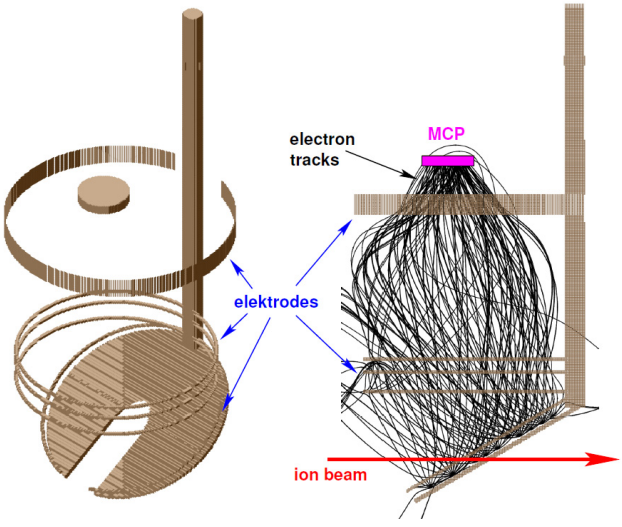

Figure 1: Electrode representation and simulated electron tracks calculated with the SIMION package.

The new detection system will be used for a measurement of the $^3P_0 - ^3P_1$ splitting in beryllium-like krypton in an anti-collinear laser spectroscopy experiment at the ESR [4]. The meta-stable state $(1s^2 2s2p)^3P_0$ (see figure 2) is populated during the production of the $^{84}Kr^{32+}$ ions. For the excitation to the $(1s^2 2s2p)^3P_1$ state, a laser-beam is injected anti-collinear to the ions which are stored at a velocity of $\beta = 0.69$. Due to the Doppler shift, the required wavelength is red-shifted from 118 nm to 276 nm. The photons emitted during de-excitation to the ground state in the forward direction are in turn blue shifted to energies up to 170 eV.

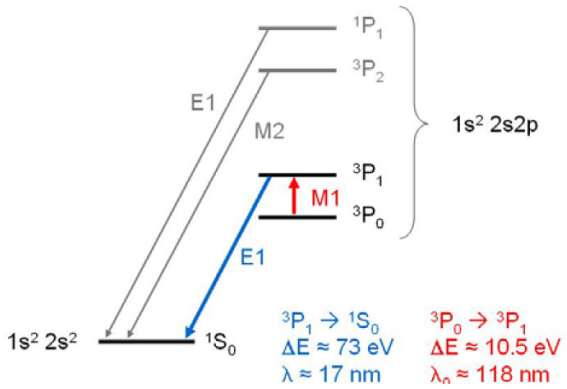

Figure 2: Excerpt of the level-scheme of beryllium-like krypton.

References

[1] M. Lochmann *et al.*, GSI Scientific Report 2011, PNI-AP-01

[2] J. Mader *et al.*, GSI Scientific Report 2011, PNI-AP-24

[3] SIMION package, Scientific Instrument Services, Inc., http://simion.com

[4] D.F.A. Winters et al., *Laser spectroscopy of the* $(1s^2 2s2p)^3P_0 - ^3P_1$ *level splitting in Be-like krypton*, GSI Experiment E104

* Supported by BMBF under contract number 06MS7191

† hannen@uni-muenster.de

First imaging of cold magnesium ion clouds in SpecTrap*

S. Schmidt[1,2,3], T. Murböck[4], W. Nörtershäuser[1,2,3], Z. Andelkovic[3], M. Vogel[4], A. Martin[4], G. Birkl[4], V. Hannen[5], J. Vollbrecht[5], C. Weinheimer[5], D. Segal[6], and R. Thompson[6]

[1]Institut für Kernphysik, TU Darmstadt; [2]Institut für Kernchemie, Johannes Gutenberg-Universität, Mainz; [3]GSI Helmholtzzentrum für Schwerionenforschung, Darmstadt; [4]Institut für Angewandte Physik, TU Darmstadt; [5]Westfälische Wilhems-Universität, Münster; [6]Imperial College London

In recent years, sympathetic cooling has been established as an important tool for the study of exciting quantum phenomena and applications, ranging from microwave quantum logic gates [1] to ultracold chemical reactions [2]. It is mostly used when other cooling methods such as Doppler laser cooling cannot be applied. This also holds for Highly Charged Ions (HCIs), which are the subject of our current investigations at SpecTrap. We will therefore exploit a cooling strategy based on laser cooled singly charged magnesium ions for cooling any species of HCIs down to the mK regime for high precision laser spectroscopy experiments.

The experimental apparatus, the preparation scheme, and first experimental results of laser cooled Mg^+ are described in detail in [3]. In brief, singly charged magnesium ions are produced in an electron impact ion source and are subsequently transfered in bunches of 1–10 μs at an energy of 200 eV into a cylindrical Penning trap. By dynamically switching the trap electrodes it is possible to stack multiple ion bunches. The precise timing even allows isotope selective loading by this means. All experimental parameters, such as electrode or ion optic voltages, are controlled by our newly developed experimental control system, which was successfully tested in 2012.

After completion of the loading procedure, the ion cloud is efficiently cooled by 280 nm laser light irradiated in axial direction. For this purpose, a new seed laser was installed to provide more than 10 mW ultraviolet laser light after frequency quadrupling. A frequency stability of the seed laser of a few hundred kHz on a long-term scale was achieved by locking it to a high-precision wavemeter. Fluorescence detection of the scattered cooling light is performed in radial direction. During the cooling phase of approximately six seconds, the ionic sample undergoes a transition to a strongly coupled state. The rearrangement of the ion cloud becomes apparent in form of a precooling peak visible in the fluorescence spectra while scanning across the resonance [3]. Detailed analysis of the obtained fluorescence signal reveals an upper limit for the ion temperature of roughly 60 mK.

Usually, the laser frequency is tuned to the closed $\left|3^2\mathrm{S}_{1/2}, \mathrm{m_j} = -1/2\right\rangle \rightarrow \left|3^2\mathrm{P}_{3/2}, -3/2\right\rangle$ transition to ensure permanent cooling of the confined ionic ensemble. By observing the fluorescence signal, the lifetime of the magnesium ions in the trap was estimated. A single measurement of the lifetime shows that the ion cloud could be stored for 75 minutes without significant losses.

Additionally to the fluorescence detection with photomultiplier tubes, a UV-CCD camera was used to image the ion cloud. In figure 1 a sequence of four images of the laser cooled ion cloud is depicted. It shows a compression of the cloud during the cooling phase. By varying the trap voltages, precise control of the spatial position of the ion cloud was possible and even the manipulation of the ion cloud density might be possible using the rotating wall technique [4]. In future, an improvement of the imaging system will help us to study in more detail the ion dynamics of low-Z ions, HCIs and their mixtures in the Penning trap.

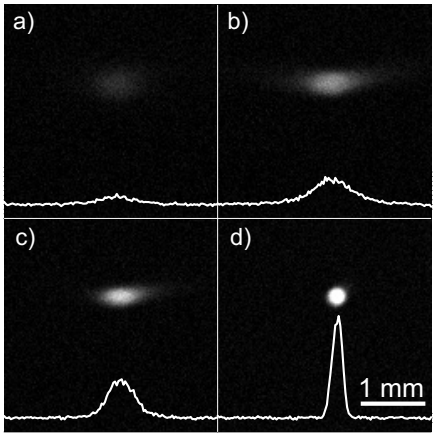

Figure 1: Images of the ion cloud during laser cooling together with the corresponding radial profiles.

In summary, the experimental results show that we can prepare an ideal source of cold and dense singly charged magnesium ions, by optimizing the vacuum conditions, implementation of an experimental control system and optimizing the existing laser system. As soon as the beamline from the HITRAP facility to SpecTrap is finished, first high precision spectroscopy measurements on HCIs will be possible.

References

[1] C. Ospelkaus et. al., Nature 476, 181-184 (2011)

[2] P. F. Staanum et. al., Phys. Rev. Lett. 100, 234003 (2008)

[3] Z. Andelkovic, R. Cazan et. al., submitted to Phys. Rev. A, arXiv:1211.2106 (2012)

[4] S. Bharadia, et al., Appl. Phys. B 107 1105-1115 (2012)

*This work has been supported financially by BMBF (05P12RDFA4, 06DA9020I), DFG, EPSRC, GSI, the Helmholtz Association (VH-NG-148), HGS-HiRe and HIM.

Controlled interaction of ions with high-intensity laser light

M. Vogel[1,2], *W. Quint*[2,3], *Th. Stöhlker*[2,4,5], *and G. Paulus*[5]

[1]TU Darmstadt; [2]GSI, Darmstadt; [3]Ruprecht Karls-Universität Heidelberg; [4]Helmholtz-Institut Jena; [5]Universität Jena

We are currently preparing an experimental setup which features a Penning trap for preparation and control of suitable ion targets for irradiation with high-intensity laser light and study of subsequent reactions. Of particular interest is the detailed investigation of multiphoton-ionisation of confined particles by highly intense laser light. One important aspect is control over the confined particles' mass, charge, density, localization and optimized overlap with the laser light by Penning trap techniques like the use of trap electrodes as 'electrostatic tweezers' and by application of a 'rotating wall', respectively. Also, the non-destructive detection of reaction products is a central property. The Penning trap setup is designed in a portable fashion, such that it can be attached to existing laser systems easily [1].

The interaction of highly intense radiation with matter and the corresponding non-linear effects have been subject of lively research, both theoretical and experimental, especially in the infrared and visible photon energy regimes. Laser systems capable of producing high intensities also at photon energies in the extreme ultra-violet (EUV) and (soft) X-ray regime open access to novel effects like non-linear Compton effects or simultaneous elastic and inelastic photon scattering, and allow multiphoton-ionisation experiments in a new domain. However, experiments have so far not been able to prepare and investigate well-defined particle ensembles and to non-destructively analyse the reaction products with high accuracy, nor were they able to select or prepare products for further studies in a well-defined way.

The particles (atomic or molecular ions) are confined in the Penning trap following in-trap production or capture of externally produced ions. Confined ions can be cooled, compressed, positioned and selected with respect to their mass and charge prior to laser irradiation. The reaction products are analysed by non-destructive methods and hence remain confined for further studies. Such measurements are, for example, able to determine cross sections for multiphoton-ionisation in an energy- and intensity- regime so far not or not sufficiently examined. Additionally, the created electrons may be extracted from the trap and analysed externally. Hence, the reaction energetics may be reconstructed as completely as possible.

Figure 1 shows an example of a multiphoton ionization study using these techniques: ions are dynamically loaded into the trap from external sources or produced in the trap by electron impact or laser ionization (A). One or more specific ion species are selected (B), these ions are then cooled, compressed by a rotating wall and positioned. Thus, the ion target is well-prepared for interaction with the high-intensity laser. During and following the laser interaction, the charge state evolution of the confined ions is monitored

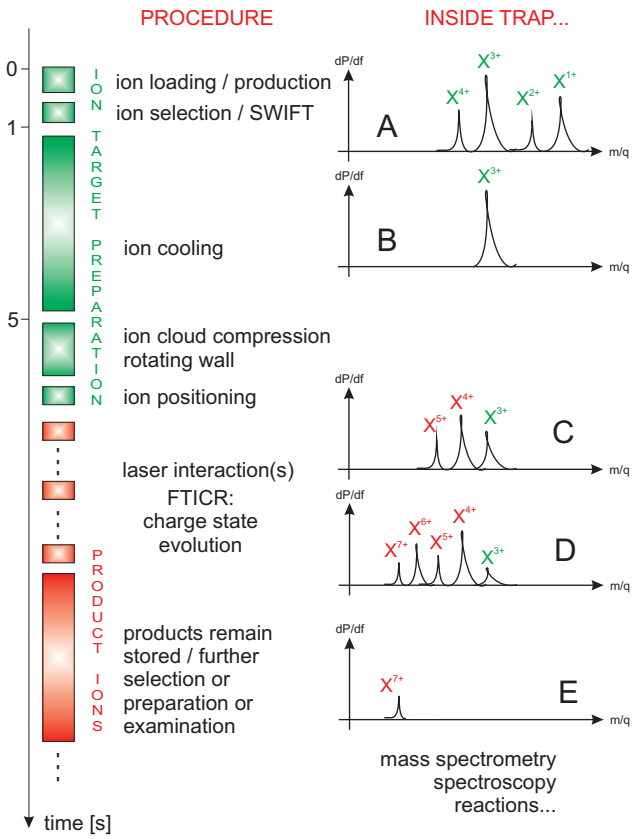

Figure 1: Example of an experimental timing scheme for a study of multiphoton ionization. The individual durations are meant to reflect the typical order of magnitude. The right hand side shows the corresponding mass-to-charge spectra of the trap content, for details see text.

by FT-ICR-spectrometry (C and D). Specific product ions can be selected and remain stored for further use (E).

Ion positioning along the experimental axis has some interesting features when a focused laser is considered since it allows to determine the position of the focus with high resolution. At the same time, especially for strongly focused lasers, ion positions can be chosen such that the reaction takes place at different field intensities and thus allows a study of the reaction as a function of laser field intensity without the need to change laser parameters.

References

[1] M. Vogel, W. Quint, Th. Stöhlker and G.G. Paulus, Nucl. Inst. Meth. B **285**, 65 (2012).

Access to the quadratic and cubic Zeeman effects at ARTEMIS

M. Vogel[1,2], *G. Birkl*[1], *D. von Lindenfels*[2,3], *A. Martin*[1], *W. Quint*[2,3], *and M. Wiesel*[1,2,3]
[1]Institut für Angewandte Physik, TU Darmstadt; [2]GSI, Darmstadt; [3]Ruprecht Karls-Universität Heidelberg

We have conceived an experiment for laser-microwave double-resonance spectroscopy of highly charged ions in a Penning trap. Such spectroscopy allows a highly precise measurement of the Zeeman splittings of fine- and hyperfine-structure levels due the magnetic field of the trap. We also have performed detailed calculations of the Zeeman effect in the framework of quantum electrodynamics of bound states as present in such highly charged ions. We find that apart from the linear Zeeman effect, also second- and third-order Zeeman effects contribute to the splittings on a level of 10^{-4} and 10^{-8}, respectively, and hence are accessible to a determination within the achievable spectroscopic resolution of the currently prepared ARTEMIS experiment.

A quadratic contribution to the Zeeman effect has first been discovered by Segré and Jenkins in the 1930s. Since then, there have been numerous studies, both experimental and theoretical, of higher-order Zeeman contributions in atoms, molecules and singly charged ions in laboratory magnetic fields. Corresponding studies in observational astronomy have identified a quadratic Zeeman effect in abundant species like hydrogen and helium. Although highly charged ions are both abundant in the universe and readily accessible in laboratories, to our knowledge, no higher-order Zeeman effect in highly charged ions has been observed so far.

We are currently setting up a laser-microwave double-resonance spectroscopy experiment with highly charged ions in a Penning trap, which combines precise spectroscopy both of optical transitions and microwave Zeeman splittings [1, 2]. The experiment aims at spectroscopic precision measurements of such energy level splittings and magnetic moments of bound electrons on the ppb level of accuracy and better. At the same time, it allows access to the nuclear magnetic moment in absence of diamagnetic shielding. For first tests, the $^{40}Ar^{13+}$ ion has been chosen. It has a spinless nucleus, such that only a fine structure is present. Similar measurements in hyperfine structures are to be performed with ions of higher charge states such as for example $^{207}Pb^{81+}$ and $^{209}Bi^{82+}$ as available to ARTEMIS within the framework of the HITRAP facility.

In an external magnetic field, the Zeeman effect lifts the degeneracy of energies within fine- and hyperfine-structure levels. For highly charged ions in magnetic fields of a few Tesla strength, the Zeeman splitting is well within the microwave domain and thus accessible for precision spectroscopy. In addition, in case of fine- and hyperfine-structure transitions, the strong scaling with Z eventually shifts the corresponding energies into the laser-accessible region and thus makes them available for precision optical spectroscopy. Figure 1 schematically shows the Zeeman splitting of the $2\,^2P_J$ states of boron-like argon Ar^{13+} in an external magnetic field with higher-order contributions to the Zeeman effect. While the linear effect separates the two ground-state ($2\,^2P_{1/2}$) levels by about 65 GHz and the four excited-state ($2\,^2P_{3/2}$) levels by about 130 GHz, the quadratic effect shifts both $(1/2, \pm 1/2)$ levels down and the two $(3/2, \pm 1/2)$ levels up by about 3 MHz. The $(3/2, \pm 3/2)$ levels are shifted up by 74 kHz. The cubic effect increases the splitting between the ground-state levels by about 306 Hz, thus simulating a contribution of $3 \cdot 10^{-9}$ to $g_{1/2}$ which is still within achievable experimental resolution. The experimental approach chosen allows a separation of the respective higher-order contributions to the linear Zeeman effect and will hence be valuable as a benchmark of theoretical calculations which include QED effects in extreme fields [3].

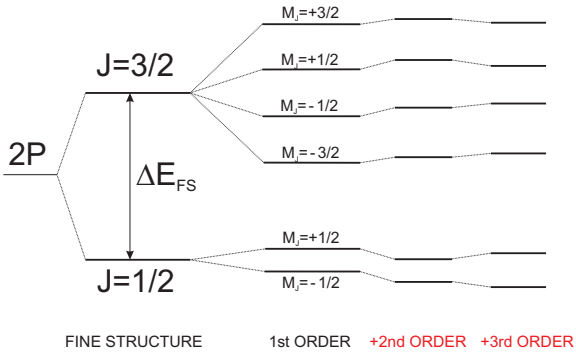

Figure 1: Level scheme of the $2\,^2P_J$ states of boron-like argon Ar^{13+} in an external magnetic field with higher-order contributions to the Zeeman effect (not true to scale)

This work has been performed in collaboration with D.A. Glazov, V.M. Shabaev, M.M. Sokolov, A.V. Volotka and G. Plunien from the St. Petersburg State University and the Technische Universität Dresden.

This work has been supported in part by DFG (Grants VO 1707/1-2 and BI 647/4-1), by GSI, HGS-HiRe, and by the IMPRS for Quantum Dynamics Heidelberg.

References

[1] W. Quint, D. Moskovkin, V.M. Shabaev and M. Vogel, Phys. Rev. A **78** (2008) 032517.

[2] D. von Lindenfels, N. Brantjes, G. Birkl, W. Quint, V. Shabaev and M. Vogel, Can. J. Phys. **89**, 79 (2011).

[3] D. von Lindenfels, G. Birkl, D.A. Glazov, A. Martin, G. Plunien, W. Quint, V.M. Shabaev, M.M. Sokolov, M. Vogel, A.V. Volotka, and M. Wiesel, accepted for Phys. Rev. A (2013).

Versatile cold atom apparatus

B. Höltkemeier[1], S. Götz[1], C. Hofmann[1], Dominic Litsch[1], B. DePaola[2], M. Weidemüller[1]

[1]Physikalisches Institut, Universität Heidelberg, Germany; [2]Kansas State University, Manhattan, KS, U.S.A.

We present a compact apparatus that consists of a cold atomic target at the center of a high resolution recoil ion momentum spectrometer (RIMS) [1] which will be implemented in the HITRAP beamline at GSI.

With our current setup densities of up to a few 10^{11} atoms/cm^{-3} can be achieved. Therefore a dark spontaneous force optical trap [2] loaded by a 2D MOT [3] is used which not only overcomes the density limit of a normal magneto optical trap but also reduces loading times of the trap to as low as 300ms. This allows measurements of processes with very low probability such as multi electron charge transfer, which are otherwise disguised by the far more dominant single charge transfer channel. To resolve the dynamics of such processes a new recoil ion momentum spectrometer has been build (Fig. 1).

The whole setup has been tested using a pulsed laser beam. The inset of Fig. 1 shows the recoil ions' angular momentum distribution depending on the polarization of this pulsed laser. It can be clearly seen that the very small momentum transferred to the ion during the ionization process can be well resolved. The determined resolution of the recoil ions' momentum is 0.10 a.u. which is sufficient to study multiple charge transfer in highly charged ion – atom collisions. With these measurements also the target could be characterized in great detail and the use of the 2D MOT as an independent target has been explored [4].

As a next step the target will be upgraded by implementing a dipole trap where the atoms are trapped at the focus of a far detuned, intense laser beam. This technique allows the reach densities of some 10^{13} atoms/cm^{-3} and by letting the warmest atoms evaporate from the trap a Bose-Einstein-Condensate (BEC) can be reached. This way a completely new target will be provided where not only the interactions between single atoms and ions but also collective effects which are only present in BECs can be investigated.

In addition, using a dipole trap allows to trap atoms without the use of a magnetic field which has several advantages. Firstly the trap can be run continuously whereas in the present setup the magnetic field as well as the MOT lasers have to be switched of several milli-seconds before any recoil momentum can be measured with high accuracy. Secondly it is possible to state prepare the atoms in the dipole trap which makes it possible to explore the dependence of multiple charge transfer on the polarization of the target.

We acknowledge financial support by the BMBF within the framework of "FAIR-SPARC", the Heidelberg Center for Quantum Dynamics and HGS-Hire.

References

[1] B. DePaola et al., Adv. At. Mol. Opt. Phy. 55 (2008)
[2] W. Ketterle et al., Phys.Rev.Lett. 70, 2253 (1993)
[3] K. Dieckmann et al., Phys. Rev. A 58, 3891 (1998)
[4] S. Götz et al., Rev. Sci. Instr. 83, 073112 (2012)

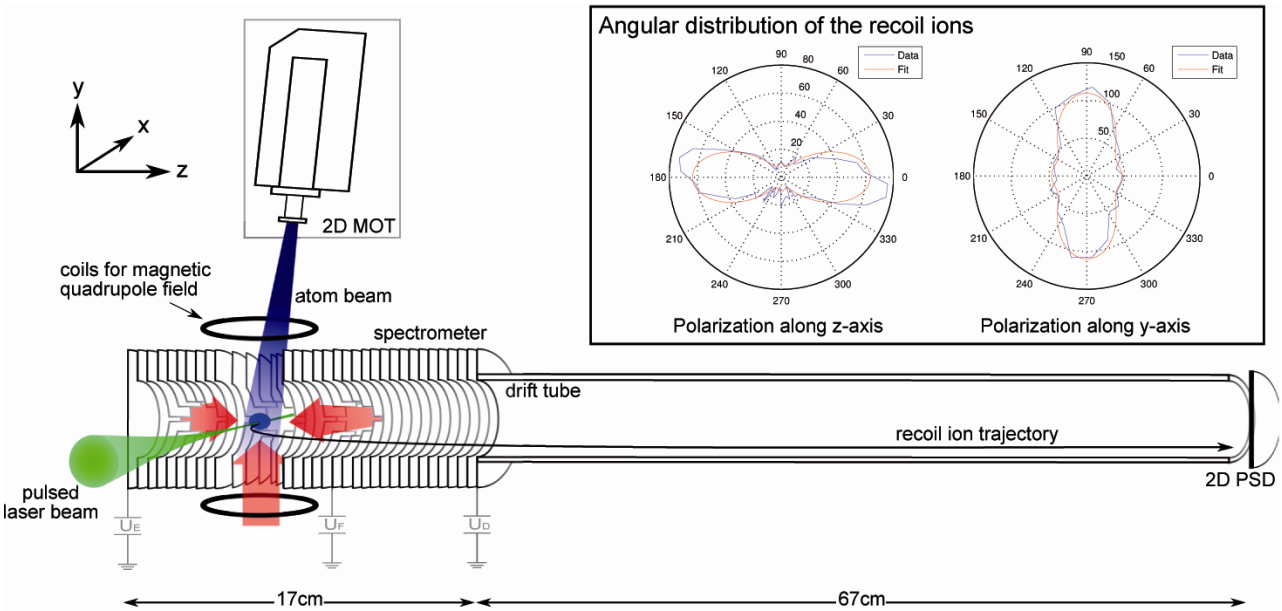

Figure 1: MOTRIMS setup. The inlet shows the recoil ions' angular momentum distribution when atoms are photoionized with a pulsed laser beam. The two graphs correspond to the different polarizations of the laser.

Towards Precision Laser Spectroscopy of Forbidden Transitions in Highly-Charged Ions

S. Albrecht[1], *T. Murböck*[1], *M. Vogel*[1,2], *G. Birkl*[1], *and the SPECTRAP collaboration*[2]
[1]TU Darmstadt, Darmstadt, Germany; [2]GSI, Darmstadt, Germany

Introduction

The SPECTRAP experiment for the investigation of highly charged ions (HCI) at rest with methods of high-resolution laser spectroscopy is under development at GSI. The spectroscopic data can be used to test atomic structure and bound-state quantum electrodynamics (QED). Systematic measurements on several species of highly charged ions will be possible with up to three orders of magnitude better spectroscopic resolution than in former experiments [1]. Amongst others, related earlier measurements have been realized on bunches of $^{209}Bi^{82+}$-ions in the experimental storage ring ESR. The value of the transition wavelength was determined to be $243.87(4)$ nm in the lab-frame [2, 3]. For improved precision in the measurement the ions will be now be decelerated by the HITRAP-facility and cooled to liquid helium temperatures inside the SPECTRAP Penning trap.

Spectroscopic Apparatus

For spectroscopy on $^{209}Bi^{82+}$, the necessary laser system has to produce laser light with a power of several mW at 243.87 nm and a tuning range significantly larger than the standard deviation of 100 GHz of the previous measurement [2, 3]. In addition, the laser frequency should be stable to a precision and accuracy comparable to or below the expected Doppler-width of the transition of the ions inside the Penning trap which is expected to be approximately 30 MHz. For the generation of the light at the target wavelength we use a commercial frequency-quadrupled diode laser system. Through the successive frequency doubling we have access to laser fields at 244 nm, 488 nm and 976 nm. The light at 488 nm is used for frequency diagnostics on $^{130}Te_2$ vapour while the light at 976 nm is used for frequency stabilization to a cavity. Tuning of the output frequency with high precision is achieved via a tunable rf offset lock and coupling to the cavity.

For stabilization and frequency diagnostic, vapour of molecular tellurium $^{130}Te_2$ is used as spectroscopic reference. We recorded and analysed a set of resonances, delivering precise spectroscopic references on a continuous spectrum between 488.36 nm and 487.28 nm with an absolute accuracy of 3 MHz (one standard deviation). The data were compared to previous highly precise measurements of known tellurium features. The uncertainty of 3 MHz is caused by ambient pressure fluctuation and the limitations in the corresponding corrections. In a recent set of measurements, our absolute accuracy for some lines has been improved to 0.9 MHz.

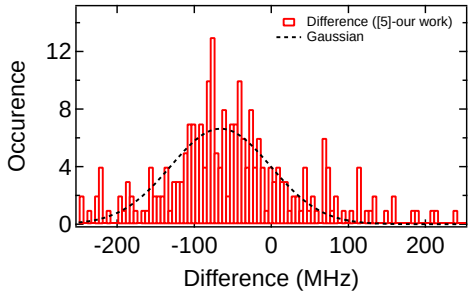

Figure 1: Histogram for the offset frequency between our Doppler-broadened measurements and the ones from [5].

To constitute a map of $^{130}Te_2$ vapour, we switch between the zero crossings of the 976 nm cavity signal for stabilization. We took two sets of measurements which were then combined to one final average. For analysis, Gaussian and Lorentzian profiles were fitted to the averaged ensemble map. Those features which could be correlated to the ones listed in [5] were assigned accordingly. Additionally, we took five measurements scanning the previously calibrated features from the literature with the cavity placed inside a vacuum chamber. Taking several runs on known tellurium references gives us the possibility to quantify our precision by calibrating each run to two features with known absolute frequency. Comparing our Doppler broadened lines to the ones in [5], we could confirm previous results [6], that the atlas delivers smaller values by an average offset of 65.8 MHz (Fig. 1). As a result, we now have a high-precision map of tellurium lines in the range of 488.36 nm and 487.28 nm and a table with over 900 spectroscopic references.

References

[1] M. Vogel, D.F.A. Winters, D.M. Segal, R.C. Thompson, Rev. Sci. Ins. **76**, 103102 (2005).

[2] I. Klaft et al.: Phys. Rev. Lett. **73**, 2425 (1994).

[3] S. Borneis et al.: Hyp. Int. **127**, 305 (2000).

[4] S. Albrecht et al.: Appl. Phys. B. **107**, 1069 (2012).

[5] J. Cariou, P. Luc: *Atlas du Spectre d'Absorption de la Molécule Tellure, 20300cm-1 - 21195cm-1* (Lab. Aime-Cotton CNRS, Paris, 1980).

[6] J. D. Gillaspy and Craig J. Sansonetti: J. Opt. Soc. Am B **8**, 2414 (1991).

Production and diagnostics of spin-polarized heavy ions in the sequential two-electron radiative recombination *

A. V. Maiorova† [1], A. Surzhykov[2,3,4], S. Tashenov[2,3], V. M. Shabaev[1], and T. Stöhlker[3,4]
[1]SPbSU, St. Petersburg, Russia; [2]PI, Heidelberg, Germany; [3]GSI, Darmstadt, Germany; [4]HI, Jena, Germany

Within the last decades the radiative recombination (RR) by highly charged heavy ions remains the subject of intense theoretical and experimental research (see [1] and references therein). The RR is an effective tool for studying of the photoionization in the relativistic regime, which is not approachable directly at the present time. Moreover, the RR is interesting due to its sensitivity to the spin, relativistic and QED effects in the structure and dynamics of heavy atomic systems (see, e.g. [2, 3]).

In the recent years several experiments on researching the RR with polarized ion beams were proposed [4, 5]. Furthermore, it was proposed to use the RR into polarized H-like ions as the tool for beam spin diagnostic [6]. Information about the ion polarization is required for studying, for example, the parity nonconservation effects in highly charged ions or in heavy-ion collisions. But all of proposed experiments are hampered now by the lack of polarized ions.

In the present work we propose the method, that can be used for investigations of the RR into spin-polarized H-like ions. This approach is based on a subsequent capture of two electrons from two spatially separated targets by initial bare (finally He-like) ion and measurements of two emitted photons in coincidence. We choose the quantization axis (Z-axis) along the momentum $\mathbf{p}_i$ of the incoming electron. After the capture of the first electron, a photon is emitted in the direction $\mathbf{k}_1$, determined by polar angle θ_1. It turns out that the relative magnetic sublevel population of the resulting H-like ion depends on θ_1. Hence the properties of the second photon, emitted in the direction $\mathbf{k}_2$ characterized by two angles (θ_2, φ_2), should be also dependent on θ_1.

The population of the intermediate H-like ion can be parameterized in terms of the polarization vector $\mathbf{P} = (P_x, P_y, P_z)$. From the symmetry considerations in our case, when the photons, emitted in course of recombination of unpolarized electrons with bare ions, are observed in a particular setup, only single parameter P_y is non-zero [7].

Information about the polarization of the H-like ions can be obtained from the analysis of the linear polarization of the second recombination photons. From the practical viewpoint it is more convenient to use the polarization ellipse parameters P_L (the degree of linear polarization) and χ_0 (the orientation of the principal axis with respect to the reaction plane) for the description of the x-ray linear polarization.

* Work supported by DFG, Helmholtz association, RFBR, FAIR-Russia Research Center, Emmy Noether Programm and GSI.

† maiorova@pcqnt1.phys.spbu.ru

In Fig. 1, we display P_y as a function of θ_1 and χ_0 as a function of θ_2 in the case of $\varphi_2 = 90^o$. The calculations have been performed in the ion–rest frame for the incident electron energies ε_i =109.7 keV, which correspond to the projectile energy T_p = 200 MeV/u in the laboratory frame. As one can see from the figure, the polarization of the H-like ions following RR is very sensitive to the geometry of the photon emission. For example, a very significant degree of polarization, $P_y \sim 85\%$, can be achieved for those ions, whose production is accompanied by the photon emission under the angle $\theta \simeq 150°$. You can also see that χ_0 shows strong dependence on the θ_1 and, hence, on the degree of ion polarization. Thereby in the proposed scheme the characteristics of the first and the second RR photons are correlated through the spin states of intermediate H-like ions. Hence, using the proposed method we can "emulate" not only the production but also the diagnostics of heavy ion beams.

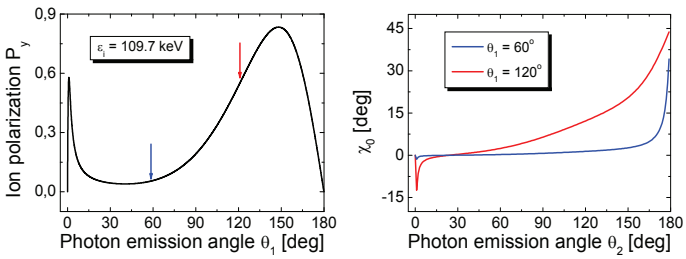

Figure 1: Component P_y of the polarization vector of H-like uranium ions ($Z = 92$) as a function of first photon emission direction θ_1 (left panel) and angle χ_0 as a function of the emission angle of the second photon θ_2 at $\varphi_2 = 90^o$ (right panel). The calculations are performed in the ion–rest frame for the kinetic energy $\varepsilon_i = 109.7$ keV of the incoming electron.

References

[1] J. Eichler, Th. Stöhlkler, Phys. Rep. **439**, 1 (2007).

[2] Th. Stöhlkler *et al.*, Phys. Rev. Lett. **82**, 3232 (1999).

[3] S. Tashenov *et al.*, Phys. Rev. Lett. **97**, 223202 (2006).

[4] A. Surzhykov *et al.* Phys. Rev. A **68**, 022710 (2003).

[5] A. E. Klasnikov *et al.*, NIMB **235**, 284 (2005).

[6] A. Surzhykov *et al.* Phys. Rev. Lett. **94**, 203202 (2005).

[7] V. V. Balashov *et al.*, *Polarization and Correlation Phenomena in Atomic Collisions* (New York: Kluwer Academic, 2000).

Characterization of a Si(Li) Compton polarimeter for the hard x-ray regime, using synchrotron radiation.*

M. Schwemlein[1,2,3], K.-H. Blumenhagen[4,5], A. Gumberidze[1,6], R. Märtin[5,7], N. Schell[8], U. Spillmann[9], G. Weber[7,9], and Th. Stöhlker[5,7,9]

[1]ExtreMe Matter Institute EMMI and Research Division, Darmstadt, Germany, [2]PI, Universität Heidelberg, Germany, [3]Staatliches Seminar für Didaktik und Lehrerbildung, Heidelberg, Germany, [4]Helmholtz-Institut Jena, Germany, [5]IOQ, Universität Jena, Germany, [6]Frankfurt Institute for Advanced Studies, Frankfurt, Germany, [7]Helmholtz-Institut Jena, Germany, [8]Helmholtzzentrum Geesthacht, Germany, [9]GSI, Darmstadt, Germany

Novel highly-segmented semiconductor detectors which combine a good detection efficiency, energy and time resolution, together with millimetre to sub-millimetre position sensitivity, represent a versatile tool for Compton polarimetry in the hard x-ray regime [1]. Such detection systems have recently been introduced for the investigation of radiative processes involving high-Z ions in collisions with gaseous matter at the storage ring ESR [2,3,4] as well as in electron-atom collisions at the TU Darmstadt [5].

In the present experiment, a novel Si(Li) Compton polarimeter [6], which was developed for experiments at the international FAIR facility, has been tested at the DESY PETRA III beamline P07-EH1. For this purpose, the detector was exposed to the synchrotron radiation. Since the synchrotron radiation is nearly 100% linearly polarized, we were able to test the detector performance as an x-ray polarimeter for photons in the hard x-ray regime.

Figure 1 shows the Si(Li) detector response to the incident synchrotron radiation. The monochromator of the beamline was set to 57.3 keV. The clearly visible line at 161.1 keV could be identified as the third harmonic. The broad structures at lower energies belong to recoil electrons of the Compton-scattered photons.

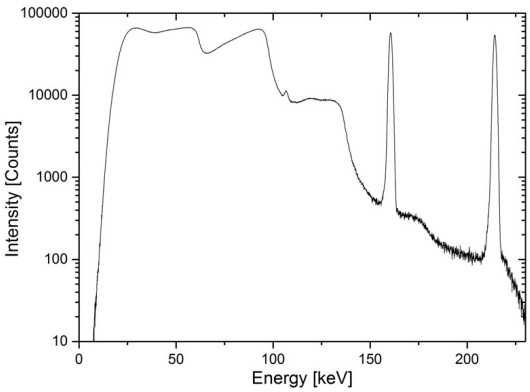

Figure 1: Si(Li) detector response to the incident synchrotron radiation.

Figure 2 shows the position distribution of Compton scattered photons inside the Si(Li) detector crystal. In this case, only the 161.1 keV incident photons of Figure 1 and only polar scattering angles of 90°+-10° are taken into account. The incoming x-ray beam was centred on the centre of the detector. Compton recoil electrons (spot in the centre of Figure 2) have been detected in coincidence with the corresponding Compton scattered photons. To reconstruct the whole kinematic process, each pair of Compton-electron and Compton-photon has been quantified in position and energy.

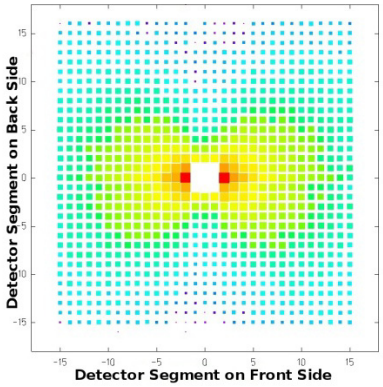

Figure 2: The position distribution of Compton scattered photons inside the Si(Li) detector crystal for 161.1 keV incident photons. The strong anisotropy indicates the high degree of linear polarization of the incident synchrotron radiation.

According to Klein-Nishina equation, the photons are scattered mostly perpendicular to the incident photon electric field vector (polarization axis). This is clearly reflected in the strong azimuthal anisotropy of Figure 2, which indicates a very high degree of linear polarization, typical for synchrotron radiation facilities. The degree of linear polarization as well as the polarization orientation of the incident radiation can be reconstructed apllying a least-squares adjustment to the azimuthal scattering distribution [7].

We have acquired the Compton scattering data for different x-ray energies as well as different detector orientations. The evaluation is currently under way.

References

[1] U. Spillmann et al., Rev. Sci. Instr. **79**, 083101 (2008).
[2] S. Tashenov et al., PRL **97**, 223202 (2006).
[3] S. Hess et al., J. Phys.: Conf. Ser. **163,** 012072 (2009)
[4] G. Weber et al., PRL **105**, 243002 (2010).
[5] R. Märtin et al., PRL **108**, 264801 (2012).
[6] G. Weber et al., JINST **5**, C07010 (2010)
[7] F. Lei et al., Space Sci. Rev.**82**, 309 (1997)

* Work supported by Helmholtz Alliance EMMI.

Characterization of a novel setup for hard x-ray spectroscopy and polarimetry at very high fluxes

G. Weber[*1,2], *C. Hahn*[1,3], *A. Paz*[1,3], *and R. Märtin*[1,2]
[1]HI-Jena, Jena, Germany; [2]GSI, Darmstadt, Germany; [3]IOQ, FSU, Jena, Germany

X-ray spectroscopy is a powerful tool for the diagnosis of plasmas being produced in fusion devices, celestial objects and in the interaction of high-power lasers or ion beams with matter. It is also known that radiative processes like bremsstrahlung, radiative recombination and characteristic transitions occurring in plasmas may exhibit distinct anisotropic and polarization features. In general, an anisotropic plasma tends to produce polarized radiation, and by photon polarimetry and/or angular resolved measurements one can investigate the anisotropic, and thus non-thermal features of the plasma [1, 2].
While single photon spectroscopy up to roughly 20 keV can be performed using standard x-ray CCD cameras, precise studies in the hard x-ray regime are often hampered by the lack of adequate detector technology. This is due to extremely high fluxes in combination with low repetition rates being typically found at plasma sources which generate x-rays up to the MeV regime, e. g. high-power laser facilities. Here, the operation of standard unsegmented, large-volume detectors leads to photon pile-up in the detector or requires unrealistic long acquisition times in order to obtain single photon spectra. Thus, state-of-art studies of hard x-ray spectra originating from plasmas still rely on low-precision techniques like stacks of several filter materials in front of an image plate [3]. However, with the recent development of pixelated CdTe sensors equipped with the Timepix readout chip [4, 5], energy-resolving detectors have become available that combine a high granularity comparable to x-ray CCDs with the high-stopping power of a high-Z detector material.

In this report, we present a setup optimized for Compton spectroscopy and linear polarimetry of incident x-rays up to a few hundred keV based on such detector systems, see Fig. 1. Here, two 1 mm thick CdTe detectors with up to 256×256 pixels record the radiation which is Compton scattered within a low-Z target. Compton spectroscopy aims for the reconstruction of the incident x-ray spectrum from the spectral distribution of the scattered photons and is in particular well-suited for fluxes being too high to expose the detector directly to the incident radiation [6]. As for photon energies below about 1 MeV the Compton cross section varies only slightly, the efficiency and consequently the amount of flux reduction of the scattering setup is mainly determined by geometry, namely the solid angle covered by the CdTe detectors. Similarly, the spectral broadening due to the dependence of the scattered photon energy on the longitudinal Compton scattering angle ϑ can be adjusted.

* g.weber@gsi.de

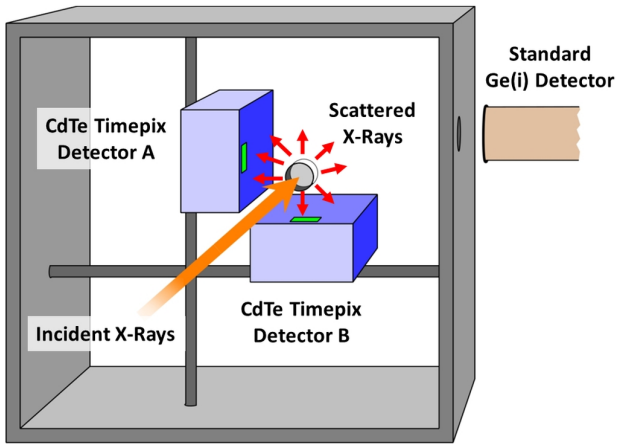

Figure 1: Setup for Compton spectroscopy and polarimetry consisting of two pixelated CdTe detectors and a scatter target, as it was used in the test measurement at DESY.

Moreover, the degree of linear polarization P_L of the incident radiation can be obtained by means of Compton polarimetry, which is based on the asymmetry of the scattered photon emission pattern with respect to the azimuthal scattering angle φ, see [7]. Assuming that the CdTe detectors are located at 0° and 90° with respect to the incident photon electric field vector, the linear polarization is given by $P_L = M(N_{0°} - N_{90°})/(N_{0°} + N_{90°})$, with M denoting the modulation factor depending on the photon energy and the experimental setup. If the orientation of the polarization is unknown, this quantity can also be obtained by rotation the detectors around the scattering target.
Recently the setup from Fig. 1 was used in a test measurement at the PETRA III synchrotron facility at DESY where high-intensity, highly polarized photon beams between 50 and a few hundred keV were impinging on the scatter target. The analysis of the obtained data is still ongoing.

References

[1] D. Giulietti and L. A. Gizzi, La Rivista del Nuovo Cimento **21**, 1 (1998).
[2] *Plasma polarization spectroscopy* edited by T. Fujimoto and A. Iwamae, Springer (2008).
[3] B. R. Maddox et al., Rev. Sci. Instrum. **82**, 023111 (2011).
[4] X. Llopart et al., NIM A **581**, 485 (2007).
[5] P. Cermak et al., NSS '08. IEEE, 444 (2008).
[6] H. I. Amols et al., NIM A **227**, 373 (1984).
[7] F. Lei et al., Space Sci. Rev. **82**, 309 (1997).

Monte Carlo simulations of Compton polarimeter systems

K.-H. Blumenhagen[*1,2,3], *A. Fleischmann*[4], *Th. Stöhlker*[1,2,3], *and G. Weber*[1,2]

[1]GSI, Darmstadt, Germany; [2]HI Jena, Germany; [3]IOQ, Universität Jena, Germany; [4]KIP, Universität Heidelberg, Germany

Compton polarimetry has proven to be a powerful tool to measure the linear polarization of hard x-rays. In the GSI atomic physics department, several measurements of this type have been carried out using a lithium-drifted silicon (Si(Li)) double-sided strip detector (DSSD) [1,2]. This device works well in a photon energy range of about 60 keV to 150 keV. An extension to higher energies can be achieved by using a heavier detector material. In this work, germanium DSSD has been simulated, using concepts from previous simulations of the same type [3]. For the low-energy region of about 20 keV to 80 keV, an entirely new concept for Compton polarimetry is proposed: the polarimeter consists of a low-Z cylindrical scatterer and - around it - a ring of individual high-Z absorber plates. Each of these plates is a high-resolution microcalorimeter which is a novel development of the "Magnetic Calorimeters" group in Heidelberg [4]. In this work, the efficiencies of both polarimeter systems have been investigated in Monte Carlo simulations using EGS5 [5]. In both cases, this quantity was given by the fraction of identified Compton events. Simulations were carried out for different polarimeter configurations and for different photon energies.

The geometry the germanium DSSD has always been choosen to be symmetric in x- and y-direction. Also, the strip width was fixed at 1 mm. The parameters varied were the number of strips (this number for each direction x and y) and the detector thickness (z-direction). First, results were obtained for a point-like (p) incidence in the center of the detector, then the incoming photons were spread over the detector area (s). Results are shown in figure 1.

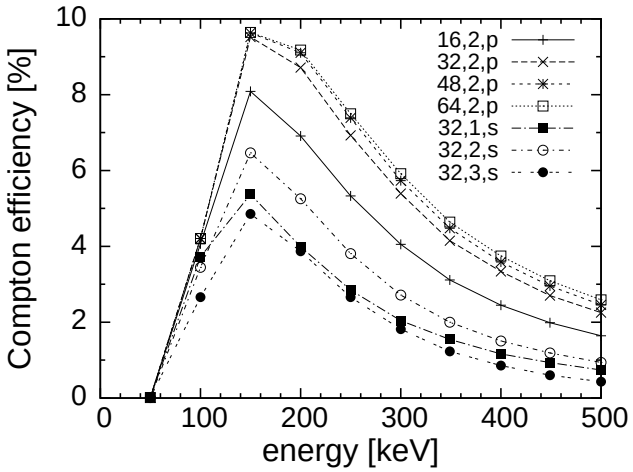

Figure 1: DSSD results. Legend format: number of strips, detector thickness [cm], incidence spread (p=no, s=yes).

For the microcalorimeter polarimeter, the following geometry has been considered: the scattering cylinder had a diameter and length of 1 mm. The area of the absorber plates (here: gold) facing the scatterer was 1 mm by 1 mm, the absorber thickness 0.2 mm. The radius of the absorber ring was dervied from the requirement that one absorber covers the θ-range of $90° \pm \Delta\theta$. The angular acceptance $\Delta\theta$ was choosen here according the number of absorbers to minimize the gaps between them. So far, three configurations have been simulated: 40 absorbers and $\Delta\theta = 3.5°$ with (1) a beryllium and (2) a carbon scatterer, and (3) 31 absorbers and $\Delta\theta = 5.8°$ with a carbon scatterer. Figure 2 shows the microcalorimeter simulation results.

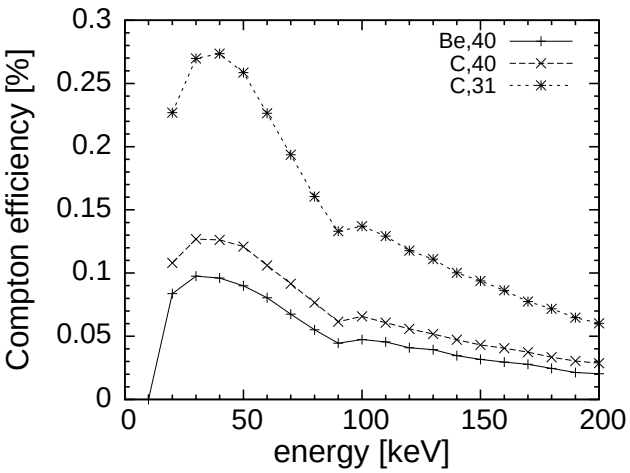

Figure 2: Microcalorimeter results. Legend format: scatterer material, number of absorbers.

References

[1] H. Bräuning et al., Polarization Measurements of Radiative Electron Capture Transitions in Highly Charged Ions, AIP Conference Proceedings, 1099, 117-120 (2009).

[2] G. Weber et al., Performance of a position sensitive Si(Li) x-ray detector dedicated to Compton polarimetry of stored and trapped highly-charged ions, JINST 5,C07010 (2010).

[3] G. Weber et al., Monte Carlo simulations for the characterization of position-sensitive x-ray detectors dedicated to Compton polarimetry, Physica Scripta, T144, 014034 (2011).

[4] C. Pies et al., Microcalorimeter Arrays for High-Resolution X-Ray Spectroscopy at GSI/FAIR, Journal of Low Temperature Physics, 167, 3-4, 269-279 (2012).

[5] H. Hirayama et al., The EGS5 code system (2005), `http://rcwww.kek.jp/research/egs/egs5_manual/slac730-070620.pdf`.

[*] k.-h.blumenhagen@gsi.de

Direct mass measurement of ^{45}Cr and its impact on Ca-Sc cycle in X-ray burst*

X. L. Yan[1,2,3,4], Y. H. Zhang[1], H. S. Xu[1], Yu. A. Litvinov†[4,1], H. Schatz[5], X. L. Tu[1], K. Blaum[3], X. H. Zhou[1], B. H. Sun[6], J. J. He[1], Y. Sun[7,1], M. Wang[1,3,8], Y. J. Yuan[1], J. W. Xia[1], J. C. Yang[1], G. Audi[8], G. B. Jia[1,2], Z. G. Hu[1], X. W. Ma[1], R. S. Mao[1], B. Mei[1], P. Shuai[1,9], Z. Y. Sun[1], S. T. Wang[1,2], G. Q. Xiao[1], X. Xu[1,2], T. Yamaguchi[10], Y. Yamaguchi[11], Y. D. Zang[1,2], H. W. Zhao[1], T. C. Zhao[1], W. Zhang[1,2], and W. L. Zhan[1]

[1]IMPCAS, Lanzhou; [2]UCAS, Beijing; [3]MPIK Heidelberg; [4]GSI Darmstadt; [5]MSU, East Lansing; [6]BUAA, Beijing; [7]SJTU, Shanghai; [8]CSNSM-IN2P3-CNRS, Orsay; [9]USTC, Hefei; [10]Uni Saitama; [11]RIKEN Wako

The experimental program on mass measurements of exotic nuclei has been continued at the storage ring CSRe in Lanzhou by addressing neutron-deficient ^{58}Ni projectile fragments. Masses of ^{41}Ti, ^{45}Cr, ^{49}Fe and ^{53}Ni were measured by applying the isochronous mass spectrometry technique [1, 2]. Details of the experiment can be found in Ref. [3]. It turned out that the mass of ^{45}Cr nucleus has an affect on the modelling of the astrophysical rapid proton capture process (rp-process) of nucleosynthesis in X-ray bursts.

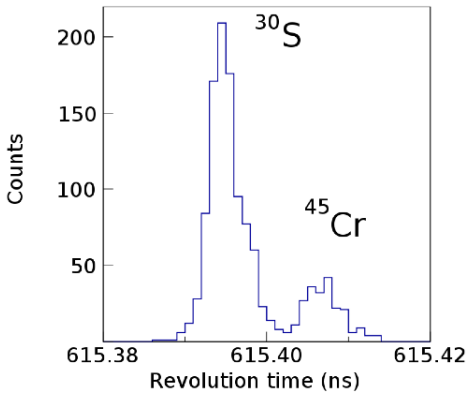

Figure 1: Revolution time spectrum zoom in at ^{30}S and ^{45}Cr.

In total 218 bare ions of ^{45}Cr were collected, see Figure 1, and a statistical mass error of 16 keV was achieved for ^{45}Cr. A special data analysis method was conducted to account for a possible contamination by a recently discovered isomeric state ($E_x = 107$ keV) [4], which resulted the final mass excess of $ME(^{45}\mathrm{Cr}) = -19515(35)$ keV.

Signal zone X-ray burst model [5] calculation was carried out to test the impacts of new masses on the rp-process. With our new mass value the matter flow through ^{43}Ti could be constrained [6].

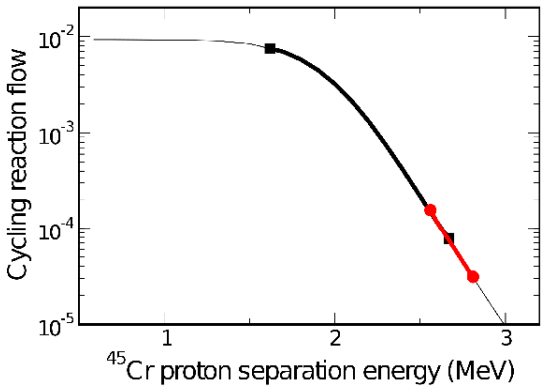

Figure 2: Time intergrated reaction flow through the Ca-Sc cycle during an X-ray burst as a function of $S_p(^{45}\mathrm{Cr})$. The graph spans the 3σ uncertainty of $S_p(^{45}\mathrm{Cr})$ in AME 2003. The thick black line limited by filled squares indicates the 1σ uncertainty of $S_p(^{45}\mathrm{Cr})$ in AME2003, while the thick red line limited by filled circles indicates the 1σ uncertainty when using the experimental data from this work. Taken from Ref. [6].

For a low ^{45}Cr proton separation energy, ^{45}Cr(γ,p) reaction becomes effective, hampering the proton capture flow at ^{43}Ti. As a result, a significant β-decay branch develops at ^{43}Ti driving the reaction flow into ^{43}Sc, which follows by a ^{43}Sc(p,α)^{40}Ca reaction. Thus a so-called Ca-Sc cycle can be forms [7]. With our new ^{45}Cr mass value, a p-capture on ^{44}V becomes effective and a formation of a strong Ca-Sc cycle is practically excluded, see Figure 2.

References

[1] M. Hausmann *et al.*, Nucl. Instr. Meth. A **446** (2000) 569.
[2] X. L. Tu *et al.*, Nucl. Instr. Meth. A **654** (2011) 213.
[3] Y. H. Zhang *et al.*, Phy. Rev. Lett. **109** (2012) 102501.
[4] R. Hoischen *et al.*, J. Phys. G **38** (2011) 035104.
[5] H. Schatz *et al.*, Phys. Rev. Lett. **86** (2001) 3471.
[6] X. L. Yan *et al.*, ApJ Lett. (2013) in press.
[7] L. Van Wormer *et al.* ApJ **432** (1004) 326.
[8] G. Audi *et al.*, Nucl. Phys. A **729** (2003) 337.

*This work is supported by CAS and NNSFC grants 10975008, 10925526, 11035007, 10675147, 10805059, 10875077, 11075103, 11105010 and 11128510 the Major State Basic Research Development Program of China (Contract No. G2007CB815000), the NECT (Grant No. NCET-09-0031), External Cooperation Program of the Chinese Academy Sciences, Grant No. GJHZ1305, Helmholtz-CAS Joint Research Group HCJRG-108, BMBF grant in the framework of the Internationale Zusammenarbeit in Bildung und Forschung Projekt-Nr. CHN 11/012. H.S. is supported by NSF grants PHY06-06007 and PHY08-22648. Y.A.L is supported by CAS visiting professorship for senior international scientists (Grant No. 2009J2-23). K.B. acknowledges support by the Nuclear Astrophysics Virtual Institute (NAVI) of the Helmholtz Association. K.B. and Y.A.L. thank ESF for support within the EuroGENESIS program.

† Email: Y.Litvinov@GSI.de

Direct mass measurement of ^{53}Ni and first test of IMME in fp-shell nuclei*

Y. H. Zhang[1], H. S. Xu[1], X. L. Tu[1], X. L. Yan[1,2,3,4], Yu. A. Litvinov†[4,1], B. A. Brown[5], K. Blaum[3], S. Typel[4], X. H. Zhou[1], B. H. Sun[6], J. J. He[1], Y. Sun[7,1], M. Wang[1,3,8], Y. J. Yuan[1], J. W. Xia[1], J. C. Yang[1], G. Audi[8], G. B. Jia[1,2], Z. G. Hu[1], X. W. Ma[1], R. S. Mao[1], B. Mei[1], P. Shuai[1,9], Z. Y. Sun[1], S. T. Wang[1,2], G. Q. Xiao[1], X. Xu[1,2], T. Yamaguchi[10], Y. Yamaguchi[11], Y. D. Zang[1,2], H. W. Zhao[1], T. C. Zhao[1], W. Zhang[1,2], and W. L. Zhan[1]

[1]IMPCAS, Lanzhou; [2]UCAS, Beijing; [3]MPIK Heidelberg; [4]GSI Darmstadt; [5]MSU, East Lansing; [6]BUAA, Beijing; [7]SJTU, Shanghai; [8]CSNSM-IN2P3-CNRS, Orsay; [9]USTC, Hefei; [10]Uni Saitama; [11]RIKEN Wako

New mass measurements were conducted at the storage ring CSRe in Lanzhou, employing the isochronous mass spectrometry (IMS) technique [1, 2]. Nuclides of interested were produced in projectile fragmentation of ^{58}Ni primary beam. Masses of a series of short-lived neutron-deficient nuclides including ^{41}Ti, ^{45}Cr, ^{49}Fe and ^{53}Ni were measured with a typical mass uncertainty of 30 keV/c^2 [5]. The measured revolution time spectrum is illustrated in Figure 1.

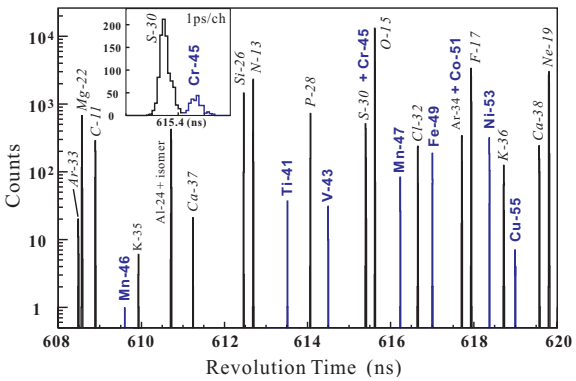

Figure 1: The revolution time spectrum of neutron-deficient ^{58}Ni projectile fragments. The insert shows the well-resolved peaks of ^{30}S and ^{45}Cr nuclei. Nuclei with masses determined in this experiment and those used as references are indicated with bold and italic letters, respectively. Adopted from Ref. [5].

New data enabled us to perform the first ever test of the Isobaric Multiplet Mass Equation (IMME) in fp-shell nuclei [5]. Based on the concept of isospin symmetry, the states in nuclei can be classified according to the isospin quantum number T with a projection $T_z = (N - Z)/2$. Assuming the two-body nature for any charge-dependent effects and the Coulomb force between the nucleons, the masses of $2T + 1$ members of an isobaric multiplet are related by the isobaric multiplet mass equation (IMME) [3, 4]. To test a possible deviation of the IMME from the predicted parabolic form, described by polynomial coefficients a, b and c, an additional cubic term with coefficient d can be considered.

Experimental d-coefficients obtained in this work are plotted in Figure 2 together with precision data on lighter nuclei, see Ref. [5] and references cited therein. A 3.5σ deviation from the parabolic shape is observed for $A = 53$ isobaric multiplet, which is a striking result.

This large d coefficient cannot be explained by either the existing or the new dedicated theoretical calculations of isospin mixing. If this breakdown of the IMME is confirmed by improved experimental data, both the new ground-state masses as well as the energies of the isobaric analog states, possible reasons, such as enhanced effects of isospin mixing and/or charge-dependent nuclear forces in the fp-shell, should be investigated.

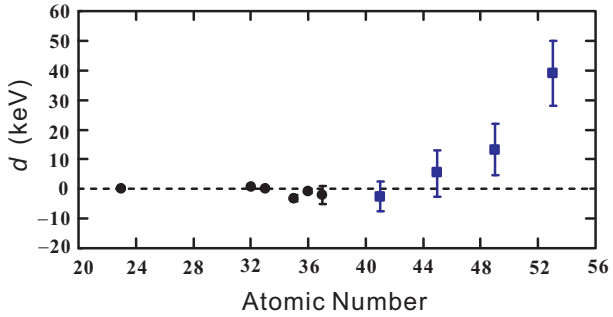

Figure 2: d coefficients for the four $T = 3/2$ isobaric multiplets in pf-shell (squares). Data for lighter nuclei (circles) are shown for comparison. Taken from Ref. [5].

*This work is supported by CAS and NNSFC grants 10975008, 10925526, 11035007, 10675147, 10805059, 10875077, 11075103, 11105010 and 11128510 the Major State Basic Research Development Program of China (Contract No. G2007CB815000), the NECT (Grant No. NCET-09-0031), External Cooperation Program of the Chinese Academy Sciences, Grant No. GJHZ1305, Helmholtz-CAS Joint Research Group HCJRG-108, BMBF grant in the framework of the Internationale Zusammenarbeit in Bildung und Forschung Projekt-Nr. CHN 11/012. H.S. is supported by NSF grants PHY06-06007 and PHY08-22648. Y.A.L is supported by CAS visiting professorship for senior international scientists (Grant No. 2009J2-23). K.B. acknowledges support by the Nuclear Astrophysics Virtual Institute (NAVI) of the Helmholtz Association. K.B. and Y.A.L. thank ESF for support within the EuroGENESIS program.

†Email: Y.Litvinov@GSI.de

References

[1] M. Hausmann *et al.*, Nucl. Instr. Meth. A **446** (2000) 569.
[2] X. L. Tu *et al.*, Nucl. Instr. Meth. A **654** (2011) 213.
[3] E. P. Wigner, Proc. Welch Found. Conf. Chem. Res. (1957).
[4] S. Weinberg and S. B. Treiman, Phys. Rev. **116** (1959) 465.
[5] Y. H. Zhang *et al.*, Phy. Rev. Lett. **109** (2012) 102501.

A new particle detector manipulator for ESR, CRYRING and HESR*

C. Brandau[1,2,4], *R. Reifarth*[3], *M. Heil*[2], *A. Müller*[4], *A. Gumberidze*[1,2], *A. Hennig*[2,5], *C. Kozhuharov*[2], *S. Litvinov*[2], *Yu.A. Litvinov*[2,6], *B. Mei*[2,3], *M. Meister*[2], *G. Rastrepina*[2,3], *and T. Stöhlker*[2,7,8]

[1]EMMI/FIAS, Darmstadt; [2]GSI, Darmstadt; [3]Universität Frankfurt; [4]Universität Gießen; [5]Universität Köln; [6]MPI-K, Heidelberg; [7]Helmholtz-Institut Jena; [8]Universität Jena

In a collaboration of GSI, EMMI and the universities Frankfurt and Giessen, a new particle detector manipulator for use at storage rings is presently being designed (Fig. 1). A central feature of this new device is that all detector installations can be completely retracted and can be separated from the ring vacuum using suitable translational motion devices and gate valves. With this design we obtain a high degree of flexibility that allows for easy and quick changes in the set-up between two experiments even with in-vacuum detectors. This new manipulator is ideally adapted to the high vacuum requirements ($\sim 10^{-11}$ mbar) of storage rings such as the ESR, the CRYRING@GSI and the HESR. After opening for service, only the small volume of the bellow has to be heated and not the full ring sector. For the movement of the detector, both, a step motor for slow, fine-tunable movement of the full travel distance, and an additional pneumatic drive for fast short-distance travels (e.g. out/in during injection) are foreseen.

Installation of different modules offers a wide range of applications such as: (i) The use of detector pockets with metal-foil windows for detectors that cannot operate in the ultra-high vacuum of the ring. (ii) In-vacuum window-less detectors for atomic and nuclear collision studies at low ion energies. For example, such a low ion energy is favorable for precision x-ray spectroscopy (low Doppler shift) but also for nuclear reactions around the Coulomb barrier or around the Gamov window. (iii) Arbitrarily positionable scraper or slit systems. (iv) Thin-foil in-vacuum detectors for time-of-flight, particle tracking or even in-ring channeling experiments.

It is planned to have two prototype systems set up, tested and put into operation in the ESR's first dipole magnets in the south and the north arc, respectively, by the end of 2013. Especially for the ESR, the present design allows for the installation of detectors *in* the dipole magnets (C-type). A special optional detector mount enables the placement of a detector in-vacuum on the inside of the ring. A first experiment envisaged at the ESR is the measurement of (p,γ) cross sections in inverse kinematics near or at astrophysically interesting energies for the p-process [1]. The p-process nucleosynthesis is responsible for the production of the rare, proton-rich heavy isotopes (p-nuclei) that cannot be made by neutron-induced processes. It occurs in supernovae, where (p,γ) and (γ,n) reactions modify the seed of s- and r- nuclei at high temperatures. A second immediate application with detectors in the ESR dipole magnets arises for atomic collision studies employing a permanently stochastically cooled ion beam. The electron cooler is then available as a full-time free-electron target for precision collision-spectroscopy experiments [2, 3]. For stochastic cooling the ion beam is stored on an orbit in the outside of the of the ring at a displacement of $\delta p/p = +1\%$. For this setting recombined ions hit the wall before the nominal particle detector positions in the scraper chambers [2]. Therefore, for cooler experiments with such ring settings a detector position inside the first dipole close to the exit of the magnet is required. Experiments with a stochastically cold beam open many new opportunities and significant enhancements over the standard measurement procedure at the cooler (cf. [2, 3]). With stochastic cooling beam losses due to cooling are essentially negligible and the beam lifetime in the ring is hours up to days. For example, this helps to make at least an order of magnitude more efficient use of expensive beams such as radioisotopes and additionally improves the duty cycle by a factor of 2-4. The technique also increases the available collision energy range from 0 up to 200 keV, and appears ideally suited for lifetime studies via recombination resonances. As discussed in [4] it may also be a very important building brick towards experimental verification of the elusive process of nuclear excitation by electron capture (NEEC) [4].

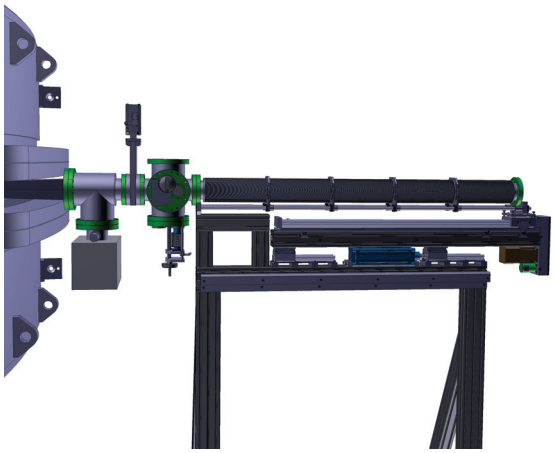

Figure 1: Design study of a detector manipulator for implementation at the ESR, or CRYRING@GSI and HESR. The mobile part of the assembly can be retracted and disconnected from the ring-vacuum by means of gate valves.

*Work is supported by BMBF (contracts 06GI911I and 06GI7127/05P12R6FAN), by the Alliance Program of the Helmholtz Association (HA216/EMMI), by the HGF Young Investigators Project VH-NG-327 and by HIC for FAIR.

References

[1] Q. Zhong, et al., J Phys: Conf. Ser. **202** (2010) 012011.

[2] D. Bernhardt et al., Phys. Rev. A **783** (2011), 020701.

[3] C. Brandau and C. Kozhuharov, in: Atom. Proc. in Basic and Appl. Phys., Springer, V. Shevelko and H. Tawara (Eds.), (2012) 283ff.

[4] A. Pálffy, et al., Phys. Lett. B **661** (2008) 330.

Construction of four position sensitive proportional counters for soft x-ray spectroscopy*

A. Georgiadis and M. Dumchev[#]

Institute for Product- und Process innovation (PPI), Leuphana University Lueneburg.

Introduction: Two crystal spectrometers in a symmetrical set up have been demonstrated at the ESR yet for QED investigations on H, He and Li-like high Z ions. Position sensitive x-ray detectors have been used, a micro-strip germanium for high energy x-rays and CCD based detectors for the soft x-rays. CCD cameras for x-rays show sufficient energy and position but not time resolution according to the requirements (< 100 ns) of ongoing and future experiments within the SPARC collaboration. For these purposes four position sensitive proportional counters have been built.

Construction of the Detectors: The detectors are of the backgammon type [H.F. Beyer at all, annual report 1985] where the positions signal is derived by charge division on a split cathode. The main components of the detectors are an anode frame with seven gold-plated tungsten wires with ~ 20 µm diameters, a backgammon cathode made as a printed circuit. The housing of the detector is made of a stainless steel (1.4301, non-magnetic) front plate and aluminium side and rear plates.

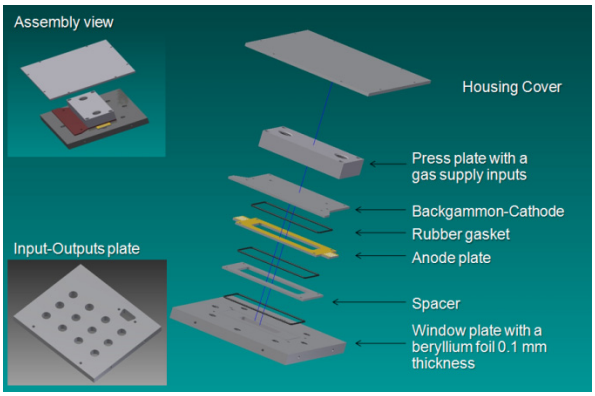

Figure 1: Exploded drawing of the detector chamber.

A beryllium foil 0.1mm thickness is used for the entrance window of 12 × 40 mm on the front plate.

Active Area	12 × 40 x 4 (mm)
Detection gas	90% Argon+10% CO2
Anode wires	Diameter ~20 µm
Windows sizes / material	12×40 mm / beryllium
Window thickness	0.1 µm
Cathode plate	Printed circuit board
Connector for HV supply	50 ohms SHV
Valve and fittings for gas	Swagelok 316 WHL
Dimension of the housing	105 x 130x 105 (mm)

Table1: Mechanical characteristics of the counter

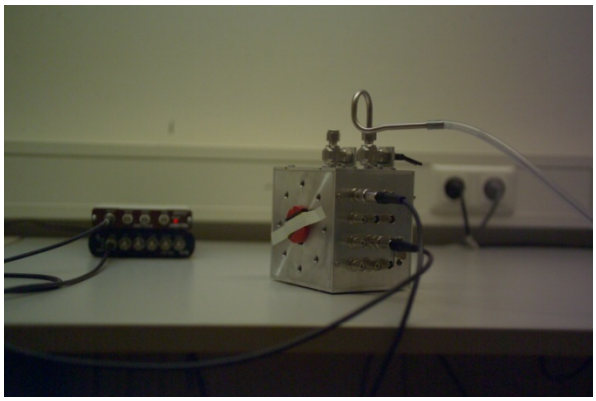

Figure 2: Counter overview during first testing.

Figure 2 shows the pprincipal setup with the Fe-55 radiation source fixed at the entrance window during the very first tests of the counter´s function. An ORTEC EASY-MCA and a MC USB-1604 are also presented on the picture. The detector operates with an A/CO2 (90%/10%) mixture at one atmosphere.

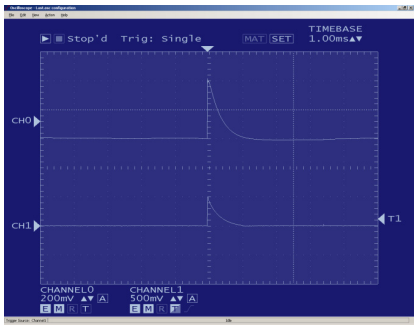

Figure 3: Oscilloscope screen shot with anode signals, Ch0 after the preamplifier, Ch1 after the amplifier.

Testing of function and next steps:

The characterisation of the four counters concerning energy, time and position resolution is going on at the moment. A Fe-55 source and standard NIM electronic components are used. In the next step the counters could be integrated into the crystal spectrometer. Furthermore, the development of a new type 3D miniaturized Multi Tube Proportional Counter is planned for the next phase.

* Work supported by GSI Helmholzzentrum für Schwerionenforschung GmbH, Projekt-Nr: LGGEOR1012 und dem Institute for Product and Process Innovation at the Leuphana University Lueneburg.

Development of a VUV-VIS-Spectrometer for Target Characterisation

Ph. Reiß[*1], *A. Knie*[1], *and A. Ehresmann*[†1]

[1]Institute of Physics and CINSaT, University of Kassel, Heinrich-Plett-Str. 40, 34132 Kassel, Germany

Fluorescence Spectroscopy in the visible, ultraviolet and VUV spectral range is a powerful experimental technique for the investigation of quantum-mechanical interference and electron correlative processes in atoms, molecules, and their ions. Energy differences between the two involved levels of the radiative transitions can be determined accurately, the recorded fluorescence intensity is a measure for the population probability of the fluorescence transitions initial state and a polarization analysis enables an analysis of the population of the energetically degenerate magnetic sublevels.

Advantages of Fluorescence Spectrometry

In synchrotron radiation experiments fluorescence spectrometry has proven to be an outstanding tool due to its state selectivity. The possibility to determine energies of doubly excited states in rare gas atoms demonstrates this feature nicely. In these experiments energies of individual autoionizing Rydberg states of two-electron excitations were determined. The state specificity of the autoioinzation processes into particular final states (which have been the initial states of the fluorescence transitions) enabled an individual determination of Rydberg states energies, being completely impossible in absorption experiments due to the high density of all doubly excited Rydberg states contributing to the absorption signal [1]. An example of such an experiment is shown in Figure 1 for Rydberg series of Kr doubly excited states.

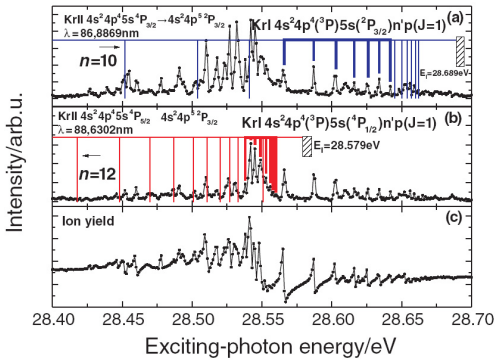

Figure 1: Dispersed fluorescence intensities from excited KrII $4s^2 4p^4 5s\ ^4\mathrm{P}_{3/2}$ (a) and $4s^2 4p^4 5s\ ^4\mathrm{P}_{3/2}$ (b) satellite states after photon excitation with energies around 28.55eV as well as the total photoion yield (c). Rydberg series of autoionizing two-electron resonances are clearly visible and can be distinguished.

* Work supported by the HGS-HIRe for FAIR

† ehresmann@physik.uni-kassel.de

Usage at Heavy-Ion Storage Rings

Fluorescence spectrometry used for the investigations of atomic or molecular ions formed after impact of heavy ions will be invaluable to conclude on the possible formation processes and on the involved electronic states. Also, a diagnosis of the ion beam itself after an impact in gaseous targets and foils is an intended aim of the project. Processes to be investigated will be radiative electron capture and dielectronic recombination.

Experimental setup and status of the project

The setup consists of a McPherson Model 225 1m-normal-incidence spectrometer that can be equipped with interchangeable diffraction gratings for the dispersion of the fluorescence radiation, each optimized for a different spectral range (VUV-VIS spectral range).

The detection of the photons is performed by 2-dimensional position- and time-resolving single-photon detectors that allow the simultaneous measurement of several fluorescence lines within a certain fluorescence wavelength range. Time resolution offers the option for lifetime or coincidence measurements.

Two detectors with wavelength ranges of 190nm to 700nm for the visible and 115nm to 300nm for the UV and VUV spectral range have been ordered from Quantar Technology and will be tested upon delivery. A third detector for the EUV spectral range from 30nm to 150nm will be assembled at the University of Kassel and also tested after completion.

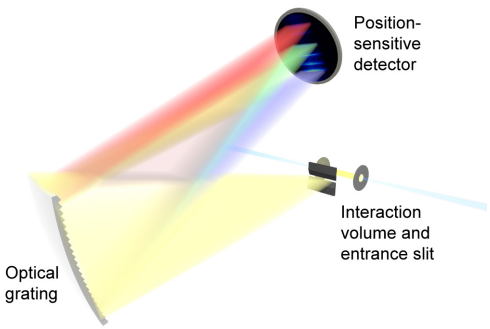

Figure 2: Sketch of the spectrometer setup.

References

[1] A. Ehresmann, et. al., J. Phys. B: At. Mol. Opt. Phys: 37, L251

Measurements of the Heavy Ion Stopping in X-ray heated low-density nanostructured targets

R. Maeder[2] , T. Rienecker[1,2] , O.N. Rosmej[1] , D. Martsovenko[3] , L. Borisenko[4] , A. Malikova, M. Schachinger [2], A. Schönlein[2], S. Zaehter[2] , Ge Xu [2] , J. Jacoby[2]

[1]GSI, Darmstadt, Germany; [2]University Frankfurt, Germany; [3] VNIIEF, Sarov, Russia; [4]Moscow State University

Measurements of the enhanced ion energy loss in plasma compared to those in non-ionized matter have been carried out in the frame of the project U272. The plasma targets were produced via volumetric heating of CHO-foam layers (cellulose-triacetate-TAC; $C_{12}H_{16}O_8$) by soft X-rays. X-ray source with close to the Planckian spectral distribution was generated by irradiation of a gold cylindrical hohlraum with the PHELIX-laser at 0.54 µm, 150J, 1 ns, 5.10^{14} W/cm^2 [1]. 80% conversion of the laser energy into soft X-rays with $T_{Planck} \sim 45$eV has been reached. Hydrodynamic stable homogeneous plasma with electron density of $n_e \sim 10^{21}$ cm^{-3} and 20-30 eV temperature is then produced in the state close to the thermodynamic equilibrium. This plasma is partially ionized and presented by He-like states of Carbon and Oxygen and fully ionized Hydrogen ions. Calculations of the 4.7 MeV/u Ti-ions energy loss on free and bound target electrons in dependence on plasma temperature/ionization degree (see Fig.1) have been done using a numerical code, described in [2].

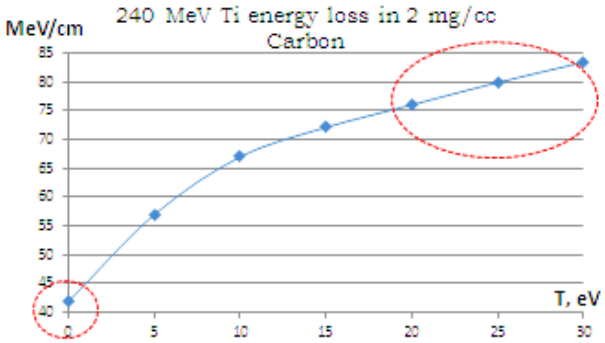

Figure 1: Expected energy loss of 240 MeV Ti-ions in a 1mm thick 2 mg/cm^3 carbon–plasma layer in dependence on plasma temperature.

The experimental set-up for the plasma production and ion energy loss measurements was similar to those used in [3]. Plasma target was probed by Ti-ions with a variable delay between the laser pulse and the ion micro-bunch. The ion velocity after interaction with target was measured using Time of Flight method. The results are shown in Fig. 2. Comparison of the TOF data for vacuum and cold target conditions results into the time of flight difference of 6.9 ns. After interaction with plasma layer the ions reached the stop detector 2.8 ns later than in the case of the cold target, this corresponds to1.4-times enhancement of the ion energy loss due interaction with free electrons in plasma. Energy loss of Ti-ions in plasma was measured for different time-delays and two plasma target densities, the results are presented in Fig. 3. At later times (>10ns) plasma temperature in the interaction region, placed 0.75mm apart from the hohlraum bottom, reached 20-30 eV and for both densities the enhancement of the ion energy loss is between 1.4 – 1.8 in accordance with [2]. The low enhancement factor at earlier times can be explained by lower plasma temperatures (see Fig.1) as a results of finite time needed for the heating process.

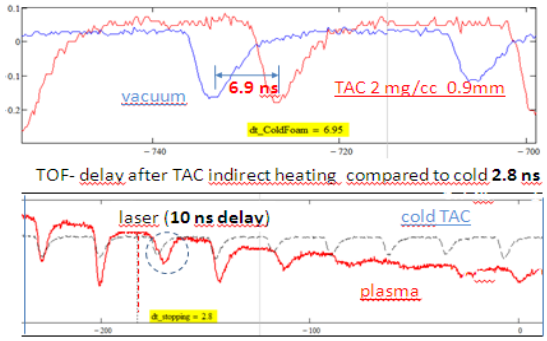

Figure 2: Ti –ion beam micro-bunch structure measured in vacuum and after interaction with foam and plasma.

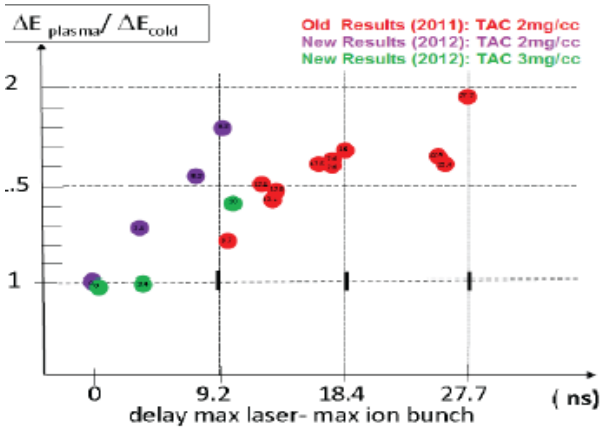

Figure 3: Enhancement of the ion energy loss in plasma depending on the delay between the laser and ion pulses.

References:

[1] O. Rosmej, V. Bagnoud, U. Eisenbarth, et al, "Nucl. Instr. and Meth. A 653 (2011), p.52-57.

[2] M. M. Basko, Ion stopping in dense plasmas, Physika Plazmi, **10**, V6 (1984)1195-1203

[3] R. Maeder, T. Rienecker, et al, Annual GSI-Report 2011, PNI-PP-17, p. 450.

Ion energy loss at maximum stopping power in a laser-generated plasma*

W. Cayzac[1,2], V. Bagnoud[3,5], M. Basko[6], S. Bedacht[1], A. Blažević[3], O. Deppert[1], A. Frank[5], D. Gericke[8], L. Hallo[4], A. Knetsch[1], D. Kraus[1], G. Malka[2], A. Ortner[1], K. Pépitone[4], M. Roth[1], G. Schaumann[1], T. Schlegel[3], D. Schumacher[3], An. Tauschwitz[7], J. Vorberger[9], and F. Wagner[1]

[1]TU Darmstadt; [2]CELIA; [3]GSI; [4]CEA/CESTA; [5]Helmholtzinstitut Jena; [6]KIAM Moscow; [7]University of Frankfurt; [8]University of Warwick; [9]MPI for physics of complex systems

Ion stopping in plasma is relatively well-understood for projectile velocities much higher than the thermal velocity of plasma electrons ($v_{ion}/v_{th} >> 1$), but large uncertainties remain for the region of maximum stopping power, where $v_{ion}/v_{th} \approx 1$. This parameter region, of crucial importance for ICF, is very difficult to model theoretically [1] and, to our knowledge, no experimental data exists in order to benchmark the existing theories and numerical codes. The purpose of this work, led in collaboration with the CEA and CELIA in France, is to carry out such measurements, and the first campaign was conducted in 2012.

100 μg/cm^2 carbon foils were irradiated from both sides with frequency-doubled pulses from the PHELIX and *nhelix* laser systems, as in [2]. The generated hot (200 eV) and dense (10^{20-21} cm^{-3}) plasma has been well-characterized by using multi-frame interferometry [3] and hydrodynamic simulations with the RALEF2D code [4], both approaches being consistent with each other [2,3]. The plasma was fully ionized and ideal (coupling coefficient $\Gamma \approx 0{,}01$). The projectile energy was $0{,}5$ MeV/u, and carbon ions were employed, as they are expected to be fully stripped in plasma in these conditions, according to Monte-Carlo calculations. In this way, no charge variation affects the stopping power and only the Coulomb logarithm of the interaction is expected to play a role. Theoretical calculations of the stopping power of C^{6+} in a fully ionized carbon plasma reveal discrepancies reaching $30\,\%$ between the various approaches.

The experimental setup is shown in Fig.1. The ions were decelerated to $0{,}5$ MeV/u by using a graphite foil of 45μm thickness. This led to a beam straggling of $10\,\%$ in energy and 1-2° in angle, as calculated with the TRIM and Geant4 codes. The decelerating foil was positioned only 10 mm from the plasma target, allowing about $90\,\%$ of the ion beam to interact with a transversally homogeneous plasma according to TRIM and RALEF2D results, while keeping the foil outside of the laser beam path. To avoid the overlapping of consecutive ion beams, a time-of-flight distance of only 50 cm had to be used.

A new 15×15 mm^2 large and 13 μm thick polycrystalline CVD-diamond detector was therefore specially developed for the experiment, allowing to register $10\,\%$ of the beam. Due to their proximity to the plasma, the detector and the signal transmission line had to be properly shielded against X-rays and EMP. In particular, a 2 mg/cm^2 gold foil on the beam path blocked most of direct X-rays without stopping the ions.

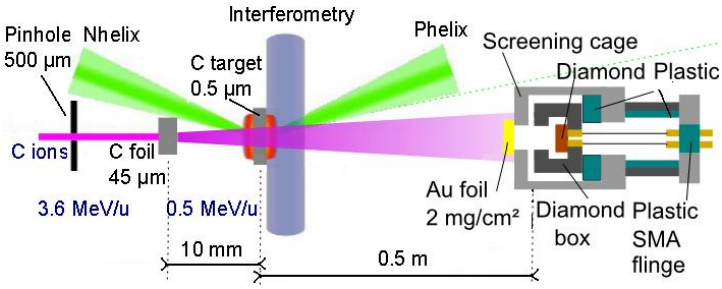

Figure 1: Experimental setup.

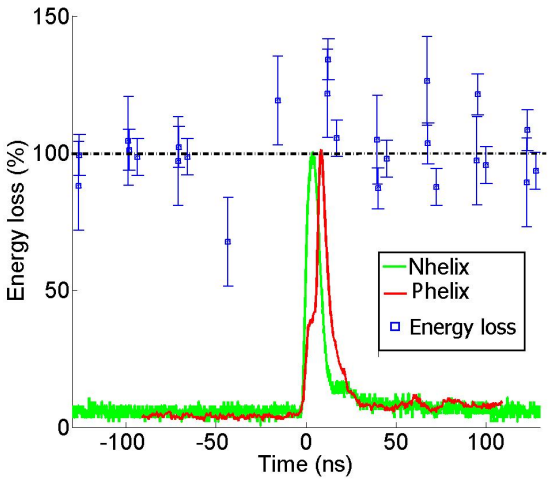

Figure 2: Energy loss as a function of time. $100\,\%$ corresponds to the energy loss in the solid foil.

First data was successfully gathered, and preliminary results are shown in Fig.2. An increase in energy loss in plasma of $34\,\%$ in relation to the cold target is observed.

References

[1] D.O. Gericke and M. Schlanges, Phys. Rev. E, Vol.60, 1999

[2] A. Frank et al., submitted to *Physical Review Letter*

[3] M. Boerner et al., *Review of Scientific Instruments*, 2012

[4] An. Tauschwitz et al., *High Energy Density Physics*, 2013

*This project is supported by CEA/CESTA and the Région Aquitaine as well as by BMBF and HIC4FAIR

Transport and focusing of laser-accelerated protons at Z6*

S. Busold[1], *D. Schumacher*[4], *O. Deppert*[1], *C. Brabetz*[2], *F. Kroll*[3], *M. Joost*[3], *H. Al Omari*[2], *A. Blazevic*[4,5], *B. Zielbauer*[4,5], *V. Bagnoud*[4,5], *I. Hofmann*[4,5], *and M. Roth*[1]

[1]TU Darmstadt, IKP, Germany; [2]JWG Universität Frankfurt, IAP, Germany; [3]Helmholtzzentrum Dresden-Rossendorf, Germany; [4]GSI, Darmstadt, Germany; [5]Helmholtz Institut Jena, Germany

LIGHT

Irradiation of μm-thin foils with high-intensity laser pulses ($> 10^{19}$ W/cm^2) became a reliable tool during the last decade for producing high-intensity proton bunches, providing up to 10^{14} protons in about a pico-second from a sub-millimeter source. However, the proton energy distribution is of an exponential shape with a currently achievable cut-off energy < 100 MeV (TNSA mechanism) and the beam is highly divergent with an energy-dependent envelope-divergence of up to 60 degrees. Thus, for most possible applications it is necessary to be able to capture and control these protons as well as select a specific energy. Therefore, the LIGHT collaboration (**L**aser **I**on **G**eneration, **H**andling and **T**ransport) was formed, dedicated to investigate the possibilities of compact laser-driven ion sources for ions in the multi-MeV range. In this context, a lot of preperative work had been done at GSI in the last years and the most promising results could be obtained with small quadrupol magnets [1] and pulsed high-field solenoids [2, 3]. And since the commissioning of the PHELIX 100 TW beamline [4] some experiments could already move to the Z6 area, where now short-pulse laser technology and conventional accelerator infrastructure can be merged in a unique way.

pulsed high-field solenoid

The first experiment in 2012 for transport and focusing of laser-accelerated protons was done at the Z6 area, where PHELIX can deliver about 15 J of laser energy on target, exceeding 10^{19} W/cm^2. While the laser hits the front of the target, a 5–10 μm thin metal foil, the protons are accelerated targetnormal from the back side. The pulsed solenoid, placed 80 mm behind the target, is 150 mm long, has an open aperture of 40.5 mm diameter and can reach a maximum field of 10 T.

The magnetic field was adjusted to focus 4.5 MeV protons at 695 mm behind the solenoid (925 mm behind the target). The Detection of the proton beam in front of the solenoid and directly behind (still inside the targetchamber) showed the expected energy-dependet focusing and beam rotation. A proton focus could be reached inside the attached Z6 ion beamline at 695 mm behind the solenoid, containing 5×10^8 particles and with a spot size of 3 mm (FWHM).

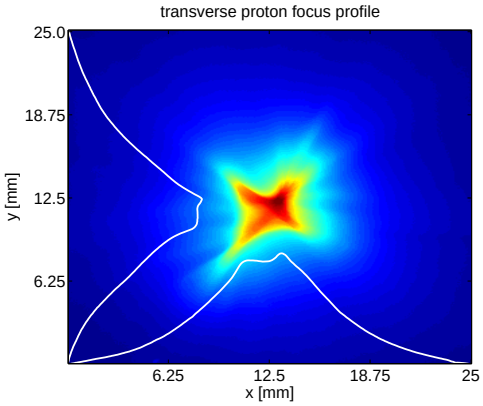

Figure 1: Transverse focus profile of 4.5 MeV protons at nearly 1 m from source, produced with the pulsed high-field solenoid.

The results are in good agreement with accompanying simulation studies, which are performed with CST particle studio and TraceWin.

permanent-magnetic quadrupole triplet

In a second experimental campaign in 2012, the transport and focusing of laser-accelerated protons could be tested in the PHELIX laserbay with a permanent-magnetic quadrupole triplet. Here, intensities of 5×10^{19} W/cm^2 were used with about 60 J laser energy on target; i.e. more particles are produced initially.

A sub-aperture of the full beam (40 mrad divergence) was transported through the triplet and at 630 mm distance to the source, 10 MeV protons were focused in a 3x6 mm (FWHM) spot size, containing up to 10^9 particles.

References

[1] M. Schollmeier *et al.*, PRL **101**, 055004 (2008)

[2] K. Harres *et al.*, Phys. Plas. **17**, 023107 (2010)

[3] T. Burris-Mog *et al.*, PRSTAB **14**, 121301 (2011)

[4] S. Busold *et al.*, GSI scientific report (2011)

*This work is supported by the Helmholtz Institute Jena and HIC for FAIR.

Ultra-thin foils for laser ion acceleration in the radiation-pressure regime

B. Aurand[1,2], L.-O. Heim[3], B. Elkin[4], B. Lommel[1], B. Kindler[1], O. Jäckel[2,5], S. Kuschel[2,5], C. Rödel[2,5] and T. Kuehl[1,2,6]

[1] GSI , Darmstadt, Germany; [2] Helmholtz Institute Jena, Jena, Germany; [3] Center for Smart Interfaces, Darmstadt, Germany; [4] Fraunhofer Institute for Interfacial Engineering and Biotechnology, Stuttgart, Germany; [5] Institute for Optic and Quantum Electronics, Jena, Germany; [6] Johannes Gutenberg University, Mainz, Germany;

Introduction

Recent developments by our and other groups on the mechanism of radiation-pressure driven acceleration of protons and heavy ions [1,2,3,4] emphasizes the strong dependence of the results on a very high laser contrast of > 10^9, as well as the development of suitable targets. Since a few years diamond-like-carbon (DLC) foils are an appropriate choice. The drawback is the low mechanical stability for foils having a thickness of just a few. We developed an alternative process using a polymer based film which is produced by vapor deposition. Test of the surface roughness as well as the mechanical stability show great advantage for this kind of material compared to normal DLC foil.

Setup

We use parylene, an industrial coating material which is hydrophobic and optical transparent [5]. Starting from a glass substrate which is wiped with a hydrophilic barrier layer (detergent) the polymer is attached by pyrolytic chemical vapor deposition (p-CVD) forming a homogeneous layer on all surfaces within the deposition chamber, see fig, 1

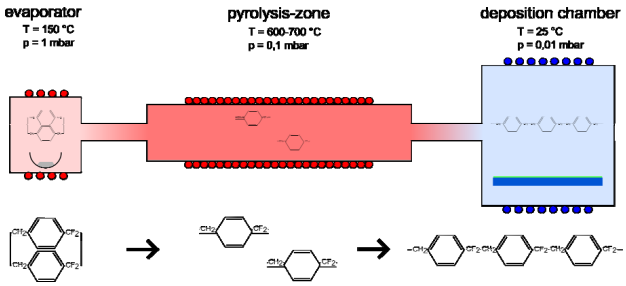

Fig.1 : Process of pyrolytic chemical vapour deposition (p-CVD) of parylene onto the glass substrates.

After deposition the glass substrate is removed and stored in inert gas, allowing storage times of more than one year before mounting as a target.
The foil can be flooded of the substrate by slowly casting in a bath of water and being attached to a target mount by adhesion, afterwards. For laser-acceleration experiments we used in previous experiments a 15nm thick foil attached on a special target mount (fig. 2a) creating more than 400 targets which can be used without opening the chamber in between shots. It was also possible to attach the foils self-supporting on very large apertures, up to 20mm, see fig. 2b

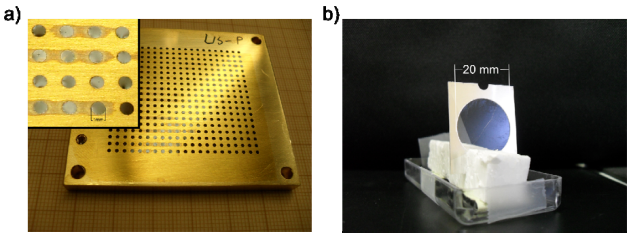

Fig.2 : a) Parylene foil attached to target mount used for laser-acceleration experiments. B) Self-supporting 15 nm foil freestanding on 20 mm aperture.

Characterization

For a proper characterization we measured the thickness of each processed foil by ellipsometry, resulting in a thickness derivation of not more than 1nm at different positions of a large (150 x 100 mm) foil sample and a average thickness of 15nm.
The mechanical stability of the parylene foil was compared to the stability of a DLC foil of the same thickness Here 30 nm thick foils were used. For this purpose both foils were attached on TEM-grids creating small self-supporting samples. The force-distance relation was measured via nanoindentation using an atomic-force microscpe (AFM). The measured elasticity of the parylene is 5 times higher than the one of the DLC, which explains the higher resistance against mechanical shock and temperature variation observed during hadling. Using AFM topography mode, we measured the surface roughness in addition. Both samples hade more or less the same average roughness of R_{DLC}= 5.7 ± 0.9 nm and $R_{Parylen}$= 8.6 ± 2.3 nm.

References

[1] B. Aurand et al. , in CLEO: QELS-Fundamental Science, OSA Techn. Digest (2012), paper JTh3I.2.
[2] A. Henig *et al.*, PRL 103, 245003 (2009)
[3] S. Kar *et al.*, PRL 109, 185006 (2012)
[4] B. Qiao et al., PRL 105, 155002 (2010)
[5] A. Greiner *et al.*, Acta Polymer 48, 1 (1997)

X-ray Laser Developments at PHELIX

B. Ecker[1,2], B. Aurand[2,3,4], D. C. Hochhaus[3,7], P. Neumayer[3], B. Zielbauer[1,4], K. Cassou[5], S. Dabousi[5], O. Guilbaud[5], S. Kazamias[5], T. T. T. Le[6], E. Oliva[6], L. Li[6], H. Zhao[8], Q. Jin[8], D. Ros[5], P. Zeitoun[6] and T. Kuehl[2,4]

[1]Helmholtz Institute Jena , [2]Johannes-Gutenberg Universität Mainz, [3]ExtreMe Matter Institute EMMI, [4]GSI Helmholtzzentrum fuer Schwerionenforschung, [5]LASERIX-CLUPS / Université Paris-Sud 11 [6]Laboratoire d'Optique Appliquée, [7]Goethe-Universität Frankfurt, [8]Institute of Modern Physics, CAS

Introduction

We report on results of a double-stage molybdenum x-ray laser experiment. The two targets were pumped using the double-pulse grazing incidence pumping technique, which includes travelling wave excitation for both the seed- and the amplifier-target..

The main motivation for X-ray laser (XRL) research at GSI is to perform spectroscopy experiments on highly-charged heavy-ions stored in the experimental storage ring (ESR) of the GSI accelerator facility[1]. The first experiment of this kind will aim at measuring the 2s1/2 – 2p1/2 transition in Li-like ions. For ions of an atomic number between 50 (Sn) and 92 (Ur), this transition energy lies between 100 eV and 300 eV [1], which corresponds to wavelengths between 12 nm and 4 nm. Setting up the experiment in a way, where the XRL is counter propagating to the ion bunch, one can exploit the relativistic Doppler effect. The use of laser-pumped plasma XRL's, with typical photon energy up to 100 eV [2,3,3] can address the whole range of lithium-like ions for the lowest lying transitions The perspective for FAIR, given by the even higher ion velocities at HESR , opens a completely new range of experiments.

Experiment

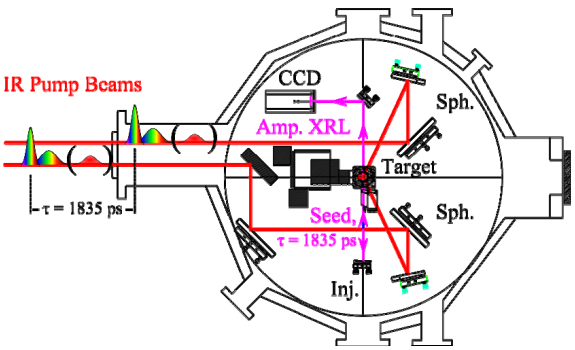

Fig. 1. Sketch of the experimental setup. A more detailed description is given in the text.

A Mach-Zehnder like interferometer, which was implemented in the short-pulse frontend of the PHELIX laser, was used to create the chirped double-pulse structure required for the DGRIP scheme [2]. After compression, the pulse duration of the two pulses was 200 ps (prepulse) and 2 ps (main pulse). Using the PHELIX pre-amplifier section, the total pump energy on the target amounted to 600 mJ, equally distributed between two individual pumping beams. Inside the target chamber, the two beams were focused in opposite direction onto the Mo slab target by two spherical mirrors, as illustrated in Fig. 1. The line foci were vertically separated by ~ 3 mm. The output of the lower XRL – the seed pulse - was focused into the upper – amplifying- medium by a spherical XUV mirror.

Results

Seeded x-ray laser operation has been demonstrated, resulting in x-ray laser pulses of up to 240 nJ and 2 mrad × 2 mrad divergence. The peak brilliance of the amplified x-ray laser of 4×10^{23} photons /s /mm² /mrad² in 5×10^{-5} relative bandwidth was more than two orders of magnitude larger compared to the original seed pulses.Figure 1 shows the typical beam patterns of the HH observed (filters: Zr and Ti) under (a) only He gas jet (valve stagnation pressure: 4000 mbar), (b) Ne 400 mbar jet, and (c) both gas jets for Ne 400-He 4000 mbar.

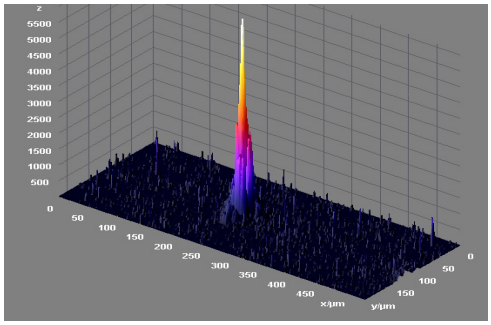

Fig. 2: Beam quality of the seeded XRL. showing 2 mrad × 2 mrad divergence.

References

1. D.Winters et al., GSI Annual report 2012
2. B. Ecker et al., Opt. Express **20**(23), 25391 (2012).
3. D. Zimmer et al., Optics Express, 13, 2403, 2008
4.D. Ros et al., NIM A, 653,, 76, 2011

Hollow Beam creation with continuous diffractive phase mask at PHELIX*

C. Brabetz[2], V. Bagnoud[1], S. Busold[4], T. E. Cowan[3], O. Deppert[4], U. Eisenbarth[1], S. Götte[1], O. Kester[1,2], D. Schumacher[1], B. Zielbauer[1]

[1]GSI Darmstadt, Germany; [2]Johann Wolfgang Goethe University, Frankfurt, Germany;
[3]HZDR, Helmholtz center Dresden Rossendorf, Germany; [4]TU Darmstadt, Darmstadt, Germany

Overview

In the framework of the Laser Ion Generation Handling and Transport (LIGHT) project, the reduction of the divergence of the laser accelerated ions is a central issue. One solution relies on engineering the electron sheath used in standard laser-driven proton acceleration (target normal sheath acceleration, TNSA) for reducing the initial divergence of the ion beam. In 2012, we conducted an experimental campaign in which "donut" focal spot have been used to drive proton acceleration. From that we have found two interesting features:

• One sees a qualitative effect of the focal spot beam shape on the ion beam divergence as expected, and

• The energy cut-off in the proton spectrum was nearly higher when a donut focus was applied, although this resulted in contradiction with the scaling law of TNSA.

Report on the 2012 beamtime

During the beamtime, we did a first run on laser-ion acceleration with engineered beams. We also focused particularly on avoiding strong wavefront distortion in the laser amplifier (astigmatism) because we saw how crucial it is for that kind of experiment. In 2012 a new PHELIX off-axis parabolic mirror was installed and produced a good hollow focus profile during alignment. However, we found that the on-shot aberrations also strongly alter the beam quality. Therefore a bending mechanism was installed to the main-mirror 1 in the main amplifier of PHELIX to correct for the thermal aberrations happening on shot and measured with a wavefront sensor. Using this pre-compensation, the alignment- beam profile looks distorted but the on-shot profile looks more promising.

Results on ion acceleration with engineered laser beam

In total we had 29 successful high-energy experiment shots on gold foils with different thicknesses with and without hollow beam.

In comparison to a standard Gaussian beam (blue dots in Figure 1) the focal spot diameter of the hollow beam focus increases by a factor of about 2 and therefore the peak intensity drops nearly by a factor of 4. A troubling feature is that the maximum proton energy for the hollow beams (in red) does not depend on the laser intensity contrarily to what laser-ion acceleration scaling laws predict. For higher-order hollow beams (green dots), the focal spot was heavily distorted and resulted in a speckle-like energy distribution at low intensity. In this case a significant reduction of the proton energies was observed.

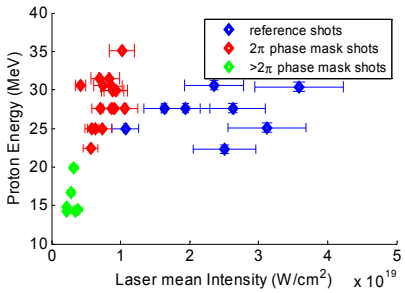

Figure 1: Proton Energy dependency on laser intensity.

From an angular distribution stand-point, the proton beams created with the hollow laser beam clearly show a systematic trend to lower divergences and higher proton yields. Taking the more aberrated shots into account we observe other effects on the ion beam. Some type of shots with a hollow beam profile broke down to 2 similar strong focal spots shows a divergence reduction in only on dimension while other shots with the hollow beam phase on thick targets shows unexpected high proton energies.

3w on-shot focus diagnostics

We set up a new imaging diagnostic for measuring the laser focal spot on target during the shot [1]. The idea was to look at the relativistic oscillation plasma surface that generates harmonics. Then filter for only the 3w light that is specular reflected from the target surface and is linked directly to the laser focal spot and the TNSA source size. As the components were not available in the beginning of the experiment it was just installed in the last two days. Therefore there was not enough time for optimization of the diagnostic. We know that the imaging system was strongly affected by astigmatism (duo to passing through a thick glass substrate). But still we can say that the source size was smaller than 80x80 µm^2 (Figure 2).

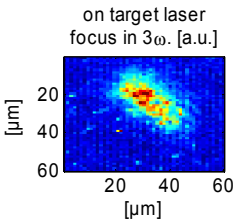

Figure 2: on-shot focus in 3w.

References

[1] B. Dromey et al., Laser and Particle Beams **27**, 243-248 (2009).

* Work supported by HIC for FAIR.

Amplification of high harmonic generation signal by double gas jet scheme

J. Seres[1], E. Seres[1], B. Aurand[2,3], S. Namba[4], B. Landgraf[1,2], C. Spielmann[1,2] and T. Kuehl[2,3,5,6]

[1] Institute for Optic and Quantum Electronics, Jena, Germany; [2] GSI , Darmstadt, Germany; [3] Helmholtz Institute Jena, Jena, Germany; [4] Hiroshima University, Japan; [5] Johannes Gutenberg University, Mainz, Germany; [6] EMMI Extreme Matter Institute, Darmstadt, Germany

Introduction

High-harmonic (HH) radiation due to nonlinear interaction of rare gas with an ultrashort, high intensity laser pulse has attracted a great deal of interest for various applications, such as, attosecond pulses [1] and a seeding light for an X-ray free electron laser (XFEL) [2]. On the other hand, we have observed X-ray parametric stimulated amplification of the HH emission for the first time [3]. However, the output of the HH in high photon energy regime is still weak, so that practical applications are limited in some particular physical and chemical research. In order to increase the output energy and obtain much shorter wavelength radiation, a double gas jet method was used in this study. As a result, we succeeded in a significant enhancement of the HH output. Moreover, the appearance of a high intensity, hot spot emission was observed.

Experiment

The experiment was carried out at the JETI laser-system, delivering pulses of 200 mJ, 10 Hz in 26 fs, with a pulse contrast in the range of better than 10^6. The beam was focused by a spherical mirror to an intensity of $< 5\times10^{15}$ W/cm^2. In order to enhance the HH lights, we employed a double gas jet scheme, in which the first gas was Ne as a seeder and the second jet (He) served as an amplifier. Both gases were supplied by electro-magnetic pulsed gas valves. An extreme ultraviolet (EUV) spectrometer was used to measure the HH spectra and their intensity distribution. The beam pattern of the HH was observed by a back-illuminated soft X-ray CCD camera, at which some appropriate filters (Ti and Zr) were inserted to select wavelength region and block the fundamental laser light.

Results

Fig. 1 shows the typical beam patterns of the HH observed under (a) only He gas jet (valve stagnation pressure: 4000 mbar), (b) Ne jet 400 mbar, and (c) both gas jets for Ne 400-He 4000 mbar.

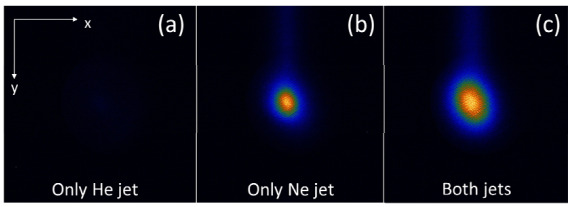

Fig. 1: Two dimensional image of the high harmonic radiations for (a) only He jet (4000 mbar), (b) Ne (400 mbar), and (c) both jets operated. For comparison, the graphs are shown in the same color scale. Significant enhancement of the HH signal was obtained.

The distance of the jets was set to d=0 mm. The figures are shown in the same color scale. As clearly seen, no HH was observed for only He gas jet, whereas by operating both jets the HH signal becomes higher by two times than that by only the Ne jet.

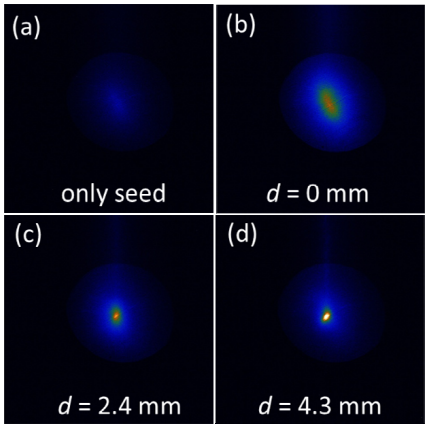

Fig. 2: Variation of the HH image on the gas jet distance. Above d~2mm, the hot spot appeared, where the gain coefficient increased by ~20 times.

On the other hand, the hot spot where the HH intensity is locally enhanced is obtained as shown in Fig. 2. The experimental conditions are as follows: stagnation pressures of Ne 250 mbar, He 4000 mbar, Zr-Ti filters, for various jet distances were used. The seed lights generated in Ne gas jet were amplified significantly at d=0 mm, which is similar with that in Fig. 1. However, in the case of the jet distances above d~2 mm, we obtain the intense spot radiation near the beam center. At optimal condition, we demonstrate that the gain coefficient at the hot spot, which is defined by the ratio of HH intensity with both gas jets to that of Ne one, is around 20.

References

[1] M. Hentschel *et al*., "Attosecond metrology", Nature 414, 509 (2001).

[2] T. Togashi *et al*., "Extreme ultraviolet free electron laser seeded with high-order harmonic of Ti:sapphire laser", Opt. Express, 19, 317 (2011).

[3] J. Seres *et al*.," Laser-driven amplification of soft X-rays by parametric stimulated emission in neutral gases", Nature Phys. 6, 455 (2010).

Supersonic radiation driven heat waves in foam target heated by X-rays

O. N. Rosmej[1], D. Klir[2], K. Rezak[2], M. Schächinger[3], T. Rienecker[3], G. Vergunova[4], N. Borisenko[4], L. Borisenko[5], A. Malikova[5]

[1]GSI, Darmstadt, Germany; [2] Czech Technical University in Prague; [3]University of Frankfurt, Germany,

[4] Lebedev Physical Institute, Moscow, Russia; [5]Moscow State University, Russia

A combined hohlraum-target concept have been investigated in order to gain a high degree of plasma homogeneity in experiment on the energy loss of heavy ions in ionized matter and approach plasma with a coupling parameter Γ~0.5-1. In this scheme, low density mm-thick foam layers were heated by means of X-rays generated in the gold hohlraum. The application of low density CHO-foam layers for plasma production has demonstrated a very high hydrodynamic stability of the created plasma and its uniformity [1]. A wide verity of diagnostic methods has been applied for measurements on the thermal wave propagation, plasma opacities and plasma self-radiation.

In Hydrodynamic 1-D calculations, 2 mg/cc cellulose triacetate $C_{12}H_{16}O_8$ of 2 mm thickness was heated from the right side by an X-ray flux with the Planckian spectral distribution at temperature of 30 eV and 10 ns duration (experimental conditions), see Fig.1. For radiation transport in the diffusion approximation $C_{12}H_{16}O_8$ - opacities calculated in [,2] have been used.

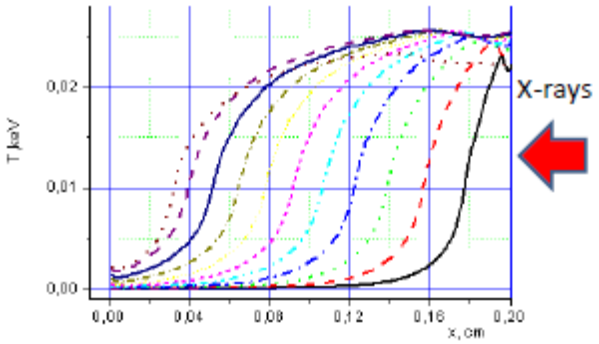

Figure 1: Propagation of the heating front through a 2 mm thick CHO-foam in time window from 1 to 10 ns..

Depending on the hohlraum spectra and foam density two different scenarios of a foam target heating by X-rays can be realized. If the mean photon pass in plasma is shorter than a plasma size, optically thick case, target heating occurs step by step (Fig.1) via propagation of the radiation driven supersonic thermal waves. If created plasma is optically thin (low target density or more energetic spectra of photons due to higher hohlraum temperature) volumetric heating takes place.

Propagation of the radiation driven supersonic thermal waves has been obsurved experimentally using a pin-hole camera coupled to the 4-frame gated MCP (microchannel plate) [3] and imaging the CHO-foam at different times of the heating process. An exposition time for every frame, in experiment 3-5 ns, and time delay between two subsequent frames can be variied. Frig. 2 shows the geometry of the combined target (picture left), the MCP-cheep with four imaging areas (right) and a measured time history of the heat-front propagating from the cylindrical hohlraum into the foam (center).

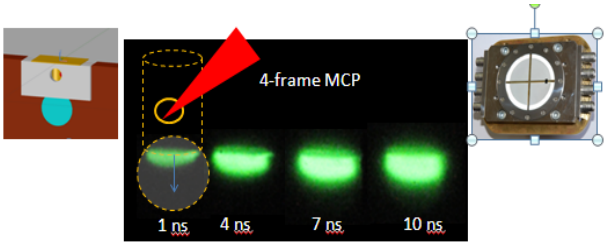

Figure 2: 2-D image of the foam region heated to plasma by hohlraum x-rays in the regime of supersonic radiation-driven heat waves, measured at different times.

The supersonic heat wave velocity $V \sim \dfrac{T^{m+4}}{\rho \sim const}$ (1)

is a strong function of the plasma temperature T (in our case m~3) and doesn't depend on plasma density for hydrodynamic stable plasmas (ρ=const). After analyses of the radiation front position at different times one comes up with the averaged over the exposition time heat wave velocities and corresponding plasma temperatures.

$V(1ns) = 1.2x10^7\ cm/s \rightarrow T \sim 25\,eV$

$V(4ns) = 8.3x10^6\ cm/s \rightarrow T \sim 23\,eV$

$V(7ns) = 4.0x10^6\ cm/s \rightarrow T \sim 20\,eV$

$V(10\,ns) = 1.4x10^6\ cm/s \rightarrow T \sim 15\,eV$

In coming experiments this method will be applied for measurements of the plasma temperature in the time window of ion-plasma interaction.

References

[1] G. Vergunova et a,lJournal of Russian Laser Research, Volume 31, Number 5, 2010

[2] N. Orlov et al, LPB 29 (2011), 69–80.

[3] D. Klir, PhD 2005, Czech Technical University in Prague

Comparison of measured time resolved hohlraum radiation temperature with data produced by RALEF II-Code

T. Rienecker[2], R. Maeder[2], O. N. Rosmej[1], D. Martsovenko[3], N. Suslov[3], S. Faik[2], M. Basko[5], An. Tauschwitz[2], L. Borisenko[4], A. Malikova[3], M. Schadinger[2], A. Schönlein[2], S. Zaehter[2], Xu Ge[2], and J. Jacoby[2]

[1]GSI, Darmstadt, Germany; [2]Goethe-University Frankfurt, Germany; [3]VNIIEF-Sarov, Russia; [4]Moscow State Univversity, Russia; [5]Keldysh Institute of Applied Mathematics, Moscow

For indirect homogeneous heating of low-Z triacetate-cellulose (TAC) foam targets, used in experiments on ion energy loss in plasma, a large (Ø > 1 mm) soft X-ray source with a Planckian equivalent radiative temperature of 30 to 50 eV is required. In this temperature region soft X-rays are effectively absorbed by low Z low density polymer layers. More energetic radiation above 1 keV passes through the 200 µg/cm^2 TAC-layer without attenuation giving no input into the process of foam heating.

The experiments have been supported by RALEF II simulations, made by S. Faik from University Frankfurt. One important data, the hohlraum temperature show a heating during the shot of the laser in the first ns, it leads to a peak temperature of about 70 eV. After some additional Nanoseconds the Temperature in the hohlraum is homogenized and stays nearly constant for a long (>10 ns) while (see figure 2a).

Figure 1a: The picture shows a scheme of the setup, with

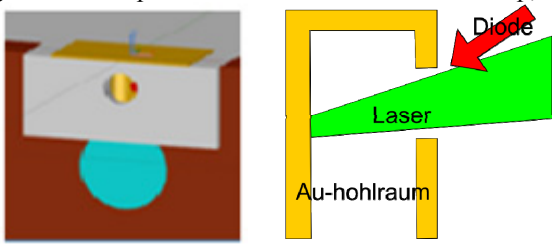

a view in the Au-Hohlraum from the same position as the X-ray-diode.
Figure 1b: The scheme shows the laser and the diode, using the same hole for heating and diagnostic.

The temperature in experiment was measured by X-ray-diodes. The X-ray-diodes are composed once of a carbon and second of an aluminium cathodes, a grid with and a filter. The combination of different filters allow measuring the absolute photon flux in different parts of the hohlraum spectrum and deduce a time-history of the hohlraum temperature radiation. dows for different wavelength (see Figure 2).

According to earlier experiments [1,2], we can assume a short time of 5-7 ns after the beginning of the laser pulse of X-ray imission and reemission. After this homogenisation the radiation fits to the normal hohlraum radiation. Folding the this radiation with the filters and the electron efficiency of the cathodes leading to different currents, produced by the X-ray diodes (see Figure 2).

The described measurement assumes an absolute calibrated X-ray-diode, like the one we had. For a better verifiability and a second method, we use a second X-ray-diode, with different filers. On this way it was possible to compare the two signals in a proportional, witch not necessary needs absolute calibrated X-ray-diodes.

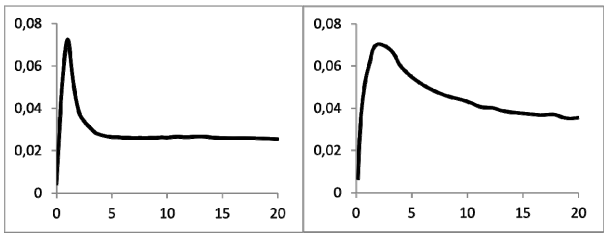

Figure 2a: Simulated temperature [k eV], time resolved [ns] integrated over a line across the hohlraum. Figure 2b: Measured temperature [keV], time resolved [ns] integrated over the view line to the rear wall.

The simulated data (see figure 1) shows a very small peak in the first ns, an a flat temperature after the 5th ns. The measured curve is some eV higher in the temperature, after the homogenisation. This may be caused by the fact, that the X-ray-diode views a part of the laser spot. The important parameter, the long lasting temperature, is reached in the simulation and the measurement, and both fit together.

References

[1] O.N. Rosmej et al. NIMA 653(2011)52-57
[2] T. Rienecker, et al. GSI-report 2011
[3] M. Basko, An. Tauschwitzt et al, GSI-Preprint N 2011

* Work supported by GSI; Extreme Matter Institute EMMI

Hard X-Ray backlighting for Warm Dense Matter at FAIR*

A. Schoenlein[1], *J.Wiechula*[1], *O. Rosmej*[2], *B. Aurand*[2], *D. Hochhaus*[3], *Paul Neumayer*[3], *O. V. Chefonov*[3], *A. V. Ovchinnikov*[3], *and J. Jacoby*[1]

[1]Goethe University, Frankfurt, Germany; [2]GSI, Darmstadt, Germany; [3]Extreme Matter Institute EMMI, Germany; [4]Joint Institute for High Temperatures, Moscow

FAIR opens new possibilities to study the fundamental properties of matter under extreme conditions. In experiments like HIHEX or LAPLAS [1] the Warm Dense Matter will be generated by high-energy, high-intensity ion beams heating large (mm^3) high Z-targets (Al-Pb). For backlighting these targets, it is necessary to generate photons with energies in the keV-MeV range. Hard X-ray and Gamma sources can be generated by processes that occur during interaction of high intensity lasers with matter. When a laser pulse impacts onto the target, collective absorption mechanisms transfer up to 20% of the laser energy into hot electrons, which are accelerated to multi-keV and MeV energies. The deceleration of the hot electrons penetrating the target causes bremstrahlung radiation. Attenuation and scattering of x-rays can be used to determine the electron plasma temperature and density[2]. The advantage of a hard x-ray generation using short-pulse lasers over a common x-ray tube is, that it gives the possibility to generate short bursts (fs-ps) of x-rays which provide the possibility to investigate a time history of dynamic processes in the plasma.

The experiment was carried out in the frame of the PHELIX - project P42. The applied laser parameters ($E_L \approx 150J$, $\tau_L = 500fs$, focal spot size of $15 - 20\mu m$) lead to the maximum intensity of $3 * 10^{19} \frac{W}{cm^2}$. Ag foils (10-100$\mu$m) and Ag bulks (3mm) were used as targets. The experiment setup includes several pinhole cameras for spatial diagnostics, a single hit CCD for the measurement of Ag-Kα radiation, **H**ard **X**-**r**ay **D**etectors (HXRD) for spectral diagnostics and a x-ray knife to determine the energy of hot electrons.

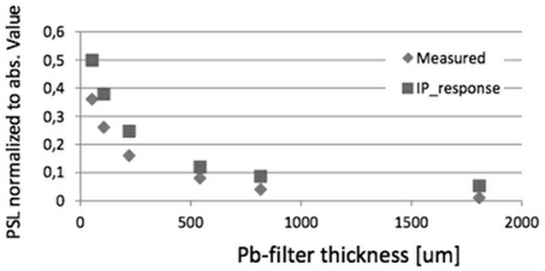

Figure 1: comparison of calculated and measured IP-response

The HXRD mainly consists of an image plate (IP), which is placed behind filters of different thicknesses (Pb 53-1807μm). The x-ray absorption of the filter set takes place in accordance with the Lambert-Beer-Law $I = I_0 \cdot e^{-\alpha\rho d}$, where d is the thickness of the filter, α is the attenuation coefficient of the filter material and ρ is the filter density. The bremsstrahlung spectrum will then be reconstructed using a fitting procedure in which a synthetic spectrum with a temperature of hot electrons, defined in a zero approximation by the laser intensity[3], is sent through the filter set. By varying the temperature of hot electrons, one tries to achieve the best agreement between theoretical and experimental data. Fig.1 shows the comparison of calculated and measured IP-responses in the laser shot at $2 \cdot 10^{19} \frac{W}{cm^2}$ The best fit is achieved for hot electron temperature of 1,5MeV. The x-ray knife diagnostic consists of a 500μm thick Au-plate placed between the target and an IP. Due to the bremsstrahlung, generated by hot electrons penetrating the target, this arrangement allows to obtain an 1-D image of the interaction region and to estimate the electron energy depending on the electron penetration depth in target.

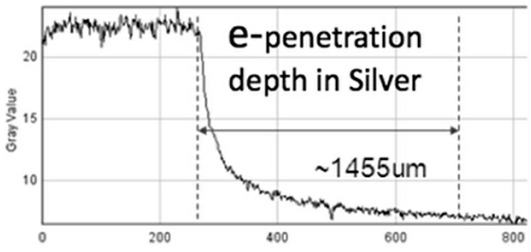

Figure 2: penetration depth of hot electrons in Ag

Fig.2 shows that the hot electrons are stopped after 1455μm of propagation in silver target. A stopping range of $\sim$1,5mm in Ag refers to electron energies of 2MeV. This is in good agreement with results of the HXRD-diagnostic.

For backlighting of the 4mm-thick LAPLAS target tamper [1] made from Nb or W, laser induced photons with energies above 0.5-1MeV, electrons >20MeV and protons >100MeV are required. The current progress in advanced laser driven sources will allow generating short, quasi-monochromatic bursts of protons, electrons, neutrons and coherent x- and gamma-rays of high energies.

References

[1] N.A. Tahir et al, New J. Phys. 12(2010) 073022

[2] S.H. Glenzer, G. Gregori, R.W. Lee et al. // Phys. Rev. Lett. 90 (2003) 175002.

[3] Wilks S.C., Kruer W.L., Tabak M., Langdon A.B. // Phys. Rev. Lett. 69 (1992) 1383-1386

* work supported by EMMI

Melting of carbon under extreme conditions characterized by X-ray scattering

D. Kraus[*1], *V. Bagnoud*[2], *A. Blazevic*[2], *A. Frank*[3], *D. O. Gericke*[4], *G. Gregori*[5], *A. Ortner*[1], *A. Otten*[1], *F. Roth*[1], *G. Schaumann*[1], *K. Siegenthaler*[1], *J. Vorberger*[4], *F. Wagner*[1], *K. Wünsch*[4], *and M. Roth*[1]

[1]TU Darmstadt, Germany; [2]GSI, Darmstadt, Germany; [3]Helmholtz-Institut Jena, Germany;
[4]University of Warwick, UK; [5]University of Oxford, UK

Introduction

X-ray scattering is a very powerful technique to study warm dense matter which means materials around solid density and temperatures of from several thousand to several hundred thousand kelvins [1]. It gives the possibility for the direct measurement of plasma parameters like temperature, density of free electrons, degree of ionization and the microscopic structure of a warm dense matter sample. Therefore, X-ray scattering is a central diagnostics for all three upcoming plasma physics experiments at FAIR (HIHEX, LAPLAS, WDM) which aim for a precise characterization of warm dense matter [2]. Hence, the accumulation of experience with X-ray scattering experiments at GSI and using the laser system PHELIX as pulsed X-ray source of high brilliance is of major importance for the success of these future experiments at FAIR.

Experiment

After a first successful proof-of-principle experiment on X-ray scattering from shock-compressed matter at GSI in 2011 [3], an advanced campaign was performed in February/March 2012 at the Z6 experimental area. The aim was to investigate the microscopic structure of carbon at the melting regime around 100 GPa (=1 Mbar) pressure. The laser system nhelix with pulse energies of 65 J at 1064 nm and pulse durations of 10 ns was used for the compression of graphite samples. The ns-option of the PHELIX system at Z6 (150 J, 1 ns, 527 nm) was focused on a Ti foil and created enough X-rays of Ti-He-α line radiation (4.75 keV) for a successful X-ray scattering experiment. In fact, a conversion efficiency of up to 5×10^{-3} could be achieved. The scattering angles were chosen to be 105° and 125° which ensures scattering in the non-collective regime (scattering on single electrons). Comparing the intensity of elastic scattering from tightly bound electrons to inelastic scattering from weakly bound electrons gives the possibility to determine an absolute value of the atomic/ionic structure factor S_{ii} of the shocked samples (see figure 1). Density and pressure inside the shock wave could be characterized by a classical measurement of shock and particle velocity resulting in 3.9 ± 0.2 g/cm^3 and 145 ± 17 GPa for the 2012 campaign as well as 3.9 ± 0.2 g/cm^3 and 86 ± 11 GPa for the 2011 campaign.

Simulations and results

In addition to the experiment, DFT-MD simulations calculating the microscopic structure of possible carbon phases which might be present inside the laser-driven shock have been perforemd. Comparing the experimentally obtained strucutre factors to the simulations gives the definite result that liquid carbon is present inside the laser-driven shock in both experiments [4]. This is in fact the first direct measurement which proves the existence of the liquid phase in this density and pressure regime and can be used to test corresponding theoretical phase diagrams. Thus, a successful method to characterize phase transitions in warm dense matter has been developed. Concerning the carbon solid-liquid phase transition, more sophisticated experiments at the VULCAN laser are scheduled for February/March 2013 and high precision experiments at the LCLS facility are proposed for end of 2013.

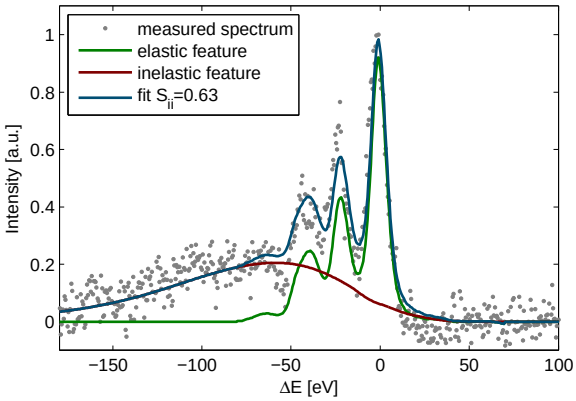

Figure 1: X-ray scattering spectrum from which the structure factor is deduced by determining the ratio of elastic and inelastic scattering. The elastic scattering profile is given by the source radiation spectrum which was measured in the experiment whereas the inelastic feature consists of the convolution of the source spectrum and a typical Compton profile of bound electrons.

References

[1] S. H. Glenzer, R. Redmer, Rev. Mod. Phys. 81, 1625 (2009)

[2] FAIR Baseline Technical Report (2006)

[3] D. Kraus et al., High Energy Density Physics 8, 46-49 (2012)

[4] D. Kraus et al., in preperation

* d.kraus@gsi.de

S- and P-polarized reflectivities of strongly correlated plasma

Yu. Zaporozhets[1], V. Mintsev[1], V. Gryaznov[1], V.Fortov[2], H. Reinholz[3] and G. Röpke[3]

[1]IPCP RAS, Chernogolovka, Russia; [2]JIHT RAS, Moscow, Russia; [3]University of Rostock, Germany

The experimental data from investigations of optical properties of a strongly correlated plasma is an important cornerstone to construct theoretical models for the description of warm dense matter. The analysis of the response of a dense plasma to electromagnetic waves of moderate intensity can be used as a tool to investigate the validity of the physical models describing the behavior of matter under extreme conditions, high temperatures and pressures.

The plasma created has transitive surfaces with a density profile. The research of the transitive layer of a explosively driven dense plasma can be carried out using the technique of inclined probing by polarized electromagnetic waves. Angular dependence of S- and P-polarized reflectivities at several wavelengths can be used in the integration of Maxwell equations to construct the spatial profile of the density of charge carriers. In this paper, we report new results of S- and P-polarized reflectivity measurements of a non-ideal plasma at $\nu_{las} = 2.83 \cdot 10^{14}$ s^{-1} (λ_{las} = 1064 nm), $\nu_{las} = 4.33 \cdot 10^{14}$ s^{-1} (λ_{las} = 694 nm) and $\nu_{las} = 5.66 \cdot 10^{14}$ s^{-1} (λ_{las} = 532 nm).

To generate the non-ideal plasma, we used explosively driven shock waves which lead to compression and irreversible heating of xenon and to measure the dense xenon plasma polarized reflectivity index, a pulsed RUBY and YAG+KTP system with a four-channel pulse high-speed device for determination of the Stokes vector components was used [1]. The device allowes to measure the intensity of the reflected laser beam for four azimuthal angles and was equipped with filters for selection of probing frequency.

In order to determine the thermodynamic parameters and composition of plasma suitable calculations have been carried out. Working with a grand canonical ensemble, virial corrections have been taken into account due to charge-charge interactions (Debye approximation). Short-range repulsion of heavy particles was considered within the framework of a soft sphere model [2-3].

In Figure 1, the experimental data and results of solving of Maxwell equations using the generalized Drude formula and the dynamical collision frequency in Born approximation [4] are shown. Results of calculations with layer temperature profile and ea-collisions as factor are shown in Figure 1 too.

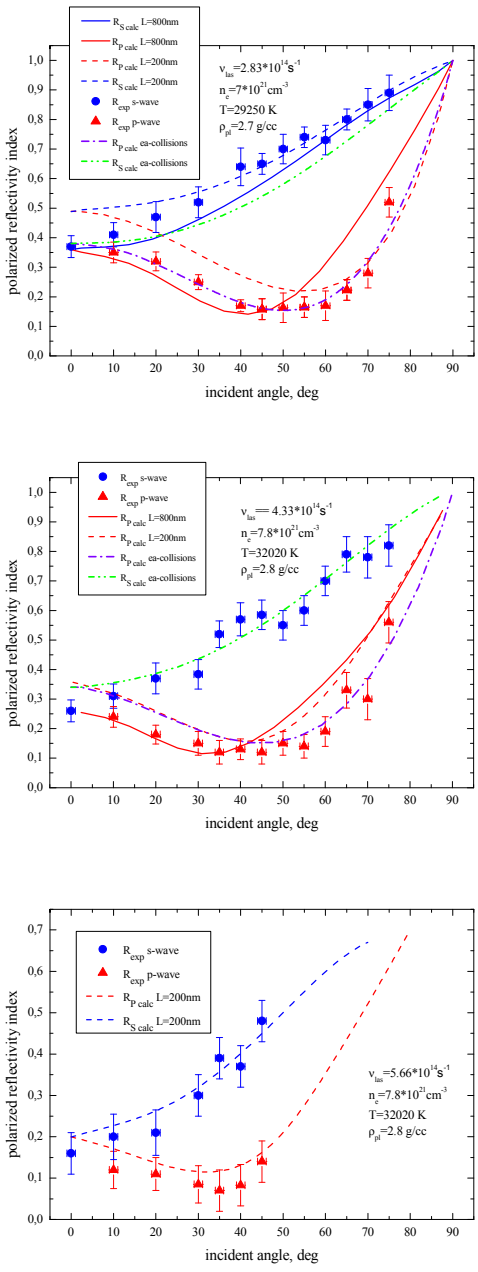

Figure 1: S- and P-polarized reflectivities calculated in comparison to the experimental data.

References

[1] Zaporoghets Yu.B., Mintsev V.B., Gryaznov V.K., Fortov V.E., Reinholz H., and Röpke G. // J. Phys. A: Math. Theor. 2009. V. 42. P. 214063.

[2] Ebeling W., F¨orster A., Fortov V., Gryaznov V. and Polishchuk A. Thermophysical Properties of Hot Dense Plasmas. Stuttgart: Teubner, 1991.

[3] Fortov V.E., Gryaznov V.K., Mintsev V.B., Ternovoi V.Ya., Iosilevski I. L., Zhernokletov M.V. and Mochalov M.A. // Contrib.Plasma Phys. 2001. V. 41. P. 215.

[4] Reinholz H., Röpke G., Wierling A., Mintsev V.B. and Gryaznov V.K. // CPP. 2003. V. 43. P. 3.

Prototype of Real-time Hard X-ray Imaging System and Spectrometer

K.Li[1,2,3], P.Neumayer[1,2,3]

[1] *ExtreMe Matter Institute, Darmstadt, Germany*; [2] *Helmholtzzentrum fur Schwerionenforschung GSI, Germany*; [3] *Frankfurt Institute for Advanced Studies (FIAS).*

Large scale (~mm), high-z targets are used in many laboratories as well as in the future FAIR in the research of warm dense matter and high energy density plasmas, and sub-GeV photon radiography is one important diagnostic. Besides sub-GeV photons, hard x-ray photons (E>100 keV) can also penetrate ~mm thick high-Z material, and such photons can be generated in the interaction of intense laser pulse with target, with conversion efficiency up to 10^{-4} and spot size as small as 10 μm [1,2]. This bremsstrahlung radiation then becomes another candidate for the above radiography. In many experiments, in-line or real-time diagnostic is necessary either due to long pump/vent time or high repetition rate of sources, which makes the popular image plate no longer useful. In this way, we are building a scintillator/screen-based hard x-ray imaging system to perform real-time imaging, and aiming to achieve ~10 ps temporal resolution, ~10 μm spatial resolution, ~1mm field of view for ~1mm thick high-Z targets. It should also work as a real-time x-ray spectrometer, working below 1 MeV.

The prototype is a point-projection, scintillator-based, lens-coupling, visible-ccd-measurement portable system. The scintillators/screen are LYSO, BGO and LANEX. In October 2012, the prototype was first tested in Phelix laser facility, compared with image-plate-based system. The laser parameters are ~100 Joules, ~picosecond, ~10 μm foci, intensity up to 10^{19} Wcm^{-2}. The irradiated bremsstrahlung images the objects to scintillators/screen, and then the fluorescence from scintillator/screen is imaged by lens pair to pco ccd camera. For some shots, we mount copper and tantalum filters of various thickness to measure the spectra. Fig.1 shows that ~10 mm thick, middle/high-Z target can really be imaged in our condition. From other results and analysis, it is known that ~100 μm spatial resolution can be achieved on scintillator/screens, corresponding to 20 μm resolution on object with 5x magnification. And in the energy range 50 keV~1MeV, the system can achieve single-photon imaging, bypassing the detection capability of image plate. The x-ray spectra measured in the system fits with that of electron spectra measure by e-spec for energy range of 20~200 keV. By changing filters and thickness of scintillators, we will be able to measure energy spectra up to 1 MeV.

To better understand the system, we plan to do calibration with 5 keV radioactive source and 1~2 MeV DALINAC photon source, also Monte Carlo simulation of transport processes of high-energy photons in both filters and scintillators will be performed. Expensive fiber bundle coupling will also be utilized if we have enough funding. We hope to have better results in the next experiment.

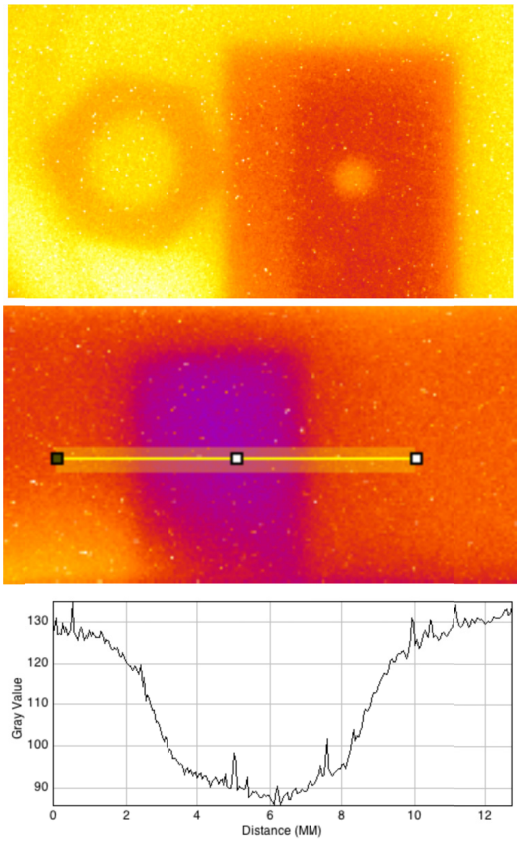

Figure 1: Images of objects by LYSO-based system. Above: M4 nut (3 mm thick iron) and Tantalum layers (1 mm and 0.5 mm thick) with 1.5 mm through hole on 5 mm thick copper; Middle: 6-mm diameter Tantalum cylinder on 5 mm thick copper: Below: lineout of Tantalum cylinder.

References

[1] R. Tommasini, S. P. Hatchett, D. S. Hey, C. Iglesias, N. Izumi, et al. Physics of Plasmas 18, 056309 (2011)

[2] R. Tommasini et al. Review of Scientific Instruments, 79, 10E901 (2008).

Development of a high current gas discharge switch for the FAIR magnetic horn*

C. Hock[1], B. Brünner[1], A. Faber[1],M. Iberler[1], J. Jacoby[1], G. Loisch[1], A. Schönlein[1] and J. Wiechula[1]
[1]IAP - Goethe Universität, Frankfurt, Germany

The planned Facility for Antiproton and Ion Research (FAIR) is a new international accelerator laboratory at the GSI in Darmstadt, Germany. The main focus at this facility is aimed to heavy-ion research as well as protons and antiprotons colliding experiments. To produce these antiprotons (3 GeV), protons (29 GeV) will be aimed at a target (e.g. Copper). In order to focus these antiprotons for the storage in a synchrotron, a strong magnetic field will be applied by a so called magnetic horn. To generate the necessary high magnetic field for this application the designed stripline of the pulse forming network (PFN) has to handle a peak current of 400 kA with a pulse length of 20µs. Currently the only possibility to handle this amplitude is are mercury filled Ignitrons. Another application for high-power switches is the FAIR SIS injection and extraction magnets. The requirements for this switch are a hold-off voltage of about 80 kV and maximum currents of about 8 kA with a pulse length of a few µs.

The plasma physics working group at the University of Frankfurt develops a mercury free switch, which is able to replace the Ignitrons in the PFN of the magnetic horn. The challenge for the development of a switch for such high currents is to reduce the local electrode erosion. For that we propose a gas switch that generates an accelerated plasma to minimize the attrition.

The experimental setup of the switch consists of coaxial electrodes, similar to the geometry used for plasma focus devices [1]. To reach a high hold-off voltage, the setup is designed for the left hand side of the Paschen branch. One important feature of a high-voltage and high-current switch is the reliability for triggering. The main discharge between the coaxial electrode system will be initiated by a trigger predischarge. With an external triggering a gas breakdown is initiated at the outer electrodes and forms a conductive plasma sheath which penetrates through holes to the inner electrodes.

After the ignition of the main discharge between the coaxial electrode system and due to the interaction of the induced radial magnetic field with the plasma, the gas discharge will be accelerated to the open end of the coaxial electrode system. This acceleration of the plasma sheet is due to the Lorentz force, which interacts with the discharge. It is given by:

$$\vec{F} = \int dV \; J \times B$$

Therefore the switch will be called a Lorentz Drift Switch (LDS). For already designed LDSs the maximum current is 33 kA with a current rise time of 15 kA/µs. As a working gas Nitrogen and Argon were used.

For a further reduction of erosion and to provide enough charged particles for the current transport, several of these coaxial devices will be stacked together in a parallel, multiple electrode system. In order to synchronize the plasma sheets, the single tubes will be connected with each other across a vertical arrangement of boreholes at the outer electrodes. The following Fig. 1 shows a schematic drawing of the experimental set up of the first prototype of the multi-channel Lorentz Drift Switch.

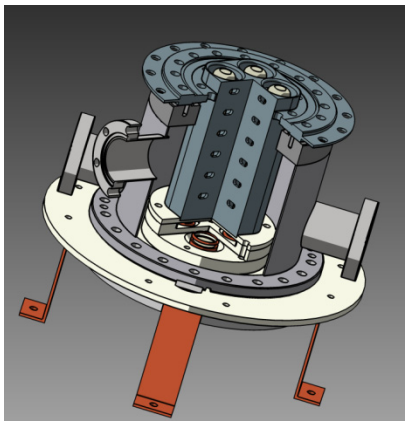

Figure 1: Schematic drawing of a multi-channel LDS.

The designed multi-channel LDS is a low inductive, fast current, low pressure gas discharge switch. Due to the simple setup and the reduction of erosion we will introduce a low cost, and rugged high-current switch for applications in further high-energy experiments. With the introduced setup we hope to provide a real alternative for such high-current applications, when common Ignitrons were used at FAIR so far.

* Work supported by a HGS-HIRe scholarship.

References

[1] J. Jacoby, C. Bickes, D.H.H. Hoffmann, C. Hofmann, J. Philipps, Experimental Study to Accumulate, Accelerate and Focus a Massive Plasma Beam onto a Target Fusion Engineering and Design 44 (1999) 331.

[2] A. Görtler, “Untersuchungen von gepulsten Oberflächenentladungen an Dielektrika und deren Anwendung zur Triggerung eines Pseudofunkenschalters”, Diplomarbeit, Universität Erlangen-Nürnberg (1986)

[3] M. Iberler, R. Bischoff, K. Frank, I. Petzenhauser, A. Rainer, J. Urban, Fundamental investigation in two flashover-based trigger methods for low-pressure gas discharge switches, IEEE on Plasma Science, Vol 32 (1), 208-214, 2004.

Investigation of the parameters of a dense, inductively generated stripping plasma for the FAIR-Project*

A. Fedjuschenko, J. Jacoby, and C. Teske

Plasma physics Group, Institute of Applied Physics, Goethe University, 60438 Frankfurt, Germany

As higher charge states are essential for short acceleration distances in modern facilities like FAIR, a screw-pinch plasma device is set up at the IAP Plasma physics group in the Goethe University Frankfurt. This screw-pinch device is set up as an alternative solution to the theta-pinch device[1] and as possible alternative solution to the established stripping foils.

The objective of the experiment is the investigation of a new coil configuration, and the generation and maintenance of dense plasmas with different ignition parameters.

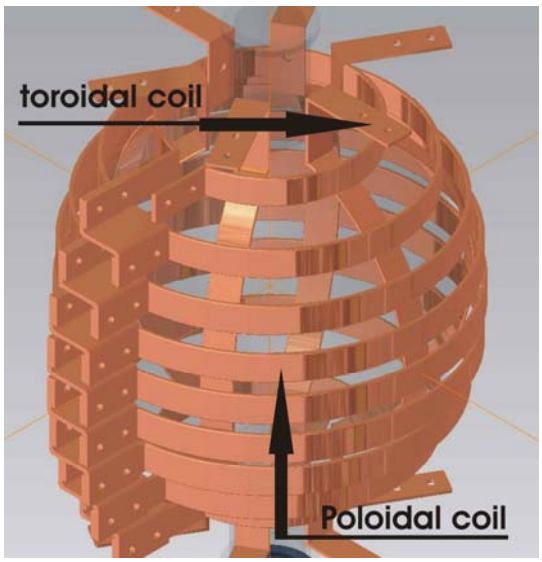

Figure 1: The construction of the coil

Figure 1 shows the configuration of the screw-pinch coils. This configuration consists of two coils, which are superimposed. The inner coil has 6 poloidal turns which are oriented along the Z-axis. The outer coil has 9 toroidal turns, which are in the XY-plane. The total inductance of the set up is L≈11 µH. The energy storage of the device consists of four capacitors with a capacitance of 25 µF each at a maximum charging voltage of 9300 V. The modular design of the capacitor bank can use capacitors single (25µF), parallel (50, 75, 100 µF) and in series (12,5 and 25 µF). A thyratron (TDI1-200k/25H) is used in order to switch the high voltage and current. The argon gas is used for the experiment.

Figure 2 shows a signal of the photodiode with a signal of a current curve. The photodiode signal is detected in the center of the recipient. The duration of the plasma discharge is about 500 µs, and is repeatedly compressed

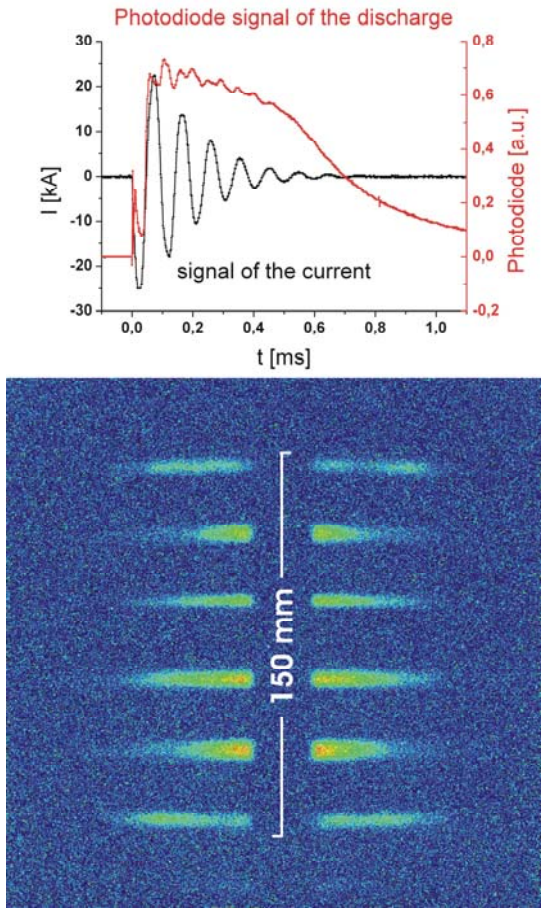

Figure 2: Above-the signal of the photodiode and current; below- plasma discharge at 74 µs

to a cylindrical shape. The duration of the compression phase is about 10 µs and the length of the discharge is 150mm. The achieved average electron density of the plasma is $1{,}6*10^{16}$ cm^{-3}. The maximum efficiency of the structure is achieved at a pressure of about 140 ± 20 Pa and is approximately η = 70% for frequency of 10 kHz (Capacitance 25 µF) and charging voltage 18 kV.

References

[1] C. Teske, Y. Liu, S. Blaes and J. Jacoby, "Electron density and plasma dynamics of a spherical thete pinch", Phys. Plasmas 19, 033505 (2012)

* This project was supported by BMBF and HGS-HIRe

Interaction of Ca^{10+} ion beam with a hydrogen theta-pinch plasma*

G.Xu[1, 3, 5], J. Jacoby[1], Y.Zhao[3], G.Xiao[3], G.Loisch[1], T. Rienecker[1], K.Weyrich[2], K.Cistakov[1], S.Savin[4], A.Schönlein[1], O.Rosmej[2], J. Wiechula[1], R. Gavrilin[4], A.Blazevic[2], M.Iberler[1], C.Hock[1], R.Maeder[1]

[1]Goethe University of Frankfurt, Frankfurt am Main, Germany; [2]GSI, Darmstadt, Germany; [3]IMP, Lanzhou, China; [4]ITEP, Moscow, Russia; [5]UCAS, Beijing, China

Introduction

The interaction of heavy ions with plasma is important for research in a field like warm dense matter (WDM), laboratory astrophysics and inertial confinement fusion (ICF), where the high repetition rate of ion-beam pulses are of an advantage as a driver. Also applications like using the plasma as an efficient beam-stripper are of importance with respect for the future Facility for Antiproton and Ion Research (FAIR).

Experiment

The Plasma Physics Group of the Goethe University in Frankfurt has developed and built a spherical Theta-pinch device [1, 2]. Different than in a Z-pinch, there is no need for electrodes in direct contact with the plasma.

Fig. 1 shows the set-up of the Theta pinch device. A spherical glass vessel is encircled by 7 segments of a copper coil. The coils together with a capacitor bank (37.5 µF) and a thyristor-stack [3] is part of a LRC electric circuit. At an operation voltage of 14 kV the stored energy in the capacitors is 3.7 kJ. Once triggered by the thyristor-stack, the energy will be released in the discharge in several milliseconds. The peak current in the circuit reaches up to 50 kA. Hydrogen is chosen as target gas in the vessel because hydrogen is easily fully ionized which is an advantage for obtaining a high charge state of the beam ions. The plasma is created by discharging the energy of the capacitor bank into the gas volume, which leads to an alternating strong current in the coil ionizing the gas and resulting also in a strong magnetic field compressing the plasma (pinch-effect). The Theta-pinch is differentially pumped over a two-stage aperture-system on both sides of the glass vessel, reducing the initial gas pressure of up to 1 mbar to the vacuum of 10^{-5} mbar of accelerator beam line the device is integrated in for measurements.

The interaction experiments were carried out at the Z6 experimental area of GSI. The Theta-pinch was integrated in the accelerator beam line, where a 3.6 MeV/u Calcium^{10+} pulsed ion beam with a 108 MHz frequency is provided, resulting in a time-structure with 9 ns distance between the micro beam-pulses, while the maximum duration of the macro-pulse is 5 ms. The ion-beam-pulse, triggering of the discharge and timing of diagnostic tools were synchronized by a high precision trigger system.

Results

Figure 2 shows the Ca-beam signal obtained by a stop detector, black curve. The blue curve is the light emission from the plasma which is detected by a photo diode. Here the beam micro pulse was 4 ms. During the first 100 µs, until the discharge is triggered, the beam is interacting

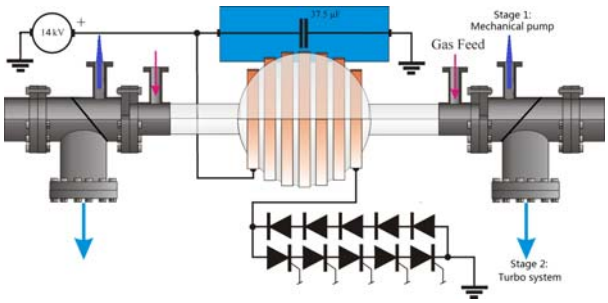

Figure 1: Schema of the set-up of the Theta-pinch device

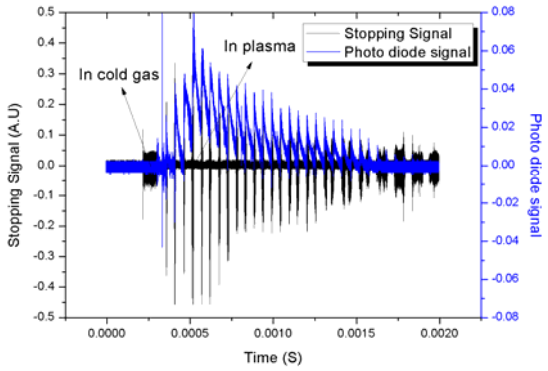

Figure 2: Beam transmission and plasma light emission

with cold gas. Later when the hydrogen is ionized, visible in figure 2 by the start of the signal from the light emission (blue curve) the target is in the plasma state. The light emission is not constant but oscillating, following the oscillations in the discharge current. Fig. 2 also shows the transmission of the ion beam during the whole time of the plasma duration. The ion-beam signals show the same oscillating behaviour like the light emission, the pulse intensity increases even over the transmitted pulse intensity in cold gas and disappears at other times, this result depends probably from the time dependent magnetic field imaging the beam ions like a solenoid.

References

[1] C. Teske, J. Jacoby, F. Senzel, and W. Schweizer, Physics of plasmas 17, 043501 (2010)

[2] C. Teske, Y. Liu, S. Blaes, and J. Jacoby, Physics of plasmas 19, 033505 (2012)

[3] C. Teske, J. Jacoby, W. Schweizer, and J. Wiechula, Review of scientific instruments 80, 034702(2009)

*This project has been funded by BMBF (06FY9082I), HIC for FAIR , GSI HIRe and HGS-HIRe.

First preparatory experiments on NEET at GSI

A. Frank[1], *V. Bagnoud*[1], *M. Basko*[6], *A. Blazevic*[1], *T. Bonnet*[2], *M. Comet*[2], *J.M. Daugas*[3], *D. Denis-Petit*[2], *A. Ebran*[3], *L. Gaudefroy*[3], *F. Gobet*[2], *G. Gosselin*[3], *V. Meot*[3], *P. Morel*[3], *O. Roig*[3], *M. Roth*[4], *M. Tarisien*[2], *An. Tauschwitz*[5], *M. Versteegen*[2], *and F. Hannachi*[2]

[1]GSI/Helmholtz-Institute Jena, Germany; [2]CENBG, France; [3]CEA DIM DIF, France; [4]TU Darmstadt, Germany; [5]Univ. of Frankfurt, Germany; [6]KIAM Moscow, Russia

Nuclear excitation by electronic transition (NEET) [1] designates a mechanism of nuclear excitation induced by a transition between two bound states of the atomic system. Depending on the considered element, the surrounding environment of different atomic configurations may influence the decay rates of isomeric states.

This is supposed to be the case for ^{84}Rb in a plasma environment [2]. As shown in Fig. 1, it is possible to excite a nucleus from an isomeric state to a higher state with different half-life. In ^{84}Rb this transition is around 3.5 keV. The ^{84}Rb isomeric state could be efficiently produced by the Unilac with a 76Ge(11B, 3n)84Rb reaction, alternatively with a 76Ge(12C, p3n)84Rb reaction. For an efficient NEET rate, high charge states (30-34+) are needed to have an efficient energy matching. Depending on different plasma models, especially for higher Z-elements the ionic structure depending on the temperature becomes hard to predict - LTE calculations suggest 300-400 eV, while non-LTE calculations suggest 2-3 keV to reach the desired ionization degrees.

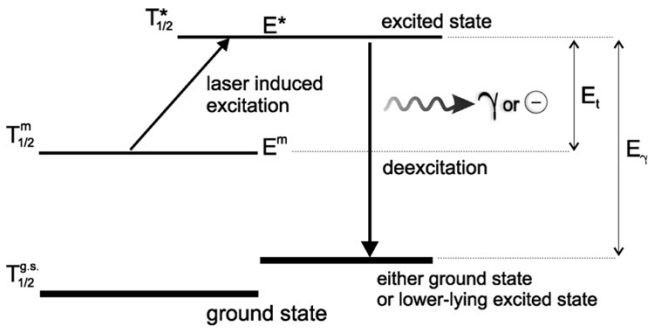

Figure 1: Principle of the NEET process

To determine whether the PHELIX parameters available at Z6 in the long pulse option are sufficient to reach these high charge states, we did a first test run to record the spectra of a RbF target. Two spectrometers recorded time integrated spectra of the target and they were used in different configurations to observe different energy ranges. One was based on a HoPG crystal for high reflectivity, the other one was a Mica crystal for high spectral resolution.

The Phelix laser was used at an energy of 150 J(2ω) at a pulse length of 1.4 ns with a focus diameter of d=100μm. This corresponds to an intensity of 10^{15}W/cm^2 on target. Additionally, we tried to increase the laser energy by using a pulse train of Phelix, each laser pulse at an energy of 150 J, but separated by 3-4 ns to fulfill the damage threshold criterions.

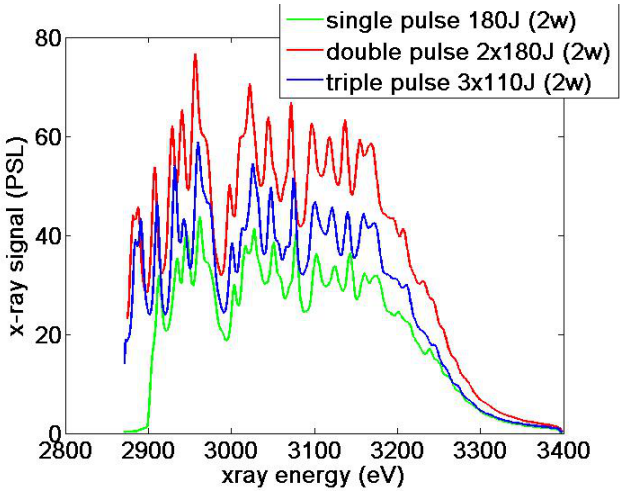

Figure 2: Different spectra recorded with a HoPG crystal

Some of the spectra recorded with the HoPG spectrometer are shown in Fig. 2. They do not show dramatic differences when the energy is increased, however the overall amount of x-rays is increased.

The analysis of the spectra in detail is still ongoing. The difficulty is that there are no experimental data and only limited theoretical calculations available for Rb plasmas to compare them to. The results of a first analysis indicate that we observed charge-states in the range of 25-27+, which would be a bit too low for our experiment. However we intend to continue our efforts into this direction. The laser focus will be further optimized by using a deformable mirror at the Phelix laser and we intend to exploit the advantages of undercritical foam targets which are highly doped with high-Z elements to reach higher temperatures. In addition, we want to specifically analyze the corona of the target to see, whether the undercritical part reaches a sufficiently high temperature and charge states to perform a final experiment at GSI to observe and measure the NEET rate of ^{84}Rb in a plasma.

References

[1] M.Morita, Progr. Theor. Phys. 49, 1574 (1973)

[2] F.Gobet et al., Nucl.Instr. and Meth. A 653, 80 (2011)

g factor of few-electron highly charged ions *

D. A. Glazov[1,2], *A. V. Volotka*[1,2], *V. M. Shabaev*[1], *I. I. Tupitsyn*[1], *and G. Plunien*[2]

[1]St. Petersburg State University, Russia; [2]Technische Universität Dresden, Germany

The g factor of highly charged ions is an excellent instrument for probing bound-state QED effects in the presence of a magnetic field, and, moreover, gives access to an accurate determination of fundamental physical constants and nuclear parameters. Few-electron ions are of particular interest: On the one hand, apart from to one-electron QED effects they provide an excellent possibility to probe also many-electron QED corrections. On the other hand, simultaneous investigations of one- and few-electron ions allow us to construct specific differences, where the uncertainty originating from the lack of knowledge of the nuclear properties can be almost eliminated. Studying of a specific difference of the g factors of H- and B-like ions [1] can provide an independent determination of the fine structure constant in the domain of strong external field.

The high-precision measurement of the g factor has been recently accomplished for Li-like $^{28}Si^{11+}$ [2]. The measurement for B-like $^{40}Ar^{13+}$ is already in preparation in the framework of the ARTEMIS project [3]. Here we report on recent progress in the theoretical predictions for these systems.

The theoretical contributions to the g factor of Li-like ions can be split into one-electron and many-electron parts, respectively. The former are similar to the corresponding corrections to the g factor in H-like ions. The latter, which define the difference between the g factors of H- and Li-like ions, are mainly due to screened QED-radiative and the interelectronic-interaction corrections. Until now, the interelectronic-interaction contributions have mainly determined the total theoretical uncertainty of the g factor of Li-like ions for all values of Z. Recently, we have performed the rigorous QED evaluation of the two-photon exchange corrections to the g factor [2, 4], and, thus, improved the total theoretical accuracy for the g factor of $^{28}Si^{11+}$ by almost a factor of 2. A comparison of the experimental value $g_{\rm exp}[2s] = 2.000\,889\,889\,9(21)$ with the corresponding theoretical prediction $g_{\rm th}[2s] = 2.000\,889\,909(51)$ allows to probe the two-photon exchange correction on a level of about 1%. This provides the most stringent test of many-electron QED effects in the presence of a magnetic field.

The ARTEMIS project will implement the laser-microwave double resonance spectroscopy to measure with ppb accuracy the Zeeman splittings of both ground state $(1s)^2\,(2s)^2\,2p_{1/2}$ and first excited state $(1s)^2\,(2s)^2\,2p_{3/2}$ in boron-like argon [3]. Recently, we have performed accurate QED calculations of the g factor of these states [5]. The $1/Z$-term of the interelectronic interaction is calculated within the rigorous QED approach. For the ground state the higher-order contributions are evaluated within the large-scale configuration-interaction method with the Dirac-Fock and Dirac-Fock-Sturm basis functions (CI-DFS). The one-loop self-energy correction for P_J-states is calculated employing the Kohn-Sham potential, that partly takes into account the screening effect. The higher-order (two-loop) QED effects are accounted for to zeroth order in αZ. The recoil correction is evaluated to first order in m/M, also with the Kohn-Sham screening potential. The present results $g_{\rm th}[2p_{1/2}] = 0.663\,647(1)$ and $g_{\rm th}[2p_{3/2}] = 1.332\,285(3)$ are in agreement with those reported in Ref. [6] and are by order of magnitude more precise.

We also considered the effects of second- and third-order in the magnetic field, which can be expressed in the following way: $\Delta E_A^{(2)}(B) = g_J^{(2)}(M_J)(\mu_0 B)^2/(mc^2)$ and $\Delta E_A^{(3)}(B) = g_J^{(3)}(M_J)(\mu_0 B)^3/(mc^2)^2$, where μ_0 is the Bohr magneton and m is the electron mass. Accordingly, the results for $g_J^{(2)}$ and $g_J^{(3)}$ for B-like Ar are obtained as:

$$
\begin{aligned}
g^{(2)}_{1/2}(\pm 1/2) &= -39.5\times 10^3, \quad g^{(3)}_{1/2}(\pm 1/2) = \pm 2.5\times 10^9,\\
g^{(2)}_{3/2}(\pm 1/2) &= 41.0\times 10^3, \quad g^{(3)}_{3/2}(\pm 1/2) = \mp 2.5\times 10^9,\\
g^{(2)}_{3/2}(\pm 3/2) &= 1.0\times 10^3, \quad g^{(3)}_{3/2}(\pm 3/2) = \mp 5.7\times 10^3.
\end{aligned}
$$

The ARTEMIS experimental setup implies the presence of a magnetic field of about 7 Tesla. This leads to the relative contribution of the quadratic effect $|\Delta E_A^{(2)}/\Delta E_A^{(1)}| = 0.9\times 10^{-4}$ for the $2p_{1/2}$ state and 0.5×10^{-4} for the $2p_{3/2}$ state. The relative contribution of the cubic effect yields $|\Delta E_A^{(3)}/\Delta E_A^{(1)}| = 4.7\times 10^{-9}$ for the $2p_{1/2}$ state and 2.3×10^{-9} for the $2p_{3/2}$ state. Therefore, the second- and third-order contributions can clearly be disregarded at the anticipated ppb-level of accuracy. The above results are closely related to recent experimental investigations [3], where details on the measurement procedure and the identification of higher-order effects can be found.

References

[1] V. M. Shabaev *et al.*, Phys. Rev. Lett. **96**, 253002 (2006).

[2] A. Wagner *et al.*, Phys. Rev. Lett. **110**, 033003 (2013).

[3] D. von Lindenfels *et al.*, accepted to Phys. Rev. A.

[4] A. V. Volotka *et al.*, in preparation.

[5] D. A. Glazov *et al.*, accepted in Phys. Scr. (2013).

[6] R. Soria Orts *et al.*, Phys. Rev. A **76**, 052501 (2007).

* Work supported by GSI and DFG

Parity nonconservation effects in the dielectronic recombination of polarized electrons with heavy He-like ions *

V. A. Zaytsev[1], *A. V. Maiorova*[1], *V. M. Shabaev*[1], *A. V. Volotka*[1,2], *and G. Plunien*[2]

[1]St. Petersburg State University, Russia; [2]Technische Universität Dresden, Germany

Parity nonconservation (PNC) experiments with heavy few-electron ions can provide new possibilities for tests of the Standard Model in the low-energy regime [1, 2]. In contrast to neutral atoms, the atomic structure of heavy few-electron ions can be calculated to a high accuracy. To date, various schemes [3, 4, 5, 6, 7, 8, 9] for PNC measurements in highly-charged ions were suggested. Here we report on recent studies of the PNC effect in the dielectronic recombination of polarized electrons with He-like ions.

The enhancement of PNC-effect in atomic systems takes place for close-lying opposite-parity levels. As such levels, we consider the $((1s2s)_0\, ns)_{1/2}$ and $\left(\left(1s2p_{1/2}\right)_0 ns\right)_{1/2}$ states, which are found to be close for $4 \leq n \leq 7$, $Z \sim 60$, and $Z \sim 90$, where n is the principal quantum number of the third electron and Z is the nuclear charge number. The related energy differences are listed in Table 1.

Table 1: The energy difference $E_{\left(\left(1s2p_{1/2}\right)_0 ns\right)_{1/2}} - E_{\left((1s2s)_0 ns\right)_{1/2}}$, in eV, for the values of Z and n, which seem to be the most promising for enhancement of the PNC effect.

Z	$n=4$	$n=5$	$n=6$	$n=7$
54	-0.489(35)	-0.787(34)	-1.21(4)	-1.47(4)
60	3.49(6)	1.42(6)	-0.222(56)	-0.376(56)
62	3.90(6)	1.66(6)	0.818(64)	-0.103(64)
64	4.40(7)	2.06(7)	1.14(7)	0.699(74)
88	9.17(30)	5.34(29)	3.86(29)	3.17(29)
90	8.27(47)	4.13(47)	2.51(47)	1.75(47)
92	6.69(27)	2.97(28)	-1.07(28)	-1.60(28)

We consider the process of the dielectronic recombination of a polarized electron with a heavy He-like ion, being originally in the ground state, into the doubly-excited $d_1 = \left(\left(1s2p_{1/2}\right)_0 ns\right)_{1/2}$ and $d_2 = ((1s2s)_0\, ns)_{1/2}$ states. In order to evaluate the PNC effect, we consider the cross section without the PNC effect, $\sigma_0 = \left(\sigma_{1/2} + \sigma_{-1/2}\right)/2$, and the P-violating contribution, $\sigma_{\rm PNC} = \left(\sigma_{1/2} - \sigma_{-1/2}\right)/2$, where $\sigma_{\pm 1/2}$ are the cross sections for the $\pm 1/2$ helicity (spin projection onto the electron momentum direction) of the incident electron, respectively.

In the process under investigation, the most pronounced PNC effect is expected in the uranium ($Z = 92$) ion, when the energy of the incident electron tuned in resonance with $\left(\left(1s2p_{1/2}\right)_0 6s\right)_{1/2}$ state. The corresponding behaviour of $\sigma_{\rm PNC}$ as a function of the energy of the incident electron is presented in Fig. 1. In this case the PNC asymmetry, $|\sigma_{\rm PNC}|/\sigma_0$, reaches a value of about 1.5×10^{-5}. The analogous process of the dielectronic recombination of polarized electrons with the H-like ions at $Z < 60$ was studied by Gribakin *et al.* in Ref. [10]. The PNC asymmetry of that process was found to amount of about 5×10^{-9}, which is by several orders of magnitude smaller than the effect as we have reported here.

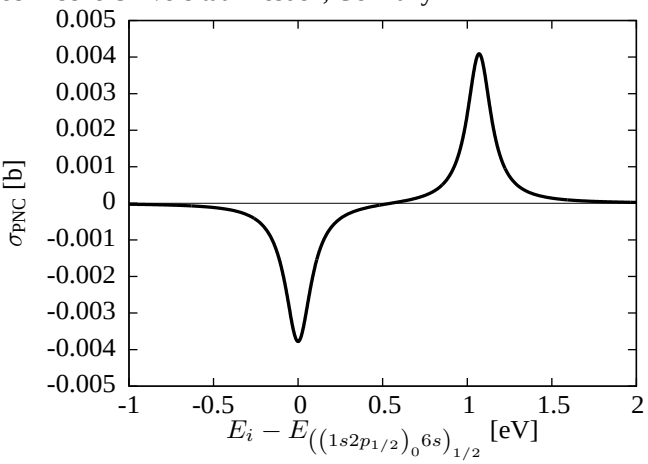

Figure 1: PNC cross section of the dielectronic recombination process into the states $\left(\left(1s2p_{1/2}\right)_0 6s\right)_{1/2}$ and $((1s2s)_0\, 6s)_{1/2}$ for $Z = 92$. The difference $E_i - E_{\left(\left(1s2p_{1/2}\right)_0 6s\right)_{1/2}}$ determines uniquely the energy of the incident electron.

References

[1] I. B. Khriplovich, Phys. Scr. **T112**, 52 (2004).

[2] J. S. M. Ginges and V. V. Flambaum Phys. Rep. **397**, 63 (2004).

[3] V. G. Gorshkov and L. N. Labzowsky, JETP Lett. **19**, 394 (1974).

[4] A. Schäfer *et al.*, Phys. Rev. A **40**, 7362 (1989).

[5] L. N. Labzowsky *et al.*, Phys. Rev. A **63**, 054105 (2001).

[6] A. V. Maiorova *et al.*, J. Phys. B: At. Mol. Opt. Phys. **42**, 205002 (2009).

[7] V. M. Shabaev *et al.*, Phys. Rev. A **81**, 052102 (2010).

[8] F. Ferro *et al.*, Phys. Rev. A **83**, 052518 (2011).

[9] A. V. Maiorova *et al.*, J. Phys. B: At. Mol. Opt. Phys. **44**, 225003 (2011).

[10] G. F. Gribakin *et al.*, Phys. Rev. A **72**, 032109 (2005); Phys. Rev. A **80**, 049901(E) (2009).

* Work supported by GSI and DFG

Parity–violating transitions in beryllium–like ions*

A. Surzhykov† [1,2,3], *S. Fritzsche*[3,4], *A. V. Maiorova*[5], *V. M. Shabaev*[5], *and Th. Stöhlker*[1,3,4]

[1]GSI, Darmstadt, Germany; [2]University of Heidelberg, Germany; [3]Helmholtz Institute Jena, Germany; [4]University of Jena, Germany; [5]St. Petersburg State University, Russia

Parity–violation (PV) phenomena in highly–charged ions currently attract much attention (see e.g. [1, 2]). In particular, many studies are focused on the mixing between opposite–parity atomic levels caused by the weak electron–nucleus interaction. A number of proposals have been made to detect such a mixing and, hence, to explore the basic parameters of the electroweak theory. Most of theses proposals have dealt up to now with the near–degenerate $1s2s$ and $1s2p_{1/2}$ states of helium–like *heavy* ions for which the PV effects are significantly enhanced. In the high–Z domain, however, the lifetimes of such singly–excited states are shorter than $\tau \sim 10^{-10}$ seconds which makes the observation of the parity–violating phenomena in two–electron systems rather challenging. During the recent years, therefore, particular interest has been given to other few–electron species whose *long–lived* levels might be mixed by the weak interaction.

Owing to their shell structure, beryllium–like heavy ions may provide an alternative and promising tool for studying atomic PV phenomena. For the case of *zero* nuclear spin, the first excited state of these ions, $1s^2\,2s\,2p\;{}^3P_0$, can decay to the $1s^2\,2s^2\;{}^1S_0$ ground level solely by the strongly suppressed two–photon $E1M1$ emission and, hence, has a lifetime of the order of seconds. Moreover, the energy splitting between these two levels does not exceed 260 eV even for the heaviest ions, thus leading to a rather remarkable ${}^1S_0$–${}^3P_0$ parity–violating mixing [3]. To observe such a mixing, we have recently proposed to utilize the source of the coherent extreme ultraviolet (EUV) radiation and to induce a single–photon transition between the metastable $1s^2\,2s\,2p\;{}^3P_0$ and short–lived $1s^2\,2s\,2p\;{}^3P_1$ levels [4]. Since the ${}^3P_0$ state has a small PV–admixture of the ground one, such an absorption can proceed not only via the allowed $M1$ but also the parity–violating $E1$ channel (see Fig. 1).

The interference between the $M1$ and PV–$E1$ excitation channels becomes "visible" if the $1s^2\,2s\,2p\;{}^3P_0 \to 1s^2\,2s\,2p\;{}^3P_1$ transition is induced by the circularly polarized light. In this case the photoexcitation cross section reads as [4]:

$$\sigma_\lambda = \sigma_{M1}\,(1 + \lambda\epsilon)\;, \qquad (1)$$

where $\lambda = \pm 1$ for the right– and left–hand polarization, σ_{M1} describes the leading, parity–preserved ${}^3P_0 \to {}^3P_1$ magnetic dipole channel, and the so–called asymmetry coefficient ϵ is given by:

$$\epsilon = -2\,\eta_{PV}\,\frac{\langle 1s^2 2s2p\;{}^3P_1\,\|E1\|\,1s^2 2s^2\;{}^1S_0\rangle}{\langle 1s^2 2s2p\;{}^3P_1\,\|M1\|\,1s^2 2s2p\;{}^3P_0\rangle}\,. \qquad (2)$$

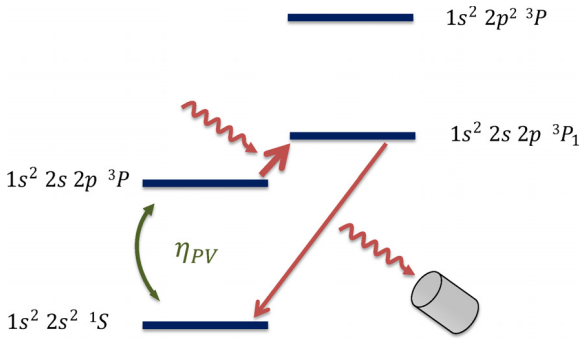

Figure 1: Proposed scheme for measuring the PV–mixing between the ground $1s^2\,2s^2\;{}^1S_0$ and the first excited $1s^2\,2s\,2p\;{}^3P_0$ states of beryllium–like heavy ions. For the case of U^{88+}, the energies $E_{^3P_0}$ and $E_{^3P_1}$ if defined relative to the ground state energy are 258.3 and 298.2 eV, correspondingly. From Ref. [4].

In this expression, $\langle ...\,\|E1, M1\|\,...\rangle$ are the reduced matrix elements for the ${}^1S_0 \to {}^3P_1$ ($E1$) and ${}^3P_0 \to {}^3P_1$ ($M1$) transitions, and the parameter η_{PV} describes the PV–mixing between the ${}^1S_0$ and ${}^3P_0$ states.

The asymmetry parameter ϵ is the physical observable in the proposed experiment. It can be determined by inducing the $1s^2\,2s\,2p\;{}^3P_0 \to 1s^2\,2s\,2p\;{}^3P_1$ transition separately with left– and right– circularly polarized light and by recording then the intensity difference of the x–rays from the decay of the ${}^3P_1$ state. Since these intensities are proportional to the photo–excitation cross sections (1), $I_\lambda({}^3P_1 \to {}^1S_0) \sim \sigma_\lambda$, we can find:

$$\epsilon = \frac{I_+ - I_-}{I_+ + I_-}\,. \qquad (3)$$

In order to provide an estimate of this asymmetry parameter, detailed calculations have been performed within the framework of the multi–configuration Dirac–Fock (MCDF) approach [4]. Based on these calculations, we argue that the most suitable candidate for the experimental realization of the proposed scheme is beryllium–like uranium U^{88+}. For this ion, the PV–mixing between the $1s^2\,2s\,2p\;{}^3P_0$ and $1s^2\,2s^2\;{}^1S_0$ states gives rise to $\eta_{PV} = -1.0\times10^{-8}$ and the asymmetry parameter $\epsilon = 3.1\times10^{-7}$.

References

[1] V. M. Shabaev *et al.*, Phys. Rev. A 81 (2010) 052102.

[2] A. Bondarevskaya *et al.*, Phys. Rep. 507 (2011) 1.

[3] M. Maul *et al.*, J. Phys. B: At. Mol. Phys. 31 (1998) 2725.

[4] A. Surzhykov *et al.*, Phys. Scr. (2013), accepted.

* Work supported by Helmholtz Association under the project VH–NG–421.

† surz@physi.uni-heidelberg.de

Relativistic calculations of charge transfer probabilities in heavy-ion collisions using the basis set of cubic Hermite splines *

I. A. Maltsev[1], *G. B. Deyneka*[2], *I. I. Tupitsyn*[1], *V. M. Shabaev*[1], *Y. S. Kozhedub*[1], *G. Plunien*[4], *and Th. Stöhlker*[3,5,6]

[1]St. Petersburg State University, Russia; [2]St. Petersburg State University of Information Technologies, Mechanics and Optics, Russia; [3]GSI, Darmstadt, Germany; [4]TU Dresden, Germany; [5]Universität Heidelberg, Germany; [6]Helmholtz-Institut Jena, Jena, Germany

Low-energy heavy-ion collisions provide a unique opportunity to test quantum electrodynamics effects in supercritical electromagnetic fields [1]. The investigation of related phenomena requires first the development suitable numerical methods for solving the two-center time-dependent Dirac equation in the external electromagnetic field generated by the colliding heavy ions. In previous works we developed a numerical method using the basis of atomic-like Dirac-Fock-Sturm orbitals [2, 3], which allows us to calculate charge transfer and electron excitation probabilities in ion-ion and ion-atom collisions.

Here we report on an alternative approach for the treatment of exact two-center Dirac problem based on utilizing the finite basis set of cubic Hermite splines on a two-dimensional uniform lattice. Previously, the Hermite splines have been employed for relativistic calculations of electron excitation probabilities within the monopole approximation [4]. An advantage of this basis set is, that only adjacent Hermite splines overlap. Accordingly, the Hamiltonian and overlapp matrix are sparse. Moreover, since the overlapping area is small, the matrix elements can be obtained by numerical integration at a smaller number of points. The Dirac equation is solved in the reference frame which rotates together with the internuclear axis. It allows using the two-dimensional lattice instead of a three-dimensional one. The influence of the rotational couplings is taken into account by the inclusion of the states with different projection of the total angular momentum into the basis set. The time-dependent Dirac equation is solved by expansion of evolution operator into the Taylor series.

At first, collisions of a bare nucleus U^{92+} (projectile) with one-electron ion $\mathrm{U}^{91+}(1\mathrm{s})$ (target) were considered. The target is considered to by at rest, while the projectile moves along a straight-line trajectory with a constant velocity. Charge transfer probabilities were calculated at the projectile energy $E = 6$ MeV/u for a wide range of the impact parameters b. The calculations were performed including several channels with different projection of the total angular momentum onto the internuclear axis. In the case of one channel the rotation of the internuclear axis is not taken into account. The results of calculations are shown in Fig. 1. As one can see from Fig. 1, the six channel results are in a good agreement with the corresponding values of Ref. [2]. We observed that four channels are quite sufficient to describe the charge transfer process. Since for impact parameter $b < 600$ fm the one-channel results differ significantly from those including six channels, we can conclude that the influence of the rotational coupling due to the rotation of the internuclear axis becomes essential for small values of b.

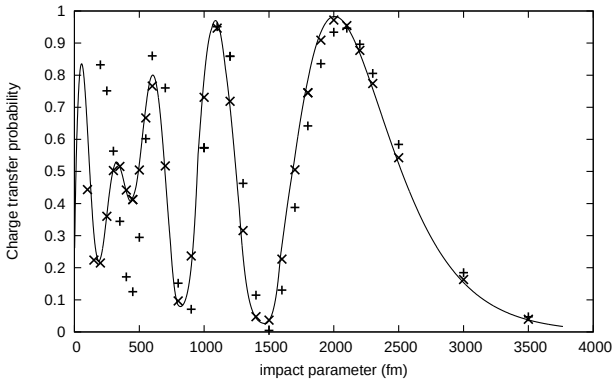

Figure 1: The charge transfer probability as a function of the impact parameter for $\mathrm{U}^{92+} - \mathrm{U}^{91+}(1\mathrm{s})$ collision at the projectile energy $E = 6$ MeV/u. Symbols "+" and "×" indicate the results of one- and six-channel calculations, respectively. The solid line indicates the results of Ref. [2]

We plan to extend the developed method to describe ionization and pair-creation processes in heavy-ion collisions. The negative-energy Dirac continuum will be considered to be fully occupied by electrons. The amplitudes of corresponding processes will be calculated utilizing many-body techniques as described in [5, 6]. We expect that this work will be required for the future experiments at GSI and FAIR.

References

[1] W. Greiner, B. Müller, J. Rafelski, *Quantum Electrodynamics of Strong Fields*, (Springer-Verlag, Berlin, 1985).

[2] I.I. Tupitsyn *et al.*, Phys. Rev. A **82**, 042701 (2010).

[3] I.I. Tupitsyn *et al.*, Phys. Rev. A **85**, 032712 (2012).

[4] G.B. Deyneka *et al.*, Russian Journal of Physical Chemistry B **6**, Issue 2, 224-228 (2012).

[5] E. S. Fradkin, D. M. Gitman, and S. M. Shvartsman, *Quantum Electrodynamics with Unstable Vacuum*, (Springer-Verlag, Berlin, 1991).

[6] H.J. Lüdde and R.M. Dreizler, J. Phys. B **18**, 107 (1985).

* Work supported by DFG and GSI

Relativistic calculations of inner-shell atomic processes in low-energy ion-atom collisions*

Y. S. Kozhedub[1], *I. I. Tupitsyn*[1], *V. M. Shabaev*[1], *S. Hagmann*[2], *G. Plunien*[3], *and Th. Stöhlker*[2,4]
[1]St. Petersburg State University, Russia; [2]GSI, Darmstadt, Germany; [3]TU Dresden, Germany; [4]Helmholtz-Institut Jena, Jena, Germany

In the recent work [1] we developed a relativistic method for evaluation of charge-transfer and electron-excitation processes in low-energy ion-atom collisions. Here we report on a recent application of this method for the evaluation of K-shell-vacancy production and K-K-shell charge transfer probabilities versus the impact parameters in low-energy collisions of H-like ions with neutral atoms. The calculations are performed for systems already studied experimentally and theoretically [2, 3, 4, 5], as well as for systems, which will be investigated experimentally at GSI and FAIR (Darmstadt) in the near future [6].

The method of calculations is based on the independent particle model, where the many-particle Hamiltonian $\hat{H}$ is approximated by a sum of effective single-particle Hamiltonians $\hat{H}^{\rm eff} = \sum \hat{h}^{\rm eff}$ reducing the electron many-particle problem to a set of single-particle equations. The latter is solved by means of the coupled-channel approach with atomic-like Dirac-Fock-Sturm orbitals [1], localized at the ions (atoms). The solutions of these equations allow one to describe the many-electron collision dynamics. The Dirac-Kohn-Sham Hamiltonians with the exchange-correlation potential taken in the Perdew-Zunger parametrization [7] are used as effective single-particle Hamiltonians.

In our calculations the projectile (H-like ion) moves along a straight line with a constant velocity and the target (neutral atom) is fixed. Only the $1s$ electron of the target is considered as the active electron and participates in excitation and charge-transfer processes, while the electrons of the target provide a screening potential. In Fig. 1 we present the results of the calculations for the Ne – $F^{8+}(1s)$ collision at the projectile energy 525 keV/u. We note that the K-shell-vacancy production is mainly determined by the K-K-shell charge transfer. At small impact parameters the contribution from the charge-transfer excitation into the $2s$, $2p$, and higher vacant states of the projectile become also important. The related calculations of the K-shell-vacancy production are performed for the Xe – $Xe^{53+}(1s)$ collision at the projectile energy of 5.9 MeV/u in the relativistic and nonrelativistic limits. As one can see from Fig. 2 the role of the relativistic effects is rather strong. We note that both curves have the same oscillatory behavior but the nonrelativistic curve is shifted toward larger impact parameters.

In our further investigation we plan to continue investigation of inner-shell electron processes in low-energy ion-atom collisions. Special attention will be paid to the many-particle effects.

* Work supported by GSI and DFG.

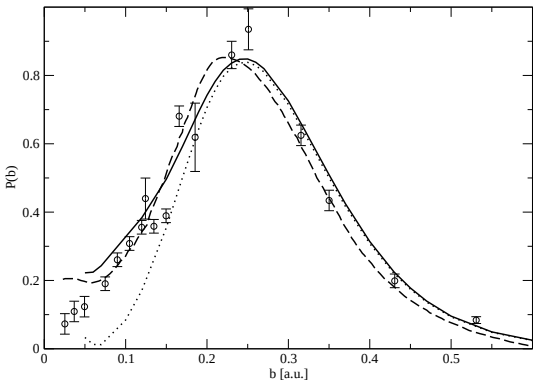

Figure 1: The probabilities $P(b)$ of the Ne K-shell-vacancy production (solid line) and of the K-K-shell charge transfer (dotted line) as functions of the impact parameter b for the Ne-$F^{8+}(1s)$ collision at the projectile (fluorine) energy of 525 keV/u. The circles indicate experimental results by Hagmann *et al.* [2]. The dashed line presents theoretical results by Fritsch and Lin [3].

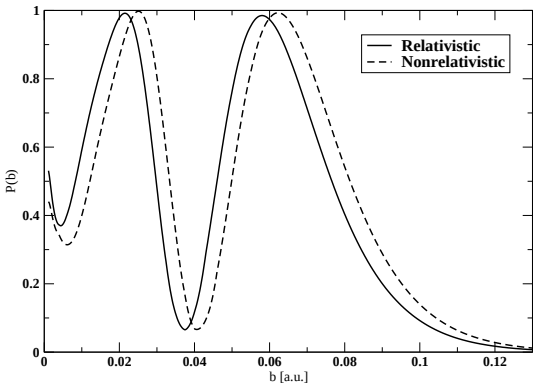

Figure 2: The probability $P(b)$ of the Xe K-shell-vacancy production in the Xe-$Xe^{53+}(1s)$ collision as a function of the impact parameter b at the projectile energy of 5.9 MeV/u.

References

[1] I.I. Tupitsyn *et al.*, Phys. Rev. A **85**, 032712 (2012).
[2] S. Hagmann *et al.*, Phys. Rev. A **25**, 1918 (1982).
[3] W. Fritsch and C. D. Lin, Phys. Rev. A **31**, 1164 (1985).
[4] S. Hagmann *et al.*, Phys. Rev. A **36**, 2603 (1987).
[5] A. Toepfer *et al.*, Phys. Lett. A **126**, 11 (1987).
[6] S. Hagmann *et al.*, AIP Conf. Proc. 1336, 115-118 (2011).
[7] J. P. Perdew and A. Zunger, Phys. Rev. B **23**, 5048 (1981).

Magnetic interactions and retardation in the electron emission from highly-charged ions

S. Fritzsche[1,2,3], *A. Surzhykov*[*1,2,4], *A. Gumberidze*[1,5,6], *and T. Stöhlker*[1,2,3]

[1]GSI, Darmstadt, Germany; [2]Helmholtz Institute Jena, Germany; [3]University of Jena, Germany; [4]University of Heidelberg, Germany; [5]FIAS, Frankfurt, Germany; [6]EMMI, Darmstadt, Germany

X-ray studies from multiple and highly charged ions have been found a unique tool for exploring the electron-electron (e-e) and electron-photon interactions in the presence of strong fields [1]. The x-ray spectroscopy of such systems have demonstrated for a long time that accurate energies and cross sections are obtained only if, apart from the static Coulomb repulsion among the electrons, the magnetic interactions and retardation as well as leading quantum-electrodynamical effects are taken into account. In contrast to the spectrocopy of hard x-rays, however, much less is known how relativistic interactions among the electrons affect their emission and, hence, the dynamics of electrons in strong fields.

To obtain further insight into the strong-field dynamics of electrons, we re-analyzed the excitation and autoionization of highly charged ions with the goal to separate the magnetic and retardation contributions to the e-e interaction from the static Coulomb repulsion. A remarkable change in the electron angular distribution due to the relativistic terms in the e-e interaction was found especially for the autoionization of (initially) beryllium-like projectiles, following a $1s \rightarrow 2p_{3/2}$ Coulomb excitation in collision with some target nuclei. In this process, the angular distribution of the emitted electron is given by

$$W(\theta) \propto 1 + \sum_{k=2,4,\ldots} \mathcal{A}_k(\alpha_r J_r)\, f_k(\alpha_r J_r, \alpha_f J_f)\, P_k(\cos\theta),$$

where $\mathcal{A}_k(\alpha_r J_r)$ characterizes the alignment of the intermediate state after the excitation, θ is the polar angle with regard to the beam direction and where the $f_k(\alpha_r J_r, \alpha_f J_f)$ are characteristic functions that describe the dynamics of the autoionization. The function f_k in this distribution merely depends on the (reduced) matrix elements of the (frequency-dependent) e-e interaction

$$V = V^{\rm Coulomb} + V^{\rm Breit}$$

that comprises both, the instantaneous Coloumb repulsion and the (so-called) Breit interaction, i.e. the magnetic and retardation contributions.

For the excitation-autoionization process via the $1s2s^22p_{3/2}\ ^3P_2$ resonance, a diminished (electron) emission in forward direction as well as oscillations in the electron angular distribution due to the magnetic and retarded interactions are predicted especially for the electron emission into the $1s^22s\ ^2S_{1/2}$ ground and $1s^22p\ ^2P_{1/2}$ excited levels of the finally lithium-like ions. This emission pattern is in strong contrast to a pure Coulomb repulsion between the bound and the outgoing electrons. For example, Figure 1 displays the angular distribution of electrons emitted in the $1s2s^22p_{3/2}\ ^3P_2 - 1s^22s\ ^2S_{1/2}$ (left panel) and $1s2s^22p_{3/2}\ ^3P_2 - 1s^22p\ ^2P_{1/2}$ (right panel) autoionization of U^{88+} projectiles with energy T_p = 5 MeV/u. Results are shown in the laboratory frame and by incorporating only the Coulomb repulsion into the Auger amplitude (blue dashed lines) as well as for a full account of the e-e interaction (black solid lines). The lowering of the electron emission in forward direction ($\theta \approx 0^o$) is significant and enhanced in the laboratory frame due to the Lorentz transformation of the energetic electrons

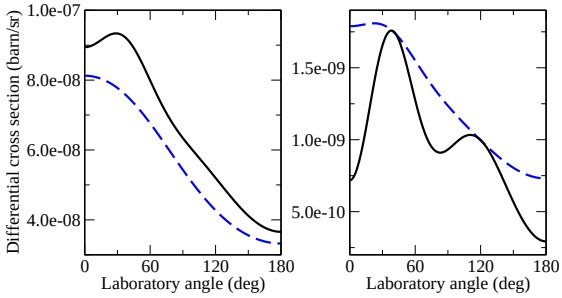

Figure 1: Angular distribution of electrons emitted in the $1s2s^22p_{3/2}\ ^3P_2 - 1s^22s\ ^2S_{1/2}$ (left panel) and $1s2s^22p_{3/2}\ ^3P_2 - 1s^22p\ ^2P_{1/2}$ (right panel) autoionization of U^{88+} projectiles with energy T_p = 5 MeV/u.

In conclusion, the proposed excitation-autoionization process can be observed at existing storage rings and will provide novel insight into the dynamics of electrons in strong fields. The most simple signatures of the relativistic contributions to the e-e interaction in high-Z ions is the reduced electron emission in forward direction ($\theta < 5^o$) as well as the double-peak structure in the expected angular distribution; these signatures arise especially at low projectile energies < 10 MeV/u and for beryllium-like ions with nuclear charge $Z > 70$. The electron angular distribution from such projectiles can be analyzed with present-day electron spectrometers and provide complementary information about the electron dynamics in strong fields that is not accessible from x-ray spectra alone.

References

[1] S. Fritzsche *et al.*, J. Phys. B 38, S707 (2005).

[2] S. Fritzsche et al., New J. Phys. 14, 083018 (2012).

*Work is supported by Helmholtz Association under the project VH–NG–421.

Excitation of autoionizing states of helium-like ions by scattering of high-energy particles*

A.I. Mikhailov[1], *A.V. Nefiodov*[1], *and G. Plunien*[2]

[1]PNPI, 188300 Gatchina, St. Petersburg, Russia; [2]TU Dresden, Mommsenstr. 13, D-01062 Dresden, Germany

Two-electron excitations of atoms and ions induced by impact of charged particles and photons are fundamental processes, which have been studied since decades. Along with double ionization and ionization accompanied by simultaneous excitation, double excitation is caused by the interelectronic interaction. Accordingly, the cross sections of these processes turn out to be extremely sensitive to the quality of which dynamic correlations are taken into account. This allows one to test different theoretical approaches. In experiments, the neutral helium atom is perferably used as a target, since it is the simplest multielectron system. Helium-like ions with moderate values of nuclear charge Z are even more attractive for investigation of correlated processes, since the corresponding cross sections exhibit a universal scaling behavior. However, such processes are rather rare. Their cross sections decrease rapidly with increasing Z values.

In a most recent paper [1], we have studied two-electron excitations of helium-like ions into the two lower autoionizing $2s^2\,(^1S)$ and $2p^2\,(^1S)$ states (in the following denoted, for simplicity, by numbers 1 and 2, respectively) by collisions with high-energy electrons and photons. The calculations are performed analytically within the framework of non-relativistic perturbation theory with respect to the interelectronic interaction. The atomic targets are assumed to be characterized by the small parameters $1/Z \ll 1$ and $\alpha Z \ll 1$, where α is the fine-structure constant. The Auger widths of the levels are equal to $\Gamma_1 = 0.226$ eV and $\Gamma_2 = 0.011$ eV.

In high-energy non-relativistic domain characterized by $3/2 \ll \varepsilon \ll 2(\alpha Z)^{-2}$, the total cross section can be cast into the following scaling form ($\hbar = 1$, $c = 1$) [1]:

$$\sigma^{**} = \frac{\sigma_0}{Z^6 \varepsilon} B(\varepsilon), \qquad B(\varepsilon) = \int_{x_1}^{x_2} Q(x) dx, \qquad (1)$$

where $\sigma_0 = \pi a_0^2 = 87.974$ Mb and $a_0 = 1/(m\alpha)$ is the Bohr radius. The limits of integration over the dimensionless momentum transfer x are given by $x_1 = 9/(4x_2)$ and $x_2 = (\sqrt{\varepsilon} + \sqrt{\varepsilon - 3/2})^2$, respectively. The dimensionless energy ε is related to the asymptotic velocity v of projectile according to $\varepsilon = v^2/(\alpha Z)^2$.

The universal functions $Q(x)$ and $B(\varepsilon)$ are independent of the values of Z. The excitation process is characterized by a rather small momentum transfer $x \lesssim 4$ (see Fig. 1). The scalings $B(\varepsilon)$ are saturated already at $\varepsilon \gtrsim 10$. For the lower autoionizing states, the asymptotic high-energy limits amount to the values $B_1 = 0.0231$ and $B_2 = 0.0072$. Then for fast projectiles ($\varepsilon \gg 3/2$), the total cross sections have a simple scaling behavior like $\sigma^{**} \sim \varepsilon^{-1}$, which is similar to that for single-electron excitations $1s \to ns$ [2]. Note, that in this case, the formula (1) can also be employed for collisions with heavy charged particles, which are nevertheless much lighter than the atomic nucleus of target. If the charge number of the incident particle is equal to $\pm z$ (in units of the elementary charge e), then the cross section should be multiplied by the factor z^2. Although $\Gamma_2 \ll \Gamma_1$, both the autoionizing $2s^2\,(^1S)$ and $2p^2\,(^1S)$ levels can be efficiently excited by high-energy particle scattering.

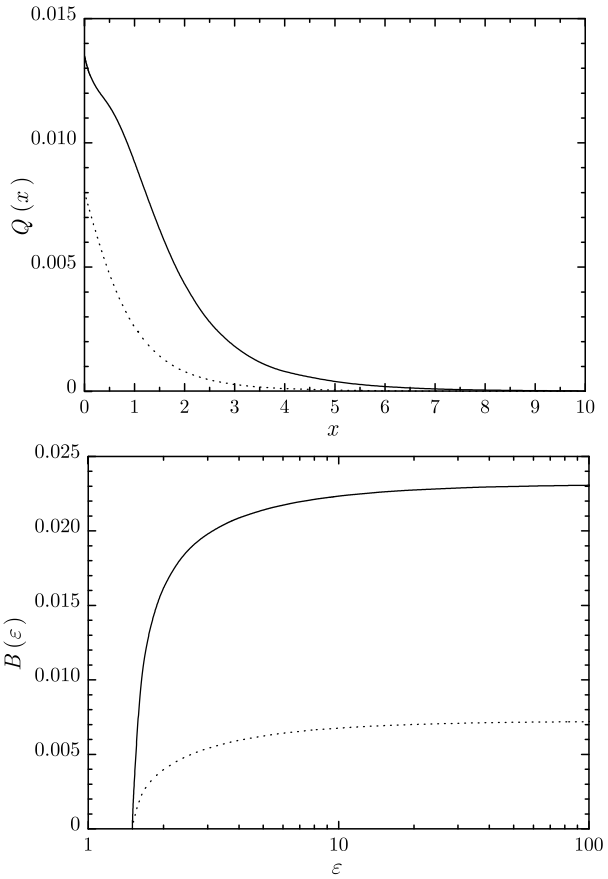

Figure 1: The universal functions $Q(x)$ and $B(\varepsilon)$: solid line, $2s^2\,(^1S)$ state; dotted line, $2p^2\,(^1S)$ state.

References

[1] A. I. Mikhailov, A. V. Nefiodov, and G. Plunien, JETP 116 (2013) (in press).

[2] A. V. Nefiodov and G. Plunien, J. Phys. B 43 (2010) 165206.

* Work supported by GSI

High-temperature plasma of Ge generated by the PHELIX laser *

M. M. Basko[1,2,3], *J. Maruhn*[1,2], *An. Tauschwitz*[1,2], *A. Grushin*[3], *V. G. Novikov*[3], *A. Frank*[4], *V. Bagnoud*[5], *and F. Hannachi*[6]

[1]EMMI-GSI, Darmstadt, Germany; [2]University of Frankfurt, Germany; [3]KIAM, Moscow, Russia ; [4]Helmholtz-Institut Jena, Germany; [5]GSI, Darmstadt, Germany; [6]CENBG, France

Certain nuclear transitions, accompanied by release of large amounts of energy, can be induced by appropriate atomic resonances. One potential candidate is an isomeric state of ^{84}Rb, whose γ-decay could be initiated by resonant $ns \rightarrow 2s$ transitions in strongly ($z_{ion} > 27$) ionized Rb atoms [1]. The required degree of ionization could be achieved by heating the medium, where the ^{84}Rb isomers are created, with the PHELIX laser at GSI. Since the Rb isomers are expected to be created in the ^{76}Ge(12C,p3n)^{84}Rb reaction, i.e. by irradiating Ge with a carbon beam, it is the Ge plasma where one should demonstrate the ability to achieve the necessary temperatures under laser irradiation.

Here we present the results of RALEF-2D [2] simulations of a 4 μm thick Ge foil, irradiated normally by a $\lambda = 532$ nm laser pulse of 150 J over a focal spot of radius $r_f = 100$ μm; the 1.4-ns long pulse was ramped with 0.2-ns linear rise and fall intervals. As a preliminary step, spectral opacities and the equation of state of Ge in the approximation of local thermodynamic equilibrium (LTE) were generated with the THERMOS code [3]. The RALEF runs were performed in the newly developed axial rz mode of the radiation transport, which was treated with 22 spectral groups and the S_{12} angular quadrature.

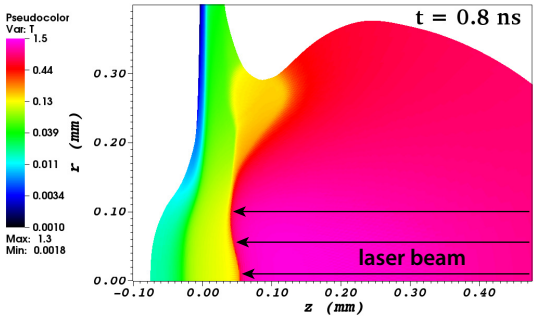

Figure 1: 2D color contour plot of Ge-plasma temperature (in keV) at $t = 0.8$ ns.

The calculated 2D temperature distribution in the Ge plasma shortly after the middle of the laser pulse ($t = 0.8$ ns) is displayed in Fig. 1. The corresponding 1D profiles along the laser-beam axis are shown in Fig. 2. The laser heated plasma consists of two distinct zones: a low-density hot corona behind the critical surface, whose temperature reaches $T_{max} \approx 1.3$ keV, and a radiation-driven heat wave before the critical surface with a relatively high density of $\rho \approx 0.1$–0.2 g/cc, where the matter and radiation temperatures are practically equal and lie in the range $T \approx T_r \approx 100$–$150$ eV. The whole structure is dominated by x-ray energy transport: our simulation indicates that about 70% of the absorbed laser energy escapes the target in the form of keV-range x-rays. The calculated time- and space-integrated emission spectrum (in the direction opposite to the laser beam) is shown in Fig. 3.

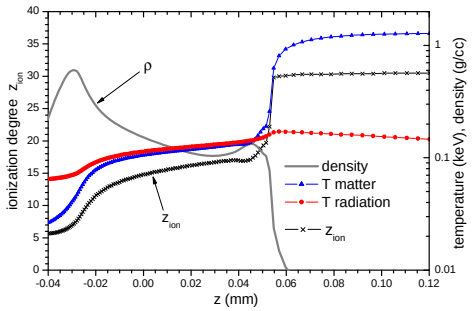

Figure 2: Profiles along the laser-beam axis at $t = 0.8$ ns.

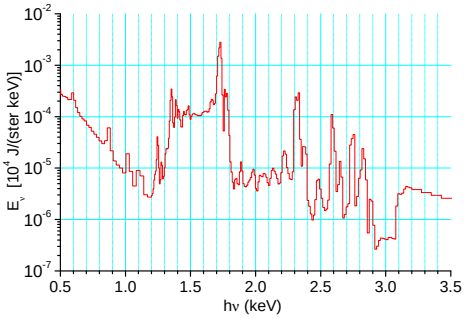

Figure 3: Time- and space-integrated emission spectrum.

Of principal interest for studying the nuclear transitions in Rb would be a narrow ablation front, where the matter temperature jumps from $T \lesssim 0.2$ keV to $T > 1$ keV. It is within this layer that, similar to Ge, the admixture Rb atoms should undergo sharp increase in their ionization degree from $z_{ion} \approx 15$–20 up to a helium-like state with $z_{ion} = 35$ assuming LTE.

References

[1] F. Gobet et al., Nucl.Instr. and Meth. A **653** (2011) 80.

[2] M. M. Basko et al., GSI Report 2010-1 , p. 410.

[3] A.F. Nikiforov, V.G. Novikov, V.B. Uvarov, *Quantum-statistical models of hot dense matter: methods for computation of opacity and equation of state*, Birkhäuser, 2005.

* The project is a collaboration between CENBG, CEA DAM, GSI, University of Frankfurt and KIAM and is supported by the Extreme Matter Institute EMMI.

Radiation-hydrodynamic simulations of foams heated by hohlraum radiation*

S. Faik[1], *An. Tauschwitz*[1,2], *J. A. Maruhn*[1,2], *M. M. Basko*[2,3], *O. N. Rosmej*[1,2], *T. Rienecker*[1], *V. G. Novikov*[3], *and A. S. Grushin*[3]

[1]Goethe University, Frankfurt am Main, Germany; [2]EMMI, GSI, Darmstadt, Germany; [3]KIAM, Moscow, Russia

Undergoing experiments at GSI use a cylindrical hohlraum target irradiated by the PHELIX laser for the indirect x-ray heating of a carbon foam to create a homogeneously ionized plasma state for measurements of the ion stopping power [1]. Simulations with the newly developed code RALEF-2D [2] have been performed to investigate the dynamics of the hohlraum and of the plasma [3]. Figure 1a shows the lateral cut of the simulated Cartesian (x, y) configuration which extends to infinity along the z-axis.

The RALEF-2D code solves the one-fluid one-temperature hydrodynamic equations in two spatial dimensions on a multi-block structured quadrilateral grid by a second-order Godunov-type numerical scheme using the ALE approach. Thermal conduction, radiation transport, and laser energy deposition by means of inverse bremsstrahlung absorption have been implemented within the unified symmetric semi-implicit approach with respect to time discretization. The applied EOS, thermal conductivity, and spectral opacities were provided by the THERMOS code. In combination with the Planckian source function, this involves that the radiation transport is treated in the LTE approximation.

The frequency-doubled PHELIX laser pulse in the experiment has a pulse duration of 1.4 ns with a total energy of 180 J, which corresponds to 122.8 J/mm after conversion to the simulated 2D case. In the simulation, the radiative transfer equation was solved for 7 spectral opacity groups and for 960 discrete ray directions over the entire 4π solid angle. The spatial laser intensity profile was approximated by a Gaussian curve with a FWHM of 0.2 mm.

The calculated x-ray hohlraum spectrum close to the end of the laser pulse (Figure 1b) shows a highly non-Planckian spectrum, which mimics the spectral opacity profile of carbon. The matter and radiation temperatures at the center of the hohlraum equilibrate to ≈ 31 eV at $t = 3$ ns. For times $t > 7$ ns a thin and dense filament of shock-compressed gold plasma is formed and stays close to the hohlraum center due to the collision of the expanding clouds of the ablated material from both hohlraum walls.

For a large portion of the hohlraum radiation emitted during the laser pulse the carbon foam with the initial mean density $\rho_C = 2.0$ mg/cm^3 has an optical thickness of ≈ 1. For this reason the carbon foam is practically instantaneously heated by a flash of x-rays from the laser spot over the entire foam volume to an average temperature of $T \approx 30$ eV, varying by about a factor 4 across a distance of 1 mm. After the laser pulse, the plasma temperature relaxes while the x-ray heating from the hohlraum continues. At $t = 14$ ns (Figure 1c) the dynamics of the carbon plasma is dominated by lateral expansion and by a shock wave propagating from the Cu-C interface. Nevertheless, the simulations show that the time and space variations of such key parameters as the column mass density along the ion trajectories and the plasma ionization degree ($Z \approx 3.9$ at $T \approx 30$ eV) over the ion beam aperture remain sufficiently small for the measurements in the range 3 ns $\lesssim t \lesssim$ 10 ns.

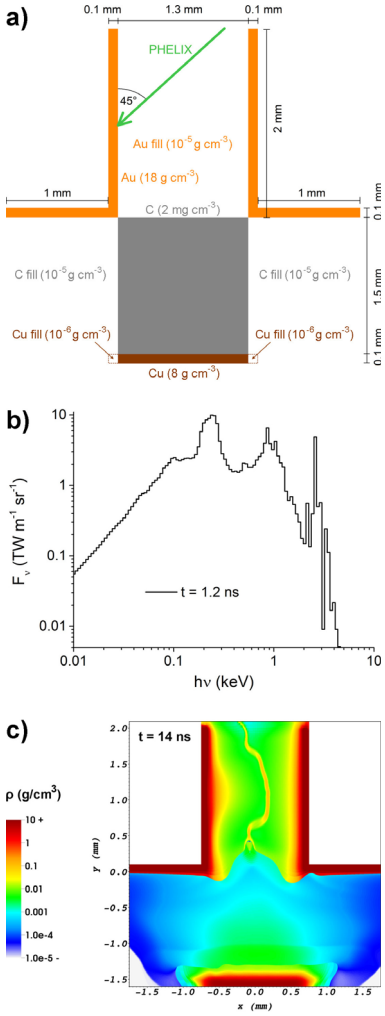

Figure 1: a) 2D lateral cut of the simulated configuration; b) calculated x-ray spectrum as observed through the lower hohlraum hole at $t = 1.2$ ns; c) density ρ at $t = 14$ ns.

References

[1] O. N. Rosmej et al., NIM-A 653 (2011) 52.

[2] M. M. Basko et al., GSI Report 2010-1 410.

[3] S. Faik et al., in preparation.

* supported by BMBF (Project 05P09RFFTA) and by EMMI

Study of Materials at Negative Pressures Using Picosecond Laser Pulses*

I.A. Stuchebryukhov†[1], *S.A. Abrosimov*[1], *A.P. Bazhulin*[1], *V.V. Voronov*[1], *I.K. Krasyuk*[1], *P.P. Pashinin*[1], *A.Yu. Semenov*[1], *and K.V. Khishchenko*[2]

[1]GPI RAS, Moscow, Russia; [2]JIHT RAS, Moscow, Russia

In the present work, the dynamic strength of Al, Pb, Cu, and Ta was studied by the method of generation of shock waves under the action of laser pulses of 70 ps duration. The use of such short pulse make it possible to realize in these experiments strain rates exceeding 10^7 s^{-1}.

We used a neodymium glass laser of the Kamerton-T facility in GPI RAS. The basic radiation was transformed to the second harmonic with the wavelength of 0.527 μm and the laser pulse energy of 2.5 J. Irradiated spot on a target surface was of 0.2 to 0.8 mm in diameter. Then the maximum energy density of the laser radiation flux in the focal area was $6.2 \cdot 10^{13}$ W/cm^2; the ablation pressure was about 1.35 TPa. Targets made of Al, Pb, Cu, and Ta had the form of plates 50 to 100 μm thick.

In our study, we have used an approach [1] that has allowed us to determine the strain rate and the spall strength of the material. This approach is based on both the measurement of the spallation depth after the laser-pulse action on the target and the subsequent numerical simulation of the shock-wave process in the matter under study.

For calculations, we used a numerical code [2], which is based on the hydrodynamic equations solving on the Courant–Isaacson–Rees scheme. Equations of state for the materials in question were taken from [3].

Figure 1 presents the obtained in this work spall strength values for Al versus the strain rate. Data from previous experiments [4–11] are also shown.

The data obtained under conditions of laser action on the target with pulse duration of 70 ps show that, at moderate amplitudes of shock loading, spall strength values are in agreement with the known functional dependencies of the strength upon the rate of deformation. With greater loading pressure (data set 4 in figure 1), there is a sharp growth of spall strength, that indicates the strengthening of the material as a result of loading. The registered growth of spall strength of aluminum is connected with the fact that, in the experiments, the increase of the rate of deformation was achieved not only by shortening of the pulse duration, but also by the increase of the amplitude of loading. The latter increase leads to hardening of the material under study. In this case, defects, which cause the premature spallation of the material, may be disappeared.

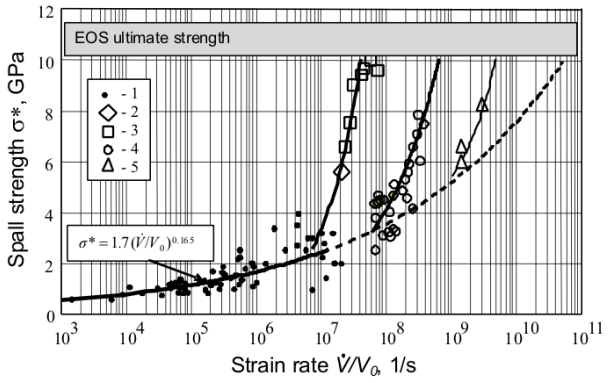

Figure 1: Spall strength of Al versus the strain rate. Solid curve (marked by arrow) approximates 70 experimental points reported in [4–9]. Dashed curve extends the solid curve into a region of high strain rates. Experimental data: 1 — [4–9], 2 — [4], 3 — [10], 4 — this study, 5 — [11].

References

[1] McQueen R. G., March D. // J. Appl. Phys. 1962. V. 33. N. 2. P. 654.

[2] Kulikovskii A. G., Pogorelov N. V., Semenov A. Yu. Mathematical Problems of Numerically Solving Hyperbolic Systems of Equations. Moscow: FIZMATLIT, 2001.

[3] Fortov V. E., Khishchenko K. V., Levashov P. R., Lomonosov I. V. // Nucl. Instr. Meth. Phys. Res. A. 1998. V. 415. N. 3. P. 604.

[4] Moshe E., Eliezer S., Henis Z., et al. // Appl. Phys. Lett. 2000. V. 76. N. 12. P. 1555.

[5] Eliezer S., Gilath I., Bar-Noy T. // J. Appl. Phys. 1990. V. 67. N. 2. P. 715.

[6] Fortov V. E., Kostin V. V., Eliezer S. // J. Appl. Phys. 1991. V. 70. N. 8. P. 4524.

[7] Moshe E., Eliezer S., Dekel E., et al. // J. Appl. Phys. 1998. V. 83. N. 8. P. 4004.

[8] Bachmann H., Baumung K., Kanel G. I., et al. // Proceedings of the IX Intern. Conference on High Power Particle Beams. Washington (DC), May 25–29, 1992. Springfield (VA): NTIS, 1993. V. 2. P. 963–968.

[9] Kanel' G. I., Razorenov S. V., Utkin A. V., Fortov V. E. Shock-Wave Phenomena in Condense Matter. Moscow: Yanus-K, 1996.

[10] Vovchenko V. I., Krasyuk I. K., Pashinin P. P., Semenov A. Yu. // Prikl. Fiz. 2009. N. 1. P. 12.

[11] Ashitkov S. I., Agranat M. B., Kanel' G. I., et al. // Pis'ma Zh. Eksp. Teor. Fiz. 2010. V. 92. N. 8. P. 568.

* This work is supported by the Russian Foundation for Basic Research (projects 11-02-12003, 11-08-01225, 12-02-00625, 12-02-00746, and 13-02-91057), the Russian Academy of Sciences (programs 2P and 13P), and the President of the Russian Federation (grants NSh-368.2012.2 and NSh-7241.2012.2).

† st777@kapella.gpi.ru

ESR Operation and Development

C. Dimopoulou, S. Litvinov, C. Kleffner, W. Maier, F. Nolden, C. Peschke, P. Petri, U. Popp, M. Steck, and D. Winters[1]

[1]GSI, Darmstadt, Germany

The ESR storage ring was operated for physics experiments as well as for FAIR-related machine development.

Internal target experiments included tests of the FOCAL detector and the electron spectrometer. The series of laser cooling experiments was continued successfully, and beams were decelerated for HITRAP.

An experiment on dielectronic recombination (DR) aimed at comparing DR spectra in both ground and isomeric states of $^{235}\mathrm{U}^{89+}$. An almost pure isomeric state was populated through the β^- decay of $^{235}\mathrm{Pa}^{88+}$. The latter was identified among other fragmentation products by Schottky spectroscopy, and a pure $^{235}\mathrm{Pa}^{88+}$ beam was produced by appropriate scraping.

A completely new type of experiments was launched in autumn 2012 with the advent of the first nuclear reaction experiments at the internal gas jet target. In particular, a sufficiently intense secondary $^{56}\mathrm{Ni}^{28+}$ from the fragment separator was accumulated before being used by the experiment. This experiment is covered in a separate contribution to this report [1].

Another nuclear reaction experiment aimed at the measurement of the $^{20}\mathrm{Ne}^{10+}$ (p,d) reaction. This experiment was successfully performed in autumn 2012.

The ESR internal target was run with different types of gases. Hydrogen operation was remarkably reliable, for the first time a helium cluster jet was successfully used for experiments with a density of almost $6 \cdot 10^{12}\ \mathrm{cm}^{-2}$.

An obstacle impeding beam transport into the inner parts of the ESR aperture without dedicated vertical bumps [2] has been identified by now. All stochastic cooling pickup and kicker stations are equipped with resistively coated ceramic cylinders in order to supress undesired higher microwave modes in the beam chamber. Due to mechanical problems which are not yet understood completely, one such cylinder had fallen down into the beam aperture, leading to severe practical problems in beam handling. This obstacle will be removed before the autumn 2013 beam period.

The machine experiments focused on comparative studies of the different longitudinal stochastic cooling systems. These experiment made use of the newly developed optical notch filter [3]. Here the ESR is an important test bench for components of the FAIR project, as a similar device will be installed at the CR of FAIR.

Three different longitudinal stochastic cooling methods are available at the ESR: Palmer cooling, time of flight (TOF) cooling, and notch filter cooling (see [4]). All of these are also planned to be applied at the CR. The components of the optical notch filter worked reliably. The prescise setting of the notch frequencies by changing the position of an optical mirror was a necessary prerequisite for the low momentum width equilibria achieved. The same is true for the optical attenuator settings. First preliminary tests in April confirmed quantitatively the expectation that the momentum acceptance of notch filter cooling is smaller than for TOF or Palmer cooling [5]. Another series of measurements were performed in October with a 400 MeV $^{58}\mathrm{Ni}^{28+}$ beam in order to determine optimum cooling times. The measurements were made with a beam of $6 \cdot 10^6$ particles. The second moment of the momentum distribution $\sigma(t)$ was evaluated and fitted with an exponential decay towards an equilibrium as a model:

$$\sigma(t) = (\sigma_0 - \sigma_\infty)\exp(-t/\tau) + \sigma_\infty$$

A preliminary evaluation of the data confirms the expectation that the equilibrium value for notch filter cooling ($\sigma_\infty = 2.47 \cdot 10^{-5}$) is much lower than for TOF cooling ($\sigma_\infty = 4.33 \cdot 10^{-5}$). Also the cooling time for notch filter cooling ($\tau = 0.18\,\mathrm{s}$) is much shorter than for TOF cooling ($\tau = 4.33\,\mathrm{s}$). The latter is mainly due to the much larger amplification (22 dB higher!) which is affordable in the case of notch filter cooling. This is due to the well-known fact that notch filtering reduces largely the random noise in the vicinity of the revolution frequency. It is planned to provide a fast switching from TOF cooling (with its large momentum acceptance in the beginning of the cooling process) to final notch filter cooling in order to profit from both schemes in an optimized fashion..

During the shutdown period in 2013 the high voltage power supply of the electron cooler will be repaired, as the high voltage was less stable than usual from time to time.

It is planned to establish a new model for the supply of data to the quadrupole magnet power supplies during deceleration, because it has turned out that there are deviations between the set values and the measured values of both tunes, particularly during deceleration. A more flexible programming of the rf voltage and frequency ramps during deceleration is under work, as well.

References

[1] F. Nolden et al., this report

[2] C. Dimopoulou et al., GSI scientific report 2011, 470

[3] C. Peschke et al., GSI scientific report 2011, 328

[4] D. Möhl, Stochastic Cooling of Particle Beams, Lecture Notes in Physics 866

[5] F. Nolden et al.; *Nucl. Inst. Meth A* 564 (2006) 87-93

Radioactive Beam Accumulation in the ESR

F. Nolden, C. Dimopoulou, C. Kleffner, S. Litvinov, W. Maier, C. Peschke, P. Petri, U. Popp, M. Steck, H. Weick, D. Winters[1]

[1]GSI, Darmstadt, Germany

A radioactive $^{56}Ni^{28+}$ was accumulated for the first time in the ESR to an amount usable for a nuclear physics experiment with the ESR internal target. The $^{56}Ni^{28+}$ ions were produced in the fragment separator (FRS) by shooting an intense 600 MeV/u $^{58}Ni^{28+}$ beam from the SIS synchrotron on a fragmentation target. By proper settings of the FRS degrader, contaminants like $^{54}Co^{27+}$ could be reduced to a total fraction of $< 10^{-3}$. Typically $8 \cdot 10^4$ ions were injected at each shot from the SIS. This beam was precooled in two steps (5 s coasting beam + 5 s bunched beam) by stochastic cooling using the newly established time of flight method [1]. The precooled bunched beam was transferred by rf stacking towards an inner orbit of the ESR, where it was neither disturbed by the magnetic field of the injection kicker nor by the rf fields of the stochastic cooling kickers. Here it was gradually moved by electron cooling towards an orbit at a somewhat lower energy. At this orbit, the beam was accumulated using up to 60 injections. The average time between injections was 36 s, as the SIS synchrotron had to serve several different experiments in parallel. Typically $4.8 \cdot 10^6$ secondary $^{56}Ni^{28+}$ ions interacted with the internal target after properly aligning the beam with the (hydrogen or helium) gas jet.

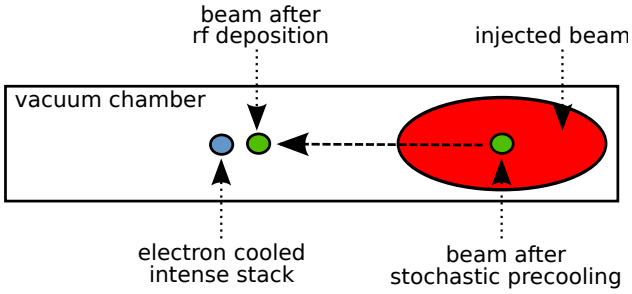

Figure 1: Scheme of beam orbits during accumulation

Fig. 2 shows stochastic precooling of a fresh secondary beam. As long as the beam is coasting the second moment of the momentum width ($\sigma(\delta p/p)$) is decreased by a factor of 3. Due to the non-adiabatic turning on of the rf, $\sigma(\delta p/p)$ increases slightly and is then reduced anew.

Fig. 3 is a waterfall diagram of Schottky spectra (124^{th} harmonic of the revolution frequency) taken just before and after the end of the rf stacking procedure. The distance between stack and deposited beam ($\delta p/p = 4.3 \cdot 10^{-4}$) is chosen such that the two beams are close enough for fast merging by electron cooling without disturbing the stack by the rf. Therefore a low final rf voltage (200 V) was set which corresponds to a full bucket height $(\delta p/p)_{max} = 3.9 \cdot 10^{-4}$.

Fig. 4 displays a series of measured data points from the DC beam current transformer. Although its resolution is limited, the data points are rather linear, indicating that the stacking procedure is working practically lossless.

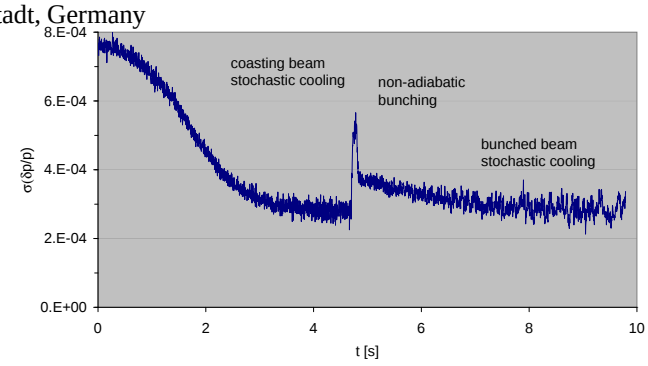

Figure 2: Momentum cooling of freshly injected beam

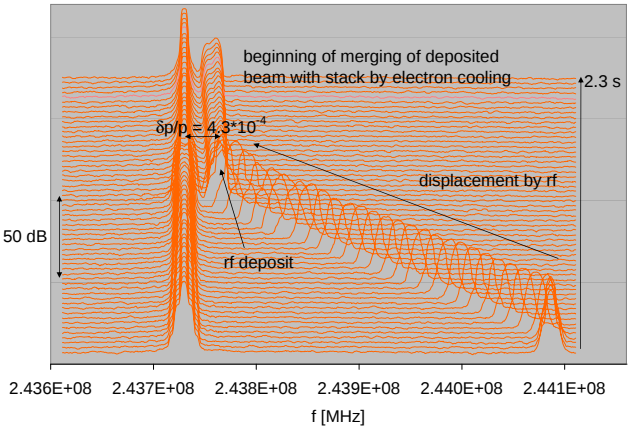

Figure 3: Schottky spectra around beam deposit (see text)

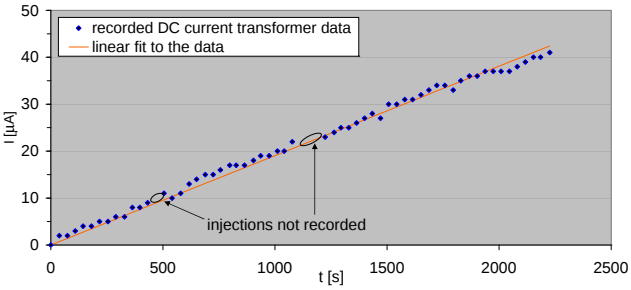

Figure 4: DC beam current transformer data as a function of time

References

[1] C. Dimopoulou et al., this report

Sensitivity measurements of the resonant pickup in the ESR

M. S. Sanjari[1,2], P.-M. Hillenbrand[1,3], R. DuBois[4], F. Bosch[1], S. Hagmann[1], P. Hülsmann[1,2], C. Kozhuharov[1], Yu. A. Litvinov[1], F. Nolden[1], C. Peschke[1], P. Petri[1], A. Schempp[2], D. Shubina[1], M. Steck[1], N. Winckler[1], and X. L. Yan[1]

[1]GSI Darmstadt; [2]Goethe Universität Frankfurt am Main; [3]Universiät Gießen; [4]University of Missouri-Rolla

Qualitative measurements were carried out to determine the sensitivity of the ESR resonant pickup ([1], [2]) using short-lived uranium beams at different energies.

Conventional beam current monitors such as transformers can determine the amount of beam current. But even those devices with high sensitivity suffer from a limited bandwidth which results in reduced performance at higher frequency components of the beam current. To achieve measurements of beams with very few ions, one can make use of the high sensitivity of resonant pickups at a harmonic band of the Schottky signal.

The Schottky process can be shown to be wide sense stationary with the expected (average) value equal to the macroscopic beam current I_B as $\mathsf{E}[i(t)] = qf_rN = I_B$, where q is the charge, f_r is the revolution frequency and N is the number of particles [2]. Its autocorrelation corresponds to the expected instantaneous power of the signal, which in turn is related to its power spectral density (PSD) via the inverse Fourier transform. The integral under the curve of the PSD shows the total average power in a given frequency band. In this case the area is the same in every (non-overlapping) Schottky band and is equal to

$$\langle I_s^2 \rangle = 2q^2 f_r^2 N = 2qf_r I_B \qquad (1)$$

Absolute power values may be difficult to obtain after several stages of signal processing. Also the noise level depends on the number of points within a given frame of sampled data, making it hard to determine at what level signals can be distinguished from noise. A solution is to use an external DC current transformers (DCCT) as a calibration reference to determine I_B and to scale the area under the curve such that it corresponds to it. The number of ions N can also be determined using Eqn. 1.

In August 2012 beams of ^{238}U were stored in the ESR at relatively low energies. Signals from both the DCCT and the resonant pickup were corrected for offset and prepared as described in detail in [2]. After scaling, the number of ions were calculated accordingly using the Schottky spectra.

The beams of $^{238}U^{88+}$ were injected at 90 MeV/u. The N_2 gas target was used to reduce the number of ions over several orders of magnitude during the measurement time. Beams of $^{238}U^{28+}$ were injected at energies of 30 MeV/u without gas target. The results can be seen in Fig. 1. The resonant pickup is several orders of magnitude more sensitive than the DCCT, but of course its sensitivity depends on the total charge and energy of the beam. The DCCT has an estimated uncertainty of ± 1 μA which propagates into the calculation of the number of ions, but it is not shown in the figure. Using a high precision DCCT with known uncertainties could improve measurement results in the future.

It is seen in Fig. 1 that the decrease of beam intensity is not strictly exponential. At higher beam intensities coherent Schottky signals cause amplitude suppression, while at lower signal intensities, noise background accounts for loss of precision. A detailed study of these effects may be crucial for in-ring decay studies.

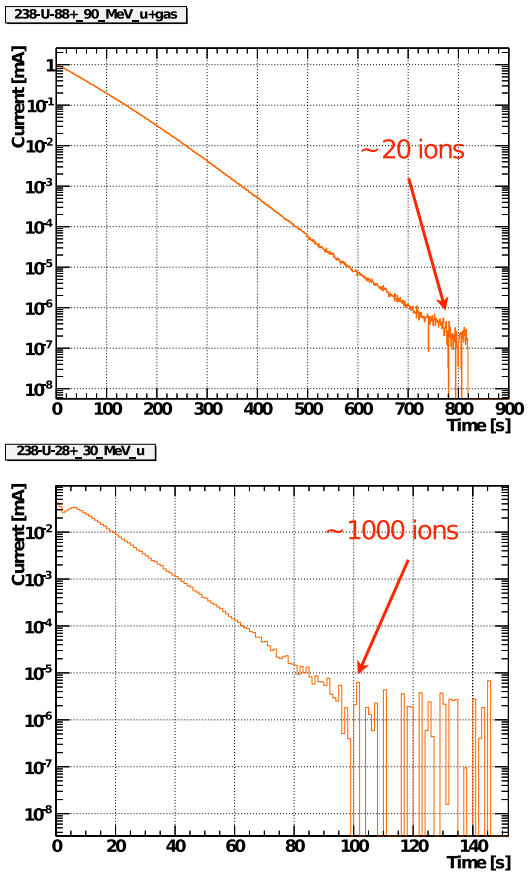

Figure 1: Number of ions after injection for $^{238}U^{88+}$ at 90 and $^{238}U^{28+}$ at 30 MeV/u.

References

[1] F. Nolden *et. al. Nucl. Instr. Meth. A* **659** (2011) p. 69–77.

[2] M. S. Sanjari *PhD Thesis*, submitted to the Goethe University, Frankfurt am Main, Germany (2013).

The CRYRING@ESR Project

F. Herfurth[1], M. Lestinsky[1], R. Bär[1], A. Bräuning-Demian[1], S. Litvinov[1], O. Dolinskii[1], W. Enders[1], M. Engström[2], B. Franzke[1], O. Gorda[1], A. Källberg[2], Y. Litvinov[1], A. Simonsson[2], J. Sjöholm[2], M. Steck[1], Th. Stöhlker[1], G. Vorobjev[1], N. Winckler[1]

[1]GSI, Darmstadt, Germany; [2]MSL, Stockholm University, Stockholm, Sweden

The low energy storage ring LSR shall provide low energy, highly charged ions and antiprotons at FAIR used by two collaborations, SPARC and FLAIR, for precision experiments. The LSR is a Swedish in-kind contribution to the FAIR facility in Darmstadt,

The LSR [1] evolves from the heavy-ion storage ring CRYRING, which has been operated at the Manne Siegbahn Laboratory in Stockholm until 2010. Instead of storing the ring components until installation at the Facility for Antiproton and Ion Research, FAIR, the immediate installation behind the existing Experimental Storage Ring, ESR, has been proposed and worked out in detail by a Swedish-German working group. The estimated efforts for installation and operation of CRYRING at the ESR have been summarized in a report [2] published by that working group in 2012.

A schematic overview of the storage ring and its facilities is shown in fig. 1. CRYRING can decelerate, cool and store heavy, highly charged ions down to a few 100 keV/nucleon. It provides a high performance electron cooler as well as a gas jet target. It is equipped with it's own injector and ion source, to allow for standalone commissioning.

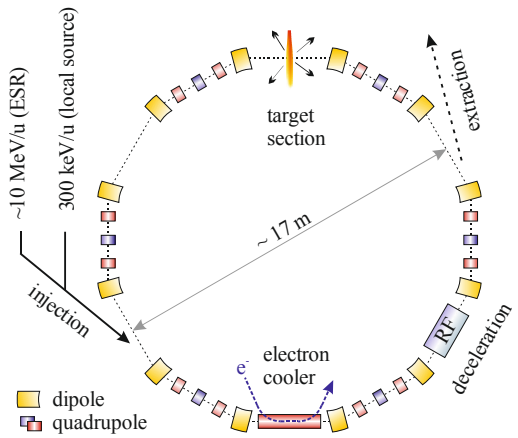

Figure 1: CRYRING at ESR.

The ions are kept in orbit by twelve 30° magnetic dipoles and a number of magnetic quadrupoles and sextupoles (not shown in the figure) in six of the twelve straight sections. The other six sections house an injection and an extraction system, the deceleration and acceleration section, and the electron cooler. One section is used for experimental installations as for instance a gas target.

The storage ring is capable of accelerating ions with mass to charge ratio below four injected at only 300 keV/nucleon from the off-line ion source to the maximum rigidity of 1.44 Tm. It also decelerates ions injected at the maximal rigidity down to the lower rigidity limit of 0.054 Tm. The magnets are designed for fast ramping, such that the whole decelerating (accelerating) process could be done in only 150 ms.

One of the key features is an electron cooler with adiabatic expansion of the electron beam. This yields about 100 times lower transversal electron temperature than in the ESR and yields directly higher resolution in recombination spectroscopy with merged ion – electron beams.

The proposed installation behind the ESR in combination with its own injector makes CRYRING@ESR the perfect machine for FAIR related tests of diagnostics, software and concepts on one hand, and atomic physics experiments with heavy, highly charged ions stored at low energy on the other hand.

The new control system of FAIR will be implemented for the first time in a machine that delivers beam and hence will be the perfect occasion to test not only the cooperation of the design concepts but also the performance of the system. Since the ring can be operated any time it is the perfect training ground for operators on the new control system and this allows for valuable feedback on the operational concept well in advance before the commissioning of FAIR's key machines.

Physics applications range from "classical" atomic physics experiments like the determination of the lamb shift using X-ray spectroscopy, but with increased resolution, over measurements at the borderline of atomic and nuclear physics for instance to determine the charge radius, to a yet unexplored energy regime for astrophysically interesting nuclear reactions. The details of planned experiments are laid down in the "Physics book" that is close to completion [3].

Most components have been shipped by now to GSI and on-site tests are on going. CRYRING@ESR will be installed in the existing Cave B and the necessary reconstruction work has been started.

References

[1] H. Danared, et al. (2011) "LSR - Low-energy Storage Ring, Technical design report", Manne-Siegbahn Laboratory, Stockholm University, version 1.3.

[2] M. Lestinsky, et al. (2012) "CRYRING@ESR: A study group report", Project study, GSI, Darmstadt, https://www.gsi.de/fileadmin/SPARC/documents/Cryring/ReportCryring_40ESR.PDF

[3] M. Lestinsky, et al. (2013) "Physics Book: CRYRING@ESR", in preparation.

Department "SPARC Detectors" in the FAIR@GSI Project*

Yu.A. Litvinov[1], *Th. Stöhlker*[1,2,3], *R. Schuch*[4], *and M. Steck*[1]

[1]GSI Helmholtzzentrum für Schwerionenforschung; [2]F. Schiller Universität Jena; [3]Helmholtz Institut Jena; [4]Stockholm University

In the last decades, accelerator-based atomic physics has advanced into hitherto unexplored areas of research, encompassing high energies, high atomic charge states and strong electromagnetic fields. Here, the heavy-ion storage rings play an indispensable role. A worldwide unique research program is being pursued at the experimental storage ring ESR of GSI by conducting precision spectroscopy of relativistic few-electron ions and interaction studies of relativistic ions with atoms, electrons and photons. The atomic physics groups at GSI and HIJ have gained an unparalleled expertise in this field which ensures that the unprecedented possibilities of the future Facility for Antiproton and Ion Research (FAIR) [1] – concerning energy, intensity and experimental tools – can optimally be exploited to provide access to the fundamental facets of relativistic atomic physics and neighbouring fields. Realisation of this rich research program is the main aim of a large international collaboration, the SPARC Collaboration [2].

The envisioned experiments were initially foreseen in several areas of the FAIR complex: in a dedicated APPA multi-purpose cave, at the SIS-100/SIS-300 synchrotrons, at the FLAIR facility and at the New Experimental Storage Ring NESR. However, the SPARC research program was dramatically reduced by the Modularised Start Version (MSV) [3] of FAIR, where the construction of the central facilities for the SPARC experiments, the NESR and the connected FLAIR facility have been moved to later modules. Therefore, intense investigations of various possibilities to rescue the SPARC science at FAIR by using the facilities available within the MSV have been conducted in the last two years.

One of the solutions is to explore the unique opportunity offered by the High Energy Storage Ring (HESR) [4], which was primarily designed for experiments with stored and cooled antiprotons. However, it turned out to be a well-suited facility which can accommodate a range of SPARC experiments with high-energy stored heavy-ion beams [5, 6]. In particular, the HESR can store cooled beams at energies of up to 5 GeV/u and can thus enable unique atomic physics experiments which are not feasible at any other place in the world. Furthermore, installation of the CRYRING – the storage ring which was operated until very recently at the University of Stockholm – at the present ESR facility will open up the possibility of precision experiments with cooled highly-charged heavy ions at low energies already in the MSV of FAIR [7].

A dedicated department within the FAIR@GSI Project, SPARC Detectors, has been organised, the primary task of which is to accomplish working packages assigned by the SPARC collaboration as the GSI contribution to the SPARC experiments at FAIR. These are the integration of the overall SPARC setup including the necessary infrastructure in the HESR and – if required by the collaboration – the construction of SPARC instrumentation, like internal targets, spectrometers, particle detectors, etc.

* This work is supported by the Helmholtz Association (HCJRG-108) and by Helmholtz Institute Jena

References

[1] W. F. Henning (Ed.), *Internal Accelerator Facility for Beams of Ions and Antiprotons*, GSI-Darmstadt, November, 2001, http://www.gsi.de/GSI-Future/cdr/

[2] SPARC Technical Proposal, http://www.gsi.de/forschung/fair_experiments/sparc/documents.html (2005).

[3] *FAIR Green Paper: The Modularized Start Version*, Oktober 2009, http://www.gsi.de/documents/DOC-2009-Nov-124-1.pdf

[4] R. Maier *et al.*, HESR Technical Design Report V. 3.1.2 (2008), http://www-win.gsi.de/fair-eoi/PDF/TDR_PDF/TDR_HESR-TRV3.1.2.pdf

[5] T. Stöhlker *et al.*, Physica Scripta, *in press* (2013).

[6] T. Stöhlker *et al.*, *SPARC Experiments at the HESR: A Feasibility Study*, 2012, http://www.gsi.de/index.php?eID=tx_nawsecuredl&u=0&file=/fileadmin/SPARC/documents/SPARC@HESR_FS_V26.pdf&t=1348670739&hash=de961710768d9d9ceccdf799f4eac0b463bfc6c8

[7] M. Lestinsky *et al.*, *CRYRING@ESR: A Study Group Report*, GSI, 2012.

A target station design study for future in-ring applications

N. Petridis[*1,2], *Th. Stöhlker*[3,4], *and R. E. Grisenti*[1,3]
[1]IKF, J.W.G.-University Frankfurt; [2]EMMI, Darmstadt; [3]GSI, Darmstadt; [4]Helmholtz-Institut, Jena

Recent experimental findings [1, 2] led to the elaboration of an internal target design study, which is based on the prototype target station currently deployed at the experimental storage ring (ESR). The initial motivation for starting the redesign process of the former target station, which was assembled in the original setup in 1989 for the first time, was mainly driven by the limited maximum target densities for the light gases helium and hydrogen. Previously, the behavior of cryogenically cooled, thus liquified helium expanded into vacuum through a micrometer sized orifice nozzle was investigated experimentally [3] and set the foundation for the modification process. Therefore, in order to optimize the target performance, the modification of the target inlet chamber started in 2008 by decreasing the working temperature of the target nozzle using a high cooling-power cryostat. In the course of numerous successful target beamtimes performed at the ESR the prototype target setup was further improved in terms of usability and target stability by applying, i.e., a closed-cycle cryostat featuring push-button operation and a trumpet shaped (CERN) nozzle geometry, kindly provided by A. Khoukaz from the Münster University. As a result, an extremely versatile and reliable prototype target station was developed during the past years, capable of providing target beams of all desired species in a wide range of adjustable target densities (see Table 1 below).

Target gas	Area density [cm^{-2}]	T_0 [K]
Helium	1×10^{13}	20
Hydrogen	3×10^{13}	40
Nitrogen	8×10^{12}	130
Argon	3.5×10^{12}	300
Krypton	1.5×10^{12}	300
Xenon	6×10^{12}	300

Table 1: A survey of actual area densities for different target gases achieved at the ESR by employing a 12 ± 1 μm diameter CERN nozzle.

The prototype target station, with which those improvements were accomplished, essentially consists of the former target station including the important modifications, i.e. the cryostat and the nozzle. Hence, in order to exploit the full potential of the implemented parts, a dedicated and specialized inlet chamber design is crucial. For instance, geometrical considerations regarding the skimmer geometry suggest an improvement in target density at shorter distance of the nozzle to the interaction point (assuming equal

* petridis@atom.uni-frankfurt.de

Investigation and Optimization of Transverse Beam Dynamics in HESR@FAIR for Experiments with Highly-Charged Heavy Ions*

O. Kovalenko[1,2], *A. Dolinskii*[1], *Yu. A. Litvinov*[1], *and Th. Stöhlker*[1,3,4]

[1]GSI Helmholzzentrum, Darmstadt, Germany; [2]University of Heidelberg, Germany; [3]F. Schiller Universität Jena; [4]Helmholtz Institut Jena

Introduction

The High-Energy Storage Ring (HESR) was primarily designed for experiments with stored and cooled antiprotons. But it also appeared to be most suitable facility to maintain a wide range of experiments with high-energy stored heavy-ion beams. In this study the transverse nonlinear beam dynamics for heavy ions in the HESR were investigated.

Beam optics optimization for heavy ion experiments

Within PHELIX project at FAIR@GSI an appropriate place for an experiment, where laser and ion beams are overlapped, has to be found. Available free space and flexible optics are important factors in search for the right location. As an optimal solution a place in the straight section in between two quadrupole triplets is proposed. To maximize the brightness of the ion beam in the above-mentioned location (which is crucial for the experiment) we have to minimize a beam profile as much as possible. For this purpose with the help of MIRKO code an algorithm for decreasing the beam transverse profile was developed.

The technique of variation the quadrupole magnets strengths along the ring allowed to locally decrease the β_x-function in the place of beams interaction. As a result, in modified ring optics in the location of interaction the β_x-function was reduced to the value of 3.1 m, which is 7 times less than in standard optics. Optics variation didn't require any change of the designed quadrupoles parameters.

The emittance of a transferred (from the CR to the HESR) beam is about $\epsilon_{x,y}$ = 0.5 mm mrad and the momentum spread about $7 \cdot 10^{-4}$ [1]. Thus one can calculate the size of the beam. The following results are obtained: the horizontal and the vertical beam widths after changing the optics equal to 1.2 mm and 1.5 mm correspondingly.

With the existing set of sextupoles the chromaticities ξ_x = -14.35 and ξ_y = -13.71 can be corrected up to 0.

Frequency map analysis

Frequency map analysis for both ring optics has been performed. The field errors of dipole and quadrupole magnets [2] were included. An ordinary tracking was used to define the dynamic aperture (DA). From the DA plot for modified optics (see figure 1): A_x = 3.1 mm, A_y = 15.0 mm. The emittances which correspond to the dynamic aperture are ϵ_x = 0.7 mm mrad and ϵ_y = 17.8 mm mrad. For standard optics we have ϵ_x = 11.2 mm mrad and ϵ_y = 13.3 mm mrad. One can see that the horizontal DA decreased significantly (from 11.2 mm mrad to 0.7 mm mrad). The betatron tunes are: Q_x = 7.94, Q_y = 7.62 for modified and Q_x = 7.62 Q_y = 7.62 for standard optics. Further investigation and analysis are needed in order to find out and possibly eliminate the causes of DA shrinking.

A revised Fourier technique [3] with data windowing was used in order to obtain a frequency map with a diffusion coefficient (see figure 2).

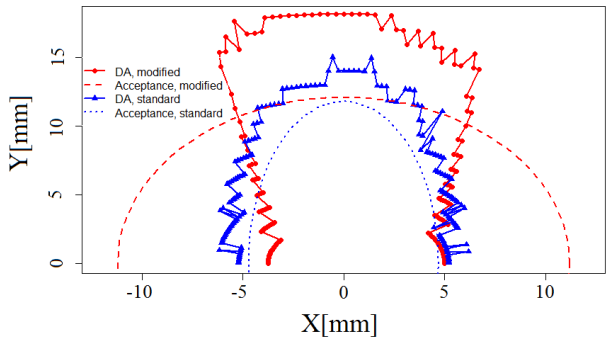

Figure 1: Calculated dynamic aperture for modified (β_x = 13.7 m, β_y = 12.6 m) and standard optics (β_x = 2.4 m, β_y = 11.9 m) for Δp/p = 0.

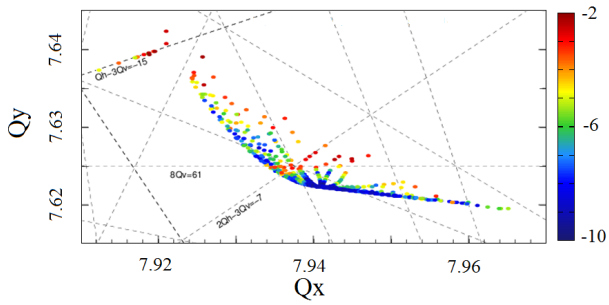

Figure 2: Frequency diagram for modified optics

References

[1] T. Stöhlker *et al.*, "SPARC Experiments at the HESR: A Feasibility Study" (2012).

[2] D.M. Welsch, "Investigation and Optimization of Transverse Non-linear Beam Dynamics in the High-Energy Storage Ring HESR" (2009).

[3] J. Laskar, C. Froeschle and A. Celetti, Physica D 56 (1992).

*This work is supported by the Helmholtz Association (HCJRG-108), Helmholtz Institute Jena, and GSI F&E program

HITRAP – Status of On-Line Commissioning and Installations

F. Herfurth[1], W. Barth[1], G. Clemente[1], L. A. Dahl[1], P. Gerhard[1], O. K. Kester[1], H.-J. Kluge[1], C. Krantz[2], N. Kotovskiy[1], C. Kozhuharov[1], M. Maier[1], D. Neidherr[1], W. Quint[1], U. Ratzinger[3], A. Reiter[1], A. Schempp[3], A. Sokolov[1], Th. Stöhlker[1], H. Vormann[1], G. Vorobjev[1], A. Wolf[2], and S. Yaramishev[1]

[1]GSI, Darmstadt, Germany; [2]MPI-K, Heidelberg, Germany, [3]IAP Uni-Frankfurt, Germany

Heavy, highly charged ions (HCI) are interesting systems for many different experiments as for instance precision tests of the theory of quantum electrodynamics (QED). In order to transform heavy HCI produced at 400 MeV/u to stored and cooled HCI at low energy the linear decelerator facility HITRAP has been conceived behind the experimental storage ring (ESR). Its setup has been started in 2006 and commissioning is underway [1].

In the ESR ions are decelerated from 400 to 4 MeV/nucleon, cooled and extracted; meanwhile a routine operation. Up to ten million ions can be extracted at 4 MeV/nucleon and sent to HITRAP.

The ions are then matched to an interdigital H-type structure (IH) using a double drift buncher, decelerated from 4 to 0.5 MeV/nucleon in the IH, and then down to 6 keV/nucleon in a radio frequency quadrupole (RFQ).

About one million highly charged ions are typically decelerated with the IH from 400 MeV/nucleon to about 0.5 MeV/nucleon per cycle. However, the optimization of the combination of two bunchers (combined in the double drift buncher) and the IH is still difficult and not completely understood. The large parameter space given by three RF amplitudes and two phases requires the investigation of many different settings.

In 2012, the rebuncher between IH and RFQ structures was taken into operation. With a measured loaded Q-value of about 5000 and an effective impedance of 29 MΩ it yields a gap voltage of 100 kV for A/q=3. For $^{50}Ti^{22+}$ ions the effective gap voltage of 80 kV corresponds to a change in energy of less than 35 keV/nucleon.

To measure the action of the buncher on the beam, the phase of the rebuncher RF was changed relative to the master oscillator driving the IH radio frequency (fig. 1). Effectively, this makes the ions experience different gap voltages. The largest measured dispersion on the energy analysing detector of about 0.8 mm corresponds to an approximate change in energy of 40 keV/nucleon, pretty close to the expected value.

The full-width-half-maximum of the peak on the detector is 45 keV/nucleon. This is the result of a convolution of geometrical spread due to imaging, slit size and camera issues with the actual energy spread of the ion beam. This has not yet been disentangled, but first estimates show that at least half of that spread is due to the energy spread.

All efforts to decelerate the beam further with the RFQ structure failed so far. The most probable reason is a slight mismatch of the IH output energy distribution and the energy range accepted by the RFQ. This was found in recently updated simulations of the RFQ structure using the code DYNAMION accompanied by detailed 3D measurements of the electrodes and verified in off-line test. Consequently, a new electrode set has been designed, built and tested off-line [2,3,4] with an on-line test pending autumn 2013.

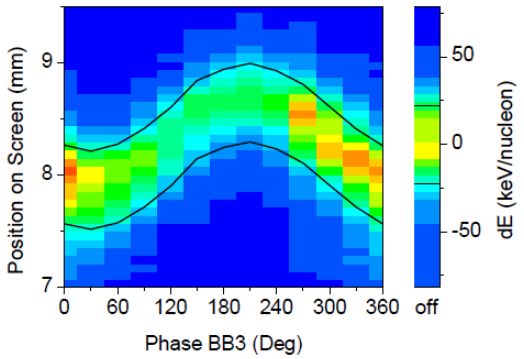

Figure 1: Commissioning of the spiral rebuncher between IH and RFQ. Shown are position on the screen, corresponding energy shift, and intensity (in arbitrary units) of the beam on the energy analysing detector versus the phase of the radio frequency driving the buncher cavity. A power of 1.1 kW was used for all phases. The lines are the FWHM limits of a Gaussian fit of the beam profile at each phase.

The cooler Penning trap was tested offline with deuterium ions from a cross beam ion source, an electron source to provide the electrons for the electron cooling scheme and medium heavy, highly charged ions from a compact, room temperature electron beam ion trap (EBIT) [5]. Finally, O^{8+} ions have been stored for an extended period of time. The simultaneous storage of ions and electrons is the next item on the test schedule.

References

[1] F. Herfurth *et al.*, "The HITRAP Decelerator and Beam Instrumentation", HIAT'12, Chicago, July 2012, p. 217, http://www.jacow.org.

[2] S. Yaramyshev *et al.*, "A new Design of the RFQ-Decelerator for HITRAP", this annual report.

[3] K. Dermati *et al.*, "Manufacturing and Assembly of the Electrode Structure of the HITRAP RFQ", this annual report.

[4] M. Maier *et al.*, "Offline commissioning of the old and new HITRAP RFQ", this annual report.

[5] A Sokolov *et al.*, "SPARC EBIT — a charge breeder for the HITRAP project", J. Instrum. 5 (2010), C11001.

Simulation of Resistive Cooling in cylindrical Penning Traps*

J. Steinmann[1,2], *J. Groß*[2], *F. Herfurth*[1], *and G. Zwicknagel*[3]

[1]GSI Helmholtzzentrum, Darmstadt, Germany; [2]University of Applied Sciences, Darmstadt, Germany; [3]University, Erlangen-Nuernberg, Germany

The simulation of ion clouds in traps taking ion-ion interaction into account is associated with large computational effort. This applies especially for the simulation of cooling methods like e.g. resistive cooling, where the cooling force has a complex structure. In [1] a simulation method for the resistive cooling was presented, using a particle in cell code. There the ion-ion interaction was treated by a mean-field approximation which, however, neglects the influence of ion-ion correlations on the dynamics. We thus developed an algorithm for the simulation of resistive cooling including the complete ion-ion interactions.

Charged particles moving between two conductive electrodes induce a surface charge Q on both of them and cause a potential imbalance u. Connecting the electrodes to an external RLC-circuit leads to an electrical current i. Energy dissipation in the resistor of the circuit then leads to changes in the induced charges on the electrodes and the related electric field which acts back on the ions as a cooling force $\vec{F}_D$. This non-trivial coupling between the circuit and the ion motion is described by the equations:

$$\frac{d^2u}{dt^2} + \frac{R}{L}\frac{du}{dt} + \frac{1}{LC}u = \frac{1}{C}\left(\frac{R}{L}\frac{di}{dt} + i\right) \quad (1)$$

$$i = \sum_{k=1}^{N} \frac{d}{dt} \cdot \Delta Q(\vec{r}_k)$$

$$\ddot{\vec{r}}_j = \frac{1}{m_j} \cdot \Big(\vec{F}_E(\vec{r}_j) + \vec{F}_B(\dot{\vec{r}}_j) + \cdots + \vec{F}_C(\vec{r}_1, \cdots, \vec{r}_N) + \vec{F}_D(\vec{r}_j, u)\Big) \quad (2)$$

R represent the resistance, C the capacitance and L the inductance of the circuit which is driven by the current i and ΔQ is the difference of the induced charges on the Pick-Up electrodes. $\vec{F}_E$, $\vec{F}_B$, $\vec{F}_C$ and $\vec{F}_D := -q_j\vec{\nabla}V_D$ represents the forces from the electrical field, magnetic field, the Coulomb interaction and the induced Potential. N is the number of ions and $\vec{r}_j$ the position vector of the j-th particle. The induced charge on one of the Pick-Up electrodes is given by the equation:

$$Q = a \cdot \sum_{k=1}^{N} \int_{z_<}^{z_>} \int_0^{2\pi} \epsilon_0 \frac{\partial V(r, \phi, z; r_k, \phi_k, z_k)}{\partial r}\bigg|_a d\phi dz, \quad (3)$$

where $z_<$, $z_>$ representing the z coordinates of the electrode, V_k the potential of the k-th ion using cylindrical coordinates and a the radius of the trap.

* Work supported by FE, Project-Number DAGROS1012.

In figure 1, the workflow of the resistive cooling algorithm is shown. The algorithm starts with an inital distribution of the positions and velocities of the ions, while the electrical Potential V_D caused by the induced current is neclegted at first. Next equation (2) is solved numerically to calculate a new set of positions, velocities and accelerations from which the right hand side of equation (1) is evaluated. After solving equation (1), finally the electrical potential V_D is calculated and serves together with the new positions and velocities as a starting point for the subsequent cycle.

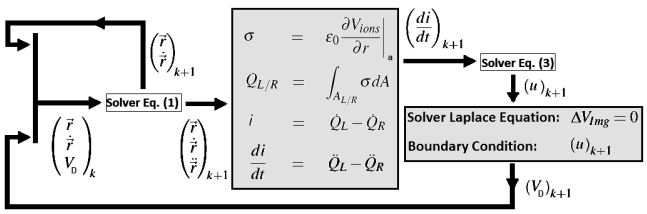

Figure 1: Workflow of the resistive cooling algorithm

Currently we work on the implementation of this algorithm into our existing code [2]. First simulations done with single ions show the expected cooling behavior. Figure 2 shows the simulation result of a single $^{12}C^{5+}$ ion in a cylindrical geometry with radius of $3.5\ mm$. The parameters of the circuit were chosen as $(R,\ L,\ C) \approx (10\ \Omega,\ 1.22\ mH,\ 14.22\ pF)$. The simulation was done on a GPU device using an parallelized Adam-Bashforth method of fourth order.

Next steps are the comparsion of the simulation results with experimental data were the circuit parameters are well known and investigating the cooling behavior for an increasing ion number.

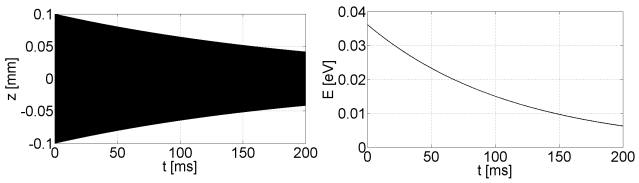

Figure 2: Left: Amplitude of the axial motion, Right: Total axial energy of the ion during resistive cooling.

References

[1] G. Maero , Springer , Applied Physics B , vol. 107 , p. 1087-1096.

[2] J. Steinmann , GSI Report 2009-1 , p. 307.

Demonstration of the Sensitive Schottky-System for CR *

A. Penirschke[1], *M. Hansli*[1], *W. Kaufmann*[2], *P. Hülsmann*[2], *M. Schwickert*[2], *A. Angelovski*[1], *W. Ackermann*[3], *W. Müller*[3], *T. Weiland*[3], *and R. Jakoby*[1]

[1]IMP, TU Darmstadt, Germany; [2]GSI, Darmstadt, Germany; [3]TEMF, TU Darmstadt, Germany

Introduction

This report summarizes the development of a sensitive longitudinal and transversal Schottky-Sensor for the Collector Ring CR at FAIR. Based on the equivalent circuit model, numerical simulations with CST Microwave Studio, controlled by MATLAB were accomplished to optimize the performance of the sensor structure to the needs of the CR. To demonstrate the performance, a scaled non-hermetic demonstrator was optimized, fabricated and characterized.

Schottky-System Design

Resonant cavities exhibit excellent performances with moderate size for schottky measurements at the ESR [1]. The evaluation of the monopole mode TM_{010} and the dipole mode TM_{110} allows longitudinal as well as transversal schottky measurements. Due to the weak excitation of the dipole mode, both modes need to be coupled out independently and, to suppress the monopole mode for the extraction of the transversal signal, rectangular waveguide resonators are foreseen for the CR [2, 3].

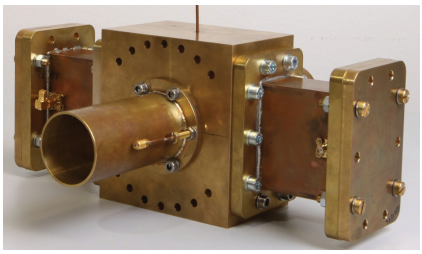

Figure 1: Non-hermetic demonstrator with a beampipe dimension of 46.5 mm.

Structure Optimization

Due to the strong inter-dependence of the relevant parameters and the complex structure, the sensor system cannot be separated into subsystems. To optimize the coupling geometry, the simulations with CST Microwave studio are iteratively controlled by MATLAB. The algorithm optimizes the length of the waveguide for maximum coupling between the pillbox and the waveguide resonators under condition that the monopole mode is kept constant at 200 MHz, which can be adjusted by the radius of the pillbox. The algorithm closes with the adaption of the coupling geometry, until the goal, the maximum gradient of the $\frac{R}{Q}$-value of the dipole mode is achieved.

* Work supported by BMBF: 06DA90351

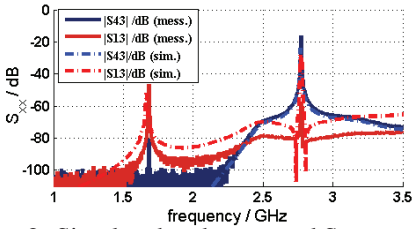

Figure 2: Simulated and measured S-parameters.

Non-hermetic demonstrator

To prove the simulation results, a non hermetic demonstrator scaled down by a factor of 8.6 was realized at TU Darmstadt (see fig.1). S-parameter results exhibit very good agreement between simulation and measurement (fig. 2). Preliminary perturbation measurements of the system exhibits good agreement with the expected behavior for both, the longitudinal and transversal detection (fig. 3).

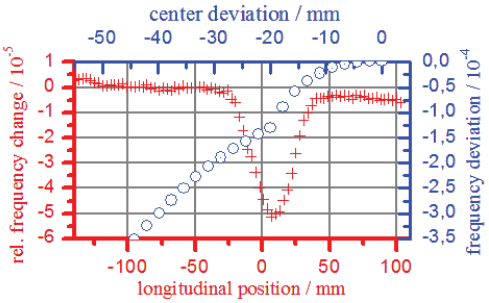

Figure 3: Preliminary results of the perturbation measurements.

Summary and Outlook

An iterative optimization algorithm based on Matlab controlled CST Microwave Studio simulations have been verified by a realized non-hermetic demonstrator. The optimization of the sensor geometry for the CR is ongoing.

References

[1] F. Nolden *et al.*, "A Fast and Sensitive Resonant Schottky Pick-up for Heavy Ion Storage Rings", Nuclear Instruments and Methods in Physics Research Section A, 2011.

[2] M. Hansli, *et al.*, "T. Conceptual Design of a high Sensitive Versatile Schottky Sensor for the Collector Ring at FAIR , Proceedings DIPAC11, 2011

[3] M. Hansli, *et al.*, "Coupling Methods for the Highly Sensitive Cavity Sensor for Longitudinal and Transverse Schottky Measurements, Proceedings BIW12, 2012

Studies for the radioactive waste management of copular air filters

M. M. Günther[1], E. Kozlova[1], A. Sokolov[1], K. Vogt[1] and G. Fehrenbacher[1]

[1]GSI, department of radiation protection, Darmstadt, Germany

One of the main tasks of the radiation protection department at GSI is the radioactive waste management. Among the duties around the radioactive waste management (see other annual reports of 2012) are the inspection and utilization of used air filter systems, fig. 1 a). As the filters could contain radioactive isotopes, it is mandatory to analyze the possible radioactive nuclides and their activities within the filter. The isotopes emitting distinctive γ ray decay lines allow identification using a High Purity Germanium (HPGe) detector. The remaining difficulty is the determination of the efficiency calibration and thus the determination of the minimum detectable activity (MDA) [1]. In the following we introduce results from simulation and experimental studies of the MDA determination.

The main difficulty for the determination of the MDA is the complicated internal structure of the copular air filter. Each filter consists of an inlet and an outlet section, see fig. 1 b) and c).

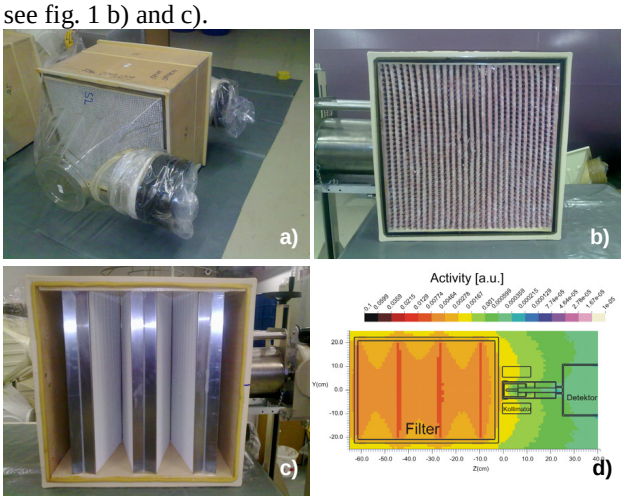

Figure 1: a) Copular air filter. b) charcoal filter of the incoming air section. c) Micro structure filter fins of exhaust section. d) Simulated activity distribution of the air filter.

The HPGe detector is used with a tungsten collimator reducing the background counts. To determine the MDA we used several calibration point sources (^{241}Am, ^{152}Eu, ^{210}Pb) in combination with an unused copular air filter (fig.1). These sources were placed behind and in the middle of the filter, while the detector was placed right in front. The experimental results are compared to the simulation using the Monte Carlo radiation transport code FLUKA [2]. The comparison of the results from FLUKA and the experiment for the point sources shows relative agreement with 20% discrepancy means the differences in the ideal to real terms of the detector-filter system. Additional simulations were done for expanded sources to be compared with point sources. Figure 1 d) shows example of the simulated activity distribution for expanded sources related to the activated filter fins. Figure 2 shows the detector efficiency as a function of the γ ray energy.

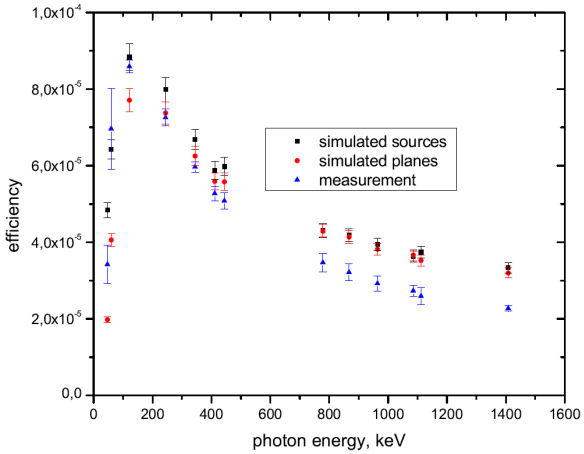

Figure 2: Detector efficiency as a function of γ ray energy.

The difference between the efficiency of a point source and an expanded source is not significant with a discrepancy of less than 5%. So, for future measurements of copular air filters we can use point sources for the efficiency calibration instead of complicated expanded sources.

Nuclide	Energy keV	Iγ %	MDA (Bq)	
			Middle	Behind
Pb-210	46,54	4,25	1,13E+02	2,58E+03
Cs-137	661,66	85,10	4,04E+00	5,65E+01
K-40	1461,00	10,67	6,04E+01	4,43E+02
Tl-208	2614,53	99,16	1,04E+00	7,53E+01

Table 1: MDA of different background lines of detector-filter system. The detector efficiency was used in terms of the calibration using point sources in the middle and the back of the filter element.

Table 1 shows the MDA of the detector-filter system for the γ ray lines of naturally occurring isotopes. It demonstrates the high accuracy for the determination of a low MDA for different γ decay lines using the mentioned results.

The consolidated results of the detector efficiency study lead to the determination of isotopes with very low activities satisfying the DIN norms [1]. Furthermore, future measurements of used copular air filters can be done with high accuracy which lead to a proper and routine radioactive waste management.

References:

[1] Nachweisgrenze DIN 25 4825

[2] http://www.fluka.org

Electron spectroscopy at the high-energy endpoint of electron-nucleus bremsstrahlung

P.-M. Hillenbrand[1,2], S. Hagmann[1,3], D. Banas[4], C. Brandau[1,5], K.-H. Blumenhagen[6], W. Chen[1], A. Gumberidze[5], D. Guo[7], E. DeFilippo[8], C. Kozhuharov[1], M. Lestinsky[1], Y.A. Litvinov[1], A. Müller[2], H. Rothard[9], S. Schippers[2], M. Schöffler[3], U. Spillmann[1], S. Trotsenko[1,6], N. Winckler[1], X. Yan[7], and Th. Stöhlker[1,6]

[1]GSI Darmstadt; [2]Universität Giessen; [3]Universität Frankfurt; [4]JKU, Kielce, Poland; [5]EMMI Darmstadt; [6]Helmholtz Institut Jena; [7]IMP, Lanzhou, China; [8]INFN, Catalania, Italy; [9]CIRIL-Ganil, Caen, France

In electron-nucleus bremsstrahlung an electron with kinetic energy E_0 scatters inelastically off an atomic nucleus and emits a photon of energy E_γ under energy conservation $E_0 = E_f + E_\gamma$:

$$e_0(E_0) + A \rightarrow e_f(E_f, \vartheta_f) + A + \gamma(E_\gamma, \vartheta_\gamma) \qquad (1)$$

The coincident detection of scattered electron $e_f(E_f, \vartheta_f)$ and bremsstrahlung photon $\gamma(E_\gamma, \vartheta_\gamma)$ provides the most stringent tests for our understanding of the coupling between a matter field and an electromagnetic field.

Of particular theoretical interest is the case, when the entire kinetic energy of the incident electron is transferred to the photon; the theoretical description of the resulting high-energy endpoint of the electron-nucleus bremsstrahlung spectrum is closely related with photoionization PI and radiative electron capture REC. This process is not accessible in classical setups, where energetic electrons are scattered off high-Z target atoms at rest.

However, using a setup in inverse kinematics, namely highly charged heavy projectiles from the ESR, like U^{88+}, scattering off quasi-free electrons, enables us to perform coincidence measurements at the high-energy endpoint, as the scattered electron at rest in the moving frame appears in the 0°-cusp in the laboratory frame. Here the electron can be understood alternatively as radiatively captured into the continuum of the projectile (RECC).

In order to measure triple differential cross-sections $d^3\sigma/dE_e/d\Omega_e/d\Omega_\gamma$ of the RECC process a beam of U^{88+} was injected into the ESR at 90MeV/u intersecting a supersonic N_2 gas target. Cusp-electrons emitted from the gas target into the forward direction ϑ_f=0° at velocities close to the projectile velocity where detected with the ESR electron spectrometer. The spectrometer consists of two 60°-dipole magnets for momentum analysis and an iron-free quadrupol-triplett in between the dipols to enable telescopic imaging onto a position sensitve MCP-delayline-detector (cf. last annual report [1]). To measure the X-rays five standard Ge-detectors where used at angels $\vartheta_\gamma = +35^\circ, +90^\circ, +150^\circ, -90^\circ$, and -145° around the interaction point. Particle detectors in the ESR dipole magnets where used to detect capture and ionization events.

Using this setup we were able to measure for the RECC process the electron energy distribution for five different photon emission angles, and accordingly the photon angular distribution of the electron-nucleus bremsstrahlung at the high-energy endpoint.

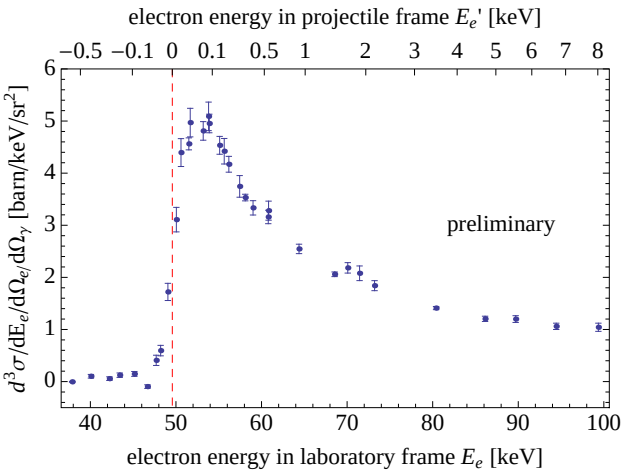

Figure 1: Electron energy distribution for forward emitted electrons in coincidence with a photon emitted at $\vartheta_\gamma = +90^\circ$.

Fig. 1 shows examples of preliminary results for the electron energy distributions. The cross section is given differentially in electron energy dE_e, electron emission angle $d\Omega_e$ and the photon emission angle $d\Omega_\gamma$ while being integrated over the energy of the coincident photon energy E_γ. The distribution is peaked above the electron energy of $E_0 = 49.6keV$ corresponding to $E'_f = 0$ projectile frame energy. The strong asymmetry of the cusp shows that electrons are in the projectile frame predominately emitted into the forward direction. The spectra will be compared with state-of-the-art theories such as [2].

P.-M. H. greatfully acknowledges support by HGS-HIRe.

References

[1] P.-M. Hillenbrand, Commissioning of the electron spectrometer at the ESR, GSI Scientific Report 2011

[2] D.H. Jakubassa-Amundsen, Radiative ionization: The link between radiative electron capture and bremsstrahlung, Radiation Physics Research Progress, 2008, pp.155-191

Two-electron one-photon transition in Li-like Bi

S.Trotsenko[1,2], A. Gumberidze[3], K. Sosnova[4], E. Rozenbaum[4], M. Lestinsky[2], and Th. Stöhlker[1,2,5]

[1]Helmholtz-Institut Jena, Jena, Germany; [2]GSI, Darmstadt, Germany; [3]ExtreMe Matter Institute/GSI, Darmstadt, Germany; [4]Sankt-Petersburg University, Sankt-Petersburg, Russia; [5]Friedrich-Schiller-University Jena, Germany

We report on experimental study of the decay properties of $1s(2s^2)$ state in Li-like bismuth (Z=83), adopting a state selective K-shell ionization technique [1]. This state is expected to undergo predominantly an exotic $1s(2s)^2 \rightarrow (1s)^2 2p_{1/2}$ two-electron one-photon decay (TEOP) [2, 3], which is interesting because of its sensitivity to electron correlation effects. In the high-Z ions the $1s(2s^2)$ state can also decay to the ground $(1s)^2 2s$ state via a radiative magnetic dipole M1-transition. The strong variation of the decay properties of the states along the isoelectronic sequence is an ideal testing ground for our understanding of the interplay of electron correlation and relativistic effects in a few-electron ions. The experiment was performed at

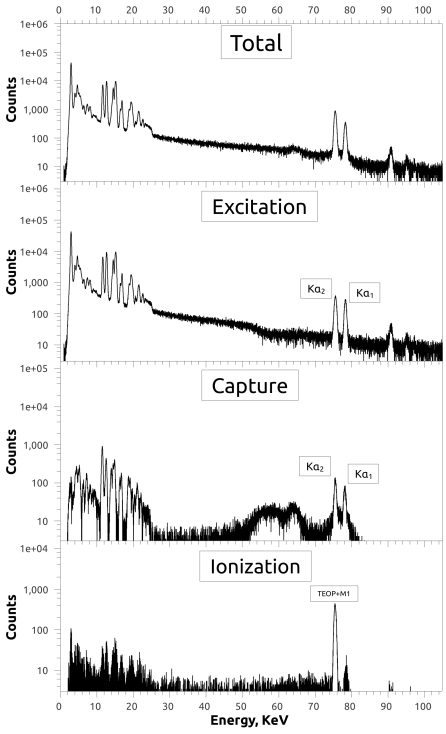

Figure 1: Preliminary x-ray spectra recorded for $Bi^{79+} \rightarrow N_2$ (see text for details).

the ESR (GSI) with 98 MeV/u Be-like bismuth ions colliding with a gas jet target (N_2). The x-rays produced in this process (see Fig. 1) were measured under an angle of 35° with respect to the propagation direction of the ion beam (for details concerning the setup see [1]). By the coincident registration of x-rays with the charge state of the ions after the collision, few different radiative processes can be separated: K-shell excitation of the Be-like ions, the radiative electron capture and the formation of excited states of the Li-like ions produced by K-shell ionization. As can be seen in the ionization spectrum (Fig 1:Ionization), K-shell ionization appears to be a very selective population process, because in the associated photon spectrum only one single x-ray line is observed stemming from the decay of the $1s(2s^2)$ state.

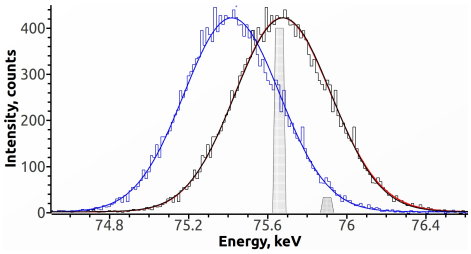

Figure 2: Preliminary analysed ionization spectrum peak; blue steps / blue line: the peak position defined by radiative sources calibration/ the corresponding fitting curve; black steps / black line: the peak position obtained by the calibration based on the theoretical Kα1 and Kα2 lines / the corresponding fitting curve; grey boxes: theoretical predictions for the TEOP (left) and M1 (right) transitions with the widths corresponding to the theoretical uncertainties; red line: convolution of the theoretical predictions [3].

The energy separation between the two transitions of interest, TEOP[$1s(2s^2) \rightarrow (1s)^2 2p_{1/2}$] and M1[$1s(2s^2) \rightarrow (1s)^2 2s_{1/2}$], is close to 250 eV in the emitter frame. Due to the lack of high resolution x-ray detectors within the current investigation, the goal of the current data analysis is to determine M1/TEOP branching ratio, i.e. the contamination of the TEOP by the M1 decay, using an accurate line centroid determination of the observed x-ray line. Apart from a conventional method utilising an accurate calibration of the detector with radioactive sources, a complementary calibration method was used based on corresponding energies of the Kα1- and Kα2-lines, produced by excitation (Fig. 1:Excitation), as an energy reference. The latter provides an important cross-check for the Doppler corrections to be applied. This, however, is based on the assumption that K-shell excitation of the Be-like ions occurs to the $1s(2s)^2 p_{3/2}$ and $1s(2s)^2 p_{1/2}$ levels exclusively. Preliminary results are presented in the Fig. 2, suggesting a dominance of the TEOP over the M1 transition. The data analysis is in progress.

References

[1] J. Rzadkiewicz et al., Phys. Rev. A 74, 012511 (2006)

[2] C. Z. Dong et al., J. Phys. B: At. M. Op. Ph. 39, 3121 (2006).

[3] A. Volotka and Y. Kozhedub, Private communication.

Single Differential Cross Section $d\sigma/dE_{electron}$ for Projectile Ionization of U^{28+} Ions at 30-50AMeV measured in the ESR

S. Hagmann[1,2], P.-M. Hillenbrand[1,3], W. Chen[1], G. Dalong[4], Ch. Dimopoulou[1], R. Dörner[2], R. Dubois[5], R. Grisenti[1,2], A. Gumberidze[1,6] , Ch. Kozhuharov[1], M. Lestinsky[1], Yu. Litvinov[1], A. Müller[3], F. Nolden[1], N. Petridis[2], S. Sanjari[1,2], S. Schippers[3], U. Spillmann[1], M. Steck[1], G. Weber[7], D. F. A. Winters[1], N. Winckler[1], X. L. Yan[4], and Th. Stöhlker[1,7,8]

[1]GSI Darmstadt, [2]Univ. Frankfurt, [3]IAMP, Univ. Giessen, [4]IMP, Lanzhou, China, [5]Univ. of Missouri, Rolla, USA, [6]Extreme Matter Inst. EMMI, Darmstadt, [7]Helmholtz Inst. Jena, [8]Physikal. Inst., Univ. Jena,

For heavy ion projectiles with specific beam energies from 1 AMeV to beyond 10 AGeV, the overwhelming contribution to beam loss in accelerator facilities at GSI/FAIR is quantitatively described as collisions of the swift projectile (in a charge state q) with quasifree target electrons which are ionized into the continuum.

Remarkably, for non-bare projectiles another contribution to stopping power and beam loss appears; besides the electron continua attributed to target ionization a prominent and strong cusp shaped feature at 0^0 with respect to the projectile direction and with $v_e \approx v_{projectile}$ is observed and is attributed to electron emission from ionization of a projectile carrying electrons, this cusp is normally labelled as electron loss to continuum (ELC) cusp.

The magnitude of the cross section indicates the relevance this ionization channel has for swift structured projectiles. It so comes as no surprise so see this channel also as the dominant loss rate for multi-electron U^{28+} beams in SIS and ESR and future FAIR facilities [1].

For the future accelerator project FAIR high intensity beams of relativistic high-Z projectiles like Uranium are envisaged. The needed luminosity of the beam –subject to the space charge limit $\sim A/q^2$ -can only be achieved for such ions of high-Z when a low charge state q of the ion to be accelerated keeps the number density at a higher level than the one which would be expected for a higher charge state of the projectile. A technically optimal solution for the existing UNILAC accelerator facilities serving FAIR are Uranium beams with a mean charge state 28+ (i.e...$4f^{14}5s^25p^2$) accelerated to 7.1 AMeV in the UNILAC and then further in the SIS 18 to 50 AMeV. The SIS18 needs to inject 1.3 10^{11} ions at 2.6 Hz into the SIS100 synchrotron which then provides beams from 400 AMeV to 2.7AGeV for experiments.

As the charge state 28+ of the U beam is nearly over the entire acceleration phase in both synchrotrons far below the average charge state for the near relativistic beam velocity, the dominant beam loss is projectile ionization $U^{28+} + \{A\} \rightarrow U^{(28+n)+} + \{A^{+*}\}$ with $n \geq 1$; a fraction exceeding 40% has been calculated [1] for multiple loss $n \geq 2$ arising from the large number of weakly bound electrons on the projectile (E_B= 930eV for the ionization potential of U^{28+}). Attempts for first order theoretical description of ionization of U^{28+} in fast collisions ($v_e \ll v_{projectile}$ for outermost electrons) have surprisingly produced mixed results.

Detailed calculations by A. Voitkiv et al. from the MPI-K [2] incorporate in their *ab initio* theoretical approach the symmetric eikonal model for relativistic ion-atom collisions and provide total ionization cross sections, but also differential projectile ionization cross sections for the ELC cusp. Importantly, the eikonal approximation gives at low collision energies 5 to 10 lower total cross sections than the first order theory [2].

We have embarked on an extensive experimental study to investigate single differential ionization cross sections $d\sigma/dE_{electron}$ (SDCS) for single and multiple U^{28+} projectiles [3]. Using the imaging forward electron spectrometer in the supersonic target zone of the ESR we have measured SDCS $d\sigma/dE_{electron}$ for the electron loss to continuum (ELC) cusp in collisions at 30 and 50 AMeV

$$U^{28+} + [H_2, N_2, Xe] \rightarrow U^{q+} + e_{cusp}(0^0) \quad (1).$$

The preliminary absolute SDCS exhibit strong asymmetries of the (ELC) cusp (see fig. 1), which are at variance with simple first order Born approximation theories. Future experiments with electrons measured in coincidence with the outgoing projectile charge state in order to distinguish SDCS from single and multiple electron loss of the projectile are in preparation.

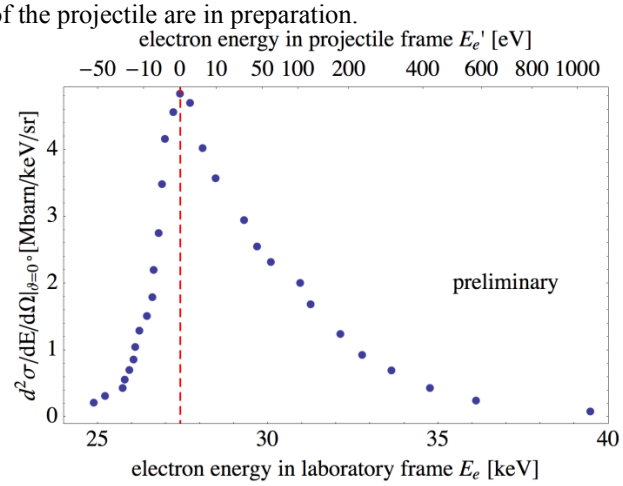

Fig.1 absolute SDCS (±70%) for projectile ionization in 50 AMeV U^{28+} +Xe collisions

References

[1] M. Song et al., NIM **B267** 2369 (2009)
[2] A. Voitkiv et al., Phys. Rev.**A82,** 022707 (2010)
[3] S. Hagmann et al., Proposal E117, GSI (2012).

Charge transfer in collisions between highly charged Xe ions and Mg atom

W. Chen, G. Vorobyev, F. Herfurth, and T. Stöhlker
GSI Helmholtzzentrum für Schwerionenforschung , Darmstadt, Germany

In this report, we study the charge transfer process between slow, highly charged xenon ions and magnesium vapor. In general the process can be described as

$$\mathrm{Xe}^{q+} + \mathrm{Mg} \rightarrow \mathrm{Xe}^{(q-p)+} + \mathrm{Mg}^{r+} + (r-p)e^{-} \qquad (1)$$

The cross section for that process is $\sigma_r^{q,q-p}$. Within the main process we can distinguish three different sub processes, electron capture ($r - p = 0$), ionization transfer ($r - p > 0$) and ionization ($p = 0$, and $r > 0$). The latter is negligible for the here studied velocity regime..

The setup is shown schematically in Fig. 1. Highly charged xenon ions ($^{132}\mathrm{Xe}^{q+}$) were extracted from an electron beam ion trap at GSI [1] with an energy of $5.5\,q$ keV continuously. After charge to mass selective bending, the ion beam collided with the magnesium vapor produced by an oven. Finally, the projectiles were dispersed by another bending magnet to separate primary ions and ions with one or more captured electrons, recorded by a position sensitive multi-channel plate (MCP) detector. The recoiled Mg^{r+} were accelerated by an electric field perpendicular to the beam axis towards a second MCP detector. The signals of both detectors were measured in coincidence to get the time of flight (TOF) of the recoiled magnesium ion from the reaction zone to the detector. The detected position of the projectiles and the TOF of the recoiled magnesium ions allows one to separate the above mentioned sub processes and, hence, to measure the differential charge exchange cross sections. A typical position spectrum at the projectile detector and a TOF spectrum from the recoil detector are shown in Fig. 2. Unexpectedly, almost no Mg^{3+} ions were produced in the collision.

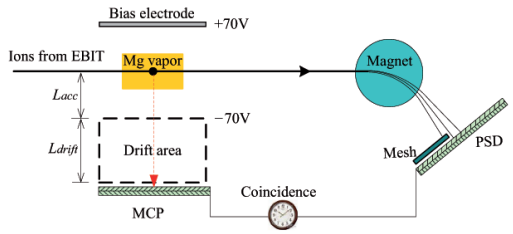

Figure 1: Schematic setup as explained in the text.

After appropriate background subtraction, the peak areas are proportional to the corresponding cross section. The cross section ratio $\sigma_2^{q,q-1}/\sigma_2^{q,q-2}$ as a function of projectile charge state is shown in Fig. 3. It shows that for the system we studied, transfer ionization dominates the two-electron removal process.

Theoretically, the charge transfer process is described in a two-step picture. First the projectile ion and target

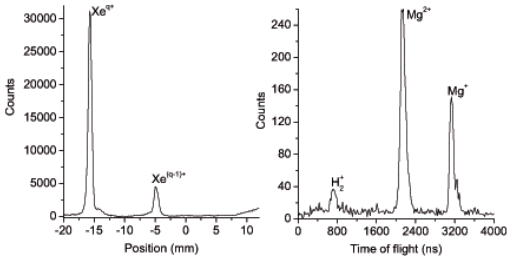

Figure 2: Left: charge-state distribution of projectile ions after collision with the magnesium target. The primary beam of Xe^{q+} is attenuated by a dense mesh on front of the PSD. Right: TOF spectrum from the recoil detector with the projectile as trigger.

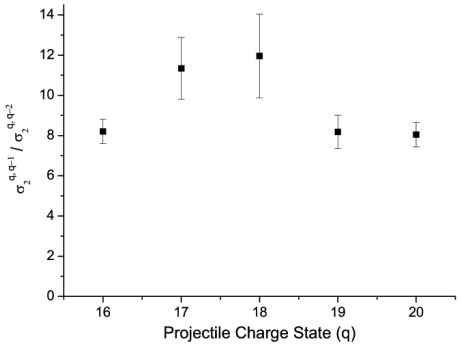

Figure 3: The cross section ratio of transfer ionization to pure two electron capture as a function of the projectile charge state.

atom form a quasi-molecule, while the projectile captures two electrons from the target to Rydberg orbitals, forming a doubly-excited state. Then the doubly excited ions release their excess energy by radiative decay or by the Auger process. Especially for highly charged ions with large potential and metal targets with loosely bound electrons, the Auger process dominates the relaxation. This situation is studied for the first time, and shows large deviation from theoretical calculations based on a classic over-barrier model or semiempirical calculations [2].

References

[1] A Sokolov et al., “SPARC EBIT — a charge breeder for the HITRAP project”, J. Instrum. **5** (2010), C11001.

[2] N. Selberg, C. Biedermann and H. Cederquist, Phys. Rev. A 56 (1997) 4623.

Characterization of a croygenic adsorption valve for inert gases

D. von Lindenfels[1,2], *J. Glässel*[3], *M. Wiesel*[3,4], *G. Birkl*[4], *W. Quint*[1,3], *and M. Vogel*[1,4]
[1]GSI, Darmstadt; [2]MPIK, Heidelberg; [3]PI, Uni Heidelberg; [4]IAP, TU Darmstadt

We are currently setting up ARTEMIS (AsymmetRic Trap for the measurement of Electron Magnetic moments in IonS) in the framework of the HITRAP facility. This experiment with highly charged ions in a cryogenic Penning trap combines precise spectroscopy both of optical transitions and microwave Zeeman splittings. The latter determine the magnetic magnetic moments (g factors) of bound electrons.

Argon ions are produced in the trap chamber by consecutive electron-impact ionization. To this end, neutral gas enters the trap chamber via a cryogenic valve and are bombarded with an electron beam coming from a field emission source.

The valve is depicted in Fig. 1: A narrow stainless steel tube comes from outside the outer vacuum chamber, which maintains a low pressure for the operation of the cryostat. We hook up a standard shutoff valve and a gas bottle on the lower end of the tube. The upper end is soldered to a cylindrical copper box, partially divided by several baffles. Another short tube guides the gas into the inner vacuum chamber, which will host the trap. The thermal contact to the trap chamber at 4 K via OFHC copper wire ensures a low temperature in the cold, i.e. 'closed', mode of the valve, while an attached resistor can locally heat it and regulate the temperature in the range of 15 to at least 100 K.

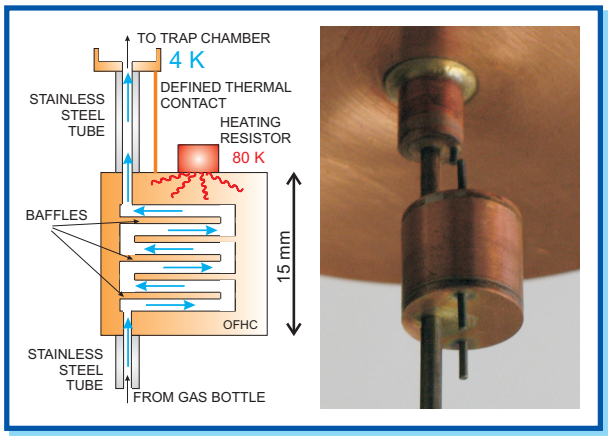

Figure 1: Schematic drawing of the adsorption valve with heater mounted, viewed in vertical section, and photograph of the ca. 1.5 cm long valve with tubes, soldered to the vacuum chamber.

The working principle relies on cryogenic adsorption: Atoms coming into the valve have to hit the baffles many times in order to travel through. They will most probably stick to a cold wall, so the box acts like a closed valve. When heated, sticking probability for incoming gas particles decreases, so that the valve is open. Additionally, the walls release adsorbed matter. Depending on the temperature, this allows a controlled flow of gas into the vacuum chamber [1, 2].

We have tested the valve with pulses of argon gas at defined pressure (1 mbar and below) and duration of 100 ms, applied at varying temperature. For the course of 10 s, the transmitted amount was recorded, using an IKR vacuum gauge as time-resolving detector inside the copper vacuum chamber, next to its gas port. It ranges down to 10^{-9} mbar.

The traces in Fig. 2 have been taken with 1.0 mbar pulse pressure, after several days of operation. No signal can be detected below 34 K. Above, a series of peaks appear. At increasing temperature they come with shorter delay and more intensity.

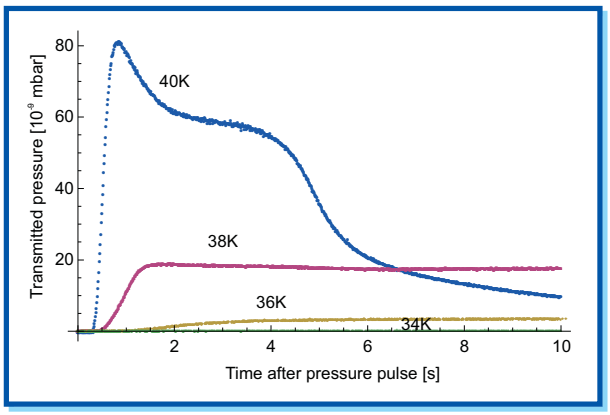

Figure 2: Time-resolved pressure in the vacuum chamber after the gas pulse, background corrected.

We are confident that the home-made gas valve will in the cold state maintain a pressure below 10^{-12} mbar in the vacuum chamber, mainly containing residual helium, hydrogen and neon gas, which are not cryo-pumped. When heated, it will supply enough argon for our measurement.

We thank E.E. Donets (supported by the BMBF programme JINR project no. 5.1) for the inspiration and Christoph Marzini for simulations. Great acknowledgement to Technologielabor for advising us and constructing the valve. Julian Glässel thanks the organizers of the summer student program.

References

[1] D. von Lindenfels, N. Brantjes, G. Birkl, W. Quint, V. Shabaev and M. Vogel, Can. J. Phys. 89 (2011) 79.

[2] D. von Lindenfels, Diploma Thesis, University of Heidelberg (2010), URL: http://www.gsi.de/documents/DOC-2011-Feb-63-1.pdf.

Interaction of heavy ions with warm dense plasma using hohlraum targets (combined experiment with PHELIX and UNILAC)

A. Ortner[*2], *A. Blazevic*[1], *M. Basko*[7], *S. Bedacht*[2], *W. Cayzac*[4], *A. Frank*[5], *S. Faik*[6], *D. Kraus*[2], *T. Rienecker*[6], *G. Schaumann*[2], *D. Schumacher*[1], *An. Tauschwitz*[6], *F. Wagner*[2], *and M. Roth*[2]

[1]GSI, Darmstadt, Germany; [2]Technical University Darmstadt, Germany ; [4]CELIA, France ; [5]Helmholtz Institut Jena, Germany ; [6]University Frankfurt, Germany ; [7]KIAM Moscow, Russia

Measurement of the energy loss and the charge state distribution of heavy ions in dense plasma, generated by indirect laser heating with double hohlraum cavities.
In 2011 we carried out a first proof of principle experiment using a double gold hohlraum to convert laser light into x-rays and to use them to generate a warm dense carbon plasma. The main result of this campaign was the measurement of the radiation temperature inside hohlraum [3,4]. The laser light, coming from PHELIX with 150 J in 1.5 ns at 528 nm, generates 100 eV of Planck radiation in the primary hohlraum, which leads to 33 eV radiation temperature in the secondary hohlraum. These measurements are in good agreement with theory and simulations. However, we found that the gold flow off of the walls inside the secondary hohlraum is expanding too quickly into the path of the probing ion beam and disturbs the energy loss measurement (see Fig. 2 a). Hence, in 2012, we put a lot of effort into improving the hohlraum geometry and the shielding. The new design as shown in Fig. 2 b) was studied in RALEF2D simulations [5] and experimentally verified. As shown in Fig. 1 a) the interaction area stays free of gold plasma for more then 4 ns which is enough time to probe the plasma with the ion beam. Fig. 1 b) shows a simulation with carbon foils attached to the back and front side of the hohlraum where electron densities of up to 10^{22} cm^{-3}, an electron temperature of 15 eV and an ionization degree of 3.5 can be reached. All simulations were benchmarked by experimental temperature and density measurements.

* a.ortner@gsi.de

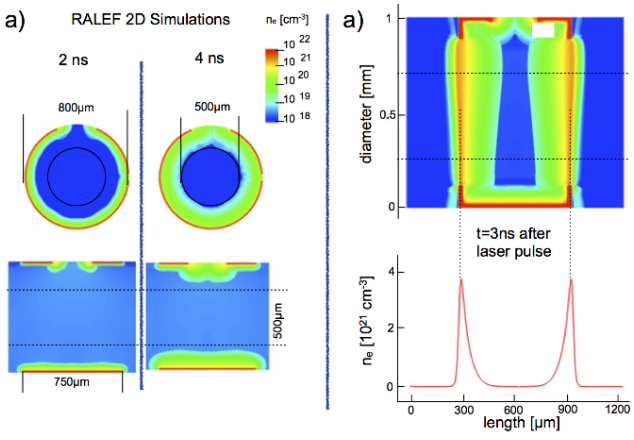

Figure 1: RALEF2D simulations: **a)** Gold flow in an empty hohlraum. With 1000 μm in diameter the hohlraum stays free of gold for more than 4 ns. **b)** Hohlraum with attached carbon foils and the resulting electron density of the carbon plasma after 3 ns of heating.

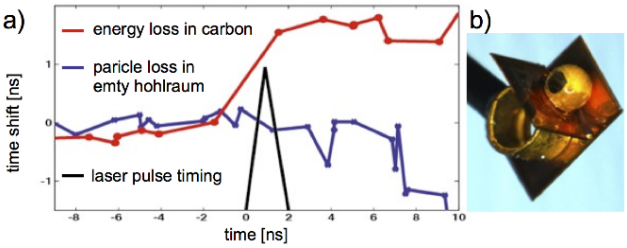

Figure 2: **a)** Results of the energy loss measurement. The upper (red) curve shows the measurement in dense carbon, the lower curve (blue) the signal drop in an empty hohlraum due to gold plasma flowing in **b)** New sub millimeter hohlraum targets with shielding.

The upper curve (red) in Fig. 2 a) shows the measured energy loss in the plasma which increases by about 40% compared to cold carbon. The lower curve (blue) shows a reference measurement in an empty hohlraum. After 6 ns the signal drops due to gold plasma completely stopping the ion beam. These results will be compared to theoretical models. Especially, we enhance a microscopic description of the energy loss as developed by [1,2] to enter this new regime. As we have an interaction of a partly ionized projectile with a partly ionized plasma, charge exchange processes will become relevant for the energy loss process. For this reason we are going to conduct a another experimental campaign at the end of 2013 where the charge state distribution after interaction will be measured precisely.
This project is supported by BMBF and HIC4FAIR

References

[1] A.Frank et al., Physical Review E, 81,02640 (2010)

[2] A.Frank et al., submitted to Physical Review Letters

[3] T. Hessling et al, Physical Review E, vol. 84, id. 016412 (2011)

[4] D.Schumacher et al, in preparation

[5] An.Tauschwitz et al., High Energy Density Physics, Vol. 9, 1, p. 158166 (2013)

Characteristic X-rays from silver foils for backlighting of WDM

O.F. Kostenko[1], *N.E. Andreev*[1], *O.V. Chefonov*[1], *A.V. Ovchinnikov*[1], *O.N. Rosmej*[2], *A. Schönlein*[3], *J. Wiechula*[3], *P. Neumayer*[3], *and J.Jacoby*[4]

[1]JIHT RAS, Moscow, Russia; [2]GSI, Darmstadt, Germany; [3]EMMI, Germany; [4]Goethe Universität, Frankfurt, Germany

The goal of experiments carried out at GSI with high intensity laser system PHELIX is the investigation of mechanisms leading to effective production of photons with energies above 20 keV required for monochromatic backlighting of Warm Dense Matter (WDM). In experiments, 1ω, 500fs, 100J laser pulses were used for irradiation of 3 mm thick Ag targets and thin foils deposited on Al and plastic substrates. The laser intensity was varied between 10^{18} and 4×10^{19} W/cm^2 by changing the laser focal spot size. In this report we present a comparison of numerical simulations of the silver K_α-photon yield with experimental results obtained by means of a single-hit CCD technique [1].

In simulations, the K_α-photon yields from Ag foils in given direction into a unit of solid angle per laser pulse energy, N_k, were calculated according to the model [2], which takes into account dependencies of the conversion efficiency of laser energy into hot electrons $\eta(I_\mathrm{L})$ [1] and average energy of hot electrons $T_\mathrm{h}(I_\mathrm{L})$ [3] on the laser pulse intensity $I_\mathrm{L}(r,t)$, as well as a self-absorption of 22.1 keV K_α photons in a foil of arbitrary thickness. In the case of Gaussian laser pulse, $I_\mathrm{L}(\upsilon) = I_0 \exp(-\upsilon)$, $\upsilon = r^2/r_0^2 + t^2/t_0^2$, we get

$$N_\mathrm{k} = \frac{2}{\sqrt{\pi}} \int_0^\infty \sqrt{\upsilon}\, \mathrm{d}\upsilon \frac{\eta(\upsilon)\, e^{-\upsilon}}{T_\mathrm{h}^2(\upsilon)} \times \times \int_{E_\mathrm{k}}^\infty \mathrm{d}E_0 \exp\left[-\frac{E_0}{T_\mathrm{h}(\upsilon)}\right] \frac{\mathrm{d}N_\mathrm{em}(E_0)}{\mathrm{d}\Omega},$$

were $\mathrm{d}N_\mathrm{em}(E_0)/\mathrm{d}\Omega$ is the number of photons per steradian, emitted by an electron, normally incident with initial energy E_0, from the front side of the foil in given direction.

Theoretical dependencies $N_\mathrm{k}(I_0)$, calculated with the assumption of suppression of hot electron refluxing, describe well features revealed in experiments: sharp increase of K_α-photon yield in the intensity range (1.5–2)$\times 10^{18}$ W cm^{-2}, and then relatively small decrease of N_k with growth of the intensity up to 3.4$\times 10^{19}$ W cm^{-2} (Fig. 1(a)). The K_α-photon yield increases up to 3 times with increase of foil thickness from 10 to 100 μm (cf. Figs. 1(a) and (b)). The last two features confirm the assumption about suppression of hot electron refluxing in foils deposited on the bulk substrates, even at high laser intensities. The K_α yield from the foil of 10 μm thickness with refluxing electrons, calculated for intensity $I_0 \approx 2.5 \times 10^{19}$ W cm^{-2} [2], exceeds shown in Fig. 1(a) value for the foil with single-pass electrons about 44 times, so only very small input from refluxing electrons could cause insignificant deviations of the experimental value from calculated one (see Fig. 1(a)).

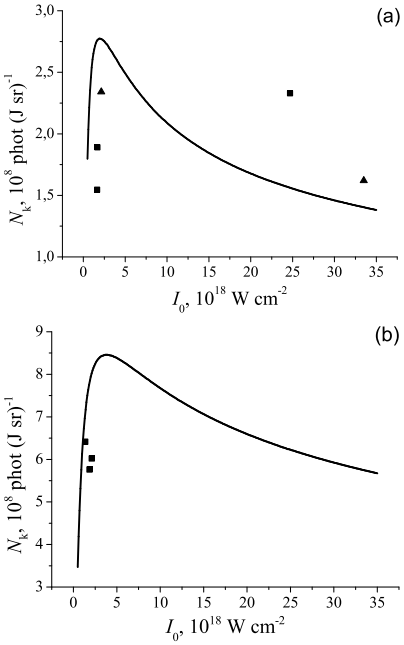

Figure 1: The K_α photon yield vs laser pulse intensity. Solid lines correspond to calculated values with Ag foils of thicknesses: (a) 10 μm and (b) 100 μm. Points correspond to measured values, multiplied by a factor 3: (a) Ag foil of 10 μm thickness deposited on bulk plexiglass (squares) and bulk Al (triangles); (b) Ag foil of 100 μm thickness deposited on bulk plexiglass.

It is important to point out that strong suppression of hot electron refluxing takes place as well for non-conductive substrates like a plexiglass. The last allows supposing the presence of plasma channels in dielectric substrates which occur due to ionization caused by the self-consistent electric field of the electron bunch [4]. Systematic overestimation by a factor about 3 of calculated K_α-photon yields over measured absolute values will be a subject of future analysis (see also [5]).

References

[1] P. Neumayer *et al.*, Phys. Plasmas **17**, 103103 (2010).

[2] O.F. Kostenko, N.E. Andreev, Quntum Electron. (submitted).

[3] S.C. Wilks *et al.*, Phys. Rev. Lett. **69**, 1383 (1992).

[4] V.T. Tikhonchuk, Phys. Plasmas **9**, 1416 (2002).

[5] M.N. Quinn *et al.*, Plasma Phys. Control. Fusion **53**, 025007 (2011).

Imaging Interferometer for Pressure Measurements in Ion-Beam Driven HEDP Experiments*

B.F. Ionita[1], S. El Moussati[1], D.H.H. Hoffmann[1], P.M. Lang[1], L. Shestov[1], S. Udrea[1], D. Varentsov[2], K. Weyrich[2], D. Nikolaev[3], N. Shilkin[3], V. Ternovoi[3], A. Kantsyrev[4], and N. Markov[4]

[1]TUD, Darmstadt, Germany; [2]GSI, Darmstadt, Germany;
[3]IPCP, Chernogolovka, Russia; [4]ITEP, Moscow, Russia

The relatively poorly explored near critical region of Pb ($T_c \approx 5500$ K, $p_c \approx 2.3$ kbar) was reached at HHT using sub-microsecond SIS-18 uranium beams at 350 AMeV and ~$3 \cdot 10^9$ particles/pulse, with a sub-millimetre spot on target, leading to uniform isochoric heating, evaporation and expansion of the material across a gap (Fig. 1a).

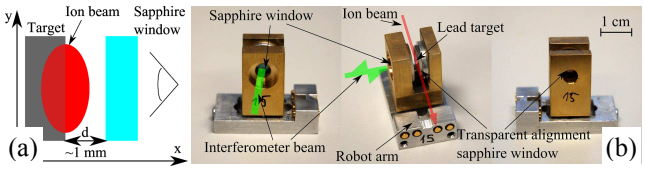

Figure 1: Target - ion beam - diagnostics configuration: (a) experimental principle; (b) target holder.

The behaviour of Pb during isentropic compression on the front surface of a sapphire window (Fig. 1) was analyzed using a fast multi-channel pyrometer [1] and a specially developed imaging displacement interferometer (Fig. 2), designed to permit for the first time simultaneous temperature and pressure measurements (Fig. 3) by integrating the light collection optics for both systems on the pyrometer head. The specularly reflecting sapphire surface is imaged on a 50% beam-splitter through a doubly afocal system in order to keep the optical front flat. It is further relayed to the surface of the reference mirror which can be tilted remotely to allow for fringe tuning, and to an alignment camera and a streak camera, at a final resolution of ~50 µm. The imaging capability is used to solve fringe movement uncertainties.

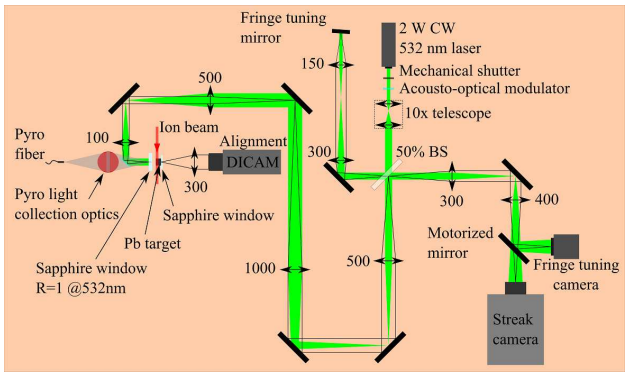

Figure 2: Optical schematics of the diagnostic devices.

Pressure is calculated as the product of acoustic impedance of sapphire and particle velocity (half of the surface velocity obtained through time derivation of the measured displacement, given no impedance matching).

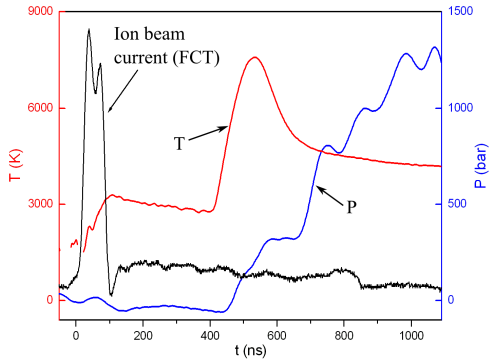

Figure 3: Simultaneous temperature (red), pressure (blue) and ion beam intensity (black) temporal profiles.

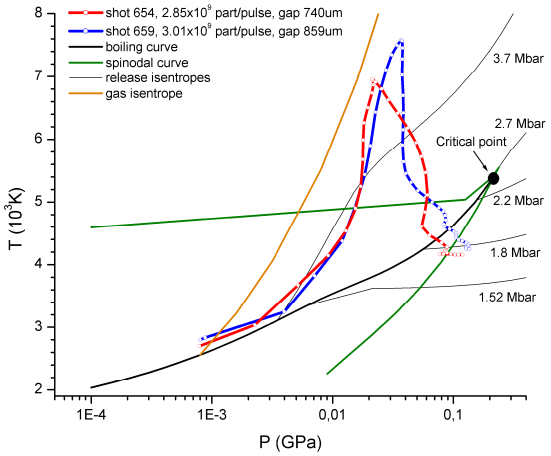

Figure 4: Explored region of the T-P phase diagram.

Two obtained temperature-pressure curves are shown in Fig. 4, as they start from a point on the boiling curve, approximately follow the 3.7 Mbar release isentrope [3] until it intersects the spinodal curve, afterwards kinematic effects govern the dynamics of the superheated material, to finally reach an area near the boiling curve.

Using higher intensities up to ~$5 \cdot 10^{11}$ particles/pulse available at FAIR, the near critical region of other metals, especially refractory ones (e.g. Ta, Ti, W) can be probed.

References

[1] P. Ni et al., Las. Part. Beams 26 (04), 583 (2008).
[2] D. Varentsov et al., Nucl. Instrum. Meth. Phys. Res. A 577, 262 (2007).
[3] V. Ternovoi et al., in *Physics of Strongly Coupled Plasmas*, eds. W.D. Kraeft et al., World Scientific Publishing Ltd, Singapore, 1996, pp.119-124.

* Work supported by Helmholtz-Russia Joint Research Group HRJRG-112 and BMBF 06DA9033I.

Status of the PRIOR Project*

P.-M. Lang[1], *A. Bogdanov*[2], *D.H.H. Hoffmann*[1], *A. Kantsyrev*[2], *Ya. Krasik*[3], *C. La Tessa*[4], *F. Merrill*[5], *M. Prall*[4], *M. Rodionova*[1,4], *A. Semennikov*[2], *L. Shestov*[1,6], *V. Skachkov*[2], *S. Udrea*[1], *D. Varentsov*[4], *and K. Weyrich*[4]

[1]TUD, Darmstadt, Germany; [2]ITEP, Moscow, Russia; [3]Technion, Haifa, Israel; [4]GSI, Darmstadt, Germany; [5]LANL, Los Alamos, USA; [6]EMMI, Darmstadt, Germany

High energy proton microscopy (HEPM) is a novel diagnostic technique for probing the interior of dense objects. Using HEPM, it is possible to image an object with high spatial resolution and to reconstruct its density distribution with sub-percent accuracy. The PRIOR (Proton Microscope for FAIR) facility will be the first magnifying proton radiography system, which will use mono-energetic protons in the multi-GeV-range. This will allow to reach a spatial resolution of less than 10 μm and a time resolution of about 10 ns.

The GSI accelerator facility is able to deliver up to 4.5 GeV protons in bunches of 10^{10} particles from the SIS-18 synchrotron to the HHT experimental area, where PRIOR is being installed. The HHT area had to be modified due to a large drift length needed for the imaging system. Additional shielding and beam dump have been built in order to fit safety requirements.

The ion optical system of PRIOR contains four permanent magnetic quadrupoles (PMQs) made of an NdFeB alloy. Their pole tip field is about 1.83 T with an inner aperture of 30 mm. Between the second and the third PMQ, the protons are sorted by their scattering angle in a Fourier plane by a collimator (Fig. 1).

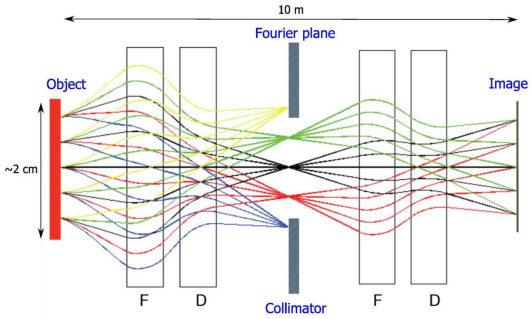

Figure 1: Proton trajectories in the ion optical system of PRIOR.

The PRIOR PMQs have been manufactured at ITEP, Moscow, and were assembled at GSI on a high precision rail with motorized tables. The next step will be to perform high accuracy field measurements in order to adjust the lenses precisely and include the obtained results into the simulation codes. Furthermore, vacuum and alignment systems have to be constructed and cameras and a scintillator screen as detectors have to be installed. Comissioning of PRIOR as well as first experiments will start within 2013.

*This work is supported by the BMBF project 05K10RD1, HRJRG-112 and DFG.

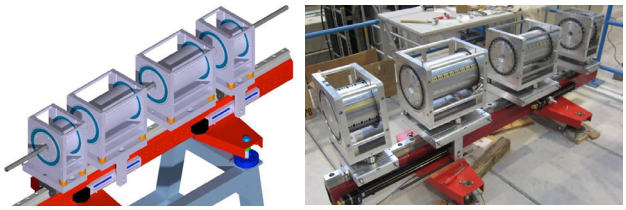

Figure 2: PRIOR PMQ setup

One of the first proposed experiments with PRIOR will be related to the PaNTERA (Proton Therapy and Radiography) project [1], to investigate the feasibility of using HEPM as an imaging method in particle therapy. First studies have already been made at ITEP in 2011 [3], producing the first radiograph of a zebra fish using an 800 MeV proton beam. Those experiments were continued at the pRad facility at the Los Alamos National Laboratory. A set of PMMA-targets, encapsulated fishes, a mouse and the MATROSHKA human phantom (Fig. 3) were used as test objects with a biologically relevant structure [2]. This experiments will be contiuned with PRIOR at GSI and at FAIR making it possible to achieve much higher precision.

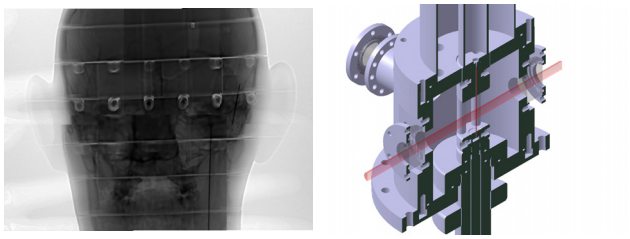

Figure 3: Proton radiograph of the MATROSHKA head taken at pRad (left) and the new setup for UEWE experiments (right).

PRIOR will be also used in HEDP dynamic experiments. The first one will use a setup for Underwater Electrical Wire Explosions (UEWE), which is currently designed in cooperation with Technion, Haifa. At FAIR, PRIOR will be the key diagnostic tool for the HEDgeHOB collaboration experiments.

References

[1] M. Durante and H. Stöcker, Journal of Physics: Conference Series **373** (2012), 012016.

[2] C. La Tessa et al. “First high-energy proton tomography of a mouse” 2012, this report

[3] D. Varentsov et al., “First biological images with high-energy proton microscopy”, Phys. Med. (2012), doi:10.1016/j.ejmp.2012.03.002

Operation and Improvements of PHELIX*+

V. Bagnoud[1], C. Brabetz[2], U. Eisenbarth[1], J. Fils[1], S. Götte[1], T. Kühl[1,3], S. Kunzer[1], M. Kreutz[1], D. Reemts[1], T. Stöhlker[1,4], L. Tymura[1], F. Wagner[5], B. Zielbauer[4]

[1]GSI, Darmstadt, Germany; [2]Johann Wolfgang Goethe University Frankfurt, Germany; [3]Johannes Gutenberg University Mainz, Germany; [4]Helmholtz Institute Jena, Germany, [5]Technical University Darmstadt, Germany

General overview

The general mission of GSI has undergone some tremendous changes in 2012 with the increased focusing of the laboratory's activities on the construction of FAIR. In view of the foreseen scarce ion-beamtime availability in the coming years, PHELIX[1], the high-energy short-pulse laser facility of GSI, has been used in 2012 almost exclusively to provide beamtime for users as well as internal developments.

Completed in 2008, PHELIX, a Helmholtz user facility opened to the international scientific community, is a dual front end high-energy laser capable of delivering long nanosecond high-energy as well as short sub-picosecond high-intensity laser pulses. It offers also a world-wide unique opportunity for combined ion-laser experiments to support the science programs of the Plasma Physics and Atomic Physics departments of GSI.

From an operation stand point, PHELIX supported 16 experiments distributed over 18 beamtimes and accounting for 245 shifts. The average duration of a beamtime at PHELIX including setup is about ten working days. At the end of 2012, nearly all remaining experiments in the backlog of approved experiment proposals have been scheduled for the beginning of 2013. A call for proposal has run in November and December and new experiments will be scheduled as soon as the evaluation process is over.

From a machine stand point and as recommended by the PHELIX advisory committee, the generation and amplification of temporally-clean short laser pulses has been a central issue for internal developments. In particular the development of an ultra-high temporal contrast module, the elimination of pre-pulses and the commissioning of plasma mirrors have been pursued

Operation of the laser facility

As can be seen in Figure 1, the time dedicated to user operation of the facility (experiment and setup time) exceeds 2/3 of the total time in 2012. This corresponds to nearly 35 weeks. This unusual high value has been dictated by the need to complete experiments in combination with the UNILAC before the 2013 shutdown. In order to provide this support, many important maintenance operations have been delayed. In particular, some repairs at the nanosecond front end have been postponed to 2013 and will result in a long downtime when they are being performed. In addition, the time dedicated to internal development has been reduced and internal development projects have been slowed down.

A recent feature of PHELIX that has been ramped up in the last years has been the use of the shot database (PSDB)[2]. Besides recording all relevant shot data during operation, this database allows for generating statistics on the laser usage and performance. In the last 12 months, PHELIX has delivered about 3500 shots, from which 2500 shots are target shots while serving experiments The low portion of failed experiment shots of 1.1 % demonstrates the reliability of the facility. So far, this does not include difference between effective and target parameters (energy, pulse duration etc…) as success criteria. The origin of a failed shot can be due to the machine and during test shots it is in majority due to debugging of the control system, which is normal. However, during beamtime the origin of failed shots is mostly due to the operators. For this reason, the failed shots are actively documented and the appropriate safety guards and checks are constantly added to the control system to help operators.

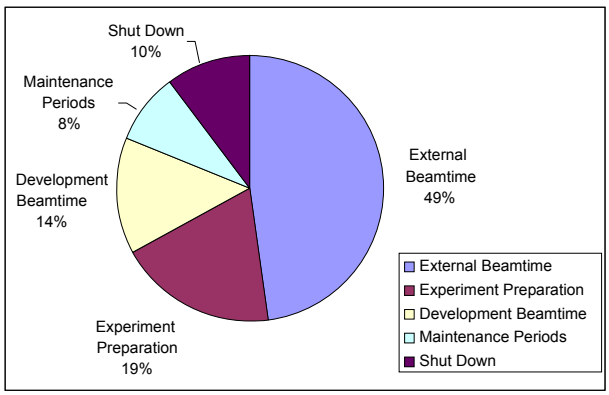

Figure 1: PHELIX usage in 2012

Internal developments and beamtime

An important development in the course of the year has been the first results and target shots with the temporal-contrast boosting module at PHELIX. In the last two years, the pump laser for this temporally-clean non-linear amplifier has been developed by the Helmholtz Institute Jena; and it led its first results at the beginning of the year. The module allows for a decrease of more than 4 orders of magnitude of the nanosecond pedestal of the pulse; and in the second part of the year a first glance at its impact on laser-driven proton acceleration has been done. More details about this work can be found elsewhere[3]. During this work, we discovered that the laser

* The acronym stands for **P**etawatt **H**igh **E**nergy **L**aser for heavy **I**on e**X**periments.

+ This work is supported by EMMI, the Helmholtz Institude Jena and GSI

temporal structure also includes weak pre-pulses that originate from the interplay between nonlinear effects in the amplifiers and internal reflections from the plan-parallel surfaces of optical components. These pre-pulses could be observed only when the general background was reduced sufficiently using the contrast boosting module. A way around this problem relies on the step-wise identification of defective optical components and their replacement with a component having wedged surfaces. However, this procedure is time consuming as the largest pre-pulses have been hiding pre-pulses of lower energy that must be taken care of in an iterative way[4].

Similarly important for the temporal contrast of short laser pulses, the use of plasma mirrors as fast optical switches has been continued in collaboration with the STFC/Strathclyde University groups of Prof David Neely and Prof. Paul McKenna in the U. K. There, a characterization of the laser focus after the plasma mirror has been conducted at high energies, bringing new insights on the influence of the plasma mirror on the focus quality of the reflected laser pulses[5].

On the infrastructure side, PHELIX has continued the upgrade of the petawatt target area to be able to operate at full power during the down-time of the accelerator and support user operation as well as the preparatory phase of the FAIR science program. After the successful integration of a new shielding scheme relying on 15 cm-thick steel plates aiming at containing radiation within the target area, the procurement and delivery of a target chamber with improved performance was realized. The new chamber, which can be seen in Figure 2, offers among others the possibility to work with two or more beams in order to build the pump-probe setups required by nearly all users.

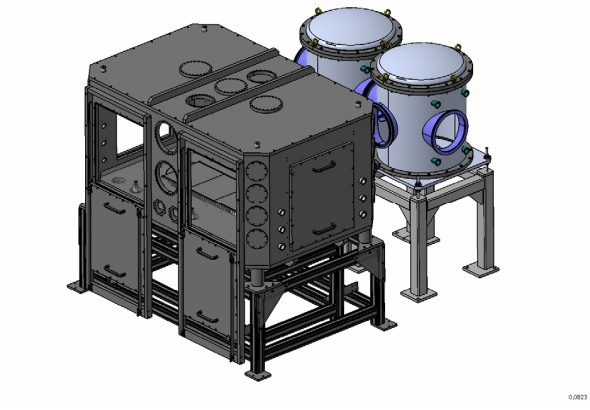

Figure 2: 3-D CAD view of the PHELIX target chamber

Another important infrastructure development concerns the end of chain sensor at the Z6 area that has been finalized and integrated in the PHELIX control system. This sensor is built on standard blocks (such as camera an energy attenuation systems) already used at other places of the laser and therefore easier to maintain than its predecessor. It includes also new features to ease the routine beam alignment together with spatial, energy and time information over the on-shot of both 1ω and 2ω.pulses delivered at Z6.

Contribution to the scientific program and outreach

This year, 10 peer-reviewed articles[6,7,8,9,10,11,12,13,14,15] were published on data collected at PHELIX. Typically, these publications report on results obtained during beamtime that occurred in the last 18 months.

In May, GSI held a joined meeting between IZEST[16] and the people involved in the Helmholtz Beamline project. The 4-day meeting gathered more than 120 participants from around the globe to explore synergies between the IZEST proposal and the scientific program with lasers at FAIR. The variety of the presentations and the vitality of the discussions at the meeting showed the attractiveness and uniqueness of the Helmholtz beamline project for FAIR.

Outlook for 2013

In the last part of 2012, a call for proposal for experiments at PHELIX received a great success as the requested number of shifts exceeded the offer by a factor of three. The selected experiments will be planned starting in the second semester of 2013.

References

[1] V. Bagnoud et al., Appl. Phys. B **100** (1), 137-150 (2010)
[2] U. Eisenbarth et al., GSI Scientific Report 2011 /PNI-PP-02, 435 (2011)
[3] F. Wagner et al., submitted to Optics Express
[4] F. Wagner et al., this report
[5] B. Zielbauer et al., this report
[6] N. Kugland and al., Appl. Phys. Lett. **101**, 024102 (2012)
[7] G. Scott et al., Appl. Phys. Lett. **101**, 024101 (2012)
[8] B. Ecker et al., Optics Express **20** (23), 25391-25399 (2012)
[9] D. Kraus et al., High Energy Density Physics **8** (1), 46–49 (2012)
[10] M. Börner et al., Rev. Sci. Instrum. **83**, 043501 (2012)
[11] I. Hofmann et al., Nuclear Instrum. and Meth. in Physics Research Section A: Accelerators, Spectrometers, Detectors and Associated Equipment **681**, 44 – 54 (2012)
[12] A. Almomani et al., Phys. Rev. ST Accel. Beams, American Physical Society **15**, 051302 (2012)
[13] P. Neumayer et al., Phys. Plasmas **19**, 122708 (2012)
[14] M. M. Günther et al., Fus. Sci. and Technol. **61** (1), 231-236 (2012)
[15] M. E. Povarnitsyn et al., Phys. Plasmas **19**, 023110 (2012)
[16] http://www.izest.polytechnique.edu

Isentropic Compression of Iron with PHELIX*

B.F. Ionita[1], D.H.H. Hoffmann[1], A. Ortner[1], S. Udrea[1], F. Wagner[1], V. Bagnoud[2], A. Blazevic[2], A. Frank[2], D. Varentsov[2], K. Weyrich[2], N. Amadou[3], and E. Brambrink[3]

[1]TUD, Darmstadt, Germany; [2]GSI, Darmstadt, Germany; [3]LULI, Paris, France

Laser-driven isentropic compression is an important technique to reach high-pressure low-temperature states, which are of interest for planetary physics (especially the relatively poorly known multi-Mbar range of the phase diagram of iron found in Earth's interior). This technique requires relatively long compression times (>10 ns), times which can be achieved with the PHELIX laser.

The experimental setup deployed in this work is shown in Fig. 1: thin iron foils (10-50 µm) were compressed isentropically by irradiating with a flat-top PHELIX beam (15 ns, ~150 J @2ω, Ø1 mm), while velocity on the free surface was recorded simultaneously by two line VISARs [1,2] (Fig. 2), with spatial resolution of ~20 µm (Fig. 3a).

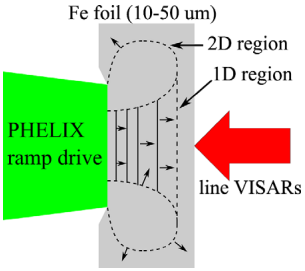

Figure 1: Experimental principle.

The velocity interferometers were equipped with fused silica etalons of 15.04 mm and 50 mm, corresponding to velocity sensitivities of 3415 m/s/fringe and 1027 m/s/fringe, respectively, using the frequency doubled beam (532 nm) of nhelix as diagnostic laser.

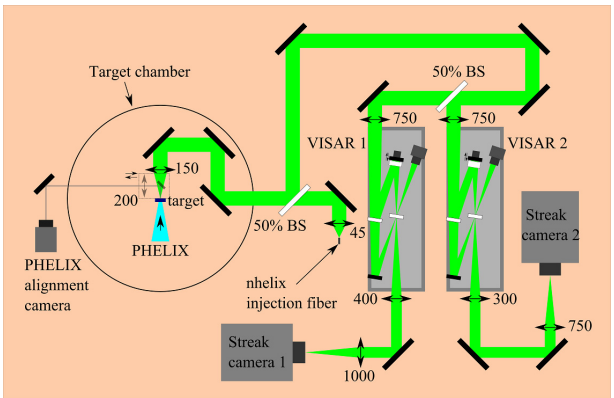

Figure 2: Optical schematics of the dual line VISAR setup in the Z6 experimental area.

Raw interferometric data obtained with the system are shown in Fig. 4b. A smooth fringe shift indicates shock-less compression, as expected for isentropic compression.

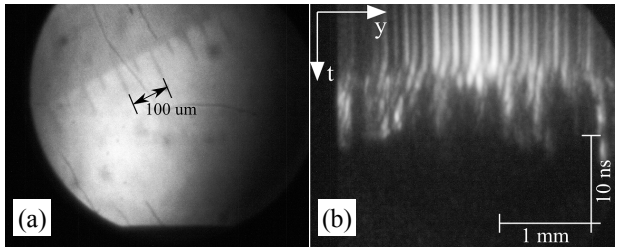

Figure 3: (a) Spatial calibration; (b) raw interferogram.

Surface velocity profiles were obtained by tracing the fringe shifts, from which particle velocity was determined as half of the surface velocity, given that expansion takes place in vacuum (therefore no impedance matching). Pressure was further derived from an iron isentrope starting at room conditions.

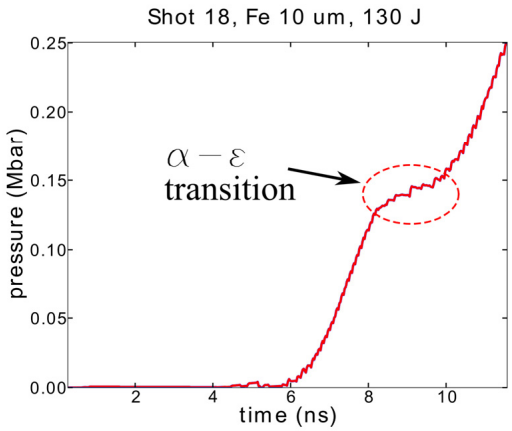

Figure 4: Pressure temporal profile with α–ε phase transition plateau.

In Fig. 4, the plateau on the profile between 8 and 10 ns is related to the well known α–ε phase transition in iron at ~130 kbar, its length and starting velocity comparable to other results [3]. The study of dynamics of phase transitions [4] can be thus studied.

The shape of the temporal intensity profile of PHELIX as well as its spatial intensity profile will be optimized in future experiments to increase the maximum reachable pressure to several Mbar.

References

[1] L. M. Barker et al., J. Appl. Phys. 43, 4669 (1972).
[2] P. Celliers et al., Rev. Sci. Instrum. 75, 4916 (2004).
[3] N. Amadou et al., AIP Conf. Proc. 1426, 1525 (2011).
[4] M. Bastea et al., Appl. Phys. Lett. 95, 241911 (2009).

* Work supported by Helmholtz-Russia Joint Research Group HRJRG-112 and BMBF 06DA9033I.

Plasma mirror far field characteristics of PHELIX *

B. Zielbauer[1,2,#], C. Brabetz[1], G. Scott[3,4], H. Powell[4], P. McKenna[4], D. Neely[3,4], V. Bagnoud[1,2]

[1]GSI Helmholtz Center for Heavy-Ion Research, Darmstadt, Germany; [2]Helmholtz Institute Jena, Jena, Germany;
[3]Central Laser Facility, STFC Rutherford Appleton Laboratory, Didcot, UK;
[4]Department of Physics SUPA, University of Strathclyde, Glasgow, UK

In the last ten years, plasma mirrors [1] have been often used to improve the temporal contrast of high-intensity short-pulse lasers, so that deleterious pre-ionization effects in laser-matter interaction experiments are avoided. Indeed, the use of an anti-reflection-coated mirror close to a focus in the laser beam allows one to gain up to 3 orders of magnitude in temporal contrast per reflecting surface. For petawatt-class lasers that are very complicated machines, this turns out to be one of the few solutions that one has at hand to reach the temporal contrast required by many experiments. Much work has been published on the temporal characterization of plasma mirror setups at low energy [2]; however the impact of the plasma mirror on the focal spot quality of high-energy sub-picosecond lasers has been much less studied. We propose and demonstrate an experimental setup capable of handling many 10's of Joules, allowing for the direct characterization of the focal spot of a petawatt-class laser after a plasma mirror. On the one hand we have observed that the focal spot shape of the laser is qualitatively not affected by the mirror, even at high working intensities. On the other hand, the Strehl ratio of the beam is largely reduced at high intensities because of scattering on the expanding plasma. Together with the measurement of the mirror reflectivity, we could define precisely the optimal working condition of the mirror.

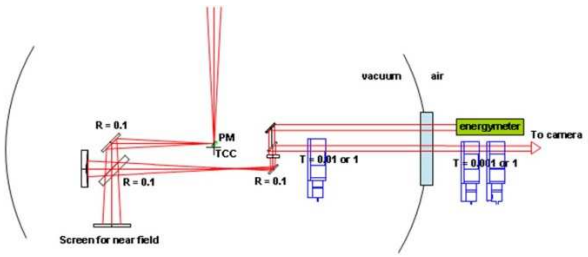

Figure 1: Experimental setup. PM: plasma mirror, TCC: Target chamber center.

The setup depicted in figure 1 has been implemented at the PHELIX laser facility [3]. An S-polarized laser beam is focused with a 90-degree off-axis f/5 parabolic mirror. During the initial alignment, a standard alignment system made of a magnifying telescope is used to image the laser spot outside the target chamber, allowing for an optimal alignment of the parabolic mirror. The 45-dregree plasma mirror is then inserted at a distance of 15 to 45 mm before the focal spot. The main problem of the setup resides in energy mitigation: for that, we rely on multiple reflections on uncoated fused silica substrates to bring the energy down to the millijoule level and density filters based on HR coated plates to get a dynamic range in energy of 7 orders of magnitude. The first part of the setup uses a 150-mm diameter spherical mirror that makes a 1:1 image of the focus while allowing for a decrease of the energy by a factor 100. The second part of the setup is a standard magnifying telescope that images the beam outside the target chamber onto a CMOS camera. During the alignment all filters are taken out of the beam and replaced by AR coated plates so that one can verify the fidelity of the imaging system. At this stage, a powermeter is used to measure the transmission of the whole setup. During high-energy shots, the reflected energy and the image of the focus are simultaneously recorded using the HR coated filters to keep the energy density on the camera constant.

After ignition at 10^{12} W/cm^2, the plasma mirror reflectivity reaches a maximum at about 90% and falls down below 80% above 2x10^{15}W/cm^2 (see figure 2). In parallel, the far field images recorded by the CMOS camera show no visible sign of alteration below the saturation level. On the plateau, the focal spot images also show very little reduction in quality. However, at higher energies, a strong scattering background can be measured around the focus, resulting in a strong reduction of the encircled energy and focal spot intensity.

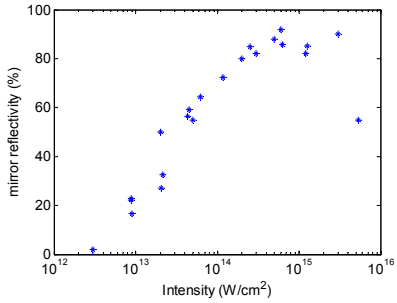

Figure 2: Measured reflectivity for different pulse intensities on the plasma mirror

References

[1] M. Nantel et al. "Temporal Contrast in Ti:Sapphire Lasers: Characterization and Control" JSTQE, **4** 449 (1998)

[2] G. Doumy et al. "Complete characterization of a plasma mirror for the production of high-contrast ultraintense laser pulses" Phys. Rev. E **69**, 026402 (2004)

[3] V. Bagnoud et al. "Commissioning and early experiments of the PHELIX facility" Appl. Phys. B **100** 137 (2010)

* Work supported by LaserLab III.

#b.zielbauer@gsi.de

Prepulse removal at the PHELIX short-pulse facility

F. Wagner[1] and V. Bagnoud[2,3]
[1]Inst. für Kernphysik, TU Darmstadt, Germany; [2]GSI Helmholtzzentrum für Schwerionenforschung GmbH, Germany;
[3]Helmholtz-Institute Jena, Germany;

Introduction

The temporal contrast of short-pulse laser systems is defined as the ratio of the peak-intensity and the intensity at a given time before the peak. With intensities exceeding 10^{20} W/cm^2 this parameter has become very critical for high-power laser systems like PHELIX [1]. Since the minimum for plasma generation is between 10^9 and 10^{12} W/cm^2 depending on the target properties a contrast of at least 9 orders of magnitude is mandatory to guarantee an undisturbed target at the arrival of the main pulse. Particularly for several lately proposed experiments such as probing new mechnisms for laser ion acceleration like BOA or RPA with thin targets in the sub µm range as well as experiments for surface high-harmonic generation which calls for a steep density gradient at the target surface high temporal-contrast is required.

Temporal-contrast at CPA systems

Several effects contribute to the imperfect temporal-contrast in a chirped-pulse amplification (CPA) system:

- Noise in the amplifiers due to amplified spontaneous emission (ASE) results in a pedestal that is typically 6 to 7 orders below the maximum and ranges over a few ns.
- Multiple reflections between parallel optical surfaces may generate postpulses which can be shifted to the front of the peak due to nonlinear effects in a CPA system. Furthermore compressed prepulses can arise due to the finite extinciton ratio of optical switches.
- Clipping of the spectrum in the stretcher or compressor as well as spectral phase noise due to imperfect surfaces of the gratings induce a slowly rising slope ranging over some tens of ps.

All these effects are independent from each other and therefore have to be treated separately.
The ASE-pedestal can be decreased by increasing the seeding energy of the amplifiers. For this purpose an ultrafast optical parametric amplifier (uOPA) has been developed and successfully implemented at PHELIX. This new module enables an ASE-contrast better than 10 orders of magnitude. For more detailed information about the uOPA see Ref. [2,3].

Prepulses at PHELIX

Parallel surfaces can generate postpulses which may become prepulses due to nonlinear effects. Therefore the temporal separation between the prepulse and the peak is defined by the optical path which enables to identify the element that is responsible for the prepulse by its thickness. By switching to wedged optical elements the particular prepulse can be removed.

Figure 1 shows the contrast improvement in the course of 2012. The measurement was performed with a scanning third-order cross correlator with high dynamic range (Sequoia, Amplitude Technology).

The main prepulse (no. 1) was attributed to a Pockels cell (PC) with parallel surfaces in a regenerative amplifier of the frontend. By switching to a PC with tilted surfaces the prepulse could be removed as shown in the measurement from August 2012. The prepulse 2 could also be eliminated by changing a PC (see measurement from January 2013). The remaining pulses (2, 3 and 4) should be removed in the beginning of 2013. The prepulse 3 is correlated with a one inch optical element. Furthermore there are four more PCs in the PHELIX frontend which could be responsible for the pulses 4 and 5 and which will be investigated in 2013.

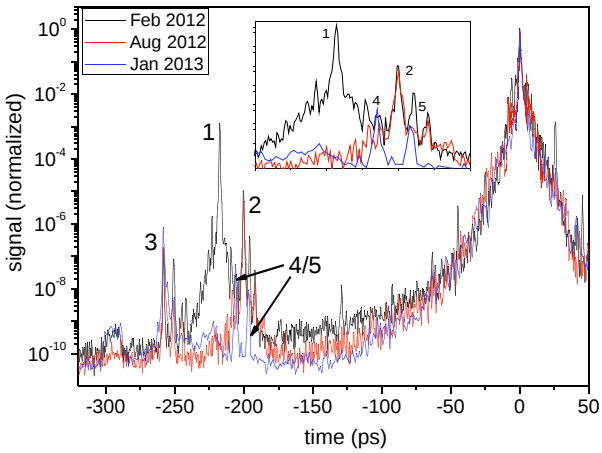

Figure 1: Contrast improvement at PHELIX in 2012

Conclusion and Outlook

The main prepulses of the PHELIX short-pulse beam were successfully removed. The remaining prepulses have been identified and will be investigated in 2013. Together with the new uOPA this enables a contrast level exceeding 10 orders of magnitude.

Reference

[1] V. Bagnoud et al., "Commissioning and early experiments of the PHELIX facility" Appl. Phys. B **100** 137–150 (2010).
[2] F. Wagner et al., "A compact temporal contrast-boosting module for petawatt-class lasers" submitted to Optics Express.
[3] C. P. João, F. Wagner et al., are preparing a manuscript to be called "Diode-pumped Yb:KYW regenerative amplifier for optical parametric amplifier pumping"

Target surface cleaning by fs laser desorption at PHELIX

G. Hoffmeister[*1], *M. Bender*[2], *H. Kollmus*[2], *R. Jaeger*[1], *F. Wagner*[1], *M. Wengenroth*[2], *B. Zielbauer*[2,3], *and M. Roth*[1]

[1]Institut für Kernphysik, TU Darmstadt, 64289 Darmstadt; [2]GSI Helmholtzzentrum für Schwerionenforschung GmbH, 64291 Darmstadt; [3]Helmholtz Institut Jena, 07743 Jena

In laser ion acceleration experiments like the target normal sheath acceleration (TNSA) the target design has an essential influence on the resulting ion spectra. Apart from studies about elaborate geometries like cone or hemispherical targets [1] the target surface structure plays a crucial role. In almost all laser proton acceleration experiments it is the contamination on top of the target surface -mainly consisting of hydrocarbons and oxygen- which is ionized and accelerated.
The fs laser desorption constitutes a promising technique which enables to remove these surface contaminants successively, thereby learning more about their amount and composition. Due to the ultrashort laser pulse duration the energy transfer from the laser to the target is nonthermal i.e. melting is almost no issue [2]. The target surface remains undamaged and smooth. Combining this method with a sophisticated target design like a characterized multilayer target could allow to scan through the TNSA field distribution giving information about its penetration depth and about the TNSA field strength.

Experimental setup We performed a fs laser desorption experiment using the PHELIX laser frontend at GSI Helmholtzzentrum für Schwerionenforschung GmbH. The PHELIX laser frontend delivered pulses of 400 fs pulse duration with 10 Hz repetition rate. The pulse energies were varied between 0.1 mJ and 3 mJ. With a focal spot size of 560 μm this led to laser intensities between (10^{10} - 10^{12}) W/cm^2.
The laser irradiated 1 mm thick aluminum, copper and gold foils which were mounted in a special ultrahigh vacuum (UHV) chamber at a pressure of 10^{-10} mbar realized by a titanium sublimation pump and an ion pump. The UHV was necessary to observe even small pressure increases. The analysis of the gas composition was performed by a residual gas analyzer (RGA) represented by the quadrupole mass spectrometer QMA 200 by Pfeiffer Vacuum.

Results The intention of this experiment was to determine the threshold intensity for plasma formation as well as to investigate the target cleaning in dependence of the laser parameters. At intensities of $I = (5 - 10) \times 10^{10}$ W/cm^2 there were no explicit desorption effects visible. The total pressure rise was negligible. With increasing intensity in the mid 10^{11} W/cm^2 regime we observed clear signals of target surface cleaning. Figure 1 shows the total pressure rise during the continuous laser irradiatiation at 10 Hz on a 1 mm thick gold foil. In the left image, three irradiation cycles with 1000 s, 2100 s and 500 s, respectively, were applied. The first two cycles show an initial pressure rise due to the desorption of surface contaminants. Probably the laser spot was slightly shifted between those two cycles since the UHV conditions prevent the re-establishment of a contamination layer on the desorbed surface. In the third irradiation cycle this pressure rise did not occur any more, indicating that the irradiated region had been cleaned and there were no more surface contaminants to be removed. Additionally, the laser intensity was still low enough such that plasma formation was no issue. In contrast, the right image of Figure 1 demonstrates that at a laser intensity of $I = 8.5 \times 10^{11}$ W/cm^2 the total pressure rise shows a completely different behavior. Instead of decreasing after a short time of laser irradiation it increased more and more. Plasma formation set in and the laser intensity sufficed to immediately ionize the contaminants as well as the gold atoms.

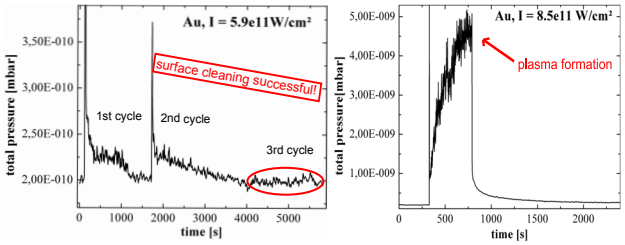

Figure 1: Total pressure as function of time of laser desorption at 10 Hz with $I = 5.9 \times 10^{11}$ W/cm^2 (left) and $I = 8.5 \times 10^{11}$ W/cm^2 (right).

Similar results were obtained by irradiating aluminum and copper foils. While for copper the plasma threshold turned out to be at the same intensitiy as it was observed for gold foils, for aluminum we determined a minor threshold intensity for the plasma formation at $I = 3.5 \times 10^{11}$ W/cm^2.
With this desorption experiment at the PHELIX laser we could experimentally determine a plasma threshold intensity for gold, copper and aluminum targets. Furthermore, we found clear evidence of a complete target surface cleaning in the intensity regime of $I = (2 - 6) \times 10^{11}$ W/cm^2.

Acknowledgements

This work was funded by the BMBF, support code 06DA9044I, and HIC4FAIR.

References

[1] P. K. Patel *et al.*, Phys. Rev. Lett., **91**, 125004 (2003)

[2] R.E. Russo *et al.*, J. Anal. At. Spectrom. **17**, 1072 (2002)

* g.hoffmeister@gsi.de

Swift Heavy Ion Tracks in $Gd_2Ti_2O_7$ Pyrochlore: Effect of Electronic Energy Loss*

Maik Lang[1,#], Marcel Toulemonde[2], Jiaming Zhang[1], Fuxiang Zhang[1], Cameron Tracy[1], Jie Lian[3], William J. Weber[4], Daniel Severin[5], Markus Bender[5], Christina Trautmann[5], and Rodney C. Ewing[1]

[1]University of Michigan, Ann Arbor, MI, U.S.A.; CIMAP, Caen, France; [3]Rensselaer Polytechnic Institute, Troy, NY, U.S.A.; [4]Oak Ridge National Laboratory & University of Tennessee, Knoxville, TN, U.S.A.; [5]GSI Helmholtzzentrum and Technische Universität Darmstadt, Germany

Pyrochlore oxides ($A_2B_2O_7$) have recently been studied in detail with respect to their response to swift heavy ion irradiation. Characterization using complementary analytical techniques revealed a complex track-damage morphology consisting of an amorphous core surrounded by a disordered, defect-fluorite structured shell. Molecular dynamics (MD) simulations based on the inelastic thermal spike model were performed in which the time and temperature evolution of individual tracks is followed [1]. In order to provide further experimental insights into the formation of concentric nanoscale damage zones, the influence of the electronic energy loss dE/dx of GeV ions is investigated in gadolinium-titanate pyrochlore [2].

Polycrystalline samples of $Gd_2Ti_2O_7$ were polished down to 40 µm and irradiated with ^{58}Ni, ^{101}Ru, ^{129}Xe, ^{181}Ta, and ^{197}Au ions at the UNILAC accelerator with a specific energy of 11.1 MeV/u. The ions passed completely though the samples. The applied fluence of 5×10^{10} ions/cm^2 was low enough to avoid extensive track overlapping. The irradiated samples were crushed to a fine powder and investigated by means of high-resolution transmission electron microscopy (HR-TEM).

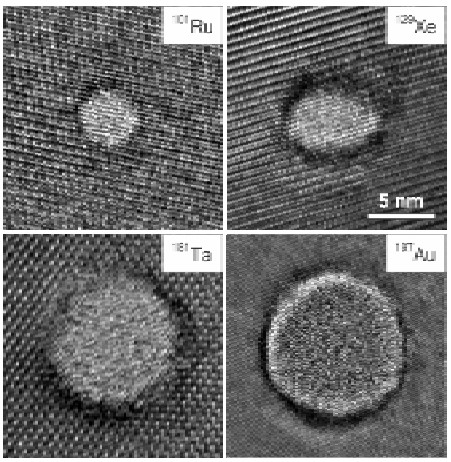

Figure 1: Cross-sectional HR-TEM images of cylindrical ion tracks in $Gd_2Ti_2O_7$ displaying a core-shell damage morphology. The dE/dx of the respective ions is 21.7 (Ru), 28.5 (Xe), 37.0 (Ta), and 40.1 (Au) keV/nm.

* Work was supported as part of the Materials Science of Actinides, an Energy Frontier Research Center funded by the U.S. DOE, Office of Science, Office of Basic Energy Sciences under Award Number DE-SC0001089.

#mklang@umich.edu

The track damage is characterized by a core-shell structure (Fig. 1) changing from a defect-fluorite dominated shell at low dE/dx to predominantly amorphous tracks at high dE/dx. From Ru to Au ions, the amorphous fraction increases from 11 to 67% (Fig. 2) following an exponential growth with dE/dx, while the respective overall track diameter increases by about a factor of two (Fig. 2).

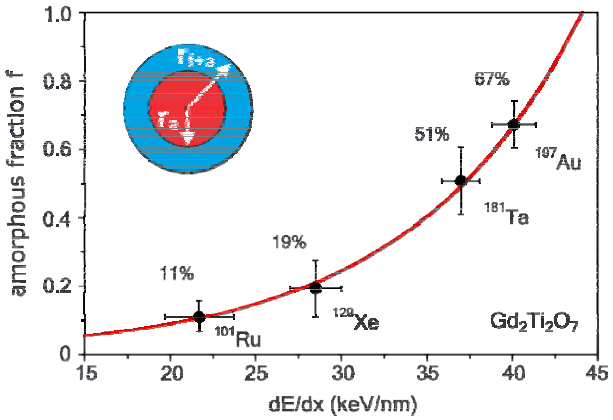

Figure 2: Amorphous fraction f of tracks in $Gd_2Ti_2O_7$ as a function of energy loss. f is estimated by the area ratio of the amorphous core (radius r_a) to the full track (radius r_{f+a}). The errors represent the dE/dx variation throughout the sample thickness, and the uncertainties of determining the area of amorphous core and entire track, respectively.

The size increase of tracks is primarily due to an expanding amorphous core, while the defect-fluorite structured shell radius remains almost constant. Thermal-spike calculations show that the molten track cross section increases with the energy deposition of the ions [2]. MD simulations reveal that the track shell results of a crystallization process from the track melt [1]. Thus, the shell thickness may be limited kinetically by material dependent crystallization front velocities. However, thermodynamic constraints on stabilization of a non-equilibrium phase may also contribute.

References

[1] J.W. Wang, M. Lang, R.C. Ewing, and U. Becker, *J. Phys.: Condens. Matter* 25 (2013) 135001.

[2] M. Lang, M. Toulemonde, J.M. Zhang, F.X. Zhang, C.L. Tracy, J. Lian, Z.W. Wang, W.J. Weber, D. Severin, M. Bender, C. Trautmann, R.C. Ewing, to be submitted (2013).

Structural Response of A_2TiO_5 (A = La, Nd, Sm, Gd) to Swift Heavy Ion Irradiation*

Cameron L. Tracy[1#], Maik Lang[1], Jiaming Zhang[1], Fuxiang Zhang[1], Zhongwu Wang[2], Markus Bender[3], Daniel Severin[3], Christina Trautmann[3], and Rodney C. Ewing[1]

[1] University of Michigan, Ann Arbor, MI, U.S.A.; [2] Cornell High Energy Synchrotron Source, Ithaca, NY, U.S.A; [3] GSI Helmholtzzentrum and Technische Universität Darmstadt, Germany

Pyrochlore-structured titanates ($A_2Ti_2O_7$) have been extensively studied as radiation-resistant materials for nuclear fuel cycle applications. Here we investigate related compounds A_2TiO_5, where A is a lanthanide element. They are orthorhombic at ambient conditions for A-site elements with a lower Z than Ho. The radiation response of A_2TiO_5 in general, and comparison with $A_2Ti_2O_7$ materials is of interest as a means of investigating the role of structure in swift heavy ion-induced amorphization of ternary complex oxides.

Powders of A_2TiO_5 (A = La, Nd, Sm, Gd) were pressed into 40 μm thick pellets and irradiated with 1.47 GeV ^{132}Xe ions at the X0 beamline of the UNILAC accelerator [1]. Irradiation was performed to several fluences in the range 5×10^{10} to 1×10^{13} ions/cm^2. For the energies used, the nuclear energy loss remained at least three orders of magnitude lower than the electronic energy loss. The ions passed completely though the thin samples, producing damage tracks of cylindrical geometry. All materials were characterized using synchrotron x-ray diffraction (XRD), transmission electron microscopy (TEM), and Raman spectroscopy.

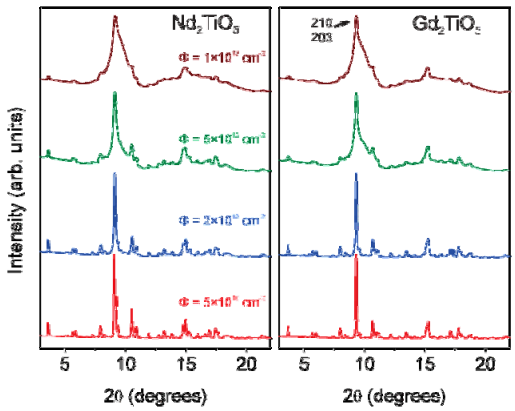

Figure 1: XRD patterns of irradiated Nd_2TiO_5 and Gd_2TiO_5. The decrease in amorphization with substitution of smaller cations is evident in the (210) and (203) peaks.

Both XRD and Raman spectroscopy showed evidence of increasing amorphization as a function of fluence for all compositions. The Raman spectra exhibited a systematic decrease in the intensity of the vibrational modes along with growth of a broad band at ~750 cm^{-1}, a vibrational mode also observed in pyrochlore titanates following swift heavy ion-induced amorphization. The XRD patterns displayed both peak broadening and the growth of broad peaks at approximately 7-12°, 12-20°, and 22-30° resulting from diffuse scattering by the amorphized sample volume (Fig. 1).

The XRD patterns were anaylzed by deconvoluting the intensity and peak area of the crystalline and amorphous contributions, The amorphization cross section per ion was calculated by fitting a direct-impact model to the extracted amorphous volume as a function of irradiation fluence. These cross sections were found to decrease as lanthanides of smaller ionic radius (higher Z) were substituted on the A-site. This relation between the ionic radius ratio of the cations and the amorphization per ion is similar to that previously observed in pyrochlores as a result of their propensity to resist amorphization. The effect is ascribed to the recrystallization of a disordered fluorite structure when the thermal spike region is quenched [2]. The occurrence of this phenomenon in A_2TiO_5 and its dependence on the cation radius ratio was confirmed by high-resolution TEM of single tracks shown in Fig. 2. La_2TiO_5, for which the cations differ greatly in ionic radius, exhibits only amorphous material within the track while Sm_2TiO_5 features a defect fluorite track shell surrounding the amorphous core. The presence of this non-equilibrium phase suggests that it forms as an intermediate phase during solidification of the melted track and is quenched before further ordering occurs.

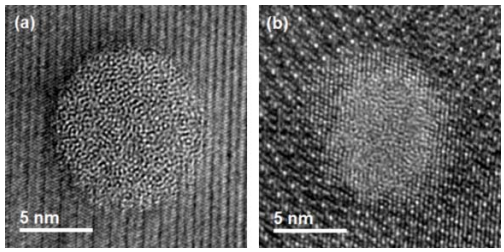

Figure 2: Cross-sectional TEM images of individual tracks in (a) La_2TiO_5 and (b) Sm_2TiO_5. The latter shows a defect-fluorite shell around the amorphous track core.

* This work was supported as part of the Materials Science of Actinides, an Energy Frontier Research Center funded by the U.S. Department of Energy, Office of Science, Office of Basic Energy Sciences under Award Number DE-SC0001089.

#cltracy@umich.edu

[1] C.L Tracy, M. Lang, J. Zhang, F.X. Zhang, Z. Wang, R.C. Ewing, Acta Mater. **60** (2012) 4477.

[2] M. Lang, J. Lian, J. Zhang, F.X. Zhang, W.J. Weber, C. Trautmann, R.C. Ewing, Phys. Rev. B **79** (2009) 1.

Temperature dependent formation of ion tracks in quartz studied using small angle x-ray scattering *

D. Schauries[1], M. Lang[2], S. Botis[2], B. Afra[1], M. D. Rodriguez[1], M. Toulemonde[3], O. H. Pakarinen[4], K. Nordlund[4], R. Ewing[2], M. Bender[5], D. Severin[5], C. Trautmann[5,6], N. Kirby[7], and P. Kluth[1,#]

[1]The Australian National University, Canberra, Australia; [2]University of Michigan, Ann Arbor, USA; [3]CIMAP, Caen, France; [4]University of Helsinki, Finland; [5]GSI Helmholtzzentrum, Darmstadt, Germany, [6]Technische Universität Darmstadt, Germany, [7]Australian Synchrotron, Clayton, Australia.

Ion tracks are narrow cylindrical defects of displaced atoms, a few nanometres in diameter and up to tens of micrometres in length. They result from the interaction of high-energy heavy ions with the electrons of a target material. We have performed a systematic investigation of the effects of the temperature during track formation in natural quartz samples, using synchrotron-based small angle x-ray scattering (SAXS). SAXS is a powerful and non-destructive technique well suited to measure ion track radii with high precision [1].

Natural quartz samples were irradiated at the UNILAC accelerator with 2.2-GeV Au ions and a fluence of 5×10^{10} ions/cm^2. This leads to the formation of ion tracks of ~95 µm length, as estimated by SRIM2008 [2]. The irradiation was carried out at room-temperature (RT) as well as at elevated temperatures. The quartz was cut parallel to the c-axis, thus leading to a track alignment perpendicular to the crystal's c-axis. Reference samples, irradiated at RT, underwent the same heat cycles as the samples irradiated at elevated temperatures. For characterization of the track radii, SAXS measurements were carried out at the SAXS/WAXS beamline at the Australian Synchrotron and analysed using our existing protocols [1].

Figure 1 shows the SAXS spectra of Au-ion tracks in quartz together with the corresponding fits and plots of track radii as a function of temperature for both reference and high temperature irradiated samples. The error bars display the standard deviation of the respective fits; they are below visibility for most SAXS radii. The track radius increases as a function of irradiation temperature with 0.1 nm/100K. The reference samples also exhibit an increase in track radii, although about one order of magnitude lower than samples irradiated at high temperature. This small increase is possibly a result of heat-induced stress relaxation and will be discussed elsewhere. We can thus attribute the increase in track radii for the high temperature irradiated samples predominately to the conditions during track formation. For verification, thermal spike model calculations [3] as well as molecular dynamics simulations were carried out yielding a similar track size increase of 0.08 and 0.10 nm/100K, respectively. We conclude that at elevated temperatures the energy required for melting of the quartz is lowered and thus the melting

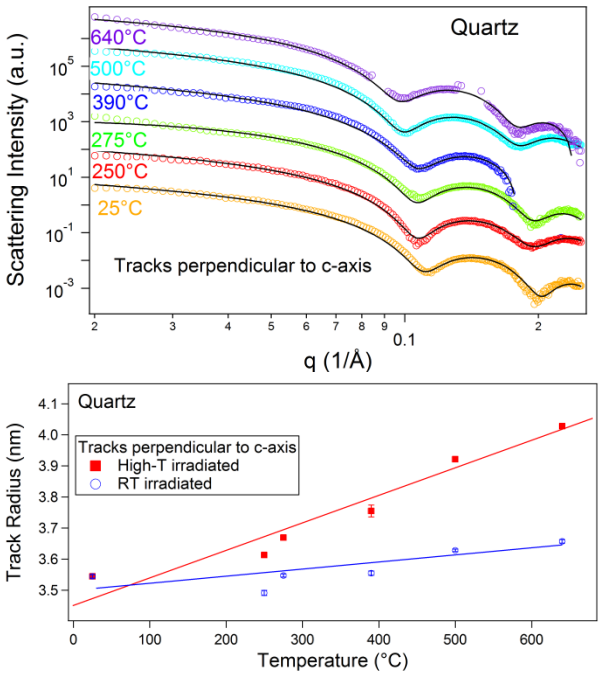

Figure 1: (top) SAXS intensities and corresponding fits of ion tracks in quartz, irradiated at different temperatures; (bottom) radii deduced from SAXS data of samples irradiated at RT (blue circles) and at high temperatures (red squares).

radius or equivalently the ion track radius is increased. We note that the small changes observed in the track radii are challenging to resolve with conventional analytical techniques such as transmission electron microscopy. Thus SAXS becomes an important tool in studying high temperature effects on ion track formation.

References

[1] B. Afra et al, J. Phys.: Condens. Matter **25,** 045006 (2013)

[2] J. F. Ziegler, J. P. Biersack, and U. Littmark, The Stopping and Range of Ions in Matter (Pergamon, New York, 1985)

[3] M. Toulemonde, C. Dufour, A. Meftah, E. Paumier, Nucl. Instr. Meth. B, **166**, 903 (2000)

* Work supported by the Australian Research Council and by Office of Basic Energy Sciences of the USDOE (DE-FG02-97ER45656)

#patrick.kluth@anu.edu.au

In situ annealing studies of ion tracks in amorphous Fe-B alloys

M. D. Rodríguez[1,#], C.Trautmann[2,3], B. Afra[1], T. Bierschenk[1], N. Kirby[4], and P. Kluth[1]

[1]Australian National University, Australia, [2]GSI, Darmstadt, Germany, [3]Technische Universität Darmstadt, Germany, [4]Australian Synchrotron, Australia.

Ion tracks in amorphous materials are characterized only by subtle differences in structure and density between track and matrix material [1, 2]. This lack of contrast leaves the complex structure of ion tracks inaccessible with most experimental techniques. As a consequence, there is currently little information about ion tracks in metallic glasses while still in the amorphous phase.

We investigated the morphology of ion tracks produced in Fe-B based (amorphous) metallic glasses and their influence on the recrystallisation behaviour upon *ex situ* annealing [3] using synchrotron based small angle x-ray scattering (SAXS). The tracks are cylindrical and show a density difference to the matrix material of less than 0.1 % [2]. The ion tracks were generated with various heavy ion beams with energies ranging from 500 MeV to 2.2 GeV. The fluence varied between 1×10^{10} and 3×10^{11} ions/cm^2 which is sufficiently low to form individual ion tracks with negligible overlap. The annealing kinetics of the ion tracks were studied with simultaneous SAXS and wide angle x-ray scattering (WAXS) in combination with *ex situ* isochronal annealing experiments. The *ex situ* annealing of the samples showed a clear change of the track radii due to the relaxation of the ion track boundaries. Such track recovery occurs while the material still is amorphous and gradually becomes brittle [3].

SAXS/WAXS *in situ* annealing measurements were performed at the Australian Synchrotron, in Melbourne, to further investigate the recovery of the ion tracks. Series of regular isothermal annealing steps of 15 to 25 min, comprised of 15 s exposure time measurements, were collected between room temperature and 550°C.

Figure 1 shows the SAXS intensity profiles of annealed tracks of $Fe_{80}B_{20}$. The positions for the minima in the track intensity profiles determine the track radius. The intensity data were fitted assuming cylindrical track geometry of constant radial density difference with respect to the matrix material. The radii extracted from the fits show a nearly constant value (Fig. 2), which is in contrast to the earlier *ex situ* annealing experiments. However, the maximum intensities from the track signals (at $q \approx 0.001$ *Å*$^{-1}$)) decrease with increasing annealing time (not shown here) and temperature (see Figure 2). These results suggest that the track radius remains approximately constant during the annealing process. Whereas the intensity decrease is an indication of different scenarios: the number of ion tracks in the material decreases (unlikely), the density difference between the matrix and tracks decreases and/or the ion tracks gradually reduce their length. Further studies are in progress to clarify the differences found between *ex situ* and *in situ* annealing processes.

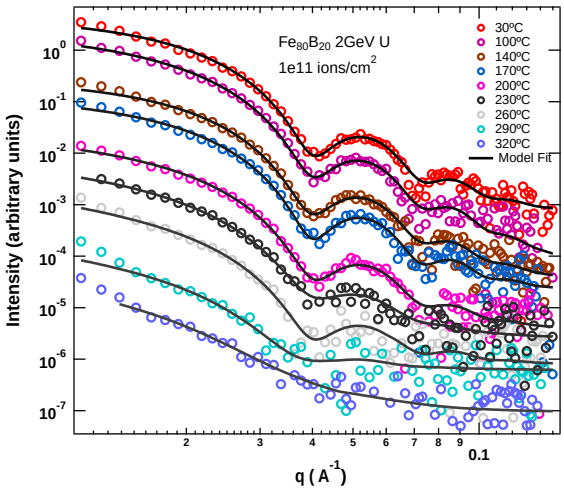

Figure 1: SAXS intensities as a function of scattering vector q (symbols) and corresponding fits (lines) with the hard cylinder model for different annealing temperatures. Vertical shifts of are applied for better visualization.

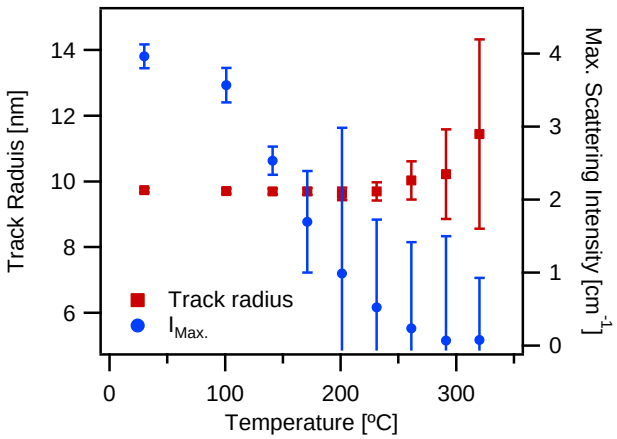

Figure 2: Track radii extracted from fits to SAXS data and experimental maximum SAXS scattering intensity (at q≈0.001Å^{-1}) versus annealing temperature for 15 min isothermal steps.

References

[1] P. Kluth et al., Phys. Rev. Lett. 101 (2008) 175503

[2] M. D. Rodriguez *et al.*, J. of Non-Cryst. Solids 358 (2012) 571

[3] M. D. Rodriguez et al., Microelect. Engineering 102 (2013) 64

Matias.rodriguez@anu.edu.au

Effect of doping on the radiation response of conductive Nb-$SrTiO_3$*

W.X. Li[1,#], M. Rodriguez[2], P. Kluth[2], M. Lang[1], N. Medvedev[3], M. Sorokin[4], J. Zhang[1], B. Afra[2], M. Bender[5], D. Severin[5], C. Trautmann[5,6] and R. Ewing[1]

[1]University of Michigan, Ann Arbor, U.S.A.; [2]The Australian National University, Australia; [3]DESY, Germany; [4]Kurchatov Institute, Moscow, Russia; [5]GSI, Darmstadt, Germany; [6]TU Darmstadt, Germany

Based on the Coulomb-spike model, track formation is expected to depend on the electrical resistivity of a given material. Here, we report the first systematic study on ion tracks in doped $SrTiO_3$ (STO) [1]. With the addition of low concentrations of Nb the resistivity of STO dramatically decreases covering the entire electronic regime from an insulating to conducting material.

Tracks were produced by exposing Nb-doped STO single crystals (thickness ~40 μm) to 1.7-GeV Au or 2.0-GeV U ions (see Table 1 for details) at the UNILAC accelerator. The Nb concentrations varied from 0, 0.1, and 1 wt % with corresponding resistivities of ~10^4, 8×10^{-2}, and 3.5×10^{-3} Ωcm, respectively. The irradiated samples were investigated using transmission small-angle x-ray scattering (SAXS) at the Australian Synchrotron in Melbourne. Crushed samples were inspected by transmission electron microscopy (TEM).

Tracks are observed by TEM in both undoped and Nb-doped STO samples, despite the significant decrease in resistivity (Fig. 1). The tracks are parallel aligned and evident by the dark contrast of their damage trails with respect to the unirradiated matrix. In comparison to the sharp contrast between the track core and boundary in apatite [2], the contrast of tracks in undoped and Nb-doped STO is rather weak. Independent of the Nb-doping level, the track radius deduced from TEM images is rather similar (~20-30 Å) for all samples. However, the weak contrast prevents a precise determination of the track radii by TEM. Track radii were also deduced from SAXS measurements by fitting the intensities data of the tracks as a function of the scattering vector. The SAXS track radii are consistent with the values as observed by TEM (Table 1). In contrast to the limited number of tracks in a localized area as observed by TEM, the strong scattering oscillations from a very large number of well aligned, identical tracks in a bulk sample, as detected by SAXS, provide a very reliable means for determining the mean track radius. The SAXS measurements further confirm that the Nb-doping has no evident influence on the track size in STO.

There are two different possibilities that explain the independence of track formation on the Nb-doping level. Firstly, although the density of the conduction electrons significantly increases up to ~10^{20} cm^{-3} upon doping, this number is still too low to influence the cooling of the electronic subsystem as compared with the number of excited electrons (~10^{22} cm^{-3}) in the track core. Secondly, as implied by the non-thermal model, the difference in the type of bonding between metals and dielectrics may be important for track formation because ionization might not so much change metallic bonds, while the covalent or ionic bonds can be broken. However, the low concentration doping in this study does not change the bonding type, just the electronic conductivity, and therefore has probably no significant effect on track formation.

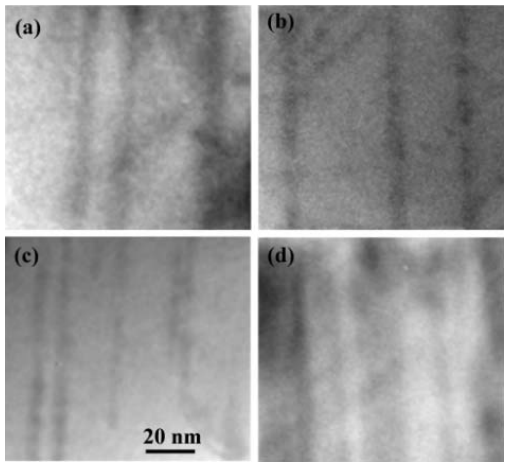

Figure 1: TEM images showing the morphologies of tracks created by 2.0-GeV U ions at room temperature in (a) undoped STO and (b) 1 wt % Nb-doped STO, and by 1.7-GeV Au ions at 24 K in (c) undoped STO and (d) 1 wt % Nb-doped STO.

Table 1: Irradiation parameters and track radii deduced from SAXS measurements.

Doping Nb (wt%)	Irradiation temperature	Ions (GeV)	*R*(Å)
0	RT	U (2.0)	31.3 (0.1)
0.1	RT	U (2.0)	30.7 (0.2)
1	RT	U (2.0)	31.2 (0.2)
0	RT	Au (1.7)	22.8 (0.5)
0.1	RT	Au (1.7)	23.6 (0.5)
1	RT	Au (1.7)	N.A.
0	24 K	Au (1.7)	22.8 (0.2)
0.1	24 K	Au (1.7)	19.8 (0.3)
1	24 K	Au (1.7)	N.A.

[1] W.X. Li et al., accepted in Nucl. Instr. Meth. (2013).
[2] W.X. Li, L.M. Wang, M. Lang, C. Trautmann, and R. Ewing, Earth Planet. Sci. Lett. 302 (2011) 227.

* Work supported by the Office of Basic Energy Sciences of the U.S. DOE (DE-FG02-97ER45656).

#wxli@umich.edu

Swift heavy ion induced radiation damage of $TmPO_4$*

A. Romanenko[1,2,#], M.Lang[3], F. Fujara[2], and C. Trautmann[1,2]

[1]GSI, Darmstadt, Germany; [2]TU Darmstadt, Darmstadt, Germany; [3]University of Michigan, USA

One of the key questions in ion-irradiation induced material degradation is why certain materials are easily damaged while others exhibit high radiation hardness. This work is part of a project investigating the response of lanthanide phosphates $LnPO_4$ to high electronic excitation. Using synthetic single crystals with lanthanide ions varying from Y, Sc, La, … up to Lu allows us to perform a systematic damage study. Depending on the lanthanide ion, the crystals are divided into two groups with similar structures. Crystals with the lanthanide ions of diameter larger that the one of Gd (Ln = La…Gd) form monoclinic ($P2_1/n$) crystal lattices, whereas the other phosphates (Ln = Y, Sc or Tb…Lu) form tetragonal ($I4_1/amd$) crystals. Here we present first results on $TmPO_4$.

The irradiation of $TmPO_4$ single crystals was performed at the UNILAC using 2.2 GeV Au ions. At this energy, the ion range is of the order of 80 µm. We applied fluences between 5×10^{10} and 5×10^{13} ions/cm^2 and a beam flux of either 10^8 or 10^9 ions/cm^{2}s. The irradiated crystals were analyzed by Raman spectroscopy using a Horiba LabRAM spectrometer with a laser of λ= 632 nm.

For radiation studies, an important information is the damage cross section which is directly related to the track radius. We thus analyzed the Raman spectra of crystals exposed to a fluence series (fig. 1) and deduced a track radius according to the Poison equation (single-impact model) assuming that each ion creates a cylindrical track:

$$A = A_0 \cdot \exp(-\pi r_{tr}^2 \Phi) \qquad (1)$$

where r_{tr} is the track radius, Φ denotes the fluence, and A is the intensity ratio of the Raman bands at 1004 and 977 cm^{-1}. The band at 1004 cm^{-1} corresponds to symmetrical stretching of the PO_4 tetrahedron and is the most intense peak in Raman spectra of the virgin sample, whereas the 977 cm^{-1} band appears as a result of the irradiation. Figure 2 shows the evolution of the intensity ratio as a function of fluence. Fitting Eq.(1) to the data yields a track radius of 2.8±0.8 nm which is in agreement with track radii in other compound insulators such as $Y_3Fe_5O_{12}$ [1] or $NiFe_2O_4$ [2].

Figure 3 presents Raman spectra from irradiations with different fluence and flux parameters showing that the ion flux plays a significant role. For a fixed fluence, the spectrum from the irradiation with 10^8 ions/cm^{2}s shows higher degradation than under 10^9 ions/cm^{2}s (cf. black and red spectrum). At a flux increased by one order of magnitude twice as large a fluence is requires to provide the same amount of damage in the material (cf. blue and black spectrum).

* Work supported by GSI-TUD cooperation contract and HGS-HIRe

#an.romanenko@gsi.de

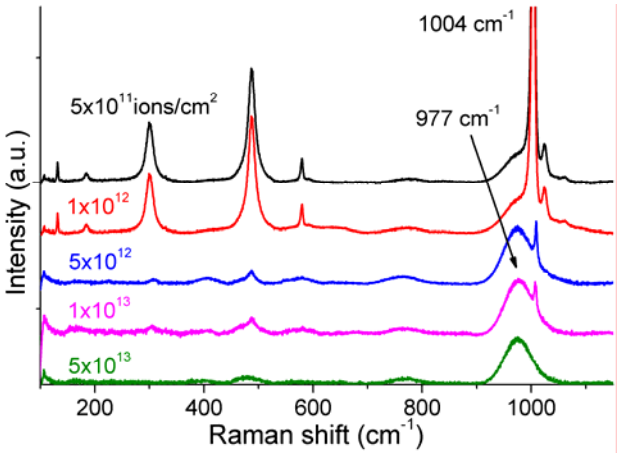

Figure 1: Raman spectra of $TmPO_4$ crystals exposed to 2.2-GeV Au ions. Damage creation increasing with fluence is indicated by significant broadening and intensity decrease of all bands.

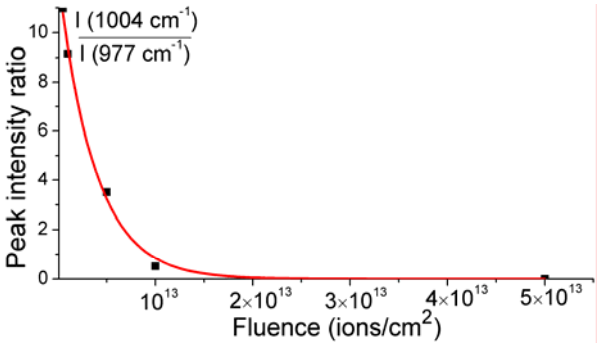

Figure 2: analysis of track radius fitting the ratio of 1004 to 977 cm^{-1} band intensities.

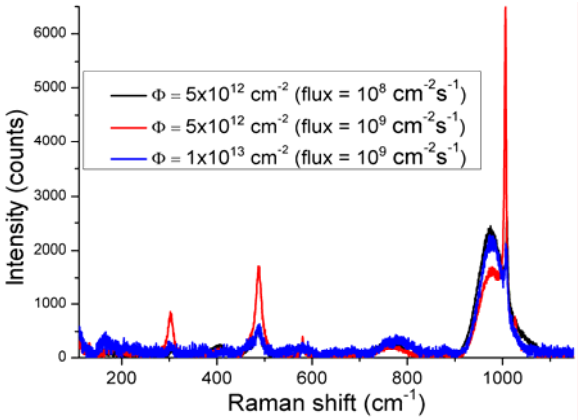

Figure 3: Raman spectra of $TmPO_4$ crystals irradiated at two different fluxes.

[1] A. Meftah et al., Phys. Rev. B 48 (1993) 920.
[2] M. Toulemonde et al., Sol. Stat. Phen. 30 (1993) 477.

Electronic excitation effects on yttria-stabilized zirconia by high-energy ion irradiation

K. Nakano[1], A. Iwase [1,#], and C. Trautmann[2]

[1]Osaka Prefecture University, Sakai, Osaka, Japan; [2]GSI and Technische Universität, Darmstadt, Germany

Introduction

In pure zirconia the irradiation with swift heavy ions induces a phase transformation. Details such as the damage cross section are known to depend on the electronic energy loss of the ions [1,2]. However, according to our recent experiments with heavy ions in the energy range between 7 and 200 MeV, irradiation effects on lattice expansion of yttria stabilized zirconia (YSZ) depend on the elastic energy loss or displacements per atom (dpa) [3]. To clarify the effect of electronic excitation on the lattice structure of YSZ, we performed irradiations with ions of much higher energy in the GeV range.

Experimental

YSZ pellets (8% Y_2O_3 in ZrO_2) were irradiated with 2.2-GeV Au ions at the UNILAC. Fluences in the range from 10^{10} – 2×10^{12} ions/cm^2 were applied. To evaluate the irradiation effects on the lattice structure, the samples were analyzed by x-ray diffraction (XRD). The results are compared with data from irradiations with 16-MeV Au ions.

Results and discussion

After ion irradiation the fluorite structure of YSZ remains unchanged. No new phases appear, neither when exposed to 2.2 GeV nor to 16 MeV Au ions. However, when analyzing the XRD peaks at each diffraction angle, we observed a peak shift that allows us to estimate the beam-induced change in lattice constant. Figures 1(a) and 1(b) show the change in the lattice constant as a function of the energy deposited through electronic excitation and by averaged dpa, respectively. The lattice expansion from the irradiation with 16-MeV Au ions is much larger than that for 2.2-GeV Au ions when comparing same energy depositions through electronic excitation (Fig. 1(a)). As can be seen in Fig. 1(b), the lattice constants are well scaled by dpa for both irradiations, 2.2-GeV and 16 MeV Au ions. This result shows that the irradiation effect on lattice constants of YSZ is dominated by the elastic energy loss unlike in the case of pure zirconia, which is quite sensitive to electronic excitation.

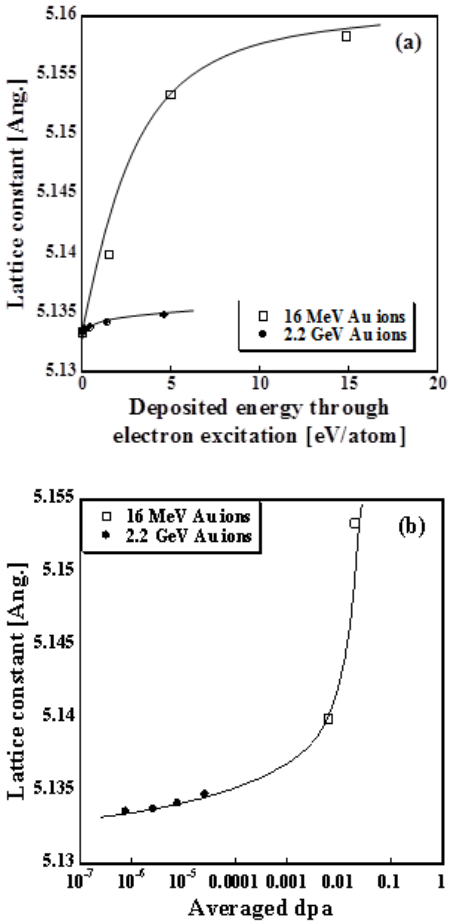

Fig. 1. Lattice constant for YSZ samples irradiated with 2.2-GeV and 16-MeV Au ions as a function of (a) the energy deposited through electronic excitation and (b) averaged dpa.

References

[1] A. Benyagoub, F. Couvreur, S. Bouffard, F. Levesque, C. Dufour, E. Paumier, Nucl. Instr. Meth. B 175-177 (2001) 417.
[2] A. Benyagoub, Nucl. Instr. Meth. B 206 (2003) 132.
[3] K. Nakano et al., SHIM 2012 (Kyoto October 2012)

#iwase@mtr.osakafu-u.ac.jp

Ion induced grain rotation – a general phenomenon?

M. Bender[1], F. Garrido[2], S. Klaumünzer[3], and D. Severin[1, #]

[1]GSI, Darmstadt; [2]CSNSM, Orsay, France; [3]Helmholtz-Zentrum Berlin;

Various amorphous materials show the so-called ion hammering effect [1]. It is supposed that this effect is driven by shear stress relaxation during the transient, fluid state of the ion track while the surrounding solid matrix responds perfectly elastically [1]. Ion hammering was also invoked to explain ion-beam-induced nanostructuring of NiO and other metal oxides [2,3]. But online X-ray diffraction of NiO indicated the absence of any amorphous material. Rather, the observed shear deformation is probably the result of grain boundary motion and grain rotation. In fact, when ion beam and specimen normal subtend an angle $\alpha \geq 20°$, single crystalline NiO rapidly transforms into nanocrystallites with diameters around 30 nm and the nanocrystals rotate. Their tilt is easily detectable as a change of the lattice orientation Ω and increases with ion fluence Φt [4,5].

To test if the observation for NiO is a more general material response, we exposed single crystals of NiO, MgO, UO_2, and LiF to 709-MeV Au ions. The irradiations were performed at the M2-beamline of the UNILAC using a scanned beam. The irradiation chamber is equipped with a 4-circle X-ray diffractometer (Seifert 3003TT, see fig. 1). The samples had a typical size of 0.5-1 cm^2 and a thickness of 0.5 to 1 mm. The information depth of the X-rays is larger than the ion range so that the unirradiated sample part serves as reference. The irradiation temperature was kept below 80°C. The irradiation angle α was 45°.

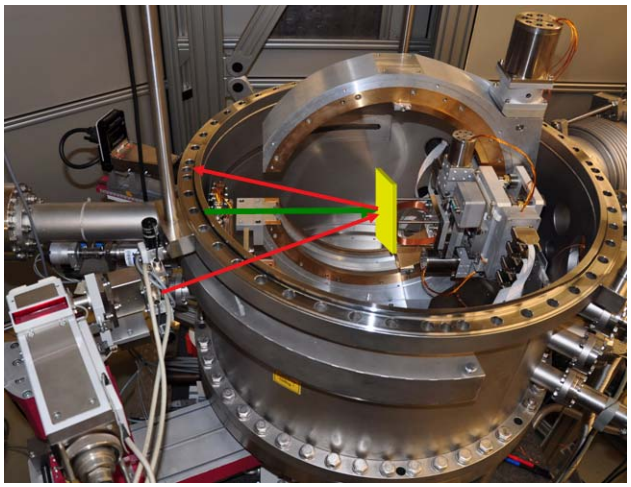

Figure 1: In-situ XRD setup at beamline M2 (M-branch, UNILAC). The green arrow indicates the ion beam (here at $\alpha = 0°$). The red arrows indicate the incident and diffracted X-ray beam.

#d.severin@gsi.de

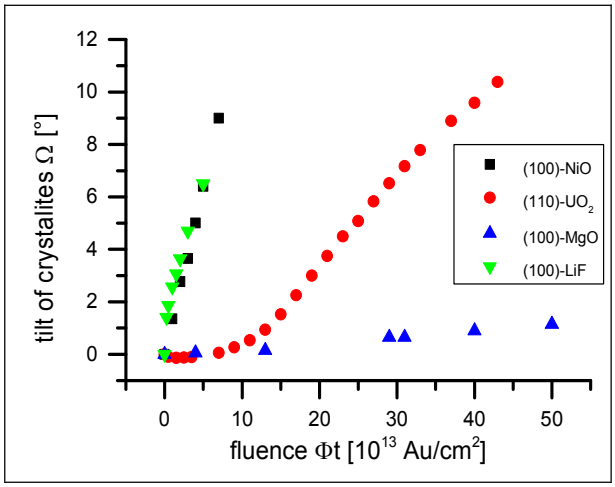

Figure 2: Lattice tilt Ω vs. ion fluence for irradiation with Au ions under $\alpha = 45°$. The beam energy was 945 MeV (NiO, UO_2, and MgO) and 709 MeV (LiF).

All four materials exhibit grain rotation (figure 2). There is no indication of amorphization and the crystals stay mechanically intact. In the case of MgO, the effect of grain rotation is rather weak compared to the other crystals. Grain rotation of UO_2 shows a non-linear evolution and a kind of incubation fluence of $\sim 7\times10^{13}$ ions/cm^2. Above this value, the rotation rate $d\Omega/d\Phi t$ gradually increases followed by a constant rotation rate above $\sim 3\times10^{14}$ ions/cm^2. A similar behaviour was also found for ω-titanium [4]. Grain rotation is nearly reversible if the rotation axis coincides with a high-symmetry crystal axis. Changing α from +45° to -45° reverses the sign but leaves the magnitude of the rotation rate almost unchanged [5]. When the rotation axis is not a crystal axis of high symmetry, additional crystallite tilts occur which destroy gradually the memory on the original orientation of the single crystal and are the starting point for the formation of a polycrystal.

Our results give evidence that grain rotation seems to be a rather common phenomenon in non-amorphizing materials. The basic mechanism is not yet clear, but it is probably linked to loop punching in the immediate surroundings of the extremely hot and thus over pressurized ion tracks.

[1] H. Trinkaus and A. I. Ryazanov, Phys. Rev. Lett. 74 (1995) 5072.
[2] W. Bolse, Nucl. Instr. Meth B 244 (2006) 8.
[3] W. Bolse et al., Appl. Phys. A77 (2003) 11.
[4] I. Zizak et al., Phys. Rev. Lett. 101 (2008) 065503.
[5] S. Klaumünzer et al., GSI annual report PNI-MR-01.

Laboratory simulation of heavy-ion irradiation effects in astrophysical ices*

M. Bender[1], Ph. Boduch[2], V. Bordalo[3], J. J. Ding[2], A. Domaracka[2], H. Kollmus[1], Th. Langlinay[2], X. Y. Lv[2], H. Rothard[2,#], D. Severin[1], C. Trautmann[1,4], M. Toulemonde[2], M. Wengenroth[1]

[1]GSI, Darmstadt; [2]CIMAP-CIRIL-Ganil, Caen, France; [3]PUC, Rio de Janeiro, Brazil, [4]TU Darmstadt Germany

In space, ices such as H_2O, CO, CO_2, and NH_3 are omnipresent on comets, moons of giant planets, and dust grains in dense clouds (the birthplaces of stars and planetary systems). They are exposed to cosmic rays, which in turn induce radiolysis, i.e., molecule fragmentation, formation of radicals, and subsequent synthesis of new molecular species. Even complex pre-biotic molecules such as amino acids can be formed [1]. Due to their high electronic energy loss, the heavy ion fraction in cosmic rays yields non negligible contributions to sputtering and radiolysis, even if protons and alpha particles are more abundant [1,2]. In the laboratory heavy ions accelerated to high energies allow us to simulate the specific effects induced by the heavy ion fraction of cosmic radiation. A first test experiment was successfully performed at the M-branch of the UNILAC exposing CO_2 ice (deposited at approx. 35K on a CsI substrate) to 570-MeV Ti ions. Molecular changes such as destruction and synthesis of new species were monitored by Fourier transform infrared absorption spectroscopy (FTIR) (Fig. 1). Simultaneously, sputtered and outgassing species released from the ice surface were identified and monitored by quadruple mass spectrometry (QMS).

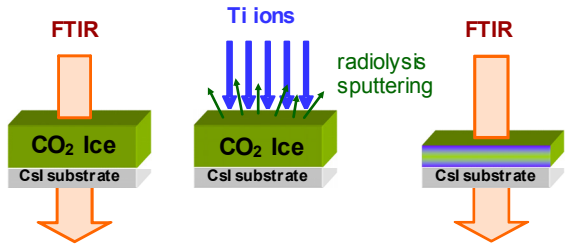

Figure 1: Laboratory simulation of heavy-ion irradiation effects in ices monitored by infrared spectroscopy.

Figure 2 shows the change of column densities ("thickness") of CO_2 (top) and CO (bottom) during ion irradiation. The amount of CO_2 decreases exponentially with a corresponding destruction cross section of $\sigma_d = 4.3\times10^{-14}$ cm^2. The initial density increase is assumed to result from a change of optical properties of the ice due to compaction [1]. One of the daughter molecules appearing during irradiation is CO. The formation cross section deduced from the exponential increase is $\sigma_f = 1.2\times10^{-14}$ cm^2. Synthesis of CO_3, O_3, and C_3 is also observed [2]. Taking into account the amount of deposited energy in the ice by electronic energy loss, the observed cross sections are in good agreement with values observed for 50-MeV Ni ions used earlier at the Ganil facility in France [2].

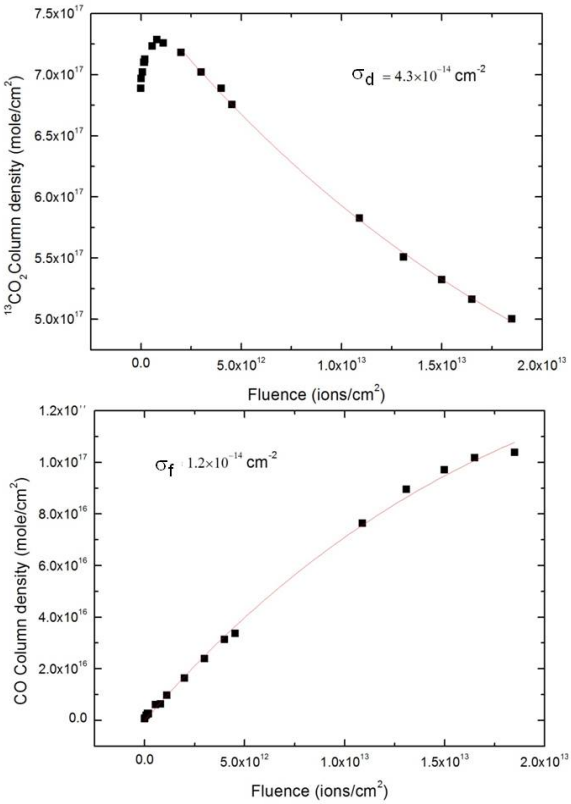

Figure 2: Irradiation of CO_2 ice with 570-MeV Ti ions. Preliminary results of column density of CO_2 (top) and CO (bottom) as a function of ion fluence.

References

[1] S. Pilling, E. Seperuelo Duarte, E. F. da Silveira, E. Balanzat, H. Rothard, A. Domaracka, P. Boduch, Astronomy & Astrophysics 509 (2010) A87.

[2] E. Seperuelo Duarte, P. Boduch, H. Rothard, T. Been, E. Dartois, L. S.Farenzena, E. F. da Silveira, Astronomy & Astrophysics 502 (2009) 599.

*Work co-funded by the European Commission, FP7 for RTD (2007-2013), Capacities Program (Contract No. 262010, ENSAR); supported by the CAPES-COFECUB French-Brazilian exchange program and the CRC Chinese Research Council.

#rothard@ganil.fr

Analysis of radiation damage in heavy-ion irradiated ionic crystals by magnetic resonance*

M. Ditter[1,#], K-C. Meyer[1], S. Orth[1], S. Quittek[1], A. Mansouri[1], K. Schwartz[2], C. Trautmann[1,2] and F. Fujara[1]

[1] TU Darmstadt; Germany, [2] GSI, Darmstadt, Germany.

We explore and expand the capabilities of magnetic resonance techniques, mainly nuclear magnetic resonance (NMR) but also electron spin resonance (ESR), as a tool for the characterization of radiation damage in solids. At present, we are focussing on ionic crystals, mainly lithium fluoride (LiF), which offers two suitable probe nuclei for NMR. In contrast, ESR is directly susceptible to paramagnetic defects and conduction electrons e.g. in metallic colloids. In 2012 our research concentrated on three topics: (a) Utilizing spatially resolved field-cycling (FC) NMR data to obtain information about the distribution of ion-beam induced defects, (b) using NMR spectroscopy to detect the presence of fluorine gas within irradiated samples, and (c) examining defect dynamics above room temperature by ESR and spatially resolved NMR after a series of stepwise annealing experiments.

(a) Common NMR relaxation theory in the presence of paramagnetic centres in alkali halides predicts a strong B-field dependence of the relaxation rate, depending on the distribution of defects within the sample [1]. This effect is supported by our data recorded by FC NMR. However, so far literature provides only analytical and approximate solutions of the resulting differential equation for homogeneous distributions. We are currently working on a numerical approach to calculate relaxation rates for any given distribution. By comparing our model with data derived from samples with known distributions, we hope to deduce from FC NMR the topology of unknown defect structures.

(b) The formation of molecular fluorine gas formed in neutron-irradiated LiF was first observed by CW-NMR spectroscopy some five decades ago [2]. Until now it was just speculated that fluorine gas also forms in samples irradiated with heavy ions having a strong radial gradient of the dose deposited around the ion track. Recently, we identified for the first time F_2 molecules in several LiF crystals irradiated with 6×10^{11} to 2×10^{12} ions/cm² by NMR spectroscopy. We have evidence that the appearance of fluorine molecules requires an energy loss above 10 keV/nm where tracks consist of a heavily damaged core zone of few nm in diameter [3]. At present, the nature of this track core is not yet fully understood.

c) With CW-ESR spectroscopy we detected the formation of metallic Li colloids in LiF at temperatures above 600 K during annealing experiments. Li colloids in heavy-ion irradiated LiF samples were already identified by optical absorption spectroscopy [4]. However, ESR allows us to gain access to more heavily irradiated samples where the large color centers concentration leads to a high optical density preventing quantitative analysis of optical absorption spectra.

By spatially resolved NMR relaxation rate measurements on a stepwise annealed LiF crystal, we observed a remarkable drop of the relaxation rate below the level found in the unirradiated part of the crystal (Figure 1). This effect appeared at a temperature which corresponds to the recently observed ion-beam induced formation of impurity magnesium colloids [4]. We thus tentatively attribute this effect also to the formation of impurity clusters. The concentration of paramagnetic impurities is decisive for the relaxation rate in unirradiated crystals.

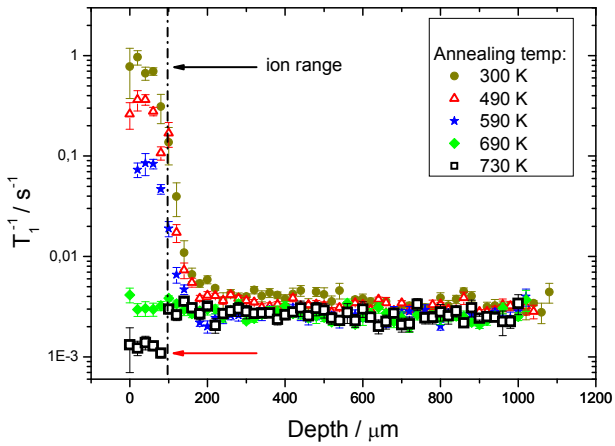

Figure 1: Depth profiles of nuclear spin-lattice relaxation rates recorded for a LiF crystal irradiated with 2.2-GeV ions of 6×10^{11} ions/cm². The sample was stepwise annealed for 20 min at different temperatures up to 730 K. Note the drop of relaxation rates at 730 K (red arrow) to a level below the value of the unirradiated, crystal (depth >100 μm).

References

[1] I.J. Lowe and D. Tse, Phys. Rev. 166 (1968) 279.

[2] C.D. Knutson, H.O. Hooper, P.J. Bray, J. Phys. Chem. Solids 27 (1966) 147.

[3] C. Trautmann, K. Schwartz, J.M. Constantini, T. Steckenreiter, M. Toulemonde, Nucl. Instr. Meth. B 146 (1998) 367.

[4] K. Schwartz, A.E. Volkov, M.V. Sorokin, R. Neumann, C. Trautmann, Phys. Rev. B 82 (2010) 144116.

* Work supported by DFG, No. FU 308/12.

michael.ditter@physik.tu-darmstadt.de

Ion-induced luminescence of radiation defects in ZnO

R. Stübner[1,#], M. Bender[2], D. Severin[2], and J. Weber[1]

[1]Technische Universität Dresden, Germany; [2]GSI, Darmstadt, Germany

Ion-induced luminescence (IL) experiments and photoluminescence investigations (PL) were performed to study the properties of irradiation induced intrinsic point defects in ZnO single crystals.

In these experiments, we irradiated vapour phase grown n-type ZnO single crystals perpendicular to the c-axis with 4.8 MeV/amu Ti^{12+} ions up to a fluence of 2.5×10^{10} ions/cm^2. The ion beam had a frequency of 1 Hz and a pulse length of 5 ms corresponding to 6×10^7 ions/cm^2 per pulse. The samples were mounted on a closed-cycle He-cryostat and kept at constant temperatures between T = 25 and 140 K. The luminescence was analyzed with a fixed grating outside the vacuum chamber and detected with a CCD detector. The PL was excited by the 355 nm line of a frequency tripled Nd:YAG laser. After each IL measurement a PL spectrum was recorded at the same temperature within 30 s.

The PL and IL spectra at T=25 K and T=75 K are shown in Fig. 1 and 2, respectively. At a temperature of T=25 K the PL spectrum shows a dominant peak at 3.360 eV which is caused by aluminium donor bound exciton transitions. At higher energies, smaller peaks caused by hydrogen (H) and free exciton transitions (FX) are visible. The IL spectrum has a dominant peak at 3.355 eV (I_x), and a correlated two-phonon transition at 3.210 eV (I_x-2LO).

At higher temperatures, the FX transition and its phonon replica increase in intensity (Fig. 2). While the phonon-related transitions are visible in PL and IL as well, the FX zero-phonon transition is only visible in the PL spectra. The difference between the PL and IL spectra can be understood, if one considers the different electronic excitation volumes in both cases. In PL the excitation is located in the surface region, while in IL the excitation is distributed along the ion track. In the latter case the emission has to pass a thicker layer of material before reaching the surface, which leads to a stronger absorption of luminescence close to the band-edge.

The temperature dependence of the emission intensity of I_x was measured in the range of 50 to 90 K. A two-level model of free and bound excitons is used to fit the measured intensity at increasing temperatures. As preliminary result, we obtain a localization energy of 23 meV, and under the assumption of a donor bound exciton transition, a donor binding energy of 74 meV. These values are comparable with the so far unidentified I_{10} defect in ZnO (Tab. 1).

Possible candidates for the I_x defect are generally all native point defects. Based on literature data, vacancies and oxygen interstitials can be excluded as origin of the I_x defect. The zinc interstitial, however, seems to be a reasonable candidate for the observed defect.

ronald.stuebner@physik.tu-dresden.de

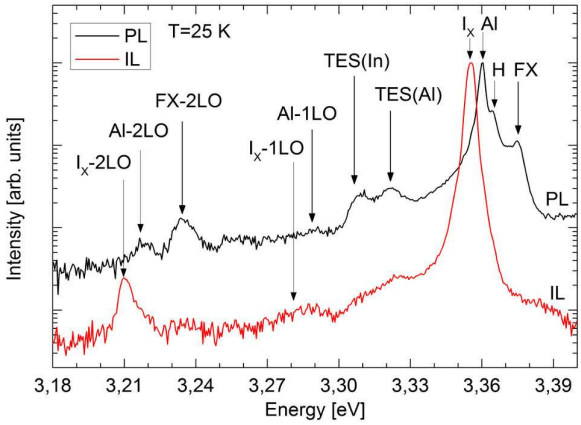

Figure 1: PL and IL spectra of ZnO crystals at T=25K.

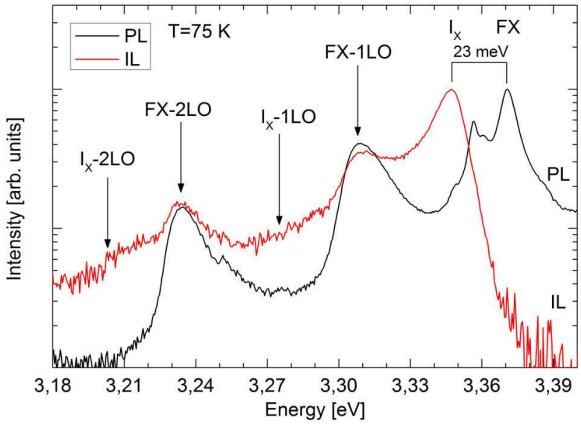

Figure 2: PL and IL spectra of ZnO crystals at T=75K.

Defect	E_{loc}	E_D (meV)	Ref.
I_x	23 meV	74	This work
I_{10}	22.8 meV	72.6	[1]
I_{10}	23.1 meV		[2]
IID*		75	[3]
I_{10}	23.5 meV	76.7	[4]

* Irradiation induced donor

Table 1: Measured values and literature data.

References

[1] B.K. Meyer *et al.*, phys. stat. sol. (b), **241**, 231 (2004)
[2] Y.S. Jung *et al.*, J. of Appl. Phys. **99**, 013502 (2006)
[3] D.C. Look *et al.*, Phys. Rev. Lett. **95**, 225502 (2005)
[4] L. Bergman and J.L. McHale, *Handbook of luminescent semiconductor materials*, CRC Press, Boca Raton, 2012

Conductivity enhancement of single ion tracks in tetrahedral amorphous carbon by matrix doping with B, N, Cu and Fe*

J. Krauser[1,#], A.-K. Nix[2], H.-G. Gehrke[2], H. Hofsäss[2], C. Trautmann[3,4], A. Weidinger[5]

[1]Hochschule Harz, Wernigerode, Germany; [2]Universität Göttingen, Germany; [3]GSI Helmholtzzentrum, Darmstadt, Germany; [4]Technische Universität Darmstadt, Germany; [5]Helmholtz-Zentrum Berlin, Germany

The irradiation of diamond-like tetrahedral amorphous carbon (ta-C) with swift heavy ions leads to conductive tracks. The increased conductivity along the ion trajectories is due to a transformation of the sp^3-rich phase (insulating) into a more sp^2-rich phase (conducting) of the material [1]. For any applications of conducting ion tracks [2], it is important that their conductivity exhibits Ohmic behavior and that the track conductivity is significantly larger than that of the surrounding matrix material. In the present study, we investigate if the conductivity of the ion tracks can be selectively enhanced by adding metal atoms (Cu and Fe) or other typical doping materials (B and N) during the growth process of the ta-C matrix layer.

The ta-C samples with film thickness of ~ 100 nm were produced at the University of Göttingen by means of low energy mass selected ion beam deposition (MSIBD) on heavily doped n-Si substrates. Doping of the ta-C films was performed by injecting the desired dopant into the ion source and then rapidly switching the mass separation magnet from ^{12}C to the dopant ion periodically. The doping concentration for all samples is about 1 at. % except for the ta-C:B sample which has a doping concentration of 2 at. %. Doped and undoped samples were exposed to 1-GeV Au or U ions at the UNILAC. The fluence was in the range of 1 - 5×10^9 ions/cm^2. The conductivity of individual ion tracks was analyzed by atomic force microscopy (AFM) using a conducting tip.

Figure 1 shows I-V characteristics of single tracks in undoped and doped films. It is evident that the doping changes the current through the tracks drastically: N- and B-doping induces a moderate and Cu and Fe doping a strong increase of the currents. The I-V curves for B- and N-doped samples are still slightly bend whereas those for Cu- and Fe- doped samples are straight lines.

Figure 2 shows the conductivity of the tracks calculated from the slopes of the I-V curves at low voltages. Doping significantly improves the track conductivity. Cu is identified as most suitable, while B, N, and Fe dopants have the disadvantage to enhance the conductivity not only of the tracks but also of the unirradiated ta-C matrix. The incorporation of Fe can produce conducting paths through the ta-C matrix, degrading the resistivity of the unirradiated film and thus leading to a low conductivity contrast (not shown here).

* Work supported by by DFG (HO 1125/17-1 and KR 3298/1-1) and BMBF (05KK4MGA/9).

jkrauser@hs-harz.de

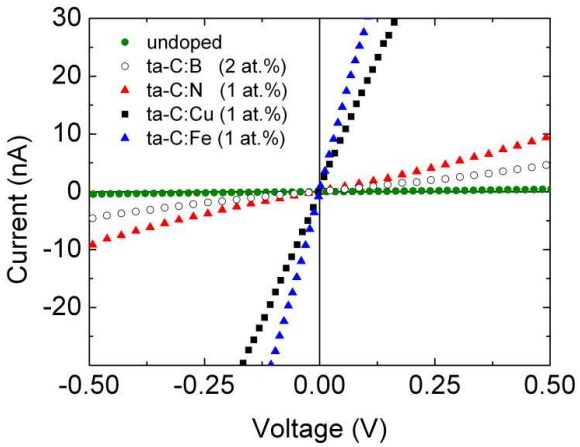

Figure 1: I-V characteristics of single ion tracks in undoped and differently doped ta-C samples. The dopant species and their concentrations are indicated.

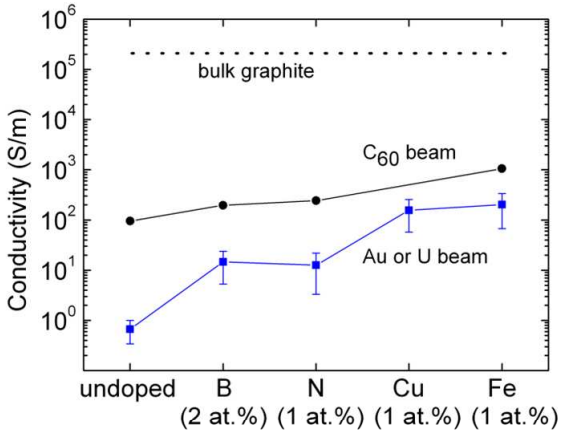

Figure 2: Conductivity of ion tracks for differently doped ta-C films. The beams were 1-GeV Au or U ions (for Cu) and 30-MeV C60 clusters [3]. The conductivities were calculated assuming a cylinder of 8 nm diameter and a length corresponding to the film thickness (100 nm).

References

[1] M. Waiblinger et al., Appl. Phys. A 69 (1999) 239
[2] A. Weidinger, Europhysics News, 35/5 (2004) 152
[3] J. Krauser et al., Nucl. Instr. Meth. B 272 (2012) 28

Preparation, irradiation, and characterization of surfaces under ultra high vacuum conditions

F. Meinerzhagen[1], H. Bukowska[1], T. Peters[1], O. Picht[1,2], D. Severin[2], M. Bender[2], A. Siegmund[2], H. Lebius[3], F. Weiss[1], and M. Schleberger[1,#]

[1]Universität Duisburg-Essen, 47057 Duisburg, Germany; [2]GSI, 64291 Darmstadt, Germany; [3]CIMAP, 14070 Caen Cedex 5, France .

A scanning probe microscope (SPM) in an ultra-high-vacuum (UHV) enviroment was built up at the M-branch of GSI. With this new facility it is possible to characterize modifications caused by ion irradiation in-situ with a resolution down to atomic scales.

Experimental setup

A picture of the experimental setup is shown in fig. 1. Tips for the SPM, samples or substrates can be transferred to UHV from a load-lock. Samples can be heated with an electron beam or a direct current heater on a manipulator in the preparation chamber. An electron beam evaporator in this chamber allows to deposit two different materials on the sample. For controlling the mass flow a microbalance can be used. A low energy electron diffraction (LEED) unit enables the investigation of sample crystallinity. The main part of the setup is the commercially available VT SPM (Omicron NanoTechnology). It allows atomic force microscopy (AFM), scanning tunneling microscopy (STM), and special modes of AFM like Kelvin probe force microscopy (KPFM) for spatially resolved measurements of surface potentials. The irradiation chamber permits irradiation of samples under glancing incidence ($\theta < 5°$). Currently the accuracy of the angle is ± 1°, but in the final stage it will be down to ± 0.05°. In addition to the angle, the energy deposition is an important parameter for our experiments. The ions are accelerated by the linear accelerator UNILAC and have energies in the range of 3.6 to 11.4 MeV/u. We are interested in single ion induced modifications in low-dimensional solids and therefore use fluences on the order of 10^{10} ions/cm^{-2}.

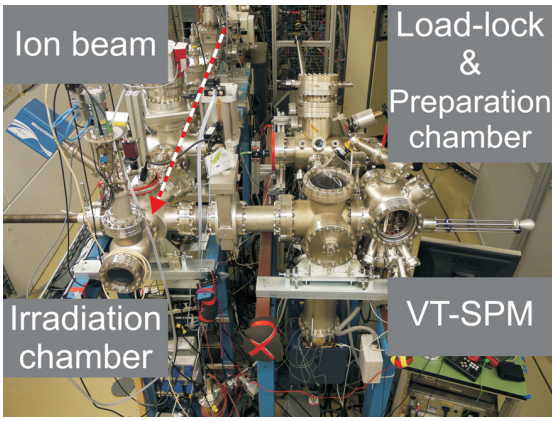

Figure 1: Picture of the setup. The irradiation chamber is mounted at the end of the ion beam line (marked with the arrow). In the upper right part of the picture the preparation chamber can be seen, below the chamber with the SPM.

First results

At the first beamtimes we could demonstrate that the newly built system works as planned. Figure 2 shows an AFM image of a successfull irradiated strontium titanate ($SrTiO_3$) surface with stopping power of 48 keV/nm. On the crystalline $SrTiO_3$ chains of hillocks with a height up to 6 nm are observable. This phenomenon has been observed before for $SrTiO_3$ irradiated with ions with stopping powers up to 25 keV/nm [1-3].

We also found a new structural feature in form of a few Ångström deep rift at the beginning of the trajecory (see inset in fig. 2). This effect will be studied in future experiments with our new setup.

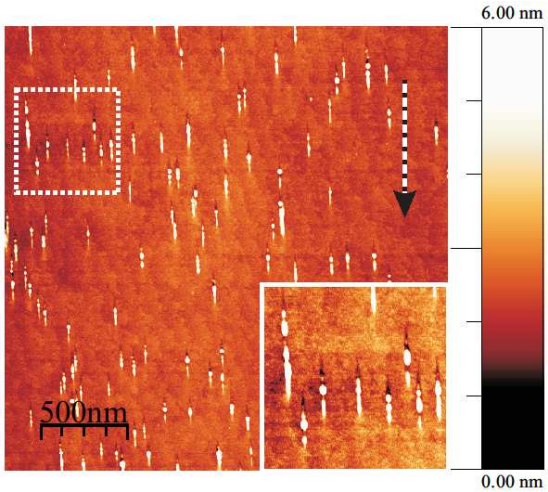

Figure 2: AFM image of a $SrTiO_3$ surface (Δf = -23 Hz). The sample was irradiated under an angle of $\theta = 4° \pm 1°$ with $^{238}U^{28+}$ and an energy of 857 MeV. The stopping power was 48 keV/nm. The arrow marks the direction of the ion beam.

References

[1] E. Akcöltekin, T. Peters et al., Nature Nanotech. 2 (2007) 290
[2] E. Akcöltekin, S. Akcöltekin et al., New J. Phys. 10 (2008) 053007
[3] S. Akcöltekin, E. Akcöltekin et al., Nucl. Instr. Meth. B 267 (2009) 1386

#marika.schleberger@uni-due.de

A micro-manipulator system for characterization of irradiation induced thin film modifications at the in-situ high-resolution SEM at UNILAC*

C. Kiener, R. Ferhati, and W. Bolse[#]

Institute for Semiconductor Optics and Functional Interfaces, University of Stuttgart, Germany.

In order to be able to track the development of swift heavy ion (SHI) induced material modifications on surfaces and in thin films on a nm-scale, we have recently installed our in-situ high-resolution scanning electron microscope (HR-SEM) at the M-Branch of the UNILAC beam line [1]. The microscopy chamber is utilized for the ion irradiation as well as for SEM analysis and allows us to investigate the evolution of individual µm- and nm-sized objects from the first ion impact throughout the entire irradiation experiment. In a first extension stage an EDX-detector has been added to the system that enables us to also follow compositional changes besides the SHI induced structure formation. This way we were able to investigate SHI-induced dewetting of thin oxide films and to discover a dewetting mechanism, which is very similar to the spinodal dewetting of liquid films. But instead on capillary waves, the effect is based on a surface instability caused by irradiation induced mechanical stresses [2].

Here we present a new extension of our setup with a micro-manipulator (MM) system consisting of two MM3A devices from Kleindiek Nanotechnik [3]. The MM3A is a telescopic robotic arm, which can be rotated around its two perpendicular axes. It is attached to the microscopes 5-axes eutectic stage such that it follows the tilt and the up-down movement of the stage, but no lateral translation and azimuthal rotation. This way it can be assured that the tips of the MMs stay in the focus of the electron beam, while the sample can be adjusted on a nm-scale for precise handling (see also Fig. 1).

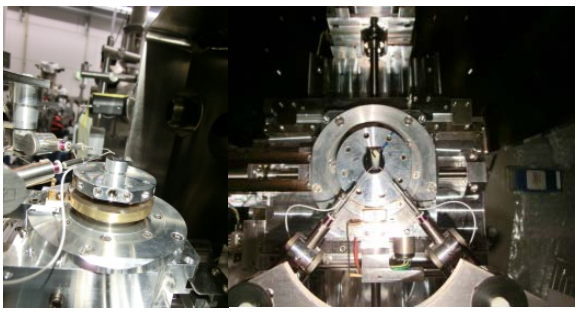

Figure 1: The micro-manipulators in the SEM.

Besides the prober tips (metallic needles with some tens of nm curvature radius), the MM3A can be equipped with various plug-in tools for different applications. The ROTIP device allows for axial rotation of the manipulator arms. For grabbing, removing and repositioning of µm and sub-µm sized particles a micro-gripper (MGS2) is available.

A force measurement system (FMS) allows for the investigation of (sub)micro-mechanical properties and a low current measurement kit (LCMK) can be used for electrical characterization on that length scale.

This system significantly enhances the potential of the in-situ setup, since it extends the possibility of in-situ tracking SHI-induced structural and compositional changes by simultaneous investigation of important other physical properties. Moreover, it will allow us to perform SEM- and EDX-analyses on submicron objects without the heavily disturbing substrate by separating them using the micro-gripper or glueing them on a prober tip. In combination with the ROTIP the object can then be inspected from any direction.

After installation of the MM system, first tests were performed. SiO_2 spheres with 3µm diameter were grabbed and repositioned on a Si-wafer (Fig.2). The FMS system was calibrated and a nano-indentation experiment was performed on a thin SiO_2-film on Si by measuring the indentation depth and force relationship. The LCMK was applied for conductivity measurements on gold-nanowires on NiO-lamellae formed by grazing incidence SHI irradiation of a Au-coated NiO-layer on oxidized Si. Publication of the results of these experiments is in preparation.

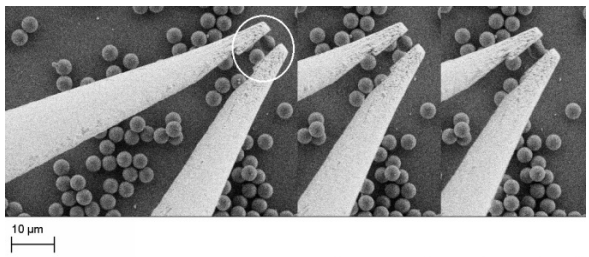

Figure 2: Test run of the MGS2 micro-gripper with microspheres.

We like to acknowledge GSI for hosting the experiment and especially M. Bender and D. Severin for valuable help.

References

[1] S. Amirthapandian, F. Schuchart, W. Bolse, Review of Scientific Instruments 81 (2010)

[2] S. Amirthapandian, F. Schuchart, D. Garmatter, W. Bolse, J. Appl. Phys, 112 (2012)

[3] Kleindiek Nanotechnik, www.nanotechnik.com

* Work supported by Deutsches Bundesministerium für Bildung und Forschung under contract 05K10VS1.

w.bolse@ihfg.uni-stuttgart.de

High-Energy Elastic Recoil Ion Detection Analysis

M. Bender[*1], *D. Severin*[1], *H. Kollmus*[1], *M. Wengenroth*[1], *T. Steinbach*[2], *and W. Wesch*[2]
[1]GSI, Darmstadt, Germany; [2]FSU Jena, IFK, Jena, Germany

Elastic recoil detection analysis (ERDA) with heavy ions has become a powerful tool for stoichiometrical analysis of multifaceted samples. The method uses the information of atoms elastically scattered out of the target in forward direction. These ejectiles are analyzed concerning their atomic number and energy, the latter reveals the depth of the scattering collision inside of the sample. The differential cross section for scattering the target atom into the detector is:

$$\frac{d\sigma}{d\Omega} = \left(\frac{Z_1 Z_2 e^2 (M_1 + M_2)}{8\pi\epsilon_0 M_2 E_1} \right)^2 \cdot \frac{1}{cos^3\phi} \qquad (1)$$

with the scattering angle ϕ. Especially with heavy ions, (e. g., Xe or heavier), element specific depth profiles for atomic masses up to Cr, Fe and Ni, the components of steel, can be obtained easily.
ERDA as a standard analytical tool in research and in industry is typically performed with projectile energies below 1 MeV/u at small electrostatic accelerators.
In recent years, ERDA has been tested at the high charge state injector using 1.4 MeV/u Xe ions [1]. In 2012 a similar setup was installed at the M3-branch of the UNILAC. Here, we have performed ERDA for the first time with 3.6 MeV/u Au ions. At this energy the Coulomb threshold is not reached and thus, the necessary elasticity of the binary collision is still guaranteed.
The figures show qualitative results, demonstrating the promising capabilities of high energy-ERDA. Various samples were probed under an incident angle of 67.5° to surface normal. The scattered atoms have been analyzed under 45° with respect to the incident beam by a $\Delta E/E_{rest}$-telescope similar to the one used in [2]. The detector consists of an ionization chamber working with isobuthane at 30 mbar pressure, decoupled from the experimental vacuum by a $1\mu m$ mylar foil and a silicon detector for E_{rest}. It has a solid angle of 1.7 msr and an acceptance angle of 2.8° in scattering plane.
From eq. 1, the difficulty of high energy-ERDA is visible, as the differential cross section goes down with the energy square. This problem is mitigated by choosing Au as projectile and a longer measuring time as compared to [2].
Within the limited beamtime available, we concentrated on the depth profiling of non-evaporable getter (NEG) coatings on stainless steel as a well known system [2]. Furthermore NEG getters are of active interest because of their use in the FAIR project [1] and the LHC.
Figure 1 shows the raw ERDA data of a getter-coated stainless steel target. All elements are clearly resolved in the plot. The getter layer consists of Ti, V, and Zr and has a thickness of roughly 1.2 μm. Under the getter layer, the steel substrate is clearly visible. The substrate composition and cleanliness of the interface is essential for the life time of the getter coatings. The data illustrate the capability and impact of high energy ERDA to investigate buried layers and interfaces of layer samples to the substrate.

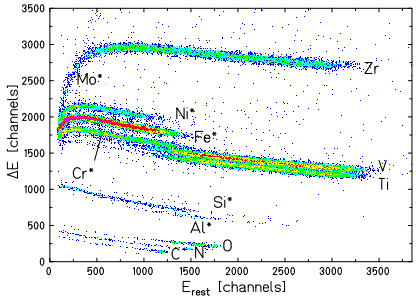

Figure 1: Raw data plot of the NEG getter sample.

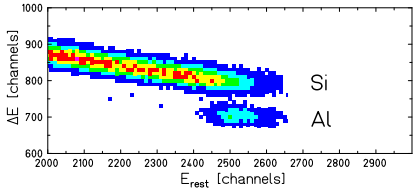

Figure 2: Zoomed into raw data plot of an Al layer on Si.

Figure 2 shows a zoomed area of the $\Delta E - E_{rest}$ plot of Si coverd by a 100 nm thick Al coating. The neighboring elements Si and Al are clearly resolved. However, the 100 nm thickness of the Al layer is distributed on roughly 100 channels of the acquisition chain. With respect to the gauss-shaped borders (front and back edge) of the layer, the depth resolution of the system is towards several 10 nm, being yet poor as compared to low energy ERDA systems [3]. We are presently working on improvements for the depth resolution. This includes the elimination of the binning combined with minimization of noise in the analog signal chain of the electronics. Moreover, an improved E_{rest}-detector with a better energy resolution should be used. Lastly, the implementation of kinematic correction is necessary to eliminate the haziness in energy due to the acceptance angle in scattering plane.

References

[1] M.C. Bellachioma, et al., Vacuum 82 (2008) 435.
[2] M. Bender, et al., NIM **B** 268 (1997) 1986.
[3] K. Kimura, et al., Analytical Sciences 26 (2010) 223.

* corresponding author: m.bender@gsi.de

Installation of diamond window in Paris-Edinburgh press for sample analysis before, during, and after ion irradiation *

Michael Burchard[1], Ulrich A. Glasmacher[1#], Sebastian Dedera[1], Christina Trautmann[2,3]

[1]Institute of Earth Sciences, University of Heidelberg, [2]GSI Darmstadt, [3]Technische Universität Darmstadt

To investigate matter under extreme conditions, materials have been simultaneously exposed to pressure and ion irradiation. Most experiments have been performed by pressurizing miniature samples (<0.001 mm^3) in diamond anvil cells (DAC). Larger samples (up to 1 mm^3) can be pressurized in a Paris-Edinburgh (PE) press where the sample in placed between two hard anvils made, e.g., from cubic boron nitride, allowing quasi-hydrostatic compression up to ~ 10 GPa.

In the recent past, we successfully tested our PE press as a tool to expose large-volume samples under pressure to energetic heavy ions in Cave A [1]. To perform spectroscopic investigations of the sample under pressure (advantage of diamond anvil cells), the PE cell anvil was equipped with a diamond stamp in beam direction [1, 2]). This new diamond window (Fig. 1) provides access to a laser beam in order to perform "in situ" Raman spectroscopy measurements of pressurized samples (Fig. 2). Besides many handling advantages, the modification also allows us to determine the real pressure inside the PE-cell by means of Raman line shifts (Fig. 3).

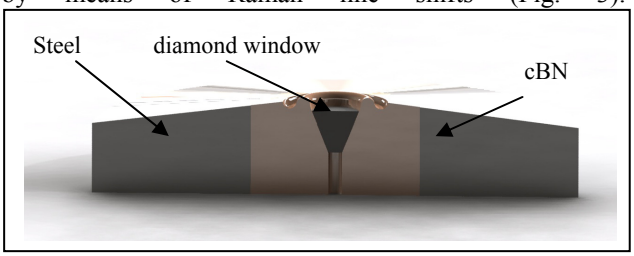

Figure 1: Cross section of pressure stamp of PE-cell with the new diamond window.

For the first test irradiation of the new setup in August 2012 we mounted a calcite crystal ($CaCO_3$) and pressurized it to 0.9 GPa. Calcite is quite suitable for this test, because it has well defined Raman bands. The irradiation was performed in cave A at the SIS18 using a focused beam of U ions of 250 MeV/n initial energy. A total fluence of 1×10^{11} ions/cm^2 was applied.

The mounting and positioning of the PE cell with the overhead gantry resulted in no further problem. The deactivation time of the irradiated PE cell was remarkably short. Most of the activation disappeared two days after the irradiation. After two weeks, the cell could be handled safely.

The new setup of the Paris Edinburgh cell provides many new possibilities for "in situ" measurements of irradiated samples under pressure, although some design details are still on a preliminary status.

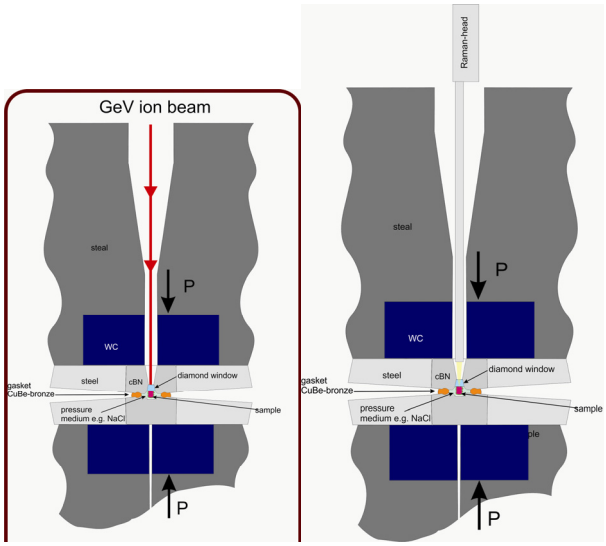

Figure 2: Cross section of new PE-cell design, (left) under ion irradiation and (right) for spectroscopic analysis.

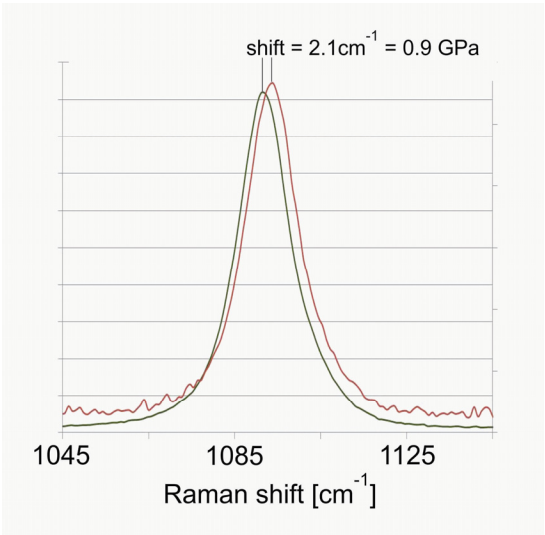

Figure 3: Raman spectra of calcite recorded through the new diamond window of the PE cell at ambient pressure (smooth black line and in pressurized state (red line).

References

[1] M. Burchard et al. "Ion irradiation under pressure using the Paris-Edinburgh press: first results", GSI Scientific Report 2009, p. 345

[2] A New Design for Diamond Window Equipped Paris-Edinburgh-Calls - First Tests and Results, Eos Trans AGU Fall Meet Suppl., Abstract MR23A-2390:

* Work supported by BMBF Verbundprojekt 05K10VH1

ulrich.a.glasmacher@geow.uni-heidelberg.de

Optimized etching of swift heavy ion tracks in calcite*

Sebastian Dedera[1], Ulrich A. Glasmacher[1#], Michael Burchard[1], Christina Trautmann[2,3]

[1]Institute of Earth Sciences, University of Heidelberg, [2]GSI Darmstadt, [3]Technische Universität Darmstadt

Carbonate minerals are of interest for thermochronology (fission-track dating). By irradiating calcite ($CaCO_3$) with swift heavy ions, we perform systematic track etching studies to develop and optimize the track etching process.

For optimal etching several properties need to be fulfilled: (i) Each ion track should lead to a single etch pit, i.e., the etching efficiency should be 100%. (ii) The etching solution should be selective, i.e., the track etch rate should be larger than the bulk etch rate. (iii) The overall etching process should be slow enough to handle the samples in a controllable manner. (iv) The etch pits should be as homogeneous allowing automated analysis by optical microscopy (standard method in geology).

Earlier investigations revealed etched tracks in calcite crystals using HNO_3 [2, 3] or a 1:1 mixture of ethylenediaminetetraacetic acid (EDTA) and 0-5% acetic acid as etchant [1], but the results were far from being optimal.

Natural calcite crystals were irradiated with 11.1 MeV/u ^{197}Au ions at the UNILAC accelerator applying a fluence of 10^6 ions/cm^2. During irradiation, the crystals were covered with a hexagonal mask to provide neighboring irradiated and non-irradiated surfaces.

Knowing that calcite crystals are very sensitive to nitric acid, etching series were performed at two temperatures (15 and 21°C) in highly diluted HNO_3 of concentrations of 0.91, 0.091, and 0.0091%. Regarding shape and size of the etch pits, best results are obtained for 4 s etching in 0.091% HNO_3 at 15°C. As expected [3], the etch pit geometry depends on the solution: tracks etched in EDTA + 5% acetic acid have an elongated hexagonal shape while 0.091% HNO_3 produces pentagon-shaped pits (Fig.1).

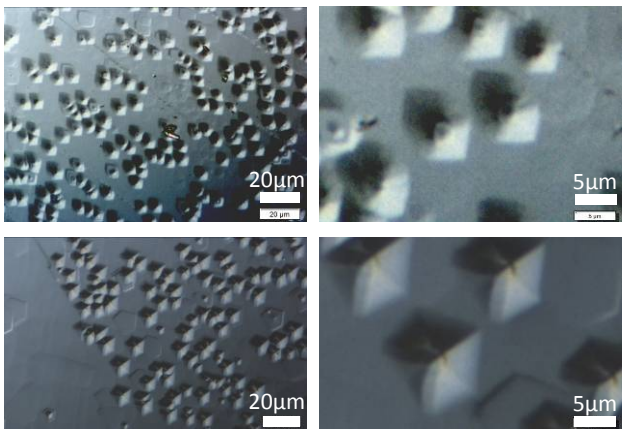

Fig.1: Optical images of etched tracks in calcite crystals at different magnifications: (top) 20 s etching in EDTA + 5% acetic acid; (bottom) 4 s etching in 0.091% HNO_3. Note the different shape of the etch pits.

* Work supported by BMBF Verbundprojekt 05K10VH1

ulrich.a.glasmacher@geow.uni-heidelberg.de

Figure 2 compares the size of the etch pits as a function of etching time for HNO_3 and EDTA. Compared to EDTA, the etch rate of HNO_3 is by a factor of about five higher. Besides that, the development of the etch pits regarding length and width is the same, both show linear growth with length > width.

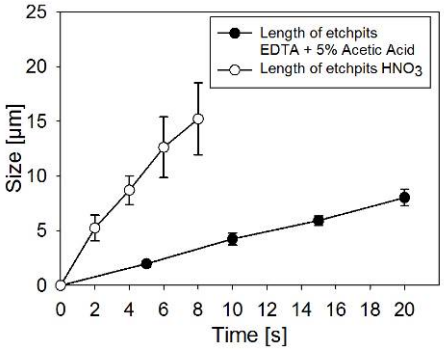

Fig. 2: Length of etch pits as a function of etching time for two etching solutions at 21°C: (open symbol) EDTA + 5% acetic acid and (full symbol) 0.091% HNO_3

Another promising aspect of HNO_3 as etching solution is given by the fact that the contrast of the etch pits in calcite under the optical microscope is excellent. This allows automated counting by image analyzing software (Fig. 3), an important issue for fission track dating.

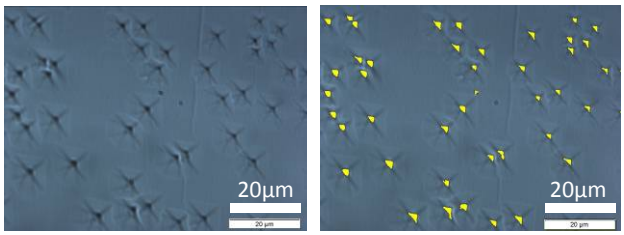

Fig.3: Optical image of HNO_3-etched tracks recorded in transmission mode. The excellent contrast allows automated counting indicated by the white detection marks (right image) produced by the analyzing software.

In conclusion, HNO_3 is a very promising option for etching heavy ion tracks in calcite crystals. The solution is easier to produce and it fulfils the above mentioned requirements for thermochronological track application.

[1] S. Dedera et al., "Etching of heavy ion tracks in calcite", GSI-Report 2011 (2012) PNI-MR-23

[2] R. E. Keith & J.J. Gilman, „Dislocation Etch Pits and Plastic Deformation in Calcite", Acta Metallurgica, Vol. 8, 1960

[3] A. Boos, "Ätzversuche an Calcit, Rhodochrosit und Siderit", N. Jahrbuch f. Mineralogie, 1943

Irradiation-induced effects in organic thin PMMA films

R. Thomaz[1,2], C. Trautmann[1,3], M. R. da Silva[2], L. G. Barbosa[2] and R. Papaléo[2]

[1]GSI, Darmstadt, Germany; [2] Pontifical Catholic University of Rio Grande do Sul, Brazil, [3]Technische Universität Darmstadt

Individual heavy ions impacting insulators at high velocities (few tenths of MeV/u or higher) cause the ejection of material and plastic deformation at the surface, resulting in permanent rims and craters [1-4]. Recent studies on the interaction of individual ions in polymeric thin films indicate that the surface effects are altered as the thickness of the material is reduced [5]. The effects of fast ions on confined structures are not completely understood [6] and may vary from those observed for bulk matter. In this contribution, we report on the impact features produced by 4.8 MeV/u Pb ions on poly(methyl methacrylate) (PMMA) films as a function of the thickness t at normal incidence. The results observed indicated a clear thickness dependent effect on the crater formation process for very thin layers.

Thin films of PMMA were spin-coated onto Si substrates with a thicknesses t ranging from 2 to 100 nm. The films were bombarded with 4.8 MeV/u Pb ions at a fluence of ~10^8 cm^{-2} at the UNILAC accelerator. The size and shape of the surface tracks were characterized offline with a Nanoscope IIIa scanning force microscope (SFM).

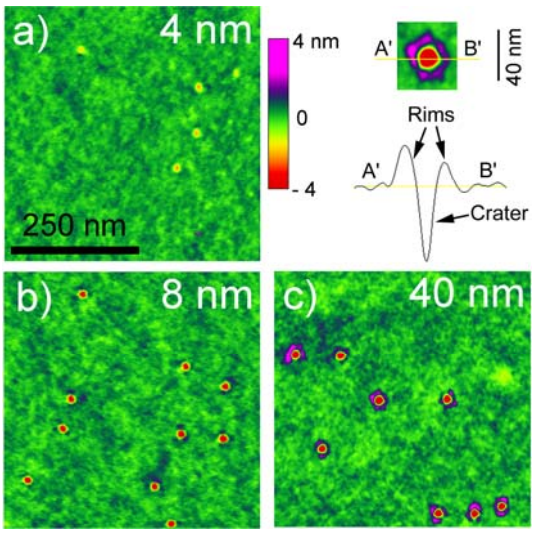

Figure 1: SFM images of PMMA films of indicated thickness, bombarded normal to the surface by 4.8 MeV/u Pb ions. The inset shows typical profile of impact features.

Typical images of impact features at normal beam incidence are shown in Fig. 1. For the thicker films, two different structures are observed at the impact site: crater-like holes and rims. Figure 2 and 3 depict quantitative data on the averaged sizes of rims and craters as a function of thickness t, respectively. For a critical thickness, the impact features show changes in size and morphology: below 40 nm, the rim volume decreases linearly and disappears completely below $t \sim 4$ nm. This strong change of rim dimension indicates a deeper depth of origin for protrusion formation, related to long-range cooperative interactions. The crater dimensions on the other hand, showed only slight changes even for very thin samples, reducing from ~20 nm for thicker layers down to ~15 nm for the thinnest films. The weaker thickness effect suggests their formation is very much dependent on the near surface excitation events, as was indicated recently by charge-state dependent impact craters produced with 600-MeV Au ions [5].

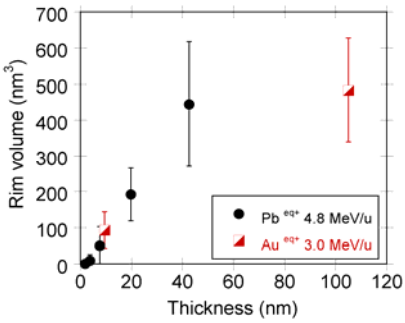

Figure 2: Average volume of rims produced by 4.8 MeV/u Pb ions and 3.0 MeV/u Au ions [5] on PMMA films of different thickness.

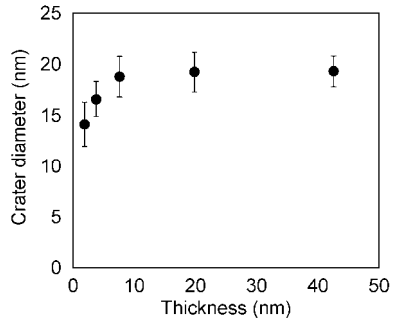

Figure 3: Average diameter of craters produced by 4.8 MeV/u Pb ions on PMMA films of different thickness.

[1] F. Thibaudau et al., Phys Rev Lett. 67 (1991) 1582.
[2] I. H. Wilson, Surf. Interface Anal. 20 (1993) 637.
[3] R. Neumann, Nucl Instr. Meth B. 151 (1999) 42.
[4] R.M. Papaléo, *Transport Processes in Ion – Irradiated Polymers*, in *Surface tracks and cratering in polymers* (Berlin: Springer, 2004).
[5] R. M. Papaleo, et al. Phys Rev Lett 101 (2008).
[6] A.V. Krasheninnikov; K. Nordlund J. Appl. Phys. 107 (2010).

* Work supported by Brazilian agency CAPES.
#R.Thomaz@gsi.de

Analysis of ion-beam induced degradation of poly(vinylidene fluoride) and post-irradiation treatment for efficient track etching

T. Yamaki[1,#], M. Asano[1], H. Koshikawa[1], Y. Maekawa[1], D. Severin[2], T. Seidl[2], C. Trautmann[2,3]

[1]Japan Atomic Energy Agency (JAEA), Takasaki, Japan; [2]GSI, Darmstadt, [3]Technische Universität Darmstadt, Germany

Ion-track membranes of poly(vinylidene fluoride) (PVDF), a type of fluoropolymer, could find wide applications due to its superior chemical and mechanical properties. In order to produce track-etched pores in PVDF films, a highly-concentrated alkaline solution with a strong oxidizing agent (e.g., $KMnO_4$) has mostly been used at a high temperature. Yet this provides irreversible chemical damage over the entire film including the non-irradiated part [1]. Thus, we have developed much milder etching conditions without any oxidant additives in the alkaline etching solution [2]. The goal of this work is to investigate the effect of post-irradiation treatment to pursue the possibility of accelerating the track etching rate. The discussion is given to this based on the detailed chemistry of heavy-ion-induced degradation, which was analyzed at the M-branch.

Commercially-available 25-μm thick PVDF films were irradiated at room temperature with 450-MeV ^{129}Xe ions at the TIARA cyclotron of JAEA, and with 2.2-GeV ^{197}Au ions at the UNILAC. The irradiation at UNILAC was performed in the multi-purpose chamber of the M3 beamline equipped with a Fourier-transform infrared (FT-IR) transmission spectrometer and a quadrupole mass. analyzer. The FT-IR spectra and the residual gas data were recorded in-situ as a function of fluence up to 6×10^{11} ions/cm^2. For the track-etching experiments, the irradiation at TIARA was performed at a lower fluence of 3×10^7 ions/cm^2. The irradiated film was etched in a 9 mol/dm^3 aqueous potassium hydroxide (KOH) solution at 80°C. The track etch rate was determined via measuring the breakthrough time (T_B) in a conductometric etching cell.

The FT-IR analyses undoubtedly confirm that the irradiation efficiently produces C=C double bonds, both within and at the end of the main chain [3]. Main outgassing fragments were seen at mass-to-charge ratios (m/z) equal to or below 20. The most dominant peak appeared at m/z = 20 assigned to hydrogen fluoride (HF), which was predicted as degradation product for the formation of unsaturations in the main chain [4]. Additional large signals were located at m/z = 2, 18, and 19 from hydrogen (H_2), residual water (H_2O), and fluorine (F), respectively. Other masses are assigned to CH_x fragments from the degradation of hydrocarbons. Importantly, dehydrofluorination occurs very efficiently to produce the C=C double bonds.

Therefore, we finally consider how the C=C double bonds could be oxidized efficiently. When the oxidant coexists, they are readily converted to C=O groups with a high water wettability enabling faster attack by the etchant. We chose ozone as the oxidant for the pre-etching treatment. PVDF films irradiated with 450-MeV ^{129}Xe ions were exposed to ozonized O_2 for 6 h at room temperature. Figure 1 shows our preliminary conductometry results. The conductance values on the ordinate are not converted to an effective pore diameter, d_{eff}, because the measurement was intended to analyze T_B for samples with and without the ozone treatment. The breakthrough time T_B of the ozone-treated film is about seven times shorter than that of the untreated film. This clearly demonstrates that the pre-etching treatment with a gaseous oxidant greatly accelerated the track etching rate. The reason for this effect is possibly linked to a quick reaction between ozone and alkenes to yield products in which the double bond is cleaved, such as ketones and carboxylic acids. It should be emphasized that this post-irradiation treatment method was achieved by the feedback from our findings regarding the basic chemistry in the track, quite in contrast to the previous study on ozone-induced track sensitization of PET films [5].

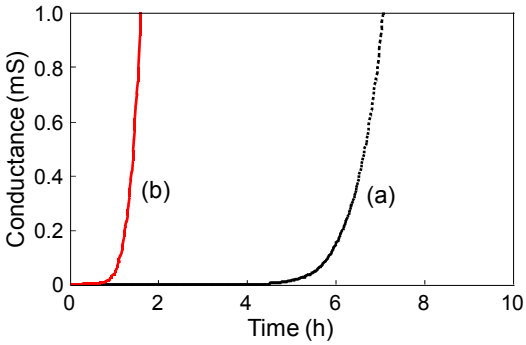

Fig. 1: Measured conductance vs. etching time for PVDF films irradiated with 450-MeV ^{129}Xe ions (a) with and (b) without treatment with ozone gas before the etching.

[1] C. Daubresse, T. Sergent-Engelen, E. Ferain, Y.-J. Schneider, R. Legras, Nucl. Instr. Meth. B, 105 (1995) 126.

[2] T. Yamaki, N. Nuryanthi, H. Koshikawa, M. Asano, S.Sawada, S. Hasegawa, Y. Maekawa, K.-O. Voss, C. Trautmann, R. Neumann, Trans. Mater. Res. Soc. Japan, 37 (2012) 223.

[3] T. Yamaki, M. Asano, H. Koshikawa, Y. Maekawa, D. Severin, T. Seidl, C. Trautmann, GSI Scientific Report 2011 (2012) 420.

[4] For example, A Le Bouëdec, N. Betz, S. Esnouf, A. Le Moël, Nucl. Instr. Meth. B, 151 (1999) 89.

[5] T.E. Laricheva, A.A. Machula, V.K. Milinchuk, Colloid J.,66 (2004) 57.

[#] yamaki.tetsuya@jaea.go.jp

Impedance Spectroscopy on High Performance Polymers

B. Körber[1,2], *D. Severin*[1], *and M. Bender*[*1]
[1]GSI, Darmstadt, Germany; [2]HS RheinMain, Wiesbaden, Germany

Due to the outstanding properties, polyimide films such as Kapton are widely used as electrical and thermal insulation in harsh environments. Compared to other organic insulators, Kapton exhibits enhanced radiation hardness and can be applied in a wide temperature range from 4 up to 670 K.

For the new FAIR accelerators, Kapton will be used as insulating material in superconducting magnet coils. Here it is exposed to a continuous particle shower of primary and secondary ions, e.g. from scattering events with residual gas. In the long run, this leads to degeneration of the material and might cause the insulator to fail. To follow the aging process of the insulator under radiation exposure and to predict its life time, we have developed an *in-situ* monitor of the dielectric strength by means of an impedance measurement as possible low-cost device for the FAIR magnets [1]. Briefly, the dielectric value is measured by the resonance frequency of an LC oscillator, where the foil represents the dielectric medium of the capacitor. Here, we will report on results obtained with different ion beams and energies, corresponding to different dose loads. The radiation dose accumulated over time equals the total energy deposited per mass unit of the test sample and is thus independent of the different beam parameters such as species and energy of ions. A direct comparison of the irradiation effects is scaled by the dose D:

$$D = \frac{E}{m} = \frac{e \cdot \Delta E \cdot \Phi}{d \cdot \rho}, \qquad (1)$$

where e is the elementary charge, ρ the mean target density, ΔE is the deposited energy as $\int_0^x \frac{\delta E}{\delta x}\Delta x$ and Φ the total irradiation fluence in projectile ions per area.

In our irradiation experiments, we used a flux of $1.4 \cdot 10^8 cm^{-2}s^{-1}$ for Xe and Au and $4 \cdot 10^8 cm^{-2}s^{-1}$ for Ti ions. The beam energy was varied between 1.4 and 4.8 MeV/u. The Kapton foils had a thickness of 7.6 μm and were coated with Al on both sides. For beam exposure, the foils were mounted in a supporting frame to ensure reliable electrical contact. The initial capacity of the pristine foil varied within $\pm 15\%$ around the mean value of 4 nF for all investigated foils. For an overall comparison of the different experiments, we plot the change in capacity $\Delta C/C_0$ against the applied dose. The change in capacity is a direct transformation of dielectric changes, since no geometrical change of the target is observed such as swelling or shrinking.

The irradiation experiments were performed at the high charge state injector (HLI) of GSI with 1.4 MeV/u Xe ions and at the M3 branch of the UNILAC with Au and Ti ions of 4.8 MeV/u. The energy loss of the Ti, Xe, and Au ions in the Kapton target was 4, 12, and 16 MeV/μm respectively. Figure 1 shows the capacity change of the various irradiation runs with Ti, Xe, and Au beams. The end of irradiation is marked in red; maximum dose of foils that broke due to brittleness are marked in black.

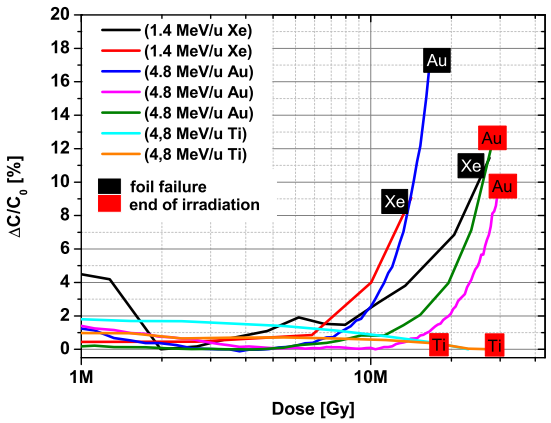

Figure 1: Capacity change of 7.6 μm thick aluminized Kapton foils from different irradiation experiments vs. respective dose.

The foils irradiated with Ti do not show a significant change in capacity up to a dose far above 10 MGy ($5 \cdot 10^{12}$ ions per cm^2). This effect is ascribed to the low energy loss of the Ti ions being below the threshold for severe damage formation reported earlier [2].

All other irradiations lead to a steep capacity change between 10 and 20 MGy, which is in good agreement with earlier results from beam-induced structural changes [3]. At low dose values, i.e. at the initial stage of the irradiation, the capacity change shows a slightly decreasing slope. This effect is ascribed to water desorption. Virgin Kapton is known to incorporate water with a dielectric constant of 80 compared to 3.4 for Kapton. Thus, small amounts of water are sufficient to change the foil capacity. For the planned on-line monitoring, the water desorption is not relevant, because the desorption is finalized within the initial irradiation phase.

References

[1] B. Körber, et al., GSI annual report 2011-PNI-MR-21

[2] P. Salvetat, et al., Phys. Rev. **B** 55 (1997) 6238

[3] D. Severin, et al., Nucl. Inst. Meth. **B** 236 (2005) 456

* corresponding author: m.bender@gsi.de

In-Situ High Voltage Tests on Pristine and Irradiated Polyimide *

V. Lima[1,2,#], T. Seidl[1,2], E. Mustafin[1], E. Floch[1], C. Trautmann[1,2], and W. Ensinger[2]

[1]GSI, Darmstadt, Germany; [2]Technische Universität Darmstadt, Germany

Concerning radiation hardness, organic materials such as polymeric insulators are identified as highly sensitive towards ionizing radiation compared to inorganic materials [1]. Despite this fact, these materials are widely used in accelerator components since they have favourable properties for application, often better than comparable inorganic materials. Due to their superior mechanical and dielectric properties, even if irradiated with swift heavy ions [1], polyimides are commonly used as insulator in beam-guiding magnets in ion beam facilities such as the synchrotrons and storage rings of the planned *Facility for Antiproton and Ion Research* (FAIR). FAIR will provide highest beam intensities, and beam losses will partly induce high secondary radiation fields during the pulsed operation of the accelerator. Former studies of radiation induced modifications of electrical properties of polyimide focused on ex-situ measurements of (i) breakdown voltage [1] and (ii) electrical conductivity and dielectric constant [2].

During accelerator operation, the insulators in the magnets are exposed to particle radiation and additionally to electromagnetic fields. Because irradiation-induced damage can initiate electrical breakdowns events [3], this study tackles in-situ breakdown voltage tests during the direct exposure of the material to ion beams. For this purpose, a setup was built where non-irradiated and ion irradiated polyimide samples are mounted between two electrodes and a potential is applied between them.

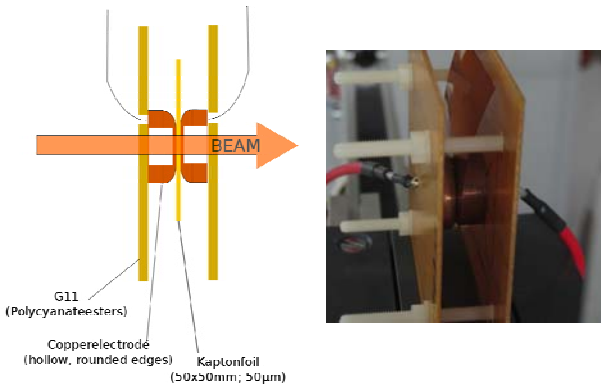

Figure 1: Schematic presentation (left) and photograph (right) of experiment setup.

50-µm thick Kapton™-type polyimide foils with an area of 50 × 50 mm^2 were cut from commercial rolls. Samples were irradiated at the UNILAC (X0-beamline) with 11.1-MeV/u ruthenium ions and fluences up to 10^{12} cm^{-2} (corresponding to a radiation dose of 8 MGy). For the in-situ breakdown voltage test, samples were mounted between two copper electrodes (see scheme Fig.1 left). These electrodes had a rounded-edge-geometry to avoid increased electrical fields at the edges. The thickness of the electrodes was 2 mm, suitable for the irradiation experiment due to the penetration depth of the ion beam (6 mm in copper, calculated with SRIM-2010 code). The electrode-sample configuration was attached to a glassfiber/composite sample holder having a thickness of 1 mm. Breakdown measurements were conducted using a high voltage power supply (max. voltage: 7 kV) via current measurements with a current clamp. Additionally, the dark current of the high voltage power supply was monitored with an oscilloscope.

The in-situ-irradiation experiment was carried out at SIS 100 (Cave A). At first, a voltage of 500 V was applied to the electrodes. Subsequently, several spills of uranium ions (E= 500 MeV/u) were applied for. The flux of the beam was about 2×10^8 cm^{-2}s^{-1}, while the size of the beam spot was about 0.5 cm^2. When no breakdown occurred, the potential was increased in 500-V-steps and the irradiation procedure was continued for each potential.

For pristine non-irradiated samples no breakdown was detected after irradiation with about 20 spills (~ 4×10^9 cm^{-2}) up to the maximum potential of 7 kV. However, during a spill of ions, the dark current shortly increased. Samples pre-irradiated with Ru ions of fluences $\leq5\times10^{11}$ cm^{-2}, failed without or after a few U spills at electrical fields >1 kV.. This is ascribed to the dielectric strength reduced by the Ru ion irradiation. Below 1 kV we did not observe break down events of pre-irradiated samples. However, due to time constraints this stability was not tested over extended time periods.

Samples pre-irradiated with 10^{12} Ru-ions cm^{-2} showed surface flashovers at already low electrical fields ~1 kV. Due to ion-induced carbonization, the samples were black indicating that the surface conductivity is already too high to be used as insulator.

In summary, ion irradiated samples have in general a lower dielectric strength, but there was no correlation observed between direct ion irradiation and in situ breakdown events

[1] T. Seidl, A. Plotnikov, E. Mustafin, R. Lopez, D. Severin, E. Floch, C. Trautmann, A. Golubev, A. Smolyakov, D. Tommasini, and W. Ensinger, Polymer Degradation and Stability 97 (2012) 2396.

[2] J.-P. Salvetat, J.-M. Costantini, F. Brisard, and L. Zuppiroli, Phys. Rev. B 55 (1997) 6238.

[3] C. L. Wadhwa, "High Voltage Engineering". New Age International Publishers, New Delhi, 2007.

* Work supported by BMBF project No. 06DA7027.

v.lima@gsi.de

Ion induced weight loss and thermal gravimetric analysis of ion-irradiated polyvinyl formal

U. H. Hossain[1, 2#], T. Seidl[1, 2], C. Fasel[1], D. Severin[2] and W. Ensinger[1]
[1]Technische Universität Darmstadt, Germany; [2]GSI, Darmstadt, Germany.

Polyvinyl polymers are high-performance insulating materials used in many applications. At the new *Facility for Antiproton and Ion Research* (FAIR) polyvinyl polymers are foreseen as wire insulation in some parts of the superconducting magnets [1]. During the operation of FAIR, beam losses will result in secondary radiation fields consisting of various energetic particles and gamma radiation. Ion-induced radiolysis of polymers involves bond scission, cross-linking and other chemical reactions leading to outgassing of small volatile degradation products and finally to loss of functional properties. At operational cryogenic temperatures, these gases may accumulate and raise problems during thermal cycling of the superconducting magnets [2]. This study extends existing data of beam-induced weight loss in polymers and shows results of thermal gravimetric analysis (TGA) of irradiated polyvinyl formal. Results are complementary to previous reports on infrared spectroscopy (IR) and qualitative interpretation of residual gas analysis [3].

20-µm thick Formvar® foils were synthesized and irradiated at the X0 beamline of the UNILAC with Au and U ions of 11.1 MeV/u. The applied fluences were 1×10^{9} - 6×10^{11} Au/cm^2 for TGA measurements and 1×10^{10} - 1×10^{12} U/cm^2 for weight-loss measurements. TGA was performed using a Netzsch TG209 F1 instrument with a heating rate of 4 K/min in argon atmosphere. For weight loss analysis a chemical balance with a resolution of about 0.1 mg was used.

TGA measures the weight of a material as a function of temperature in a controlled atmosphere. Figure 1 compares the decomposition behavior of a pristine and an ion-irradiated polyvinyl formal sample from room temperature to 650 °C. The pristine Formvar® foil shows two steps, first a small initial weight loss occurring between 104 and 153ºC which is commonly attributed to the release of water absorbed in the polymer. Between ~300 and 420°C a significant weight loss occurs with a 5% of char residue. The decomposition of nearly the entire polymer indicates that the thermal degradation follows a depolymerisation process and not a so-called random scission process, which would lead to a great amount of char. The TGA curve of the irradiated sample shows only one broad degradation phase occurring between 110 and 420°C with a residual char of 10%. The temperatures for maximum mass loss rate ($T_{d\ (max)}$) of both samples are indicated in the derivative curves (Fig. 1, bottom). The ion irradiation leads to a slight increase of $T_{d\ (max)}$. Both effects are explained by ion induced synthesis of carbon clusters which are not decomposed at the used temperatures.

* work was partially financed by BMBF 06DA7027
# u.h.hossain@gsi.de

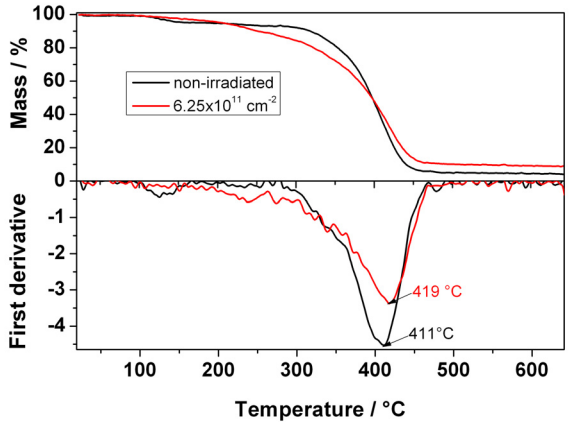

Figure 1: TGA curves of Formvar® foils (black) before and (red) after irradiation with 6×10^{11} Au-ions/cm^2 (top) and their derivatives (bottom).

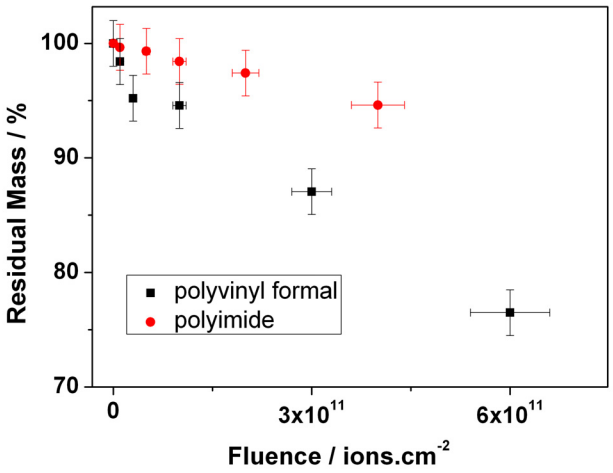

Figure 2: Residual mass as a function of ion fluence for polyvinyl formal (black) and polyimide (red) [2] irradiated with 11.1-MeV/u U ions.

Figure 2 depicts the residual mass of irradiated polyvinyl formal in comparison with results from irradiated polyimide samples from previous work [2]. All irradiated samples show a strong decrease in weight with increasing ion fluence. Compared with polyimide a greater decrease is found for polyvinyl formal. Polyimide insulation obviously forms less outgassing radiolysis products which could accumulate when used in cryogenic environment.

[1] T. Seidl et al. Nucl. Instr. Meth. B 272, (2012), 400.
[2] D. Severin, PhD thesis, Univ. Marburg (2008).
[3] U.H. Hossain et. al., GSI Scientific Report; PNI-MR-20 (2011).

Dielectric strength of two fiber reinforced plastics irradiated with heavy ions*

T. Seidl[1,2,#], E. Floch[2], V. Lima[1,2], U.H. Hossain[1,2], T. Wietoska[1], C. Trautmann[1,2], W. Ensinger[1]

[1]Technische Universität Darmstadt, Germany; [2]GSI, Darmstadt, Germany.

Glass-fiber reinforced plastics (GFRP) are considered as structure support and electrical insulator for the new superconducting magnets at the Facility for Antiproton and Ion Research (FAIR). At FAIR, materials close to the beam tube will be exposed to high doses of secondary radiation of neutrons, protons, and heavier particles, possibly limiting reliable function and lifetime of device components. Typical GFRP used in accelerator magnets consist of woven glass-fiber fabrics embedded in a thermosetting polymer matrix. In superconducting magnets most commonly a G11-type composite [1] is used which consists of ~60% E-glass-fibers and an amine cured polyepoxy matrix.

Radiation hardness studies motivated by the International Thermonuclear Experimental Reactor (ITER) showed that neutron-irradiated composites consisting of a cyanate-ester matrix and S-glass fibers exhibit increased radiation resistance when compared with classical epoxy-systems [2]. In this study a classical G11-type epoxy/E-glass and an ITER-type cyanate-ester/S-glass composite were irradiated with heavy ions. For the irradiated samples, the dielectric strength (maximum electrical field strength at which the insulator fails) was determined.

G11-type epoxy/E-glass (thickness 1.0 mm) and ITER-type cyanate-ester/S-glass (thickness 1.4 mm) composites were provided by ISOVOLTA AG (ISOVAL® 11 HKB and cured ISOPREG CN). The G11-type epoxy is a commercially available product whereas the cyanate-ester composite is only available in the form of prepregs and was especially cured by the company for our tests.

The irradiation was performed at the Cave A of SIS18 with a 400 MeV/u Au-beam and slow extraction mode. The beam spot size was about 0.5 cm^2 and the flux of the order of 10^8 $cm^{-2}s^{-1}$. For each material three stacks consisting of three samples were irradiated. According to the SRIM-2010 code, the penetration depth of the Au ions is about 7 mm. The thickness of the sample-stack was 3 mm in case of G11-type and 4.2 mm in case of ITER-type material.

Breakdown voltage measurements were performed in silicon oil using an AC high voltage tester with round stainless steel electrodes 15 mm in diameter. The dielectric strength was normalized by the thickness and is presented in kV/mm.

Figure 1 shows the (AC)-dielectric strength of non-irradiated and irradiated glass-fiber reinforced plastics plotted as a function of irradiation fluence. The dielectric strength of the cyanate-ester/S-glass system is generally lower than the one of the commercial epoxy system. For irradiated classical G11-type composite, the dielectric strength decreases as a function of fluence and seems to evolve towards a limiting value of approximately 32 kV/mm at higher fluences. In contrast to this, the change in dielectric strength of irradiated cyanate-ester/S-glass composites is insignificant. Although, the ITER-composite is less affected by degradation, the irradiated classical G11 system has still a superior dielectric strength even at the highest fluence. It needs to be clarified whether the initial dielectric strength of the ITER-composite could be raised with an optimized curing procedure.

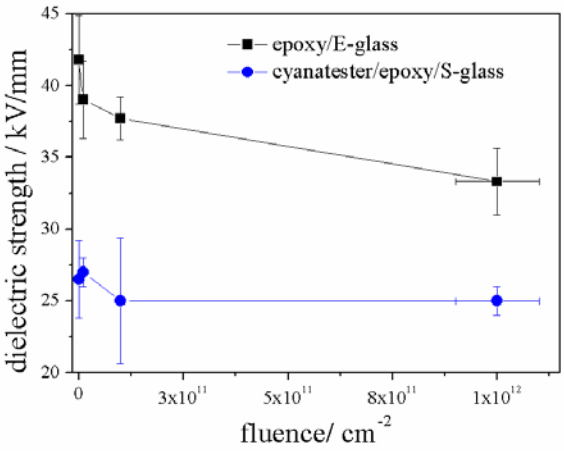

Figure 1: Dielectric strength of G11 and ITER-type plastic/glass-fiber composites versus fluence of 400-MeV/u Au ions. Lines are guides to the eye.

Earlier studies on ion-irradiated polyimide films showed a drastic decrease of insulating properties at rather low fluences [3]. The effect of ion irradiation for the analyzed composites is less pronounced probably because of the reinforcement with the inorganic glass-fibers prohibiting the formation of conductive ion tracks throughout the material.

For its usage at FAIR, both investigated composites show a tolerable decrease of dielectric strength within the tested range of ion fluences. However, a little caveat because the dielectric strength tests were performed ex-situ at room temperature and not considering low operation temperatures, thermal cycles or degradation due to dynamic mechanical forces.

[1] National Electrical Manufacturers Association, Standard LI-1, (1998).
[2] P.E. Fabian et al., Fusion Engineering and Design 61–62 (2002) 795.
[3] T. Seidl et al., Polymer Degradation and Stability 97 (2012) 2396.

* Work supported by BMBF, Project No. 06DA90251 and 06DA7027.
# t.seidl@gsi.de

Beam Monitoring on Graphite Targets by Infrared Thermography

M. Tomut[1,2,#], C. Hubert[1,3], K. Kupka[1,3], B. Lommel[1], A. Beusch[1], D. Severin[1], C. Trautmann[1,3]

[1]GSI, Darmstadt, Germany; [2] NIMP, Bucharest, Romania; [3]Technische Universität Darmstadt, Germany

The thermal print of an ion beam on a target is related to the power density deposited in the target [1]. Infrared (IR) radiometry is one of the few methods suitable for the monitoring of high-intensity primary beams on production targets at FAIR. This work summarizes first results on online infrared imaging of beamspot size on thin graphite targets in experiments with ion beams at MeV-GeV energies using a FLIR SC 7500 high sensitivity, cooled IR camera. Due to their good thermo-mechanical properties and high emissivity, graphite targets are ideal for thermography-based beam diagnostic.

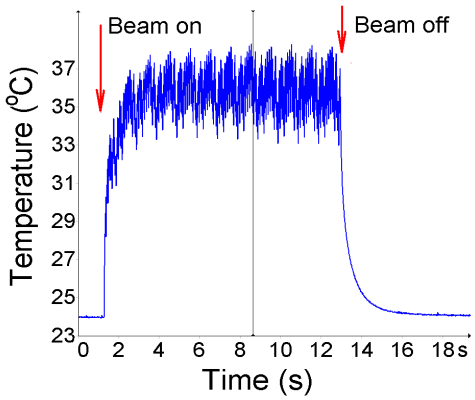

Figure 1: Temporal evolution of temperature within the center of the beam spot during irradiation with 1x10^9 i/cm^{2}s ^{197}Au ions with a energy of 3.6 MeV/u, 4 ms pulse length and a repetition rate of 38 Hz.

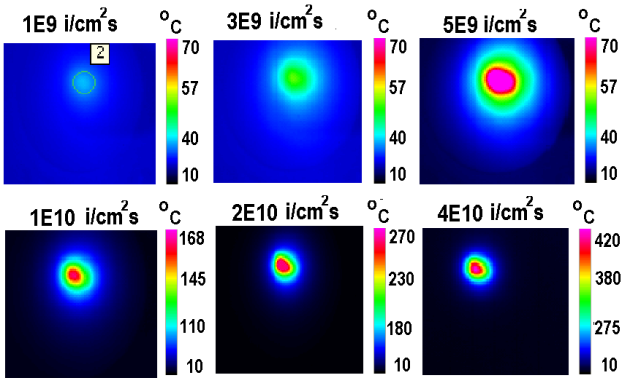

Figure 2: Sequence of infrared images of beam spot on thin graphite targets with increasing beam flux. Each image corresponds to maximum intensity during a pulse, for a 3.6 MeV/u, 4 ms, 38 Hz ^{197}Au beam.

#m.tomut@gsi.de

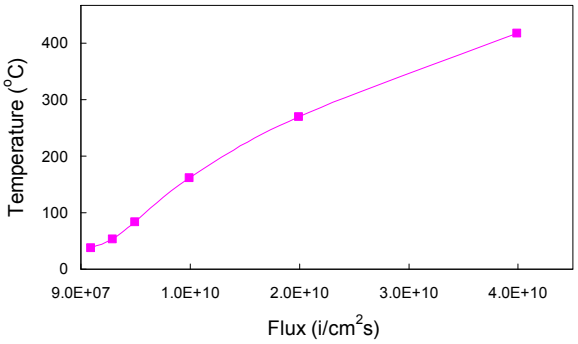

Figure 3: Maximum temperature recorded within the beamspot on thin graphite targets exposed to 3.6 MeV/u ^{197}Au ions, with increasing beam intensity, as a function of beam flux.

Figure 1 presents the time evolution of the temperature maximum within the beamspot of 3.6 MeV/u Au ions. The high sensitivity and low integration time of the camera provide a high accuracy monitoring of intensity variation during individual pulses. This type of information was used as input in finite element calculations of beam-induced thermal stress in targets. About 2 s are necessary for the temperature in the target to reach the steady state at the beginning of the irradiation, for the given beam parameters. Upon the beam stop, the time constant of the temperature decay in the target can be related to the thermal conductivity of the target materials.

To get accurate temperature distribution from the radiometric image of the ion heated target, previous calibration of the emissivity of the target and environment and of the transmittance of the beamline IR viewport are necessary. Figure 2 shows a series of thermal prints of Au ion beam pulses with increasing intensity on graphite targets. Snapshots are taken after the temperature in the targets reached a steady state condition (> 2 s) and at the maximum pulse intensity. The increase of the maximum temperature in the beamspot with increasing ion flux is shown in Figure 3. A detailed analysis of the fully radiometric image will be used for inferring the beam power density profiles providing the beam intensity profile. To validate these results, cross-checks using luminescence targets will also be done. This beam diagnostic technique is particularly suited for high intensity cases where other techniques would fail. Thermographic screens made out of carbon materials are also a cheaper alternative to luminescence screens.

[1] H. Buttig, “Beam Diagnostic by Infrared Thermography” ZKF-453 Report Forschungszentrum Rossendorf, Aug. 1981.

High Resolution Synchrotron X-Ray Diffraction of Swift Heavy Ion Irradiated Graphite

C. Hubert [1,2 #], M. Tomut[1,3 ##], K. Kupka[1,2], A. Romanenko[1,2], B. Schuster[1,2], H-P.Liermann[4] and C. Trautmann[1,2]

[1]GSI, Darmstadt, Germany; [2]TU Darmstadt, Germany; [3]NIMP Bucharest, Romania; [4]DESY Petra III Beam line P02, Hamburg, Germany

The use of graphite as material for the Super-FRS target and beam catchers at FAIR requires a proper understanding of ion-beam induced structural changes and defect formation.

The irradiation of high-density isotropic graphite was performed at the UNILAC with a flux of 1×10^9 ions/cm²s. The samples were exposed to 3.6-MeV/u Au ions of fluences up to 1×10^{14} ions/cm^2.

For structural analysis, synchrotron XRD measurements were performed at the P02 beam-line of Petra III (DESY, Hamburg) using a wavelength of 0.29135Å. The facility provides x-ray beams of very high brilliance, allowing transmission experiments with high resolution in real and reciprocal space [1]. The micro-focused beam spot and the high precision sample positioning made it possible to perform spatially resolved X-ray diffraction along the ion trajectories of the irradiated samples.

Diffractograms of graphite exposed to different fluences are show in Fig. 1. In contrast to the 100 and 101 peaks significant broadening and intensity reduction are observed for the 002and 004 diffraction peaks. This process is ascribed to a distribution of increased inter-planar distances along the c-axis of the graphite crystal due to interstitial clusters formation. With increasing fluence, the interstitial clusters coalesce to new crystalline planes, leading to turbostratic graphite formation.

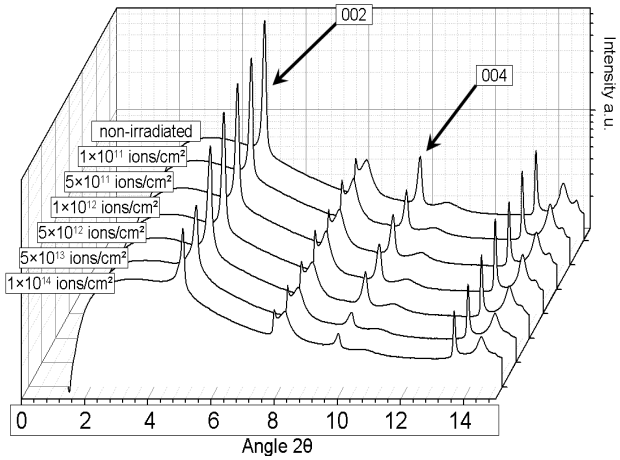

Figure 1: Synchrotron XRD patterns of isotropic graphite samples irradiated with 3.6-MeV/u Au ions and increasing fluences (x-rays collinear with ion tracks)

* Work supported by GSI-TUD cooperation contract and HGS-HIRe.

c.hubert@gsi.de, ## m.tomut@gsi.de

The second type of measurements focused on monitoring structural changes along the ion trajectory. The x-ray beam thus scanned through the cross-section of the sample (x-rays normal to ion tracks). The X-ray beam spot has a size of 2 µm × 2 µm. As presented in Fig. 2, a maximum of structural disordering occurs at a sample depth of around 45 µm, as evident by the decreased intensity and broadening of the 002 diffraction peak. According to the SRIM code, this depth position correlates well with the energy deposition due to the elastic collision cascade.

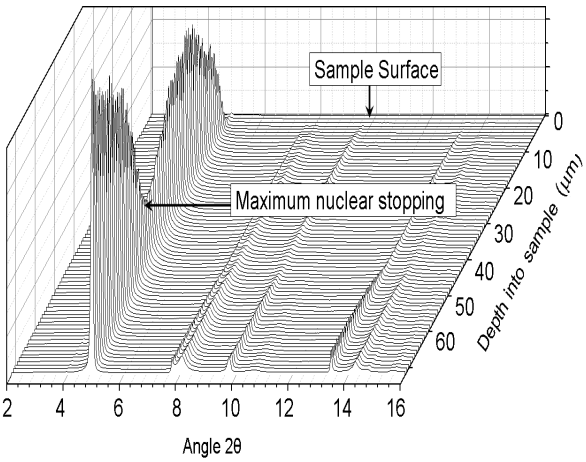

Figure 2: XRD-spectra of isotropic graphite recorded in cross-sectional geometry (x-rays perpendicular to ion tracks). The irradiation was performed with 3.6-MeV/u Au ions of 5×10^{13} ions/cm²

The analysis shows that the irradiation of graphite with 3.6-MeV/u Au ions mainly induces disordering due to defect cluster formation. Increasing ion fluence enhances the disordering. At the stopping end of the ions, elastic collisions are more effective than electronic excitation in inducing structural disorder. A perfect alignment of the sample and beam was difficult. The gradual intensity increase of the 002 peak at the surface is due to the finite X-ray beam-spot size and sample positioning. The broadening of the disorder effect at a range of 45 µm is due to irradiation-induced bending of the sample.

[1] H.-P. Liermann et al., The Extreme Conditions Beamline at PETRA III, DESY: Possibilities to conduct time resolved monochromatic diffraction experiments in dynamic and laser heated DAC. J. Phys., Conf. Ser. 215 (2010) 012029.

Measurements of Carbon Stripper Foils Emissivity for Quantitative On-line Infrared Thermography

K. Kupka[1,2,#], M. Tomut[1,3], C. Hubert[1,2], R. Danjoux[4], B. Lommel[1], J. Steiner[1], and C. Trautmann[1,2]

[1] GSI, Darmstadt, Germany; [2]Technische Universität Darmstadt, Germany; [3]NIMP, Bucharest, Romania, [4]FLIR Systems, Inc., Croissy-Beaubourg, France.

Attempting to mitigate space charge limitation during the foreseen high-intensity operation of SIS at FAIR, the replacement of the gas stripper at 1.4 MeV/u and the foil stripper at 11.4 MeV/u (TK) by one carbon stripper foil at 1.4 MeV/u for directly delivering an intermediate charge state has been investigated.

Experiments with solid carbon stripper foils installed at the 1.4 MeV/u-stripper section revealed the capability of 20 µg/cm² amorphous carbon foils produced by the GSI Target Laboratory for delivering U^{39+} ions to SIS18. The foils exhibited an average lifetime of 11 h [1].

In order to predict and increase the life time of the stripper foils, systematic investigations of the processes leading to failure are needed. In this work, we strive to better understand which are the contributions of radiation damage, high temperature and stress waves induced by the pulsed beam to final failure. We report on emissivity measurements of amorphous carbon foils of different thicknesses. The data are needed for monitoring temperature evolution and gradients within the beam spot with an infrared (IR) camera during foil irradiation. Due to semi-transparency of the stripper foils, a method for measuring the emissivity in consideration with the background had to be developed.

Amorphous carbon stripper foils of different thicknesses (20, 30, 50, 97 µg/cm²) were installed in front of a box heating the foil and acting as a black body (Fig. 1 right). Additionally, a copper sheet of known emissivity was placed between the foil and the heat box. In order to subtract the background, the radiance was measured with the infrared camera on the copper sheet (location 1, Fig. 1 left) and on the heat box, not covered by any foil (location 2). The deviation of these two radiance values served as a background function. The same measurement was repeated for the area covered by the semitransparent carbon foil (location 3 and 4). The ratio of the difference function for the area covered by the foil, *Df*, and the background function, *Bf*, yielded the transmittance τ of the amorphous carbon foil ($\tau = Df / Bf$). Emissivity values for foils of different thicknesses were calculated by applying conservation of energy: $\varepsilon = 1 - \rho - \tau$, where ε is the emissivity, ρ the reflectance and τ the transmittance of the foil. The reflectance was assumed to be 4%. Resulting emissivity and transmittance values for different stripper foils are presented in Fig 1 (left). The emissivity increases exponentially with the thickness of the amorphous carbon foils. The calculated values were used as input parameters for the measurement of the temperature evolution during beam exposure of the foils (Fig. 2). The transmittance of a CaF_2 window similar to that of the infrared viewport of the irradiation chamber was measured. The resulting value of 87.2% was also used in the calculations.

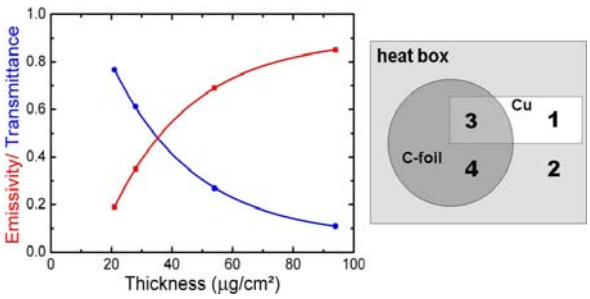

Figure 1: (left) Measured emissivity values for foils of different thicknesses, (right) radiance measurement setup.

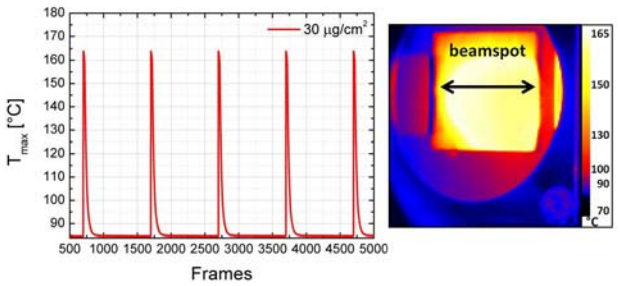

Figure 2: (left) Time and (right) temperature evolution in the beamspot during irradiation of the 30 µg/cm² foil with a 4.8 MeV/u ^{238}U beam.

Table 1 shows flux, energy density, and observed temperatures. A significant increase of peak temperature with increasing foil thickness is visible, reaching a maximum temperature of 353°C in the 97 µg/cm² foil.

Table 1: Irradiation parameters and measured temperatures for amorphous carbon foils of different thicknesses.

Thickness [µg/cm²]	Flux [ions/pulse cm²]	Power Density [kW/g pulse]	T(max) [°C]
20	7.30E+09	388.8	155
30	7.50E+09	399.4	163
50	7.00E+09	372.8	205
97	7.70E+09	410.1	353

The use of a multiple integration time mode upgrade of the IR camera is planned to increase accuracy of the IR measurements above 350°C.

*Work supported by BMBF (contract No. 05P12RDRBL) and HGS-HIRe.

k.kupka@gsi.de

[1] W. Barth et al., LINAC2010, Tsukuba, Japan (2010)

Simulation of Stress Waves Induced by Pulsed Heavy Ion Beams in Thin Graphite Targets*

Duy C. Nguyen[1,2,#], M. Tomut[2,3,##], C. Hubert[2,4], K. Kukpa[2,4], B. Xu[4], and C. Trautmann[2,4]

[1]HS RheinMain Rüsselsheim; [2]GSI Darmstadt, Germany; [3]NIMP, Bukarest, Romania; [4]TU Darmstadt, Germany

Graphite is used as material for production targets for in-flight radioactive ions and neutrino facilities. At the future Super-FRS at FAIR and at several neutrino facilities, the driving beam will be a pulsed beam. Failure of the targets is a combined effect of radiation damage and fatigue due to cyclic thermo-mechanical loads. This work is part of the efforts to understand and mitigate the effects of beam-induced stress waves on the lifetime of the graphite targets. A Finite Element method (FEM) simulation using a simplified model of the target is applied to describe the thermo-mechanical behaviour [1].

FEM simulations require realistic input parameters on the beam spot in particular with respect to the temperature distribution [2]. We therefore performed irradiation experiments with 45-µm thin SGL R6650 graphite foils (density of 1.84 g/cm^3 [3]) mounted on Al frames with a radius of 1.5 cm . The foils were exposed to 1.14-GeV ^{238}U ions (0.7 Hz, 0.15 ms pulse length). The energy deposition by the ions induces target heating within the beam spot localised in the foil centre. A fast FLIR SC7500 infrared (IR) camera recorded the spatial distribution and time profile of the temperature on the target.

Thermal expansion within the beam spot causes a compressive stress wave that spreads out and reflects at the foil frame. The succeeding waves interfere leading to high stress amplitudes within the material. The temperature distribution as recorded by the IR camera was mapped onto the generated mesh of the target as shown in Figure 1 (a). The rise of thermal load *T(t)* to a recorded maximum temperature T_{max} = 820K was fitted by a sin^2 function (Fig. 1 (b)). The simulation used a temporal temperature profile with one temperature rise after the other to save calculation time.

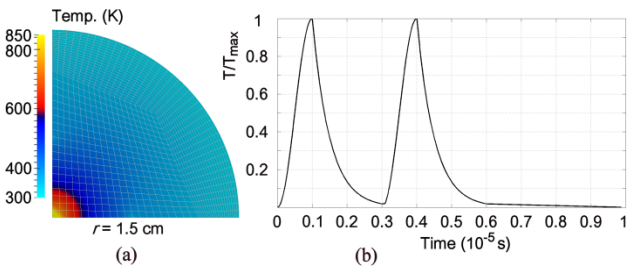

Figure 1: (a) Radial temperature distribution caused by a single ion beam pulse superimposed on the FEM mesh. (b) Simulated temporal evolution of temperature induced by two consecutive beam shots in the centre of the target.

The FEM simulations are limited to a linear elastic behaviour [4]. The material properties are inserted as constants, i.e. changes with temperature were neglected. The distribution of the stress amplitude was calculated and plotted as function of target radius. Stress wave reflexions at the foil frame and their interferences were simulated, without considering damping. To save comuting time, the calculations used axial symmetry of the target-beam configuration. Figure 2 shows the magnitudes of the shear and compressive stress caused by the initial beam pulse (blue lines) and the amplitude of the stress caused by interferences with a second pulse (red lines).

To simulate the response of the irradiated target to beam-induced stresses, a future approach will take into account different material properties within the beam spot under the effect of radiation damage.

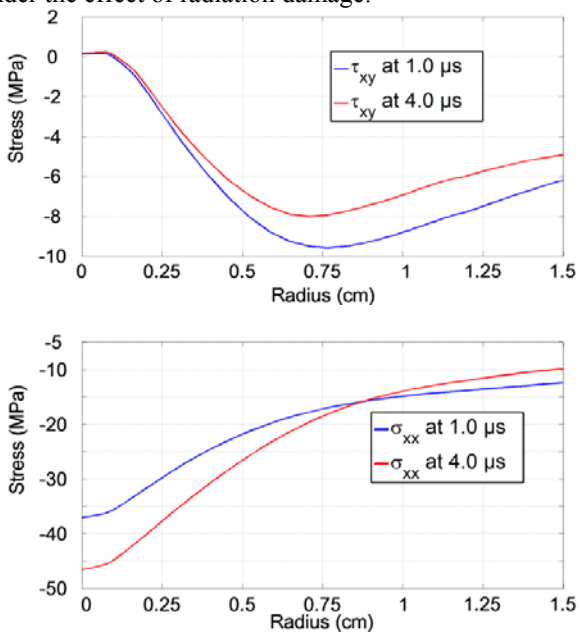

Figure 2: Distribution of shear stress (top) and compressive stress (bottom) after initial ion pulse (blue) and after second pulse (red)

[1] Bernd Klein, FEM - Grundlagen und Anwendungen der Finite-Element-Methode im Maschinen- und Fahrzeugbau, 2007.

[2] C. Plate, Untersuchung von Spannungswellen im Produktionstarget des Super-FRS Fragmentseperators an der Beschleuningungsanlage FAIR, Bachelor Thesis, TU Darmstadt, 2006.

[3] R. Chavan, A thermomechanical analysis of central column tiles, Internal report INT 195/99, 1999.

[4] R. Taylor, FEAP Theory Manual, 2011.

* Work supported by GSI-TUD cooperation contract, BMBF (project OSP12RDRBL) and HGS-HIRe

#d.c.nguyen@gsi.de; ##m.tomut.@gsi.de

Application of track-etched nanopore in nanofluidic*

C. Wang[1], L. Cao[1], J. Xue[1], M.E. Toimil-Molares[2], C. Trautmann[2,3], M. Ali[2,3] and Y. Wang[1,#]

[1]State Key Laboratory of Nuclear Physics and Technology, Peking University, China; [2]GSI, Darmstadt, Germany; [3]Technische Universität Damrstadt, Germany

Track-etched nanopores have broad application prospects in nanofluidic research fields, such as mimicking current rectification in ion channels, drug delivery systems, and micro-machines. Our research activities focus on current rectification in conical nanopores [1] and on electroosmotic pumps [2]. In both projects we use track-etched nanopores produced by irradiating thin polymer foils with GeV heavy ions followed by chemical etching.

Ion current rectification (ICR) in negatively charged conical nanopores is shown to be controlled by the electrolyte concentration gradient depending on the direction of ion diffusion. The degree of ICR is enhanced with the increasing forward concentration difference. An unusual rectification inversion is observed when the concentration gradient is reversely applied. A numerical simulation based on the coupled Poisson and Nernst Planck (PNP) equations is proposed to solve the ion distribution and ionic flux in the charged and structurally asymmetric nanofluidic channel with diffusive ion flow.

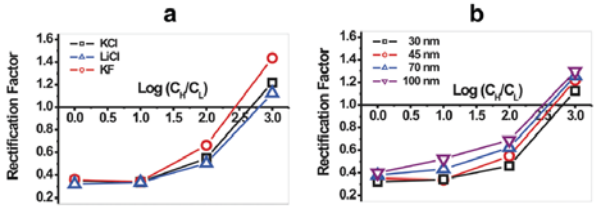

Figure 1: Model calculations qualitatively predict the trends in rectification inversion. (a) For KCl, LiCl, and KF, the degree of ICR initially decreases with increasing reverse concentration gradient. Under highest concentration gradient (1000-fold), rectification inversion occurs. (b) This trend depends on the diameter of the pore tip.

When the concentration gradient is reversely applied, an unusual rectification inversion is observed. Simulation results qualitatively describe the ICR behavior in conical nanopores suggested by experimental data and demonstrate the cooperation and competition between geometry-induced asymmetric ion transport and concentration-gradient driven ion flow (fig. 1). The present study improves our understanding of the ICR in asymmetric nanofluidic channels associated with the ion concentration difference. The diffusive and ion-rectifying of nanofluidic systems have promising use in constructing bio-inspired energy-conversion devices of high efficiency.

Track-etched polymer membranes are also used to realize low-voltage electroosmotic (EO) pumps. The diameter of the nanopores in polycarbonate (PC) and polyethylene terephthalate (PET) films was limited to 100 - 250 nm by adjusting the etching time. Low voltages (2–5 V) applied across the membrane results in high flow rates (fig. 2). The maximum normalized flow rate is as high as 0.12 ml min^{-1} V^{-1} cm^2, which is comparable to best values of previously demonstrated EO pumps. We attribute this to the unique properties of the track-etched nanopores.

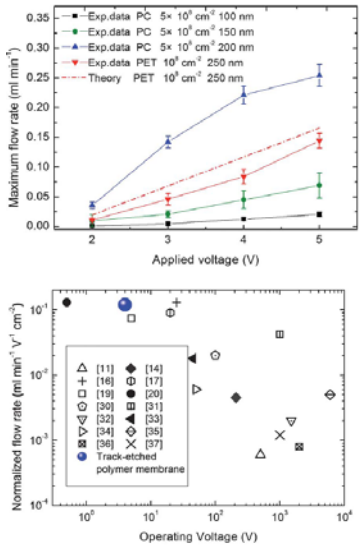

Figure 2: (top) flow rate versus applied voltage for EO pumps fabricated from three track-etched PC membranes with pore density of 10^8 cm^{-2} and pore diameters of 100, 150, and 200 nm in PC and 250 nm in PET membranes. (bottom) Comparison of the normalized flow rate obtained from track etched polymer membrane EO pump against flow rates reported in the literature.

We successfully demonstrated that the utilization of track-etched polymer membranes enables EO pumping to achieve flow rates that are higher than most values reported so far especially at low operating voltage. The simple and cost-effective fabrication of track-etched polymer membrane EO pumps makes them attractive for future applications in micro- or nanofluidic chips. These EO pumps are also capable of providing pressure/flow rate capacity sufficiently large for drug delivery applications and micro-electronics cooling.

[1] Liuxuan Cao, Wei Guo, Yugang Wang, and Lei Jiang, Langmuir 28 (2012) 2194.
[2] Ceming Wang, Lin Wang, Xiaorui Zhu, Yugang Wang and Jianming Xue, Lab Chip 12(2012) 1710.

* Supported by NSFC (grant No. 10975009 & 90923004
# ygwang@pku.edu.cn

Nanopores in Track-Etched Polymer Membranes as Substitutes for the Tight Junctions in a Novel Concept of an Artificial Corneal Endothelium *

T. V. Chirila[1,#], T. Nann [2], M. E. Toimil-Molares[3] and C. Trautmann[3,4]

[1]Queensland Eye Institute, Brisbane, Australia; [2] Ian Wark Research Institute, University of South Australia, Adelaide, Australia; [3]GSI Helmholtz Centre, Darmstadt, Germany; [4]Technische Universität Darmstadt, Germany

This collaborative project is aimed at creating an artificial substitute for the eye's corneal endothelium. The availability of an artificial endothelium able to duplicate the transendothelial ion-and-fluid transport function of the natural endothelium will remove the need for donor tissue or cell-based constructs in the treatment of corneal blindness. To date, no attempts were successful to substitute a dysfunctional corneal endothelium with an artificial membrane.

The natural endothelium consists of a monolayer of specialized cells, and has an essential role in maintaining the transparency of our cornea by performing a process called "pump-barrier function", which assures a constant hydration of the corneal stroma. The loss of this function leads eventually to blindness.

The mechanism of the pump-barrier function is still disputed. Based on Fischbarg's hypothesis [1] that the fluid transport through the endothelium is achieved by electroosmosis through the leaky tight junctions between cells, we proposed [2] that the nanopores in track-etched membranes can mimic the natural tight junctions. An essential condition for the electoosmosis is fulfilled by the fact that the internal pore walls are electrically charged.

Poly(ethylene terephthalate) (PET) membranes (12-µm thick) were irradiated at the UNILAC using Au ions (11.1 MeV/u) and a fluence of either 10^6 or 10^7 ions/cm^2. Subsequent track etching was performed at 50 ºC in 2M NaOH for various times (5, 25, 125 and 250 min) yielding cylindrical, parallel oriented pores of diameter 20, 100, 500 and 1000 nm, respectively.

Preliminary experiments have been performed to quantify the electroosmotic flow (EOF) through track-etched polymer membranes. Wang and co-workers did perform similar experiments earlier, where they recorded a mass flow by direct displacement of the electrolyte [3, 4]. In our work, we used a fluorophore to monitor the mass transport through the membrane, with the view that the fluorophore will also allow to account for other effects such as diffusion and electrophoresis.

In our experiment, two compartments were separated by a track-etched polymer membrane where the average pore diameter was 100 nm. One compartment was loaded with an electrolyte containing 100 mM KCl and 1 mg/ml Eosin Y, and the other was filled with exactly 1 ml of electrolyte without the dye. Then, gold electrodes were placed in each compartment and a potential of 500 mV was applied for two hours.

Figure 1 shows photoluminescence spectra of a diluted aliquot of the electrolyte-only compartment after two hours of application of the potential. The red spectrum shows the results when the anode was placed in the electrolyte-only compartment, the black spectrum corresponds to the reverse polarisation. The arrows indicate the direction of the respective flow components. By comparing these two spectra, it is evident that EOF is the dominating contribution, however, diffusion plays a significant role as well. Further studies will be necessary to quantify all transport mechanisms systematically.

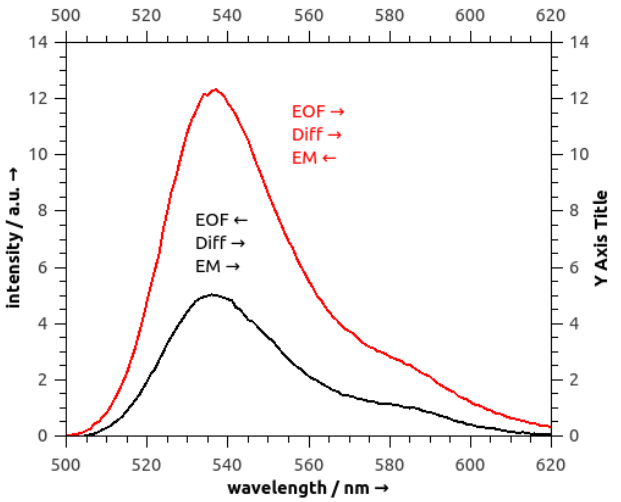

Figure 1: Photoluminescence spectra from electrolyte-only compartment after two hours of voltage application indicating the electroosmotic transport of Eosin Y. For the red (black) spectrum the anode (cathode) was placed in the electrolyte-only compartment. EOF is the direction of the electroosmotic flow, Diff denotes diffusion, and EM means electrophoretic flow.

References

[1] J. Fischbarg, Physiol. Rev. 90 (2010) 1271
[2] T.V. Chirila et al., J. Biomim. Biomater. Tissue Eng. 5 (2010) 13
[3] C. Wang et al., Nucl. Instr. Meth. B 286 (2012) 223
[4] C. Wang et al., Lab Chip 12 (2012) 1710

* This work has been supported in part by the Prevent Blindness Foundation (Queensland), Australia
# Traian.Chirila@qei.org.au

Integration of nanowires onto 100 mm wafers by the growth in-place method*

F. Greiner[1], F. Dassinger[1], S. Quednau[1], R. Sarwar[1], M. Hottes[1], C. Stegmann[1], M. Rauber[1], C. Trautmann[1,2], H. F. Schlaak[1], and W. Ensinger[1]

[1]Technische Universität Darmstadt, Germany; [2]GSI, Darmstadt, Germany.

The synthesis of submicron wires and nanowires based on ion-track-etched polymer templates and subsequent electrodeposition is an important expertise [1] this work relies on. Our approach [2] describes the growth in-place of metallic micro and nano-wires onto rigid and planar wafers of 100 mm diameter. These wafers are designed to be used for high-resolution UV lithography for batch fabrication of microstructures. Thereby, the approach paves the way to the integration of free standing submicron wires and nanowires in micro-electro-mechanical systems (MEMS) with manifold opportunities of application.

The process starts with the physical vapor deposition (PVD) of a 150 nm thick Ni film followed by microstructuring by lithography and wet etching (fig. 1 a). After stripping the photoresist, these circuit paths are gold plated by immersion. Then another photoresist layer is applied onto the wafer surface lithographically in such a way that specific areas remain open for later wire growth (fig. 1 b). In parallel, ion-irradiated polycarbonate membranes are etched to produce parallel-oriented cylindrical channels vertically perforating the membranes (fig. 1 c and d) [3]. Subsequently, the track-etched membrane is laminated onto the wafer (fig. 1 e). By applying heat and pressure, the photoresist becomes adhesive and reliably fixes the membrane on the wafer surface.

In the following, the channels are filled with a metal by electrodeposition. The control of the process parameters allows us to taylor the shape of the wire array. The wire growth can be stopped before reaching the membrane surface (fig. 1 f). Alternatively, the growth can be continued to obtain a closed top layer on the wire array (fig. 1 g). Another option is to apply PVD, thick film lithography, and electrodeposition on top of this structure and to grow another metallic microstructure on the upper layer of the wire array (fig. 1 h). By means of plasma etching, all polymer material can finally be removed releasing the wires with clean functional surfaces and without sticking of adjacent wires.

Currently, three system configurations with integrated vertical wires are investigated.

Gold submicron wires without overgrowth are studied to minimize the electrical resistance of contact systems in MEMS (fig. 1 i). The wires are very flexible and are supposed to need minimal forces to build up small resistance micro contacts (a-spots).

Wire arrays made of vertical submicron wires with a closed overgrown top layer are investigated for gas flow analyzing MEMS (fig. 1 j). The large surface-to-volume ratio is expected to accelerate the system response.

A similar configuration applies a larger microstructure on top of the flexible wire array for an acceleration detection MEMS (fig. 1 k).

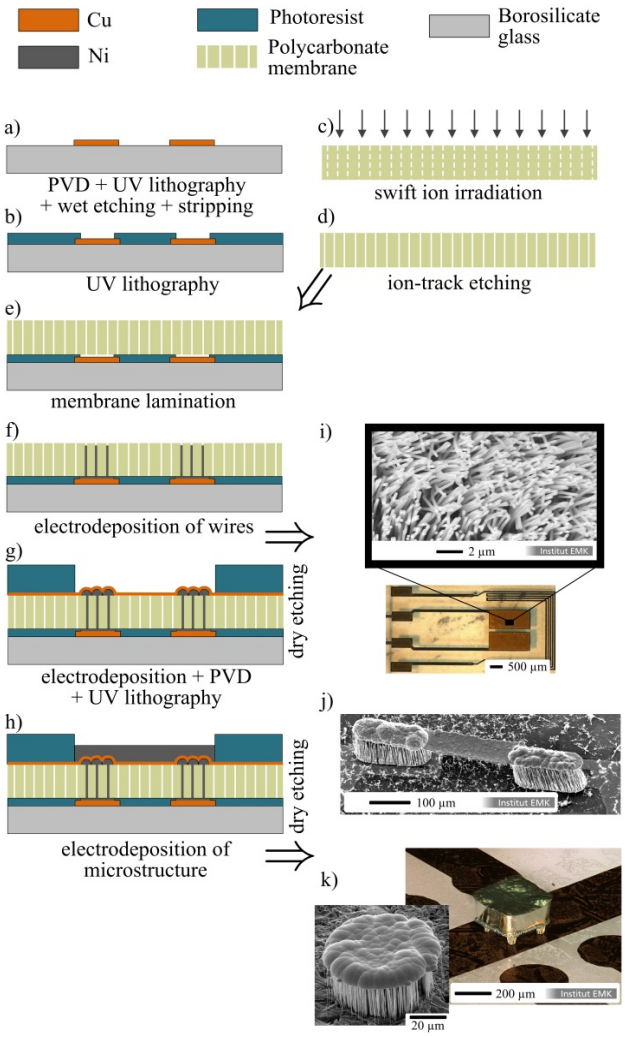

Figure 1: (a-h): Process flow of micro- and nano-wire integration by the growth in-place method; (i-k) Scanning electron and optical microscopy images of MEMS with grown in-place wire arrays.

* Work supported by BMBF, grant numbers 16SV5053, 16SV5475, 16SV5476 and 16SV5511.
Corresponding authors: mems@emk.tu-darmstadt.de

References

[1] S. Karim et al, Appl. Phys. A 84, 403-407 (2006)
[2] F Greiner et al, J. Micromech. Microeng. 23 025018 (2013)
[3] W Ensinger, P Vater, Mat. Sci. Eng. C 25, 609-619, (2005)

Antimony Nanowire Networks*

M. F. Wagner[1,2], *S. Müller*[1], *C. Trautmann*[1,2], *and M. E. Toimil-Molares*[†1]
[1]GSI, Darmstadt, Germany; [2]TU Darmstadt, Germany

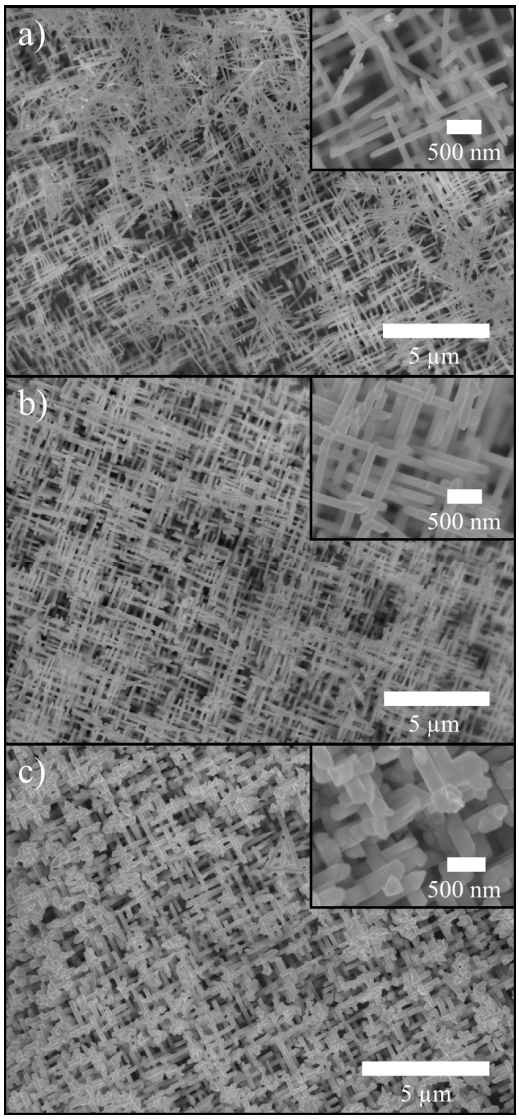

Figure 1: SEM images of Sb nanowire networks electrodeposited in etched ion-track membranes. Membranes with channels oriented under different angles were obtained by irradiating PC foils under four different beam incidence ($4 \times 5 \cdot 10^8$ ions/cm^2) followed by track etching to a mean wire diameter of a) 80, b) 130, and c) 220 nm.

Theoretical calculations predict an enhanced thermoelectric (TE) performance for materials that are confined in one dimension such as nanowires [1]. Sb as bulk material is p-type and Sb nanowire (NW) arrays could be employed for example as p-type element in nanostructured Peltier elements or thermocouples. However, bulk Sb and NWs made of Sb (as well as other TE materials, e. g., Bi and Bi_2Te_3) are very brittle and prone to break. The mechanical instability exhibited by arrays of parallel TE NWs constitutes thus a challenge towards their implementation in TE devices.

Here, we present the synthesis of 3D Sb nanowire networks (NWNWs). By ion-track technology and electrodeposition, we adjust integration density and NW diameter independently to provide mechanically stable and self-supporting structures of interconnected Sb NWs.

To create templates suitable for the electrochemical deposition of NWNWs, polymer foils were irradiated sequentially four times at the UNILAC facility with ~ 2 GeV Au ions under an angle of $45°$. After each irradiation step, the foils were rotated by $90°$ about the surface normal [3]. Thus, after etching the tracks for 5, 7.5, and 10 min with 6 mol/l NaOH solution at 50 °C, networks of interconnected nanochannels were obtained. During etching, the mean diameter increased by (29 ± 3) nm/min [4]. These channels were then filled by electrodeposition from an Sb electrolyte based on hydrochloric acid and Sb(III)-chloride [5].

Homogeneous Sb NWNWs were grown at a temperature of 40 °C, applying pulsed deposition with an on-potential of -265 mV vs. a saturated calomel electrode (SCE) for 20 ms and an off-potential of -100 mV vs. SCE for 100 ms. After the deposition, the polymer template was removed with dichloromethane and the remaining NWNWs were investigated by scanning electron microscopy (SEM) [4].

Figure 1 shows SEM images of NWNWs with mean wire diameters of about a) 80, b) 130, and c) 220 nm with a fixed fluence of $4 \times 5 \cdot 10^8$ ions/cm^2 in all cases. The fluence of ions during the irradiation steps determines the integration density. With increasing etching time (i. e., increasing wire diameter), the interconnectivity is increased leading to more stable NWNWs.

In conclusion, we have shown that mechanically stable Sb NWNWs can be created by electrodeposition in etched ion-track membranes by adjusting NW diameter and track density. These results are promising for the device integration of quasi-1D materials. Thermoelectric transport properties and the crystalline structure of these networks will be further investigated.

References

[1] Hicks, Dresselhaus, Phys. Rev. B 47 (1993) 12727–12731.
[2] Huber, Graf, Phys. Rev. B 60 (1999) 16880–16884.
[3] Rauber et al., Nano Lett. 11 (2011) 2304–2310.
[4] Wagner, diploma thesis, TU Darmstadt (2012).
[5] Müller et al., J. of Crystal Growth 12 (2012) 615–621.

* funding within DFG priority program 1386
† M.E.ToimilMolares@gsi.de

Influence of Electrolyte Concentration on Crystal Orientation and Seebeck Coefficient of Bi_2Te_3 Nanowires Arrays

O. Picht[1], J. Gronefeld[1], M. Cassinelli[1], S. Mueller[1], C. Trautmann[1,2], M.E. Toimil-Molares[1,#]

[1]GSI, Darmstadt, Germany, [2] Technische Universität Darmstadt, Germany.

Bulk materials based on bismuth telluride (Bi_2Te_3) exhibit high thermoelectric efficiency at room temperature, being thus common constituents of thermoelectric devices operating at ambient conditions. The efficiency of a thermoelectric device is described by the figure of merit $ZT = S^2\sigma T/\lambda$, where S denotes the Seebeck coefficient, σ electrical, λ thermal conductivity, and T the absolute temperature. Theoretical calculations predicted an enhancement of the thermoelectric efficiency in low-dimensional Bi_2Te_3 structures, such as nanowires (NWs), due to finite- and quantum-size effects [1]. For NWs, the diameter clearly represents one of the crucial parameters for the enhancement of ZT. Bi_2Te_3 NWs had been synthesized by electrodeposition mainly in porous alumina membranes [2] displaying in most cases diameters above 50 nm. Recently, we have reported the electrodeposition of Bi_2Te_3 NWs with diameters as small as ~17 nm in the pores of etched ion-track membranes [3]. In addition, Bi_2Te_3 has a highly anisotropic crystal structure and the electrodeposition parameters can thus influence its crystal orientation and physical properties. Here we present systematic studies on the influence of electrolyte concentration on the crystallographic characteristics and Seebeck coefficient of 25-nm diameter Bi_2Te_3 NW arrays [4].

Polycarbonate foils (thickness 30 µm) were irradiated with ~GeV U ions at the UNILAC accelerator. The ion tracks were etched in 6M NaOH solution at 50 °C for 60 s to fabricate channels with diameter ~25 nm. Bi_2Te_3 NWs were electrodeposited in the channels using a thermostated three-electrode cell and a saturated calomel reference (SCE) electrode. The deposition was performed applying U = 0 mV vs. SCE at T = 4°C. The electrolytes were based on 1 M nitric acid, 5 mM tellurium powder and three different bismuth nitrate pentahydrate concentrations, namely 10 mM, 7.5 mM, and 3.5 mM Bi.

Bi_2Te_3 NW arrays synthesized with different electrolytes were characterized by x-ray diffraction (XRD) to study the preferential crystallographic orientation (Fig. 1). The XRD spectra display reflections assigned to the polycarbonate membrane, the Au cathode layer and the (101), (105), and (205) reflections from the Bi_2Te_3 NWs. The (101) reflection is small in all cases, while the NW array deposited with lowest Bi:Te ratio (green) displays the strongest, but still relatively weak, signal for (015) orientation. Finally, with increasing Bi:Te ratio in the electrolyte, an increase of the (205) reflection, i.e. (205) planes parallel to membrane surface, is noticeable.

* Work supported by DFG (No. SPP 1386).

M.E.Toimilmolares@gsi.de

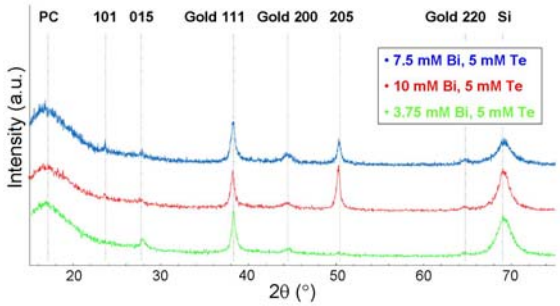

Fig. 1: XRD patterns of Bi_2Te_3 NW arrays deposited with electrolytes of Bi:Te ratio 3.75:5 (green), 7.5:5 (blue), and 10:5 (red) at T=4°C applying U=0 mV vs. SCE.

All samples show negative S values, indicating n-type behaviour, with a linear T dependence. The sample synthesized with the lowest Bi:Te electrolyte ratio exhibits highest S in the whole range, achieving S = -55.0 µV/K at 270°C, while NWs deposited with 7.5 mM Bi and 10 mM Bi, displayed S ~ -49.6 µV/K and -38.6 µV/K at 270 °C, respectively.

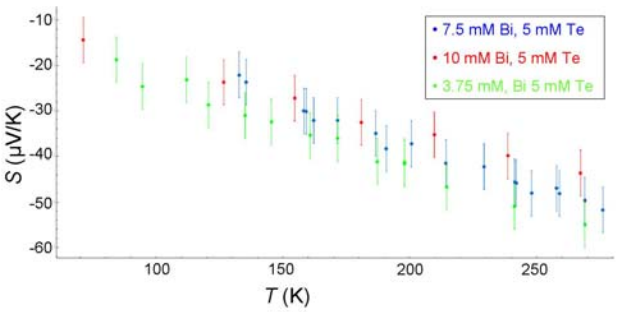

Fig. 2: Seebeck coefficient vs. temperature.

In conclusion, Bi_2Te_3 NWs arrays were electrodeposited in etched ion-track membranes using electrolytes with three different Bi:Te ratios. XRD measurements revealed an increasing (205) preferred crystallographic orientation for higher Bi concentrations in the electrolyte. Seebeck measurements indicate only a weak dependence of the S coefficient on the different Bi:Te ratio of the electrolyte.

[1] L.D. Hicks and M.S. Dresselhaus, Phys. Rev. B 47, 12727 (1993).
[2] S.A. Sapp et al., Adv. Mater. 11, 402 (1999).
[3] O. Picht et al., J.of Phys. Chem.. C 116, 5367 (2012).
[4] J. Gronefeld, Bachelor Thesis, TU-Darmstadt.
[5] S. Mueller, PhD Thesis, Univ. of Heidelberg.

Seebeck Measurements on $Bi_{1-x}Sb_x$ Nanowire Arrays*

S. Müller[1], *M. Cassinelli*[1], *K.–O. Voss*[1], *C. Trautmann*[1,2], *and M. E. Toimil-Molares*[†1]
[1]GSI, Darmstadt, Germany; [2]TU Darmstadt, Germany

In thermoelectrics, the efficiency of a material is expressed by the dimensionless figure-of-merit ZT. ZT and the Seebeck coefficient S are defined by

$$Z \cdot T := \frac{\sigma S^2}{\kappa} T \quad \text{and} \quad S(T) := \frac{\mathrm{d}U}{\mathrm{d}T}$$

being T the absolute temperature, σ the electrical conductivity, κ the thermal conductivity, and U the thermovoltage.

One dimensional materials such as nanowires (NWs) are of interest because it was predicted that they exhibit an enhanced value of ZT due to quantum confinement of the charge carriers [1, 2]. Also finite-size effects, e. g., enhanced scattering of phonons at the wire surface [3], could contribute to increase their ZT to values interesting for thermoelectric (TE) commercial applications.

To investigate the influence of size-effects on the TE properties of nanomaterials, it requires the development of new techniques able to measure reliably temperature gradients, thermovoltages, as well as electrical and thermal conductivities along a nanostructure. Here, we present a setup developed and optimized at GSI to measure S of NW arrays fabricated by electrodeposition in etched ion-track membranes. These membranes were produced by irradiation with $\sim$ 2 GeV Au heavy ions at the UNILAC facility. The ion tracks were etched in 6 mol/l NaOH at 50 °C to form channels with diameters between 25 and 200 nm. Nanowires were grown by electrodeposition inside the nanochannels [4, 5].

In Figure 1, the setup for the measurement of S is depicted. The NWs remained in the PC template and were electrically contacted by a Au layer sputtered on top. The array was clamped between two copper plates placed in a stainless steel frame. This frame was mounted on a cooling finger in a cryostat. Contacts are attached from top and bottom as well as Si diodes to measure the temperatures T_1 and T_2 at both sides of the membrane. The polymer matrix has only a small thermal conductivity and, therefore, a temperature difference $\Delta T = T_2 - T_1$ was readily created and varied by heating and cooling the bottom part around a predefined set-point that can be selected from 30 to 300 K. The slopes of the obtained $U - \Delta T$ curves provide S.

Figure 2 shows S as function of temperature T for four different NW arrays: Cu (green), Bi (black), Sb (blue), and $Bi_{0.9}Sb_{0.1}$ (red). The Cu NW array (d $\sim$120 nm) served as a reference sample for NW configuration, since no size effects are expected for Cu NWs of such dimensions. The Cu NW sample exhibited $S = (2.0 \pm 0.5)$ µV/K, which is in excellent agreement with S of bulk Cu, namely

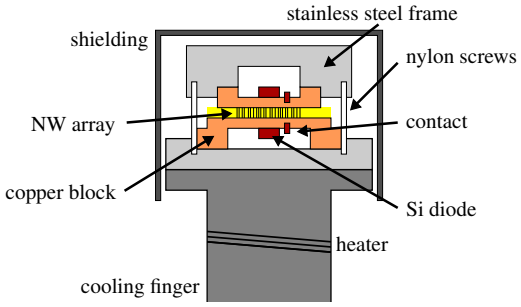

Figure 1: Schematic of the setup for the measurement of the Seebeck coefficient.

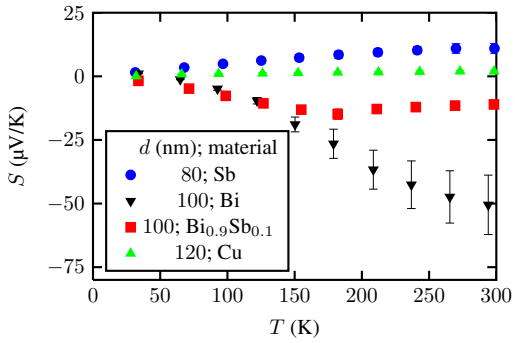

Figure 2: Seebeck coefficients of nanowire arrays of different materials as function of temperature.

S =1.83 µV/K [6]. In the case of Bi compound nanowires, the diameter $\sim$ 100 nm is comparable to the mean free path of charge carriers and thus size effects are expected. At room temperature, S was (-50 ± 12), (11 ± 2), and (-11 ± 2) µV/K for Bi, Sb, and $Bi_{0.9}Sb_{0.1}$, respectively. While the NW arrays were p- and n-type materials as their bulk counterparts, the Seebeck values measured at room temperature were considerably smaller.

Further measurements are underway to study the influence of nanowire diameter, crystallite size, crystallographic orientation, and thermal contacts on the value of S.

References

[1] Hicks, Dresselhaus, Phys. Rev. B 47 (1993) 16631.
[2] Rabin et al., Appl. Phys. Lett. 79 (2001) 81.
[3] Hochbaum et al., Nature 451 (2008) 163.
[4] Müller et al., J. of Crystal Growth 12 (2012) 615.
[5] Müller, PhD thesis, University of Heidelberg (2012).
[6] Cusack and Kendall, Proc. Phys. Soc. 72 (1958) 898.
[7] Issi, Australian J. of Phys. 32 (1979) 585.

* funding within DFG priority program 1386
† M.E.ToimilMolares@gsi.de

Thermal Instability of Porous Gold Nanowires

L. Burr[#,1], I. Alber[1], M.E. Toimil-Molares[1] and C. Trautmann[1,2]

[1]GSI, Darmstadt, Germany, [2]Technische Universität Darmstadt, Germany

Due to their high surface-to-volume ratio, porous metal and semiconductor nanowires (NWs) are attracting strong interest as promising devices e.g. in electronics, catalysis and sensorics. Under working conditions, NW devices should stand elevated temperatures, it is thus necessary to investigate their thermal stability.

Theoretical modelling by Nichols and Mullins predicted that, while annealing, solid cylinders with initial radius R_0 break into a row of spheres with diameter $3.78R_0$ spaced by $2\sqrt{2}\pi R_0$ in a process governed by surface diffusion [1]. Recent publications showed that Cu and Au NWs are thermally instable at temperatures much lower than the melting point of their bulk counterpart, and transform into a row of spheres [2,3]. Here we study the thermal instability of porous Au NWs by annealing and scanning electron microscopy (SEM) investigations.

AuAg alloy solid NWs were electrochemically grown in the nanochannels of etched ion-track polycarbonate templates. The membranes were fabricated by irradiation with Au ions (~ GeV) at the UNILAC accelerator and subsequent chemical etching.

Nanowires with length ~ 2 μm and diameter ~ 110 nm were synthesized inside the etched channels using a cyanidic electrolyte containing $KAu(CN)_2$ and $KAg(CN)_2$ in 1:1 ratio, applying a potential U = -1.1V vs. Ag/AgCl reference electrode. Details of the synthesis process are given in [4]. After deposition, the polymer membrane is removed in a dichloromethane solution, and the nanowires were drop-casted on Si wafers.

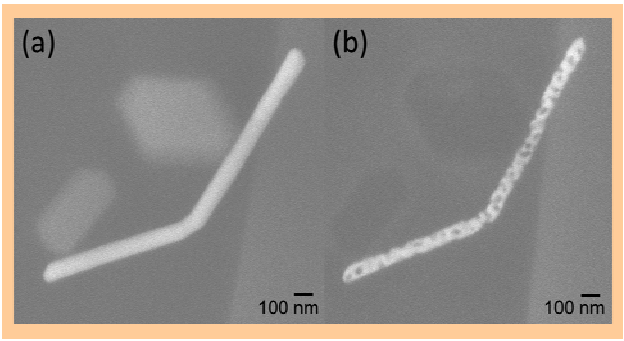

Figure 1: SEM images of a given AuAg NW (a) before and (b) after HNO_3 treatment.

To create porous NWs, the Si wafer with AuAg alloy NWs is dipped for 3h in concentrated nitric acid. Figure 1 depicts the same AuAg alloy NW (a) before and (b) after the nitric acid treatment. In this case, the diameter of the wire is reduced from 105 to 85 nm. Nitric acid dissolves Ag atoms but does not react with Au. The formation of nanoscale porosity can be explained by diffusion of Au adatoms on the NW surface and formation of Au-rich clusters during Ag dissolution [4]. We observe that the porosity and the diameter reduction depend sensitively on the initial Au/Ag composition and NW diameter.

Figure 2 depicts the porous NWs after annealing at 200, 300, and 500 °C for 1h on 290-μm thick silicon wafers (heating rate of 9 °C/min).

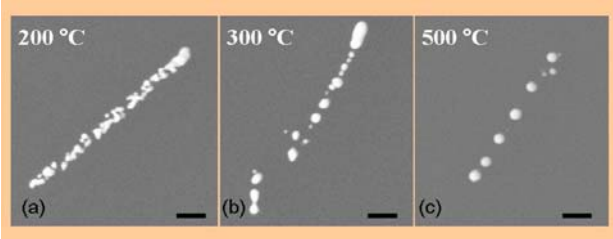

Figure 2: SEM pictures of porous nanowires after 1h annealing at temperatures (a) 200 °C, (b) 300 °C, and (c) 500 °C (Scale bar: 100nm).

Karim et al. previously reported that several μm-long solid Au NWs with diameter ~ 80 nm maintain their cylindrical morphology during 1 hour annealing at temperatures between 200 and 500 °C, and display morphological instabilities after annealing at 600 °C.

In contrast, the morphology of the porous NWs as synthesized in this work starts to change already at 200 °C (Fig. 2a). At higher temperatures, they transform into chains of spheres (Fig. 2b). At 500 °C, spheres with sizes varying between ~ 30 and 120 nm, and inter-sphere separations ranging between 30 and 200 nm are observed (Fig. 2c). Further experiments are currently underway to understand the relation between initial wire porosity and dimensions, and the final morphology of the chain of spheres.

These first results indicate that porous nanostructures undergo morphological transformation at lower temperatures as their solid counterparts due to their higher surface-to-volume ratio. At the same time, this behaviour enables the fabrication of chains of closely spaced nanoparticles interesting for, e.g., surface plasmon investigations.

*Work supported by HGS-HIRe.

l.Burr@gsi.de

References

[1] F. A. Nichols and W. W. Mullins, *J. Appl. Phys.* 36 (1965) 1826..

[2] M. E. Toimil Molares et al. *Appl. Phys. Lett.* 85 (2004) 5337.

[3] S. Karim et al. *Nanotechnology* 17 (2006) 5954.

[4] I. Alber, "Synthesis and Plasmonic Properties of Metallic Nanowires and Nanowires Dimers," Ruprecht - Karls - Universität Heidelberg, PhD Thesis 2012.

Surface Plasmons in Conductively Coupled Nanowire Dimers

I. Alber[1], W. Sigle[2], F. Demming-Janssen[3], R. Neumann[1], C. Trautmann[1,4], P. A. van Aken[2], and M.E. Toimil-Molares[1]*

[1]GSI, Darmstadt, Germany; [2]MPI, Stuttgart, Germany, [3]CST GmbH, Darmstadt, Germany, [4]TU Darmstadt, Germany.

Localized surface plasmon resonances (SPR) in nanowires separated by nanogaps are attracting strong interest due to the high electric field enhancement generated at the position of the gap. These structures are called nanowire dimers and are, due to the high field enhancement, interesting e.g. for surface enhanced Raman spectroscopy.[1]

We have synthesized nanowire dimers by electrodeposition of Au-rich/Ag-rich/Au-rich wires in ion-track etched polymer membranes and subsequent dissolution of the Ag segments. Applying this technique we find that not all Ag segments are transformed into a gap but that in some cases two Au segments remain connected by a small metallic junction. These junctions enable current flow between two wires, and modify the plasmonic properties. We have analyzed these differences for dimers with gaps or connections of varying dimensions.[2] Precise knowledge of the SPR energies is crucial for their applications.

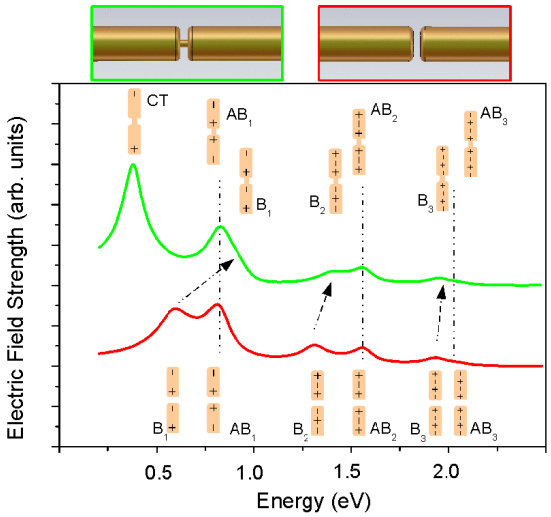

Figure 1: Calculated electric field strength of dimer with gap (red) and with nano-connection (green) vs. excitation energy.#

Figure 1 shows simulations with CST microwave studio[3] of the multipole SPR of two dimers with same length and diameter. The lower (red) spectrum corresponds to a dimer with a gap of 19 nm, while the upper (green) line depicts a spectrum of a connected dimer with junction of length 19 nm and diameter 20 nm. The two spectra show the electric field strength at a distance of 1 nm from an end of the dimers. The nanowire schemes illustrate the surface charge distributions of the corresponding SPR.

The two spectra reveal SPR at varying energies: For the dimer with connection, the so-called charge transfer mode (CT) is excited at low energy. It is not observable in the spectrum of the dimer with gap since in this case current flow between the two wires is prevented. For both dimers three pairs of SPR can be identified. Each pair consists of two modes called bonding mode (B) and antibonding mode (AB), that are close in energy. For the dimer with gap the B-modes are usually excited at lower energies than the corresponding AB-modes.[4] The energies of the three AB-modes are almost identical for the dimer with gap and that with connection. In contrast, the three B-modes are shifted to higher energies for the dimer with connection compared to the one with gap. This blue-shift is caused by a decreasing field strength at the center of the structure with increasing connection diameter.

To compare with simulations, we have performed SPR measurements on dimers. The SPR were excited using the electric field of a monochromated 200 keV electron beam in a TEM and analyzed with an electron spectrometer. The resonances can be identified in the electron spectra as energies of high energy-loss probability.

Figure 2 shows exemplarily a map consisting of 100 spectra measured along a connected dimer. Each horizontal line represents the spectral distribution at the corresponding wire position. The energy increases from 0.25 to 2 eV from left to right. The colors indicate the number of counts. The map confirms our simulation results, revealing the excitation of the CT mode at low energy, and the blue-shift of the B_1-mode compared to the AB_1-mode, which is not observed for dimers with gaps.

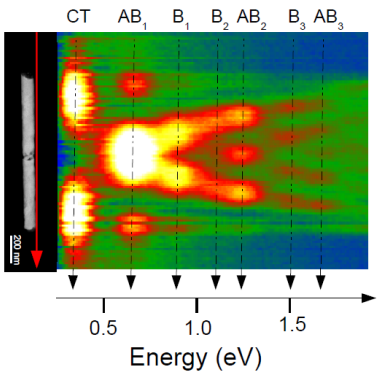

Figure 2: Electron energy-loss map consisting of 100 spectra measured along a dimer with connection (red arrow in TEM image on the left).#

Work is part of HGS-HIRe.

[1] S. Li et al., Nano Lett. 10 (2010), 1722- 1727.
[2] I. Alber et al., ACS Nano 6 (2012) 9711–9717.
[3] CST AG Darmstadt, www.cst.de.
[4] B. Willingham et al., Appl. Phys. B 28 (2008) 209-216.

* i.alber@gsi.de

Synthesis of Cu-Ni core-shell nanowires by a two-step etching and electrodeposition

Y.H. Chen[1, 2], M.E. Toimil Molares[1,#], S. Müller[1], I. Alber[1], M. Cassinelli[1,3], J. Liu[2], C. Trautmann[1,3]

[1]GSI, Darmstadt, Germany; [2]IMP, Lanzhou, China, [3]TU-Darmstadt, Darmstadt.

In recent years, one-dimensional nanostructures such as nanowires and nanotubes have inspired extensive research efforts because of their potential applications in physics, chemistry, materials science, and many other fields [1]. In this work, nanocables with a core-shell structure are synthesized consisting of a Cu core that is surrounded by a Ni layer. According to theoretical calculations [2,3], such nanostructures are expected to display interesting physical properties as a function of size, crystal structure, and thickness of the core and shell layer. We describe an approach to fabricate core-shell nanocables by two-step etching in combination with electrochemical deposition.

Polycarbonate (PC) foils were first irradiated with swift heavy ions (fluence ~ 5×10^8 ions/cm^2) and subsequently exposed to UV light on each side of the foils for 2 h in order to enhance the track-etching rate. The ion tracks in the foils were etched in a 5 M NaOH solution at 50 °C for 3 minutes leading to cylindrical channels with diameters 80-90 nm. In the following step, Cu was electrochemically deposited in the channels in a two-electrode arrangement at constant applied cell voltage of U = -0.27 V. A thin Au layer sputtered on one side of the PC template and a copper cone, served as cathode and anode, respectively. The electrolyte consisted of 75 g/l $CuSO_4{\cdot}5H_2O$ and 30 g/l H_2SO_4. After that, the membrane with embedded Cu nanowires was immersed once more in a 5 M NaOH solution at 50 ºC to form an annular tube around each Cu nanowire. Finally, Ni was potentiostatically deposited in the annular free space between the template and the Cu wire, applying U = -1.5 V with a nickel cone as anode and using an electrolyte of 250 g/l $NiSO_4.6H_2O$, 50 g/l $NiCl_2{\cdot}6H_2O$ and 30 g/l H_3BO_3.

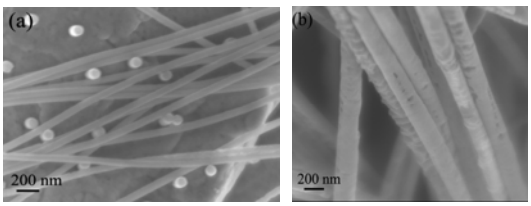

Figure 1: SEM images of Cu nanowires (diameter 80 nm) before (a) and after (b) deposition of a Ni shell. The diameter of the Ni/Cu nanocables is 200 nm.

For characterization, the PC template was dissolved in dichloromethane, and the morphology of the Cu nanowires and Ni/Cu nanocables was investigated by scanning electron microscopy (SEM) (JSM 7401F, JEOL). Figure 1(a) displays the Cu nanowires with cylindrical shape, smooth surface and uniform diameter (d ~ 80 nm). After the second etching step and subsequent deposition of Ni, the diameter of the structures is significantly increased to about ~ 200 nm (Fig. 1(b)), demonstrating that Ni shell has been successfully grown onto the Cu nanowires. The Ni/Cu nanocables display a not so homogeneous diameter contour and a relatively rough surface. Further investigations are underway to clarify if the roughness is due to contour inhomogeneities formed during the second etching step or during the Ni deposition process. Figure 2 shows the cross section of a single nanocable analysed by energy dispersive x-ray analysis (EDX). The elemental map reveals a Cu-rich core (red) and a Ni-rich shell (blue) as expected. EDX compositional line profiles are displayed in Fig. 2(b).

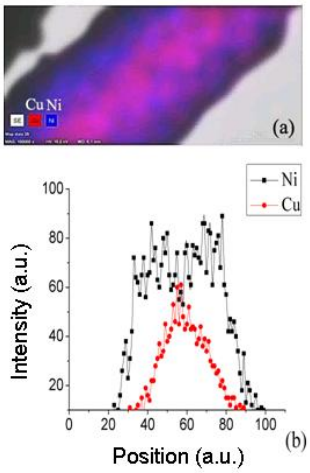

Figure 2: Elemental composition of single Ni/Cu nanocable analysed by EDX (a), composition mapping (b) line profiles of wire cross section with Cu-rich (red) and Ni-rich (blue) regions.

In conclusion, a multi-step process is demonstrated to synthesize nanocables with a Cu core surrounded by a Ni shell. The fabrication involves standard electrodeposition of Cu nanowires followed by a second chemical etching process. The tube region formed around the Cu wires is subsequently electrochemically filled resulting in a Ni shell. The existence and elemental composition of the core-shell structure is confirmed by EDX.

References

[1] A.R Madaria, A. Kumar and C. Zhou, Nanotechnology 22(2011) 245201.

[2] Y. Tak, S.J. Hong, J.S. Lee and K. Yong, J. Mater. Chem. 19 (2009) 5945.

[3] B. Wang, X. Chen, G. Chen and J. Zhao, Solid State Commun. 129 (2004) 25.

#m.e.toimilmolares@gsi.de

Optimization of copper nanocones for field emission cathodes

P. Serbun[1], F. Jordan[1], G. Müller[1*], I. Alber[2], M. E. Toimil-Molares[2], C. Trautmann[2,3]

[1]Physics Department, University of Wuppertal, [2]GSI Helmholtz Centre, [3]Technische Universität, Darmstadt, Germany

We have optimized the fabrication of copper nanocones (Cu-NCs) for flat structured field emission (FE) cathodes [1]. Stacks of three polycarbonate foils (PC ~30 µm) were irradiated with ^{238}U or ^{136}Xe ions (11.1 MeV/u, 10^6-10^7 cm^{-2}). The ion tracks were asymmetrically etched in a 40:60 mixture of 9 M NaOH and methanol. Depending on the etching time, conical pores of different size were obtained. The membrane surface with the large pore opening (2-4 µm) was sputter-coated with ~60 nm Au, reinforced with ~20 µm Cu, and glued on an Al plate, to obtain a flat template for the electrochemical deposition of NCs as described in detail in [2, 3]. Flat cathodes of 25 mm^2 size with mechanically stable Cu-NCs were achieved (Fig.1).

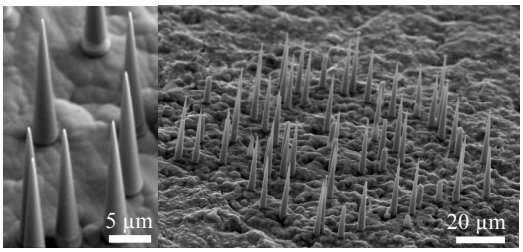

Figure 1: SEM images (60° view) of Cu-NCs with sharp tips (left) and of a patch (right) (PC irradiated with ^{136}Xe).

The average values and standard deviations of the NC tips on various cathodes derived from SEM images are summarized in Fig. 2. A systematic increase of the mean tip diameter with etching time is obvious up to 17 min, and the aging of the etchant is considered to be responsible for the rather low values for the 20 min etching which was performed one day later. As expected for the different total energy loss, the complete pore opening required a longer etching time for ^{136}Xe (~20 min) than for ^{238}U ion tracks (~15 min). Moreover, there is some evidence for a weak dependence of the NC size on the stack position. It is most remarkable that the sharpest Cu-NCs were grown in the ^{136}Xe ion tracks.

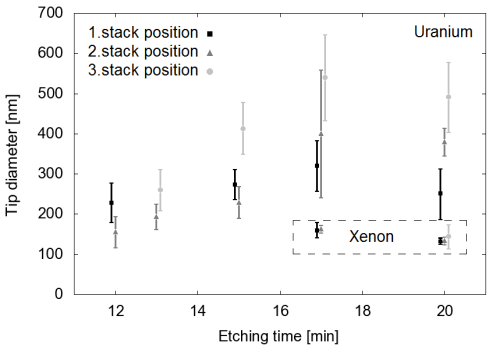

Figure 2: Mean tip diameter of Cu-NCs as function of the polycarbonate (PC) etching time for three stack positions. The dashed rectangle marks the data for ^{136}Xe ion tracks.

The FE homogeneity of selected Cu-NC cathodes was measured before and after sputter-coating with Au by means of the FESM as described in [1]. W anodes with small tip diameter $Ø_a$ and gap Δz were used to obtain high resolution maps. In Fig. 3 the best result is given showing at least 8 emitters/patch (of ~180 µm diameter) for the bare Cu-NCs grown in etched Xe-ion tracks, and ~20 % more after 60 nm Au coating probably due to less oxide.

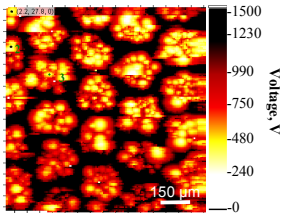

Figure 3: High resolution voltage maps (1 nA FE current, $Ø_a$=12 µm, Δz = 30 µm) of bare (left, ~1 mm^2) and 60 nm Au-coated (right, ~0.9 mm^2) structured Cu-NC cathodes.

The integral FE properties of selected Cu-NC patches were measured with a truncated-cone anode of adjusted size ($Ø_a$ = 150 µm). The typical current-field curve of a Au-coated patch in the left Fig. 4 confirms a rather stable Fowler-Nordheim (FN) behavior up to 90 µA at 43 V/µm with a field enhancement factor of ~338. Current jumps occurred on all patches, but at higher current levels for the Au-coated CuNCs as shown in the right Fig 4. Correlated SEM images revealed a partial destruction of the CuNCs by FE currents of ~20 µA for bare and ~100 µA for the Au-coated ones. On average these patches yielded 151 µA at 50 V/m, i.e. much higher FE current carrying capability as compared to Au nanowire patches. In conclusion, these results are very promising for high current FE devices based on Au-NC cathodes grown in ^{136}Xe ion tracks.

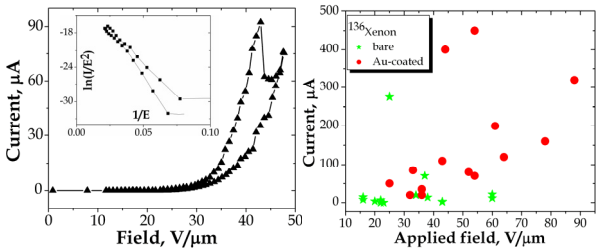

Figure 4: Typ. I(E)-curve and FN-plot (inset) of a patch in the right map of Fig. 3 (left) and maximum current vs. field for all measured patches of various Cu-NC cathodes.

References

[1] P. Serbun et al., Eur. Phys. J. Appl. Phys. **58**, 10402 (2012).
[2] F. Jordan et al., Techn. Dig. IVNC 2012, Jeju Korea, IEEE Cat. No. CFP12VAC-ART, p. 58 (2012).
[3] F. Jordan, Univ. Wuppertal, ext. Report, Dec. 2012.

*contact: gmueller@uni-wuppertal.de

High-Precision Heating Stage for the Bio Endstation of the Microprobe

K.-O. Voss[*1] *and B. Merk*[1,2]

[1]GSI Helmholtzzentrum für Schwerionenforschung GSI; [2]Technische Universität Darmstadt

Introduction

For single-particle irradiation with sub-micron accuracy temperature control of the entire microprobe facility is essential. With relevant lengths of the most sensitive parts of the setup ranging around tens of cm and a thermal expansion coefficient of steel or aluminum around 15-25 µm per meter and Kelvin one can expect a temperature change of 100 mK to introduce a shift of a few hundred nanometers. With the current absolute targeting accuracy of our system being 700 nm such a shift is not negligible and we are thus continuously striving for improvements of this situation. For this reason, sources of heat have either been eliminated whenever possible (e.g. use of LED illumination as soon as commercially available [1]) or thoroughly separated from the most critical components. At the same time, these components have been kept at minimum lengths and are allowed to thermally stabilize before precision irradiations are conducted.

In conflict with this struggle, the vast majority of experiments depend on the introduction of various heat sources. Here, we report on a heat source with up to a whopping 25 Watts being flanged onto the thermally sensitive microscope stage of the bio endstation. This heat source allows for accurate irradiation of cell cultures at 37 °C instead of the constant but unregulated 30 °C with the unheated stage. The temperature is deemed to be a contributing parameter for absolute measurements of protein kinetics [2], where temperature is expected to strongly modify micro-'viscosity'.

Lazy Man's Approach – On/Off Thermostat

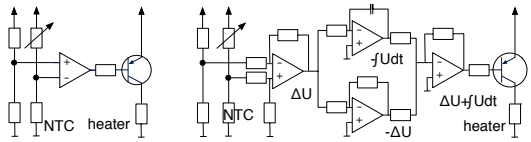

Figure 1: Schematic of a simple on/off-type thermostat (left) and a slightly more elaborate PI regulator (right).

A simple circuit that reads from a temperature sensor and drives current through heating resistors whenever the measured temperature is smaller than 37 °C is shown in fig. 1 (left). Here, a negative-temperature-coefficient resistor (NTC) mounted as close to the sample position as possible is part of a voltage devider. The thermo-voltage is compared to a reference voltage, with the full comparator sweep switching the current through the heating resistor on or off when the sensor reading is too low or too high, respectively. Using this regulator, we found a temperature hysteresis at the sample position of 0.4 K resulting in a thermal drift measured to be 1.2 µm. The hysteresis depends on the distance of heating and sensing elements as well as heat capacity and thermal conductivity of the stage and is as such difficult to improve while sticking with the thermostat approach.

OK, That Didn't Work – PI Regulation

To cater for the thermal 'inertia' of the stage, the circuit in fig. 1 (right) introduces an integrating branch yielding a signal that represents the past difference between set-point and measured temperature. This slow integral (I) part is summed up with a voltage proportional (P) to the current temperature deviation from the set-point to speed up recovery from temperature excursions. The sum then adjusts the collector-emitter resistance of a power transistor, effectively regulating the current flowing through the heater.

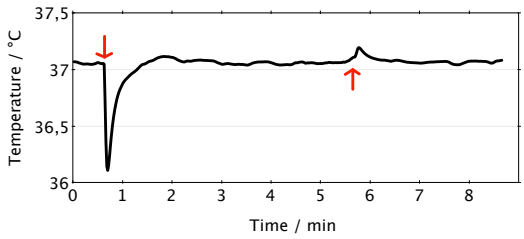

Figure 2: Recovery of the set-point temperature after a forced temperature excursion (arrow at 30 s). For this 1 K excursion, temperature returns to set point within roughly 100 s and remains stable to less than 1/20 K. Arrow at 5 minutes marks small forced excursion to higher temperatures. Temperature measured at sample site, fully integrated into microbeam setup.

Figure 2 shows the response of the well admixed proportional and integral branches to an excursion one might expect from a sample exchange (1 K) with a very small overshoot on the way back to 37 °C. When locked to 37 °C, no movement of the stage is detectable.

References

[1] B. Merk, B.E. Fischer, R. Neumann, K.-O. Voss, GSI Scientific Report 2008, 361

[2] B. Merk, K.-O. Voss, I. Müller, B.E. Fischer, B. Jakob, G. Taucher-Scholz, C. Trautmann, M. Durante, Biophysics section of this GSI Scientific Report

* K.-O.Voss@gsi.de

A transverse electron target for the FAIR storage rings

S. Geyer[1], O. Meusel[1] and O. Kester[1,2]

[1]Goethe-Universität Frankfurt, Germany; [2]GSI, Darmstadt, Germany

Electron-ion interaction processes are of fundamental interest for several research fields like for atomic and astrophysics as well as for plasma physics. To address this topic, a transverse electron target, dedicated to the FAIR storage rings, is under development.

Target Design

The transverse electron target uses a sheet beam of free electrons in crossed-beam geometry. This allows the realization of a small and flexible design with access to the interaction region for spectroscopy (fig.1, left). The electron beam is produced by an indirectly heated BaO cathode. The cathode has a length of 100 mm in ion beam direction and a height of 12 mm. To focus the sheet beam only electrostatic fields are used. For beam formation the cathode is surrounded by a Wehnelt electrode on negative potential relative to the cathode. The anode is the first of three electrodes placed in front of the interaction region. Another three electrodes with mirrored potential configuration are installed behind it. This design gives independency of the electron current from the electron beam energy and assures a symmetric potential distribution in the interaction region. The adjustable electron energy in the interaction region ranges between several 10 eV and a few keV. To gain a large solid angle for spectroscopy the electrodes next to the interaction region are shaped accordingly. Behind the second lens the electron beam is defocused, decelerated and dumped in a collector. For critical electrodes - such as the Wehnelt, the anode and the collector - water-cooling has been implemented. The other electrodes are cooled indirectly by their isolating aluminium oxide ceramics.

For absolute cross section measurements, the overlap between the electron and the stored ion beam has to be determined. Therefore a manipulator system with a stepper motor will be integrated in the setup (fig. 1, right). The target is vertically mounted on a CF160 flange upside down. A bellow allows the stepper motor to mechanically scan the electron beam through the ion beam.

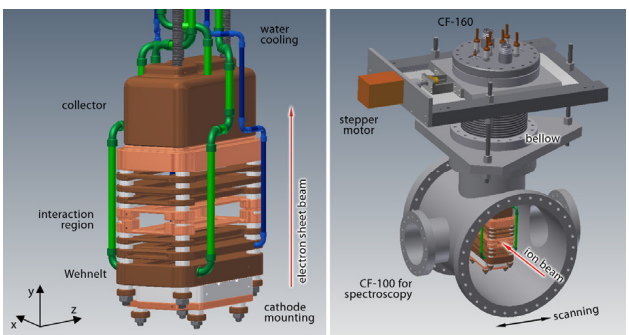

Fig. 1: The design of the transversal electron target (left). The mounted target with its manipulator system (right).

A control and interlock system monitors the water-cooling system, the vacuum system and the beam losses on the different electrodes to protect the target parts from heating by beam losses.

Simulation and beam parameter

To optimize the beam optics in the interaction region, simulations with the Amaze© code have been performed. They give a perveance for the electron target of 5.1 µA/V$^{3/2}$. In the interaction region the beam has a height of ~ 5 mm and a density of up to 10^9 electrons /cm^3 (fig. 2), both depending on the voltage setting. The example in figure 3 depicts the emittance of the beam for the direction of the crossing ion beam angle in direction toward the ion beam. Also investigations concerning the energy resolution and the line width in collisions experiments have been performed.

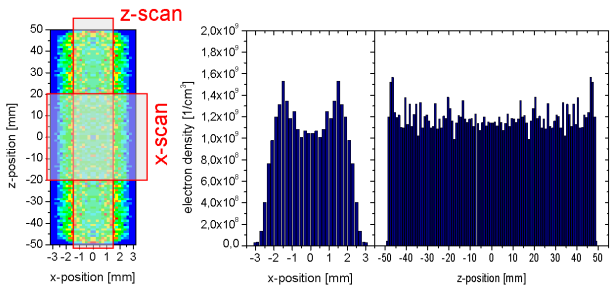

Fig. 2: Simulated cross section (left) and electron density profiles for the marked regions (right).

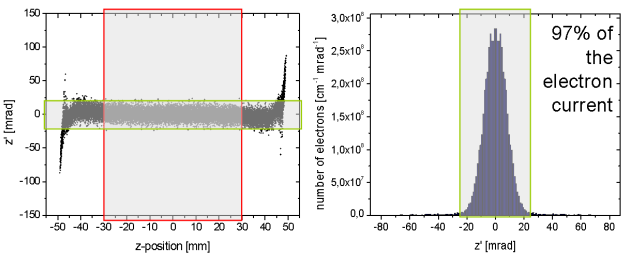

Fig. 3: Simulated emittance in direction of the ion beam (left) and the corresponding density distribution (right).

Summary and Outlook

All parts of the target are currently built at the IAP (Institut für Angewandte Physik) workshop. A test beam line for first characterization measurements of the target is already prepared. Experiments with molecule and ion beams from a volume source and an XEBIS are envisaged. Also the influence of the space charge of the electron beam on the ion optics in storage rings is part of further studies by simulations as well as subsequent measurements.

Simulation study of TNSA from a double-layer target

Zsolt Lecz[1], *Oliver Boine-Frankenheim*[2], *and Vladimir Kornilov*[2]
[1]TU, Darmstadt, Germany; [2]GSI, Darmstadt, Germany

For intensities of the PHELIX laser [1] the Target Normal Sheath Acceleration (TNSA) is the relevant acceleration mechanism. In our simulation work we found that the phase-space distribution of the accelerated proton beam strongly depends on the thickness of the contamination layer, deposited on the target surface. In this report we present a parameter-scan over the layer thickness in 1D geometry. The simulations were performed using the VORPAL PIC code [2].

The laser-produced relativistic electrons create strong charge separation field at the plasma surface. The spatial profile of the electric field is known analytically [3] and it allows us to set up the initial electron density profiles with thermal Boltzmann distribution. The temperature ratio of hot (h) and cold (c) electrons is $T_h/T_c = 20$ and the density ratio is $n_c/n_h = 5$. The target consists of heavy ions and a proton layer on the surface.

The electric field penetrating into the target can be approximated with an exponential function [3] with the scale length: λ_D/r where $\lambda_D = (\epsilon_0 T_h/(e^2 n_h))^{1/2}$ and $r = \sqrt{1+(n_c/n_h)(T_h/T_c)}$. The proton layer thickness should be compared to this length, therefore we introduce the dimensionless parameter:

$$D = \frac{rd}{\lambda_D} \qquad (1)$$

where d is the layer thickness. The quantity D characterizes the layer and defines in which regime will the protons be accelerated.

In Fig. 1 the resulting proton energy distribution is shown for different initial layer thicknesses. The main features of the two extreme cases are clearly visible: quasi-monoenergetic beam in the case of thin layer ($D \ll 1$, quasi-static acceleration [3]) and exponential energy distribution with large energy spread [4] in the case of thick layer ($D \gg 1$, plasma expansion).

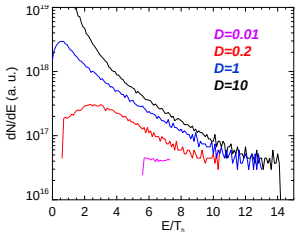

Figure 1: The energy spectrums of protons for different normalized layer thicknesses.

In the intermadiate regime the proton layer detaches from the target and expands in the Debye sheath, while it traps electrons, which means that the energy spread increases. Based on the work of Albright et al. [5] we could deduce an expression for the potential drop between the heavy target and the proton layer after detachment:

$$\varphi_d = 2\ln\left(e^{-\varphi_0/2} + \frac{\sqrt{2}n_h}{n_p(D/r + d_{min}/\lambda_D)}\right) \qquad (2)$$

where $d_{min} = \lambda_D n_p^{-1}\sqrt{2}/(e^{-\varphi_{min}/2} - e^{-\varphi_0/2})$, $n_p = n_c + n_h$ is the initial proton density and φ_0 is the potential at the surface of the heavy ion plasma. The minimum potential is defined by the maximum electron energy (ϵ_{max}): $-\varphi_{min} = \epsilon_{max}/T_h - 1$. In our simulations $\epsilon_{max} = 7.5T_h$ is arbitrary chosen. The potential is normalized to T_h/e.

The comparison of simulation results with our analytical estimation is shown in Fig. 2. We performed simulations with two plasma lengths: $L_p = 4\lambda_D$ (blue) and $L_p = 20\lambda_D$. The discrepancy at larger layer thicknesses is due to the different cooling time of the hot electrons.

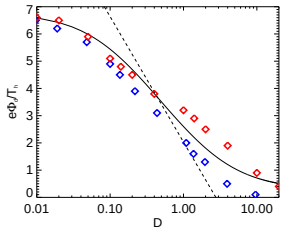

Figure 2: Potential drop measured from 2T simulations with $L_p = 4\lambda_D$ (blue) and $L_p = 20\lambda_D$ (red). The black full line represents Eq. (2) and the dashed line corresponds to the case, when $\epsilon_{max} \to \infty$.

The expression given in Eq. 2 can be used to estimate the energy conversion from the hot electrons to protons. If $D \ll 1$ the mean energy of the short bunch will be $-\varphi_{min}T_h/e$, while in the expansion regime the total energy of protons is the integral of the hot electron energy distribution form φ_d up to ϵ_{max}.

References

[1] F. Nürnberg, Journal of Physics: Conference Series **244**, 022052 (2010)
[2] Web page: http://www.txcorp.com/products/VORPAL
[3] M. Passoni et al., Phys Rev E **69**, 026411 (2004)
[4] P. Mora, Phys. Rev. Lett., **90**, 185002 (2003)
[5] B. J. Albright et al., PRL **97**, 115002 (2006)

The Ion-irradiation Induced Pan-nuclear H2AX Phosphorylation depends on the kinases ATM and DNA-PK*

B. Meyer[1], KO. Voss[1], G. Becker[1], A. L. Leifke[1], M. Durante[1,2] and G. Taucher-Scholz[1,2]

[1]GSI, Darmstadt, Germany; [2]TUD, Darmstadt, Germany

Introduction

DNA double-strand breaks (DSBs) elicit the phosphorylation of the histone H2AX around the break to form distinct γH2AX foci detectable by immunofluorescence microscopy. Additionally, heavy ion irradiation provokes H2AX phosphorylation across the whole cell nucleus, also in undamaged chromatin regions distant from the breaks. This pan-nuclear γH2AX is not connected to apoptosis, increases with dose [1] and is fully active only within few hours after irradiation [2]. At DSBs H2AX is phosphorylated by the phosphatidylinositol 3-kinase-related kinases ataxia telangiectasia mutated (ATM) and the DNA-dependent protein kinase (DNA-PK). We investigated the role of both kinases in the ion-induced pan-nuclear H2AX phosphorylation.

Results

Normal human fibroblasts were treated with either specific ATM or specific DNA-PKcs inhibitor, or simultaneously with both inhibitors. Dimethyl sulfoxide (DMSO) treatment served as a control. Cells were irradiated with xenon ions and the pan-nuclear γH2AX signal detected by immunofluorescence staining. In DMSO-treated cells nuclear-wide γH2AX formed and treatment with ATM or DNA-PKcs inhibitor did not eliminate the response (Fig. 1). Only the suppression of both ATM and DNA-PKcs fully impeded the pan-nuclear H2AX phosphorylation.

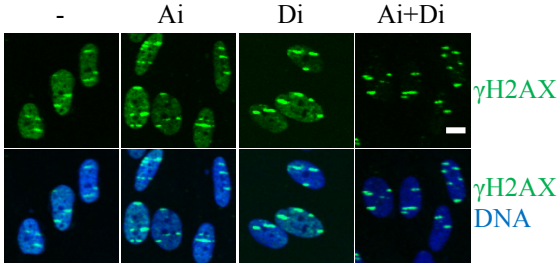

Figure 1: Pan-nuclear H2AX phosphorylation by ATM and DNA-PK. Confluent human skin fibroblasts were incubated with DMSO (-), ATM inhibitor (Ai, KU55933, 10 µM), DNA-PKcs inhibitor (Di, IC86621, 200 µM) or both ATM and DNA-PKcs (Ai+Di) inhibitor from at least 1 h before irradiation until fixation 1 h after irradiation. Cells were irradiated at low angle with xenon ions (8700 keV/µm, $3 \cdot 10^6$ p/cm^2) and γH2AX and the DNA (propidium iodide) detected. Scale bar: 10 µm.

The role of ATM and DNA-PK was further confirmed by the investigation of kinase deficient cell lines. While in ATM deficient human fibroblasts a pan-nuclear γH2AX was induced after ion irradiation, it could be suppressed by additional inhibition of DNA-PKcs (Fig. 2A). In DNA-PKcs deficient mouse embryonic fibroblasts (MEF) an ion irradiation-induced nuclear-wide H2AX phosphorylation was observed but was eliminated by treatment of these cells with ATM inhibitor (Fig. 2B).

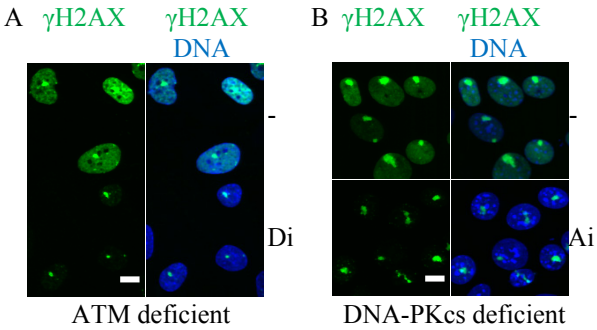

Figure 2: Pan-nuclear H2AX phosphorylation in ATM- and DNA-PKcs-deficient cells. (A) Human ATM-deficient fibroblasts (AT1BR) and (B) DNA-PKcs-deficient MEFs were irradiated at the heavy ion microprobe with 5 nickel ions (3800 keV/µm) targeted to 1 spot within the nucleus. Cells were treated with DMSO (-), DNA-PKcs inhibitor (Di) or ATM inhibitor (Ai) as in Figure 1. 1 h after irradiation γH2AX and the DNA (To-pro-3) were detected. Scale bar: 10 µm.

Conclusion

We show that the ion-induced nuclear-wide phosphorylation of H2AX is clearly dependent on both ATM and DNA-PK that also mediate H2AX phosphorylation at DSBs. The activity of only one of the two kinases is sufficient to induce pan-nuclear γH2AX. Our results suggest that high LET irradiation causes the nuclear-wide activity of ATM and DNA-PK which usually is locally restricted to chromatin areas surrounding DSBs. The impact of the nuclear-wide response on other repair factors is the matter of further studies.

References

[1] B. Meyer et al., "Characterization of the Nuclear-wide γH2AX Response after Ion Irradiation", GSI Scientific Report 2010, 2011, p.440

[2] B. Meyer et al., "Transient Ion Irradiation-induced Pan-nuclear H2AX Phosphorylation", GSI Scientific Report 2011, 2012, p. 492

* Work supported by BMBF Grant 02NUK001A.

X-rays-induced γH2AX accumulates at moderately transcribed genes*

F. Natale[1,2,#], Y. Yokota[3], M. Durante[1,2] and G. Taucher-Scholz[2]

[1]FIAS, Frankfurt; [2]GSI, Darmstadt; [3]Microbeam Radiation Biology Group, Japan Atomic Energy Agency, Takasaki

Introduction

Despite the DNA double strand break (DSB) marker γH2AX being extensively studied, its distribution in the context of diverse genomic features (e.g. transcription) is yet to be fully elucidated. Several indications suggest that gene transcription may hinder γH2AX propagation, altough most of the data were collected after endonuclease-induced DSB[1].

We previously showed that γH2AX distribution after exposure to ionizing radiation (IR) is positively correlated to GC usage[2] and, thus, gene content. To investigate the effect of gene transcription (TX) on γH2AX spreading during different stages of DNA damage response (DDR) to IR, we have measured γH2AX levels at nine specific loci on human chromosome 1 presenting different TX levels.

Methods

Unsynchronized HepG2 cells were exposed to 10 Gy X-rays (250 kV, 16 mA, 2 Gy/min) and incubated for 0.25, 0.5, 3 and 24 hours to allow γH2AX propagation and DSB repair. The DNA associated to γH2AX-enriched chromatin fractions was collected as previously described [2] and employed for quantitative PCR analysis. 31 primer pairs were designed on five regions of human chromosome 1, presenting different GC content and TX levels. Serial dilutions of genomic DNA were used to set standard curves and estimate the amplification efficiency for each primer pair. Only primer pairs showing efficiency higher than 84% and no primer-dimer amplification were selected for further studies. Such cut-off reduced the number of selected primer pairs to 9.

TX levels of the selected loci were retrieved from publicly available database under the accession number GSE30240.

γH2AX accumulates at moderately but not at highly transcribed genes

First, we assigned each primer pair to "genic" or "non-genic" groups. 3 out of 9 primer pairs were designed in non-genic regions; thus, the corresponding TX value was considered null. Primer pairs designed in genic regions (6 out of 9) were then assigned the TX value of their corresponding genes.

Next, we quantified the amount of γH2AX-associated DNA at the different loci, during early (0.25, 0.5 hours), middle (3 hours) or late (24 hours) stages of DDR (Fig. 1). We found that during the early stage, non-genic rgions are poorly modified by γH2AX, while moderately transcribed genes (TX levels ranging from 3 to 4 arbitrary units) showed a five-fold accumulation of the phosphorylation marker. Notably, highly transcribed genes (TX levels >4) showed low γH2AX levels, which were comparable to those observed under physiological conditions in both non-genic regions and highly transcribed genes, though a two-fold accumulation in moderately transcribed genes was still observed. During the late stage of DDR, γH2AX levels were even lower than those observed under physiological conditions.

Figure 1

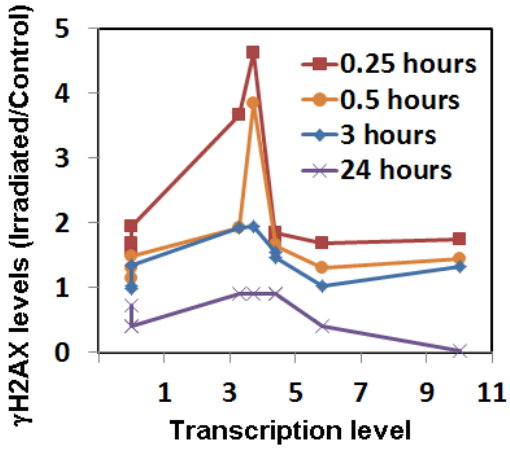

Figure 1: γH2AX levels at indicated times post IR relative to γH2AX levels under physiological conditions. TX levels are indicated in arbitrary units.

Conclusions and Perspectives

In this preliminary study, we showed that TX affects γH2AX distribution post IR. Namely, high TX levels hinder γH2AX propagation, while moderate levels are more permissive. Similarly to highly transcribed genes, non-genic regions are poorly permissive to γH2AX propagation. Such similarity may originate from different reasons. On the one hand, high TX rate may induce nucleosome remodelling and histone H2AX eviction, ultimately leading to lower γH2AX levels. On the other hand, non-genic regions present a lower nucleosome density which translates in low γH2AX levels.

References

[1] J. S. Jacovoni *et al.*, "High-resolution profiling of gamma-H2AX around DNA double strand breaks in the mammalian genome", EMBO J. 2010

[2] F. Natale *et al.*, "X-rays or heavy ions-induced γH2AX distribution is correlated to the GC content in the human genome", GSI Report 2011

* Work supported by Beilstein Stiftung (NanoL project)

f.natale@gsi.de

The histone H2AX does not inhibit resection of DNA double strand breaks induced by heavy ions

N. B. Averbeck[1], O. Ringel[1], B. Jakob[1], A. L. Leifke[1], G. Becker[1], M. Durante[1, 2], and G. Taucher-Scholz[1, 2]

[1]GSI Helmholtzzentrum für Schwerionenforschung GmbH, Darmstadt, Germany;
[2]Technical University Darmstadt, Germany

The histone H2A variant H2AX plays an important role in the repair of DNA double strand breaks (DSBs) within eukaryotes. Very rapidly upon DSB induction this H2A variant becomes phosphorylated at Ser139 [1]; H2AX phosphorylated at this site is named γH2AX. It serves as a platform for several DSB repair factors [reviewed in 2] and further is thought to stabilize the loose ends of a DSB [3]. In addition, γH2AX controls the end processing of recombination activating gene (RAG) endonuclease induced DSBs within V(D)J recombination, which takes place in the G1 cell cycle phase of lymphocytes. Absence of γH2AX within this process allows CtIP-mediated DSB resection [4]. Hence, γH2AX prevents resection within the V(D)J recombination and it is conceivable that resection of genotoxic caused DSBs is as well under the control of γH2AX [4], especially in the cell cycle phase G1 when DSB resection would lead to genomic instability.

Studies here at GSI clearly demonstrated that CtIP-driven resection of heavy ion induced DSBs occurs not only in the late S and G2 cell cycle phase but in G1 as well [5] sustaing the notion that resection of ion induced DSBs in G1 is not inhibited by γH2AX. This is further supported by the observation that in ion irradiated confluent human fibroblasts (AG1522D) (figure 1), where 98 % of cells were in the G1/G0 cell cycle phase, most DSBs are resected and the resection marker pRPA always colocalizes with γH2AX at ion induced DSBs. There was not one cell where RPA was recruited to a break site where H2AX was not phosphorylated. This was observed in three independent experiments (2x ^{238}U irradiation, LET: 15 000 keV/µm, fluence: 3 x 10^6 p./cm^2; 1x ^{207}Pb irradiation, LET 13500 keV/µm, fluence 3 x 10^6 p./cm^2). Thus, γH2AX seems not to inhibit DSB resection of heavy ion induced lesions.

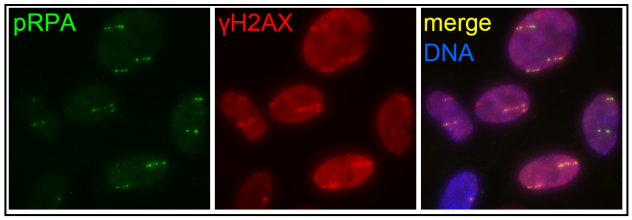

Figure 1: **Resection of ion induced DSBs is never observed independently of γH2AX.** Confluent human fibroblasts were irradiated with ^{207}Pb ions (LET: 13500 keV/µm; fluence: 3 x 10^6 p/cm^2) and fixed 1 h after irradiation. Cells were immuno-stained for γH2AX (DSB marker) and pRPA (resection marker). DNA was visualized by DAPI staining.

In order to further characterize whether or not DSB resection in G1 is controlled by H2AX and in particular by γH2AX we studied DSB resection in H2AX deficient cells. Murine H2AX -/- and wild-type cells were ^{12}C ion irradiated (LET: 170 keV/µm; fluence: 3 x 10^6 p/cm^2) and immuno-stained against RPA (resection marker) and 53BP1 (DSB marker) 1 h after irradiation. If γH2AX were inhibiting ion induced DSB resection in the G1 cell cycle phase one would expect that the H2AX deficient cells show an increase in resected DSBs. However, H2AX deficient and wild type cells both show about 20 % of resected DSBs. A different cell cycle distribution cannot be responsible for the obtained result as approximately 50 % of both populations were in the G1 cell cycle phase (determined by flow cytometry). As H2AX deficiency did not influence the fraction of resected ion induced DSBs in G1 we conclude that γH2AX indeed does not inhibit resection of heavy ion induced DSBs in cells within the G1 cell cycle phase.

Taken together, from these observations we conclude that H2AX most likely has no function in controlling end resection of genotoxic-induced DSBs. Its influence on DSB resection might, thus, be unique to V(D)J recombination.

References

[1] E.P. Rogakou *et al.*, DNA double-stranded breaks induce histone H2AX phosphorylation on serine 139, J Biol Chem, 273 (1998) 5858-5868.
[2] J. Yuan *et al.*, Focus on histone variant H2AX: to be or not to be, FEBS Lett, 584 (2010) 3717-3724.
[3] B. Yin *et al.*, Histone H2AX stabilizes broken DNA strands to suppress chromosome breaks and translocations during V(D)J recombination, J Exp Med, 206 (2009) 2625-2639.
[4] B.A. Helmink *et al.*, H2AX prevents CtIP-mediated DNA end resection and aberrant repair in G1-phase lymphocytes, Nature, 469 (2011) 245-249.
[5] N. Averbeck *et al.*, DNA double strand break resection after heavy ion irradiation, in: K. Große (Ed.) GSI Scientific Report 2011, GSI Helmholtzzentrum für Schwerionenforschung GmbH, Darmstadt, 2012.

Acknowledgements

This work is partially funded by the BMBF grant 02NUK001A.

Visualization of DNA double-strand breaks induced by heavy ions in murine tissues

M. Steinlage[1], S. Conrad[1], Michael Scholz[2], C. Fournier[2], G. Taucher-Scholz[2] and M. Löbrich[1]
[1]Darmstadt University of Technology, Germany; [2]GSI, Darmstadt, Germany

DNA double-strand breaks (DSBs) constitute the most lethal and hence the biologically most significant damage in response to ionizing radiation (IR). Particle radiation results in DNA damage that is more complex than the damage evoked by photon radiation, therefore these DSBs are repaired with much slower kinetics [1].

As part of the GREWIS project, the goal of this study is the biodosimetric measurement of inhaled radon gas in different mouse tissues. Radon (Rn-222) is a radioactive noble gas that has been used for its therapeutic anti-inflammatory effects in Central Europe for over a century. Patients with painful inflammatory or degenerative joint and spine diseases are treated in radon therapy caves in Bad Gastein and Bad Kreuznach [2]. During the radioactive decay of radon and radon progeny, three biologically relevant α-particles are emitted. In this project, the goal is to detect α-particle induced DSB tracks in various murine tissues to gain insight into the diffusion patterns of radon gas inside the body and information about potential accumulation in specific organs.

An ^{241}Americium source was used for preliminary *in vitro* experiments with α-particles. Due to the low penetration depth of α-particles, HeLa cells were seeded on Mylar® polyester film (2 µm thickness). The cells were irradiated with up to 300 mGy, and α-particle induced DNA DSBs were visualized by γH2AX immunofluorescence staining. We were able to successfully visualize tracks of DNA DSBs in HeLa cells after α-particle irradiation (Fig. 1 A).

Prior to *in vivo* radon experiments, wild type C57BL/6 mice were irradiated with low fluence carbon ions at the GSI particle accelerator. This experiment served as a positive control to assess the staining efficacy of heavy ion induced DNA DSB tracks in various murine tissues. Using 53BP1 immunofluorescence staining, paraffin embedded sections of murine brain tissue was analyzed. We were able to visualize ion tracks in brain tissue, especially in the granular cell layer of the cerebellum, as this region contains very densely packed cell nuclei (Fig. 1 B).

Future efforts will focus on the visualization and quantification of carbon ion induced DNA DSBs in other murine tissues, such as lung, kidney, and intestine. Upon completion of the radon exposure chamber, *in vivo* radon experiments will be conducted.

A) α-particle tracks in HeLa cells

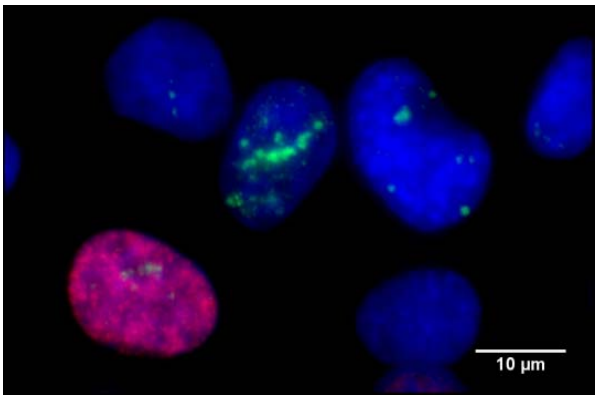

B) Carbon ion tracks in murine brain tissue

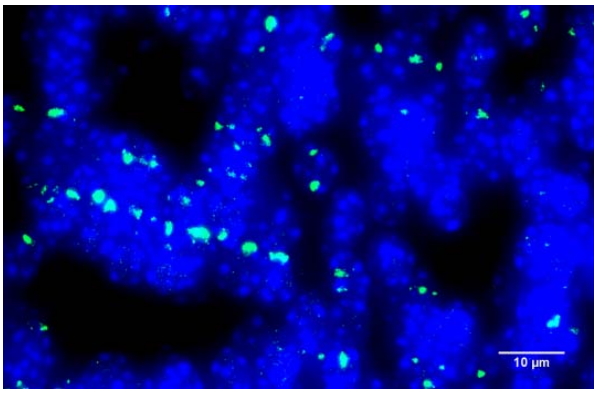

Fig.1: Visualization of DNA DSBs: (A) γH2AX foci in HeLA cells after α-particle irradiation. (B) Tracks of 53BP1 foci in murine brain tissue (granular cell layer of the cerebellum) after carbon ion irradiation.

References

[1] R. Okayasu. Int. J. Cancer:130 (2012) 991-1000
[2] K. Becker. Int. J. Low Radiation Vol. 1 (2004) 334-356

Funded by German federal ministry of research and education (BMBF/ 02NUK017E).

STED Microscopy of DNA Damage Markers*

M. Beuke[1], B. Jakob[1], T. Staudt[2], J. Engelhardt[2] , G. Becker[1], M. Durante[1,3], G. Taucher-Scholz[1,3]
[1]GSI, Darmstadt, Germany; [2]DKFZ, Heidelberg, Germany; [3]TUD, Darmstadt, Germany

STED (stimulated emission depletion) is a specialized form of immunofluorescence microscopy that overcomes the resolution limitations by diffraction. 1873 Ernst Abbe defined the diffraction limit [1] as:

$$\Delta d = \frac{\lambda}{2n \sin \alpha}$$

λ wavelength of light, n refractive index, α semiaperture angle of the lens.

With λ being typically between 400 and 700 nm and α < 70° this means, that classical light microscopy is limited to 200 nm resolution at its best.

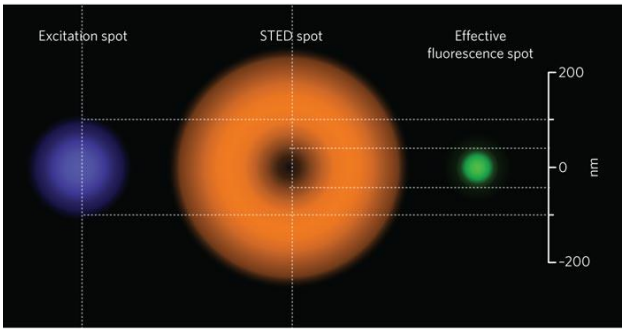

Figure 1: Coupling the excitation beam (blue) with a doughnut-shaped STED beam (orange) shrinks the fluorescence area (green) below the diffraction limit (200 nm). [2]

However, STED microscopy [3] makes use of the RESOLFT (reversible saturable optical fluorescent transitions) concept to reach below this barrier. A usual excitation beam is coupled with a doughnut-shaped STED beam depleting all of the fluorescence except of the emission of the very centre of the focus (Figure 1). By scanning with this sharpened spot across the sample images can be recorded with resolutions below the diffraction barrier.

53BP1 (p53 binding protein 1) shares common features with the commonly used DNA damage marker γH2AX [4]. Both are phosphorylated by ATM in response to ionising radiation (IR) and form IR induced foci (IRIFs) which colocalize.

Here, we show a biological application for the high resolution STED technique.

Results and Discussion

Recent work in our group [5] indicated that high resolution 4 Pi microscopy can provide a more precise insight in IRIF organisation. We tried to further improve this effort by making use of the STED microscopy. 53BP1 foci, which appear as large, homogeneous spots in confocal microscopy (Figure 2 A, red) show distinct substructure in STED microscopy (green). In our biological sample we were able to reach a resolution of 60 nm (Figure 2 B), well below the diffraction limit.

Future work will possibly be able to give a much deeper insight in IRIF organisation, DNA damage response factor recruitment and repair complex formation, especially by performing multi colour STED.

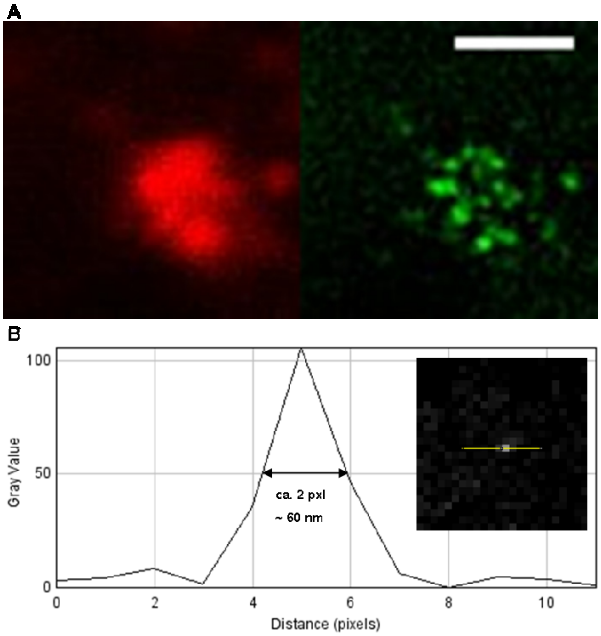

Figure 2: (**A**) MEF wt cells irradiated with Ne ions, 9.6 MeV/u, 460 keV/µm at UNILAC, fixed 1 h post irradiation. Red: 53BP1 confocal; green: 53BP1 STED. Scalebar 1 µm. (**B**) Focus measurement, full width half maximum ~ 60 nm.

References

[1] Abbe, E. (1873); Beitrage zur Theorie des Mikroskops und der mikroskopischen Wahrnehmung. *Arch. Mikr. Anat.* 9: 413–420.

[2] Alison Abbott (2009); Microscopic marvels: The glorious resolution. *Nature* 459, 638-639.

[3] Hell, S.W. et al (2006); Fluoreszenzmikroskopie ohne Beugungsgrenze. *BIOspektrum*, 12. Jahrgang

[4] Noon, A.T. et al. (2011); 53BP1-mediated DNA double strand break repair. *DNA Repair* 10, 1071-1076.

[5] Splinter, J. et al. (2010); Biological dose estimation of UVA laser microirradiation utilizing charged particle-induced protein foci. *Mutagenesis* 1-9.

*This work was partly supported by BMBF contract [02NUK001A].
This work is part of HGS-Hire.

Influence of the chromatin remodeler ACF1 on the dynamic behaviour of 53BP1 foci after heavy ion irradiation

A. Becker[1], B. Jakob[1], R. Khan[1], A.L. Leifke[1], G. Becker[1], M. Durante[1,2] and G. Taucher-Scholz[1,2]

[1]GSI, Darmstadt, Germany; [2] TU-Darmstadt

By exposure to heavy ion irradiation, a cell nucleus accumulates multiple double strand breaks (DSBs) along the ion traversal. DNA repair proteins accumulate at these lesions and can be detected as irradiation induced foci (IRIF) by fluorescence microscopy (Fig.1a). As it is still an open question how the outcome of DNA repair is influenced by the dynamic behavior of damaged chromatin, we investigated foci movement after irradiation with charged particles. By tracking of 53BP1-GFP foci over two hours using live cell microscopy we observed a random walk behavior in wt cells which leads to a mobility of damaged sites well below 1 µm per hour (Fig.1b) [1].

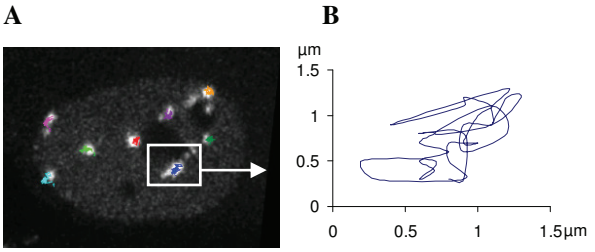

Figure 1: (a) U2OS cell expressing 53BP1-GFP 2 hours after irradiation with Cr ions (LET 2630 keV/µm). Movement of occurring foci is tracked and marked in different colours. (b) Motional trajectory of a 53BP1 foci over 2 hours in 2D.

To investigate if the motion of IRIFs is an active process relying on energy consumption, we depleted ATP 30 min before irradiation with heavy ions and tracked the motion of occurring 53BP1 foci. A strong reduction in mobility from 0.6 µm^2/h in wild type cells to a msd of 0.3 µm^2/h could be observed (Fig 2). This demonstrates a strong energy dependence of chromatin dynamics. However, ATP depletion might also influence the chromatin structure and compaction.

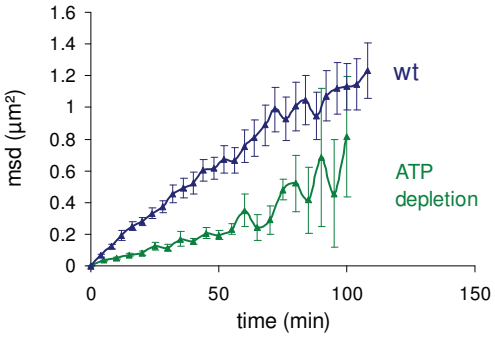

Figure 2: Mean square displacement (msd) of 53BP1 foci after irradiation with Cr ions in ATP depleted and wt U2OS cells.

To investigate the influence of changes in chromatin structure in more detail we knocked down the chromatin remodeler ACF1 which is involved in DNA repair, especially NHEJ, and contributes to chromatin relaxation [2]. By siRNA mediated knockdown of this remodeler, local decondensation should be diminished and thus DNA repair by NHEJ suppressed. As a result of the reduced decondensation, leading to a less opened chromatin network, we expected a more confined mobility. The msd plot of IRIFs after ACF1 knockdown as well as in wt cells is shown in Fig. 3.

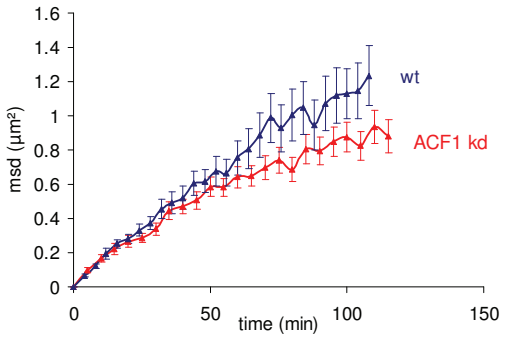

Figure 3: Mean square displacement (msd) of 53BP1 foci after irradiation with Cr ions (LET 2630 keV/µm) in ACF1 knockdown and mock treated U2OS cells.

A trend of a slight reduction in mobility can be observed in ACF1 knockdown cells. However this is presently not statistically significant. As there are many remodelers working together and in part redundantly way, it is highly probable, that a single knockdown does not create major differences in chromatin structure. In addition, chromatin alterations by the remodeler might be restricted to a smaller scale of only few nucleosomes, which would not influence the mobility of the whole IRIF significantly. Further experiments generating more pronounced changes in the chromatin are needed to solve the still open question in how far chromatin structure influences the foci mobility and if this mobility can be linked to the formation of chromosomal aberrations.

References

[1] B. Jakob et al., PNAS (2009)
[2] L. Lan et al., Mol. Cell (2010)

This work is part of HGS-HIRe and supported by DFG-funded Graduiertenkolleg (GRK 1657) TU-Darmstadt, BMBF Grant 02NUK001A and BMBF Grant 02NUK001C.

Active DNA Methylation Changes in Response to Ionizing Radiation*

M. Herrlitz[1,2], F. Natale[1,2], A.L. Leifke[1], M. Durante[1,2,3] and G. Taucher-Scholz[1,3]

[1]GSI, Darmstadt, Germany; [2]FIAS, Frankfurt Institute for Advanced Studies, Germany; [3]TUD, Darmstadt, Germany

Introduction

Eukaryotic DNA methylation, which consists in the addition of a methyl group on cytosine bases, is an epigenetic mechanism controlling a variety of biological processes. Previous work reported that ionizing radiation (IR) can induce epigenetic aberrations, including genomic instability [1]. Moreover, several attempts to correlate radiation-induced genomic instability to changes in DNA methylation patterns have been pursued. However, in these studies DNA methylation levels were measured several population doublings after exposure to IR [2]. Whether DNA methylation changes may take place also at short times post irradiation remains controversial. In this study we aim to investigate global DNA methylation levels in several cell types before and after exposure to IR. Preliminary results on fibroblast and tumor cell lines suggest that X-rays induce changes in global DNA methylation levels, even at short times (0.5 hours) after exposure. Both increased and decreased DNA methylation levels were observed which were dependent on the cell line.

Results

We investigated different cell lines for their global DNA methylation levels before and after irradiation with 10Gy X-rays (Fig.1). We observed that DNA methylation levels do not change in MEF (mouse embryonic fibroblasts), while decreasing in AG1522 (human foreskin fibroblasts) and HeLa and increasing in U2OS (human osteosarcoma cells), NFF hTERT (immortalized human fibroblasts) and HCT116 (human colorectal carcinoma cells).

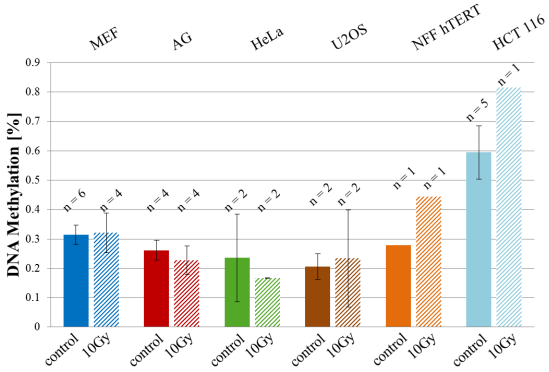

Figure 1: Fibroblast cell lines (MEF, AG1522 and NFF hTERT) or tumor cell lines (HeLa, U2OS and HCT116) were irradiated with 10Gy X-ray. Genomic DNA was isolated 30 minutes post irradiation and global DNA methylation analysis was performed using an ELISA-based technique quantifying 5-Methylcytosine colorimetrically. N indicates the number of experiments. 2 duplicates per sample were used. Error bar: standard error

Due to the different behaviour of the investigated cell lines, we thought that considering additional timepoints might reveal a common tendency of all cell lines towards DNA hypo- or hypermethylation. In a preliminary attempt we analyzed MEF and AG1522 cells. In MEF cells global DNA methylation increased 10 minutes and 3 hours after exposure to IR while 30 minutes and 24 hours after irradiation there was almost no change compared to control level. In contrast DNA methylation in AG1522 cells seemed to steadily decrease with increasing incubation time until the 3 hour timepoint. In both cell lines we observed complete (MEF) or partial (AG1522) recovery of DNA methylation after 24 hours relative to control level.

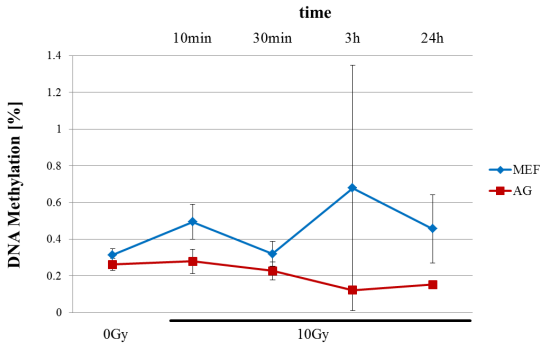

Figure 2: MEF and AG1522 cells were irradiated with 10Gy X-rays. DNA was isolated at the indicated timepoints and global DNA methylation was analyzed as described in Fig.1. Results for control, 10 min and 30 min are shown as mean for 3 experiments, results for 3h and 24h are from 2 experiments. 2 duplicates per sample were used in each experiment. Error bar: standard error

Conclusions

Our preliminary results show that global DNA methylation changes up to one duplication after irradiation are dependent on the cell line. While there is no clear tendency for methylation changes in MEF cells, a steady hypomethylation tendency is shown in AG cells. Further experiments are needed to elucidate methylation changes more closely and to characterize differences between different cell lines.

References

[1] Aypar et al. (2011) Int. J. Radiat. Biol., Vol. 87, No. 2, pp. 179–191

[2] Goetz et al. (2011) Radiation Research, Vol. 175, No. 5, p. 575-587

*Supported by the Beilstein – Institut, Frankfurt/Main, Germany, within the research collaboration Nano BiC
Work is part of HGS – HIRe and partially funded by BMBF grant 02NUK001A.

Apoptotic response to ionizing radiation in human skin cells.

P. Simoniello[1], J. Wiedemann[1,2], M. Stange[1], J. Zink[1], M. Durante[1,2], C. Fournier[1]

[1]GSI, Darmstadt, Germany; [2]TU Darmstadt, Germany

Numerous studies indicate that radiation exposure leads to inflammatory responses in skin cells and tissue [1, 2]. On the other hand, low doses of irradiation with α-particles emitted from a radon source exert anti-inflammatory effects in patients suffering from chronic inflammation. This indicates a complex dependence of the regulation of inflammation on radiation quality, dose and the interaction of irradiated cells with the tissue environment. In general the two major types of cell death, apoptosis and necrosis, are involved in processes related to inflammation [3]. In contrast to necrosis, apoptosis is a controlled process which leads to the elimination of the cells without triggering inflammation. In this project we want to investigate changes induced by ionizing radiation that are potentially related to induction or inhibition of inflammation in skin, i.e. the occurrence of apoptosis and the release of cytokines and other relevant factors.

Methods

To investigate the effect of different irradiation types, primary keratinocytes (NHEK; Lonza) and a human full-thickness skin equivalent (MatTek; Ashland) were irradiated with X-ray and carbon ions (186keV/µm).The effects were compared with previous results obtained in immortalized HaCaT cells. For each irradiation type a low dose and a high dose was used. Doses have been chosen to obtain nearly equivalent survival levels. 24 hours and 3 days after irradiation, cells were stained with DAPI to investigate changes in the morphology or fixed with 4 % of PFA. The skin equivalent was used for protein extraction with RIPA-Buffer or was fixed with Bouin's solution, dehydrogenated and embedded in paraffin. Serial sections (5 µm) of irradiated and unirradiated skin equivalents were stained with hematoxylin and eosin (H & E) according to commonly used procedures. In order to detect apoptotic cells, sections were stained with an antibody against cleaved caspase3 (Cell signaling). All sections were counterstained with hematoxylin. Protein extracts of monolayer cell culture and full thickness skin equivalents were used for Western Blot analysis.

Results and Discussion

In NHEK, no morphological changes indicating primary apoptosis could be detected in DAPI stainings 24 hours after irradiation with high doses of X-ray (fig.1). HaCaT cells respond similarly at this early time point, but 3 days after irradiation a significant amount of the cleaved form of caspase 3 was detected, indicating late apoptosis [4], whereas no cleaved caspase 3 could be detected in NHEK cells, also not after carbon ion exposure (data not shown). Growth kinetics analysis performed with NHEK suggests that the cells stop to proliferate after irradiation but do not undergo primary and late apoptosis (data not shown).

Fig. 1: DAPI stained cell nuclei of NHEK cells 3 days after X-ray irradiation (10 Gy).

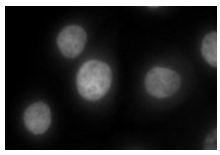

To compare the effects of ionizing irradiation on monolayer and 3-D cultures we irradiated a human full-thickness skin equivalent with different doses of X-rays and carbon ions. In our first experiments the cells of the human skin equivalent turned out to be very resistant to ionizing irradiation. After irradiation with a high dose of carbon ions or X-rays cleaved caspase 3 could not be detected in antibody stainings (fig.2) and Western Blot analysis (fig.3).

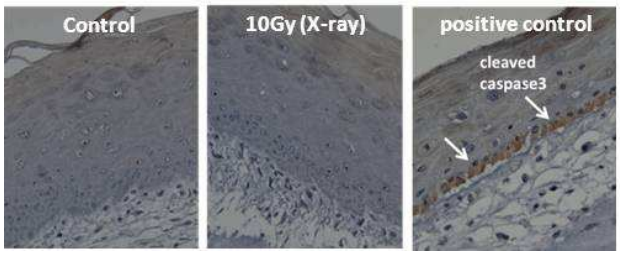

Fig. 2: Immunolocalization of cleaved caspase3 in EpiDermFT-400 3 days post irradiation with X-rays. Cells which express cleaved caspase 3 are indicated with a brown staining (arrows).

Fig. 3: Western blot analysis of Caspase-3 in skin equivalents 24hours and 3 days after irradiation with carbon-ions. PC: positive Control (Lysats of HaCaT cells 3 days after irradiation with 10 Gy of X-ray); kDa: Kilodalton; fl:full-length; cl: cleaved length.

Taken together, primary keratinocytes do not respond with early or late apoptosis to ionizing irradiation. This is in contrast to HaCaT cells that undergo secondary apoptosis after continued proliferation, probably due to mutated p53 in HaCat cells [5]. Epidermal keratinocytes of skin equivalents do not undergo apoptosis irrespective of dose and radiation quality.

We conclude that apoptosis of keratinocytes is not a direct trigger for pro- or anti-inflammatory responses in skin after exposure to ionizing radiation.

References

[1] Bogdandi et al. (2010), Radiat Res. 174:480–9.
[2] Varum et al. (2012), Radiat Res. 178. 591–599.
[3] Voll et al. (1997), Nature. 390: 350-351.
[4] Zink et al. (2011), GSI Scientific Report. 507.
[5] Boukamp et al. (1988), J. Cell Biol. 106: 761-771.

Work supported by GREWIS No. 02NUK017A, DFG (GRK 1657) and HGS-HIRe.

Biodosimetry of heavy-ion induced DNA double-strand breaks in murine tissues

J.Mirsch[1], A.Frohns[1], A.Maier[2], M.Scholz[2], G.Taucher-Scholz[2], S.Conrad[1] and M.Löbrich[1]

[1]Darmstadt University of Technology, Darmstadt, Germany. [2]GSI, Darmstadt, Germany.

Heavy ion irradiation is of special interest in radiobiology, clinical tumor therapy and space radiation research. Astronauts, for example, are exposed to solar and cosmic radiation consisting of energetic protons and high atomic number high-energy (HZE) particles. These particles contribute significantly to the radiation risk of long-term space missions. The damage distribution of HZE particles is distinct from that after X-rays, involving cells which are directly hit by the particle receiving fairly high doses (core) and cells in the surrounding area. These cells in the so-called penumbra are hit by δ-electrons and receive much lower doses (Figure 1A).

Recent work from our group has shown that cells in culture as well as in various tissues of living mice fail to repair DNA double strand breaks (DSBs) which are induced by few milli-Gray of X-rays [1,2]. In this study (grant number AO-10-IBER), we investigated if low doses of heavy ions also modify the DSB repair. For this we irradiated murine retina (*ex vivo*) and living C57BL/6 mice with low fluencies of HZE-particles (1 GeV/u $_{22}$Ti-or $_{28}$Ni-ions). Immunostaining of γH2AX and 53BP1 allowed us to find ion tracks in various tissues of irradiated mice as defined lines of γH2AX-foci as well as single δ-electron-induced DSBs in the penumbra. For first analysis we chose the murine retina as model tissue to follow an ion track though a cell multilayer because murine photoreceptor cells are uniformly arranged and tightly packed (Figure 1B). Currently we determine the lateral distance of each δ-electron induced DSB in the penumbra to the corresponding core track. Using the lateral distances of each DSB and each cell nucleus we will be able to calculate the dose distribution around the ion trajectory. The next step of our low dose study will be a repair analysis of δ-electron-induced DSBs in the penumbra in different tissues.

As a long-term goal, we plan to modify the cellular capacity to repair DSBs after low doses by pretreating cells and mice with agents that reduce or increase the intra-cellular radical level. These studies are of outmost importance to evaluate and modify the carcinogenic risk of HZE particle irradiation.

A) schematic figure

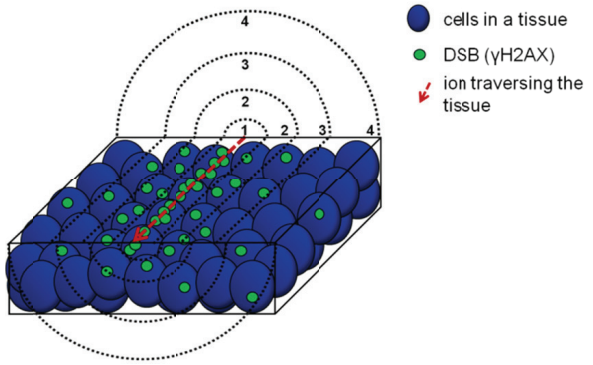

B) 3D model of image stacks

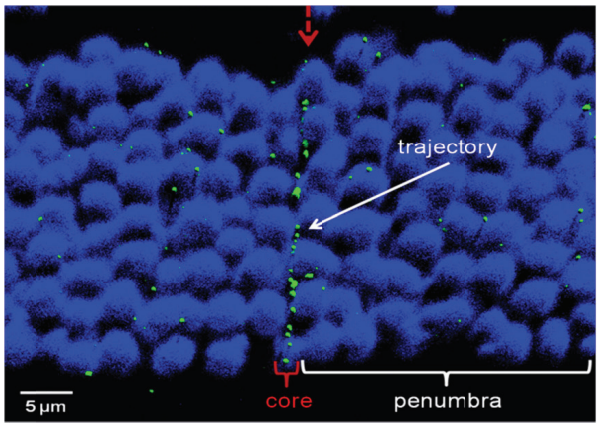

Figure 1: Schematic (A) and experimental figure (B) of a single ion crossing cells in a tissue. The numbered circles in the schematic figure indicate different dose-regions applied by δ-electrons in the penumbra of the ion track. The 3D model was calculated using image stack from a Ti ion (1 GeV/u, 114 keV/µm) crossing the murine photoreceptor cells. The core track (dashed arrow) can be visualized as a defined line of induced DSBs (γH2AX, green). DSBs induced by δ-electrons outside the core track (penumbra) are present. DNA was counterstained with DAPI (blue).

References

[1] K. Rothkamm and M. Lobrich, "Evidence for a lack of DNA double-strand break repair in human cells exposed to very low x-ray doses", PNAS 2003 April 29;100(9):5706-15

[2] Grudzenski et al., "Inducible response required for repair of low-dose radiation damage in human fibroblasts", PNAS 2010 Aug 10 107(32):14205-10.

Biological studies using the proton beam produced at the PHELIX laser at GSI

F. Tobias[1], O. Deppert[2], D. Pignalosa[1], G. Lenz[1] , P Hessel, [1]l S. Ritter[1], M. Roth[2], G. Kraft[1], and M. Durante[12]

[1]Department of Biophysics, GSI; [2]Department of Plasma Physics, GSI and TU Darmstadt

Developments in the field of laser-plasma-acceleration of ions have made progress over the last decades. It was proposed that this technique could replace linear and synchrotron accelerators used for therapy by smaller and more cost efficient devices [1,2]. However up to now progress is much slower and the necessary ion energies are neither in sight in near future nor a technique for a conform beam

However the very short pulses in the femto and pico second range make it interesting to use the existing ion beams from PHELIX to study fast reaction responses especially chemical and biochemical reactions [3,4]. Therefore we have continued the investigation of laser accelerated ion beams and established the necessary irradiation conditions for biological samples .

To extract the beam in air an re-entry tube with a 10 µm Ti vacuum window was constructed .Cells were mounted vertically in a special designed holder behind the Ti window. With this setup DNA damage and chromosomal aberrations in biological cells can be studied

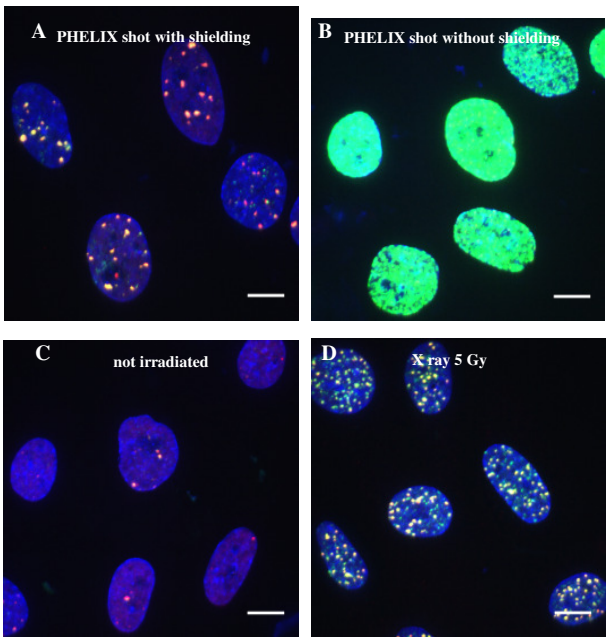

Fig 1: Foci analysis after PHELIX irradiation. Human Skin Fibroblasts (AG-D cells) were irradiated as indicated and fixed 2 h after irradiation. DNA was stained with DAPI (blue) and γH2AX (green) and 53BP1 (red) were stained with antibodies. A and B: DNA damage foci after PHELIX irradiation with and without shielding by a MD-V2 Gafchromic film; C: Not irradiated cells. D: Cells after X-ray irradiation with a dose of 5 Gy. Scalebar: 10 µm.

The foci assay is a method to analyze DNA damage. Results from experiments after PHELIX and X-ray irradiation are shown in Fig. 1. Cells were chemically fixed 2h after irradiation. After PHELIX exposure the cells showed a clear reaction forming gH2AX and 53BP1 foci. Shielding the cells with one MD-V2 Gafchromic film drastically reduced the cell reaction, but foci were still clearly visible. The comparison to the X-ray irradiated sample yielded doses well below and above 5 Gy in the shielded and unshielded case, respectively.

Besides the foci assay, analysis of chromosomal aberrations is certainly the most established method to quantify DNA damage. Results after PHELIX irradiation are shown in Fig. 2. Obviously the exposure to laser accelerated ions largely influences the chromosome structure and produces small chromosomal fragments.

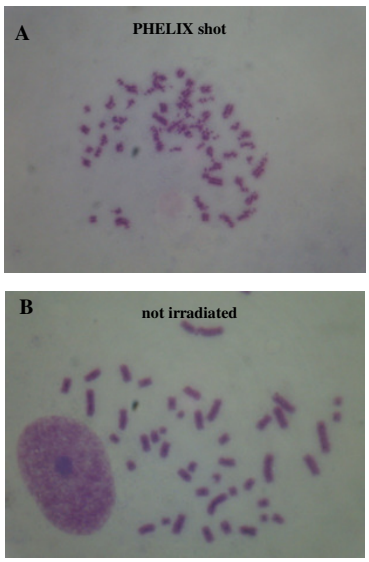

Fig 2: Analysis of chromosomal aberrations after PHELIX irradiation. Human Skin Fibroblasts (AG-D cells) were irradiated as indicated and fixed 2 h after irradiation: a large amount of chromosomal damage in form of small fragment is visible.

1. Fourkal E, Li JS, Ding M, Tajima T, Ma CM (2003). Medical physics 30: 1660–1670.
2. Ledingham KWD, Galster W, Sauerbrey R (2007) The British journal of radiology 80: 855–858.
3. Kraft SD, Richter C, Zeil K, et al. (2010) New Journal of Physics 12: 085003.
4. Fiorini F, Kirby D, Borghesi M.et al. (2011) PMB 56: 6969–6982.

Carbon ions and protons elicit an equal amount of late effects in irradiated rat lungs*

T. Dettmering[1], S. van der Veen[2], P. Simoniello[1], H. Faber[2], M. Durante[1], C. Fournier[1], R. P. Coppes[2], P. van Luijk[2]

[1]GSI, Darmstadt, Germany; [2]University Medical Center Groningen, The Netherlands

The application of charged particles such as carbon ions and protons in modern radiotherapy represents an important step towards a successful treatment of surgically untreatable tumors, such as in the head and neck region. A beneficial feature of charged particles is the *inverted depth dose profile,* which spares the normal tissue in the entrance channel, but deposits high doses inside the tumor [1]. As the development of particle therapy continues, new applications are emerging, for instance irradiation of moving tumors in the thorax with scanned particle beams [2]. In Germany, lung cancer ranks among the top three cancers with the highest mortality [3]. Efforts are being made to treat lung cancer using charged particles, but the normal tissue response to these radiation qualities is not well investigated. Selection of the appropriate charged particle for therapy of a specific tumor type—carbon ions or protons—requires knowledge about possible differences in the normal tissue response such as fibrosis in the patient. Here we investigated the response of lung tissue to doses of carbon ions and protons and scored the amount of fibrosis 10 months after irradiation in order to determine possible differences in the effect of both particles.

Materials and Methods

Groups of 3 (C-ions) or 5 (protons) adult male albino Wistar rats of the Hsd/Cpb:WU strain weighing 300 ± 10 g at the beginning of the experiment were irradiated at a physical dose of 18 Gy with 150 MeV/u protons or 270 MeV/u carbon ions. 50% of the lung volume was irradiated. After 42 weeks, animals were sacrificed and 5 µm lung slices were Hemotoxylin-Eosin (HE) stained and scored as described in [4]. Significance between datasets was assessed with the Mann-Whitney-U test, null hypothesis (protons and carbon ions elicit an equal amount of fibrosis) was rejected at $p < 0.05$.

Results and Discussion

Both radiation qualities elicited a fibrotic reaction in the radiation field (Fig. 1). A disorganization of the lung parenchyma was visible, with strongly damaged alveoli. Infiltrates containing inflammatory cells were visible in the tissue, which indicates a chronic inflammation. Blood vessels showed signs of edema and thickening of the *tunica media*. Qualitative assessment of the histological features did not reveal a difference of the morphology after exposure to carbon ions or protons.

Scoring of the lungs substantiated this assessment, as both qualities elicited an equal amount of fibrosis in the lung parenchyma (Fig. A, inset). Scoring for inflammation and vascular damage did not reveal a difference between both radiation qualities (not shown). The differences were also not significant in other dose ranges of carbon ions and protons (13–15 Gy physical dose).

We conclude that, comparing the same physical doses of carbon ions and protons, typical late radiation damage is elicited in the rat lung at a comparable severness, which predestines both radiation qualities for lung cancer treatment. This first result provides a basis for further studies of late effects of both radiation qualities, where more doses and additional endpoints will be taken into account.

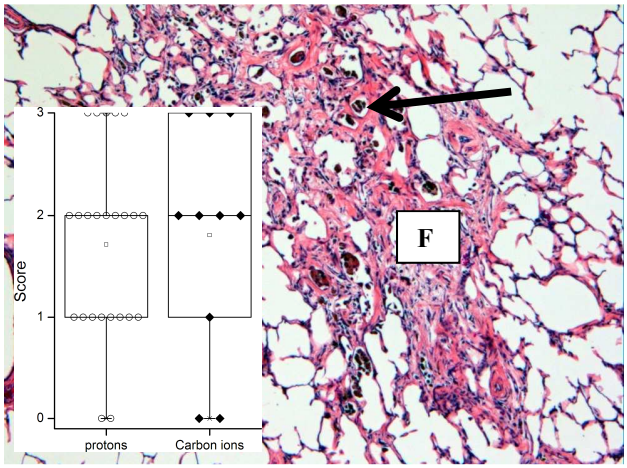

Fig. 1: Representative example of a fibrotic reaction in HE stained lung tissue irradiated with 18 Gy carbon ions. The alveolar structure is disrupted by a fibrotic clot (F). Inflammatory cells can be observed (arrow). Inset: Scoring results for fibrosis in tissue irradiated with protons (left) and carbon ions (right).

References

[1] M. Durante, J.S. Loeffler (2010). Nat. Rev. Clin. Oncol 7 37.

[2] Bert, C., M. Durante (2011). Phys Med Biol 56(16): R113-144.

[3] German Cancer Research Society, Heidelberg. 2010 data.

[4] Coppes, R. P., C. T. Muijs, et al. (2011). Int J Radiat Oncol Biol Phys.

* *Supported by HGS-HIRe and grant CBR-754842 from the University of Groningen*

Comparison of anti-inflammatory effects between UV and ionizing radiation in co-cultures of macrophages and lymphocytes*

J. Klinger[1], F. Engert[1], U. Gaipl[3], B. Frey[3], M. Durante[1,2], C. Fournier[1],
[1]GSI, Darmstadt, Germany; [2]TU Darmstadt, Germany; [3]Universitätsklinkum Erlangen, Germany

Introduction

Chronic inflammatory diseases such as arthritic disorders are efficiently treated by irradiation with low doses of photons or α-particles [1,2]. However, the molecular and cellular background of the anti-inflammatory effects by low dose irradiation remains widely unknown. It was shown that the phagocytosis of UV induced apoptotic cells has an immunosuppressive effect on human macrophages, monocytes or leukocytes [3,4,5]. Up to now, the immune-suppressive effects of ionizing radiation have not been investigated yet. In the present work the question was raised if the induction of apoptosis through ionizing radiation would have the same effect on human macrophages as described for UV irradiation. To achieve this goal a simple phagocytosis assay of mature macrophages and apoptotic lymphocytes was established for a quantitative measurement of cytokine release.

Materials and Methods

Mature macrophages were generated by *in vitro* differentiation for 7d with M-CSF [50ng/ml]. For the phagocytosis assay human peripheral blood lymphocytes (PBL) were irradiated using X-rays (250kV, 16mA) or UV-B. After irradiation PBL and macrophages were co-cultured for 20h. For all experiments macrophages were cultured alone as controls for the cytokine release of the monocultures. After co-incubation the supernatant was removed, centrifuged und subsequently stored at -80°C. The remaining unbound PBL were removed by washing with PBS, afterwards macrophages were detached and the cell number was determined. The concentration of the cytokines: TGF-β and IL-10 (anti-inflammatory) and TNF-α (pro-inflammatory) were measured with ELISA technique (eBiosciences), according to the manufacture instructions.

Results and Conclusion

The results for the release of TGF-β, IL-10 and TNF-α of the co-cultures are shown in figure 1. For a better comparison between unirradiated and irradiated samples, the released amount of cytokines was normalized on the cell number of each sample. The results are shown as relative cytokine release, in which the release of the monocultures of macrophages was set as 1. The concentrations of the three cytokines were ranging from: 130-220pg (TGF-β), 24-220pg (IL-10) and 2-4pg (TNF-α). As can be seen from figure 1 only minor changes could be detected for the release of TGF-β and TNF-α. However the release of IL-10 was remarkably increased (6 fold) after co-incubation of macrophages with apoptotic PBL which were irradiated with UV-B (180mJ/cm²), while irradiation with X-rays (6Gy) had no effect on the IL-10 release.

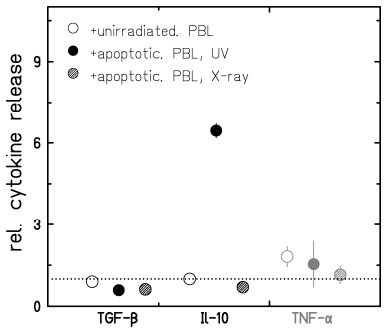

Figure 1: *Relative cytokine release of human macrophages, co-cultivated with unirradiated- or apoptotic PBL. Apoptosis was induced by irradiation with X-ray (6Gy) or UV-B (180mJ/cm²)). Co-incubation was performed for 20h. Error bars are shown as SEM.* (N=2, n=4)

The observed increased release of the anti-inflammatory cytokine IL-10 by macrophages after co-incubation with PBL, that were apoptotic after UV-B exposure is in good agreement to published data [4]. However this effect could not be observed after irradiation with X-rays, where overall no modification of the cytokine release related to immune-suppressive effects was observed. Taken together, or results clearly show differences between X-rays and UV-B in their immunosuppressive effect.

A possible reason for the huge differences of the IL-10 release might be a different amount of induced late apoptosis or necrosis of the PBL. The relatively high UV-B irradiation caused a much higher induction of late apoptosis and necrosis in PBL compared to X-ray irradiation. For UV-B irradiation after 24h almost 90% of the cells were late apoptotic or necrotic, whereas for X-ray irradiation only 40% were apoptotic, without any necrotic cells. The higher amount of apoptotic or necrotic cells following UV exposure at the investigated time point may lead to an increased phagocytotic activity of the macrophages which in turn could influence the cytokine release. These questions will be assessed in future experiments.

References

[1] Seegenschmiedt et al., *Strahlenther. Onkol.* 180: 718-730 (2004).
[2] Falkenbach et al., *Rheumatol Int.* 25(3): 205-10 (2005)
[3] Fadok et al., *J. Clin. Invest.* 101(4): 890–898 (1998)
[4] Voll et al., *Nature* 390(6658): 350–351 (1997)
[5] Munoz et al., *J. Leukoc. Biol.* 81(1): 6–14 (2007)

*Work is supported by HGS-HIRe, FOI Gastein (Austria) and financed by BMBF (GREWIS, 02NUK017A)

Cytogenetic analysis of mouse bone marrow cells after radiation exposure *

N. Paz[1], J. Kramer[2], F. Frohns[2], M. Durante [1, 2], E. Nasonova [1,3]and S. Ritter[1]

[1]GSI, Darmstadt, Germany; [2]TU, Darmstadt, Germany; [3]JINR, Dubna, Russia

Chromosome analysis is an established technique to estimate the absorbed dose and to assess radiation risk. Most studies rely on damage produced in peripheral blood lymphocytes that represent mature cells. Yet, little information is available on the damage produced in their progenies that are found in the bone marrow. Studies in mice have shown that genetic background and dose play a role in the immediate induction of aberrations in bone marrow cells and in maintaining genetic stability [1-3].

To contribute to this issue we examine the quantity and the quality of chromosomal damage induced in mouse bone marrow cells by X-rays, α-particles or heavier ions. First, we optimized the isolation and in vitro cultivation of bone marrow cells for chromosome analysis (Fig. 1). Bones (femurs and tibias of hind legs) from C57BL/6 and rhodopsin (*Rho*) mutant mice were kindly provided by Prof. Layer (TU-Darmstadt). Both femurs and tibias were dissected and bone marrow cells were isolated by repeated flushing with culture medium. From each bone marrow specimen one culture was set-up in 4ml medium, respectively.

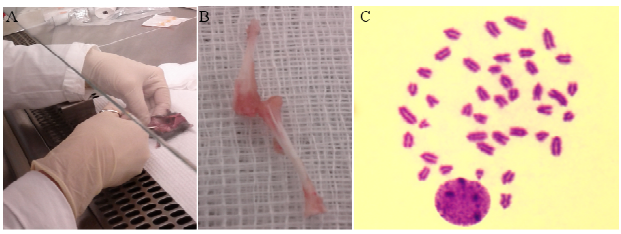

Figure 1: Isolation of bone marrow cells for chromosome analysis. (A) Preparation of bones, (B) Isolated femur and tibia, (C) Giemsa stained chromosome sample of bone marrow cells.

Cells were exposed in a flask to 1Gy X-rays (135kV, and 33,7mA) and chromosomes were prepared directly after exposure as well as 2, 6, 8, 24h post-irradiation. Briefly, colcemid (0.25µg/ml) was added to the culture medium 1h prior harvest to accumulate metaphase cells. Hypotonic treatment (0,075 M KCl) was performed at room temperature for 10 min. Then, cells were fixed with methanol and acetic acid (3:1) and dropped onto wet slides. Samples were stained with 3% Giemsa (Fig. 1C) and the mitotic index was determined. At 2h and 6h post-irradiation the mitotic index was <0.5%, while at 8h and 24h about 1.4 and 1.6% reached mitosis. Based on these measurements samples collected at 8h and 24h were selected for aberration scoring.

In *Rho* mutant mice the proportion of aberrant cells was 45% at 8h and increased to 68% at 24h post-irradiation (Fig. 2A). At both time points the most frequent aberrations were chromatid-type breaks accounting for 88% and 81% of all aberrations. On the other hand, 40% of the bone marrow cells of C57BL/6 mice were aberrant at 8 and 24h, respectively. At 8h the majority of aberrations (i.e. 87%) were chromatid-type breaks as observed in the mutant strain, but at 24 h this proportion decreased to 44% and chromosome-type aberrations such as chromosome-type breaks and dicentrics dominate. For a more detailed karyotype analysis the multicolour fluorescence in situ hybridisation technique (mFISH) is currently being used. An example is shown in Fig. 2B

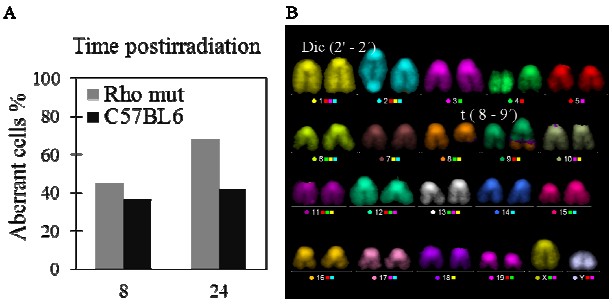

Figure 2: Cytogenetic analysis: (A) Percentage of aberrant cells measured at 8 and 24h post-irradiation following Giemsa staining (B) C57BL/6 bone marrow metaphase cell harvested 24h after exposure to 1Gy X-rays visualized with mFISH. The cell has 41 chromosomes and a dicentric chromosome (dic 2'-2') and a translocation (t (8-9') are indicated by an arrow.

The observed differences in the aberration spectrum at 24h post-irradiation point to a shorter cell cycle time of C57BL/6 bone marrow cells compared to the rho mutant cells, because aberration types reflect the duplication status of the chromosomes at the time of exposure. The appearance of only chromosome-type aberrations indicates that the cell was exposed in G0 or G1. Chromatid-type aberrations are formed when the affected chromosome region is already split or duplicated, i.e. during S or G2 phase. Yet, it cannot be excluded that a subset of C57BL/6 bone marrow cells has already undergone cell division. To account for the cell cycle effects, we are currently establishing a technique that allows both aberration analysis and identification of cells that were in S-phase at the time of exposure.

References

[1] G. E. Watson et al, Int. J. Radiat. Biol 71 (1997)
[2] M. A. Kadhim, Oncogene 22(2003)
[3] K. N. Rithidech et al, Dose-Response 10 (2012)

* Work supported by BMBF, grant 02NUK017A.

Does Radon act via the cholinergic anti-inflammatory signaling pathway in arthritic mice and mesenchymal stem cells?

Gopenath Thangaraj[1], Claudia Fournier[2], Paul G. Layer[1]
[1] Technische Universität Darmstadt, Germany; [2] GSI, Darmstadt, Germany

Introduction

Treatment with Radon is believed to suppress the severity of the autoimmune disorder *Rheumatoid Arthritis* (RA). Thereby, associated with excess pain, cartilage undergoes severe destruction and synovial fluids accumulate in the joints. One of the mechanisms supposedly involved in RA is the *cholinergic anti-inflammatory pathway* (CAIP). Roles of the cholinergic system in CNS functioning are well established. But also, non-neural, e.g. developmental functions of the cholinergic system are now well accepted. Recently, we have shown improper formation of cartilage in an AChE/BChE double knockout mouse, thus providing evidence for the involvement of cholinesterases in cartilage development (J. Klaczinski, Dissertation 2012). In AP6 of the GREWIS project, we analyse the effects of Radon treatment on the expression of cholinergic components (ACh receptors, particularly the α7-nAChRs, a main player of CAIP, and AChE, ChAT) during the formation of cartilage, both *in vivo* and *in vitro*.

Materials and Methods

11 day-old pregnant mice and chicken embryos up to stages HH23 are used. Mesenchymal cells were isolated from limb buds of both mouse and chick embryos, plated as high density micro-mass cultures and incubated for 2 weeks at 37°C. Also, human primary osteoblast cells were cultured until passage 4 and collected for mRNA isolation. Alcian blue staining marks cartilage development, while Alizarin red and alkaline phosphatase stainings indicates differentiation of osteoblasts. Cholinesterase enzyme activity was visualized by Karnovsky-Roots staining. cDNA was synthesized and used for PCR analysis.

Results

Human primary osteoblast cells express an entire set of cholinergic components

First results showed that human osteoblast cells expressed cholinesterases (AChE and BChE); they also synthesize ACh and express both muscarinic and nicotinic ACh receptors (Fig. 1), suggesting the involvement of an entire cholinergic system in the differentiation of osteoblasts.

Fig. 1: PCR analyses of human osteoblast cells. *They express all tested cholinergic components.*

Micromass cultures as 3D *in vitro*-systems for cartilage formation

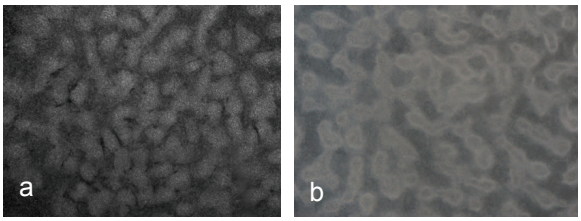

Fig. 2: Light microscopy of micromass cultures. *Chondrocytes condense to form nodules which later differentiate to osteoblasts, both for chick (a) and mouse mesenchymal cells(b). Such cultures will be exposed to radon and to analyze the effects on cartilage formation.*

Formation of cartilage in vitro

In mouse micromass cultures, cartilage formation starts as early as div 2, as visualized by Alcian blue staining. It rises until 6 days and drops from 8 days, when osteoblast differentiation takes over.

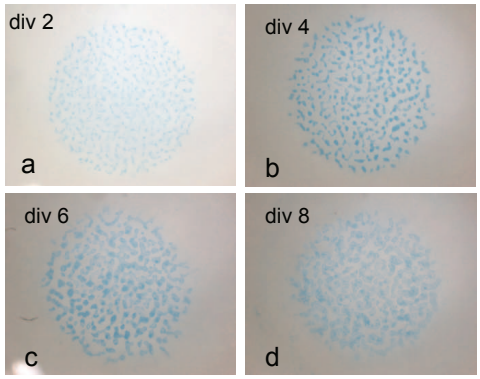

Fig. 3: *Cartilage nodules from mouse mesenchymal cells from div2-8, stained with Alcian blue.*

Cholinesterase activity during cartilage formation

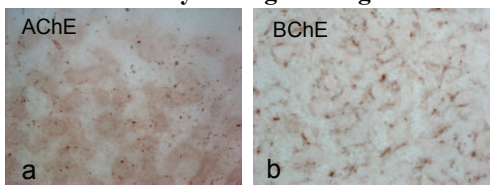

Fig. 4: *Note different expression patterns of AChE and BChE in mouse cartilage nodules after 4 div. AChE supposedly supports further osteoblast differentiation.*

Future work

Treatment of osteoblasts, MSC-derived chondrogenic cells (to be established) and micromass cultures with cholinesterase and nAChR inhibitors, +/- radon exposure. Correlate changes of cholinergic components with results of other APs (cytokines, NF-kB, TRP channels).

Work is funded by BMBF (GREWIS, 02NUK017A).

Dosimetry of the MicroLeman Collimated X-ray Setup for Cell Irradiation*

A. Tütüncü[1], R. Khan[1,2], M. Durante[1,2], G. Taucher-Scholz[1,2] and B. Jakob[1]

[1]GSI, Darmstadt, Germany; [2]TUD, Darmstadt, Germany

Introduction

Collimated x-rays may be used for subnuclear exposure of cells to ionizing irradiation to compare the biological response to that induced by charged particles. Collimation was done using wafer stacks of silicon or GaAs with etched groves in the order of some µm using the MicroLeman setup (Fig.1 left). To determine appropriate irradiation conditions for the evaluation of biological damage, we started to establish a spatially resolving dosimetry utilizing different radiochromic films and microscopic readout.

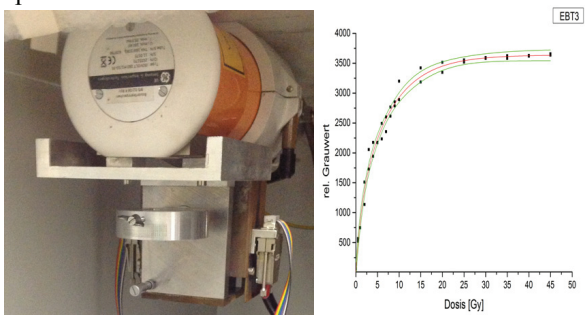

Figure 1: Left: X-ray tube G&E 160M1 equipped with the MicroLeman irradiator device. Right: Dose response curve of the EBT3 film for 35kV irradiation.

Method

Irradiation was done using a G&E ISOVOLT 160 M1 / 10-55 x-ray tube. Omitting the collimators, we recorded calibration curves at different tube voltages (20 to 35 kV) using Gafchromic EBT3 and MD-V2-55 radiochromic films and an ionization chamber as reference. Absorption changes of the films were measured either in 48-bit RGB modus of a Canon LIDE210 flatbed scanner (Fig. 2 left) or using the transmission channel in a Leica confocal microscope (Fig. 2 right and Fig 3 left).

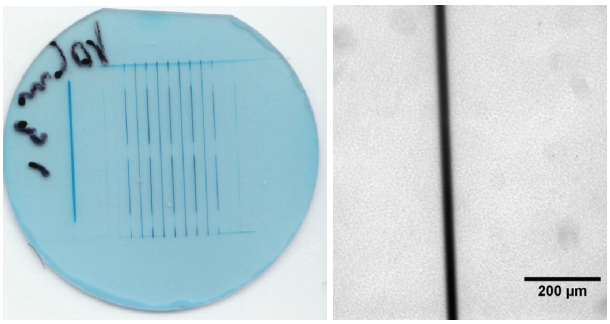

Figure 2: Left: EBT film irradiated for 3 min using the 10 µm GaAs collimator. Film was scanned with the scanner (left) or with higher resolution under the microscope (right).

Results

Recorded grey or colour values of the radiochromic films were plotted against the applied dose and fitted by exponential functions (Fig. 1). The EBT3 films showed a higher sensitivity compared to the MD-V2-55 (not shown), However a saturation behaviour above 12 Gy in EBT3 limits the usable range, whereas the MD V2-55 could be used up to doses of >100 Gy. The obtained calibration curves for different radiation energies (20-35 kV) allowed the assignment of the corresponding local dose using the different collimators (1 to 10 µm slits). Dose was colour coded for better visualization (Fig. 3).

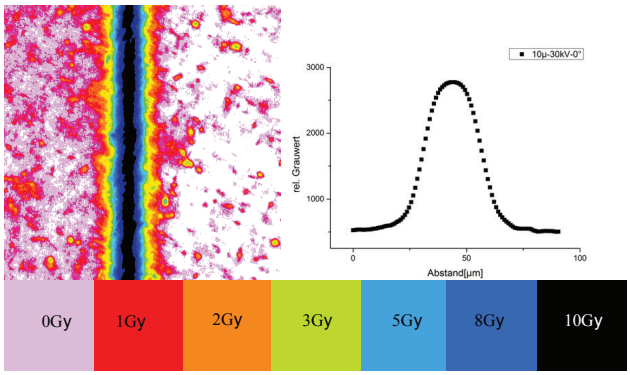

Figure 3: Left: High resolution microscopic image of the EBT film shown above. Colours indicate the applied dose Central dose exceeds 10 Gy whereas the dose in the shielded areas was below 1 Gy. The profile (right) showed a fwhm of around 30 µm for the 10 µm collimator.

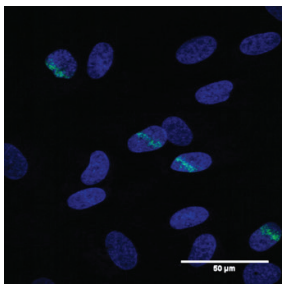

Figure 4: Irradiated AG1522 cells using the 1 µm collimator stained against γ-H2AX (green) and DNA (blue)

First cell irradiation experiments were done using the Microleman setup. Fig.4 exemplarily shows human fibroblasts irradiated with the 1 µm GaAs collimator for 5 min at 35 kV. A green band of γ-H2AX indicates the presence of double-strand breaks (DSBs) along the slit.

* Work supported by BMBF grant [02NUK001A and C]

Effects of heavy ionizing radiation on neuronal development, as analyzed in the retina of chick embryos

Florian Frohns[1], Margot Mayer[2], Marco Durante[1,3], Claudia Fournier[3], Paul G. Layer[1]
[1] Technische Universität Darmstadt, Germany; [2] University of Applied Sciences Aschaffenburg, Germany
[3] GSI, Darmstadt, Germany

Introduction

The developing central nervous system (CNS) is well known to be particularly sensitive against ionizing radiation. However, only little is known about the impact of high LET radiation on CNS development. Therefore we have developed an experimental approach to analyze the consequences of high LET radiation on the retina of chick embryos, as a comparably simple structured part of the CNS. Hereby, fertilized chicken eggs of different developmental stages become bombarded with heavy ion radiation, allowing us to investigate high LET effects on survival, proliferation and differentiation in an *in vivo* situation. To compare these effects with low LET radiation, control experiments with X-radiation have been carried out.

Materials and Methods

Fertilized chicken eggs were incubated for five or seven days, allowing chick embryos to grow to an appropriate developmental stage that is ideal for the analysis of the effects of radiation on retinal development. After five to seven days, irradiation was carried out with nickel or titanium ions (1GeV/u, see Fig. 1) or X-ray (135kV, 19mA), respectively. Doses that were used for the irradiation accounted between 1-2Gy. For the investigations of the effects, embryos were sacrified at defined time points after the treatment and eyes were harvested for retinal analysis by immunohistochemistry in paraffin sections. Determination of apoptotic events was done by counting of pyknotic nuclei, visualized by DAPI staining.

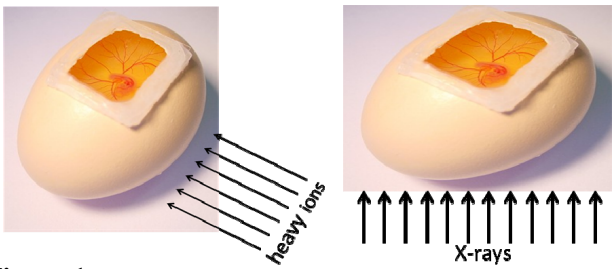

Figure 1: Irradiation setup for chick embryos with high and low LET-radiation. *For high LET treatment, fertilized chicken eggs were laterally scanned with the nickel- or titanium-beam, whereas for X-irradiation the X-ray-source was placed below the egg. Note that the embryo is localized at the top of the yolk. Therefore, a dosimeter was placed directly above the embryo to determine the applied dose during X-irradiation (not shown).*

Results and Conclusion

Preliminary results of our experiments showed that chick embryos are an adequate model system for heavy ion irradiation experiments. Both, five (E5) and seven (E7) day old embryos survived the high LET treatment and could be further incubated until the seventeenth day after fertilization.

No deviations from the phenotype of control embryos could be detected by first glance. However, the results from retinal analysis are still pending.

Control experiments with X-rays instead have already been analyzed for the impact of low LET radiation on cellular survival within the different embryonic stages of the retina, showing not only a time- but also an age-dependency in the occurrence of radiation-induced apoptotic events (see Fig. 1).

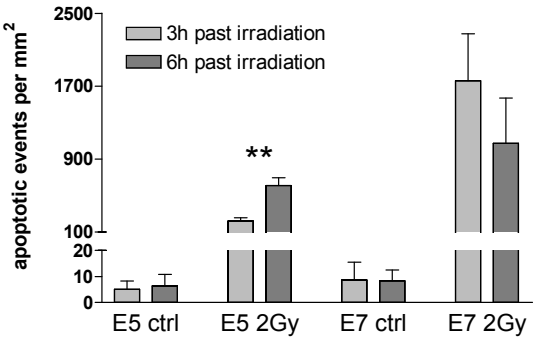

Figure 2: Time- and age-dependent occurrence of apoptotic events within the embryonic chick retina after low LET radiation. *Numbers of apoptotic events within were determined 3 and 6 hours after exposure to 2 Gy of X-rays by counting of pyknotic nuclei in DAPI-stained paraffin sections of the 5 and 7 day-old chick retinae.*

In fact, after 2 Gy of X-rays, the number of apoptotic events per mm^2 was doubled from 3 to 6 hours in 5 day old embryos. In contrast, apoptosis dropped from 1760 to 1072 events per mm^2 within the same time period in seven day old embryos.

Conclusion and Outlook

Our preliminary results show that the chick embryo is an appropriate model system to investigate the impact of high and low LET-radiation on the developing CNS in an *in vivo* situation. In further analyses, differences between comparable doses of high and low LET exposures will be determined, regarding not only survival, but also cell cycle regulation and/or radiation-induced cell cycle arrests as well as differentiation of retina-specific cell types.

Aknowledgements

We thank ESA-IBER for the funding of this project and Prof. M. Löbrich for providing X-ray facilities.

First electrophysiological studies on mouse embryonic stem cell-derived cardiomyocytes

M. Materna[1,2], A. Helm[1], P. Hessel[1], J. Frieß[3], C. Thielemann[3], D. Pignalosa[1], W. Mäntele[2], M. Durante[1,4] and S. Ritter[1,#]

[1]GSI, Darmstadt, Germany; [2] Goethe University Frankfurt/Main, Germany; [3]University of Applied Sciences Aschaffenburg, Germany; [4]TU Darmstadt, Darmstadt, Germany

There is emerging epidemiological evidence of an increased risk of adverse cardiovascular effects at low or moderate doses of ionizing radiation occurring many years after the exposure [1]. However, essentially no information is available on the potential cardiovascular effects associated with the exposure to heavy ions. To address this issue, we recently established in our laboratory an effective protocol for generating functional (i.e. beating) cardiomyocytes from mouse embryonic stem cells (mESC). In the present study, first electrophysiological measurements were performed employing microelectrode array chips (MEA).

Briefly, commercially available mESC (line D3) were differentiated by means of the hanging drop method [2]. ESC aggregate and form embryoid bodies (EBs). Seven days after initiation of the differentiation process, EBs were plated onto MEAs (1 EB/MEA). The MEAs used have a field with 60 electrodes arranged in an 8x8 grid. Each electrode has a diameter of 30 µm and the interelectrode distance spans 200 µm. The system allows non-invasive electrophysiological measurements. At day 10, EBs start beating, pointing to the formation of cardiomyocyte-networks. In general, the number of beating EBs increased during the subsequent days and declined around day 20. Western Blot analysis and histological staining of cardio-specific markers confirmed the formation of true cardiomyocytes. Accordingly, electrophysiological measurements were conducted between day 10 and 20.

Electrophysiological activity of untreated control samples was measured for 60 sec at a sampling rate of 10 kHz. The obtained data was then analysed with the MATLAB based program *DrCell* developed at the University of Applied Sciences Aschaffenburg [3]. The recorded data were analysed in terms of signal amplitude, shape and beat rate. Additionally, the origin of the signal, its spreading direction and velocity was registered and the number of active electrodes was determined. Representative recordings of the signal spreading, number of active electrodes and beat rate are shown in figures 1-3.

Detailed analysis of the data revealed that the cell system is highly variable; large differences were observed both within a sample and between samples. This is illustrated in figure 2 and 3, where changes in the number of active electrodes and in the beat rate are depicted for 2 EBs. Based on these results we conclude that mESC-derived cardiomyocytes are an unsuitable model system for studying the electrophysiological responses of cardiac cells after radiation exposure which are expected to be small.

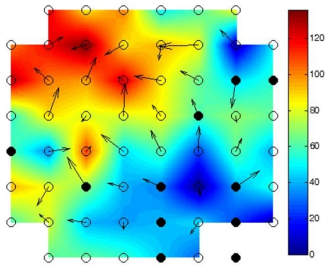

Fig. 1: Pseudocolor plot showing the delay time (ms) of action-potentials. One EB was seeded per MEA chip and 10 days after initiation of the differentiation electrical activity of cardiomyocytes was measured. Dark blue regions indicate the origin of the signal. Circles are electrodes.

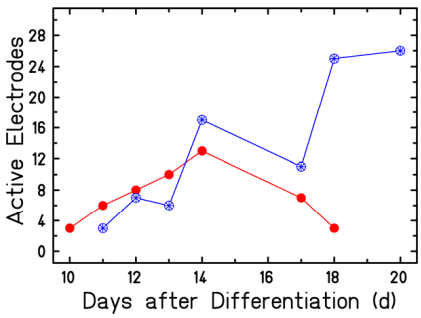

Fig. 2: Number of active electrodes during the observation period (day 10 to day 20). The graphs display recordings from 2 EBs.

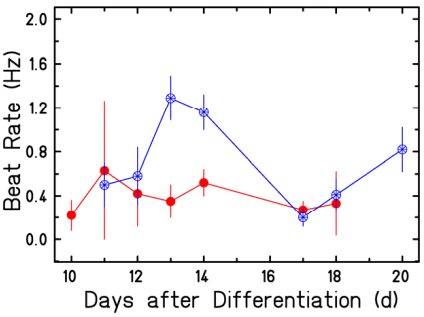

Fig.3. Beat rate of rhythmically contracting clusters in 2 EBs.

References

[1] Little et al., Radiat Environ Biophys, 2009, 49(2), 139-53
[2] Helm et al., GSI Scientific Report 2010, 455
[3] Nick et al., IEEE Trans. on TBME, submitted 2013

[#]s.ritter@gsi.de

*Funded by Euratom 7th Framework Programme (no.295823), Verein für Förderung der Tumortherapie mit schweren Ionen e.V. and HGS-HIRe.

First experiments using human embryonic stem cells as a model to examine radiation effects on early embryonic development: emphasis on gene expression

D. Pignalosa[1], S. Luft[1], O. Arrizabalaga[1], A. Helm[1], F. Natale[1], Durante[1,2], S. Ritter[1]
[1]GSI, Darmstadt; Germany; [2]TUD, Darmstadt, Germany.

Embryonic stem cells (ESC) are derived from the inner cell mass of the blastocyst and are characterized by an unlimited self-renewal capability. They are pluripotent due to their ability to generate all tissues and cell types of an individual. Because of their key biological role, it has been proposed that ESC have a strict control of their genome integrity to prevent the transmission of the genetic damage to their progeny. Indeed, there is that the repair of DNA damage is more precise in hESC than in their differentiated counterparts (e.g. [1]). Little is known about the effects of ionizing radiation (IR) on the developing human embryo and the few data available come mostly from the atomic bomb survivors (2). This hinders an accurate estimate of the risk from a prenatal exposure. To this end, human embryonic stem cells (hESC) represent an excellent model to investigate the effects of IR on early embryonic development.

Recently we set up the protocol for hESC cultivation (line H9), characterized the cell and performed first radiation experiments. Karyotype analysis of control cultures by means of the mFISH technique (fig.1, left) revealed a low percentage of cells with numerical or structural aberrations (1.7 ± 1.1 and 3.3 ± 1.6, respectively). Apoptosis was detected by flow cytometry based on caspase-3 activity. As shown in fig.1 (right) cells exposed to 1 Gy Ni-ions (1 GeV/n) showed a significant higher number of caspase-3 positive cells (6 fold) compared to the control. Additionally, we examined by flow cytometry the presence of the pluripotency marker SSEA4 in cells exposed to 1 Gy X-rays or Ni-ions and no statistical difference was observed up to 50h post-irradiation (data not shown).

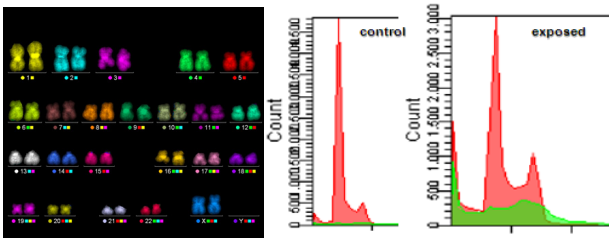

Figure 1: Normal karyotype of hESC visualized by the mFISH staining (left); Flow cytometric analysis of hESC immunolabeled against active Caspase 3 (green profile) and counterstained with DAPI (red profile) (right).

Since the signalling network of hESC is extremely intricate, the analysis of a few pluripotency markers is not conclusive. For a more detailed analysis of this complex network, gene expression profiling has to be performed. For that purpose we used the RT^2 Profiler PCR array system (Qiagen) that allows the analysis of the expression of 84 key genes involved in ESC maintenance and differentiation. Briefly, for RNA isolation sham irradiated and exposed cells were detached by 20 minutes incubation in 1% EDTA PBS, centrifuged, re-suspended in PBS and after another centrifugation stored at -80° in a tissue and cell lysis buffer (Epibio) with 0.3% proteinase K. RNA was harvested with the MasterPure™ Complete DNA and RNA Purification Kit (Epibio) following manufacturer's instructions. RNA concentration and purity were tested with a NanoDrop spectrophotometer and integrity was verified by agarose gel electrophoresis (Fig. 2, left).

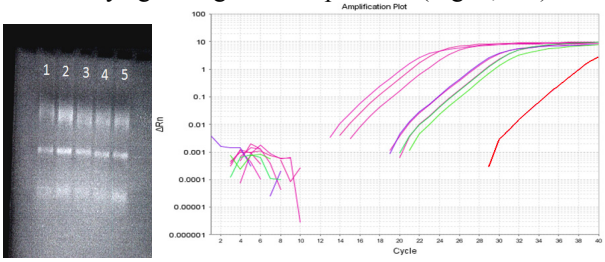

Figure 2: Agarose gel with RNA samples (left) from control (lanes 1-2, 5) and exposed samples (X-ray, lane 3 and Ti-ions, lanes 4). Amplification plot of representative genes from the Ti sample (right): The pink curves correspond to the housekeeping genes (ACTB, B2M, GAPDH, HPRT1, RPLP0), green curves represent genes for receptors (IL6ST, LIFR) and violet for transcription factor STAT3 involved in the pluripotency maintenance pathway. The red curve represents human genomic contamination.

The cDNA was obtained from 0.5 µg RNA using the RT^2 First Strand kit (Qiagen) following manufacturer's protocol. The cDNA from the exposed sample was used to test the first stem cell signalling RT^2 Profiler PCR array (Qiagen). A StepOne instrument (Applied Biosystem) was used to perform the real time PCR assay; data were collected and visualized with the Step One software.

After correction of the threshold line, the C_T (threshold cycle) values were examined and compared with the reference values reported by the manufacturer: no significant genomic DNA contamination was detected (Fig. 2, right, red line). The comparison between the C_T values for reverse transcription control and positive PCR control indicated that no inhibition of the reverse transcription occurred. The positive PCR control value is lower than the expected one reported in the manual. A high sensitivity of the Real-time cycler might be responsible for this discrepancy. Nonetheless, this deviation from the reference number is acceptable, if it is consistently observed in subsequent experiments. Further tests are needed to verify the reliability of the system used.

References

[1] Fung et al. 2011 Plos One, 6 (5): e20514.
[2] Streffer et al. 2003 Annals of the ICRP, 33: 5-206.

This work is funded by the BMBF, grant 02NUK025A

First irradiation results using the neurosphere formation assay

C. Hartel[1], Z. Yu[1,2,3], W. Weyrather[1], E. Kim[4], A. Giese[4] and M. Durante[1,5]

[1]GSI, Darmstadt, Germany; [2]Department of Radiation Oncology, Fudan University Shanghai Cancer Center, Shanghai, China; [3]Department of Oncology, Shanghai Medical School, Fudan University, Shanghai,China;, [4]Uniklinikum Mainz, Germany, [5]Condensed Matter Physics, TU Darmstadt, Darmstadt, Germany;

Introduction

The neurosphere formation assay is used to culture neural stem cells *in vitro*. The cells grow in suspension into round cell clusters, so-called neurospheres. The neurosphere assay is used to investigate the stemness properties of the neural stem cells. One criterion for stemness is the ability of the cells to proliferate and self-renew. This property of the cells is promoted by the neurosphere culture conditions.

In the last decade, cancer stem cells were found in many different types of cancer. These cancer stem cells share some characteristic properties with normal stem cells, including their ability for unlimited growth and self-renewal, as well as the ability to differentiate into all the types of cancer cells found in the specific cancer type. It is assumed that cancer stem cells are responsible for the formation of metastasis and for failure of therapy and tumor relapse. Moreover, it was fond that tumor stem cells are more resistant to radiotherapy and chemotherapy than the bulk tumor cells. The relative biological effectiveness RBE of high-LET radiation is generally high for radioresistant cells, thus accelerated ions should be very effective in killing radioresistant cancer stem cells[1].

At GSI, the neurosphere assay was established using glioma stem cells kindly provided by Dr. E. Kim, Neurosurgery Department, University Hospital Mainz, Germany. First irradiation experiments were carried out using accelerated Carbon-ions, Titanium-ions and X-rays.

Materials and Methods

A glioma stem cell line (#10) was cultured in serum-free neurobasal A medium supplemented with B27, EGF and FGF. Before irradiation, cells were typsinized and counted. A defined number of cells was irradiated with X-rays, Carbon-ions (extended Bragg peak, LET=60-85 keV/µm) or Titanium-ions (energy = 1 GeV/u, LET=107 keV/µm) and seeded in T25 tissue culture flasks for neurosphere formation test. From each irradiated sample, four tissue culture flasks were prepared. After two weeks of incubation the number of neurospheres was determined in each flask. Examples of neurospheres are shown in Figure 1.

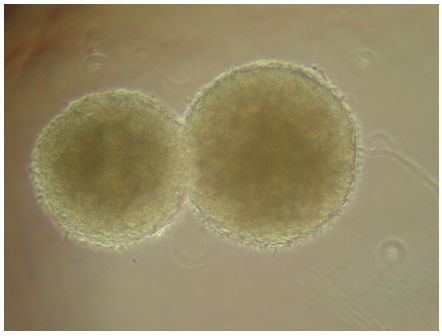

Figure 1: Microscope image of neurospheres.

Results

The fraction of neurospheres which formed after doses of 1 and 2,5 Gy X-rays, Carbon-ions and Titanium-ions is shown in Figure 2. Titanium-ions and Carbon-ions were more effective in reducing the neurosphere formation rate than X-rays, indicating that accelerated heavy ions can indeed inactivate glioma stem cells effectively. To further investigate the effects of heavy ion irradiation on glioma stem cells, experiments using additional cell lines, a wider dose-range and other biological endpoints are planned.

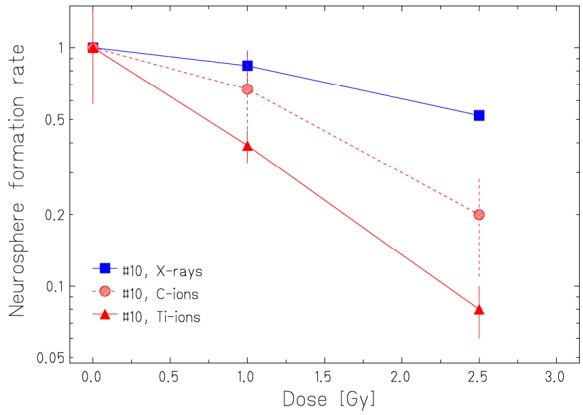

Figure 2: Fraction of neurospheres (normalized to unirradiated control) which formed after 1 and 2,5 Gy of X-rays (squares), C-ions (circles) and Ti-ions (triangels).

References

[1] Pignalosa, D. & Durante, M. Overcoming resistance of cancer stem cells. *Lancet Oncol.* **13**, e187-e188 (2012)

FRAP measurements after targeted irradiation of heterochromatin and euchromatin at the GSI microbeam*

B. Merk[1,2,#], K.-O. Voss[1], I. Müller[1], B.E. Fischer[1], B. Jakob[1], G. Taucher-Scholz[1,2], C. Trautmann[1,2], and M. Durante[1,2]

[1]GSI, Darmstadt, Germany; [2]Technische Universität Darmstadt, Germany

Introduction

The GSI microbeam is routinely employed for targeted irradiation of living cells in culture [1]. Over the last years the custom-build epifluorescence microscope was improved, and a laser system was integrated [2].

Now the microscope has a temporal and spatial resolution to image fast repair protein kinetics after irradiation with heavy ions. This gives an insight into the kinetics of repair proteins recruiting at the damage sites (foci) [3].

By a laser system the fluorescent markers at these foci can be locally bleached and the fluorescence recovery after photobleaching (FRAP) can be recorded. This yields information about the protein exchange at the damage sites [4].

Here we use the microbeam to irradiate heterochromatic (HC) and euchromatic (EC) regions followed by FRAP analysis to see if there is a difference in protein exchange for high (HC) and low (EC) chromatin density [2].

Experiment

In the mouse embryonic fibroblast cell line NIH3T3 HC and EC can be easily visualized by a DNA staining (Hoechst 33342) (Figure 1 a). After targeted irradiation of these sub-cellular compartments by single gold ions (LET of 12900 keV/u) (Figure 1 at red crosses) the DNA repair is starting by accumulation of repair proteins to the damage sites. These cells are in addition transfected with an green fluorescent protein (GFP) fused to repair protein Ku80, a important protein for the non-homologous end joining repair pathway. Figure 1 b shows foci of Ku80-GFP one minute after ion irradiation, which act as targets for bleaching by the laser system (Figure 1 c green crosses) [2]. Afterwards these targets are bleached and time-lapse images are recorded. Figure 2 shows typical FRAP curves of HC and EC measured in the cell depicted in Figure 1. Evaluation of several of these curves yields FRAP times of $t_{1/2}$ = 4.2 ± 0.4 s (N=35) for HC and $t_{1/2}$ = 2.8 ± 0.5 s (N=38) for EC and resulting diffusion coefficients of D_{HC} = 0.24 ± 0.02 $\mu m^2 s^{-1}$ and D_{EC} = 0.36 ± 0.06 $\mu m^2 s^{-1}$ [2]. The diffusion coefficient reported in HeLa cells for Ku80 is ~ 0.35 $\mu m^2 s^{-1}$ [5] and in excellent agreement with our measurements in EC. In addition a significant difference in protein exchange of Ku80 in EC and HC is visible.

B.Merk@gsi.de

*Work supported by HGS-HIRe.

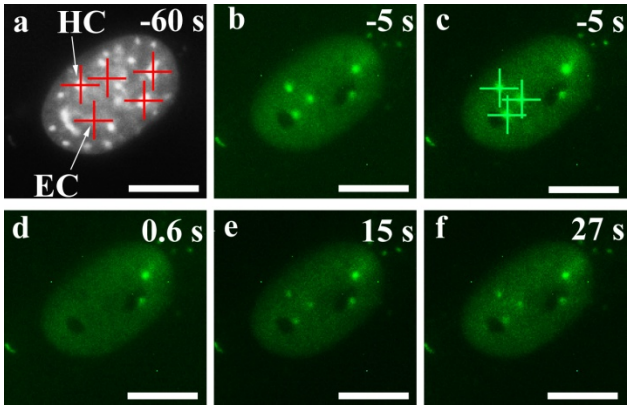

Figure 1: DNA staining image of a NIH3T3 cell nucleus before targeted irradiation with 4.8 MeV/u gold ions (a). After accumulation of repair protein Ku80-GFP to the DNA damage (b) targets to bleach are selected (c) and a fluorescence recovery is imaged (d-f). Scale bar 5 µm.

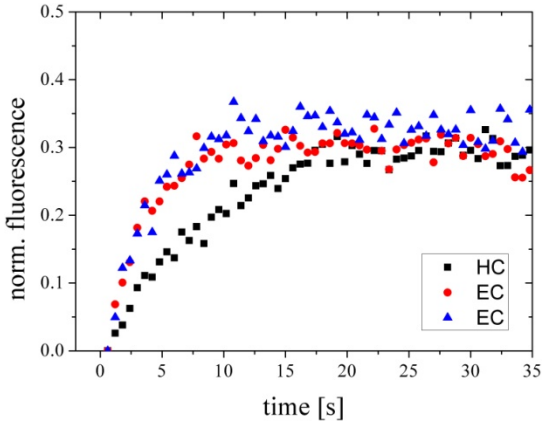

Figure 2: FRAP curves of Ku80-GFP in one cell nucleus. Significant difference of HC and EC curves is visible. Normalized to pre-bleach intensity.

References

[1] M. Heiß, B.E. Fischer, B. Jakob, C. Fournier, G. Becker, G. Taucher-Scholz, Rad Res 165 (2006) 231

[2] B. Merk, K.-O. Voss, I. Müller, B.E. Fischer, B. Jakob, G. Taucher-Scholz, C. Trautmann, M. Durante, NIMB, in press

[3] B. Jakob, J.H. Rudolph, N. Gueven, M.F. Lavin, G. Taucher-Scholz, Rad Res 163 (2005) 681-690

[4] D. Axelrod, D. E. Koppel, J. Schlessinger, E. Elson, W. W. Webb, Biophysical Journal 16 (1976) 1055-1069

[5] W. Rodgers, S. Jordan, J. Capra, J Immunol 168 (2002) 2348-2355

Impact of carbon ion irradiation on epidermal growth factor receptor and glioma cell migration in comparison to photon irradiation*

C. Stahler[1], N. Cordes[2], G. Taucher-Scholz[3] and W. Mueller-Klieser[1]

[1]University Medical Center Mainz, Germany; [2]OncoRay, University of Technology, Dresden, Germany; [3]GSI, Darmstadt, Germany

Introduction

Radiotherapy of malignant gliomas may be limited by an interference of radiation with the migratory potential of tumour cells. Thus, the cellular motility of certain tumour cell lines is enhanced by sublethal doses of photon irradiation as we previously reported *in vitro* [1]. Furthermore, conventional radiotherapy has been shown to result in an elevated phosphorylation of the epidermal growth factor receptor (EGFR) in different cancer types [2] and EGFR activation is known to promote tumour cell migration suggesting a causal relationship between the two phenomena. In contrast, recent data is suggestive of carbon ion radiotherapy to reduce the migratory potential of tumour cells [3]. To date no data exist regarding the influence of particle irradiation on the EGFR.

Considering this background information, the present study was performed in order to investigate the impact of carbon ion irradiation on glioblastoma cell motility and EGFR phosphorylation *in vitro*.

Materials and Methods

EGFR overexpressing glioblastoma cell lines U87 EGFR++ and LN229 EGFR++ were irradiated with a single absorbed dose of 2 Gy photons or ^{12}C heavy ions (LET ≈ 100 keV/µm, 1 cm SOBP). Migration was analyzed 24 h after treatment in a standardized Boyden Chamber assay. At different time points EGFR Y1173 phosphorylation was analyzed by Western blotting and quantified by densitometric analysis.

Results

The effect of irradiation on cell migration depends on the type of radiation (Figure 1). 24 h after photon treatment U87 EGFR++ cells showed a significantly enhanced migration to 122% compared to untreated cells (100%), while after ^{12}C irradiation motility was reduced down to 58%. With LN229 EGFR++ cells, a decrease of cell migration after 2 Gy photons and ^{12}C was observed, indicating that the effect of irradiation is also cell line dependent.

Western blotting of EGFR showed a significant time-dependent upregulation of EGFR Y1173 phosphorylation in U87 EGFR++ cells after photon irradiation (Figure 2). ^{12}C ion irradiation did not induce any EGFR phosphorylation. For LN229 EGFR++ no modifications of the EGFR could be observed (data not shown).

When cells were treated with an EGFR tyrosine kinase inhibitor prior to photon irradiation, no EGFR phosphorylation and enhanced cell migration could be observed (data not shown).

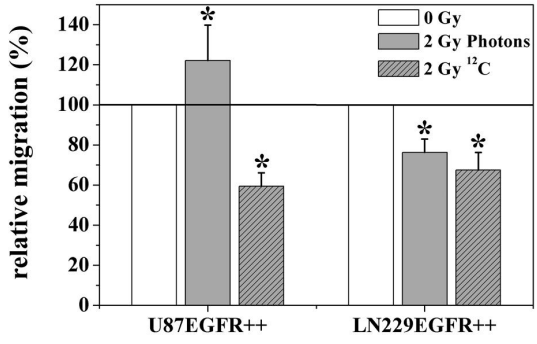

Figure 1: Relative migration of U87 EGFR++ and LN229 EGFR++ 24 h after irradiation with 2 Gy photons or ^{12}C ions (N ≥ 3), (*p < 0.05, t-test).

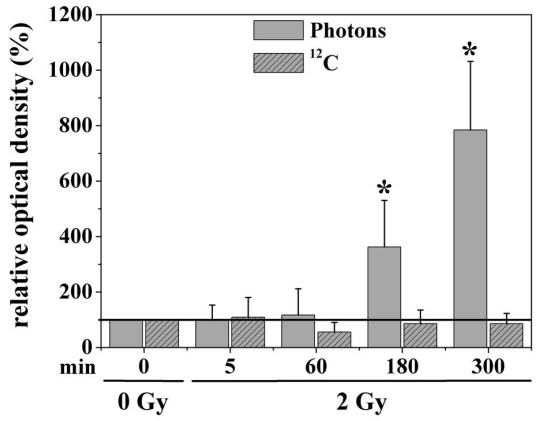

Figure 2: Relative phosphorylation of EGFR Y1173 in U87 EGFR++ cells 5 to 300 min after irradiation with 2 Gy photons or ^{12}C ions (N ≥ 3), (* p < 0.05, t-test).

Conclusions

These results suggest that the impact of irradiation on tumour cell migration and EGFR phosphorylation depends on radiation type and cell line. Photons, but not heavy ions, potentially contribute to treatment failure by increasing EGFR-related tumour cell migration.

References

[1] Goetze K, Scholz M, Taucher-Scholz G, Mueller-Klieser W, Int. J. Radiat. Biol. 83:889-896, 2007.

[2] Dent P, Reardon DB, Park JS, Bowers G, Logsdon C, Valerie K, Schmidt-Ullrich R, Mol. Biol. Cell. 10:2493-2506, 1999.

[3] Rieken S, Habermehl D, Wuerth L, Brons S, Mohr A, Lindel K, Weber K, Haberer T, Debus J, Combs SE, Int. J. Radiat. Oncol. Biol. Phy. 83:394-399, 2012.

* Work supported by DFG Mu 576/17, CO 668/4-1, TA 548/2-1

Impact of ionizing radiation on differentiation and proliferation of human osteoblasts

A.Groo[1], D.Kraft[1], S.Meyer[2], M.Durante[1,2], M.C.Cardoso[2], C.Fournier[1]*
[1]Helmholtzzentrum für Schwerionenforschung GSI, [2]Technische Universität Darmstadt

Introduction

Bone metabolism is a highly regulated process in which the balance between bone-resorbing osteoclasts (OCs) and bone-forming osteoblasts (OBs) is influenced by hematopoietic and mesenchymal stem and progenitor cells (MSC) in the bone marrow (BM). The progenitor cells affect each other in their differentiation by release of migration factors (i.e. SCF-1) or direct cell adhesion interactions (1, 2). The deregulation of the balance between OBs and OCs can lead to chronic inflammatory diseases like osteoporosis or rheumatoid arthritis (RA) (3). This is reflected in the synovial fluid of RA patients, where OCs are present at pathological levels. An efficient treatment of these pathologies is the exposure to low doses of ionizing irradiation, either photons or exposure to α- particles in radon galleries.
Therefore we want to assess whether low dose irradiation influences differentiation or survival of BM progenitor cells. We focused first on OB progenitors as well as differentiated cells.

Materials and Methods

MSC were isolated from BM aspirates of healthy donors via their adherence to plastic and further differentiated into OBs with ß-glycerophosphate and ascorbic acid treatment. The differentiation status was controlled by staining of $Ca2^{+}$ deposits with Alizarin red S (4). Immunofluorescence staining (IF) was performed with DAPI to highlight the nuclei, and antibodies to NF-kB/p65 or to its phosphorylated form to score the presence and activation of NF-κB.

Results and Discussion

First experiments revealed that the characteristic deposition of $Ca2^{+}$ during differentiation of OBs increased not only with increasing cell passage numbers and cultivation time (Fig.1a) but also after X-ray exposure in a dose-dependent manner (0.5 and 2 Gy) (Fig.1b). Furthermore, OBs showed reduced clonogenic survival (26% after exposure to 2Gy X-rays) and were more radiosensitive than other mesenchymal cells, i.e. fibroblasts (5). With further differentiation, osteoblasts became even more radiosensitive (not shown).

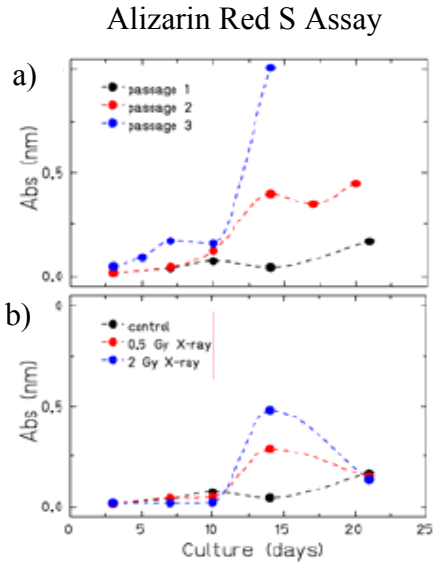

Fig.1: Alizarin Red S absorbance (450 nm) measured in cell extracts of OBs throughout cultivation time (a) and after irradiation with X-ray (0.5 and 2Gy) (b). Increasing absorbance values indicates enhanced Ca^{2+} deposition as result of faster cell differentiation.

The radiation induced enhanced differentiation and reduced survival could potentially impact the balance between OBs and OCs after irradiation. To investigate the involvement of NF-κB, which is an important factor regulating survival and differentiation, we have established the conditions to score its activation by measuring its phosphorylation as well as its nuclear translocation in osteoblasts *in situ* (Fig.2) and *in vitro*.

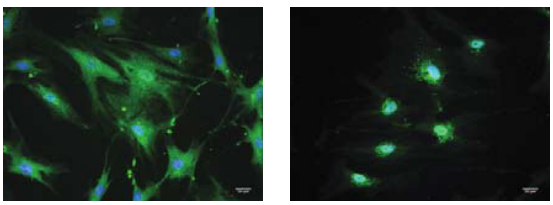

Fig.2: IF staining (green) of NF-κB/p65 (a) and NF-κB/p65phospho (b) in TNF-α stimulated primary osteoblasts. DAPI is used for nuclei staining; Activated NF-κB/p65phospho is located in nucleus of OBs.

References

1. Kiel MJ et al. 2008. Nat rev immunol 8 (4), pp 290-301
2. Lapidot T et al. 2002. Exp. Hematol. 30. pp 973–981
3. Udagawa et al . 2002. Arthritis Res. 4: 281-289.
4. Gregory et al. 2004. Anal Biochem 329 77–84.
5. Fournier et al. 2001. Int J Radiat Biol 77, 713-722,

Work is funded by BMBF (GREWIS 02NUK017A)
* Work is supported by HGS-HIRe

Increased RBE of carbon ions in tumor growth inhibition using an in vivo lung adenocarcinoma model

F. Subtil[1], S. Scheel[1], B. Bischoff[1], F. Rose[1], R. Engenhart-Cabillic[1], A. Arenz[1], M. Scholz[2], C. Fournier[2], G. Taucher-Scholz[2], and J. Hänze[3]

[1]Dept. of Radiotherapy and Radiooncology, University of Marburg, Germany; [2]GSI, Darmstadt, Germany; [3]Department of Urology and Pediatric Urology, University of Marburg, Germany

Carbon ion irradiation is an emerging therapy option for various tumor entities, including lung cancer [1]. This irradiation quality with a high linear energy transfer (LET) induces more complex and irreparable clustered DNA damage. Compared with low-LET photons and protons, carbon ions have a higher relative biological effectiveness (RBE) with less oxygen-dependent radiosensitivity [2]. Based on the colony formation assay we previously revealed a RBE of 3 for 10% cell survival in A549 cells [3].

Here we compared the effect of different irradiation qualities (carbon ions (^{12}C) and photon irradiations) on the tumor growth using a mouse tumor model of the human non small lung adenocarcinoma cell line (A549).

Adult BALBc nu/nu mice were maintained under pathogen-free conditions and handled in accordance with the recommendations for animal experimentation of European Community. After subcutaneous tumor initiation and a starting tumor volume of 200 mm³, local tumor irradiation with biologically equivalent doses of ^{12}C (LET 50-70 keV/µm, energy 122.36-183.74 MeV/u on target, 40 mm spread out bragg peak [SOBP]) and photons (6 MV-X) were performed. The tumor volumes were measured 3 times per week until reaching a target tumor volume of 400 mm³ or after an observation time of 40 days. The tumor volume (TV) was calculated by the formula: TV [mm ³] = (L x W²)/2; where L is the longest dimension of the tumor [mm], and W is the shortest dimension of the tumor [mm].

We found a tumor volume doubling time of 37.8 ± 1.6 days in the carbon ion irradiated group compared to 18.3 ± 1.2 days in the photon irradiated group and 11.9 ± 1.0 days in the unirradiated control group (Figure 1). Thus, the RBE of in vivo tumor growth is above 3 and clearly greater than for cell survival measurements, providing further support for a clinical application. However, it should be mentioned that 3 of 6 carbon ion irradiated tumors did not reach the target tumor volume of 400 mm³ within the observation time of 40 days.

In further experiments, we will focus on the analysis of the effects of carbon ion irradiation on the tumor microenvironment. These experiments will consider effects on tumor cells, tumor vasculature as well as distribution of immune cells.

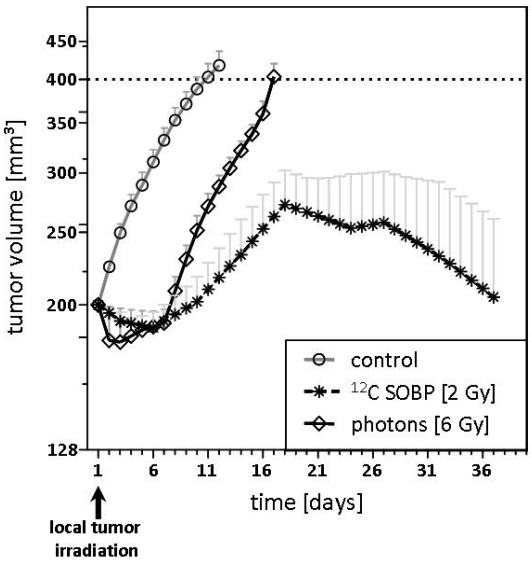

Figure 1: Growth curves of A549 tumors after irradiation with carbon ions (^{12}C SOBP) or photons. All data represent the means ± S.E.M.

References

[1] Miyamoto, T., Baba, M., Sugane, T., Nakajima, M., Yashiro, T., Kagei, K., Hirasawa, N., Sugawara, T., Yamamoto, N., Koto, M., Ezawa, H., Kadono, K., Tsujii, H., Mizoe, J. E., Yoshikawa, K., Kandatsu, S., and Fujisawa, T. (2007) Carbon ion radiotherapy for stage I non-small cell lung cancer using a regimen of four fractions during 1 week. *J Thorac Oncol* **2**, 916-926

[2] Weber, U., and Kraft, G. (2009) Comparison of carbon ions versus protons. Cancer J 15, 325-332

[3] Kamlah, F., Hänze, J., Arenz, A., Seay, U., Hasan, D., Juricko, J., Bischoff, B., Gottschald, O. R., Fournier, C., Taucher-Scholz, G., Scholz, M., Seeger, W., Engenhart-Cabillic, R., and Rose, F. (2011) Comparison of the effects of carbon ion and photon irradiation on the angiogenic response in human lung adenocarcinoma cells. Int J Radiat Oncol Biol Phys 80, 1541-1549

Influence of Ionizing radiation on the potency state of murine embryonic stem cells*

S. Luft[1], A. Helm[1], P. Hesse1[1], D. Pignalosa[1], S. Brons[2], P.G. Layer[3], M. Durante[1,3], S. Ritter[1,#]

[1]GSI, Darmstadt, Germany, [2]HIT, Heidelberg, Germany, [3]Technische Universität Darmstadt, Germany.

The cell potency describes the differentiation potential of a cell. There are different levels of cell potency, ranging from the ability to differentiate into any cell type and therefore being able to create a whole organism (totipotency) to the ability to differentiate into only one cell type (unipotency). Embryonic stem cells (ESCs) are the most potent cells that can be cultured *in vitro*. They can give rise to cells of all the three germ layers of an organism and are therefore called pluripotent (overview in [1]). Under appropriate culture conditions, ESCs closely resemble the embryonic development *in vitro*, providing a model system to investigate the effects of external factors like ionizing radiation on the early mammalian development.

To investigate whether ionizing radiation affects the potency state of ESCs, the murine ESC line D3 was chosen as a model. Cells were exposed to X-rays or C-ions. C-ion irradiation was performed at SIS, GSI and at HIT, Heidelberg (25 mm extended Bragg peak with energies ranging from 106 to 147 MeV/u, dose averaged LET=75 keV/µm), D3 cells were harvested at 10 h and 8 d after exposure and chromosome aberrations were analysed by means of the mFISH technique. Furthermore, at 0, 8 and 16 days after exposure the presence of pluripotency markers was examined by flow cytometry. In first experiments cells were stained with fluorescent labelled antibodies against Oct3/4 and SOX2, both being transcription factors that play a key role in the complex interactive network establishing pluripotency.

Analysis of chromosome aberrations in first cycle cells (at 10h) and in the progeny of cells which survived the exposure (at 8 d) demonstrates that damaged cells are efficiently removed from the culture after X-ray irradiation, while in the offspring of C-ion exposed cells the number of aberrant cells was still significantly higher than in the control sample (data not shown).

The flow cytometric quantification of the Oct3/4 presence over time is shown in figure 1A. The fluorescence signal intensity shows a noticeable inter-experimental variation. For example, between control samples there is a 2.5-fold difference. Nevertheless, in the same experiment the signal intensity of irradiated and corresponding control cells is similar indicating that the presence of the pluripotency marker Oct3/4 in the surviving cells is not affected by ionizing radiation up to16 d after exposure. This has also been shown for the presence of a second pluripotency marker, SOX2 (see figure 1B), even though its relative median fluorescence intensity was much lower compared to Oct3/4.

To verify the data, the activity of alkaline phosphatase, an enzyme which is highly expressed in pluripotent cells, was examined by performing a colour reaction assay. As shown in figure 2, D3 cells exhibit the typical red stain indicating the pluripotent state. In between the colonies, single unstained cells appear, demonstrating minor differentiation processes in the culture.

However, drawing conclusions from the expression of only few pluripotency markers is questionable, since pluripotency is established by a complex network of proteins and molecules, influencing and interacting with each other. Furthermore, Oct3/4 plays a role not only in relation to pluripotency, but is also known to accumulate at chromatin lesions, like double strand breaks [2].

Therefore, in subsequent studies we will examine the expression of a larger number of pluripotency markers by both flow cytometry and a specific stem cell signalling rtPCR array (see also [3]). The latter technique allows quantifying the expression of 96 different stem cell-characteristic genes.

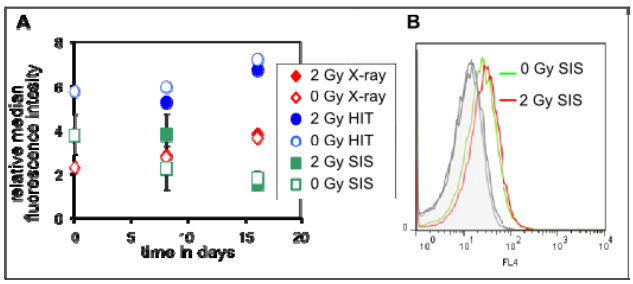

Figure 1: Immunochemical detection of Oct3/4 and Sox2 measured by flow cytometry. A: Median fluorescence intensity for Oct3/4, normalized to isotype control over time. B: One-parameter-histograms showing the fluorescence intensity for SOX2 in control (green) and 2-Gy C-ions exposed cells (red) 16 d after exposure; tinted grey: isotype control.

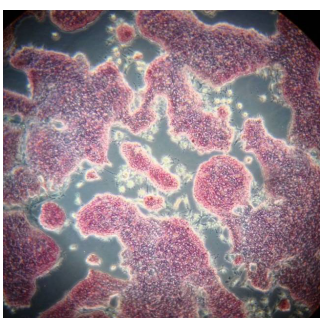

Figure 2: Alkaline Phosphatase Staining (red) of murine ESC colonies confirms the pluripotent state.

References

[1] S. Yamanaka et al., Cell and tissue research 331, 5 (2008)

[2] E. Bartova et al.,. PloS one 6, e27281 (2011)

[3] Pignalosa et al. GSI scientific report 2012 (this issue)

*Work supported by BMBF grant 02NUK025A and HGS-HIRe.

s.ritter@gsi.de

Inhibitory effect of ionizing radiation on cellular adhesion of lymphocytes to endothelial cells under dynamic conditions*

J. Klinger[1], A.S. Bothe[1], N. Erbeldinger[1], M.Durante[1,2], F.Rödel[3],C. Fournier[1]
[1]GSI, Darmstadt, Germany; [2]TU Darmstadt, Germany; [3]Goethe Universität Frankfurt, Germany

Introduction

Chronic inflammatory diseases are efficiently treated by irradiation with low doses of photons (low dose radiotherapy) or α-particles (radon treatment), but the cellular and molecular background remains widely unknown [1,2]. Adhesion of PBMC on the endothelial cell (EC) wall of the blood vessels is one of the initial steps in the inflammation cascade to recruit immune cells to inflamed tissue. An inhibitory effect of photon irradiation on the adhesion process is discussed as part of the anti-inflammatory mechanisms of low dose radiotherapy [3,4]. In our previously reported experiments EC were all cultured under static conditions, whereas in vivo EC are exposed to constant shear stress of the blood stream. Therefore the goal of the present study was to investigate possible changes in the adhesion of peripheral blood lymphocytes (PBL) to primary EC under dynamic cultivation conditions and after irradiation with X-rays or carbon ions. Because of physical differences in the energy deposition between photons and α-particles, both radiation qualities were compared with respect to their anti-inflammatory effectiveness. Carbon ions with similar LET values were used as a surrogate for α-particles.

Materials and Methods

A flow-chamber system was built, based on a publication by Freyberg et al. [5]. Human dermal microvascular endothelial cells (HMVEC) were used for the experiments. They were cultivated for 72h prior to exposure to X-rays (250kV, 16mA) or carbon ions (LET: 168keV/µm). After irradiation EC were stimulated with TNF-α (1ng/ml) and incubated for 24h under laminar flow conditions. Afterwards the complete medium was exchanged by medium w/o TNF-α supplementation. Afterwards stained PBL were streamed over the EC monolayer for 30min. The unbound PBL were removed by washing the samples with PBS and afterwards EC were fixed with paraformaldehyde. Analysis was performed using a fluorescent microscope. As a comparison all experiments were performed as well under static conditions.

Results and Conclusion

The adhesion of PBL on HMVEC was measured after exposure to a low (0.5Gy) or a high dose of photons or carbon ions (2 or 6Gy, respectively). The results are shown in figure 1. The relative adhesion indicates the amount of attached PBL normalized on the positive controls (unirradiated and stimulated) which were set as 100%. As can be seen from figure 1, the relative adhesion of the unstimulated controls is only about 30% compared to the positive controls. After irradiation of HMVEC with a low dose of either photons or carbon ions, the adhesion of PBL was remarkably reduced (to about 30%). This corresponds roughly to the level of the unstimulated controls. However, after irradiation with a high dose a reduced adhesion was only observed for carbon ions (2Gy) but not for X-rays. The dose response remains to be investigated in more detail. By these results we can show a clear inhibitory effect of sparsely- and densely ionizing radiation on adhesion of PBL to EC.

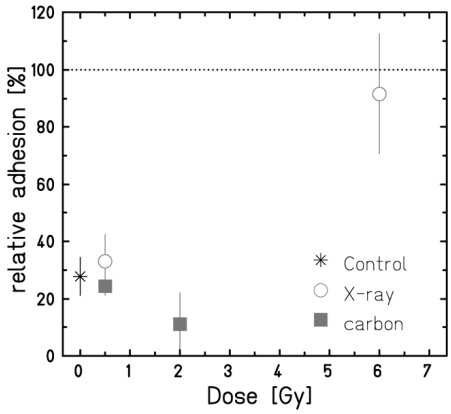

Figure 1: *Influence of irradiation with X-rays or carbon ions (LET: 168keV/µm) on adhesion related interaction of TNF-α stimulated ECs and PBL under dynamic conditions (100% adhesion corresponds to unirradiated, TNF-α stimulated EC).* (X-ray: N=2-4, n=5-9; carbon ions: N=1, n=2)

Although we did not find a specific low dose effect in previously performed experiments under static conditions, we observed a high effectiveness of low doses for both radiation qualities with primary EC under dynamic conditions [6]. In accordance to our results a low dose effect was also observed in human genetically engineered EC or murine endothelioma cells [3,4,7] as well *in vivo* for gastrointestinal venules of mice [8]. This points to complex molecular interactions promoting or inhibiting the adhesion processes which are influenced by sheer forces of the bloodstream.

References

[1] Seegenschmiedt et al., *Strahlenther. Onkol.* 180: 718-730 (2004).
[2] Falkenbach et al., *Rheumatol Int*. 25(3): 205-10 (2005)
[3] Rödel et al., *Strahlenter Onkol*., 180:194-200 (2004)
[4] Rödel et al. *Strahlenter Onkol.,* 184:41-47 (2008)
[5] Freyberg et al, *Cytotechnology* 26: 49–58 (1998)
[6] Klinger et al., *GSI Scientific Report*, 452 (2010)
[7] Kern et al. *Radiother Oncol*. 54:273-282 (2000)
[8] Arenas et al. *Int.J.Radiat.Oncol.Biol.Phys*. 66:560-567 (2006)

*Work is supported by HGS-HIRe, FOI Gastein (Austria) and financed by BMBF (GREWIS, 02NUK017A)

Ionizing irradiation causes rapid activation of the human intermediate K^+ channel in A549 cells: link to cell migration and proliferation

Roth B[1], Knoop J[2], Fournier C[2] and Thiel G[1]

[1]Membrane Biophysics, Technische Universität Darmstadt; [2]GSI, Darmstadt, Germany

Introduction

In previous experiments it was shown that radiation with photons and high-energy ions results in a rapid activation of K^+ channels in the epithelial lung cancer cell line A549 [1]. Among the responsive channels is the human intermediate potassium channel hIK [1]. This channel is known to regulate in other types of cells the cell-cycle transition and cell migration via hyperpolarization of the plasma membrane [2]. To further test the contribution of hIK channels to the irradiation induced rise in conductance we exposed responsive cells after irradiation to the specific inhibitor 10 µM Clotrimazole. Since this treatment was effective to block the hIK channel in A549 cells we tested whether an inhibition of the hIK channel in A549 cells is able to influence proliferation and migration.

Material and Methods

We examined the conductance of ion-channels in A549 cells by a planar patch-clamp technique combined with an external perfusion system [3]. Migration and motility was observed under a microscope with a scratch assay. Proliferation rates were determined in a particle counter and cell-cycle analysis was performed by flow cytometer after DAPI staining.

Results

The data in figure 1 show that the high conductance of A549 cells, which were obtained by irradiation, were restored back to the control level by treating cells with Clotrimazole. The results of these experiments underscore the view that irradiation augments the conductance of hIK type channels. To monitor the proliferation behavior of the A549 cells in the presence of Clotrimazole the cell density was counted over a period of 96 hours. The data show a 5times lower proliferation rate in the presence of the channel blocker compared to the control.

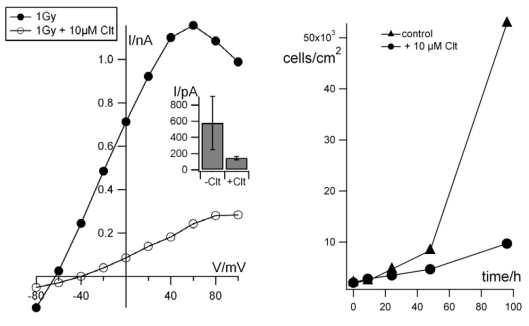

Figure 1: *Current response of an A549 cell to a standard pulse-protocol (a). The irradiation augmented conductance can be inhibited by 10 µM Clotrimazole, a specific blocker of Ca^{2+}-activated K^+ channels (hIK). Blocking the same ion-channel slowed down the proliferation-rate dramatically (b).*

The scratch wound healing assay was used to measure two-dimensional movement of the A549 cells (Fig 2). The result of this assay showed that the specific hIK channel blocker Tram-34 decreases the motility of the cells and their ability to migrate.

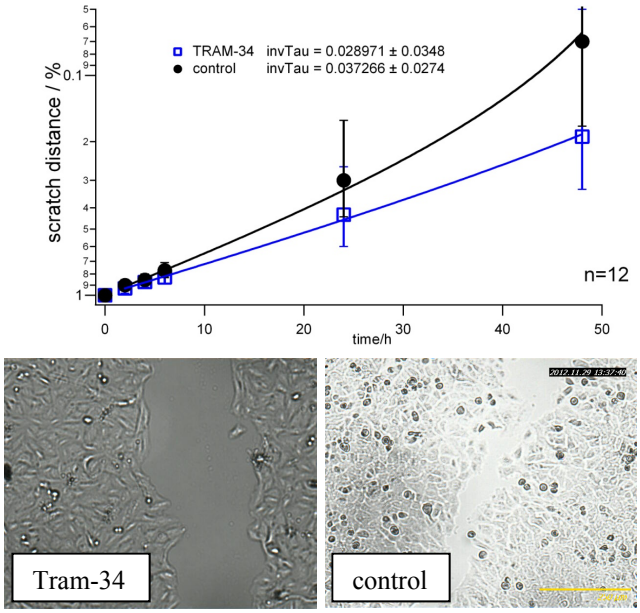

Figure 2: *Effects of hIK ion-channel blocker (Tram-34) on migration of A549 cell line. Scratch wound healing assay was performed to compare the migratory capabilities of cells. The images were acquired 12h after scratch.*

Discussion

The present data verify and extend a previous report, which has shown that ionizing irradiation increases already at low doses the conductance of the human intermediate conductance potassium channel hIK. On the other hand the hIK channel has been identified as a key player in regulation of proliferation and migration in A549 cells. Hence it is reasonable to speculate that an irradiation-induced activation of the hIK channel can stimulate the proliferation and motility via hyperpolarization of the plasma membrane.

Funded by BMBF 02NUK017B and HGS-HIRe

References

[1] Roth B, unpublished (2012)

[2] Ouadid-Ahidouch (2008), The Journal of membrane biology, 221: 1-6

[3] Fertig N, Blick RH, Behrends JC (2002) 82: 3056-3062.

Live cell observation of chromatin decondensation after heavy ion irradiation at the microbeam*

I. Müller[1], B. Merk[1,2], K.-O. Voss[1], A. L. Leifke[1], G. Becker[1], M. Durante[1,2] and G. Taucher-Scholz[1,2]

[1]GSI, Darmstadt, Germany; [2] TUD, Darmstadt, Germany.

Introduction

The inaccurate repair of DNA double strand breaks (DSBs), as generated by heavy ion irradiation, can result in chromosome aberrations, cell death and various forms of cancer. To keep genomic stability the cell uses different repair mechanisms with diverse signalling factors and repair proteins assembling at the lesion in a highly ordered spatial and time-dependent manner. Within this orchestrated response local as well as global chromatin decondensation has been found at various stages, thought to enable the access of repair factors to the damage site [1]. However the direct visualisation of these relaxation steps is difficult and usually only global decondensation, via indirect methods, is detectable. Recently we described local chromatin decondensation visible as a depletion of DNA staining within the highly compacted chromocenters in fixed mouse embryonic fibroblast, and due to low hitting probability at the UNILAC broad beam, also in a small numbers of living cells [2].

Results and Conclusions

To increase the number of live cell observations and to study the decondensation process within chromocenter after heavy ion irradiation in more detail we used the GSI microbeam, allowing the defined and targeted irradiation of subnuclear compartments [3].

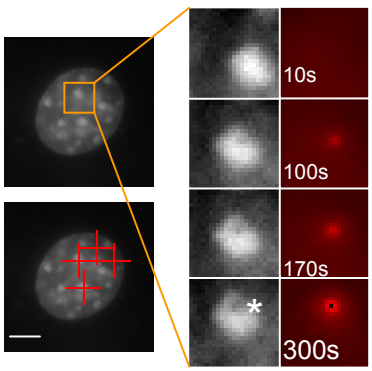

Figure 1: Chromatin decondensation within chromocenters of living cells at the microbeam. DNA of NIH3T3 cells were stained with Hoechst 33342 (left). Chromocenters, which are visible as areas of more intensive DNA staining, were targeted using the in-situ microscope (see red crosses). Cells were irradiated with gold ions (LET 12.800 keV/µm) and a time series was recorded with one picture every 10s for at least 5 min. Zoomed in pictures at the indicated timepoints (right) show a single hit chromocenter verified by the accumulation of XRCC1-RFP (red) an early repair protein. Decondensation is visible as an emerging, less stained area (white asterisk) within the chromocenter. (Scale bar 5µm)

Chromatin decondensation at the microbeam-hit sites within chromocenters is visible as an appearing darker area at sites of damage (Figure 1). Single line measurements of DNA staining intensities over time verify that depletion is a continuous process with the fluorescence decreasing over time leading to the typical dip formation (Figure 2) attesting to the assumptions made before [2] that dip formation is a printout of decondensation.

While little is known about the chromatin decondensation mechanism within compacted chromocenters after ion irradiation, the establishment of live cell observations of this process at the microbeam is a breakthrough that will help to elucidate the pathways behind.

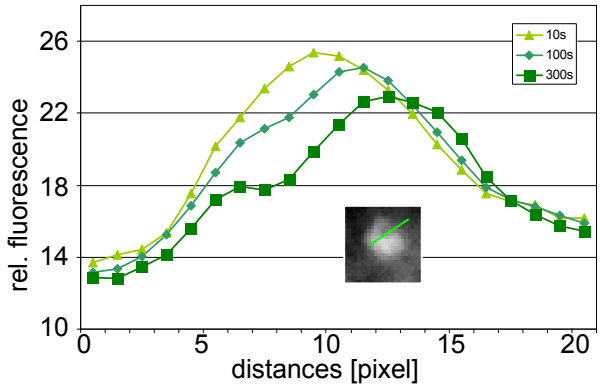

Figure 1: Dip formation as the printout for chromatin decondensation. Recorded sequences of live cell observation (Figure 1) were corrected for bleaching and cell movement and normalised to 1. Plot shows the DNA fluorescence intensities measured at the depicted single green line within the picture at the specific timepoints after irradiation. The staining intensities at the damage sites decrease, leading to the formation of a dip.

References

[1] Misteli and Soutoglou (2009), *Nat Rev Mol Cell Biol* 10, 243-254

[2] Jakob et al, Nucleic acids research (2011) 39, 6489-6499

[3] Heiss et al (2006), *Radiat Res* 165, 231-239.

* Work supported by BMBF 02NUK001A and HGS-HIRe

Modulation of chemokine release in cardiac endothelial cells by low doses of ionizing radiation *

J. Klinger[1], N. Erbeldinger[1], T. Dettmering[1], M. Durante[1,2], C. Fournier[1]
[1]GSI, Darmstadt, Germany; [2]TU Darmstadt, Germany

Introduction

More and more evidence has been provided, that exposure of the heart to even low doses (0.5Gy) of ionizing radiation significantly increase the risk for cardiovascular disease and in consequence leads to increased mortality [1-4]. The term "cardiovascular disease" describes different types of pathologies which affect the cardiovascular systems (e.g. coronary heart disease, heart failure, etc.). Several processes are discussed to be involved, e.g. pericardial or myocardial fibrosis, accelerated atherosclerosis, etc. [4]. In this context the endothelial dysfunction plays an important role in promoting fibrotic and inflammatory processes after irradiation [5]. Endothelial dysfunction is mainly characterized by a loss of thrombo-resistence of the endothelium, which is accompanied by an increased expression of adhesion molecules and van-Willebrand factor [5]. However the cellular and molecular mechanisms underlying the disease progression are not completely understood. Our part in this project is the investigation of the modulation of cytokine release by EC of the cardiovascular system after irradiation with low doses of high- and low LET radiation, in collaboration with partner institutes within the Procardio project, namely: the Helmholtz centre Munich, Germany and the Health protection agency (HPA) Chilton, UK.

Materials and Methods

For irradiation experiments, primary cardiac microvascular endothelial cells (HCMEC) were obtained from Lonza. In a first experiment, the cells have been irradiated with γ-rays at Helmholtz centre Munich and with nickel ions (175keV/µm) at GSI facilities (Darmstadt, Germany). Supernatant was taken 4 and 24h after irradiation and stored at -80°C. Measurements of the cytokine concentration were performed with ELISA technique and multiplex bead arrays (both from eBiosciences).

Results and Conclusion

The results of the first experiment where monocultures of HCMEC have been irradiated with nickel ions are shown in Figure 1. Measurements of the concentration of more than 20 cytokines or chemokines (e.g. TNF-α, MCP-1, MIP-1, IL-1α, IL-6, IL-8 etc.) revealed a tendency for a increased release of 2 chemokines (MCP-1 and IL-8) 24h after exposure, already at a dose of 0.5Gy. The other factors that have been investigated remained unchanged or the changes were statistically not significant (data not shown). No significant changes have been detected for all cytokines and chemokines measured after γ-exposure (not shown).

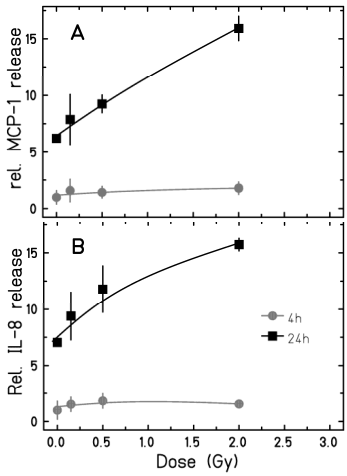

Figure 1: *Relative release of MCP-1 (***A***) or IL-8 (***B***) of HCMEC 4 and 24h after irradiation with nickel ions (LET: 175keV/µm).* (N=1, n=2)

The tendency for an increased release of the chemokines MCP-1 and IL-8 clearly points to an inflammatory reaction of HCMEC even after irradiation with low doses of ionizing radiation. The chemokine MCP-1 is mainly responsible to trigger monocyte recruitment into inflamed tissue [6], whereas IL-8 is responsible for recruitment of neutrophils and T-cells [7]. The higher amount of chemokines points to an increased migration of immune cells into the heart tissue after exposure to ionizing radiation, which than in turn could promote inflammatory processes like fibrosis or endothelial dysfunction. In future experiments the release of chemokines will be assessed more in detail, to clarify if the effect is statistically significant. As a next step the question will be addressed if a co-cultivation with other relevant cell types influences the responding cytokine/chemokine release.

References

[1] Hoel DG., *Ann N Y Acad Sci*; 1076:309-317 (2006)
[2] Little MP et al., *Radiat Res*; 169(1):99-109 (2008)
[3] McGale P. et al., *Radiat Res*; 163(3):247-257 (2005)
[4] Adams MJ. et al., *Crit Rev Oncol/Hematol*. 45: 55-75 (2003)
[5] Boerma et al., *Card Res Prac, Article ID 858262* (2011)
[6] Gullestade et al., *Cardiology*, 122:23–35 (2012)
[7] Damas et al., *Cardiovasc. Res.,* 47(4):778-87 (2000)

* Work is financed by the EURATOM 7th Framework Program under grant agreement n° 295823.

Processing of radiation-induced DNA double-strand breaks (DSBs) differs in human hematopoietic stem and progenitor cells versus mature lymphocytes

D. Kraft[1,2], M. Volcic[3], A. Groo[1], A. Stahl[3], D. Salles[3], H. Bönig[2], M. Durante[1], G. Taucher-Scholz[1], C. Fournier[1] and L. Wiesmüller[3]

[1]GSI, Darmstadt, Germany; [2]Institute for Transfusion Medicine and Immunohaematology, Frankfurt, Germany; [3]Department of Obstetrics and Gynecology, University of Ulm, Germany

Introduction

Stem and progenitor cells of the hematopoietic system (HSPC) are the origin of radiation-induced leukemogenesis [1]. Ionizing radiation generates DNA double-strand breaks (DSBs) and error-prone DSB repair activities are thought to be responsible for generating chromosomal rearrangements that can lead to hematopoietic malignancies [2]. Regarding repair of radiation-induced DSBs and its accuracy in HSPC, data are scarce, in part contradictory and were obtained almost exclusively in murine model systems [e.g. 2]. Having identified differences in DSB repair pathway usage in HSPC versus mature peripheral blood lymphocytes (PBLs) (see report 2011), we exposed cells to different radiation qualities (X rays, heavy Titanium/Calcium ions), which may induce different types of chromosomal damage and thus different DSB repair mechanisms [3,4], and monitored processing of radiation-induced DNA lesions in HSPC versus PBLs.

Materials and Methods

Human CD34$^+$ HSPC and PBLs were isolated from healthy donors. While HSPC were pooled from 4-9 donors and cultivated for 72h as described [4] PBLs were individually cultivated in RPMI 1640 medium supplemented with 20% FCS, 3mM Glutamine and 3% phytohemagglutinin (PHA). Cell cultures were irradiated with 2 Gy of X rays or particle irradation (Titanium, Calcium, 1GeV/u) and further cultivated for the indicated times. After cytospin harvest cells were fixed, extracted, and immunolabeled as in [5]. Fluorescence micrographs were collected on an Olympus BX51 epifluorescence microscope equipped with AnalySIS software including mFIP module (3.2, Soft Imaging System) for image acquisition and automated identification. Antibodies used were: 53BP1 rabbit (Novus), phospho-RPA (p-RPA) mAb clone S33 (Bethyl), Rad51 rabbit H-92 (sc-8349, Santa Cruz), and Alexa Fluor® 555 conjugated secondary antibodies (Invitrogen).

Results

Recently, we observed that HSPC and PBLs differ in the usage of DSB repair pathways and fidelity of the same, even though the cell cycle distribution under the assay conditions following *ex vivo* cultivation for 72h was comparable (see report 2011 and data not shown). Next, we dissected DSB processing in response to treatment with ionizing radiation by quantitative immunofluorescence microscopy of discrete nuclear signals (foci) indicative for the accumulation and/or removal of DNA lesions (53BP1), single-stranded DNA (p-RPA) and the assembly/disassembly of the machinery for homologous recombination (Rad51), as this repair activity had differed up to 16-fold between the two cell types. Exposure to 2Gy of X rays caused a sharp increase of 53BP1, p-RPA and Rad51 foci in HSPC. Strikingly, PBLs displayed 2-3fold lower foci numbers per nuclear area 1h (53BP1, p-RPA) and 2h (Rad51) after irradiation. Interestingly, 53BP1 foci numbers were equivalent when irradiating cells with Titanium or Calcium ions (not shown) suggesting that with complex chromosomal damage differences in damage processing between HSPC and PBLs disappear.

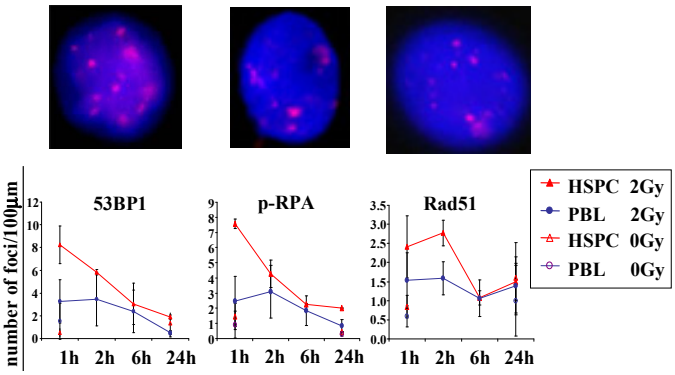

Figure 1: Analysis of DNA damage processing in human HSPC versus PBLs *ex vivo*. HSPC and PBLs were cultivated for 72h followed by exposure to 2Gy X rays and further cultivation for the indicated times. HSPC and PBLs were processed for immunofluorescence analysis and 53BP1, p-RPA, and Rad51 foci quantified (representative images for HSPCs). Mean values and SDs from 50-100 nuclei for N=2-3 HSPC cultures and N=6-9 PBL donors are shown graphically.

References

[1] Rithidech et al (2007), Radiat Environ Biophys, 46(2):137-145
[2] Mohrin et al (2010), Cell Stem Cell, 7(2):174-185
[3] Durante et al (2001), Radiat Res, 156(5 Pt 2):662–667
[4] Becker et al (2009), Int J Radiat Biol, 85(11):1051-1059
[5] Volcic et al. (2012), Nucleic Acids Res, 40(1):181-195

* Work financed by DLR/BMWi contract No. 50 WB 1225.

Organotypic slice cultures of human glioblastoma reveal different susceptibility to treatments*

Felicitas Merz[1], Frank Gaunitz[2], Faramarz Dehghani[1], Christof Renner[2], Jürgen Meixensberger[2], Angelika Gutenberg[3], Alf Giese[3], Kosta Schopow[4], Christian Hellwig[5], Michael Schäfer[5], Manfred Bauer[6], Horst Stöcker[7,8], Gisela Taucher-Scholz[7], Marco Durante[7,8], Ingo Bechmann[1,8]

[1]Institute of Anatomy, University of Leipzig, Leipzig, Germany; [2]Department of Neurosurgery, University Hospital Leipzig, Leipzig, Germany; [3]Department of Neurosurgery, University of Mainz, Mainz, Germany; [4]Dr. Senckenberg Foundation, Frankfurt/Main, Germany; [5]Institute of Pharmacology, University of Leipzig, Leipzig, Germany; [6]Institute of Pathology, University of Leipzig, Leipzig, Germany; [7]GSI Helmholtz Center for Heavy Ion Research, Darmstadt, Germany; [8]FIAS Frankfurt Institute for Advanced Sciences Darmstadt, Germany

Introduction

Glioblastoma multiforme (GBM) is an aggressive brain tumor with no efficient treatment at present. We have developed a method to culture human GBM tissue obtained from surgery as organotypic slice cultures which allows for testing the effects of known treatment options including X-irradiation or chemotherapy as well as applying novel compounds as well as Carbon ions [1, 2].

Method

GBM tissue was transported to the lab and processed into organotypic slice cultures as described before . At different timepoints after treatments, slices were fixed, embedded, sectioned and used for morphological evaluation (HE staining, Fig. 2) or analysis of proliferation or cell death with immunofluorescent stainings (Fig. 1).

Results

GBM slices were viable in culture for up to two weeks with preservation of general GBM hallmarks (protein expression, morphologic features) as well as the individual characteristics of the initial tumor. When irradiated with X-rays or Carbon ions, a time-dependent decrease of proliferation in GBM slices was detected (Fig. 1 E and F). This was visualized by using an antibody against Ki-67 which marks cells going through the cell cycle (Fig. 1 A-D).

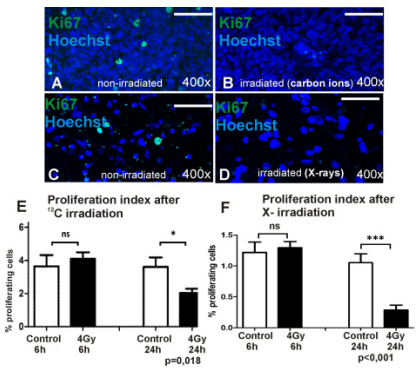

Figure 1: Human GBM slice cultures were irradiated with X-rays or Carbon ions and fixed after 6 or 24 hours. Staining with Ki-67 for proliferating cells revealed a significant decrease in proliferation after 24h. A and C= Control; B= Carbon irradiated (SOBP, 2 Gy); D= X-irradiated (4 Gy); E= proliferation index 6 or 24h after Carbon; F= proliferation index 6 or 24h after X-rays

When treated with the common chemotherapeutic drug temozolomide (TMZ) alone or in combination with irradiation, cell death was induced in slices. Morphological changes and cell loss were visible in HE stainings (Fig. 2 A-D), and apoptosis induction was quantified by staining for activated caspase-3. In the tissues examined here, Carbon irradiation and TMZ induced more cell death and decreased cellular density (Fig. 2 E and F) than treatment with X-rays and TMZ (G and H).

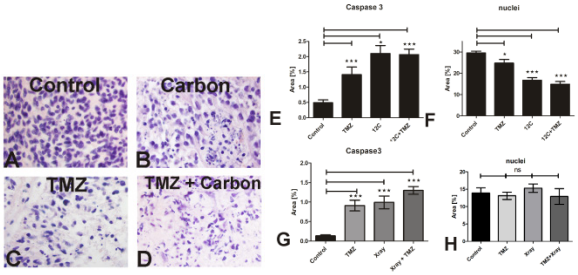

Figure 2: Human GBM slice cultures were treated with TMZ and Carbon ions (SOBP, 2 Gy) or X-rays (4 Gy). In HE stained sections, cell loss and morphological changes are visible (A-D). Fluorescent staining for activated caspase-3 and nuclei revealed induction of apoptosis and cell loss after treatment. The area covered by positive cells in at least 20 pictures per group was analyzed using ImageJ.

The details of this study are now being published in Neuro-Oncology [3].

Discussion

Our model can be used to test effects of different known or novel therapeutic options in one tumor at a time. It can help exposing mechanisms of tumor resistance and cell survival after treatment. In future, it could be used to identify the most suitable therapy strategy for a patient before starting a treatment.

References

[1] Merz F et al, Radiat Environ Biophys (2010) 49(3):457-62

[2] Merz F, Bechmann I. Future Oncol. (2011) 7(4):489-91

[3] Merz F et al, accepted in Neuro-Oncology (2013)

* Work supported by ESA and DLR

Survival of chemoresistant cancer cells exposed to x-rays and heavy ions

Z. Yu[1,2,3] , C. Hartel[1] , W. K. Weyrather[1], D. Diaz-Carballo[4] and M. Durante[1,5]

[1]GSI, Darmstadt, Germany; [2]Department of Radiation Oncology, Fudan University Shanghai Cancer Center, Shanghai, China; [3]Department of Oncology, Shanghai Medical School, Fudan University, Shanghai, China; [4]Marienhospital Herne Klinikum der Ruhr-Universität Bochum, Bochum, Germany; [5]TU Darmstadt, Germany;

Introduction

Cancer stem-cells (CSCs) are more resistant to most conventional therapy than differentiated tumor cells. A rapid relapse after treatment can occur, caused by CSCs which were not eliminated by the applied therapy [1]. CSCs are supposed to be radioresistant and/or chemoresistant. Culturing cancer cells in the presence of a low dose of a chemotherapeutic agent is one of the methods to enrich CSCs. In this study, etoposide is used to enrich CSCs in glioblastoma and neuroblastoma cell lines. Etoposide is a topoisomerase inhibitor and causes errors in DNA synthesis and promotes apoptosis of cancer cells. It is used as a form of chemotherapy for cancers such as glioblastoma multiforme.

In this report, the survival of chemoresistant cancer cells is shown compared with original ones exposed to x-rays and heavy ions. All cell lines in the report are kindly given by Dr. D. Diaz-Carballo, Marienhospital Herne, Klinikum der Ruhr-Universität Bochum, Bochum, Germany.

Material and Methods

Four cell lines (LAN-1 WT, LAN-1 RETO, ASTRO WT, ASTRO RETO) derived from human tumor tissue of patients are cultured in DMEM medium, supplemented with 10% fetal calf serum (FCS) and 1% Penicillin/Streptomycin, and kept in a humidified atmosphere of 5% CO_2 at 37°C. All cells show adherent growth. ASTRO cell lines are derived from glioblastoma multiforme and LAN-1 cell lines are derived from neuroblastoma. RETO cells are cultured in Medium containing 4µg/ml etoposide. Carbon ion irradiation was performed using a 1cm extended Bragg peak at a dose-averaged LET of 100 keV/µm. X-ray irradiation was performed using 250 kVp. Cell survival was measured with a colony formation assay.

Results

The survival curves show that carbon ion irradiation is more effective than x-ray in all four cell lines (figure 1, figure 2). For LAN-1 cells, RETO cells (cultured in the presence of etoposide) are more resistant than WT cells (cultured without etoposide) after x-ray and carbon ion irradiation (figure 1), but for ASTRO cells, RETO cells (cultured with etoposide) are more sensitive than WT cells (cultured without etoposide) after x-ray and carbon ion irradiation (figure 2).

Conclusions

Carbon ion irradiation is more effective than x-ray for both untreated cancer cell lines and chemoresistant cell lines. For LAN-1 cells, chemoresistant cells (RETO) are more radioresistant than untreated cells (WT), while this effect was not found in ASTRO cells.

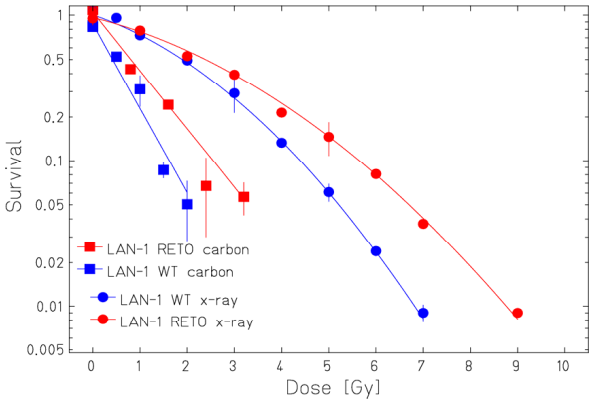

Figure 1: Survival of LAN-1 WT and LAN-1 RETO cells irradiated by x-ray and carbon ions.

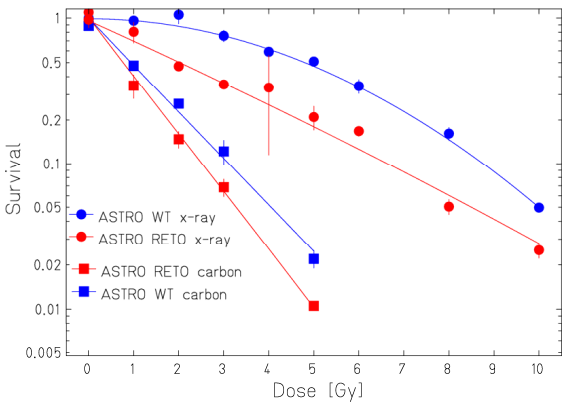

Figure 2: Survival of ASTRO WT and ASTRO RETO cells irradiated by x-ray and carbon ions.

References

[1] L. Vermeulen et al. "The developing cancer stem-cell model: clinical challenges and opportunities." *Lancet Oncol*, February 2012, 13(2), p.e83-89

Telomere Length Measurements of Human and Mouse Cells by Fluorescence in situ Hybridization

D. Nieri[1], E. Nasonova[2,3], C. Hartel[2], D. Diaz-Carballo[4], M. Durante[2,5] and S. Ritter[2,#]

[1]Università Roma Tre, Roma, Italy; [2]GSI, Darmstadt, Germany; [3]JINR, Dubna, Russia; [4]Marienhospital Herne Klinikum der Ruhr-Universität Bochum, Bochum, Germany;[5]TU Darmstadt, Darmstadt, Germany

Telomeres are located at the ends of chromosomes and consist of tandemly repeated DNA sequence (5'-TTAGGG-3') associated with proteins. Telomeres confer stability to the chromosome termini, i.e. protect the chromosome ends from being recognized and processed as double strand breaks. Telomere dysfunction results in genetic instability and is implicated in aging and cancer. A sensitive method to determine the telomere length in single metaphase cells is the so-called Quantitative Fluorescence in situ Hybridization technique (Q-FISH). Telomeres are visualized by means of a fluorescent labeled PNA probe as shown in Fig. 1. The signal intensity is directly proportional to the telomere length [1] and is quantified from digital microscopy images.

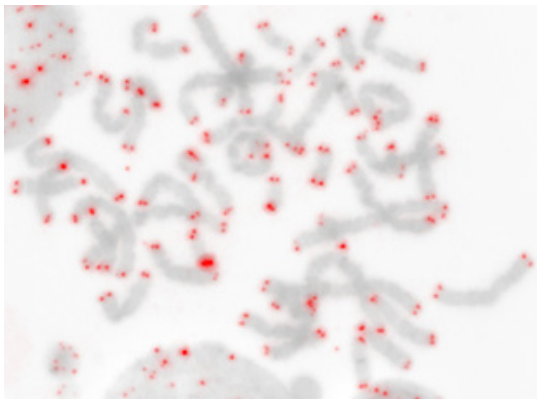

Fig 1: Typical Q-FISH image: Telomere sequences of a human metaphase spread stained with a Cy3-conjugated PNA probe (red spots, focus stack image). Chromosomes are counterstained with DAPI (gray).

Recently we set up the Q-FISH method and characterized human and mouse primary cells and established cell lines used in current radiobiological studies: human cells include primary lymphocytes, glioblastoma cells (line LAN1-WT) and embryonic stem cells (line H9); mouse cells include primary bone marrow cells, embryonic fibroblasts and embryonic stem cells (line D3). In each case >40 metaphases were analyzed.

Examples of chromosomes with stained telomeres are shown in Fig. 2. Analysis of the data clearly demonstrated that the telomeres of human cells are much shorter in comparison with mouse cells (Fig. 3). Moreover, in both species embryonic stem cells had longer telomeres than somatic cells. These observations are consistent with published data [2-4]. In subsequent studies we will use this method to uncover the relationship between telomere length and radiation induced chromosomal instability.

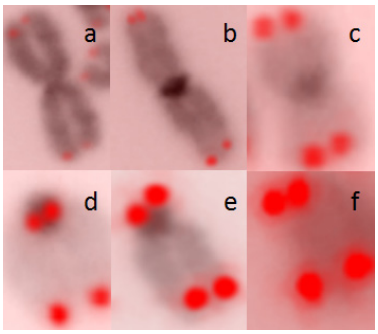

Fig 2: Increase in telomeric Cy3-signal intensity reflecting telomere length: (a) human glioblastoma cells (hGlio), (b) human lymphocytes (hLymph), (c) human embryonic stem cells (hESC), (d) mouse bone marrow cells (mBM), (e) mouse embryonic fibroblasts (mEF), (f) mouse embryonic stem cells (mESC); (b,d) are primary cells, while the others are established cell lines.

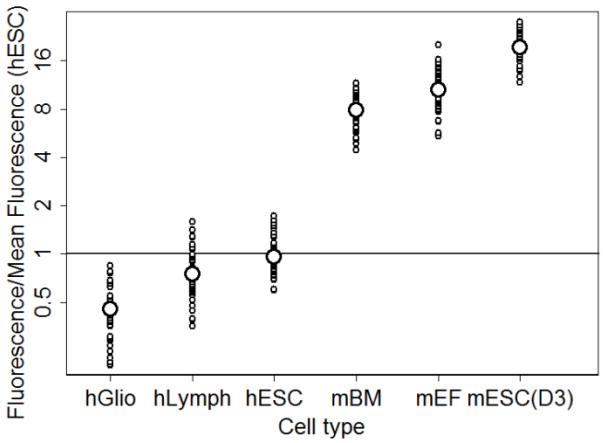

Fig. 3: Fluorescence measures of Cy3 telomere-stained metaphases. Data are normalized on the mean fluorescence of hESC. Abbreviations as in Fig. 2.

References

[1] Perner et al., Am J Pathol 163(5):1751-6 (2003)
[2] Marion et al., Cell Stem Cell 4(2):141-154 (2009)
[3] Allen et al., Biochim Biophys Acta 1792(4):324-328 (2009)
[4] Hakin-Smith et al., Lancet. 361(9360):836-8 (2003)

Supported by BMBF grants 02NUK017A and 02NUK025A.

s.ritter@gsi.de

Testing of a 3D-human skin equivalent for radiation experiments.

J. Wiedemann[1,2], P. Simoniello[1], L. Madl[1], M. Durante[1,2], C. Fournier[1]

[1]GSI, Darmstadt, Germany; [2]TU Darmstadt, Germany.

Introduction

Despite the increasing concern about the effect of ionising radiation on living organisms, the majority of radiobiological studies have been conducted *in vitro*, i.e. in 2-dimensional (2D) monocultures. Accumulating evidence suggests that cells behave differently when they are cultivated in a 3D extra-cellular matrix where they also interact with other cells [1-5]. In order to be able to extrapolate the *in vitro* results closer to the *in vivo* situation, it is of great benefit to develop tissue systems suitable for radiobiological assays.

In this project we want to use commercially available 3D-tissue skin equivalents, composed of an epidermal and dermal layer of human keratinocytes and fibroblasts. The extracellular matrix and other cell types resident in skin may have an impact on the occurrence of apoptosis and/or the release of inflammation-related cytokines.

Materials and Methods

To investigate the effect of different irradiation types (UVB; X-rays and carbon ions) a human full-thickness skin equivalent from MatTek was used. Histological stainings and protein extraction methods have been established for morphological and immunological analysis.

After irradiation cultures were fixed in Bouin`s solution, paraffin embedded, sectioned, and stained with hematoxylin and eosin (H & E) to check the morphology. In order to detect differentiation markers, sections were stained with an antibody against cytokeratin 10 (Abcam) and counterstained with hematoxylin.

Lysis with RIPA-buffer was performed after separating mechanically the epidermis from the dermis. The lysates were used for Western Blot analysis to detect E-cadherin, Vimentin (Abcam) and GAPDH (Cell signaling).

Results and Discussion

We could successfully establish methods for fixation, embedding and cutting of the tissue equivalent. Morphological analysis showed a well-organized epiderm with basal, spinous, granular and cornified layers. The dermis is composed of a collagen matrix containing numerous viable normal human fibroblasts (fig.1). The impression of a typical morphology of the skin equivalent could be confirmed by a comparison of tissue slices from normal human skin (courtesy of the dermatological department of the Darmstadt Hospital).

Immunostaining (fig. 1b) shows that cytokeratin 10, a marker for differentiation [6] is expressed in the upper layers of the epiderm (brown staining) but not in the basal layer where the cells remain undifferentiated. A high cell-number in the basal layer is a sign for viable tissue.

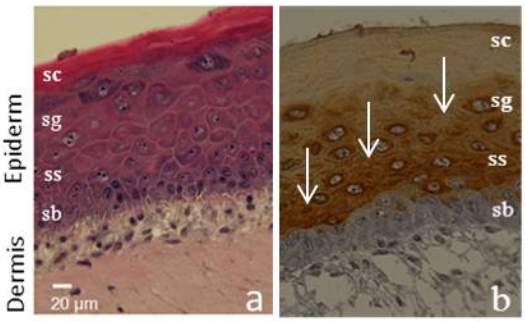

Fig. 1: (a) H&E Staining and (b) immunolocalization of cytokeratin 10 (b) in EpiDermFT400. Cells which express cytokeratin 10 display a brown staining in the cytoplasm (arrows).Stratum basale (sb), stratum spinosum (ss), stratum granulosum (sg) and stratum corneum (sc).

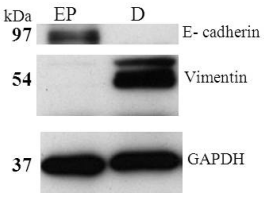

Fig. 2: Western blot analysis of E-cadherin and Vimentin in skin equivalent EFT 400. E-cadherin is detectable in the epiderm (EP) at 97 kDa and Vimentin in the dermis (D) at 37 kDa.GAPDH is used as a loading control; kDa: Kilodalton; EP: epiderm; D: Dermis.

To overcome problems to lyse the tissue samples we tested a combination of mechanical lysis with a douncer homogenizer and ultrasound (bath-type sonicator) which worked very well. EFT-400 offers the possibility to separate the epidermis from the dermis mechanically. Western Blot analysis shows the presence of E-cadherin exclusively in the epiderm and of vimentin in the dermis (fig. 2).

Our study establishes EpiDerm-FT 400 (MatTek) as a suitable model to study the underlying mechanisms of tissue responses to radiation. Analysis of 3D skin equivalents, bridging the gap between in vitro and in vivo models, are important for a better understanding of radiation effects on normal tissues, in particular inflammation and fibrosis during radiotherapy [7].

Reference

[1] Sun et al. (2006), *J Biotechnol*. **122** (3), 372-81.
[2] Smalley et al. (2006), *In Vitro Cell Dev Biol Anim*. **42** (8-9), 242-7.
[3] Sun et al. (2007), *Biotechnol Bioeng*. **97** (5), 1318-28
[4] Kremer et al. (2001), *Langenbecks Arch Surg*. **386** (5), 357-63.
[5] Escámez et al. (2004), *Invest Dermatol*. **123** (6), 1182-91.
[6] Deepak et al. (2006), *J Invest Dermatol.* **126**, 243–257.
[7] Eke & Cordes et al. (2011), *Radiotherapy and Oncology*. **99,** 271–278.

Work supported by EU, PARTNER PROJECT No. 215840, DFG (GRK 1657) and HGS-HIRe.

A LEM based DNA DSB kinetic rejoining model*

F. Tommasino[1], T. Friedrich[1], U. Scholz[1], G. Taucher-Scholz[1], M. Durante[1, 2] and M. Scholz[1]

[1]GSI, Darmstadt, Germany; [2]Institut für Festkörperphysik, Technische Universität, Darmstadt, Germany

In the context of ionising radiation induced DNA damage, the DNA double strand breaks (DSB) are actually considered the dominant effect of radiation action leading to cell killing. Several experimental methods have been developed in order to measure the DSB induction and repair in cells. By means of gel electrophoresis techniques, for example, is possible to measure the DSB induction and the following rejoining over time after irradiation [1, 2]. The resulting curve is often fitted with a combination of two exponential functions, representing the fast and the slow component of rejoining. When comparing the effect of different radiation qualities on the rejoining kinetics, a delay is in general observed in the rejoining process when high ionisation densities are involved (i.e. high LET ion irradiation) and consequently more clustered damage is induced.

The recent version of the Local Effect Model (LEM) combines the photon input data and an amorphous track structure model with a detailed consideration of the spatial distribution of the initial damage (DSB) [3, 4]. The high order chromatin structure is actually taken into account, assuming that the DNA content inside the cell nucleus is organised in "giant loops" of DNA [5], each one comprising around 2Mbp of DNA. This allows the definition of two different classes of damage, namely 'isolated' (iDSB) and 'clustered' (cDSB) double strand breaks, when only one and two or more DSB are induced in the loop structure respectively. Obviously, cDSB are expected to be more difficult for the cell to process because the integrity of the loop structure is lost. The fractions of induced iDSB and cDSB strongly depend on the ionisation density, with a higher fraction of cDSB being the result of a high LET irradiation, compared to the photon case.

The LEM predictions in terms of iDSB and cDSB can be used to develop a DSB kinetic rejoining model. The basic assumption is that a correspondence can be found between the two classes of DSB defined in the LEM and the two components of DSB rejoining which are usually observed in the experimental curves. According to this concept, an increase in the fraction of DSB rejoined with a slow kinetic would be the effect of an increase in the fraction of induced cDSB. In this context, once experimental data are available and experimental conditions are known (radiation quality, cell line), we can use the LEM to predict the fractions of iDSB and cDSB corresponding to the particular case (in the photon case, Poissonian distribution of DSB is assumed). These values are then used to derive the fraction of unrejoined DSB:

$$U(t) = F_{iDSB} e^{-\frac{\ln(2)}{\tau_{fast}}t} + F_{cDSB} e^{-\frac{\ln(2)}{\tau_{slow}}t} \qquad (1)$$

where F_{iDSB} and F_{cDSB} are the fractions of induced iDSB and cDSB respectively, and τ_{fast} and τ_{slow} are the half-lives of the two components. After the input parameters are available from simulations, we can use the function to fit experimental data, obtaining τ_{fast} and τ_{slow} as fitted parameters. In Fig. 1 a preliminary application of the model is shown; it demonstrates, that a consistent simultaneous description of low- and high-LET rejoining data can be achieved based on half-lives derived from the photon data (τ_{fast}=16±1min, τ_{slow}=146±28min) and the different contributions of iDSB and cDSB for the different radiation qualities.

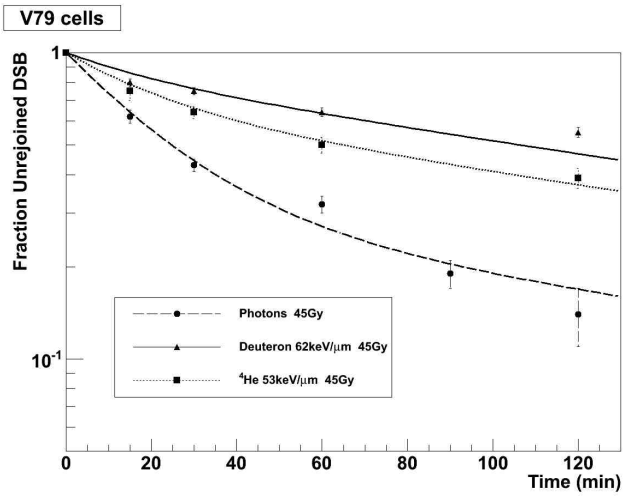

Figure 1: application of the rejoining model to experimental data shown in [1], the points refer to experimental data, while lines show the results obtained with the model.

A successful application of the model presented here to a wide spectrum of experimental data, involving different cell lines and different radiation qualities, would represent a partial validation for the mechanistic bases of DNA damage on which the LEM is built. Work is actually ongoing in this direction.

References

[1] Belli et al., Int. J. Rad. Bio. 76 (2000) 1095
[2] Stenerlow et al., Int. J. Rad. Bio. 76 (2000) 549
[3] M. Scholz et al., Radiat. Envir. Biophys. 36 (1997) 59.
[4] Friedrich et al., Int. J. Radiat. Biol., 88 (2012) 103.
[5] Yokota et al., J. Cell Biol., 130 (1995) 1239.

* This work is supported by DFG-funded Graduiertenkolleg (GRK 1657) and is part of HGS-HIRe

A kinetic extension for the Giant Loop Binary Lesion model

L.Herr[1,2,], T.Friedrich[1], M. Durante[1,2], and M. Scholz[1]*

[1]GSI, Darmstadt, Germany; [2]TU Darmstadt, Germany

In 2012 the Giant LOop Binary LEsion model (GLOBLE) was proposed [1] and a formalism for the description of dose dependent cell survival probabilities after instantaneous photon irradiation was given. The concept of the model suggests an extension which takes into account dose rate effects. This contribution will summarize an extract of the research that has been done towards this aim.

Theory

DNA double strand breaks (DSBs) are supposed to be the main reason for cell death after irradiation. The GLOBLE is based on a classification of DSB according to their spatial distribution in the chromatin, specifically in giant loops (~ 2Megabasepairs) whose terminal ends are attached to the nuclear matrix.

It is assumed that a single (isolated) DSB within a giant loop is relatively easy to rejoin due to the fixation of the two parts of the loop to the nuclear matrix. However, multiple (clustered) DSBs within a loop imply a high risk for misrejoining followed by cell death since larger fragments of the DNA might get lost in this case. Therefore, a significant higher lethality ε is assigned to clustered DSBs as compared to isolated DSBs: $\varepsilon_c >> \varepsilon_i$.

Given dose dependent expected numbers of isolated and clustered DSBs after irradiation (N_i and N_c) one is able to calculate the corresponding cell survival probability as the Poisson probability for no lethal event:

(1)

In order to adapt the GLOBLE to the application of arbitrary dose rates during the irradiation the interaction between damage induction and cellular repair has to be accounted for.

The yield of initial DSBs is expected to depend only on the total dose, but not on the dose rate. However, the frequency of clustered DSBs is significantly affected by the dose rate, since a simultaneous existence of at least 2 DSBs in a loop is required to form them. The competition between the rate of DSB induction and rejoining/repair thus determines the relative fraction of isolated and clustered DSBs. In the GLOBLE it is assumed that the rate of DSB induction is proportional to the dose rate and that isolated and clustered DSBs are rejoined with fast and slow kinetics, respectively.

The dynamics involved in damage induction and repair can be expressed in five differential equations – one for each state that a giant loop might take. There are loops without DSB or lethal event, loops with non-processed isolated/clustered DSBs and loops with lethal events after misrejoining of isolated/clustered DSBs. With these differential equations and appropriate initial values one can calculate the expected number of lethal events and the corresponding survival probability.

Applications

With the kinetic extension of the GLOBLE cell survival probabilities after photon irradiation with arbitrary dose rates can be described. For the specific case of constant dose rates and for split dose experiments good agreement between model predictions and experimental data has been found.

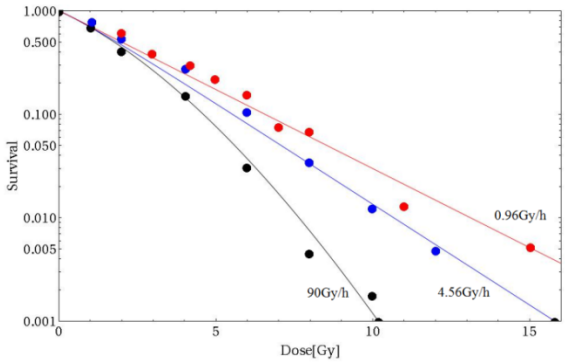

The figure above shows that the model (full lines) reflects the increase in cell survival probabilities with decreasing dose rate as observed in the experimental data [2] (dots). The model predictions are based on a single set of parameters (lethalities and rejoining rates) simultaneously describing the whole range of dose rates for the given cell line. The analysis of 15 other published dose rate experiments and of 5 split dose experiments in different cell lines support the conclusion that one is able to find cell line specific parameters with the GLOBLE.

Outlook

The Local Effect Model (LEM) which predicts effects of high LET radiation is based on the same classification of DSBs as the GLOBLE. In analogy to the approach presented here, future work will focus on an extension of the LEM which allows for the description of dose rate effects for ion beam radiation.

References

[1] Friedrich T, Durante M, Scholz M.; Radiat. Res 2012; 178: 385-394.

[2] Kelland LR, Steel GG.; Radioth. and Oncol. 1986; 7:259-268.

*Supported by HGS-HIRe and Studienstiftung des deutschen Volkes

Carbon beam dosimetry in bony tissue inhomogeneties: TRiP98 validation with experimental measurements

A. Eichhorn[1,2], *C. La Tessa*[2], *E. Scifoni*[2], *A. Carlino*[3], *M. Krämer*[2], *and M. Durante*[1,2]
[1]GSI, Darmstadt, Germany; [2]TU Darmstadt, Germany; [3]University of Palermo, Italy

Recent Measurements of the attenuation of a therapeutical carbon beam in bone-like materials [1] showed that the experimental values are slightly higher than the theoretical predictions obtained with a simple density scaling of measurements in water. In TRiP98, the heavy ion treatment planning system developed at GSI [2], the interaction between primary radiation and tissue is modeled from experimental data measured in water and rescaled to all other biological materials. As the attenuation experiment showed, this approximation is not accurate enough for materials whose elemental composition besides density deviates significantly from water.

The influence of this discrepancy on the dose profile has to be investigated in order to assess the accuracy of the treatment planning. The dose inhomogeneity predicted by TRiP98 at the interface between water and bone targets was investigated and measured at the Heavy Ion Therapy center (HIT) in Heidelberg, Germany. The inhomogeneity region is obtained by shooting the beam in a composite target so that the particles pass partly directly through water and partly through a layer of bone before entering water. The dose spikes are induced by two different effects: a macroscopic one due to the finite size of the pencil beam and in addition a microscopic one due to the scattering of the particles at the interface. How exactly the latter influences the dose inhomogeneities is not completely understood yet and a further investigation is needed.

Experimental setup

For the experiment, a water phantom was exposed to a carbon beam for irradiating a tumor volume of 5x3x3 cm^3 placed at a depth of 10 cm. A scheme of the experimental is shown in Fig. 1.

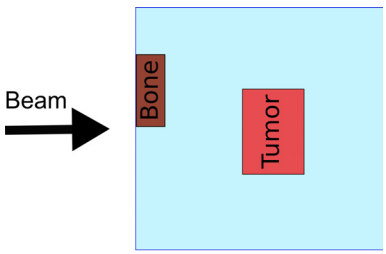

Figure 1: Scheme of the experimental setup.

The 3D treatment plan was optimized by TRiP98. The inhomogeneity region was obtained by equipping the water phantom with different bone targets at beam entrance channel. The measurements were repeated with two types of target: 1 cm thick compact bone (Gammex RMI 450) and a multilayer composed by 2 pieces of compact bone, 1 cm each, separated by 1 cm of spongious bone (Gammex RMI 456). Measurements without bone target were collected as a reference. The dose profile was measured with thermoluminescence detectors of the type TLD-700 (^{7}LiF:Mg), Pin-Point Ionization Chambers and X-ray dosimetric films (Kodax X-Omat V). The detectors were placed at several depths along the beam direction and in the perpendicular plane to understand the dose contributions over the whole treatment area, especially nearby the critical areas, i.e the bone target and the tumor volume.

Results

The lateral and depth-dose profiles measured with the Pin-Point Ionization Chambers show differences when compared to the values predicted by TRiP98 (Fig. 2). Two effects can be identified in the comparison. First of all, only the data points measured in the pure water pathway fit perfectly to the TRiP98 calculation. The values collected in the region containing the bone target are smaller than the predicted data, which is in agreement with the trend showed by the attenuation measurements. The other effect is the presence of dose spikes at the interface between the bone target and water. This effect is patently reproduced by TRiP98 and can be clearly seen in Fig. 2.

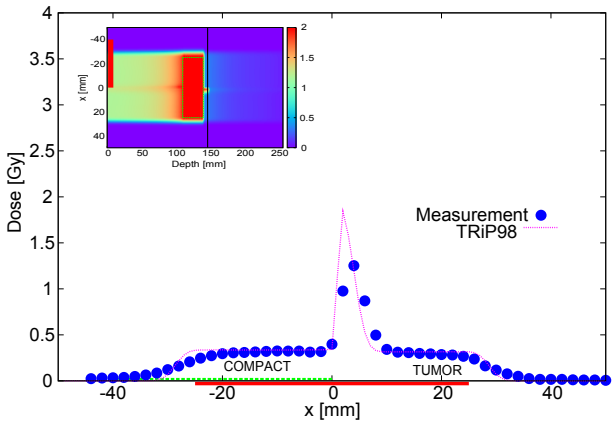

Figure 2: Dose distribution measured with the Pin-Point Ionization Chambers at a water depth of 146.3 mm directly behind the tumor volume (Longitudinal cut-line shown in the coronal plot inset

References

[1] A. Eichhorn et al., GSI Scientific Report (2011)
[2] M. Krämer et al., Phys. Med. Biol. 45, 3319 (2000)

Effect of spatially correlated ions predicted by LEM IV*

U. Scholz[†1,2], *T. Friedrich*[1], *M. Durante*[1,2], *and M. Scholz*[1]

[1]GSI, Darmstadt, Germany; [2]Institut für Festkörperphysik, Technische Universität Darmstadt, Darmstadt, Germany

In previous work, the full simulation of cell survival curves has been implemented in the Local Effect Model LEM IV [1]. With this implementation, biological effects resulting from intertrack effects can be modeled, allowing the accurate simulation of cell survival probabilities up to arbitrarily high doses. This approach is particularly suitable also to analyse in detail the effect of spatially correlated ions, as they were used e.g. in the "Molecular Beam" experiment [2]. The results showed an increased biological effectiveness with decreasing separation distance in the submicrometer range.

As described in [3], LEM IV predicts the effect E_1 of an ionizing particle based on the linear-quadratic-linear (LQ-L) photon dose response curve and the spatial distribution of double strand breaks (DSBs) in the cell nucleus. According to the number of DSB induced in 2Mbp chromatin domains, they are classified as isolated DSB (iDSB), if exactly 1 DSB is induced, or clustered DSB (cDSB), if 2 or more DSB are induced. The photon equivalent dose is defined by the photon dose generating the same ratio cDSB to the total number of damages, iDSB+cDSB, for a given pattern of particle traversals. The biological effect E_1 is then determined by rescaling the corresponding photon equivalent effect according to the total number of affected domains in both cases.

In contrast to the LQ-L model, the recently developed GLOBLE model [4] evaluates the biological effect of photon radiation by directly assigning mean numbers of lethal events to every iDSB and cDSB, respectively. In this work, photon dose response curves as predicted by the GLOBLE have been also used in LEM IV as an alternative to the standard LQ-L representation.

For simplicity, instead of deuterons, protons with the same linear energy transfer (LET) are simulated. The mean numbers of iDSBs and cDSBs for different track distances are compared in Figure 1. It is obvious that the numbers of iDSBs and cDSBs are influenced at track distances up to 0.5 µm, although the track radius is less then 0.1 µm. In the experiment, the zero separation distance was mimicked by using helium ions with twice the LET of single deuterons. Therefore, we also present the corresponding calculation for He ions in Table 1. They show a slightly increased number of iDSBs and cDSBs, even though the energy deposition is the same as for two protons.

The initial slope α of an ion dose response curve is calculated by

$$\alpha = [1 - \exp(-E_1)]\, d^{-1}\,,$$

where d is the dose of one ion traversal through the cell nucleus (doubled for spatially correlated ions). Table 1 shows the ratio of the initial slope of correlated (α_{dd}) and uncorrelated (α_d) particle radiation.

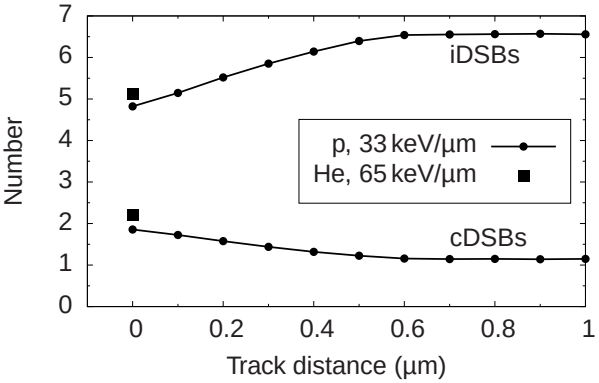

Figure 1: Modeled mean numbers of iDSBs and cDSBs for spatially correlated protons and single helium ions.

Table 1: Experimental and modeled ratio of α_{dd} and α_d. The given model errors are based on Monte Carlo fluctuations.

(mean) track distance (µm)	α_{dd}/α_d Experiment	α_{dd}/α_d LEM IV LQ-L	LEM IV GLOBLE
0.255	1.21(22)	1.005(2)	1.123(4)
0.156	1.33(22)	1.024(2)	1.211(4)
0.091	1.33(22)	1.033(2)	1.256(4)
0	—	1.046(2)	1.319(4)
He	2.09(27)	1.188(2)	1.532(5)

The model findings clearly demonstrate an increased biological effect of correlated ions even at larger track distances, where no physical overlap between the tracks occurs. Furthermore, LEM IV with GLOBLE based photon dose response curve shows a better agreement with the experimental data than LEM IV with the LQ-L based photon dose response curve.

References

[1] U. Scholz et al., GSI Scientific Report, 2011.

[2] A. M. Kellerer et al., Radiat. Res., 83(**3**) (1980), 511-528.

[3] T. Friedrich et al., Int. J. Radiat. Biol., 88(**1-2**) (2011), 103-7.

[4] T. Friedrich et al., Rad. Res., 178(**5**) (2012), 385-94.

* Work is part of HGS-HIRe.

† u.scholz@gsi.de

Predictions of cell survival along proton spread out Bragg-peaks based on the Local Effect Model

R. Grün [*1,2,3], *T. Friedrich*[1], *M. Krämer*[1], *M. Durante*[1,4], *and M. Scholz*[1]

[1]GSI, Darmstadt, Germany; [2]Institut für Medizinische Physik und Strahlenschutz,TH-Mittelhessen, Gießen, Germany; [3]Medical Faculty of Philipps-University Marburg, Germany; [4]TU Darmstadt, Germany

Introduction: Proton beam radiotherapy is a common clinical treatment procedure. For the clinical practice the biological effectiveness of protons is assumed to be constant (RBE=1.1). Nevertheless, in-vitro studies show that protons have an increased RBE at the end of their range [1, 2]. This increase of the RBE can be explained by the increasing LET at the declining edge of the spread out Bragg-peak (SOBP). The recently published version of the Local Effect Model (LEM IV; [3]) has shown to be applicable for a wide range of particles and energies. In the present work we focus on the comparison of measured cell survival data along proton SOBP with the predicted cell survival of the LEM IV to validate the predictions for further analysis.

Methods: The LEM IV predictions are compared to cell survival of CHO cells after irradiation measured by Tang et al. [1] and for SCC25 cells measured by Bettega et al. [2]. Both used a 65 MeV proton beam to produce an SOBP with 15 mm and 17.5 mm extension, respectively. Cells were irradiated at differnt positions of the SOBP with different doses levels. Irradiations were simulated with the treatment planning software TRiP98 [4]. As input parameters for the LEM IV calculations the RBE-table AB-CHO with the photon parameters given in Tang et al. [1] and the RBE-table AB-SCC25 with photon parameters given in Bettega et al. [2] were used and listed in Tab. 1:

RBE-table	$\alpha\,[\mathrm{Gy}^{-1}]$	$\beta\,[\mathrm{Gy}^{-2}]$	$\alpha/\beta\,[Gy]$	$D_t[Gy]$
AB-CHO	0.16	0.0246	6.5	13
AB-SCC25	0.57	0.012	47.5	15

Results: Fig. 1a shows the cell survival measurements from Tang et al. [1] with CHO cells in different depths for 2 Gy also in the entrance channel. Fig. 1b shows the cell survival measurements from Bettega et al. [2] with SCC25 cells in different depths for 2, 5 and 7 Gy. For both data sets the model predictions are in accordance with the experimentally observed survival. In particular, for SCC25 cells the steep increase of RBE values significantly above 1.1 at the distal egde is reproduced by the model predictions very well (Tab. 2), thus clearly demonstrating the relevance of RBE effects at the distal end of the SOBP.

Conclusion: The depth and dose dependence of RBE as predicted by LEM IV for proton SOBPs was shown to be consistent with experimental data. LEM IV thus represents a useful tool to implement variable RBE values in treatment planning for protons, aiming at overcoming limitations that might result from the currently used constant RBE value of 1.1 for clinical applications.

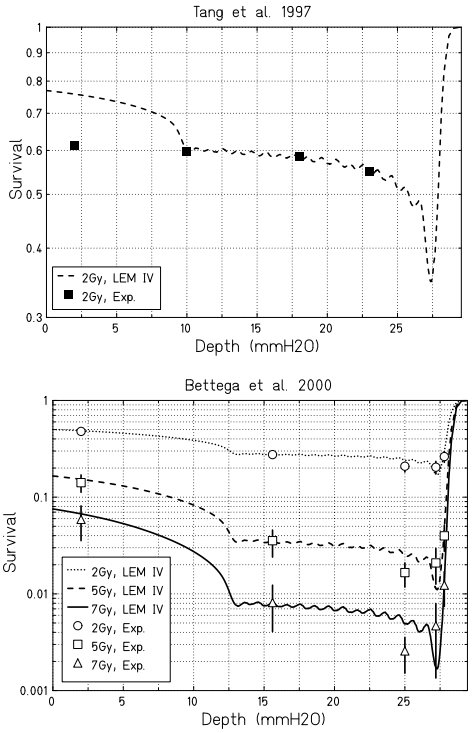

Figure 1: a) Comparison of measured and predicted cell survival (LEM IV) for a) CHO cells [1] for 2 Gy physical dose and b) SCC25 cells [2] for 2, 5 and 7 Gy physical dose at different positions of the SOBP (symbols). The lines correspond to the predictions of LEM IV.

Table 2:

Position	Dose	RBE exp. Bettega [2]			LEM prediction		
(mm)	(%)	2 Gy	5 Gy	7 Gy	2 Gy	5 Gy	7 Gy
2	65	1.00	1.00	1.00	0.97	0.97	0.98
15.6	100	1.058	1.043	1.035	1.071	1.058	1.056
25	101.5	1.23	1.23	1.23	1.18	1.15	1.13
27.2	91	1.39	1.30	1.26	1.42	1.35	1.31
27.8	52	2.064	1.95	1.89	1.79	1.70	1.65

References

[1] J. Tang et al., Brit J Cancer (1997) **76**:220.

[2] D. Bettega et al., Int J Radiat Biol (2000) **76**:1297.

[3] T. Elsässer et al., Int J Radiat Onc Biol Phys (2010) **78**:1177.

[4] M. Krämer and M. Scholz, Phys Med Biol, (2000) **45**:3319.

[*] Work is part of HGS-HIRe

Parallelization of plan-optimization for TRiP98 *

S. Hild[1,2], K.Zink[2], M.Durante[1,3] C.Bert[1,4] and C. Graeff[1,#]

[1]GSI, Darmstadt, Germany; [2]TH Mittelhessen, Germany; [3]TU Darmstadt, Germany; [4]Universität Erlangen , Germany .

Introduction

In clinical practice treatment protocols of inter-fractional moving tumours like the prostate carcinoma foresee only one optimization of a treatment plan. The margins are therefore enlarged to compensate the expected daily variation [1]. Organs adjacent to the prostate (e.g. bladder, rectum) however will in part be enclosed in the high dose regions when increasing the margins. Their tolerance dose limits the maximum therapeutic target dose. Variations of geometrical changes could also be considered via adaptive treatment methods that modify a treatment plan on a daily bases. This approach guarantees the best compromise between target coverage and sparing healthy tissue.

We aim on speeding up the complete therapy planning procedure for particles (e.g. daily CT-scan, contouring, plan-optimization and plan-verification) to a point where treatment delivery can directly follow a daily CT-scan and the patient can be kept in the immobilisation device. Amongst other requirements this demands fast optimization of treatment plans. In this scope the optimization part of the treatment planning code for particles TRiP98 [2;3] has been modified to run on a multi-core environment.

Material and Methods

The dose calculation of TRiP98 has already been modified to support multi threaded calculations [4]. All calculations carried out for dose verification are independent so that parallelizing this sector worked very well. Plan optimization starts with setting up a large dose correlation matrix (DCM) which contains a list of beam positions per target voxel that contribute to its total dose. During optimization the complete DCM has to be accessible and be kept in memory. The iterative optimization process can therefore not be calculated in parallel. However the dose calculation which is needed prior to each iteration has no such dependency and can be spread over multiple cores.

In the current implementation setting up the DCM and inter step dose calculation has been parallelized according to the scheme shown in figure 1.

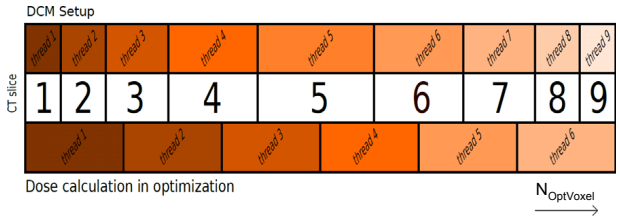

Figure 1: Illustration of OptVoxel distribution along the different threads.

Results / Current status

The speed up factor for parallel DCM set up increases with the DCM's size (figure 2). For small DCMs (e.g. single field (SF)) the time needed to create a thread restricts the total calculation speed. Also the performance of the parallel optimization depends on the DCM size. Multi field (MF) calculations therefore benefit more from utilising multiple cores.

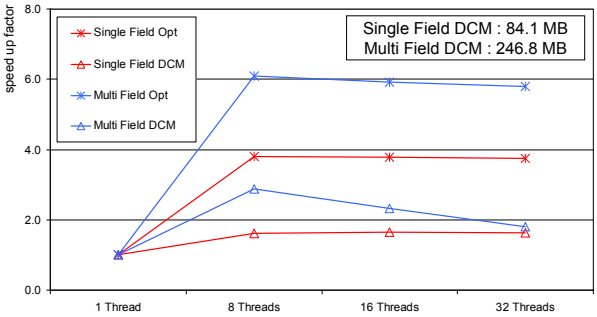

Figure 2: Performance of the parallelized code

The calculations have been carried out with an IBM Blade-Server PS701 (8 Cores, 4 Hyper-threads each). Due to the underlying architecture the algorithms show their peak performance when calculating on 8 threads.

The example calculation shown in figure 2 represents an optimization of the biological effective dose for a prostate cancer case using a grid spacing of 2mm and a planning CT with 256x256 voxels per slice. On the target with 4853 voxels (~55.5cm^3) 200 optimization steps were carried out. Calculations with one thread took 1290 sec and 1780 sec for SF and MF respectively. These times could be reduced to 340 sec for SF and 290 sec for MF.

References

[1] van Herk et.al. "The probability of correct target dosage: Dose-population histograms for deriving treatment margins in radiotherapy" Int J Radiat Oncol Biol Phys 47 (2000)1121-1135

[2] Krämer et al. "Treatment planning for heavy-ion radiotherapy: physical beam model and dose optimization" Phys. Med. Biol. 45 (2000) 3299–3317

[3] Krämer et al. "Treatment planning for heavy-ion radiotherapy: calculation and optimization of biologically effective dose" Phys. Med. Biol. 45 (2000) 3319–3330

[4] Trautmann et. al. "TRiP98: Parallelization of Dose Calculation" GSI Scientific Report HEALTH39 (2010) 478

* In part funded by HGS-HIRe

#c.graeff@gsi.de

Status of the TRiP98 Treatment Planning System *

M. Krämer[1], *M. Horcicka*[1,2,4], *E.Scifoni*[1], *and M. Durante*[1,3,4]

[1]GSI, Darmstadt, Germany; [3]FIAS, Frankfurt, Germany; [2]ITWM Kaiserslautern, Germany; [4]TU Darmstadt, Germany

Dose Optimization Algorithms

Various iterative algorithms to solve the dose optimization problem have been investigated in recent years [1]. The BFGS method as well as the popular Levenberg-Marquardt minimization (LMM) have now been integrated in the upcoming TRiP98 production version. Figure 1 shows that for problem sizes we usually encounter in ion beam radiotherapy, i.e. free parameter numbers up to and above 70000, text book wisdom (LMM and BFGS) tends to loose against the much simpler gradient based methods (steepest descent, SD, and conjugated gradients, CGFR).

Multi-material beam modelling

In ion beam treatment plans all tissue is treated as water, and even obvious deviations like lung or bone are only accounted for their influence on penetration depth. In particular bone, however, might have a different transport characteristic due to its significantly different elemental composition. To this end, materials other than water have been introduced in the TRiP98 transport model. Figure 2 shows a comparison with experimental data [2]. Whereas "spongious bone" data agree with density scaled water as well as with preliminary transport calculations, deviations are seen for "compact bone", which are still under investigation.

New modalities

In view of upcoming irradiations with protons above 1 GeV, exploratory treatment plans have been performed for this new potential modality. Since at these energies the Bragg peak can no longer be used, cross fire techniques have to be implemented. A semi-empirical depth dose profile was constructed from the experimental data in [3]. As a proof-of-principle, figure 3 shows a planned four-field irradiation of a simulated tumour in the biophantom. The entrance dose is roughly 50% of the target dose.

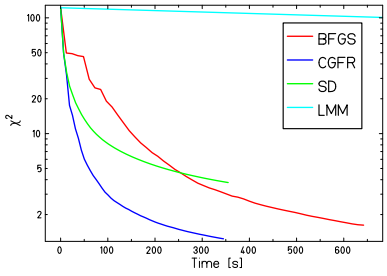

Figure 1: Convergence speed of optimization algorithms.

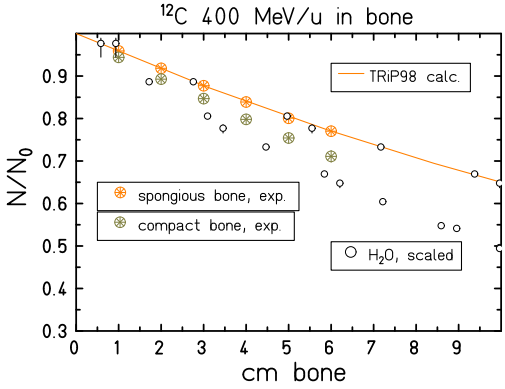

Figure 2: Primary beam attenuation in bone.

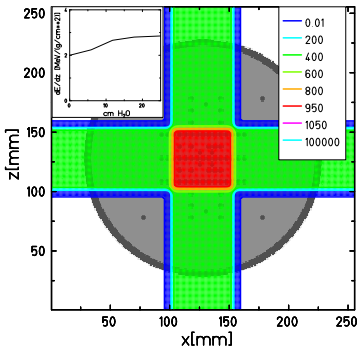

Figure 3: Treatment plan for 2.5 GeV protons. The assumed depth dose profile is shown in the insert.

Technical developments

With more demanding treatment plans, in particular high resolution CTs as well as 4D irradiations, the computational footprint of TPS calculations has dramatically increased in comparison to the initial TRiP98 version introduced in 1999. Thus the support of large (64bit) address spaces, large files and multicore CPUs have finally reached the production version. The underlying batch system (LoadLeveler) has been tuned accordingly.

References

[1] Horcicka M. et al., Phys. Med. Biol., 58 (2): 275-286 (2013)

[2] Eichhorn A., et al., GSI Report 2011

[3] Z.Yu, et al., J. Radiat. Res. 53(4): 620-627 (2012)

*Work co-funded by the European Commission under FP7 Grant Agreement Number 228436

Systematic investigation of RBE using the particle irradiation data ensemble*

T. Friedrich[1], *U. Scholz*[1,2], *T. Elsässer*[†1], *M. Durante*[1,2], *and M. Scholz*[1]
[1]GSI, Darmstadt, Germany; [2]TUD, FKP, Darmstadt, Germany

Introduction

Survival assays of cultured cells are frequently used to investigate the response to both photon and ion radiation. Its dose dependence is commonly visualized as survival curves. An enhanced efficacy of ion irradiation compared to photon irradiation is evident for many endpoints and is expressed by the relative biological effectiveness (RBE), which is the ratio of doses of ion and photon radiation needed to cause the same effect [1]. The experimental investigation of the systematics of RBE and dose response curves is complemented by predictive models such as the Local Effect Model (LEM). To probe their accuracy a global view on available data is needed. Therefore the Particle Irradiation Data Ensemble (PIDE) was set up [2], which is a collection of ion and photon survival curves from the literature. Meanwhile it comprises 855 dose response experiments, parameterized by the linear-quadratic (LQ) model for photons and ions, from 77 publications [3].

Results

For ion irradiation survival decreases usually linearly with increasing dose. This makes it difficult to perform reliable fits in particular for the quadratic parameter β_I. It is not clear up to now how β_I evolves with LET. Here PIDE allows model comparisons with good statistics.

Figure 1 presents β_I normalized to the photon β_γ parameter vs LET for different particle types and cell lines. The spread of the data points is large, and it is unclear if β_I systematically exceeds β_γ or falls off starting from small LET. Hence a running average procedure was applied. The emerging average curves suggest a small initial increase of β_I and a final falloff to zero. It may be explained by saturation effects, as for very large LET each hit cell is killed anyway, and hence only hit statistics matters, resulting in a straight survival curve.

Experimental findings do not precisely reveal the nature of β_I, and also RBE models reflect a huge variability in the predictions. This can be seen in Fig. 2 where β_I for three models is compared with data from two cell lines. The figure indicates that neither experimental nor model data show a clear systematics, so some aspects of high LET cell survival are still unclear. With respect to clinical applications the accurate modelling of β_I presumably becomes relevant in hypofractionation, whereas for more conventional fractionation schemes treatment plans are comparably robust against larger variation of β_I.

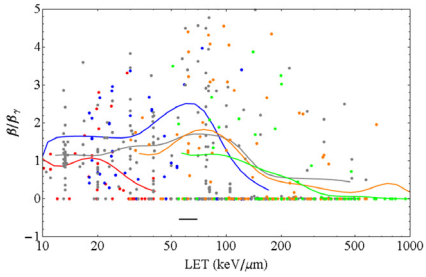

Figure 1: Ratio of the LQ parameter β_I of ions to that of photons vs LET for monoenergetic ions for different ion species (p: red; He: blue; C: grey; Ne: orange; heavier ions than Ne: green). The solid lines are running averages with correlation length as indicated by the horizontal bar.

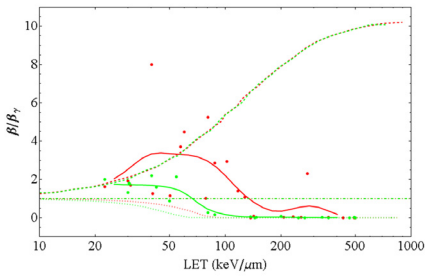

Figure 2: As Fig. 1 for two individual cell lines (V79: red, HSG: green). Thick lines: running averages of the data. Dashed, dotted and dashed-dotted lines: model predictions of the repair-misrepair-fixation model, the LEM, and the microdosimetric-kinetic model, respectively.

Conclusions

The presented example demonstrates that the PIDE is appropriate to identify open points in the dose response systematics. It is helpful for model evaluation and accessible to the research community (http://www.gsi.de/bio-pide).

References

[1] ICRP Report 92, Elsevier (2003).
[2] T. Friedrich, GSI Sci.-Rep. 2010, Health-22.
[3] T. Friedrich et al., J Radiat Res 2012, in press.

* Work supported by Siemens Healthcare. Work is part of HGS Hire.
† Now working at Siemens Healthcare.

Radon exposure setup for cells and small animals – preparation for experiments on inflammation related effects*

A. Maier[1], C. Fournier[1], M. Durante[1,2] and G. Kraft[1]

[1]GSI, Darmstadt, Germany; [2]TU Darmstadt, Germany

There is a large interest in the radiobiological response to the exposure to Radon gas because of two reasons: In many areas, radon gas emanates from the soil containing uranium isotopes and its daughter nuclei .There, a chronic exposure to radon gas and its decay products is probably the main reason for tumor induction after smoking. [1] But radon is also used in the medical treatment of inflammatory diseases such as ankolysing spondilitis. Every year some ten thousand rheumatic patients undergo radon inhalations, total body exposure or bathing in radon containing water. [2]

In the past, the effects of the chronic exposure have been mainly studied in epidemiologic projects in the radon exposed areas while separately the anti-inflammatory reaction was mainly studied in patients after radon exposure. [3] In both cases the dosimetry, i.e. the amount and the time-distribution of incorporated radon-progenies over the body, is not very well known.

In future experiments we want to study the radiobiological effects of radon exposure *in vitro* and *in vivo* under precisely controlled conditions concerning the radon activity, the exposure timing, the temperature and other parameters that might influence the radon uptake and the metabolism of the biological objects. For this purpose a radon exposure chamber has been constructed in the last year and is presently under initial operation in order to study both effects, the anti-inflammatory behaviour and the mutagenic alterations in cell culture and in mice.

Requirements for measurement setup

In the radon exposure chamber the same conditions like in radon galleries and in the vapour bath both at Bad Gastein should be simulated (temperature 37°C, relative humidity 70-100%, activity-concentration 44-440kBq/m³). These variables must be monitored and regulated during the experiments. For experiments with cells the CO_2-concentration has to be controlled.

As we want to do experiments with cells and also with small animals, there must be space for a cage inside the chamber and the whole system must meet the requirements of the Protection of Animals Act.

Results

The chamber in its present design is a barrel made of stainless steel with plane surfaces and has a content of 50 l. There is a hermetic seal between the cover plate and the body.

For a schematic drawing of the whole system see figure 1. The chamber is immersed in a water bath. So the temperature can be regulated. The gas is coming from a Radium-226 source which emanates Radon-222. The radon is guided into the chamber or - when the radon is not needed for experiments - directly into an absorption filter of activated carbon where it is absorbed completely.

For the air moistening system controlled volumes of gas and fluid are mixed and evaporated. The steam is then routed to the chamber. With this system contaminations of the chamber can be avoided.

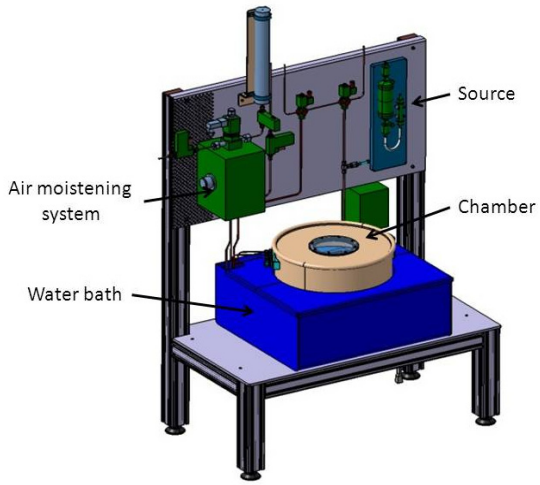

Figure 1: schematic drawing.

After the experiment the system is flushed with normal air to get rid of the radon inside the chamber and one can open the system and take out the samples without any risk of contamination

References

[1] Potential Health Effects of Indoor Radon Exposure, E. Radford, Experimental Health Perspectives, Vol. 62, pp.281-287, 1985

[2] Radon als Heilmittel: Therapeutische Wirkung biologischer Wirkungsmechanismus und vergleichende Risikobewertung, P. Deetjen et. al., Verlag Dr. Kovac, 2005.

[3] Modulation of Inflammatory Immune Reactions by Low-dose Ionizing Radiation: Molecular Mechanisms and Clinical Application, F. Rödel et. al., Current Medicinal Chemistry, 2012.

* Work is part of HGS-Hire and supported by BMBF project funding reference number 02NUK017A

Experimental verification of TRiP-OER *

E. Scifoni † [1], *W. Tinganelli*[1,2], *W. Kraft-Weyrather*[1], *M. Durante*[1,2,3], *A. Maier*[1], *and M. Krämer*[1]
[1]GSI, Darmstadt, Germany; [2]IOL GSI-NIRS, Chiba, Japan; [3]TUD, Darmstadt, Germany

One of the key challenges for advanced radiotherapy is the possibility to adapt the treatment to patient-specific features, i.e. to perform an *adaptive treatment planning*. Among these features, increased radioresistence of tumor regions due to hypoxia (lower degree of cells' oxigenation) assumes a crucial importance, given the extremely poor prognosis connected with this phenomenon. Ion beam radiation allows in principle a larger flexibility and a higher potential for achieving an efficient adaptive treatment planning, but specific tools are lacking.

The TRiP98 code [1], pioneer treatment planning system for ion beams, which contributed to the success of the GSI pilot therapy project, was then recently extended toward this direction, and specifically, to implement the biological optimization including the hypoxia-induced radioresistence, i.e., the oxygen enhancement ratio (OER).

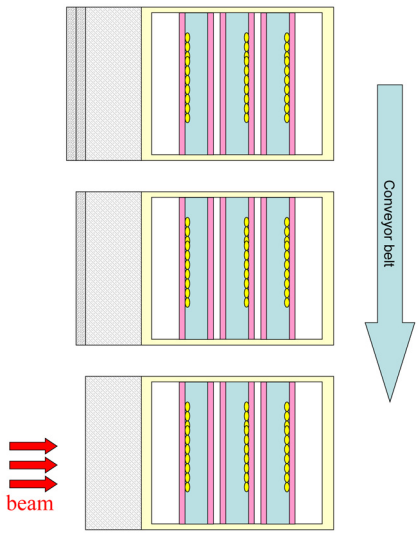

Figure 1: Experimental setup (see text).

The TRiP-OER extension mainly consist in the possibility to introduce a selective treatment of differently oxygenated areas of a tumor, once its spatial oxygenation map is provided as an input (e.g. exploiting the recent PET functional imaging techniques [2]), through an effect-based optimization aiming at restoring a prescribed survival level in the overall tumor. The extension relies on a semiempirical model description of the OER as a function of LET and oxygen concentration (pO_2) [3], and the modification of the biological effect calculations introduced into the code and allowing to perform not only forward but also inverse planning, obtaining an effective OER driven optimization [4,5].

Dedicated experiments were then designed to verify the expected survival predicted by the code in a carbon ion extended target irradiation, and specifically, with a focus on the very last part of the extended volume, where the LET effect in suppressing the OER is maximum and has a steep gradient. This has been done by exposing CHO-K1 cells in the GSI patented hypoxic triple ring chambers [6] in a sequence designed to cover densely the relevant depth region (Fig.1): the chambers containing the rings filled with medium were exposed to the beam by a conveyor belt in anoxic and normoxic conditions.

The experiments, performed during several carbon beamtimes in 2011 and 2012, returned, despite a consistent experimental uncertainty, a remarkable agreement with the calculations of TRiP-OER (Figure 2).

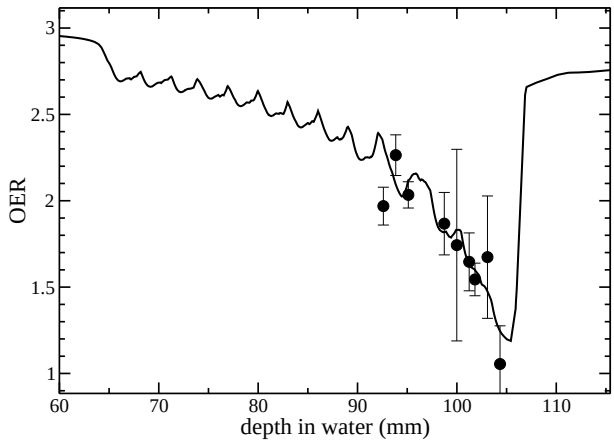

Figure 2: TRiP-OER computed OER values across a single field extended target irradiation (line) and corresponding experimental data (points).

References

[1] M. Kramer and M. Durante, Eur. Phys. J. D. 60 (2010) 195.

[2] S. M. Bentzen and V. Gregoire, Semin Radiat Oncol 21, 101 (2011).

[3] E. Scifoni, M. Krämer and M. Durante, GSI Sci. Rep. 2011 (2012) 521.

[4] M. Krämer, E. Scifoni, C. Wälzlein and M. Durante, J. Phys. Conf. Ser. 373 (2012) 012017.

[5] E. Scifoni, W. Tinganelli, W. Kraft-Weyrather, M. Durante, A. Maier and M. Krämer, Phys. Med. Biol., submitted.

[6] C. Schicker et al., Pat Ep 09002 402 (2009), 7.

* Work supported by the European Commission under FP7 Grant Agreement Number 228436, project ULICE

† e.scifoni@gsi.de

GSI-NIRS International Open Laboratory: filling the gap of oxygen effect measurements*

M. Durante[1,2,3], W. Tinganelli[1,3,4], E. Scifoni[1], R. Hirayama[4] and Y. Furusawa[3, 4]

[1]GSI, Darmstadt, Germany; [2]TUD, Darmstadt, Germany; [3] IOL, International Open Laboratory; [4]NIRS, Chiba, Japan

The main goal of the GSI-NIRS International Open Laboratory (IOL) "Radiation Quality Research Unit" is the verification, with a set of experimental OER (Oxygen Enhancement Ratio) data points of a semi-empirical model developed at GSI that is being used for the implementation of adaptive treatment planning in TRiP98 [1,2], for specifically targeting hypoxic tumors. The longstanding lack of experimental measurements exactly in those conditions of oxygen concentration (pO_2) and linear energy transfer (LET) most relevant for a clinical application of the method, guided the need of this project, joining the two most experienced groups worldwide (GSI and NIRS) on hypoxic irradiation with ion beams. The IOL kick-off meeting was held in Darmstadt on 05.09.2011. The last progress report meeting was held in Chiba, Japan on 22.01.2013, where actual results were presented and further projects and collaborations between units were discussed.

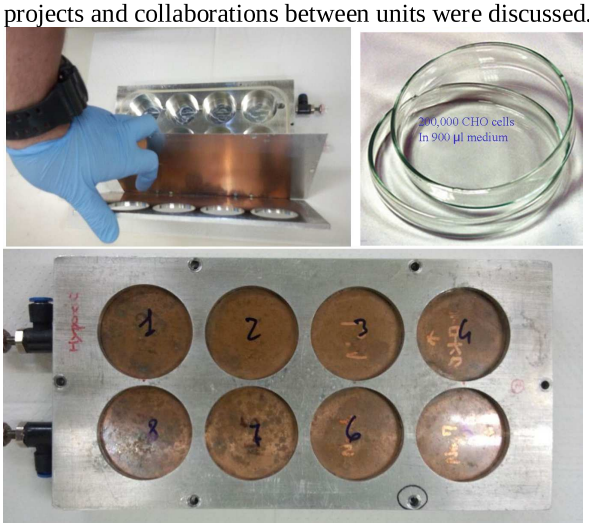

Figure1: Experimental setup for hypoxic irradiation at several tunable oxygen concentrations adopted at NIRS for the present project, with ion beams and X-rays.

IOL Status report

Experimental points about the complete anoxic condition (0%) and a partially hypoxic (0.5%) one have been measured at NIRS with CHO cells and a dedicated experimental setup (Figure 1) to verify our model. The results (Figure 2) shown a reasonable agreement with the prediction model, especially in the slope region, suggesting a slight adjustment of the low LET asymptote for the specific cell line. The higher OER value found for the very high LET, is due to the large ions fragmentation, since we used the HIMAC-NIRS passive beam experimental room.

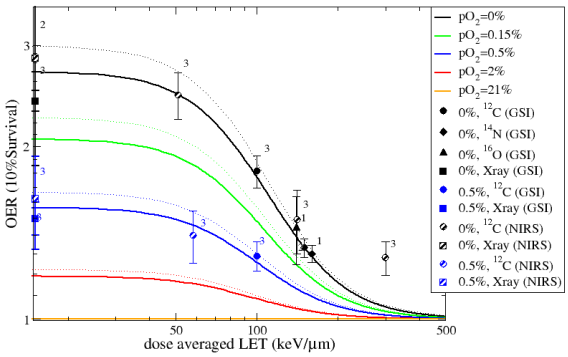

Figure 2: Model of the dependence of OER from LET for different oxygen partial pressures under implementation in TRiP98 and independent experiments performed at GSI-IOL/NIRS (points).

Collaborations

In the same time, our unit started the planned collaborations with the Particle Therapy Molecular Target Unit (Profs. Nickoloff, Colorado State University and Jeggo, University of Sussex). Several other projects related to the hypoxic irradiation with ion beams were initiated, namely related to the *Phoenix rising* effect [3], and suppression of the tumor immunogenicity capacity [4]. A link with the Radiation Response Model Unit for alternative OER modeling is also planned.

OUTLOOK

Further OER experiments are planned at 2% and 0.15% oxygen concentrations. Selected other experiments at LET 75-30 keV/µm at anoxia and 0.5% oxygen will be also performed. About the *Phoenix rising* effect we planned to verify with a specific experiment the molecular pathway. In February 2013 we will start the immune system-mediated radiation effect experiments.

References

[1] E. Scifoni et al., Phys. Med . Biol. submitted
[2] E.Scifoni et al., this report.
[3] Q. Huang et al., Nat. Med. 17 (2011): 860-6.
[4] S. Formenti and S. Demaria, Lancet Oncol. 10 (2009) 718-726

* Supported by the NIRS IOL grant to GSI.
#m.durante@gsi.de

Response of organotypic slice cultures to ionizing radiation

Mareike Müller[1,2,3,], Marco Durante[2,3,4], Francesco Natale[2], Horst Stöcker[2,3], Horst-Werner Korf[1]*

[1]Dr. Senckenbergisches Chronomedizinisches Institut, Goethe-Universität Frankfurt/Main [2]GSI Darmstadt, Germany
[3]Frankfurt Institute for Advanced Studies, Frankfurt/Main [4]Technische Universität Darmstadt.

The aim of this work was to evaluate the response of liver and pancreas tissue to sparsely and densely ionizing radiation. For this, organotypic slice cultures (OSC) of liver (OLSC) and organotypic explant cultures (OEC) of pancreas (OPEC) were prepared from C3H wildtype (wt) mice and transgenic c-myc/TGF-α mice with an inducible liver tumor. OLSC from the transgenic c-myc/TGF-α mice were prepared from healthy (OHLSC) and neoplastic (ONLSC) parts of the liver. The pancreas from these animals was cultured as well (OTPEC). In order to evaluate a possible timedependence of the tissue response to ionizing radiation, OLSC and OPEC, OHLSC, ONLSC, and OTPEC were prepared at two different times of day: at the middle of the subjective day and at the middle of the subjective night.

Samples were cultured in a membrane-based culturing system with a liquid-air interface for several days. OLSC and OPEC from C3H wt-mice were irradiated with X-rays at doses of 2Gy, 5Gy, or 10Gy. OHLSC, ONLSC, OTPEC were irradiated with ^{12}C-ion extended Bragg peaks at the same doses. Mock-irradiated samples served as controls. All samples were fixed 1h and 24hrs post-irradiation, respectively, and immunohistochemically analyzed for markers of proliferation (Ki67), apoptosis (Caspase3), and DNA double-strand breaks (γH2Ax).

While the pancreas samples, unfortunately, did not produce any meaningful results with regard to the evaluated parameters, healthy liver tissue showed distinct day-night differences with regard to all three analyzed parameters: the proliferation rate was significantly increased at the middle of the subjective day compared to the middle of the subjective night. Contrariwise, the apoptosis rate and rate of DNA double-strand breaks was significantly increased at the middle of the subjective night. These day-night differences were not detected in ONLSC. Regardless of the radiation type and dose, irradiation of healthy liver tissue did not influence the evaluated parameters. In ONLSC, however, the rate of DNA double-strand breaks increased dose-dependently.

The effects of ionizing radiation on the circadian clockwork were further examined in tissue samples of transgenic Per2^{luc}-mice [1]. Per2^{luc}-mice express the enzyme luciferase under the control of the *Per2*-promoter, an important element of the circadian clockwork. Therefore, the analysis of these animals allowed to record the circadian rhythm of the molecular clockwork in liver and other tissues via realtime recordings of the luciferase-activity. As could be shown in OLSC and OEC from adrenal glands, ionizing radiation leads to a dose-dependent phase advance of the circadian clockwork.

The results of this project lead to the conclusion that ionizing radiation alter the circadian clockwork, but barely influence proliferation and apoptosis in healthy liver tissue.

References

[1] [Yoo2004]Yoo SH, Yamazaki S, Lowrey PL, Shimomura K, Ko CH, Buhr ED, Siepka SM, Hong HK, Oh WJ, Yoo OJ, Menaker M, Takahashi JS „PERIOD2::LUCIFERASE real-time reporting of circadian dynamics reveals persistent circadian oscillations in mouse peripheral tissues“ Proc Natl Acad Sci U S A. 2004; 101(15): 5339–5346

* M. Müller is supported by a Puschmann scholarship.

A VOI-based 4D optimization method for the ion beam therapy of intrafractionally moving tumours

C. Graeff, R. Lüchtenborg, M. Durante, C. Bert

GSI, Darmstadt, Germany

Introduction

Ion beam therapy permits highly conformal dose delivery. It results in significantly improved therapy outcome in a number of cancer types. The treatment of moving tumour is especially challenging in ion beam therapy due to the high sensitivity to radiological depth which changes with e.g. breathing motion. For scanned beam delivery also interplay effects between pencil beam and tumour motion have to be considered.

Motion mitigation strategies such as tracking inherently use a 3D optimization on a static reference phase of a 4DCT. The treatment plan is then adapted, in part online during delivery, to deliver dose to the moving tumour; especially range-adaptation is challenging [1]. We propose a method that includes the motion information already during optimization, resulting in a 4D treatment plan as conformal as tracking.

Material and Methods

To enable 4D optimization, a correlation between tumour motion and delivery progress has to be defined. This also has to be upheld during delivery. In the present method, the target volume (VOI) is divided into subsections, with each subsection to be irradiated in a specific motion phase. A single treatment plan is prepared for each subsection transformed to the corresponding motion phase. The resulting combined 4D treatment plan is optimized simultaneously for all motion phases. In this way, correct geometrical motion and resulting changes in radiological depth is already factored into the optimization process.

The subsections were chosen as pie slices from beam's eye view, so that each motion phase has similar dose contributions to each iso-energy slice (IES). The pie slices were arranged such that the breathing motion moved them apart during delivery creating a broad, low-dose entry channel.

For delivery, a dedicated treatment control system (TCS) is needed together with precise motion monitoring to keep up the motion correlation assumed during optimization.

At GSI, this 4D-TCS was realized as an addition to the original Cave M TCS. The main control structures of the original TCS were unchanged, but the actual pencil beam to be delivered were determined as a function of motion phase and this motion phase's progress from the external 4D-TCS. The 4D-TCS also controlled the change of IES. If for a given IES a certain motion phase's plan was completely delivered, the beam would be gated using fast KO extraction.

The feasibility of the 4D optimization was investigated in a planning study in a lung cancer patient using a single A-P field with a physical target dose of 1 Gy. The feasibility of the 4D TCS was tested in a simple film experiment in a Ca beam time at Cave M.

Results

The patient study resulted in a conformal dose to the target with V95=97% in spite of a 22 mm motion amplitude. Figure 1 shows the conformal dose as well as the dose in the entry channel, which is smooth and without hot spots as opposed to tracking which experiences inverse interplay [1].

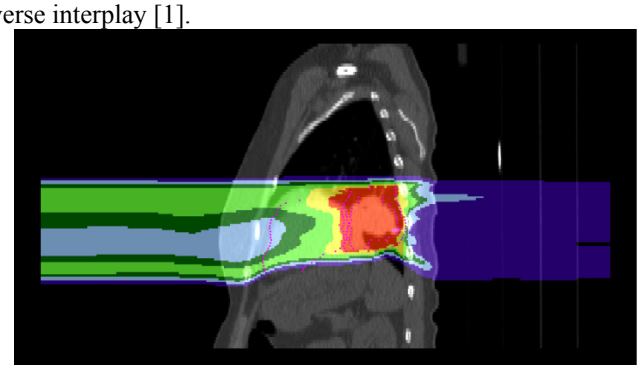

Figure 1: Sagittal dose cut of the patient study, showing conformal dose also in the main S-I motion direction.

The film experiments resulted in a large improvement of dose homogeneity and conformity in comparison to an interplay irradiation (Fig. 2). It also revealed the impact of residual motion of up to 3 mm within the motion phases, which was not considered during the patient study.

Figure 2: Interplay, static and 4D optimized (left to right) dose to a 3cm circular target on a radiographic film.

Conclusion

4D optimization allows conformal dose delivery without additional equipment for online range adaptation. Residual motion within the quasi-static motion phases would have to be countered by re-scanning or fractionation.

References

[1] C. Bert et al. "Dosimetric precision of an ion beam tracking system," Radiat Oncol **5**, 61 (2010).

Confirmation of the tumour motion extraction method*

R.Brevet[1], C.Graeff[1], C.Bert[2] and M. Durante[1,3]

[1]GSI, Darmstadt, Germany; [2]Universitätsklinikum, Erlangen, Germany; [3]Technical University Darmstadt, Darmstadt, Germany

Introduction

Radiotherapy treatment of tumours located in the thorax or in the abdomen has to take into account a motion which can be caused by breathing or heart pulsation. [1] During scanned beam ion therapy, this intra-fractional motion can be responsible of dose delivery on organs at risk (OAR) and underdosage on the tumour. Several motion compensation techniques exist, such as the association of internal monitoring and external surrogates.

The motion of the tumour must be extracted from patient imaging datasets and correlated to the extern signals so that extern surrogates only can then be used to avoid additional imaging dose to the patient. Motions were extracted from MegaVoltage (MV) fluoroscopy sequences [2], but had to be confirmed as the real motions and positions of the tumours.

Algorithm validity

To find out if the obtained motions correspond to the real tumour trajectories and to confirm the validity of the algorithm, several comparisons with 4DCT datasets of the corresponding patients were investigated.

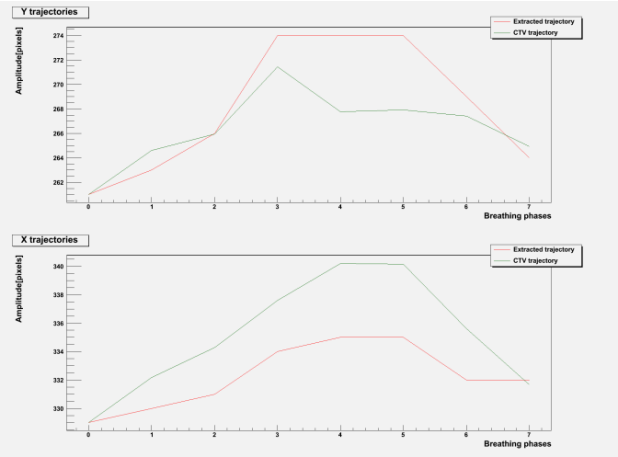

Figure 1: Comparison of trajectories obtained with the clinical target volumes (CTV) of the 8 phases of the 4DCT datasets (green) and as a result of the tracking algorithm applied on the 4DCT datasets (red)

A first example is displayed on Figure 1. The algorithm was here applied on the 4DCT datasets in order to evaluate its ability to yield a motion from this kind of imaging data.

* RB is funded as an ESR within the EU-FP-7 ENTERVISION framework, Grant Agreement no. 264552. Further funds received by DFG KFO 214.

Extracted motion confirmation

Figure 2 shows another type of comparison, which here aims at looking at the behaviours of extracted trajectories from MV-fluoroscopy sequences and CTV-based trajectories from 4DCT datasets.

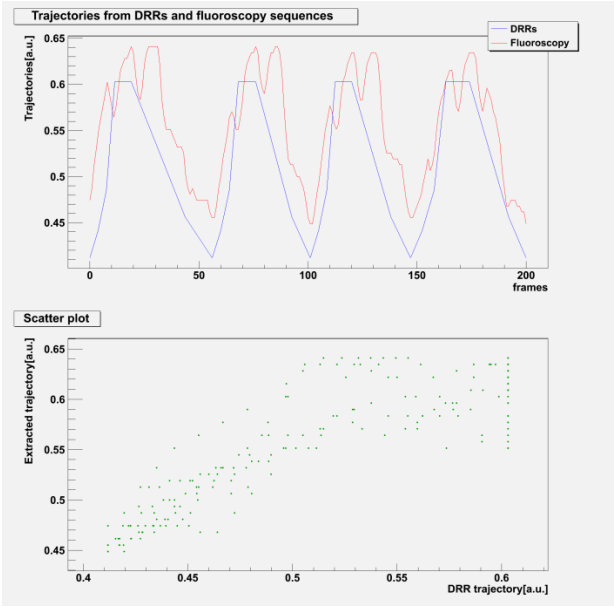

Figure 2: *(top graph)* Comparison of trajectories obtained with digitally reconstructed radiographs (DRR, blue) and with the motion extraction algorithm (red), *(bottom graph)* scatter plot used to compare the behaviours of both trajectories with each other.

For all five lung tumour patients, different parameters, such as different starting points or different DRR settings, had to be used to achieve a correlation of $r > 0.75$ and to obtain good contrast on DRRs.

Conclusion

Comparison to traces extracted from 4DCT data turned out to be strongly depending on the patient. Thus more data are needed to make conclusions.

References

[1] C. Bert and M. Durante, 2011 Phys. Med. Biol. 56, R113-R144.

[2] R. Brevet et al, “Analysis of internal/external motion correlation”, 2012 GSI Scientific Report

Influence of cardiac motion on pulmonary veins for the non-invasive treatment of atrial fibrillation with a scanned cabon ion beam*

A. Constantinescu[1,2], *H.I.Lehmann*[3], *C. Graeff*[1], *D.Packer*[3], *M. Durante*[1,2], *and C. Bert*[1,4]

[1]GSI, Darmstadt, Germany; [2]Technische Universität Darmstadt, Germany; [3]Mayo Clinic College of Medicine, Rochester, USA; [4]Universitätsklinik Erlangen, Germany

Introduction

Arrhythmias describe a wide range of caridac conditions associated with abnormal heart beats. The most common arrhythmia is atrial fibrillation (AF), describing an irregular and often rapid heart beat. Although not considered life treathening, it causes a range of complications and significantly increases the risk of suffering a stroke. AF is often treated by radiofrequency ablation aiming for an electrical isolation of the pulmonary veins (PVs). This is a complicated and time consuming procedure with varying success rates [1]. Recently, animals studies showed that a non-invasive albation with photons is feasible [2]. Based on the experience gained in cancer treatment lesion creation with ions seems promising. In order to study the treatment delivery for such an irradiation, the cardiac motion due to respiration and heart beat was studied. The resulting motion volume histograms (MVHs) of the PVs will be presented for one patient case.

Material and Methods

A time resolved Computed Tomography scan of an AF patient, gated on the respiration as well as on heart beat (5DCT) was acquired. Forty quasi-stationary sections (motion phases) resulted as each of the two respiratory phases (exhale, inhale) included twenty cardiac phases (5% intervals of the cardiac cycle). PV ablation lines for the left PV (LPV) and right PV (RPV) were contoured (x≈5 mm, y≈20 mm, z≈35 mm, respectively for LPV and RPV). A non-rigid registration of the motion phases was carried out with the open source software Plastimatch. The MVHs were calculated with the in-house treatment planning software TRiP4D [3]. The motion of the PVs due to the influence of the heart beat was investigated by studying the difference between the minimal and maximal phase of the cardiac cycle at the exhale position of the patient. The influence of the respiration was studied by keeping the cardiac phase constant and looking at the displacement vectors between inhale and exhale.

Results

In fig.1 the MVH for the motion of the PVs due to the heart beat is shown (left column) and under respiratory influence (right column) for the different motion directions as well as the LPV and RPV, respectively.

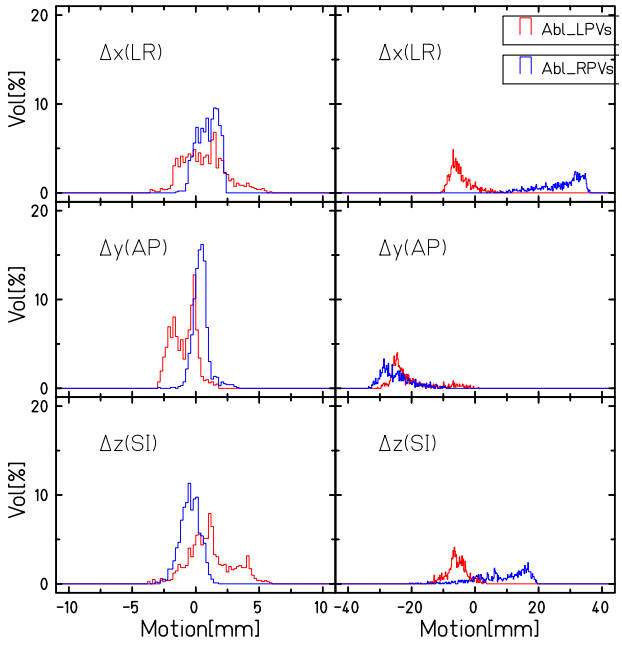

Figure 1: MVHs of PV motion. The left column shows the displacement due to the cardiac cycle, the right column due to respiration. The top row shows the motion in the left-right (LR) direction, the second row in the anterior-posterior (AP) direction and the third row in the superior-inferior (SI) direction.

As expected, the motion of the PVs due to respiration is big (∼ 20 mm), while the motion due to heart beat alone is relatively small (∼ 5 mm). Nevertheless, taking into account the small size of the target as well as the planned beam spot size (x=1 mm, y=1 mm), the motion due to heart beat can not be neglected.

Conclusion

From the investigation of one single patient CT it seems as if the irradiation of the PVs for a non-invasive treatment of AF motion mitigation technqiues need to be applied not only on the respiration of the patient but also on the heart beat itself.

References

[1] Cappato et al., Circulation 111(9), 2005

[2] Sharma et al., HeartRhythm 7(6), 2010

[3] Richter, Dissertation, TU Darmstadt, 2012

* Work is part of HGS-HIRE

Integration of an optical tracking system for beam guidance in radiotherapy of moving targets using carbon ions*

R Kaderka[1], G Fattori[2], A Pella[2], M Seregni[2], A Constantinescu[1], N Saito[1], P Cerveri[2,3], M Riboldi[2,3], G Baroni[2,3], M Durante[1,4] and C Bert[1,5]

[1]GSI, Darmstadt, Germany; [2]Politecnico di Milano, Milano, Italy; [3]CNAO foundation, Pavia, Italy; [4]Technische Universität, Darmstadt, Germany; [5]Universitätsklinikum, Erlangen, Germany

In the therapy pilot project from 1997 to 2008 over 400 patients with tumours in the head and neck region or in the prostate were treated at GSI with carbon ions. The aim of several research groups is to extend carbon ion therapy to moving targets such as lung tumours. Interplay of the scanned ion beam and tumour motion can lead to unacceptable dose profiles in the patient.

In order to compensate for tumour motion, several mitigation strategies have been developed and implemented at GSI. For applying the compensation it is vital to have an accurate observation of the target position over time.

In this study we present the implementation of an infrared based optical tracking system (OTS) and its experimental validation using an anthropomorphic breathing phantom in order to simulate the clinical workflow of a lung tumour treatment.

Methods and materials

Breathing phantom

A homemade breathing phantom was chosen for the treatment. It consists of PVC bones in the thorax region covered with rubber acting as patient skin. A string is attached to the chest wall which can be pulled with an electrical motor. This leads to a contraction of the phantom resulting in a breathing-like motion.

The phantom is filled with a PMMA block containing 20 pinpoint ionization chambers. This block serves as target and is moved in three-dimensions using an industrial robot arm synchronized with the thorax deformation. (A video is shown in [1])

Among the motion compensation techniques implemented at GSI, beam tracking was chosen for the experiment. In this approach, the scanner magnets are used to steer the ions following the target motion. The motion can also lead to ion range changes, for example when traversing rib bones. To compensate for the changes in range a double wedge system is employed to adjust the amount of material in front of the target. [2]

Motion detection

To fully exploit the potential of beam tracking the target position must be known with high-frequency and accuracy. Fluoroscopy represents a possible solution, but results in high additional dose to the patient. Therefore different approaches using external motion surrogates are investigated.

In this approach an infrared OTS was implemented in the treatment room of GSI. Several markers coated with a reflective surface are attached on the phantom surface. Three cameras and IR emitters capture the reflected light and thus determine the marker position. The target position is estimated from the marker signal using external-internal correlation models. The correlation models are based on the 4DCT taken for treatment planning.

Experimental setup

The breathing phantom was setup in the cave using the OTS cameras. The goal of the irradiation was to deliver 1 Gy dose in the target with carbon ions.

To assess the impact of the motion compensation, several irradiations were performed with different parameters. The motion was varied from a regular breathing to irregular breathing patterns with baseline shifts or phase shifts between thorax and target motion. The dose measured during motion was compared to a static reference case.

Results and conclusion

For the regular breathing, a mean dose difference of 0.8±3.7% (mean ± std. deviation) was measured for the pinpoint chambers relative to the static case when using correlation models. This represents a significant ($p<0.001$) improvement over the non-compensated irradiation where the difference was -13±25%. A significant improvement was also found when introducing baseline drifts (2.5±3.2%) or phase shifts (0.2±4.3%).

The experimental results show that beam tracking using an OTS for beam guidance is able to deliver the treatment in a clinical scenario with dose profiles that are comparable to a static case.

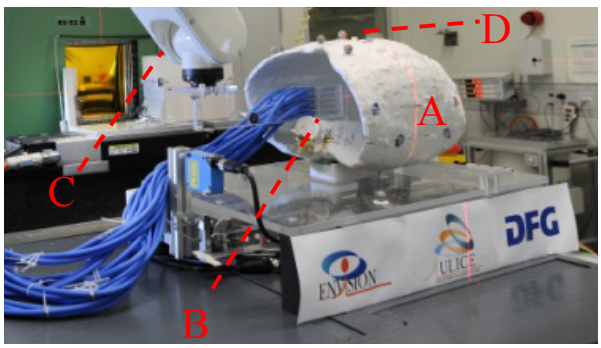

Figure 1: Breathing thorax (A), ion chambers (B), robotic arm (C), reflective markers (D). Picture by G.Otto, GSI

References

[1] http://www.youtube.com/watch?v=4QjsM2xUC3I
[2] Bert et al, Radiat. Oncol, 2010

* supported by EU-FP7, grant agreement no. 228436

Ion Beam Tracking using Ultrasound Motion Detection

Matthias Prall[1], *R. Kaderka*[1], *J. Jenne*[2,4], *N. Saito*[1], *C. Sarti*[2], *J. Schwaab*[2], *and Ch. Bert*[1,3]

[1]GSI, Darmstadt, Germany; [2]Mediri GmbH, Vangerowstrae 18, 69115 Heidelberg; [3]Universitätsklinikum Erlangen, Universitätsstrae 27, 91054 Erlangen; [4]Fraunhofer MEVIS, Universitätsallee 29, 28359 Bremen

Motivation

In particle therapy of moving tumors, currently being implemented at several sites, beam scanning is the preferred option to conform the dose distribution to the target. This technique allows to follow the motion of e.g. a tumor in the lung via motion mitigation techniques [1]. Real-time knowledge of target position with mm precision is a requirement for these techniques. We investigated the feasibility of motion detection using ultrasound (US) at the heavy ion tumor treatment facility of GSI Darmstadt.

Materials and Methods

In our feasibility study (cf. Figure 1), a robotic arm (KUKA KR 5 sixx R850) generated various periodic two-dimensional trajectories in a plane perpendicular to the beam. A field of 3×3 cm^2 was homogenously irradiated with a E=200 MeV/u, FWHM=6 mm beam of calcium ions on radiosenstive films (Kodak X-Omat) using the beam tracking technique [1]. A US position measurement system (mediri GmbH, Heidelberg) was integrated into the GSI therapy control system. A rubber ball was used as tumor surrogate. Its position in water was continously measured by the US system with a sampling rate of about $\Delta t = 35$ ms. The films were attached to the robot arm and thus moved with the rubber ball. Position reconstruction from US and data communication introduced a delay of $D = 70 - 80$ ms until irradiation, resulting in a deviation of up to about 5 mm. We compensated this delay using an artificial neural network (ANN). ANNs are nonlinear computational models which can be used to predict the evolution of a discrete time-series from previous values [2]. We performed several measurement series with a moving and one with a static target (reference). For each motion axis we used the trajecory $A \cdot \sin^{2n}(\frac{2\pi}{T}t)$ with $n = 1, 2, 4$, $T = 3$ s and $A = 10$ mm. We have chosen these trajectories as they are known to model diaphragm motion due to breathing [3].

Results and Conclusions

Figure 2 proofs that we could produce homogenous irradiation patterns with mm precision if ANN prediction was used. In order to quantify the similarity to the static case, we computed three measures for each case: The average FWHM of the blackening was determined from four equidistant lines across each pattern in x and y direction. The inhomogeneity IH $= \sigma/G$ of the blackening is given by the standard deviation σ of the grey values divided by average G around the center of each pattern. Our feasibility study has successfully shown that ion beam tracking using US motion detection is feasible. It could be a dose-free alternative to X-ray based motion detection techniques and would not depend on implanted markers. US allows to track target motion directly. No correlation model between the actual internal anatomy (determined via 4DCT) and an external motion surrogate (e.g. moving patient surface) has to be implemented.

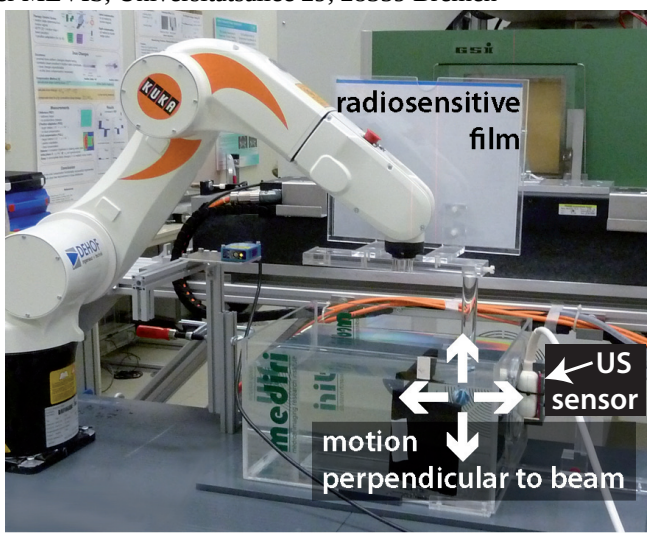

Figure 1: Experimental setup in cave M at GSI.

	static	A·sin($\frac{2\pi}{T}$t)	A·sin^2($\frac{2\pi}{T}$t)	A·sin^4($\frac{2\pi}{T}$t)
without ANN				
IH (%)	0.8	> 15	> 18	> 13
FWHM X (mm)	32.1 ± 0.1	24 ± 5	19 ± 10	36 ± 2
FWHM Y (mm)	32.5 ± 0.1	24 ± 4	26 ± 6	37 ± 2
with ANN				
IH (%)		5.5	6.3	3.5
FWHM X (mm)		33.5 ± 0.5	33.1 ± 0.5	31.3 ± 0.5
FWHM Y (mm)		34.1 ± 0.5	33.4 ± 0.5	31.9 ± 0.5

Figure 2: Irradiated films. Top: Without ANN prediction. Bottom: With ANN prediction.

References

[1] C Bert and M Durante Phys. Med. Biol. **56** (2011) R113-R144

[2] MJ Murphy and S Dieterich Phys. Med. Biol. **51** 5903-5914 (2006)

[3] E Lujan *et al.* Med. Phys. **26** 715 (1999)

[4] N Saito *et al.* Phys. Med. Biol. **55 3499-513 (2010)**

Solid target extensions in TRAX

C. Wälzlein[*1,2], *M. Krämer*[1], *E. Scifoni*[1], *and M. Durante*[1,2]
[1]GSI, Darmstadt, Germany; [2]FIAS, Frankfurt, Germany

The GSI track structure Monte Carlo (MC) code TRAX [1], whose main purpose is to properly describe creation and transport of low-energy electrons, has been further extended. TRAX is intended to be suitable for a variety of different target materials and projectiles. In ion irradiation the distribution of produced secondary electrons is dominated by energies below 100 eV. Therefore electrons with initial energies in this range are the most relevant for radiation damage.
One of our goals is to reproduce the data from the GSI Toroid experiment [2] to gain further insight on low-energy electron creation and transport in solids. Therefore our cross section database was extended to account for electron induced excitations. Consideration of excitation reduces the cut-off energy, below which electrons are considered to be stopped, as no further cross sections for inelastic interactions are available below. Cross sections for electron induced ionization can be easily calculated for all target materials using a simplified formula based on binary encounter theory according to Kim and Rudd [3]. With a few input parameters like the binding and kinetic energy of electrons in any target atom or molecule, we can easily access ionization cross sections. For electron induced excitation neither a complete database nor a simple model exists which could calculate all desired cross sections. With the Toroid experiment in mind we consider the target materials carbon, nickel, silver and gold.

Carbon

The cross section database for low energy electrons incident on carbon has been extended to account for electronic excitations. Collision strengths from a review of Suno [4] have been used to calculate cross sections for 21 individual excitation channels. Considered are excitations from 2s to 2p states (6 channels), 2p→3s (2 ch), 2p→3p (6 ch), 2p→3d (5 ch) and 2p→2p (2 ch). Below ≈ 100 eV the excitation cross sections exceed the ionization cross sections. and below the ionization threshold (11.26 eV) excitation is the only source of energy deposition in our simulation. With the newly introduced excitation cross sections, the cut-off energy is reduced from 11.26 eV to 1.26 eV. More details are given in [5].

Gold

We consider 3 single excitation channels (6s-6p and 5d-6s excitations) by using experimental cross sections from Maslov and Zatsarinny et al. [6, 7]. The cross sections were extrapolated to higher energies using the Bethe-Born approximation [8]. We also consider plasmon excitation by using the formula given by Quinn [9]. This reduces the cut-off energy from 9.23 eV to 2.7 eV. More details are given in [10].

Nickel and Silver

For excitations in Nickel and Silver we used the ACE code [11] which is a collision code based on distorted wave methods by Mann [12]. We account for 9(Ni) and 11(Ag) dielectric excitation channels. For Ni we have transitions with energy losses down to 0.12 eV (4s-3d) and for Ag down to 3.28 eV (5s-5p).

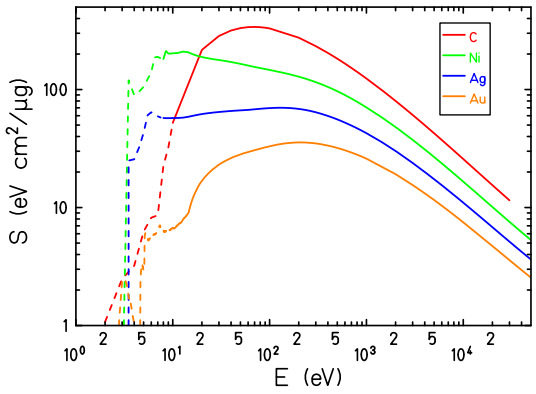

Figure 1: Energy dependent electron stopping power for target materials used in the Toroid experiment. The stopping powers were calculated using the ionization and excitation cross sections and the corresponding energy losses.

References

[1] M. Krämer and M. Durante, Eur. Phys. J. D, 60 (2010) 195.
[2] N. Lineva et al., NIM B 267 (2009) 891.
[3] Y.K. Kim and E. Rudd, Phys. Rev. A 50 (1994) 3954.
[4] H. Suno et al., At. Data and Nucl. Data Tabl. 92 (2006) 407.
[5] C. Wälzlein et al., Phys. Rev. E., submitted.
[6] M. Maslov et al., Phys. Rev. A 77 (2008) 062711.
[7] O. Zatsarinny et al., Phys. Rev. A 78 (2008) 042713.
[8] G.W. Bransden et al., Int. J. Radiat. Biol. Stud. Phys. Chem. Med. 10 (1966) 317.
[9] J.J. Quinn, Phys. Rev. 126(4) (1962) 1453.
[10] C. Wälzlein et al., Appl. Rad. and Isot., in press.
[11] R.E.H. Clark et al., Manual LA-11436-M, Los Alamos Laboratory (1988).
[12] J.B. Mann, At. Dat. Nuc. Data Tables 29 (1983), 407.

*Work supported by Beilstein Institute (NanoBiC project). Work is part of HGS-HIRe.

Overview of the FIRST Project at GSI

R. Pleskac[1] on behalf of the FIRST collaboration

[1]GSI, Darmstadt, Germany

In this contribution one reviews the run of the whole project.

The FIRST collaboration was formed in December 2008 and the proposal for the experiments on nuclear fragmentation of carbon, oxygen, silicon and iron beams on different targets relevant both for the particle therapy and space research was presented in front of the G-PAC committee at GSI in February 2009 [1]. From 2009 till summer 2011 a part of the former ALADIN detector set-up was restarted and new detectors for the interaction region were built and tested in the beam [2]. In August 2011 the experiment with the carbon beam on thin graphite and gold target at 400 MeV/u was performed at GSI accelerator facility in cave C [3]. Charged reaction fragments were measured in coincidence by means of small and big detectors. The small detectors ([4] and see Fig. 1 – 3) are positioned around the target and cover a big solid angle relative to the beam. Very forward reaction products were analysed in the magnetic field of the ALADIN dipole and then detected in the big detectors (ToF scintillator wall and LAND detector). An independent reference measurement was performed in cave A at the same time. In this case charged reaction fragments were detected in ΔE – E telescope consisting of thin plastic and thick BaF_2 scintillator and positioned at different angles relative to the beam. The data analysis of the measurement performed in cave C has started in autumn 2011. Calibration runs were analysed and particle identification and tracking reconstruction were done all small and big detectors. At present a global reconstruction algorithm for charged particle tracks is tested with data obtained from the experiment and Monte-Carlo simulations.

The FIRST collaboration plans to carry out next experiments in near future. In order to perform high-accuracy measurements on double-differential cross sections of charged reaction fragments the experimental setup will be upgraded. Position sensitive big area gaseous drift chambers will be placed in front and behind the magnetic field to strengthen the global particle tracking.

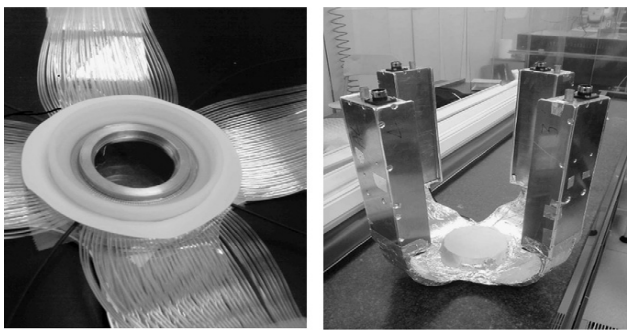

Figure 1: The thin scintillator foil of the Start Counter read out by scintillating fibres.

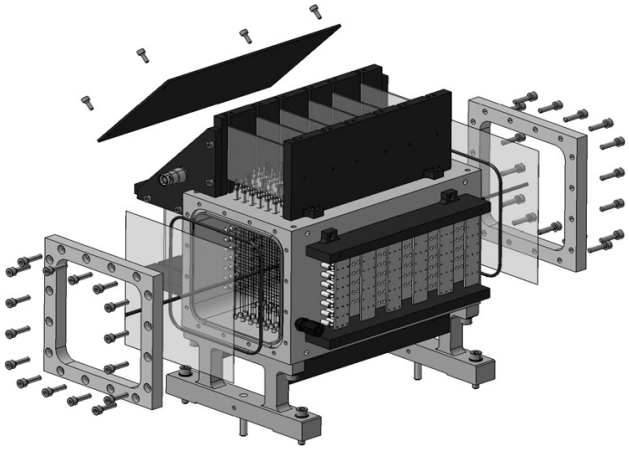

Figure 2: Technical drawing of the Beam Monitor Drift chamber.

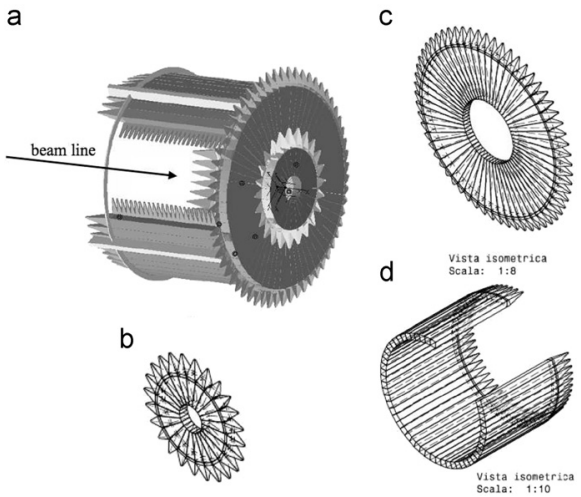

Figure 3: Technical drawing of the KENTROS Proton Tagger: (a) general assembly, (b) small end-cap, (c) big end-cap and (d) barrel.

References

[1] FIRST collaboration, "Extensive study of nuclear reaction of interest for medical and space applications", Project proposal, January 2009

[2] R. Pleskac, "The status of the FIRST experiment", GSI Scientific Report 2009 and 2011, Darmstadt

[3] R. Pleskac et al., "The FIRST experiment at GSI", NIM A, Vol. 678, 21 June 2012, p. 130-138

[4] Z. Abou-Haidar et al., "Performance of upstream interaction region detectors for the FIRST experiment at GSI", JINST 7, Vol. 7, 13 February 2012

Characterization of Alanine EPR detectors response in clinical ^{12}C ion beams

A. Carlino[1,3], E. Scifoni[2], M. Kraemer[2], C. La Tessa[2], M. Durante[2], S. Panzeca[1], A. Longo[1,3], M. Marrale[1,3], M. Brai[1,3]

[1]University of Palermo, Italy; [2]GSI, Darmstadt, Germany; [3]INFN Section of Catania, Italy

Among solid state detectors the alanine electron paramagnetic resonance (EPR) detectors present several advantages such as tissue equivalence, wide range linearity of its dose-response, high stability of radiation induced free radicals, non-destructive read-out procedure.

The main goal of the present work is to investigate the response behaviour of alanine EPR pellets in clinical carbon ion beams. In particular, alanine dose response at selected locations within a carbon ion radiation field has been measured with alanine dosimeters in water and in presence of medium inhomogeneities (such as bone-water) to simulate different quasi-clinical scenarios.

Moreover, a model based on the Local Effect Model (LEM) together with the dedicated treatment planning system for particles TRiP98 [1] has been applied to calculate alanine pellets response.

Materials and Methods

All measurements have been carried out with the alanine pellets placed at several depths along the primary beam direction in a water phantom. At each depth 8 alanine pellets of 4.5 mm in diameter and 3 mm in thickness have been placed.

With the treatment planning system TRiP98, a target volume of 6x3x3 cm^3 placed at 12.5 cm in water depth has been simulated for two different scenarios:

- Irradiation in an homogeneous water medium.
- Irradiation in an inhomogeneous medium.

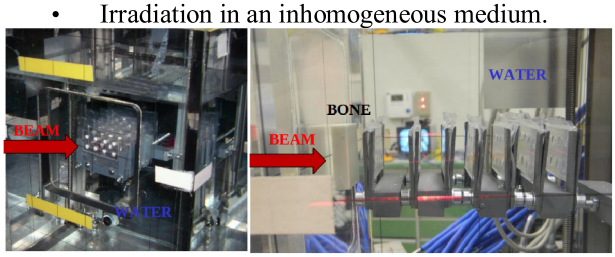

Figure 1: Homogeneous water phantom (left side) and inhomogeneous medium created by a bone target (dimension 4x4x1cm^3, density 1.8 g/cm^3) placed at the entrance window inside the water phantom (right side).

Alanine Response Model Calculation

The alanine dosimeter suffers from a non linear dose response as a function of the particle charge Z and energy E, then the detailed knowledge of the resulting mixed radiation field at each point of the treatment area is crucial to calculate the detector response.

A Relative Effectiveness (RE) look-up table for each charge Z and energy E based on "LEM like" model [2] has been implemented in TRiP98. This way, the single contributions have been properly combined and the alanine dosimeters' response has been computed.

Results and Discussion

Experimental data, simulated response values and TPS values are shown below for the two irradiation set-ups. The percentage deviation between EPR readings and calculated response increases with depth up to 7% in the target. Moreover, the figure on top shows how TRiP98 estimates slightly better the dose for the beam which goes through the water than through the bone.

In conclusion, a 3D dose distribution in water and in the presence of medium inhomogeneities for clinical carbon ion beams has been measured by means of alanine dosimeters. A model based on LEM has been applied to calculate the Relative Effectiveness (RE) for each charge Z and energy E of a mixed radiation field. Implementing this data set in TRiP98 we are able to compute the alanine dose in a mixed radiation field, with a relevant accuracy, considering the uncertainties of EPR response.

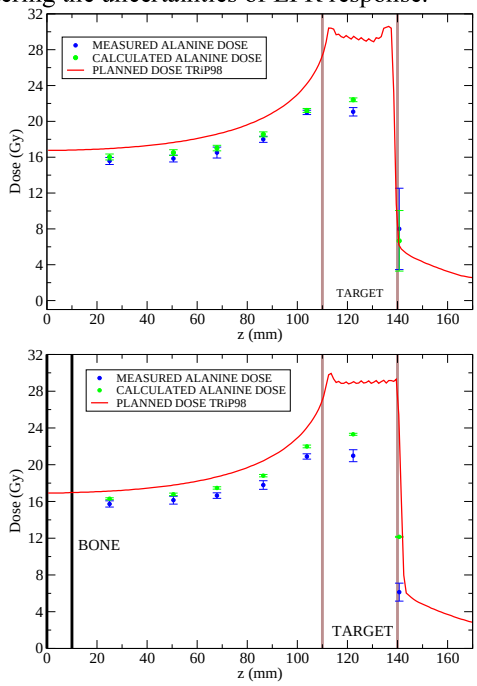

Figure 2: Computed and measured responses along a pure water pathway (up) and after passing a bone (down).

References

[1] M. Krämer et al., Phys Med Biol. 2000, 45, 3319
[2] Geiss et al, Nucl. Instr. Met. B 142 (1998) 592-598

Detection of prompts γ produced by ^{12}C fragmentation in a PMMA target for Bragg-Peak position monitoring

M. Vanstalle[1], *C. La Tessa*[1], *C. Schuy*[1], *M. Marafini*[2], *L. Piersanti*[2], *A. Sarti*[2], *V. Patera*[2], *A. Sciubba*[2], *and M. Durante*[1,3]

[1]GSI, Darmstadt, Germany; [2]University "La Sapienza" of Rome, Italy; [3]TUD, Darmstadt, Germany

The determination of the irradiated volume position is a major concern in modern ion therapy as it allows to check that the maximal dose is deposited in the tumor and not in the peripheral healthy tissue. At the moment, this verification is accomplished with the Positron Emission Tomography technique, which offers an offline control on the dose. A real time monitoring of the irradiated volume position would allow a direct check of the patient alignment in combination with the treatment planning delivered. A method to achieve this goal is to exploit the fragmentation of the primary ions in the patient, correlating the production of secondary particles (prompt γ, protons,...) with the tumor position.

An experiment in collaboration with University "La Sapienza" of Rome (Italy) was carried out at GSI (cave A) in May 2012. In this measurement, a PMMA phantom was irradiated with 220 MeV/u carbon ions. One goal of the experiment was to characterize the field of prompt γ produced through the nuclear interaction ^{12}C ions with the target. The energy spectra of secondary photons were acquired at 60 and 90 degrees with respect to the primary beam direction. Furthermore, the yield of γ emitted at 90 degrees was investigated at different target depths to find a correlation between the former and the Bragg Peak position.

Calibration of the BaF_2

The experimental setup was similar to the one described in [1]. The secondary particles produced by the fragmentation of ^{12}C were detected by a $\Delta E - E$ telescope composed of a plastic scintillator (VETO) for measuring energy loss and a barium fluoride crystal (BaF_2) to determine the residual energy. Particle identification was achieved with a combination of the energy loss information and Time-Of-Flight (TOF) measurement between the start counter (placed between the beam exit window and the target) and the BaF_2 detector.

In order to convert the charge spectra acquired by the detector in kinetic energy spectra, the barium fluoride was irradiated with γ sources : ^{22}Na (0.511 and 1.275 MeV), ^{137}Cs (0.662 MeV), ^{60}Co (1.17 and 1.33 MeV) and ^{239}PuBe (peak at 4.4 MeV from ^{12}C* decay). The obtained calibration curve is shown in Fig. 1. The average energy resolution is around 20%.

Monte Carlo simulations of the experiment have been performed with Geant4 [2]. First results predicting the kinetic energy spectra of secondary photons are shown in Fig.2. The spectra take into account the detector resolution of 20%.

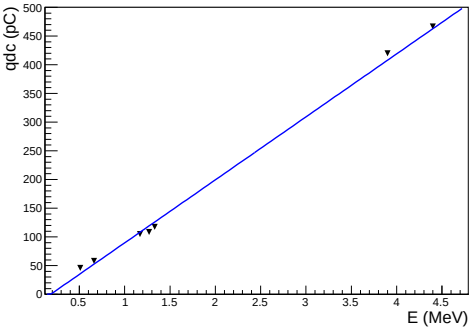

Figure 1: Charge-to-energy photon calibration curve for the BaF_2 detector.

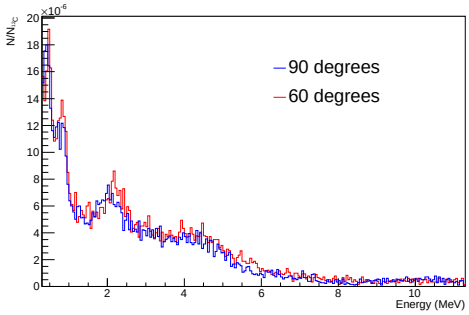

Figure 2: Expected γ energy spectra for two positions of the BaF_2 (at 60 and 90 degrees with respect to the primary ions direction).

Prospects

The data analysis is still in progress. Once the kinetic energy spectra of the photons are finalized, the yield of the prompt γ as a function of the depth of the target will be determined. Futures experiments will also be carried out in medical conditions: anthropomorphic phantom, irradiated volume,...

References

[1] K. Gunzert-Marx, H. Iwase, D. Schardt et al., New J. Phys. 10:1-21 (2008).

[2] GEANT4 COLLABORATION, `http://www.geant4.org/geant4/`

Development of a VME data acquisition system

L. Piersanti[1,2], *C. Schuy*[3], *C. La Tessa*[3], *and M. Durante*[3,4]

[1]University of Rome "Sapienza", Italy; [2]INFN Laboratori Nazionali di Frascati, Italy; [3]GSI, Darmstadt, Germany; [4]TU Darmstadt, Germany

The increasing interest in nuclear fragmentation measurements, both for ion therapy and space radiation protection applications, demands a large amount of data takings often performed in various facilities around the world. In order to minimize the discrepancies between different data acquisition systems (DAQ), e.g. charge and time resolution, maximum acquisition rate, dead time efficiency and so on, a portable DAQ system, based on standard VME bus and developed at "Scienze di Base e Applicate per l'Ingegneria" (SBAI) Department of "Sapienza" University of Rome, has been successfully installed and operated. In contrast to the Multi Branch System (MBS) [1] currently used at GSI, this system is more suitable for small-scale experiments, i.e. where few detectors are involved and hence few channels need to be read out. The software can run on any Linux platform, hence maximizing its portability, and currently supports two different boards that can be alternatively used as crate controller: a 2.0 USB link bridge (CAEN V1718) and an optical link bridge (CAEN V2718). The former allows to use as DAQ PC even a laptop (with a maximum acquisition rate, limited by USB data transfer rate), while the latter requires only one standard PCI slot for the optical link card (with a maximum acquisition rate of $\sim$20 kHz). This new system has been successfully used during GSI fall beam-time [2], [3] showing promising results.

DAQ setup

In the last decades, the VME bus has proved to be a reliable and versatile tool for data acquisition systems in experimental physics. Moreover, the availability of *bridge boards*, that allow a simple and quite fast VME bus readout, has increased the interest in this standard. For this reason, a portable DAQ system relying on VME bus has been installed and successfully operated at GSI. This system, formerly developed by A. Sarti and V. Patera at "Scienze di Base e Applicate per l'Ingegneria" (SBAI) Department of "Sapienza" University of Rome, has been built in order to guarantee a high modularity (including or excluding a board is, in fact, a straightforward process). Furthermore, the software includes a built-in decoding tool that converts acquired data (standard binary files) directly in a ROOT file.

The core of the DAQ is the bridge board that has been programmed to work simoultaneously as crate controller and I/O register. The system supports both USB (CAEN V1718) and optical link (CAEN V2718) bridge boards. In the former case even a laptop can be used as DAQ PC (with a maximum allowed transfer rate limited by USB port $\sim$1 kHz) while the latter requires only a PCI slot to be accessed. The acquisition and the decoding software has been written in standard C/C++ language in order to enhance its customization capabilities. The system already supports several commercial VME boards (mostly CAEN TDC, QDC, ADC, Scaler) and has been tested and used in a "minimal" and in a "typical" configuration to benchmark its performances. In order to prevent multiple trigger events, a dedicated dead-time logic has been implemented too.

A first test has been performed with a NIM pulsed signal (100 kHz) used as trigger and only the bridge (CAEN V2718) and a QDC (CAEN V792N) have been acquired. In this basic configuration, a rate of $\sim$ 20 kHz has been reached, hence defining the acquisition rate upper limit. The "typical" configuration comprised the bridge (CAEN V2718), two QDCs (CAEN V792N), one peak sensing ADC (CAEN V785N) and a scaler (CAEN V560) resulting in an acquisition rate of $\sim$ 10 kHz.

In the experiments performed at GSI in the fall 2012, this latter setup was used to measure the shielding properties of different materials for astronauts protection in outer space (in the framework of ROSSINI project [2],[3]) showing very promising results.

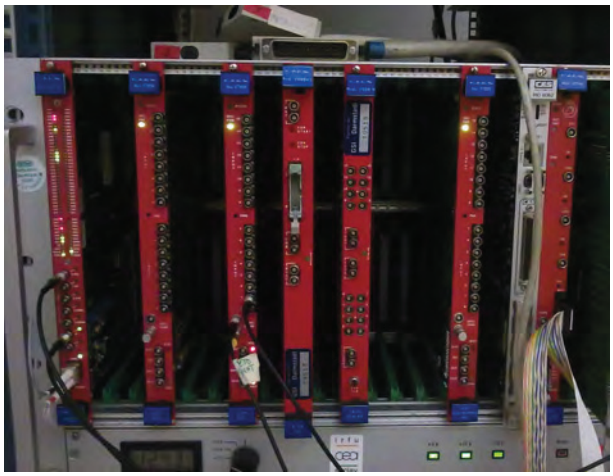

Figure 1: The DAQ system used during a calibration measurement.

References

[1] H.G. Essel, N. Kurz, *The general purpose data acquisition system MBS*, IEEE Transactions on Nuclear Science, vol.47, no.2, pp.337-339 (2000)

[2] C. Schuy et al., GSI Scientific Report (2012).

[3] M. Rovituso et al., GSI Scientific Report (2012).

Electrophysiological Effects of Heavy Ion Irradiation on Cardiomyocytes*

J. Frieß[1], A. Heselich[2], S. Ritter[3] A. W. Daus[1], P. G. Layer[2], and C. Thielemann[1]

[1] University of Applied Sciences Aschaffenburg, Germany; [2]TU Darmstadt, Germany
[3]GSI, Darmstadt, Germany

Motivation

Several effects of ionising radiation at low or moderate doses on the cardiovascular system are known [1, 2], but there is essentially no information available on the effects of high-LET radiation on the heart. Therefore, an assessment of possible late effects on the cardiovascular system after irradiation with high-LET radiation is needed, for instance with respect to particle therapy or the planning of long-term space missions [3]. In both cases the emergence of adverse effects following radiation exposure must be taken into consideration.

To address the question if and to what extent the cells in the heart muscle are affected by an exposure to high doses of heavy ions, primary avian cardiomyocytes were used. In parallel experiments cells were grown on microelectrode array chips (MEAs) or culture dishes and changes in the electrophysiological behaviour as well as in cell cycle propagation were investigated.

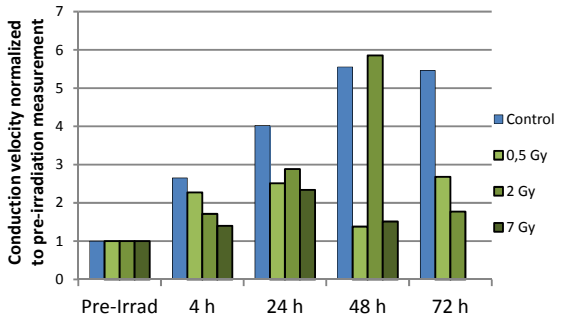

Figure 1: Conduction velocity of cardiomyocyte networks after titanium ion irradiation.

Material and Methods

Cardiac cells were isolated from chicken at developmental embryonic stage E8 and cultivated [4]. As a means to investigate electrophysiological signals, cells were seeded onto 60 electrode MEAs.

To analyse intracellular damage accumulation, cell cycle arrests and cell proliferation, cells were also seeded onto fibronectin coated glass coverslips cultured in multiwall plates.

In order to study the effects of high-LET radiation on the cells, the cultures were exposed to carbon (25 mm Bragg Peak, mean energy 75 keV/µm at sample position) and titanium (1 GeV/u) ions at the SIS-facility (GSI, Germany).

Electrophysiological properties of the cell cultures were measured before and after exposure. Cardiac signals could be recorded for approximately one week and were analysed in terms of beat rate, conduction velocity, field action potential duration and general spike shape. Cardiomyocytes cultured on coverslips were fixed at different time points after exposure and by immunohistochemistry double strand break (DSB) accumulation and repair, oxidative stress and apoptosis, were measured.

Results

As previously shown, the cardiac cultures exhibit a high resistance towards ionising radiation [5], since all cell networks maintained their contractive activity. In cultures irradiated with titanium ions, a reduction of the conduction velocity compared to the untreated controls was observed (see Figure 1). This effect might result from an alteration in gap junction activity due to irradiation. Further assays addressing the expression of connexion 43 could give insights into this phenomenon in future experiments.

Immunohistological stainings for γH2AX-phosphorylated DSBs in the nuclear DNA showed ion tracks through the cell nucleus in cultures fixed shortly after exposure to titanium ions (see Figure 2). Furthermore, our data show that independent of applied dose the cells were able to repair the induced genetic damage within 24 hours (data not shown).

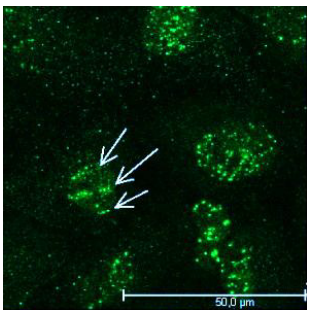

Figure 2: γH2AX-stained cardiac cell culture, fixed 15 min after exposure to titanium. Arrows indicate ion tracks through one nucleus.

References

[1] R. Roychoudhuri et al., BMC Cancer. 2007 Jan 15;7:9.
[2] M. Hooning et al., J Natl Cancer Inst. 2007 Mar 7;99(5):365-75.
[3] M. Durante and F. Cucinotta, Nat Rev Cancer. 2008 Jun 8(6):465-72.
[4] A.W. Daus, et al., Bioelectromagnetics. 2011 Jul; 32(5):351-9.
[5] Steger et al., GSI Report 2011-1, p450.

* This work is supported by the DLR and ESA in the frame of the ESA IBER-10 program.

Extension of the treatment planning system TRiP by the beam mixing model proposed by Lam*§

O. Steinsträter[1], T. Friedrich[1], U. Scholz[1], M. Krämer[1], M. Durante[1], and M. Scholz[1]

[1]GSI, Darmstadt, Germany

The treatment planning system TRiP [1,2] developed at GSI for heavy ion radiotherapy predicts the biological effect of an ion beam based on the Local Effect Model (LEM), also developed at GSI [3]. Here, LEM is used to derive the biological effect of monoenergetic ion beams, typically provided as parameters according to the Linear-Quadratic-Linear (LQL) model (α, β and threshold dose D_t). Since for the treatment planning the effect of mixed radiation (the primary projectile and its fragments in a wide energy range) has to be predicted, in addition a beam mixing model is required. Currently a monte-carlo based model [1] and a model based on the Theory of Dual Radiation Action (TDRA) [2] are implemented in TRiP. The monte-carlo based model is highly flexible but for many application too time consuming. On the other hand, the calculation time for the TDRA based model could substantially be reduced by moving a significant part of the total calculation into a pre-processing step which has to be performed only once [2]. Unfortunately the TDRA based model cannot directly use ion specific threshold parameters D_t, which are provided by the most recent version of the LEM [4]. Although an extension of the TDRA based model is possible [5], this model is significantly more complex and does not allow a comparable pre-processing technique as in the original model. We therefore introduced the beam mixing model provided by Lam [6], which is independent of the underlying model for the dose-response curves of the contributing monoenergetic ions and therefore highly flexible. In addition, similar to the implemented TDRA based model, a significant part of the calculation could be moved to a pre-calculation step.

The beam mixing model proposed by Lam [6] relates the slope of the effect of the mixed beam, ϵ_{mix}, to the slopes of the effects of the contributing monoenergetic beams, ϵ_i: $\frac{d\epsilon_{\mathrm{mix}}}{dD} = \sum_i \frac{D_i}{D_{\mathrm{mix}}} \frac{d\epsilon_i}{dD}$ (total dose $D_{\mathrm{mix}} = \sum_i D_i$).

The irradiation system developed at GSI uses an active dose shaping technique which superimposes many narrow ion beams (pencil beams). The irradiation field at a position (x, y, z) can therefore be expressed in terms of the initial fluences of the contributing pencil beams, F_u, comprised as vector $\boldsymbol{F} = (F_1, \cdots, F_N)$. Hence, TRiP internally calculates effects with respect to $\boldsymbol{F}$: $\epsilon(\boldsymbol{F})$. In addition, for the optimization of the target dose, the algorithms implemented in TRiP also need the derivatives of ϵ with respect to the fluences: $\partial\epsilon/\partial F_v$. For the Lam based beam mixing method this results in a weakly-coupled system of ordinary differential equations (ODE) for $t \mapsto \epsilon(t\boldsymbol{F})$ and $t \mapsto \partial\epsilon(t\boldsymbol{F})/\partial F_v$, $0 \le t \le 1$,

$$\frac{d}{dt}\epsilon = f_0(\epsilon), \qquad \frac{d}{dt}\left(\frac{\partial\epsilon}{\partial F_v}\right) = f_v\left(t, \epsilon, \frac{\partial\epsilon}{\partial F_v}\right), 1 \le v \le n,$$

which have to be solved for each position (x, y, z). The functions f_v are quite complicated and depend on the depth z and on other more general properties of the irradiation field, but not on the fluence vector $\boldsymbol{F}$. Therefore, significant parts of the calculation of the f_v can be moved to a pre-calculation step, which only has to be repeated if general parameters like the initial projectile or the irradiated cell type have to be changed.

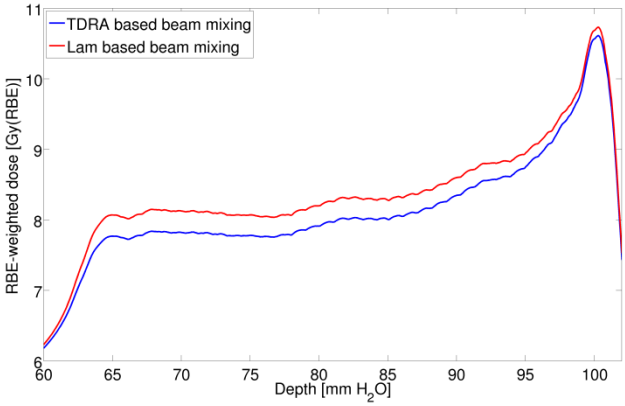

In the figure, TRiP estimations for the RBE-weighted dose of a carbon irradiation of CHO (Chinese Hamster Ovary) cells with an SOBP (Spread Out Bragg Peak) of 4 cm are shown (the plot is restricted to the SOBP region). Whereas both curves have been based on the same LEM data, the beam mixing models were different: TDRA model in blue, the newly implemented Lam model in red.

Conclusion

Although significantly more complex than the TDRA based method, especially the pre-calculation technique reduces the calculation time for the Lam based method to a value acceptable for the most applications.

The new beam mixing model tends to emphasize higher β values (around 5% higher RBE-weighted dose values in the SOBP) which might be of particular interest for the new full simulation LEM method [4].

References

[1] M. Krämer et al., Phys. Med. Biol., 45 (2000) 3319.
[2] M. Krämer et al., Phys. Med. Biol., 51 (2006) 1959.
[3] T. Elsässer et al., Int. J. Radiation Oncology Biol. Phys. 78 (2010) 1177.
[4] U. Scholz et al., GSI Sci. Report, (2011) 517.
[5] O. Steinsträter et al., GSI Sci Rep, (2011) 524.
[6] G. K. Y. Lam, Radiat. Res., 110 (1987) 232.

* Work supported by Siemens Healthcare.
§ Work is part of HGS-HIRe.

First high-energy proton tomography of a mouse

C. La Tessa[1], *M. Durante*[1,2], *P. M. Lang*[2], *F. Merrill*[3], *M. Prall*[1], *L. Shestov*[1], *and D. Varentsov*[1]
[1]GSI, Darmstadt, Germany; [2]TU Darmstadt, Germany; [3]Los Alamos National Laboratory, NM, USA

Relativistic protons have been proposed as an alternative to low-energy ions in the treatment of cancer and non cancer diseases [1]. The increase of the primary beam energy to the GeV region will overcome several limitations of Bragg-Peak therapy with protons, such as the broadening of the primary beam due to multiple scattering and uncertainties on the particle range and Relative Biological Effectiveness (RBE). These processes lead to a reduced dose gradient between the tumor volume and the surrounding tissue and thus to an increase of side effects. The main advantage of relativistic protons is that the beam crossing the patient can be exploited for imaging purposes. Proton radiography was investigated for many years because of its low radiation dose and high density resolution, but until recently the image blurring caused by scattering was limiting its practical applications in medicine. In the past years, the Los Alamos National Laboratory (LANL) system based on a magnetic lens after the object for imaging and chromatic aberration corrections pushed the technique to unprecedented time and spatial resolution [2]. This technique exploits differences in the lateral scattering of the primary ions due to the material thickness and density they encounter. The application of this methodology to medical imagining has been tested at the pRad facility (LANL) in December 2012. The experiment was performed within the framework of the PANTERA (Proton Therapy and Radiography) project. Radiographies of simple (plastic tissue-equivalent targets) and complex (antropomorphic phantom, zebra fishes) geometries were acquired using 800 MeV protons. Furthermore, the first proton tomography of a formalin-preserved mouse was obtained. First preliminary results of the latter target are shown in this report.

The experiment

The mouse was placed with its main axis perpendicular to the beam direction. A rotational stage was used to allow a 360 degrees movement of the sample with a 0.5 degrees step. Examples of the mouse profile acquired in the orthogonal and parallel direction with respect to the beam axis are reported in Figs. 1 and 2. The former has been obtained from a direct acquisition of the target radiography while the latter was achieved through a more advanced data analysis. Using filtered backprojection (employing a ramp filter), tomographic slices were reconstructed from transmission images, of which Fig. 2 is an example. The shape of the mouse can be clearly distinguished in the full picture (Fig. 1). Furthermore, internal bony structures are well visible especially in the parallel reconstruction (Fig. 2).

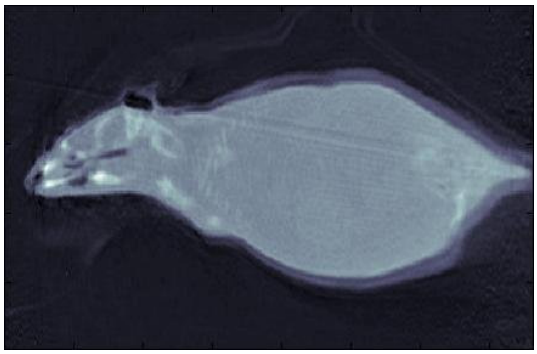

Figure 1: Profile of the mouse acquired in the direction orthogonal to the beam axis.

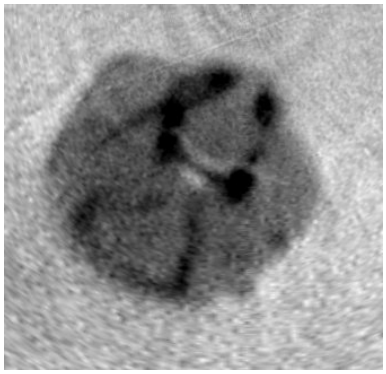

Figure 2: Tomographic reconstruction of a mouse slice acquired in the direction parallel to the beam axis. The image contains a section of the head, where the skull bones (dark areas) and nasal cavities (light areas) are visible.

Conclusions

The application of relativistic protons to diagnostic has shown promising results. Further tests on live animals are planned at pRad in 2013 and at the proton microscope PRIOR located in the FAIR facility, where energies above 1 GeV will be available. The experiments will focus on optimizing the technique for the image of lesions implanted in the animals and couple the irradiation with standard radiotherapy.

References

[1] M. Durante and H. Stöcker, J. Phys.: Conf. Ser. **373** (2012), 012016.

[2] F. E. Merrill et *al.*, Rev Sci Instr **82** (2011), 103709.

Proton radiography of cells administered with gold nanoparticles

B.Wezorke[1, 2], Z.Yu[1,3], C.Hartel[1], W.K.Weyrather[1], A.Rusek[4] and M.Durante[1, 2]

[1]GSI, Darmstadt, Germany; [2] TU Darmstadt, Germany; [3] Department of Radiation Oncology, Fudan University Shanghai Cancer Center, Shanghai, China; [4] NASA Space Radiation Laboratory, Brookhaven, USA

Introduction

Radiopaque materials are commonly used to enhance radiographic contrast. Gold nanoparticles are a new type of contrast agent, providing a very small size and a high atomic number (Z=79). As they have a radiosensitizing effect [1] they are not only beneficial for radiodiagnostics but turn out to be very valuable in radiotumortherapy. They enable a better delineation of the tumor and also amplify the effect of X-irradiation. To investigate whether gold nanoparticles are also applicable as a contrast agent for high energy particle radiation, they were incorporated in CHO (Chinese Hamster ovary) cells which were irradiated with a proton beam. Further tests have been performed to investigate, whether gold nanoparticles show a radiosensitizing effect with Carbon-Ion irradiation.

Methods and Material

The CHO cells were grown on polystyrol-sticks to enable a 2 dimensional view in the headphantom [2]. Cultivation was in DMEM medium supplemented with 10% fetal calv serum and 1% penicillin/streptavidin and kept in a humidified atmosphere of 5% CO_2 at 37° C. Gold nanoparticles of a diameter of 1,9 nm were added to a concentration of 100 µM and incubated for 24 hours. After incubation the cells were fixed on the sticks with methanol at -20°C. Irradiation took place in the NASA Space Radiation Laboratory, Brookhaven with a beam of 2.5 GeV protons. This beam had an estimated range of 10.4 m and an LET of 0.21 keV/µm in water. The size of the beam was about 20 x 20 cm², with an intensity approximately 1,3 Gy/min. After the experiment the sticks were stained for 10 minutes with methylenblue, to prove the presence of cells on the sticks. To investigate the radio sensitizing effect survival curves were made. AG1522D (human foreskin) cells were cultivated in EMEM medium with 1% glutamine, 10% FCS and 1% P/S under standard conditions. Gold nanoparticles of a diameter of 1,9 nm were added to a concentration of 50 µM and incubated for 24 hours. Irradiation was performed with an average LET of 100 and an extended Bragg-peak of 1 cm.

Results

The sticks were irradiated together in a holder perpendicular to the beam direction, with a dose of 100 Gy. The obtained image can be seen in Fig. 1. On the left side is the original image, on the right side the contrast has been enhanced with imageJ software. Analysis indicates an evident enhancement of contrast on the sticks with the gold nanoparticles at an average of 20%.

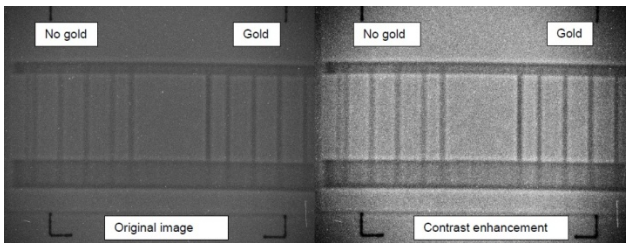

Figure 1: Proton radiography of CHO cells on sticks, with and without incorporated Gold Nanoparticles.

The staining with methyleneblue proofed the existence of cells on the stick, regardless if they contain gold nanoparticles or not, concluding that gold nanoparticles are in fact a possible contrast agent for high energy particle radiation. The experiment also indicates that the protocol of cell treatment leads to the incorporation of gold nanoparticles. The survival curve comparing AG-D cells with and without gold nanoparticle is displayed in Fig. 2. Preliminary results show no increase in radio sensitization for the addition of gold nanoparticles.

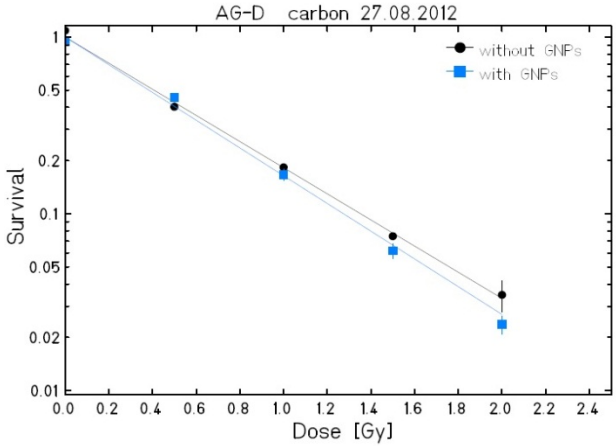

Figure 2: Survival curve of AG-D cells and AG-D cells administered with Gold Nanoparticles

References

[1] Jain et al. “Gold nanoparticles as novel agents for cancer therapy” British Journal of Radiology 2012, 101–113

[2] C. von Neubeck “Aufbau eines 3-dimensionalen Systems zur biologischen Verifikation der Bestrahlungsplanung mit Schwerionen” Diploma thesis 2006

"Mosaic": a new start (sCVD) detector for nuclear fragmentation measurements

R. Pleskac[1]

[1]GSI, Darmstadt, Germany

Introduction

Nuclear fragmentation cross-sections are of high interest both for radiation therapy and space research. The aim of measurements is to benchmark different Monte Carlo codes with new data sets. The main observable is the double-differential cross-section for charged fragments and neutrons. The number of produced fragments is measured as a function of emission angle relative to the beam and their kinetic energy. Different experimental setups were used for such measurements at GSI in cave A and also in cave C during last years. Information on energy loss of charged fragments, their time-of-flight between target and detection place in combination with magnetic field and/or pulse shape technique is used to perform identification of fragments both in charge and mass.

Mosaic detector

In order to perform time-of-flight measurements mentioned above for big angles (> 30°) relative to the beam in reasonable time the primary beam intensity has to be increased up to 10^7 or even 10^8 pps. It requires a start detector with excellent performance properties [1]. The start detector positioned in front of the target is counting number of primary beam particles, starting or stopping all time-of-flight measurements and providing a fast trigger signal for the data acquisition system. The "mosaic" detection system (CIVIDEC) consisting of an array of 3 x 3 sCVD diamonds (Element6) was proposed as a new start detector for future nuclear fragmentation experiments.

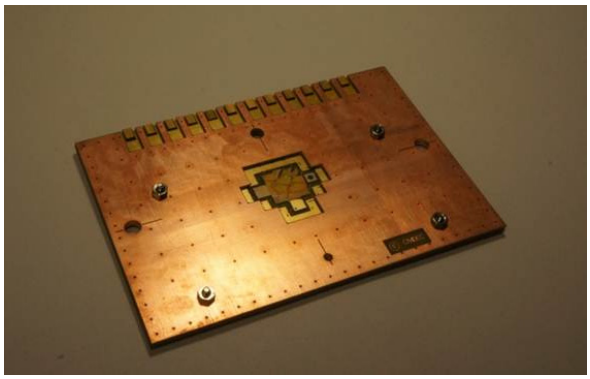

Figure 1: mosaic-detector for the n_ToF-collaboration.

The diamond has an excellent time resolution (tens of ps), works stably in very high rates (factor of 100 or higher than plastic scintillator) and is much more radiation resistant then other detectors. The size of one diamond is 4,5 x 4,5 mm^2 x 300 µm with an active area of 4,0 x 4,0 mm^2 (about 80 % of the total area). The total area of the "mosaic" detector is 13,5 x 13,5 mm^2 (a typical size of the beam spot on target is between 5–10 mm FWHM). Three printed circuit boards make a mechanical support for diamonds and interface signals from diamonds to further signal processing.

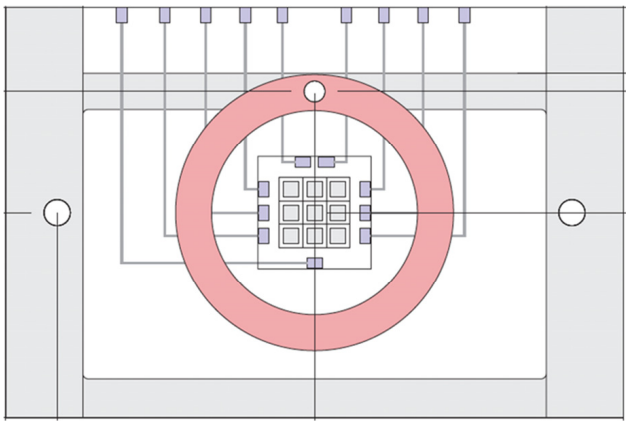

Figure 2: scheme of mechanical layout.

Special preamplifiers for diamond detectors were developed in order to apply the "mosaic" detection system in beams from proton up to uranium in an kinetic energy range from 100 – 1000 MeV/u. For example, in the case of proton and oxygen beam at 500 MeV/u a charge of 3.2 and 350 µC is collected. After passing 40 dB amplifier (f = 100) the output signal has a level of 4 and 200 mV. This corresponds to a signal-to-background ratio of 1.6 and 62.5. Therefore in the case of protons a fast charge amplifier has to be used (4 mV/fC) to get signal-to-background ration of 21.3. The time resolution for protons and oxygen beam at 500 MeV/u is 150 and 10 ps. The energy information provided by sCVD diamonds is used to identify primary beam particles in charge.

Outlook

The "mosaic" detection system is one part of a new experimental setup developed in order to perform future measurements on nuclear fragmentation at GSI and worldwide. A combination of two "mosaic" detectors (positioned on the beam axis upstream and downstream relative to target) offers a possibility to build a high precision start-veto system providing direct information on total reaction cross section and beam-on-target position during measurement. The project is financed by BMBF.

References

[1] R. Pleskac, "Mosaic Detector: Experiments for Therapy and Space Research", 1st ADAMAS Workshop, GSI Darmstadt, December 2012, http://www-adamas.gsi.de.

Impact of various motion state identification methods on simulated 4D dose distributions in scanned ion beam therapy.

D. Richter[1], *M. Durante*[1,2], *and C. Graeff*[1]

[1]GSI, Darmstadt, Germany; [2]Technische Universität Darmstadt, Physics Dep., Germany

Introduction

External (surrogate) motion monitoring data, e.g., from a pressure sensor in a waist belt, are commonly used to facilitate image reconstruction of time-resolved computed tomography (4DCT)[1]. In the GSI 4D treatment planning system, TRiP4D, these data are required for 4D simulation of dose delivery to mobile tumors with scanned ion beams[2]. For each delivered raster point the surrogate signal is correlated to the respective phase of the 4DCT. Motion state identification (ID) can, e.g., be based on the relative signal amplitude, the time between successive breathing cycles or the signal phase[2]. In this work, we assess the impact of these methods on the 4D dose distribution for irregular and regular breathing trajectories.

Materials and Methods

We performed 4D dose simulations for one patient using four measured breathing trajectories (pressure sensor). One regular $\cos^2$ motion acc. Lujan et al.[3] with a 3.6 s breathing period was also included. Relative amplitude-based (RB), time-based (TB) and phase-based (PB) motion state ID was performed for each trajectory. The signals were pre-processed with in-house software to obtain the relative amplitude, time and signal phase for each breathing cycle. The derived signals featured a fixed amplitude range (e.g. 0 % to 100 %) per cycle. State ID in TRiP4D was based on the pre-processed trajectories using 14 equally distributed motion states over the amplitude range. Irradiation timing was simulated for typical beam pauses and spill lengths used at the Heidelberg Ion Therapy Center. The resulting 15 dose distributions were assessed with respect to dose coverage (V_{95}), over dose (V_{107}) and dose homogeneity ($HI = D_5 - D_{95}$). V_X denotes the target volume fraction receiving at least X % of the planned dose, D_X is the dose covering X % of the target volume.

Results

Table 1 lists the resulting V_{95}, V_{107} and HI values for the different trajectories and state ID methods. V_{107} and HI in all cases are larger for the RB method (less than 5 % and 3 %, respectively). While for the Lujan trajectory V_{95} values are similar for all state ID methods, differences of up to 9 % occur for the irregular trajectories, e.g., for fraction 3. Variability of all parameters between different breathing trajectories due to modulated interplay patterns was also observed, as expected.

trajectory	method	V_{95}[%]	V_{107}[%]	HI[%]
fraction 1	RB	92.7	11.9	15.1
	TB	93.9	8.7	13.7
	PB	94.1	9.4	13.6
fraction 2	RB	88.6	2.5	12.4
	TB	93.1	2.3	11.6
	PB	89.1	1.3	11.4
fraction 3	RB	80.3	10.5	17.2
	TB	86.2	5.7	14.3
	PB	89.3	8.0	14.9
fraction 4	RB	92.1	11.5	15.2
	TB	88.8	6.5	14.3
	PB	92.7	9.6	14.3
Lujan	RB	92.3	10.1	14.7
	TB	93.7	5.3	12.6
	PB	92.9	6.3	13.1

Table 1: V_{95}, V_{107} and HI values for the 4D simulations using different motion trajectories and state ID methods.

Discussion

In this study the employed state ID methods had a non-negligible impact on the simulated 4D dose distribution, especially for irregular motion trajectories. For the RB method, frequency distributions of the motion state per raster point featured pronounced maxima around the extrema of the motion trajectory. This is a likely cause for the dosimetric differences observed in this case w.r.t to the TB and PB methods, especially in V_{107}. It can be assumed that the employed state ID method should ideally match the one used during 4DCT reconstruction. However, these methods are vendor-specific and can be difficult to access.

Conclusion

The selected motion state ID method in 4D treatment simulations for scanned beam delivery can have a non-negligible impact on the simulated 4D dose distributions.

References

[1] E. Rietzel, "Four-dimensional computed tomography: image formation and clinical protocol.", *Med. Phys.* (2005) **32**(4):874-889

[2] D. Richter, "Treatment Planning for tumors with residual motion in scanned ion beam therapy", *PhD Thesis* (2012) 29-48

[3] A.E. Lujan, "A method for incorporating organ motion due to breathing in 3D dose calculations", *Med. Phys.* (1999) **26**(5) 715-720

Gated phantom irradiation for 4D in-beam and 4D off-beam PET comparison*

K. Laube[1], *C. Bert*[2], *W. Enghardt*[1,3], *S. Helmbrecht*[1], *R. Kaderka*[2], *C. Kurz*[4], *K. Parodi*[4], *N. Saito*[2], *Y. Tian*[1], *and F. Fiedler*[3]

[1]OncoRay, Dresden; [2]GSI, Darmstadt; [3]HZDR, Dresden; [4]HIT and Heidelberg University Clinics, Heidelberg

Introduction

Treatment of intra-fractional moving tumours in the thorax and upper abdominal region using ion beams requires motion compensated beam delivery [1] but also reliable dose monitoring. Positron emission tomography (PET) can be applied to image the autoactivation occuring along the beam path during irradiation and it has turned out that PET delivers valuable information when evaluating the radiation induced activity in static targets. Depending on the available scanner type the PET measurement is carried out with a double-head scanner during irradiation (in-beam), immediatly afterwards with a scanner inside the treatment room (in-room) or with a conventional full-ring scanner in close vicinity to the treatment room (off-beam) [2]. Since 2008 a lot of experience was gained from time-resolved (4D) in-beam PET measurements with moving phantoms using the double-head PET scanner BASTEI at the former medical beam line at GSI [3].

Materials and Methods

Since there is no in-beam PET installation in clinical operation it has to be validated whether gained knowledge coincides with experiences collected at existing off-beam PET installations. Therefore, first phantom experiments with 4D PET measurements were performed under almost equal conditions at GSI and the Heidelberg Ion-Beam Therapy Center (HIT). Same motion system (commercial motion table QUASAR) and targets (made of polymethyl methacrylate) were used at both installations. A rather simple ^{12}C treatment plan including only two adjacent energies and horizontal pencil-beam scanning was delivered within a 50% amplitude gating window regarding the ± 10 mm target elongation of a $\cos^4$-motion pattern. The quite complex target geometry induced well defined range variations that have to be reproduced in the PET images. Measurements performed at GSI where reconstructed with an in-house 4D reconstruction algorithm [4] concerning in-beam (irradiation + 40 s) and in-room (1–4 min after irradiation end) time regime. Off-beam measurements at HIT started about 7 min after irradiation due to target transport to the scanner but lasted then 30 min.

Results

Reconstructed activity distributions from measurements with a static and a moving target performed at GSI are shown as color coded distribution with additional contour plot in figure 1. Range modifications are well detectable in the scanner midplane after 4D reconstruction but resolution in perpendicular direction suffers from limited angle artefacts. Detailed comparison of counting statistics and resultig image quality for 4D in-beam and 4D off-beam PET measurements at the different facilities will follow soon.

References

[1] C. Bert & M. Durante, Phys. Med. Biol. 56, R113–44 (2011)
[2] G. Shakirin *et al.*, Phys. Med. Biol. 56, 1281–98 (2011)
[3] K. Laube *et al.*, Radiother. Oncol. 102, S43–4 (2012)
[4] K. Laube *et al.*, Phys. Med. Biol. (submitted 2013)

* Work supported by EU, ENVISION contract No. 241851.

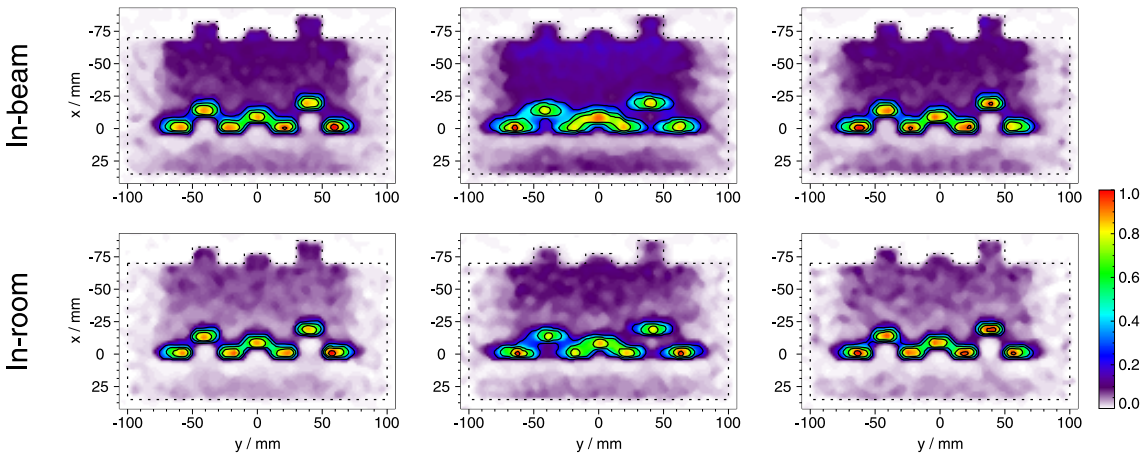

Figure 1: Reconstructed activity distributions in the irradiated phantom (dotted contour) shown for the midplane between detector heads. Images are shown for a static target (left), a moving traget without motion consideration during reconstruction (middle) and performing correct 4D reconstruction, in each case for in-beam and in-room time regime. Beam direction was along the x-axis and motion parallel to the y-axis.

Fragmentation of therapeutical carbon ions in bone-like materials

M. Rovituso[1,2,3], *C. La Tessa*[1], *L. Piersanti*[4,5], *C. Schuy*[1], *and M. Durante*[1,6]

[1]GSI, Darmstadt, Germany; [2]INFN Laboratori Nazionali del Sud, Catania, Italy; [3]University of Catania, Italy; [4]University "Sapienza" of Rome, Italy; [5]INFN Laboratori Nazionali di Frascati, Italy; [6]TU Darmstadt, Germany

Heavy-ion beams offer favourable conditions for the therapy of cancer diseases. The type of tumors treated with such method is still limited but increasing. An important step for widening and improving its application is to characterize the interaction of the primary ions with specific material, like bones, which are encountered by the primary radiation before reaching the tumor.

This work focuses on the characterization of nuclear interaction processes occurring when carbon ions in the therapeutical energy range transverse bone-like materials. In the measurements, 200 and 400 MeV/u ^{12}C beams interacted with compact bone targets (Gammex RMI 450) of different thickness (1, 3 and 5 cm). For each beam energy and target thickness, the yield and kinetic energy spectra of neutral and charged particles were acquired at 0, 2.5, 5, 10, 15, 20 and 30 degrees with respect to the primary beam direction.

The experiment

A scheme of the experimental setup is shown in Fig. 1. Two plastic scintillators of 2 and 9 mm thickness (START and VETO, respectively), and a 14 cm long barium fluoride scintillator (BaF_2) were used.

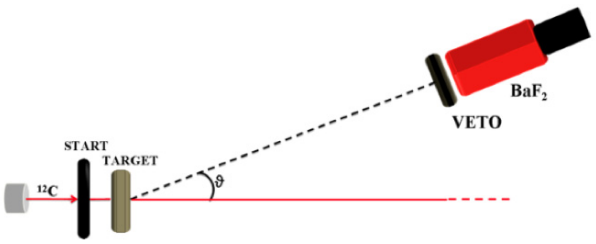

Figure 1: Scheme of the experimental setup.

The identification of the primary ions surviving the target as well as of the secondary particles produced by fragmentation of the former with the target nuclei was achieved with deposited energy (ΔE) and residual energy (E) measured with the VETO-BaF_2 telescope. Once a particle species is selected, the kinetic energy spectrum are obtained from the Time-Of-Flight (TOF) data measured between the START and BaF_2 detectors.

An example of a 2D plot of the ΔE and E signals collected with the telescope is shown in Fig 2.

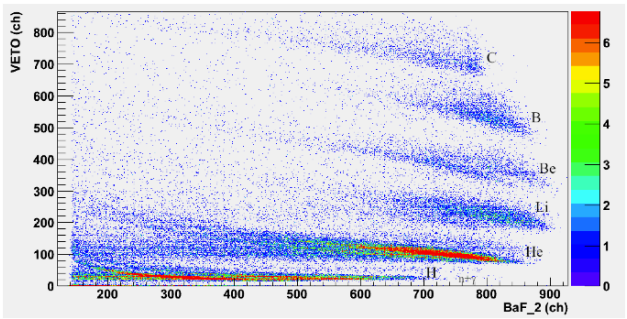

Figure 2: ΔE-E plot for a 200 MeV/u ^{12}C beam interacting with 3 cm compact bone at 5 deg with respect to the primary beam direction.

The trend of the particle yield as a function of the angle is shown in Fig 3.

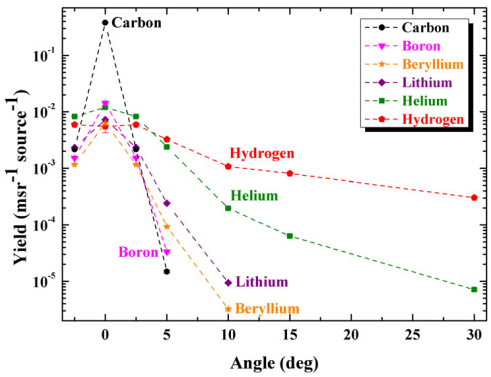

Figure 3: Angular distributions of particles measured at forward angles from -2.5° to 30° for a 400 MeV/u ^{12}C interacting with 5 cm compact bone target.

The angular distributions are all forward peaked. Primary ions and heavy fragments down to Li are detected in the range from 0 to 10 deg and cannot be found at larger angles. Neutrons, helium and hydrogen fragments present a different shape of the distribution, broader for the latter (hydrogen particles and neutrons) than for the former.

AO-10-IBER-13: Osteoblast Like Cell Culture Model Systems In Response to Space relevant Qualities of Ionizing Radiation (OSIRIS 2.0)

P. Lau[1], Y. Hu[1], C.E. Hellweg[1], C. Baumstark-Khan[1], A. Groo[3], E. Tobiasch[2], and G. Reitz[1]

[1]DLR, Köln, Germany; [2]University of Applied Sciences, Bonn Rhein-Sieg, Rheinbach, Germany; [3]GSI, Germany.

Space travel produces many challenges to human health, including radiation exposure and musculoskeletal disuse. Bone forming osteoblasts are derived from undifferentiated mesenchymal stem cells. In this study, we used human adipose tissue derived stem cells (ATSCs) to investigate cellular survival (**Fig.1**), and differentiation after radiation exposure, as well as supplementation through osteogenic medium additives (50 µM L-ascorbic acid, 10 mM β-glycerophosphate and 10^{-8} M dexamethasone), (**Fig.2**).

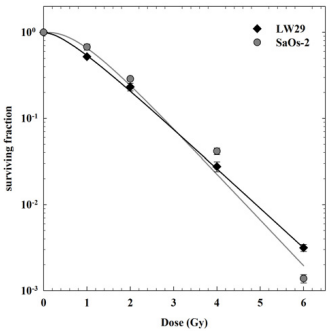

Figure 1: Survival curves of LW29 and SAOS-2 cells exposed to radiation doses up to 6 Gy.

Quantitative determination of bone cell differentiation was performed by analyzing the hydroxyapatite content of the ECM. Three days after seeding, culture medium was changed to osteogenic medium. Calcium rich deposits were confirmed less well formed regarding LW24 in comparison to the osteosarcoma cell line SAOS-2.

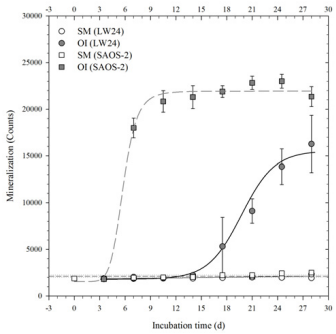

Figure 2: Cells were seeded three days before addition of osteogenic medium additives. Fluorescence was read out by using the microplate reader Lambda Fluoro 320 by using excitation / emission wavelengths of 485 / 535 nm.

Up to know few studies have evaluated the effects of low- and high-LET exposure on cell cycle regulation of ATSCs. In this study, cells were exposed to X-rays as well as to Ti-ions (1000 MeV/A; LET 107.7 keV/µm) in a dose range between 1 and 4 Gy, respectively.

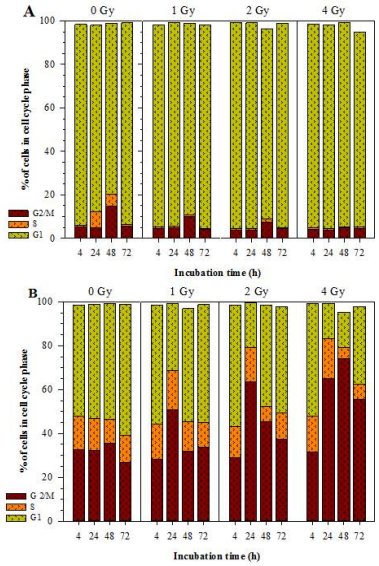

Figure 3: Cell cycle distribution after exposure to Ti-ions. Data for SAOS-2 (A) and LW24 (B) are shown as percentage of cells in the cell cycle phases G1, S and G2/M.

Cell cycle distribution of LW24 cells were only marginally affected (**Fig. 3A**) whereas a significant and dose-dependent arrest of SAOS-2 cells was detected after exposure to Ti-ions (**Fig. 3B**).

Outlook

Our findings provide a better understanding of radiation-induced biological response of ATSCs and may lead to the development of better strategies for stem cell treatment and cancer therapy. However, a detailed gene expression analysis in future work is required, to unravel intracellular responses after exposure to high-LET radiation.

Acknowledgement

We would like to thank all physicists at the GSI for their outstanding help. Bikash Konda, Claudia Schmitz and Sebastian Feles are acknowledged for their valuable help during all performed beam times.

AO-10-IBER-16 – Ground based radiation field simulation of the MATROSHKA experiment: Physical and Biological Experiments for Radiation Risk Assessment - PART II

T. Berger[1], G. Reitz[1], C. Baumstark-Khan[1], C.E. Hellweg[1], K. Koch[1], A. A. Chishti[1], M. Hajek[2], P. Bilski[3], J. K. Pálfalvi[4], L. Hager[5], S. Burmeister[6], L. Sihver[7], C. La Tessa[8]

[1]DLR, Germany; [2]TU Vienna, ATI, Austria; [3]IFJ, Poland; [4]AERI, Hungary; [5]HPA, UK; [6]CAU, Germany; [7]CTH, Sweden; [8]GSI, Germany

One goal of the AO-10-IBER-16 is the irradiation of the ground based model (phantom head) of the MATROSHKA phantom equipped with passive (Thermoluminescence (TLDs) detectors. At the same time the biological part of the experiment includes the survival reflected by radiation-dependent reduction of growth of stably and constitutively tdTomato expressing human embryonic kidney cells exposed outside and inside the phantom head.

Fig. 1. shows the dose distribution inside the phantom head after irradiation with 2Gy 1GeV/n Ti ions as a baseline for intercomparison with cell survival inside the phantom head.

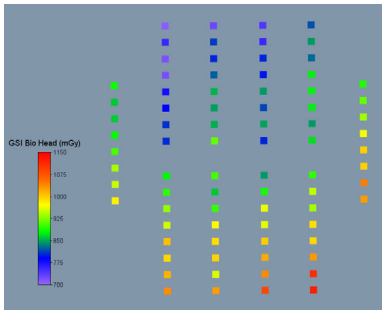

Figure 1: Dose distribution inside the phantom head measured with thermoluminescence detectors (2 Gy 1MeV/n Ti ions)

Stress-induced gene expression mediated by Nuclear Factor κB (NF-κB) was monitored by means of stably transfected HEK-pNF-κB-d2EGFP/Neo L2 cells. In these cells, d2EGFP expression is operated by four NF-κB binding sites (Hellweg et al., J. Biomol. Screen. 8, 511-521, 2003; Hellweg et al., Annals of the New York Academy of Sciences 1091, 191–204, 2006; Hellweg et al., Advances in Space Research 44, 907–916, 2009). NF-κB-dependent gene expression was monitored by flow cytometric detection of d2EGFP, a destabilized form of Enhanced Green Fluorescent Protein (EGFP).

Using these cell lines, it was recently shown that NF-κB activation depends on LET and reaches a maximum in the range of 80-300 keV/µm (Hellweg et al., International Journal of Radiation Biology, 87(9), 954–963, 2011; Hellweg et al. Radiation Research 175, 424-431, 2011). The highest biological effectiveness (RBE) in NF-κB activation was observed with argon ions (LET 172 keV/µm) with an RBE of ~9. The experiments at GSI with Ti ions (1GeV/n, LET 108 keV/µm) and Ni ions (1GeV/n, LET 175 keV/µm) complemented these results and give further inside into the dose-effect relationship and the kinetics of NF-κB dependent gene expression (**Fig. 2 A and B**). The RBE for NF-κB activation was 4.8 after Ti ions exposure, compared to 200 kV X-rays as reference radiation.

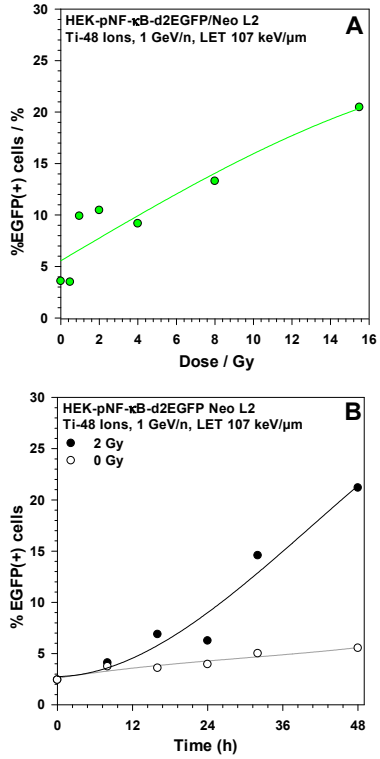

Figure 2: Induction of NF-κB dependent gene expression in HEK-pNF-κB-d2EGFP/Neo L2 cells after exposure to Ti ions. The expression of the reporter EGFP increases dose-dependently 18 h after exposure (**A**). The NF-κB activation continuously increases over two days after exposure to 2 Gy Ti ions (**B**).

Outlook

The data acquired during the beam times at GSI in 2011-2012 are being currently further evaluated. These investigations include also simulations of the physics experiment with GEANT4 Monte Carlo code. Publications on NF-κB dependent gene expression are currently under preparation.

Gene expression and cytokine monitoring for biodosimetry and radiation sensitivity screening (GYMBRASS)*

R. Quintens[1], S. Baatout[1], E. Macaeva[1], A. Michaux[1], M. Moreels[1] and K. Tabury[1]

[1]Radiobiology Unit, Belgian Nuclear Research Centre, SCK•CEN, Mol, Belgium

Introduction

The radiation environment in deep space is very different from the one on Earth and consists mainly of the galactic cosmic rays and solar particle events. Although present at only minor fractions, high-charge and high-energy particles ("heavy ions") constitute the main risk for the crew's health due to their large ionization power [1]. In contrast to low linear energy transfer (LET) radiation such as X- or γ-rays, the relationship between the early biological effects of heavy ions and the probability of cancer development in humans, is not well understood. Therefore, large uncertainties exist in estimating cancer risk as well as other adverse health effects (e.g. cataract, vascular diseases and cognitive defects) during deep space exploration. This is considered as one of the major hurdles for safe manned interplanetary space exploration [2].

Due to obvious mass constraints and physical reasons related to the very high energy of the particles of space radiation, shielding is only practical to a certain extent. Therefore, other radiation protection measures, such as on-board biodosimetry and therapeutic countermeasures should also be considered. Another possible, more preventive measure, although ethically questionable, could be to select-out those crew applicants for interplanetary missions with high resistance to the induction of early as well as late effects of radiation exposure.

Our study aims at identifying new biomarkers for radiation exposure to low- and high-LET radiation. We will focus on the use of gene, exon and/or cytokine expression signatures in human peripheral blood mononuclear cells (PBMCs) as biomarkers. These data will be integrated with those from DNA double strand break (DSB) repair kinetics in order to identify biomarkers of individual radiosensitivity.

Results and discussion

Comparison of radiation-induced gene expression after irradiation of PBMCs with 1 Gy of X-rays or C-ions

Using microarrays, we analysed genome-wide gene expression changes in non-stimulated, cultured PBMCs 8 h after irradiation with 1 Gy of X-rays (250 kV, 15 mA; n=10) or C-ions (LET = 50-75 keV/µm; n=4). Data analysis revealed that the changes were very similar between the different types of radiation. Because of the different number of donors for both experiments, yielding very different ANOVA *p*-values, we used rank-rank hypergeometric overlap analysis to detect and to visualise overlap trends between both gene expression profiles. This showed that there was a very high degree of overlap (minimum hypergeometric *p*-value ~10^{-63}) among the genes that are upregulated by both X-ray as well as C-ion irradiation.

Radiation quality-specific gene expression changes

Besides overlapping genes, we also identified gene expression signatures that were only responsive to either X-ray or C-ion irradiation. Whether these signatures can be used as biomarkers for prediction of exposure to radiation of different qualities is still under investigation.

Analysis of individual DNA repair kinetics by γH2AX

To identify biomarkers for individual radiation sensitivity, we will integrate gene/exon/cytokine expression data with data from individual DNA repair kinetics based on microscopic analysis of γH2AX positive DSB foci. First results show that there are indeed differences in radiation-induced foci formation among the donors.

Conclusions and perspectives

Our preliminary data indicate that there is a high degree of overlap in gene expression changes in PBMCs that are irradiated with similar doses of high- and low-LET radiation, although specific expression signatures were identified for both radiation qualities. We also analysed transcriptional changes at the level of single exons, which indicate that exon expression signatures are also useful as biomarkers of exposure and may explain differences in inter-individual radiation sensitivity.

Further experiments using multiplex protein assays will be performed to verify cytokines as possible biomarkers. Integration of DNA repair kinetics from individual donors with their radiation-responsive expression profiles will be performed as a final step of the project.

References

[1] F.A. Cucinotta and M. Durante. Risk of radiation carcinogenesis, *Human health and performance risk of Space exploration missions*, J.S. Mcphee and J.B. Charles, Houston, Texas, USA, 2009.

[2] M. Durante and F.A. Cucinotta. Heavy ion carcinogenesis and human space exploration, *Nat. Rev. Cancer*, Vol. 8(6), 465-472, 2008.

* Work supported by Belspo, Prodex-9 project "MOSAIC-2" (42-000-90-380) and by the ESA IBER-10 program (AO-10-IBER-26)

Mucositis represents a potential risc for astronauts on extended space flights*

V. Tschachojan[1], N. Averbeck[2], W. Mueller-Klieser[1]

[1] Institute of Physiology and Pathophysiology, University Medical Center Mainz, Germany;
[2]GSI Helmholtz Centre for Heavy Ion Research, Darmstadt, Germany.

Radiation-induced mucositis is a severe complication of heavy ion radiotherapy [1] and may also represent a health risk during extended space flights [2].

To evaluate the risk of developing a radiation-induced mucositis through highly energetic heavy ions in space, a three-dimensional organotypic oral mucosa model of immortalized human keratinocytes and fibroblasts was irradiated with ^{12}C particles (150 MeV/u) at the SIS accelerator at GSI. The focus of this study was on immediate and early effects after irradiation, where NFκB activation and increased expression of the cytokines are precursors of oral mucositis. 3D cultures were irradiated with 2 or 4 Gy and NFκB activation as well as IL6/IL8 expression was analyzed 4, 8, 24 and 48 h after treatment. In order to study NFκB activation NFκB p50 was immunofluorescence stained in cryosections of irradiated 3D cultures. This revealed a translocation of NFκB p50 from the cytoplasm to the nucleus after irradiation. The nuclear NFκB p50 signal was quantified and normalized against the nuclear DAPI signal. The relative change of the NFκB p50 amount in the nucleus upon irradiation is shown in Figure 1. In cultures exposed to 2 Gy ^{12}C heavy ions we observed a translocation of the transcription factor to the nucleus 24 h and 48 h after treatment. 4 Gy of ^{12}C irradiation caused a nuclear increase of NFκB p50 already after 4 h; this localization could still be seen after 8 h, 24 h and 48 h.

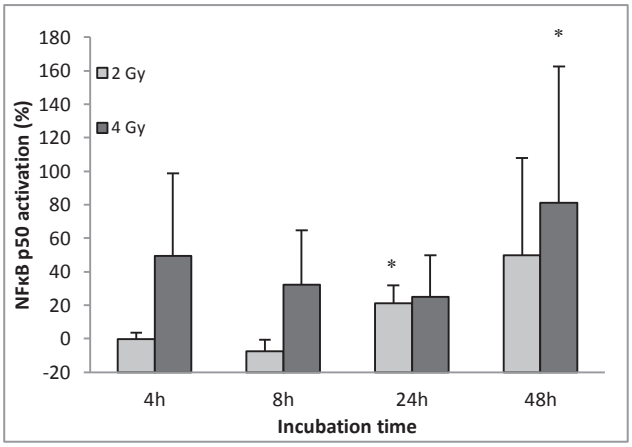

Figure 1: The percentage change of the NFκB p50 amount in cell nuclei upon ^{12}C irradiation. Cryosections of 3D cultures were immunofluorescence stained against NFκB p50. Only nuclear NFκB p50 stained areas were related to whole DAPI stained areas (n=4, mean ± sd;
*p < 0,02 with reference to not irradiated cultures).

The pro-inflammatory cytokines IL6 and IL8 were analyzed in the culture's supernatants in four independent experiments (Figure 2). In general, a tendency of dose-dependent increase of IL6 and IL8 could be detected for up to 24 h after irradiation. 48 h after irradiation the IL6 and IL8 level was back to the initial value.

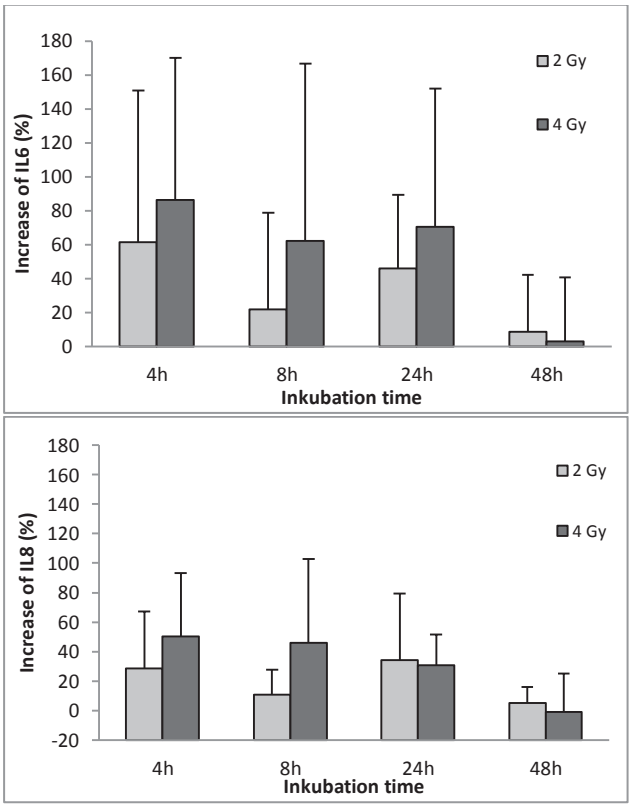

Figure 2: ELISA analyzes of cytokines IL6 and IL8 from supernatants of organotypic cultures. The relative increase compared to the control level (untreated) in IL6 or IL8 is shown. (n=4, mean ± sd)

Taken together, inflammatory responses as a sign of the initiation stage of oral mucositis could be detected in organotypic mucosa models exposed to highly energetic carbon ions. This suggests that mucositis indeed poses a risk for astronauts on extended space flights.

References

[1] Schultz-Ertner, D et al., (2002). Radiotherapy and Oncology 64; 189–195.
[2] Gonda, TA et al., (2009). Cell Cycle 8:13:2005-2013.

* Support: ESA, Deutsches Zentrum für Luft- und Raumfahrt e. V. (DLR), Bundesministerium für Wirtschaft und Technologie (BMWi), #50 WB 0926.

Status of the ROSSINI project at GSI*

C. Schuy† [1,2], *C. La Tessa*[1], *M. Rovituso*[1,2], *L. Piersanti*[1,3], *E. Tracino*[4], *C. Lobascio*[4], *and M. Durante*[1,2]

[1]GSI, Darmstadt, Germany; [2]TU Darmstadt, Germany; [3]University of Rome "La Sapienza", Italy; [4]Thales Alenia Space, Italy

Overview

Since the end of the Apollo missions, human spaceflight concentrated on missions in Low Earth Orbit thus reducing one of the major risk for man in space - radiation. Due to Earth's magnetic field, astronauts are largely protected from cosmic radiation originating from the sun or outside our galaxy. This situation will change significantly when the final destination is beyond this protection and deeper into the solar system. The feasibility of missions into deep space is strongly connected to the capability of protecting astronauts from the harsh radiation environment in interplanetary space [1]. Passive shielding, a well known technique in radiation protection, shows great promises in reducing the health risk induced by the space radiation environment.

The ROSSINI project

The ROSSINI(RadiatiOn Shielding by ISRU and/or INnovative MaterIals for EVA, Vehicle and Habitat) project is funded by ESA and started in 2012. The goal of the experiment is to select innovative shielding materials and provide recommendations and guidelines for space radioprotection in different mission scenarios. These include the protection of spaceships, which require light and durable shielding materials, as well as the shielding of possible permanent bases on Mars or Moon, where available material like regolith can offer the needed protection.
The project is a common effort of Thales Alenia Space, GSI, SpaceIT and ESA.

Experiments

The shielding effectivness of all candidate materials is assessed through dose reduction curves and/or Bragg-Peak measurments similar to the experimental setup in [2].
For the most promising materials a characterization of the mixed radiation field produced by heavy ions impinging on the targets is perfomed. Particle identification is achieved with a BaF_2 telescope and kinetic energy with the time-of-flight technique [3].
First experiments were performed in June 2012 at NSRL/Brookehaven National Laboratory (USA), and in August and October 2012 at Cave A/GSI using high energy heavy ion beams.

Status and outlook

Experimental data taken during the measurment campaign in 2012 at GSI is currently being analysed [Fig 1]. Based on the gained experience, optimizations of the detectors and electronics are currently in progress, as well as changes of the experimental site Cave A. Further experiments are expected to be performed at the end of 2013.

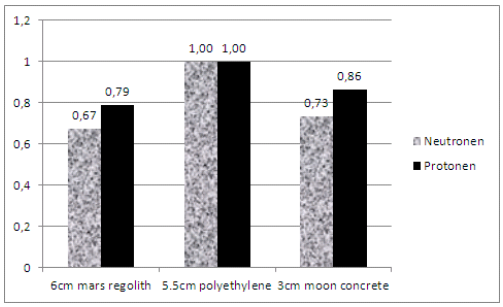

Figure 1: Preliminary relative proton and neutron production rate for 1 GeV/u Ti beam impinging on different shielding materials of 5 g/cm^2 thickness. All results are scaled to Polyethelene, which is a widely used radiation shielding material.

Acknowledgment

Adam Rusek and Michael Sivertz of the Brookhaven National Laboratory, Stephen Bennington and Zeynep Kurban of Cella Energy, Enrico Dini of Dinitech and Markus Kayser for the test of Solar Sinter machine.

References

[1] M. Durante and F. Cucinotta, "Heavy ion carcinogenesis and human space exploration", Nature Reviews Cancer 8 (June 2008), 465-472

[2] D. Schardt et. al, "Precision Bragg-Curve Measurements for Light-Ion Beams in Water", GSI Scientific report, 2007

[3] E. Haettner,H. Iwase and D. Schardt, "Experimental fragmentation studies with ^{12}C therapy beams ", Radiat Prot Dosimetry (December 2006) 122 (1-4): 485-487

* Work supported by ESA(RF: SGI-TASI-PRO-0226)
† Work supported by HGSHire

Status of the FairRoot framework

M. Al-Turany[1], *D. Bertini*[1], *R. Karabowicz*[1], *D. Kresan*[1], *T. Stockmanns*[2], *and F. Uhlig*[1]
[1]GSI, Darmstadt, Germany; [2]FZJ, Juelich, Germany

The FairRoot framework is an object oriented simulation, reconstruction and data analysis framework based on ROOT [1]. It includes core services for detector simulation and offline analysis. The framework delivers base classes which enable the users to easily construct their experimental setup in a fast and convenient way. By using the Virtual Monte Carlo concept it is possible to perform the simulations using either Geant3 or Geant4 without changing the user code or the geometry description. Extending the task mechanism of ROOT it is possible to implement complex analysis tasks in a convenient way. Using the FairCuda interface of the framework it is possible to run special tasks also on GPU. Data I/O, as well as parameter handling and data base connections are also handled by the framework. Since some of the experiments will not have a experimental setup with a conventional trigger system, the framework can handle also free flowing input stream of detector data. For this task the framework provides classes to create out of event based simulation data the needed time sorted input stream of detector data. There are also tools to do radiation studies and to visualize the simulated data. A CMake-CDash based building and monitoring system is also part of the FairRoot services which helps to build and test the framework on many different platforms in an automatic way, including also Continuous Integration.

The framework, is designed to optimize the accessibility for beginners and developers, to be flexible (i.e. able to cope with future developments), and to enhance synergy between the different physics experiments within the FAIR project. However the framework is meanwhile also used outside FAIR project by the MPD project at Dubna [2] and the EIC project at BNL [3]

Time based simulation

The time based simulation support in FairRoot is available for all experiments. At present only some detectors in PANDA did the full implementation of there detectors to handle the time based simulation (i.e: MVD, LMD and STT have the full implementation). Work is ongoing by the different detector groups and soon the system should be ready for PANDA.

Database support

The parameter handling in FairRoot has been extended. The connection to storage database is implemented via a database interface which provides a simple and uniform concept regardless of the data being accessed, this is described in details in this report by D. Bertini. et.al [4]

Support the realtime pipeline-processing

Extensions for supporting realtime pipeline-processing scenarios of the online analysis are being developed within the FairRoot framework. This new development is described in more details in a separate report [5].

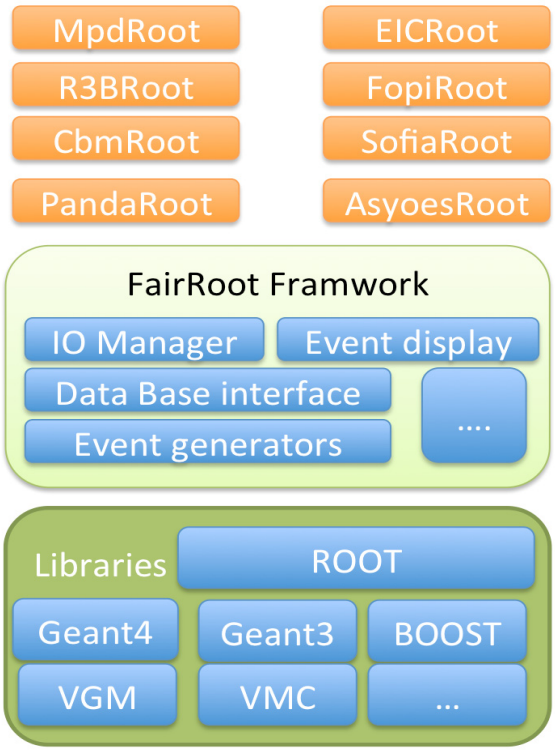

Figure 1: FairRoot at different experiments

References

[1] R. Brun and F. Rademakers. Root - an object oriented data analysis framework. *Nuclear Instruments and Methods in Physics Research A*, 389:81–86, Sep. 1997.

[2] MpdRoot software team, Simulation and Analysis Framework for NICA/MPD Detectors Webpage, available online at http://mpd.jinr.ru/dr/;

[3] EIC Collaboration, Letter of Intent for Detector R+D, Towards an EIC Detector, Webpage, available online at https://wiki.bnl.gov/conferences/images/6/69/RD 2011-2 EICTrackingPIDproposal.pdf;

[4] D. Bertini, Y. G. Rozas and M. Babai. Database support within FairRoot, this report.

[5] D. Klein and M. Al-Turany, Flexible data transport for the online analysis of a particle physics experiment, this report

Alignment in FairRoot

M. Al-Turany[1], D. Bertini[1], R. Karabowicz[1], D. Kresan[1], and F. Uhlig[1]
[1]GSI, Darmstadt, Germany

Alignment means to create the geometry used in simulation, reconstruction, and data analysis as close as possible to the real one in the experiment. The agreement between these two geometries is needed to achieve for example the required experimental resolution.

The problem is to know the real position of the detectors and detector subcomponents as accurate as possible which cannot be taken from a technical drawing. During their assembly the detectors and detector subcomponents cannot be placed at the expected position, since the positions of subcomponents may change for example due to mechanical deformations.

The alignment procedure needs as a starting point a geometry which is as close as possible to the real geometry in the experiment. This geometry can be taken from the technical drawings, but in most cases it comes from an optical survey. The alignment procedure then improves the accuracy of the positions of the different volumes by using signals generated in the active parts of the detector. Depending on the experiment and the detector system these signals can be produced by a laser calibration system, cosmic particles or particles from collision events.

Alignment Procedures

One approximate alignment procedure is to fit data from single tracks assuming fixed alignment parameters. The deviations between the measured hit position and the fitted one (residuals) are then used afterwards to extract the alignment parameters.

The problem with this method is that the result and hence the extracted alignment parameters are biased, since one uses wrong hit positions for the track fit. In repeated fits using the alignment parameters extracted in the previous iteration one can reduce the residuals, but it is not clear if the procedure converges [1].

A more efficient and faster method is an overall least squares fit, with all the global parameters (alignment parameters) and local parameters (track parameters for one track), perhaps from thousands or millions of events, determined simultaneously. For this task the Millepede program [2] was developed. The global parameters are the different degrees of freedom for each volume to be aligned. Assuming a 3 dimensional cartesian coordinate system this can be up to 6 different degrees of freedom. 3 for shifts in the x-, y-, and z-direction and another 3 for the rotations around the 3 axis of the coordinate system. Not all of these parameters have to be free in the minimization process.

Using Millepede in FairRoot

The program Millepede actually consist of two program parts. One is the writer component called mille, which writes the required input data for the minimizer (pede) in the correct binary format. This split, and the fact that there is also a c++ implementation of the writer component make the usage of Millepede in the FairRoot framework rather easy.

A reconstruction or analysis run within the FairRoot framework [3] is always build out of one or more tasks which are executed in a given order. To use Millepede within this scheme one has only to create a task which collects for each event all the information needed by the minimizer component and uses the writer component to create the input data in the correct binary format.

The data to be written are the derivatives of the local and global parameters, the residual and the error for each measured hit together with labels to define which global parameters are correlated with this hit. This data is very much dependent on the track model used by the experiment and the global parameters and hence the implementation of the writer task is very much experiment specific.

The FairRoot framework contains a toy model experiment (Tutorial4) which is meant to explain how to write an experiment specific class to create the binary data file for the minimization part of Millepede. The ”experiment” has 40 silicon detector planes, which can measure the x- and y-coordinates of particles traversing the detector volume. In the simulation run for each event one particle from different vertices and with different incident angles is tracked through the experimental setup. In the reconstruction run as the first step the hit positions are calculated taking into account parametrized shifts of the detector planes (misalignment) and an uncertainty due to detector response. For each event the hits are now fitted to extract the track parameters. The used track model for this fit is a straight line. In the last step the derivatives of the local and global parameters and the residuals for each hit are written to the binary data file for the minimizer component of Millepede.

The calculated alignment parameters (shifts of the detector planes in x-, and y-direction) using the minimizer component of Millepede are in very good agreement with the simulated misalignment.

References

[1] http://www.desy.de/˜blobel/

[2] https://www.wiki.terascale.de/index.php/Millepede_II

[3] http://fairroot.gsi.de/

Flexible data transport for the online analysis in a particle physics experiment.*

D. Klein[1,2] *and M. Al-Turany*[1]

[1]GSI, Darmstadt, Germany; [2]University of Applied Sciences, Darmstadt, Germany

Motivation

The next generation of experiments at GSI/FAIR share the common software framework *FairRoot*[1] which provides the building blocks for offline analysis. The software is well-suited for batch-processing.

Online analysis processes the data on-the-fly, filters the interesting physics data and it needs to reduce the raw data rates by three orders of a magnitude.

The FairRoot framework must be extended to support the continuous pipeline-processing scenario of the online analysis.

During prototyping it is very important to be able to often change data paths and processing elements in the pipeline. The inter-process data transport must be reliable and efficient within one node and over the network between nodes.

The Data Transport Framework

A data transport framework has been proposed and implemented[3]. Each framework component, a so-called device, runs in its own operating system process. A device has a variable number of inputs and outputs which can be flexibly interconnected to each other. The data transport of each connection is built upon a highly efficient message queuing library (ZeroMQ[2]). The message queuing technology itself is reliable by definition. For inter-node connections the transport relies on the Linux TCP/IP stack which works over Ethernet and Infiniband. Intra-node connections are realized on Unix' named pipes.

The framework provides a basic set of devices: *sampler*, *processor*, *splitter*, and *merger*.

A sampler device starts any pipeline during simulation. It feeds simulated data from root files into the pipeline. The current implementation supports control over the sending speed in events per second.

Processors are devices which operate on the contents of the messages (events) - they constitute the actual processing instance in the pipeline. The current implementation features a plugin system for processing algorithms via *ProcessorTask* similar to the *FairTask* class in FairRoot.

Splitters and mergers are devices to de/multiplex the data path. Whenever a processing instance must be distributed over serveral nodes/processes due to bandwidth and/or cpu limitations data paths can be splitted and merged before and after processor devices.

Let $n, m \in \mathbb{N}$, then a many-to-many mesh of n splitters to m mergers serves as a transposing engine (with n inputs and m outputs) of signals from n subdetector links to an over m nodes/processes distributed processing instance. Fig. 1 illustrates an example which was successfully run with the current implementation, monte-carlo data generated with PandaRoot[1] and a dummy processor task.

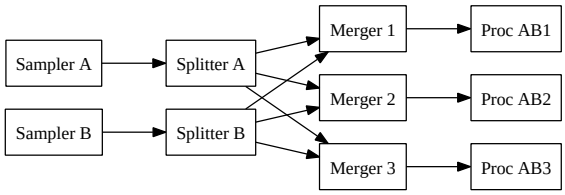

Figure 1: 3-way distributed processor fed from two sources.

TCP throughput

A bandwidth utilization of 99.7% of the theoretical maximum for TCP over GigabitEthernet has been seen. In the test a sampler was connected to a processor on two identical nodes - CPU load was 25% of one core (2.13 GHz Intel Xeon) per device.

Next Steps

- Integration into FairRoot repository,
- configuration management via directory service,
- adding support for time-series simulated data,
- improving the user interface,
- reducing latency even more by using shared memory transport of ZeroMQ between processor tasks each running in their own thread,
- collecting runtime monitoring information.

References

[1] http://fairroot.gsi.de

[2] http://www.zeromq.org

[3] D. Klein, "Flexible data transport for the online analysis in a particle physics experiment", Feb 2013, Bachelor thesis.

* thanks to the KoSI program

Track finding and fitting on GPUs, first steps toward a software trigger

M. Al-Turany[1], A. Herten[2], and A. Rybalchenko[1]
[1]GSI, Darmstadt, Germany; [2]FZJ, Juelich, Germany

The graphics processing units (GPUs) have evolved into high performance co-processors that can be easily programmed with common high-level language such as C, Fortran and C++. Todays GPUs greatly outpace CPUs in arithmetic performance and memory bandwidth, making them the ideal co-processor to accelerate a variety of data parallel applications. For the online processing (i.e: Software triggers and online event selection with high data rates as in CBM [1] and PANDA[2] experiments) GPUs present an attractive solution.

Online applications include high level processing, which requires floating point operations. However, the widely used FPGA (Field Programmable Gate Array) does not have such capabilities. The users have to program in the low-level hardware description language (HDL). GPUs, on the contrary, are programmable with high-level languages and meanwhile provide support even for double precision. In order to evaluate GPU solution in a practical way, an algorithm based upon conformal mapping and Hough transform was implemented on GPUs using NVIDIA CUDA (Compute Unified Device Architecture). The algorithm is tested with the PANDA central tracker simulated data. The results of the same algorithm are compared with CPU and FPGA implementations.

To evaluate the run-time and the precision of the algorithm, the GPU implementation was compared against CPU implementation. Used hardware included NVIDIA GeForce GTX 480 GPU and Intel Xeon W3505 CPU clocked at 2.53 GHz. Already with a trivial GPU implementation it was possible to decrease the run-time of the algorithm by over a 100 times. After applying various memory optimization techniques, GPU configuration optimizations and program flow optimizations the performance was further improved, with total run-time decrease of around 200 times. The precision of the results is comparable within 5% to the CPU solution.

	CPU	GPU
tracks segments in first step	1615	1609
After first iteration	158	151
After last iteration	14	14

Table 1: Comparison of number of tracks found for the same event when analyzed on CPU or GPU

Compared to the FPGA, the GPU implementation is about 30% faster. However, one should keep in mind that on both systems we still have a huge space for improvement. With the new release of the CUDA compiler (CUDA 5.0) the same code runs 20% faster on the same hardware. This is an important illustration of the current state of the GPU and GPU compiler technology, which, although already offering promising performance, is still at an early development stage and further improvements are likely to happen.

The newest GPU generation from NVIDIA (so called Kepler architecture [3]) includes various new hardware improvements and allows more functionality on the GPU side. The new features have the potential to further improve the performance of track finding and fitting. The new features (e.g: GPUDirect [4] and "Dynamic Parallelism" [3]) will have a huge impact on the whole design of the software running on GPUs, moreover, it will releases the host CPU almost completely and the whole fork could be done on the GPU.

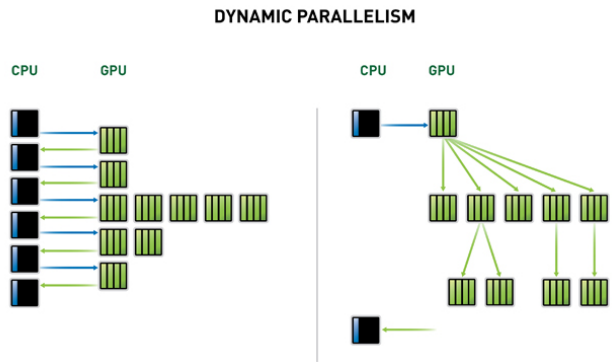

Figure 1: Dynamic Parallelism on Kepler GPU dynamically spawns new threads by adapting to the data without going back to the CPU, greatly simplifying GPU programming and accelerating a broader set of popular algorithms. (From nvidia.com)

As an alternative to the traditional Hough transform, an adaptive approach needs to be considered, which holds the potential to greatly reduce the size of the data to analyze. Although it reduces the data parallelism of the algorithm, it also frees up GPU resources for more task parallelism, which now can be implemented very efficiently with Dynamic Parallelism.

References

[1] https://www.gsi.de/work/forschung/cbmnqm/cbm.htm
[2] http://www-panda.gsi.de/
[3] http://www.nvidia.com/object/nvidia-kepler.html
[4] https://developer.nvidia.com/gpudirect

E-Science Activities at GSI

K. Schwarz for the e-science group/Scientific Computing[1]
[1]GSI, Darmstadt, Germany

This article describes the work of the GSI e-science Group with the aim to enlarge and operate an ALICE tier2 centre within the global environment of the LHC Computing Grid and to prototype a distributed computing environment for FAIR.

ALICE tier2 centre at GSI and ALICE Grid in Germany

The ALICE tier2 centre at GSI provides a computing infrastructure for ALICE Grid and for the local usage of the German ALICE groups. The available disk space is distributed among an xroot cluster (300 TB) and Lustre (1.4 PB on /lustre and 2.1 PB on /hera). A new Grid Storage Element on top of /hera has been configured which is connected to the outside world via GSI's 10 Gb network interface to HEPPI net. New data-sets are being transferred to GSI continuously and are processed on the local batch farm via daily running analysis trains.

Throughout the year GSI participates in centrally managed ALICE Grid productions and data analysis activities. The overall job share of GSI, Forschungszentrum Karlsruhe (ALICE tier1 centre) and the HHLR compute cluster at Goethe University in Frankfurt has been 15% of all ALICE jobs worldwide.

Local farm management at GSI

The GSI e-science group contributes significantly to local farm management with the GSI batch farm being an integral part of the ALICE tier2 centre. One of the major projects has been the successful transition from the commercial LSF scheduler to the open source scheduler (Sun)GridEngine [1] in close collaboration with the HPC group.

PROOF on Demand

The in the context of the D-Grid project developed "PROOF on Demand (PoD) utilities" enjoy a high popularity [2]. The development is going on and and new releases are being published. Most recently an interface to Slurm is being developed.

CRISP

The Cluster of Research Infrastructures for Synergies in Physics (CRISP) project is a collaboration between different institutions and facilities related to physics research. In this scope, a pan-European Federated Identity Management (FIM) system is under development [3].

LSDMA

The work of the Data Life Cycle Lab "Structure of Matter/FAIR" is being defined by the computing requests of the FAIR project. A project plan has been created and first discussions have to be done with the FAIR experiments. New positions are to be advertised.

KOSI

The KOSI programm (Kooperativer Studiengang Informatik) from Hochschule Darmstadt starts to become a very efficient way to attract good students to GSI. Within the context of this joint venture programm a new visualisation tool for accounting data at the GSI batch farm [4] came into life. Moreover in collaboration with the GSI theory group a general framework to predict and analyze hadronic final-state interactions is being prepared [5].

Preparation for FAIR

PANDA-Grid consists currently of 15 sites from 12 institutes in 10 countries. The most recent sites which joined the project are Mainz, SUT in Thailand, and Talca in Chile. Currently Northwestern University, USA, is in the process of joining. The single most defining event of 2012 [6] was the withdrawal of the Glasgow University from the PandaGrid activities. Therefore the PandaGrid Central Services had to be moved from Scotland to GSI as well as the central Grid monitoring MonaLisa service to Torino. The movement, although more challenging than anticipated, consolidated and brought experience to the GSI Grid group.

The collaboration between ALICE and PandaGrid intensified significantly. In joint workshops on regular basis (PandaGrid Workshop in conjunction with AliEn Developers Week) as well as in frequent telephone meetings the ongoing work is organised.

References

[1] C. Preuss, K. Schwarz, "Batch Computing Support", this report.

[2] A. Manafov, P. Malzacher, "PROOF on Demand", this report.

[3] A. Montiel Gonzalez, K. Schwarz, P. Malzacher, "Federated Identity Manangement within CRISP", this report.

[4] S. Jovanovic, C. Preuss, K. Schwarz, "A Visualisation Tool for Accounting Data", this report.

[5] J. Knedlik, M.F.M. Lutz, K. Schwarz, "Distributed matrix computations via MPI on the GSI cluster", this report.

[6] R. Karabowicz, A. Montiel-Gonzalez, J. Behrendt, K. Schwarz, "Annual Activities in PandaGrid", this report.

A Visualisation Tool for Accounting Data *

S. Jovanovic[1,2], *C. Preuss*[1], *and K. Schwarz*[1]
[1]GSI, Darmstadt, Germany; [2]Hochschule Darmstadt, Germany

This article describes the project ”Computing Cluster Usage Visualization Tool” which has been developed in the context of the KoSI (Kooperativer Studiengang Informatik) project in cooperation between the ”Hochschule Darmstadt” and the GSI.

Introduction and background

The ”Hochschule Darmstadt” offers in the faculty of Information Technology a dual study course during which a pre defined project is being developed in cooperation between the university and the participating company within three praxis semesters distributed over the whole course of studies. The ”Computing Cluster Usage Visualization Tool” came into existence during the 3rd praxis semester - the 7th semester in total - and had the aim to provide a visualisation system for the capacity utilisation of the Prometheus compute cluster at GSI.

Users and groups have the possibility to get information about their computed jobs and their efficiency in a fast way via an easy to understand graphical display. By giving the time interval the degree of capacity usage within certain periods of time can be visualised. Most of the times recently computed jobs are available for such capacity usage visualisation. Also a time interval larger than a single month can be defined. The visualisation system is accessible in the intranet of the GSI under the following address http://webdocs.gsi.de/~jsinisa/accountingApp/mainAjax.html. An example view is given in fig. 1.

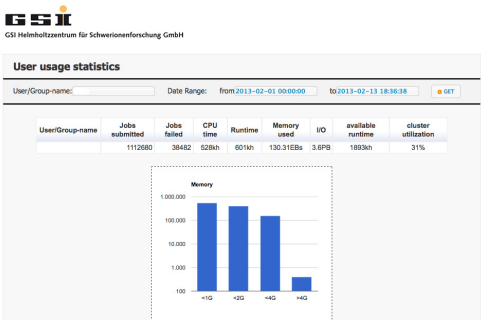

Figure 1: An example view of the Computing Cluster Usage Visualisation Tool.

Visualisation of resources

The ”Computing Cluster Usage Visualization Tool” offers a visualisation for whole groups as well as for single users. The following information about computed jobs in a given time interval can be displayed:

- number of computed jobs
- number of failed jobs
- consumed CPU time
- memory consumption
- storage consumption of I/O operations
- cluster capacity utilisation with respect to run time/wall clock in percentage

Additional graphs give more detailed information about the jobs. The charts are ordered according to time periods and memory consumption. Depending on how many jobs in a given time gap have been computed or on how many jobs consume a certain amount of memory corresponding bars will be plotted. This results in bar charts ordered in a way as described above.

Benefit and results

The job management system of Sun Microsystems, Sun GridEngine, which is powering the compute cluster Prometheus, is documenting each computed job in a accounting file. A copy of this accounting file will be placed into the intranet of GSI and will be updated in periodical time spans. Via this method a permanent insight into the current capacity utilisation is available. At the end of each month a report is being created summarising the capacity utilisation of the cluster. This report is presented on a regular basis in the monthly Technical Computing Meeting where representatives of GSI IT and the experiments are present and are thus regularly informed. This may simplify estimates related to the currently available hardware and also estimates related to future resource distribution plans. Statistics of individual experiments can be discussed and also how to proceed in future.

Outview

The project ”Computing Cluster Usage Visualization Tool” has been developed during a praxis semester of a KOSI study course. The visualisation system can be further extended though with regards to functionality and simplified visualisation. Another possibility is to further develop and to integrate the current system into a larger monitoring project at GSI IT.

* Work supported by the KOSI program

PROOF on Demand

A. Manafov, P. Malzacher

GSI, Darmstadt, Germany

PROOF on Demand (PoD) [1][2] is a tool-set that automats and dramatically simplifies the process of creating private PROOF [3] clusters.

PoD dynamically sets up a PROOF cluster at a user's request on any resource management system (RMS). It provides a plug-in based system, in order to use different job submission front-ends.

PoD plug-ins

Currently PoD supports the following plug-ins: gLite, LSF, PBS (PBSPro/OpenPBS/Torque), Grid Engine (OGE/SGE), Condor, LoadLeveler, and SSH plug-ins. PoD makes it possible just within a few seconds to get a private PROOF cluster on those systems. If there is no RMS, then the SSH plug-in can be used, which dynamically turns a bunch of machines to PROOF workers. The SSH plug-in has been widely improved during a 2012 development cycle.

In 2012 the plug-in set has been also extended to support PanDA [4] a distributed software system developed for the ATLAS experiment. The PanDA PoD plug-in is already used by ATLAS and CMS users.

Binary payload attachment

Recently a new major step in PoD development has been made. To simplify PoD work packages a multilayer binary payload attachment (BPL) has been introduced.

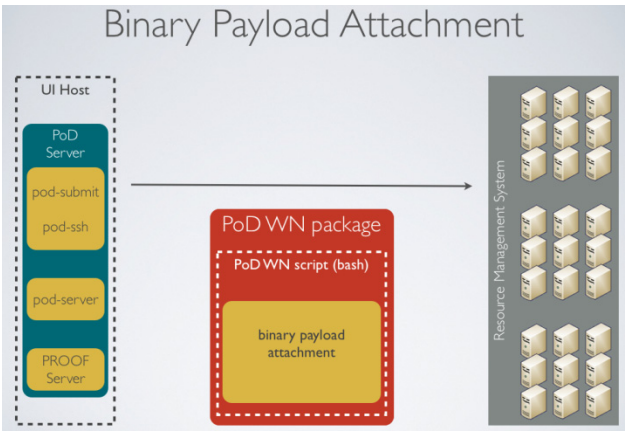

Figure 1: A multilayer binary payload attachment.

Now PoD doesn't require shared file systems on worker nodes or input sandboxes. There is only a single worker script, which is submitted to worker nodes and which contains everything PoD workers need, including precompiled binaries, configuration files, and user resources.

BPL also helped to simplify all plug-ins of PoD, as requirements for PoD workers were dramatically reduced.

User community

PoD is being very successfully used by German ALICE collaboration and has been chosen as a standard PROOF tool for FAIR computing [5].

The tool-set is also official distributed to all Tier3 ATLAS sites via standard ATLAS software deployment machinery [6].

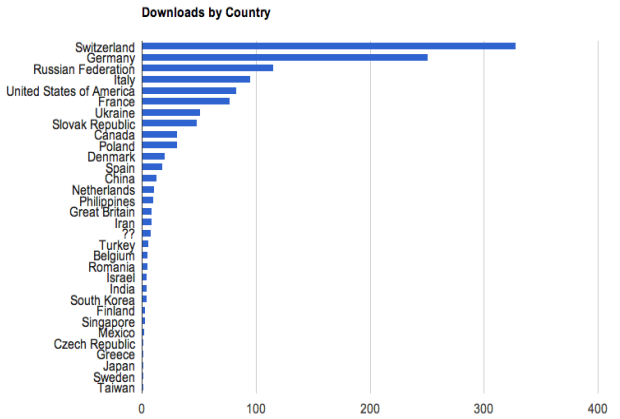

Figure 2: ~1300 downloads from 31 countries (since June, 2010), with 220 downloads/year from unique IPs. It's 20% more unique IPs and additionally 9 new countries than in 2011.

Summary

As PoD matures as a product, it is used more and more as a standard for setting up dynamic PROOF clusters in many different institutions in the HEP community. With PoD there is no need to maintain a dedicated PROOF analysis facility. PoD users create themselves private dynamic PROOF clusters on general purpose batch farms, Grid or Cloud systems.

References

[1] A. Manafov et al, "PROOF on Demand", PHN-IS-IT-07, GSI Scientific Report 2010.

[2] PROOF on Demand (PoD), http://pod.gsi.de

[3] The Parallel ROOT Facility (PROOF), http://root.cern.ch/drupal/content/proof

[4] ATLAS PanDA, https://twiki.cern.ch/twiki/bin/view/Atlas/Panda

[5] M. Al-Turany et al, "PROOF integration in FairRoot, GSI", Scientific Report 2011.

[6] ATLAS Wiki, https://twiki.atlas-canada.ca/bin/view/AtlasCanada/ManageTier3SW

Annual activities in PandaGrid

R. Karabowicz[1], *J. Behrendt*[1], *A. Montiel González*[1], *and K. Schwarz*[1]
[1]GSI, Darmstadt, Germany

Abstract

PandaGrid, started as a project in 2005, and since then proved itself to be a successful tool in large scale data production for the Panda collaboration. The variety of use spans from individual jobs of more than 50 PandaGrid users to massive physics simulation and reconstruction for the Panda Technical Design Report. The passing year stands for important changes in the structure of the PandaGrid.

Introduction

The single most defining event of 2012 was the withdrawal of the Glasgow University from the PandaGrid activities and movement of the Central Services to GSI and MonaLisa to Torino. The movement, although more challenging than anticipated, consolidated and brought experience to our GSI Grid group. In the course of last year 3 new sites joined PandaGrid: Mainz, SUT in Thailand and Talca in Chile. Currently we are in the process of integrating Northwestern University, USA, as a new site. Altogether the infrastructure comprises 15 sites from 12 institutes in 10 countries, see Fig. 1.

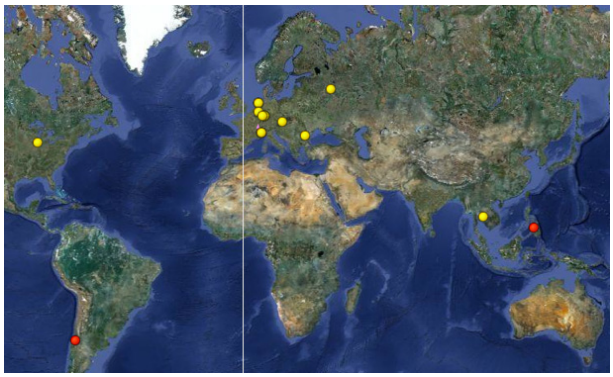

Figure 1: Map of PandaGrid sites.

Software and Middleware Tools

PandaGrid is based on AliEn [1], middleware developed and maintained by the ALICE Collaboration. The software for simulation and reconstruction, PandaRoot, bases on FairRoot [2], and is distributed on the Grid via built-in package management mechanism of AliEn. The system supervision and monitoring is provided by the MonaLisa webpage [3].

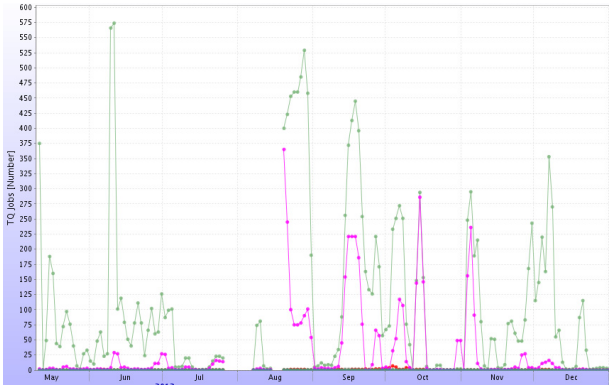

Figure 2: PandaGrid usage.

Testing and Development

As part of our obligation to the middleware development we are testing and debugging the newest releases of AliEn. This year's most important contributions included:

- fixing the database structure description,
- fixing the package manager,
- migrating the communication message protocol from SOAP to JSON,
- implementing new fuctionalities.

Numerous other issues have been reported to the AliEn developers. These changes helped keeping not only PandaGrid stable, but also improved the original ALICE Grid performance.

Results

The PandaGrid running jobs in year 2012 are plotted in the Figure 2 as a function of time.

The close collaboration with the AliEn development group resulted in 2 PandaGrid Workshops in SUT, Thailand and Talca, Chile, where we focused on fixing and developing AliEn as well as setup the new PandaGrid sites. In the coming year we would like to focus on further consolidating the existing infrastructure and integrating new sites.

References

[1] AliEn: http://alien2.cern.ch

[2] FairRoot, M. Al-Turany *et al*, this report.

[3] MonaLisa: http://serpiero.to.infn.it

Batch Computing Support

C. Preuss[1] *and K. Schwarz*[1]
[1]GSI, Darmstadt, Germany

Current State

After getting good experiences with GridEngine [1] on our (Icarus) cluster in 2011 [2], we decided to use the same technique also for the new larger cluster (Prometheus), which was delivered and installed in spring 2012. The compute clusters and their properties are listed in table 1.

With now two additional clusters and the phase-out of Debian Etch at GSI, we decided to shutdown the old LSF cluster end of 2012. Due to the circumstances that we have two clusters with GE not differing only in the size but also in the used Lustre instances, CPUs/memory, location, and network (and a new Debian version) the movement of the last users from LSF to GE had taken more time than expected, but was in the end successful.

Cluster	**Icarus**	**Prometheus**
Cores	1600	9000
Cores/Node	16	24
Memory	2GB/core	2.7GB/core
Lustre instance	/lustre	/hera
Network	Ethernet	InfiniBand
Location	BG2	MiniCube

Table 1: The compute clusters at GSI and their properties.

BlackHole detection script

As the batch farm has become larger over the years, the demand for a tool which can identify problematic nodes automatically came up. The decision was made to develop a so called ”BlackHole” detector script which monitors the job flow on the batch nodes, identifies anomalies and decides whether an alert is raised or not.

During the test phase we have identified several show stoppers preventing us from using it as a fully automated system, so currently it is in an adjustment and configuration phase. A proper balance between finding a good and fast automatic detection and not too many blind alerts still needs to be found.

Accounting and Visualization Tool

As some experiments are curious about their resource usage we decided to develop an accounting tool for the batch farm, which was done by one of our KoSI students, Sinisa Jovanovic. He will describe his work in another article [3], ”A Visualisation Tool for Accounting Data”.

Outview

As we are still using the last GE version developed by SUN (6.2.5) the problems described in the Scientific Report from last year (memory restrictions, MPI scheduling) are still existing.

Luckily the development of GE is now ongoing, but unfortunately in several different branches.

So there are now OracleGE and UnivaGE as commercial versions, and two open source trunks, OpenGE and SonOfGE [4].

As one reason for using GE was that it is for free we will stay with the open source trunks of GE, favoured is here SonOfGE as it seems to be more alive than OpenGE.

A test setup will be deployed during the next months, together with a database for the accounting data, a mechanism for shutting down unused batch nodes and the new Debian Wheezy as operating system.

References

[1] web site of gridengine:
http://gridengine.org

[2] Wiki page with GridEngine Documentation:
http://wiki.gsi.de/cgi-bin/view/Linux/GridEngineUsage

[3] S. Jovanovic, C. Preuss, K. Schwarz, “A Visualisation Tool for Accounting Data”, this report.

[4] web site of SGE:
http://arc.liv.ac.uk/SGE

Distribution of security-sentive data

A. Montiel González[1] *and M. Pausch*[1]
[1]GSI, Darmstadt, Germany

A new system for authentication and authorization has been implemented to substitute the old Network Information System (NIS). This is based in the integration of Heimdal and OpenLDAP, which together combine remarkable security aspects and a reliable replication engine. In this infrastructure security items need to be installed on every *kerberized* network service. These are the so called keytabs, which hold one or more keys.

This system is going to be deployed by using Chef as configuration management system[1].

The process of creating a keytab requires a privileged user to invoke the Kerberos administration application and to access it with an authorized principal, generating a key to be installed on the system. Therefore, there is intervention by a human to enter a password. The use of Chef implies automation in such steps. Hence, it is required to automatically and securely distribute these keytabs and, eventually, any other security-sensitive data.

Two solutions to this problem are described here.

Wallet

Wallet[2] is a system for managing secure data for systems. In this system, secure data could be any file or Kerberos keytabs. It stores and retrieves these data, and can automatically create keytabs on demand. It applies ACLs, and audits trail of operations.

It is a client/server tool, where communication is accomplished via remctl. This protocol uses Kerberos for authentication and encryption. It runs simple commands on a remote host and returns the output.

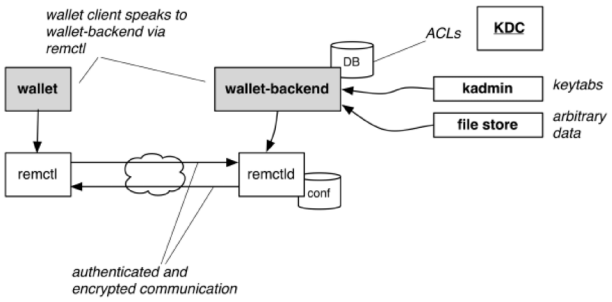

Figure 1: Wallet system. Figure taken from Ref[6]

As seen in Figure 1, the wallet-backend will keep the ACLs in a local database. Those ACLs control access to normal and administrative operations. The server also implements a front-end to the Kerberos kadmin, which retrieves keytabs. When retrieving a keytab, by default, the key is changed in the KDC and hence the invalidation of any existing keytabs for that principal. It also maintains an encrypted file bucket, where secure files are stored.

A wallet client will run on every node where secure data need to be provisioned. They must hold a keytab to communicate with the wallet server. For this purpose, a service principal for the wallet is created on Kerberos. This keytab is exported and copied onto all clients as part of the basic system. With this in place, and having configured the connection to the KDC and to the wallet server, the node could generate on demand any keytab and retrieve secure files, like the master key of KDC.

Chef

Chef[3] is a server/client based configuration management system for GNU/Linux. A *Chef-client* is running on every computer in the infrastructure that is managed by Chef. This Client uses RESTful communication to talk to the Chef-server, which is encrypted using public key cryptography. Since a cryptographic system is already in place when using Chef as configuration management system, this system can be used for encryption of other data.

In order to securely transport sensitive data from one node to another, the data are encrypted using a hybrid cryptographic system consisting of RSA and AES. The data are then uploaded to the Chef-server, from which the Chef-client can download and decrypt the data with the appropriate private key. The implementation of Chef allows easy extension in Ruby[4], which offers an interface to the OpenSSL[5] library that is used to handle the encryption of the data.

This approach should only be taken into account for small files, since big files can quickly lead to a lot of storage consumption on the Chef-server.

Conclusions

Both solutions are sound. The one extending Chef has been taken as first approach. The Wallet is a good alternative that prevents from relying on the Chef server reliability.

References

[1] C. Huhn et al, "Configuration Management Evolution in the GSI HPC farm", GSI Annual Report 2012.

[2] http://www.eyrie.org/ eagle/software/wallet/design.html

[3] http://www.opscode.com/chef/

[4] http://www.ruby-lang.org/en/

[5] http://www.openssl.org/

[6] http://jpmens.net/2012/06/25/streamlining-distribution-of-kerberos-keytabs-and-other-secure-data/

Federated Identity Management within CRISP*

A. Montiel González[1], *K. Schwarz*[1], *and P. Malzacher*[1]
[1]GSI, Darmstadt, Germany

The Cluster of Research Infrastructures for Synergies in Physics (CRISP) project is a collaboration between different institutions and facilities related to physics research. In this scope, a pan-European Federated Identity Management (FIM) system is under development.

Introduction

FIM solves the Single-Sign-On (SSO) access across multiple organizations using the same identification data.

The core protocol for enabling federated access to applications is Security Access Markup Language (SAML)[1]. SAML is the standard for exchanging authentication and authorization data between security domains, with Shibboleth[2] being its most extended implementation.

FIM especially benefits research communities, which try to have a common vision and follow the same roadmap[3].

At GSI/FAIR, like in most distributed high energy physics communities, the implementation to solve authentication and authorization is done with x.509. Besides, access to traditional web services is supported by local accounts as well as access to local computing resources. Shibboleth would enable browser-based applications to be accessed in a federated way through a wide set of authentication methods, including: x.509, OpenID and Kerberos. But this infrastructure would not solve the non-web-based applications. In this case, Moonshot[4] is interesting as it also relies on SAML for exchanging identity assertions.

The approach within CRISP is to continue developing the Shibboleth based Umbrella[5] system to bridge to other federations. In addition, we also evaluate Moonshot.

Umbrella

Umbrella is a FIM solution adopted from the Photon/Neutron community to provide federated access to experimental data. It provides a unique EU-wide identifier of users and solves the problem of having to remember accounts spread in the different web user offices(WUO)-web interface to the resources. This tool is currently implemented in several organizations within this community and it is under development at GSI/FAIR. Umbrella has only one Identity Provider(IdP) provisioning identification of users. This Umbrella account is the only one to be remembered by the user. The IdP stores minimal information about the users, enough to uniquely identify them. The users can link their account in the local organizations to their Umbrella account, so they are able to access already existing resources through this single account.

The authorization phase is completely delegated to the local WUOs.

Implementation and ongoing activities

An Umbrella system has been deployed as a testbed in a virtual machine(VM), with both IdP and Service Provider(SP) components. Since many users hold a x.509 certificate already, the first development is to create a bridge that would authenticate users holding such certificate to Umbrella resources, and, eventually, vice-versa. To accomplish this, another VM has been deployed with Shibboleth IdP and SP. The IdP handles login through x.509 and the SP federates access to a secured resource by using such certificate installed in the browser. It is still ongoing work to develop the software needed to bridge these credentials to the Umbrella.

Another line of development is to provide federated access to non web based applications. Moonshot proposes a solution for this case. It relies on three key security technologies: Extensible Authentication Protocol, Generic Security Services API and SAML. The main advantage lies on leaving the authentication phase to the eduroam infrastructure, which is extensively adopted, and to enable enriching of edu-tokens via SAML. A testing infrastructure has been deployed to try this solution. This testbed consist of a Home Institution(HI) and a Visited Institution(VI). The eduroam federation has been simulated with local RADIUS servers and clients. The HI has several VMs connected to the same internal network running the following services: Kerberos-Ldap implementation as Authentication-Authorization-Accounting system, IdP from Shibboleth, a RADIUS server, and a Moonshot ssh server. These are connected to the visited institution through two channels: JRadius, which is an open-source application that allows to simulate RADIUS traffic, and through SAML messages between the IdP and the SP. The VI runs the following services: the visited RADIUS server, the SP and the moonshot ssh client. The functionality of HI and VI has been demonstrated. Integration between them still needs to be implemented.

References

[1] https://www.oasis-open.org/standards/#samlv2.0

[2] http://shibboleth.net/

[3] D. Broeder et al, “Federated Identity Management for Research Collaborations”, TNC 2012, April 2012

[4] https://community.ja.net/groups/moonshot

[5] https://umbrella.psi.ch

* Work supported by the European Commission under the 7th Framework Program Grant Agreement 283745.

Distributed matrix computations via MPI on the GSI cluster *

J. Knedlik[1,2], *M.F.M. Lutz*[1], *and K. Schwarz*[1]
[1]GSI, Darmstadt, Germany; [2]Hochschule Darmstadt, Germany

The theory group in collaboration with the scientific computing group at GSI is preparing a general framework to predict and analyze hadronic final-state interactions. This is of crucial importance for a successful interpretation of data to be taken by the PANDA collaboration at FAIR. The main challenge is to combine constraints from micro-causality and coupled-channel unitarity using the concepts of effective field theories. A general scheme was proposed recently and already tested successfully in various well studied sectors of hadronic interactions [1, 2, 3, 4]. An application to proton-antiproton annihilation requires an extension to a huge number of channels. Part of the corresponding framework has been prepared in [5, 6]. In this report we explore the computational needs of such a project.

The proper treatment of final state interaction requires the solution of large, dense linear systems, that cannot be solved by a single CPU. To meet the enormous memory requirements, a distribution of the problem on a computer cluster is required. Available software, like GSL or LAPACK, for solving linear equations is proven, but most of them are not designed to be scalable on a computer cluster. ScaLAPACK is an extension to LAPACK which fits this purpose by supplying functions to build and solve linear systems efficiently in a scalable distributed memory environment by utilizing 2D Block Cyclic Mapping. ScaLAPACK is capable to be configured with a customized BLAS, and to be tinkered to our clusters' hardware environment. As inter process communication protocol OpenMPI came into use since this is already supported in the GSI cluster. In order to minimize the usage of cluster resources ScaLAPACK must use an optimized BLAS. To find a good BLAS implementation for our hardware, Intels MKL- and AMD's ACML have been bench marked against the non optimized reference BLAS. ScaLAPACK can be further optimized, by setting the right size of blocks, in which the linear system is divided, that are evenly distributed onto the available CPU's. The best block size is determined by the hardware environment through networkpacket-, cachesize etc. In order to find the best block size another set of benchmarks have been conducted.

A C++-interface to ScaLAPACK, for building and solving linear systems, has been implemented for easy access to ScaLAPACK's routines. In conclusion a solution to the computational need by the theory group has been found by utilizing ScaLAPACK to distribute the computation in the cluster. Many linear systems of order 50000 have already been successfully solved on the cluster, but there are still crashes when scaled over 100 CPU's. Also no real data have been used in these computations so far. An important task for the near future is to solve the the scalability-issues on the cluster.

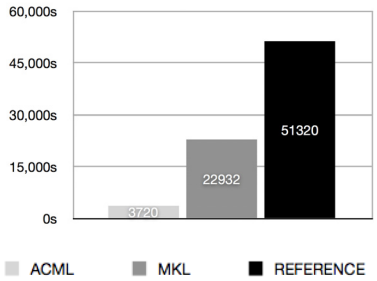

Figure 1: This figure shows the runtime of the different BLAS implementations solving a linear system of order 20000. The fastest result of 30 runs has been used. AMD's implementation of BLAS proves to be the most optimized.

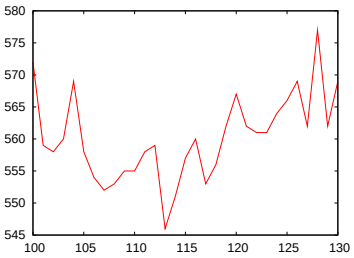

Figure 2: runtime with different block sizes solving a linear system of order 10000, filled with random values. The range of the best block size has been found in previous tests. The average of 50 runs has been taken. The best block size is 113.

References

[1] A. Gasparyan and M. F. M. Lutz, Nucl. Phys. A **848** (2010) 126.

[2] I. V. Danilkin, L. I. R. Gil and M. F. M. Lutz, Phys. Lett. B **703** (2011) 504.

[3] I. V. Danilkin, M. F. M. Lutz, S. Leupold and C. Terschlusen, arXiv:1211.1503 [hep-ph].

[4] A. M. Gasparyan, M. F. M. Lutz and E. Epelbaum, arXiv:1212.3057 [nucl-th].

[5] S. Stoica, M. F. M. Lutz and O. Scholten, Phys. Rev. D **84** (2011) 125001.

[6] M. F. M. Lutz and I. Vidana, Eur. Phys. J. A **48** (2012) 124.

* Work supported by the KOSI program

gStore - a High Performance Experiment Data Archive Storage

H.Göringer, M. Feyerabend, and S. Sedykh

GSI, Darmstadt, Germany

Overview

Archive and storage for experiment data is provided 24 hours a day and 7 days a week by **gStore,** a client/server middleware developed at GSI. Data are archived in automatic tape libraries (ATL), which can be accessed with high performance and in parallel via data movers (DM) with large read and write disk caches.
Design principles and functionality of gStore are described in detail in GSI reports, talks, and two papers [1].

Hardware Status

The eight IBM 3592 tape drives in the ATL located in the computer centre (RZ) have been upgraded from E06 to E07. As a result the I/O speed of each drive has been increased from 160 MByte/s to 250 MByte/s, and up to 4 TByte of uncompressed data can be written to the actual tape media. The current storage capacity for experiment and user backup data has been increased to 8.8 PByte, and the overall I/O bandwidth amounts to 2 GByte/s now. With additional frames for tape media and tape drives, the data capacity could be enhanced to 50 PByte, which is already in the order of magnitude needed for FAIR.
The second ATL located in the remote BG2 building contains copies of experiment (raw) and of user backup data. This concept prevents from loss of valuable data in case of media damage and enables disaster recovery.
Three outdated data movers have been replaced by new ones with larger disk arrays thus increasing the available disk space for read and write cache from 170 TB to nearly 220 TB. A summary of the current hardware resources can be found in table 1.

resource	used	max
storage capacities:		
3584-L23 ATL RZ:	700 TB	8.8 PB
3584-L23 ATL BG2:	240 TB	1.3 PB
overall data mover disk cache	< 90%	0.22 PB
lustre/hera file system	~80%	3.5 PB
overall gStore I/O bandwith:		
DM disk <-> tape (SAN)		2.0 GB/s
DM disk <-> clients (LAN)		5.0 GB/s

Table 1: Hardware Status GSI Storage in December 2012

gStore Enhancements

Access to /hera. Now all data movers have also mount connections with the new lustre file system /hera residing in the testing hall. As /hera is only reachable via Infiniband, data transfers between gStore data movers and /hera file servers take place via so-called LNET routers connecting Ethernet with Infiniband hosts and vice versa. The current I/O bandwidth amounts to 2.5 GByte/s.
Access from Icarus and Prometheus. On the GSI batch farms connected with /lustre (Icarus) and /hera (Prometheus) the gStore clients are made available via cvmfs [2].
New Storage Pool for large data transfers. Large data transfers, e.g. between gStore and lustre/hera, or between tape and disk cache, need the highest performance possible. Therefore they should be made in parallel and on the fastest data movers. However, some of these transfers need read cache and others write cache resources, which were completely separate in gStore in the past. Therefore a new pool has been created for these transfers. It is located on the data movers connected with 10 Gbit and used for both, writing to gStore and reading from gStore.

Data Movements

In 2012, from April to December the online data storage capabilities of gStore were heavily used by up to four experiments running in parallel.
For nearly five weeks, data from Hades event builders, divided into 16 data streams, were written to gStore write cache with an overall average data rate of 100 MByte/s. Additionally, the data were copied automatically from write cache to lustre and migrated to tape afterwards[1] .
The long term stability of gStore was also utilized by the Tasca experiment, which was running for nearly half a year. Nearly all the time data were stored online in gStore with data rates of 10 MByte/s.
Taking into account all data transfers between gStore clients, disk cache, and tape, in 2012 overall 1.37 million files were moved with a data volume of nearly 1.1 PByte.

Outlook

The concept of automatic process parallelization, which is already realized for staging processes from tape to read cache, will also be implemented for data transfer processes between lustre/hera and gStore using the new fast storage pool. Then handling many files in parallel can be done with single gstore commands enabling transfer rates between lustre/hera and gStore with full I/O bandwidth of up to 5 GB/s.

References

[1] see http://www.gsi.de/informationen/wti/it/exp_daten/daten_speicherung_e.html as starting point for more info
[2] http://wiki.gsi.de/cgi-bin/view/Linux/CvmFs

[1] Parts of the data were test data not permanently stored on tape.

ALICE HLT TPC GPU Tracker*

D. Rohr[1], *S. Gorbunov*[1], *V. Lindenstruth*[1] *for the ALICE Collaboration*

[1]Frankfurt Institute for Advanced Studies, Frankfurt, Germany

The Alice High Level Trigger

The Large Hadron Collider (LHC) at the European Center for Particle Physics (CERN) is today's most powerful particle collider built to search for rare particles such as the Higgs boson and to study properties of dense hot medium. Alice is one of its four major detectors designed specifically for the second purpose. The ALICE High Level Trigger (HLT) is a compute farm of about 250 nodes and it is the first point where all data from the various subdetectors are available together. The HLT is capable of a full online event reconstruction and uses data compression techniques in order to reduce the data rate stored to the tapes to a feasible level.

The Alice HLT TPC Tracker

Reconstruction of the trajectories (tracking) of particles measured in the Time Projection Chamber (TPC) is one critical part of event reconstruction and requires significant compute resources. The HLT implements a parallel tracking algorithm that can make use of GPUs. It is based on the cellular automation and the Kalman filter [1]. The tracker employs a pipeline which ensures continuous GPU utilization. Results of the GPU and the CPU version of the tracker match exactly except for artifacts caused by different rounding due to non-associative floating point arithmetic [5] [2] [3]. A direct comparison of the GPU tracker to a hexa-core CPU demonstrates a speedup factor of about three [4].

The HLT compute nodes are not exclusively used for tracking but also for other tasks such as cluster transformation and vertexing. Hence, not all CPU cores are available for tracking. The below figure shows the speedup of both the GPU and the CPU implementation of the HLT tracker running on four CPU cores and, in the case of the GPU tracker, also on the GPU. The HLT tracker is 12 to 15 times faster than the offline version and the GPU tracker is faster by another order of magnitude [2] (see figure 1).

If the CPU tracker employs all available cores of one node, tracking takes about as long as tracking on the GPU. Hence, plugging a GPU in an existing node saves an entire node - and the required additional infrastructure. Overall, the GPU tracker enables TPC tracking with only about one tenth the investment which would be required otherwise.

During the Pb-Pb run in 2010 the GPU tracker was first tested under real conditions. This led to some minor improvements, e.g. with respect to memory consumption. Some other improvements coped with irreproducible results caused by concurrency, which - even though they did not affect physical observables - complicated QA efforts. Later on, the GPU tracker was operated during the lead run in 2011, and it ran stably in 24/7 operation during the full proton phase of 2012. For the current proton-lead run the HLT was upgraded with more GPUs to cope with the increased rate.

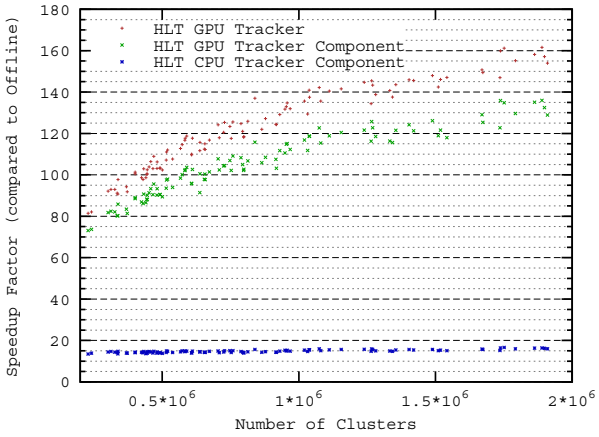

Figure 1: HLT Tracker Speedup.

At the moment, the HLT is equipped with about 60 Fermi GPUs achieving a maximum data rate of more than 200 Hz in central lead-lead collisions.

References

[1] S. Gorbunov, D. Rohr, et al. ALICE HLT high speed tracking on GPU, IEEE Transactions on Nuclear Science 58 (2011) 1845

[2] D. Rohr, S. Gorbunov, et al. ALICE HLT TPC Tracking of Pb-Pb Events on GPUs, Journal of Physics: Conference Series (2012, Vol. 396, p. 12044)

[3] D. Rohr ALICE TPC Online Tracker on GPUs for Heavy-Ion Events, Proceedings of 13th International Workshop on Cellular Nanoscale Networks and their Applications (2012, pp. 298303)

[4] S. Gorbunov, M. Kretz, D. Rohr, ALICE TPC Online Tracking on GPU, GSI Scientific Report 2009

[5] D. Rohr, ALICE TPC Tracking on GPU for Pb-Pb Run in December 2010, GSI Scientific Report 2010

* Work supported by GSI, BMBF, HGS-HIRe

WOS publications to the programme Physics of hadrons and nuclei published in 2012

WOS-PHN-1 Aamodt, K.; Abelev, B.; Abrahantes Quintana, A.; Adamova, D.; Adare, A.M.; Aggarwal, M.M.; Aglieri Rinella, G.; Agocs, A.G.; Agostinelli, A.; Aguilar Salazar, S.; Ahammed, Z.; Ahmad, N.; Ahmad Masoodi, A.; Ahn, S.U.; Akindinov, A.; Aleksandrov, D.; Alessandro, B.; Alfaro Molina, R.; Alici, A.; Alkin, A.; Almaraz Avina, E.; Alme, J.; Alt, T. ; Altini, V.; Altinpinar, S.; Altsybeev, I.; Andrei, C.; Andronic, A.; Anguelov, V.; Anielski, J.; Anticic, T.; Antinori, F.; Antonioli, P.; Aphecetche, L.; Appelshäuser, H.; Arbor, N.; Arcelli, S.; Arend, A.; Armesto, N.; Arnaldi, R. ; Aronsson, T.; Arsene, I.C.; Arslandok, M.; Asryan, A.; Augustinus, A.; Averbeck, R.; Awes, T.C.; Äystö J.; Azmi, M.D.; Bach, M.; Badala, A.; Baek, Y.W.; Bailhache, R.; Bala, R. ; Baldini Ferroli, R.; Baldisseri, A.; Baldit, A. ; Baltasar Dos Santos Pedrosa, F.; Ban, J.; Baral, R.C.; Barbera, R.; Barile, F.; Barnaföldi, G.G. ; Barnby, L.S.; Barret, V.; Bartke, J.; Basile, M.; Bastid, N.; Bathen, B.; Batigne, G.; Batyunya, B.; Baumann, C.; Bearden, I.G.; Beck, H. ; Belikov, I.; Bellini, F.; Bellwied, R.; Belmont-Moreno, E.; Beole, S.; Berceanu, I.; Bercuci, A.; Berdnikov, Y.; Berenyi, D.; Bergmann, C.; Betev, L.; Bhasin, A.; Bhati, A.K.; Bianchi, L.; Bianchi, N.; Bianchin, C.; Bielcik, J.; Bielcikova, J.; Bilandzic, A.; Biolcati, E.; Blanco, F.; Blanco, F.; Blau, D.; Blume, C.; Bock, N.; Bogdanov, A.; Boggild, H.; Bogolyubsky, M.; Boldizsar, L.; Bombara, M.; Bombonati, C.; Book, J.; Borel, H.; Borissov, A.; Bortolin, C.; Bose, S.; Boss, F.; Botje, M.; Böttger, S.; Boyer, B.; Braun-Munzinger, P.; Bregant, M.; Breitner, T.; Broz, M.; Brun, R.; Bruna, E.; Bruno, G.E.; Budnikov, D.; Buesching, H.; Bufalino, S.; Bugaiev, K.; Busch, O.; Buthelezi, Z.; Caffarri, D.; Cai, X.; Caines, H.; Calvo Villar, E. ; Camerini, P.; Canoa Roman, V.; Cara Romeo, G.; Carena, F.; Carena, W.; Carminati, F.; Casanova Diaz, A.; Caselle, M.; Castillo Castellanos, J.; Casula, E.A.R.; Catanescu, V.; Cavicchioli, C.; Cepila, J.; Cerello, P.; Chang, B.; Chapeland, S. ; Charvet, J.L.; Chattopadhyay, S.; Chattopadhyay, S.; Cherney, M.; Cheshkov, C.; Cheynis, B.; Chiavassa, E.; Chibante Barroso, V.; Chinellato, D.D. ; Chochula, P.; Chojnacki, M.; Christakoglou, P.; Christensen, C.H.; Christiansen, P.; Chujo, T.; Chung, S.U.; Cicalo, C.; Cifarelli, L.; Cindolo, F. ; Cleymans, J.; Coccetti, F.; Coffin, J.-P.; Colamaria, F.; Colella, D.; Conesa Balbastre, G.; Conesa del Valle, Z.; Constantin, P.; Contin, G.; Contreras, J.G.; Cormier, T.M.; Corrales Morales, Y. ; Cortes Maldonado, I.; Cortese, P.; Cosentino, M.R.; Costa, F.; Cotallo, M.E.; Crochet, P.; Cruz Alaniz, E.; Cuautle, E.; Cunqueiro, L.; Erasmo, G.D.; Dainese, A.; Dalsgaard, H.H.; Danu, A.; Das, D.; Das, I.; Das, K.; Dash, A.; Dash, S.; De, S.; De Azevedo Moregula, A.; de Barros, G.O.V.; De Caro, A.; de Cataldo, G.; de Cuveland, J.; De Falco, A.; De Gruttola, D.; De Marco, N.; De Pasquale, S.; de Rooij, R.; Del Castillo Sanchez, E.; Delagrange, H.; Deloff, A.; Demanov, V.; Denes, E.; Deppman, A.; Di Bari, D. ; Di Giglio, C.; Di Liberto, S.; Di Mauro, A.; Di Nezza, P.; Dietel, T.; Divia, R.; Djuvsland, O. ; Dobrin, A.; Dobrowolski, T.; Dominguez, I.; Dönigus, B.; Dordic, O.; Driga, O.; Dubey, A.K. ; Ducroux, L.; Dupieux, P.; Dutta Majumdar, A.K.; Dutta Majumdar, M.R.; Elia, D.; Emschermann, D.; Engel, H.; Erdal, H.A.; Espagnon, B.; Estienne, M. ; Esumi, S.; Evans, D.; Eyyubova, G.; Fabris, D. ; Faivre, J.; Falchieri, D.; Fantoni, A.; Fasel, M.; Fearick, R.; Fedunov, A.; Fehlker, D.; Felea, D.; Fenton-Olsen, B.; Feofilov, G.; Fernandez Tellez, A.; Ferreiro, E.G.; Ferretti, A. ; Ferretti, R.; Figiel, J.; Figueredo, M.A.S.; Filchagin, S.; Fini, R.; Finogeev, D.; Fionda, F.M. ; Fiore, E.M.; Floris, M.; Foertsch, S.; Foka, P. ; Fokin, S.; Fragiacomo, E.; Fragkiadakis, M.; Frankenfeld, U.; Fuchs, U.; Furget, C.; Fusco Girard, M.; Gaardhoje, J.J.; Gagliardi, M.; Gago, A.; Gallio, M.; Gangadharan, D.R.; Ganoti, P.; Garabatos, C.; Garcia-Solis, E.; Garishvili, I.; Gerhard, J.; Germain, M.; Geuna, C.; Gheata, A.; Gheata, M.; Ghidini, B.; Ghosh, P.; Gianotti, P. ; Girard, M.R.; Giubellino, P.; Gladysz-Dziadus, E. ; Glässel, P.; Gomez, R.; Gonzalez-Trueba, L.H. ; Gonzalez-Zamora, P.; Gorbunov, S.; Goswami, A. ; Gotovac, S.; Grabski, V.; Graczykowski, L.K.; Grajcarek, R.; Grelli, A.; Grigoras, A.; Grigoras, C.; Grigoriev, V.; Grigoryan, A.; Grigoryan, S.; Grinyov, B.; Grion, N.; Grosse-Oetringhaus, J.F.; Grossiord, J.-Y.; Guber, F.; Guernane, R.; Guerra Gutierrez, C.; Guerzoni, B.; Guilbaud, M.; Gulbrandsen, K.; Gunji, T.; Gupta, A.; Gupta, R. ; Gutbrod, H.; Haaland, O.; Hadjidakis, C.; Haiduc, M.; Hamagaki, H.; Hamar, G.; Hanratty, L.D. ; Harmanova, Z.; Harris, J.W.; Hartig, M.; Hasegan, D.; Hatzifotiadou, D.; Hayrapetyan, A.; Heide, M.; Helstrup, H.; Herghelegiu, A.; Herrera Corral, G.; Herrmann, N.; Hetland, K.F.; Hicks, B. ; Hille, P.T.; Hippolyte, B.; Horaguchi, T.; Hori, Y.; Hristov, P.; Hrivnacova, I.; Huang, M.; Huber, S.; Humanic, T.J.; Hwang, D.S.; Ichou, R.; Ilkaev, R.; Ilkiv, I.; Inaba, M.; Incani, E.; Innocenti, G.M.; Ippolitov, M.; Irfan, M.; Ivan, C.; Ivanov, A.; Ivanov, M.; Ivanov, V. ; Ivanytskyi, O.; Jacobs, P.M.; Jancurova, L.; Jangal, S.; Janik, M.A.; Janik, R.; Jayarathna, P.H.S.Y.; Jena, S.; Jimenez Bustamante, R.T.; Jirden, L.; Jones, P.G.; Jung, H.; Jung, W.; Jusko, A.; Kalcher, S.; Kalinak, P.; Kalisky, M. ; Kalliokoski, T.; Kalweit, A.; Kanaki, K.; Kang, J.H.; Kaplin, V.; Karasu Uysal, A.; Karavichev, O. ; Karavicheva, T.; Karpechev, E.; Kazantsev, A.; Kebschull, U.; Keidel, R.; Khan, M.M.; Khan, P.; Khan, S.A.; Khanzadeev, A.; Kharlov, Y.; Kileng, B. ; Kim, B.; Kim, D.J.; Kim, D.W.; Kim, J.H.; Kim, J.S.; Kim, M.; Kim, S.; Kim, S.H.; Kim, T. ; Kirsch, S.; Kisel, I.; Kiselev, S.; Kisiel, A. ; Klay, J.L.; Klein, J.; Klein-Bösing, C.; Kliemant, M.; Kluge, A.; Knichel, M.L.; Koch, K. ; Köhler, M.K.; Kolojvari, A.; Kondratiev, V.; Kondratyeva, N.; Konevskikh, A.; Kottachchi Kankanamge Don, C.; Kour, R.; Kowalski, M.; Kox, S.; Koyithatta Meethaleveedu, G.; Kral, J.; Kralik, I. ; Kramer, F.; Kraus, I.; Krawutschke, T.; Kretz, M.; Krivda, M.; Krizek, F.; Krus, M.; Kryshen, E.; Krzewicki, M.; Kucheriaev, Y.; Kuhn, C.; Kuijer, P.G.; Kurashvili, P.; Kurepin, A.; Kurepin, A.B.; Kuryakin, A.; Kushpil, S.; Kushpil, V.; Kweon, M.J.; Kwon, Y.; La Rocca, P.; Ladron de Guevara, P.; Lakomov, I.; Lara, C.; Lardeux, A.; Larsen, D.T.; Lazzeroni, C.; Le Bornec, Y.; Lea, R. ; Lechman, M.; Lee, K.S.; Lee, S.C.; Lefevre, F. ; Lehnert, J.; Leistam, L.; Lenhardt, M.; Lenti, V.; Leon Monzon, I.; Leon Vargas, H.; Levai, P. ; Li, X.; Lien, J.; Lietava, R.; Lindal, S.; Lindenstruth, V.; Lippmann, C.; Lisa, M.A.; Liu, L. ; Loenne, P.I.; Loggins, V.R.; Loginov, V.; Lohn, S.; Lohner, D.; Loizides, C.; Loo, K.K.; Lopez, X.; Lopez Torres, E.; Lovhoiden, G.; Lu, X.-G. ; Luettig, P.; Lunardon, M.; Luo, J.; Luparello, G.; Luquin, L.; Luzzi, C.; Ma, R.; Maevskaya, A. ;

Mager, M.; Mahapatra, D.P.; Maire, A.; Malaev, M.; Maldonado Cervantes, I.; Malinina, L.; MalKevich, D.; Malzacher, P.; Mamonov, A.; Manceau, L.; Manko, V.; Manso, F.; Manzari, V.; Mao, Y.; Marchisone, M.; Mares, J.; Margagliotti, G.V.; Margotti, A.; Marin, A.; Markert, C.; Martashvili, I.; Martinengo, P.; Martinez, M.I.; Martinez Davalos, A.; Martinez Garcia, G.; Martynov, Y.; Mas, A.; Masciocchi, S.; Masera, M. ; Masoni, A.; Massacrier, L.; Mastromarco, M.; Mastroserio, A.; Matthews, Z.L.; Matyja, A.; Mayani, D.; Mayer, C.; Mazzoni, M.A.; Meddi, F.; Menchaca-Rocha, A.; Mercado Perez, J.; Meres, M.; Miake, Y.; Michalon, A.; Midori, J.; Milano, L.; Milosevic, J.; Mischke, A.; Mishra, A.N.; Mikowiec, D.; Mitu, C.; Mlynarz, J.; Mohanty, A.K.; Mohanty, B.; Molnar, L.; Montano Zetina, L. ; Monteno, M.; Montes, E.; Moon, T.; Morando, M. ; Moreira De Godoy, D.A.; Moretto, S.; Morsch, A. ; Muccifora, V.; Mudnic, E.; Müller, H.; Muhuri, S.; Munhoz, M.G.; Musa, L.; Musso, A.; Nagle, J.L.; Nandi, B.K.; Nania, R.; Nappi, E.; Nattrass, C.; Naumov, N.P.; Navin, S.; Nayak, T.K. ; Nazarenko, S.; Nazarov, G.; Nedosekin, A.; Nicassio, M.; Nielsen, B.S.; Niida, T.; Nikolaev, S.; Nikolic, V.; Nikulin, S.; Nikulin, V.; Nilsen, B.S.; Nilsson, M.S.; Noferini, F.; Nomokonov, P.; Nooren, G.; Novitzky, N.; Nyanin, A. ; Nyatha, A.; Nygaard, C.; Nystrand, J.; Obayashi, H.; Ochirov, A.; Oeschler, H.; Oh, S.K. ; Oleniacz, J.; Oppedisano, C.; Ortiz Velasquez, A. ; Ortona, G.; Oskarsson, A.; Otterlund, I.; Otwinowski, J.; Ovrebekk, G.; Oyama, K.; Pachmayer, Y.; Pachr, M.; Padilla, F.; Pagano, P. ; Paic, G.; Painke, F.; Pajares, C.; Pal, S.; Pal, S.K.; Palaha, A.; Palmeri, A.; Pappalardo, G.S.; Park, W.J.; Passfeld, A.; Patalakha, D.I.; Paticchio, V.; Pavlinov, A.; Pawlak, T.; Peitzmann, T.; Pereira De Oliveira Filho, E.; Peresunko, D.; Perez Lara, C.E.; Perez Lezama, E.; Perini, D.; Perrino, D.; Peryt, W.; Pesci, A.; Peskov, V.; Pestov, Y.; Petracek, V.; Petran, M.; Petris, M. ; Petrov, P.; Petrovici, M.; Petta, C.; Piano, S. ; Piccotti, A.; Pikna, M.; Pillot, P.; Pinazza, O.; Pinsky, L.; Pitz, N.; Piuz, F.; Piyarathna, D.B.; Ploskon, M.; Pluta, J.; Pocheptsov, T.; Pochybova, S.; Podesta-Lerma, P.L.M.; Poghosyan, M.G. ; Polichtchouk, B.; Pop, A.; Porteboeuf-Houssais, S. ; Pospisil, V.; Potukuchi, B.; Prasad, S.K.; Preghenella, R.; Prino, F.; Pruneau, C.A.; Pshenichnov, I.; Puddu, G.; Pulvirenti, A.; Punin, V.; Putis, M.; Putschke, J.; Quercigh, E.; Qvigstad, H.; Rachevski, A.; Rademakers, A.; Radomski, S.; Räihä T.S.; Rak, J.; Rakotozafindrabe, A.; Ramello, L.; Ramirez Reyes, A. ; Raniwala, R.; Raniwala, S.; Räsänen, S.S.; Rascanu, B.T.; Rathee, D.; Read, K.F.; Real, J.S. ; Redlich, K.; Reichelt, P.; Reicher, M.; Renfordt, R.; Reolon, A.R.; Reshetin, A.; Rettig, F.; Revol, J.-P.; Reygers, K.; Ricaud, H.; Riccati, L.; Ricci, R.A.; Richter, M.; Riedler, P. ; Riegler, W.; Riggi, F.; Rodriguez Cahuantzi, M. ; Rohr, D.; Röhrich, D.; Romita, R.; Ronchetti, F.; Rosnet, P.; Rossegger, S.; Rossi, A.; Roukoutakis, F.; Roy, C.; Roy, P.; Rubio Montero, A.J.; Rui, R.; Ryabinkin, E.; Rybicki, A.; Sadovsky, S.; Safarik, K.; Sahu, P.K.; Saini, J. ; Sakaguchi, H.; Sakai, S.; Sakata, D.; Salgado, C.A.; Sambyal, S.; Samsonov, V.; Sanchez Castro, X. ; Sandor, L.; Sandoval, A.; Sano, M.; Sano, S. ; Santo, R.; Santoro, R.; Sarkamo, J.; Scapparone, E.; Scarlassara, F.; Scharenberg, R.P.; Schiaua, C.; Schicker, R.; Schmidt, C.; Schmidt, H.R.; Schreiner, S.; Schuchmann, S.; Schukraft, J. ; Schutz, Y.; Schwarz, K.; Schweda, K.; Scioli, G.; Scomparin, E.; Scott, P.A.; Scott, R.; Segato, G.; Selyuzhenkov, I.; Senyukov, S.; Serci, S.; Serradilla, E.; Sevcenco, A.; Sgura, I.; Shabratova, G.; Shahoyan, R.; Sharma, N.; Sharma, S.; Shigaki, K.; Shimomura, M.; Shtejer, K.; Sibiriak, Y.; Siciliano, M.; Sicking, E.; Siddhanta, S.; Siemiarczuk, T.; Silvermyr, D.; Simonetti, G.; Singaraju, R.; Singh, R.; Singha, S. ; Sinha, B.C.; Sinha, T.; Sitar, B.; Sitta, M. ; Skaali, T.B.; Skjerdal, K.; Smakal, R.; Smirnov, N.; Snellings, R.; Sogaard, C.; Soltz, R. ; Son, H.; Song, J.; Song, M.; Soos, C.; Soramel, F.; Spyropoulou-Stassinaki, M.; Srivastava, B.K.; Stachel, J.; Stan, I.; Stefanek, G.; Stefanini, G.; Steinbeck, T.; Steinpreis, M.; Stenlund, E.; Steyn, G.; Stocco, D.; Stolpovskiy, M.; Strmen, P.; Suaide, A.A.P.; Subieta Vasquez, M.A.; Sugitate, T.; Suire, C.; Sukhorukov, M.; Sultanov, R.; Sumbera, M.; Susa, T.; Szanto de Toledo, A.; Szarka, I.; Szostak, A.; Tagridis, C. ; Takahashi, J.; Tapia Takaki, J.D.; Tauro, A.; Tejeda Munoz, G.; Telesca, A.; Terrevoli, C.; Thäder, J.; Thomas, D.; Thomas, J.H.; Tieulent, R. ; Timmins, A.R.; Tlusty, D.; Toia, A.; Torii, H. ; Tosello, F.; Traczyk, T.; Trzaska, W.H.; Tsuji, T.; Tumkin, A.; Turrisi, R.; Turvey, A.J.; Tveter, T.S.; Ulery, J.; Ullaland, K.; Ulrich, J. ; Uras, A.; Urban, J.; Urciuoli, G.M.; Usai, G.L.; Vajzer, M.; Vala, M.; Valencia Palomo, L.; Vallero, S.; van der Kolk, N.; van Leeuwen, M.; Vande Vyvre, P.; Vannucci, L.; Vargas, A.; Varma, R.; Vasileiou, M.; Vasiliev, A.; Vechernin, V.; Veldhoen, M.; Venaruzzo, M.; Vercellin, E.; Vergara, S.; Vernekohl, D.C.; Vernet, R.; Verweij, M.; Vickovic, L.; Viesti, G.; Vikhlyantsev, O.; Vilakazi, Z.; Villalobos Baillie, O.; Vinogradov, A. ; Vinogradov, L.; Vinogradov, Y.; Virgili, T.; Viyogi, Y.P.; Vodopyanov, A.; Voloshin, K.; Voloshin, S.; Volpe, G.; von Haller, B.; Vrlakova, J.; Vulpescu, B.; Vyushin, A.; Wagner, B.; Wagner, V.; Wan, R.; Wang, D.; Wang, M.; Wang, Y.; Wang, Y.; Watanabe, K.; Wessels, J.P.; Westerhoff, U.; Wiechula, J.; Wikne, J.; Wilde, M. ; Wilk, A.; Wilk, G.; Williams, M.C.S.; Windelband, B.; Xaplanteris Karampatsos, L.; Yang, H. ; Yasnopolskiy, S.; Yi, J.; Yin, Z.; Yokoyama, H. ; Yoo, I.-K.; Yoon, J.; Yu, W.; Yuan, X.; Yushmanov, I.; Zach, C.; Zampolli, C.; Zaporozhets, S.; Zarochentsev, A.; Zavada, P.; Zaviyalov, N. ; Zbroszczyk, H.; Zelnicek, P.; Zgura, I.; Zhalov, M.; Zhang, X.; Zhou, D.; Zhou, F.; Zhou, Y.; Zhu, X.; Zichichi, A.; Zimmermann, A.; Zinovjev, G.; Zoccarato, Y.; Zynovyev, M.; Vranic, D.: **Harmonic decomposition of two particle angular correlations in PbPb collisions at $\sqrt{s_{NN}} = 2.76$ TeV.** *Physics letters / B* 708: 249 - 264, 2012. DOI:10.1016/j.physletb.2012.01.060

WOS-PHN-2 Aamodt, K.; Abelev, B.; AbrahantesQuintana, A.; Adamova, D.; Adare, A. M.; Aggarwal, M. M.; AglieriRinella, G.; Agocs, A. G.; Agostinelli, A. ; Aguilar Salazar, S.; Ahammed, Z.; Ahmad, N.; AhmadMasoodi, A.; Ahn, S. U.; Akindinov, A.; Aleksandrov, D.; Alessandro, B.; AlfaroMolina, R. ; Alici, A.; Alkin, A.; Almaraz Avina, E.; Alme, J.; Alt, T.; Altini, V.; Altinpinar, S.; Altsybeev, I.; Andrei, C.; Andronic, A.; Anguelov, V.; Anielski, J.; Anticic, T.; Antinori, F.; Antonioli, P.; Aphecetche, L.; Appelshäuser, H.; Arbor, N.; Arcelli, S.; Arend, A.; Armesto, N.; Arnaldi, R.; Aronsson, T.; Arsene, I. C.; Arslandok, M.; Asryan, A.; Augustinus, A.; Averbeck, R.; Awes, T. C.; Äystö J.; Azmi, M. D. ; Bach, M.; Badala, A.; Baek, Y. W.; Bailhache, R.; Bala, R.; Baldini Ferroli, R.; Baldisseri, A. ; Baldit, A.; BaltasarDosSantosPedrosa, F.; Ban, J.; Baral, R. C.; Barbera, R.; Barile, F.; Barnaföldi, G. G.; Barnby, L. S.; Barret, V.; Bartke, J.; Basile, M.; Bastid, N.; Bathen, B.; Batigne, G.; Batyunya, B.; Baumann, C.; Bearden, I. G.; Beck, H.; Belikov, I.; Bellini, F.; Bellwied, R.; Belmont-Moreno, E.; Beole, S.; Berceanu, I.; Bercuci, A.; Berdnikov, Y.; Berenyi, D.; Bergmann, C.; Betev, L.; Bhasin, A.; Bhati, A. K.; Bianchi, L.; Bianchi, N.; Bianchin, C.; Bielcik, J.; Bielcikova, J.; Bilandzic, A.; Biolcati, E.; Blanco, F.; Blanco, F.; Blau, D.; Blume, C.; Bock, N.; Bogdanov, A.; Boggild, H.; Bogolyubsky, M.; Boldizsar, L.; Bombara, M.; Bombonati, C.; Book, J.; Borel, H.; Borissov,

A. ; Bortolin, C.; Bose, S.; Boss, F.; Botje, M. ; Böttger, S.; Boyer, B.; Braun-Munzinger, P.; Bregant, M.; Breitner, T.; Broz, M.; Brun, R.; Bruna, E.; Bruno, G. E.; Budnikov, D.; Buesching, H.; Bufalino, S.; Bugaiev, K.; Busch, O.; Buthelezi, Z.; Caffarri, D.; Cai, X.; Caines, H. ; Calvo Villar, E.; Camerini, P.; Canoa Roman, V. ; Cara Romeo, G.; Carena, F.; Carena, W.; Carminati, F.; CasanovaDiaz, A.; Caselle, M.; Castillo-Castellanos, J.; Casula, E. A. R.; Catanescu, V.; Cavicchioli, C.; Cepila, J.; Cerello, P.; Chang, B.; Chapeland, S.; Charvet, J. L.; Chattopadhyay, S.; Chattopadhyay, S.; Cherney, M.; Cheshkov, C.; Cheynis, B.; Chiavassa, E.; ChibanteBarroso, V.; Chinellato, D. D.; Chochula, P. ; Chojnacki, M.; Christakoglou, P.; Christensen, C. H.; Christiansen, P.; Chujo, T.; Chung, S. U.; Cicalo, C.; Cifarelli, L.; Cindolo, F.; Cleymans, J.; Coccetti, F.; Coffin, J.-P.; Colamaria, F.; Colella, D.; ConesaBalbastre, G.; ConesadelValle, Z.; Constantin, P.; Contin, G.; Contreras, J. G.; Cormier, T. M.; CorralesMorales, Y.; CortesMaldonado, I.; Cortese, P.; Cosentino, M. R.; Costa, F.; Cotallo, M. E.; Crochet, P.; CruzAlaniz, E.; Cuautle, E.; Cunqueiro, L.; Erasmo, G. D.; Dainese, A.; Dalsgaard, H. H.; Danu, A.; Das, D.; Das, I.; Das, K.; Dash, A.; Dash, S.; De, S.; DeAzevedo Moregula, A.; de Barros, G. O. V.; DeCaro, A.; deCataldo, G.; deCuveland, J.; DeFalco, A.; DeGruttola, D.; DeMarco, N.; DePasquale, S.; deRooij, R.; DelCastilloSanchez, E.; Delagrange, H.; Deloff, A. ; Demanov, V.; Denes, E.; Deppman, A.; DiBari, D.; DiGiglio, C.; DiLiberto, S.; DiMauro, A. ; DiNezza, P.; Dietel, T.; Divia, R.; Djuvsland, O.; Dobrin, A.; Dobrowolski, T.; Dominguez, I.; Dönigus, B.; Dordic, O.; Driga, O. ; Dubey, A. K.; Ducroux, L.; Dupieux, P.; DuttaMajumdar, A. K.; DuttaMajumdar, M. R.; Elia, D.; Emschermann, D.; Engel, H.; Erdal, H. A.; Espagnon, B.; Estienne, M.; Esumi, S.; Evans, D. ; Eyyubova, G.; Fabris, D.; Faivre, J.; Falchieri, D.; Fantoni, A.; Fasel, M.; Fearick, R. ; Fedunov, A.; Fehlker, D.; Felea, D.; Fenton-Olsen, B.; Feofilov, G.; FernandezTellez, A.; Ferreiro, E. G.; Ferretti, A.; Ferretti, R.; Figiel, J.; Figueredo, M. A. S.; Filchagin, S.; Fini, R.; Finogeev, D.; Fionda, F. M.; Fiore, E. M. ; Floris, M.; Foertsch, S.; Foka, P.; Fokin, S. ; Fragiacomo, E.; Fragkiadakis, M.; Frankenfeld, U. ; Fuchs, U.; Furget, C.; FuscoGirard, M.; Gaardhoje, J. J.; Gagliardi, M.; Gago, A.; Gallio, M.; Gangadharan, D. R.; Ganoti, P.; Garabatos, C. ; Garcia-Solis, E.; Garishvili, I.; Gerhard, J.; Germain, M.; Geuna, C.; Gheata, A.; Gheata, M.; Ghidini, B.; Ghosh, P.; Gianotti, P.; Girard, M. R. ; Giubellino, P.; Gladysz-Dziadus, E.; Glässel, P. ; Gomez, R.; Gonzalez-Trueba, L. H.; Gonzalez-Zamora, P.; Gorbunov, S.; Goswami, A.; Gotovac, S.; Grabski, V.; Graczykowski, L. K.; Grajcarek, R.; Grelli, A.; Grigoras, A.; Grigoras, C.; Grigoriev, V.; Grigoryan, A.; Grigoryan, S.; Grinyov, B.; Grion, N.; Grosse-Oetringhaus, J. F.; Grossiord, J.-Y.; Guber, F.; Guernane, R.; GuerraGutierrez, C.; Guerzoni, B.; Guilbaud, M.; Gulbrandsen, K.; Gunji, T.; Gupta, A.; Gupta, R. ; Gutbrod, H.; Haaland, O.; Hadjidakis, C.; Haiduc, M.; Hamagaki, H.; Hamar, G.; Hanratty, L. D.; Harmanova, Z.; Harris, J. W.; Hartig, M.; Hasegan, D.; Hatzifotiadou, D.; Hayrapetyan, A.; Heide, M.; Helstrup, H.; Herghelegiu, A.; Herrera Corral, G.; Herrmann, N.; Hetland, K. F.; Hicks, B. ; Hille, P. T.; Hippolyte, B.; Horaguchi, T.; Hori, Y.; Hristov, P.; Hrivnacova, I.; Huang, M.; Huber, S.; Humanic, T. J.; Hwang, D. S.; Ichou, R.; Ilkaev, R.; Ilkiv, I.; Inaba, M.; Incani, E.; Innocenti, G. M.; Ippolitov, M.; Irfan, M.; Ivan, C.; Ivanov, A.; Ivanov, M.; Ivanov, V. ; Ivanytskyi, O.; Jacobs, P. M.; Jancurova, L.; Jangal, S.; Janik, M. A.; Janik, R.; Jayarathna, P. H. S. Y.; Jena, S.; JimenezBustamante, R. T.; Jirden, L.; Jones, P. G.; Jung, H.; Jung, W.; Jusko, A.; Kalcher, S.; Kalinak, P.; Kalisky, M. ; Kalliokoski, T.; Kalweit, A.; Kanaki, K.; Kang, J. H.; Kaplin, V.; KarasuUysal, A.; Karavichev, O.; Karavicheva, T.; Karpechev, E.; Kazantsev, A. ; Kebschull, U.; Keidel, R.; Khan, M. M.; Khan, P.; Khan, S. A.; Khanzadeev, A.; Kharlov, Y.; Kileng, B.; Kim, B.; Kim, D. J.; Kim, D. W.; Kim, J. H.; Kim, J. S.; Kim, M.; Kim, S.; Kim, S. H.; Kim, T.; Kirsch, S.; Kisel, I.; Kiselev, S.; Kisiel, A.; Klay, J. L.; Klein, J.; Klein-Bösing, C.; Kliemant, M.; Kluge, A.; Knichel, M. L.; Koch, K.; Köhler, M. K.; Kolojvari, A.; Kondratiev, V.; Kondratyeva, N.; Konevskikh, A.; KottachchiKankanamgDon, C.; Kour, R.; Kowalski, M.; Kox, S.; KoyithattaMeethaleveedu, G.; Kral, J.; Kralik, I. ; Kramer, F.; Kraus, I.; Krawutschke, T.; Kretz, M.; Krivda, M.; Krizek, F.; Krus, M.; Kryshen, E.; Krzewicki, M.; Kucheriaev, Y.; Kuhn, C.; Kuijer, P. G.; Kurashvili, P.; Kurepin, A.; Kurepin, A. B.; Kuryakin, A.; Kushpil, S.; Kushpil, V.; Kweon, M. J.; Kwon, Y.; La Rocca, P.; Ladron de Guevara, P.; Lakomov, I.; Lara, C.; Lardeux, A.; Larsen, D. T.; Lazzeroni, C.; Le Bornec, Y.; Lea, R.; Lechman, M.; Lee, K. S.; Lee, S. C.; Lefevre, F.; Lehnert, J.; Leistam, L. ; Lenhardt, M.; Lenti, V.; LeonMonzon, I.; LeonVargas, H.; Levai, P.; Li, X.; Lien, J.; Lietava, R.; Lindal, S.; Lindenstruth, V.; Lippmann, C.; Lisa, M. A.; Liu, L.; Loenne, P. I. ; Loggins, V. R.; Loginov, V.; Lohn, S.; Lohner, D.; Loizides, C.; Loo, K. K.; Lopez, X.; LopezTorres, E.; Lovhoiden, G.; Lu, X.-G.; Luettig, P.; Lunardon, M.; Luo, J.; Luparello, G. ; Luquin, L.; Luzzi, C.; Ma, R.; Maevskaya, A. ; Mager, M.; Mahapatra, D. P.; Maire, A.; Malaev, M.; MaldonadoCervantes, I.; Malinina, L.; MalKevich, D.; Malzacher, P.; Mamonov, A.; Manceau, L.; Manko, V.; Manso, F.; Manzari, V.; Mao, Y.; Marchisone, M.; Mares, J.; Margagliotti, G. V.; Margotti, A.; Marin, A.; Markert, C.; Martashvili, I.; Martinengo, P.; Martinez, M. I.; Martinez Davalos, A.; MartinezGarcia, G.; Martynov, Y.; Mas, A.; Masciocchi, S.; Masera, M. ; Masoni, A.; Massacrier, L.; Mastromarco, M.; Mastroserio, A.; Matthews, Z. L.; Matyja, A.; Mayani, D.; Mayer, C.; Mazzoni, M. A.; Meddi, F. ; Menchaca-Rocha, A.; MercadoPerez, J.; Meres, M. ; Miake, Y.; Michalon, A.; Midori, J.; Milano, L. ; Milosevic, J.; Mischke, A.; Mishra, A. N.; Mikowiec, D.; Mitu, C.; Mlynarz, J.; Mohanty, A. K.; Mohanty, B.; Molnar, L.; MontanoZetina, L. ; Monteno, M.; Montes, E.; Moon, T.; Morando, M. ; MoreiraDeGodoy, D. A.; Moretto, S.; Morsch, A. ; Muccifora, V.; Mudnic, E.; Müller, H.; Muhuri, S.; Munhoz, M. G.; Musa, L.; Musso, A.; Nandi, B. K.; Nania, R.; Nappi, E.; Nattrass, C.; Naumov, N. P.; Navin, S.; Nayak, T. K.; Nazarenko, S.; Nazarov, G.; Nedosekin, A.; Nicassio, M.; Nielsen, B. S.; Niida, T.; Nikolaev, S.; Nikolic, V.; Nikulin, S.; Nikulin, V.; Nilsen, B. S.; Nilsson, M. S.; Noferini, F.; Nomokonov, P.; Nooren, G.; Novitzky, N.; Nyanin, A.; Nyatha, A. ; Nygaard, C.; Nystrand, J.; Obayashi, H.; Ochirov, A.; Oeschler, H.; Oh, S. K.; Oleniacz, J. ; Oppedisano, C.; Ortiz Velasquez, A.; Ortona, G. ; Oskarsson, A.; Otterlund, I.; Otwinowski, J.; Ovrebekk, G.; Oyama, K.; Pachmayer, Y.; Pachr, M. ; Padilla, F.; Pagano, P.; Paic, G.; Painke, F. ; Pajares, C.; Pal, S.; Pal, S. K.; Palaha, A. ; Palmeri, A.; Pappalardo, G. S.; Park, W. J.; Passfeld, A.; Patalakha, D. I.; Paticchio, V.; Pavlinov, A.; Pawlak, T.; Peitzmann, T.; PereiraDeOliveiraFilho, E.; Peresunko, D.; Perez Lara, C. E.; Perez Lezama, E.; Perini, D.; Perrino, D.; Peryt, W.; Pesci, A.; Peskov, V.; Pestov, Y.; Petracek, V.; Petran, M.; Petris, M. ; Petrov, P.; Petrovici, M.; Petta, C.; Piano, S. ; Piccotti, A.; Pikna, M.; Pillot, P.; Pinazza, O.; Pinsky, L.; Pitz, N.; Piuz, F.; Piyarathna, D. B.; Ploskon, M.; Pluta, J.; Pocheptsov, T.; Pochybova, S.; Podesta-Lerma, P. L. M.; Poghosyan, M. G.; Polichtchouk, B.; Pop, A.; Porteboeuf-Houssais, S.; Pospisil, V.;

Potukuchi, B.; Prasad, S. K. ; Preghenella, R.; Prino, F.; Pruneau, C. A.; Pshenichnov, I.; Puddu, G.; Pulvirenti, A.; Punin, V.; Putis, M.; Putschke, J.; Quercigh, E.; Qvigstad, H.; Rachevski, A.; Rademakers, A.; Radomski, S.; Räihä T. S.; Rak, J.; Rakotozafindrabe, A.; Ramello, L.; RamirezReyes, A. ; Raniwala, R.; Raniwala, S.; Räsänen, S. S.; Rascanu, B. T.; Rathee, D.; Read, K. F.; Real, J. S.; Redlich, K.; Reichelt, P.; Reicher, M.; Renfordt, R.; Reolon, A. R.; Reshetin, A.; Rettig, F.; Revol, J.-P.; Reygers, K.; Ricaud, H.; Riccati, L.; Ricci, R. A.; Richter, M.; Riedler, P. ; Riegler, W.; Riggi, F.; RodriguezCahuantzi, M. ; Rohr, D.; Röhrich, D.; Romita, R.; Ronchetti, F.; Rosnet, P.; Rossegger, S.; Rossi, A.; Roukoutakis, F.; Roy, C.; Roy, P.; RubioMontero, A. J.; Rui, R.; Ryabinkin, E.; Rybicki, A.; Sadovsky, S.; Safarik, K.; Sahu, P. K.; Saini, J.; Sakaguchi, H.; Sakai, S.; Sakata, D.; Salgado, C. A.; Sambyal, S.; Samsonov, V.; SanchezCastro, X.; Sandor, L.; Sandoval, A.; Sano, M.; Sano, S.; Santo, R.; Santoro, R.; Sarkamo, J.; Scapparone, E.; Scarlassara, F.; Scharenberg, R. P.; Schiaua, C.; Schicker, R.; Schmidt, C.; Schmidt, H. R.; Schreiner, S.; Schuchmann, S.; Schukraft, J.; Schutz, Y.; Schwarz, K.; Schweda, K.; Scioli, G.; Scomparin, E.; Scott, P. A.; Scott, R.; Segato, G.; Selyuzhenkov, I.; Senyukov, S.; Serci, S.; Serradilla, E.; Sevcenco, A.; Sgura, I.; Shabratova, G.; Shahoyan, R.; Sharma, N.; Sharma, S.; Shigaki, K.; Shimomura, M.; Shtejer, K.; Sibiriak, Y.; Siciliano, M.; Sicking, E.; Siddhanta, S.; Siemiarczuk, T.; Silvermyr, D.; Simonetti, G.; Singaraju, R.; Singh, R.; Singha, S.; Sinha, B. C. ; Sinha, T.; Sitar, B.; Sitta, M.; Skaali, T. B. ; Skjerdal, K.; Smakal, R.; Smirnov, N.; Snellings, R.; Sogaard, C.; Soltz, R.; Son, H.; Song, J.; Song, M.; Soos, C.; Soramel, F.; Spyropoulou-Stassinaki, M.; Srivastava, B. K.; Stachel, J.; Stan, I.; Stefanek, G.; Stefanini, G. ; Steinbeck, T.; Steinpreis, M.; Stenlund, E.; Steyn, G.; Stocco, D.; Stolpovskiy, M.; Strmen, P. ; Suaide, A. A. P.; SubietaVasquez, M. A.; Sugitate, T.; Suire, C.; Sukhorukov, M.; Sultanov, R.; Sumbera, M.; Susa, T.; Szanto de Toledo, A. ; Szarka, I.; Szostak, A.; Tagridis, C.; Takahashi, J.; TapiaTakaki, J. D.; Tauro, A.; TejedaMunoz, G.; Telesca, A.; Terrevoli, C.; Thäder, J.; Thomas, D.; Thomas, J. H.; Tieulent, R.; Timmins, A. R.; Tlusty, D.; Toia, A.; Torii, H.; Tosello, F.; Traczyk, T.; Trzaska, W. H.; Tsuji, T.; Tumkin, A.; Turrisi, R.; Turvey, A. J. ; Tveter, T. S.; Ulery, J.; Ullaland, K.; Ulrich, J.; Uras, A.; Urban, J.; Urciuoli, G. M.; Usai, G. L.; Vajzer, M.; Vala, M.; Valencia Palomo, L. ; Vallero, S.; van der Kolk, N.; van Leeuwen, M.; Vande Vyvre, P.; Vannucci, L.; Vargas, A.; Varma, R.; Vasileiou, M.; Vasiliev, A.; Vechernin, V.; Veldhoen, M.; Venaruzzo, M.; Vercellin, E.; Vergara, S.; Vernekohl, D. C.; Vernet, R.; Verweij, M.; Vickovic, L.; Viesti, G.; Vikhlyantsev, O.; Vilakazi, Z.; VillalobosBaillie, O.; Vinogradov, A. ; Vinogradov, L.; Vinogradov, Y.; Virgili, T.; Viyogi, Y. P.; Vodopyanov, A.; Voloshin, K.; Voloshin, S.; Volpe, G.; vonHaller, B.; Vrlakova, J.; Vulpescu, B.; Vyushin, A.; Wagner, B.; Wagner, V.; Wan, R.; Wang, D.; Wang, M.; Wang, Y.; Wang, Y.; Watanabe, K.; Wessels, J. P. ; Westerhoff, U.; Wiechula, J.; Wikne, J.; Wilde, M.; Wilk, A.; Wilk, G.; Williams, M. C. S.; Windelband, B.; XaplanterisKarampatsos, L.; Yang, H. ; Yasnopolskiy, S.; Yi, J.; Yin, Z.; Yokoyama, H. ; Yoo, I.-K.; Yoon, J.; Yu, W.; Yuan, X.; Yushmanov, I.; Zach, C.; Zampolli, C.; Zaporozhets, S.; Zarochentsev, A.; Zavada, P.; Zaviyalov, N. ; Zbroszczyk, H.; Zelnicek, P.; Zgura, I.; Zhalov, M.; Zhang, X.; Zhou, D.; Zhou, F.; Zhou, Y.; Zhu, X.; Zichichi, A.; Zimmermann, A.; Zinovjev, G.; Zoccarato, Y.; Zynovyev, M.; Vranic, D.: **Particle-Yield Modification in Jetlike Azimuthal Dihadron Correlations in Pb-Pb Collisions at $\sqrt{s_{NN}} = 2.76$TeV.** *Physical review letters* 108: 092301, 2012. DOI:10.1103/PhysRevLett.108.092301

WOS-PHN-3 Abelev, B.; Abrahantes Quintana, A.; Adamova, D.; Adare, A. M.; Aggarwal, M. M.; Aglieri Rinella, G.; Agocs, A. G.; Agostinelli, A.; Aguilar Salazar, S.; Ahammed, Z.; Ahmad, N.; Ahmad Masoodi, A.; Ahn, S. U.; Akindinov, A.; Aleksandrov, D.; Alessandro, B. ; Alfaro Molina, R.; Alici, A.; Alkin, A.; Almaraz Avina, E.; Alt, T.; Altini, V.; Altinpinar, S.; Altsybeev, I.; Andrei, C.; Andronic, A.; Anguelov, V.; Anson, C.; Anticic, T.; Antinori, F.; Antonioli, P.; Aphecetche, L.; Appelshäuser, H.; Arbor, N.; Arcelli, S.; Arend, A.; Armesto, N.; Arnaldi, R.; Aronsson, T.; Arsene, I. C.; Arslandok, M.; Asryan, A.; Augustinus, A.; Averbeck, R.; Awes, T. C.; Äystö J.; Azmi, M. D.; Bach, M.; Badala, A.; Baek, Y. W.; Bailhache, R.; Bala, R.; Baldini Ferroli, R. ; Baldisseri, A.; Baldit, A.; Baltasar Dos Santos Pedrosa, F.; Ban, J.; Baral, R. C.; Barbera, R. ; Barile, F.; Barnaföldi, G. G.; Barnby, L. S.; Barret, V.; Bartke, J.; Basile, M.; Bastid, N.; Bathen, B.; Batigne, G.; Batyunya, B.; Baumann, C. ; Bearden, I. G.; Beck, H.; Belikov, I.; Bellini, F.; Bellwied, R.; Belmont-Moreno, E.; Beole, S.; Berceanu, I.; Bercuci, A.; Berdnikov, Y.; Berenyi, D.; Bergmann, C.; Berzano, D.; Betev, L.; Bhasin, A.; Bhati, A. K.; Bianchi, N.; Bianchi, L. ; Bianchin, C.; Bielcik, J.; Bielcikova, J.; Bilandzic, A.; Blanco, F.; Blanco, F.; Blau, D.; Blume, C.; Boccioli, M.; Bock, N.; Bogdanov, A.; Boggild, H.; Bogolyubsky, M.; Boldizsar, L.; Bombara, M.; Book, J.; Borel, H.; Borissov, A.; Bortolin, C.; Bose, S.; Boss, F.; Botje, M.; Böttger, S.; Boyer, B.; Braun-Munzinger, P.; Bregant, M.; Breitner, T.; Broz, M.; Brun, R.; Bruna, E.; Bruno, G. E.; Budnikov, D.; Buesching, H.; Bufalino, S.; Bugaiev, K.; Busch, O.; Buthelezi, Z.; Caffarri, D.; Cai, X.; Caines, H. ; Calvo Villar, E.; Camerini, P.; Canoa Roman, V. ; Cara Romeo, G.; Carena, W.; Carena, F.; Carlin Filho, N.; Carminati, F.; Carrillo Montoya, C. A.; Casanova Diaz, A.; Caselle, M.; Castillo Castellanos, J.; Castillo Hernandez, J. F.; Casula, E. A. R.; Catanescu, V.; Cavicchioli, C.; Cepila, J.; Cerello, P.; Chang, B.; Chapeland, S.; Charvet, J. L.; Chattopadhyay, S.; Chattopadhyay, S.; Cherney, M.; Cheshkov, C.; Cheynis, B.; Chiavassa, E.; Chibante Barroso, V.; Chinellato, D. D.; Chochula, P. ; Chojnacki, M.; Christakoglou, P.; Christensen, C. H.; Christiansen, P.; Chujo, T.; Chung, S. U.; Cicalo, C.; Cifarelli, L.; Cindolo, F.; Cleymans, J.; Coccetti, F.; Coffin, J.-P.; Colamaria, F.; Colella, D.; Conesa Balbastre, G.; Conesa del Valle, Z.; Constantin, P.; Contin, G.; Contreras, J. G. ; Cormier, T. M.; Corrales Morales, Y.; Cortese, P. ; Cortes Maldonado, I.; Cosentino, M. R.; Costa, F. ; Cotallo, M. E.; Crescio, E.; Crochet, P.; Cruz Alaniz, E.; Cuautle, E.; Cunqueiro, L.; Dainese, A. ; Dalsgaard, H. H.; Danu, A.; Das, D.; Das, I. ; Das, K.; Dash, S.; Dash, A.; De, S.; Azevedo Moregula, A.; Barros, G. O. V.; Caro, A.; Cataldo, G.; Cuveland, J.; Falco, A.; Gruttola, D.; Delagrange, H.; Castillo Sanchez, E.; Deloff, A.; Demanov, V.; Marco, N.; Denes, E.; Pasquale, S. ; Deppman, A.; Erasmo, G. D; Rooij, R.; Bari, D. ; Dietel, T.; Giglio, C.; Liberto, S.; Mauro, A. ; Nezza, P.; Divia, R.; Djuvsland, O.; Dobrin, A.; Dobrowolski, T.; Dominguez, I.; Dönigus, B. ; Dordic, O.; Driga, O.; Dubey, A. K.; Ducroux, L.; Dupieux, P.; Dutta Majumdar, M. R.; Dutta Majumdar, A. K.; Elia, D.; Emschermann, D.; Engel, H.; Erdal, H. A.; Espagnon, B.; Estienne, M.; Esumi, S.; Evans, D.; Eyyubova, G.; Fabris, D.; Faivre, J.; Falchieri, D.; Fantoni, A.; Fasel, M. ; Fearick, R.; Fedunov, A.; Fehlker, D.; Feldkamp, L.; Felea, D.; Feofilov, G.; Fernandez Tellez, A.; Ferretti, A.; Ferretti, R.; Figiel, J. ; Figueredo, M. A. S.; Filchagin, S.; Fini, R.; Finogeev, D.; Fionda, F. M.; Fiore, E. M.; Floris, M.; Foertsch, S.; Foka,

P.; Fokin, S.; Fragiacomo, E.; Fragkiadakis, M.; Frankenfeld, U.; Fuchs, U.; Furget, C.; Fusco Girard, M.; Gaardhoje, J. J.; Gagliardi, M.; Gago, A.; Gallio, M.; Gangadharan, D. R.; Ganoti, P.; Garabatos, C. ; Garcia-Solis, E.; Garishvili, I.; Gerhard, J.; Germain, M.; Geuna, C.; Gheata, A.; Gheata, M.; Ghidini, B.; Ghosh, P.; Gianotti, P.; Girard, M. R. ; Giubellino, P.; Gladysz-Dziadus, E.; Glässel, P. ; Gomez, R.; Ferreiro, E. G.; Gonzalez-Trueba, L. H.; Gonzalez-Zamora, P.; Gorbunov, S.; Goswami, A. ; Gotovac, S.; Grabski, V.; Graczykowski, L. K.; Grajcarek, R.; Grelli, A.; Grigoras, A.; Grigoras, C.; Grigoriev, V.; Grigoryan, S.; Grigoryan, A.; Grinyov, B.; Grion, N.; Gros, P.; Grosse-Oetringhaus, J. F.; Grossiord, J.-Y.; Grosso, R.; Guber, F.; Guernane, R.; Guerra Gutierrez, C. ; Guerzoni, B.; Guilbaud, M.; Gulbrandsen, K.; Gunji, T.; Gupta, A.; Gupta, R.; Gutbrod, H.; Haaland, O.; Hadjidakis, C.; Haiduc, M.; Hamagaki, H.; Hamar, G.; Han, B. H.; Hanratty, L. D.; Hansen, A.; Harmanova, Z.; Harris, J. W.; Hartig, M.; Hasegan, D.; Hatzifotiadou, D.; Hayrapetyan, A. ; Heide, M.; Helstrup, H.; Herghelegiu, A.; Herrera Corral, G.; Herrmann, N.; Hetland, K. F.; Hicks, B.; Hille, P. T.; Hippolyte, B.; Horaguchi, T.; Hori, Y.; Hristov, P.; Hrivnacova, I.; Huang, M.; Huber, S.; Humanic, T. J.; Hwang, D. S. ; Ichou, R.; Ilkaev, R.; Ilkiv, I.; Inaba, M.; Incani, E.; Innocenti, P. G.; Innocenti, G. M.; Ippolitov, M.; Irfan, M.; Ivan, C.; Ivanov, A.; Ivanov, M.; Ivanov, V.; Ivanytskyi, O.; Jacholkowski, A.; Jacobs, P. M.; Jancurova, L.; Jangal, S.; Janik, M. A.; Janik, R.; Jayarathna, P. H. S. Y.; Jena, S.; Jimenez Bustamante, R. T.; Jirden, L.; Jones, P. G.; Jung, H.; Jung, W.; Jusko, A.; Kaidalov, A. B.; Kakoyan, V.; Kalcher, S.; Kalinak, P.; Kalisky, M.; Kalliokoski, T.; Kalweit, A.; Kanaki, K.; Kang, J. H.; Kaplin, V. ; Karasu Uysal, A.; Karavichev, O.; Karavicheva, T. ; Karpechev, E.; Kazantsev, A.; Kebschull, U.; Keidel, R.; Khan, M. M.; Khan, S. A.; Khan, P.; Khanzadeev, A.; Kharlov, Y.; Kileng, B.; Kim, S. ; Kim, D. W.; Kim, J. H.; Kim, J. S.; Kim, M.; Kim, S. H.; Kim, T.; Kim, B.; Kim, D. J.; Kirsch, S.; Kisel, I.; Kiselev, S.; Kisiel, A.; Klay, J. L.; Klein, J.; Klein-Bösing, C.; Kliemant, M.; Kluge, A.; Knichel, M. L.; Koch, K. ; Köhler, M. K.; Kolojvari, A.; Kondratiev, V.; Kondratyeva, N.; Konevskikh, A.; Kottachchi Kankanamge Don, C.; Kour, R.; Kowalski, M.; Kox, S.; Koyithatta Meethaleveedu, G.; Kral, J.; Kralik, I. ; Kramer, F.; Kraus, I.; Krawutschke, T.; Kretz, M.; Krivda, M.; Krizek, F.; Krus, M.; Kryshen, E.; Krzewicki, M.; Kucheriaev, Y.; Kuhn, C.; Kuijer, P. G.; Kurashvili, P.; Kurepin, A. B.; Kurepin, A.; Kuryakin, A.; Kushpil, V.; Kushpil, S. ; Kvaerno, H.; Kweon, M. J.; Kwon, Y.; Ladron de Guevara, P.; Lakomov, I.; Langoy, R.; Lara, C.; Lardeux, A.; Rocca, P.; Larsen, D. T.; Lazzeroni, C.; Lea, R.; Bornec, Y.; Lee, S. C.; Lee, K. S. ; Lefevre, F.; Lehnert, J.; Leistam, L.; Lenhardt, M.; Lenti, V.; Leon, H.; Leon Monzon, I.; Leon Vargas, H.; Levai, P.; Li, X.; Lien, J.; Lietava, R.; Lindal, S.; Lindenstruth, V.; Lippmann, C.; Lisa, M. A.; Liu, L.; Loenne, P. I. ; Loggins, V. R.; Loginov, V.; Lohn, S.; Lohner, D.; Loizides, C.; Loo, K. K.; Lopez, X.; Lopez Torres, E.; Lovhoiden, G.; Lu, X.-G.; Luettig, P. ; Lunardon, M.; Luo, J.; Luparello, G.; Luquin, L.; Luzzi, C.; Ma, R.; Ma, K.; Madagodahettige-Don, D. M.; Maevskaya, A.; Mager, M. ; Mahapatra, D. P.; Maire, A.; Malaev, M.; Maldonado Cervantes, I.; Malinina, L.; MalKevich, D.; Malzacher, P.; Mamonov, A.; Manceau, L.; Mangotra, L.; Manko, V.; Manso, F.; Manzari, V.; Mao, Y.; Marchisone, M.; Mares, J.; Margagliotti, G. V.; Margotti, A.; Marin, Ana; Markert, C.; Martashvili, I.; Martinengo, P.; Martinez, M. I.; Martinez Davalos, A.; Martinez Garcia, G.; Martynov, Y.; Mas, A.; Masciocchi, S.; Masera, M. ; Masoni, A.; Massacrier, L.; Mastromarco, M.; Mastroserio, A.; Matthews, Z. L.; Matyja, A.; Mayani, D.; Mayer, C.; Mazzoni, M. A.; Meddi, F. ; Menchaca-Rocha, A.; Mercado Perez, J.; Meres, M. ; Miake, Y.; Michalon, A.; Midori, J.; Milano, L. ; Milosevic, J.; Mischke, A.; Mishra, A. N.; Miskowiec, D.; Mitu, C.; Mlynarz, J.; Mohanty, A. K.; Mohanty, B.; Molnar, L.; Montano Zetina, L. ; Monteno, M.; Montes, E.; Moon, T.; Morando, M. ; Moreira De Godoy, D. A.; Moretto, S.; Morsch, A. ; Muccifora, V.; Mudnic, E.; Muhuri, S.; Müller, H.; Munhoz, M. G.; Musa, L.; Musso, A.; Nandi, B. K.; Nania, R.; Nappi, E.; Nattrass, C.; Naumov, N. P.; Navin, S.; Nayak, T. K.; Nazarenko, S.; Nazarov, G.; Nedosekin, A.; Nicassio, M.; Nielsen, B. S.; Niida, T.; Nikolaev, S.; Nikolic, V.; Nikulin, V.; Nikulin, S.; Nilsen, B. S.; Nilsson, M. S.; Noferini, F.; Nomokonov, P.; Nooren, G.; Novitzky, N.; Nyanin, A.; Nyatha, A. ; Nygaard, C.; Nystrand, J.; Obayashi, H.; Ochirov, A.; Oeschler, H.; Oh, S. K.; Oleniacz, J. ; Oppedisano, C.; Ortiz Velasquez, A.; Ortona, G. ; Oskarsson, A.; Ostrowski, P.; Otterlund, I.; Otwinowski, J.; Oyama, K.; Ozawa, K.; Pachmayer, Y. ; Pachr, M.; Padilla, F.; Pagano, P.; Paic, G. ; Painke, F.; Pajares, C.; Pal, S.; Pal, S. K. ; Palaha, A.; Palmeri, A.; Papikyan, V.; Pappalardo, G. S.; Park, W. J.; Passfeld, A.; Pastircak, B.; Patalakha, D. I.; Paticchio, V.; Pavlinov, A.; Pawlak, T.; Peitzmann, T.; Perales, M.; Pereira De Oliveira Filho, E.; Peresunko, D.; Perez Lara, C. E.; Perez Lezama, E.; Perini, D.; Perrino, D.; Peryt, W.; Pesci, A.; Peskov, V.; Pestov, Y.; Petracek, V.; Petran, M.; Petris, M. ; Petrov, P.; Petrovici, M.; Petta, C.; Piano, S. ; Piccotti, A.; Pikna, M.; Pillot, P.; Pinazza, O.; Pinsky, L.; Pitz, N.; Piuz, F.; Piyarathna, D. B.; Ploskon, M.; Pluta, J.; Pocheptsov, T.; Pochybova, S.; Podesta-Lerma, P. L. M.; Poghosyan, M. G.; Polak, K.; Polichtchouk, B.; Pop, A.; Porteboeuf-Houssais, S.; Pospisil, V.; Potukuchi, B. ; Prasad, S. K.; Preghenella, R.; Prino, F.; Pruneau, C. A.; Pshenichnov, I.; Puddu, G.; Pulvirenti, A.; Punin, V.; Putis, M.; Putschke, J. ; Quercigh, E.; Qvigstad, H.; Rachevski, A.; Rademakers, A.; Radomski, S.; Räihä T. S.; Rak, J.; Rakotozafindrabe, A.; Ramello, L.; Ramirez Reyes, A.; Raniwala, S.; Raniwala, R.; Räsänen, S. S.; Rascanu, B. T.; Rathee, D.; Read, K. F.; Real, J. S.; Redlich, K.; Reichelt, P.; Reicher, M. ; Renfordt, R.; Reolon, A. R.; Reshetin, A.; Rettig, F.; Revol, J.-P.; Reygers, K.; Ricaud, H. ; Riccati, L.; Ricci, R. A.; Richter, M.; Riedler, P.; Riegler, W.; Riggi, F.; Rodriguez Cahuantzi, M.; Rohr, D.; Röhrich, D.; Romita, R. ; Ronchetti, F.; Rosnet, P.; Rossegger, S.; Rossi, A.; Roukoutakis, F.; Roy, C.; Roy, P.; Rubio Montero, A. J.; Rui, R.; Ryabinkin, E.; Rybicki, A.; Sadovsky, S.; Safarik, K.; Sahu, P. K.; Saini, J.; Sakaguchi, H.; Sakai, S.; Sakata, D.; Salgado, C. A.; Sambyal, S.; Samsonov, V.; Sanchez Castro, X.; Sandor, L.; Sandoval, A.; Sano, M.; Sano, S.; Santo, R.; Santoro, R.; Sarkamo, J.; Scapparone, E.; Scarlassara, F.; Scharenberg, R. P.; Schiaua, C.; Schicker, R.; Schmidt, H. R.; Schmidt, C.; Schreiner, S.; Schuchmann, S.; Schukraft, J.; Schutz, Y.; Schwarz, K.; Schweda, K.; Scioli, G.; Scomparin, E.; Scott, R.; Scott, P. A.; Segato, G.; Selyuzhenkov, I.; Senyukov, S.; Seo, J.; Serci, S.; Serradilla, E.; Sevcenco, A.; Sgura, I.; Shabratova, G.; Shahoyan, R.; Sharma, N.; Sharma, S.; Shigaki, K.; Shimomura, M.; Shtejer, K.; Sibiriak, Y.; Siciliano, M.; Sicking, E.; Siddhanta, S.; Siemiarczuk, T.; Silvermyr, D.; Simonetti, G.; Singaraju, R.; Singh, R.; Singha, S. ; Sinha, T.; Sinha, B. C.; Sitar, B.; Sitta, M. ; Skaali, T. B.; Skjerdal, K.; Smakal, R.; Smirnov, N.; Snellings, R.; Sogaard, C.; Soltz, R. ; Son, H.; Song, J.; Song, M.; Soos, C.; Soramel, F.; Spyropoulou-Stassinaki, M.; Srivastava, B. K.; Stachel, J.; Stan, I.; Stan, I.; Stefanek, G.; Stefanini, G.; Steinbeck, T.; Steinpreis, M.; Stenlund, E.; Steyn, G.; Stocco, D. ; Stolpovskiy, M.; Strmen, P.; Suaide, A. A. P.; Subieta Vasquez,

M. A.; Sugitate, T.; Suire, C.; Sukhorukov, M.; Sultanov, R.; Sumbera, M.; Susa, T.; Szanto de Toledo, A.; Szarka, I.; Szostak, A. ; Tagridis, C.; Takahashi, J.; Tapia Takaki, J. D. ; Tauro, A.; Tejeda Munoz, G.; Telesca, A.; Terrevoli, C.; Thäder, J.; Thomas, J. H.; Thomas, D.; Tieulent, R.; Timmins, A. R.; Tlusty, D.; Toia, A.; Torii, H.; Toscano, L.; Tosello, F.; Traczyk, T.; Truesdale, D.; Trzaska, W. H.; Tsuji, T.; Tumkin, A.; Turrisi, R.; Tveter, T. S.; Ulery, J.; Ullaland, K.; Ulrich, J.; Uras, A.; Urban, J.; Urciuoli, G. M.; Usai, G. L.; Vajzer, M.; Vala, M.; Valencia Palomo, L.; Vallero, S.; Kolk, N.; Vyvre, P. Vande; Leeuwen, M.; Vannucci, L.; Vargas, A.; Varma, R.; Vasileiou, M.; Vasiliev, A.; Vechernin, V.; Veldhoen, M.; Venaruzzo, M.; Vercellin, E.; Vergara, S.; Vernekohl, D. C.; Vernet, R.; Verweij, M.; Vickovic, L.; Viesti, G.; Vikhlyantsev, O.; Vilakazi, Z.; Villalobos Baillie, O.; Vinogradov, A. ; Vinogradov, L.; Vinogradov, Y.; Virgili, T.; Viyogi, Y. P.; Vodopyanov, A.; Voloshin, K.; Voloshin, S.; Volpe, G.; Haller, B.; Vranic, D.; Ovrebekk, G.; Vrlakova, J.; Vulpescu, B.; Vyushin, A.; Wagner, V.; Wagner, B.; Wan, R.; Wang, Y.; Wang, D.; Wang, Y.; Wang, M.; Watanabe, K.; Wessels, J. P.; Westerhoff, U.; Wiechula, J.; Wikne, J.; Wilde, M.; Wilk, G.; Wilk, A.; Williams, M. C. S.; Windelband, B.; Xaplanteris Karampatsos, L.; Yang, H.; Yano, S.; Yasnopolskiy, S.; Yi, J.; Yin, Z.; Yokoyama, H.; Yoo, I.-K.; Yoon, J.; Yu, W.; Yuan, X.; Yushmanov, I.; Zach, C.; Zampolli, C.; Zaporozhets, S.; Zarochentsev, A.; Zavada, P.; Zaviyalov, N. ; Zbroszczyk, H.; Zelnicek, P.; Zgura, I.; Zhalov, M.; Zhang, X.; Zhou, F.; Zhou, D.; Zhou, Y.; Zhu, X.; Zichichi, A.; Zimmermann, A.; Zinovjev, G.; Zoccarato, Y.; Zynovyev, M.: **Measurement of charm production at central rapidity in proton-proton collisions at $\sqrt{s}$ = 7TeV.** *Journal of high energy physics* 2012: 128, 2012. DOI:10.1007/JHEP01(2012)128

WOS-PHN-4 Abelev, B.; Abrahantes Quintana, A.; Adamova, D.; Adare, A. M.; Aggarwal, M. M.; Aglieri Rinella, G.; Agocs, A. G.; Agostinelli, A.; Aguilar Salazar, S.; Ahammed, Z.; Ahmad, N.; Ahmad Masoodi, A.; Ahn, S. U.; Akindinov, A.; Aleksandrov, D.; Alessandro, B. ; AlfaroMolina, R.; Alici, A.; Alkin, A.; Almaraz Avina, E.; Alt, T.; Altini, V.; Altinpinar, S.; Altsybeev, I.; Andrei, C.; Andronic, A.; Anguelov, V.; Anson, C.; Anticic, T.; Antinori, F.; Antonioli, P.; Aphecetche, L.; Appelshäuser, H.; Arbor, N.; Arcelli, S.; Arend, A.; Armesto, N.; Arnaldi, R.; Aronsson, T.; Arsene, I. C.; Arslandok, M.; Asryan, A.; Augustinus, A.; Averbeck, R.; Awes, T. C.; Äystö J.; Azmi, M. D.; Bach, M.; Badala, A.; Baek, Y. W.; Bailhache, R.; Bala, R.; Baldini Ferroli, R. ; Baldisseri, A.; Baldit, A.; Baltasar Dos Santos Pedrosa, F.; Ban, J.; Baral, R. C.; Barbera, R. ; Barile, F.; Barnaföldi, G. G.; Barnby, L. S.; Barret, V.; Bartke, J.; Basile, M.; Bastid, N.; Bathen, B.; Batigne, G.; Batyunya, B.; Baumann, C. ; Bearden, I. G.; Beck, H.; Belikov, I.; Bellini, F.; Bellwied, R.; Belmont-Moreno, E.; Beole, S.; Berceanu, I.; Bercuci, A.; Berdnikov, Y.; Berenyi, D.; Bergmann, C.; Berzano, D.; Betev, L.; Bhasin, A.; Bhati, A. K.; Bianchi, N.; Bianchi, L. ; Bianchin, C.; Bielcik, J.; Bielcikova, J.; Bilandzic, A.; Blanco, F.; Blanco, F.; Blau, D.; Blume, C.; Boccioli, M.; Bock, N.; Bogdanov, A.; Boggild, H.; Bogolyubsky, M.; Boldizsar, L.; Bombara, M.; Book, J.; Borel, H.; Borissov, A.; Bortolin, C.; Bose, S.; Boss, F.; Botje, M.; Böttger, S.; Boyer, B.; Braun-Munzinger, P.; Bregant, M.; Breitner, T.; Broz, M.; Brun, R.; Bruna, E.; Bruno, G. E.; Budnikov, D.; Buesching, H.; Bufalino, S.; Bugaiev, K.; Busch, O.; Buthelezi, Z.; Caffarri, D.; Cai, X.; Caines, H. ; Calvo Villar, E.; Camerini, P.; Canoa Roman, V. ; Cara Romeo, G.; Carena, W.; Carena, F.; Carlin Filho, N.; Carminati, F.; Carrillo Montoya, C. A.; Casanova Diaz, A.; Caselle, M.; Castillo Castellanos, J.; Castillo Hernandez, J. F.; Casula, E. A. R.; Catanescu, V.; Cavicchioli, C.; Cepila, J.; Cerello, P.; Chang, B.; Chapeland, S.; Charvet, J. L.; Chattopadhyay, S.; Chattopadhyay, S.; Cherney, M.; Cheshkov, C.; Cheynis, B.; Chiavassa, E.; Chibante Barroso, V.; Chinellato, D. D.; Chochula, P. ; Chojnacki, M.; Christakoglou, P.; Christensen, C. H.; Christiansen, P.; Chujo, T.; Chung, S. U.; Cical, C.; Cifarelli, L.; Cindolo, F.; Cleymans, J.; Coccetti, F.; Coffin, J.-P.; Colamaria, F.; Colella, D.; Conesa Balbastre, G.; Conesa del Valle, Z.; Constantin, P.; Contin, G.; Contreras, J. G. ; Cormier, T. M.; Corrales Morales, Y.; Cortese, P. ; Cortes Maldonado, I.; Cosentino, M. R.; Costa, F. ; Cotallo, M. E.; Crescio, E.; Crochet, P.; Cruz Alaniz, E.; Cuautle, E.; Cunqueiro, L.; Dainese, A. ; Dalsgaard, H. H.; Danu, A.; Das, D.; Das, I. ; Das, K.; Dash, S.; Dash, A.; De, S.; De Azevedo Moregula, A.; de Barros, G. O. V.; De Caro, A. ; de Cataldo, G.; de Cuveland, J.; De Falco, A.; De Gruttola, D.; Delagrange, H.; Del Castillo Sanchez, E.; Deloff, A.; Demanov, V.; De Marco, N.; Denes, E.; De Pasquale, S.; Deppman, A.; DErasmo, G.; de Rooij, R.; Di Bari, D.; Dietel, T.; Di Giglio, C.; Di Liberto, S.; Di Mauro, A.; Di Nezza, P.; Divia, R.; Djuvsland, O.; Dobrin, A.; Dobrowolski, T.; Dominguez, I.; Dönigus, B. ; Dordic, O.; Driga, O.; Dubey, A. K.; Ducroux, L.; Dupieux, P.; Dutta Majumdar, M. R.; Dutta Majumdar, A. K.; Elia, D.; Emschermann, D.; Engel, H.; Erdal, H. A.; Espagnon, B.; Estienne, M.; Esumi, S.; Evans, D.; Eyyubova, G.; Fabris, D.; Faivre, J.; Falchieri, D.; Fantoni, A.; Fasel, M. ; Fearick, R.; Fedunov, A.; Fehlker, D.; Feldkamp, L.; Felea, D.; Feofilov, G.; Fernandez Tellez, A.; Ferreiro, E. G.; Ferretti, A.; Ferretti, R.; Figiel, J.; Figueredo, M. A. S.; Filchagin, S.; Fini, R.; Finogeev, D.; Fionda, F. M.; Fiore, E. M.; Floris, M.; Foertsch, S.; Foka, P.; Fokin, S.; Fragiacomo, E.; Fragkiadakis, M.; Frankenfeld, U.; Fuchs, U.; Furget, C.; Fusco Girard, M.; Gaardhoje, J. J.; Gagliardi, M.; Gago, A.; Gallio, M.; Gangadharan, D. R.; Ganoti, P.; Garabatos, C.; Garcia-Solis, E.; Garishvili, I. ; Gerhard, J.; Germain, M.; Geuna, C.; Gheata, A. ; Gheata, M.; Ghidini, B.; Ghosh, P.; Gianotti, P.; Girard, M. R.; Giubellino, P.; Gladysz-Dziadus, E.; Glässel, P.; Gomez, R.; Gonzalez-Trueba, L. H.; Gonzalez-Zamora, P.; Gorbunov, S.; Goswami, A. ; Gotovac, S.; Grabski, V.; Graczykowski, L. K.; Grajcarek, R.; Grelli, A.; Grigoras, A.; Grigoras, C.; Grigoriev, V.; Grigoryan, S.; Grigoryan, A.; Grinyov, B.; Grion, N.; Gros, P.; Grosse-Oetringhaus, J. F.; Grossiord, J.-Y.; Grosso, R.; Guber, F.; Guernane, R.; Guerra Gutierrez, C. ; Guerzoni, B.; Guilbaud, M.; Gulbrandsen, K.; Gunji, T.; Gupta, A.; Gupta, R.; Gutbrod, H.; Haaland, O.; Hadjidakis, C.; Haiduc, M.; Hamagaki, H.; Hamar, G.; Han, B. H.; Hanratty, L. D.; Hansen, A.; Harmanova, Z.; Harris, J. W.; Hartig, M.; Hasegan, D.; Hatzifotiadou, D.; Hayrapetyan, A. ; Heide, M.; Helstrup, H.; Herghelegiu, A.; Herrera Corral, G.; Herrmann, N.; Hetland, K. F.; Hicks, B.; Hille, P. T.; Hippolyte, B.; Horaguchi, T.; Hori, Y.; Hristov, P.; Hrivnacova, I.; Huang, M.; Huber, S.; Humanic, T. J.; Hwang, D. S. ; Ichou, R.; Ilkaev, R.; Ilkiv, I.; Inaba, M.; Incani, E.; Innocenti, P. G.; Innocenti, G. M.; Ippolitov, M.; Irfan, M.; Ivan, C.; Ivanov, A.; Ivanov, M.; Ivanov, V.; Ivanytskyi, O.; Jacholkowski, A.; Jacobs, P. M.; Jancurova, L.; Jangal, S.; Janik, M. A.; Janik, R.; Jayarathna, P. H. S. Y.; Jena, S.; Jimenez Bustamante, R. T.; Jirden, L.; Jones, P. G.; Jung, H.; Jung, W.; Jusko, A.; Kaidalov, A. B.; Kakoyan, V.; Kalcher, S.; Kalinak, P.; Kalisky, M.; Kalliokoski, T.; Kalweit, A.; Kanaki, K.; Kang, J. H.; Kaplin, V. ; Karasu Uysal, A.; Karavichev, O.; Karavicheva, T. ; Karpechev, E.; Kazantsev, A.; Kebschull, U.; Keidel, R.; Khan, M. M.; Khan, S. A.; Khan, P.; Khanzadeev, A.; Kharlov,

Y.; Kileng, B.; Kim, S. ; Kim, D. W.; Kim, J. H.; Kim, J. S.; Kim, M.; Kim, S. H.; Kim, T.; Kim, B.; Kim, D. J.; Kirsch, S.; Kisel, I.; Kiselev, S.; Kisiel, A.; Klay, J. L.; Klein, J.; Klein-Bösing, C.; Kliemant, M.; Kluge, A.; Knichel, M. L.; Koch, K. ; Köhler, M. K.; Kolojvari, A.; Kondratiev, V.; Kondratyeva, N.; Konevskikh, A.; Kottachchi Kankanamge Don, C.; Kour, R.; Kowalski, M.; Kox, S.; Koyithatta Meethaleveedu, G.; Kral, J.; Kralik, I. ; Kramer, F.; Kraus, I.; Krawutschke, T.; Kretz, M.; Krivda, M.; Krizek, F.; Krus, M.; Kryshen, E.; Krzewicki, M.; Kucheriaev, Y.; Kuhn, C.; Kuijer, P. G.; Kurashvili, P.; Kurepin, A. B.; Kurepin, A.; Kuryakin, A.; Kushpil, V.; Kushpil, S. ; Kvaerno, H.; Kweon, M. J.; Kwon, Y.; Ladron de Guevara, P.; Lakomov, I.; Langoy, R.; Lara, C.; Lardeux, A.; La Rocca, P.; Larsen, D. T.; Lazzeroni, C.; Lea, R.; Le Bornec, Y.; Lee, S. C. ; Lee, K. S.; Lefevre, F.; Lehnert, J.; Leistam, L.; Lenhardt, M.; Lenti, V.; Leon, H.; Leon Monzon, I.; Leon Vargas, H.; Levai, P.; Li, X. ; Lien, J.; Lietava, R.; Lindal, S.; Lindenstruth, V.; Lippmann, C.; Lisa, M. A.; Liu, L.; Loenne, P. I.; Loggins, V. R.; Loginov, V.; Lohn, S.; Lohner, D.; Loizides, C.; Loo, K. K.; Lopez, X.; Lopez Torres, E.; Lovhoiden, G.; Lu, X.-G.; Luettig, P.; Lunardon, M.; Luo, J.; Luparello, G.; Luquin, L.; Luzzi, C.; Ma, R.; Ma, K.; Madagodahettige-Don, D. M.; Maevskaya, A.; Mager, M.; Mahapatra, D. P.; Maire, A.; Malaev, M. ; Maldonado Cervantes, I.; Malinina, L.; MalKevich, D.; Malzacher, P.; Mamonov, A.; Manceau, L.; Mangotra, L.; Manko, V.; Manso, F.; Manzari, V.; Mao, Y.; Marchisone, M.; Mares, J. ; Margagliotti, G. V.; Margotti, A.; Marin, Ana; Markert, C.; Martashvili, I.; Martinengo, P.; Martinez, M. I.; Martinez Davalos, A.; Martinez Garcia, G.; Martynov, Y.; Mas, A.; Masciocchi, S. ; Masera, M.; Masoni, A.; Massacrier, L.; Mastromarco, M.; Mastroserio, A.; Matthews, Z. L.; Matyja, A.; Mayani, D.; Mayer, C.; Mazzoni, M. A. ; Meddi, F.; Menchaca-Rocha, A.; Mercado Perez, J. ; Meres, M.; Miake, Y.; Michalon, A.; Midori, J. ; Milano, L.; Milosevic, J.; Mischke, A.; Mishra, A. N.; Mikowiec, D.; Mitu, C.; Mlynarz, J.; Mohanty, A. K.; Mohanty, B.; Molnar, L.; Montano Zetina, L.; Monteno, M.; Montes, E.; Moon, T.; Morando, M.; Moreira De Godoy, D. A.; Moretto, S.; Morsch, A.; Muccifora, V.; Mudnic, E.; Muhuri, S. ; Müller, H.; Munhoz, M. G.; Musa, L.; Musso, A. ; Nandi, B. K.; Nania, R.; Nappi, E.; Nattrass, C.; Naumov, N. P.; Navin, S.; Nayak, T. K.; Nazarenko, S.; Nazarov, G.; Nedosekin, A.; Nicassio, M.; Nielsen, B. S.; Niida, T.; Nikolaev, S.; Nikolic, V.; Nikulin, V.; Nikulin, S.; Nilsen, B. S.; Nilsson, M. S.; Noferini, F.; Nomokonov, P.; Nooren, G.; Novitzky, N.; Nyanin, A. ; Nyatha, A.; Nygaard, C.; Nystrand, J.; Obayashi, H.; Ochirov, A.; Oeschler, H.; Oh, S. K. ; Oleniacz, J.; Oppedisano, C.; Ortiz Velasquez, A. ; Ortona, G.; Oskarsson, A.; Ostrowski, P.; Otterlund, I.; Otwinowski, J.; Ovrebekk, G.; Oyama, K.; Ozawa, K.; Pachmayer, Y.; Pachr, M.; Padilla, F.; Pagano, P.; Paic, G.; Painke, F.; Pajares, C.; Pal, S.; Pal, S. K.; Palaha, A.; Palmeri, A.; Papikyan, V.; Pappalardo, G. S.; Park, W. J.; Passfeld, A.; Pastircak, B.; Patalakha, D. I.; Paticchio, V.; Pavlinov, A.; Pawlak, T.; Peitzmann, T.; Perales, M.; Pereira De Oliveira Filho, E.; Peresunko, D.; Perez Lara, C. E.; Perez Lezama, E.; Perini, D.; Perrino, D.; Peryt, W.; Pesci, A.; Peskov, V.; Pestov, Y.; Petracek, V. ; Petran, M.; Petris, M.; Petrov, P.; Petrovici, M.; Petta, C.; Piano, S.; Piccotti, A.; Pikna, M.; Pillot, P.; Pinazza, O.; Pinsky, L.; Pitz, N.; Piuz, F.; Piyarathna, D. B.; Ploskon, M.; Pluta, J.; Pocheptsov, T.; Pochybova, S.; Podesta-Lerma, P. L. M.; Poghosyan, M. G.; Polak, K. ; Polichtchouk, B.; Pop, A.; Porteboeuf-Houssais, S. ; Pospisil, V.; Potukuchi, B.; Prasad, S. K.; Preghenella, R.; Prino, F.; Pruneau, C. A.; Pshenichnov, I.; Puddu, G.; Pulvirenti, A.; Punin, V.; Putis, M.; Putschke, J.; Quercigh, E.; Qvigstad, H.; Rachevski, A.; Rademakers, A.; Radomski, S.; Räihä T. S.; Rak, J.; Rakotozafindrabe, A.; Ramello, L.; Ramirez Reyes, A. ; Raniwala, S.; Raniwala, R.; Räsänen, S. S.; Rascanu, B. T.; Rathee, D.; Read, K. F.; Real, J. S.; Redlich, K.; Reichelt, P.; Reicher, M.; Renfordt, R.; Reolon, A. R.; Reshetin, A.; Rettig, F.; Revol, J.-P.; Reygers, K.; Ricaud, H.; Riccati, L.; Ricci, R. A.; Richter, M.; Riedler, P. ; Riegler, W.; Riggi, F.; Rodriguez Cahuantzi, M. ; Rohr, D.; Röhrich, D.; Romita, R.; Ronchetti, F.; Rosnet, P.; Rossegger, S.; Rossi, A.; Roukoutakis, F.; Roy, C.; Roy, P.; Rubio Montero, A. J.; Rui, R.; Ryabinkin, E.; Rybicki, A.; Sadovsky, S.; Safarik, K.; Sahu, P. K.; Saini, J.; Sakaguchi, H.; Sakai, S.; Sakata, D.; Salgado, C. A.; Sambyal, S.; Samsonov, V.; Sanchez Castro, X.; Sandor, L.; Sandoval, A.; Sano, M. ; Sano, S.; Santo, R.; Santoro, R.; Sarkamo, J. ; Scapparone, E.; Scarlassara, F.; Scharenberg, R. P.; Schiaua, C.; Schicker, R.; Schmidt, H. R.; Schmidt, C.; Schreiner, S.; Schuchmann, S.; Schukraft, J.; Schutz, Y.; Schwarz, K.; Schweda, K. ; Scioli, G.; Scomparin, E.; Scott, R.; Scott, P. A.; Segato, G.; Selyuzhenkov, I.; Senyukov, S.; Seo, J.; Serci, S.; Serradilla, E.; Sevcenco, A. ; Sgura, I.; Shabratova, G.; Shahoyan, R.; Sharma, N.; Sharma, S.; Shigaki, K.; Shimomura, M. ; Shtejer, K.; Sibiriak, Y.; Siciliano, M.; Sicking, E.; Siddhanta, S.; Siemiarczuk, T.; Silvermyr, D.; Simonetti, G.; Singaraju, R.; Singh, R.; Singha, S.; Sinha, T.; Sinha, B. C.; Sitar, B.; Sitta, M.; Skaali, T. B.; Skjerdal, K.; Smakal, R.; Smirnov, N.; Snellings, R.; Sogaard, C.; Soltz, R.; Son, H.; Song, J.; Song, M.; Soos, C.; Soramel, F.; Spyropoulou-Stassinaki, M.; Srivastava, B. K.; Stachel, J.; Stan, I.; Stan, I. ; Stefanek, G.; Stefanini, G.; Steinbeck, T.; Steinpreis, M.; Stenlund, E.; Steyn, G.; Stocco, D. ; Stolpovskiy, M.; Strmen, P.; Suaide, A. A. P.; Subieta Vasquez, M. A.; Sugitate, T.; Suire, C.; Sukhorukov, M.; Sultanov, R.; Sumbera, M.; Susa, T.; Szanto de Toledo, A.; Szarka, I.; Szostak, A. ; Tagridis, C.; Takahashi, J.; Tapia Takaki, J. D. ; Tauro, A.; Tejeda Munoz, G.; Telesca, A.; Terrevoli, C.; Thäder, J.; Thomas, J. H.; Thomas, D.; Tieulent, R.; Timmins, A. R.; Tlusty, D.; Toia, A.; Torii, H.; Toscano, L.; Tosello, F.; Traczyk, T.; Truesdale, D.; Trzaska, W. H.; Tsuji, T.; Tumkin, A.; Turrisi, R.; Tveter, T. S.; Ulery, J.; Ullaland, K.; Ulrich, J.; Uras, A.; Urban, J.; Urciuoli, G. M.; Usai, G. L.; Vajzer, M.; Vala, M.; Valencia Palomo, L.; Vallero, S.; van der Kolk, N.; Vande Vyvre, P.; van Leeuwen, M.; Vannucci, L.; Vargas, A.; Varma, R.; Vasileiou, M. ; Vasiliev, A.; Vechernin, V.; Veldhoen, M.; Venaruzzo, M.; Vercellin, E.; Vergara, S.; Vernekohl, D. C.; Vernet, R.; Verweij, M.; Vickovic, L.; Viesti, G.; Vikhlyantsev, O.; Vilakazi, Z.; Villalobos Baillie, O.; Vinogradov, A. ; Vinogradov, L.; Vinogradov, Y.; Virgili, T.; Viyogi, Y. P.; Vodopyanov, A.; Voloshin, K.; Voloshin, S.; Volpe, G.; von Haller, B.; Vranic, D. ; Vrlakova, J.; Vulpescu, B.; Vyushin, A.; Wagner, V.; Wagner, B.; Wan, R.; Wang, Y.; Wang, D.; Wang, Y.; Wang, M.; Watanabe, K.; Wessels, J. P.; Westerhoff, U.; Wiechula, J.; Wikne, J.; Wilde, M.; Wilk, G.; Wilk, A.; Williams, M. C. S. ; Windelband, B.; Xaplanteris Karampatsos, L.; Yang, H.; Yano, S.; Yasnopolskiy, S.; Yi, J.; Yin, Z. ; Yokoyama, H.; Yoo, I.-K.; Yoon, J.; Yu, W.; Yuan, X.; Yushmanov, I.; Zach, C.; Zampolli, C.; Zaporozhets, S.; Zarochentsev, A.; Zavada, P.; Zaviyalov, N.; Zbroszczyk, H.; Zelnicek, P.; Zgura, I.; Zhalov, M.; Zhang, X.; Zhou, F.; Zhou, D. ; Zhou, Y.; Zhu, X.; Zichichi, A.; Zimmermann, A. ; Zinovjev, G.; Zoccarato, Y.; Zynovyev, M.: **J/ψ Polarization in pp Collisions at $\sqrt{s} = 7$TeV.** *Physical review letters* 108: 082001, 2012. DOI:10.1103/PhysRevLett.108.082001

WOS-PHN-5 Abelev, B.; Abrahantes Quintana, A.; Adamova, D.; Adare, A.M.; Aggarwal, M.M.; Aglieri Rinella, G.; Agocs, A.G.; Agostinelli, A.; Aguilar Salazar, S.; Ahammed, Z.; Ahmad, N.; Ahmad Masoodi, A.; Ahn, S.U.; Akindinov, A.; Aleksandrov, D.; Alessandro, B.; Alfaro Molina, R.; Alici, A.; Alkin, A.; Almaraz Avina, E.; Alt, T.; Altini, V.; Altinpinar, S.; Altsybeev, I.; Andrei, C.; Andronic, A.; Anguelov, V.; Anson, C.; Anticic, T.; Antinori, F.; Antonioli, P.; Aphecetche, L.; Appelshäuser, H.; Arbor, N.; Arcelli, S.; Arend, A.; Armesto, N.; Arnaldi, R.; Aronsson, T.; Arsene, I.C.; Arslandok, M.; Asryan, A.; Augustinus, A.; Averbeck, R.; Awes, T.C.; Äystö J.; Azmi, M.D.; Bach, M.; Badala, A.; Baek, Y.W.; Bailhache, R.; Bala, R.; Baldini Ferroli, R. ; Baldisseri, A.; Baldit, A.; Baltasar Dos Santos Pedrosa, F.; Ban, J.; Baral, R.C.; Barbera, R.; Barile, F.; Barnaföldi, G.G.; Barnby, L.S.; Barret, V.; Bartke, J.; Basile, M.; Bastid, N.; Bathen, B.; Batigne, G.; Batyunya, B.; Baumann, C. ; Bearden, I.G.; Beck, H.; Belikov, I.; Bellini, F.; Bellwied, R.; Belmont-Moreno, E.; Beole, S.; Berceanu, I.; Bercuci, A.; Berdnikov, Y.; Berenyi, D.; Bergmann, C.; Berzano, D.; Betev, L.; Bhasin, A.; Bhati, A.K.; Bianchi, L.; Bianchi, N. ; Bianchin, C.; Bielcik, J.; Bielcikova, J.; Bilandzic, A.; Blanco, F.; Blanco, F.; Blau, D.; Blume, C.; Boccioli, M.; Bock, N.; Bogdanov, A.; Boggild, H.; Bogolyubsky, M.; Boldizsar, L.; Bombara, M.; Book, J.; Borel, H.; Borissov, A.; Bortolin, C.; Bose, S.; Boss, F.; Botje, M.; Böttger, S.; Boyer, B.; Braun-Munzinger, P.; Bregant, M.; Breitner, T.; Broz, M.; Brun, R.; Bruna, E.; Bruno, G.E.; Budnikov, D.; Buesching, H. ; Bufalino, S.; Bugaiev, K.; Busch, O.; Buthelezi, Z.; Caffarri, D.; Cai, X.; Caines, H. ; Calvo Villar, E.; Camerini, P.; Canoa Roman, V. ; Cara Romeo, G.; Carena, W.; Carena, F.; Carlin Filho, N.; Carminati, F.; Carrillo Montoya, C.A.; Casanova Diaz, A.; Caselle, M.; Castillo Castellanos, J.; Castillo Hernandez, J.F.; Casula, E.A.R.; Catanescu, V.; Cavicchioli, C.; Cepila, J.; Cerello, P.; Chang, B.; Chapeland, S.; Charvet, J.L.; Chattopadhyay, S.; Chattopadhyay, S.; Cherney, M.; Cheshkov, C.; Cheynis, B.; Chiavassa, E.; Chibante Barroso, V.; Chinellato, D.D.; Chochula, P.; Chojnacki, M.; Christakoglou, P.; Christensen, C.H.; Christiansen, P.; Chujo, T.; Chung, S.U.; Cicalo, C.; Cifarelli, L.; Cindolo, F. ; Cleymans, J.; Coccetti, F.; Coffin, J.-P.; Colamaria, F.; Colella, D.; Conesa Balbastre, G.; Conesa del Valle, Z.; Constantin, P.; Contin, G.; Contreras, J.G.; Cormier, T.M.; Corrales Morales, Y. ; Cortese, P.; Cortes Maldonado, I.; Cosentino, M.R.; Costa, F.; Cotallo, M.E.; Crescio, E.; Crochet, P.; Cruz Alaniz, E.; Cuautle, E.; Cunqueiro, L.; Dainese, A.; Dalsgaard, H.H.; Danu, A.; Das, K.; Das, D.; Das, I.; Dash, S.; Dash, A.; De, S.; De Azevedo Moregula, A.; de Barros, G.O.V.; De Caro, A.; de Cataldo, G.; de Cuveland, J.; De Falco, A.; De Gruttola, D.; Delagrange, H.; Del Castillo Sanchez, E.; Deloff, A. ; Demanov, V.; De Marco, N.; Denes, E.; De Pasquale, S.; Deppman, A.; D Erasmo, G.; de Rooij, R.; Di Bari, D.; Dietel, T.; Di Giglio, C.; Di Liberto, S.; Di Mauro, A.; Di Nezza, P.; Divia, R. ; Djuvsland, O.; Dobrin, A.; Dobrowolski, T.; Dominguez, I.; Dönigus, B.; Dordic, O.; Driga, O. ; Dubey, A.K.; Ducroux, L.; Dupieux, P.; Dutta Majumdar, A.K.; Dutta Majumdar, M.R.; Elia, D.; Emschermann, D.; Engel, H.; Erdal, H.A.; Espagnon, B.; Estienne, M.; Esumi, S.; Evans, D.; Eyyubova, G.; Fabris, D.; Faivre, J.; Falchieri, D. ; Fantoni, A.; Fasel, M.; Fearick, R.; Fedunov, A.; Fehlker, D.; Feldkamp, L.; Felea, D.; Feofilov, G.; Fernandez Tellez, A.; Ferretti, A.; Ferretti, R.; Figiel, J.; Figueredo, M.A.S.; Filchagin, S.; Fini, R.; Finogeev, D.; Fionda, F.M. ; Fiore, E.M.; Floris, M.; Foertsch, S.; Foka, P. ; Fokin, S.; Fragiacomo, E.; Fragkiadakis, M.; Frankenfeld, U.; Fuchs, U.; Furget, C.; Fusco Girard, M.; Gaardhoje, J.J.; Gagliardi, M.; Gago, A.; Gallio, M.; Gangadharan, D.R.; Ganoti, P.; Garabatos, C.; Garcia-Solis, E.; Garishvili, I.; Gerhard, J.; Germain, M.; Geuna, C.; Gheata, M.; Gheata, A.; Ghidini, B.; Ghosh, P.; Gianotti, P. ; Girard, M.R.; Giubellino, P.; Gladysz-Dziadus, E. ; Glässel, P.; Gomez, R.; Ferreiro, E.G.; Gonzalez-Trueba, L.H.; Gonzalez-Zamora, P.; Gorbunov, S.; Goswami, A.; Gotovac, S.; Grabski, V. ; Graczykowski, L.K.; Grajcarek, R.; Grelli, A.; Grigoras, C.; Grigoras, A.; Grigoriev, V.; Grigoryan, A.; Grigoryan, S.; Grinyov, B.; Grion, N.; Gros, P.; Grosse-Oetringhaus, J.F.; Grossiord, J.-Y.; Grosso, R.; Guber, F.; Guernane, R.; Guerra Gutierrez, C.; Guerzoni, B.; Guilbaud, M.; Gulbrandsen, K.; Gunji, T.; Gupta, A.; Gupta, R. ; Gutbrod, H.; Haaland, O.; Hadjidakis, C.; Haiduc, M.; Hamagaki, H.; Hamar, G.; Han, B.H.; Hanratty, L.D.; Hansen, A.; Harmanova, Z.; Harris, J.W.; Hartig, M.; Hasegan, D.; Hatzifotiadou, D. ; Hayrapetyan, A.; Heide, M.; Helstrup, H.; Herghelegiu, A.; Herrera Corral, G.; Herrmann, N.; Hetland, K.F.; Hicks, B.; Hille, P.T.; Hippolyte, B.; Horaguchi, T.; Hori, Y.; Hristov, P.; Hrivnacova, I.; Huang, M.; Huber, S.; Humanic, T.J.; Hwang, D.S.; Ichou, R.; Ilkaev, R.; Ilkiv, I.; Inaba, M.; Incani, E.; Innocenti, G.M.; Innocenti, P.G.; Ippolitov, M.; Irfan, M.; Ivan, C. ; Ivanov, M.; Ivanov, A.; Ivanov, V.; Ivanytskyi, O.; Jacholkowski, A.; Jacobs, P.M.; Jancurova, L. ; Jang, H.J.; Jangal, S.; Janik, R.; Janik, M.A. ; Jayarathna, P.H.S.Y.; Jena, S.; Jimenez Bustamante, R.T.; Jirden, L.; Jones, P.G.; Jung, W. ; Jung, H.; Jusko, A.; Kaidalov, A.B.; Kakoyan, V.; Kalcher, S.; Kalinak, P.; Kalisky, M.; Kalliokoski, T.; Kalweit, A.; Kanaki, K.; Kang, J.H.; Kaplin, V.; Karasu Uysal, A.; Karavichev, O. ; Karavicheva, T.; Karpechev, E.; Kazantsev, A.; Kebschull, U.; Keidel, R.; Khan, M.M.; Khan, P.; Khan, S.A.; Khanzadeev, A.; Kharlov, Y.; Kileng, B. ; Kim, D.W.; Kim, M.; Kim, J.H.; Kim, S.H.; Kim, S.; Kim, B.; Kim, T.; Kim, D.J.; Kim, J.S. ; Kirsch, S.; Kisel, I.; Kiselev, S.; Kisiel, A. ; Klay, J.L.; Klein, J.; Klein-Bösing, C.; Kliemant, M.; Kluge, A.; Knichel, M.L.; Koch, K. ; Köhler, M.K.; Kolojvari, A.; Kondratiev, V.; Kondratyeva, N.; Konevskikh, A.; Korneev, A.; Kottachchi Kankanamge Don, C.; Kour, R.; Kowalski, M. ; Kox, S.; Koyithatta Meethaleveedu, G.; Kral, J. ; Kralik, I.; Kramer, F.; Kraus, I.; Krawutschke, T.; Kretz, M.; Krivda, M.; Krizek, F. ; Krus, M.; Kryshen, E.; Krzewicki, M.; Kucheriaev, Y.; Kuhn, C.; Kuijer, P.G.; Kurashvili, P.; Kurepin, A.B.; Kurepin, A.; Kuryakin, A.; Kushpil, V.; Kushpil, S.; Kvaerno, H.; Kweon, M.J. ; Kwon, Y.; Ladron de Guevara, P.; Lakomov, I.; Langoy, R.; Lara, C.; Lardeux, A.; La Rocca, P.; Lazzeroni, C.; Lea, R.; Le Bornec, Y.; Lee, K.S. ; Lee, S.C.; Lefevre, F.; Lehnert, J.; Leistam, L.; Lenhardt, M.; Lenti, V.; Leon, H.; Leon Monzon, I.; Leon Vargas, H.; Levai, P.; Li, X. ; Lien, J.; Lietava, R.; Lindal, S.; Lindenstruth, V.; Lippmann, C.; Lisa, M.A.; Liu, L. ; Loenne, P.I.; Loggins, V.R.; Loginov, V.; Lohn, S.; Lohner, D.; Loizides, C.; Loo, K.K.; Lopez, X.; Lopez Torres, E.; Lovhoiden, G.; Lu, X.-G. ; Luettig, P.; Lunardon, M.; Luo, J.; Luparello, G.; Luquin, L.; Luzzi, C.; Ma, R.; Ma, K.; Madagodahettige-Don, D.M.; Maevskaya, A.; Mager, M. ; Mahapatra, D.P.; Maire, A.; Malaev, M.; Maldonado Cervantes, I.; Malinina, L.; MalKevich, D. ; Malzacher, P.; Mamonov, A.; Manceau, L.; Mangotra, L.; Manko, V.; Manso, F.; Manzari, V.; Mao, Y.; Marchisone, M.; Mares, J.; Margagliotti, G.V.; Margotti, A.; Marin, Ana; Markert, C.; Martashvili, I.; Martinengo, P.; Martinez, M.I.; Martinez Davalos, A.; Martinez Garcia, G.; Martynov, Y.; Mas, A.; Masciocchi, S.; Masera, M. ; Masoni, A.; Massacrier, L.; Mastromarco, M.; Mastroserio, A.; Matthews, Z.L.; Matyja, A.; Mayani, D.; Mayer, C.; Mazer, J.; Mazzoni, M.A.; Meddi, F.;

Menchaca-Rocha, A.; Mercado Perez, J.; Meres, M.; Miake, Y.; Michalon, A.; Midori, J.; Milano, L.; Milosevic, J.; Mischke, A.; Mishra, A.N.; Mikowiec, D.; Mitu, C.; Mlynarz, J.; Mohanty, A.K.; Mohanty, B.; Molnar, L.; Montano Zetina, L.; Monteno, M.; Montes, E.; Moon, T.; Morando, M.; Moreira De Godoy, D.A.; Moretto, S.; Morsch, A.; Muccifora, V.; Mudnic, E.; Muhuri, S. ; Müller, H.; Munhoz, M.G.; Musa, L.; Musso, A. ; Nandi, B.K.; Nania, R.; Nappi, E.; Nattrass, C. ; Naumov, N.P.; Navin, S.; Nayak, T.K.; Nazarenko, S.; Nazarov, G.; Nedosekin, A.; Nicassio, M.; Nielsen, B.S.; Niida, T.; Nikolaev, S.; Nikolic, V.; Nikulin, S.; Nikulin, V.; Nilsen, B.S.; Nilsson, M.S.; Noferini, F.; Nomokonov, P.; Nooren, G.; Novitzky, N.; Nyanin, A. ; Nyatha, A.; Nygaard, C.; Nystrand, J.; Obayashi, H.; Ochirov, A.; Oeschler, H.; Oh, S.K. ; Oh, S.; Oleniacz, J.; Oppedisano, C.; Ortiz Velasquez, A.; Ortona, G.; Oskarsson, A.; Ostrowski, P.; Otterlund, I.; Otwinowski, J.; Oyama, K.; Ozawa, K.; Pachmayer, Y.; Pachr, M.; Padilla, F.; Pagano, P.; Paic, G.; Painke, F.; Pajares, C.; Pal, S.; Pal, S.K.; Palaha, A.; Palmeri, A.; Papikyan, V.; Pappalardo, G.S.; Park, W.J.; Passfeld, A.; Pastircak, B.; Patalakha, D.I.; Paticchio, V.; Pavlinov, A.; Pawlak, T.; Peitzmann, T.; Perales, M.; Pereira De Oliveira Filho, E.; Peresunko, D.; Perez Lara, C.E.; Perez Lezama, E.; Perini, D.; Perrino, D.; Peryt, W.; Pesci, A.; Peskov, V.; Pestov, Y.; Petracek, V.; Petran, M.; Petris, M.; Petrov, P.; Petrovici, M. ; Petta, C.; Piano, S.; Piccotti, A.; Pikna, M. ; Pillot, P.; Pinazza, O.; Pinsky, L.; Pitz, N. ; Piuz, F.; Piyarathna, D.B.; Ploskon, M.; Pluta, J.; Pocheptsov, T.; Pochybova, S.; Podesta-Lerma, P.L.M.; Poghosyan, M.G.; Polak, K.; Polichtchouk, B.; Pop, A.; Porteboeuf-Houssais, S.; Pospisil, V.; Potukuchi, B.; Prasad, S.K.; Preghenella, R.; Prino, F.; Pruneau, C.A.; Pshenichnov, I.; Puchagin, S.; Puddu, G.; Pulvirenti, A.; Punin, V.; Putis, M.; Putschke, J. ; Quercigh, E.; Qvigstad, H.; Rachevski, A.; Rademakers, A.; Radomski, S.; Räihä T.S.; Rak, J.; Rakotozafindrabe, A.; Ramello, L.; Ramirez Reyes, A.; Raniwala, R.; Raniwala, S.; Räsänen, S.S.; Rascanu, B.T.; Rathee, D.; Read, K.F.; Real, J.S.; Redlich, K.; Reichelt, P.; Reicher, M. ; Renfordt, R.; Reolon, A.R.; Reshetin, A.; Rettig, F.; Revol, J.-P.; Reygers, K.; Riccati, L. ; Ricci, R.A.; Richter, M.; Riedler, P.; Riegler, W.; Riggi, F.; Rodriguez Cahuantzi, M.; Rohr, D. ; Röhrich, D.; Romita, R.; Ronchetti, F.; Rosnet, P.; Rossegger, S.; Rossi, A.; Roukoutakis, F.; Roy, C.; Roy, P.; Rubio Montero, A.J.; Rui, R.; Ryabinkin, E.; Rybicki, A.; Sadovsky, S.; Safarik, K.; Sahu, P.K.; Saini, J.; Sakaguchi, H.; Sakai, S.; Sakata, D.; Salgado, C.A.; Sambyal, S.; Samsonov, V.; Sanchez Castro, X.; Sandor, L.; Sandoval, A.; Sano, M.; Sano, S.; Santo, R.; Santoro, R.; Sarkamo, J.; Scapparone, E. ; Scarlassara, F.; Scharenberg, R.P.; Schiaua, C. ; Schicker, R.; Schmidt, C.; Schmidt, H.R.; Schreiner, S.; Schuchmann, S.; Schukraft, J.; Schutz, Y.; Schwarz, K.; Schweda, K.; Scioli, G. ; Scomparin, E.; Scott, P.A.; Scott, R.; Segato, G.; Selyuzhenkov, I.; Senyukov, S.; Seo, J.; Serci, S.; Serradilla, E.; Sevcenco, A.; Sgura, I. ; Shabetai, A.; Shabratova, G.; Shahoyan, R.; Sharma, N.; Sharma, S.; Shigaki, K.; Shimomura, M. ; Shtejer, K.; Sibiriak, Y.; Siciliano, M.; Sicking, E.; Siddhanta, S.; Siemiarczuk, T.; Silvermyr, D.; Simonetti, G.; Singaraju, R.; Singh, R.; Singha, S.; Sinha, B.C.; Sinha, T.; Sitar, B.; Sitta, M.; Skaali, T.B.; Skjerdal, K.; Smakal, R.; Smirnov, N.; Snellings, R.; Sogaard, C.; Soltz, R.; Son, H.; Song, M.; Song, J.; Soos, C.; Soramel, F.; Sputowska, I.; Spyropoulou-Stassinaki, M.; Srivastava, B.K.; Stachel, J.; Stan, I.; Stan, I.; Stefanek, G.; Stefanini, G.; Steinbeck, T.; Steinpreis, M.; Stenlund, E.; Steyn, G.; Stocco, D.; Stolpovskiy, M.; Strabykin, K.; Strmen, P.; Suaide, A.A.P.; Subieta Vasquez, M.A.; Sugitate, T.; Suire, C.; Sukhorukov, M.; Sultanov, R.; Sumbera, M.; Susa, T.; Szanto de Toledo, A.; Szarka, I.; Szostak, A.; Tagridis, C. ; Takahashi, J.; Tapia Takaki, J.D.; Tauro, A.; Tejeda Munoz, G.; Telesca, A.; Terrevoli, C.; Thäder, J.; Thomas, D.; Thomas, J.H.; Tieulent, R. ; Timmins, A.R.; Tlusty, D.; Toia, A.; Torii, H. ; Toscano, L.; Tosello, F.; Traczyk, T.; Truesdale, D.; Trzaska, W.H.; Tsuji, T.; Tumkin, A. ; Turrisi, R.; Tveter, T.S.; Ulery, J.; Ullaland, K.; Ulrich, J.; Uras, A.; Urban, J.; Urciuoli, G.M.; Usai, G.L.; Vajzer, M.; Vala, M.; Valencia Palomo, L.; Vallero, S.; van der Kolk, N.; Vande Vyvre, P.; van Leeuwen, M.; Vannucci, L.; Vargas, A.; Varma, R.; Vasileiou, M.; Vasiliev, A.; Vechernin, V.; Veldhoen, M.; Venaruzzo, M.; Vercellin, E.; Vergara, S.; Vernekohl, D.C.; Vernet, R.; Verweij, M.; Vickovic, L.; Viesti, G. ; Vikhlyantsev, O.; Vilakazi, Z.; Villalobos Baillie, O.; Vinogradov, L.; Vinogradov, A.; Vinogradov, Y.; Virgili, T.; Viyogi, Y.P.; Vodopyanov, A.; Voloshin, S.; Voloshin, K.; Volpe, G.; von Haller, B.; Vranic, D.; Ovrebekk, G.; Vrlakova, J.; Vulpescu, B.; Vyushin, A.; Wagner, V.; Wagner, B.; Wan, R.; Wang, Y.; Wang, M.; Wang, Y.; Wang, D.; Watanabe, K.; Wessels, J.P.; Westerhoff, U.; Wiechula, J.; Wikne, J.; Wilde, M. ; Wilk, A.; Wilk, G.; Williams, M.C.S.; Windelband, B.; Xaplanteris Karampatsos, L.; Yang, S. ; Yang, H.; Yano, S.; Yasnopolskiy, S.; Yi, J. ; Yin, Z.; Yokoyama, H.; Yoo, I.-K.; Yoon, J.; Yu, W.; Yuan, X.; Yushmanov, I.; Zach, C.; Zampolli, C.; Zaporozhets, S.; Zarochentsev, A.; Zavada, P.; Zaviyalov, N.; Zbroszczyk, H.; Zelnicek, P.; Zgura, I.; Zhalov, M.; Zhang, X.; Zhou, D.; Zhou, Y.; Zhou, F.; Zhu, X.; Zichichi, A.; Zimmermann, A.; Zinovjev, G.; Zoccarato, Y.; Zynovyev, M.: **Light vector meson production in pp collisions at $\sqrt{s} = 7$ TeV.** *Physics letters / B* 710: 557 - 568, 2012. DOI:10.1016/j.physletb.2012.03.038

WOS-PHN-6 Abelev, B.; Abrahantes Quintana, A.; Adamova, D.; Adare, A.M.; Aggarwal, M.M.; Aglieri Rinella, G.; Agocs, A.G.; Agostinelli, A.; Aguilar Salazar, S.; Ahammed, Z.; Ahmad, N.; Ahmad Masoodi, A.; Ahn, S.U.; Akindinov, A.; Aleksandrov, D.; Alessandro, B.; Alfaro Molina, R.; Alici, A.; Alkin, A.; Almaraz Avina, E.; Alt, T.; Altini, V.; Altinpinar, S.; Altsybeev, I.; Andrei, C.; Andronic, A.; Anguelov, V.; Anson, C.; Anticic, T.; Antinori, F.; Antonioli, P.; Aphecetche, L.; Appelshäuser, H.; Arbor, N.; Arcelli, S.; Arend, A.; Armesto, N.; Arnaldi, R.; Aronsson, T.; Arsene, I.C.; Arslandok, M.; Asryan, A.; Augustinus, A.; Averbeck, R.; Awes, T.C.; Äystö J.; Azmi, M.D.; Bach, M.; Badala, A.; Baek, Y.W.; Bailhache, R.; Bala, R.; Baldini Ferroli, R. ; Baldisseri, A.; Baldit, A.; Baltasar Dos Santos Pedrosa, F.; Ban, J.; Baral, R.C.; Barbera, R.; Barile, F.; Barnaföldi, G.G.; Barnby, L.S.; Barret, V.; Bartke, J.; Basile, M.; Bastid, N.; Bathen, B.; Batigne, G.; Batyunya, B.; Baumann, C. ; Bearden, I.G.; Beck, H.; Belikov, I.; Bellini, F.; Bellwied, R.; Belmont-Moreno, E.; Beole, S.; Berceanu, I.; Bercuci, A.; Berdnikov, Y.; Berenyi, D.; Bergmann, C.; Berzano, D.; Betev, L.; Bhasin, A.; Bhati, A.K.; Bianchi, N.; Bianchi, L. ; Bianchin, C.; Bielcik, J.; Bielcikova, J.; Bilandzic, A.; Blanco, F.; Blanco, F.; Blau, D.; Blume, C.; Boccioli, M.; Bock, F.; Bock, N.; Bogdanov, A.; Boggild, H.; Bogolyubsky, M.; Boldizsar, L.; Bombara, M.; Book, J.; Borel, H. ; Borissov, A.; Bortolin, C.; Bose, S.; Boss, F.; Botje, M.; Böttger, S.; Boyer, B.; Braun-Munzinger, P.; Bregant, M.; Breitner, T.; Broz, M.; Brun, R.; Bruna, E.; Bruno, G.E.; Budnikov, D.; Buesching, H.; Bufalino, S.; Bugaiev, K.; Busch, O.; Buthelezi, Z.; Caffarri, D.; Cai, X.; Caines, H.; Calvo Villar, E.; Camerini, P.; Canoa Roman, V.; Cara Romeo, G.; Carena, F.; Carena, W.; Carlin Filho, N.; Carminati, F.; Carrillo Montoya, C.A.; Casanova Diaz, A.; Caselle, M.;

Castillo Castellanos, J.; Castillo Hernandez, J.F. ; Casula, E.A.R.; Catanescu, V.; Cavicchioli, C.; Cepila, J.; Cerello, P.; Chang, B.; Chapeland, S. ; Charvet, J.L.; Chattopadhyay, S.; Chattopadhyay, S.; Cherney, M.; Cheshkov, C.; Cheynis, B.; Chiavassa, E.; Chibante Barroso, V.; Chinellato, D.D. ; Chochula, P.; Chojnacki, M.; Christakoglou, P.; Christensen, C.H.; Christiansen, P.; Chujo, T.; Chung, S.U.; Cicalo, C.; Cifarelli, L.; Cindolo, F. ; Cleymans, J.; Coccetti, F.; Coffin, J.-P.; Colamaria, F.; Colella, D.; Conesa Balbastre, G.; Conesa del Valle, Z.; Constantin, P.; Contin, G.; Contreras, J.G.; Cormier, T.M.; Corrales Morales, Y. ; Cortese, P.; Cortes Maldonado, I.; Cosentino, M.R.; Costa, F.; Cotallo, M.E.; Crescio, E.; Crochet, P.; Cruz Alaniz, E.; Cuautle, E.; Cunqueiro, L.; Dainese, A.; Dalsgaard, H.H.; Danu, A.; Das, I.; Das, K.; Das, D.; Dash, A.; Dash, S.; De, S.; De Azevedo Moregula, A.; de Barros, G.O.V.; De Caro, A.; de Cataldo, G.; de Cuveland, J.; De Falco, A.; De Gruttola, D.; Delagrange, H.; Del Castillo Sanchez, E.; Deloff, A. ; Demanov, V.; De Marco, N.; Denes, E.; De Pasquale, S.; Deppman, A.; D Erasmo, G.; de Rooij, R.; Di Bari, D.; Dietel, T.; Di Giglio, C.; Di Liberto, S.; Di Mauro, A.; Di Nezza, P.; Divia, R. ; Djuvsland, O.; Dobrin, A.; Dobrowolski, T.; Dominguez, I.; Dönigus, B.; Dordic, O.; Driga, O. ; Dubey, A.K.; Ducroux, L.; Dupieux, P.; Dutta Majumdar, M.R.; Dutta Majumdar, A.K.; Elia, D.; Emschermann, D.; Engel, H.; Erdal, H.A.; Espagnon, B.; Estienne, M.; Esumi, S.; Evans, D.; Eyyubova, G.; Fabris, D.; Faivre, J.; Falchieri, D. ; Fantoni, A.; Fasel, M.; Fearick, R.; Fedunov, A.; Fehlker, D.; Feldkamp, L.; Felea, D.; Feofilov, G.; Fernandez Tellez, A.; Ferretti, A.; Ferretti, R.; Figiel, J.; Figueredo, M.A.S.; Filchagin, S.; Fini, R.; Finogeev, D.; Fionda, F.M. ; Fiore, E.M.; Floris, M.; Foertsch, S.; Foka, P. ; Fokin, S.; Fragiacomo, E.; Fragkiadakis, M.; Frankenfeld, U.; Fuchs, U.; Furget, C.; Fusco Girard, M.; Gaardhoje, J.J.; Gagliardi, M.; Gago, A.; Gallio, M.; Gangadharan, D.R.; Ganoti, P.; Garabatos, C.; Garcia-Solis, E.; Garishvili, I.; Gerhard, J.; Germain, M.; Geuna, C.; Gheata, A.; Gheata, M.; Ghidini, B.; Ghosh, P.; Gianotti, P. ; Girard, M.R.; Giubellino, P.; Gladysz-Dziadus, E. ; Glässel, P.; Gomez, R.; Ferreiro, E.G.; Gonzalez-Trueba, L.H.; Gonzalez-Zamora, P.; Gorbunov, S.; Goswami, A.; Gotovac, S.; Grabski, V. ; Graczykowski, L.K.; Grajcarek, R.; Grelli, A.; Grigoras, C.; Grigoras, A.; Grigoriev, V.; Grigoryan, A.; Grigoryan, S.; Grinyov, B.; Grion, N.; Gros, P.; Grosse-Oetringhaus, J.F.; Grossiord, J.-Y.; Grosso, R.; Guber, F.; Guernane, R.; Guerra Gutierrez, C.; Guerzoni, B.; Guilbaud, M.; Gulbrandsen, K.; Gunji, T.; Gupta, A.; Gupta, R. ; Gutbrod, H.; Haaland, O.; Hadjidakis, C.; Haiduc, M.; Hamagaki, H.; Hamar, G.; Han, B.H.; Hanratty, L.D.; Hansen, A.; Harmanova, Z.; Harris, J.W.; Hartig, M.; Hasegan, D.; Hatzifotiadou, D. ; Hayrapetyan, A.; Heckel, S.T.; Heide, M.; Helstrup, H.; Herghelegiu, A.; Herrera Corral, G.; Herrmann, N.; Hetland, K.F.; Hicks, B.; Hille, P.T. ; Hippolyte, B.; Horaguchi, T.; Hori, Y.; Hristov, P.; Hrivnacova, I.; Huang, M.; Huber, S.; Humanic, T.J.; Hwang, D.S.; Ichou, R.; Ilkaev, R.; Ilkiv, I.; Inaba, M.; Incani, E.; Innocenti, P.G.; Innocenti, G.M.; Ippolitov, M.; Irfan, M.; Ivan, C.; Ivanov, M.; Ivanov, V.; Ivanov, A.; Ivanytskyi, O.; Jacholkowski, A.; Jacobs, P.M.; Jancurova, L.; Jang, H.J.; Jangal, S.; Janik, R.; Janik, M.A.; Jayarathna, P.H.S.Y. ; Jena, S.; Jimenez Bustamante, R.T.; Jirden, L.; Jones, P.G.; Jung, W.; Jung, H.; Jusko, A.; Kaidalov, A.B.; Kakoyan, V.; Kalcher, S.; Kalinak, P.; Kalisky, M.; Kalliokoski, T.; Kalweit, A.; Kanaki, K.; Kang, J.H.; Kaplin, V.; Karasu Uysal, A.; Karavichev, O.; Karavicheva, T.; Karpechev, E.; Kazantsev, A.; Kebschull, U.; Keidel, R.; Khan, P.; Khan, M.M.; Khan, S.A.; Khanzadeev, A.; Kharlov, Y.; Kileng, B.; Kim, J.H. ; Kim, D.J.; Kim, D.W.; Kim, J.S.; Kim, M.; Kim, S.H.; Kim, S.; Kim, B.; Kim, T.; Kirsch, S. ; Kisel, I.; Kiselev, S.; Kisiel, A.; Klay, J.L. ; Klein, J.; Klein-Bösing, C.; Kliemant, M.; Kluge, A.; Knichel, M.L.; Koch, K.; Köhler, M.K. ; Kolojvari, A.; Kondratiev, V.; Kondratyeva, N.; Konevskikh, A.; Korneev, A.; Kottachchi Kankanamge Don, C.; Kour, R.; Kowalski, M.; Kox, S.; Koyithatta Meethaleveedu, G.; Kral, J.; Kralik, I. ; Kramer, F.; Kraus, I.; Krawutschke, T.; Kretz, M.; Krivda, M.; Krizek, F.; Krus, M.; Kryshen, E.; Krzewicki, M.; Kucheriaev, Y.; Kuhn, C.; Kuijer, P.G.; Kurashvili, P.; Kurepin, A.B.; Kurepin, A.; Kuryakin, A.; Kushpil, S.; Kushpil, V. ; Kvaerno, H.; Kweon, M.J.; Kwon, Y.; Ladron de Guevara, P.; Lakomov, I.; Langoy, R.; Lara, C.; Lardeux, A.; La Rocca, P.; Lazzeroni, C.; Lea, R. ; Le Bornec, Y.; Lee, S.C.; Lee, K.S.; Lefevre, F.; Lehnert, J.; Leistam, L.; Lenhardt, M.; Lenti, V.; Leon, H.; Leon Monzon, I.; Leon Vargas, H.; Levai, P.; Li, X.; Lien, J.; Lietava, R.; Lindal, S.; Lindenstruth, V.; Lippmann, C.; Lisa, M.A.; Liu, L.; Loenne, P.I.; Loggins, V.R.; Loginov, V.; Lohn, S.; Lohner, D. ; Loizides, C.; Loo, K.K.; Lopez, X.; Lopez Torres, E.; Lovhoiden, G.; Lu, X.-G.; Luettig, P. ; Lunardon, M.; Luo, J.; Luparello, G.; Luquin, L.; Luzzi, C.; Ma, R.; Ma, K.; Madagodahettige-Don, D.M.; Maevskaya, A.; Mager, M. ; Mahapatra, D.P.; Maire, A.; Malaev, M.; Maldonado Cervantes, I.; Malinina, L.; MalKevich, D. ; Malzacher, P.; Mamonov, A.; Manceau, L.; Mangotra, L.; Manko, V.; Manso, F.; Manzari, V.; Mao, Y.; Marchisone, M.; Mares, J.; Margagliotti, G.V.; Margotti, A.; Marin, Ana; Markert, C.; Martashvili, I.; Martinengo, P.; Martinez, M.I.; Martinez Davalos, A.; Martinez Garcia, G.; Martynov, Y.; Mas, A.; Masciocchi, S.; Masera, M. ; Masoni, A.; Massacrier, L.; Mastromarco, M.; Mastroserio, A.; Matthews, Z.L.; Matyja, A.; Mayani, D.; Mayer, C.; Mazer, J.; Mazzoni, M.A.; Meddi, F.; Menchaca-Rocha, A.; Mercado Perez, J.; Meres, M.; Miake, Y.; Michalon, A.; Midori, J.; Milano, L.; Milosevic, J.; Mischke, A.; Mishra, A.N.; Mikowiec, D.; Mitu, C.; Mlynarz, J.; Mohanty, A.K.; Mohanty, B.; Molnar, L.; Montano Zetina, L.; Monteno, M.; Montes, E.; Moon, T.; Morando, M.; Moreira De Godoy, D.A.; Moretto, S.; Morsch, A.; Muccifora, V.; Mudnic, E.; Muhuri, S. ; Müller, H.; Munhoz, M.G.; Musa, L.; Musso, A. ; Nandi, B.K.; Nania, R.; Nappi, E.; Nattrass, C. ; Naumov, N.P.; Navin, S.; Nayak, T.K.; Nazarenko, S.; Nazarov, G.; Nedosekin, A.; Nicassio, M.; Nielsen, B.S.; Niida, T.; Nikolaev, S.; Nikolic, V.; Nikulin, V.; Nikulin, S.; Nilsen, B.S.; Nilsson, M.S.; Noferini, F.; Nomokonov, P.; Nooren, G.; Novitzky, N.; Nyanin, A. ; Nyatha, A.; Nygaard, C.; Nystrand, J.; Obayashi, H.; Ochirov, A.; Oeschler, H.; Oh, S.K. ; Oh, S.; Oleniacz, J.; Oppedisano, C.; Ortiz Velasquez, A.; Ortona, G.; Oskarsson, A.; Ostrowski, P.; Otterlund, I.; Otwinowski, J.; Oyama, K.; Ozawa, K.; Pachmayer, Y.; Pachr, M.; Padilla, F.; Pagano, P.; Paic, G.; Painke, F.; Pajares, C.; Pal, S.; Pal, S.K.; Palaha, A.; Palmeri, A.; Papikyan, V.; Pappalardo, G.S.; Park, W.J.; Passfeld, A.; Pastircak, B.; Patalakha, D.I.; Paticchio, V.; Pavlinov, A.; Pawlak, T.; Peitzmann, T.; Perales, M.; Pereira De Oliveira Filho, E.; Peresunko, D.; Perez Lara, C.E.; Perez Lezama, E.; Perini, D.; Perrino, D.; Peryt, W.; Pesci, A.; Peskov, V.; Pestov, Y.; Petracek, V.; Petran, M.; Petris, M.; Petrov, P.; Petrovici, M. ; Petta, C.; Piano, S.; Piccotti, A.; Pikna, M. ; Pillot, P.; Pinazza, O.; Pinsky, L.; Pitz, N. ; Piuz, F.; Piyarathna, D.B.; Ploskon, M.; Pluta, J.; Pocheptsov, T.; Pochybova, S.; Podesta-Lerma, P.L.M.; Poghosyan, M.G.; Polak, K.; Polichtchouk, B.; Pop, A.; Porteboeuf-Houssais, S.; Pospisil, V.; Potukuchi, B.; Prasad, S.K.; Preghenella, R.; Prino, F.; Pruneau, C.A.; Pshenichnov, I.; Puchagin, S.; Puddu, G.; Pulvirenti, A.; Punin, V.; Putis, M.; Putschke, J. ; Quercigh, E.;

Qvigstad, H.; Rachevski, A.; Rademakers, A.; Radomski, S.; Räihä T.S.; Rak, J.; Rakotozafindrabe, A.; Ramello, L.; Ramirez Reyes, A.; Raniwala, S.; Raniwala, R.; Räsänen, S.S.; Rascanu, B.T.; Rathee, D.; Read, K.F.; Real, J.S.; Redlich, K.; Reichelt, P.; Reicher, M. ; Renfordt, R.; Reolon, A.R.; Reshetin, A.; Rettig, F.; Revol, J.-P.; Reygers, K.; Riccati, L. ; Ricci, R.A.; Richter, M.; Riedler, P.; Riegler, W.; Riggi, F.; Rodriguez Cahuantzi, M.; Rohr, D. ; Röhrich, D.; Romita, R.; Ronchetti, F.; Rosnet, P.; Rossegger, S.; Rossi, A.; Roukoutakis, F.; Roy, P.; Roy, C.; Rubio Montero, A.J.; Rui, R.; Ryabinkin, E.; Rybicki, A.; Sadovsky, S.; Safarik, K.; Sahu, P.K.; Saini, J.; Sakaguchi, H.; Sakai, S.; Sakata, D.; Salgado, C.A.; Sambyal, S.; Samsonov, V.; Sanchez Castro, X.; Sandor, L.; Sandoval, A.; Sano, M.; Sano, S.; Santo, R.; Santoro, R.; Sarkamo, J.; Scapparone, E. ; Scarlassara, F.; Scharenberg, R.P.; Schiaua, C. ; Schicker, R.; Schmidt, C.; Schmidt, H.R.; Schreiner, S.; Schuchmann, S.; Schukraft, J.; Schutz, Y.; Schwarz, K.; Schweda, K.; Scioli, G. ; Scomparin, E.; Scott, R.; Scott, P.A.; Segato, G.; Selyuzhenkov, I.; Senyukov, S.; Seo, J.; Serci, S.; Serradilla, E.; Sevcenco, A.; Sgura, I. ; Shabetai, A.; Shabratova, G.; Shahoyan, R.; Sharma, N.; Sharma, S.; Shigaki, K.; Shimomura, M. ; Shtejer, K.; Sibiriak, Y.; Siciliano, M.; Sicking, E.; Siddhanta, S.; Siemiarczuk, T.; Silvermyr, D.; Simonetti, G.; Singaraju, R.; Singh, R.; Singha, S.; Sinha, B.C.; Sinha, T.; Sitar, B.; Sitta, M.; Skaali, T.B.; Skjerdal, K.; Smakal, R.; Smirnov, N.; Snellings, R.; Sogaard, C.; Soltz, R.; Son, H.; Song, J.; Song, M.; Soos, C.; Soramel, F.; Sputowska, I.; Spyropoulou-Stassinaki, M.; Srivastava, B.K.; Stachel, J.; Stan, I.; Stan, I.; Stefanek, G.; Stefanini, G.; Steinbeck, T.; Steinpreis, M.; Stenlund, E.; Steyn, G.; Stocco, D.; Stolpovskiy, M.; Strabykin, K.; Strmen, P.; Suaide, A.A.P.; Subieta Vasquez, M.A.; Sugitate, T.; Suire, C.; Sukhorukov, M.; Sultanov, R.; Sumbera, M.; Susa, T.; Szanto de Toledo, A.; Szarka, I.; Szostak, A.; Tagridis, C. ; Takahashi, J.; Tapia Takaki, J.D.; Tauro, A.; Tejeda Munoz, G.; Telesca, A.; Terrevoli, C.; Thäder, J.; Thomas, J.H.; Thomas, D.; Tieulent, R. ; Timmins, A.R.; Tlusty, D.; Toia, A.; Torii, H. ; Toscano, L.; Tosello, F.; Traczyk, T.; Truesdale, D.; Trzaska, W.H.; Tsuji, T.; Tumkin, A. ; Turrisi, R.; Tveter, T.S.; Ulery, J.; Ullaland, K.; Ulrich, J.; Uras, A.; Urban, J.; Urciuoli, G.M.; Usai, G.L.; Vajzer, M.; Vala, M.; Valencia Palomo, L.; Vallero, S.; van der Kolk, N.; Vande Vyvre, P.; van Leeuwen, M.; Vannucci, L.; Vargas, A.; Varma, R.; Vasileiou, M.; Vasiliev, A.; Vechernin, V.; Veldhoen, M.; Venaruzzo, M.; Vercellin, E.; Vergara, S.; Vernekohl, D.C.; Vernet, R.; Verweij, M.; Vickovic, L.; Viesti, G. ; Vikhlyantsev, O.; Vilakazi, Z.; Villalobos Baillie, O.; Vinogradov, L.; Vinogradov, Y.; Vinogradov, A.; Virgili, T.; Viyogi, Y.P.; Vodopyanov, A.; Voloshin, S.; Voloshin, K.; Volpe, G.; von Haller, B.; Vranic, D.; Ovrebekk, G.; Vrlakova, J.; Vulpescu, B.; Vyushin, A.; Wagner, B.; Wagner, V.; Wan, R.; Wang, Y.; Wang, M.; Wang, D.; Wang, Y.; Watanabe, K.; Wessels, J.P.; Westerhoff, U.; Wiechula, J.; Wikne, J.; Wilde, M. ; Wilk, G.; Wilk, A.; Williams, M.C.S.; Windelband, B.; Xaplanteris Karampatsos, L.; Yang, H. ; Yang, S.; Yano, S.; Yasnopolskiy, S.; Yi, J. ; Yin, Z.; Yokoyama, H.; Yoo, I.-K.; Yoon, J.; Yu, W.; Yuan, X.; Yushmanov, I.; Zach, C.; Zampolli, C.; Zaporozhets, S.; Zarochentsev, A.; Zavada, P.; Zaviyalov, N.; Zbroszczyk, H.; Zelnicek, P.; Zgura, I.S.; Zhalov, M.; Zhang, X. ; Zhou, F.; Zhou, Y.; Zhou, D.; Zhu, X.; Zichichi, A.; Zimmermann, A.; Zinovjev, G.; Zoccarato, Y.; Zynovyev, M.: **Neutral pion and η meson production in protonproton collisions at $\sqrt{s} = 0.9$ TeV and $\sqrt{s} = 7$ TeV.** *Physics letters / B* 717: 162 - 172, 2012. DOI:10.1016/j.physletb.2012.09.015

WOS-PHN-7 Abelev, B.; Adam, J.; Adamova, D.; Adare, A. M.; Aggarwal, M. M.; Aglieri Rinella, G.; Agocs, A. G. ; Agostinelli, A.; Aguilar Salazar, S.; Ahammed, Z. ; Ahmad Masoodi, A.; Ahmad, N.; Ahn, S. U.; Akindinov, A.; Aleksandrov, D.; Alessandro, B.; Alfaro Molina, R.; Alici, A.; Alkin, A.; Almaraz Avina, E.; Alme, J.; Alt, T.; Altini, V.; Altinpinar, S.; Altsybeev, I.; Andrei, C.; Andronic, A.; Anguelov, V.; Anielski, J.; Anticic, T.; Antinori, F.; Antonioli, P.; Aphecetche, L.; Appelshäuser, H.; Arbor, N.; Arcelli, S.; Armesto, N.; Arnaldi, R.; Aronsson, T. ; Arsene, I. C.; Arslandok, M.; Augustinus, A.; Averbeck, R.; Awes, T. C.; Äystö J.; Azmi, M. D. ; Bach, M.; Badala, A.; Baek, Y. W.; Bailhache, R.; Bala, R.; Baldini Ferroli, R.; Baldisseri, A. ; Baldit, A.; BaltasarDosSantos Pedrosa, F.; Ban, J.; Baral, R. C.; Barbera, R.; Barile, F.; Barnaföldi, G. G.; Barnby, L. S.; Barret, V.; Bartke, J.; Basile, M.; Bastid, N.; Basu, S.; Bathen, B.; Batigne, G.; Batyunya, B.; Baumann, C. ; Bearden, I. G.; Beck, H.; Behera, N. K.; Belikov, I.; Bellini, F.; Bellwied, R.; Belmont-Moreno, E.; Bencedi, G.; Beole, S.; Berceanu, I.; Bercuci, A.; Berdnikov, Y.; Berenyi, D.; Bergognon, A. A. E.; Berzano, D.; Betev, L.; Bhasin, A.; Bhati, A. K.; Bhom, J.; Bianchi, L.; Bianchi, N.; Bianchin, C.; Bielcik, J.; Bielcikova, J.; Bilandzic, A.; Bjelogrlic, S.; Blanco, F.; Blanco, F.; Blau, D.; Blume, C.; Bock, N.; Böttger, S.; Bogdanov, A.; Boggild, H. ; Bogolyubsky, M.; Boldizsar, L.; Bombara, M.; Book, J.; Borel, H.; Borissov, A.; Bose, S.; Boss, F.; Botje, M.; Boyer, B.; Braidot, E.; Braun-Munzinger, P.; Bregant, M.; Breitner, T.; Browning, T. A.; Broz, M.; Brun, R.; Bruna, E.; Bruno, G. E.; Budnikov, D.; Buesching, H.; Bufalino, S.; Busch, O.; Buthelezi, Z.; Caffarri, D.; Cai, X.; Caines, H.; Calvo Villar, E.; Camerini, P.; Canoa Roman, V.; Cara Romeo, G.; Carena, F.; Carena, W.; Carminati, F.; Casanova Diaz, A.; Castillo Castellanos, J.; Casula, E. A. R. ; Catanescu, V.; Cavicchioli, C.; Ceballos Sanchez, C.; Cepila, J.; Cerello, P.; Chang, B.; Chapeland, S.; Charvet, J. L.; Chattopadhyay, S.; Chattopadhyay, S.; Chawla, I.; Cherney, M.; Cheshkov, C.; Cheynis, B.; Chiavassa, E.; Chibante Barroso, V.; Chinellato, D. D.; Chochula, P.; Chojnacki, M.; Choudhury, S.; Christakoglou, P.; Christensen, C. H.; Christiansen, P.; Chujo, T.; Chung, S. U.; Cicalo, C.; Cifarelli, L.; Cindolo, F.; Cleymans, J.; Coccetti, F.; Colamaria, F.; Colella, D.; Conesa Balbastre, G.; ConesadelValle, Z.; Constantin, P.; Contin, G.; Contreras, J. G. ; Cormier, T. M.; Corrales Morales, Y.; Cortes Maldonado, I.; Cortese, P.; Cosentino, M. R.; Costa, F.; Cotallo, M. E.; Crochet, P.; Cruz Alaniz, E.; Cuautle, E.; Cunqueiro, L.; D Erasmo, G.; Dainese, A.; Dalsgaard, H. H.; Danu, A.; Das, D.; Das, I.; Das, K.; Dash, A.; Dash, S. ; De, S.; Barros, G. O. V.; Caro, A.; Cataldo, G. ; Cuveland, J.; Falco, A.; Gruttola, D.; Marco, N.; Pasquale, S.; Rooij, R.; Delagrange, H.; Deloff, A.; Demanov, V.; Denes, E.; Deppman, A. ; Bari, D.; Giglio, C.; Liberto, S.; Mauro, A. ; Nezza, P.; Diaz Corchero, M. A.; Dietel, T.; Divia, R.; Djuvsland, O.; Dobrin, A.; Dobrowolski, T.; Dominguez, I.; Dönigus, B.; Dordic, O.; Driga, O.; Dubey, A. K.; Dubla, A.; Ducroux, L.; Dupieux, P.; Dutta Majumdar, A. K.; Dutta Majumdar, M. R.; Elia, D.; Emschermann, D.; Engel, H.; Erazmus, B.; Erdal, H. A.; Espagnon, B. ; Estienne, M.; Esumi, S.; Evans, D.; Eyyubova, G.; Fabris, D.; Faivre, J.; Falchieri, D.; Fantoni, A.; Fasel, M.; Fedunov, A.; Fehlker, D. ; Feldkamp, L.; Felea, D.; Fenton-Olsen, B.; Feofilov, G.; Fernandez Tellez, A.; Ferretti, A.; Ferretti, R.; Festanti, A.; Figiel, J.; Figueredo, M. A. S.; Filchagin, S.; Finogeev, D.; Fionda, F. M.; Fiore, E. M.; Floris, M.; Foertsch, S.; Foka, P.; Fokin, S.; Fragiacomo, E.; Francescon, A. ; Frankenfeld, U.; Fuchs, U.; Furget, C.; Fusco Girard, M.; Gaardhoje, J. J.; Gagliardi, M.; Gago, A.; Gallio,

M.; Gangadharan, D. R.; Ganoti, P.; Garabatos, C.; Garcia-Solis, E.; Garishvili, I.; Gerhard, J.; Germain, M.; Geuna, C.; Gheata, A.; Gheata, M.; Ghidini, B.; Ghosh, P.; Gianotti, P. ; Girard, M. R.; Giubellino, P.; Gladysz-Dziadus, E. ; Glässel, P.; Gomez, R.; Ferreiro, E. G.; Gonzalez-Trueba, L. H.; Gonzalez-Zamora, P.; Gorbunov, S.; Goswami, A.; Gotovac, S.; Grabski, V. ; Graczykowski, L. K.; Grajcarek, R.; Grelli, A.; Grigoras, A.; Grigoras, C.; Grigoriev, V.; Grigoryan, A.; Grigoryan, S.; Grinyov, B.; Grion, N.; Grosse-Oetringhaus, J. F.; Grossiord, J.-Y.; Grosso, R.; Guber, F.; Guernane, R.; Guerra Gutierrez, C.; Guerzoni, B.; Guilbaud, M.; Gulbrandsen, K.; Gunji, T.; Gupta, A.; Gupta, R. ; Gutbrod, H.; Haaland, O.; Hadjidakis, C.; Haiduc, M.; Hamagaki, H.; Hamar, G.; Hanratty, L. D.; Hansen, A.; Harmanova, Z.; Harris, J. W.; Hartig, M.; Hasegan, D.; Hatzifotiadou, D.; Hayrapetyan, A.; Heckel, S. T.; Heide, M.; Helstrup, H.; Herghelegiu, A.; Herrera Corral, G.; Herrmann, N.; Hess, B. A.; Hetland, K. F.; Hicks, B.; Hille, P. T.; Hippolyte, B.; Horaguchi, T.; Hori, Y.; Hristov, P.; Hrivnacova, I.; Huang, M.; Humanic, T. J.; Hwang, D. S.; Ichou, R.; Ilkaev, R.; Ilkiv, I.; Inaba, M.; Incani, E.; Innocenti, G. M.; Ippolitov, M.; Irfan, M.; Ivan, C.; Ivanov, A.; Ivanov, M.; Ivanov, V.; Ivanytskyi, O.; Jacholkowski, A.; Jacobs, P. M.; Janik, M. A.; Janik, R.; Jayarathna, P. H. S. Y.; Jena, S.; Jha, D. M.; Jimenez Bustamante, R. T.; Jirden, L.; Jones, P. G.; Jung, H.; Jusko, A.; Kakoyan, V.; Kalcher, S.; Kalinak, P.; Kalliokoski, T.; Kalweit, A.; Kang, J. H.; Kaplin, V.; Karasu Uysal, A.; Karavichev, O.; Karavicheva, T.; Karpechev, E.; Kazantsev, A.; Kebschull, U.; Keidel, R.; Khan, M. M.; Khan, P.; Khan, S. A.; Khanzadeev, A.; Kharlov, Y.; Kileng, B.; Kim, B. ; Kim, D. J.; Kim, D. W.; Kim, J. H.; Kim, J. S. ; Kim, M.; Kim, M.; Kim, S.; Kim, S. H.; Kim, T.; Kirsch, S.; Kisel, I.; Kiselev, S.; Kisiel, A.; Klay, J. L.; Klein, J.; Klein-Bösing, C.; Kluge, A.; Knichel, M. L.; Knospe, A. G.; Koch, K. ; Köhler, M. K.; Kollegger, T.; Kolojvari, A.; Kondratiev, V.; Kondratyeva, N.; Konevskikh, A.; Korneev, A.; Kour, R.; Kowalski, M.; Kox, S.; Koyithatta Meethaleveedu, G.; Kral, J.; Kralik, I. ; Kramer, F.; Kraus, I.; Krawutschke, T.; Krelina, M.; Kretz, M.; Krivda, M.; Krizek, F.; Krus, M.; Kryshen, E.; Krzewicki, M.; Kucheriaev, Y.; Kugathasan, T.; Kuhn, C.; Kuijer, P. G.; Kulakov, I.; Kumar, J.; Kurashvili, P.; Kurepin, A. ; Kurepin, A. B.; Kuryakin, A.; Kushpil, S.; Kushpil, V.; Kweon, M. J.; Kwon, Y.; Pointe, S. L. ; Rocca, P.; LadrondeGuevara, P.; Lakomov, I. ; Langoy, R.; Lara, C.; Lardeux, A.; Lazzeroni, C.; Bornec, Y.; Lea, R.; Lechman, M.; Lee, G. R. ; Lee, K. S.; Lee, S. C.; Lefevre, F.; Lehnert, J.; Leistam, L.; Lemmon, R. C.; Lenti, V.; Leon Monzon, I.; Leon Vargas, H.; Leoncino, M.; Levai, P.; Lien, J.; Lietava, R.; Lindal, S.; Lindenstruth, V.; Lippmann, C.; Lisa, M. A.; Liu, L.; Loggins, V. R.; Loginov, V.; Lohn, S.; Lohner, D.; Loizides, C.; Loo, K. K.; Lopez, X.; Lopez Torres, E.; Lovhoiden, G.; Lu, X.-G.; Luettig, P.; Lunardon, M.; Luo, J.; Luparello, G. ; Luquin, L.; Luzzi, C.; Ma, R.; Maevskaya, A. ; Mager, M.; Mahapatra, D. P.; Maire, A.; MalKevich, D.; Malaev, M.; Maldonado Cervantes, I. ; Malinina, L.; Malzacher, P.; Mamonov, A.; Manceau, L.; Manko, V.; Manso, F.; Manzari, V.; Mao, Y.; Marchisone, M.; Mares, J.; Margagliotti, G. V.; Margotti, A.; Marin, Ana; Marin Tobon, C. A. ; Markert, C.; Martashvili, I.; Martinengo, P.; Martinez, M. I.; Martinez Davalos, A.; Martinez Garcia, G.; Martynov, Y.; Mas, A.; Masciocchi, S. ; Masera, M.; Masoni, A.; Mastroserio, A.; Matthews, Z. L.; Matyja, A.; Mayer, C.; Mazer, J. ; Mazzoni, M. A.; Meddi, F.; Menchaca-Rocha, A.; Mercado Perez, J.; Meres, M.; Miake, Y.; Milano, L.; Milosevic, J.; Mischke, A.; Mishra, A. N.; Mikowiec, D.; Mitu, C.; Mlynarz, J.; Mohanty, B. ; Molnar, L.; Montano Zetina, L.; Monteno, M.; Montes, E.; Moon, T.; Morando, M.; MoreiraDeGodoy, D. A.; Moretto, S.; Morsch, A.; Muccifora, V.; Mudnic, E.; Muhuri, S.; Mukherjee, M.; Müller, H.; Munhoz, M. G.; Musa, L.; Musso, A.; Nandi, B. K.; Nania, R.; Nappi, E.; Nattrass, C.; Naumov, N. P.; Navin, S.; Nayak, T. K.; Nazarenko, S.; Nazarov, G.; Nedosekin, A.; Nicassio, M.; Niculescu, M.; Nielsen, B. S.; Niida, T.; Nikolaev, S.; Nikulin, S.; Nikulin, V.; Nilsen, B. S.; Nilsson, M. S.; Noferini, F.; Nomokonov, P.; Nooren, G.; Novitzky, N.; Nyanin, A. ; Nyatha, A.; Nygaard, C.; Nystrand, J.; Oeschler, H.; Oh, S.; Oh, S. K.; Oleniacz, J.; Oppedisano, C.; Ortona, G.; Oskarsson, A.; Otwinowski, J.; Oyama, K.; Pachmayer, Y.; Pachr, M. ; Padilla, F.; Pagano, P.; Paic, G.; Painke, F. ; Pajares, C.; Pal, S. K.; Palaha, A.; Palmeri, A.; Papikyan, V.; Pappalardo, G. S.; Park, W. J. ; Passfeld, A.; Patalakha, D. I.; Paticchio, V.; Pavlinov, A.; Pawlak, T.; Peitzmann, T.; PereiraDaCosta, H.; PereiraDeOliveira Filho, E. ; Peresunko, D.; Perez Lara, C. E.; Perez Lezama, E.; Perini, D.; Perrino, D.; Peryt, W.; Pesci, A.; Peskov, V.; Pestov, Y.; Petracek, V.; Petran, M.; Petris, M.; Petrov, P.; Petrovici, M. ; Petta, C.; Piano, S.; Piccotti, A.; Pikna, M. ; Pillot, P.; Pinazza, O.; Pinsky, L.; Pitz, N. ; Piuz, F.; Piyarathna, D. B.; Ploskon, M.; Pluta, J.; Pochybova, S.; Podesta-Lerma, P. L. M.; Poghosyan, M. G.; Polichtchouk, B.; Pop, A.; Porteboeuf-Houssais, S.; Pospisil, V.; Potukuchi, B. ; Prasad, S. K.; Preghenella, R.; Prino, F.; Pruneau, C. A.; Pshenichnov, I.; Puchagin, S.; Puddu, G.; Pujahari, P.; Pulvirenti, A.; Punin, V. ; Putis, M.; Putschke, J.; Quercigh, E.; Qvigstad, H.; Rachevski, A.; Rademakers, A.; Räihä T. S.; Rak, J.; Rakotozafindrabe, A.; Ramello, L.; Ramirez Reyes, A.; Raniwala, R.; Raniwala, S.; Räsänen, S. S.; Rascanu, B. T.; Rathee, D.; Read, K. F.; Real, J. S.; Redlich, K. ; Rehman, A.; Reichelt, P.; Reicher, M.; Renfordt, R.; Reolon, A. R.; Reshetin, A.; Rettig, F.; Revol, J.-P.; Reygers, K.; Riccati, L.; Ricci, R. A.; Richert, T.; Richter, M.; Riedler, P. ; Riegler, W.; Riggi, F.; Rodrigues Fernandes Rabacal, B.; Rodriguez Cahuantzi, M.; Rodriguez Manso, A.; Roed, K.; Rohr, D.; Röhrich, D.; Romita, R.; Ronchetti, F.; Rosnet, P.; Rossegger, S.; Rossi, A.; Roy, C.; Roy, P.; Rubio Montero, A. J.; Rui, R.; Russo, R.; Ryabinkin, E.; Rybicki, A.; Sadovsky, S.; Safarik, K.; Sahoo, R.; Sahu, P. K.; Saini, J.; Sakaguchi, H.; Sakai, S.; Sakata, D.; Salgado, C. A.; Salzwedel, J.; Sambyal, S.; Samsonov, V.; Sanchez Castro, X. ; Sandor, L.; Sandoval, A.; Sano, M.; Sano, S. ; Santo, R.; Santoro, R.; Sarkamo, J.; Scapparone, E.; Scarlassara, F.; Scharenberg, R. P. ; Schiaua, C.; Schicker, R.; Schmidt, C.; Schmidt, H. R.; Schreiner, S.; Schuchmann, S.; Schukraft, J.; Schutz, Y.; Schwarz, K.; Schweda, K. ; Scioli, G.; Scomparin, E.; Scott, P. A.; Scott, R.; Segato, G.; Selyuzhenkov, I.; Senyukov, S.; Seo, J.; Serci, S.; Serradilla, E.; Sevcenco, A. ; Shabetai, A.; Shabratova, G.; Shahoyan, R.; Sharma, N.; Sharma, S.; Shigaki, K.; Shimomura, M. ; Shtejer, K.; Sibiriak, Y.; Siciliano, M.; Sicking, E.; Siddhanta, S.; Siemiarczuk, T.; Silvermyr, D.; Silvestre, C.; Simatovic, G.; Simonetti, G.; Singaraju, R.; Singh, R.; Singha, S. ; Singhal, V.; Sinha, B. C.; Sinha, T.; Sitar, B. ; Sitta, M.; Skaali, T. B.; Skjerdal, K.; Smakal, R.; Smirnov, N.; Snellings, R. J. M.; Sogaard, C. ; Soltz, R.; Son, H.; Song, J.; Song, M.; Soos, C.; Soramel, F.; Sputowska, I.; Spyropoulou-Stassinaki, M.; Srivastava, B. K.; Stachel, J.; Stan, I.; Stefanek, G.; Stefanini, G. ; Steinpreis, M.; Stenlund, E.; Steyn, G.; Stiller, J. H.; Stocco, D.; Stolpovskiy, M.; Strabykin, K.; Strmen, P.; Suaide, A. A. P.; Subieta Vasquez, M. A.; Sugitate, T.; Suire, C.; Sukhorukov, M.; Sultanov, R.; Sumbera, M.; Susa, T.; SzantodeToledo, A.; Szarka, I.; Szczepankiewicz, A.; Szostak, A.; Szymanski, M.; Takahashi, J.; Tapia Takaki, J. D.; Tarazona Martinez, A.; Tauro,

A.; Tejeda Munoz, G.; Telesca, A.; Terrevoli, C.; Thäder, J.; Thomas, D.; Tieulent, R.; Timmins, A. R.; Toia, A.; Torii, H.; Tosello, F.; Trubnikov, V.; Trzaska, W. H.; Tsuji, T.; Tumkin, A.; Turrisi, R.; Tveter, T. S.; Ulery, J.; Ullaland, K.; Ulrich, J.; Uras, A.; Urban, J.; Urciuoli, G. M.; Usai, G. L.; Vajzer, M.; Vala, M.; Valencia Palomo, L.; Vallero, S.; Kolk, N.; Leeuwen, M.; Vande Vyvre, P.; Vannucci, L.; Vargas, A.; Varma, R.; Vasileiou, M.; Vasiliev, A.; Vechernin, V.; Veldhoen, M.; Venaruzzo, M.; Vercellin, E.; Vergara, S.; Vernet, R.; Verweij, M.; Vickovic, L.; Viesti, G.; Vikhlyantsev, O.; Vilakazi, Z.; Villalobos Baillie, O. ; Vinogradov, A.; Vinogradov, L.; Vinogradov, Y.; Virgili, T.; Viyogi, Y. P.; Vodopyanov, A.; Voloshin, K.; Voloshin, S.; Volpe, G.; Haller, B. ; Vranic, D.; Ovrebekk, G.; Vrlakova, J.; Vulpescu, B.; Vyushin, A.; Wagner, B.; Wagner, V. ; Wan, R.; Wang, D.; Wang, M.; Wang, Y.; Wang, Y.; Watanabe, K.; Weber, M.; Wessels, J. P.; Westerhoff, U.; Wiechula, J.; Wikne, J.; Wilde, M. ; Wilk, A.; Wilk, G.; Williams, M. C. S.; Windelband, B.; Xaplanteris Karampatsos, L.; Yaldo, C. G.; Yamaguchi, Y.; Yang, H.; Yang, S.; Yasnopolskiy, S.; Yi, J.; Yin, Z.; Yoo, I.-K.; Yoon, J.; Yu, W.; Yuan, X.; Yushmanov, I.; Zach, C.; Zampolli, C.; Zaporozhets, S.; Zarochentsev, A. ; Zavada, P.; Zaviyalov, N.; Zbroszczyk, H.; Zelnicek, P.; Zgura, I. S.; Zhalov, M.; Zhang, H. ; Zhang, X.; Zhou, D.; Zhou, F.; Zhou, Y.; Zhu, J.; Zhu, X.; Zichichi, A.; Zimmermann, A.; Zinovjev, G.; Zoccarato, Y.; Zynovyev, M.; Zyzak, M.: **Production of K(892)0 and (1020) in pp collisions at $\sqrt{s}$ =7 TeV.** *The European physical journal / C* 72: 2183, 2012. DOI:10.1140/epjc/s10052-012-2183-y

WOS-PHN-8 Abelev, B.; Adam, J.; Adamova, D.; Adare, A. M.; Aggarwal, M. M.; Aglieri Rinella, G.; Agocs, A. G. ; Agostinelli, A.; Aguilar Salazar, S.; Ahammed, Z. ; Ahmad Masoodi, A.; Ahmad, N.; Ahn, S. U.; Akindinov, A.; Aleksandrov, D.; Alessandro, B.; Alfaro Molina, R.; Alici, A.; Alkin, A.; Almaraz Avina, E.; Alme, J.; Alt, T.; Altini, V.; Altinpinar, S.; Altsybeev, I.; Andrei, C.; Andronic, A.; Anguelov, V.; Anielski, J.; Anson, C. ; Anticic, T.; Antinori, F.; Antonioli, P.; Aphecetche, L.; Appelshäuser, H.; Arbor, N.; Arcelli, S.; Arend, A.; Armesto, N.; Arnaldi, R. ; Aronsson, T.; Arsene, I. C.; Arslandok, M.; Asryan, A.; Augustinus, A.; Averbeck, R.; Awes, T. C.; Äystö J.; Azmi, M. D.; Bach, M.; Badala, A.; Baek, Y. W.; Bailhache, R.; Bala, R.; Baldini Ferroli, R.; Baldisseri, A.; Baldit, A.; Baltasar Dos Santos Pedrosa, F.; Ban, J.; Baral, R. C.; Barbera, R.; Barile, F.; Barnaföldi, G. G.; Barnby, L. S.; Barret, V.; Bartke, J.; Basile, M. ; Bastid, N.; Bathen, B.; Batigne, G.; Batyunya, B.; Baumann, C.; Bearden, I. G.; Beck, H.; Belikov, I.; Bellini, F.; Bellwied, R.; Belmont-Moreno, E.; Bencedi, G.; Beole, S.; Berceanu, I.; Bercuci, A.; Berdnikov, Y.; Berenyi, D.; Bergmann, C.; Berzano, D.; Betev, L.; Bhasin, A.; Bhati, A. K.; Bianchi, L.; Bianchi, N. ; Bianchin, C.; Bielcik, J.; Bielcikova, J.; Bilandzic, A.; Bjelogrlic, S.; Blanco, F.; Blanco, F.; Blau, D.; Blume, C.; Boccioli, M.; Bock, N. ; Bogdanov, A.; Boggild, H.; Bogolyubsky, M.; Boldizsar, L.; Bombara, M.; Book, J.; Borel, H. ; Borissov, A.; Bose, S.; Boss, F.; Botje, M. ; Böttger, S.; Boyer, B.; Braidot, E.; Braun-Munzinger, P.; Bregant, M.; Breitner, T.; Browning, T. A.; Broz, M.; Brun, R.; Bruna, E.; Bruno, G. E.; Budnikov, D.; Buesching, H.; Bufalino, S.; Bugaiev, K.; Busch, O.; Buthelezi, Z. ; Caballero Orduna, D.; Caffarri, D.; Cai, X.; Caines, H.; Calvo Villar, E.; Camerini, P.; Canoa Roman, V.; Cara Romeo, G.; Carena, W.; Carena, F. ; Carlin Filho, N.; Carminati, F.; Carrillo Montoya, C. A.; Casanova Diaz, A.; Castillo Castellanos, J. ; Castillo Hernandez, J. F.; Casula, E. A. R.; Catanescu, V.; Cavicchioli, C.; Cepila, J.; Cerello, P.; Chang, B.; Chapeland, S.; Charvet, J. L.; Chattopadhyay, S.; Chattopadhyay, S.; Chawla, I.; Cherney, M.; Cheshkov, C.; Cheynis, B.; Chiavassa, E.; Chibante Barroso, V.; Chinellato, D. D. ; Chochula, P.; Chojnacki, M.; Christakoglou, P.; Christensen, C. H.; Christiansen, P.; Chujo, T.; Chung, S. U.; Cicalo, C.; Cifarelli, L.; Cindolo, F.; Cleymans, J.; Coccetti, F.; Colamaria, F.; Colella, D.; Conesa Balbastre, G.; Conesa del Valle, Z.; Constantin, P.; Contin, G.; Contreras, J. G. ; Cormier, T. M.; Corrales Morales, Y.; Cortese, P. ; Cortes Maldonado, I.; Cosentino, M. R.; Costa, F. ; Cotallo, M. E.; Crescio, E.; Crochet, P.; Cruz Alaniz, E.; Cuautle, E.; Cunqueiro, L.; Dainese, A. ; Dalsgaard, H. H.; Danu, A.; Das, K.; Das, I. ; Das, D.; Dash, A.; Dash, S.; De, S.; de Barros, G. O. V.; De Caro, A.; de Cataldo, G.; de Cuveland, J.; De Falco, A.; De Gruttola, D.; Delagrange, H.; Del Castillo Sanchez, E.; Deloff, A. ; Demanov, V.; De Marco, N.; Denes, E.; De Pasquale, S.; Deppman, A.; DErasmo, G.; de Rooij, R.; Diaz Corchero, M. A.; Di Bari, D.; Dietel, T.; Di Giglio, C.; Di Liberto, S.; Di Mauro, A.; Di Nezza, P.; Divia, R.; Djuvsland, O. ; Dobrin, A.; Dobrowolski, T.; Dominguez, I.; Dönigus, B.; Dordic, O.; Driga, O.; Dubey, A. K. ; Ducroux, L.; Dupieux, P.; Dutta Majumdar, A. K. ; Dutta Majumdar, M. R.; Elia, D.; Emschermann, D. ; Engel, H.; Erdal, H. A.; Espagnon, B.; Estienne, M.; Esumi, S.; Evans, D.; Eyyubova, G. ; Fabris, D.; Faivre, J.; Falchieri, D.; Fantoni, A.; Fasel, M.; Fearick, R.; Fedunov, A.; Fehlker, D.; Feldkamp, L.; Felea, D.; Feofilov, G. ; Fernandez Tellez, A.; Ferretti, A.; Ferretti, R. ; Figiel, J.; Figueredo, M. A. S.; Filchagin, S.; Finogeev, D.; Fionda, F. M.; Fiore, E. M.; Floris, M.; Foertsch, S.; Foka, P.; Fokin, S.; Fragiacomo, E.; Fragkiadakis, M.; Frankenfeld, U.; Fuchs, U.; Furget, C.; Fusco Girard, M.; Gaardhoje, J. J.; Gagliardi, M.; Gago, A.; Gallio, M.; Gangadharan, D. R.; Ganoti, P.; Garabatos, C. ; Garcia-Solis, E.; Garishvili, I.; Gerhard, J.; Germain, M.; Geuna, C.; Gheata, A.; Gheata, M.; Ghidini, B.; Ghosh, P.; Gianotti, P.; Girard, M. R. ; Giubellino, P.; Gladysz-Dziadus, E.; Glässel, P. ; Gomez, R.; Ferreiro, E. G.; Gonzalez-Trueba, L. H.; Gonzalez-Zamora, P.; Gorbunov, S.; Goswami, A. ; Gotovac, S.; Grabski, V.; Graczykowski, L. K.; Grajcarek, R.; Grelli, A.; Grigoras, A.; Grigoras, C.; Grigoriev, V.; Grigoryan, A.; Grigoryan, S.; Grinyov, B.; Grion, N.; Gros, P.; Grosse-Oetringhaus, J. F.; Grossiord, J.-Y.; Grosso, R.; Guber, F.; Guernane, R.; Guerra Gutierrez, C. ; Guerzoni, B.; Guilbaud, M.; Gulbrandsen, K.; Gunji, T.; Gupta, A.; Gupta, R.; Gutbrod, H.; Haaland, O.; Hadjidakis, C.; Haiduc, M.; Hamagaki, H.; Hamar, G.; Han, B. H.; Hanratty, L. D.; Hansen, A.; Harmanova, Z.; Harris, J. W.; Hartig, M.; Hasegan, D.; Hatzifotiadou, D.; Hayrapetyan, A. ; Heckel, S. T.; Heide, M.; Helstrup, H.; Herghelegiu, A.; Herrera Corral, G.; Herrmann, N.; Hetland, K. F.; Hicks, B.; Hille, P. T.; Hippolyte, B.; Horaguchi, T.; Hori, Y.; Hristov, P.; Hrivnacova, I.; Huang, M.; Huber, S.; Humanic, T. J.; Hwang, D. S.; Ichou, R.; Ilkaev, R.; Ilkiv, I.; Inaba, M.; Incani, E.; Innocenti, G. M. ; Innocenti, P. G.; Ippolitov, M.; Irfan, M.; Ivan, C.; Ivanov, V.; Ivanov, A.; Ivanov, M.; Ivanytskyi, O.; Jacholkowski, A.; Jacobs, P. M.; Jancurova, L.; Jang, H. J.; Jangal, S.; Janik, M. A.; Janik, R.; Jayarathna, P. H. S. Y.; Jena, S. ; Jimenez Bustamante, R. T.; Jirden, L.; Jones, P. G.; Jung, H.; Jusko, A.; Kaidalov, A. B.; Kakoyan, V.; Kalcher, S.; Kalinak, P.; Kalisky, M.; Kalliokoski, T.; Kalweit, A.; Kanaki, K.; Kang, J. H.; Kaplin, V.; Karasu Uysal, A.; Karavichev, O.; Karavicheva, T.; Karpechev, E.; Kazantsev, A.; Kebschull, U.; Keidel, R.; Khan, M. M.; Khan, S. A.; Khan, P.; Khanzadeev, A.; Kharlov, Y.; Kileng, B.; Kim, M.; Kim, J. S.; Kim, D. J.; Kim, T.; Kim, B.; Kim, S.; Kim, S. H.; Kim, D. W.; Kim, J. H.; Kirsch, S.; Kisel, I.; Kiselev, S.; Kisiel, A.; Klay, J. L.;

Klein, J.; Klein-Bösing, C.; Kliemant, M.; Kluge, A.; Knichel, M. L.; Knospe, A. G.; Koch, K.; Köhler, M. K.; Kolojvari, A.; Kondratiev, V.; Kondratyeva, N.; Konevskikh, A.; Korneev, A.; Kottachchi Kankanamge Don, C.; Kour, R.; Kowalski, M.; Kox, S. ; Koyithatta Meethaleveedu, G.; Kral, J.; Kralik, I.; Kramer, F.; Kraus, I.; Krawutschke, T.; Krelina, M.; Kretz, M.; Krivda, M.; Krizek, F.; Krus, M.; Kryshen, E.; Krzewicki, M.; Kucheriaev, Y.; Kuhn, C.; Kuijer, P. G.; Kurashvili, P.; Kurepin, A.; Kurepin, A. B.; Kuryakin, A.; Kushpil, S.; Kushpil, V.; Kvaerno, H.; Kweon, M. J.; Kwon, Y.; Ladron de Guevara, P.; Lakomov, I.; Langoy, R.; Lara, C.; Lardeux, A.; La Rocca, P.; Lazzeroni, C.; Lea, R.; Le Bornec, Y.; Lee, S. C. ; Lee, K. S.; Lefevre, F.; Lehnert, J.; Leistam, L.; Lenhardt, M.; Lenti, V.; Leon, H.; Leon Monzon, I.; Leon Vargas, H.; Levai, P.; Lien, J. ; Lietava, R.; Lindal, S.; Lindenstruth, V.; Lippmann, C.; Lisa, M. A.; Liu, L.; Loenne, P. I. ; Loggins, V. R.; Loginov, V.; Lohn, S.; Lohner, D.; Loizides, C.; Loo, K. K.; Lopez, X.; Lopez Torres, E.; Lovhoiden, G.; Lu, X.-G.; Luettig, P. ; Lunardon, M.; Luo, J.; Luparello, G.; Luquin, L.; Luzzi, C.; Ma, K.; Ma, R.; Madagodahettige-Don, D. M.; Maevskaya, A.; Mager, M. ; Mahapatra, D. P.; Maire, A.; Malaev, M.; Maldonado Cervantes, I.; Malinina, L.; MalKevich, D.; Malzacher, P.; Mamonov, A.; Manceau, L.; Mangotra, L.; Manko, V.; Manso, F.; Manzari, V.; Mao, Y.; Marchisone, M.; Mares, J.; Margagliotti, G. V.; Margotti, A.; Marin, Ana; Marin Tobon, C. A. ; Markert, C.; Martashvili, I.; Martinengo, P.; Martinez, M. I.; Martinez Davalos, A.; Martinez Garcia, G.; Martynov, Y.; Mas, A.; Masciocchi, S. ; Masera, M.; Masoni, A.; Massacrier, L.; Mastromarco, M.; Mastroserio, A.; Matthews, Z. L.; Matyja, A.; Mayani, D.; Mayer, C.; Mazer, J.; Mazzoni, M. A.; Meddi, F.; Menchaca-Rocha, A.; Mercado Perez, J.; Meres, M.; Miake, Y.; Milano, L.; Milosevic, J.; Mischke, A.; Mishra, A. N.; Mikowiec, D.; Mitu, C.; Mlynarz, J.; Mohanty, A. K.; Mohanty, B.; Molnar, L.; Montano Zetina, L. ; Monteno, M.; Montes, E.; Moon, T.; Morando, M. ; Moreira De Godoy, D. A.; Moretto, S.; Morsch, A. ; Muccifora, V.; Mudnic, E.; Muhuri, S.; Müller, H.; Munhoz, M. G.; Musa, L.; Musso, A.; Nandi, B. K.; Nania, R.; Nappi, E.; Nattrass, C.; Naumov, N. P.; Navin, S.; Nayak, T. K.; Nazarenko, S.; Nazarov, G.; Nedosekin, A.; Nicassio, M.; Nielsen, B. S.; Niida, T.; Nikolaev, S.; Nikolic, V.; Nikulin, V.; Nikulin, S.; Nilsen, B. S.; Nilsson, M. S.; Noferini, F.; Nomokonov, P.; Nooren, G.; Novitzky, N.; Nyanin, A.; Nyatha, A. ; Nygaard, C.; Nystrand, J.; Ochirov, A.; Oeschler, H.; Oh, S. K.; Oh, S.; Oleniacz, J.; Oppedisano, C.; Ortiz Velasquez, A.; Ortona, G.; Oskarsson, A.; Ostrowski, P.; Otwinowski, J.; Oyama, K.; Ozawa, K.; Pachmayer, Y.; Pachr, M.; Padilla, F.; Pagano, P.; Paic, G.; Painke, F.; Pajares, C.; Pal, S. K.; Pal, S.; Palaha, A.; Palmeri, A.; Papikyan, V.; Pappalardo, G. S.; Park, W. J.; Passfeld, A.; Pastircak, B.; Patalakha, D. I.; Paticchio, V.; Pavlinov, A.; Pawlak, T.; Peitzmann, T.; Pereira De Oliveira Filho, E.; Peresunko, D.; Perez Lara, C. E.; Perez Lezama, E. ; Perini, D.; Perrino, D.; Peryt, W.; Pesci, A. ; Peskov, V.; Pestov, Y.; Petracek, V.; Petran, M.; Petris, M.; Petrov, P.; Petrovici, M.; Petta, C.; Piano, S.; Piccotti, A.; Pikna, M.; Pillot, P.; Pinazza, O.; Pinsky, L.; Pitz, N.; Piuz, F.; Piyarathna, D. B.; Ploskon, M.; Pluta, J.; Pocheptsov, T.; Pochybova, S.; Podesta-Lerma, P. L. M.; Poghosyan, M. G.; Polak, K.; Polichtchouk, B.; Pop, A.; Porteboeuf-Houssais, S.; Pospisil, V.; Potukuchi, B.; Prasad, S. K.; Preghenella, R.; Prino, F.; Pruneau, C. A.; Pshenichnov, I.; Puchagin, S.; Puddu, G.; Pujol Teixido, J.; Pulvirenti, A.; Punin, V.; Putis, M. ; Putschke, J.; Quercigh, E.; Qvigstad, H.; Rachevski, A.; Rademakers, A.; Radomski, S.; Räihä T. S.; Rak, J.; Rakotozafindrabe, A.; Ramello, L.; Ramirez Reyes, A.; Raniwala, S.; Raniwala, R.; Räsänen, S. S.; Rascanu, B. T.; Rathee, D.; Read, K. F.; Real, J. S.; Redlich, K. ; Reichelt, P.; Reicher, M.; Renfordt, R.; Reolon, A. R.; Reshetin, A.; Rettig, F.; Revol, J.-P.; Reygers, K.; Riccati, L.; Ricci, R. A.; Richert, T.; Richter, M.; Riedler, P.; Riegler, W. ; Riggi, F.; Rodriguez Cahuantzi, M.; Roed, K.; Rohr, D.; Röhrich, D.; Romita, R.; Ronchetti, F. ; Rosnet, P.; Rossegger, S.; Rossi, A.; Roukoutakis, F.; Roy, C.; Roy, P.; Rubio Montero, A. J.; Rui, R.; Ryabinkin, E.; Rybicki, A.; Sadovsky, S.; Safarik, K.; Sahoo, R.; Sahu, P. K.; Saini, J.; Sakaguchi, H.; Sakai, S.; Sakata, D.; Salgado, C. A.; Salzwedel, J.; Sambyal, S.; Samsonov, V.; Sanchez Castro, X.; Sandor, L.; Sandoval, A.; Sano, S.; Sano, M.; Santo, R.; Santoro, R.; Sarkamo, J.; Scapparone, E.; Scarlassara, F.; Scharenberg, R. P.; Schiaua, C.; Schicker, R.; Schmidt, H. R.; Schmidt, C.; Schreiner, S.; Schuchmann, S.; Schukraft, J.; Schutz, Y.; Schwarz, K.; Schweda, K.; Scioli, G. ; Scomparin, E.; Scott, P. A.; Scott, R.; Segato, G.; Selyuzhenkov, I.; Senyukov, S.; Seo, J.; Serci, S.; Serradilla, E.; Sevcenco, A.; Sgura, I. ; Shabetai, A.; Shabratova, G.; Shahoyan, R.; Sharma, N.; Sharma, S.; Shigaki, K.; Shimomura, M. ; Shtejer, K.; Sibiriak, Y.; Siciliano, M.; Sicking, E.; Siddhanta, S.; Siemiarczuk, T.; Silvermyr, D.; Silvestre, c.; Simonetti, G.; Singaraju, R.; Singh, R.; Singha, S.; Sinha, T.; Sinha, B. C.; Sitar, B.; Sitta, M.; Skaali, T. B. ; Skjerdal, K.; Smakal, R.; Smirnov, N.; Snellings, R. J. M.; Sogaard, C.; Soltz, R.; Son, H.; Song, M.; Song, J.; Soos, C.; Soramel, F. ; Sputowska, I.; Spyropoulou-Stassinaki, M.; Srivastava, B. K.; Stachel, J.; Stan, I.; Stan, I. ; Stefanek, G.; Stefanini, G.; Steinbeck, T.; Steinpreis, M.; Stenlund, E.; Steyn, G.; Stocco, D. ; Stolpovskiy, M.; Strabykin, K.; Strmen, P.; Suaide, A. A. P.; Subieta Vasquez, M. A.; Sugitate, T.; Suire, C.; Sukhorukov, M.; Sultanov, R.; Sumbera, M.; Susa, T.; Szanto de Toledo, A.; Szarka, I.; Szostak, A.; Tagridis, C.; Takahashi, J.; Tapia Takaki, J. D.; Tauro, A.; Tejeda Munoz, G.; Telesca, A.; Terrevoli, C.; Thäder, J.; Thomas, D.; Tieulent, R.; Timmins, A. R.; Tlusty, D.; Toia, A.; Torii, H.; Toscano, L.; Tosello, F.; Truesdale, D.; Trzaska, W. H.; Tsuji, T.; Tumkin, A.; Turrisi, R.; Tveter, T. S.; Ulery, J. ; Ullaland, K.; Ulrich, J.; Uras, A.; Urban, J. ; Urciuoli, G. M.; Usai, G. L.; Vajzer, M.; Vala, M.; Valencia Palomo, L.; Vallero, S.; van der Kolk, N.; Vande Vyvre, P.; van Leeuwen, M.; Vannucci, L. ; Vargas, A.; Varma, R.; Vasileiou, M.; Vasiliev, A.; Vechernin, V.; Veldhoen, M.; Venaruzzo, M.; Vercellin, E.; Vergara, S.; Vernekohl, D. C.; Vernet, R.; Verweij, M.; Vickovic, L.; Viesti, G. ; Vikhlyantsev, O.; Vilakazi, Z.; Villalobos Baillie, O.; Vinogradov, A.; Vinogradov, Y.; Vinogradov, L.; Virgili, T.; Viyogi, Y. P.; Vodopyanov, A.; Voloshin, S.; Voloshin, K.; Volpe, G.; von Haller, B.; Vranic, D.; Ovrebekk, G.; Vrlakova, J.; Vulpescu, B.; Vyushin, A.; Wagner, B.; Wagner, V.; Wan, R.; Wang, Y.; Wang, D.; Wang, Y.; Wang, M.; Watanabe, K.; Wessels, J. P. ; Westerhoff, U.; Wiechula, J.; Wikne, J.; Wilde, M.; Wilk, G.; Wilk, A.; Williams, M. C. S.; Windelband, B.; Xaplanteris Karampatsos, L.; Yang, H. ; Yang, S.; Yasnopolskiy, S.; Yi, J.; Yin, Z.; Yokoyama, H.; Yoo, I.-K.; Yoon, J.; Yu, W.; Yuan, X.; Yushmanov, I.; Zach, C.; Zampolli, C.; Zaporozhets, S.; Zarochentsev, A.; Zavada, P.; Zaviyalov, N.; Zbroszczyk, H.; Zelnicek, P.; Zgura, I. S.; Zhalov, M.; Zhang, X.; Zhou, D.; Zhou, Y. ; Zhou, F.; Zhu, X.; Zichichi, A.; Zimmermann, A. ; Zinovjev, G.; Zoccarato, Y.; Zynovyev, M.: **J/ψ Suppression at Forward Rapidity in Pb-Pb Collisions at $\sqrt{s_{NN}}$ =2.76TeV.** *Physical review letters* 109: 072301, 2012. DOI:10.1103/PhysRevLett.109.072301

WOS-PHN-9 Abelev, B.; Adam, J.; Adamova, D.; Adare, A. M.;

Aggarwal, M. M.; Aglieri Rinella, G.; Agocs, A. G. ; Agostinelli, A.; Aguilar Salazar, S.; Ahammed, Z. ; Ahmad, N.; Ahmad Masoodi, A.; Ahn, S. A.; Ahn, S. U.; Akindinov, A.; Aleksandrov, D.; Alessandro, B.; Alfaro Molina, R.; Alici, A.; Alkin, A.; Almaraz Avina, E.; Alme, J.; Alt, T.; Altini, V. ; Altinpinar, S.; Altsybeev, I.; Andrei, C.; Andronic, A.; Anguelov, V.; Anielski, J.; Anson, C. ; Anticic, T.; Antinori, F.; Antonioli, P.; Aphecetche, L.; Appelshäuser, H.; Arbor, N.; Arcelli, S.; Arend, A.; Armesto, N.; Arnaldi, R. ; Aronsson, T.; Arsene, I. C.; Arslandok, M.; Asryan, A.; Augustinus, A.; Averbeck, R.; Awes, T. C.; Äystö J.; Azmi, M. D.; Bach, M.; Badala, A.; Baek, Y. W.; Bailhache, R.; Bala, R.; Baldini Ferroli, R.; Baldisseri, A.; Baldit, A.; Baltasar Dos Santos Pedrosa, F.; Ban, J.; Baral, R. C.; Barbera, R.; Barile, F.; Barnaföldi, G. G.; Barnby, L. S.; Barret, V.; Bartke, J.; Basile, M. ; Bastid, N.; Basu, S.; Bathen, B.; Batigne, G. ; Batyunya, B.; Baumann, C.; Bearden, I. G.; Beck, H.; Behera, N. K.; Belikov, I.; Bellini, F. ; Bellwied, R.; Belmont-Moreno, E.; Bencedi, G.; Beole, S.; Berceanu, I.; Bercuci, A.; Berdnikov, Y. ; Berenyi, D.; Bergognon, A. A. E.; Berzano, D.; Betev, L.; Bhasin, A.; Bhati, A. K.; Bhom, J.; Bianchi, L.; Bianchi, N.; Bianchin, C.; Bielcik, J.; Bielcikova, J.; Bilandzic, A.; Bjelogrlic, S.; Blanco, F.; Blanco, F.; Blau, D.; Blume, C. ; Boccioli, M.; Bock, N.; Böttger, S.; Bogdanov, A.; Boggild, H.; Bogolyubsky, M.; Boldizsar, L. ; Bombara, M.; Book, J.; Borel, H.; Borissov, A. ; Bose, S.; Boss, F.; Botje, M.; Botta, E.; Boyer, B.; Braidot, E.; Braun-Munzinger, P.; Bregant, M.; Breitner, T.; Browning, T. A.; Broz, M.; Brun, R.; Bruna, E.; Bruno, G. E.; Budnikov, D.; Buesching, H.; Bufalino, S.; Busch, O.; Buthelezi, Z.; Caballero Orduna, D.; Caffarri, D.; Cai, X.; Caines, H.; Calvo Villar, E.; Camerini, P. ; Canoa Roman, V.; Cara Romeo, G.; Carena, F.; Carena, W.; Carlin Filho, N.; Carminati, F.; Casanova Diaz, A.; Castillo Castellanos, J.; Castillo Hernandez, J. F.; Casula, E. A. R.; Catanescu, V.; Cavicchioli, C.; Ceballos Sanchez, C.; Cepila, J.; Cerello, P.; Chang, B.; Chapeland, S.; Charvet, J. L.; Chattopadhyay, S.; Chattopadhyay, S.; Chawla, I.; Cherney, M.; Cheshkov, C.; Cheynis, B.; Chibante Barroso, V.; Chinellato, D. D.; Chochula, P. ; Chojnacki, M.; Choudhury, S.; Christakoglou, P. ; Christensen, C. H.; Christiansen, P.; Chujo, T. ; Chung, S. U.; Cicalo, C.; Cifarelli, L.; Cindolo, F.; Cleymans, J.; Coccetti, F.; Colamaria, F.; Colella, D.; Conesa Balbastre, G.; Conesa del Valle, Z.; Constantin, P.; Contin, G.; Contreras, J. G.; Cormier, T. M.; Corrales Morales, Y.; Cortese, P.; Cortes Maldonado, I.; Cosentino, M. R. ; Costa, F.; Cotallo, M. E.; Crescio, E.; Crochet, P.; Cruz Alaniz, E.; Cuautle, E.; Cunqueiro, L.; Dainese, A.; Dalsgaard, H. H.; Danu, A.; Das, I.; Das, D.; Das, K.; Dash, S.; Dash, A.; De, S.; de Barros, G. O. V.; De Caro, A. ; de Cataldo, G.; de Cuveland, J.; De Falco, A.; De Gruttola, D.; Delagrange, H.; Deloff, A.; Demanov, V.; De Marco, N.; Denes, E.; De Pasquale, S.; Deppman, A.; Erasmo, G. D.; de Rooij, R.; Diaz Corchero, M. A.; Di Bari, D.; Dietel, T.; Di Giglio, C.; Di Liberto, S.; Di Mauro, A.; Di Nezza, P.; Divia, R.; Djuvsland, O.; Dobrin, A.; Dobrowolski, T.; Dominguez, I.; Dönigus, B.; Dordic, O.; Driga, O.; Dubey, A. K.; Dubla, A.; Ducroux, L.; Dupieux, P.; Dutta Majumdar, A. K.; Dutta Majumdar, M. R.; Elia, D.; Emschermann, D.; Engel, H.; Erazmus, B.; Erdal, H. A.; Espagnon, B. ; Estienne, M.; Esumi, S.; Evans, D.; Eyyubova, G.; Fabris, D.; Faivre, J.; Falchieri, D.; Fantoni, A.; Fasel, M.; Fearick, R.; Fedunov, A. ; Fehlker, D.; Feldkamp, L.; Felea, D.; Fenton-Olsen, B.; Feofilov, G.; Fernandez Tellez, A. ; Ferretti, A.; Ferretti, R.; Festanti, A.; Figiel, J.; Figueredo, M. A. S.; Filchagin, S.; Finogeev, D.; Fionda, F. M.; Fiore, E. M.; Floris, M.; Foertsch, S.; Foka, P.; Fokin, S.; Fragiacomo, E.; Francescon, A.; Frankenfeld, U.; Fuchs, U.; Furget, C.; Fusco Girard, M.; Gaardhoje, J. J.; Gagliardi, M.; Gago, A.; Gallio, M.; Gangadharan, D. R.; Ganoti, P.; Garabatos, C. ; Garcia-Solis, E.; Garishvili, I.; Gerhard, J.; Germain, M.; Geuna, C.; Gheata, M.; Gheata, A.; Ghidini, B.; Ghosh, P.; Gianotti, P.; Girard, M. R. ; Giubellino, P.; Gladysz-Dziadus, E.; Glässel, P. ; Gomez, R.; Ferreiro, E. G.; Gonzalez-Trueba, L. H.; Gonzalez-Zamora, P.; Gorbunov, S.; Goswami, A. ; Gotovac, S.; Grabski, V.; Graczykowski, L. K.; Grajcarek, R.; Grelli, A.; Grigoras, C.; Grigoras, A.; Grigoriev, V.; Grigoryan, S.; Grigoryan, A.; Grinyov, B.; Grion, N.; Gros, P.; Grosse-Oetringhaus, J. F.; Grossiord, J.-Y.; Grosso, R.; Guber, F.; Guernane, R.; Guerra Gutierrez, C. ; Guerzoni, B.; Guilbaud, M.; Gulbrandsen, K.; Gunji, T.; Gupta, R.; Gupta, A.; Gutbrod, H.; Haaland, O.; Hadjidakis, C.; Haiduc, M.; Hamagaki, H.; Hamar, G.; Han, B. H.; Hanratty, L. D.; Hansen, A.; Harmanova-Tothova, Z.; Harris, J. W. ; Hartig, M.; Hasegan, D.; Hatzifotiadou, D.; Hayrapetyan, A.; Heckel, S. T.; Heide, M.; Helstrup, H.; Herghelegiu, A.; Herrera Corral, G.; Herrmann, N.; Hess, B. A.; Hetland, K. F.; Hicks, B.; Hille, P. T.; Hippolyte, B.; Horaguchi, T.; Hori, Y.; Hristov, P.; Hrivnacova, I.; Huang, M.; Humanic, T. J.; Hwang, D. S.; Ichou, R.; Ilkaev, R.; Ilkiv, I.; Inaba, M.; Incani, E.; Innocenti, G. M.; Innocenti, P. G.; Ippolitov, M.; Irfan, M.; Ivan, C.; Ivanov, M.; Ivanov, A.; Ivanov, V.; Ivanytskyi, O.; Jacobs, P. M.; Jang, H. J.; Janik, R.; Janik, M. A.; Jayarathna, P. H. S. Y.; Jena, S.; Jha, D. M.; Jimenez Bustamante, R. T. ; Jirden, L.; Jones, P. G.; Jung, H.; Jusko, A. ; Kaidalov, A. B.; Kakoyan, V.; Kalcher, S.; Kalinak, P.; Kalliokoski, T.; Kalweit, A.; Kang, J. H.; Kaplin, V.; Karasu Uysal, A.; Karavichev, O. ; Karavicheva, T.; Karpechev, E.; Kazantsev, A.; Kebschull, U.; Keidel, R.; Khan, P.; Khan, M. M. ; Khan, S. A.; Khanzadeev, A.; Kharlov, Y.; Kileng, B.; Kim, M.; Kim, D. J.; Kim, D. W.; Kim, J. H.; Kim, J. S.; Kim, T.; Kim, M.; Kim, S. H.; Kim, S.; Kim, B.; Kirsch, S.; Kisel, I. ; Kiselev, S.; Kisiel, A.; Klay, J. L.; Klein, J. ; Klein-Bösing, C.; Kliemant, M.; Kluge, A.; Knichel, M. L.; Knospe, A. G.; Koch, K.; Köhler, M. K.; Kollegger, T.; Kolojvari, A.; Kondratiev, V. ; Kondratyeva, N.; Konevskikh, A.; Korneev, A.; Kour, R.; Kowalski, M.; Kox, S.; Koyithatta Meethaleveedu, G.; Kral, J.; Kralik, I.; Kramer, F.; Kraus, I.; Krawutschke, T.; Krelina, M.; Kretz, M.; Krivda, M.; Krizek, F.; Krus, M.; Kryshen, E.; Krzewicki, M.; Kucheriaev, Y.; Kugathasan, T.; Kuhn, C.; Kuijer, P. G.; Kulakov, I.; Kumar, J.; Kurashvili, P.; Kurepin, A. B.; Kurepin, A.; Kuryakin, A.; Kushpil, S.; Kushpil, V. ; Kvaerno, H.; Kweon, M. J.; Kwon, Y.; Ladron de Guevara, P.; Lakomov, I.; Langoy, R.; La Pointe, S. L.; Lara, C.; Lardeux, A.; La Rocca, P.; Lazzeroni, C.; Lea, R.; Le Bornec, Y.; Lechman, M. ; Lee, K. S.; Lee, G. R.; Lee, S. C.; Lefevre, F.; Lehnert, J.; Leistam, L.; Lenhardt, M.; Lenti, V.; Leon, H.; Leoncino, M.; Leon Monzon, I.; Leon Vargas, H.; Levai, P.; Lien, J.; Lietava, R.; Lindal, S.; Lindenstruth, V.; Lippmann, C.; Lisa, M. A.; Liu, L.; Loggins, V. R. ; Loginov, V.; Lohn, S.; Lohner, D.; Loizides, C. ; Loo, K. K.; Lopez, X.; Lopez Torres, E.; Lovhoiden, G.; Lu, X.-G.; Luettig, P.; Lunardon, M.; Luo, J.; Luparello, G.; Luquin, L.; Luzzi, C.; Ma, K.; Ma, R.; Madagodahettige-Don, D. M.; Maevskaya, A.; Mager, M.; Mahapatra, D. P.; Maire, A.; Malaev, M.; Maldonado Cervantes, I.; Malinina, L.; MalKevich, D.; Malzacher, P.; Mamonov, A. ; Manceau, L.; Mangotra, L.; Manko, V.; Manso, F. ; Manzari, V.; Mao, Y.; Marchisone, M.; Mares, J.; Margagliotti, G. V.; Margotti, A.; Marin, A. ; Marin Tobon, C. A.; Markert, C.; Martashvili, I. ; Martinengo, P.; Martinez, M. I.; Martinez Davalos, A.; Martinez Garcia, G.; Martynov, Y.; Mas, A.; Masciocchi, S.; Masera, M.; Masoni, A.; Massacrier, L.; Mastroserio, A.;

Matthews, Z. L.; Matyja, A.; Mayer, C.; Mazer, J.; Mazzoni, M. A. ; Meddi, F.; Menchaca-Rocha, A.; Mercado Perez, J. ; Meres, M.; Miake, Y.; Milano, L.; Milosevic, J. ; Mischke, A.; Mishra, A. N.; Mikowiec, D.; Mitu, C.; Mlynarz, J.; Mohanty, B.; Molnar, L.; Montano Zetina, L.; Monteno, M.; Montes, E.; Moon, T.; Morando, M.; Moreira De Godoy, D. A.; Moretto, S.; Morsch, A.; Muccifora, V.; Mudnic, E.; Muhuri, S.; Mukherjee, M.; Müller, H.; Munhoz, M. G.; Musa, L.; Musso, A.; Nandi, B. K.; Nania, R. ; Nappi, E.; Nattrass, C.; Naumov, N. P.; Navin, S.; Nayak, T. K.; Nazarenko, S.; Nazarov, G.; Nedosekin, A.; Nicassio, M.; Niculescu, M.; Nielsen, B. S.; Niida, T.; Nikolaev, S.; Nikolic, V.; Nikulin, S.; Nikulin, V.; Nilsen, B. S.; Nilsson, M. S.; Noferini, F.; Nomokonov, P.; Nooren, G.; Novitzky, N.; Nyanin, A.; Nyatha, A. ; Nygaard, C.; Nystrand, J.; Ochirov, A.; Oeschler, H.; Oh, S.; Oh, S. K.; Oleniacz, J.; Oppedisano, C.; Ortiz Velasquez, A.; Ortona, G.; Oskarsson, A.; Ostrowski, P.; Otwinowski, J.; Oyama, K.; Ozawa, K.; Pachmayer, Y.; Pachr, M.; Padilla, F.; Pagano, P.; Paic, G.; Painke, F.; Pajares, C.; Pal, S. K.; Palaha, A.; Palmeri, A. ; Papikyan, V.; Pappalardo, G. S.; Park, W. J.; Passfeld, A.; Pastircak, B.; Patalakha, D. I.; Paticchio, V.; Pavlinov, A.; Pawlak, T.; Peitzmann, T.; Pereira Da Costa, H.; Pereira De Oliveira Filho, E.; Peresunko, D.; Perez Lara, C. E.; Perez Lezama, E.; Perini, D.; Perrino, D.; Peryt, W.; Pesci, A.; Peskov, V.; Pestov, Y.; Petracek, V. ; Petran, M.; Petris, M.; Petrov, P.; Petrovici, M.; Petta, C.; Piano, S.; Piccotti, A.; Pikna, M.; Pillot, P.; Pinazza, O.; Pinsky, L.; Pitz, N.; Piyarathna, D. B.; Planinic, M.; Ploskon, M. ; Pluta, J.; Pocheptsov, T.; Pochybova, S.; Podesta-Lerma, P. L. M.; Poghosyan, M. G.; Polak, K. ; Polichtchouk, B.; Pop, A.; Porteboeuf-Houssais, S. ; Pospisil, V.; Potukuchi, B.; Prasad, S. K.; Preghenella, R.; Prino, F.; Pruneau, C. A.; Pshenichnov, I.; Puchagin, S.; Puddu, G.; Pulvirenti, A.; Punin, V.; Putis, M.; Putschke, J. ; Quercigh, E.; Qvigstad, H.; Rachevski, A.; Rademakers, A.; Räihä T. S.; Rak, J.; Rakotozafindrabe, A.; Ramello, L.; Ramirez Reyes, A. ; Raniwala, S.; Raniwala, R.; Räsänen, S. S.; Rascanu, B. T.; Rathee, D.; Read, K. F.; Real, J. S.; Redlich, K.; Reichelt, P.; Reicher, M.; Renfordt, R.; Reolon, A. R.; Reshetin, A.; Rettig, F.; Revol, J.-P.; Reygers, K.; Riccati, L.; Ricci, R. A.; Richert, T.; Richter, M.; Riedler, P. ; Riegler, W.; Riggi, F.; Rodrigues Fernandes Rabacal, B.; Rodriguez Cahuantzi, M.; Rodriguez Manso, A.; Roed, K.; Rohr, D.; Röhrich, D.; Romita, R.; Ronchetti, F.; Rosnet, P.; Rossegger, S.; Rossi, A.; Roy, P.; Roy, C.; Rubio Montero, A. J.; Rui, R.; Russo, R.; Ryabinkin, E.; Rybicki, A.; Sadovsky, S.; Safarik, K.; Sahoo, R.; Sahu, P. K.; Saini, J.; Sakaguchi, H.; Sakai, S.; Sakata, D.; Salgado, C. A.; Salzwedel, J.; Sambyal, S.; Samsonov, V.; Sanchez Castro, X. ; Sandor, L.; Sandoval, A.; Sano, M.; Sano, S. ; Santo, R.; Santoro, R.; Sarkamo, J.; Scapparone, E.; Scarlassara, F.; Scharenberg, R. P. ; Schiaua, C.; Schicker, R.; Schmidt, H. R.; Schmidt, C.; Schreiner, S.; Schuchmann, S.; Schukraft, J.; Schutz, Y.; Schwarz, K.; Schweda, K. ; Scioli, G.; Scomparin, E.; Scott, P. A.; Scott, R.; Segato, G.; Selyuzhenkov, I.; Senyukov, S.; Seo, J.; Serci, S.; Serradilla, E.; Sevcenco, A. ; Shabetai, A.; Shabratova, G.; Shahoyan, R.; Sharma, N.; Sharma, S.; Rohni, S.; Shigaki, K.; Shimomura, M.; Shtejer, K.; Sibiriak, Y.; Siciliano, M.; Sicking, E.; Siddhanta, S.; Siemiarczuk, T.; Silvermyr, D.; Silvestre, C.; Simatovic, G.; Simonetti, G.; Singaraju, R.; Singh, R.; Singha, S.; Singhal, V.; Sinha, T.; Sinha, B. C.; Sitar, B.; Sitta, M.; Skaali, T. B.; Skjerdal, K.; Smakal, R.; Smirnov, N.; Snellings, R. J. M.; Sogaard, C.; Soltz, R.; Son, H.; Song, J.; Song, M.; Soos, C.; Soramel, F.; Sputowska, I.; Spyropoulou-Stassinaki, M.; Srivastava, B. K.; Stachel, J.; Stan, I.; Stan, I.; Stefanek, G.; Steinpreis, M.; Stenlund, E.; Steyn, G.; Stiller, J. H.; Stocco, D.; Stolpovskiy, M.; Strabykin, K.; Strmen, P.; Suaide, A. A. P.; Subieta Vasquez, M. A.; Sugitate, T.; Suire, C.; Sukhorukov, M.; Sultanov, R.; Sumbera, M.; Susa, T.; Symons, T. J. M.; Szanto de Toledo, A.; Szarka, I.; Szczepankiewicz, A.; Szostak, A.; Szymanski, M.; Takahashi, J.; Tapia Takaki, J. D.; Tauro, A. ; Tejeda Munoz, G.; Telesca, A.; Terrevoli, C.; Thäder, J.; Thomas, D.; Tieulent, R.; Timmins, A. R.; Tlusty, D.; Toia, A.; Torii, H.; Toscano, L. ; Trubnikov, V.; Truesdale, D.; Trzaska, W. H.; Tsuji, T.; Tumkin, A.; Turrisi, R.; Tveter, T. S. ; Ulery, J.; Ullaland, K.; Ulrich, J.; Uras, A. ; Urban, J.; Urciuoli, G. M.; Usai, G. L.; Vajzer, M.; Vala, M.; Valencia Palomo, L.; Vallero, S.; Vande Vyvre, P.; van Leeuwen, M.; Vannucci, L. ; Vargas, A.; Varma, R.; Vasileiou, M.; Vasiliev, A.; Vechernin, V.; Veldhoen, M.; Venaruzzo, M.; Vercellin, E.; Vergara, S.; Vernet, R.; Verweij, M. ; Vickovic, L.; Viesti, G.; Vikhlyantsev, O.; Vilakazi, Z.; Villalobos Baillie, O.; Vinogradov, Y. ; Vinogradov, A.; Vinogradov, L.; Virgili, T.; Viyogi, Y. P.; Vodopyanov, A.; Voloshin, S.; Voloshin, K.; Volpe, G.; von Haller, B.; Vranic, D. ; Ovrebekk, G.; Vrlakova, J.; Vulpescu, B.; Vyushin, A.; Wagner, V.; Wagner, B.; Wan, R.; Wang, Y.; Wang, M.; Wang, D.; Wang, Y.; Watanabe, K.; Weber, M.; Wessels, J. P.; Westerhoff, U.; Wiechula, J.; Wikne, J.; Wilde, M. ; Wilk, A.; Wilk, G.; Williams, M. C. S.; Windelband, B.; Xaplanteris Karampatsos, L.; Yaldo, C. G.; Yamaguchi, Y.; Yang, S.; Yang, H.; Yasnopolskiy, S.; Yi, J.; Yin, Z.; Yoo, I.-K.; Yoon, J.; Yu, W.; Yuan, X.; Yushmanov, I.; Zaccolo, V.; Zach, C.; Zampolli, C.; Zaporozhets, S.; Zarochentsev, A.; Zavada, P.; Zaviyalov, N. ; Zbroszczyk, H.; Zelnicek, P.; Zgura, I. S.; Zhalov, M.; Zhang, H.; Zhang, X.; Zhou, D.; Zhou, Y.; Zhou, F.; Zhu, J.; Zhu, X.; Zhu, J. ; Zichichi, A.; Zimmermann, A.; Zinovjev, G.; Zoccarato, Y.; Zynovyev, M.; Zyzak, M.: **Pion, Kaon, and Proton Production in Central Pb-Pb Collisions at $\sqrt{s_{NN}}$=2.76TeV.** *Physical review letters* 109: 252301, 2012. DOI:10.1103/PhysRevLett.109.252301

WOS-PHN-10 Abelev, B.; Adam, J.; Adamova, D.; Adare, A. M.; Aggarwal, M. M.; Aglieri Rinella, G.; Agocs, A. G. ; Agostinelli, A.; Aguilar Salazar, S.; Ahammed, Z. ; Ahmad, N.; Ahmad Masoodi, A.; Ahn, S. U.; Akindinov, A.; Aleksandrov, D.; Alessandro, B.; Alfaro Molina, R.; Alici, A.; Alkin, A.; Almaraz Avina, E.; Alt, T.; Altini, V.; Altinpinar, S.; Altsybeev, I.; Andrei, C.; Andronic, A.; Anguelov, V.; Anielski, J.; Anson, C.; Anticic, T.; Antinori, F.; Antonioli, P.; Aphecetche, L.; Appelshäuser, H.; Arbor, N.; Arcelli, S.; Arend, A.; Armesto, N.; Arnaldi, R.; Aronsson, T.; Arsene, I. C.; Arslandok, M.; Asryan, A.; Augustinus, A.; Averbeck, R.; Awes, T. C.; Äystö J.; Azmi, M. D.; Bach, M.; Badala, A.; Baek, Y. W.; Bailhache, R.; Bala, R.; Baldini Ferroli, R. ; Baldisseri, A.; Baldit, A.; Baltasar Dos Santos Pedrosa, F.; Ban, J.; Baral, R. C.; Barbera, R. ; Barile, F.; Barnaföldi, G. G.; Barnby, L. S.; Barret, V.; Bartke, J.; Basile, M.; Bastid, N.; Bathen, B.; Batigne, G.; Batyunya, B.; Baumann, C. ; Bearden, I. G.; Beck, H.; Belikov, I.; Bellini, F.; Bellwied, R.; Belmont-Moreno, E.; Beole, S.; Berceanu, I.; Bercuci, A.; Berdnikov, Y.; Berenyi, D.; Bergmann, C.; Berzano, D.; Betev, L.; Bhasin, A.; Bhati, A. K.; Bianchi, N.; Bianchi, L. ; Bianchin, C.; Bielcik, J.; Bielcikova, J.; Bilandzic, A.; Blanco, F.; Blanco, F.; Blau, D.; Blume, C.; Boccioli, M.; Bock, N.; Bogdanov, A.; Boggild, H.; Bogolyubsky, M.; Boldizsar, L.; Bombara, M.; Book, J.; Borel, H.; Borissov, A.; Bose, S.; Boss, F.; Botje, M.; Böttger, S.; Boyer, B.; Braun-Munzinger, P.; Bregant, M.; Breitner, T.; Broz, M.; Brun, R.; Bruna, E.; Bruno, G. E.; Budnikov, D.; Buesching, H.; Bufalino, S.;

Bugaiev, K.; Busch, O.; Buthelezi, Z. ; Caballero Orduna, D.; Caffarri, D.; Cai, X.; Caines, H.; Calvo Villar, E.; Camerini, P.; Canoa Roman, V.; Cara Romeo, G.; Carena, F.; Carena, W. ; Carlin Filho, N.; Carminati, F.; Carrillo Montoya, C. A.; Casanova Diaz, A.; Caselle, M.; Castillo Castellanos, J.; Castillo Hernandez, J. F.; Casula, E. A. R.; Catanescu, V.; Cavicchioli, C.; Cepila, J. ; Cerello, P.; Chang, B.; Chapeland, S.; Charvet, J. L.; Chattopadhyay, S.; Chattopadhyay, S.; Cherney, M.; Cheshkov, C.; Cheynis, B.; Chiavassa, E.; Chibante Barroso, V.; Chinellato, D. D.; Chochula, P.; Chojnacki, M.; Christakoglou, P.; Christensen, C. H.; Christiansen, P.; Chujo, T.; Chung, S. U.; Cicalo, C.; Cifarelli, L.; Cindolo, F.; Cleymans, J.; Coccetti, F.; Coffin, J.-P.; Colamaria, F.; Colella, D.; Conesa Balbastre, G.; Conesa del Valle, Z.; Constantin, P.; Contin, G.; Contreras, J. G.; Cormier, T. M.; Corrales Morales, Y. ; Cortese, P.; Cortes Maldonado, I.; Cosentino, M. R.; Costa, F.; Cotallo, M. E.; Crescio, E.; Crochet, P.; Cruz Alaniz, E.; Cuautle, E.; Cunqueiro, L.; Dainese, A.; Dalsgaard, H. H.; Danu, A.; Das, K.; Das, D.; Das, I.; Dash, A.; Dash, S.; De, S.; Azevedo Moregula, A.; Barros, G. O. V.; Caro, A.; Cataldo, G.; Cuveland, J.; Falco, A.; Gruttola, D.; Delagrange, H.; Castillo Sanchez, E.; Deloff, A.; Demanov, V.; Marco, N.; Denes, E.; Pasquale, S.; Deppman, A.; Erasmo, G. D ; Rooij, R.; Bari, D.; Dietel, T.; Giglio, C.; Liberto, S.; Mauro, A.; Nezza, P.; Divia, R.; Djuvsland, O.; Dobrin, A.; Dobrowolski, T.; Dominguez, I.; Dönigus, B.; Dordic, O.; Driga, O. ; Dubey, A. K.; Ducroux, L.; Dupieux, P.; Dutta Majumdar, A. K.; Dutta Majumdar, M. R.; Elia, D.; Emschermann, D.; Engel, H.; Erdal, H. A.; Espagnon, B.; Estienne, M.; Esumi, S.; Evans, D.; Eyyubova, G.; Fabris, D.; Faivre, J.; Falchieri, D. ; Fantoni, A.; Fasel, M.; Fearick, R.; Fedunov, A.; Fehlker, D.; Feldkamp, L.; Felea, D.; Feofilov, G.; Fernandez Tellez, A.; Ferretti, A.; Ferretti, R.; Figiel, J.; Figueredo, M. A. S.; Filchagin, S.; Fini, R.; Finogeev, D.; Fionda, F. M.; Fiore, E. M.; Floris, M.; Foertsch, S.; Foka, P.; Fokin, S.; Fragiacomo, E.; Fragkiadakis, M.; Frankenfeld, U.; Fuchs, U.; Furget, C.; Fusco Girard, M.; Gaardhoje, J. J.; Gagliardi, M.; Gago, A.; Gallio, M.; Gangadharan, D. R.; Ganoti, P.; Garabatos, C.; Garcia-Solis, E.; Garishvili, I. ; Gerhard, J.; Germain, M.; Geuna, C.; Gheata, A. ; Gheata, M.; Ghidini, B.; Ghosh, P.; Gianotti, P.; Girard, M. R.; Giubellino, P.; Gladysz-Dziadus, E.; Glässel, P.; Gomez, R.; Ferreiro, E. G.; Gonzalez-Trueba, L. H.; Gonzalez-Zamora, P.; Gorbunov, S.; Goswami, A.; Gotovac, S.; Grabski, V. ; Graczykowski, L. K.; Grajcarek, R.; Grelli, A.; Grigoras, C.; Grigoras, A.; Grigoriev, V.; Grigoryan, S.; Grigoryan, A.; Grinyov, B.; Grion, N.; Gros, P.; Grosse-Oetringhaus, J. F.; Grossiord, J.-Y.; Grosso, R.; Guber, F.; Guernane, R.; Guerra Gutierrez, C.; Guerzoni, B.; Guilbaud, M.; Gulbrandsen, K.; Gunji, T.; Gupta, A.; Gupta, R. ; Gutbrod, H.; Haaland, O.; Hadjidakis, C.; Haiduc, M.; Hamagaki, H.; Hamar, G.; Han, B. H.; Hanratty, L. D.; Hansen, A.; Harmanova, Z.; Harris, J. W.; Hartig, M.; Hasegan, D.; Hatzifotiadou, D. ; Hayrapetyan, A.; Heckel, S. T.; Heide, M.; Helstrup, H.; Herghelegiu, A.; Herrera Corral, G.; Herrmann, N.; Hetland, K. F.; Hicks, B.; Hille, P. T.; Hippolyte, B.; Horaguchi, T.; Hori, Y.; Hristov, P.; Hrivnacova, I.; Huang, M.; Huber, S.; Humanic, T. J.; Hwang, D. S.; Ichou, R.; Ilkaev, R.; Ilkiv, I.; Inaba, M.; Incani, E.; Innocenti, G. M.; Innocenti, P. G.; Ippolitov, M.; Irfan, M.; Ivan, C.; Ivanov, A.; Ivanov, V.; Ivanov, M.; Ivanytskyi, O.; Jacholkowski, A.; Jacobs, P. M.; Jancurova, L.; Jang, H. J.; Jangal, S.; Janik, R.; Janik, M. A.; Jayarathna, P. H. S. Y.; Jena, S.; Jimenez Bustamante, R. T.; Jirden, L. ; Jones, P. G.; Jung, H.; Jung, W.; Jusko, A.; Kaidalov, A. B.; Kakoyan, V.; Kalcher, S.; Kalinak, P.; Kalisky, M.; Kalliokoski, T.; Kalweit, A.; Kanaki, K.; Kang, J. H.; Kaplin, V. ; Karasu Uysal, A.; Karavichev, O.; Karavicheva, T. ; Karpechev, E.; Kazantsev, A.; Kebschull, U.; Keidel, R.; Khan, P.; Khan, M. M.; Khan, S. A.; Khanzadeev, A.; Kharlov, Y.; Kileng, B.; Kim, D. J. ; Kim, D. W.; Kim, J. H.; Kim, J. S.; Kim, M.; Kim, S. H.; Kim, S.; Kim, T.; Kim, B.; Kirsch, S.; Kisel, I.; Kiselev, S.; Kisiel, A.; Klay, J. L.; Klein, J.; Klein-Bösing, C.; Kliemant, M.; Kluge, A.; Knichel, M. L.; Koch, K.; Köhler, M. K. ; Kolojvari, A.; Kondratiev, V.; Kondratyeva, N.; Konevskikh, A.; Korneev, A.; Kottachchi Kankanamge Don, C.; Kour, R.; Kowalski, M.; Kox, S.; Koyithatta Meethaleveedu, G.; Kral, J.; Kralik, I. ; Kramer, F.; Kraus, I.; Krawutschke, T.; Krelina, M.; Kretz, M.; Krivda, M.; Krizek, F.; Krus, M.; Kryshen, E.; Krzewicki, M.; Kucheriaev, Y.; Kuhn, C.; Kuijer, P. G.; Kurashvili, P.; Kurepin, A.; Kurepin, A. B.; Kuryakin, A.; Kushpil, V.; Kushpil, S.; Kvaerno, H.; Kweon, M. J.; Kwon, Y.; Ladron de Guevara, P.; Lakomov, I.; Langoy, R.; Lara, C.; Lardeux, A.; Rocca, P.; Lazzeroni, C.; Lea, R.; Bornec, Y.; Lee, K. S.; Lee, S. C.; Lefevre, F.; Lehnert, J.; Leistam, L. ; Lenhardt, M.; Lenti, V.; Leon, H.; Leon Monzon, I.; Leon Vargas, H.; Levai, P.; Li, X. ; Lien, J.; Lietava, R.; Lindal, S.; Lindenstruth, V.; Lippmann, C.; Lisa, M. A.; Liu, L.; Loenne, P. I.; Loggins, V. R.; Loginov, V.; Lohn, S.; Lohner, D.; Loizides, C.; Loo, K. K.; Lopez, X.; Lopez Torres, E.; Lovhoiden, G.; Lu, X.-G.; Luettig, P.; Lunardon, M.; Luo, J.; Luparello, G.; Luquin, L.; Luzzi, C.; Ma, K.; Ma, R.; Madagodahettige-Don, D. M.; Maevskaya, A.; Mager, M.; Mahapatra, D. P.; Maire, A.; Malaev, M. ; Maldonado Cervantes, I.; Malinina, L.; MalKevich, D.; Malzacher, P.; Mamonov, A.; Manceau, L.; Mangotra, L.; Manko, V.; Manso, F.; Manzari, V.; Mao, Y.; Marchisone, M.; Mares, J. ; Margagliotti, G. V.; Margotti, A.; Marin, A.; Markert, C.; Martashvili, I.; Martinengo, P.; Martinez, M. I.; Martinez Davalos, A.; Martinez Garcia, G.; Martynov, Y.; Mas, A.; Masciocchi, S. ; Masera, M.; Masoni, A.; Massacrier, L.; Mastromarco, M.; Mastroserio, A.; Matthews, Z. L.; Matyja, A.; Mayani, D.; Mayer, C.; Mazer, J.; Mazzoni, M. A.; Meddi, F.; Menchaca-Rocha, A.; Mercado Perez, J.; Meres, M.; Miake, Y.; Michalon, A.; Milano, L.; Milosevic, J.; Mischke, A.; Mishra, A. N.; Miskowiec, D.; Mitu, C.; Mlynarz, J. ; Mohanty, B.; Mohanty, A. K.; Molnar, L.; Montano Zetina, L.; Monteno, M.; Montes, E.; Moon, T.; Morando, M.; Moreira De Godoy, D. A.; Moretto, S.; Morsch, A.; Muccifora, V.; Mudnic, E.; Muhuri, S.; Müller, H.; Munhoz, M. G.; Musa, L. ; Musso, A.; Nandi, B. K.; Nania, R.; Nappi, E. ; Nattrass, C.; Naumov, N. P.; Navin, S.; Nayak, T. K.; Nazarenko, S.; Nazarov, G.; Nedosekin, A. ; Nicassio, M.; Nielsen, B. S.; Niida, T.; Nikolaev, S.; Nikolic, V.; Nikulin, S.; Nikulin, V. ; Nilsen, B. S.; Nilsson, M. S.; Noferini, F.; Nomokonov, P.; Nooren, G.; Novitzky, N.; Nyanin, A. ; Nyatha, A.; Nygaard, C.; Nystrand, J.; Ochirov, A.; Oeschler, H.; Oh, S.; Oh, S. K.; Oleniacz, J.; Oppedisano, C.; Ortiz Velasquez, A.; Ortona, G. ; Oskarsson, A.; Ostrowski, P.; Otterlund, I.; Otwinowski, J.; Oyama, K.; Ozawa, K.; Pachmayer, Y. ; Pachr, M.; Padilla, F.; Pagano, P.; Paic, G. ; Painke, F.; Pajares, C.; Pal, S. K.; Pal, S. ; Palaha, A.; Palmeri, A.; Papikyan, V.; Pappalardo, G. S.; Park, W. J.; Passfeld, A.; Pastircak, B.; Patalakha, D. I.; Paticchio, V.; Pavlinov, A.; Pawlak, T.; Peitzmann, T.; Perales, M.; Pereira De Oliveira Filho, E.; Peresunko, D.; Perez Lara, C. E.; Perez Lezama, E.; Perini, D.; Perrino, D.; Peryt, W.; Pesci, A.; Peskov, V.; Pestov, Y.; Petracek, V.; Petran, M.; Petris, M. ; Petrov, P.; Petrovici, M.; Petta, C.; Piano, S. ; Piccotti, A.; Pikna, M.; Pillot, P.; Pinazza, O.; Pinsky, L.; Pitz, N.; Piuz, F.; Piyarathna, D. B.; Ploskon, M.; Pluta, J.; Pocheptsov, T.; Pochybova, S.; Podesta-Lerma, P. L. M.; Poghosyan, M. G.;

Polak, K.; Polichtchouk, B.; Pop, A.; Porteboeuf-Houssais, S.; Pospisil, V.; Potukuchi, B. ; Prasad, S. K.; Preghenella, R.; Prino, F.; Pruneau, C. A.; Pshenichnov, I.; Puchagin, S.; Puddu, G.; Pulvirenti, A.; Punin, V.; Putis, M. ; Putschke, J.; Quercigh, E.; Qvigstad, H.; Rachevski, A.; Rademakers, A.; Radomski, S.; Räihä T. S.; Rak, J.; Rakotozafindrabe, A.; Ramello, L.; Ramirez Reyes, A.; Raniwala, S.; Raniwala, R.; Räsänen, S. S.; Rascanu, B. T.; Rathee, D.; Read, K. F.; Real, J. S.; Redlich, K. ; Reichelt, P.; Reicher, M.; Renfordt, R.; Reolon, A. R.; Reshetin, A.; Rettig, F.; Revol, J.-P.; Reygers, K.; Riccati, L.; Ricci, R. A.; Richert, T.; Richter, M.; Riedler, P.; Riegler, W. ; Riggi, F.; Rodriguez Cahuantzi, M.; Roed, K.; Rohr, D.; Röhrich, D.; Romita, R.; Ronchetti, F. ; Rosnet, P.; Rossegger, S.; Rossi, A.; Roukoutakis, F.; Roy, P.; Roy, C.; Rubio Montero, A. J.; Rui, R.; Ryabinkin, E.; Rybicki, A.; Sadovsky, S.; Safarik, K.; Sahu, P. K.; Saini, J.; Sakaguchi, H.; Sakai, S.; Sakata, D.; Salgado, C. A.; Salzwedel, J.; Sambyal, S.; Samsonov, V.; Sanchez Castro, X.; Sandor, L.; Sandoval, A.; Sano, M.; Sano, S.; Santo, R.; Santoro, R.; Sarkamo, J.; Scapparone, E.; Scarlassara, F.; Scharenberg, R. P.; Schiaua, C.; Schicker, R.; Schmidt, C.; Schmidt, H. R.; Schreiner, S.; Schuchmann, S.; Schukraft, J.; Schutz, Y.; Schwarz, K.; Schweda, K.; Scioli, G. ; Scomparin, E.; Scott, P. A.; Scott, R.; Segato, G.; Selyuzhenkov, I.; Senyukov, S.; Seo, J.; Serci, S.; Serradilla, E.; Sevcenco, A.; Sgura, I. ; Shabetai, A.; Shabratova, G.; Shahoyan, R.; Sharma, N.; Sharma, S.; Shigaki, K.; Shimomura, M. ; Shtejer, K.; Sibiriak, Y.; Siciliano, M.; Sicking, E.; Siddhanta, S.; Siemiarczuk, T.; Silvermyr, D.; Simonetti, G.; Singaraju, R.; Singh, R.; Singha, S.; Sinha, T.; Sinha, B. C.; Sitar, B.; Sitta, M.; Skaali, T. B.; Skjerdal, K.; Smakal, R.; Smirnov, N.; Snellings, R.; Sogaard, C.; Soltz, R.; Son, H.; Song, M.; Song, J.; Soos, C.; Soramel, F.; Sputowska, I.; Spyropoulou-Stassinaki, M.; Srivastava, B. K.; Stachel, J.; Stan, I.; Stan, I.; Stefanek, G.; Stefanini, G.; Steinbeck, T.; Steinpreis, M.; Stenlund, E.; Steyn, G.; Stocco, D.; Stolpovskiy, M.; Strabykin, K.; Strmen, P.; Suaide, A. A. P.; Subieta Vasquez, M. A.; Sugitate, T.; Suire, C.; Sukhorukov, M.; Sultanov, R.; Sumbera, M.; Susa, T.; Szanto de Toledo, A.; Szarka, I.; Szostak, A. ; Tagridis, C.; Takahashi, J.; Tapia Takaki, J. D. ; Tauro, A.; Tejeda Munoz, G.; Telesca, A.; Terrevoli, C.; Thäder, J.; Thomas, D.; Thomas, J. H.; Tieulent, R.; Timmins, A. R.; Tlusty, D.; Toia, A.; Torii, H.; Toscano, L.; Tosello, F.; Traczyk, T.; Truesdale, D.; Trzaska, W. H.; Tsuji, T.; Tumkin, A.; Turrisi, R.; Tveter, T. S.; Ulery, J.; Ullaland, K.; Ulrich, J.; Uras, A.; Urban, J.; Urciuoli, G. M.; Usai, G. L.; Vajzer, M.; Vala, M.; Valencia Palomo, L.; Vallero, S.; Kolk, N.; Vande Vyvre, P.; Leeuwen, M.; Vannucci, L.; Vargas, A.; Varma, R.; Vasileiou, M.; Vasiliev, A.; Vechernin, V.; Veldhoen, M.; Venaruzzo, M.; Vercellin, E.; Vergara, S.; Vernekohl, D. C.; Vernet, R.; Verweij, M.; Vickovic, L.; Viesti, G.; Vikhlyantsev, O.; Vilakazi, Z.; Villalobos Baillie, O.; Vinogradov, A. ; Vinogradov, Y.; Vinogradov, L.; Virgili, T.; Viyogi, Y. P.; Vodopyanov, A.; Voloshin, S.; Voloshin, K.; Volpe, G.; Haller, B.; Vranic, D.; Ovrebekk, G.; Vrlakova, J.; Vulpescu, B.; Vyushin, A.; Wagner, B.; Wagner, V.; Wan, R.; Wang, Y.; Wang, M.; Wang, D.; Wang, Y.; Watanabe, K.; Wessels, J. P.; Westerhoff, U.; Wiechula, J.; Wikne, J.; Wilde, M.; Wilk, G.; Wilk, A.; Williams, M. C. S.; Windelband, B.; Xaplanteris Karampatsos, L.; Yang, H.; Yang, S.; Yasnopolskiy, S.; Yi, J.; Yin, Z.; Yokoyama, H.; Yoo, I.-K.; Yoon, J.; Yu, W.; Yuan, X.; Yushmanov, I.; Zach, C.; Zampolli, C.; Zaporozhets, S.; Zarochentsev, A.; Zavada, P.; Zaviyalov, N. ; Zbroszczyk, H.; Zelnicek, P.; Zgura, I. S.; Zhalov, M.; Zhang, X.; Zhou, F.; Zhou, D.; Zhou, Y.; Zhu, X.; Zichichi, A.; Zimmermann, A.; Zinovjev, G.; Zoccarato, Y.; Zynovyev, M.: **Measurement of event background fluctuations for charged particle jet reconstruction in Pb-Pb collisions at $\sqrt{s_{NN}}$ = 2.76 TeV.** *Journal of high energy physics* 2012: 53, 2012. DOI:10.1007/JHEP03(2012)053

WOS-PHN-11 Abelev, B.; Adam, J.; Adamova, D.; Adare, A. M.; Aggarwal, M. M.; Aglieri Rinella, G.; Agocs, A. G. ; Agostinelli, A.; Aguilar Salazar, S.; Ahammed, Z. ; Ahmad, N.; Ahmad Masoodi, A.; Ahn, S. U.; Akindinov, A.; Aleksandrov, D.; Alessandro, B.; Alfaro Molina, R.; Sanchez-Lorente, Alicia; Alkin, A. ; Almaraz Avina, E.; Alme, J.; Alt, T.; Altini, V.; Altinpinar, S.; Altsybeev, I.; Andrei, C.; Andronic, Anton; Anguelov, V.; Anielski, J.; Anson, C.; Anticic, T.; Antinori, F.; Antonioli, P.; Aphecetche, L.; Appelshäuser, H.; Arbor, N.; Arcelli, S.; Arend, A.; Armesto, N.; Arnaldi, R. ; Aronsson, T.; Arsene, Ionut Cristian; Arslandok, M.; Asryan, A.; Augustinus, A.; Averbeck, Ralf; Awes, T. C.; Äystö J.; Azmi, M. D.; Bach, M.; Badala, A.; Baek, Y. W.; Bailhache, R.; Bala, R. ; Baldini Ferroli, R.; Baldisseri, A.; Baldit, A. ; Baltasar Dos Santos Pedrosa, F.; Ban, J.; Baral, R. C.; Barbera, R.; Barile, F.; Barnaföldi, G. G. ; Barnby, L. S.; Barret, V.; Bartke, J.; Basile, M.; Bastid, N.; Basu, S.; Bathen, B.; Batigne, G.; Batyunya, B.; Baumann, C.; Bearden, I. G.; Beck, H.; Belikov, I.; Bellini, F.; Bellwied, R. ; Belmont-Moreno, E.; Bencedi, G.; Beole, S.; Berceanu, I.; Bercuci, A.; Berdnikov, Y.; Berenyi, D.; Berzano, D.; Betev, L.; Bhasin, A.; Bhati, A. K.; Bhom, J.; Bianchi, N.; Bianchi, L.; Bianchin, C.; Bielcik, J.; Bielcikova, J.; Bilandzic, A.; Bjelogrlic, S.; Blanco, F.; Blanco, F.; Blau, D.; Blume, C.; Boccioli, M.; Bock, N. ; Bogdanov, A.; Boggild, H.; Bogolyubsky, M.; Boldizsar, L.; Bombara, M.; Book, J.; Borel, H. ; Borissov, A.; Bose, S.; Boss, F.; Botje, M. ; Böttger, S.; Boyer, B.; Braidot, E.; Braun-Munzinger, Peter; Bregant, M.; Breitner, T.; Browning, T. A.; Broz, M.; Brun, R.; Bruna, E.; Bruno, G. E.; Budnikov, D.; Buesching, H.; Bufalino, S.; Bugaiev, K.; Busch, O.; Buthelezi, Z. ; Caballero Orduna, D.; Caffarri, D.; Cai, X.; Caines, H.; Calvo Villar, E.; Camerini, P.; Canoa Roman, V.; Cara Romeo, G.; Carena, W.; Carena, F. ; Carlin Filho, N.; Carminati, F.; Carrillo Montoya, C. A.; Casanova Diaz, A.; Castillo Castellanos, J. ; Castillo Hernandez, J. F.; Casula, E. A. R.; Catanescu, V.; Cavicchioli, C.; Ceballos Sanchez, C. ; Cepila, J.; Cerello, P.; Chang, B.; Chapeland, S.; Charvet, J. L.; Chattopadhyay, S.; Chattopadhyay, S.; Chawla, I.; Cherney, M.; Cheshkov, C.; Cheynis, B.; Chibante Barroso, V.; Chinellato, D. D.; Chochula, P.; Chojnacki, M.; Choudhury, S.; Christakoglou, P.; Christensen, C. H. ; Christiansen, P.; Chujo, T.; Chung, S. U.; Cicalo, C.; Cifarelli, L.; Cindolo, F.; Cleymans, J.; Coccetti, F.; Colamaria, F.; Colella, D.; Conesa Balbastre, G.; Conesa del Valle, Z.; Constantin, P.; Contin, G.; Contreras, J. G.; Cormier, T. M.; Corrales Morales, Y.; Cortese, P.; Cortes Maldonado, I.; Cosentino, M. R.; Costa, F.; Cotallo, M. E.; Crescio, E.; Crochet, P.; Cruz Alaniz, E.; Cuautle, E.; Cunqueiro, L.; Dainese, A. ; Dalsgaard, H. H.; Danu, A.; Das, K.; Das, I. ; Das, D.; Dash, A.; Dash, S.; De, S; Barros, G. O. V.; De Caro, A.; Cataldo, G.; Cuveland, J. ; Falco, A.; Gruttola, D.; Delagrange, H.; Castillo Sanchez, E.; Deloff, A.; Demanov, V.; Marco, N.; Denes, E.; Pasquale, S.; Deppman, A. ; Erasmo, G. D; Rooij, R.; Diaz Corchero, M. A.; Bari, D.; Dietel, T.; Giglio, C.; Liberto, S.; Mauro, A.; Nezza, P.; Divia, R.; Djuvsland, O. ; Dobrin, A.; Dobrowolski, T.; Dominguez, I.; Dönigus, Benjamin; Dordic, O.; Driga, O.; Dubey, A. K.; Ducroux, L.; Dupieux, P.; Dutta Majumdar, A. K.; Dutta Majumdar, M. R.; Elia, D.; Emschermann, D.; Engel, H.; Erdal, H. A.; Espagnon, B.; Estienne, M.; Esumi, S.; Evans, D.; Eyyubova, G. ; Fabris, D.;

Faivre, J.; Falchieri, D.; Fantoni, A.; Fasel, Markus; Fearick, R.; Fedunov, A.; Fehlker, D.; Feldkamp, L.; Felea, D.; Fenton-Olsen, B.; Feofilov, G.; Fernandez Tellez, A.; Ferretti, A.; Ferretti, R.; Figiel, J.; Figueredo, M. A. S. ; Filchagin, S.; Finogeev, D.; Fionda, F. M.; Fiore, E. M.; Floris, M.; Foertsch, S.; Foka, Panagiota; Fokin, S.; Fragiacomo, E.; Fragkiadakis, M.; Frankenfeld, Ulrich; Fuchs, U.; Furget, C.; Fusco Girard, M.; Gaardhoje, J. J.; Gagliardi, M.; Gago, A.; Gallio, M.; Gangadharan, D. R.; Ganoti, P.; Garabatos, C.; Garcia-Solis, E.; Garishvili, I. ; Gerhard, J.; Germain, M.; Geuna, C.; Gheata, M. ; Gheata, A.; Ghidini, B.; Ghosh, P.; Gianotti, P.; Girard, M. R.; Giubellino, P.; Gladysz-Dziadus, E.; Glässel, P.; Gomez, R.; Ferreiro, E. G.; Gonzalez-Trueba, L. H.; Gonzalez-Zamora, P.; Gorbunov, S.; Goswami, A.; Gotovac, S.; Grabski, V. ; Graczykowski, L. K.; Grajcarek, R.; Grelli, A.; Grigoras, C.; Grigoras, A.; Grigoriev, V.; Grigoryan, S.; Grigoryan, A.; Grinyov, B.; Grion, N.; Gros, P.; Grosse-Oetringhaus, J. F.; Grossiord, J.-Y.; Grosso, R.; Guber, F.; Guernane, R.; Guerra Gutierrez, C.; Guerzoni, B.; Guilbaud, M.; Gulbrandsen, K.; Gunji, T.; Gupta, R.; Gupta, A. ; Gutbrod, H.; Haaland, O.; Hadjidakis, C.; Haiduc, M.; Hamagaki, H.; Hamar, G.; Han, B. H.; Hanratty, L. D.; Hansen, A.; Harmanova, Z.; Harris, J. W.; Hartig, M.; Hasegan, D.; Hatzifotiadou, D. ; Hayrapetyan, A.; Heckel, S. T.; Heide, M.; Helstrup, H.; Herghelegiu, A.; Herrera Corral, G.; Herrmann, N.; Hetland, K. F.; Hicks, B.; Hille, P. T.; Hippolyte, B.; Horaguchi, T.; Hori, Y.; Hristov, P.; Hrivnacova, I.; Huang, M.; Humanic, T. J.; Hwang, D. S.; Ichou, R.; Ilkaev, R. ; Ilkiv, I.; Inaba, M.; Incani, E.; Innocenti, P. G.; Innocenti, G. M.; Ippolitov, M.; Irfan, M.; Ivan, Cristian George; Ivanov, V.; Ivanov, A.; Ivanov, Marian; Ivanytskyi, O.; Jacholkowski, A.; Jacobs, P. M.; Jancurova, L.; Jang, H. J.; Jangal, S.; Janik, R.; Janik, M. A.; Jayarathna, P. H. S. Y.; Jena, S.; Jha, D. M.; Jimenez Bustamante, R. T. ; Jirden, L.; Jones, P. G.; Jung, H.; Jusko, A. ; Kaidalov, A. B.; Kakoyan, V.; Kalcher, S.; Kalinak, P.; Kalisky, M.; Kalliokoski, T.; Kalweit, A.; Kanaki, K.; Kang, J. H.; Kaplin, V. ; Karasu Uysal, A.; Karavichev, O.; Karavicheva, T. ; Karpechev, E.; Kazantsev, A.; Kebschull, U.; Keidel, R.; Khan, M. M.; Khan, S. A.; Khanzadeev, A.; Kharlov, Y.; Kileng, B.; Kim, J. S.; Kim, D. W.; Kim, S. H.; Kim, J. H.; Kim, M.; Kim, D. J. ; Kim, B.; Kim, T.; Kim, S.; Kirsch, S.; Kisel, I.; Kiselev, S.; Kisiel, A.; Klay, J. L.; Klein, J.; Klein-Bösing, C.; Kliemant, M.; Kluge, A.; Knichel, Michael Linus; Knospe, A. G.; Koch, K. ; Köhler, M. K.; Kolojvari, A.; Kondratiev, V.; Kondratyeva, N.; Konevskikh, A.; Korneev, A.; Kour, R.; Kowalski, M.; Kox, S.; Koyithatta Meethaleveedu, G.; Kral, J.; Kralik, I.; Kramer, F.; Kraus, I.; Krawutschke, T.; Krelina, M.; Kretz, M.; Krivda, M.; Krizek, F.; Krus, M.; Kryshen, E.; Krzewicki, Mikolaj; Kucheriaev, Y.; Kuhn, C.; Kuijer, P. G.; Kurashvili, P.; Kurepin, A.; Kurepin, A. B.; Kuryakin, A.; Kushpil, V.; Kushpil, S.; Kvaerno, H.; Kweon, M. J.; Kwon, Y. ; Ladron de Guevara, P.; Lakomov, I.; Langoy, R. ; Pointe, S. L.; Lara, C.; Lardeux, A.; Rocca, P. ; Lazzeroni, C.; Lea, R.; Bornec, Y.; Lechman, M. ; Lee, S. C.; Lee, K. S.; Lefevre, F.; Lehnert, J.; Leistam, L.; Lenhardt, M.; Lenti, V.; Leon, H.; Leon Monzon, I.; Leon Vargas, H.; Levai, P. ; Lien, J.; Lietava, R.; Lindal, S.; Lindenstruth, V.; Lippmann, C.; Lisa, M. A.; Liu, L.; Loenne, P. I.; Loggins, V. R.; Loginov, V.; Lohn, S.; Lohner, D.; Loizides, C.; Loo, K. K.; Lopez, X.; Lopez Torres, E.; Lovhoiden, G.; Lu, X.-G.; Luettig, P.; Lunardon, M.; Luo, J.; Luparello, G.; Luquin, L.; Luzzi, C.; Ma, R.; Ma, K.; Madagodahettige-Don, D. M.; Maevskaya, A.; Mager, M.; Mahapatra, D. P.; Maire, A.; Malaev, M. ; Maldonado Cervantes, I.; Malinina, L.; MalKevich, D.; Malzacher, Peter; Mamonov, A.; Manceau, L.; Mangotra, L.; Manko, V.; Manso, F.; Manzari, V.; Mao, Y.; Marchisone, M.; Mares, J. ; Margagliotti, G. V.; Margotti, A.; Marin, Ana; Marin Tobon, C. A.; Markert, C.; Martashvili, I.; Martinengo, P.; Martinez, M. I.; Martinez Davalos, A.; Martinez Garcia, G.; Martynov, Y.; Masciocchi, Silvia; Masciocchi, Silvia; Masera, M.; Masoni, A.; Massacrier, L.; Mastromarco, M.; Mastroserio, A.; Matthews, Z. L.; Matyja, A.; Mayani, D.; Mayer, C.; Mazer, J.; Mazzoni, M. A. ; Meddi, F.; Menchaca-Rocha, A.; Mercado Perez, J. ; Meres, M.; Miake, Y.; Milano, L.; Milosevic, J. ; Mischke, A.; Mishra, A. N.; Miskowiec, Dariusz; Mitu, C.; Mlynarz, J.; Mohanty, A. K.; Mohanty, B. ; Molnar, L.; Montano Zetina, L.; Monteno, M.; Montes, E.; Moon, T.; Morando, M.; Moreira De Godoy, D. A.; Moretto, S.; Morsch, A.; Muccifora, V.; Mudnic, E.; Muhuri, S.; Mukherjee, M.; Müller, H.; Munhoz, M. G.; Musa, L.; Musso, A.; Nandi, B. K.; Nania, R.; Nappi, E.; Nattrass, C. ; Naumov, N. P.; Navin, S.; Nayak, T. K.; Nazarenko, S.; Nazarov, G.; Nedosekin, A.; Nicassio, M.; Nielsen, B. S.; Niida, T.; Nikolaev, S.; Nikolic, V.; Nikulin, V.; Nikulin, S.; Nilsen, B. S.; Nilsson, M. S.; Noferini, F.; Nomokonov, P.; Nooren, G.; Novitzky, N.; Nyanin, A. ; Nyatha, A.; Nygaard, C.; Nystrand, J.; Ochirov, A.; Oeschler, H.; Oh,; Oh, S. K.; Oleniacz, J. ; Oppedisano, C.; Ortiz Velasquez, A.; Ortona, G. ; Oskarsson, A.; Ostrowski, P.; Otwinowski, Jacek ; Oyama, K.; Ozawa, K.; Pachmayer, Y.; Pachr, M. ; Padilla, F.; Pagano, P.; Paic, G.; Painke, F. ; Pajares, C.; Pal, S. K.; Pal, S.; Palaha, A. ; Palmeri, A.; Papikyan, V.; Pappalardo, G. S.; Park, Woo Jin; Passfeld, A.; Pastircak, B.; Patalakha, D. I.; Paticchio, V.; Pavlinov, A.; Pawlak, T.; Peitzmann, T.; Pereira Da Costa, H.; Pereira De Oliveira Filho, E.; Peresunko, D.; Perez Lara, C. E.; Perez Lezama, E.; Perini, D.; Perrino, D.; Peryt, W.; Pesci, A.; Peskov, V.; Pestov, Y. ; Petracek, V.; Petran, M.; Petris, M.; Petrov, P.; Petrovici, M.; Petta, C.; Piano, S.; Piccotti, A.; Pikna, M.; Pillot, P.; Pinazza, O. ; Pinsky, L.; Pitz, N.; Piyarathna, D. B.; Ploskon, M.; Pluta, J.; Pocheptsov, T.; Pochybova, S.; Podesta-Lerma, P. L. M.; Poghosyan, M. G.; Polak, K.; Polichtchouk, B.; Pop, A.; Porteboeuf-Houssais, S.; Pospisil, V.; Potukuchi, B. ; Prasad, S. K.; Preghenella, R.; Prino, F.; Pruneau, C. A.; Pshenichnov, I.; Puchagin, S.; Puddu, G.; Pujol Teixido, J.; Pulvirenti, A.; Punin, V.; Putis, M.; Putschke, J.; Quercigh, E. ; Qvigstad, H.; Rachevski, A.; Rademakers, A.; Radomski, S.; Räihä T. S.; Dvorak, Jan; Rakotozafindrabe, A.; Ramello, L.; Ramirez Reyes, A. ; Raniwala, R.; Raniwala, S.; Räsänen, S. S.; Rascanu, B. T.; Rathee, D.; Read, K. F.; Real, J. S.; Redlich, K.; Reichelt, P.; Reicher, M.; Renfordt, R.; Reolon, A. R.; Reshetin, A.; Rettig, F.; Revol, J.-P.; Reygers, K.; Riccati, L.; Ricci, R. A.; Richert, T.; Richter, M.; Riedler, P. ; Riegler, W.; Riggi, F.; Rodrigues Fernandes Rabacal, B.; Rodriguez Cahuantzi, M.; Rodriguez Manso, A.; Roed, K.; Rohr, D.; Röhrich, D.; Romita, R.; Ronchetti, F.; Rosnet, P.; Rossegger, S.; Rossi, A.; Roukoutakis, F.; Roy, P.; Roy, C. ; Rubio Montero, A. J.; Rui, R.; Ryabinkin, E.; Rybicki, A.; Sadovsky, S.; Safarik, K.; Sahoo, R.; Sahu, P. K.; Saini, J.; Sakaguchi, H.; Sakai, S.; Sakata, D.; Salgado, C. A.; Salzwedel, J.; Sambyal, S.; Samsonov, V.; Sanchez Castro, X. ; Sandor, L.; Sandoval, A.; Sano, S.; Sano, M. ; Santo, R.; Santoro, R.; Sarkamo, J.; Scapparone, E.; Scarlassara, F.; Scharenberg, R. P. ; Schiaua, C.; Schicker, R.; Schmidt, Christian Alberto; Schmidt, Hans Rudolf; Schreiner, S.; Schuchmann, S.; Schukraft, J.; Schutz, Y.; Schwarz, Kilian; Schweda, Kai; Scioli, G.; Scomparin, E.; Scott, R.; Scott, P. A.; Segato, G.; Selyuzhenkov, Ilya; Senyukov, S.; Seo, J.; Serci, S.; Serradilla, E.; Sevcenco, A.; Sgura, I.; Shabetai, A.; Shabratova, G.; Shahoyan, R.; Sharma, N.; Sharma, S.;

Shigaki, K.; Shimomura, M.; Shtejer, K. ; Sibiriak, Y.; Siciliano, M.; Sicking, E.; Siddhanta, S.; Siemiarczuk, T.; Silvermyr, D.; Silvestre, c.; Simonetti, G.; Singaraju, R.; Singh, R.; Singha, S.; Sinha, B. C.; Sinha, T.; Sitar, B.; Sitta, M.; Skaali, T. B.; Skjerdal, K.; Smakal, R.; Smirnov, N.; Snellings, R. J. M.; Sogaard, C.; Soltz, R.; Johansson, H.; Song, M. ; Song, J.; Soos, C.; Soramel, F.; Sputowska, I. ; Spyropoulou-Stassinaki, M.; Srivastava, B. K.; Stachel, J.; Stan, I.; Stan, I.; Stefanek, G.; Steinbeck, T.; Steinpreis, M.; Stenlund, E.; Steyn, G.; Stiller, J. H.; Stocco, D.; Stolpovskiy, M.; Strabykin, K.; Strmen, P.; Suaide, A. A. P.; Subieta Vasquez, M. A.; Sugitate, T.; Suire, C.; Sukhorukov, M.; Sultanov, R.; Sumbera, M.; Susa, T.; Szanto de Toledo, A.; Szarka, I.; Szostak, A. ; Tagridis, C.; Takahashi, J.; Tapia Takaki, J. D. ; Tauro, A.; Tejeda Munoz, G.; Telesca, A.; Terrevoli, C.; Thäder, Jochen; Thomas, D.; Tieulent, R.; Timmins, A. R.; Tlusty, D.; Toia, A. ; Torii, H.; Toscano, L.; Truesdale, D.; Trzaska, W. H.; Tsuji, T.; Tumkin, A.; Turrisi, R.; Tveter, T. S.; Ulery, J.; Ullaland, K.; Ulrich, J. ; Uras, A.; Urban, J.; Urciuoli, G. M.; Usai, G. L.; Vajzer, M.; Vala, M.; Valencia Palomo, L.; Vallero, S.; Kolk, N.; Vande Vyvre, P.; Leeuwen, M. ; Vannucci, L.; Vargas, A.; Varma, R.; Vasileiou, M.; Vasiliev, A.; Vechernin, V.; Veldhoen, M.; Venaruzzo, M.; Vercellin, E.; Vergara, S.; Vernet, R.; Verweij, M.; Vickovic, L.; Viesti, G.; Vikhlyantsev, O.; Vilakazi, Z.; Villalobos Baillie, O. ; Vinogradov, A.; Vinogradov, L.; Vinogradov, Y.; Virgili, T.; Viyogi, Y. P.; Vodopyanov, A.; Voloshin, S.; Voloshin, K.; Volpe, G.; Haller, B. ; Vranic, D.; Ovrebekk, G.; Vrlakova, J.; Vulpescu, B.; Vyushin, A.; Wagner, B.; Wagner, V. ; Wan, R.; Wang, Y.; Wang, D.; Wang, Y.; Wang, M.; Watanabe, K.; Wessels, J. P.; Westerhoff, U. ; Wiechula, J.; Wikne, J.; Wilde, M.; Wilk, G. ; Wilk, A.; Williams, M. C. S.; Windelband, B.; Xaplanteris Karampatsos, L.; Yaldo, C. G.; Yang, H. ; Yang, S.; Yasnopolskiy, S.; Yi, J.; Yin, Z.; Yoo, I.-K.; Yoon, J.; Yu, W.; Yuan, X.; Yushmanov, I.; Zach, C.; Zampolli, C.; Zaporozhets, S.; Zarochentsev, A.; Zavada, P.; Zaviyalov, N. ; Zbroszczyk, H.; Zelnicek, P.; Zgura, I. S.; Zhalov, M.; Zhang, H.; Zhang, X.; Zhou, D.; Zhou, F.; Zhou, Y.; Zhu, X.; Zhu, J.; Zhu, J. ; Zichichi, A.; Zimmermann, A.; Zinovjev, G.; Zoccarato, Y.; Zynovyev, M.: **Suppression of high transverse momentum D mesons in central Pb-Pb collisions at $\sqrt{s_{NN}}$=2.76 TeV.** *Journal of high energy physics* 2012: 112, 2012. DOI:10.1007/JHEP09(2012)112

WOS-PHN-12 Abelev, B.; Adam, J.; Adamova, D.; Adare, A.M.; Aggarwal, M.M.; Aglieri Rinella, G.; Agocs, A.G. ; Agostinelli, A.; Aguilar Salazar, S.; Ahammed, Z. ; Ahmad Masoodi, A.; Ahmad, N.; Ahn, S.A.; Ahn, S.U.; Akindinov, A.; Aleksandrov, D.; Alessandro, B.; Alfaro Molina, R.; Alici, A.; Alkin, A.; Almaraz Avina, E.; Alme, J.; Alt, T.; Altini, V. ; Altinpinar, S.; Altsybeev, I.; Andrei, C.; Andronic, A.; Anguelov, V.; Anielski, J.; Anson, C. ; Anticic, T.; Antinori, F.; Antonioli, P.; Aphecetche, L.; Appelshäuser, H.; Arbor, N.; Arcelli, S.; Arend, A.; Armesto, N.; Arnaldi, R. ; Aronsson, T.; Arsene, I.C.; Arslandok, M.; Asryan, A.; Augustinus, A.; Averbeck, R.; Awes, T.C.; Äystö J.; Azmi, M.D.; Bach, M.; Badala, A.; Baek, Y.W.; Bailhache, R.; Bala, R. ; Baldini Ferroli, R.; Baldisseri, A.; Baldit, A. ; Baltasar Dos Santos Pedrosa, F.; Ban, J.; Baral, R.C.; Barbera, R.; Barile, F.; Barnaföldi, G.G. ; Barnby, L.S.; Barret, V.; Bartke, J.; Basile, M.; Bastid, N.; Basu, S.; Bathen, B.; Batigne, G.; Batyunya, B.; Baumann, C.; Bearden, I.G.; Beck, H.; Belikov, I.; Bellini, F.; Bellwied, R. ; Belmont-Moreno, E.; Bencedi, G.; Beole, S.; Berceanu, I.; Bercuci, A.; Berdnikov, Y.; Berenyi, D.; Bergognon, A.A.E.; Berzano, D.; Betev, L.; Bhasin, A.; Bhati, A.K.; Bhom, J.; Bianchi, L.; Bianchi, N.; Bianchin, C.; Bielcik, J.; Bielcikova, J.; Bilandzic, A.; Bjelogrlic, S.; Blanco, F.; Blanco, F.; Blau, D.; Blume, C.; Boccioli, M.; Bock, N.; Böttger, S.; Bogdanov, A. ; Boggild, H.; Bogolyubsky, M.; Boldizsar, L.; Bombara, M.; Book, J.; Borel, H.; Borissov, A.; Bose, S.; Boss, F.; Botje, M.; Boyer, B.; Braidot, E.; Braun-Munzinger, P.; Bregant, M.; Breitner, T.; Browning, T.A.; Broz, M.; Brun, R. ; Bruna, E.; Bruno, G.E.; Budnikov, D.; Buesching, H.; Bufalino, S.; Bugaiev, K.; Busch, O. ; Buthelezi, Z.; Caballero Orduna, D.; Caffarri, D. ; Cai, X.; Caines, H.; Calvo Villar, E.; Camerini, P.; Canoa Roman, V.; Cara Romeo, G.; Carena, F.; Carena, W.; Carlin Filho, N.; Carminati, F.; Carrillo Montoya, C.A.; Casanova Diaz, A.; Castillo Castellanos, J.; Castillo Hernandez, J.F. ; Casula, E.A.R.; Catanescu, V.; Cavicchioli, C.; Ceballos Sanchez, C.; Cepila, J.; Cerello, P.; Chang, B.; Chapeland, S.; Charvet, J.L.; Chattopadhyay, S.; Chattopadhyay, S.; Chawla, I.; Cherney, M.; Cheshkov, C.; Cheynis, B.; Chibante Barroso, V.; Chinellato, D.D.; Chochula, P.; Chojnacki, M.; Choudhury, S.; Christakoglou, P.; Christensen, C.H.; Christiansen, P.; Chujo, T.; Chung, S.U.; Cicalo, C.; Cifarelli, L.; Cindolo, F. ; Cleymans, J.; Coccetti, F.; Colamaria, F.; Colella, D.; Conesa Balbastre, G.; Conesa del Valle, Z.; Constantin, P.; Contin, G.; Contreras, J.G.; Cormier, T.M.; Corrales Morales, Y.; Cortese, P.; Cortes Maldonado, I.; Cosentino, M.R.; Costa, F.; Cotallo, M.E.; Crescio, E.; Crochet, P.; Cruz Alaniz, E.; Cuautle, E.; Cunqueiro, L.; Dainese, A. ; Dalsgaard, H.H.; Danu, A.; Das, D.; Das, I.; Das, K.; Dash, S.; Dash, A.; De, S.; de Barros, G.O.V.; De Caro, A.; de Cataldo, G.; de Cuveland, J.; De Falco, A.; De Gruttola, D.; Delagrange, H. ; Deloff, A.; Demanov, V.; De Marco, N.; Denes, E.; De Pasquale, S.; Deppman, A.; D Erasmo, G.; de Rooij, R.; Diaz Corchero, M.A.; Di Bari, D.; Dietel, T.; Di Liberto, S.; Di Mauro, A.; Di Nezza, P.; Divia, R.; Djuvsland, O.; Dobrin, A.; Dobrowolski, T.; Dominguez, I.; Dönigus, B.; Dordic, O.; Driga, O.; Dubey, A.K.; Ducroux, L.; Dupieux, P.; Dutta Majumdar, M.R.; Dutta Majumdar, A.K.; Elia, D.; Emschermann, D.; Engel, H.; Erdal, H.A.; Espagnon, B.; Estienne, M.; Esumi, S. ; Evans, D.; Eyyubova, G.; Fabris, D.; Faivre, J. ; Falchieri, D.; Fantoni, A.; Fasel, M.; Fearick, R.; Fedunov, A.; Fehlker, D.; Feldkamp, L.; Felea, D.; Fenton-Olsen, B.; Feofilov, G.; Fernandez Tellez, A.; Ferretti, A.; Ferretti, R.; Figiel, J.; Figueredo, M.A.S.; Filchagin, S.; Finogeev, D.; Fionda, F.M.; Fiore, E.M.; Floris, M. ; Foertsch, S.; Foka, P.; Fokin, S.; Fragiacomo, E.; Frankenfeld, U.; Fuchs, U.; Furget, C.; Fusco Girard, M.; Gaardhoje, J.J.; Gagliardi, M.; Gago, A.; Gallio, M.; Gangadharan, D.R.; Ganoti, P. ; Garabatos, C.; Garcia-Solis, E.; Garishvili, I. ; Gerhard, J.; Germain, M.; Geuna, C.; Gheata, A. ; Gheata, M.; Ghidini, B.; Ghosh, P.; Gianotti, P.; Girard, M.R.; Giubellino, P.; Gladysz-Dziadus, E.; Glässel, P.; Gomez, R.; Gonschior, A.; Ferreiro, E.G.; Gonzalez-Trueba, L.H.; Gonzalez-Zamora, P.; Gorbunov, S.; Goswami, A.; Gotovac, S.; Grabski, V.; Graczykowski, L.K.; Grajcarek, R.; Grelli, A.; Grigoras, C.; Grigoras, A.; Grigoriev, V.; Grigoryan, A.; Grigoryan, S.; Grinyov, B.; Grion, N.; Gros, P.; Grosse-Oetringhaus, J.F.; Grossiord, J.-Y.; Grosso, R. ; Guber, F.; Guernane, R.; Guerra Gutierrez, C.; Guerzoni, B.; Guilbaud, M.; Gulbrandsen, K.; Gunji, T.; Gupta, A.; Gupta, R.; Gutbrod, H.; Haaland, O.; Hadjidakis, C.; Haiduc, M.; Hamagaki, H.; Hamar, G.; Han, B.H.; Hanratty, L.D.; Hansen, A. ; Harmanova, Z.; Harris, J.W.; Hartig, M.; Hasegan, D.; Hatzifotiadou, D.; Hayrapetyan, A.; Heckel, S.T.; Heide, M.; Helstrup, H.; Herghelegiu, A.; Herrera Corral, G.; Herrmann, N.; Hess, B.A. ; Hetland, K.F.; Hicks, B.; Hille, P.T.; Hippolyte, B.; Horaguchi, T.; Hori, Y.; Hristov,

P. ; Hrivnacova, I.; Huang, M.; Humanic, T.J.; Hwang, D.S.; Ichou, R.; Ilkaev, R.; Ilkiv, I.; Inaba, M.; Incani, E.; Innocenti, G.M.; Innocenti, P.G.; Ippolitov, M.; Irfan, M.; Ivan, C.; Ivanov, V.; Ivanov, M.; Ivanov, A.; Ivanytskyi, O. ; Jacholkowski, A.; Jacobs, P.M.; Jang, H.J.; Janik, M.A.; Janik, R.; Jayarathna, P.H.S.Y.; Jena, S.; Jha, D.M.; Jimenez Bustamante, R.T.; Jirden, L. ; Jones, P.G.; Jung, H.; Jusko, A.; Kaidalov, A.B.; Kakoyan, V.; Kalcher, S.; Kalinak, P.; Kalliokoski, T.; Kalweit, A.; Kanaki, K.; Kang, J.H.; Kaplin, V.; Karasu Uysal, A.; Karavichev, O. ; Karavicheva, T.; Karpechev, E.; Kazantsev, A.; Kebschull, U.; Keidel, R.; Khan, S.A.; Khan, M.M. ; Khan, P.; Khanzadeev, A.; Kharlov, Y.; Kileng, B.; Kim, T.; Kim, D.W.; Kim, J.H.; Kim, J.S.; Kim, M.; Kim, B.; Kim, M.; Kim, S.H.; Kim, S. ; Kim, D.J.; Kirsch, S.; Kisel, I.; Kiselev, S. ; Kisiel, A.; Klay, J.L.; Klein, J.; Klein-Bösing, C.; Kliemant, M.; Kluge, A.; Knichel, M.L.; Knospe, A.G.; Koch, K.; Köhler, M.K.; Kolojvari, A.; Kondratiev, V.; Kondratyeva, N.; Konevskikh, A.; Korneev, A.; Kour, R.; Kowalski, M.; Kox, S.; Koyithatta Meethaleveedu, G. ; Kral, J.; Kralik, I.; Kramer, F.; Kraus, I. ; Krawutschke, T.; Krelina, M.; Kretz, M.; Krivda, M.; Krizek, F.; Krus, M.; Kryshen, E.; Krzewicki, M.; Kucheriaev, Y.; Kuhn, C.; Kuijer, P.G.; Kulakov, I.; Kumar, J.; Kurashvili, P.; Kurepin, A.; Kurepin, A.B.; Kuryakin, A.; Kushpil, V.; Kushpil, S.; Kvaerno, H.; Kweon, M.J.; Kwon, Y.; Ladron de Guevara, P.; Lakomov, I.; Langoy, R. ; La Pointe, S.L.; Lara, C.; Lardeux, A.; La Rocca, P.; Lazzeroni, C.; Lea, R.; Le Bornec, Y. ; Lechman, M.; Lee, S.C.; Lee, G.R.; Lee, K.S. ; Lefevre, F.; Lehnert, J.; Leistam, L.; Lenhardt, M.; Lenti, V.; Leon, H.; Leoncino, M. ; Leon Monzon, I.; Leon Vargas, H.; Levai, P. ; Lien, J.; Lietava, R.; Lindal, S.; Lindenstruth, V.; Lippmann, C.; Lisa, M.A.; Liu, L. ; Loenne, P.I.; Loggins, V.R.; Loginov, V.; Lohn, S.; Lohner, D.; Loizides, C.; Loo, K.K.; Lopez, X.; Lopez Torres, E.; Lovhoiden, G.; Lu, X.-G. ; Luettig, P.; Lunardon, M.; Luo, J.; Luparello, G.; Luquin, L.; Luzzi, C.; Ma, R.; Ma, K.; Madagodahettige-Don, D.M.; Maevskaya, A.; Mager, M. ; Mahapatra, D.P.; Maire, A.; Malaev, M.; Maldonado Cervantes, I.; Malinina, L.; MalKevich, D. ; Malzacher, P.; Mamonov, A.; Manceau, L.; Mangotra, L.; Manko, V.; Manso, F.; Manzari, V.; Mao, Y.; Marchisone, M.; Mares, J.; Margagliotti, G.V.; Margotti, A.; Marin, Ana; Marin Tobon, C.A. ; Markert, C.; Martashvili, I.; Martinengo, P.; Martinez, M.I.; Martinez Davalos, A.; Martinez Garcia, G.; Martynov, Y.; Mas, A.; Masciocchi, S. ; Masera, M.; Masoni, A.; Massacrier, L.; Mastromarco, M.; Mastroserio, A.; Matthews, Z.L.; Matyja, A.; Mayani, D.; Mayer, C.; Mazer, J.; Mazzoni, M.A.; Meddi, F.; Menchaca-Rocha, A.; Mercado Perez, J.; Meres, M.; Miake, Y.; Milano, L.; Milosevic, J.; Mischke, A.; Mishra, A.N.; Mikowiec, D.; Mitu, C.; Mlynarz, J.; Mohanty, B. ; Mohanty, A.K.; Molnar, L.; Montano Zetina, L.; Monteno, M.; Montes, E.; Moon, T.; Morando, M.; Moreira De Godoy, D.A.; Moretto, S.; Morsch, A.; Muccifora, V.; Mudnic, E.; Muhuri, S.; Mukherjee, M.; Müller, H.; Munhoz, M.G.; Musa, L.; Musso, A.; Nandi, B.K.; Nania, R.; Nappi, E.; Nattrass, C.; Naumov, N.P.; Navin, S.; Nayak, T.K.; Nazarenko, S.; Nazarov, G.; Nedosekin, A.; Niculescu, M.; Nielsen, B.S.; Niida, T.; Nikolaev, S.; Nikolic, V.; Nikulin, S.; Nikulin, V.; Nilsen, B.S.; Nilsson, M.S.; Noferini, F.; Nomokonov, P.; Nooren, G.; Novitzky, N.; Nyanin, A. ; Nyatha, A.; Nygaard, C.; Nystrand, J.; Ochirov, A.; Oeschler, H.; Oh, S.; Oh, S.K.; Oleniacz, J. ; Oppedisano, C.; Ortiz Velasquez, A.; Ortona, G. ; Oskarsson, A.; Ostrowski, P.; Otwinowski, J.; Oyama, K.; Ozawa, K.; Pachmayer, Y.; Pachr, M.; Padilla, F.; Pagano, P.; Paic, G.; Painke, F.; Pajares, C.; Pal, S.; Pal, S.K.; Palaha, A.; Palmeri, A.; Papikyan, V.; Pappalardo, G.S.; Park, W.J.; Passfeld, A.; Pastircak, B.; Patalakha, D.I.; Paticchio, V.; Pavlinov, A.; Pawlak, T.; Peitzmann, T.; Pereira Da Costa, H.; Pereira De Oliveira Filho, E.; Peresunko, D.; Perez Lara, C.E. ; Perez Lezama, E.; Perini, D.; Perrino, D.; Peryt, W.; Pesci, A.; Peskov, V.; Pestov, Y.; Petracek, V.; Petran, M.; Petris, M.; Petrov, P. ; Petrovici, M.; Petta, C.; Piano, S.; Piccotti, A.; Pikna, M.; Pillot, P.; Pinazza, O.; Pinsky, L.; Pitz, N.; Piyarathna, D.B.; Ploskon, M.; Pluta, J.; Pocheptsov, T.; Pochybova, S.; Podesta-Lerma, P.L.M.; Poghosyan, M.G.; Polak, K.; Polichtchouk, B.; Pop, A.; Porteboeuf-Houssais, S.; Pospisil, V.; Potukuchi, B.; Prasad, S.K.; Preghenella, R.; Prino, F.; Pruneau, C.A.; Pshenichnov, I.; Puchagin, S.; Puddu, G.; Pujol Teixido, J.; Pulvirenti, A.; Punin, V.; Putis, M. ; Putschke, J.; Quercigh, E.; Qvigstad, H.; Rachevski, A.; Rademakers, A.; Radomski, S.; Räihä T.S.; Rak, J.; Rakotozafindrabe, A.; Ramello, L.; Ramirez Reyes, A.; Raniwala, S.; Raniwala, R.; Räsänen, S.S.; Rascanu, B.T.; Rathee, D.; Read, K.F.; Real, J.S.; Redlich, K.; Reichelt, P.; Reicher, M.; Renfordt, R.; Reolon, A.R.; Reshetin, A.; Rettig, F.; Revol, J.-P.; Reygers, K.; Riccati, L.; Ricci, R.A.; Richert, T. ; Richter, M.; Riedler, P.; Riegler, W.; Riggi, F.; Rodrigues Fernandes Rabacal, B.; Rodriguez Cahuantzi, M.; Rodriguez Manso, A.; Roed, K.; Rohr, D.; Röhrich, D.; Romita, R.; Ronchetti, F. ; Rosnet, P.; Rossegger, S.; Rossi, A.; Roy, C. ; Roy, P.; Rubio Montero, A.J.; Rui, R.; Ryabinkin, E.; Rybicki, A.; Sadovsky, S.; Safarik, K.; Sahoo, R.; Sahu, P.K.; Saini, J. ; Sakaguchi, H.; Sakai, S.; Sakata, D.; Salgado, C.A.; Salzwedel, J.; Sambyal, S.; Samsonov, V.; Sanchez Castro, X.; Sandor, L.; Sandoval, A.; Sano, S.; Sano, M.; Santo, R.; Santoro, R.; Sarkamo, J.; Scapparone, E.; Scarlassara, F.; Scharenberg, R.P.; Schiaua, C.; Schicker, R.; Schmidt, C.; Schmidt, H.R.; Schreiner, S.; Schuchmann, S.; Schukraft, J.; Schutz, Y.; Schwarz, K.; Schweda, K.; Scioli, G.; Scomparin, E.; Scott, R.; Scott, P.A.; Segato, G.; Selyuzhenkov, I.; Senyukov, S.; Seo, J.; Serci, S.; Serradilla, E.; Sevcenco, A.; Shabetai, A.; Shabratova, G.; Shahoyan, R.; Sharma, N.; Sharma, S.; Rohni, S.; Shigaki, K.; Shimomura, M.; Shtejer, K.; Sibiriak, Y.; Siciliano, M.; Sicking, E.; Siddhanta, S.; Siemiarczuk, T.; Silvermyr, D. ; Silvestre, C.; Simatovic, G.; Simonetti, G.; Singaraju, R.; Singh, R.; Singha, S.; Singhal, V. ; Sinha, T.; Sinha, B.C.; Sitar, B.; Sitta, M. ; Skaali, T.B.; Skjerdal, K.; Smakal, R.; Smirnov, N.; Snellings, R.J.M.; Sogaard, C.; Soltz, R.; Son, H.; Song, M.; Song, J.; Soos, C. ; Soramel, F.; Sputowska, I.; Spyropoulou-Stassinaki, M.; Srivastava, B.K.; Stachel, J.; Stan, I.; Stan, I.; Stefanek, G.; Steinbeck, T.; Steinpreis, M.; Stenlund, E.; Steyn, G.; Stiller, J.H.; Stocco, D.; Stolpovskiy, M.; Strabykin, K.; Strmen, P.; Suaide, A.A.P.; Subieta Vasquez, M.A.; Sugitate, T.; Suire, C.; Sukhorukov, M.; Sultanov, R.; Sumbera, M.; Susa, T.; Szanto de Toledo, A.; Szarka, I.; Szczepankiewicz, A.; Szostak, A.; Szymanski, M.; Takahashi, J.; Tapia Takaki, J.D.; Tauro, A.; Tejeda Munoz, G.; Telesca, A.; Terrevoli, C.; Thäder, J.; Thomas, D.; Tieulent, R.; Timmins, A.R.; Tlusty, D.; Toia, A.; Torii, H.; Toscano, L.; Truesdale, D.; Trzaska, W.H.; Tsuji, T.; Tumkin, A.; Turrisi, R.; Tveter, T.S.; Ulery, J. ; Ullaland, K.; Ulrich, J.; Uras, A.; Urban, J. ; Urciuoli, G.M.; Usai, G.L.; Vajzer, M.; Vala, M.; Valencia Palomo, L.; Vallero, S.; van der Kolk, N.; Vande Vyvre, P.; van Leeuwen, M.; Vannucci, L. ; Vargas, A.; Varma, R.; Vasileiou, M.; Vasiliev, A.; Vechernin, V.; Veldhoen, M.; Venaruzzo, M.; Vercellin, E.; Vergara, S.; Vernet, R.; Verweij, M. ; Vickovic, L.; Viesti, G.; Vikhlyantsev, O.; Vilakazi, Z.; Villalobos Baillie, O.; Vinogradov, A. ; Vinogradov, L.; Vinogradov, Y.; Virgili, T.; Viyogi, Y.P.; Vodopyanov, A.; Voloshin, K.; Voloshin, S.; Volpe, G.; von Haller, B.; Vranic, D. ;

Ovrebekk, G.; Vrlakova, J.; Vulpescu, B.; Vyushin, A.; Wagner, V.; Wagner, B.; Wan, R.; Wang, M.; Wang, D.; Wang, Y.; Wang, Y.; Watanabe, K.; Weber, M.; Wessels, J.P.; Westerhoff, U.; Wiechula, J.; Wikne, J.; Wilde, M.; Wilk, G. ; Wilk, A.; Williams, M.C.S.; Windelband, B.; Xaplanteris Karampatsos, L.; Yaldo, C.G.; Yamaguchi, Y.; Yang, H.; Yang, S.; Yasnopolskiy, S.; Yi, J. ; Yin, Z.; Yoo, I.-K.; Yoon, J.; Yu, W.; Yuan, X.; Yushmanov, I.; Zach, C.; Zampolli, C.; Zaporozhets, S.; Zarochentsev, A.; Zavada, P.; Zaviyalov, N.; Zbroszczyk, H.; Zelnicek, P.; Zgura, I.S.; Zhalov, M.; Zhang, X.; Zhang, H.; Zhou, F. ; Zhou, D.; Zhou, Y.; Zhu, J.; Zhu, J.; Zhu, X.; Zichichi, A.; Zimmermann, A.; Zinovjev, G.; Zoccarato, Y.; Zynovyev, M.; Zyzak, M.: $K^0_s K^0_s$ **correlations in pp collisions at** $\sqrt{s}$ **=7 TeV from the LHC ALICE experiment.** *Physics letters / B* 717: 151 - 161, 2012. DOI:10.1016/j.physletb.2012.09.013

WOS-PHN-13 Abelev, B.; Adam, J.; Adamova, D.; Adare, A.M.; Aggarwal, M.M.; Aglieri Rinella, G.; Agocs, A.G. ; Agostinelli, A.; Aguilar Salazar, S.; Ahammed, Z. ; Ahmad Masoodi, A.; Ahmad, N.; Ahn, S.U.; Akindinov, A.; Aleksandrov, D.; Alessandro, B.; Alfaro Molina, R.; Alici, A.; Alkin, A.; Almaraz Avina, E.; Alme, J.; Alt, T.; Altini, V.; Altinpinar, S.; Altsybeev, I.; Andrei, C.; Andronic, A.; Anguelov, V.; Anielski, J.; Anson, C. ; Anticic, T.; Antinori, F.; Antonioli, P.; Aphecetche, L.; Appelshäuser, H.; Arbor, N.; Arcelli, S.; Arend, A.; Armesto, N.; Arnaldi, R. ; Aronsson, T.; Arsene, I.C.; Arslandok, M.; Asryan, A.; Augustinus, A.; Averbeck, R.; Awes, T.C.; Äystö J.; Azmi, M.D.; Bach, M.; Badala, A.; Baek, Y.W.; Bailhache, R.; Bala, R. ; Baldini Ferroli, R.; Baldisseri, A.; Baldit, A. ; Baltasar Dos Santos Pedrosa, F.; Ban, J.; Baral, R.C.; Barbera, R.; Barile, F.; Barnaföldi, G.G. ; Barnby, L.S.; Barret, V.; Bartke, J.; Basile, M.; Bastid, N.; Bathen, B.; Batigne, G.; Batyunya, B.; Baumann, C.; Bearden, I.G.; Beck, H. ; Belikov, I.; Bellini, F.; Bellwied, R.; Belmont-Moreno, E.; Bencedi, G.; Beole, S.; Berceanu, I.; Bercuci, A.; Berdnikov, Y.; Berenyi, D.; Bergmann, C.; Berzano, D.; Betev, L.; Bhasin, A.; Bhati, A.K.; Bianchi, L.; Bianchi, N. ; Bianchin, C.; Bielcik, J.; Bielcikova, J.; Bilandzic, A.; Bjelogrlic, S.; Blanco, F.; Blanco, F.; Blau, D.; Blume, C.; Boccioli, M.; Bock, N. ; Bogdanov, A.; Boggild, H.; Bogolyubsky, M.; Boldizsar, L.; Bombara, M.; Book, J.; Borel, H. ; Borissov, A.; Bose, S.; Boss, F.; Botje, M. ; Böttger, S.; Boyer, B.; Braidot, E.; Braun-Munzinger, P.; Bregant, M.; Breitner, T.; Browning, T.A.; Broz, M.; Brun, R.; Bruna, E.; Bruno, G.E.; Budnikov, D.; Buesching, H.; Bufalino, S.; Bugaiev, K.; Busch, O.; Buthelezi, Z.; Caballero Orduna, D.; Caffarri, D.; Cai, X.; Caines, H.; Calvo Villar, E.; Camerini, P.; Canoa Roman, V.; Cara Romeo, G.; Carena, W.; Carena, F. ; Carlin Filho, N.; Carminati, F.; Carrillo Montoya, C.A.; Casanova Diaz, A.; Castillo Castellanos, J.; Castillo Hernandez, J.F.; Casula, E.A.R.; Catanescu, V.; Cavicchioli, C.; Cepila, J.; Cerello, P.; Chang, B.; Chapeland, S.; Charvet, J.L.; Chattopadhyay, S.; Chattopadhyay, S.; Chawla, I.; Cherney, M.; Cheshkov, C.; Cheynis, B.; Chiavassa, E.; Chibante Barroso, V.; Chinellato, D.D.; Chochula, P.; Chojnacki, M.; Christakoglou, P.; Christensen, C.H.; Christiansen, P.; Chujo, T.; Chung, S.U.; Cicalo, C.; Cifarelli, L.; Cindolo, F. ; Cleymans, J.; Coccetti, F.; Colamaria, F.; Colella, D.; Conesa Balbastre, G.; Conesa del Valle, Z.; Constantin, P.; Contin, G.; Contreras, J.G.; Cormier, T.M.; Corrales Morales, Y.; Cortese, P.; Cortes Maldonado, I.; Cosentino, M.R.; Costa, F.; Cotallo, M.E.; Crescio, E.; Crochet, P.; Cruz Alaniz, E.; Cuautle, E.; Cunqueiro, L.; Dainese, A. ; Dalsgaard, H.H.; Danu, A.; Das, K.; Das, I.; Das, D.; Dash, A.; Dash, S.; De, S.; de Barros, G.O.V.; De Caro, A.; de Cataldo, G.; de Cuveland, J.; De Falco, A.; De Gruttola, D.; Delagrange, H. ; Del Castillo Sanchez, E.; Deloff, A.; Demanov, V. ; De Marco, N.; Denes, E.; De Pasquale, S.; Deppman, A.; D Erasmo, G.; de Rooij, R.; Diaz Corchero, M.A.; Di Bari, D.; Dietel, T.; Di Giglio, C.; Di Liberto, S.; Di Mauro, A.; Di Nezza, P.; Divia, R.; Djuvsland, O.; Dobrin, A.; Dobrowolski, T.; Dominguez, I.; Dönigus, B.; Dordic, O.; Driga, O.; Dubey, A.K.; Ducroux, L.; Dupieux, P.; Dutta Majumdar, A.K.; Dutta Majumdar, M.R.; Elia, D.; Emschermann, D.; Engel, H.; Erdal, H.A.; Espagnon, B.; Estienne, M.; Esumi, S. ; Evans, D.; Eyyubova, G.; Fabris, D.; Faivre, J. ; Falchieri, D.; Fantoni, A.; Fasel, M.; Fearick, R.; Fedunov, A.; Fehlker, D.; Feldkamp, L.; Felea, D.; Feofilov, G.; Fernandez Tellez, A.; Ferreiro, E.G.; Ferretti, A.; Ferretti, R.; Figiel, J.; Figueredo, M.A.S.; Filchagin, S.; Finogeev, D. ; Fionda, F.M.; Fiore, E.M.; Floris, M.; Foertsch, S.; Foka, P.; Fokin, S.; Fragiacomo, E. ; Fragkiadakis, M.; Frankenfeld, U.; Fuchs, U.; Furget, C.; Fusco Girard, M.; Gaardhoje, J.J.; Gagliardi, M.; Gago, A.; Gallio, M.; Gangadharan, D.R.; Ganoti, P.; Garabatos, C.; Garcia-Solis, E. ; Garishvili, I.; Gerhard, J.; Germain, M.; Geuna, C.; Gheata, A.; Gheata, M.; Ghidini, B.; Ghosh, P.; Gianotti, P.; Girard, M.R.; Giubellino, P.; Gladysz-Dziadus, E.; Glässel, P.; Gomez, R. ; Gonzalez-Trueba, L.H.; Gonzalez-Zamora, P.; Gorbunov, S.; Goswami, A.; Gotovac, S.; Grabski, V. ; Graczykowski, L.K.; Grajcarek, R.; Grelli, A.; Grigoras, A.; Grigoras, C.; Grigoriev, V.; Grigoryan, A.; Grigoryan, S.; Grinyov, B.; Grion, N.; Gros, P.; Grosse-Oetringhaus, J.F.; Grossiord, J.-Y.; Grosso, R.; Guber, F.; Guernane, R.; Guerra Gutierrez, C.; Guerzoni, B.; Guilbaud, M.; Gulbrandsen, K.; Gunji, T.; Gupta, A.; Gupta, R. ; Gutbrod, H.; Haaland, O.; Hadjidakis, C.; Haiduc, M.; Hamagaki, H.; Hamar, G.; Han, B.H.; Hanratty, L.D.; Hansen, A.; Harmanova, Z.; Harris, J.W.; Hartig, M.; Hasegan, D.; Hatzifotiadou, D. ; Hayrapetyan, A.; Heckel, S.T.; Heide, M.; Helstrup, H.; Herghelegiu, A.; Herrera Corral, G.; Herrmann, N.; Hetland, K.F.; Hicks, B.; Hille, P.T. ; Hippolyte, B.; Horaguchi, T.; Hori, Y.; Hristov, P.; Hrivnacova, I.; Huang, M.; Huber, S.; Humanic, T.J.; Hwang, D.S.; Ichou, R.; Ilkaev, R.; Ilkiv, I.; Inaba, M.; Incani, E.; Innocenti, G.M.; Innocenti, P.G.; Ippolitov, M.; Irfan, M.; Ivan, C.; Ivanov, V.; Ivanov, A.; Ivanov, M.; Ivanytskyi, O.; Jacholkowski, A.; Jacobs, P.M.; Jancurova, L.; Jang, H.J.; Jangal, S.; Janik, M.A.; Janik, R.; Jayarathna, P.H.S.Y. ; Jena, S.; Jimenez Bustamante, R.T.; Jirden, L.; Jones, P.G.; Jung, H.; Jusko, A.; Kaidalov, A.B. ; Kakoyan, V.; Kalcher, S.; Kalinak, P.; Kalisky, M.; Kalliokoski, T.; Kalweit, A.; Kanaki, K.; Kang, J.H.; Kaplin, V.; Karasu Uysal, A.; Karavichev, O.; Karavicheva, T.; Karpechev, E.; Kazantsev, A.; Kebschull, U.; Keidel, R.; Khan, M.M.; Khan, S.A.; Khan, P.; Khanzadeev, A.; Kharlov, Y.; Kileng, B.; Kim, M.; Kim, J.S.; Kim, D.J.; Kim, T.; Kim, B.; Kim, S.; Kim, S.H. ; Kim, D.W.; Kim, J.H.; Kirsch, S.; Kisel, I.; Kiselev, S.; Kisiel, A.; Klay, J.L.; Klein, J.; Klein-Bösing, C.; Kliemant, M.; Kluge, A.; Knichel, M.L.; Knospe, A.G.; Koch, K.; Köhler, M.K.; Kolojvari, A.; Kondratiev, V.; Kondratyeva, N.; Konevskikh, A.; Korneev, A.; Kottachchi Kankanamge Don, C.; Kour, R.; Kowalski, M.; Kox, S. ; Koyithatta Meethaleveedu, G.; Kral, J.; Kralik, I.; Kramer, F.; Kraus, I.; Krawutschke, T.; Krelina, M.; Kretz, M.; Krivda, M.; Krizek, F.; Krus, M.; Kryshen, E.; Krzewicki, M.; Kucheriaev, Y.; Kuhn, C.; Kuijer, P.G.; Kurashvili, P.; Kurepin, A.; Kurepin, A.B.; Kuryakin, A.; Kushpil, S.; Kushpil, V.; Kvaerno, H.; Kweon, M.J.; Kwon, Y.; Ladron de Guevara, P.; Lakomov, I.; Langoy, R. ; Lara, C.; Lardeux, A.; La Rocca, P.; Lazzeroni, C.; Lea, R.; Le Bornec, Y.; Lee, S.C.; Lee, K.S. ; Lefevre, F.; Lehnert, J.; Leistam, L.;

Lenhardt, M.; Lenti, V.; Leon, H.; Leon Monzon, I.; Leon Vargas, H.; Levai, P.; Lien, J.; Lietava, R.; Lindal, S.; Lindenstruth, V.; Lippmann, C.; Lisa, M.A.; Liu, L.; Loenne, P.I.; Loggins, V.R.; Loginov, V.; Lohn, S.; Lohner, D. ; Loizides, C.; Loo, K.K.; Lopez, X.; Lopez Torres, E.; Lovhoiden, G.; Lu, X.-G.; Luettig, P. ; Lunardon, M.; Luo, J.; Luparello, G.; Luquin, L.; Luzzi, C.; Ma, K.; Ma, R.; Madagodahettige-Don, D.M.; Maevskaya, A.; Mager, M. ; Mahapatra, D.P.; Maire, A.; Malaev, M.; Maldonado Cervantes, I.; Malinina, L.; MalKevich, D. ; Malzacher, P.; Mamonov, A.; Manceau, L.; Mangotra, L.; Manko, V.; Manso, F.; Manzari, V.; Mao, Y.; Marchisone, M.; Mares, J.; Margagliotti, G.V.; Margotti, A.; Marin, Ana; Marin Tobon, C.A. ; Markert, C.; Martashvili, I.; Martinengo, P.; Martinez, M.I.; Martinez Davalos, A.; Martinez Garcia, G.; Martynov, Y.; Mas, A.; Masciocchi, S. ; Masera, M.; Masoni, A.; Massacrier, L.; Mastromarco, M.; Mastroserio, A.; Matthews, Z.L.; Matyja, A.; Mayani, D.; Mayer, C.; Mazer, J.; Mazzoni, M.A.; Meddi, F.; Menchaca-Rocha, A.; Mercado Perez, J.; Meres, M.; Miake, Y.; Milano, L.; Milosevic, J.; Mischke, A.; Mishra, A.N.; Mikowiec, D.; Mitu, C.; Mlynarz, J.; Mohanty, A.K.; Mohanty, B.; Molnar, L.; Montano Zetina, L. ; Monteno, M.; Montes, E.; Moon, T.; Morando, M. ; Moreira De Godoy, D.A.; Moretto, S.; Morsch, A. ; Muccifora, V.; Mudnic, E.; Muhuri, S.; Müller, H.; Munhoz, M.G.; Musa, L.; Musso, A.; Nandi, B.K.; Nania, R.; Nappi, E.; Nattrass, C.; Naumov, N.P.; Navin, S.; Nayak, T.K.; Nazarenko, S. ; Nazarov, G.; Nedosekin, A.; Nicassio, M.; Nielsen, B.S.; Niida, T.; Nikolaev, S.; Nikolic, V. ; Nikulin, V.; Nikulin, S.; Nilsen, B.S.; Nilsson, M.S.; Noferini, F.; Nomokonov, P.; Nooren, G.; Novitzky, N.; Nyanin, A.; Nyatha, A.; Nygaard, C.; Nystrand, J.; Ochirov, A.; Oeschler, H.; Oh, S.K.; Oh, S.; Oleniacz, J.; Oppedisano, C.; Ortiz Velasquez, A.; Ortona, G.; Oskarsson, A. ; Ostrowski, P.; Otwinowski, J.; Ovrebekk, G.; Oyama, K.; Ozawa, K.; Pachmayer, Y.; Pachr, M.; Padilla, F.; Pagano, P.; Paic, G.; Painke, F.; Pajares, C.; Pal, S.K.; Pal, S.; Palaha, A.; Palmeri, A.; Papikyan, V.; Pappalardo, G.S.; Park, W.J.; Passfeld, A.; Pastircak, B.; Patalakha, D.I.; Paticchio, V.; Pavlinov, A.; Pawlak, T.; Peitzmann, T.; Pereira De Oliveira Filho, E.; Peresunko, D.; Perez Lara, C.E.; Perez Lezama, E.; Perini, D.; Perrino, D.; Peryt, W.; Pesci, A.; Peskov, V.; Pestov, Y.; Petracek, V.; Petran, M. ; Petris, M.; Petrov, P.; Petrovici, M.; Petta, C.; Piano, S.; Piccotti, A.; Pikna, M.; Pillot, P.; Pinazza, O.; Pinsky, L.; Pitz, N.; Piuz, F. ; Piyarathna, D.B.; Ploskon, M.; Pluta, J.; Pocheptsov, T.; Pochybova, S.; Podesta-Lerma, P.L.M. ; Poghosyan, M.G.; Polak, K.; Polichtchouk, B.; Pop, A.; Porteboeuf-Houssais, S.; Pospisil, V.; Potukuchi, B.; Prasad, S.K.; Preghenella, R.; Prino, F.; Pruneau, C.A.; Pshenichnov, I.; Puchagin, S.; Puddu, G.; Pujol Teixido, J.; Pulvirenti, A.; Punin, V.; Putis, M.; Putschke, J. ; Quercigh, E.; Qvigstad, H.; Rachevski, A.; Rademakers, A.; Radomski, S.; Räihä T.S.; Rak, J.; Rakotozafindrabe, A.; Ramello, L.; Ramirez Reyes, A.; Raniwala, S.; Raniwala, R.; Räsänen, S.S.; Rascanu, B.T.; Rathee, D.; Read, K.F.; Real, J.S.; Redlich, K.; Reichelt, P.; Reicher, M. ; Renfordt, R.; Reolon, A.R.; Reshetin, A.; Rettig, F.; Revol, J.-P.; Reygers, K.; Riccati, L. ; Ricci, R.A.; Richert, T.; Richter, M.; Riedler, P.; Riegler, W.; Riggi, F.; Rodriguez Cahuantzi, M.; Roed, K.; Rohr, D.; Röhrich, D.; Romita, R.; Ronchetti, F.; Rosnet, P.; Rossegger, S.; Rossi, A.; Roukoutakis, F.; Roy, C.; Roy, P.; Rubio Montero, A.J.; Rui, R.; Ryabinkin, E.; Rybicki, A.; Sadovsky, S.; Safarik, K.; Sahoo, R.; Sahu, P.K.; Saini, J.; Sakaguchi, H.; Sakai, S.; Sakata, D.; Salgado, C.A.; Salzwedel, J.; Sambyal, S.; Samsonov, V.; Sanchez Castro, X.; Sandor, L.; Sandoval, A.; Sano, S.; Sano, M.; Santo, R.; Santoro, R.; Sarkamo, J.; Scapparone, E. ; Scarlassara, F.; Scharenberg, R.P.; Schiaua, C. ; Schicker, R.; Schmidt, H.R.; Schmidt, C.; Schreiner, S.; Schuchmann, S.; Schukraft, J.; Schutz, Y.; Schwarz, K.; Schweda, K.; Scioli, G. ; Scomparin, E.; Scott, P.A.; Scott, R.; Segato, G.; Selyuzhenkov, I.; Senyukov, S.; Seo, J.; Serci, S.; Serradilla, E.; Sevcenco, A.; Sgura, I. ; Shabetai, A.; Shabratova, G.; Shahoyan, R.; Sharma, N.; Sharma, S.; Shigaki, K.; Shimomura, M. ; Shtejer, K.; Sibiriak, Y.; Siciliano, M.; Sicking, E.; Siddhanta, S.; Siemiarczuk, T.; Silvermyr, D.; Silvestre, C.; Simonetti, G.; Singaraju, R.; Singh, R.; Singha, S.; Sinha, T.; Sinha, B.C.; Sitar, B.; Sitta, M.; Skaali, T.B.; Skjerdal, K.; Smakal, R.; Smirnov, N.; Snellings, R.J.M.; Sogaard, C.; Soltz, R.; Son, H.; Song, M.; Song, J.; Soos, C.; Soramel, F.; Sputowska, I.; Spyropoulou-Stassinaki, M.; Srivastava, B.K.; Stachel, J.; Stan, I.; Stan, I.; Stefanek, G.; Stefanini, G.; Steinbeck, T.; Steinpreis, M.; Stenlund, E.; Steyn, G.; Stocco, D.; Stolpovskiy, M.; Strabykin, K.; Strmen, P.; Suaide, A.A.P.; Subieta Vasquez, M.A.; Sugitate, T.; Suire, C.; Sukhorukov, M.; Sultanov, R.; Sumbera, M.; Susa, T.; Szanto de Toledo, A.; Szarka, I.; Szostak, A. ; Tagridis, C.; Takahashi, J.; Tapia Takaki, J.D. ; Tauro, A.; Tejeda Munoz, G.; Telesca, A.; Terrevoli, C.; Thäder, J.; Thomas, D.; Tieulent, R.; Timmins, A.R.; Tlusty, D.; Toia, A.; Torii, H.; Toscano, L.; Tosello, F.; Truesdale, D.; Trzaska, W.H.; Tsuji, T.; Tumkin, A.; Turrisi, R. ; Tveter, T.S.; Ulery, J.; Ullaland, K.; Ulrich, J.; Uras, A.; Urban, J.; Urciuoli, G.M.; Usai, G.L.; Vajzer, M.; Vala, M.; Valencia Palomo, L.; Vallero, S.; van der Kolk, N.; Vande Vyvre, P.; van Leeuwen, M.; Vannucci, L.; Vargas, A.; Varma, R. ; Vasileiou, M.; Vasiliev, A.; Vechernin, V.; Veldhoen, M.; Venaruzzo, M.; Vercellin, E.; Vergara, S.; Vernekohl, D.C.; Vernet, R.; Verweij, M.; Vickovic, L.; Viesti, G.; Vikhlyantsev, O.; Vilakazi, Z.; Villalobos Baillie, O.; Vinogradov, A. ; Vinogradov, Y.; Vinogradov, L.; Virgili, T.; Viyogi, Y.P.; Vodopyanov, A.; Voloshin, S.; Voloshin, K.; Volpe, G.; von Haller, B.; Vranic, D. ; Vrlakova, J.; Vulpescu, B.; Vyushin, A.; Wagner, B.; Wagner, V.; Wan, R.; Wang, Y.; Wang, D.; Wang, Y.; Wang, M.; Watanabe, K.; Wessels, J.P.; Westerhoff, U.; Wiechula, J.; Wikne, J.; Wilde, M.; Wilk, G.; Wilk, A.; Williams, M.C.S.; Windelband, B.; Xaplanteris Karampatsos, L.; Yang, H. ; Yang, S.; Yasnopolskiy, S.; Yi, J.; Yin, Z.; Yokoyama, H.; Yoo, I.-K.; Yoon, J.; Yu, W.; Yuan, X.; Yushmanov, I.; Zach, C.; Zampolli, C.; Zaporozhets, S.; Zarochentsev, A.; Zavada, P.; Zaviyalov, N.; Zbroszczyk, H.; Zelnicek, P.; Zgura, I.S.; Zhalov, M.; Zhang, X.; Zhou, D.; Zhou, Y. ; Zhou, F.; Zhu, X.; Zichichi, A.; Zimmermann, A. ; Zinovjev, G.; Zoccarato, Y.; Zynovyev, M.: **Inclusive J/psi production in pp collisions at $\sqrt{s} = 2.76TeV$.** *Physics letters / B* 718: 295 - 306, 2012. DOI:10.1016/j.physletb.2012.10.078

WOS-PHN-14 Abelev, B.; Adam, J.; Adamova, D.; Adare, A.M.; Aggarwal, M.M.; Aglieri Rinella, G.; Agocs, A.G. ; Agostinelli, A.; Aguilar Salazar, S.; Ahammed, Z. ; Ahmad Masoodi, A.; Ahmad, N.; Ahn, S.U.; Akindinov, A.; Aleksandrov, D.; Alessandro, B.; Alfaro Molina, R.; Alici, A.; Alkin, A.; Almaraz Avina, E.; Alme, J.; Alt, T.; Altini, V.; Altinpinar, S.; Altsybeev, I.; Andrei, C.; Andronic, A.; Anguelov, V.; Anielski, J.; Anson, C. ; Anticic, T.; Antinori, F.; Antonioli, P.; Aphecetche, L.; Appelshäuser, H.; Arbor, N.; Arcelli, S.; Arend, A.; Armesto, N.; Arnaldi, R. ; Aronsson, T.; Arsene, I.C.; Arslandok, M.; Asryan, A.; Augustinus, A.; Averbeck, R.; Awes, T.C.; Äystö J.; Azmi, M.D.; Bach, M.; Badala, A.; Baek, Y.W.; Bailhache, R.; Bala, R. ; Baldini Ferroli, R.; Baldisseri, A.; Baldit, A. ; Baltasar Dos Santos Pedrosa, F.; Ban, J.; Baral, R.C.; Barbera, R.; Barile, F.;

Barnaföldi, G.G. ; Barnby, L.S.; Barret, V.; Bartke, J.; Basile, M.; Bastid, N.; Bathen, B.; Batigne, G.; Batyunya, B.; Baumann, C.; Bearden, I.G.; Beck, H. ; Belikov, I.; Bellini, F.; Bellwied, R.; Belmont-Moreno, E.; Bencedi, G.; Beole, S.; Berceanu, I.; Bercuci, A.; Berdnikov, Y.; Berenyi, D.; Bergmann, C.; Berzano, D.; Betev, L.; Bhasin, A.; Bhati, A.K.; Bianchi, N.; Bianchi, L. ; Bianchin, C.; Bielcik, J.; Bielcikova, J.; Bilandzic, A.; Bjelogrlic, S.; Blanco, F.; Blanco, F.; Blau, D.; Blume, C.; Boccioli, M.; Bock, N. ; Bogdanov, A.; Boggild, H.; Bogolyubsky, M.; Boldizsar, L.; Bombara, M.; Book, J.; Borel, H. ; Borissov, A.; Bose, S.; Boss, F.; Botje, M. ; Böttger, S.; Boyer, B.; Braun-Munzinger, P.; Bregant, M.; Breitner, T.; Browning, T.A.; Broz, M. ; Brun, R.; Bruna, E.; Bruno, G.E.; Budnikov, D. ; Buesching, H.; Bufalino, S.; Bugaiev, K.; Busch, O.; Buthelezi, Z.; Caballero Orduna, D.; Caffarri, D.; Cai, X.; Caines, H.; Calvo Villar, E. ; Camerini, P.; Canoa Roman, V.; Cara Romeo, G.; Carena, F.; Carena, W.; Carlin Filho, N.; Carminati, F.; Carrillo Montoya, C.A.; Casanova Diaz, A.; Castillo Castellanos, J.; Castillo Hernandez, J.F. ; Casula, E.A.R.; Catanescu, V.; Cavicchioli, C.; Cepila, J.; Cerello, P.; Chang, B.; Chapeland, S. ; Charvet, J.L.; Chattopadhyay, S.; Chattopadhyay, S.; Cherney, M.; Cheshkov, C.; Cheynis, B.; Chiavassa, E.; Chibante Barroso, V.; Chinellato, D.D. ; Chochula, P.; Chojnacki, M.; Christakoglou, P.; Christensen, C.H.; Christiansen, P.; Chujo, T.; Chung, S.U.; Cicalo, C.; Cifarelli, L.; Cindolo, F. ; Cleymans, J.; Coccetti, F.; Colamaria, F.; Colella, D.; Conesa Balbastre, G.; Conesa del Valle, Z.; Constantin, P.; Contin, G.; Contreras, J.G.; Cormier, T.M.; Corrales Morales, Y.; Cortese, P.; Cortes Maldonado, I.; Cosentino, M.R.; Costa, F.; Cotallo, M.E.; Crescio, E.; Crochet, P.; Cruz Alaniz, E.; Cuautle, E.; Cunqueiro, L.; Dainese, A. ; Dalsgaard, H.H.; Danu, A.; Das, I.; Das, K.; Das, D.; Dash, S.; Dash, A.; De, S.; De Azevedo Moregula, A.; de Barros, G.O.V.; De Caro, A.; de Cataldo, G.; de Cuveland, J.; De Falco, A.; De Gruttola, D.; Delagrange, H.; Del Castillo Sanchez, E. ; Deloff, A.; Demanov, V.; De Marco, N.; Denes, E.; De Pasquale, S.; Deppman, A.; Erasmo, G.D.; de Rooij, R.; Di Bari, D.; Dietel, T.; Di Giglio, C.; Di Liberto, S.; Di Mauro, A.; Di Nezza, P.; Divia, R.; Djuvsland, O.; Dobrin, A.; Dobrowolski, T.; Dominguez, I.; Dönigus, B.; Dordic, O.; Driga, O.; Dubey, A.K.; Ducroux, L.; Dupieux, P.; Dutta Majumdar, A.K.; Dutta Majumdar, M.R.; Elia, D.; Emschermann, D.; Engel, H.; Erdal, H.A.; Espagnon, B.; Estienne, M.; Esumi, S. ; Evans, D.; Eyyubova, G.; Fabris, D.; Faivre, J. ; Falchieri, D.; Fantoni, A.; Fasel, M.; Fearick, R.; Fedunov, A.; Fehlker, D.; Feldkamp, L.; Felea, D.; Feofilov, G.; Fernandez Tellez, A.; Ferretti, R.; Ferretti, A.; Figiel, J.; Figueredo, M.A.S.; Filchagin, S.; Finogeev, D.; Fionda, F.M. ; Fiore, E.M.; Floris, M.; Foertsch, S.; Foka, P. ; Fokin, S.; Fragiacomo, E.; Fragkiadakis, M.; Frankenfeld, U.; Fuchs, U.; Furget, C.; Fusco Girard, M.; Gaardhoje, J.J.; Gagliardi, M.; Gago, A.; Gallio, M.; Gangadharan, D.R.; Ganoti, P.; Garabatos, C.; Garcia-Solis, E.; Garishvili, I.; Gerhard, J.; Germain, M.; Geuna, C.; Gheata, A.; Gheata, M.; Ghidini, B.; Ghosh, P.; Gianotti, P. ; Girard, M.R.; Giubellino, P.; Gladysz-Dziadus, E. ; Glässel, P.; Gomez, R.; Ferreiro, E.G.; Gonzalez-Trueba, L.H.; Gonzalez-Zamora, P.; Gorbunov, S.; Goswami, A.; Gotovac, S.; Grabski, V. ; Graczykowski, L.K.; Grajcarek, R.; Grelli, A.; Grigoras, A.; Grigoras, C.; Grigoriev, V.; Grigoryan, A.; Grigoryan, S.; Grinyov, B.; Grion, N.; Gros, P.; Grosse-Oetringhaus, J.F.; Grossiord, J.-Y.; Grosso, R.; Guber, F.; Guernane, R.; Guerra Gutierrez, C.; Guerzoni, B.; Guilbaud, M.; Gulbrandsen, K.; Gunji, T.; Gupta, A.; Gupta, R. ; Gutbrod, H.; Haaland, O.; Hadjidakis, C.; Haiduc, M.; Hamagaki, H.; Hamar, G.; Han, B.H.; Hanratty, L.D.; Hansen, A.; Harmanova, Z.; Harris, J.W.; Hartig, M.; Hasegan, D.; Hatzifotiadou, D. ; Hayrapetyan, A.; Heckel, S.T.; Heide, M.; Helstrup, H.; Herghelegiu, A.; Herrera Corral, G.; Herrmann, N.; Hetland, K.F.; Hicks, B.; Hille, P.T. ; Hippolyte, B.; Horaguchi, T.; Hori, Y.; Hristov, P.; Hrivnacova, I.; Huang, M.; Huber, S.; Humanic, T.J.; Hwang, D.S.; Ichou, R.; Ilkaev, R.; Ilkiv, I.; Inaba, M.; Incani, E.; Innocenti, G.M.; Innocenti, P.G.; Ippolitov, M.; Irfan, M.; Ivan, C.; Ivanov, M.; Ivanov, A.; Ivanov, V.; Ivanytskyi, O.; Jacholkowski, A.; Jacobs, P.M.; Jancurova, L.; Jang, H.J.; Jangal, S.; Janik, M.A.; Janik, R.; Jayarathna, P.H.S.Y. ; Jena, S.; Jimenez Bustamante, R.T.; Jirden, L.; Jones, P.G.; Jung, H.; Jung, W.; Jusko, A.; Kaidalov, A.B.; Kakoyan, V.; Kalcher, S.; Kalinak, P.; Kalisky, M.; Kalliokoski, T.; Kalweit, A.; Kanaki, K.; Kang, J.H.; Kaplin, V.; Karasu Uysal, A.; Karavichev, O.; Karavicheva, T.; Karpechev, E.; Kazantsev, A.; Kebschull, U.; Keidel, R.; Khan, S.A.; Khan, M.M.; Khan, P.; Khanzadeev, A.; Kharlov, Y.; Kileng, B.; Kim, M. ; Kim, T.; Kim, S.; Kim, D.J.; Kim, J.H.; Kim, J.S.; Kim, S.H.; Kim, D.W.; Kim, B.; Kirsch, S. ; Kisel, I.; Kiselev, S.; Kisiel, A.; Klay, J.L. ; Klein, J.; Klein-Bösing, C.; Kliemant, M.; Kluge, A.; Knichel, M.L.; Knospe, A.G.; Koch, K. ; Köhler, M.K.; Kolojvari, A.; Kondratiev, V.; Kondratyeva, N.; Konevskikh, A.; Korneev, A.; Kottachchi Kankanamge Don, C.; Kour, R.; Kowalski, M. ; Kox, S.; Koyithatta Meethaleveedu, G.; Kral, J. ; Kralik, I.; Kramer, F.; Kraus, I.; Krawutschke, T.; Krelina, M.; Kretz, M.; Krivda, M. ; Krizek, F.; Krus, M.; Kryshen, E.; Krzewicki, M.; Kucheriaev, Y.; Kuhn, C.; Kuijer, P.G.; Kurashvili, P.; Kurepin, A.B.; Kurepin, A.; Kuryakin, A.; Kushpil, V.; Kushpil, S.; Kvaerno, H. ; Kweon, M.J.; Kwon, Y.; Ladron de Guevara, P.; Lakomov, I.; Langoy, R.; Lara, C.; Lardeux, A.; La Rocca, P.; Lazzeroni, C.; Lea, R.; Le Bornec, Y. ; Lee, K.S.; Lee, S.C.; Lefevre, F.; Lehnert, J. ; Leistam, L.; Lenhardt, M.; Lenti, V.; Leon, H. ; Leon Monzon, I.; Leon Vargas, H.; Levai, P. ; Lien, J.; Lietava, R.; Lindal, S.; Lindenstruth, V.; Lippmann, C.; Lisa, M.A.; Liu, L. ; Loenne, P.I.; Loggins, V.R.; Loginov, V.; Lohn, S.; Lohner, D.; Loizides, C.; Loo, K.K.; Lopez, X.; Lopez Torres, E.; Lovhoiden, G.; Lu, X.-G. ; Luettig, P.; Lunardon, M.; Luo, J.; Luparello, G.; Luquin, L.; Luzzi, C.; Ma, K.; Ma, R.; Madagodahettige-Don, D.M.; Maevskaya, A.; Mager, M. ; Mahapatra, D.P.; Maire, A.; Malaev, M.; Maldonado Cervantes, I.; Malinina, L.; MalKevich, D. ; Malzacher, P.; Mamonov, A.; Manceau, L.; Mangotra, L.; Manko, V.; Manso, F.; Manzari, V.; Mao, Y.; Marchisone, M.; Mares, J.; Margagliotti, G.V.; Margotti, A.; Marin, Ana; Marin Tobon, C.A. ; Markert, C.; Martashvili, I.; Martinengo, P.; Martinez, M.I.; Martinez Davalos, A.; Martinez Garcia, G.; Martynov, Y.; Mas, A.; Masciocchi, S. ; Masera, M.; Masoni, A.; Massacrier, L.; Mastromarco, M.; Mastroserio, A.; Matthews, Z.L.; Matyja, A.; Mayani, D.; Mayer, C.; Mazer, J.; Mazzoni, M.A.; Meddi, F.; Menchaca-Rocha, A.; Mercado Perez, J.; Meres, M.; Miake, Y.; Milano, L.; Milosevic, J.; Mischke, A.; Mishra, A.N.; Mikowiec, D.; Mitu, C.; Mlynarz, J.; Mohanty, B. ; Mohanty, A.K.; Molnar, L.; Montano Zetina, L.; Monteno, M.; Montes, E.; Moon, T.; Morando, M.; Moreira De Godoy, D.A.; Moretto, S.; Morsch, A.; Muccifora, V.; Mudnic, E.; Muhuri, S.; Müller, H. ; Munhoz, M.G.; Musa, L.; Musso, A.; Nandi, B.K. ; Nania, R.; Nappi, E.; Nattrass, C.; Naumov, N.P.; Navin, S.; Nayak, T.K.; Nazarenko, S.; Nazarov, G.; Nedosekin, A.; Nicassio, M.; Nielsen, B.S.; Niida, T.; Nikolaev, S.; Nikolic, V.; Nikulin, S.; Nikulin, V.; Nilsen, B.S.; Nilsson, M.S.; Noferini, F.; Nomokonov, P.; Nooren, G.; Novitzky, N.; Nyanin, A.; Nyatha, A.; Nygaard, C. ; Nystrand, J.; Ochirov, A.; Oeschler, H.; Oh, S.K.; Oh, S.; Oleniacz, J.; Oppedisano, C.; Ortiz Velasquez,

A.; Ortona, G.; Oskarsson, A.; Ostrowski, P.; Otwinowski, J.; Oyama, K.; Ozawa, K. ; Pachmayer, Y.; Pachr, M.; Padilla, F.; Pagano, P.; Paic, G.; Painke, F.; Pajares, C.; Pal, S.K.; Pal, S.; Palaha, A.; Palmeri, A.; Papikyan, V.; Pappalardo, G.S.; Park, W.J.; Passfeld, A.; Pastircak, B.; Patalakha, D.I.; Paticchio, V.; Pavlinov, A.; Pawlak, T.; Peitzmann, T.; Pereira De Oliveira Filho, E.; Peresunko, D.; Perez Lara, C.E.; Perez Lezama, E.; Perini, D.; Perrino, D.; Peryt, W.; Pesci, A.; Peskov, V.; Pestov, Y.; Petracek, V.; Petran, M.; Petris, M. ; Petrov, P.; Petrovici, M.; Petta, C.; Piano, S. ; Piccotti, A.; Pikna, M.; Pillot, P.; Pinazza, O.; Pinsky, L.; Pitz, N.; Piuz, F.; Piyarathna, D.B.; Ploskon, M.; Pluta, J.; Pocheptsov, T.; Pochybova, S.; Podesta-Lerma, P.L.M.; Poghosyan, M.G. ; Polak, K.; Polichtchouk, B.; Pop, A.; Porteboeuf-Houssais, S.; Pospisil, V.; Potukuchi, B. ; Prasad, S.K.; Preghenella, R.; Prino, F.; Pruneau, C.A.; Pshenichnov, I.; Puchagin, S.; Puddu, G.; Pujol Teixido, J.; Pulvirenti, A.; Punin, V.; Putis, M.; Putschke, J.; Quercigh, E. ; Qvigstad, H.; Rachevski, A.; Rademakers, A.; Radomski, S.; Räihä T.S.; Rak, J.; Rakotozafindrabe, A.; Ramello, L.; Ramirez Reyes, A. ; Raniwala, S.; Raniwala, R.; Räsänen, S.S.; Rascanu, B.T.; Rathee, D.; Read, K.F.; Real, J.S. ; Redlich, K.; Reichelt, P.; Reicher, M.; Renfordt, R.; Reolon, A.R.; Reshetin, A.; Rettig, F.; Revol, J.-P.; Reygers, K.; Riccati, L.; Ricci, R.A.; Richert, T.; Richter, M.; Riedler, P. ; Riegler, W.; Riggi, F.; Rodriguez Cahuantzi, M. ; Roed, K.; Rohr, D.; Röhrich, D.; Romita, R. ; Ronchetti, F.; Rosnet, P.; Rossegger, S.; Rossi, A.; Roukoutakis, F.; Roy, C.; Roy, P.; Rubio Montero, A.J.; Rui, R.; Ryabinkin, E.; Rybicki, A.; Sadovsky, S.; Safarik, K.; Sahoo, R.; Sahu, P.K.; Saini, J.; Sakaguchi, H.; Sakai, S.; Sakata, D.; Salgado, C.A.; Salzwedel, J.; Sambyal, S.; Samsonov, V.; Sanchez Castro, X.; Sandor, L.; Sandoval, A.; Sano, S.; Sano, M.; Santo, R.; Santoro, R.; Sarkamo, J.; Scapparone, E. ; Scarlassara, F.; Scharenberg, R.P.; Schiaua, C. ; Schicker, R.; Schmidt, C.; Schmidt, H.R.; Schreiner, S.; Schuchmann, S.; Schukraft, J.; Schutz, Y.; Schwarz, K.; Schweda, K.; Scioli, G. ; Scomparin, E.; Scott, P.A.; Scott, R.; Segato, G.; Selyuzhenkov, I.; Senyukov, S.; Seo, J.; Serci, S.; Serradilla, E.; Sevcenco, A.; Sgura, I. ; Shabetai, A.; Shabratova, G.; Shahoyan, R.; Sharma, N.; Sharma, S.; Shigaki, K.; Shimomura, M. ; Shtejer, K.; Sibiriak, Y.; Siciliano, M.; Sicking, E.; Siddhanta, S.; Siemiarczuk, T.; Silvermyr, D.; Simonetti, G.; Singaraju, R.; Singh, R.; Singha, S.; Sinha, B.C.; Sinha, T.; Sitar, B.; Sitta, M.; Skaali, T.B.; Skjerdal, K.; Smakal, R.; Smirnov, N.; Snellings, R.; Sogaard, C.; Soltz, R.; Son, H.; Song, J.; Song, M.; Soos, C.; Soramel, F.; Sputowska, I.; Spyropoulou-Stassinaki, M.; Srivastava, B.K.; Stachel, J.; Stan, I.; Stan, I.; Stefanek, G.; Stefanini, G.; Steinbeck, T.; Steinpreis, M.; Stenlund, E.; Steyn, G.; Stocco, D.; Stolpovskiy, M.; Strabykin, K.; Strmen, P.; Suaide, A.A.P.; Subieta Vasquez, M.A.; Sugitate, T.; Suire, C.; Sukhorukov, M.; Sultanov, R.; Sumbera, M.; Susa, T.; Szanto de Toledo, A.; Szarka, I.; Szostak, A.; Tagridis, C. ; Takahashi, J.; Tapia Takaki, J.D.; Tauro, A.; Tejeda Munoz, G.; Telesca, A.; Terrevoli, C.; Thäder, J.; Thomas, D.; Tieulent, R.; Timmins, A.R.; Tlusty, D.; Toia, A.; Torii, H.; Toscano, L.; Tosello, F.; Truesdale, D.; Trzaska, W.H.; Tsuji, T.; Tumkin, A.; Turrisi, R.; Tveter, T.S. ; Ulery, J.; Ullaland, K.; Ulrich, J.; Uras, A. ; Urban, J.; Urciuoli, G.M.; Usai, G.L.; Vajzer, M.; Vala, M.; Valencia Palomo, L.; Vallero, S.; van der Kolk, N.; Vande Vyvre, P.; van Leeuwen, M.; Vannucci, L.; Vargas, A.; Varma, R.; Vasileiou, M. ; Vasiliev, A.; Vechernin, V.; Veldhoen, M.; Venaruzzo, M.; Vercellin, E.; Vergara, S.; Vernekohl, D.C.; Vernet, R.; Verweij, M.; Vickovic, L.; Viesti, G.; Vikhlyantsev, O.; Vilakazi, Z.; Villalobos Baillie, O.; Vinogradov, A.; Vinogradov, L. ; Vinogradov, Y.; Virgili, T.; Viyogi, Y.P.; Vodopyanov, A.; Voloshin, K.; Voloshin, S.; Volpe, G.; von Haller, B.; Vranic, D.; Ovrebekk, G.; Vrlakova, J.; Vulpescu, B.; Vyushin, A.; Wagner, B.; Wagner, V.; Wan, R.; Wang, D.; Wang, M.; Wang, Y.; Wang, Y.; Watanabe, K.; Wessels, J.P.; Westerhoff, U.; Wiechula, J.; Wikne, J.; Wilde, M. ; Wilk, G.; Wilk, A.; Williams, M.C.S.; Windelband, B.; Xaplanteris Karampatsos, L.; Yang, H. ; Yang, S.; Yasnopolskiy, S.; Yi, J.; Yin, Z.; Yokoyama, H.; Yoo, I.-K.; Yoon, J.; Yu, W.; Yuan, X.; Yushmanov, I.; Zach, C.; Zampolli, C.; Zaporozhets, S.; Zarochentsev, A.; Zavada, P.; Zaviyalov, N.; Zbroszczyk, H.; Zelnicek, P.; Zgura, I.S.; Zhalov, M.; Zhang, X.; Zhou, Y.; Zhou, D. ; Zhou, F.; Zhu, X.; Zichichi, A.; Zimmermann, A. ; Zinovjev, G.; Zoccarato, Y.; Zynovyev, M.: J/ψ **production as a function of charged particle multiplicity in pp collisions at** $\sqrt{s}$ **= 7TeV.** *Physics letters / B* 712: 165 - 175, 2012. DOI:10.1016/j.physletb.2012.04.052

WOS-PHN-15 Abelev, B.; Adam, J.; Adamova, D.; Adare, A.M.; Aggarwal, M.M.; Aglieri Rinella, G.; Agocs, A.G. ; Agostinelli, A.; Aguilar Salazar, S.; Ahammed, Z. ; Ahmad, N.; Ahmad Masoodi, A.; Ahn, S.A.; Ahn, S.U.; Akindinov, A.; Aleksandrov, D.; Alessandro, B.; Alfaro Molina, R.; Alici, A.; Alkin, A.; Almaraz Avina, E.; Alme, J.; Alt, T.; Altini, V. ; Altinpinar, S.; Altsybeev, I.; Andrei, C.; Andronic, A.; Anguelov, V.; Anielski, J.; Anson, C. ; Anticic, T.; Antinori, F.; Antonioli, P.; Aphecetche, L.; Appelshäuser, H.; Arbor, N.; Arcelli, S.; Arend, A.; Armesto, N.; Arnaldi, R. ; Aronsson, T.; Arsene, I.C.; Arslandok, M.; Asryan, A.; Augustinus, A.; Averbeck, R.; Awes, T.C.; Äystö J.; Azmi, M.D.; Bach, M.; Badala, A.; Baek, Y.W.; Bailhache, R.; Bala, R. ; Baldini Ferroli, R.; Baldisseri, A.; Baldit, A. ; Baltasar Dos Santos Pedrosa, F.; Ban, J.; Baral, R.C.; Barbera, R.; Barile, F.; Barnaföldi, G.G. ; Barnby, L.S.; Barret, V.; Bartke, J.; Basile, M.; Bastid, N.; Basu, S.; Bathen, B.; Batigne, G.; Batyunya, B.; Baumann, C.; Bearden, I.G.; Beck, H.; Belikov, I.; Bellini, F.; Bellwied, R. ; Belmont-Moreno, E.; Bencedi, G.; Beole, S.; Berceanu, I.; Bercuci, A.; Berdnikov, Y.; Berenyi, D.; Bergognon, A.A.E.; Berzano, D.; Betev, L.; Bhasin, A.; Bhati, A.K.; Bhom, J.; Bianchi, L.; Bianchi, N.; Bianchin, C.; Bielcik, J.; Bielcikova, J.; Bilandzic, A.; Bjelogrlic, S.; Blanco, F.; Blanco, F.; Blau, D.; Blume, C.; Boccioli, M.; Bock, N.; Böttger, S.; Bogdanov, A. ; Boggild, H.; Bogolyubsky, M.; Boldizsar, L.; Bombara, M.; Book, J.; Borel, H.; Borissov, A.; Bose, S.; Boss, F.; Botje, M.; Botta, E.; Boyer, B.; Braidot, E.; Braun-Munzinger, P.; Bregant, M.; Breitner, T.; Browning, T.A.; Broz, M. ; Brun, R.; Bruna, E.; Bruno, G.E.; Budnikov, D. ; Buesching, H.; Bufalino, S.; Busch, O.; Buthelezi, Z.; Caballero Orduna, D.; Caffarri, D.; Cai, X.; Caines, H.; Calvo Villar, E.; Camerini, P. ; Canoa Roman, V.; Cara Romeo, G.; Carena, F.; Carena, W.; Carlin Filho, N.; Carminati, F.; Casanova Diaz, A.; Castillo Castellanos, J.; Castillo Hernandez, J.F.; Casula, E.A.R.; Catanescu, V.; Cavicchioli, C.; Ceballos Sanchez, C.; Cepila, J.; Cerello, P.; Chang, B.; Chapeland, S.; Charvet, J.L.; Chattopadhyay, S.; Chattopadhyay, S.; Chawla, I.; Cherney, M.; Cheshkov, C.; Cheynis, B.; Chibante Barroso, V.; Chinellato, D.D.; Chochula, P. ; Chojnacki, M.; Choudhury, S.; Christakoglou, P. ; Christensen, C.H.; Christiansen, P.; Chujo, T.; Chung, S.U.; Cicalo, C.; Cifarelli, L.; Cindolo, F. ; Cleymans, J.; Coccetti, F.; Colamaria, F.; Colella, D.; Conesa Balbastre, G.; Conesa del Valle, Z.; Constantin, P.; Contin, G.; Contreras, J.G.; Cormier, T.M.; Corrales Morales, Y.; Cortese, P.; Cortes Maldonado, I.; Cosentino, M.R.; Costa, F.; Cotallo, M.E.; Crescio,

E.; Crochet, P.; Cruz Alaniz, E.; Cuautle, E.; Cunqueiro, L.; Dainese, A. ; Dalsgaard, H.H.; Danu, A.; Das, I.; Das, D.; Das, K.; Dash, S.; Dash, A.; De, S.; de Barros, G.O.V.; De Caro, A.; de Cataldo, G.; de Cuveland, J.; De Falco, A.; De Gruttola, D.; Delagrange, H. ; Deloff, A.; Demanov, V.; De Marco, N.; Denes, E.; De Pasquale, S.; Deppman, A.; D Erasmo, G.; de Rooij, R.; Diaz Corchero, M.A.; Di Bari, D.; Dietel, T.; Di Giglio, C.; Di Liberto, S.; Di Mauro, A.; Di Nezza, P.; Divia, R.; Djuvsland, O. ; Dobrin, A.; Dobrowolski, T.; Dominguez, I.; Dönigus, B.; Dordic, O.; Driga, O.; Dubey, A.K. ; Dubla, A.; Ducroux, L.; Dupieux, P.; Dutta Majumdar, A.K.; Dutta Majumdar, M.R.; Elia, D.; Emschermann, D.; Engel, H.; Erazmus, B.; Erdal, H.A.; Espagnon, B.; Estienne, M.; Esumi, S.; Evans, D.; Eyyubova, G.; Fabris, D.; Faivre, J.; Falchieri, D.; Fantoni, A.; Fasel, M.; Fearick, R. ; Fedunov, A.; Fehlker, D.; Feldkamp, L.; Felea, D.; Fenton-Olsen, B.; Feofilov, G.; Fernandez Tellez, A.; Ferretti, A.; Ferretti, R.; Festanti, A.; Figiel, J.; Figueredo, M.A.S.; Filchagin, S. ; Finogeev, D.; Fionda, F.M.; Fiore, E.M.; Floris, M.; Foertsch, S.; Foka, P.; Fokin, S.; Fragiacomo, E.; Francescon, A.; Frankenfeld, U.; Fuchs, U.; Furget, C.; Fusco Girard, M.; Gaardhoje, J.J.; Gagliardi, M.; Gago, A.; Gallio, M.; Gangadharan, D.R.; Ganoti, P.; Garabatos, C. ; Garcia-Solis, E.; Garishvili, I.; Gerhard, J.; Germain, M.; Geuna, C.; Gheata, M.; Gheata, A.; Ghidini, B.; Ghosh, P.; Gianotti, P.; Girard, M.R. ; Giubellino, P.; Gladysz-Dziadus, E.; Glässel, P. ; Gomez, R.; Ferreiro, E.G.; Gonzalez-Trueba, L.H. ; Gonzalez-Zamora, P.; Gorbunov, S.; Goswami, A. ; Gotovac, S.; Grabski, V.; Graczykowski, L.K.; Grajcarek, R.; Grelli, A.; Grigoras, C.; Grigoras, A.; Grigoriev, V.; Grigoryan, S.; Grigoryan, A.; Grinyov, B.; Grion, N.; Gros, P.; Grosse-Oetringhaus, J.F.; Grossiord, J.-Y.; Grosso, R. ; Guber, F.; Guernane, R.; Guerra Gutierrez, C.; Guerzoni, B.; Guilbaud, M.; Gulbrandsen, K.; Gunji, T.; Gupta, R.; Gupta, A.; Gutbrod, H.; Haaland, O.; Hadjidakis, C.; Haiduc, M.; Hamagaki, H.; Hamar, G.; Han, B.H.; Hanratty, L.D.; Hansen, A. ; Harmanova-Tothova, Z.; Harris, J.W.; Hartig, M. ; Hasegan, D.; Hatzifotiadou, D.; Hayrapetyan, A. ; Heckel, S.T.; Heide, M.; Helstrup, H.; Herghelegiu, A.; Herrera Corral, G.; Herrmann, N.; Hess, B.A.; Hetland, K.F.; Hicks, B.; Hille, P.T. ; Hippolyte, B.; Horaguchi, T.; Hori, Y.; Hristov, P.; Hrivnacova, I.; Huang, M.; Humanic, T.J.; Hwang, D.S.; Ichou, R.; Ilkaev, R. ; Ilkiv, I.; Inaba, M.; Incani, E.; Innocenti, G.M.; Innocenti, P.G.; Ippolitov, M.; Irfan, M.; Ivan, C.; Ivanov, M.; Ivanov, A.; Ivanov, V.; Ivanytskyi, O.; Jacobs, P.M.; Jang, H.J.; Janik, R. ; Janik, M.A.; Jayarathna, P.H.S.Y.; Jena, S.; Jha, D.M.; Jimenez Bustamante, R.T.; Jirden, L.; Jones, P.G.; Jung, H.; Jusko, A.; Kaidalov, A.B. ; Kakoyan, V.; Kalcher, S.; Kalinak, P.; Kalliokoski, T.; Kalweit, A.; Kang, J.H.; Kaplin, V.; Karasu Uysal, A.; Karavichev, O.; Karavicheva, T.; Karpechev, E.; Kazantsev, A.; Kebschull, U.; Keidel, R.; Khan, P.; Khan, M.M.; Khan, S.A.; Khanzadeev, A.; Kharlov, Y.; Kileng, B.; Kim, M. ; Kim, D.J.; Kim, D.W.; Kim, J.H.; Kim, J.S.; Kim, T.; Kim, M.; Kim, S.H.; Kim, S.; Kim, B. ; Kirsch, S.; Kisel, I.; Kiselev, S.; Kisiel, A. ; Klay, J.L.; Klein, J.; Klein-Bösing, C.; Kliemant, M.; Kluge, A.; Knichel, M.L.; Knospe, A.G.; Koch, K.; Köhler, M.K.; Kollegger, T.; Kolojvari, A.; Kondratiev, V.; Kondratyeva, N.; Konevskikh, A.; Korneev, A.; Kour, R.; Kowalski, M. ; Kox, S.; Koyithatta Meethaleveedu, G.; Kral, J. ; Kralik, I.; Kramer, F.; Kraus, I.; Krawutschke, T.; Krelina, M.; Kretz, M.; Krivda, M. ; Krizek, F.; Krus, M.; Kryshen, E.; Krzewicki, M.; Kucheriaev, Y.; Kugathasan, T.; Kuhn, C.; Kuijer, P.G.; Kulakov, I.; Kumar, J.; Kurashvili, P.; Kurepin, A.B.; Kurepin, A.; Kuryakin, A.; Kushpil, S.; Kushpil, V.; Kvaerno, H.; Kweon, M.J. ; Kwon, Y.; Ladron de Guevara, P.; Lakomov, I.; Langoy, R.; La Pointe, S.L.; Lara, C.; Lardeux, A. ; La Rocca, P.; Lazzeroni, C.; Lea, R.; Le Bornec, Y.; Lechman, M.; Lee, K.S.; Lee, G.R.; Lee, S.C.; Lefevre, F.; Lehnert, J.; Leistam, L. ; Lenhardt, M.; Lenti, V.; Leon, H.; Leoncino, M.; Leon Monzon, I.; Leon Vargas, H.; Levai, P. ; Lien, J.; Lietava, R.; Lindal, S.; Lindenstruth, V.; Lippmann, C.; Lisa, M.A.; Liu, L. ; Loggins, V.R.; Loginov, V.; Lohn, S.; Lohner, D.; Loizides, C.; Loo, K.K.; Lopez, X.; Lopez Torres, E.; Lovhoiden, G.; Lu, X.-G.; Luettig, P. ; Lunardon, M.; Luo, J.; Luparello, G.; Luquin, L.; Luzzi, C.; Ma, K.; Ma, R.; Madagodahettige-Don, D.M.; Maevskaya, A.; Mager, M. ; Mahapatra, D.P.; Maire, A.; Malaev, M.; Maldonado Cervantes, I.; Malinina, L.; MalKevich, D. ; Malzacher, P.; Mamonov, A.; Manceau, L.; Mangotra, L.; Manko, V.; Manso, F.; Manzari, V.; Mao, Y.; Marchisone, M.; Mares, J.; Margagliotti, G.V.; Margotti, A.; Marin, Ana; Marin Tobon, C.A. ; Markert, C.; Martashvili, I.; Martinengo, P.; Martinez, M.I.; Martinez Davalos, A.; Martinez Garcia, G.; Martynov, Y.; Mas, A.; Masciocchi, S. ; Masera, M.; Masoni, A.; Massacrier, L.; Mastroserio, A.; Matthews, Z.L.; Matyja, A.; Mayer, C.; Mazer, J.; Mazzoni, M.A.; Meddi, F.; Menchaca-Rocha, A.; Mercado Perez, J.; Meres, M.; Miake, Y.; Milano, L.; Milosevic, J.; Mischke, A. ; Mishra, A.N.; Mikowiec, D.; Mitu, C.; Mlynarz, J.; Mohanty, B.; Molnar, L.; Montano Zetina, L.; Monteno, M.; Montes, E.; Moon, T.; Morando, M.; Moreira De Godoy, D.A.; Moretto, S.; Morsch, A.; Muccifora, V.; Mudnic, E.; Muhuri, S. ; Mukherjee, M.; Müller, H.; Munhoz, M.G.; Musa, L.; Musso, A.; Nandi, B.K.; Nania, R.; Nappi, E. ; Nattrass, C.; Naumov, N.P.; Navin, S.; Nayak, T.K.; Nazarenko, S.; Nazarov, G.; Nedosekin, A.; Nicassio, M.; Niculescu, M.; Nielsen, B.S.; Niida, T.; Nikolaev, S.; Nikolic, V.; Nikulin, S.; Nikulin, V.; Nilsen, B.S.; Nilsson, M.S.; Noferini, F.; Nomokonov, P.; Nooren, G.; Novitzky, N.; Nyanin, A.; Nyatha, A.; Nygaard, C.; Nystrand, J. ; Ochirov, A.; Oeschler, H.; Oh, S.; Oh, S.K.; Oleniacz, J.; Oppedisano, C.; Ortiz Velasquez, A.; Ortona, G.; Oskarsson, A.; Ostrowski, P.; Otwinowski, J.; Oyama, K.; Ozawa, K.; Pachmayer, Y. ; Pachr, M.; Padilla, F.; Pagano, P.; Paic, G. ; Painke, F.; Pajares, C.; Pal, S.K.; Palaha, A. ; Palmeri, A.; Papikyan, V.; Pappalardo, G.S.; Park, W.J.; Passfeld, A.; Pastircak, B.; Patalakha, D.I.; Paticchio, V.; Pavlinov, A.; Pawlak, T.; Peitzmann, T.; Pereira Da Costa, H.; Pereira De Oliveira Filho, E.; Peresunko, D.; Perez Lara, C.E.; Perez Lezama, E.; Perini, D.; Perrino, D.; Peryt, W.; Pesci, A.; Peskov, V.; Pestov, Y. ; Petracek, V.; Petran, M.; Petris, M.; Petrov, P.; Petrovici, M.; Petta, C.; Piano, S.; Piccotti, A.; Pikna, M.; Pillot, P.; Pinazza, O. ; Pinsky, L.; Pitz, N.; Piyarathna, D.B.; Planinic, M.; Ploskon, M.; Pluta, J.; Pocheptsov, T.; Pochybova, S.; Podesta-Lerma, P.L.M.; Poghosyan, M.G.; Polak, K.; Polichtchouk, B.; Pop, A.; Porteboeuf-Houssais, S.; Pospisil, V.; Potukuchi, B.; Prasad, S.K.; Preghenella, R.; Prino, F.; Pruneau, C.A.; Pshenichnov, I.; Puchagin, S.; Puddu, G.; Pulvirenti, A.; Punin, V. ; Putis, M.; Putschke, J.; Quercigh, E.; Qvigstad, H.; Rachevski, A.; Rademakers, A.; Räihä T.S.; Rak, J.; Rakotozafindrabe, A.; Ramello, L.; Ramirez Reyes, A.; Raniwala, S.; Raniwala, R.; Räsänen, S.S.; Rascanu, B.T.; Rathee, D.; Read, K.F.; Real, J.S.; Redlich, K.; Reichelt, P.; Reicher, M.; Renfordt, R.; Reolon, A.R.; Reshetin, A.; Rettig, F.; Revol, J.-P.; Reygers, K.; Riccati, L.; Ricci, R.A.; Richert, T. ; Richter, M.; Riedler, P.; Riegler, W.; Riggi, F.; Rodrigues Fernandes Rabacal, B.; Rodriguez Cahuantzi, M.; Rodriguez Manso, A.; Roed, K.; Rohr, D.; Röhrich, D.; Romita, R.; Ronchetti, F. ; Rosnet, P.; Rossegger, S.; Rossi, A.; Roy, P. ; Roy, C.; Rubio Montero, A.J.; Rui, R.; Russo, R.; Ryabinkin, E.; Rybicki, A.; Sadovsky, S.; Safarik,

K.; Sahoo, R.; Sahu, P.K.; Saini, J. ; Sakaguchi, H.; Sakai, S.; Sakata, D.; Salgado, C.A.; Salzwedel, J.; Sambyal, S.; Samsonov, V.; Sanchez Castro, X.; Sandor, L.; Sandoval, A.; Sano, M.; Sano, S.; Santo, R.; Santoro, R.; Sarkamo, J.; Scapparone, E.; Scarlassara, F.; Scharenberg, R.P.; Schiaua, C.; Schicker, R.; Schmidt, H.R.; Schmidt, C.; Schreiner, S.; Schuchmann, S.; Schukraft, J.; Schutz, Y.; Schwarz, K.; Schweda, K.; Scioli, G.; Scomparin, E.; Scott, P.A.; Scott, R.; Segato, G.; Selyuzhenkov, I.; Senyukov, S.; Seo, J.; Serci, S.; Serradilla, E.; Sevcenco, A.; Shabetai, A.; Shabratova, G.; Shahoyan, R.; Sharma, N.; Sharma, S.; Rohni, S.; Shigaki, K.; Shimomura, M.; Shtejer, K.; Sibiriak, Y.; Siciliano, M.; Sicking, E.; Siddhanta, S.; Siemiarczuk, T.; Silvermyr, D. ; Silvestre, C.; Simatovic, G.; Simonetti, G.; Singaraju, R.; Singh, R.; Singha, S.; Singhal, V. ; Sinha, T.; Sinha, B.C.; Sitar, B.; Sitta, M. ; Skaali, T.B.; Skjerdal, K.; Smakal, R.; Smirnov, N.; Snellings, R.J.M.; Sogaard, C.; Soltz, R.; Son, H.; Song, J.; Song, M.; Soos, C. ; Soramel, F.; Sputowska, I.; Spyropoulou-Stassinaki, M.; Srivastava, B.K.; Stachel, J.; Stan, I.; Stan, I.; Stefanek, G.; Steinpreis, M.; Stenlund, E.; Steyn, G.; Stiller, J.H.; Stocco, D.; Stolpovskiy, M.; Strabykin, K. ; Strmen, P.; Suaide, A.A.P.; Subieta Vasquez, M.A. ; Sugitate, T.; Suire, C.; Sukhorukov, M.; Sultanov, R.; Sumbera, M.; Susa, T.; Symons, T.J.M.; Szanto de Toledo, A.; Szarka, I.; Szczepankiewicz, A.; Szostak, A.; Szymanski, M.; Takahashi, J.; Tapia Takaki, J.D.; Tauro, A.; Tejeda Munoz, G.; Telesca, A.; Terrevoli, C.; Thäder, J.; Thomas, D.; Tieulent, R.; Timmins, A.R.; Tlusty, D.; Toia, A.; Torii, H.; Toscano, L.; Trubnikov, V.; Truesdale, D.; Trzaska, W.H.; Tsuji, T.; Tumkin, A.; Turrisi, R.; Tveter, T.S. ; Ulery, J.; Ullaland, K.; Ulrich, J.; Uras, A. ; Urban, J.; Urciuoli, G.M.; Usai, G.L.; Vajzer, M.; Vala, M.; Valencia Palomo, L.; Vallero, S.; Vande Vyvre, P.; van Leeuwen, M.; Vannucci, L.; Vargas, A.; Varma, R.; Vasileiou, M.; Vasiliev, A. ; Vechernin, V.; Veldhoen, M.; Venaruzzo, M.; Vercellin, E.; Vergara, S.; Vernet, R.; Verweij, M. ; Vickovic, L.; Viesti, G.; Vikhlyantsev, O.; Vilakazi, Z.; Villalobos Baillie, O.; Vinogradov, Y. ; Vinogradov, A.; Vinogradov, L.; Virgili, T.; Viyogi, Y.P.; Vodopyanov, A.; Voloshin, S.; Voloshin, K.; Volpe, G.; von Haller, B.; Vranic, D. ; Ovrebekk, G.; Vrlakova, J.; Vulpescu, B.; Vyushin, A.; Wagner, V.; Wagner, B.; Wan, R.; Wang, Y.; Wang, M.; Wang, D.; Wang, Y.; Watanabe, K.; Weber, M.; Wessels, J.P.; Westerhoff, U.; Wiechula, J.; Wikne, J.; Wilde, M.; Wilk, A. ; Wilk, G.; Williams, M.C.S.; Windelband, B.; Xaplanteris Karampatsos, L.; Yaldo, C.G.; Yamaguchi, Y.; Yang, S.; Yang, H.; Yasnopolskiy, S.; Yi, J. ; Yin, Z.; Yoo, I.-K.; Yoon, J.; Yu, W.; Yuan, X.; Yushmanov, I.; Zaccolo, V.; Zach, C.; Zampolli, C.; Zaporozhets, S.; Zarochentsev, A.; Zavada, P.; Zaviyalov, N.; Zbroszczyk, H.; Zelnicek, P.; Zgura, I.S.; Zhalov, M.; Zhang, H. ; Zhang, X.; Zhou, D.; Zhou, Y.; Zhou, F.; Zhu, J.; Zhu, X.; Zhu, J.; Zichichi, A.; Zimmermann, A.; Zinovjev, G.; Zoccarato, Y.; Zynovyev, M.; Zyzak, M.: D_s^+ **meson production at central rapidity in protonproton collisions at** $\sqrt{s}$ **=7TeV.** *Physics letters / B* 718: 279 - 294, 2012. DOI:10.1016/j.physletb.2012.10.049

WOS-PHN-16 Abelev, B.; Adam, J.; Adamova, D.; Adare, A.M.; Aggarwal, M.M.; Aglieri Rinella, G.; Agocs, A.G. ; Agostinelli, A.; Aguilar Salazar, S.; Ahammed, Z. ; Ahmad, N.; Ahmad Masoodi, A.; Ahn, S.U.; Akindinov, A.; Aleksandrov, D.; Alessandro, B.; Alfaro Molina, R.; Alici, A.; Alkin, A.; Almaraz Avina, E.; Alme, J.; Alt, T.; Altini, V.; Altinpinar, S.; Altsybeev, I.; Andrei, C.; Andronic, Anton; Anguelov, V.; Anielski, J.; Anson, C.; Anticic, T.; Antinori, F.; Antonioli, P.; Aphecetche, L.; Appelshäuser, H.; Arbor, N.; Arcelli, S.; Arend, A.; Armesto, N.; Arnaldi, R. ; Aronsson, T.; Arsene, Ionut Cristian; Arslandok, M.; Asryan, A.; Augustinus, A.; Averbeck, Ralf; Awes, T.C.; Äystö J.; Azmi, M.D.; Bach, M.; Badala, A.; Baek, Y.W.; Bailhache, R.; Bala, R. ; Baldini Ferroli, R.; Baldisseri, A.; Baldit, A. ; Baltasar Dos Santos Pedrosa, F.; Ban, J.; Baral, R.C.; Barbera, R.; Barile, F.; Barnaföldi, G.G. ; Barnby, L.S.; Barret, V.; Bartke, J.; Basile, M.; Bastid, N.; Basu, S.; Bathen, B.; Batigne, G.; Batyunya, B.; Baumann, C.; Bearden, I.G.; Beck, H.; Belikov, I.; Bellini, F.; Bellwied, R. ; Belmont-Moreno, E.; Bencedi, G.; Beole, S.; Berceanu, I.; Bercuci, A.; Berdnikov, Y.; Berenyi, D.; Berzano, D.; Betev, L.; Bhasin, A.; Bhati, A.K.; Bhom, J.; Bianchi, N.; Bianchi, L.; Bianchin, C.; Bielcik, J.; Bielcikova, J.; Bilandzic, A.; Bjelogrlic, S.; Blanco, F.; Blanco, F.; Blau, D.; Blume, C.; Boccioli, M.; Bock, N. ; Böttger, S.; Bogdanov, A.; Boggild, H.; Bogolyubsky, M.; Boldizsar, L.; Bombara, M.; Book, J.; Borel, H.; Borissov, A.; Bose, S.; Boss, F.; Botje, M.; Boyer, B.; Braidot, E.; Braun-Munzinger, Peter; Bregant, M.; Breitner, T.; Browning, T.A.; Broz, M.; Brun, R.; Bruna, E.; Bruno, G.E.; Budnikov, D.; Buesching, H.; Bufalino, S.; Bugaiev, K.; Busch, O.; Buthelezi, Z.; Caballero Orduna, D.; Caffarri, D.; Cai, X.; Caines, H.; Calvo Villar, E.; Camerini, P.; Canoa Roman, V.; Cara Romeo, G.; Carena, W.; Carena, F. ; Carlin Filho, N.; Carminati, F.; Carrillo Montoya, C.A.; Casanova Diaz, A.; Castillo Castellanos, J.; Castillo Hernandez, J.F.; Casula, E.A.R.; Catanescu, V.; Cavicchioli, C.; Ceballos Sanchez, C.; Cepila, J.; Cerello, P.; Chang, B.; Chapeland, S.; Charvet, J.L.; Chattopadhyay, S.; Chattopadhyay, S. ; Chawla, I.; Cherney, M.; Cheshkov, C.; Cheynis, B.; Chibante Barroso, V.; Chinellato, D.D.; Chochula, P.; Chojnacki, M.; Choudhury, S.; Christakoglou, P.; Christensen, C.H.; Christiansen, P. ; Chujo, T.; Chung, S.U.; Cicalo, C.; Cifarelli, L.; Cindolo, F.; Cleymans, J.; Coccetti, F.; Colamaria, F.; Colella, D.; Conesa Balbastre, G.; Conesa del Valle, Z.; Constantin, P.; Contin, G.; Contreras, J.G.; Cormier, T.M.; Corrales Morales, Y. ; Cortese, P.; Cortes Maldonado, I.; Cosentino, M.R.; Costa, F.; Cotallo, M.E.; Crescio, E.; Crochet, P.; Cruz Alaniz, E.; Cuautle, E.; Cunqueiro, L.; Dainese, A.; Dalsgaard, H.H.; Danu, A.; Das, I.; Das, K.; Das, D.; Dash, A.; Dash, S.; De, S.; de Barros, G.O.V.; De Caro, A. ; de Cataldo, G.; de Cuveland, J.; De Falco, A.; De Gruttola, D.; Delagrange, H.; Deloff, A.; Demanov, V.; De Marco, N.; Denes, E.; De Pasquale, S.; Deppman, A.; D Erasmo, G.; de Rooij, R.; Diaz Corchero, M.A.; Di Bari, D.; Dietel, T.; Di Liberto, S.; Di Mauro, A.; Di Nezza, P.; Divia, R. ; Djuvsland, O.; Dobrin, A.; Dobrowolski, T.; Dominguez, I.; Dönigus, Benjamin; Dordic, O.; Driga, O.; Dubey, A.K.; Ducroux, L.; Dupieux, P. ; Dutta Majumdar, A.K.; Dutta Majumdar, M.R.; Elia, D.; Emschermann, D.; Engel, H.; Erdal, H.A.; Espagnon, B.; Estienne, M.; Esumi, S.; Evans, D. ; Eyyubova, G.; Fabris, D.; Faivre, J.; Falchieri, D.; Fantoni, A.; Fasel, Markus; Fearick, R.; Fedunov, A.; Fehlker, D.; Feldkamp, L.; Felea, D.; Fenton-Olsen, B.; Feofilov, G.; Fernandez Tellez, A.; Ferretti, R.; Ferretti, A.; Figiel, J.; Figueredo, M.A.S.; Filchagin, S.; Finogeev, D.; Fionda, F.M.; Fiore, E.M.; Floris, M. ; Foertsch, S.; Foka, Panagiota; Fokin, S.; Fragiacomo, E.; Frankenfeld, Ulrich; Fuchs, U.; Furget, C.; Fusco Girard, M.; Gaardhoje, J.J.; Gagliardi, M.; Gago, A.; Gallio, M.; Gangadharan, D.R.; Ganoti, P.; Garabatos, C.; Garcia-Solis, E. ; Garishvili, I.; Gerhard, J.; Germain, M.; Geuna, C.; Gheata, A.; Gheata, M.; Ghidini, B.; Ghosh, P.; Gianotti, P.; Girard, M.R.; Giubellino, P.; Gladysz-Dziadus, E.; Glässel, P.; Gomez, R. ; Ferreiro, E.G.; Gonzalez-Trueba, L.H.; Gonzalez-Zamora, P.; Gorbunov, S.; Goswami, A.; Gotovac,

S.; Grabski, V.; Graczykowski, L.K.; Grajcarek, R.; Grelli, A.; Grigoras, A.; Grigoras, C.; Grigoriev, V.; Grigoryan, A.; Grigoryan, S.; Grinyov, B.; Grion, N.; Gros, P.; Grosse-Oetringhaus, J.F.; Grossiord, J.-Y.; Grosso, R. ; Guber, F.; Guernane, R.; Guerra Gutierrez, C.; Guerzoni, B.; Guilbaud, M.; Gulbrandsen, K.; Gunji, T.; Gupta, A.; Gupta, R.; Gutbrod, H.; Haaland, O.; Hadjidakis, C.; Haiduc, M.; Hamagaki, H.; Hamar, G.; Han, B.H.; Hanratty, L.D.; Hansen, A. ; Harmanova, Z.; Harris, J.W.; Hartig, M.; Hasegan, D.; Hatzifotiadou, D.; Hayrapetyan, A.; Heckel, S.T.; Heide, M.; Helstrup, H.; Herghelegiu, A.; Herrera Corral, G.; Herrmann, N.; Hetland, K.F. ; Hicks, B.; Hille, P.T.; Hippolyte, B.; Horaguchi, T.; Hori, Y.; Hristov, P.; Hrivnacova, I.; Huang, M.; Humanic, T.J.; Hwang, D.S.; Ichou, R.; Ilkaev, R.; Ilkiv, I.; Inaba, M.; Incani, E.; Innocenti, G.M.; Innocenti, P.G.; Ippolitov, M.; Irfan, M.; Ivan, Cristian George; Ivanov, A.; Ivanov, V.; Ivanov, Marian; Ivanytskyi, O.; Jacholkowski, A.; Jacobs, P.M.; Jancurova, L.; Jang, H.J.; Jangal, S.; Janik, R. ; Janik, M.A.; Jayarathna, P.H.S.Y.; Jena, S.; Jha, D.M.; Jimenez Bustamante, R.T.; Jirden, L.; Jones, P.G.; Jung, H.; Jusko, A.; Kaidalov, A.B. ; Kakoyan, V.; Kalcher, S.; Kalinak, P.; Kalliokoski, T.; Kalweit, A.; Kanaki, K.; Kang, J.H.; Kaplin, V.; Karasu Uysal, A.; Karavichev, O. ; Karavicheva, T.; Karpechev, E.; Kazantsev, A.; Kebschull, U.; Keidel, R.; Khan, P.; Khan, M.M.; Khan, S.A.; Khanzadeev, A.; Kharlov, Y.; Kileng, B. ; Kim, T.; Kim, D.J.; Kim, D.W.; Kim, J.H.; Kim, J.S.; Kim, M.; Kim, M.; Kim, S.H.; Kim, S. ; Kim, B.; Kirsch, S.; Kisel, I.; Kiselev, S.; Kisiel, A.; Klay, J.L.; Klein, J.; Klein-Bösing, C.; Kliemant, M.; Kluge, A.; Knichel, Michael Linus ; Knospe, A.G.; Koch, K.; Köhler, M.K.; Kolojvari, A.; Kondratiev, V.; Kondratyeva, N.; Konevskikh, A.; Korneev, A.; Kour, R.; Kowalski, M. ; Kox, S.; Koyithatta Meethaleveedu, G.; Kral, J. ; Kralik, I.; Kramer, F.; Kraus, I.; Krawutschke, T.; Krelina, M.; Kretz, M.; Krivda, M. ; Krizek, F.; Krus, M.; Kryshen, E.; Krzewicki, Mikolaj; Kucheriaev, Y.; Kuhn, C.; Kuijer, P.G.; Kulakov, I.; Kurashvili, P.; Kurepin, A.; Kurepin, A.B.; Kuryakin, A.; Kushpil, S.; Kushpil, V.; Kvaerno, H.; Kweon, M.J.; Kwon, Y.; Ladron de Guevara, P.; Lakomov, I.; Langoy, R.; La Pointe, S.L.; Lara, C.; Lardeux, A.; La Rocca, P.; Lazzeroni, C.; Lea, R.; Le Bornec, Y.; Lechman, M. ; Lee, S.C.; Lee, G.R.; Lee, K.S.; Lefevre, F. ; Lehnert, J.; Leistam, L.; Lenhardt, M.; Lenti, V.; Leon, H.; Leon Monzon, I.; Leon Vargas, H. ; Levai, P.; Lien, J.; Lietava, R.; Lindal, S. ; Lindenstruth, V.; Lippmann, C.; Lisa, M.A.; Liu, L.; Loenne, P.I.; Loggins, V.R.; Loginov, V. ; Lohn, S.; Lohner, D.; Loizides, C.; Loo, K.K. ; Lopez, X.; Lopez Torres, E.; Lovhoiden, G.; Lu, X.-G.; Luettig, P.; Lunardon, M.; Luo, J.; Luparello, G.; Luquin, L.; Luzzi, C.; Ma, K; Ma, R.; Madagodahettige-Don, D.M.; Maevskaya, A.; Mager, M.; Mahapatra, D.P.; Maire, A.; Malaev, M. ; Maldonado Cervantes, I.; Malinina, L.; MalKevich, D.; Malzacher, Peter; Mamonov, A.; Manceau, L.; Mangotra, L.; Manko, V.; Manso, F.; Manzari, V.; Mao, Y.; Marchisone, M.; Mares, J. ; Margagliotti, G.V.; Margotti, A.; Marin, Ana; Marin Tobon, C.A.; Markert, C.; Martashvili, I.; Martinengo, P.; Martinez, M.I.; Martinez Davalos, A. ; Martinez Garcia, G.; Martynov, Y.; Mas, A.; Masciocchi, Silvia; Masera, M.; Masoni, A.; Massacrier, L.; Mastromarco, M.; Mastroserio, A.; Matthews, Z.L.; Matyja, A.; Mayani, D.; Mayer, C. ; Mazer, J.; Mazzoni, M.A.; Meddi, F.; Menchaca-Rocha, A.; Mercado Perez, J.; Meres, M.; Miake, Y.; Milano, L.; Milosevic, J.; Mischke, A. ; Mishra, A.N.; Miskowiec, Dariusz; Mitu, C.; Mlynarz, J.; Mohanty, A.K.; Mohanty, B.; Molnar, L. ; Montano Zetina, L.; Monteno, M.; Montes, E.; Moon, T.; Morando, M.; Moreira De Godoy, D.A.; Moretto, S.; Morsch, A.; Muccifora, V.; Mudnic, E. ; Muhuri, S.; Mukherjee, M.; Müller, H.; Munhoz, M.G.; Musa, L.; Musso, A.; Nandi, B.K.; Nania, R.; Nappi, E.; Nattrass, C.; Naumov, N.P.; Navin, S.; Nayak, T.K.; Nazarenko, S.; Nazarov, G. ; Nedosekin, A.; Nielsen, B.S.; Niida, T.; Nikolaev, S.; Nikolic, V.; Nikulin, V.; Nikulin, S. ; Nilsen, B.S.; Nilsson, M.S.; Noferini, F.; Nomokonov, P.; Nooren, G.; Novitzky, N.; Nyanin, A. ; Nyatha, A.; Nygaard, C.; Nystrand, J.; Ochirov, A.; Oeschler, H.; Oh, S. K.; Oh, S.; Oleniacz, J.; Oppedisano, C.; Ortiz Velasquez, A.; Ortona, G. ; Oskarsson, A.; Ostrowski, P.; Otwinowski, Jacek ; Oyama, K.; Ozawa, K.; Pachmayer, Y.; Pachr, M. ; Padilla, F.; Pagano, P.; Paic, G.; Painke, F. ; Pajares, C.; Pal, S.K.; Pal, S.; Palaha, A.; Palmeri, A.; Papikyan, V.; Pappalardo, G.S.; Park, Woo Jin; Passfeld, A.; Pastircak, B.; Patalakha, D.I.; Paticchio, V.; Pavlinov, A.; Pawlak, T.; Peitzmann, T.; Pereira Da Costa, H.; Pereira De Oliveira Filho, E.; Peresunko, D.; Perez Lara, C.E. ; Perez Lezama, E.; Perini, D.; Perrino, D.; Peryt, W.; Pesci, A.; Peskov, V.; Pestov, Y.; Petracek, V.; Petran, M.; Petris, M.; Petrov, P. ; Petrovici, M.; Petta, C.; Piano, S.; Piccotti, A.; Pikna, M.; Pillot, P.; Pinazza, O.; Pinsky, L.; Pitz, N.; Piyarathna, D.B.; Ploskon, M.; Pluta, J.; Pocheptsov, T.; Pochybova, S.; Podesta-Lerma, P.L.M.; Poghosyan, M.G.; Polak, K.; Polichtchouk, B.; Pop, A.; Porteboeuf-Houssais, S.; Pospisil, V.; Potukuchi, B.; Prasad, S.K.; Preghenella, R.; Prino, F.; Pruneau, C.A.; Pshenichnov, I.; Puchagin, S.; Puddu, G.; Pujol Teixido, J.; Pulvirenti, A.; Punin, V.; Putis, M. ; Putschke, J.; Quercigh, E.; Qvigstad, H.; Rachevski, A.; Rademakers, A.; Radomski, S.; Räihä T.S.; Dvorak, Jan; Rakotozafindrabe, A.; Ramello, L.; Ramirez Reyes, A.; Raniwala, S.; Raniwala, R.; Räsänen, S.S.; Rascanu, B.T.; Rathee, D.; Read, K.F.; Real, J.S.; Redlich, K.; Reichelt, P.; Reicher, M.; Renfordt, R.; Reolon, A.R.; Reshetin, A.; Rettig, F.; Revol, J.-P.; Reygers, K.; Riccati, L.; Ricci, R.A.; Richert, T. ; Richter, M.; Riedler, P.; Riegler, W.; Riggi, F.; Rodrigues Fernandes Rabacal, B.; Rodriguez Cahuantzi, M.; Rodriguez Manso, A.; Roed, K.; Rohr, D.; Röhrich, D.; Romita, R.; Ronchetti, F. ; Rosnet, P.; Rossegger, S.; Rossi, A.; Roy, P. ; Roy, C.; Rubio Montero, A.J.; Rui, R.; Ryabinkin, E.; Rybicki, A.; Sadovsky, S.; Safarik, K.; Sahoo, R.; Sahu, P.K.; Saini, J. ; Sakaguchi, H.; Sakai, S.; Sakata, D.; Salgado, C.A.; Salzwedel, J.; Sambyal, S.; Samsonov, V.; Sanchez Castro, X.; Sandor, L.; Sandoval, A.; Sano, S.; Sano, M.; Santo, R.; Santoro, R.; Sarkamo, J.; Scapparone, E.; Scarlassara, F.; Scharenberg, R.P.; Schiaua, C.; Schicker, R.; Schmidt, Christian Alberto; Schmidt, H.R.; Schreiner, S.; Schuchmann, S.; Schukraft, J.; Schutz, Y.; Schwarz, Kilian; Schweda, Kai; Scioli, G.; Scomparin, E.; Scott, R.; Scott, P.A.; Segato, G. ; Selyuzhenkov, Ilya; Senyukov, S.; Seo, J.; Serci, S.; Serradilla, E.; Sevcenco, A.; Shabetai, A.; Shabratova, G.; Shahoyan, R.; Sharma, S.; Sharma, N.; Rohni, S.; Shigaki, K.; Shimomura, M. ; Shtejer, K.; Sibiriak, Y.; Siciliano, M.; Sicking, E.; Siddhanta, S.; Siemiarczuk, T.; Silvermyr, D.; Silvestre, C.; Simatovic, G.; Simonetti, G.; Singaraju, R.; Singh, R.; Singha, S. ; Sinha, T.; Sinha, B.C.; Sitar, B.; Sitta, M. ; Skaali, T.B.; Skjerdal, K.; Smakal, R.; Smirnov, N.; Snellings, R.J.M.; Sogaard, C.; Soltz, R.; Johansson, H.; Song, J.; Song, M.; Soos, C.; Soramel, F.; Sputowska, I.; Spyropoulou-Stassinaki, M.; Srivastava, B.K.; Stachel, J.; Stan, I.; Stan, I.; Stefanek, G.; Steinbeck, T.; Steinpreis, M.; Stenlund, E.; Steyn, G.; Stiller, J.H.; Stocco, D.; Stolpovskiy, M.; Strabykin, K.; Strmen, P.; Suaide, A.A.P.; Subieta Vasquez, M.A.; Sugitate, T.; Suire, C.; Sukhorukov, M.; Sultanov, R.; Sumbera, M.; Susa, T.; Szanto de Toledo, A.; Szarka, I.; Szczepankiewicz, A.; Szostak, A.; Szymanski, M.;

Takahashi, J.; Tapia Takaki, J.D.; Tauro, A.; Tejeda Munoz, G.; Telesca, A.; Terrevoli, C.; Thäder, Jochen; Thomas, D.; Tieulent, R.; Timmins, A.R.; Tlusty, D.; Toia, A.; Torii, H.; Toscano, L.; Truesdale, D.; Trzaska, W.H.; Tsuji, T.; Tumkin, A.; Turrisi, R.; Tveter, T.S.; Ulery, J. ; Ullaland, K.; Ulrich, J.; Uras, A.; Urban, J. ; Urciuoli, G.M.; Usai, G.L.; Vajzer, M.; Vala, M.; Valencia Palomo, L.; Vallero, S.; van der Kolk, N.; Vande Vyvre, P.; van Leeuwen, M.; Vannucci, L. ; Vargas, A.; Varma, R.; Vasileiou, M.; Vasiliev, A.; Vechernin, V.; Veldhoen, M.; Venaruzzo, M.; Vercellin, E.; Vergara, S.; Vernet, R.; Verweij, M. ; Vickovic, L.; Viesti, G.; Vikhlyantsev, O.; Vilakazi, Z.; Villalobos Baillie, O.; Vinogradov, A. ; Vinogradov, Y.; Vinogradov, L.; Virgili, T.; Viyogi, Y.P.; Vodopyanov, A.; Voloshin, S.; Voloshin, K.; Volpe, G.; von Haller, B.; Vranic, D. ; Ovrebekk, G.; Vrlakova, J.; Vulpescu, B.; Vyushin, A.; Wagner, B.; Wagner, V.; Wan, R; Wang, Y.; Wang, D.; Wang, M.; Wang, Y.; Watanabe, K.; Weber, M.; Wessels, J.P.; Westerhoff, U.; Wiechula, J.; Wikne, J.; Wilde, M.; Wilk, G. ; Wilk, A.; Williams, M.C.S.; Windelband, B.; Xaplanteris Karampatsos, L.; Yaldo, C.G.; Yamaguchi, Y.; Yang, S.; Yang, H.; Yasnopolskiy, S.; Yi, J. ; Yin, Z.; Yoo, I.-K.; Yoon, J.; Yu, W.; Yuan, X.; Yushmanov, I.; Zach, C.; Zampolli, C.; Zaporozhets, S.; Zarochentsev, A.; Zavada, P.; Zaviyalov, N.; Zbroszczyk, H.; Zelnicek, P.; Zgura, I.S.; Zhalov, M.; Zhang, X.; Zhang, H.; Zhou, Y. ; Zhou, D.; Zhou, F.; Zhu, X.; Zhu, J.; Zhu, J.; Zichichi, A.; Zimmermann, A.; Zinovjev, G.; Zoccarato, Y.; Zynovyev, M.; Zyzak, M.: **Multi-strange baryon production in pp collisions at with ALICE.** *Physics letters / B* 712: 309 - 318, 2012. DOI:10.1016/j.physletb.2012.05.011

WOS-PHN-17 Abelev, B.; Adamczewski-Musch, Jörn; Adamova, D.; Adare, A. M.; Aggarwal, M. M.; Aglieri Rinella, G. ; Agocs, A. G.; Agostinelli, A.; Aguilar Salazar, S. ; Ahammed, Z.; Ahmad Masoodi, A.; Ahmad, N.; Ahn, S. A.; Ahn, S. U.; Akindinov, A.; Aleksandrov, D. ; Alessandro, B.; Alfaro Molina, R.; Alici, A.; Alkin, A.; Almaraz Avina, E.; Alme, J.; Alt, T. ; Altini, V.; Altinpinar, S.; Altsybeev, I.; Andrei, C.; Andronic, A.; Anguelov, V.; Anielski, J.; Anson, C.; Anticic, T.; Antinori, F.; Antonioli, P.; Aphecetche, L.; Appelshäuser, H.; Arbor, N.; Arcelli, S.; Arend, A.; Armesto, N.; Arnaldi, R.; Aronsson, T.; Arsene, I. C.; Arslandok, M.; Asryan, A.; Augustinus, A.; Averbeck, R.; Awes, T. C.; Äystö J.; Azmi, M. D. ; Bach, M.; Badala, A.; Baek, Y. W.; Bailhache, R.; Bala, R.; Baldini Ferroli, R.; Baldisseri, A. ; Baldit, A.; Baltasar Dos Santos Pedrosa, F.; Ban, J.; Baral, R. C.; Barbera, R.; Barile, F.; Barnaföldi, G. G.; Barnby, L. S.; Barret, V.; Bartke, J.; Basile, M.; Bastid, N.; Basu, S.; Bathen, B.; Batigne, G.; Batyunya, B.; Baumann, C. ; Bearden, I. G.; Beck, H.; Belikov, I.; Bellini, F.; Bellwied, R.; Belmont-Moreno, E.; Bencedi, G. ; Beole, S.; Berceanu, I.; Bercuci, A.; Berdnikov, Y.; Berenyi, D.; Bergognon, A. A. E.; Berzano, D.; Betev, L.; Bhasin, A.; Bhati, A. K. ; Bhom, J.; Bianchi, L.; Bianchi, N.; Bianchin, C.; Bielcik, J.; Bielcikova, J.; Bilandzic, A. ; Bjelogrlic, S.; Blanco, F.; Blanco, F.; Blau, D.; Blume, C.; Boccioli, M.; Bock, N.; Böttger, S.; Bogdanov, A.; Boggild, H.; Bogolyubsky, M.; Boldizsar, L.; Bombara, M.; Book, J.; Borel, H. ; Borissov, A.; Bose, S.; Boss, F.; Botje, M. ; Boyer, B.; Braidot, E.; Braun-Munzinger, P.; Bregant, M.; Breitner, T.; Browning, T. A.; Broz, M.; Brun, R.; Bruna, E.; Bruno, G. E.; Budnikov, D.; Buesching, H.; Bufalino, S.; Bugaiev, K.; Busch, O.; Buthelezi, Z.; Caballero Orduna, D.; Caffarri, D.; Cai, X.; Caines, H.; Calvo Villar, E. ; Camerini, P.; Canoa Roman, V.; Cara Romeo, G.; Carena, F.; Carena, W.; Carlin Filho, N.; Carminati, F.; Carrillo Montoya, C. A.; Casanova Diaz, A.; Castillo Castellanos, J.; Castillo Hernandez, J. F.; Casula, E. A. R.; Catanescu, V.; Cavicchioli, C.; Ceballos Sanchez, C.; Cepila, J.; Cerello, P.; Chang, B.; Chapeland, S.; Charvet, J. L.; Chattopadhyay, S.; Chattopadhyay, S.; Chawla, I.; Cherney, M.; Cheshkov, C.; Cheynis, B.; Chibante Barroso, V.; Chinellato, D. D.; Chochula, P. ; Chojnacki, M.; Choudhury, S.; Christakoglou, P. ; Christensen, C. H.; Christiansen, P.; Chujo, T. ; Chung, S. U.; Cicalo, C.; Cifarelli, L.; Cindolo, F.; Cleymans, J.; Coccetti, F.; Colamaria, F.; Colella, D.; Conesa Balbastre, G.; Conesa del Valle, Z.; Constantin, P.; Contin, G.; Contreras, J. G.; Cormier, T. M.; Corrales Morales, Y.; Cortese, P.; Cortes Maldonado, I.; Cosentino, M. R. ; Costa, F.; Cotallo, M. E.; Crescio, E.; Crochet, P.; Cruz Alaniz, E.; Cuautle, E.; Cunqueiro, L.; Dainese, A.; Dalsgaard, H. H.; Danu, A.; Das, D.; Das, I.; Das, K.; Dash, S.; Dash, A.; De, S.; de Barros, G. O. V.; De Caro, A. ; de Cataldo, G.; de Cuveland, J.; De Falco, A.; De Gruttola, D.; Delagrange, H.; Deloff, A.; Demanov, V.; De Marco, N.; Denes, E.; De Pasquale, S.; Deppman, A.; Erasmo, G. D.; de Rooij, R.; Diaz Corchero, M. A.; Di Bari, D.; Dietel, T.; Di Liberto, S.; Di Mauro, A.; Di Nezza, P.; Divia, R. ; Djuvsland, O.; Dobrin, A.; Dobrowolski, T.; Dominguez, I.; Dönigus, B.; Dordic, O.; Driga, O. ; Dubey, A. K.; Ducroux, L.; Dupieux, P.; Dutta Majumdar, M. R.; Dutta Majumdar, A. K.; Elia, D.; Emschermann, D.; Engel, H.; Erdal, H. A.; Espagnon, B.; Estienne, M.; Esumi, S.; Evans, D.; Eyyubova, G.; Fabris, D.; Faivre, J.; Falchieri, D. ; Fantoni, A.; Fasel, M.; Fearick, R.; Fedunov, A.; Fehlker, D.; Feldkamp, L.; Felea, D.; Fenton-Olsen, B.; Feofilov, G.; Fernandez Tellez, A. ; Ferretti, A.; Ferretti, R.; Figiel, J.; Figueredo, M. A. S.; Filchagin, S.; Finogeev, D.; Fionda, F. M.; Fiore, E. M.; Floris, M.; Foertsch, S.; Foka, P.; Fokin, S.; Fragiacomo, E.; Frankenfeld, U.; Fuchs, U.; Furget, C.; Fusco Girard, M.; Gaardhoje, J. J.; Gagliardi, M.; Gago, A.; Gallio, M.; Gangadharan, D. R.; Ganoti, P.; Garabatos, C.; Garcia-Solis, E.; Garishvili, I.; Gerhard, J.; Germain, M.; Geuna, C.; Gheata, A.; Gheata, M.; Ghidini, B.; Ghosh, P.; Gianotti, P. ; Girard, M. R.; Giubellino, P.; Gladysz-Dziadus, E. ; Glässel, P.; Gomez, R.; Gonschior, A.; Ferreiro, E. G.; Gonzalez-Trueba, L. H.; Gonzalez-Zamora, P.; Gorbunov, S.; Goswami, A.; Gotovac, S.; Grabski, V.; Graczykowski, L. K.; Grajcarek, R.; Grelli, A.; Grigoras, C.; Grigoras, A.; Grigoriev, V.; Grigoryan, A.; Grigoryan, S.; Grinyov, B.; Grion, N.; Gros, P.; Grosse-Oetringhaus, J. F.; Grossiord, J.-Y.; Grosso, R.; Guber, F.; Guernane, R.; Guerra Gutierrez, C. ; Guerzoni, B.; Guilbaud, M.; Gulbrandsen, K.; Gunji, T.; Gupta, A.; Gupta, R.; Gutbrod, H.; Haaland, O.; Hadjidakis, C.; Haiduc, M.; Hamagaki, H.; Hamar, G.; Han, B. H.; Hanratty, L. D.; Hansen, A.; Harmanova, Z.; Harris, J. W.; Hartig, M.; Hasegan, D.; Hatzifotiadou, D.; Hayrapetyan, A. ; Heckel, S. T.; Heide, M.; Helstrup, H.; Herghelegiu, A.; Herrera Corral, G.; Herrmann, N.; Hess, B. A.; Hetland, K. F.; Hicks, B.; Hille, P. T.; Hippolyte, B.; Horaguchi, T.; Hori, Y.; Hristov, P.; Hrivnacova, I.; Huang, M.; Humanic, T. J.; Hwang, D. S.; Ichou, R.; Ilkaev, R. ; Ilkiv, I.; Inaba, M.; Incani, E.; Innocenti, G. M.; Innocenti, P. G.; Ippolitov, M.; Irfan, M.; Ivan, C.; Ivanov, V.; Ivanov, Marian; Ivanov, A. ; Ivanytskyi, O.; Jacholkowski, A.; Jacobs, P. M. ; Jang, H. J.; Jangal, S.; Janik, M. A.; Janik, R.; Jayarathna, P. H. S. Y.; Jena, S.; Jha, D. M. ; Jimenez Bustamante, R. T.; Jirden, L.; Jones, P. G.; Jung, H.; Jusko, A.; Kaidalov, A. B.; Kakoyan, V.; Kalcher, S.; Kalinak, P.; Kalliokoski, T.; Kalweit, A.; Kanaki, K.; Kang, J. H.; Kaplin, V.; Karasu Uysal, A.; Karavichev, O. ; Karavicheva, T.; Karpechev, E.; Kazantsev, A.; Kebschull, U.; Keidel, R.; Khan, P.; Khan, M. M. ; Khan, S. A.; Khanzadeev, A.; Kharlov, Y.; Kileng, B.; Kim, D. W.; Kim,

M.; Kim, M.; Kim, S. H.; Kim, D. J.; Kim, S.; Kim, J. H.; Kim, J. S.; Kim, B.; Kim, T.; Kirsch, S.; Kisel, Ivan ; Kiselev, S.; Kisiel, A.; Klay, J. L.; Klein, J. ; Klein-Bösing, C.; Kliemant, M.; Kluge, A.; Knichel, M. L.; Knospe, A. G.; Koch, K.; Köhler, M. K.; Kolojvari, A.; Kondratiev, V.; Kondratyeva, N.; Konevskikh, A.; Korneev, A.; Kour, R.; Kowalski, M.; Kox, S.; Koyithatta Meethaleveedu, G. ; Kral, J.; Kralik, I.; Kramer, F.; Kraus, I. ; Krawutschke, T.; Krelina, M.; Kretz, M.; Krivda, M.; Krizek, F.; Krus, M.; Kryshen, E.; Krzewicki, M.; Kucheriaev, Y.; Kuhn, C.; Kuijer, P. G.; Kulakov, I.; Kumar, J.; Kurashvili, P.; Kurepin, A. B.; Kurepin, A.; Kuryakin, A.; Kushpil, V.; Kushpil, S.; Kvaerno, H.; Kweon, M. J.; Kwon, Y.; Ladron de Guevara, P.; Lakomov, I.; Langoy, R.; La Pointe, S. L.; Lara, C.; Lardeux, A. ; La Rocca, P.; Lazzeroni, C.; Lea, R.; Le Bornec, Y.; Lechman, M.; Lee, S. C.; Lee, K. S.; Lee, G. R.; Lefevre, F.; Lehnert, J.; Leistam, L. ; Lenhardt, M.; Lenti, V.; Leon, H.; Leoncino, M.; Leon Monzon, I.; Leon Vargas, H.; Levai, P. ; Lien, J.; Lietava, R.; Lindal, S.; Lindenstruth, V.; Lippmann, C.; Lisa, M. A.; Liu, L.; Loenne, P. I.; Loggins, V. R.; Loginov, V.; Lohn, S.; Lohner, D.; Loizides, C.; Loo, K. K.; Lopez, X.; Lopez Torres, E.; Lovhoiden, G.; Lu, X.-G.; Luettig, P.; Lunardon, M.; Luo, J.; Luparello, G.; Luquin, L.; Luzzi, C.; Ma, R.; Ma, K.; Madagodahettige-Don, D. M.; Maevskaya, A.; Mager, M.; Mahapatra, D. P.; Maire, A.; Malaev, M. ; Maldonado Cervantes, I.; Malinina, L.; MalKevich, D.; Malzacher, P.; Mamonov, A.; Manceau, L.; Mangotra, L.; Manko, V.; Manso, F.; Manzari, V.; Mao, Y.; Marchisone, M.; Mares, J. ; Margagliotti, G. V.; Margotti, A.; Marin, Ana; Marin Tobon, C. A.; Markert, C.; Martashvili, I.; Martinengo, P.; Martinez, M. I.; Martinez Davalos, A.; Martinez Garcia, G.; Martynov, Y.; Mas, A. ; Masciocchi, S.; Masera, M.; Masoni, A.; Massacrier, L.; Mastromarco, M.; Mastroserio, A.; Matthews, Z. L.; Matyja, A.; Mayani, D.; Mayer, C. ; Mazer, J.; Mazzoni, M. A.; Meddi, F.; Menchaca-Rocha, A.; Mercado Perez, J.; Meres, M.; Miake, Y.; Milano, L.; Milosevic, J.; Mischke, A. ; Mishra, A. N.; Mikowiec, D.; Mitu, C.; Mlynarz, J.; Mohanty, B.; Mohanty, A. K.; Molnar, L.; Montano Zetina, L.; Monteno, M.; Montes, E. ; Moon, T.; Morando, M.; Moreira De Godoy, D. A.; Moretto, S.; Morsch, A.; Muccifora, V.; Mudnic, E. ; Muhuri, S.; Mukherjee, M.; Müller, H.; Munhoz, M. G.; Musa, L.; Musso, A.; Nandi, B. K.; Nania, R.; Nappi, E.; Nattrass, C.; Naumov, N. P.; Navin, S.; Nayak, T. K.; Nazarenko, S.; Nazarov, G. ; Nedosekin, A.; Niculescu, M.; Nielsen, B. S.; Niida, T.; Nikolaev, S.; Nikolic, V.; Nikulin, S. ; Nikulin, V.; Nilsen, B. S.; Nilsson, M. S.; Noferini, F.; Nomokonov, P.; Nooren, G.; Novitzky, N.; Nyanin, A.; Nyatha, A.; Nygaard, C.; Nystrand, J.; Ochirov, A.; Oeschler, H.; Oh, S.; Oh, S. K.; Oleniacz, J.; Oppedisano, C.; Ortiz Velasquez, A.; Ortona, G.; Oskarsson, A.; Ostrowski, P.; Otwinowski, J.; Oyama, K.; Ozawa, K. ; Pachmayer, Y.; Pachr, M.; Padilla, F.; Pagano, P.; Paic, G.; Painke, F.; Pajares, C.; Pal, S. ; Pal, S. K.; Palaha, A.; Palmeri, A.; Papikyan, V.; Pappalardo, G. S.; Park, W. J.; Passfeld, A. ; Pastircak, B.; Patalakha, D. I.; Paticchio, V. ; Pavlinov, A.; Pawlak, T.; Peitzmann, T.; Pereira Da Costa, H.; Pereira De Oliveira Filho, E.; Peresunko, D.; Perez Lara, C. E.; Perez Lezama, E. ; Perini, D.; Perrino, D.; Peryt, W.; Pesci, A. ; Peskov, V.; Pestov, Y.; Petracek, V.; Petran, M.; Petris, M.; Petrov, P.; Petrovici, M.; Petta, C.; Piano, S.; Piccotti, A.; Pikna, M.; Pillot, P.; Pinazza, O.; Pinsky, L.; Pitz, N.; Piyarathna, D. B.; Ploskon, M.; Pluta, J.; Pocheptsov, T.; Pochybova, S.; Podesta-Lerma, P. L. M. ; Poghosyan, M. G.; Polak, K.; Polichtchouk, B.; Pop, A.; Porteboeuf-Houssais, S.; Pospisil, V.; Potukuchi, B.; Prasad, S. K.; Preghenella, R.; Prino, F.; Pruneau, C. A.; Pshenichnov, I.; Puchagin, S.; Puddu, G.; Pujol Teixido, J.; Pulvirenti, A.; Punin, V.; Putis, M.; Putschke, J. ; Quercigh, E.; Qvigstad, H.; Rachevski, A.; Rademakers, A.; Radomski, S.; Räihä T. S.; Rak, J.; Rakotozafindrabe, A.; Ramello, L.; Ramirez Reyes, A.; Raniwala, S.; Raniwala, R.; Räsänen, S. S.; Rascanu, B. T.; Rathee, D.; Read, K. F.; Real, J. S.; Redlich, K.; Reichelt, P.; Reicher, M. ; Renfordt, R.; Reolon, A. R.; Reshetin, A.; Rettig, F.; Revol, J.-P.; Reygers, K.; Riccati, L. ; Ricci, R. A.; Richert, T.; Richter, M.; Riedler, P.; Riegler, W.; Riggi, F.; Rodrigues Fernandes Rabacal, B.; Rodriguez Cahuantzi, M.; Rodriguez Manso, A.; Roed, K.; Rohr, D.; Röhrich, D.; Romita, R.; Ronchetti, F.; Rosnet, P.; Rossegger, S.; Rossi, A.; Roy, C.; Roy, P.; Rubio Montero, A. J.; Rui, R.; Ryabinkin, E.; Rybicki, A.; Sadovsky, S.; Safarik, K.; Sahoo, R.; Sahu, P. K.; Saini, J.; Sakaguchi, H.; Sakai, S.; Sakata, D.; Salgado, C. A.; Salzwedel, J.; Sambyal, S.; Samsonov, V.; Sanchez Castro, X. ; Sandor, L.; Sandoval, A.; Sano, S.; Sano, M. ; Santo, R.; Santoro, R.; Sarkamo, J.; Scapparone, E.; Scarlassara, F.; Scharenberg, R. P. ; Schiaua, C.; Schicker, R.; Schmidt, C.; Schmidt, H. R.; Schreiner, S.; Schuchmann, S.; Schukraft, J.; Schutz, Y.; Schwarz, K.; Schweda, K. ; Scioli, G.; Scomparin, E.; Scott, R.; Scott, P. A.; Segato, G.; Selyuzhenkov, I.; Senyukov, S.; Seo, J.; Serci, S.; Serradilla, E.; Sevcenco, A. ; Shabetai, A.; Shabratova, G.; Shahoyan, R.; Sharma, N.; Sharma, S.; Rohni, S.; Shigaki, K.; Shimomura, M.; Shtejer, K.; Sibiriak, Y.; Siciliano, M.; Sicking, E.; Siddhanta, S.; Siemiarczuk, T.; Silvermyr, D.; Silvestre, C.; Simatovic, G.; Simonetti, G.; Singaraju, R.; Singh, R.; Singha, S.; Singhal, V.; Sinha, T.; Sinha, B. C.; Sitar, B.; Sitta, M.; Skaali, T. B.; Skjerdal, K.; Smakal, R.; Smirnov, N.; Snellings, R. J. M.; Sogaard, C.; Soltz, R.; Son, H.; Song, M.; Song, J.; Soos, C.; Soramel, F.; Sputowska, I.; Spyropoulou-Stassinaki, M.; Srivastava, B. K.; Stachel, J.; Stan, I.; Stan, I.; Stefanek, G.; Steinbeck, T.; Steinpreis, M.; Stenlund, E.; Steyn, G.; Stiller, J. H.; Stocco, D. ; Stolpovskiy, M.; Strabykin, K.; Strmen, P.; Suaide, A. A. P.; Subieta Vasquez, M. A.; Sugitate, T.; Suire, C.; Sukhorukov, M.; Sultanov, R.; Sumbera, M.; Susa, T.; Szanto de Toledo, A.; Szarka, I.; Szczepankiewicz, A.; Szostak, A.; Szymanski, M.; Takahashi, J.; Tapia Takaki, J. D.; Tauro, A.; Tejeda Munoz, G.; Telesca, A.; Terrevoli, C.; Thäder, J.; Thomas, D.; Tieulent, R.; Timmins, A. R.; Tlusty, D.; Toia, A.; Torii, H.; Toscano, L.; Truesdale, D.; Trzaska, W. H.; Tsuji, T.; Tumkin, A.; Turrisi, R.; Tveter, T. S. ; Ulery, J.; Ullaland, K.; Ulrich, J.; Uras, A. ; Urban, J.; Urciuoli, G. M.; Usai, G. L.; Vajzer, M.; Vala, M.; Valencia Palomo, L.; Vallero, S.; van der Kolk, N.; Vande Vyvre, P.; van Leeuwen, M.; Vannucci, L.; Vargas, A.; Varma, R.; Vasileiou, M.; Vasiliev, A.; Vechernin, V.; Veldhoen, M.; Venaruzzo, M.; Vercellin, E.; Vergara, S.; Vernet, R.; Verweij, M.; Vickovic, L. ; Viesti, G.; Vikhlyantsev, O.; Vilakazi, Z.; Villalobos Baillie, O.; Vinogradov, A.; Vinogradov, L. ; Vinogradov, Y.; Virgili, T.; Viyogi, Y. P.; Vodopyanov, A.; Voloshin, K.; Voloshin, S.; Volpe, G.; von Haller, B.; Vranic, D.; Ovrebekk, G.; Vrlakova, J.; Vulpescu, B.; Vyushin, A.; Wagner, V.; Wagner, B.; Wan, R.; Wang, M.; Wang, D.; Wang, Y.; Wang, Y.; Watanabe, K.; Weber, M.; Wessels, J. P.; Westerhoff, U.; Wiechula, J.; Wikne, J.; Wilde, M.; Wilk, G.; Wilk, A.; Williams, M. C. S.; Windelband, B.; Xaplanteris Karampatsos, L.; Yaldo, C. G.; Yamaguchi, Y.; Yang, H.; Yang, S.; Yasnopolskiy, S.; Yi, J.; Yin, Z. ; Yoo, I.-K.; Yoon, J.; Yu, W.; Yuan, X.; Yushmanov, I.; Zach, C.; Zampolli, C.; Zaporozhets, S.; Zarochentsev, A.; Zavada, P.; Zaviyalov, N. ; Zbroszczyk, H.; Zelnicek, P.; Zgura, I. S.; Zhalov, M.; Zhang, X.; Zhang, H.; Zhou, F.; Zhou, D.; Zhou, Y.; Zhu, J.; Zhu, J.; Zhu, X. ; Zichichi, A.; Zimmermann, A.; Zinovjev, G.; Zoccarato, Y.; Zynovyev, M.; Zyzak, M.: **Production of Muons**

from Heavy Flavor Decays at Forward Rapidity in pp and Pb-Pb Collisions at $\sqrt{s_{NN}}$ =2.76TeV. *Physical review letters* 109: 112301, 2012. DOI:10.1103/PhysRevLett.109.112301

WOS-PHN-18 Abelev, B.; Adamczewski-Musch, Jörn; Adamova, D.; Adare, A. M.; Aggarwal, M. M.; Aglieri Rinella, G. ; Agocs, A. G.; Agostinelli, A.; Aguilar Salazar, S. ; Ahammed, Z.; Tahir, Naeem Ahmad; Ahmad Masoodi, A. ; Ahn, S. U.; Akindinov, A.; Aleksandrov, D.; Alessandro, B.; Alfaro Molina, R.; Sanchez-Lorente, Alicia; Alkin, A.; Almaraz Avina, E.; Alme, J. ; Alt, T.; Altini, V.; Altinpinar, S.; Altsybeev, I.; Andrei, C.; Andronic, Anton; Anguelov, V.; Anielski, J.; Anson, C.; Anticic, T.; Antinori, F.; Antonioli, P.; Aphecetche, L.; Appelshäuser, H.; Arbor, N.; Arcelli, S.; Arend, A.; Armesto, N.; Arnaldi, R.; Aronsson, T.; Arsene, Ionut Cristian; Arslandok, M.; Asryan, A.; Augustinus, A. ; Averbeck, Ralf; Awes, T. C.; Äystö J.; Azmi, M. D.; Bach, M.; Badala, A.; Baek, Y. W.; Bailhache, R.; Bala, R.; Baldini Ferroli, R.; Baldisseri, A.; Baldit, A.; Baltasar DosSantos Pedrosa, F.; Ban, J.; Baral, R. C.; Barbera, R. ; Barile, F.; Barnaföldi, G. G.; Barnby, L. S.; Barret, V.; Bartke, J.; Basile, M.; Bastid, N.; Basu, S.; Bathen, B.; Batigne, G.; Batyunya, B.; Baumann, C.; Bearden, I. G.; Beck, R.; Belikov, I. ; Bellini, F.; Bellwied, R.; Belmont-Moreno, E.; Bencedi, G.; Beole, S.; Berceanu, I.; Bercuci, A. ; Berdnikov, Y.; Berenyi, D.; Berzano, D.; Betev, L.; Bhasin, A.; Bhati, A. K.; Bhom, J.; Bianchi, N.; Bianchi, L.; Bianchin, C.; Bielcik, J.; Bielcikova, J.; Bilandzic, A.; Bjelogrlic, S.; Blanco, F.; Blanco, F.; Blau, D.; Blume, C.; Boccioli, M.; Bock, N.; Böttger, S.; Bogdanov, A. ; Boggild, H.; Bogolyubsky, M.; Boldizsar, L.; Bombara, M.; Book, J.; Borel, H.; Borissov, A.; Bose, S.; Boss, F.; Botje, M.; Boyer, B.; Braidot, E.; Braun-Munzinger, Peter; Bregant, M.; Breitner, T.; Browning, T. A.; Broz, M.; Brun, R. ; Bruna, E.; Bruno, G. E.; Budnikov, D.; Buesching, H.; Bufalino, S.; Bugaiev, K.; Busch, O. ; Buthelezi, Z.; Caballero Orduna, D.; Caffarri, D. ; Cai, X.; Caines, H.; Calvo Villar, E.; Camerini, P.; Canoa Roman, V.; Cara Romeo, G.; Carena, W.; Carena, F.; Carlin Filho, N.; Carminati, F.; Carrillo Montoya, C. A.; Casanova Diaz, A.; Castillo Castellanos, J.; Castillo Hernandez, J. F.; Casula, E. A. R.; Catanescu, V.; Cavicchioli, C.; Ceballos Sanchez, C.; Cepila, J.; Cerello, P.; Chang, B.; Chapeland, S.; Charvet, J. L.; Chattopadhyay, S.; Chattopadhyay, S.; Chawla, I.; Cherney, M.; Cheshkov, C.; Cheynis, B.; Chibante Barroso, V.; Chinellato, D. D.; Chochula, P. ; Chojnacki, M.; Choudhury, S.; Christakoglou, P. ; Christensen, C. H.; Christiansen, P.; Chujo, T. ; Chung, S. U.; Cicalo, C.; Cifarelli, L.; Cindolo, F.; Cleymans, J.; Coccetti, F.; Colamaria, F.; Colella, D.; Conesa Balbastre, G.; ConesadelValle, Z.; Constantin, P.; Contin, G.; Contreras, J. G.; Cormier, T. M.; Corrales Morales, Y. ; Cortese, P.; Cortes Maldonado, I.; Cosentino, M. R.; Costa, F.; Cotallo, M. E.; Crescio, E.; Crochet, P.; Cruz Alaniz, E.; Cuautle, E.; Cunqueiro, L.; Dainese, A.; Dalsgaard, H. H.; Das, I.; Das, K.; Das, D.; Dash, A.; Dash, S.; De, S.; Barros, G. O. V.; De Caro, C.; Cataldo, G.; Cuveland, J.; Falco, A.; Gruttola, D.; Delagrange, H.; Deloff, A.; Demanov, V.; Marco, N.; Denes, E.; Pasquale, S.; Deppman, A.; D Erasmo, G.; Rooij, R.; Diaz Corchero, M. A.; Bari, D.; Dietel, T.; Liberto, S.; Mauro, A.; Nezza, P.; Divia, R.; Djuvsland, O.; Dobrin, A.; Dobrowolski, T.; Dominguez, I.; Dönigus, Benjamin; Dordic, O.; Driga, O.; Dubey, A. K.; Ducroux, L.; Dupieux, P. ; Dutta Majumdar, A. K.; Dutta Majumdar, M. R.; Elia, D.; Emschermann, D.; Engel, H.; Erdal, H. A. ; Espagnon, B.; Estienne, M.; Esumi, S.; Evans, D.; Eyyubova, G.; Fabris, D.; Faivre, J.; Falchieri, D.; Fantoni, A.; Fasel, Markus; Fearick, R.; Fedunov, A.; Fehlker, D.; Feldkamp, L.; Felea, D.; Fenton-Olsen, B.; Feofilov, G.; Fernandez Tellez, A.; Ferretti, R.; Ferretti, A.; Figiel, J.; Figueredo, M. A. S.; Filchagin, S.; Finogeev, D.; Fionda, F. M.; Fiore, E. M.; Floris, M.; Foertsch, S.; Foka, Panagiota; Fokin, S.; Fragiacomo, E.; Frankenfeld, Ulrich; Fuchs, U.; Furget, C.; Fusco Girard, M.; Gaardhoje, J. J.; Gagliardi, M.; Gago, A.; Gallio, M.; Gangadharan, D. R.; Ganoti, P.; Garabatos, C.; Garcia-Solis, E. ; Garishvili, I.; Gerhard, J.; Germain, M.; Geuna, C.; Gheata, A.; Gheata, M.; Ghidini, B.; Ghosh, P.; Gianotti, P.; Girard, M. R.; Giubellino, P.; Gladysz-Dziadus, E.; Glässel, P.; Gomez, R. ; Ferreiro, E. G.; Gonzalez-Trueba, L. H.; Gonzalez-Zamora, P.; Gorbunov, S.; Goswami, A.; Gotovac, S.; Grabski, V.; Graczykowski, L. K.; Grajcarek, R.; Grelli, A.; Grigoras, A.; Grigoras, C.; Grigoriev, V.; Grigoryan, A.; Grigoryan, S.; Grinyov, B.; Grion, N.; Gros, P.; Grosse-Oetringhaus, J. F.; Grossiord, J.-Y.; Grosso, R.; Guber, F.; Guernane, R.; Guerra Gutierrez, C. ; Guerzoni, B.; Guilbaud, M.; Gulbrandsen, K.; Gunji, T.; Gupta, A.; Gupta, R.; Gutbrod, H.; Haaland, O.; Hadjidakis, C.; Haiduc, M.; Hamagaki, H.; Hamar, G.; Han, B. H.; Hanratty, L. D.; Hansen, A.; Harmanova, Z.; Harris, J. W.; Hartig, M.; Hasegan, D.; Hatzifotiadou, D.; Hayrapetyan, A. ; Heckel, S. T.; Heide, M.; Helstrup, H.; Herghelegiu, A.; Herrera Corral, G.; Herrmann, N.; Hetland, K. F.; Hicks, B.; Hille, P. T.; Hippolyte, B.; Horaguchi, T.; Hori, Y.; Hristov, P.; Hrivnacova, I.; Huang, M.; Humanic, T. J.; Hwang, D. S.; Ichou, R.; Ilkaev, R.; Ilkiv, I.; Inaba, M.; Incani, E.; Innocenti, G. M.; Innocenti, P. G.; Ippolitov, M.; Irfan, M.; Ivan, Cristian George; Ivanova, Violetta; Ivanova, Violetta; Ivanov, Marian; Ivanytskyi, O.; Jacholkowski, A.; Jacobs, P. M.; Jancurova, L.; Jang, H. J.; Jangal, S.; Janik, R.; Janik, M. A.; Jayarathna, P. H. S. Y.; Jena, S.; Jha, D. M.; Jimenez Bustamante, R. T. ; Jirden, L.; Jones, P. G.; Jung, H.; Jusko, A. ; Kaidalov, A. B.; Kakoyan, V.; Kalcher, S.; Kalinak, P.; Kalliokoski, T.; Kalweit, A.; Kanaki, K.; Kang, J. H.; Kaplin, V.; Karasu Uysal, A.; Karavichev, O.; Karavicheva, T.; Karpechev, E. ; Kazantsev, A.; Kebschull, U.; Keidel, R.; Khan, P.; Khan, M. M.; Khan, S. A.; Khanzadeev, A.; Kharlov, Y.; Kileng, B.; Kim, T.; Kim, D. J.; Kim, D. W.; Kim, J. H.; Kim, J. S.; Kim, M.; Kim, M.; Kim, S. H.; Kim, S.; Kim, B.; Kirsch, S.; Kisel, I.; Kiselev, S.; Kisiel, A.; Klay, J. L.; Klein, J.; Klein-Bösing, C.; Kliemant, M.; Kluge, A.; Knichel, Michael Linus; Knospe, A. G.; Koch, K.; Köhler, M. K.; Kolojvari, A.; Kondratiev, V.; Kondratyeva, N.; Konevskikh, A.; Korneev, A.; Kour, R.; Kowalski, M.; Kox, S.; Koyithatta Meethaleveedu, G.; Kral, J.; Kralik, I. ; Kramer, F.; Kraus, I.; Krawutschke, T.; Krelina, M.; Kretz, M.; Krivda, M.; Krizek, F.; Krus, M.; Kryshen, E.; Krzewicki, Mikolaj; Kucheriaev, Y.; Kuhn, C.; Kuijer, P. G.; Kulakov, I.; Kurashvili, P.; Kurepin, A.; Kurepin, A. B.; Kuryakin, A.; Kushpil, S.; Kushpil, V.; Kvaerno, H. ; Kweon, M. J.; Kwon, Y.; Ladron deGuevara, P. ; Lakomov, I.; Langoy, R.; Pointe, S. L.; Lara, C.; Lardeux, A.; Rocca, P.; Lazzeroni, C.; Lea, R.; Bornec, Y.; Lechman, M.; Lee, S. C.; Lee, G. R.; Lee, K. S.; Lefevre, F.; Lehnert, J.; Leistam, L.; Lenhardt, M.; Lenti, V.; Leon, H.; Leon Monzon, I.; Leon Vargas, H.; Levai, P.; Lien, J.; Lietava, R.; Lindal, S.; Lindenstruth, V. ; Lippmann, C.; Lisa, M. A.; Liu, L.; Loenne, P. I.; Loggins, V. R.; Loginov, V.; Lohn, S.; Lohner, D.; Loizides, C.; Loo, K. K.; Lopez, X.; Lopez Torres, E.; Lovhoiden, G.; Lu, X.-G.; Luettig, P.; Lunardon, M.; Luo, J.; Luparello, G. ; Luquin, L.; Luzzi, C.; Ma, K.; Ma, R.; Madagodahettige-Don, D. M.; Maevskaya, A.; Mager, M. ; Mahapatra, D. P.; Maire, A.; Malaev, M.; Maldonado Cervantes, I.; Malinina, L.; MalKevich, D.; Malzacher, Peter; Mamonov, A.; Manceau, L.; Mangotra,

L.; Manko, V.; Manso, F.; Manzari, V.; Mao, Y.; Marchisone, M.; Mares, J.; Margagliotti, G. V.; Margotti, A.; Marin, Ana; Marin Tobon, C. A. ; Markert, C.; Martashvili, I.; Martinengo, P.; Martinez, M. I.; Martinez Davalos, A.; Martinez Garcia, G.; Martynov, Y.; Masciocchi, Silvia; Masera, M.; Masoni, A.; Massacrier, L.; Mastromarco, M.; Mastroserio, A.; Matthews, Z. L.; Matyja, A.; Mayani, D.; Mayer, C.; Mazer, J.; Mazzoni, M. A.; Meddi, F.; Menchaca-Rocha, A.; Mercado Perez, J.; Meres, M.; Miake, Y.; Milano, L.; Milosevic, J.; Mischke, A.; Mishra, A. N.; Miskowiec, Dariusz; Mitu, C.; Mlynarz, J.; Mohanty, A. K.; Mohanty, B.; Molnar, L.; Montano Zetina, L. ; Monteno, M.; Montes, E.; Moon, T.; Morando, M. ; MoreiraDeGodoy, D. A.; Moretto, S.; Morsch, A. ; Muccifora, V.; Mudnic, E.; Muhuri, S.; Mukherjee, M.; Müller, H.; Munhoz, M. G.; Musa, L. ; Musso, A.; Nandi, B. K.; Nania, R.; Nappi, E. ; Nattrass, C.; Naumov, N. P.; Navin, S.; Nayak, T. K.; Nazarenko, S.; Nazarov, G.; Nedosekin, A. ; Nielsen, B. S.; Niida, T.; Nikolaev, S.; Nikolic, V.; Nikulin, V.; Nikulin, S.; Nilsen, B. S.; Nilsson, M. S.; Noferini, F.; Nomokonov, P.; Nooren, G.; Novitzky, N.; Nyanin, A.; Nyatha, A. ; Nygaard, C.; Nystrand, J.; Ochirov, A.; Oeschler, H.; Oh, S. K.; Oh, S.; Oleniacz, J.; Oppedisano, C.; Ortiz Velasquez, A.; Ortona, G.; Oskarsson, A.; Ostrowski, P.; Otwinowski, Jacek; Oyama, K.; Ozawa, K.; Pachmayer, Y.; Pachr, M.; Padilla, F.; Pagano, P.; Paic, G.; Painke, F.; Pajares, C.; Pal, S. K.; Pal, S.; Palaha, A.; Palmeri, A.; Papikyan, V.; Pappalardo, G. S.; Park, Woo Jin; Passfeld, A.; Pastircak, B.; Patalakha, D. I.; Paticchio, V.; Pavlinov, A.; Pawlak, T.; Peitzmann, T.; Pereira DaCosta, H.; Pereira DeOliveira Filho, E.; Peresunko, D.; Perez Lara, C. E.; Perez Lezama, E.; Perini, D.; Perrino, D.; Peryt, W.; Pesci, A.; Peskov, V.; Pestov, Y.; Petracek, V.; Petran, M.; Petris, M.; Petrov, P. ; Petrovici, M.; Petta, C.; Piano, S.; Piccotti, A.; Pikna, M.; Pillot, P.; Pinazza, O.; Pinsky, L.; Pitz, N.; Piyarathna, D. B.; Ploskon, M.; Pluta, J.; Pocheptsov, T.; Pochybova, S.; Podesta-Lerma, P. L. M.; Poghosyan, M. G.; Polak, K. ; Polichtchouk, B.; Pop, A.; Porteboeuf-Houssais, S. ; Pospisil, V.; Potukuchi, B.; Prasad, S. K.; Preghenella, R.; Prino, F.; Pruneau, C. A.; Pshenichnov, I.; Puchagin, S.; Puddu, G.; Pujol Teixido, J.; Pulvirenti, A.; Punin, V.; Putis, M. ; Putschke, J.; Quercigh, E.; Qvigstad, H.; Rachevski, A.; Rademakers, A.; Radomski, S.; Räihä T. S.; Dvorak, Jan; Rakotozafindrabe, A.; Ramello, L.; Ramirez Reyes, A.; Raniwala, S.; Raniwala, R.; Räsänen, S. S.; Rascanu, B. T.; Rathee, D.; Read, K. F.; Real, J. S.; Redlich, K. ; Reichelt, P.; Reicher, M.; Renfordt, R.; Reolon, A. R.; Reshetin, A.; Rettig, F.; Revol, J.-P.; Reygers, K.; Riccati, L.; Ricci, R. A.; Richert, T.; Richter, M.; Riedler, P.; Riegler, W. ; Riggi, F.; Rodrigues Fernandes Rabacal, B.; Rodriguez Cahuantzi, M.; Rodriguez Manso, A.; Roed, K.; Rohr, D.; Röhrich, D.; Romita, R.; Ronchetti, F.; Rosnet, P.; Rossegger, S.; Rossi, A. ; Roy, P.; Roy, C.; Rubio Montero, A. J.; Rui, R. ; Ryabinkin, E.; Rybicki, A.; Sadovsky, S.; Safarik, K.; Sahoo, R.; Sahu, P. K.; Saini, J. ; Sakaguchi, H.; Sakai, S.; Sakata, D.; Salgado, C. A.; Salzwedel, J.; Sambyal, S.; Samsonov, V.; Sanchez Castro, X.; Sandor, L.; Sandoval, A.; Sano, S.; Sano, M.; Santo, R.; Santoro, R.; Sarkamo, J.; Scapparone, E.; Scarlassara, F.; Scharenberg, R. P.; Schiaua, C.; Schicker, R.; Schmidt, Christian Alberto; Schmidt, H. R.; Schreiner, S.; Schuchmann, S.; Schukraft, J.; Schutz, Y.; Schwarz, Kilian; Schweda, Kai; Scioli, G.; Scomparin, E.; Scott, R.; Scott, P. A.; Segato, G. ; Selyuzhenkov, Ilya; Senyukov, S.; Seo, J.; Serci, S.; Serradilla, E.; Sevcenco, A.; Shabetai, A.; Shabratova, G.; Shahoyan, R.; Sharma, S.; Sharma, N.; Rohni, S.; Shigaki, K.; Shimomura, M. ; Shtejer, K.; Sibiriak, Y.; Siciliano, M.; Sicking, E.; Siddhanta, S.; Siemiarczuk, T.; Silvermyr, D.; Silvestre, c.; Simatovic, G.; Simonetti, G.; Singaraju, R.; Singh, R.; Singha, S. ; Sinha, T.; Sinha, B. C.; Sitar, B.; Sitta, M. ; Skaali, T. B.; Skjerdal, K.; Smakal, R.; Smirnov, N.; Snellings, R. J. M.; Sogaard, C.; Soltz, R.; Johansson, H.; Song, J.; Song, M.; Soos, C.; Soramel, F.; Sputowska, I.; Spyropoulou-Stassinaki, M.; Srivastava, B. K.; Stachel, J.; Stan, I.; Stan, I.; Stefanek, G.; Steinbeck, T.; Steinpreis, M.; Stenlund, E.; Steyn, G.; Stiller, J. H.; Stocco, D.; Stolpovskiy, M.; Strabykin, K.; Strmen, P.; Suaide, A. A. P.; Subieta Vasquez, M. A.; Sugitate, T.; Suire, C.; Sukhorukov, M.; Sultanov, R.; Sumbera, M.; Susa, T.; SzantodeToledo, A.; Szarka, I.; Szczepankiewicz, A.; Szostak, A.; Szymanski, M.; Takahashi, J.; Tapia Takaki, J. D.; Tauro, A.; Tejeda Munoz, G.; Telesca, A.; Terrevoli, C.; Thäder, Jochen; Thomas, D.; Tieulent, R.; Timmins, A. R.; Tlusty, D.; Toia, A.; Torii, H.; Toscano, L.; Truesdale, D.; Trzaska, W. H.; Tsuji, T.; Tumkin, A.; Turrisi, R.; Tveter, T. S.; Ulery, J. ; Ullaland, K.; Ulrich, J.; Uras, A.; Urban, J. ; Urciuoli, G. M.; Usai, G. L.; Vajzer, M.; Vala, M.; Valencia Palomo, L.; Vallero, S.; Kolk, N.; Vande Vyvre, P.; Leeuwen, M.; Vannucci, L.; Vargas, A.; Varma, R.; Vasileiou, M.; Vasiliev, A.; Vechernin, V.; Veldhoen, M.; Venaruzzo, M.; Vercellin, E.; Vergara, S.; Vernet, R.; Verweij, M. ; Vickovic, L.; Viesti, G.; Vikhlyantsev, O.; Vilakazi, Z.; Villalobos Baillie, O.; Vinogradov, A. ; Vinogradov, Y.; Vinogradov, L.; Virgili, T.; Viyogi, Y. P.; Vodopyanov, A.; Voloshin, S.; Voloshin, K.; Volpe, G.; Haller, B.; Vranic, D.; Ovrebekk, G.; Vrlakova, J.; Vulpescu, B.; Vyushin, A.; Wagner, B.; Wagner, V.; Wan, R.; Wang, Y.; Wang, D.; Wang, M.; Wang, Y.; Watanabe, K.; Weber, M.; Wessels, J. P.; Westerhoff, U.; Wiechula, J.; Wikne, J.; Wilde, M. ; Wilk, G.; Wilk, A.; Williams, M. C. S.; Windelband, B.; Xaplanteris Karampatsos, L.; Yaldo, C. G.; Yamaguchi, Y.; Yang, S.; Yang, H.; Yasnopolskiy, S.; Yi, J.; Yin, Z.; Yoo, I.-K.; Yoon, J.; Yu, W.; Yuan, X.; Yushmanov, I.; Zach, C.; Zampolli, C.; Zaporozhets, S.; Zarochentsev, A. ; Zavada, P.; Zaviyalov, N.; Zbroszczyk, H.; Zelnicek, P.; Zgura, I. S.; Zhalov, M.; Zhang, X. ; Zhang, H.; Zhou, Y.; Zhou, D.; Zhou, F.; Zhu, X.; Zhu, J.; Zhu, J.; Zichichi, A.; Zimmermann, A.; Zinovjev, G.; Zoccarato, Y.; Zynovyev, M.; Zyzak, M.: **Transverse sphericity of primary charged particles in minimum bias protonproton collisions at $\sqrt{s}$=0.9, 2.76 and 7 TeV.** *The European physical journal / C* 72: 2124, 2012. DOI:10.1140/epjc/s10052-012-2124-9

WOS-PHN-19 Abelev, B.; Adamczewski-Musch, Jörn; Adamova, D.; Adare, A.M.; Aggarwal, M.M.; Aglieri Rinella, G. ; Agocs, A.G.; Agostinelli, A.; Aguilar Salazar, S. ; Ahammed, Z.; Tahir, Naeem Ahmad; Ahmad Masoodi, A. ; Ahn, S.U.; Akindinov, A.; Aleksandrov, D.; Alessandro, B.; Alfaro Molina, R.; Sanchez-Lorente, Alicia; Alkin, A.; Almaraz Avina, E.; Alt, T.; Altini, V.; Altinpinar, S.; Altsybeev, I.; Andrei, C.; Andronic, Anton; Anguelov, V.; Anielski, J.; Anson, C.; Anticic, T.; Antinori, F.; Antonioli, P.; Aphecetche, L.; Appelshäuser, Harald; Arbor, N.; Arcelli, S.; Arend, A.; Armesto, N.; Arnaldi, R.; Aronsson, T.; Arsene, Ionut Cristian; Arslandok, M.; Asryan, A.; Augustinus, A.; Averbeck, Ralf; Awes, T.C.; Äystö J.; Azmi, M.D. ; Bach, M.; Badala, A.; Baek, Y.W.; Bailhache, Raphaelle; Bala, R.; Baldini Ferroli, R.; Baldisseri, A.; Baldit, A.; Baltasar Dos Santos Pedrosa, F.; Ban, J.; Baral, R.C.; Barbera, R.; Barile, F.; Barnaföldi, G.G.; Barnby, L.S.; Barret, V.; Bartke, J.; Basile, M.; Bastid, N.; Bathen, B.; Batigne, G.; Batyunya, B.; Baumann, C. ; Bearden, I.G.; Beck, H.; Belikov, I.; Bellini, F.; Bellwied, R.; Belmont-Moreno, E.; Bencedi, G. ; Beole, S.; Berceanu, I.; Bercuci, A.; Berdnikov, Y.; Berenyi, D.;

Bergmann, C.; Berzano, D.; Betev, L.; Bhasin, A.; Bhati, A.K.; Bianchi, L.; Bianchi, N.; Bianchin, C.; Bielcik, J.; Bielcikova, J.; Bilandzic, A.; Bjelogrlic, S.; Blanco, F.; Blanco, F.; Blau, D.; Blume, C.; Boccioli, M.; Bock, N.; Bogdanov, A.; Boggild, H. ; Bogolyubsky, M.; Boldizsar, L.; Bombara, M.; Book, J.; Borel, H.; Borissov, A.; Bose, S.; Boss, F.; Botje, M.; Böttger, S.; Boyer, B.; Braun-Munzinger, Peter; Bregant, M.; Breitner, T.; Browning, T.A.; Broz, M.; Brun, R.; Bruna, E.; Bruno, G.E.; Budnikov, D.; Buesching, H.; Bufalino, S.; Bugaiev, K.; Busch, O.; Buthelezi, Z.; Caballero Orduna, D.; Caffarri, D.; Cai, X.; Caines, H.; Calvo Villar, E.; Camerini, P.; Canoa Roman, V.; Cara Romeo, G.; Carena, W.; Carena, F. ; Carlin Filho, N.; Carminati, F.; Carrillo Montoya, C.A.; Casanova Diaz, A.; Caselle, M.; Castillo Castellanos, J.; Castillo Hernandez, J.F.; Casula, E.A.R.; Catanescu, V.; Cavicchioli, C.; Cepila, J. ; Cerello, P.; Chang, B.; Chapeland, S.; Charvet, J.L.; Chattopadhyay, S.; Chattopadhyay, S.; Cherney, M.; Cheshkov, C.; Cheynis, B.; Chiavassa, E.; Chibante Barroso, V.; Chinellato, D.D.; Chochula, P.; Chojnacki, M.; Christakoglou, P.; Christensen, C.H.; Christiansen, P.; Chujo, T.; Chung, S.U.; Cicalo, C.; Cifarelli, L.; Cindolo, F. ; Cleymans, J.; Coccetti, F.; Coffin, J.-P.; Colamaria, F.; Colella, D.; Conesa Balbastre, G.; Conesa del Valle, Z.; Constantin, P.; Contin, G.; Contreras, J.G.; Cormier, T.M.; Corrales Morales, Y. ; Cortese, P.; Cortes Maldonado, I.; Cosentino, M.R.; Costa, F.; Cotallo, M.E.; Crescio, E.; Crochet, P.; Cruz Alaniz, E.; Cuautle, E.; Cunqueiro, L.; Dainese, A.; Dalsgaard, H.H.; Danu, A.; Das, K.; Das, I.; Das, D.; Dash, A.; Dash, S.; De, S.; De Azevedo Moregula, A.; de Barros, G.O.V.; De Caro, A.; de Cataldo, G.; de Cuveland, J.; De Falco, A.; De Gruttola, D.; Delagrange, H.; Del Castillo Sanchez, E.; Deloff, A. ; Demanov, V.; De Marco, N.; Denes, E.; De Pasquale, S.; Deppman, A.; D Erasmo, G.; de Rooij, R.; Di Bari, D.; Dietel, T.; Di Giglio, C.; Di Liberto, S.; Di Mauro, A.; Di Nezza, P.; Divia, R. ; Djuvsland, O.; Dobrin, A.; Dobrowolski, T.; Dominguez, I.; Dönigus, Benjamin; Dordic, O.; Driga, O.; Dubey, A.K.; Ducroux, L.; Dupieux, P. ; Dutta Majumdar, A.K.; Dutta Majumdar, M.R.; Elia, D.; Emschermann, D.; Engel, H.; Erdal, H.A.; Espagnon, B.; Estienne, M.; Esumi, S.; Evans, D. ; Eyyubova, G.; Fabris, D.; Faivre, J.; Falchieri, D.; Fantoni, A.; Fasel, Markus; Fearick, R.; Fedunov, A.; Fehlker, D.; Feldkamp, L.; Felea, D.; Feofilov, G.; Fernandez Tellez, A.; Ferretti, R.; Ferretti, A.; Figiel, J.; Figueredo, M.A.S.; Filchagin, S.; Fini, R.; Finogeev, D.; Fionda, F.M.; Fiore, E.M.; Floris, M.; Foertsch, S. ; Foka, Panagiota; Fokin, S.; Fragiacomo, E.; Fragkiadakis, M.; Frankenfeld, U.; Fuchs, U.; Furget, C.; Fusco Girard, M.; Gaardhoje, J.J.; Gagliardi, M.; Gago, A.; Gallio, M.; Gangadharan, D.R.; Ganoti, P.; Garabatos, C.; Garcia-Solis, E. ; Garishvili, I.; Gerhard, J.; Germain, M.; Geuna, C.; Gheata, M.; Gheata, A.; Ghidini, B.; Ghosh, P.; Gianotti, P.; Girard, M.R.; Giubellino, P.; Gladysz-Dziadus, E.; Glässel, P.; Gomez, R. ; Ferreiro, E.G.; Gonzalez-Trueba, L.H.; Gonzalez-Zamora, P.; Gorbunov, S.; Goswami, A.; Gotovac, S.; Grabski, V.; Graczykowski, L.K.; Grajcarek, R.; Grelli, A.; Grigoras, A.; Grigoras, C.; Grigoriev, V.; Grigoryan, S.; Grigoryan, A.; Grinyov, B.; Grion, N.; Gros, P.; Grosse-Oetringhaus, J.F.; Grossiord, J.-Y.; Grosso, R. ; Guber, F.; Guernane, R.; Guerra Gutierrez, C.; Guerzoni, B.; Guilbaud, M.; Gulbrandsen, K.; Gunji, T.; Gupta, R.; Gupta, A.; Gutbrod, H.; Haaland, O.; Hadjidakis, C.; Haiduc, M.; Hamagaki, H.; Hamar, G.; Han, B.H.; Hanratty, L.D.; Hansen, A. ; Harmanova, Z.; Harris, J.W.; Hartig, M.; Hasegan, D.; Hatzifotiadou, D.; Hayrapetyan, A.; Heckel, S.T.; Heide, M.; Helstrup, H.; Herghelegiu, A.; Herrera Corral, G.; Herrmann, N.; Hetland, K.F. ; Hicks, B.; Hille, P.T.; Hippolyte, B.; Horaguchi, T.; Hori, Y.; Hristov, P.; Hrivnacova, I.; Huang, M.; Huber, S.; Humanic, T.J.; Hwang, D.S.; Ichou, R.; Ilkaev, R.; Ilkiv, I.; Inaba, M.; Incani, E.; Innocenti, P.G.; Innocenti, G.M.; Ippolitov, M.; Irfan, M.; Ivan, Cristian George; Ivanov, A.; Ivanov, V.; Ivanov, Marian; Ivanytskyi, O.; Jacholkowski, A.; Jacobs, P.M.; Jancurova, L.; Jang, H.J.; Jangal, S.; Janik, M.A.; Janik, R.; Jayarathna, P.H.S.Y.; Jena, S.; Jimenez Bustamante, R.T.; Jirden, L.; Jones, P.G.; Jung, H.; Jung, W.; Jusko, A.; Kaidalov, A.B.; Kakoyan, V.; Kalcher, S.; Kalinak, P.; Kalisky, M.; Kalliokoski, T.; Kalweit, A.; Kanaki, K.; Kang, J.H.; Kaplin, V.; Karasu Uysal, A.; Karavichev, O.; Karavicheva, T.; Karpechev, E.; Kazantsev, A.; Kebschull, U.; Keidel, R.; Khan, S.A.; Khan, P.; Khan, M.M.; Khanzadeev, A.; Kharlov, Y.; Kileng, B.; Kim, D.J.; Kim, T.; Kim, S.; Kim, S.H.; Kim, M.; Kim, J.S.; Kim, J.H.; Kim, D.W.; Kim, B.; Kirsch, S.; Kisel, Ivan; Kiselev, S.; Kisiel, A.; Klay, J.L.; Klein, J.; Klein-Bösing, C.; Kliemant, M.; Kluge, A.; Knichel, Michael Linus; Koch, Karsten; Köhler, M.K.; Kolojvari, A.; Kondratiev, V.; Kondratyeva, N.; Konevskikh, A.; Korneev, A.; Kottachchi Kankanamge Don, C.; Kour, R.; Kowalski, M.; Kox, S. ; Koyithatta Meethaleveedu, G.; Kral, J.; Kralik, I.; Kramer, F.; Kraus, I.; Krawutschke, T.; Krelina, M.; Kretz, M.; Krivda, M.; Krizek, F.; Krus, M.; Kryshen, E.; Krzewicki, Mikolaj; Kucheriaev, Y.; Kuhn, C.; Kuijer, P.G.; Kurashvili, P.; Kurepin, A.B.; Kurepin, A.; Kuryakin, A.; Kushpil, S.; Kushpil, V.; Kvaerno, H.; Kweon, M.J. ; Kwon, Y.; Ladron de Guevara, P.; Lakomov, I.; Langoy, R.; Lara, C.; Lardeux, A.; La Rocca, P.; Lazzeroni, C.; Lea, R.; Le Bornec, Y.; Lee, S.C. ; Lee, K.S.; Lefevre, F.; Lehnert, J.; Leistam, L.; Lenhardt, M.; Lenti, V.; Leon, H.; Leon Monzon, I.; Leon Vargas, H.; Levai, P.; Li, X. ; Lien, J.; Lietava, R.; Lindal, S.; Lindenstruth, V.; Lippmann, C.; Lisa, M.A.; Liu, L. ; Loenne, P.I.; Loggins, V.R.; Loginov, V.; Lohn, S.; Lohner, D.; Loizides, C.; Loo, K.K.; Lopez, X.; Lopez Torres, E.; Lovhoiden, G.; Lu, X.-G. ; Luettig, P.; Lunardon, M.; Luo, J.; Luparello, G.; Luquin, L.; Luzzi, C.; Ma, R.; Ma, K.; Madagodahettige-Don, D.M.; Maevskaya, A.; Mager, M. ; Mahapatra, D.P.; Maire, A.; Malaev, M.; Maldonado Cervantes, I.; Malinina, L.; MalKevich, D. ; Malzacher, Peter; Mamonov, A.; Manceau, L.; Mangotra, L.; Manko, V.; Manso, F.; Manzari, V.; Mao, Y.; Marchisone, M.; Mares, J.; Margagliotti, G.V.; Margotti, A.; Marin, Ana; Markert, C.; Martashvili, I.; Martinengo, P.; Martinez, M.I.; Martinez Davalos, A.; Martinez Garcia, G.; Martynov, Y.; Mas, A.; Masciocchi, Silvia; Masera, M.; Masoni, A.; Massacrier, L.; Mastromarco, M.; Mastroserio, A.; Matthews, Z.L.; Matyja, A.; Mayani, D.; Mayer, C.; Mazer, J.; Mazzoni, M.A.; Meddi, F.; Menchaca-Rocha, A.; Mercado Perez, J.; Meres, M.; Miake, Y.; Michalon, A.; Milano, L.; Milosevic, J.; Mischke, A.; Mishra, A.N.; Miskowiec, Dariusz; Mitu, C.; Mlynarz, J.; Mohanty, A.K.; Mohanty, B.; Molnar, L.; Montano Zetina, L. ; Monteno, M.; Montes, E.; Moon, T.; Morando, M. ; Moreira De Godoy, D.A.; Moretto, S.; Morsch, A. ; Muccifora, V.; Mudnic, E.; Muhuri, S.; Müller, H.; Munhoz, M.G.; Musa, L.; Musso, A.; Nandi, B.K.; Nania, R.; Nappi, E.; Nattrass, C.; Naumov, N.P.; Navin, S.; Nayak, T.K.; Nazarenko, S. ; Nazarov, G.; Nedosekin, A.; Nicassio, Maria; Nielsen, B.S.; Niida, T.; Nikolaev, S.; Nikolic, V. ; Nikulin, V.; Nikulin, S.; Nilsen, B.S.; Nilsson, M.S.; Noferini, F.; Nomokonov, P.; Nooren, G.; Novitzky, N.; Nyanin, A.; Nyatha, A.; Nygaard, C.; Nystrand, J.; Ochirov, A.; Oeschler, H.; Oh, S.; Oh, S.K.; Oleniacz, J.; Oppedisano, C.; Ortiz Velasquez, A.; Ortona, G.; Oskarsson, A. ; Ostrowski, P.; Otterlund, I.; Otwinowski, Jacek ; Oyama, K.; Ozawa, K.; Pachmayer, Y.; Pachr, M. ; Padilla, F.; Pagano, P.; Paic, G.; Painke, F. ; Pajares, C.; Pal, S.; Pal,

S.K.; Palaha, A.; Palmeri, A.; Papikyan, V.; Pappalardo, G.S.; Park, Woo Jin; Passfeld, A.; Pastircak, B.; Patalakha, D.I.; Paticchio, V.; Pavlinov, A.; Pawlak, T.; Peitzmann, T.; Perales, M.; Pereira De Oliveira Filho, E.; Peresunko, D.; Perez Lara, C.E.; Perez Lezama, E.; Perini, D.; Perrino, D.; Peryt, W.; Pesci, A.; Peskov, V.; Pestov, Y.; Petracek, V.; Petran, M.; Petris, M.; Petrov, P.; Petrovici, M. ; Petta, C.; Piano, S.; Piccotti, A.; Pikna, M. ; Pillot, P.; Pinazza, O.; Pinsky, L.; Pitz, N. ; Piuz, F.; Piyarathna, D.B.; Ploskon, M.; Pluta, J.; Pocheptsov, T.; Pochybova, S.; Podesta-Lerma, P.L.M.; Poghosyan, M.G.; Polak, K.; Polichtchouk, B.; Pop, A.; Porteboeuf-Houssais, S.; Pospisil, V.; Potukuchi, B.; Prasad, S.K.; Preghenella, R.; Prino, F.; Pruneau, C.A.; Pshenichnov, I.; Puchagin, S.; Puddu, G.; Pulvirenti, A.; Punin, V.; Putis, M.; Putschke, J. ; Quercigh, E.; Qvigstad, H.; Rachevski, A.; Rademakers, A.; Radomski, S.; Räihä T.S.; Rak, J.; Rakotozafindrabe, A.; Ramello, L.; Ramirez Reyes, A.; Raniwala, R.; Raniwala, S.; Räsänen, S.S.; Rascanu, B.T.; Rathee, D.; Read, K.F.; Real, J.S.; Redlich, K.; Reichelt, P.; Reicher, M. ; Renfordt, R.; Reolon, A.R.; Reshetin, A.; Rettig, F.; Revol, J.-P.; Reygers, K.; Riccati, L. ; Ricci, R.A.; Richert, T.; Richter, M.; Riedler, P.; Riegler, W.; Riggi, F.; Rodriguez Cahuantzi, M.; Roed, K.; Rohr, D.; Röhrich, D.; Romita, R.; Ronchetti, F.; Rosnet, P.; Rossegger, S.; Rossi, A.; Roukoutakis, F.; Roy, P.; Roy, C.; Rubio Montero, A.J.; Rui, R.; Ryabinkin, E.; Rybicki, A.; Sadovsky, S.; Safarik, K.; Sahu, P.K.; Saini, J.; Sakaguchi, H.; Sakai, S.; Sakata, D.; Salgado, C.A.; Salzwedel, J.; Sambyal, S.; Samsonov, V.; Sanchez Castro, X.; Sandor, L. ; Sandoval, A.; Sano, S.; Sano, M.; Santo, R.; Santoro, R.; Sarkamo, J.; Scapparone, E.; Scarlassara, F.; Scharenberg, R.P.; Schiaua, C.; Schicker, R.; Schmidt, Hans Rudolf; Schmidt, Christian Alberto; Schreiner, S.; Schuchmann, S.; Schukraft, J.; Schutz, Y.; Schwarz, Kilian; Schweda, Kai; Scioli, G.; Scomparin, E.; Scott, R.; Scott, P.A. ; Segato, G.; Selyuzhenkov, Ilya; Senyukov, S.; Seo, J.; Serci, S.; Serradilla, E.; Sevcenco, A. ; Sgura, I.; Shabetai, A.; Shabratova, G.; Shahoyan, R.; Sharma, S.; Sharma, N.; Shigaki, K. ; Shimomura, M.; Shtejer, K.; Sibiriak, Y.; Siciliano, M.; Sicking, E.; Siddhanta, S.; Siemiarczuk, T.; Silvermyr, D.; Simonetti, G.; Singaraju, R.; Singh, R.; Singha, S.; Sinha, T.; Sinha, B.C.; Sitar, B.; Sitta, M.; Skaali, T.B.; Skjerdal, K.; Smakal, R.; Smirnov, N.; Snellings, R.; Sogaard, C.; Soltz, R.; Sondershaus, H.; Song, J.; Song, M.; Soos, C.; Soramel, F.; Sputowska, I.; Spyropoulou-Stassinaki, M.; Srivastava, B.K.; Stachel, Johanna; Stan, I.; Stan, I.; Stefanek, G.; Stefanini, G.; Steinbeck, T.; Steinpreis, M.; Stenlund, E.; Steyn, G.; Stocco, D. ; Stolpovskiy, M.; Strabykin, K.; Strmen, P.; Suaide, A.A.P.; Subieta Vasquez, M.A.; Sugitate, T. ; Suire, C.; Sukhorukov, M.; Sultanov, R.; Sumbera, M.; Susa, T.; Szanto de Toledo, A.; Szarka, I.; Szostak, A.; Tagridis, C.; Takahashi, J.; Tapia Takaki, J.D.; Tauro, A.; Tejeda Munoz, G.; Telesca, A.; Terrevoli, C.; Thäder, Jochen; Thomas, D.; Thomas, J.H.; Tieulent, R.; Timmins, A.R.; Tlusty, D.; Toia, A.; Torii, H.; Toscano, L.; Tosello, F.; Traczyk, T.; Truesdale, D.; Trzaska, W.H.; Tsuji, T.; Tumkin, A.; Turrisi, R. ; Tveter, T.S.; Ulery, J.; Ullaland, K.; Ulrich, J.; Uras, A.; Urban, J.; Urciuoli, G.M.; Usai, G.L.; Vajzer, M.; Vala, M.; Valencia Palomo, L.; Vallero, S.; van der Kolk, N.; Vande Vyvre, P.; van Leeuwen, M.; Vannucci, L.; Vargas, A.; Varma, R. ; Vasileiou, M.; Vasiliev, A.; Vechernin, V.; Veldhoen, M.; Venaruzzo, M.; Vercellin, E.; Vergara, S.; Vernekohl, D.C.; Vernet, R.; Verweij, M.; Vickovic, L.; Viesti, G.; Vikhlyantsev, O.; Vilakazi, Z.; Villalobos Baillie, O.; Vinogradov, L. ; Vinogradov, A.; Vinogradov, Y.; Virgili, T.; Viyogi, Y.P.; Vodopyanov, A.; Voloshin, S.; Voloshin, K.; Volpe, G.; von Haller, B.; Vranic, D. ; Ovrebekk, G.; Vrlakova, J.; Vulpescu, B.; Vyushin, A.; Wagner, V.; Wagner, B.; Wan, R.; Wang, Y.; Wang, D.; Wang, Y.; Wang, M.; Watanabe, K.; Wessels, J.P.; Westerhoff, U.; Wiechula, Jens; Wikne, J.; Wilde, M.; Wilk, G.; Wilk, A.; Williams, M.C.S.; Windelband, B.; Xaplanteris Karampatsos, L.; Yang, H.; Yang, S.; Yasnopolskiy, S.; Yi, J.; Yin, Z.; Yokoyama, H.; Yoo, I.-K.; Yoon, J.; Yu, W.; Yuan, X.; Yushmanov, I.; Zach, C.; Zampolli, C.; Zaporozhets, S.; Zarochentsev, A.; Zavada, P.; Zaviyalov, N. ; Zbroszczyk, H.; Zelnicek, P.; Zgura, I.S.; Zhalov, M.; Zhang, X.; Zhou, Y.; Zhou, D.; Zhou, F.; Zhu, X.; Zichichi, A.; Zimmermann, A.; Zinovjev, G.; Zoccarato, Y.; Zynovyev, M.: **Heavy flavour decay muon production at forward rapidity in protonproton collisions at $\sqrt{s} = 7$TeV.** *Physics letters / B* 708: 265 - 275, 2012. DOI:10.1016/j.physletb.2012.01.063

WOS-PHN-20 Abelev, Betty; Adam, Jaroslav; Adamova, Dagmar; Adare, Andrew Marshall; Aggarwal, Madan; Rinella, Gianluca Aglieri; Agocs, Andras Gabor; Agostinelli, Andrea; Salazar, Saul Aguilar; Ahammed, Zubayer; Ahmad, Arshad; Ahmad, Nazeer; Ahn, Sul-Ah; Ahn, Sang Un; Akindinov, Alexander; Aleksandrov, Dmitry; Alessandro, Bruno; Molina, Jose Ruben Alfaro; Alici, Andrea; Alkin, Anton; Avina, Erick Jonathan Almaraz ; Alme, Johan; Alt, Torsten; Altini, Valerio; Altinpinar, Sedat; Altsybeev, Igor; Andrei, Cristian ; Andronic, Anton; Anguelov, Venelin; Anielski, Jonas; Anson, Christopher Daniel; Anticic, Tome; Antinori, Federico; Antonioli, Pietro; Aphecetche, Laurent Bernard; Appelshauser, Harald; Arbor, Nicolas ; Arcelli, Silvia; Arend, Andreas; Armesto, Nestor ; Arnaldi, Roberta; Aronsson, Tomas Robert; Arsene, Ionut Cristian; Arslandok, Mesut; Asryan, Andzhey; Augustinus, Andre; Averbeck, Ralf Peter; Awes, Terry ; Aysto, Juha Heikki; Azmi, Mohd Danish; Bach, Matthias Jakob; Badala, Angela; Baek, Yong Wook; Bailhache, Raphaelle Marie; Bala, Renu; Ferroli, Rinaldo Baldini; Baldisseri, Alberto; Baldit, Alain ; Santos Pedrosa, Fernando Baltasar; Ban, Jaroslav; Baral, Rama Chandra; Barbera, Roberto; Barile, Francesco; Barnafoldi, Gergely Gabor; Barnby, Lee Stuart; Barret, Valerie; Bartke, Jerzy Gustaw; Basile, Maurizio; Bastid, Nicole; Basu, Sumit; Bathen, Bastian; Batigne, Guillaume; Batyunya, Boris ; Baumann, Christoph Heinrich; Bearden, Ian Gardner; Beck, Hans; Behera, Nirbhay Kumar; Belikov, Iouri; Bellini, Francesca; Bellwied, Rene; Belmont-Moreno, Ernesto; Bencedi, Gyula; Beole, Stefania; Berceanu, Ionela; Bercuci, Alexandru; Berdnikov, Yaroslav; Berenyi, Daniel; Bergognon, Anais Annick Erica; Berzano, Dario; Betev, Latchezar; Bhasin, Anju; Bhati, Ashok Kumar; Bhom, Jihyun; Bianchi, Livio; Bianchi, Nicola; Bianchin, Chiara; Bielcik, Jaroslav ; Bielcikova, Jana; Bilandzic, Ante; Bjelogrlic, Sandro; Blanco, F.; Blanco, Francesco; Blau, Dmitry ; Blume, Christoph; Boccioli, Marco; Bock, Nicolas ; Boettger, Stefan; Bogdanov, Alexey; Boggild, Hans ; Bogolyubsky, Mikhail; Boldizsar, Laszlo; Bombara, Marek; Book, Julian; Borel, Herve; Borissov, Alexander; Bose, Suvendu Nath; Bossu, Francesco; Botje, Michiel; Boyer, Bruno Alexandre; Braidot, Ermes ; Braun-Munzinger, Peter; Bregant, Marco; Breitner, Timo Gunther; Browning, Tyler Allen; Broz, Michal; Brun, Rene; Bruna, Elena; Bruno, Giuseppe Eugenio; Budnikov, Dmitry; Buesching, Henner; Bufalino, Stefania; Bugaiev, Kyrylo; Busch, Oliver; Buthelezi, Edith Zinhle; Orduna, Diego Caballero; Caffarri, Davide; Cai, Xu; Caines, Helen Louise; Villar, Ernesto Calvo; Camerini, Paolo; Roman, Veronica Canoa; Romeo, Giovanni Cara; Carena, Francesco; Carena, Wisla; Filho, Nelson

Carlin; Carminati, Federico; Montoya, Camilo Andres Carrillo; Diaz, Amaya Ofelia Casanova; Castellanos, Javier Ernesto Castillo; Hernandez, Juan Francisco Castillo; Casula, Ester Anna Rita; Catanescu, Vasile; Cavicchioli, Costanza; Sanchez, Cesar Ceballos; Cepila, Jan; Cerello, Piergiorgio; Chang, Beomsu; Chapeland, Sylvain; Charvet, Jean-Luc Fernand; Chattopadhyay, Subhasis; Chattopadhyay, Sukalyan; Chawla, Isha; Cherney, Michael Gerard; Cheshkov, Cvetan; Cheynis, Brigitte; Barroso, Vasco Miguel Chibante; Chinellato, David; Chochula, Peter; Chojnacki, Marek; Choudhury, Subikash; Christakoglou, Panagiotis; Christensen, Christian Holm; Christiansen, Peter; Chujo, Tatsuya; Chung, Suh-Urk; Cicalo, Corrado; Cifarelli, Luisa; Cindolo, Federico; Cleymans, Jean Willy Andre; Coccetti, Fabrizio; Colamaria, Fabio; Colella, Domenico; Balbastre, Gustavo Conesa; Valle, Zaida Conesa; Constantin, Paul; Contin, Giacomo; Contreras, Jesus Guillermo; Cormier, Thomas Michael; Morales, Yasser Corrales; Cortese, Pietro; Maldonado, Ismael Cortes; Cosentino, Mauro Rogerio; Costa, Filippo; Cotallo, Manuel Enrique; Crescio, Elisabetta ; Crochet, Philippe; Alaniz, Emilia Cruz; Cuautle, Eleazar; Cunqueiro, Leticia; Dainese, Andrea; Dalsgaard, Hans Hjersing; Danu, Andrea; Das, Debasish ; Das, Indranil; Das, Kushal; Dash, Sadhana; Dash, Ajay Kumar; De, Sudipan; Barros, Gabriel; Caro, Annalisa; Cataldo, Giacinto; Cuveland, Jan; Falco, Alessandro; Gruttola, Daniele; Delagrange, Hugues; Deloff, Andrzej; Demanov, Vyacheslav; Marco, Nora; Denes, Ervin; Pasquale, Salvatore; Deppman, Airton; DErasmo, Ginevra; Rooij, Raoul Stefan; Corchero, Miguel Angel Diaz; Bari, Domenico ; Giglio, Carmelo; Dietel, Thomas; Liberto, Sergio ; Mauro, Antonio; Nezza, Pasquale; Divia, Roberto ; Djuvsland, Oeystein; Dobrin, Alexandru Florin; Dobrowolski, Tadeusz Antoni; Dominguez, Isabel; Donigus, Benjamin; Dordic, Olja; Driga, Olga; Dubey, Anand Kumar; Ducroux, Laurent; Dupieux, Pascal ; Majumdar, Mihir Ranjan Dutta; Majumdar, A. K. Dutta ; Elia, Domenico; Emschermann, David Philip; Engel, Heiko; Erdal, Hege Austrheim; Espagnon, Bruno; Estienne, Magali Danielle; Esumi, Shinichi; Evans, David; Eyyubova, Gyulnara; Fabris, Daniela; Faivre, Julien; Falchieri, Davide; Fantoni, Alessandra; Fasel, Markus; Fearick, Roger Worsley; Fedunov, Anatoly; Fehlker, Dominik; Feldkamp, Linus; Felea, Daniel; Fenton-Olsen, Bo; Feofilov, Grigory; Tellez, Arturo Fernandez; Ferretti, Alessandro; Ferretti, Roberta; Figiel, Jan; Figueredo, Marcel; Filchagin, Sergey; Finogeev, Dmitry; Fionda, Fiorella ; Fiore, Enrichetta Maria; Floris, Michele; Foertsch, Siegfried Valentin; Foka, Panagiota; Fokin, Sergey; Fragiacomo, Enrico; Frankenfeld, Ulrich Michael; Fuchs, Ulrich; Furget, Christophe; Girard, Mario Fusco; Gaardhoje, Jens Joergen; Gagliardi, Martino; Gago, Alberto; Gallio, Mauro; Gangadharan, Dhevan Raja; Ganoti, Paraskevi; Garabatos, Jose; Garcia-Solis, Edmundo; Garishvili, Irakli; Gerhard, Jochen; Germain, Marie; Geuna, Claudio; Gheata, Andrei George; Gheata, Mihaela; Ghidini, Bruno; Ghosh, Premomoy; Gianotti, Paola; Girard, Martin Robert; Giubellino, Paolo; Gladysz-Dziadus, Ewa; Glassel, Peter; Gomez, Ramon; Gonschior, Alexey; Ferreiro, Elena Gonzalez; Gonzalez-Trueba, Laura Helena ; Gonzalez-Zamora, Pedro; Gorbunov, Sergey; Goswami, Ankita; Gotovac, Sven; Grabski, Varlen; Graczykowski, Lukasz Kamil; Grajcarek, Robert; Grelli, Alessandro; Grigoras, Costin; Grigoras, Alina Gabriela ; Grigoriev, Vladislav; Grigoryan, Ara; Grigoryan, Smbat; Grinyov, Boris; Grion, Nevio; Gros, Philippe ; Grosse-Oetringhaus, Jan Fiete; Grossiord, Jean-Yves ; Grosso, Raffaele; Guber, Fedor; Guernane, Rachid ; Gutierrez, Cesar Guerra; Guerzoni, Barbara; Guilbaud, Maxime Rene Joseph; Gulbrandsen, Kristjan Herlache; Gunji, Taku; Gupta, Anik; Gupta, Ramni ; Gutbrod, Hans; Haaland, Oystein Senneset; Hadjidakis, Cynthia Marie; Haiduc, Maria; Hamagaki, Hideki; Hamar, Gergoe; Han, Byounghee; Hanratty, Luke David; Hansen, Alexander; Harmanova, Zuzana; Harris, John William; Hartig, Matthias; Hasegan, Dumitru; Hatzifotiadou, Despoina; Hayrapetyan, Arsen ; Heckel, Stefan Thomas; Heide, Markus Ansgar; Helstrup, Haavard; Herghelegiu, Andrei Ionut; Corral, Gerardo Antonio Herrera; Herrmann, Norbert; Hess, Benjamin Andreas; Hetland, Kristin Fanebust; Hicks, Bernard; Hille, Per Thomas; Hippolyte, Boris; Horaguchi, Takuma; Hori, Yasuto; Hristov, Peter Zahariev; Hrivnacova, Ivana; Huang, Meidana; Humanic, Thomas; Hwang, Dae Sung; Ichou, Raphaelle; Ilkaev, Radiy; Ilkiv, Iryna; Inaba, Motoi; Incani, Elisa; Innocenti, Gian Michele; Innocenti, Pier Giorgio; Ippolitov, Mikhail; Irfan, Muhammad; Ivan, Cristian George; Ivanov, Vladimir; Ivanov, Marian; Ivanov, Andrey; Ivanytskyi, Oleksii; Jacholkowski, Adam Wlodzimierz; Jacobs, Peter; Jang, Haeng Jin; Jangal, Swensy Gwladys; Janik, Malgorzata Anna; Janik, Rudolf; Jayarathna, Sandun; Jena, Satyajit; Jha, Deeptanshu Manu; Bustamante, Raul Tonatiuh Jimenez; Jirden, Lennart; Jones, Peter Graham; Jung, Hyung Taik ; Jusko, Anton; Kaidalov, Alexei; Kakoyan, Vanik; Kalcher, Sebastian; Kalinak, Peter; Kalliokoski, Tuomo Esa Aukusti; Kalweit, Alexander Philipp; Kanaki, Kalliopi; Kang, Ju Hwan; Kaplin, Vladimir; Uysal, Ayben Karasu; Karavichev, Oleg; Karavicheva, Tatiana ; Karpechev, Evgeny; Kazantsev, Andrey; Kebschull, Udo Wolfgang; Keidel, Ralf; Khan, Palash; Khan, Mohisin Mohammed; Khan, Shuaib Ahmad; Khanzadeev, Alexei; Kharlov, Yury; Kileng, Bjarte; Kim, Do Won ; Kim, Mimae; Kim, Minwoo; Kim, Seon Hee; Kim, Dong Jo; Kim, Se Yong; Kim, Jonghyun; Kim, Jin Sook ; Kim, Beomkyu; Kim, Taesoo; Kirsch, Stefan; Kisel, Ivan; Kiselev, Sergey; Kisiel, Adam Ryszard; Klay, Jennifer Lynn; Klein, Jochen; Klein-Bosing, Christian; Kliemant, Michael; Kluge, Alexander; Knichel, Michael Linus; Knospe, Anders Garritt; Koch, Kathrin; Kohler, Markus; Kolojvari, Anatoly; Kondratiev, Valery; Kondratyeva, Natalia; Konevskih, Artem; Korneev, Andrey; Kour, Ravjeet; Kowalski, Marek; Kox, Serge; Meethaleveedu, Greeshma Koyithatta ; Kral, Jiri; Kralik, Ivan; Kramer, Frederick; Kraus, Ingrid Christine; Krawutschke, Tobias; Krelina, Michal; Kretz, Matthias; Krivda, Marian; Krizek, Filip; Krus, Miroslav; Kryshen, Evgeny; Krzewicki, Mikolaj; Kucheriaev, Yury; Kuhn, Christian Claude; Kuijer, Paul; Kulakov, Igor; Kumar, Jitendra; Kurashvili, Podist; Kurepin, A. B.; Kurepin, A.; Kuryakin, Alexey; Kushpil, Vasily; Kushpil, Svetlana ; Kvaerno, Henning; Kweon, Min Jung; Kwon, Youngil ; Guevara, Pedro Ladron; Lakomov, Igor; Langoy, Rune ; Pointe, Sarah Louise; Lara, Camilo Ernesto; Lardeux, Antoine Xavier; Rocca, Paola; Lazzeroni, Cristina; Lea, Ramona; Bornec, Yves; Lechman, Mateusz; Lee, Sung Chul; Lee, Ki Sang; Lee, Graham Richard; Lefevre, Frederic; Lehnert, Joerg Walter; Leistam, Lars; Lenhardt, Matthieu Laurent; Lenti, Vito ; Leon, Hermes; Leoncino, Marco; Monzon, Ildefonso Leon; Vargas, Hermes Leon; Levai, Peter; Lien, Jorgen; Lietava, Roman; Lindal, Svein; Lindenstruth, Volker; Lippmann, Christian; Lisa, Michael Annan; Liu, Lijiao; Loenne, Per-Ivar; Loggins, Vera; Loginov, Vitaly; Lohn, Stefan Bernhard ; Lohner, Daniel; Loizides, Constantinos; Loo, Kai Krister; Lopez, Xavier Bernard; Torres, Ernesto Lopez ; Lovhoiden, Gunnar; Lu, Xianguo; Luettig, Philipp ; Lunardon, Marcello; Luo, Jiebin; Luparello, Grazia ; Luquin, Lionel; Luzzi, Cinzia; Ma, Rongrong; Ma, Ke; Madagodahettige-Don, Dilan Minthaka; Maevskaya, Alla; Mager, Magnus; Mahapatra, Durga Prasad; Maire, Antonin; Malaev, Mikhail; Cervantes, Ivonne

Alicia Maldonado; Malinina, Ludmila; MalKevich, Dmitry; Malzacher, Peter; Mamonov, Alexander; Manceau, Loic Henri Antoine; Mangotra, Lalit Kumar; Manko, Vladislav; Manso, Franck; Manzari, Vito; Mao, Yaxian; Marchisone, Massimiliano ; Mares, Jiri; Margagliotti, Giacomo Vito; Margotti, Anselmo; Marin, Ana Maria; Tobon, Cesar Augusto Marin ; Markert, Christina; Martashvili, Irakli; Martinengo, Paolo; Martinez, Mario Ivan; Davalos, Arnulfo Martinez; Garcia, Gines Martinez; Martynov, Yevgen; Mas, Alexis Jean-Michel; Masciocchi, Silvia ; Masera, Massimo; Masoni, Alberto; Massacrier, Laure Marie; Mastromarco, Mario; Mastroserio, Annalisa ; Matthews, Zoe Louise; Matyja, Adam Tomasz; Mayani, Daniel; Mayer, Christoph; Mazer, Joel; Mazzoni, Alessandra Maria; Meddi, Franco; Menchaca-Rocha, Arturo Alejandro; Perez, Jorge Mercado; Meres, Michal ; Miake, Yasuo; Milano, Leonardo; Milosevic, Jovan ; Mischke, Andre; Mishra, Aditya Nath; Miskowiec, Dariusz; Mitu, Ciprian Mihai; Mlynarz, Jocelyn; Mohanty, Bedangadas; Mohanty, Ajit Kumar; Molnar, Levente; Zetina, Luis Manuel Montano; Monteno, Marco ; Montes, Esther; Moon, Taebong; Morando, Maurizio ; Godoy, Denise Aparecida Moreira; Moretto, Sandra; Morsch, Andreas; Muccifora, Valeria; Mudnic, Eugen; Muhuri, Sanjib; Mukherjee, Maitreyee; Muller, Hans; Munhoz, Marcelo; Musa, Luciano; Musso, Alfredo; Nandi, Basanta Kumar; Nania, Rosario; Nappi, Eugenio ; Nattrass, Christine; Naumov, Nikolay; Navin, Sparsh; Nayak, Tapan Kumar; Nazarenko, Sergey; Nazarov, Gleb; Nedosekin, Alexander; Nicassio, Maria ; Niculescu, Mihai; Nielsen, Borge Svane; Niida, Takafumi; Nikolaev, Sergey; Nikolic, Vedran; Nikulin, Sergey; Nikulin, Vladimir; Nilsen, Bjorn Steven; Nilsson, Mads Stormo; Noferini, Francesco; Nomokonov, Petr; Nooren, Gerardus; Novitzky, Norbert ; Nyanin, Alexandre; Nyatha, Anitha; Nygaard, Casper ; Nystrand, Joakim Ingemar; Ochirov, Alexander; Oeschler, Helmut Oskar; Oh, Saehanseul; Oh, Sun Kun ; Oleniacz, Janusz; Oppedisano, Chiara; Velasquez, Antonio Ortiz; Ortona, Giacomo; Oskarsson, Anders Nils Erik; Ostrowski, Piotr Krystian; Otwinowski, Jacek Tomasz; Oyama, Ken; Ozawa, Kyoichiro; Pachmayer, Yvonne Chiara; Pachr, Milos; Padilla, Fatima; Pagano, Paola; Paic, Guy; Painke, Florian; Pajares, Carlos; Pal, S.; Pal, Susanta Kumar; Palaha, Arvinder Singh; Palmeri, Armando; Papikyan, Vardanush ; Pappalardo, Giuseppe; Park, Woo Jin; Passfeld, Annika; Pastircak, Blahoslav; Patalakha, Dmitri Ivanovich; Paticchio, Vincenzo; Pavlinov, Alexei; Pawlak, Tomasz Jan; Peitzmann, Thomas; Costa, Hugo Denis Antonio Pereira; Oliveira Filho, Elienos Pereira ; Peresunko, Dmitri; Lara, Carlos Eugenio Perez; Lezama, Edgar Perez; Perini, Diego; Perrino, Davide ; Peryt, Wiktor Stanislaw; Pesci, Alessandro; Peskov, Vladimir; Pestov, Yury; Petracek, Vojtech; Petran, Michal; Petris, Mariana; Petrov, Plamen Rumenov; Petrovici, Mihai; Petta, Catia; Piano, Stefano; Piccotti, Anna; Pikna, Miroslav; Pillot, Philippe; Pinazza, Ombretta; Pinsky, Lawrence; Pitz, Nora; Piyarathna, Danthasinghe; Ploskon, Mateusz Andrzej; Pluta, Jan Marian; Pocheptsov, Timur; Pochybova, Sona; Lerma, Pedro Luis Manuel Podesta; Poghosyan, Martin; Polak, Karel; Polichtchouk, Boris ; Pop, Amalia; Porteboeuf-Houssais, Sarah; Pospisil, Vladimir; Potukuchi, Baba; Prasad, Sidharth Kumar; Preghenella, Roberto; Prino, Francesco; Pruneau, Claude Andre; Pshenichnov, Igor; Puchagin, Sergey; Puddu, Giovanna; Teixido, Jordi Pujol; Pulvirenti, Alberto; Punin, Valery; Putis, Marian; Putschke, Jorn Henning; Quercigh, Emanuele; Qvigstad, Henrik; Rachevski, Alexandre; Rademakers, Alphonse; Radomski, Sylwester; Raiha, Tomi Samuli; Rak, Jan; Rakotozafindrabe, Andry Malala; Ramello, Luciano; Reyes, Abdiel Ramirez; Raniwala, Sudhir; Raniwala, Rashmi; Rasanen, Sami Sakari; Rascanu, Bogdan Theodor ; Rathee, Deepika; Read, Kenneth Francis; Real, Jean-Sebastien; Redlich, Krzysztof; Reichelt, Patrick ; Reicher, Martijn; Renfordt, Rainer Arno Ernst; Reolon, Anna Rita; Reshetin, Andrey; Rettig, Felix Vincenz; Revol, Jean-Pierre; Reygers, Klaus Johannes ; Riccati, Lodovico; Ricci, Renato Angelo; Richert, Tuva; Richter, Matthias Rudolph; Riedler, Petra; Riegler, Werner; Riggi, Francesco; Rabacal, Bartolomeu Rodrigues Fernandes; Cahuantzi, Mario Rodriguez; Manso, Alis Rodriguez; Roed, Ketil; Rohr, David; Rohrich, Dieter; Romita, Rosa; Ronchetti, Federico; Rosnet, Philippe; Rossegger, Stefan; Rossi, Andrea; Roy, Christelle Sophie; Roy, Pradip Kumar; Montero, Antonio Juan Rubio; Rui, Rinaldo; Ryabinkin, Evgeny ; Rybicki, Andrzej; Sadovsky, Sergey; Safarik, Karel ; Sahoo, Raghunath; Sahu, Pradip Kumar; Saini, Jogender; Sakaguchi, Hiroaki; Sakai, Shingo; Sakata, Dosatsu; Salgado, Carlos Albert; Salzwedel, Jai; Sambyal, Sanjeev Singh; Samsonov, Vladimir; Castro, Xitzel Sanchez; Sandor, Ladislav; Sandoval, Andres; Sano, Satoshi; Sano, Masato; Santo, Rainer ; Santoro, Romualdo; Sarkamo, Juho Jaako; Scapparone, Eugenio; Scarlassara, Fernando; Scharenberg, Rolf Paul; Schiaua, Claudiu Cornel; Schicker, Rainer Martin; Schmidt, Christian Joachim; Schmidt, Hans Rudolf; Schreiner, Steffen; Schuchmann, Simone; Schukraft, Jurgen; Schutz, Yves Roland; Schwarz, Kilian Eberhard; Schweda, Kai Oliver; Scioli, Gilda; Scomparin, Enrico; Scott, Rebecca; Scott, Patrick Aaron; Segato, Gianfranco; Selioujenkov, Ilya ; Senyukov, Serhiy; Seo, Jeewon; Serci, Sergio; Serradilla, Eulogio; Sevcenco, Adrian; Shabetai, Alexandre; Shabratova, Galina; Shahoyan, Ruben; Sharma, Natasha; Sharma, Satish; Sharma, Rohini; Shigaki, Kenta; Shimomura, Maya; Shtejer, Katherin; Sibiriak, Yury; Siciliano, Melinda; Sicking, Eva; Siddhanta, Sabyasachi; Siemiarczuk, Teodor; Silvermyr, David Olle Rickard; Silvestre, Catherine; Simatovic, Goran; Simonetti, Giuseppe; Singaraju, Rama Narayana ; Singh, Ranbir; Singha, Subhash; Singhal, Vikas; Sinha, Tinku; Sinha, Bikash; Sitar, Branislav; Sitta, Mario; Skaali, Bernhard; Skjerdal, Kyrre; Smakal, Radek; Smirnov, Nikolai; Snellings, Raimond ; Sogaard, Carsten; Soltz, Ron Ariel; Son, Hyungsuk ; Song, Myunggeun; Song, Jihye; Soos, Csaba; Soramel, Francesca; Sputowska, Iwona; Spyropoulou-Stassinaki, Martha; Srivastava, Brijesh Kumar ; Stachel, Johanna; Stan, Ionel; Stan, Ionel; Stefanek, Grzegorz; Steinbeck, Timm Morten; Steinpreis, Matthew; Stenlund, Evert Anders; Steyn, Gideon Francois; Stiller, Johannes Hendrik; Stocco, Diego; Stolpovskiy, Mikhail; Strabykin, Kirill; Strmen, Peter; Passo Suaide, Alexandre Alarcon; Vasquez, Martin Alfonso Subieta; Sugitate, Toru; Suire, Christophe Pierre; Sukhorukov, Mikhail; Sultanov, Rishat; Sumbera, Michal; Susa, Tatjana; Toledo, Alejandro Szanto; Szarka, Imrich; Szczepankiewicz, Adam; Szostak, Artur Krzysztof; Szymanski, Maciej; Takahashi, Jun; Takaki, Daniel Jesus Tapia; Tauro, Arturo; Munoz, Guillermo Tejeda ; Telesca, Adriana; Terrevoli, Cristina; Thader, Jochen Mathias; Thomas, Deepa; Tieulent, Raphael Noel ; Timmins, Anthony; Tlusty, David; Toia, Alberica ; Torii, Hisayuki; Toscano, Luca; Truesdale, David Christopher; Trzaska, Wladyslaw Henryk; Tsuji, Tomoya ; Tumkin, Alexandr; Turrisi, Rosario; Tveter, Trine Spedstad; Ulery, Jason Glyndwr; Ullaland, Kjetil; Ulrich, Jochen; Uras, Antonio; Urban, Jozef; Urciuoli, Guido Marie; Usai, Gianluca; Vajzer, Michal ; Vala, Martin; Palomo, Lizardo Valencia; Vallero, Sara; Kolk, Naomi; Vyvre, Pierre Vande; Leeuwen, Marco; Vannucci, Luigi; Vargas, Aurora Diozcora;

Varma, Raghava; Vasileiou, Maria; Vasiliev, Andrey; Vechernin, Vladimir; Veldhoen, Misha; Venaruzzo, Massimo; Vercellin, Ermanno; Vergara, Sergio; Vernet, Renaud; Verweij, Marta; Vickovic, Linda; Viesti, Giuseppe; Vikhlyantsev, Oleg; Vilakazi, Zabulon; Baillie, Orlando Villalobos; Vinogradov, Alexander; Vinogradov, Leonid; Vinogradov, Yury; Virgili, Tiziano; Viyogi, Yogendra; Vodopianov, Alexander; Voloshin, Kirill; Voloshin, Sergey; Volpe, Giacomo; Haller, Barthelemy; Vranic, Danilo; vrebekk, Gaute; Vrlakova, Janka; Vulpescu, Bogdan; Vyushin, Alexey; Wagner, Vladimir; Wagner, Boris; Wan, Renzhuo; Wang, Mengliang; Wang, Dong; Wang, Yifei; Wang, Yaping; Watanabe, Kengo; Weber, Michael; Wessels, Johannes; Westerhoff, Uwe; Wiechula, Jens; Wikne, Jon; Wilde, Martin Rudolf; Wilk, Grzegorz Andrzej; Wilk, Alexander; Williams, Crispin; Windelband, Bernd Stefan; Karampatsos, Leonidas Xaplanteris; Yaldo, Chris G; Yamaguchi, Yorito; Yang, Hongyan; Yang, Shiming; Yasnopolsky, Stanislav; Yi, JunGyu; Yin, Zhongbao; Yoo, In-Kwon ; Yoon, Jongik; Yu, Weilin; Yuan, Xianbao; Yushmanov, Igor; Zach, Cenek; Zampolli, Chiara; Zaporozhets, Sergey; Zarochentsev, Andrey; Zavada, Petr; Zaviyalov, Nikolai; Zbroszczyk, Hanna Paulina ; Zelnicek, Pierre; Zgura, Sorin Ion; Zhalov, Mikhail; Zhang, Xiaoming; Zhang, Haitao; Zhou, Fengchu; Zhou, Daicui; Zhou, You; Zhu, Jianhui; Zhu, Jianlin; Zhu, Xiangrong; Zichichi, Antonino; Zimmermann, Alice; Zinovjev, Gennady; Zoccarato, Yannick Denis; Zynovyev, Mykhaylo; Zyzak, Maksym: **Measurement of prompt J/ψ and beauty hadron production cross sections at mid-rapidity in pp collisions at $\sqrt{s} = 7$ TeV.** *Journal of high energy physics* 2012: 65, 2012. DOI:10.1007/JHEP11(2012)065

WOS-PHN-21 Abelev, Betty; Quintana, Arian Abrahantes; Adamova, Dagmar; Adare, Andrew Marshall; Aggarwal, Madan; Rinella, Gianluca Aglieri; Agocs, Andras Gabor; Agostinelli, Andrea; Salazar, Saul Aguilar; Ahammed, Zubayer; Ahmad, Nazeer; Ahmad, Arshad; Ahn, Sang Un ; Akindinov, Alexander; Aleksandrov, Dmitry; Alessandro, Bruno; Molina, Jose Ruben Alfaro; Alici, Andrea; Alkin, Anton; Avina, Erick Jonathan Almaraz ; Alt, Torsten; Altini, Valerio; Altinpinar, Sedat ; Altsybeev, Igor; Andrei, Cristian; Andronic, Anton ; Anguelov, Venelin; Anson, Christopher Daniel; Anticic, Tome; Antinori, Federico; Antonioli, Pietro ; Aphecetche, Laurent Bernard; Appelshauser, Harald; Arbor, Nicolas; Arcelli, Silvia; Arend, Andreas; Armesto, Nestor; Arnaldi, Roberta; Aronsson, Tomas Robert; Arsene, Ionut Cristian; Arslandok, Mesut; Asryan, Andzhey; Augustinus, Andre; Averbeck, Ralf Peter; Awes, Terry; Aysto, Juha Heikki; Azmi, Mohd Danish; Bach, Matthias Jakob; Badala, Angela; Baek, Yong Wook; Bailhache, Raphaelle Marie; Bala, Renu; Ferroli, Rinaldo Baldini; Baldisseri, Alberto; Baldit, Alain; Pedrosa, Fernando Baltasar Dos Santos; Ban, Jaroslav; Baral, Rama Chandra; Barbera, Roberto; Barile, Francesco; Barnafoldi, Gergely Gabor; Barnby, Lee Stuart; Barret, Valerie; Bartke, Jerzy Gustaw; Basile, Maurizio; Bastid, Nicole; Bathen, Bastian; Batigne, Guillaume; Batyunya, Boris; Baumann, Christoph Heinrich; Bearden, Ian Gardner; Beck, Hans ; Belikov, Iouri; Bellini, Francesca; Bellwied, Rene ; Belmont-Moreno, Ernesto; Beole, Stefania; Berceanu, Ionela; Bercuci, Alexandru; Berdnikov, Yaroslav; Berenyi, Daniel; Bergmann, Cyrano; Berzano, Dario; Betev, Latchezar; Bhasin, Anju; Bhati, Ashok Kumar; Bianchi, Nicola; Bianchi, Livio ; Bianchin, Chiara; Bielcik, Jaroslav; Bielcikova, Jana; Bilandzic, Ante; Blanco, F.; Blanco, Francesco; Blau, Dmitry; Blume, Christoph; Boccioli, Marco; Bock, Nicolas; Bogdanov, Alexey; Boggild, Hans; Bogolyubsky, Mikhail; Boldizsar, Laszlo ; Bombara, Marek; Book, Julian; Borel, Herve; Borissov, Alexander; Bortolin, Claudio; Bose, Suvendu Nath; Bossu, Francesco; Botje, Michiel; Bottger, Stefan; Boyer, Bruno Alexandre; Braun-Munzinger, Peter ; Bregant, Marco; Breitner, Timo Gunther; Broz, Michal; Brun, Rene; Bruna, Elena; Bruno, Giuseppe Eugenio; Budnikov, Dmitry; Buesching, Henner; Bufalino, Stefania; Bugaiev, Kyrylo; Busch, Oliver; Buthelezi, Edith Zinhle; Caffarri, Davide; Cai, Xu; Caines, Helen Louise; Villar, Ernesto Calvo; Camerini, Paolo; Roman, Veronica Canoa; Romeo, Giovanni Cara; Carena, Francesco; Carena, Wisla; Filho, Nelson Carlin ; Carminati, Federico; Montoya, Camilo Andres Carrillo ; Diaz, Amaya Ofelia Casanova; Caselle, Michele; Castellanos, Javier Ernesto Castillo; Hernandez, Juan Francisco Castillo; Casula, Ester Anna Rita; Catanescu, Vasile; Cavicchioli, Costanza; Cepila, Jan ; Cerello, Piergiorgio; Chang, Beomsu; Chapeland, Sylvain; Charvet, Jean-Luc Fernand; Chattopadhyay, Sukalyan; Chattopadhyay, Subhasis; Cherney, Michael Gerard; Cheshkov, Cvetan; Cheynis, Brigitte; Chiavassa, Emilio; Barroso, Vasco Miguel Chibante; Chinellato, David; Chochula, Peter; Chojnacki, Marek ; Christakoglou, Panagiotis; Christensen, Christian Holm; Christiansen, Peter; Chujo, Tatsuya; Chung, Suh-Urk; Cicalo, Corrado; Cifarelli, Luisa; Cindolo, Federico; Cleymans, Jean Willy Andre; Coccetti, Fabrizio; Coffin, Jean-Pierre Michel; Colamaria, Fabio; Colella, Domenico; Balbastre, Gustavo Conesa; Valle, Zaida Conesa; Constantin, Paul ; Contin, Giacomo; Contreras, Jesus Guillermo; Cormier, Thomas Michael; Morales, Yasser Corrales; Cortese, Pietro; Maldonado, Ismael Cortes; Cosentino, Mauro Rogerio; Costa, Filippo; Cotallo, Manuel Enrique ; Crescio, Elisabetta; Crochet, Philippe; Alaniz, Emilia Cruz; Cuautle, Eleazar; Cunqueiro, Leticia; Dainese, Andrea; Dalsgaard, Hans Hjersing; Danu, Andrea; Das, Indranil; Das, Kushal; Das, Debasish ; Dash, Ajay Kumar; Dash, Sadhana; De, Sudipan; Azevedo Moregula, Andrea; Barros, Gabriel; Caro, Annalisa; Cataldo, Giacinto; Cuveland, Jan; Falco, Alessandro; Gruttola, Daniele; Delagrange, Hugues; Castillo Sanchez, Eduardo; Deloff, Andrzej; Demanov, Vyacheslav; Marco, Nora; Denes, Ervin; Pasquale, Salvatore; Deppman, Airton; DErasmo, Ginevra; Rooij, Raoul Stefan; Bari, Domenico; Dietel, Thomas ; Giglio, Carmelo; Liberto, Sergio; Mauro, Antonio ; Nezza, Pasquale; Divia, Roberto; Djuvsland, Oeystein; Dobrin, Alexandru Florin; Dobrowolski, Tadeusz Antoni; Dominguez, Isabel; Dönigus, Benjamin ; Dordic, Olja; Driga, Olga; Dubey, Anand Kumar; Ducroux, Laurent; Dupieux, Pascal; Majumdar, Mihir Ranjan Dutta; Majumdar, A.K. Dutta; Elia, Domenico; Emschermann, David Philip; Engel, Heiko; Erdal, Hege Austrheim; Espagnon, Bruno; Estienne, Magali Danielle ; Esumi, Shinichi; Evans, David; Eyyubova, Gyulnara ; Fabris, Daniela; Faivre, Julien; Falchieri, Davide ; Fantoni, Alessandra; Fasel, Markus; Fearick, Roger Worsley; Fedunov, Anatoly; Fehlker, Dominik; Feldkamp, Linus; Felea, Daniel; Feofilov, Grigory; Tellez, Arturo Fernandez; Ferretti, Alessandro; Ferretti, Roberta; Figiel, Jan; Figueredo, Marcel; Filchagin, Sergey; Fini, Rosa Anna; Finogeev, Dmitry ; Fionda, Fiorella; Fiore, Enrichetta Maria; Floris, Michele; Foertsch, Siegfried Valentin; Foka, Panagiota ; Fokin, Sergey; Fragiacomo, Enrico; Fragkiadakis, Michail; Frankenfeld, Ulrich Michael; Fuchs, Ulrich ; Furget, Christophe; Girard, Mario Fusco; Gaardhoje, Jens Joergen; Gagliardi, Martino; Gago, Alberto; Gallio, Mauro; Gangadharan, Dhevan Raja; Ganoti, Paraskevi; Garabatos, Jose; Garcia-Solis, Edmundo; Garishvili, Irakli; Gerhard, Jochen; Germain, Marie; Geuna, Claudio; Gheata, Andrei George ; Gheata, Mihaela; Ghidini, Bruno; Ghosh, Premomoy ; Gianotti, Paola;

Girard, Martin Robert; Giubellino, Paolo; Gladysz-Dziadus, Ewa; Glassel, Peter; Gomez, Ramon; Ferreiro, Elena Gonzalez; Gonzalez-Trueba, Laura Helena; Gonzalez-Zamora, Pedro; Gorbunov, Sergey; Goswami, Ankita; Gotovac, Sven; Grabski, Varlen; Graczykowski, Lukasz Kamil; Grajcarek, Robert; Grelli, Alessandro; Grigoras, Costin; Grigoras, Alina Gabriela; Grigoriev, Vladislav ; Grigoryan, Ara; Grigoryan, Smbat; Grinyov, Boris ; Grion, Nevio; Gros, Philippe; Grosse-Oetringhaus, Jan Fiete; Grossiord, Jean-Yves; Grosso, Raffaele; Guber, Fedor; Guernane, Rachid; Gutierrez, Cesar Guerra; Guerzoni, Barbara; Guilbaud, Maxime Rene Joseph; Gulbrandsen, Kristjan Herlache; Gunji, Taku ; Gupta, Anik; Gupta, Ramni; Gutbrod, Hans; Haaland, Oystein Senneset; Hadjidakis, Cynthia Marie; Haiduc, Maria; Hamagaki, Hideki; Hamar, Gergoe; Han, Byounghee; Hanratty, Luke David; Hansen, Alexander; Harmanova, Zuzana; Harris, John William; Hartig, Matthias; Hasegan, Dumitru; Hatzifotiadou, Despoina; Hayrapetyan, Arsen; Heckel, Stefan Thomas ; Heide, Markus Ansgar; Helstrup, Haavard; Herghelegiu, Andrei Ionut; Corral, Gerardo Antonio Herrera; Herrmann, Norbert; Hetland, Kristin Fanebust ; Hicks, Bernard; Hille, Per Thomas; Hippolyte, Boris; Horaguchi, Takuma; Hori, Yasuto; Hristov, Peter Zahariev; Hrivnacova, Ivana; Huang, Meidana; Huber, Sebastian Bernd; Humanic, Thomas; Hwang, Dae Sung; Ichou, Raphaelle; Ilkaev, Radiy; Ilkiv, Iryna ; Inaba, Motoi; Incani, Elisa; Innocenti, Pier Giorgio; Innocenti, Gian Michele; Ippolitov, Mikhail ; Irfan, Muhammad; Ivan, Cristian George; Ivanov, Marian; Ivanov, Vladimir; Ivanov, Andrey; Ivanytskyi, Oleksii; Jacholkowski, Adam Wlodzimierz; Jacobs, Peter; Jancurova, Lucia; Jang, Haeng Jin; Jangal, Swensy Gwladys; Janik, Rudolf; Janik, Malgorzata Anna; Jayarathna, Sandun; Jena, Satyajit ; Bustamante, Raul Tonatiuh Jimenez; Jirden, Lennart ; Jones, Peter Graham; Jung, Won Woong; Jung, Hyung Taik; Jusko, Anton; Kaidalov, Alexei; Kakoyan, Vanik; Kalcher, Sebastian; Kalinak, Peter; Kalisky, Matus; Kalliokoski, Tuomo Esa Aukusti; Kalweit, Alexander Philipp; Kanaki, Kalliopi; Kang, Ju Hwan; Kaplin, Vladimir; Uysal, Ayben Karasu; Karavichev, Oleg; Karavicheva, Tatiana; Karpechev, Evgeny; Kazantsev, Andrey; Kebschull, Udo Wolfgang; Keidel, Ralf; Khan, Palash; Khan, Mohisin Mohammed; Khan, Shuaib Ahmad; Khanzadeev, Alexei; Kharlov, Yury; Kileng, Bjarte; Kim, Jonghyun; Kim, Dong Jo; Kim, Do Won; Kim, Jin Sook; Kim, Minwoo; Kim, Seon Hee ; Kim, Se Yong; Kim, Beomkyu; Kim, Taesoo; Kirsch, Stefan; Kisel, Ivan; Kiselev, Sergey; Kisiel, Adam Ryszard; Klay, Jennifer Lynn; Klein, Jochen; Klein-Bosing, Christian; Kliemant, Michael; Kluge, Alexander; Knichel, Michael Linus; Koch, Kathrin; Köhler, Markus; Kolojvari, Anatoly; Kondratiev, Valery; Kondratyeva, Natalia; Konevskih, Artem; Korneev, Andrey; Don, Chamath Kottachchi Kankanamge; Kour, Ravjeet; Kowalski, Marek; Kox, Serge; Meethaleveedu, Greeshma Koyithatta; Kral, Jiri ; Kralik, Ivan; Kramer, Frederick; Kraus, Ingrid Christine; Krawutschke, Tobias; Kretz, Matthias; Krivda, Marian; Krizek, Filip; Krus, Miroslav; Kryshen, Evgeny; Krzewicki, Mikolaj; Kucheriaev, Yury ; Kuhn, Christian Claude; Kuijer, Paul; Kurashvili, Podist; Kurepin, A.B.; Kurepin, A.; Kuryakin, Alexey; Kushpil, Svetlana; Kushpil, Vasily; Kvaerno, Henning; Kweon, Min Jung; Kwon, Youngil; Guevara, Pedro Ladron; Lakomov, Igor; Langoy, Rune; Lara, Camilo Ernesto; Lardeux, Antoine Xavier; Rocca, Paola; Lazzeroni, Cristina; Lea, Ramona; Bornec, Yves; Lee, Sung Chul; Lee, Ki Sang; Lefevre, Frederic; Lehnert, Joerg Walter; Leistam, Lars; Lenhardt, Matthieu Laurent; Lenti, Vito; Leon, Hermes ; Monzon, Ildefonso Leon; Vargas, Hermes Leon; Levai, Peter; Li, Xiaomei; Lien, Jorgen; Lietava, Roman; Lindal, Svein; Lindenstruth, Volker; Lippmann, Christian; Lisa, Michael Annan; Liu, Lijiao ; Loenne, Per-Ivar; Loggins, Vera; Loginov, Vitaly ; Lohn, Stefan Bernhard; Lohner, Daniel; Loizides, Constantinos; Loo, Kai Krister; Lopez, Xavier Bernard ; Torres, Ernesto Lopez; Lovhoiden, Gunnar; Lu, Xianguo; Luettig, Philipp; Lunardon, Marcello; Luo, Jiebin; Luparello, Grazia; Luquin, Lionel; Luzzi, Cinzia; Ma, Rongrong; Ma, Ke; Madagodahettige-Don, Dilan Minthaka; Maevskaya, Alla; Mager, Magnus; Mahapatra, Durga Prasad; Maire, Antonin; Malaev, Mikhail; Cervantes, Ivonne Alicia Maldonado; Malinina, Ludmila; MalKevich, Dmitry; Malzacher, Peter; Mamonov, Alexander; Manceau, Loic Henri Antoine; Mangotra, Lalit Kumar; Manko, Vladislav; Manso, Franck ; Manzari, Vito; Mao, Yaxian; Marchisone, Massimiliano; Mares, Jiri; Margagliotti, Giacomo Vito ; Margotti, Anselmo; Marin, Ana Maria; Markert, Christina; Martashvili, Irakli; Martinengo, Paolo; Martinez, Mario Ivan; Davalos, Arnulfo Martinez; Garcia, Gines Martinez; Martynov, Yevgen; Mas, Alexis Jean-Michel; Masciocchi, Silvia; Masera, Massimo; Masoni, Alberto; Massacrier, Laure Marie; Mastromarco, Mario; Mastroserio, Annalisa; Matthews, Zoe Louise; Matyja, Adam Tomasz; Mayani, Daniel; Mayer, Christoph ; Mazer, Joel; Mazzoni, Alessandra Maria; Meddi, Franco; Menchaca-Rocha, Arturo Alejandro; Perez, Jorge Mercado; Meres, Michal; Miake, Yasuo; Michalon, Alain; Midori, Jumpei; Milano, Leonardo; Milosevic, Jovan; Mischke, Andre; Mishra, Aditya Nath; Miskowiec, Dariusz; Mitu, Ciprian Mihai; Mlynarz, Jocelyn; Mohanty, Ajit Kumar; Mohanty, Bedangadas; Molnar, Levente; Zetina, Luis Manuel Montano; Monteno, Marco; Montes, Esther; Moon, Taebong; Morando, Maurizio; Godoy, Denise Aparecida Moreira; Moretto, Sandra; Morsch, Andreas; Muccifora, Valeria; Mudnic, Eugen; Muhuri, Sanjib; Muller, Hans; Munhoz, Marcelo; Musa, Luciano; Musso, Alfredo; Nandi, Basanta Kumar; Nania, Rosario; Nappi, Eugenio ; Nattrass, Christine; Naumov, Nikolay; Navin, Sparsh; Nayak, Tapan Kumar; Nazarenko, Sergey; Nazarov, Gleb; Nedosekin, Alexander; Nicassio, Maria ; Nielsen, Borge Svane; Niida, Takafumi; Nikolaev, Sergey; Nikolic, Vedran; Nikulin, Vladimir; Nikulin, Sergey; Nilsen, Bjorn Steven; Nilsson, Mads Stormo; Noferini, Francesco; Nomokonov, Petr; Nooren, Gerardus; Novitzky, Norbert; Nyanin, Alexandre ; Nyatha, Anitha; Nygaard, Casper; Nystrand, Joakim Ingemar; Obayashi, Hideyuki; Ochirov, Alexander; Oeschler, Helmut Oskar; Oh, Sun Kun; Oh, Saehanseul ; Oleniacz, Janusz; Oppedisano, Chiara; Velasquez, Antonio Ortiz; Ortona, Giacomo; Oskarsson, Anders Nils Erik; Ostrowski, Piotr Krystian; Otterlund, Ingvar; Otwinowski, Jacek Tomasz; Oyama, Ken; Ozawa, Kyoichiro ; Pachmayer, Yvonne Chiara; Pachr, Milos; Padilla, Fatima; Pagano, Paola; Paic, Guy; Painke, Florian ; Pajares, Carlos; Pal, S.; Pal, Susanta Kumar; Palaha, Arvinder Singh; Palmeri, Armando; Papikyan, Vardanush; Pappalardo, Giuseppe; Park, Woo Jin; Passfeld, Annika; Pastircak, Blahoslav; Patalakha, Dmitri Ivanovich; Paticchio, Vincenzo; Pavlinov, Alexei; Pawlak, Tomasz Jan; Peitzmann, Thomas; Perales, Marianela; Oliveira Filho, Elienos Pereira; Peresunko, Dmitri; Lara, Carlos Eugenio Perez; Lezama, Edgar Perez; Perini, Diego; Perrino, Davide; Peryt, Wiktor Stanislaw; Pesci, Alessandro; Peskov, Vladimir ; Pestov, Yury; Petracek, Vojtech; Petran, Michal ; Petris, Mariana; Petrov, Plamen Rumenov; Petrovici, Mihai; Petta, Catia; Piano, Stefano; Piccotti, Anna; Pikna, Miroslav; Pillot, Philippe; Pinazza, Ombretta; Pinsky, Lawrence; Pitz, Nora; Piuz, Francois; Piyarathna, Danthasinghe; Ploskon, Mateusz Andrzej; Pluta, Jan Marian; Pocheptsov, Timur ; Pochybova, Sona;

Lerma, Pedro Luis Manuel Podesta; Poghosyan, Martin; Polak, Karel; Polichtchouk, Boris ; Pop, Amalia; Porteboeuf-Houssais, Sarah; Pospisil, Vladimir; Potukuchi, Baba; Prasad, Sidharth Kumar; Preghenella, Roberto; Prino, Francesco; Pruneau, Claude Andre; Pshenichnov, Igor; Puchagin, Sergey; Puddu, Giovanna; Pulvirenti, Alberto; Punin, Valery ; Putis, Marian; Putschke, Jorn Henning; Quercigh, Emanuele; Qvigstad, Henrik; Rachevski, Alexandre; Rademakers, Alphonse; Radomski, Sylwester; Raiha, Tomi Samuli; Rak, Jan; Rakotozafindrabe, Andry Malala; Ramello, Luciano; Reyes, Abdiel Ramirez; Raniwala, Sudhir; Raniwala, Rashmi; Rasanen, Sami Sakari; Rascanu, Bogdan Theodor; Rathee, Deepika; Read, Kenneth Francis; Real, Jean-Sebastien; Redlich, Krzysztof; Reichelt, Patrick; Reicher, Martijn; Renfordt, Rainer Arno Ernst; Reolon, Anna Rita; Reshetin, Andrey; Rettig, Felix Vincenz; Revol, Jean-Pierre; Reygers, Klaus Johannes; Riccati, Lodovico; Ricci, Renato Angelo; Richter, Matthias Rudolph; Riedler, Petra; Riegler, Werner; Riggi, Francesco; Cahuantzi, Mario Rodriguez; Rohr, David; Rohrich, Dieter; Romita, Rosa; Ronchetti, Federico; Rosnet, Philippe; Rossegger, Stefan; Rossi, Andrea; Roukoutakis, Filimon; Roy, Pradip Kumar; Roy, Christelle Sophie; Montero, Antonio Juan Rubio; Rui, Rinaldo; Ryabinkin, Evgeny; Rybicki, Andrzej; Sadovsky, Sergey; Safarik, Karel; Sahu, Pradip Kumar ; Saini, Jogender; Sakaguchi, Hiroaki; Sakai, Shingo ; Sakata, Dosatsu; Salgado, Carlos Albert; Sambyal, Sanjeev Singh; Samsonov, Vladimir; Castro, Xitzel Sanchez; Sandor, Ladislav; Sandoval, Andres; Sano, Masato; Sano, Satoshi; Santo, Rainer; Santoro, Romualdo; Sarkamo, Juho Jaako; Scapparone, Eugenio; Scarlassara, Fernando; Scharenberg, Rolf Paul; Schiaua, Claudiu Cornel; Schicker, Rainer Martin; Schmidt, Christian Joachim; Schmidt, Hans Rudolf; Schreiner, Steffen; Schuchmann, Simone; Schukraft, Jurgen; Schutz, Yves Roland; Schwarz, Kilian Eberhard ; Schweda, Kai Oliver; Scioli, Gilda; Scomparin, Enrico; Scott, Rebecca; Scott, Patrick Aaron; Segato, Gianfranco; Selioujenkov, Ilya; Senyukov, Serhiy; Seo, Jeewon; Serci, Sergio; Serradilla, Eulogio; Sevcenco, Adrian; Sgura, Irene; Shabetai, Alexandre; Shabratova, Galina; Shahoyan, Ruben; Sharma, Natasha; Sharma, Satish; Shigaki, Kenta; Shimomura, Maya; Shtejer, Katherin; Sibiriak, Yury; Siciliano, Melinda; Sicking, Eva; Siddhanta, Sabyasachi; Siemiarczuk, Teodor; Silvermyr, David Olle Rickard; Simonetti, Giuseppe; Singaraju, Rama Narayana ; Singh, Ranbir; Singha, Subhash; Sinha, Bikash; Sinha, Tinku; Sitar, Branislav; Sitta, Mario; Skaali, Bernhard; Skjerdal, Kyrre; Smakal, Radek; Smirnov, Nikolai; Snellings, Raimond; Sogaard, Carsten ; Soltz, Ron Ariel; Son, Hyungsuk; Song, Jihye; Song, Myunggeun; Soos, Csaba; Soramel, Francesca; Sputowska, Iwona; Spyropoulou-Stassinaki, Martha; Srivastava, Brijesh Kumar; Stachel, Johanna; Stan, Ionel; Stan, Ionel; Stefanek, Grzegorz; Stefanini, Giorgio; Steinbeck, Timm Morten; Steinpreis, Matthew ; Stenlund, Evert Anders; Steyn, Gideon Francois; Stocco, Diego; Stolpovskiy, Mikhail; Strabykin, Kirill ; Strmen, Peter; Passo Suaide, Alexandre Alarcon; Vasquez, Martin Alfonso Subieta; Sugitate, Toru; Suire, Christophe Pierre; Sukhorukov, Mikhail; Sultanov, Rishat; Sumbera, Michal; Susa, Tatjana; Toledo, Alejandro Szanto; Szarka, Imrich; Szostak, Artur Krzysztof; Tagridis, Christos; Takahashi, Jun ; Takaki, Daniel Jesus Tapia; Tauro, Arturo; Munoz, Guillermo Tejeda; Telesca, Adriana; Terrevoli, Cristina; Thader, Jochen Mathias; Thomas, Jim; Thomas, Deepa; Tieulent, Raphael Noel; Timmins, Anthony; Tlusty, David; Toia, Alberica; Torii, Hisayuki; Toscano, Luca; Tosello, Flavio; Traczyk, Tomasz; Truesdale, David Christopher; Trzaska, Wladyslaw Henryk; Tsuji, Tomoya; Tumkin, Alexandr; Turrisi, Rosario; Tveter, Trine Spedstad; Ulery, Jason Glyndwr; Ullaland, Kjetil; Ulrich, Jochen; Uras, Antonio; Urban, Jozef; Urciuoli, Guido Marie; Usai, Gianluca; Vajzer, Michal; Vala, Martin; Palomo, Lizardo Valencia; Vallero, Sara; Kolk, Naomi; Vyvre, Pierre Vande; Leeuwen, Marco; Vannucci, Luigi ; Vargas, Aurora Diozcora; Varma, Raghava; Vasileiou, Maria; Vasiliev, Andrey; Vechernin, Vladimir; Veldhoen, Misha; Venaruzzo, Massimo; Vercellin, Ermanno; Vergara, Sergio; Vernekohl, Don Constantin; Vernet, Renaud; Verweij, Marta; Vickovic, Linda; Viesti, Giuseppe; Vikhlyantsev, Oleg ; Vilakazi, Zabulon; Baillie, Orlando Villalobos; Vinogradov, Leonid; Vinogradov, Yury; Vinogradov, Alexander; Virgili, Tiziano; Viyogi, Yogendra; Vodopianov, Alexander; Voloshin, Sergey; Voloshin, Kirill; Volpe, Giacomo; Haller, Barthelemy; Vranic, Danilo; vrebekk, Gaute; Vrlakova, Janka; Vulpescu, Bogdan; Vyushin, Alexey; Wagner, Boris; Wagner, Vladimir; Wan, Renzhuo; Wang, Yifei; Wang, Mengliang; Wang, Dong; Wang, Yaping; Watanabe, Kengo; Wessels, Johannes; Westerhoff, Uwe; Wiechula, Jens; Wikne, Jon; Wilde, Martin Rudolf; Wilk, Grzegorz Andrzej; Wilk, Alexander; Williams, Crispin; Windelband, Bernd Stefan; Karampatsos, Leonidas Xaplanteris; Yang, Hongyan; Yang, Shiming; Yano, Satoshi; Yasnopolsky, Stanislav; Yi, JunGyu; Yin, Zhongbao; Yokoyama, Hiroki; Yoo, In-Kwon; Yoon, Jongik; Yu, Weilin; Yuan, Xianbao; Yushmanov, Igor; Zach, Cenek; Zampolli, Chiara; Zaporozhets, Sergey; Zarochentsev, Andrey; Zavada, Petr; Zaviyalov, Nikolai; Zbroszczyk, Hanna Paulina; Zelnicek, Pierre; Zgura, Sorin Ion; Zhalov, Mikhail ; Zhang, Xiaoming; Zhou, Fengchu; Zhou, You; Zhou, Daicui; Zhu, Xiangrong; Zichichi, Antonino; Zimmermann, Alice; Zinovjev, Gennady; Zoccarato, Yannick Denis; Zynovyev, Mykhaylo: **Underlying Event measurements in pp collisions at $\sqrt{s} = 0.9$ and 7 TeV with the ALICE experiment at the LHC.** *Journal of high energy physics* 2012: 116, 2012. DOI:10.1007/JHEP07(2012)116

WOS-PHN-22 Ablikim, M.; Achasov, M. N.; Albayrak, O.; Ambrose, D. J.; An, F. F.; An, Q.; Bai, J. Z.; Ban, Y.; Becker, J.; Bennett, J. V.; Bertani, M. ; Bian, J. M.; Boger, E.; Bondarenko, O.; Boyko, I.; Briere, R. A.; Bytev, V.; Cai, X.; Cakir, O. ; Calcaterra, A.; Cao, G. F.; Cetin, S. A.; Chang, J. F.; Chelkov, G.; Chen, G.; Chen, H. S. ; Chen, J. C.; Chen, M. L.; Chen, S. J.; Chen, X. ; Chen, Y. B.; Cheng, H. P.; Chu, Y. P.; Coccetti, F.; Cronin-Hennessy, D.; Dai, H. L.; Dai, J. P.; Dedovich, D.; Deng, Z. Y.; Denig, A.; Denysenko, I.; Destefanis, M.; Ding, W. M.; Ding, Y.; Dong, L. Y.; Dong, M. Y.; Du, S. X.; Fang, J.; Fang, S. S.; Fava, L.; Feldbauer, F.; Feng, C. Q.; Ferroli, R. B.; Fu, C. D.; Fu, J. L.; Gao, Y.; Geng, C.; Götzen, Klaus; Gong, W. X.; Gradl, W.; Greco, M.; Gu, M. H.; Gu, Y. T.; Guan, Y. H.; Guo, A. Q.; Guo, L. B.; Guo, Y. P.; Han, Y. L.; Harris, F. A.; He, K. L.; He, M.; He, Z. Y.; Held, T.; Heng, Y. K.; Hou, Z. L.; Hu, H. M.; Hu, J. F.; Hu, T.; Huang, G. M.; Huang, G. S.; Huang, J. S.; Huang, X. T.; Huang, Y. P.; Hussain, T.; Ji, C. S.; Ji, Q.; Ji, Q. P. ; Ji, X. B.; Ji, X. L.; Jiang, L. L.; Jiang, X. S.; Jiao, J. B.; Jiao, Z.; Jin, D. P.; Jin, S. ; Jing, F. F.; Kalantar-Nayestanaki, N.; Kavatsyuk, M.; Kornicer, M.; Kuehn, W.; Lai, W.; Lange, J. S.; Li, C. H.; Li, Cheng; Li, Cui; Li, D. M.; Li, F.; Li, G.; Li, H. B.; Li, J. C.; Li, K.; Li, Lei; Li, Q. J.; Li, S. L.; Li, W. D.; Li, W. G.; Li, X. L.; Li, X. N.; Li, X. Q.; Li, X. R. ; Li, Z. B.; Liang, H.; Liang, Y. F.; Liang, Y. T.; Liao, G. R.; Liao, X. T.; Liu, B. J.; Liu, C. L.; Liu, C. X.; Liu, C. Y.; Liu, F. H.; Liu, Fang; Liu, Feng; Liu, H.; Liu, H. H.; Liu, H. M. ; Liu, H. W.; Liu, J. P.; Liu, K. Y.; Liu, Kai ;

Liu, P. L.; Liu, Q.; Liu, S. B.; Liu, X.; Liu, Y. B.; Liu, Z. A.; Liu, Zhiqiang; Liu, Zhiqing ; Loehner, H.; Lu, G. R.; Lu, H. J.; Lu, J. G. ; Lu, Q. W.; Lu, X. R.; Lu, Y. P.; Luo, C. L.; Luo, M. X.; Luo, T.; Luo, X. L.; Lv, M.; Ma, C. L.; Ma, F. C.; Ma, H. L.; Ma, Q. M.; Ma, S.; Ma, T.; Ma, X. Y.; Ma, Y.; Maas, F. E.; Maggiora, M.; Malik, Q. A.; Mao, Y. J.; Mao, Z. P. ; Messchendorp, J. G.; Min, J.; Min, T. J.; Mitchell, R. E.; Mo, X. H.; Morales Morales, C.; Motzko, C.; Muchnoi, N. Yu.; Muramatsu, H.; Nefedov, Y.; Nicholson, C.; Nikolaev, I. B.; Ning, Z.; Olsen, S. L.; Ouyang, Q.; Pacetti, S.; Park, J. W.; Pelizaeus, M.; Peng, H. P.; Peters, K.; Ping, J. L.; Ping, R. G.; Poling, R.; Prencipe, E. ; Qi, M.; Qian, S.; Qiao, C. F.; Qin, X. S.; Qin, Y.; Qin, Z. H.; Qiu, J. F.; Rashid, K. H.; Rong, G.; Ruan, X. D.; Sarantsev, A.; Schaefer, B. D.; Schulze, J.; Shao, M.; Shen, C. P.; Shen, X. Y.; Sheng, H. Y.; Shepherd, M. R.; Song, X. Y.; Spataro, S.; Spruck, B.; Sun, D. H.; Sun, G. X.; Sun, J. F.; Sun, S. S.; Sun, Y. J.; Sun, Y. Z.; Sun, Z. J.; Sun, Z. T.; Tang, C. J.; Tang, X.; Tapan, I.; Thorndike, E. H.; Toth, D.; Ullrich, M. ; Varner, G. S.; Wang, B.; Wang, B. Q.; Wang, D. ; Wang, D. Y.; Wang, K.; Wang, L. L.; Wang, L. S. ; Wang, M.; Wang, P.; Wang, P. L.; Wang, Q.; Wang, Q. J.; Wang, S. G.; Wang, X. L.; Wang, Y. D. ; Wang, Y. F.; Wang, Y. Q.; Wang, Z.; Wang, Z. G. ; Wang, Z. Y.; Wei, D. H.; Wei, J. B.; Weidenkaff, P.; Wen, Q. G.; Wen, S. P.; Werner, M. ; Wiedner, U.; Wu, L. H.; Wu, N.; Wu, S. X.; Wu, W.; Wu, Z.; Xia, L. G.; Xiao, Z. J.; Xie, Y. G.; Xiu, Q. L.; Xu, G. F.; Xu, G. M.; Xu, H.; Xu, Q. J.; Xu, X. P.; Xu, Z. R.; Xue, F.; Xue, Z.; Yan, L.; Yan, W. B.; Yan, Y. H.; Yang, H. X. ; Yang, Y.; Yang, Y. X.; Ye, H.; Ye, M.; Ye, M. H.; Yu, B. X.; Yu, C. X.; Yu, H. W.; Yu, J. S.; Yu, S. P.; Yuan, C. Z.; Yuan, Y.; Zafar, A. A.; Zallo, A.; Zeng, Y.; Zhang, B. X.; Zhang, B. Y.; Zhang, C.; Zhang, C. C.; Zhang, D. H.; Zhang, H. H.; Zhang, H. Y.; Zhang, J. Q.; Zhang, J. W.; Zhang, J. Y.; Zhang, J. Z.; Zhang, S. H.; Zhang, X. J.; Zhang, X. Y.; Zhang, Y.; Zhang, Y. H. ; Zhang, Y. S.; Zhang, Z. P.; Zhang, Z. Y.; Zhao, G.; Zhao, H. S.; Zhao, J. W.; Zhao, K. X.; Zhao, Lei; Zhao, Ling; Zhao, M. G.; Zhao, Q.; Zhao, Q. Z.; Zhao, S. J.; Zhao, T. C.; Zhao, X. H.; Zhao, Y. B.; Zhao, Z. G.; Zhemchugov, A.; Zheng, B.; Zheng, J. P.; Zheng, Y. H.; Zhong, B.; Zhong, J. ; Zhong, Z.; Zhou, L.; Zhou, X. K.; Zhou, X. R. ; Zhu, C.; Zhu, K.; Zhu, K. J.; Zhu, S. H.; Zhu, X. L.; Zhu, Y. C.; Zhu, Y. M.; Zhu, Y. S.; Zhu, Z. A.; Zhuang, J.; Zou, B. S.; Zou, J. H.: **Precision measurements of branching fractions for** $\psi \rightarrow \pi^0 J/\psi$ **and** $\eta J/\psi$**.** *Physical review / D* 86: 092008, 2012. DOI:10.1103/PhysRevD.86.092008

WOS-PHN-23 Ablikim, M.; Achasov, M. N.; Albayrak, O.; Ambrose, D. J.; An, F. F.; An, Q.; Bai, J. Z.; Ban, Y.; Becker, J.; Bennett, J. V.; Bertani, M. ; Bian, J. M.; Boger, E.; Bondarenko, O.; Boyko, I.; Briere, R. A.; Bytev, V.; Cai, X.; Cakir, O. ; Calcaterra, A.; Cao, G. F.; Cetin, S. A.; Chang, J. F.; Chelkov, G.; Chen, G.; Chen, H. S. ; Chen, J. C.; Chen, M. L.; Chen, S. J.; Chen, X. ; Chen, Y. B.; Cheng, H. P.; Chu, Y. P.; Cronin-Hennessy, D.; Dai, H. L.; Dai, J. P.; Dedovich, D.; Deng, Z. Y.; Denig, A.; Denysenko, I. ; Destefanis, M.; Ding, W. M.; Ding, Y.; Dong, L. Y.; Dong, M. Y.; Du, S. X.; Fang, J.; Fang, S. S.; Fava, L.; Feldbauer, F.; Feng, C. Q.; Ferroli, R. B.; Fu, C. D.; Fu, J. L.; Gao, Y.; Geng, C.; Götzen, Klaus; Gong, W. X.; Gradl, W. ; Greco, M.; Gu, M. H.; Gu, Y. T.; Guan, Y. H. ; Guo, A. Q.; Guo, L. B.; Guo, Y. P.; Han, Y. L. ; Harris, F. A.; He, K. L.; He, M.; He, Z. Y.; Held, T.; Heng, Y. K.; Hou, Z. L.; Hu, H. M.; Hu, T.; Huang, G. M.; Huang, G. S.; Huang, J. S. ; Huang, X. T.; Huang, Y. P.; Hussain, T.; Ji, C. S.; Ji, Q.; Ji, Q. P.; Ji, X. B.; Ji, X. L.; Jiang, L. L.; Jiang, X. S.; Jiao, J. B.; Jiao, Z. ; Jin, D. P.; Jin, S.; Jing, F. F.; Kalantar-Nayestanaki, N.; Kavatsyuk, M.; Kuehn, W.; Lai, W.; Lange, J. S.; Li, C. H.; Li, Cheng; Li, Cui; Li, D. M.; Li, F.; Li, G.; Li, H. B.; Li, J. C.; Li, K.; Li, Lei; Li, Q. J.; Li, S. L. ; Li, W. D.; Li, W. G.; Li, X. L.; Li, X. N.; Li, X. Q.; Li, X. R.; Li, Z. B.; Liang, H.; Liang, Y. F.; Liang, Y. T.; Liao, G. R.; Liao, X. T.; Liu, B. J.; Liu, C. L.; Liu, C. X.; Liu, C. Y.; Liu, F. H.; Liu, Fang; Liu, Feng; Liu, H. ; Liu, H. H.; Liu, H. M.; Liu, H. W.; Liu, J. P. ; Liu, K. Y.; Liu, Kai; Liu, P. L.; Liu, Q.; Liu, S. B.; Liu, X.; Liu, Y. B.; Liu, Z. A.; Liu, Zhiqiang; Liu, Zhiqing; Loehner, H.; Lu, G. R. ; Lu, H. J.; Lu, J. G.; Lu, Q. W.; Lu, X. R.; Lu, Y. P.; Luo, C. L.; Luo, M. X.; Luo, T.; Luo, X. L.; Lv, M.; Ma, C. L.; Ma, F. C.; Ma, H. L. ; Ma, Q. M.; Ma, S.; Ma, T.; Ma, X. Y.; Ma, Y. ; Maas, F. E.; Maggiora, M.; Malik, Q. A.; Mao, Y. J.; Mao, Z. P.; Messchendorp, J. G.; Min, J.; Min, T. J.; Mitchell, R. E.; Mo, X. H.; Morales Morales, C.; Motzko, C.; Muchnoi, N. Yu.; Muramatsu, H.; Nefedov, Y.; Nicholson, C.; Nikolaev, I. B.; Ning, Z.; Olsen, S. L.; Ouyang, Q. ; Pacetti, S.; Park, J. W.; Pelizaeus, M.; Peng, H. P.; Peters, K.; Ping, J. L.; Ping, R. G.; Poling, R.; Prencipe, E.; Qi, M.; Qian, S.; Qiao, C. F.; Qin, X. S.; Qin, Y.; Qin, Z. H.; Qiu, J. F.; Rashid, K. H.; Rong, G.; Ruan, X. D. ; Sarantsev, A.; Schaefer, B. D.; Schulze, J.; Shao, M.; Shen, C. P.; Shen, X. Y.; Sheng, H. Y. ; Shepherd, M. R.; Song, X. Y.; Spataro, S.; Spruck, B.; Sun, D. H.; Sun, G. X.; Sun, J. F.; Sun, S. S.; Sun, Y. J.; Sun, Y. Z.; Sun, Z. J.; Sun, Z. T.; Tang, C. J.; Tang, X.; Tapan, I.; Thorndike, E. H.; Toth, D.; Ullrich, M.; Varner, G. S.; Wang, B.; Wang, B. Q.; Wang, D.; Wang, D. Y. ; Wang, K.; Wang, L. L.; Wang, L. S.; Wang, M. ; Wang, P.; Wang, P. L.; Wang, Q.; Wang, Q. J. ; Wang, S. G.; Wang, X. L.; Wang, Y. D.; Wang, Y. F.; Wang, Y. Q.; Wang, Z.; Wang, Z. G.; Wang, Z. Y.; Wei, D. H.; Wei, J. B.; Weidenkaff, P.; Wen, Q. G.; Wen, S. P.; Werner, M.; Wiedner, U.; Wu, L. H.; Wu, N.; Wu, S. X.; Wu, W.; Wu, Z.; Xia, L. G.; Xiao, Z. J.; Xie, Y. G.; Xiu, Q. L.; Xu, G. F.; Xu, G. M.; Xu, H.; Xu, Q. J.; Xu, X. P.; Xu, Z. R.; Xue, F.; Xue, Z.; Yan, L.; Yan, W. B.; Yan, Y. H.; Yang, H. X.; Yang, Y.; Yang, Y. X.; Ye, H.; Ye, M.; Ye, M. H.; Yu, B. X.; Yu, C. X.; Yu, H. W.; Yu, J. S.; Yu, S. P. ; Yuan, C. Z.; Yuan, Y.; Zafar, A. A.; Zallo, A. ; Zeng, Y.; Zhang, B. X.; Zhang, B. Y.; Zhang, C. ; Zhang, C. C.; Zhang, D. H.; Zhang, H. H.; Zhang, H. Y.; Zhang, J. Q.; Zhang, J. W.; Zhang, J. Y.; Zhang, J. Z.; Zhang, S. H.; Zhang, X. J.; Zhang, X. Y.; Zhang, Y.; Zhang, Y. H.; Zhang, Y. S. ; Zhang, Z. P.; Zhang, Z. Y.; Zhao, G.; Zhao, H. S.; Zhao, J. W.; Zhao, K. X.; Zhao, Lei; Zhao, Ling; Zhao, M. G.; Zhao, Q.; Zhao, Q. Z.; Zhao, S. J.; Zhao, T. C.; Zhao, X. H.; Zhao, Y. B.; Zhao, Z. G.; Zhemchugov, A.; Zheng, B.; Zheng, J. P.; Zheng, Y. H.; Zhong, B.; Zhong, J.; Zhong, Z.; Zhou, L.; Zhou, X. K.; Zhou, X. R.; Zhu, C. ; Zhu, K.; Zhu, K. J.; Zhu, S. H.; Zhu, X. L.; Zhu, Y. C.; Zhu, Y. M.; Zhu, Y. S.; Zhu, Z. A.; Zhuang, J.; Zou, B. S.; Zou, J. H.: **Measurement of** χ_{cj} **decaying into** $pn[over]\pi^-$ **and** $pn[over]\pi^-\pi^0$**.** *Physical review / D* 86: 052011, 2012. DOI:10.1103/PhysRevD.86.052011

WOS-PHN-24 Ablikim, M.; Achasov, M. N.; Albayrak, O.; Ambrose, D. J.; An, F. F.; An, Q.; Bai, J. Z.; Ban, Y.; Becker, J.; Bennett, J. V.; Bertani, M. ; Bian, J. M.; Boger, E.; Bondarenko, O.; Boyko, I.; Briere, R. A.; Bytev, V.; Cai, X.; Cakir, O. ; Calcaterra, A.; Cao, G. F.; Cetin, S. A.; Chang, J. F.; Chelkov, G.; Chen, G.; Chen, H. S. ; Chen, J. C.; Chen, M. L.; Chen, S. J.; Chen, X. ; Chen, Y. B.; Cheng, H. P.; Chu, Y. P.; Cronin-Hennessy, D.; Dai, H. L.; Dai, J. P.; Dedovich, D.; Deng, Z. Y.; Denig, A.; Denysenko, I. ; Destefanis, M.; Ding, W. M.; Ding, Y.; Dong, L. Y.; Dong, M. Y.; Du, S. X.; Fang, J.; Fang, S. S.; Fava, L.; Feldbauer, F.; Feng, C. Q.; Ferroli, R. B.; Fu, C. D.; Fu, J. L.; Gao, Y.; Geng, C.; Götzen, Klaus; Gong, W. X.; Gradl,

W. ; Greco, M.; Gu, M. H.; Gu, Y. T.; Guan, Y. H. ; Guo, A. Q.; Guo, L. B.; Guo, Y. P.; Han, Y. L. ; Harris, F. A.; He, K. L.; He, M.; He, Z. Y.; Held, T.; Heng, Y. K.; Hou, Z. L.; Hu, H. M.; Hu, T.; Huang, G. M.; Huang, G. S.; Huang, J. S. ; Huang, X. T.; Huang, Y. P.; Hussain, T.; Ji, C. S.; Ji, Q.; Ji, Q. P.; Ji, X. B.; Ji, X. L.; Jiang, L. L.; Jiang, X. S.; Jiao, J. B.; Jiao, Z. ; Jin, D. P.; Jin, S.; Jing, F. F.; Kalantar-Nayestanaki, N.; Kavatsyuk, M.; Kuehn, W.; Lai, W.; Lange, J. S.; Li, C. H.; Li, Cheng; Li, Cui; Li, D. M.; Li, F.; Li, G.; Li, H. B.; Li, J. C.; Li, K.; Li, Lei; Li, Q. J.; Li, S. L. ; Li, W. D.; Li, W. G.; Li, X. L.; Li, X. N.; Li, X. Q.; Li, X. R.; Li, Z. B.; Liang, H.; Liang, Y. F.; Liang, Y. T.; Liao, G. R.; Liao, X. T.; Liu, B. J.; Liu, C. L.; Liu, C. X.; Liu, C. Y.; Liu, F. H.; Liu, Fang; Liu, Feng; Liu, H. ; Liu, H. H.; Liu, H. M.; Liu, H. W.; Liu, J. P. ; Liu, K. Y.; Liu, Kai; Liu, P. L.; Liu, Q.; Liu, S. B.; Liu, X.; Liu, Y. B.; Liu, Z. A.; Liu, Zhiqiang; Liu, Zhiqing; Loehner, H.; Lu, G. R. ; Lu, H. J.; Lu, J. G.; Lu, Q. W.; Lu, X. R.; Lu, Y. P.; Luo, C. L.; Luo, M. X.; Luo, T.; Luo, X. L.; Lv, M.; Ma, C. L.; Ma, F. C.; Ma, H. L. ; Ma, Q. M.; Ma, S.; Ma, T.; Ma, X. Y.; Ma, Y. ; Maas, F. E.; Maggiora, M.; Malik, Q. A.; Mao, Y. J.; Mao, Z. P.; Messchendorp, J. G.; Min, J.; Min, T. J.; Mitchell, R. E.; Mo, X. H.; Morales Morales, C.; Motzko, C.; Muchnoi, N. Yu.; Muramatsu, H.; Nefedov, Y.; Nicholson, C.; Nikolaev, I. B.; Ning, Z.; Olsen, S. L.; Ouyang, Q. ; Pacetti, S.; Park, J. W.; Pelizaeus, M.; Peng, H. P.; Peters, K.; Ping, J. L.; Ping, R. G.; Poling, R.; Prencipe, E.; Qi, M.; Qian, S.; Qiao, C. F.; Qin, X. S.; Qin, Y.; Qin, Z. H.; Qiu, J. F.; Rashid, K. H.; Rong, G.; Ruan, X. D. ; Sarantsev, A.; Schaefer, B. D.; Schulze, J.; Shao, M.; Shen, C. P.; Shen, X. Y.; Sheng, H. Y. ; Shepherd, M. R.; Song, X. Y.; Spataro, S.; Spruck, B.; Sun, D. H.; Sun, G. X.; Sun, J. F.; Sun, S. S.; Sun, Y. J.; Sun, Y. Z.; Sun, Z. J.; Sun, Z. T.; Tang, C. J.; Tang, X.; Tapan, I.; Thorndike, E. H.; Toth, D.; Ullrich, M.; Varner, G. S.; Wang, B.; Wang, B. Q.; Wang, D.; Wang, D. Y. ; Wang, K.; Wang, L. L.; Wang, L. S.; Wang, M. ; Wang, P.; Wang, P. L.; Wang, Q.; Wang, Q. J. ; Wang, S. G.; Wang, X. L.; Wang, Y. D.; Wang, Y. F.; Wang, Y. Q.; Wang, Z.; Wang, Z. G.; Wang, Z. Y.; Wei, D. H.; Wei, J. B.; Weidenkaff, P.; Wen, Q. G.; Wen, S. P.; Werner, M.; Wiedner, U.; Wu, L. H.; Wu, N.; Wu, S. X.; Wu, W.; Wu, Z.; Xia, L. G.; Xiao, Z. J.; Xie, Y. G.; Xiu, Q. L.; Xu, G. F.; Xu, G. M.; Xu, H.; Xu, Q. J.; Xu, X. P.; Xu, Z. R.; Xue, F.; Xue, Z.; Yan, L.; Yan, W. B.; Yan, Y. H.; Yang, H. X.; Yang, Y.; Yang, Y. X.; Ye, H.; Ye, M.; Ye, M. H.; Yu, B. X.; Yu, C. X.; Yu, H. W.; Yu, J. S.; Yu, S. P. ; Yuan, C. Z.; Yuan, Y.; Zafar, A. A.; Zallo, A. ; Zeng, Y.; Zhang, B. X.; Zhang, B. Y.; Zhang, C. ; Zhang, C. C.; Zhang, D. H.; Zhang, H. H.; Zhang, H. Y.; Zhang, J. Q.; Zhang, J. W.; Zhang, J. Y.; Zhang, J. Z.; Zhang, S. H.; Zhang, X. J.; Zhang, X. Y.; Zhang, Y.; Zhang, Y. H.; Zhang, Y. S. ; Zhang, Z. P.; Zhang, Z. Y.; Zhao, G.; Zhao, H. S.; Zhao, J. W.; Zhao, K. X.; Zhao, Lei; Zhao, Ling; Zhao, M. G.; Zhao, Q.; Zhao, Q. Z.; Zhao, S. J.; Zhao, T. C.; Zhao, X. H.; Zhao, Y. B.; Zhao, Z. G.; Zhemchugov, A.; Zheng, B.; Zheng, J. P.; Zheng, Y. H.; Zhong, B.; Zhong, J.; Zhong, Z.; Zhou, L.; Zhou, X. K.; Zhou, X. R.; Zhu, C. ; Zhu, K.; Zhu, K. J.; Zhu, S. H.; Zhu, X. L.; Zhu, Y. C.; Zhu, Y. M.; Zhu, Y. S.; Zhu, Z. A.; Zhuang, J.; Zou, B. S.; Zou, J. H.: **Study of** $\psi(3686) \to \pi^0 h_c h_c \to \gamma\eta_c$ **via** η_c **exclusive decays.** *Physical review / D* 86: 092009, 2012. DOI:10.1103/PhysRevD.86.092009

WOS-PHN-25 Ablikim, M.; Achasov, M. N.; Albayrak, O.; Ambrose, D. J.; An, F. F.; An, Q.; Bai, J. Z.; Ban, Y.; Becker, J.; Bennett, J. V.; Bertani, M. ; Bian, J. M.; Boger, E.; Bondarenko, O.; Boyko, I.; Briere, R. A.; Bytev, V.; Cai, X.; Cakir, O. ; Calcaterra, A.; Cao, G. F.; Cetin, S. A.; Chang, J. F.; Chelkov, G.; Chen, G.; Chen, H. S. ; Chen, J. C.; Chen, M. L.; Chen, S. J.; Chen, Y. B.; Cheng, H. P.; Chu, Y. P.; Cronin-Hennessy, D. ; Dai, H. L.; Dai, J. P.; Dedovich, D.; Deng, Z. Y.; Denig, A.; Denysenko, I.; Destefanis, M.; Ding, W. M.; Ding, Y.; Dong, L. Y.; Dong, M. Y.; Du, S. X.; Fang, J.; Fang, S. S.; Fava, L.; Feldbauer, F.; Feng, C. Q.; Ferroli, R. B.; Fu, C. D.; Fu, J. L.; Gao, Y.; Geng, C.; Götzen, Klaus ; Gong, W. X.; Gradl, W.; Greco, M.; Gu, M. H. ; Gu, Y. T.; Guan, Y. H.; Guo, A. Q.; Guo, L. B. ; Guo, Y. P.; Han, Y. L.; Harris, F. A.; He, K. L.; He, M.; He, Z. Y.; Held, T.; Heng, Y. K.; Hou, Z. L.; Hu, H. M.; Hu, T.; Huang, G. M.; Huang, G. S.; Huang, J. S.; Huang, X. T.; Huang, Y. P.; Hussain, T.; Ji, C. S.; Ji, Q.; Ji, Q. P. ; Ji, X. B.; Ji, X. L.; Jiang, L. L.; Jiang, X. S.; Jiao, J. B.; Jiao, Z.; Jin, D. P.; Jin, S. ; Jing, F. F.; Kalantar-Nayestanaki, N.; Kavatsyuk, M.; Kuehn, W.; Lai, W.; Lange, J. S.; Li, C. H. ; Li, Cheng; Li, Cui; Li, D. M.; Li, F.; Li, G.; Li, H. B.; Li, J. C.; Li, K.; Li, Lei; Li, Q. J.; Li, S. L.; Li, W. D.; Li, W. G.; Li, X. L.; Li, X. N.; Li, X. Q.; Li, X. R.; Li, Z. B.; Liang, H.; Liang, Y. F.; Liang, Y. T.; Liao, G. R.; Liao, X. T.; Liu, B. J.; Liu, C. L.; Liu, C. X.; Liu, C. Y.; Liu, F. H.; Liu, Fang; Liu, Feng; Liu, H.; Liu, H. H.; Liu, H. M.; Liu, H. W.; Liu, J. P.; Liu, K. Y.; Liu, Kai; Liu, P. L. ; Liu, Q.; Liu, S. B.; Liu, X.; Liu, Y. B.; Liu, Z. A.; Liu, Zhiqiang; Liu, Zhiqing; Loehner, H.; Lu, G. R.; Lu, H. J.; Lu, J. G.; Lu, Q. W. ; Lu, X. R.; Lu, Y. P.; Luo, C. L.; Luo, M. X. ; Luo, T.; Luo, X. L.; Lv, M.; Ma, C. L.; Ma, F. C.; Ma, H. L.; Ma, Q. M.; Ma, S.; Ma, T.; Ma, X. Y.; Ma, Y.; Maas, F. E.; Maggiora, M.; Malik, Q. A.; Mao, Y. J.; Mao, Z. P.; Messchendorp, J. G.; Min, J.; Min, T. J.; Mitchell, R. E.; Mo, X. H.; Morales Morales, C.; Motzko, C.; Muchnoi, N. Yu.; Muramatsu, H.; Nefedov, Y.; Nicholson, C.; Nikolaev, I. B.; Ning, Z.; Olsen, S. L.; Ouyang, Q. ; Pacetti, S.; Park, J. W.; Pelizaeus, M.; Peng, H. P.; Peters, K.; Ping, J. L.; Ping, R. G.; Poling, R.; Prencipe, E.; Qi, M.; Qian, S.; Qiao, C. F.; Qin, X. S.; Qin, Y.; Qin, Z. H.; Qiu, J. F.; Rashid, K. H.; Rong, G.; Ruan, X. D. ; Sarantsev, A.; Schaefer, B. D.; Schulze, J.; Shao, M.; Shen, C. P.; Shen, X. Y.; Sheng, H. Y. ; Shepherd, M. R.; Song, X. Y.; Spataro, S.; Spruck, B.; Sun, D. H.; Sun, G. X.; Sun, J. F.; Sun, S. S.; Sun, Y. J.; Sun, Y. Z.; Sun, Z. J.; Sun, Z. T.; Tang, C. J.; Tang, X.; Tapan, I.; Thorndike, E. H.; Toth, D.; Ullrich, M.; Varner, G. S.; Wang, B.; Wang, B. Q.; Wang, K.; Wang, L. L. ; Wang, L. S.; Wang, M.; Wang, P.; Wang, P. L. ; Wang, Q.; Wang, Q. J.; Wang, S. G.; Wang, X. L. ; Wang, Y. D.; Wang, Y. F.; Wang, Y. Q.; Wang, Z. ; Wang, Z. G.; Wang, Z. Y.; Wei, D. H.; Weidenkaff, P.; Wen, Q. G.; Wen, S. P.; Werner, M. ; Wiedner, U.; Wu, L. H.; Wu, N.; Wu, S. X.; Wu, W.; Wu, Z.; Xia, L. G.; Xiao, Z. J.; Xie, Y. G.; Xiu, Q. L.; Xu, G. F.; Xu, G. M.; Xu, H.; Xu, Q. J.; Xu, X. P.; Xu, Z. R.; Xue, F.; Xue, Z.; Yan, L.; Yan, W. B.; Yan, Y. H.; Yang, H. X. ; Yang, Y.; Yang, Y. X.; Ye, H.; Ye, M.; Ye, M. H.; Yu, B. X.; Yu, C. X.; Yu, J. S.; Yu, S. P.; Yuan, C. Z.; Yuan, Y.; Zafar, A. A.; Zallo, A.; Zeng, Y.; Zhang, B. X.; Zhang, B. Y.; Zhang, C.; Zhang, C. C.; Zhang, D. H.; Zhang, H. H.; Zhang, H. Y.; Zhang, J. Q.; Zhang, J. W.; Zhang, J. Y.; Zhang, J. Z.; Zhang, S. H.; Zhang, X. J.; Zhang, X. Y.; Zhang, Y.; Zhang, Y. H.; Zhang, Y. S. ; Zhang, Z. P.; Zhang, Z. Y.; Zhao, G.; Zhao, H. S.; Zhao, J. W.; Zhao, K. X.; Zhao, Lei; Zhao, Ling; Zhao, M. G.; Zhao, Q.; Zhao, Q. Z.; Zhao, S. J.; Zhao, T. C.; Zhao, X. H.; Zhao, Y. B.; Zhao, Z. G.; Zhemchugov, A.; Zheng, B.; Zheng, J. P.; Zheng, Y. H.; Zhong, B.; Zhong, J.; Zhong, Z.; Zhou, L.; Zhou, X. K.; Zhou, X. R.; Zhu, C. ; Zhu, K.; Zhu, K. J.; Zhu, S. H.; Zhu, X. L.; Zhu, Y. C.; Zhu, Y. M.; Zhu, Y. S.; Zhu, Z. A.; Zhuang, J.; Zou, B. S.; Zou, J. H.: **Experimental study of** ψ **decays to** $K^+K^-\pi^0$ **and** $K^+K^-\eta$**.** *Physical review / D* 86: 072011, 2012. DOI:10.1103/PhysRevD.86.072011

WOS-PHN-26 Ablikim, M.; Achasov, M. N.; Alberto, D.; Ambrose, D. J.; An, F. F.; An, Q.; An, Z. H.; Bai, J. Z. ; Baldini Ferroli, R. B. F.; Ban, Y.; Becker, J.; Berger, N.; Bertani, M. B.; Bian, J. M.; Boger, E. ; Bondarenko, O.; Boyko, I.; Briere, R. A.; Bytev, V.; Cai, X.; Calcaterra, A. C.; Cao, G. F. ; Chang, J. F.; Chelkov, G.; Chen, G.; Chen, H. S.; Chen, J. C.; Chen, M. L.; Chen, S. J.; Chen, Y.; Chen, Y. B.; Cheng, H. P.; Chu, Y. P.; Cronin-Hennessy, D.; Dai, H. L.; Dai, J. P.; Dedovich, D.; Deng, Z. Y.; Denysenko, I.; Destefanis, M.; Ding Ding, W. L.; Ding, Y.; Dong, L. Y.; Dong, M. Y.; Du, S. X.; Fang, J.; Fang, S. S.; Feng, C. Q.; Fu, C. D.; Fu, J. L.; Gao, Y.; Geng, C.; Götzen, Klaus; Gong, W. X.; Greco, M.; Gu, M. H.; Gu, Y. T.; Guan, Y. H.; Guo, A. Q.; Guo, L. B.; Guo, Y. P.; Han, Y. L.; Hao, X. Q.; Harris, F. A.; He, K. L.; He, M.; He, Z. Y.; Heng, Y. K.; Hou, Z. L.; Hu, H. M.; Hu, J. F.; Hu, T.; Huang, B.; Huang, G. M.; Huang, J. S.; Huang, X. T.; Huang, Y. P.; Hussain, T.; Ji, C. S.; Ji, Q.; Ji, X. B.; Ji, X. L.; Jia, L. K.; Jiang, L. L.; Jiang, X. S.; Jiao, J. B. ; Jiao, Z.; Jin, D. P.; Jin, S.; Jing, F. F.; Kalantar-Nayestanaki, N.; Kavatsyuk, M.; Kuehn, W.; Lai, W.; Lange, J. S.; Leung, J. K. C.; Li, C. H. ; Li, Cheng; Li, Cui; Li, D. M.; Li, F.; Li, G.; Li, H. B.; Li, J. C.; Li, K.; Li, Lei; Li, N. B.; Li, Q. J.; Li, S. L.; Li, W. D.; Li, W. G.; Li, X. L.; Li, X. N.; Li, X. Q.; Li, X. R.; Li, Z. B.; Liang, H.; Liang, Y. F.; Liang, Y. T.; Liao, G. R.; Liao, X. T.; Liu, B. J.; Liu, C. L.; Liu, C. X.; Liu, C. Y.; Liu, F. H.; Liu, Fang; Liu, Feng; Liu, H.; Liu, H. B.; Liu, H. H.; Liu, H. M.; Liu, H. W.; Liu, J. P.; Liu, K.; Liu, K.; Liu, K. Y.; Liu, Q.; Liu, S. B.; Liu, X.; Liu, X. H.; Liu, Y. B.; Liu, Yong; Liu, Z. A.; Liu, Zhiqiang; Liu, Zhiqing; Loehner, H.; Lu, G. R.; Lu, H. J.; Lu, J. G.; Lu, Q. W.; Lu, X. R.; Lu, Y. P.; Luo, C. L.; Luo, M. X.; Luo, T.; Luo, X. L.; Lv, M.; Ma, C. L.; Ma, F. C.; Ma, H. L.; Ma, Q. M.; Ma, S.; Ma, T.; Ma, X. Y. ; Maggiora, M.; Malik, Q. A.; Mao, H.; Mao, Y. J. ; Mao, Z. P.; Messchendorp, J. G.; Min, J.; Min, T. J.; Mitchell, R. E.; Mo, X. H.; Muchnoi, N. Yu. ; Nefedov, Y.; Nikolaev, I. B.; Ning, Z.; Olsen, S. L.; Ouyang, Q.; Pacetti, S. P.; Park, J. W.; Pelizaeus, M.; Peters, K.; Ping, J. L.; Ping, R. G. ; Poling, R.; Pun, C. S. J.; Qi, M.; Qian, S.; Qiao, C. F.; Qin, X. S.; Qiu, J. F.; Rashid, K. H. ; Rong, G.; Ruan, X. D.; Sarantsev, A.; Schulze, J.; Shao, M.; Shen, C. P.; Shen, X. Y.; Sheng, H. Y.; Shepherd, M. R.; Song, X. Y.; Spataro, S. ; Spruck, B.; Sun, D. H.; Sun, G. X.; Sun, J. F. ; Sun, S. S.; Sun, X. D.; Sun, Y. J.; Sun, Y. Z. ; Sun, Z. J.; Sun, Z. T.; Tang, C. J.; Tang, X. ; Thorndike, E. H.; Tian, H. L.; Toth, D.; Varner, G. S.; Wan, X.; Wang, B.; Wang, B. Q.; Wang, K.; Wang, L. L.; Wang, L. S.; Wang, M.; Wang, P.; Wang, P. L.; Wang, Q.; Wang, Q. J.; Wang, S. G.; Wang, X. F.; Wang, X. L.; Wang, Y. D. ; Wang, Y. F.; Wang, Y. Q.; Wang, Z.; Wang, Z. G. ; Wang, Z. Y.; Wei, D. H.; Wen, Q. G.; Wen, S. P. ; Wiedner, U.; Wu, L. H.; Wu, N.; Wu, W.; Wu, Z.; Xiao, Z. J.; Xie, Y. G.; Xiu, Q. L.; Xu, G. F.; Xu, G. M.; Xu, H.; Xu, Q. J.; Xu, X. P.; Xu, Y.; Xu, Z. R.; Xue, Z.; Yan, L.; Yan, W. B. ; Yan, Y. H.; Yang, H. X.; Yang, T.; Yang, Y.; Yang, Y. X.; Ye, H.; Ye, M.; Ye, M. H.; Yu, B. X.; Yu, C. X.; Yu, S. P.; Yuan, C. Z.; Yuan, W. L.; Yuan, Y.; Zafar, A. A.; Zallo, A. Z.; Zeng, Y.; Zhang, B. X.; Zhang, B. Y.; Zhang, C. C.; Zhang, D. H.; Zhang, H. H.; Zhang, H. Y.; Zhang, J. ; Zhang, J. Q.; Zhang, J. W.; Zhang, J. Y.; Zhang, J. Z.; Zhang, L.; Zhang, S. H.; Zhang, T. R. ; Zhang, X. J.; Zhang, X. Y.; Zhang, Y.; Zhang, Y. H.; Zhang, Y. S.; Zhang, Z. P.; Zhang, Z. Y.; Zhao, G.; Zhao, H. S.; Zhao, Jingwei; Zhao, Lei; Zhao, Ling; Zhao, M. G.; Zhao, Q.; Zhao, S. J.; Zhao, T. C.; Zhao, X. H.; Zhao, Y. B.; Zhao, Z. G. ; Zhemchugov, A.; Zheng, B.; Zheng, J. P.; Zheng, Y. H.; Zheng, Z. P.; Zhong, B.; Zhong, J.; Zhou, L.; Zhou, X. K.; Zhou, X. R.; Zhu, C.; Zhu, K. ; Zhu, K. J.; Zhu, S. H.; Zhu, X. L.; Zhu, X. W. ; Zhu, Y. S.; Zhu, Z. A.; Zhuang, J.; Zou, B. S. ; Zou, J. H.; Zuo, J. X.: **First Observation of $\eta(1405)$ Decays into $f_0(980)\pi^0$.** *Physical review letters* 108: 182001, 2012. DOI:10.1103/PhysRevLett.108.182001

WOS-PHN-27 Ablikim, M.; Achasov, M. N.; Alberto, D.; Ambrose, D. J.; An, F. F.; An, Q.; An, Z. H.; Bai, J. Z. ; Baldini Ferroli, R. B. F.; Ban, Y.; Becker, J.; Berger, N.; Bertani, M. B.; Bian, J. M.; Boger, E. ; Bondarenko, O.; Boyko, I.; Briere, R. A.; Bytev, V.; Cai, X.; Calcaterra, A. C.; Cao, G. F. ; Chang, J. F.; Chelkov, G.; Chen, G.; Chen, H. S.; Chen, J. C.; Chen, M. L.; Chen, S. J.; Chen, Y.; Chen, Y. B.; Cheng, H. P.; Chu, Y. P.; Cronin-Hennessy, D.; Dai, H. L.; Dai, J. P.; Dedovich, D.; Deng, Z. Y.; Denysenko, I.; Destefanis, M.; Ding Ding, W. L.; Ding, Y.; Dong, L. Y.; Dong, M. Y.; Du, S. X.; Fang, J.; Fang, S. S.; Feng, C. Q.; Fu, C. D.; Fu, J. L.; Gao, Y.; Geng, C.; Götzen, Klaus; Gong, W. X.; Greco, M.; Gu, M. H.; Gu, Y. T.; Guan, Y. H.; Guo, A. Q.; Guo, L. B.; Guo, Y. P.; Han, Y. L.; Hao, X. Q.; Harris, F. A.; He, K. L.; He, M.; He, Z. Y.; Heng, Y. K.; Hou, Z. L.; Hu, H. M.; Hu, J. F.; Hu, T.; Huang, B.; Huang, G. M.; Huang, J. S.; Huang, X. T.; Huang, Y. P.; Hussain, T.; Ji, C. S.; Ji, Q.; Ji, X. B.; Ji, X. L.; Jia, L. K.; Jiang, L. L.; Jiang, X. S.; Jiao, J. B. ; Jiao, Z.; Jin, D. P.; Jin, S.; Jing, F. F.; Kalantar-Nayestanaki, N.; Kavatsyuk, M.; Kuehn, W.; Lai, W.; Lange, J. S.; Leung, J. K. C.; Li, C. H. ; Li, Cheng; Li, Cui; Li, D. M.; Li, F.; Li, G.; Li, H. B.; Li, J. C.; Li, K.; Li, Lei; Li, N. B.; Li, Q. J.; Li, S. L.; Li, W. D.; Li, W. G.; Li, X. L.; Li, X. N.; Li, X. Q.; Li, X. R.; Li, Z. B.; Liang, H.; Liang, Y. F.; Liang, Y. T.; Liao, G. R.; Liao, X. T.; Liu, B. J.; Liu, C. L.; Liu, C. X.; Liu, C. Y.; Liu, F. H.; Liu, Fang; Liu, Feng; Liu, H.; Liu, H. B.; Liu, H. H.; Liu, H. M.; Liu, H. W.; Liu, J. P.; Liu, K.; Liu, K.; Liu, K. Y.; Liu, Q.; Liu, S. B.; Liu, X.; Liu, X. H.; Liu, Y. B.; Liu, Yong; Liu, Z. A.; Liu, Zhiqiang; Liu, Zhiqing; Loehner, H.; Lu, G. R.; Lu, H. J.; Lu, J. G.; Lu, Q. W.; Lu, X. R.; Lu, Y. P.; Luo, C. L.; Luo, M. X.; Luo, T.; Luo, X. L.; Lv, M.; Ma, C. L.; Ma, F. C.; Ma, H. L.; Ma, Q. M.; Ma, S.; Ma, T.; Ma, X. Y. ; Maggiora, M.; Malik, Q. A.; Mao, H.; Mao, Y. J. ; Mao, Z. P.; Messchendorp, J. G.; Min, J.; Min, T. J.; Mitchell, R. E.; Mo, X. H.; Muchnoi, N. Yu. ; Nefedov, Y.; Nikolaev, I. B.; Ning, Z.; Olsen, S. L.; Ouyang, Q.; Pacetti, S. P.; Park, J. W.; Pelizaeus, M.; Peters, K.; Ping, J. L.; Ping, R. G. ; Poling, R.; Pun, C. S. J.; Qi, M.; Qian, S.; Qiao, C. F.; Qin, X. S.; Qiu, J. F.; Rashid, K. H. ; Rong, G.; Ruan, X. D.; Sarantsev, A.; Schulze, J.; Shao, M.; Shen, C. P.; Shen, X. Y.; Sheng, H. Y.; Shepherd, M. R.; Song, X. Y.; Spataro, S. ; Spruck, B.; Sun, D. H.; Sun, G. X.; Sun, J. F. ; Sun, S. S.; Sun, X. D.; Sun, Y. J.; Sun, Y. Z. ; Sun, Z. J.; Sun, Z. T.; Tang, C. J.; Tang, X. ; Thorndike, E. H.; Tian, H. L.; Toth, D.; Varner, G. S.; Wang, B.; Wang, B. Q.; Wang, K.; Wang, L. L.; Wang, L. S.; Wang, M.; Wang, P.; Wang, P. L.; Wang, Q.; Wang, Q. J.; Wang, S. G.; Wang, X. F.; Wang, X. L.; Wang, Y. D.; Wang, Y. F. ; Wang, Y. Q.; Wang, Z.; Wang, Z. G.; Wang, Z. Y. ; Wei, D. H.; Wen, Q. G.; Wen, S. P.; Wiedner, U. ; Wu, L. H.; Wu, N.; Wu, W.; Wu, Z.; Xiao, Z. J.; Xie, Y. G.; Xiu, Q. L.; Xu, G. F.; Xu, G. M. ; Xu, H.; Xu, Q. J.; Xu, X. P.; Xu, Y.; Xu, Z. R.; Xue, Z.; Yan, L.; Yan, W. B.; Yan, Y. H.; Yang, H. X.; Yang, T.; Yang, Y.; Yang, Y. X.; Ye, H.; Ye, M.; Ye, M. H.; Yu, B. X.; Yu, C. X. ; Yu, S. P.; Yuan, C. Z.; Yuan, W. L.; Yuan, Y. ; Zafar, A. A.; Zallo, A. Z.; Zeng, Y.; Zhang, B. X.; Zhang, B. Y.; Zhang, C. C.; Zhang, D. H.; Zhang, H. H.; Zhang, H. Y.; Zhang, J.; Zhang, J. Q. ; Zhang, J. W.; Zhang, J. Y.; Zhang, J. Z.; Zhang, L.; Zhang, S. H.; Zhang, T. R.; Zhang, X. J. ; Zhang, X. Y.; Zhang, Y.; Zhang, Y. H.; Zhang, Y. S.; Zhang, Z. P.; Zhang, Z. Y.; Zhao, G.; Zhao, H. S.; Zhao, Jingwei; Zhao,

Lei; Zhao, Ling ; Zhao, M. G.; Zhao, Q.; Zhao, S. J.; Zhao, T. C. ; Zhao, X. H.; Zhao, Y. B.; Zhao, Z. G.; Zhemchugov, A.; Zheng, B.; Zheng, J. P.; Zheng, Y. H.; Zheng, Z. P.; Zhong, B.; Zhong, J.; Zhou, L. ; Zhou, X. K.; Zhou, X. R.; Zhu, C.; Zhu, K.; Zhu, K. J.; Zhu, S. H.; Zhu, X. L.; Zhu, X. W.; Zhu, Y. S.; Zhu, Z. A.; Zhuang, J.; Zou, B. S.; Zou, J. H.; Zuo, J. X.: **Spin-Parity Analysis of $pp[over]$ Mass Threshold Structure in J/ψ and ψ(3686) Radiative Decays.** *Physical review letters* 108: 112003, 2012. DOI:10.1103/PhysRevLett.108.112003

WOS-PHN-28 Ablikim, M.; Achasov, M. N.; Alberto, D.; Ambrose, D. J.; An, F. F.; An, Q.; An, Z. H.; Bai, J. Z. ; Ferroli, R. B.; Ban, Y.; Becker, J.; Berger, N. ; Bertani, M. B.; Bian, J. M.; Boger, E.; Bondarenko, O.; Boyko, I.; Briere, R. A.; Bytev, V. ; Cai, X.; Calcaterra, A. C.; Cao, G. F.; Chang, J. F.; Chelkov, G.; Chen, G.; Chen, H. S.; Chen, H. X.; Chen, J. C.; Chen, M. L.; Chen, S. J.; Chen, Y.; Chen, Y. B.; Cheng, H. P.; Chu, Y. P.; Cronin-Hennessy, D.; Dai, H. L.; Dai, J. P.; Dedovich, D.; Deng, Z. Y.; Denysenko, I.; Destefanis, M.; Ding, W. L.; Ding, Y.; Dong, L. Y. ; Dong, M. Y.; Du, S. X.; Fang, J.; Fang, S. S. ; Feng, C. Q.; Fu, C. D.; Fu, J. L.; Gao, Y.; Geng, C.; Götzen, Klaus; Gong, W. X.; Greco, M. ; Gu, M. H.; Gu, Y. T.; Guan, Y. H.; Guo, A. Q. ; Guo, L. B.; Guo, Y. P.; Han, Y. L.; Hao, X. Q. ; Harris, F. A.; He, K. L.; He, M.; He, Z. Y.; Heng, Y. K.; Hou, Z. L.; Hu, H. M.; Hu, J. F.; Hu, T.; Huang, B.; Huang, G. M.; Huang, J. S.; Huang, X. T.; Huang, Y. P.; Hussain, T.; Ji, C. S. ; Ji, Q.; Ji, X. B.; Ji, X. L.; Jia, L. K.; Jiang, L. L.; Jiang, X. S.; Jiao, J. B.; Jiao, Z. ; Jin, D. P.; Jin, S.; Jing, F. F.; Kalantar-Nayestanaki, N.; Kavatsyuk, M.; Kuehn, W.; Lai, W.; Lange, J. S.; Leung, J. K. C.; Li, C. H. ; Li, Cheng; Li, Cui; Li, D. M.; Li, F.; Li, G.; Li, H. B.; Li, J. C.; Li, K.; Li, Lei; Li, N. B.; Li, Q. J.; Li, S. L.; Li, W. D.; Li, W. G.; Li, X. L.; Li, X. N.; Li, X. Q.; Li, X. R.; Li, Z. B.; Liang, H.; Liang, Y. F.; Liang, Y. T.; Liao, G. R.; Liao, X. T.; Liu, B. J.; Liu, C. L.; Liu, C. X.; Liu, C. Y.; Liu, F. H.; Liu, Fang; Liu, Feng; Liu, H.; Liu, H. B.; Liu, H. H.; Liu, H. M.; Liu, H. W.; Liu, J. P.; Liu, K.; Liu, K.; Liu, K. Y.; Liu, Q.; Liu, S. B.; Liu, X.; Liu, X. H.; Liu, Y. B.; Liu, Yong; Liu, Z. A.; Liu, Zhiqiang; Liu, Zhiqing; Loehner, H.; Lu, G. R.; Lu, H. J.; Lu, J. G.; Lu, Q. W.; Lu, X. R.; Lu, Y. P.; Luo, C. L.; Luo, M. X.; Luo, T.; Luo, X. L.; Lv, M.; Ma, C. L.; Ma, F. C.; Ma, H. L.; Ma, Q. M.; Ma, S.; Ma, T.; Ma, X. Y. ; Maggiora, M.; Malik, Q. A.; Mao, H.; Mao, Y. J. ; Mao, Z. P.; Messchendorp, J. G.; Min, J.; Min, T. J.; Mitchell, R. E.; Mo, X. H.; Muchnoi, N. Yu. ; Nefedov, Y.; Nikolaev, I. B.; Ning, Z.; Olsen, S. L.; Ouyang, Q.; Pacetti, S. P.; Park, J. W.; Pelizaeus, M.; Peters, K.; Ping, J. L.; Ping, R. G. ; Poling, R.; Pun, C. S. J.; Qi, M.; Qian, S.; Qiao, C. F.; Qin, X. S.; Qiu, J. F.; Rashid, K. H. ; Rong, G.; Ruan, X. D.; Sarantsev, A.; Schulze, J.; Shao, M.; Shen, C. P.; Shen, X. Y.; Sheng, H. Y.; Shepherd, M. R.; Song, X. Y.; Spataro, S. ; Spruck, B.; Sun, D. H.; Sun, G. X.; Sun, J. F. ; Sun, S. S.; Sun, X. D.; Sun, Y. J.; Sun, Y. Z. ; Sun, Z. J.; Sun, Z. T.; Tang, C. J.; Tang, X. ; Thorndike, E. H.; Tian, H. L.; Toth, D.; Varner, G. S.; Wang, B.; Wang, B. Q.; Wang, K.; Wang, L. L.; Wang, L. L.; Wang, L. S.; Wang, M.; Wang, P.; Wang, P. L.; Wang, Q.; Wang, Q. J.; Wang, S. G.; Wang, X. F.; Wang, X. L.; Wang, Y. D. ; Wang, Y. F.; Wang, Y. Q.; Wang, Z.; Wang, Z. G. ; Wang, Z. Y.; Wei, D. H.; Wen, Q. G.; Wen, S. P. ; Wiedner, U.; Wu, L. H.; Wu, N.; Wu, W.; Wu, Z.; Xiao, Z. J.; Xie, Y. G.; Xiu, Q. L.; Xu, G. F.; Xu, G. M.; Xu, H.; Xu, Q. J.; Xu, X. P.; Xu, Y.; Xu, Z. R.; Xue, Z.; Yan, L.; Yan, W. B. ; Yan, Y. H.; Yang, H. X.; Yang, T.; Yang, Y.; Yang, Y. X.; Ye, H.; Ye, M.; Ye, M. H.; Yu, B. X.; Yu, C. X.; Yu, S. P.; Yuan, C. Z.; Yuan, W. L.; Yuan, Y.; Zafar, A. A.; Zallo, A. Z.; Zeng, Y.; Zhang, B. X.; Zhang, B. Y.; Zhang, C. C.; Zhang, D. H.; Zhang, H. H.; Zhang, H. Y.; Zhang, J. ; Zhang, J. Q.; Zhang, J. W.; Zhang, J. Y.; Zhang, J. Z.; Zhang, L.; Zhang, S. H.; Zhang, T. R. ; Zhang, X. J.; Zhang, X. Y.; Zhang, Y.; Zhang, Y. H.; Zhang, Y. S.; Zhang, Z. P.; Zhang, Z. Y.; Zhao, G.; Zhao, H. S.; Zhao, Jingwei; Zhao, Lei; Zhao, Ling; Zhao, M. G.; Zhao, Q.; Zhao, S. J.; Zhao, T. C.; Zhao, X. H.; Zhao, Y. B.; Zhao, Z. G. ; Zhemchugov, A.; Zheng, B.; Zheng, J. P.; Zheng, Y. H.; Zheng, Z. P.; Zhong, B.; Zhong, J.; Zhou, L.; Zhou, X. K.; Zhou, X. R.; Zhu, C.; Zhu, K. ; Zhu, K. J.; Zhu, S. H.; Zhu, X. L.; Zhu, X. W. ; Zhu, Y. S.; Zhu, Z. A.; Zhuang, J.; Zou, B. S. ; Zou, J. H.; Zuo, J. X.: **Measurements of the Mass and Width of the η_c Using the Decay $\psi(3686) \rightarrow \gamma\eta_c$.** *Physical review letters* 108: 222002, 2012. DOI:10.1103/PhysRevLett.108.222002

WOS-PHN-29 Ablikim, M.; Achasov, M. N.; Ambrose, D. J.; An, F. F.; An, Q.; An, Z. H.; Bai, J. Z.; Ban, Y. ; Becker, J.; Bennett, J. V.; Bertani, M.; Bian, J. M.; Boger, E.; Bondarenko, O.; Boyko, I.; Briere, R. A.; Bytev, V.; Cai, X.; Cakir, O.; Calcaterra, A.; Cao, G. F.; Cetin, S. A.; Chang, J. F.; Chelkov, G.; Chen, G.; Chen, H. S.; Chen, J. C.; Chen, M. L.; Chen, S. J.; Chen, Y. B.; Cheng, H. P.; Chu, Y. P.; Cronin-Hennessy, D.; Dai, H. L.; Dai, J. P.; Dedovich, D.; Deng, Z. Y.; Denig, A.; Denysenko, I.; Destefanis, M.; Ding, W. M.; Ding, Y.; Dong, L. Y.; Dong, M. Y.; Du, S. X.; Fang, J.; Fang, S. S.; Fava, L.; Feldbauer, F.; Feng, C. Q.; Ferroli, R. B.; Fu, C. D.; Fu, J. L.; Gao, Y.; Geng, C.; Götzen, Klaus; Gong, W. X.; Gradl, W.; Greco, M.; Gu, M. H.; Gu, Y. T.; Guan, Y. H.; Guo, A. Q.; Guo, L. B.; Guo, Y. P.; Han, Y. L.; Harris, F. A.; He, K. L.; He, M. ; He, Z. Y.; Held, T.; Heng, Y. K.; Hou, Z. L. ; Hu, H. M.; Hu, J. F.; Hu, T.; Huang, G. M.; Huang, J. S.; Huang, X. T.; Huang, Y. P.; Hussain, T.; Ji, C. S.; Ji, Q.; Ji, X. B.; Ji, X. L.; Jiang, L. L.; Jiang, X. S.; Jiao, J. B.; Jiao, Z. ; Jin, D. P.; Jin, S.; Jing, F. F.; Kalantar-Nayestanaki, N.; Kavatsyuk, M.; Kuehn, W.; Lai, W.; Lange, J. S.; Li, C. H.; Li, Cheng; Li, Cui; Li, D. M.; Li, F.; Li, G.; Li, H. B.; Li, J. C.; Li, K.; Li, Lei; Li, Q. J.; Li, S. L. ; Li, W. D.; Li, W. G.; Li, X. L.; Li, X. N.; Li, X. Q.; Li, X. R.; Li, Z. B.; Liang, H.; Liang, Y. F.; Liang, Y. T.; Liao, G. R.; Liao, X. T.; Liu, B. J.; Liu, C. L.; Liu, C. X.; Liu, C. Y.; Liu, F. H.; Liu, Fang; Liu, Feng; Liu, H. ; Liu, H. B.; Liu, H. H.; Liu, H. M.; Liu, H. W. ; Liu, J. P.; Liu, K. Y.; Liu, Kai; Liu, P. L. ; Liu, Q.; Liu, S. B.; Liu, X.; Liu, X. H.; Liu, Y. B.; Liu, Z. A.; Liu, Zhiqiang; Liu, Zhiqing ; Loehner, H.; Lu, G. R.; Lu, H. J.; Lu, J. G. ; Lu, Q. W.; Lu, X. R.; Lu, Y. P.; Luo, C. L.; Luo, M. X.; Luo, T.; Luo, X. L.; Lv, M.; Ma, C. L.; Ma, F. C.; Ma, H. L.; Ma, Q. M.; Ma, S.; Ma, T.; Ma, X. Y.; Ma, Y.; Maas, F. E.; Maggiora, M.; Malik, Q. A.; Mao, Y. J.; Mao, Z. P. ; Messchendorp, J. G.; Min, J.; Min, T. J.; Mitchell, R. E.; Mo, X. H.; Morales Morales, C.; Motzko, C.; Muchnoi, N. Yu.; Muramatsu, H.; Nefedov, Y.; Nicholson, C.; Nikolaev, I. B.; Ning, Z.; Olsen, S. L.; Ouyang, Q.; Pacetti, S.; Park, J. W.; Pelizaeus, M.; Peng, H. P.; Peters, K.; Ping, J. L.; Ping, R. G.; Poling, R.; Prencipe, E. ; Qi, M.; Qian, S.; Qiao, C. F.; Qin, X. S.; Qin, Y.; Qin, Z. H.; Qiu, J. F.; Rashid, K. H.; Rong, G.; Ruan, X. D.; Sarantsev, A.; Schaefer, B. D.; Schulze, J.; Shao, M.; Shen, C. P.; Shen, X. Y.; Sheng, H. Y.; Shepherd, M. R.; Song, X. Y.; Spataro, S.; Spruck, B.; Sun, D. H.; Sun, G. X.; Sun, J. F.; Sun, S. S.; Sun, Y. J.; Sun, Y. Z.; Sun, Z. J.; Sun, Z. T.; Tang, C. J.; Tang, X.; Tapan, I.; Thorndike, E. H.; Toth, D.; Ullrich, M. ; Varner, G. S.; Wang, B.; Wang, B. Q.; Wang, K. ; Wang, L. L.; Wang, L. S.; Wang, M.; Wang, P. ; Wang, P. L.; Wang, Q.; Wang, Q. J.; Wang, S. G. ; Wang, X. L.; Wang, Y. D.; Wang, Y. F.; Wang, Y. Q.; Wang, Z.; Wang, Z. G.; Wang, Z. Y.; Wei, D. H.;

Weidenkaff, P.; Wen, Q. G.; Wen, S. P.; Werner, M.; Wiedner, U.; Wu, L. H.; Wu, N.; Wu, S. X.; Wu, W.; Wu, Z.; Xia, L. G.; Xiao, Z. J. ; Xie, Y. G.; Xiu, Q. L.; Xu, G. F.; Xu, G. M. ; Xu, H.; Xu, Q. J.; Xu, X. P.; Xu, Z. R.; Xue, F.; Xue, Z.; Yan, L.; Yan, W. B.; Yan, Y. H.; Yang, H. X.; Yang, Y.; Yang, Y. X.; Ye, H. ; Ye, M.; Ye, M. H.; Yu, B. X.; Yu, C. X.; Yu, J. S.; Yu, S. P.; Yuan, C. Z.; Yuan, Y.; Zafar, A. A.; Zallo, A.; Zeng, Y.; Zhang, B. X.; Zhang, B. Y.; Zhang, C. C.; Zhang, D. H.; Zhang, H. H.; Zhang, H. Y.; Zhang, J. Q.; Zhang, J. W.; Zhang, J. Y.; Zhang, J. Z.; Zhang, S. H.; Zhang, X. J.; Zhang, X. Y.; Zhang, Y.; Zhang, Y. H.; Zhang, Y. S. ; Zhang, Z. P.; Zhang, Z. Y.; Zhao, G.; Zhao, H. S.; Zhao, J. W.; Zhao, K. X.; Zhao, Lei; Zhao, Ling; Zhao, M. G.; Zhao, Q.; Zhao, S. J.; Zhao, T. C.; Zhao, X. H.; Zhao, Y. B.; Zhao, Z. G.; Zhemchugov, A.; Zheng, B.; Zheng, J. P.; Zheng, Y. H.; Zhong, B.; Zhong, J.; Zhou, L.; Zhou, X. K. ; Zhou, X. R.; Zhu, C.; Zhu, K.; Zhu, K. J.; Zhu, S. H.; Zhu, X. L.; Zhu, X. W.; Zhu, Y. C.; Zhu, Y. M.; Zhu, Y. S.; Zhu, Z. A.; Zhuang, J.; Zou, B. S.; Zou, J. H.: **Observation of χ_{cJ} decays to $\Lambda\Lambda[over]\pi^+\pi^-$.** *Physical review / D* 86: 052004, 2012. DOI:10.1103/PhysRevD.86.052004

WOS-PHN-30 Ablikim, M.; Achasov, M. N.; Ambrose, D. J.; An, F. F.; An, Q.; An, Z. H.; Bai, J. Z.; Ban, Y. ; Becker, J.; Bennett, J. V.; Bertani, M.; Bian, J. M.; Boger, E.; Bondarenko, O.; Boyko, I.; Briere, R. A.; Bytev, V.; Cai, X.; Cakir, O.; Calcaterra, A.; Cao, G. F.; Cetin, S. A.; Chang, J. F.; Chelkov, G.; Chen, G.; Chen, H. S.; Chen, J. C.; Chen, M. L.; Chen, S. J.; Chen, Y. B.; Cheng, H. P.; Chu, Y. P.; Cronin-Hennessy, D.; Dai, H. L.; Dai, J. P.; Dedovich, D.; Deng, Z. Y.; Denig, A.; Denysenko, I.; Destefanis, M.; Ding, W. M.; Ding, Y.; Dong, L. Y.; Dong, M. Y.; Du, S. X.; Fang, J.; Fang, S. S.; Fava, L.; Feldbauer, F.; Feng, C. Q.; Ferroli, R. B.; Fu, C. D.; Fu, J. L.; Gao, Y.; Geng, C.; Götzen, Klaus; Gong, W. X.; Gradl, W.; Greco, M.; Gu, M. H.; Gu, Y. T.; Guan, Y. H.; Guo, A. Q.; Guo, L. B.; Guo, Y. P.; Han, Y. L.; Harris, F. A.; He, K. L.; He, M. ; He, Z. Y.; Held, T.; Heng, Y. K.; Hou, Z. L. ; Hu, H. M.; Hu, J. F.; Hu, T.; Huang, G. M.; Huang, J. S.; Huang, X. T.; Huang, Y. P.; Hussain, T.; Ji, C. S.; Ji, Q.; Ji, X. B.; Ji, X. L.; Jiang, L. L.; Jiang, X. S.; Jiao, J. B.; Jiao, Z. ; Jin, D. P.; Jin, S.; Jing, F. F.; Kalantar-Nayestanaki, N.; Kavatsyuk, M.; Kuehn, W.; Lai, W.; Lange, J. S.; Li, C. H.; Li, Cheng; Li, Cui; Li, D. M.; Li, F.; Li, G.; Li, H. B.; Li, J. C.; Li, K.; Li, Lei; Li, Q. J.; Li, S. L. ; Li, W. D.; Li, W. G.; Li, X. L.; Li, X. N.; Li, X. Q.; Li, X. R.; Li, Z. B.; Liang, H.; Liang, Y. F.; Liang, Y. T.; Liao, G. R.; Liao, X. T.; Liu, B. J.; Liu, C. L.; Liu, C. X.; Liu, C. Y.; Liu, F. H.; Liu, Fang; Liu, Feng; Liu, H. ; Liu, H. B.; Liu, H. H.; Liu, H. M.; Liu, H. W. ; Liu, J. P.; Liu, K. Y.; Liu, Kai; Liu, P. L. ; Liu, Q.; Liu, S. B.; Liu, X.; Liu, X. H.; Liu, Y. B.; Liu, Z. A.; Liu, Zhiqiang; Liu, Zhiqing ; Loehner, H.; Lu, G. R.; Lu, H. J.; Lu, J. G. ; Lu, Q. W.; Lu, X. R.; Lu, Y. P.; Luo, C. L.; Luo, M. X.; Luo, T.; Luo, X. L.; Lv, M.; Ma, C. L.; Ma, F. C.; Ma, H. L.; Ma, Q. M.; Ma, S.; Ma, T.; Ma, X. Y.; Ma, Y.; Maas, F. E.; Maggiora, M.; Malik, Q. A.; Mao, Y. J.; Mao, Z. P. ; Messchendorp, J. G.; Min, J.; Min, T. J.; Mitchell, R. E.; Mo, X. H.; Morales, C. Morales; Motzko, C.; Muchnoi, N. Yu.; Muramatsu, H.; Nefedov, Y.; Nicholson, C.; Nikolaev, I. B.; Ning, Z.; Olsen, S. L.; Ouyang, Q.; Pacetti, S.; Park, J. W.; Pelizaeus, M.; Peng, H. P.; Peters, K.; Ping, J. L.; Ping, R. G.; Poling, R.; Prencipe, E. ; Qi, M.; Qian, S.; Qiao, C. F.; Qin, X. S.; Qin, Y.; Qin, Z. H.; Qiu, J. F.; Rashid, K. H.; Rong, G.; Ruan, X. D.; Sarantsev, A.; Schaefer, B. D.; Schulze, J.; Shao, M.; Shen, C. P.; Shen, X. Y.; Sheng, H. Y.; Shepherd, M. R.; Song, W. M.; Song, X. Y.; Spataro, S.; Spruck, B.; Sun, D. H. ; Sun, G. X.; Sun, J. F.; Sun, S. S.; Sun, Y. J. ; Sun, Y. Z.; Sun, Z. J.; Sun, Z. T.; Tang, C. J. ; Tang, X.; Tapan, I.; Thorndike, E. H.; Toth, D. ; Ullrich, M.; Varner, G. S.; Wang, B.; Wang, B. Q.; Wang, K.; Wang, L. L.; Wang, L. S.; Wang, M. ; Wang, P.; Wang, P. L.; Wang, Q.; Wang, Q. J. ; Wang, S. G.; Wang, X. L.; Wang, Y. D.; Wang, Y. F.; Wang, Y. Q.; Wang, Z.; Wang, Z. G.; Wang, Z. Y.; Wei, D. H.; Weidenkaff, P.; Wen, Q. G.; Wen, S. P.; Werner, M.; Wiedner, U.; Wu, L. H.; Wu, N.; Wu, S. X.; Wu, W.; Wu, Z.; Xia, L. G.; Xiao, Z. J.; Xie, Y. G.; Xiu, Q. L.; Xu, G. F.; Xu, G. M.; Xu, H.; Xu, Q. J.; Xu, X. P.; Xu, Z. R.; Xue, F.; Xue, Z.; Yan, L.; Yan, W. B.; Yan, Y. H.; Yang, H. X.; Yang, Y.; Yang, Y. X.; Ye, H.; Ye, M.; Ye, M. H.; Yu, B. X.; Yu, C. X. ; Yu, J. S.; Yu, S. P.; Yuan, C. Z.; Yuan, Y.; Zafar, A. A.; Zallo, A.; Zeng, Y.; Zhang, B. X.; Zhang, B. Y.; Zhang, C. C.; Zhang, D. H.; Zhang, H. H.; Zhang, H. Y.; Zhang, J. Q.; Zhang, J. W.; Zhang, J. Y.; Zhang, J. Z.; Zhang, S. H.; Zhang, X. J.; Zhang, X. Y.; Zhang, Y.; Zhang, Y. H.; Zhang, Y. S.; Zhang, Z. P.; Zhang, Z. Y.; Zhao, G. ; Zhao, H. S.; Zhao, J. W.; Zhao, K. X.; Zhao, Lei; Zhao, Ling; Zhao, M. G.; Zhao, Q.; Zhao, S. J.; Zhao, T. C.; Zhao, X. H.; Zhao, Y. B.; Zhao, Z. G.; Zhemchugov, A.; Zheng, B.; Zheng, J. P.; Zheng, Y. H.; Zhong, B.; Zhong, J.; Zhou, L.; Zhou, X. K.; Zhou, X. R.; Zhu, C.; Zhu, K.; Zhu, K. J.; Zhu, S. H.; Zhu, X. L.; Zhu, X. W.; Zhu, Y. C.; Zhu, Y. M.; Zhu, Y. S.; Zhu, Z. A.; Zhuang, J.; Zou, B. S.; Zou, J. H.: **Observation of $e^+e^- \to \eta J/\psi$ at center-of-mass energy $\sqrt{s} = 4.009$GeV.** *Physical review / D* 86: 071101, 2012. DOI:10.1103/PhysRevD.86.071101

WOS-PHN-31 Ablikim, M.; Achasov, M. N.; Ambrose, D. J.; An, F. F.; An, Q.; An, Z. H.; Bai, J. Z.; Ban, Y. ; Becker, J.; Berger, N.; Bertani, M. B.; Bian, J. M.; Boger, E.; Bondarenko, O.; Boyko, I.; Briere, R. A.; Bytev, V.; Cai, X.; Calcaterra, A. C.; Cao, G. F.; Chang, J. F.; Chelkov, G.; Chen, G.; Chen, H. S.; Chen, J. C.; Chen, M. L.; Chen, S. J.; Chen, Y.; Chen, Y. B.; Cheng, H. P.; Chu, Y. P.; Cronin-Hennessy, D.; Dai, H. L.; Dai, J. P. ; Dedovich, D.; Deng, Z. Y.; Denig, A.; Denysenko, I.; Destefanis, M.; Ding, W. M.; Ding, Y.; Dong, L. Y.; Dong, M. Y.; Du, S. X.; Fang, J.; Fang, S. S.; Fava, L.; Feldbauer, F.; Feng, C. Q.; Ferroli, R. B.; Fu, C. D.; Fu, J. L.; Gao, Y.; Geng, C.; Götzen, Klaus; Gong, W. X.; Gradl, W.; Greco, M.; Gu, M. H.; Gu, Y. T.; Guan, Y. H.; Guo, A. Q.; Guo, L. B.; Guo, Y. P.; Han, Y. L.; Hao, X. Q.; Harris, F. A.; He, K. L. ; He, M.; He, Z. Y.; Held, T.; Heng, Y. K.; Hou, Z. L.; Hu, H. M.; Hu, J. F.; Hu, T.; Huang, B.; Huang, G. M.; Huang, J. S.; Huang, X. T.; Huang, Y. P.; Hussain, T.; Ji, C. S.; Ji, Q.; Ji, X. B.; Ji, X. L.; Jia, L. K.; Jiang, L. L.; Jiang, X. S.; Jiao, J. B.; Jiao, Z.; Jin, D. P.; Jin, S.; Jing, F. F.; Kalantar-Nayestanaki, N.; Kavatsyuk, M.; Kuehn, W.; Lai, W.; Lange, J. S.; Leung, J. K. C.; Li, C. H.; Li, Cheng; Li, Cui; Li, D. M.; Li, F.; Li, G.; Li, H. B.; Li, J. C. ; Li, K.; Li, Lei; Li, N. B.; Li, Q. J.; Li, S. L.; Li, W. D.; Li, W. G.; Li, X. L.; Li, X. N.; Li, X. Q.; Li, X. R.; Li, Z. B.; Liang, H. ; Liang, Y. F.; Liang, Y. T.; Liao, G. R.; Liao, X. T.; Liu, B. J.; Liu, B. J.; Liu, C. L.; Liu, C. X.; Liu, C. Y.; Liu, F. H.; Liu, Fang; Liu, Feng; Liu, H.; Liu, H. B.; Liu, H. H.; Liu, H. M.; Liu, H. W.; Liu, J. P.; Liu, K.; Liu, K.; Liu, K. Y.; Liu, S. B.; Liu, X.; Liu, X. H.; Liu, Y. B.; Liu, Yong; Liu, Z. A.; Liu, Zhiqiang ; Liu, Zhiqing; Loehner, H.; Lu, G. R.; Lu, H. J. ; Lu, J. G.; Lu, Q. W.; Lu, X. R.; Lu, Y. P.; Luo, C. L.; Luo, M. X.; Luo, T.; Luo, X. L.; Lv, M.; Ma, C. L.; Ma, F. C.; Ma, H. L.; Ma, Q. M. ; Ma, S.; Ma, T.; Ma, X. Y.; Ma, Y.; Maas, F. E.; Maggiora, M.; Malik, Q. A.; Mao, H.; Mao, Y. J.; Mao, Z. P.; Messchendorp, J. G.; Min, J.; Min, T. J.; Mitchell, R. E.; Mo, X. H.; Morales, C. ; Motzko, C.; Muchnoi, N. Yu.; Nefedov, Y.; Nikolaev, I.B.; Ning, Z.; Olsen, S. L.; Ouyang, Q.; Pacetti, S. P.; Park, J. W.; Pelizaeus, M.; Peters, K.; Ping, J. L.; Ping, R.

G.; Poling, R. ; Prencipe, E.; Pun, C. S. J.; Qi, M.; Qian, S. ; Qiao, C. F.; Qin, X. S.; Qin, Y.; Qin, Z. H. ; Qiu, J. F.; Rashid, K. H.; Rong, G.; Ruan, X. D.; Sarantsev, A.; Schulze, J.; Shao, M.; Shen, C. P.; Shen, X. Y.; Sheng, H. Y.; Shepherd, M. R. ; Song, X. Y.; Spataro, S.; Spruck, B.; Sun, D. H.; Sun, G. X.; Sun, J. F.; Sun, S. S.; Sun, X. D.; Sun, Y. J.; Sun, Y. Z.; Sun, Z. J.; Sun, Z. T.; Tang, C. J.; Tang, X.; Thorndike, E. H.; Tian, H. L.; Toth, D.; Ulrich, M. U.; Varner, G. S. ; Wang, B.; Wang, B. Q.; Wang, K.; Wang, L. L. ; Wang, L. S.; Wang, M.; Wang, P.; Wang, P. L. ; Wang, Q.; Wang, Q. J.; Wang, S. G.; Wang, X. F. ; Wang, X. L.; Wang, Y. D.; Wang, Y. F.; Wang, Y. Q.; Wang, Z.; Wang, Z. G.; Wang, Z. Y.; Wei, D. H.; Weidenkaff, P.; Wen, Q. G.; Wen, S. P.; Werner, M.W.; Wiedner, U.; Wu, L. H.; Wu, N.; Wu, S. X.; Wu, W.; Wu, Z.; Xia, L. G.; Xiao, Z. J.; Xie, Y. G.; Xiu, Q. L.; Xu, G. F.; Xu, G. M. ; Xu, H.; Xu, Q. J.; Xu, X. P.; Xu, Y.; Xu, Z. R.; Xue, F.; Xue, Z.; Yan, L.; Yan, W. B.; Yan, Y. H.; Yang, H. X.; Yang, T.; Yang, Y.; Yang, Y. X.; Ye, H.; Ye, M.; Ye, M. H.; Yu, B. X.; Yu, C. X.; Yu, J. S.; Yu, S. P.; Yuan, C. Z. ; Yuan, W. L.; Yuan, Y.; Zafar, A. A.; Zallo, A. Z.; Zeng, Y.; Zhang, B. X.; Zhang, B. Y.; Zhang, C. C.; Zhang, D. H.; Zhang, H. H.; Zhang, H. Y.; Zhang, J.; Zhang, J. Q.; Zhang, J. W.; Zhang, J. Y. ; Zhang, J. Z.; Zhang, L.; Zhang, S. H.; Zhang, T. R.; Zhang, X. J.; Zhang, X. Y.; Zhang, Y.; Zhang, Y. H.; Zhang, Y. S.; Zhang, Z. P.; Zhang, Z. Y.; Zhao, G.; Zhao, H. S.; Zhao, Jingwei; Zhao, K. X.; Zhao, Lei; Zhao, Ling; Zhao, M. G.; Zhao, Q.; Zhao, S. J.; Zhao, T. C.; Zhao, X. H.; Zhao, Y. B.; Zhao, Z. G.; Zhemchugov, A.; Zheng, B.; Zheng, J. P.; Zheng, Y. H.; Zheng, Z. P.; Zhong, B. ; Zhong, J.; Zhou, L.; Zhou, X. K.; Zhou, X. R. ; Zhu, C.; Zhu, K.; Zhu, K. J.; Zhu, S. H.; Zhu, X. L.; Zhu, X. W.; Zhu, Y. M.; Zhu, Y. S.; Zhu, Z. A.; Zhuang, J.; Zou, B. S.; Zou, J. H.; Zuo, J. X.: **Search for a light exotic particle in J/ψ radiative decays.** *Physical review / D* 85: 092012, 2012. DOI:10.1103/PhysRevD.85.092012

WOS-PHN-32 Ablikim, M.; Achasov, M. N.; Ambrose, D. J.; An, F. F.; An, Q.; An, Z. H.; Bai, J. Z.; Ban, Y. ; Becker, J.; Berger, N.; Bertani, M.; Bian, J. M.; Boger, E.; Bondarenko, O.; Boyko, I.; Briere, R. A.; Bytev, V.; Cai, X.; Cakir, O.; Calcaterra, A.; Cao, G. F.; Cetin, S. A.; Chang, J. F.; Chelkov, G.; Chen, G.; Chen, H. S.; Chen, J. C.; Chen, M. L.; Chen, S. J.; Chen, Y.; Chen, Y. B.; Cheng, H. P.; Chu, Y. P.; Cronin-Hennessy, D. ; Dai, H. L.; Dai, J. P.; Dedovich, D.; Deng, Z. Y.; Denig, A.; Denysenko, I.; Destefanis, M.; Ding, W. M.; Ding, Y.; Dong, L. Y.; Dong, M. Y.; Du, S. X.; Fang, J.; Fang, S. S.; Fava, L.; Feldbauer, F.; Feng, C. Q.; Ferroli, R. B.; Fu, C. D.; Fu, J. L.; Gao, Y.; Geng, C.; Götzen, Klaus ; Gong, W. X.; Gradl, W.; Greco, M.; Gu, M. H. ; Gu, Y. T.; Guan, Y. H.; Guo, A. Q.; Guo, L. B. ; Guo, Y. P.; Han, Y. L.; Hao, X. Q.; Harris, F. A.; He, K. L.; He, M.; He, Z. Y.; Held, T.; Heng, Y. K.; Hou, Z. L.; Hu, H. M.; Hu, J. F.; Hu, T.; Huang, B.; Huang, G. M.; Huang, J. S.; Huang, X. T.; Huang, Y. P.; Hussain, T.; Ji, C. S. ; Ji, Q.; Ji, X. B.; Ji, X. L.; Jia, L. K.; Jiang, L. L.; Jiang, X. S.; Jiao, J. B.; Jiao, Z. ; Jin, D. P.; Jin, S.; Jing, F. F.; Kalantar-Nayestanaki, N.; Kavatsyuk, M.; Kuehn, W.; Lai, W.; Lange, J. S.; Li, C. H.; Li, Cheng; Li, Cui; Li, D. M.; Li, F.; Li, G.; Li, H. B.; Li, J. C.; Li, K.; Li, Lei; Li, N. B.; Li, Q. J. ; Li, S. L.; Li, W. D.; Li, W. G.; Li, X. L.; Li, X. N.; Li, X. Q.; Li, X. R.; Li, Z. B.; Liang, H.; Liang, Y. F.; Liang, Y. T.; Liao, G. R. ; Liao, X. T.; Liu, B. J.; Liu, C. L.; Liu, C. X. ; Liu, C. Y.; Liu, F. H.; Liu, Fang; Liu, Feng ; Liu, H.; Liu, H. B.; Liu, H. H.; Liu, H. M.; Liu, H. W.; Liu, J. P.; Liu, K. Y.; Liu, Kai; Liu, Kun; Liu, P. L.; Liu, S. B.; Liu, X.; Liu, X. H.; Liu, Y.; Liu, Y. B.; Liu, Z. A.; Liu, Zhiqiang; Liu, Zhiqing; Loehner, H.; Lu, G. R.; Lu, H. J.; Lu, J. G.; Lu, Q. W.; Lu, X. R.; Lu, Y. P.; Luo, C. L.; Luo, M. X.; Luo, T.; Luo, X. L.; Lv, M.; Ma, C. L.; Ma, F. C.; Ma, H. L.; Ma, Q. M.; Ma, S.; Ma, T.; Ma, X. Y.; Ma, Y.; Maas, F. E.; Maggiora, M.; Malik, Q. A.; Mao, H. ; Mao, Y. J.; Mao, Z. P.; Messchendorp, J. G.; Min, J.; Min, T. J.; Mitchell, R. E.; Mo, X. H.; Morales, C. Morales; Motzko, C.; Muchnoi, N. Yu.; Muramatsu, H.; Nefedov, Y.; Nicholson, C.; Nikolaev, I. B.; Ning, Z.; Olsen, S. L.; Ouyang, Q. ; Pacetti, S.; Park, J. W.; Pelizaeus, M.; Peng, H. P.; Peters, K.; Ping, J. L.; Ping, R. G.; Poling, R.; Prencipe, E.; Qi, M.; Qian, S.; Qiao, C. F.; Qin, X. S.; Qin, Y.; Qin, Z. H.; Qiu, J. F.; Rashid, K. H.; Rong, G.; Ruan, X. D. ; Sarantsev, A.; Schaefer, B. D.; Schulze, J.; Shao, M.; Shen, C. P.; Shen, X. Y.; Sheng, H. Y. ; Shepherd, M. R.; Song, X. Y.; Spataro, S.; Spruck, B.; Sun, D. H.; Sun, G. X.; Sun, J. F.; Sun, S. S.; Sun, X. D.; Sun, Y. J.; Sun, Y. Z.; Sun, Z. J.; Sun, Z. T.; Tang, C. J.; Tang, X.; Tang, X. F.; Tapan, I.; Thorndike, E. H.; Tian, H. L.; Toth, D.; Ullrich, M.; Varner, G. S.; Wang, B.; Wang, B. Q.; Wang, K.; Wang, L. L.; Wang, L. S.; Wang, M.; Wang, P.; Wang, P. L.; Wang, Q. ; Wang, Q. J.; Wang, S. G.; Wang, X. L.; Wang, Y. D.; Wang, Y. F.; Wang, Y. Q.; Wang, Z.; Wang, Z. G.; Wang, Z. Y.; Wei, D. H.; Weidenkaff, P.; Wen, Q. G.; Wen, S. P.; Werner, M.; Wiedner, U.; Wu, L. H.; Wu, N.; Wu, S. X.; Wu, W.; Wu, Z.; Xia, L. G.; Xiao, Z. J.; Xie, Y. G.; Xiu, Q. L.; Xu, G. F.; Xu, G. M.; Xu, H.; Xu, Q. J.; Xu, X. P.; Xu, Z. R.; Xue, F.; Xue, Z.; Yan, L.; Yan, W. B.; Yan, Y. H.; Yang, H. X.; Yang, Y.; Yang, Y. X.; Ye, H.; Ye, M.; Ye, M. H.; Yu, B. X.; Yu, C. X.; Yu, J. S.; Yu, S. P.; Yuan, C. Z. ; Yuan, W. L.; Yuan, Y.; Zafar, A. A.; Zallo, A. ; Zeng, Y.; Zhang, B. X.; Zhang, B. Y.; Zhang, C. C.; Zhang, D. H.; Zhang, H. H.; Zhang, H. Y.; Zhang, J.; Zhang, J. Q.; Zhang, J. W.; Zhang, J. Y. ; Zhang, J. Z.; Zhang, S. H.; Zhang, T. R.; Zhang, X. J.; Zhang, X. Y.; Zhang, Y.; Zhang, Y. H. ; Zhang, Y. S.; Zhang, Z. P.; Zhang, Z. Y.; Zhao, G.; Zhao, H. S.; Zhao, J. W.; Zhao, K. X.; Zhao, Lei; Zhao, Ling; Zhao, M. G.; Zhao, Q.; Zhao, S. J.; Zhao, T. C.; Zhao, X. H.; Zhao, Y. B.; Zhao, Z. G.; Zhemchugov, A.; Zheng, B.; Zheng, J. P.; Zheng, Y. H.; Zheng, Z. P.; Zhong, B.; Zhong, J. ; Zhou, L.; Zhou, X. K.; Zhou, X. R.; Zhu, C.; Zhu, K.; Zhu, K. J.; Zhu, S. H.; Zhu, X. L.; Zhu, X. W.; Zhu, Y. C.; Zhu, Y. M.; Zhu, Y. S.; Zhu, Z. A.; Zhuang, J.; Zou, B. S.; Zou, J. H.; Zuo, J. X.: **First observation of the isospin violating decay** $J/\psi \rightarrow \Lambda\Sigma[over]^0 + c.c.$**.** *Physical review / D* 86: 032008, 2012. DOI:10.1103/PhysRevD.86.032008

WOS-PHN-33 Ablikim, M.; Achasov, M. N.; Ambrose, D. J.; An, F. F.; An, Q.; An, Z. H.; Bai, J. Z.; Ban, Y. ; Becker, J.; Berger, N.; Bertani, M.; Bian, J. M.; Boger, E.; Bondarenko, O.; Boyko, I.; Briere, R. A.; Bytev, V.; Cai, X.; Calcaterra, A. ; Cao, G. F.; Chang, J. F.; Chelkov, G.; Chen, G. ; Chen, H. S.; Chen, J. C.; Chen, M. L.; Chen, S. J.; Chen, Y.; Chen, Y. B.; Cheng, H. P.; Chu, Y. P.; Cronin-Hennessy, D.; Dai, H. L.; Dai, J. P.; Dedovich, D.; Deng, Z. Y.; Denig, A.; Denysenko, I. ; Destefanis, M.; Ding, W. M.; Ding, Y.; Dong, L. Y.; Dong, M. Y.; Du, S. X.; Fang, J.; Fang, S. S.; Fava, L.; Feldbauer, F.; Feng, C. Q.; Ferroli, R. B.; Fu, C. D.; Fu, J. L.; Gao, Y.; Geng, C.; Götzen, Klaus; Gong, W. X.; Gradl, W. ; Greco, M.; Gu, M. H.; Gu, Y. T.; Guan, Y. H. ; Guo, A. Q.; Guo, L. B.; Guo, Y. P.; Han, Y. L. ; Hao, X. Q.; Harris, F. A.; He, K. L.; He, M. ; He, Z. Y.; Held, T.; Heng, Y. K.; Hou, Z. L. ; Hu, H. M.; Hu, J. F.; Hu, T.; Huang, B.; Huang, G. M.; Huang, J. S.; Huang, X. T.; Huang, Y. P.; Hussain, T.; Ji, C. S.; Ji, Q.; Ji, X. B. ; Ji, X. L.; Jia, L. K.; Jiang, L. L.; Jiang, X. S.; Jiao, J. B.; Jiao, Z.; Jin, D. P.; Jin, S. ; Jing, F. F.; Kalantar-Nayestanaki, N.; Kavatsyuk, M.; Kuehn, W.; Lai, W.; Lange, J. S.; Leung, J. K. C.; Li, C. H.; Li, Cheng; Li, Cui; Li, D. M. ; Li, F.; Li, G.; Li, H. B.; Li, J. C.; Li, K. ; Li, Lei; Li,

N. B.; Li, Q. J.; Li, S. L.; Li, W. D.; Li, W. G.; Li, X. L.; Li, X. N.; Li, X. Q.; Li, X. R.; Li, Z. B.; Liang, H.; Liang, Y. F.; Liang, Y. T.; Liao, G. R.; Liao, X. T.; Liu, B. J.; Liu, B. J.; Liu, C. L.; Liu, C. X.; Liu, C. Y.; Liu, F. H.; Liu, Fang; Liu, Feng; Liu, H.; Liu, H. B.; Liu, H. H.; Liu, H. M.; Liu, H. W.; Liu, J. P.; Liu, K. Y.; Liu, Kai; Liu, Kun; Liu, P. L.; Liu, S. B.; Liu, X.; Liu, X. H.; Liu, Y.; Liu, Y. B.; Liu, Z. A.; Liu, Zhiqiang; Liu, Zhiqing; Loehner, H.; Lu, G. R.; Lu, H. J.; Lu, J. G.; Lu, Q. W.; Lu, X. R.; Lu, Y. P.; Luo, C. L.; Luo, M. X.; Luo, T.; Luo, X. L.; Lv, M.; Ma, C. L.; Ma, F. C.; Ma, H. L.; Ma, Q. M.; Ma, S.; Ma, T.; Ma, X. Y.; Ma, Y.; Maas, F. E.; Maggiora, M.; Malik, Q. A.; Mao, H. ; Mao, Y. J.; Mao, Z. P.; Messchendorp, J. G.; Min, J.; Min, T. J.; Mitchell, R. E.; Mo, X. H.; Morales Morales, C.; Motzko, C.; Muchnoi, N. Yu.; Nefedov, Y.; Nicholson, C.; Nikolaev, I. B.; Ning, Z.; Olsen, S. L.; Ouyang, Q.; Pacetti, S.; Park, J. W.; Pelizaeus, M.; Peters, K.; Ping, J. L.; Ping, R. G.; Poling, R.; Prencipe, E.; Pun, C. S. J.; Qi, M.; Qian, S.; Qiao, C. F.; Qin, X. S. ; Qin, Y.; Qin, Z. H.; Qiu, J. F.; Rashid, K. H. ; Rong, G.; Ruan, X. D.; Sarantsev, A.; Schulze, J.; Shao, M.; Shen, C. P.; Shen, X. Y.; Sheng, H. Y.; Shepherd, M. R.; Song, X. Y.; Spataro, S. ; Spruck, B.; Sun, D. H.; Sun, G. X.; Sun, J. F. ; Sun, S. S.; Sun, X. D.; Sun, Y. J.; Sun, Y. Z. ; Sun, Z. J.; Sun, Z. T.; Tang, C. J.; Tang, X. ; Thorndike, E. H.; Tian, H. L.; Toth, D.; Ullrich, M.; Varner, G. S.; Wang, B.; Wang, B. Q. ; Wang, K.; Wang, L. L.; Wang, L. S.; Wang, M. ; Wang, P.; Wang, P. L.; Wang, Q.; Wang, Q. J. ; Wang, S. G.; Wang, X. F.; Wang, X. L.; Wang, Y. D.; Wang, Y. F.; Wang, Y. Q.; Wang, Z.; Wang, Z. G.; Wang, Z. Y.; Wei, D. H.; Weidenkaff, P.; Wen, Q. G.; Wen, S. P.; Werner, M.; Wiedner, U.; Wu, L. H.; Wu, N.; Wu, S. X.; Wu, W.; Wu, Z.; Xia, L. G.; Xiao, Z. J.; Xie, Y. G.; Xiu, Q. L.; Xu, G. F.; Xu, G. M.; Xu, H.; Xu, Q. J.; Xu, X. P.; Xu, Y.; Xu, Z. R.; Xue, F.; Xue, Z.; Yan, L.; Yan, W. B.; Yan, Y. H.; Yang, H. X.; Yang, T.; Yang, Y.; Yang, Y. X.; Ye, H.; Ye, M.; Ye, M. H.; Yu, B. X.; Yu, C. X.; Yu, J. S.; Yu, S. P.; Yuan, C. Z.; Yuan, W. L.; Yuan, Y.; Zafar, A. A.; Zallo, A.; Zeng, Y.; Zhang, B. X.; Zhang, B. Y.; Zhang, C. C.; Zhang, D. H.; Zhang, H. H.; Zhang, H. Y.; Zhang, J.; Zhang, J. G.; Zhang, J. Q.; Zhang, J. W.; Zhang, J. Y.; Zhang, J. Z.; Zhang, L.; Zhang, S. H.; Zhang, T. R.; Zhang, X. J.; Zhang, X. Y.; Zhang, Y.; Zhang, Y. H. ; Zhang, Y. S.; Zhang, Z. P.; Zhang, Z. Y.; Zhao, G.; Zhao, H. S.; Zhao, J. W.; Zhao, K. X.; Zhao, Lei; Zhao, Ling; Zhao, M. G.; Zhao, Q.; Zhao, S. J.; Zhao, T. C.; Zhao, X. H.; Zhao, Y. B.; Zhao, Z. G.; Zhemchugov, A.; Zheng, B.; Zheng, J. P.; Zheng, Y. H.; Zheng, Z. P.; Zhong, B.; Zhong, J. ; Zhou, L.; Zhou, X. K.; Zhou, X. R.; Zhu, C.; Zhu, K.; Zhu, K. J.; Zhu, S. H.; Zhu, X. L.; Zhu, X. W.; Zhu, Y. M.; Zhu, Y. S.; Zhu, Z. A.; Zhuang, J.; Zou, B. S.; Zou, J. H.; Zuo, J. X.: **Study of** $J/\psi \to pp[over]$ **and** $J/\psi \to nn[over]$**.** *Physical review / D* 86: 032014, 2012. DOI:10.1103/PhysRevD.86.032014

WOS-PHN-34 Ablikim, M.; Achasov, M. N.; Ambrose, D. J.; An, F. F.; An, Q.; An, Z. H.; Bai, J. Z.; Ban, Y. ; Becker, J.; Berger, N.; Bertani, M.; Bian, J. M.; Boger, E.; Bondarenko, O.; Boyko, I.; Briere, R. A.; Bytev, V.; Cai, X.; Calcaterra, A. ; Cao, G. F.; Chang, J. F.; Chelkov, G.; Chen, G. ; Chen, H. S.; Chen, J. C.; Chen, M. L.; Chen, S. J.; Chen, Y.; Chen, Y. B.; Cheng, H. P.; Chu, Y. P.; Cronin-Hennessy, D.; Dai, H. L.; Dai, J. P.; Dedovich, D.; Deng, Z. Y.; Denig, A.; Denysenko, I. ; Destefanis, M.; Ding, W. M.; Ding, Y.; Dong, L. Y.; Dong, M. Y.; Du, S. X.; Fang, J.; Fang, S. S.; Fava, L.; Feldbauer, F.; Feng, C. Q.; Ferroli, R. B.; Fu, C. D.; Fu, J. L.; Gao, Y.; Geng, C.; Götzen, Klaus; Gong, W. X.; Gradl, W. ; Greco, M.; Gu, M. H.; Gu, Y. T.; Guan, Y. H. ; Guo, A. Q.; Guo, L. B.; Guo, Y. P.; Han, Y. L. ; Hao, X. Q.; Harris, F. A.; He, K. L.; He, M. ; He, Z. Y.; Held, T.; Heng, Y. K.; Hou, Z. L. ; Hu, H. M.; Hu, J. F.; Hu, T.; Huang, B.; Huang, G. M.; Huang, J. S.; Huang, X. T.; Huang, Y. P.; Hussain, T.; Ji, C. S.; Ji, Q.; Ji, X. B. ; Ji, X. L.; Jia, L. K.; Jiang, L. L.; Jiang, X. S.; Jiao, J. B.; Jiao, Z.; Jin, D. P.; Jin, S. ; Jing, F. F.; Kalantar-Nayestanaki, N.; Kavatsyuk, M.; Kuehn, W.; Lai, W.; Lange, J. S.; Leung, J. K. C.; Li, C. H.; Li, Cheng; Li, Cui; Li, D. M. ; Li, F.; Li, G.; Li, H. B.; Li, J. C.; Li, K. ; Li, Lei; Li, N. B.; Li, Q. J.; Li, S. L.; Li, W. D.; Li, W. G.; Li, X. L.; Li, X. N.; Li, X. Q.; Li, X. R.; Li, Z. B.; Liang, H.; Liang, Y. F.; Liang, Y. T.; Liao, G. R.; Liao, X. T.; Liu, B. J.; Liu, B. J.; Liu, C. L.; Liu, C. X.; Liu, C. Y.; Liu, F. H.; Liu, Fang; Liu, Feng; Liu, H.; Liu, H. B.; Liu, H. H.; Liu, H. M.; Liu, H. W.; Liu, J. P.; Liu, K. Y.; Liu, Kai; Liu, Kun; Liu, P. L.; Liu, S. B.; Liu, X.; Liu, X. H.; Liu, Y.; Liu, Y. B.; Liu, Z. A.; Liu, Zhiqiang; Liu, Zhiqing; Loehner, H.; Lu, G. R.; Lu, H. J.; Lu, J. G.; Lu, Q. W.; Lu, X. R.; Lu, Y. P.; Luo, C. L.; Luo, M. X.; Luo, T.; Luo, X. L.; Lv, M.; Ma, C. L.; Ma, F. C.; Ma, H. L.; Ma, Q. M.; Ma, S.; Ma, T.; Ma, X. Y.; Ma, Y.; Maas, F. E.; Maggiora, M.; Malik, Q. A.; Mao, H. ; Mao, Y. J.; Mao, Z. P.; Messchendorp, J. G.; Min, J.; Min, T. J.; Mitchell, R. E.; Mo, X. H.; Morales, C. Morales; Motzko, C.; Muchnoi, N. Yu.; Nefedov, Y.; Nicholson, C.; Nikolaev, I. B.; Ning, Z.; Olsen, S. L.; Ouyang, Q.; Pacetti, S.; Park, J. W.; Pelizaeus, M.; Peng, H. P.; Peters, K.; Ping, J. L.; Ping, R. G.; Poling, R.; Prencipe, E. ; Pun, C. S. J.; Qi, M.; Qian, S.; Qiao, C. F. ; Qin, X. S.; Qin, Y.; Qin, Z. H.; Qiu, J. F.; Rashid, K. H.; Rong, G.; Ruan, X. D.; Sarantsev, A. ; Schaefer, B. D.; Schulze, J.; Shao, M.; Shen, C. P.; Shen, X. Y.; Sheng, H. Y.; Shepherd, M. R. ; Song, X. Y.; Spataro, S.; Spruck, B.; Sun, D. H.; Sun, G. X.; Sun, J. F.; Sun, S. S.; Sun, X. D.; Sun, Y. J.; Sun, Y. Z.; Sun, Z. J.; Sun, Z. T.; Tang, C. J.; Tang, X.; Thorndike, E. H.; Tian, H. L.; Toth, D.; Ullrich, M.; Varner, G. S. ; Wang, B.; Wang, B. Q.; Wang, K.; Wang, L. L. ; Wang, L. S.; Wang, M.; Wang, P.; Wang, P. L. ; Wang, Q.; Wang, Q. J.; Wang, S. G.; Wang, X. F. ; Wang, X. L.; Wang, Y. D.; Wang, Y. F.; Wang, Y. Q.; Wang, Z.; Wang, Z. G.; Wang, Z. Y.; Wei, D. H.; Weidenkaff, P.; Wen, Q. G.; Wen, S. P.; Werner, M.; Wiedner, U.; Wu, L. H.; Wu, N.; Wu, S. X.; Wu, W.; Wu, Z.; Xia, L. G.; Xiao, Z. J. ; Xie, Y. G.; Xiu, Q. L.; Xu, G. F.; Xu, G. M. ; Xu, H.; Xu, Q. J.; Xu, X. P.; Xu, Y.; Xu, Z. R.; Xue, F.; Xue, Z.; Yan, L.; Yan, W. B.; Yan, Y. H.; Yang, H. X.; Yang, T.; Yang, Y.; Yang, Y. X.; Ye, H.; Ye, M.; Ye, M. H.; Yu, B. X.; Yu, C. X.; Yu, J. S.; Yu, L.; Yu, S. P.; Yuan, C. Z.; Yuan, W. L.; Yuan, Y.; Zafar, A. A. ; Zallo, A.; Zeng, Y.; Zhang, B. X.; Zhang, B. Y. ; Zhang, C. C.; Zhang, D. H.; Zhang, H. H.; Zhang, H. Y.; Zhang, J.; Zhang, J. G.; Zhang, J. Q. ; Zhang, J. W.; Zhang, J. Y.; Zhang, J. Z.; Zhang, L.; Zhang, S. H.; Zhang, T. R.; Zhang, X. J. ; Zhang, X. Y.; Zhang, Y.; Zhang, Y. H.; Zhang, Y. S.; Zhang, Z. P.; Zhang, Z. Y.; Zhao, G.; Zhao, H. S.; Zhao, J. W.; Zhao, K. X.; Zhao, Lei ; Zhao, Ling; Zhao, M. G.; Zhao, Q.; Zhao, S. J. ; Zhao, T. C.; Zhao, X. H.; Zhao, Y. B.; Zhao, Z. G.; Zhemchugov, A.; Zheng, B.; Zheng, J. P.; Zheng, Y. H.; Zheng, Z. P.; Zhong, B.; Zhong, J. ; Zhou, L.; Zhou, X. K.; Zhou, X. R.; Zhu, C.; Zhu, K.; Zhu, K. J.; Zhu, S. H.; Zhu, X. L.; Zhu, X. W.; Zhu, Y. M.; Zhu, Y. S.; Zhu, Z. A.; Zhuang, J.; Zou, B. S.; Zou, J. H.; Zuo, J. X.: **First Observation of the M1 Transition** $\psi(3686) \to \gamma\eta_c(2S)$**.** *Physical review letters* 109: 042003, 2012. DOI:10.1103/PhysRevLett.109.042003

WOS-PHN-35 Ablikim, M.; Achasov, M. N.; Ambrose, D. J.; An, F. F.; An, Q.; An, Z. H.; Bai, J. Z.; Ban, Y. ; Becker, J.; Berger, N.; Bertani, M.; Bian, J. M.; Boger, E.; Bondarenko, O.; Boyko, I.; Briere, R. A.; Bytev, V.; Cai, X.; Calcaterra, A. ; Cao,

G. F.; Chang, J. F.; Chelkov, G.; Chen, G. ; Chen, H. S.; Chen, J. C.; Chen, M. L.; Chen, S. J.; Chen, Y.; Chen, Y. B.; Cheng, H. P.; Chu, Y. P.; Cronin-Hennessy, D.; Dai, H. L.; Dai, J. P.; Dedovich, D.; Deng, Z. Y.; Denig, A.; Denysenko, I. ; Destefanis, M.; Ding, W. M.; Ding, Y.; Dong, L. Y.; Dong, M. Y.; Du, S. X.; Fang, J.; Fang, S. S.; Fava, L.; Feldbauer, F.; Feng, C. Q.; Ferroli, R. B.; Fu, C. D.; Fu, J. L.; Gao, Y.; Geng, C.; Götzen, Klaus; Gong, W. X.; Gradl, W. ; Greco, M.; Gu, M. H.; Gu, Y. T.; Guan, Y. H. ; Guo, A. Q.; Guo, L. B.; Guo, Y. P.; Han, Y. L. ; Hao, X. Q.; Harris, F. A.; He, K. L.; He, M. ; He, Z. Y.; Held, T.; Heng, Y. K.; Hou, Z. L. ; Hu, H. M.; Hu, J. F.; Hu, T.; Huang, B.; Huang, G. M.; Huang, J. S.; Huang, X. T.; Huang, Y. P.; Hussain, T.; Ji, C. S.; Ji, Q.; Ji, X. B. ; Ji, X. L.; Jia, L. K.; Jiang, L. L.; Jiang, X. S.; Jiao, J. B.; Jiao, Z.; Jin, D. P.; Jin, S. ; Jing, F. F.; Kalantar-Nayestanaki, N.; Kavatsyuk, M.; Kuehn, W.; Lai, W.; Lange, J. S.; Leung, J. K. C.; Li, C. H.; Li, Cheng; Li, Cui; Li, D. M. ; Li, F.; Li, G.; Li, H. B.; Li, J. C.; Li, K. ; Li, Lei; Li, N. B.; Li, Q. J.; Li, S. L.; Li, W. D.; Li, W. G.; Li, X. L.; Li, X. N.; Li, X. Q.; Li, X. R.; Li, Z. B.; Liang, H.; Liang, Y. F.; Liang, Y. T.; Liao, G. R.; Liao, X. T.; Liu, B. J.; Liu, B. J.; Liu, C. L.; Liu, C. X.; Liu, C. Y.; Liu, F. H.; Liu, Fang; Liu, Feng; Liu, H.; Liu, H. B.; Liu, H. H.; Liu, H. M.; Liu, H. W.; Liu, J. P.; Liu, K. Y.; Liu, Kai; Liu, Kun; Liu, P. L.; Liu, S. B.; Liu, X.; Liu, X. H.; Liu, Y.; Liu, Y. B.; Liu, Z. A.; Liu, Zhiqiang; Liu, Zhiqing; Loehner, H.; Lu, G. R.; Lu, H. J.; Lu, J. G.; Lu, Q. W.; Lu, X. R.; Lu, Y. P.; Luo, C. L.; Luo, M. X.; Luo, T.; Luo, X. L.; Lv, M.; Ma, C. L.; Ma, F. C.; Ma, H. L.; Ma, Q. M.; Ma, S.; Ma, T.; Ma, X. Y.; Ma, Y.; Maas, F. E.; Maggiora, M.; Malik, Q. A.; Mao, H. ; Mao, Y. J.; Mao, Z. P.; Messchendorp, J. G.; Min, J.; Min, T. J.; Mitchell, R. E.; Mo, X. H.; Morales, C. Morales; Motzko, C.; Muchnoi, N. Yu.; Nefedov, Y.; Nicholson, C.; Nikolaev, I. B.; Ning, Z.; Olsen, S. L.; Ouyang, Q.; Pacetti, S.; Park, J. W.; Pelizaeus, M.; Peters, K.; Ping, J. L.; Ping, R. G.; Poling, R.; Prencipe, E.; Pun, C. S. J.; Qi, M.; Qian, S.; Qiao, C. F.; Qin, X. S. ; Qin, Y.; Qin, Z. H.; Qiu, J. F.; Rashid, K. H. ; Rong, G.; Ruan, X. D.; Sarantsev, A.; Schulze, J.; Shao, M.; Shen, C. P.; Shen, X. Y.; Sheng, H. Y.; Shepherd, M. R.; Song, X. Y.; Spataro, S. ; Spruck, B.; Sun, D. H.; Sun, G. X.; Sun, J. F. ; Sun, S. S.; Sun, X. D.; Sun, Y. J.; Sun, Y. Z. ; Sun, Z. J.; Sun, Z. T.; Tang, C. J.; Tang, X. ; Thorndike, E. H.; Tian, H. L.; Toth, D.; Ullrich, M.; Varner, G. S.; Wang, B.; Wang, B. Q. ; Wang, K.; Wang, L. L.; Wang, L. S.; Wang, M. ; Wang, P.; Wang, P. L.; Wang, Q.; Wang, Q. J. ; Wang, S. G.; Wang, X. F.; Wang, X. L.; Wang, Y. D.; Wang, Y. F.; Wang, Y. Q.; Wang, Z.; Wang, Z. G.; Wang, Z. Y.; Wei, D. H.; Weidenkaff, P.; Wen, Q. G.; Wen, S. P.; Werner, M.; Wiedner, U.; Wu, L. H.; Wu, N.; Wu, S. X.; Wu, W.; Wu, Z.; Xia, L. G.; Xiao, Z. J.; Xie, Y. G.; Xiu, Q. L.; Xu, G. F.; Xu, G. M.; Xu, H.; Xu, Q. J.; Xu, X. P.; Xu, Y.; Xu, Z. R.; Xue, F.; Xue, Z.; Yan, L.; Yan, W. B.; Yan, Y. H.; Yang, H. X.; Yang, T.; Yang, Y.; Yang, Y. X.; Ye, H.; Ye, M.; Ye, M. H.; Yu, B. X.; Yu, C. X.; Yu, J. S.; Yu, S. P.; Yuan, C. Z.; Yuan, W. L.; Yuan, Y.; Zafar, A. A.; Zallo, A.; Zeng, Y.; Zhang, B. X.; Zhang, B. Y.; Zhang, C. C.; Zhang, D. H.; Zhang, H. H.; Zhang, H. Y.; Zhang, J.; Zhang, J. G.; Zhang, J. Q.; Zhang, J. W.; Zhang, J. Y.; Zhang, J. Z.; Zhang, L.; Zhang, S. H.; Zhang, T. R.; Zhang, X. J.; Zhang, X. Y.; Zhang, Y.; Zhang, Y. H. ; Zhang, Y. S.; Zhang, Z. P.; Zhang, Z. Y.; Zhao, G.; Zhao, H. S.; Zhao, J. W.; Zhao, K. X.; Zhao, Lei; Zhao, Ling; Zhao, M. G.; Zhao, Q.; Zhao, S. J.; Zhao, T. C.; Zhao, X. H.; Zhao, Y. B.; Zhao, Z. G.; Zhemchugov, A.; Zheng, B.; Zheng, J. P.; Zheng, Y. H.; Zheng, Z. P.; Zhong, B.; Zhong, J. ; Zhou, L.; Zhou, X. K.; Zhou, X. R.; Zhu, C.; Zhu, K.; Zhu, K. J.; Zhu, S. H.; Zhu, X. L.; Zhu, X. W.; Zhu, Y. M.; Zhu, Y. S.; Zhu, Z. A.; Zhuang, J.; Zou, B. S.; Zou, J. H.; Zuo, J. X.: **Two-photon widths of the $\chi_{c0,2}$ states and helicity analysis for $\chi_{c2} \to \gamma\gamma$.** *Physical review / D* 85: 112008, 2012. DOI:10.1103/PhysRevD.85.112008

WOS-PHN-36 Ablikim, M.; Achasov, M. N.; Ambrose, D. J.; An, F. F.; An, Q.; An, Z. H.; Bai, J. Z.; Ban, Y. ; Becker, J.; Berger, N.; Bertani, M.; Bian, J. M.; Boger, E.; Bondarenko, O.; Boyko, I.; Briere, R. A.; Bytev, V.; Cai, X.; Calcaterra, A. ; Cao, G. F.; Chang, J. F.; Chelkov, G.; Chen, G. ; Chen, H. S.; Chen, J. C.; Chen, M. L.; Chen, S. J.; Chen, Y.; Chen, Y. B.; Cheng, H. P.; Chu, Y. P.; Cronin-Hennessy, D.; Dai, H. L.; Dai, J. P.; Dedovich, D.; Deng, Z. Y.; Denig, A.; Denysenko, I. ; Destefanis, M.; Ding, W. M.; Ding, Y.; Dong, L. Y.; Dong, M. Y.; Du, S. X.; Fang, J.; Fang, S. S.; Fava, L.; Feldbauer, F.; Feng, C. Q.; Ferroli, R. B.; Fu, C. D.; Fu, J. L.; Gao, Y.; Geng, C.; Götzen, Klaus; Gong, W. X.; Gradl, W. ; Greco, M.; Gu, M. H.; Gu, Y. T.; Guan, Y. H. ; Guo, A. Q.; Guo, L. B.; Guo, Y.P.; Han, Y. L. ; Hao, X. Q.; Harris, F. A.; He, K. L.; He, M. ; He, Z. Y.; Heng, Y. K.; Held, T.; Hou, Z. L. ; Hu, H. M.; Hu, J. F.; Hu, T.; Huang, B.; Huang, G. M.; Huang, J. S.; Huang, X. T.; Huang, Y. P.; Hussain, T.; Ji, C. S.; Ji, Q.; Ji, X. B. ; Ji, X. L.; Jia, L. K.; Jiang, L. L.; Jiang, X. S.; Jiao, J. B.; Jiao, Z.; Jin, D. P.; Jin, S. ; Jing, F. F.; Kalantar-Nayestanaki, N.; Kavatsyuk, M.; Kuehn, W.; Lai, W.; Lange, J. S.; Leung, J. K. C.; Li, C. H.; Li, Cheng; Li, Cui; Li, D. M. ; Li, F.; Li, G.; Li, H. B.; Li, J. C.; Li, K. ; Li, Lei; Li, N. B.; Li, Q. J.; Li, S. L.; Li, W. D.; Li, W. G.; Li, X. L.; Li, X. N.; Li, X. Q.; Li, X. R.; Li, Z. B.; Liang, H.; Liang, Y. F.; Liang, Y. T.; Liao, G. R.; Liao, X. T.; Liu, B. J.; Liu, C. L.; Liu, C. X.; Liu, C. Y.; Liu, F. H.; Liu, Fang; Liu, Feng; Liu, H.; Liu, H. B.; Liu, H. H.; Liu, H. M.; Liu, H. W.; Liu, J. P.; Liu, K. Y.; Liu, Kai; Liu, Kun; Liu, P. L.; Liu, S. B.; Liu, X.; Liu, X. H.; Liu, Y.; Liu, Y. B.; Liu, Z. A.; Liu, Zhiqiang; Liu, Zhiqing ; Loehner, H.; Lu, G. R.; Lu, H. J.; Lu, J. G. ; Lu, Q. W.; Lu, X. R.; Lu, Y. P.; Luo, C. L.; Luo, M. X.; Luo, T.; Luo, X. L.; Lu, M.; Ma, C. L.; Ma, F. C.; Ma, H. L.; Ma, Q. M.; Ma, S.; Ma, T.; Ma, X. Y.; Ma, Y.; Maas, F. E.; Maggiora, M.; Malik, Q. A.; Mao, H.; Mao, Y. J.; Mao, Z. P.; Messchendorp, J. G.; Min, J.; Min, T. J.; Mitchell, R. E.; Mo, X. H.; Morales, C. Morales ; Motzko, C.; Muchnoi, N. Yu.; Nefedov, Y.; Nicholson, C.; Nikolaev, I. B.; Ning, Z.; Olsen, S. L.; Ouyang, Q.; Pacetti, S.; Park, J. W.; Pelizaeus, M.; Peng, H. P.; Peters, K.; Ping, J. L. ; Ping, R. G.; Poling, R.; Prencipe, E.; Pun, C. S. J.; Qi, M.; Qian, S.; Qiao, C. F.; Qin, X. S. ; Qin, Y.; Qin, Z. H.; Qiu, J. F.; Rashid, K. H. ; Rong, G.; Ruan, X. D.; Sarantsev, A.; Schaefer, B. D.; Schulze, J.; Shao, M.; Shen, C. P.; Shen, X. Y.; Sheng, H. Y.; Shepherd, M. R.; Song, X. Y. ; Spataro, S.; Spruck, B.; Sun, D. H.; Sun, G. X. ; Sun, J. F.; Sun, S. S.; Sun, X. D.; Sun, Y. J. ; Sun, Y. Z.; Sun, Z. J.; Sun, Z. T.; Tang, C. J. ; Tang, X.; Thorndike, E. H.; Tian, H. L.; Toth, D.; Ullrich, M.; Varner, G. S.; Wang, B.; Wang, B. Q.; Wang, K.; Wang, L. L.; Wang, L. S.; Wang, M.; Wang, P.; Wang, P. L.; Wang, Q.; Wang, Q. J. ; Wang, S. G.; Wang, X. F.; Wang, X. L.; Wang, Y. D.; Wang, Y. F.; Wang, Y. Q.; Wang, Z.; Wang, Z. G.; Wang, Z. Y.; Wei, D. H.; Weidenkaff, P.; Wen, Q. G.; Wen, S. P.; Werner, M.; Wiedner, U.; Wu, L. H.; Wu, N.; Wu, S. X.; Wu, W.; Wu, Z.; Xia, L. G.; Xiao, Z. J.; Xie, Y. G.; Xiu, Q. L.; Xu, G. F.; Xu, G. M.; Xu, H.; Xu, Q. J.; Xu, X. P.; Xu, Y.; Xu, Z. R.; Xue, F.; Xue, Z.; Yan, L.; Yan, W. B.; Yan, Y. H.; Yang, H. X.; Yang, T.; Yang, Y.; Yang, Y. X.; Ye, H.; Ye, M.; Ye, M. H.; Yu, B. X.; Yu, C. X.; Yu, J. S.; Yu, S. P.; Yuan, C. Z.; Yuan, W. L.; Yuan, Y.; Zafar, A. A.; Zallo, A.; Zeng, Y.; Zhang, B. X.; Zhang, B. Y.; Zhang, C. C.; Zhang, D. H.; Zhang, H. H.; Zhang, H. Y.; Zhang, J.; Zhang, J. G.; Zhang, J. Q.; Zhang, J. W.; Zhang, J. Y.;

Zhang, J. Z.; Zhang, L.; Zhang, S. H.; Zhang, T. R.; Zhang, X. J.; Zhang, X. Y.; Zhang, Y.; Zhang, Y. H. ; Zhang, Y. S.; Zhang, Z. P.; Zhang, Z. Y.; Zhao, G.; Zhao, H. S.; Zhao, J. W.; Zhao, K. X.; Zhao, Lei; Zhao, Ling; Zhao, M. G.; Zhao, Q.; Zhao, S. J.; Zhao, T. C.; Zhao, X. H.; Zhao, Y. B.; Zhao, Z. G.; Zheng, J. P.; Zhemchugov, A.; Zheng, Y. H. ; Zheng, Z. P.; Zhong, B.; Zhong, J.; Zhou, L. ; Zhou, X. K.; Zhou, X. R.; Zhu, C.; Zhu, K.; Zhu, K. J.; Zhu, S. H.; Zhu, X. L.; Zhu, X. W.; Zhu, Y. M.; Zhu, Y. S.; Zhu, Z. A.; Zhuang, J.; Zou, B. S.; Zou, J. H.; Zuo, J. X.: **Determination of the number of J/ψ events with J/ψ → inclusive decays.** *Chinese physics / C* 36: 915 - 925, 2012. DOI:10.1088/1674-1137/36/10/001

WOS-PHN-37 Ablikim, M.; Achasov, M. N.; Ambrose, D. J.; An, F. F.; An, Q.; An, Z. H.; Bai, J. Z.; Ferroli, R. B.; Ban, Y.; Becker, J.; Berger, N.; Bertani, M. B.; Bian, J. M.; Boger, E.; Bondarenko, O.; Boyko, I.; Briere, R. A.; Bytev, V.; Cai, X.; Calcaterra, A. C.; Cao, G. F.; Chang, J. F.; Chelkov, G.; Chen, G.; Chen, H. S.; Chen, J. C.; Chen, M. L.; Chen, S. J.; Chen, Y.; Chen, Y. B.; Cheng, H. P.; Chu, Y. P.; Cronin-Hennessy, D.; Dai, H. L.; Dai, J. P.; Dedovich, D.; Deng, Z. Y.; Denig, A.; Denysenko, I.; Destefanis, M.; Ding, W. M.; Ding, Y.; Dong, L. Y.; Dong, M. Y.; Du, S. X.; Fang, J.; Fang, S. S.; Fava, L.; Feldbauer, F.; Feng, C. Q.; Fu, C. D.; Fu, J. L.; Gao, Y. ; Geng, C.; Götzen, Klaus; Gong, W. X.; Gradl, W.; Greco, M.; Gu, M. H.; Gu, Y. T.; Guan, Y. H. ; Guo, A. Q.; Guo, L. B.; Guo, Y. P.; Han, Y. L. ; Hao, X. Q.; Harris, F. A.; He, K. L.; He, M. ; He, Z. Y.; Held, T.; Heng, Y. K.; Hou, Z. L. ; Hu, H. M.; Hu, J. F.; Hu, T.; Huang, B.; Huang, G. M.; Huang, J. S.; Huang, X. T.; Huang, Y. P.; Hussain, T.; Ji, C. S.; Ji, Q.; Ji, X. B. ; Ji, X. L.; Jia, L. K.; Jiang, L. L.; Jiang, X. S.; Jiao, J. B.; Jiao, Z.; Jin, D. P.; Jin, S. ; Jing, F. F.; Kalantar-Nayestanaki, N.; Kavatsyuk, M.; Kuehn, W.; Lai, W.; Lange, J. S.; Leung, J. K. C.; Li, C. H.; Li, Cheng; Li, Cui; Li, D. M. ; Li, F.; Li, G.; Li, H. B.; Li, J. C.; Li, K. ; Li, Lei; Li, N. B.; Li, Q. J.; Li, S. L.; Li, W. D.; Li, W. G.; Li, X. L.; Li, X. N.; Li, X. Q.; Li, X. R.; Li, Z. B.; Liang, H.; Liang, Y. F.; Liang, Y. T.; Liao, G. R.; Liao, X. T.; Liu, B. J.; Liu, B. J.; Liu, C. L.; Liu, C. X.; Liu, C. Y.; Liu, F. H.; Liu, Fang; Liu, Feng; Liu, H.; Liu, H. B.; Liu, H. H.; Liu, H. M.; Liu, H. W.; Liu, J. P.; Liu, Kun; Liu, Kai; Liu, K. Y.; Liu, P. L.; Liu, S. B.; Liu, X.; Liu, X. H.; Liu, Y. B.; Liu, Y.; Liu, Z. A.; Liu, Zhiqiang; Liu, Zhiqing; Loehner, H.; Lu, G. R.; Lu, H. J.; Lu, J. G.; Lu, Q. W.; Lu, X. R.; Lu, Y. P.; Luo, C. L.; Luo, M. X.; Luo, T.; Luo, X. L.; Lv, M.; Ma, C. L.; Ma, F. C.; Ma, H. L.; Ma, Q. M.; Ma, S.; Ma, T.; Ma, X. Y.; Ma, Y.; Maas, F. E.; Maggiora, M.; Malik, Q. A.; Mao, H. ; Mao, Y. J.; Mao, Z. P.; Messchendorp, J. G.; Min, J.; Min, T. J.; Mitchell, R. E.; Mo, X. H.; Morales Morales, C.; Motzko, C.; Muchnoi, N. Yu.; Nefedov, Y.; Nicholson, C.; Nikolaev, I. B.; Ning, Z.; Olsen, S. L.; Ouyang, Q.; Pacetti, S. P.; Park, J. W.; Pelizaeus, M.; Peters, K.; Ping, J. L. ; Ping, R. G.; Poling, R.; Prencipe, E.; Pun, C. S. J.; Qi, M.; Qian, S.; Qiao, C. F.; Qin, X. S. ; Qin, Y.; Qin, Z. H.; Qiu, J. F.; Rashid, K. H. ; Rong, G.; Ruan, X. D.; Sarantsev, A.; Schulze, J.; Shao, M.; Shen, C. P.; Shen, X. Y.; Sheng, H. Y.; Shepherd, M. R.; Song, X. Y.; Spataro, S. ; Spruck, B.; Sun, D. H.; Sun, G. X.; Sun, J. F. ; Sun, S. S.; Sun, X. D.; Sun, Y. J.; Sun, Y. Z. ; Sun, Z. J.; Sun, Z. T.; Tang, C. J.; Tang, X. ; Thorndike, E. H.; Tian, H. L.; Toth, D.; Ulrich, M. U.; Varner, G. S.; Wang, B.; Wang, B. Q. ; Wang, K.; Wang, L. L.; Wang, L. S.; Wang, M. ; Wang, P.; Wang, P. L.; Wang, Q.; Wang, Q. J. ; Wang, S. G.; Wang, X. F.; Wang, X. L.; Wang, Y. D.; Wang, Y. F.; Wang, Y. Q.; Wang, Z.; Wang, Z. G.; Wang, Z. Y.; Wei, D. H.; Weidenkaff, P.; Wen, Q. G.; Wen, S. P.; Werner, M. W.; Wiedner, U. ; Wu, L. H.; Wu, N.; Wu, S. X.; Wu, W.; Wu, Z. ; Xia, L. G.; Xiao, Z. J.; Xie, Y. G.; Xiu, Q. L. ; Xu, G. F.; Xu, G. M.; Xu, H.; Xu, Q. J.; Xu, X. P.; Xu, Y.; Xu, Z. R.; Xue, F.; Xue, Z.; Yan, L.; Yan, W. B.; Yan, Y. H.; Yang, H. X.; Yang, T.; Yang, Y.; Yang, Y. X.; Ye, H.; Ye, M. ; Ye, M. H.; Yu, B. X.; Yu, C. X.; Yu, J. S.; Yu, S. P.; Yuan, C. Z.; Yuan, W. L.; Yuan, Y.; Zafar, A. A.; Zallo, A. Z.; Zeng, Y.; Zhang, B. X. ; Zhang, B. Y.; Zhang, C. C.; Zhang, D. H.; Zhang, H. H.; Zhang, H. Y.; Zhang, J.; Zhang, J. G. ; Zhang, J. Q.; Zhang, J. W.; Zhang, J. Y.; Zhang, J. Z.; Zhang, L.; Zhang, S. H.; Zhang, T. R. ; Zhang, X. J.; Zhang, X. Y.; Zhang, Y.; Zhang, Y. H.; Zhang, Y. S.; Zhang, Z. P.; Zhang, Z. Y.; Zhao, G.; Zhao, H. S.; Zhao, J. W.; Zhao, K. X.; Zhao, Lei; Zhao, Ling; Zhao, M. G.; Zhao, Q.; Zhao, S. J.; Zhao, T. C.; Zhao, X. H.; Zhao, Y. B. ; Zhao, Z. G.; Zhemchugov, A.; Zheng, B.; Zheng, J. P.; Zheng, Y. H.; Zheng, Z. P.; Zhong, B.; Zhong, J.; Zhou, L.; Zhou, X. K.; Zhou, X. R.; Zhu, C.; Zhu, K.; Zhu, K. J.; Zhu, S. H.; Zhu, X. L.; Zhu, X. W.; Zhu, Y. M.; Zhu, Y. S.; Zhu, Z. A.; Zhuang, J.; Zou, B. S.; Zou, J. H.; Zuo, J. X.: **Evidence for the Direct Two-Photon Transition from ψ(3686) to J/ψ.** *Physical review letters* 109: 172002, 2012. DOI:10.1103/PhysRevLett.109.172002

WOS-PHN-38 Ablikim, M.; Achasov, M.N.; Alberto, D.; Ambrose, D.J.; An, F.F.; An, Q.; An, Z.H.; Bai, J.Z.; Baldini Ferroli, R.B.F.; Ban, Y.; Becker, J.; Berger, N.; Bertani, M.B.; Bian, J.M.; Boger, E. ; Bondarenko, O.; Boyko, I.; Briere, R.A.; Bytev, V.; Cai, X.; Calcaterra, A.C.; Cao, G.F.; Chang, J.F.; Chelkov, G.; Chen, G.; Chen, H.S.; Chen, J.C.; Chen, M.L.; Chen, S.J.; Chen, Y.; Chen, Y.B.; Cheng, H.P.; Chu, Y.P.; Cronin-Hennessy, D. ; Dai, H.L.; Dai, J.P.; Dedovich, D.; Deng, Z.Y. ; Denysenko, I.; Destefanis, M.; Ding, W.M.; Ding, Y.; Dong, L.Y.; Dong, M.Y.; Du, S.X.; Fang, J.; Fang, S.S.; Feng, C.Q.; Fu, C.D.; Fu, J.L.; Gao, Y.; Geng, C.; Götzen, Klaus; Gong, W.X.; Greco, M.; Gu, M.H.; Gu, Y.T.; Guan, Y.H. ; Guo, A.Q.; Guo, L.B.; Guo, Y.P.; Han, Y.L.; Hao, X.Q.; Harris, F.A.; He, K.L.; He, M.; He, Z.Y.; Heng, Y.K.; Hou, Z.L.; Hu, H.M.; Hu, J.F. ; Hu, T.; Huang, B.; Huang, G.M.; Huang, J.S.; Huang, X.T.; Huang, Y.P.; Hussain, T.; Ji, C.S.; Ji, Q.; Ji, X.B.; Ji, X.L.; Jia, L.K.; Jiang, L.L.; Jiang, X.S.; Jiao, J.B.; Jiao, Z.; Jin, D.P.; Jin, S.; Jing, F.F.; Kalantar-Nayestanaki, N. ; Kavatsyuk, M.; Kuehn, W.; Lai, W.; Lange, J.S. ; Leung, J.K.C.; Li, C.H.; Li, Cheng; Li, Cui; Li, D.M.; Li, F.; Li, G.; Li, H.B.; Li, J.C.; Li, K.; Li, Lei; Li, N.B.; Li, Q.J.; Li, S.L. ; Li, W.D.; Li, W.G.; Li, X.L.; Li, X.N.; Li, X.Q.; Li, X.R.; Li, Z.B.; Liang, H.; Liang, Y.F. ; Liang, Y.T.; Liao, G.R.; Liao, X.T.; Liu, B.J. ; Liu, B.J.; Liu, C.L.; Liu, C.X.; Liu, C.Y.; Liu, F.H.; Liu, Fang; Liu, Feng; Liu, H.; Liu, H.B.; Liu, H.H.; Liu, H.M.; Liu, H.W.; Liu, J.P. ; Liu, K.; Liu, K.; Liu, K.Y.; Liu, Q.; Liu, S.B.; Liu, X.; Liu, X.H.; Liu, Y.B.; Liu, Yong ; Liu, Z.A.; Liu, Zhiqiang; Liu, Zhiqing; Loehner, H.; Lu, G.R.; Lu, H.J.; Lu, J.G.; Lu, Q.W.; Lu, X.R.; Lu, Y.P.; Luo, C.L.; Luo, M.X. ; Luo, T.; Luo, X.L.; Lv, M.; Ma, C.L.; Ma, F.C.; Ma, H.L.; Ma, Q.M.; Ma, S.; Ma, T.; Ma, X.Y.; Maggiora, M.; Malik, Q.A.; Mao, H.; Mao, Y.J.; Mao, Z.P.; Messchendorp, J.G.; Min, J.; Min, T.J.; Mitchell, R.E.; Mo, X.H.; Muchnoi, N.Yu. ; Nefedov, Y.; Nikolaev, I.B.; Ning, Z.; Olsen, S.L.; Ouyang, Q.; Pacetti, S.P.; Park, J.W.; Pelizaeus, M.; Peters, K.; Ping, J.L.; Ping, R.G. ; Poling, R.; Pun, C.S.J.; Qi, M.; Qian, S.; Qiao, C.F.; Qin, X.S.; Qin, Z.H.; Qiu, J.F.; Rashid, K.H.; Rong, G.; Ruan, X.D.; Sarantsev, A. ; Schulze, J.; Shao, M.; Shen, C.P.; Shen, X.Y. ; Sheng, H.Y.; Shepherd, M.R.; Song, X.Y.; Spataro, S.; Spruck, B.; Sun, D.H.; Sun, G.X.; Sun, J.F.; Sun, S.S.; Sun, X.D.; Sun, Y.J.; Sun, Y.Z.; Sun, Z.J.; Sun, Z.T.;

Tang, C.J.; Tang, X. ; Thorndike, E.H.; Tian, H.L.; Toth, D.; Ulrich, M.U.; Varner, G.S.; Wang, B.; Wang, B.Q.; Wang, K.; Wang, L.L.; Wang, L.S.; Wang, M.; Wang, P. ; Wang, P.L.; Wang, Q.; Wang, Q.J.; Wang, S.G. ; Wang, X.F.; Wang, X.L.; Wang, Y.D.; Wang, Y.F. ; Wang, Y.Q.; Wang, Z.; Wang, Z.G.; Wang, Z.Y. ; Wei, D.H.; Wen, Q.G.; Wen, S.P.; Werner, M.W. ; Wiedner, U.; Wu, L.H.; Wu, N.; Wu, W.; Wu, Z.; Xia, L.G.; Xiao, Z.J.; Xie, Y.G.; Xiu, Q.L. ; Xu, G.F.; Xu, G.M.; Xu, H.; Xu, Q.J.; Xu, X.P.; Xu, Y.; Xu, Z.R.; Xue, F.; Xue, Z.; Yan, L.; Yan, W.B.; Yan, Y.H.; Yang, H.X.; Yang, T.; Yang, Y.; Yang, Y.X.; Ye, H.; Ye, M.; Ye, M.H.; Yu, B.X.; Yu, C.X.; Yu, S.P.; Yuan, C.Z. ; Yuan, W.L.; Yuan, Y.; Zafar, A.A.; Zallo, A.Z. ; Zeng, Y.; Zhang, B.X.; Zhang, B.Y.; Zhang, C.C. ; Zhang, D.H.; Zhang, H.H.; Zhang, H.Y.; Zhang, J.; Zhang, J.Q.; Zhang, J.W.; Zhang, J.Y.; Zhang, J.Z.; Zhang, L.; Zhang, S.H.; Zhang, T.R. ; Zhang, X.J.; Zhang, X.Y.; Zhang, Y.; Zhang, Y.H.; Zhang, Y.S.; Zhang, Z.P.; Zhang, Z.Y.; Zhao, G.; Zhao, H.S.; Zhao, Jingwei; Zhao, Lei; Zhao, Ling; Zhao, M.G.; Zhao, Q.; Zhao, S.J.; Zhao, T.C.; Zhao, X.H.; Zhao, Y.B.; Zhao, Z.G.; Zhemchugov, A.; Zheng, B.; Zheng, J.P.; Zheng, Y.H. ; Zheng, Z.P.; Zhong, B.; Zhong, J.; Zhou, L.; Zhou, X.K.; Zhou, X.R.; Zhu, C.; Zhu, K.; Zhu, K.J.; Zhu, S.H.; Zhu, X.L.; Zhu, X.W.; Zhu, Y.S. ; Zhu, Z.A.; Zhuang, J.; Zou, B.S.; Zou, J.H.; Zuo, J.X.: **Precision measurement of the branching fractions of J/$\psi \to \pi + \pi\pi 0 J/\psi \to \pi + \pi\pi$0 and $\psi \to \pi + \pi\pi$0.** *Physics letters / B* 710: 594 - 599, 2012. DOI:10.1016/j.physletb.2012.03.036

WOS-PHN-39 Abou-Haidar, Z; Agodi, C; Alvarez, M A G; Anelli, M; Aumann, T; Battistoni, G; Bocci, A; Böhlen, T T; Boudard, A; Brunetti, A; Carpinelli, M; Cirrone, G A P; Cortes-Giraldo, M A; Cuttone, G; Napoli, M De; Durante, M; Fernandez-Garcia, J P; Finck, C; Gallardo, M I; Golosio, B; Iarocci, E; Iazzi, F; Ickert, G; Introzzi, R; Juliani, D; Krimmer, J; Kurz, N; Labalme, M; Leifels, Y; LeFevre, A.; Leray, S; Marchetto, F; Monaco, V; Morone, M C; Oliva, P; Paoloni, A; Patera, V; Piersanti, L; Pleskac, R; Quesada, J M; Randazzo, N ; Romano, F; Rossi, D; Rosso, V; Rousseau, M; Sacchi, R; Sala, P; Sarti, A; Schuy, C; Sciubba, A; Sfienti, C; Simon, H; Sipala, V; Spiriti, E ; Stuttge, L; Tropea, S; Younis, H: **Performance of upstream interaction region detectors for the FIRST experiment at GSI.** *Journal of Instrumentation* 7: P02006 - P02006, 2012. DOI:10.1088/1748-0221/7/02/P02006

WOS-PHN-40 Achenbach, P.; Ayerbe Gayoso, C.; Bernauer, J. C.; Bianchin, S.; Böhm, R.; Borodina, O.; Bosnar, D. ; Bösz, M.; Bozkurt, V.; Bydzovsky, P.; Debenjak, L.; Distler, M. O.; Esser, A.; Friscic, I.; Gomez Rodriguez, M.; Göküzüm, B. ; Grießinger, K.; Jennewein, P.; Kim, E.; Makek, M.; Merkel, H.; Minami, S.; Müller, U.; Nakajima, D.; Nungesser, L.; Özel-Tashenov, B.; Pochodzalla, J.; Rappold, Ch.; Saito, T. R.; Sanchez Majos, S.; Schlimme, B. S.; Sirca, S.; Weinriefer, M.; Yoon, C. J.: **Exclusive electroproduction of $K^+\Lambda$ and $K^+\Sigma^0$ final states at Q2 = 0.0300.055 (GeV/c)2.** *The European physical journal / A* 48: 14, 2012. DOI:10.1140/epja/i2012-12014-9

WOS-PHN-41 Achenbach, P.; Esser, A.; Ayerbe Gayoso, C.; Böhm, R.; Borodina, O.; Bosnar, D.; Bozkurt, V. ; Bydzovsky, P.; Debenjak, L.; Distler, M.O.; Friscic, I.; Fujii, Y.; Gogami, T.; Gomez Rodriguez, M.; Hashimoto, O.; Hirose, S.; Kim, E. ; Margaryan, A.; Merkel, H.; Müller, U.; Nagao, S.; Nakamura, S.N.; Pochodzalla, J.; Rappold, C. ; Reinhold, J.; Saito, T.R.; Sanchez Lorente, A.; Sanchez Majos, S.; Schlimme, B.S.; Schoth, M.; Schulz, F.; Sfienti, C.; Sirca, S.; Tang, L.; Thiel, M.; Tsukada, K.: **Strange hadronic physics in electroproduction experiments at the Mainz Microtron.** *Nuclear physics / A* 881: 187 - 198, 2012. DOI:10.1016/j.nuclphysa.2012.01.008

WOS-PHN-42 Adamova, D.; Agakichiev, G.; Andronic, A.; Antonczyk, D.; Appelshäuser, H.; Belaga, V.; Bielcikova, J.; Braun-Munzinger, P.; Busch, O.; Cherlin, A.; Damjanovic, S.; Dietel, T.; Dietrich, L.; Drees, A.; Dubitzky, W.; Esumi, S.I.; Filimonov, K.; Fomenko, K.; Fraenkel, Z.; Garabatos, C.; Glässel, P.; Hering, G.; Holeczek, J.; Kalisky, M.; Krobath, G.; Kushpil, V.; Maas, A.; Marin, Ana; Milosevic, J.; Mikowiec, D.; Panebrattsev, Y.; Petchenova, O.; Petracek, V.; Radomski, S.; Rak, J.; Ravinovich, I.; Rehak, P. ; Sako, H.; Schmitz, W.; Schuchmann, S.; Sedykh, S.; Shimansky, S.; Stachel, J.; Sumbera, M.; Tilsner, H.; Tserruya, I.; Tsiledakis, G.; Wessels, J.P.; Wienold, T.; Wurm, J.P.; Yurevich, S.; Yurevich, V.: **Elliptic flow of charged pions, protons and strange particles emitted in Pb+Au collisions at top SPS energy.** *Nuclear physics / A* 894: 41 - 73, 2012. DOI:10.1016/j.nuclphysa.2012.08.004

WOS-PHN-43 Adolph, C.; Alekseev, M.G.; Alexakhin, V.Yu.; Alexandrov, Yu.; Alexeev, G.D.; Amoroso, A.; Antonov, A.A.; Austregesilo, A.; Badelek, B.; Balestra, F.; Barth, J.; Baum, G.; Bedfer, Y.; Bernhard, J.; Bertini, R.; Bettinelli, M.; Bicker, K.; Bieling, J.; Birsa, R.; Bisplinghoff, J.; Bordalo, P.; Bradamante, F.; Braun, C.; Bravar, A. ; Bressan, A.; Burtin, E.; Chaberny, D.; Chiosso, M.; Chung, S.U.; Cicuttin, A.; Crespo, M.L.; Dalla Torre, S.; Das, S.; Dasgupta, S.S.; Denisov, O.Yu.; Dhara, L.; Donskov, S.V.; Doshita, N.; Duic, V.; Dünnweber, W.; Dziewiecki, M.; Efremov, A.; Elia, C.; Eversheim, P.D.; Eyrich, W.; Faessler, M.; Ferrero, A.; Filin, A.; Finger, M. ; Finger, M.; Fischer, H.; Franco, C.; du Fresne von Hohenesche, N.; Friedrich, J.M.; Garfagnini, R. ; Gautheron, F.; Gavrichtchouk, O.P.; Gazda, R.; Gerassimov, S.; Geyer, R.; Giorgi, M.; Gnesi, I. ; Gobbo, B.; Goertz, S.; Grabmüller, S.; Grasso, A.; Grube, B.; Gushterski, R.; Guskov, A.; Guthörl, T.; Haas, F.; von Harrach, D.; Heinsius, F.H.; Herrmann, F.; HeßC.; Hinterberger, F.; Horikawa, N.; Höppner, Ch.; dHose, N.; Huber, S. ; Ishimoto, S.; Ivanov, O.; Ivanshin, Yu.; Iwata, T.; Jahn, R.; Jasinski, P.; Joosten, R.; KabußE.; Kang, D.; Ketzer, B.; Khaustov, G.V.; Khokhlov, Yu.A.; Kisselev, Yu.; Klein, F.; Klimaszewski, K.; Koblitz, S.; Koivuniemi, J.H.; Kolosov, V.N.; Kondo, K.; Königsmann, K.; Konorov, I.; Konstantinov, V.F.; Korzenev, A.; Kotzinian, A.M.; Kouznetsov, O.; Krämer, M.; Kroumchtein, Z.V.; Kunne, F.; Kurek, K.; Lauser, L.; Lednev, A.A.; Lehmann, A.; Levorato, S.; Lichtenstadt, J. ; Maggiora, A.; Magnon, A.; Makke, N.; Mallot, G.K.; Mann, A.; Marchand, C.; Martin, A.; Marzec, J.; Massmann, F.; Matsuda, T.; Meyer, W. ; Michigami, T.; Mielech, A.; Mikhailov, Yu.V.; Moinester, M.A.; Morreale, A.; Mutter, A.; Nagaytsev, A.; Nagel, T.; Negrini, T.; Nerling, F. ; Neubert, S.; Neyret, D.; Nikolaenko, V.I.; Nowak, W.D.; Nunes, A.S.; Olshevsky, A.G.; Ostrick, M.; Padee, A.; Panknin, R.; Panzieri, D.; Parsamyan, B.; Paul, S.; Perevalova, E.; Pesaro, G. ; Peshekhonov, D.V.; Piragino, G.; Platchkov, S.; Pochodzalla, J.; Polak, J.; Polyakov, V.A.; Pontecorvo, G.; Pretz, J.; Quaresma, M.; Quintans, C.; Rajotte, J.-F.; Ramos, S.; Rapatsky, V.; Reicherz, G.; Richter, A.; Rocco, E.; Rondio, E. ; Rossiyskaya, N.S.; Ryabchikov, D.I.; Samoylenko, V.D.; Sandacz, A.; Sapozhnikov, M.G.; Sarkar, S. ; Savin, I.A.; Sbrizzai, G.; Schiavon, P.; Schill, C.; Schlüter, T.; Schmidt, K.; Schmitt, L. ; Schönning, K.; Schopferer, S.; Schott, M.; Shevchenko, O.Yu.; Silva, L.; Sinha,

L.; Sissakian, A.N.; Slunecka, M.; Smirnov, G.I.; Sosio, S.; Sozzi, F.; Srnka, A.; Stolarski, M.; Sulc, M.; Sulej, R.; Sznajder, P.; Takekawa, S.; Ter Wolbeek, J.; Tessaro, S.; Tessarotto, F.; Tkatchev, L.G.; Uhl, S.; Uman, I.; Vandenbroucke, M.; Virius, M. ; Vlassov, N.V.; Vossen, A.; Wang, L.; Windmolders, R.; Wilicki, W.; Wollny, H.; Zaremba, K.; Zavertyaev, M.; Zemlyanichkina, E.; Ziembicki, M.; Zhuravlev, N.; Zvyagin, A.: **Transverse spin effects in hadron-pair production from semi-inclusive deep inelastic scattering.** *Physics letters / B* 713: 10 - 16, 2012. DOI:10.1016/j.physletb.2012.05.015

WOS-PHN-44 Adolph, C.; Alekseev, M.G.; Alexakhin, V.Yu.; Alexandrov, Yu.; Alexeev, G.D.; Amoroso, A.; Antonov, A.A.; Austregesilo, A.; Badelek, B.; Balestra, F.; Barth, J.; Baum, G.; Bedfer, Y.; Bernhard, J.; Bertini, R.; Bettinelli, M.; Bicker, K.; Bieling, J.; Birsa, R.; Bisplinghoff, J.; Bordalo, P.; Bradamante, F.; Braun, C.; Bravar, A. ; Bressan, A.; Büchele, M.; Burtin, E.; Capozza, L.; Chiosso, M.; Chung, S.U.; Cicuttin, A.; Crespo, M.L.; Dalla Torre, S.; Das, S.; Dasgupta, S.S.; Dasgupta, S.; Denisov, O.Yu.; Dhara, L.; Donskov, S.V.; Doshita, N.; Duic, V.; Dünnweber, W.; Dziewiecki, M.; Efremov, A.; Elia, C.; Eversheim, P.D.; Eyrich, W.; Faessler, M.; Ferrero, A.; Filin, A.; Finger, M.; Finger, M.; Fischer, H.; Franco, C.; du Fresne von Hohenesche, N.; Friedrich, J.M.; Frolov, V.; Garfagnini, R.; Gautheron, F.; Gavrichtchouk, O.P.; Gerassimov, S.; Geyer, R.; Giorgi, M.; Gnesi, I.; Gobbo, B.; Goertz, S.; Grabmüller, S.; Grasso, A.; Grube, B. ; Gushterski, R.; Guskov, A.; Guthörl, T.; Haas, F.; von Harrach, D.; Heinsius, F.H.; Herrmann, F. ; HeßC.; Hinterberger, F.; Horikawa, N.; Höppner, Ch.; dHose, N.; Huber, S.; Ishimoto, S. ; Ivanov, O.; Ivanshin, Yu.; Iwata, T.; Jahn, R. ; Jary, V.; Jasinski, P.; Joosten, R.; KabußE. ; Kang, D.; Ketzer, B.; Khaustov, G.V.; Khokhlov, Yu.A.; Kisselev, Yu.; Klein, F.; Klimaszewski, K. ; Koblitz, S.; Koivuniemi, J.H.; Kolosov, V.N.; Kondo, K.; Königsmann, K.; Konorov, I.; Konstantinov, V.F.; Korzenev, A.; Kotzinian, A.M.; Kouznetsov, O.; Krämer, M.; Kroumchtein, Z.V.; Kunne, F.; Kurek, K.; Lauser, L.; Lednev, A.A.; Lehmann, A.; Levorato, S.; Lichtenstadt, J.; Liska, T.; Maggiora, A.; Magnon, A.; Makke, N.; Mallot, G.K.; Mann, A.; Marchand, C.; Martin, A.; Marzec, J.; Matsuda, T.; Meshcheryakov, G.; Meyer, W.; Michigami, T.; Mikhailov, Yu.V.; Morreale, A. ; Mutter, A.; Nagaytsev, A.; Nagel, T.; Negrini, T.; Nerling, F.; Neubert, S.; Neyret, D.; Nikolaenko, V.I.; Nowak, W.-D.; Nunes, A.S.; Olshevsky, A.G.; Ostrick, M.; Padee, A.; Panknin, R.; Panzieri, D.; Parsamyan, B.; Paul, S.; Perevalova, E.; Pesaro, G.; Peshekhonov, D.V.; Piragino, G.; Platchkov, S.; Pochodzalla, J.; Polak, J.; Polyakov, V.A.; Pretz, J.; Quaresma, M. ; Quintans, C.; Rajotte, J.-F.; Ramos, S.; Rapatsky, V.; Reicherz, G.; Richter, A.; Rocco, E. ; Rondio, E.; Rossiyskaya, N.S.; Ryabchikov, D.I. ; Samoylenko, V.D.; Sandacz, A.; Sapozhnikov, M.G. ; Sarkar, S.; Savin, I.A.; Sbrizzai, G.; Schiavon, P.; Schill, C.; Schlüter, T.; Schmidt, K.; Schmitt, L.; Schönning, K.; Schopferer, S.; Schott, M.; Schröder, W.; Shevchenko, O.Yu.; Silva, L.; Sinha, L.; Sissakian, A.N.; Slunecka, M. ; Smirnov, G.I.; Sosio, S.; Sozzi, F.; Srnka, A. ; Steiger, L.; Stolarski, M.; Sulc, M.; Sulej, R. ; Suzuki, H.; Sznajder, P.; Takekawa, S.; Ter Wolbeek, J.; Tessaro, S.; Tessarotto, F.; Tkatchev, L.G.; Uhl, S.; Uman, I.; Vandenbroucke, M.; Virius, M.; Vlassov, N.V.; Wang, L.; Wilfert, M. ; Windmolders, R.; Wilicki, W.; Wollny, H.; Zaremba, K.; Zavertyaev, M.; Zemlyanichkina, E.; Ziembicki, M.; Zhuravlev, N.; Zvyagin, A.: **I Experimental investigation of transverse spin asymmetries in μ-p SIDIS processes: Collins asymmetries.** *Physics letters / B* 717: 376 - 382, 2012. DOI:10.1016/j.physletb.2012.09.055

WOS-PHN-45 Adolph, C.; Alekseev, M.G.; Alexakhin, V.Yu.; Alexandrov, Yu.; Alexeev, G.D.; Amoroso, A.; Antonov, A.A.; Austregesilo, A.; Badelek, B.; Balestra, F.; Barth, J.; Baum, G.; Bedfer, Y.; Bernhard, J.; Bertini, R.; Bettinelli, M.; Bicker, K.; Bieling, J.; Birsa, R.; Bisplinghoff, J.; Bordalo, P.; Bradamante, F.; Braun, C.; Bravar, A. ; Bressan, A.; Büchele, M.; Burtin, E.; Capozza, L.; Chiosso, M.; Chung, S.U.; Cicuttin, A.; Crespo, M.L.; Dalla Torre, S.; Das, S.; Dasgupta, S.S.; Dasgupta, S.; Denisov, O.Yu.; Dhara, L.; Donskov, S.V.; Doshita, N.; Duic, V.; Dünnweber, W.; Dziewiecki, M.; Efremov, A.; Elia, C.; Eversheim, P.D.; Eyrich, W.; Faessler, M.; Ferrero, A.; Filin, A.; Finger, M.; Finger, M.; Fischer, H.; Franco, C.; du Fresne von Hohenesche, N.; Friedrich, J.M.; Frolov, V.; Garfagnini, R.; Gautheron, F.; Gavrichtchouk, O.P.; Gerassimov, S.; Geyer, R.; Giorgi, M.; Gnesi, I.; Gobbo, B.; Goertz, S.; Grabmüller, S.; Grasso, A.; Grube, B. ; Gushterski, R.; Guskov, A.; Guthörl, T.; Haas, F.; von Harrach, D.; Heinsius, F.H.; Herrmann, F. ; HeßC.; Hinterberger, F.; Horikawa, N.; Höppner, Ch.; dHose, N.; Huber, S.; Ishimoto, S. ; Ivanov, O.; Ivanshin, Yu.; Iwata, T.; Jahn, R. ; Jary, V.; Jasinski, P.; Joosten, R.; KabußE. ; Kang, D.; Ketzer, B.; Khaustov, G.V.; Khokhlov, Yu.A.; Kisselev, Yu.; Klein, F.; Klimaszewski, K. ; Koblitz, S.; Koivuniemi, J.H.; Kolosov, V.N.; Kondo, K.; Königsmann, K.; Konorov, I.; Konstantinov, V.F.; Korzenev, A.; Kotzinian, A.M.; Kouznetsov, O.; Krämer, M.; Kroumchtein, Z.V.; Kunne, F.; Kurek, K.; Lauser, L.; Lednev, A.A.; Lehmann, A.; Levorato, S.; Lichtenstadt, J.; Liska, T.; Maggiora, A.; Magnon, A.; Makke, N.; Mallot, G.K.; Mann, A.; Marchand, C.; Martin, A.; Marzec, J.; Matsuda, T.; Meshcheryakov, G.; Meyer, W.; Michigami, T.; Mikhailov, Yu.V.; Morreale, A. ; Mutter, A.; Nagaytsev, A.; Nagel, T.; Negrini, T.; Nerling, F.; Neubert, S.; Neyret, D.; Nikolaenko, V.I.; Nowak, W.-D.; Nunes, A.S.; Olshevsky, A.G.; Ostrick, M.; Padee, A.; Panknin, R.; Panzieri, D.; Parsamyan, B.; Paul, S.; Perevalova, E.; Pesaro, G.; Peshekhonov, D.V.; Piragino, G.; Platchkov, S.; Pochodzalla, J.; Polak, J.; Polyakov, V.A.; Pretz, J.; Quaresma, M. ; Quintans, C.; Rajotte, J.-F.; Ramos, S.; Rapatsky, V.; Reicherz, G.; Richter, A.; Rocco, E. ; Rondio, E.; Rossiyskaya, N.S.; Ryabchikov, D.I. ; Samoylenko, V.D.; Sandacz, A.; Sapozhnikov, M.G. ; Sarkar, S.; Savin, I.A.; Sbrizzai, G.; Schiavon, P.; Schill, C.; Schlüter, T.; Schmidt, K.; Schmitt, L.; Schönning, K.; Schopferer, S.; Schott, M.; Schröder, W.; Shevchenko, O.Yu.; Silva, L.; Sinha, L.; Sissakian, A.N.; Slunecka, M. ; Smirnov, G.I.; Sosio, S.; Sozzi, F.; Srnka, A. ; Steiger, L.; Stolarski, M.; Sulc, M.; Sulej, R. ; Suzuki, H.; Sznajder, P.; Takekawa, S.; Ter Wolbeek, J.; Tessaro, S.; Tessarotto, F.; Tkatchev, L.G.; Uhl, S.; Uman, I.; Vandenbroucke, M.; Virius, M.; Vlassov, N.V.; Wang, L.; Wilfert, M. ; Windmolders, R.; Wilicki, W.; Wollny, H.; Zaremba, K.; Zavertyaev, M.; Zemlyanichkina, E.; Ziembicki, M.; Zhuravlev, N.; Zvyagin, A.: **II Experimental investigation of transverse spin asymmetries in μ-p SIDIS processes: Sivers asymmetries.** *Physics letters / B* 717: 383 - 389, 2012. DOI:10.1016/j.physletb.2012.09.056

WOS-PHN-46 Adolph, C.; Alekseev, M.G.; Alexakhin, V.Yu.; Alexandrov, Yu.; Alexeev, G.D.; Amoroso, A.; Antonov, A.A.; Austregesilo, A.; Badelek, B.; Balestra, F.; Barth, J.; Baum, G.; Bedfer, Y.; Bernhard, J.; Bertini, R.; Bettinelli, M.; Bicker, K.; Bieling, J.; Birsa, R.; Bisplinghoff, J.; Bordalo, P.; Bradamante, F.; Braun, C.; Bravar, A. ; Bressan, A.; Büchele, M.; Burtin, E.; Capozza, L.; Chiosso, M.; Chung, S.U.; Cicuttin, A.; Crespo,

M.L.; Dalla Torre, S.; Das, S.; Dasgupta, S.S.; Dasgupta, S.; Denisov, O.Yu.; Dhara, L.; Donskov, S.V.; Doshita, N.; Duic, V.; Dünnweber, W.; Dziewiecki, M.; Efremov, A.; Elia, C.; Eversheim, P.D.; Eyrich, W.; Faessler, M.; Ferrero, A.; Filin, A.; Finger, M.; Finger, M.; Fischer, H.; Franco, C.; du Fresne von Hohenesche, N.; Friedrich, J.M.; Frolov, V.; Garfagnini, R.; Gautheron, F.; Gavrichtchouk, O.P.; Gerassimov, S.; Geyer, R.; Giorgi, M.; Gnesi, I.; Gobbo, B.; Goertz, S.; Grabmüller, S.; Grasso, A.; Grube, B. ; Gushterski, R.; Guskov, A.; Guthörl, T.; Haas, F.; von Harrach, D.; Heinsius, F.H.; Herrmann, F. ; HeßC.; Hinterberger, F.; Horikawa, N.; Höppner, Ch.; dHose, N.; Ishimoto, S.; Ivanov, O.; Ivanshin, Yu.; Iwata, T.; Jahn, R.; Jary, V. ; Jasinski, P.; Jegou, G.; Joosten, R.; KabußE.; Kang, D.; Ketzer, B.; Khaustov, G.V.; Khokhlov, Yu.A.; Kisselev, Yu.; Klein, F.; Klimaszewski, K.; Koblitz, S.; Koivuniemi, J.H.; Kolosov, V.N.; Kondo, K.; Königsmann, K.; Konorov, I.; Konstantinov, V.F.; Korzenev, A.; Kotzinian, A.M.; Kouznetsov, O.; Krämer, M.; Kroumchtein, Z.V.; Kunne, F.; Kurek, K.; Lauser, L.; Lednev, A.A.; Lehmann, A.; Levorato, S.; Lichtenstadt, J. ; Liska, T.; Maggiora, A.; Magnon, A.; Makke, N. ; Mallot, G.K.; Mann, A.; Marchand, C.; Martin, A.; Marzec, J.; Matsuda, T.; Meshcheryakov, G.; Meyer, W.; Michigami, T.; Mikhailov, Yu.V.; Moinester, M.A.; Morreale, A.; Mutter, A.; Nagaytsev, A.; Nagel, T.; Negrini, T.; Nerling, F. ; Neubert, S.; Neyret, D.; Nikolaenko, V.I.; Nowak, W.-D.; Nunes, A.S.; Olshevsky, A.G.; Ostrick, M.; Padee, A.; Panknin, R.; Panzieri, D. ; Parsamyan, B.; Paul, S.; Perevalova, E.; Pesaro, G.; Peshekhonov, D.V.; Piragino, G.; Platchkov, S.; Pochodzalla, J.; Polak, J.; Polyakov, V.A.; Pretz, J.; Quaresma, M.; Quintans, C.; Rajotte, J.-F.; Ramos, S.; Rapatsky, V.; Reicherz, G.; Richter, A.; Rocco, E.; Rondio, E. ; Rossiyskaya, N.S.; Ryabchikov, D.I.; Samoylenko, V.D.; Sandacz, A.; Sapozhnikov, M.G.; Sarkar, S. ; Savin, I.A.; Sbrizzai, G.; Schiavon, P.; Schill, C.; Schlüter, T.; Schmidt, K.; Schmitt, L. ; Schönning, K.; Schopferer, S.; Schott, M.; Schröder, W.; Shevchenko, O.Yu.; Silva, L.; Sinha, L.; Sissakian, A.N.; Slunecka, M.; Smirnov, G.I. ; Sosio, S.; Sozzi, F.; Srnka, A.; Steiger, L. ; Stolarski, M.; Sulc, M.; Sulej, R.; Suzuki, H. ; Sznajder, P.; Takekawa, S.; Ter Wolbeek, J.; Tessaro, S.; Tessarotto, F.; Tkatchev, L.G.; Uhl, S.; Uman, I.; Vandenbroucke, M.; Virius, M.; Vlassov, N.V.; Wang, L.; Wilfert, M.; Windmolders, R.; Wilicki, W.; Wollny, H.; Zaremba, K.; Zavertyaev, M.; Zemlyanichkina, E.; Ziembicki, M.; Zhuravlev, N.; Zvyagin, A.: **Exclusive muoproduction on transversely polarised protons and deuterons.** *Nuclear physics / B* 865: 1 - 20, 2012. DOI:10.1016/j.nuclphysb.2012.07.025

WOS-PHN-47 Adonin, A.; Hollinger, R.: **Development of high current Bi and Au beams for the synchrotron operation at the GSI accelerator facility.** *Review of scientific instruments* 83: 02A505 -, 2012. DOI:10.1063/1.3670743

WOS-PHN-48 Agakishiev, G.; Alvarez-Pol, H.; Balanda, A.; Bassini, R.; Böhmer, M.; Bokemeyer, H.; Boyard, J. L.; Cabanelas, P.; Chernenko, S.; Christ, T.; Destefanis, M.; Dohrmann, F.; Dybczak, A.; Eberl, T.; Fabbietti, L.; Fateev, O.; Finocchiaro, P.; Friese, J.; Fröhlich, I.; Galatyuk, T.; Garzon, J. A.; Gernhäuser, R.; Gilardi, C.; Golubeva, M. ; Gonzalez-Diaz, D.; Guber, F.; Gumberidze, M.; Hennino, T.; Holzmann, R.; Ierusalimov, A.; Iori, I.; Ivashkin, A.; Jurkovic, M.; Kämpfer, B.; Kanaki, K.; Karavicheva, T.; Koenig, I.; Koenig, W. ; Kolb, B. W.; Kotte, R.; Kozuch, A.; Krizek, F. ; Kühn, W.; Kugler, A.; Kurepin, A.; Lang, S. ; Lapidus, K.; Liu, T.; Maier, L.; Markert, J. ; Metag, V.; Michalska, B.; Moriniere, E.; Mousa, J.; Münch, C.; Müntz, C.; Naumann, L.; Otwinowski, J.; Pachmayer, Y. C.; Pechenov, V.; Pechenova, O.; Perez Cavalcanti, T.; Pietraszko, J. ; Pospisil, V.; Przygoda, W.; Ramstein, B.; Reshetin, A.; Roy-Stephan, M.; Rustamov, A.; Sadovsky, A.; Sailer, B.; Salabura, P.; Sanchez, M.; Schmah, A.; Schwab, E.; Sobolev, Yu. G.; Spataro, S.; Spruck, B.; Ströbele, H.; Stroth, J. ; Sturm, C.; Tarantola, A.; Teilab, K.; Tlusty, P.; Toia, A.; Traxler, M.; Trebacz, R.; Tsertos, H.; Wagner, V.; Wisniowski, M.; Wojcik, T.; Wüstenfeld, J.; Yurevich, S.; Zanevsky, Y.; Zumbruch, P.: **Inclusive dielectron production in proton-proton collisions at 2.2 GeV beam energy.** *Physical review / C* 85: 054005, 2012. DOI:10.1103/PhysRevC.85.054005

WOS-PHN-49 Agakishiev, G.; Alvarez-Pol, H.; Balanda, A.; Bassini, R.; Böhmer, M.; Bokemeyer, H.; Boyard, J. L.; Cabanelas, P.; Chernenko, S.; Christ, T.; Destefanis, M.; Dohrmann, F.; Dybczak, A.; Eberl, T.; Fabbietti, L.; Fateev, O.; Finocchiaro, P.; Friese, J.; Fröhlich, I.; Galatyuk, T.; Garzon, J. A.; Gernhäuser, R.; Gilardi, C.; Golubeva, M. ; Gonzalez-Daz, D.; Guber, F.; Gumberidze, M.; Hennino, T.; Holzmann, R.; Ierusalimov, A.; Iori, I.; Ivashkin, A.; Jurkovic, M.; Kämpfer, B.; Kanaki, K.; Karavicheva, T.; Koenig, I.; Koenig, W. ; Kolb, B. W.; Kotte, R.; Kozuch, A.; Krizek, F. ; Kühn, W.; Kugler, A.; Kurepin, A.; Lang, S. ; Lapidus, K.; Liu, T.; Maier, L.; Markert, J. ; Metag, V.; Michalska, B.; Moriniere, E.; Mousa, J.; Münch, M.; Müntz, C.; Naumann, L.; Otwinowski, J.; Pachmayer, Y. C.; Pechenov, V.; Pechenova, O.; Perez Cavalcanti, T.; Pietraszko, J. ; Pospsil, V.; Przygoda, W.; Ramstein, B.; Reshetin, A.; Roy-Stephan, M.; Rustamov, A.; Sadovsky, A.; Sailer, B.; Salabura, P.; Sanchez, M.; Schmah, A.; Schwab, E.; Sobolev, Yu. G.; Spataro, S.; Spruck, B.; Ströbele, H.; Stroth, J. ; Sturm, C.; Tarantola, A.; Teilab, K.; Tlusty, P.; Toia, A.; Traxler, M.; Trebacz, R.; Tsertos, H.; Wagner, V.; Wisniowski, M.; Wojcik, T.; Wüstenfeld, J.; Yurevich, S.; Zanevsky, Y.; Zumbruch, P.: **Study of exclusive one-pion and one-eta production using hadron and dielectron channels in pp reactions at kinetic beam energies of 1.25 GeV and 2.2 GeV with HADES.** *The European physical journal / A* 48: 74, 2012. DOI:10.1140/epja/i2012-12074-9

WOS-PHN-50 Agakishiev, G.; Balanda, A.; Belver, D.; Belyaev, A.; Berger-Chen, J. C.; Blanco, A.; Böhmer, M.; Boyard, J. L.; Cabanelas, P.; Castro, E.; Chernenko, S.; Christ, T.; Destefanis, M.; Dohrmann, F.; Dybczak, A.; Epple, E.; Fabbietti, L. ; Fateev, O. V.; Finocchiaro, P.; Fonte, P.; Friese, J.; Fröhlich, I.; Galatyuk, T.; Garzon, J. A.; Gernhäuser, R.; Gilardi, C.; Golubeva, M. ; Gonzalez-Diaz, D.; Guber, F.; Gumberidze, M.; Heinz, T.; Hennino, T.; Holzmann, R.; Ierusalimov, A.; Iori, I.; Ivashkin, A.; Jurkovic, M.; Kämpfer, B.; Kanaki, K.; Karavicheva, T.; Koenig, I.; Koenig, W.; Kolb, B. W.; Kotte, R.; Krasa, A.; Krizek, F.; Krücken, R.; Kuc, H.; Kühn, W. ; Kugler, A.; Kurepin, A.; Lalik, R.; Lang, S. ; Lange, J. S.; Lapidus, K.; Liu, T.; Lopes, L. ; Lorenz, M.; Maier, L.; Mangiarotti, A.; Markert, J.; Metag, V.; Michalska, B.; Michel, J. ; Moriniere, E.; Mousa, J.; Müntz, C.; Naumann, L.; Otwinowski, J.; Pachmayer, Y. C.; Palka, M.; Parpottas, Y.; Pechenov, V.; Pechenova, O.; Pietraszko, J.; Przygoda, W.; Ramstein, B.; Reshetin, A.; Rustamov, A.; Sadovsky, A.; Salabura, P.; Schmah, A.; Schwab, E.; Siebenson, J.; Sobolev, Yu. G.; Spataro, S.; Spruck, B.; Ströbele, H.; Stroth, J.; Sturm, C.; Tarantola, A. ; Teilab, K.; Tlusty, P.; Traxler, M.; Trebacz, R.; Tsertos, H.; Wagner, V.; Weber, M.; Wendisch, C.; Wüstenfeld, J.; Yurevich, S.; Zanevsky, Y.: **Baryonic resonances close to the**

$\frac{K}{N}$ **threshold: The case of $\Sigma(1385)^+$ in pp collisions.** *Physical review / C* 85: 035203, 2012. DOI:10.1103/PhysRevC.85.035203

WOS-PHN-51 Agakishiev, G.; Balanda, A.; Belver, D.; Belyaev, A.; Berger-Chen, J.C.; Blanco, A.; Böhmer, M.; Boyard, J.L.; Cabanelas, P.; Castro, E.; Chernenko, S.; Christ, T.; Destefanis, M.; Dohrmann, F.; Dybczak, A.; Epple, E.; Fabbietti, L.; Fateev, O. ; Finocchiaro, P.; Fonte, P.; Friese, J.; Fröhlich, I.; Galatyuk, T.; Garzon, J.A.; Gernhäuser, R.; Gilardi, C.; Golubeva, M.; Gonzalez-Diaz, D.; Guber, F.; Gumberidze, M.; Heinz, T.; Hennino, T.; Holzmann, R.; Ierusalimov, A.; Iori, I.; Ivashkin, A.; Jurkovic, M.; Kämpfer, B.; Kanaki, K.; Karavicheva, T.; Koenig, I.; Koenig, W.; Kolb, B.W.; Kotte, R.; Krasa, A.; Krizek, F.; Krücken, R.; Kuc, H.; Kühn, W. ; Kugler, A.; Kurepin, A.; Lalik, R.; Lang, S. ; Lange, J.S.; Lapidus, K.; Liu, T.; Lopes, L. ; Lorenz, M.; Maier, L.; Mangiarotti, A.; Markert, J.; Metag, V.; Michalska, B.; Michel, J. ; Moriniere, E.; Mousa, J.; Müntz, C.; Münzer, R.; Naumann, L.; Otwinowski, J.; Pachmayer, Y.C. ; Palka, M.; Parpottas, Y.; Pechenov, V.; Pechenova, O.; Pietraszko, J.; Przygoda, W.; Ramstein, B.; Reshetin, A.; Rustamov, A.; Sadovsky, A.; Salabura, P.; Schmah, A.; Schwab, E.; Siebenson, J.; Sobolev, Yu.G.; Spataro, S.; Spruck, B.; Ströbele, H.; Stroth, J.; Sturm, C.; Tarantola, A.; Teilab, K.; Tlusty, P.; Traxler, M. ; Trebacz, R.; Tsertos, H.; Wagner, V.; Weber, M. ; Wendisch, C.; Wüstenfeld, J.; Yurevich, S.; Zanevsky, Y.: **Production of in reactions at 3.5 GeV beam energy.** *Nuclear physics / A* 881: 178 - 186, 2012. DOI:10.1016/j.nuclphysa.2012.02.009

WOS-PHN-52 Agakishiev, G.; Balanda, A.; Belver, D.; Belyaev, A.; Berger-Chen, J.C.; Blanco, A.; Böhmer, M.; Boyard, J.L.; Cabanelas, P.; Chernenko, S.; Dybczak, A.; Epple, E.; Fabbietti, L.; Fateev, O. ; Finocchiaro, P.; Fonte, P.; Friese, J.; Fröhlich, I.; Galatyuk, T.; Garzon, J.A.; Gernhäuser, R.; Göbel, K.; Golubeva, M.; Gonzalez-Diaz, D.; Guber, F.; Gumberidze, M.; Heinz, T.; Hennino, T.; Holzmann, R.; Ierusalimov, A.; Iori, I.; Ivashkin, A.; Jurkovic, M.; Kämpfer, B.; Karavicheva, T.; Koenig, I.; Koenig, W.; Kolb, B.W.; Kornakov, G.; Kotte, R.; Krasa, A.; Krizek, F.; Krücken, R.; Kuc, H.; Kühn, W. ; Kugler, A.; Kurepin, A.; Ladygin, V.; Lalik, R. ; Lang, S.; Lapidus, K.; Lebedev, A.; Liu, T.; Lopes, L.; Lorenz, M.; Maier, L.; Mangiarotti, A. ; Markert, J.; Metag, V.; Michalska, B.; Michel, J.; Mishra, D.; Müntz, C.; Naumann, L.; Pachmayer, Y.C.; Palka, M.; Parpottas, Y.; Pechenov, V.; Pechenova, O.; Pietraszko, J.; Przygoda, W.; Ramstein, B.; Reshetin, A.; Rustamov, A.; Sadovsky, A.; Salabura, P.; Schmah, A.; Schwab, E.; Siebenson, J.; Sobolev, Yu.G.; Spataro, S.; Spruck, B.; Ströbele, H.; Stroth, J.; Sturm, C.; Tarantola, A.; Teilab, K.; Tlusty, P. ; Traxler, M.; Trebacz, R.; Tsertos, H.; Vasiliev, T.; Wagner, V.; Weber, M.; Wendisch, C. ; Wüstenfeld, J.; Yurevich, S.; Zanevsky, Y.: **First measurement of proton-induced low-momentum dielectron radiation off cold nuclear matter.** *Physics letters / B* 715: 304 - 309, 2012. DOI:10.1016/j.physletb.2012.08.004

WOS-PHN-53 Agakishiev, G.; Balanda, A.; Belver, D.; Belyaev, A.; Blanco, A.; Böhmer, M.; Boyard, J. L.; Cabanelas, P.; Castro, E.; Chen, J. C.; Chernenko, S.; Christ, T.; Destefanis, M.; Dohrmann, F.; Dybczak, A.; Epple, E.; Fabbietti, L.; Fateev, O. ; Finocchiaro, P.; Fonte, P.; Friese, J.; Fröhlich, I.; Galatyuk, T.; Garzon, J. A.; Gernhäuser, R.; Gilardi, C.; Golubeva, M.; Gonzalez-Diaz, D.; Guber, F.; Gumberidze, M.; Heinz, T.; Hennino, T.; Holzmann, R.; Ierusalimov, A.; Iori, I.; Ivashkin, A.; Jurkovic, M.; Kämpfer, B.; Kanaki, K.; Karavicheva, T.; Koenig, I.; Koenig, W.; Kolb, B. W.; Kotte, R.; Krasa, A.; Krizek, F.; Krücken, R.; Kuc, H.; Kühn, W. ; Kugler, A.; Kurepin, A.; Lalik, R.; Lang, S. ; Lange, J. S.; Lapidus, K.; Liu, T.; Lopes, L. ; Lorenz, M.; Maier, L.; Mangiarotti, A.; Markert, J.; Metag, V.; Michalska, B.; Michel, J. ; Moriniere, E.; Mousa, J.; Müntz, C.; Naumann, L.; Otwinowski, J.; Pachmayer, Y. C.; Palka, M.; Parpottas, Y.; Pechenov, V.; Pechenova, O.; Pietraszko, J.; Przygoda, W.; Ramstein, B.; Reshetin, A.; Rustamov, A.; Sadovsky, A.; Salabura, P.; Schmah, A.; Schwab, E.; Siebenson, J.; Sobolev, Yu. G.; Spataro, S.; Spruck, B.; Ströbele, H.; Stroth, J.; Sturm, C.; Tarantola, A. ; Teilab, K.; Tlusty, P.; Traxler, M.; Trebacz, R.; Tsertos, H.; Wagner, V.; Weber, M.; Wendisch, C.; Wüstenfeld, J.; Yurevich, S.; Zanevsky, Y.: **Inclusive dielectron spectra in p+p collisions at 3.5 GeV kinetic beam energy.** *The European physical journal / A* 48: 64, 2012. DOI:10.1140/epja/i2012-12064-y

WOS-PHN-54 Andronic, Anton; Braun-Munzinger, Peter; Stachel, J.; Winn, M.: **Interacting hadron resonance gas meets lattice QCD.** *Physics letters / B* 718: 80 - 85, 2012. DOI:10.1016/j.physletb.2012.10.001

WOS-PHN-55 Andronic, Anton; Wessels, J.P.: **Transition radiation detectors.** *Nuclear instruments & methods in physics research / A* 666: 130 - 147, 2012. DOI:10.1016/j.nima.2011.09.041

WOS-PHN-56 Anticic, T.; Baatar, B.; Barna, D.; Bartke, J.; Beck, Dietrich; Betev, L.; Bialkowska, H.; Blume, C.; Bogusz, M.; Boimska, B.; Book, J.; Botje, M. ; Buncic, P.; Cetner, T.; Christakoglou, P.; Chung, P.; Chvala, O.; Cramer, J. G.; Eckardt, V. ; Fodor, Z.; Foka, P.; Friese, Volker; Gadzicki, M.; Grebieszkow, K.; Höhne, C.; Kadija, K.; Karev, A.; Kolesnikov, V. I.; Kowalski, M.; Kresan, Dmytro; Laszlo, A.; Lacey, R.; van Leeuwen, M.; Mackowiak-Pawlowska, M.; Makariev, M. ; Malakhov, A. I.; Mateev, M.; Melkumov, G. L.; Mitrovski, M.; Mrowczynski, St.; Nicolic, V.; Palla, G.; Panagiotou, A. D.; Peryt, W.; Pluta, J. ; Prindle, D.; Pühlhofer, F.; Renfordt, R.; Roland, C.; Roland, G.; Rybczynski, M.; Rybicki, A.; Sandoval, A.; Schmitz, N.; Schuster, T.; Seyboth, P.; Sikler, F.; Skrzypczak, E.; Slodkowski, M.; Stefanek, G.; Stock, R.; Ströbele, H.; Susa, T.; Szuba, M.; Utvic, M.; Varga, D. ; Vassiliou, M.; Veres, G. I.; Vesztergombi, G.; Vranic, D.; Wlodarczyk, Z.; Wojtaszek-Szwarc, A.: **Antideuteron and deuteron production in midcentral Pb+Pb collisions at 158A GeV.** *Physical review / C* 85: 044913, 2012. DOI:10.1103/PhysRevC.85.044913

WOS-PHN-57 Anticic, T.; Baatar, B.; Barna, D.; Bartke, J.; Beck, H.; Betev, L.; Bialkowska, H.; Blume, C.; Bogusz, M.; Boimska, B.; Book, J.; Botje, M.; Buncic, P.; Cetner, T.; Christakoglou, P.; Chung, P.; Chvala, O.; Cramer, J. G.; Dinkelaker, P.; Eckardt, V.; Fodor, Z.; Foka, P.; Friese, V.; Gadzicki, M.; Grebieszkow, K.; Höhne, C.; Kadija, K.; Karev, A.; Kliemant, M.; Kolesnikov, V. I.; Kollegger, T.; Kowalski, M.; Kresan, D.; Laszlo, A.; Lacey, R.; van Leeuwen, M.; Lungwitz, B.; Mackowiak, M.; Makariev, M.; Malakhov, A. I. ; Mateev, M.; Melkumov, G. L.; Mitrovski, M.; Mrowczynski, St.; Nicolic, V.; Palla, G.; Panagiotou, A. D.; Peryt, W.; Pluta, J.; Prindle, D.; Pühlhofer, F.; Renfordt, R.; Roland, C.; Roland, G.; Rybczynski, M.; Rybicki, A.; Sandoval, A.; Schmitz, N.; Schuster, T.; Seyboth, P.; Sikler, F.; Skrzypczak, E.; Slodkowski, M.; Stefanek, G.; Stock, R.; Ströbele, H.; Susa, T. ; Szuba, M.; Utvic, M.; Varga, D.; Vassiliou, M. ;

Veres, G. I.; Vesztergombi, G.; Vranic, D.; Wlodarczyk, Z.; Wojtaszek-Szwarc, A.: **System-size and centrality dependence of charged kaon and pion production in nucleus-nucleus collisions at 40A GeV and 158A GeV beam energy.** *Physical review / C* 86: 054903, 2012. DOI:10.1103/PhysRevC.86.054903

WOS-PHN-58 Appel, Sabrina; Boine-Frankenheim, Oliver: **Microbunch dynamics and multistream instability in a heavy-ion synchrotron.** *Physical review / Special topics / Accelerators and beams* 15: 054201, 2012. DOI:10.1103/PhysRevSTAB.15.054201

WOS-PHN-59 Arcones, A.; Bertsch, G. F.: **Nuclear Correlations and the r Process.** *Physical review letters* 108: 151101, 2012. DOI:10.1103/PhysRevLett.108.151101

WOS-PHN-60 Arcones, A.; Fröhlich, C.; Martinez-Pinedo, G.: **Impact of supernova dynamics on the p -process.** *The astrophysical journal / 1* 750: 18 -, 2012. DOI:10.1088/0004-637X/750/1/18

WOS-PHN-61 Armbruster, P.; Münzenberg, Gottfried: **An experimental paradigm opening the world of superheavy elements.** *The European physical journal / H* 37: 237 - 309, 2012. DOI:10.1140/epjh/e2012-20046-7

WOS-PHN-62 Audi, G.; Kondev, F.G.; Wang, M.; Pfeiffer, B.; Sun, X.; Blachot, J.; MacCormick, M.: **The Nubase2012 evaluation of nuclear properties.** *Chinese physics / C* 36: 1157 - 1286, 2012. DOI:10.1088/1674-1137/36/12/001

WOS-PHN-63 Bacca, S.; Barnea, N.; Schwenk, A.: **Matter and charge radius of ^6He in the hyperspherical-harmonics approach.** *Physical review / C* 86: 034321, 2012. DOI:10.1103/PhysRevC.86.034321

WOS-PHN-64 Bacca, S.; Hally, K.; Liebendörfer, M.; Perego, A.; Pethick, C. J.; Schwenk, A.: **Neutrino processs in partially degenerate neutron matter.** *The astrophysical journal / 1* 758: 34 -, 2012. DOI:10.1088/0004-637X/758/1/34

WOS-PHN-65 Becker, R.; Kester, Oliver: **The design of an electron gun switchable between immersed and Brillouin flow.** *Review of scientific instruments* 83: 02A506 -, 2012. DOI:10.1063/1.3671737

WOS-PHN-66 Belousov, Anton; Mustafin, Edil; Ensinger, W.: **Short and long term ionizing radiation effects on charge-coupled devices in radiation environment of high-intensity heavy ion accelerators.** *Journal of Instrumentation* 7: C11002 - C11002, 2012. DOI:10.1088/1748-0221/7/11/C11002

WOS-PHN-67 Belver, D; Blanco, A; Cabanelas, P; Diaz, J; Fonte, P; Garzon, J A; Gil, A; Gonzalez Diaz, Diego; Koenig, Wolfgang; Kolb, Hermann; Kornakov, G ; Lopes, L; Palka, M; Pereira, A; Traxler, Michael; Zumbruch, Peter: **Analysis of the space-time microstructure of cosmic ray air showers using the HADES RPC TOF wall.** *Journal of Instrumentation* 7: P10007 - P10007, 2012. DOI:10.1088/1748-0221/7/10/P10007

WOS-PHN-68 Berges, Jürgen; Boguslavski, Kirill; Schlichting, Sören: **Nonlinear amplification of instabilities with longitudinal expansion.** *Physical review / D* 85: 076005, 2012. DOI:10.1103/PhysRevD.85.076005

WOS-PHN-69 Berges, Jürgen; Scheffler, Sebastian; Schlichting, Sören; Sexty, Denes: **Out-of-equilibrium dynamics of coherent non-Abelian gauge fields.** *Physical review / D* 85: 034507, 2012. DOI:10.1103/PhysRevD.85.034507

WOS-PHN-70 Berges, Jürgen; Sexty, Denes: **Bose-Einstein Condensation in Relativistic Field Theories Far from Equilibrium.** *Physical review letters* 108: 161601, 2012. DOI:10.1103/PhysRevLett.108.161601

WOS-PHN-71 Blanco, A; Fonte, P; Lopes, L; Martins, P; Michel, J; Palka, M; Kajetanowicz, M; Korcyl, G; Traxler, M; Marques, R: **TOFtracker: gaseous detector with bidimensional tracking and time-of-flight capabilities.** *Journal of Instrumentation* 7: P11012 - P11012, 2012. DOI:10.1088/1748-0221/7/11/P11012

WOS-PHN-72 Blanco, A.; Belver, D.; Cabanelas, P.; Diaz, J.; Fonte, P.; Garzon, J.A.; Gil, A.; Gonzalez Diaz, Diego; Koenig, Wolfgang; Kolb, Burkhard; Lopes, L.; Palka, M.; Pereira, A.; Traxler, Michael ; Zumbruch, Peter: **RPC HADES-TOF wall cosmic ray test performance.** *Nuclear instruments & methods in physics research / A* 661: S114 - S117, 2012. DOI:10.1016/j.nima.2010.08.068

WOS-PHN-73 Blaschke, D.; Berdermann, J.; Cleymans, J.; Redlich, K.: **Chiral Condensate and MottAnderson Freeze-Out.** *Few-body systems* 53: 99 - 109, 2012. DOI:10.1007/s00601-011-0261-6

WOS-PHN-74 Blaschke, D.; Grigorian, H.; Voskresensky, D. N.; Weber, F.: **Cooling of the neutron star in Cassiopeia A.** *Physical review / C* 85: 022802, 2012. DOI:10.1103/PhysRevC.85.022802

WOS-PHN-75 Boine-Frankenheim, O.; Gjonaj, E.; Petrov, F.; Yaman, F.; Weiland, T.; Rumolo, G.: **Energy loss and longitudinal wakefield of relativistic short proton bunches in electron clouds.** *Physical review / Special topics / Accelerators and beams* 15: 054402, 2012. DOI:10.1103/PhysRevSTAB.15.054402

WOS-PHN-76 Boine-Frankenheim, O.; Gjonaj, E.; Petrov, F.; Yaman, F.; Weiland, T.; Rumolo, G.: **Energy loss and longitudinal wakefield of relativistic short proton bunches in electron clouds.** *Physical review / Special topics / Accelerators and beams* 15: 054402, 2012. DOI:10.1103/PhysRevSTAB.15.054402

WOS-PHN-77 Bonnet, Jacqueline A.; Fischer, Christian S.; Williams, Richard: **Effects of anisotropy in (2+1)-dimensional QED.** *Progress in particle and nuclear physics* 67: 245 - 249, 2012. DOI:10.1016/j.ppnp.2011.12.026

WOS-PHN-78 Bonnet, Jacqueline A.; Fischer, Christian S.: **Critical scaling of finite temperature QED3 in anisotropic spacetime.** *Physics letters / B* 718: 532 - 537, 2012. DOI:10.1016/j.physletb.2012.11.004

WOS-PHN-79 Botvina, A.S.; Gudima, K.K.; Steinheimer, J.; Mishustin, I.N.; Pochodzalla, J.; Sanchez-Lorente, Alicia; Bleicher, M.; Stöcker, Horst: **Production of hypernuclei in**

peripheral collisions of relativistic ions. *Nuclear physics / A* 881: 228 - 239, 2012. DOI:10.1016/j.nuclphysa.2012.01.015

WOS-PHN-80 Braun-Munzinger, P.; Friman, B.; Karsch, F.; Redlich, K.; Skokov, V.: **Net charge probability distributions in heavy ion collisions at chemical freeze-out.** *Nuclear physics / A* 880: 48 - 64, 2012. DOI:10.1016/j.nuclphysa.2012.02.010

WOS-PHN-81 Bravo, Eduardo; Martinez-Pinedo, Gabriel: **Sensitivity study of explosive nucleosynthesis in type Ia supernovae: Modification of individual thermonuclear reaction rates.** *Physical review / C* 85: 055805, 2012. DOI:10.1103/PhysRevC.85.055805

WOS-PHN-82 Brodeur, M.; Brunner, T.; Champagne, C.; Ettenauer, S.; Smith, M. J.; Lapierre, A.; Ringle, R.; Ryjkov, V. L.; Bacca, S.; Delheij, P.; Drake, G. W. F.; Schwenk, A.; Lunney, D.; Dilling, J.: **First Direct Mass Measurement of the Two-Neutron Halo Nucleus ^{6}He and Improved Mass for the Four-Neutron Halo ^{8}He.** *Physical review letters* 108: 052504, 2012. DOI:10.1103/PhysRevLett.108.052504

WOS-PHN-83 Chen, H; Wang, Y; Gonzalez Diaz, Diego; Wang, J; Fan, X; Cheng, J; Linev, Sergey: **Production of long-strip multi-gap resistive plate chamber module for the STAR-MTD system.** *Journal of Instrumentation* 7: P10006 - P10006, 2012. DOI:10.1088/1748-0221/7/10/P10006

WOS-PHN-84 Comas, V.; Heinz, S.; Hofmann, S.; Ackermann, D.; Heredia, J.; Heßberger, F. P.; Khuyagbaatar, J. ; Kindler, B.; Lommel, B.; Mann, R.: **Observation of rotating nuclear molecules and determination of their lifetimes.** *The European physical journal / A* 48: 180, 2012. DOI:10.1140/epja/i2012-12180-8

WOS-PHN-85 Csernai, L.P.; Skalvik, A.M.; Magas, V.K.; Wang, D.J.; Stöcker, H.: **Flow components and initial state CM fluctuations.** *Acta physica Polonica / B* 43: 803 - 810, 2012. DOI:10.5506/APhysPolB.43.803

WOS-PHN-86 Danilkin, I. V.; Orlovsky, V. D.; Simonov, Yu. A.: **Hadron interaction with heavy quarkonia.** *Physical review / D* 85: 034012, 2012. DOI:10.1103/PhysRevD.85.034012

WOS-PHN-87 Deppner, I; Herrmann, N; Ciobanu, M; Frühauf, Jochen; Kis, M; Loizeau, P -A; Wisniewski, K; Xiang, C: **A glass type Multistrip-MRPC prototype for the low rate region of the CBM Time-of-Flight wall.** *Journal of Instrumentation* 7: P10008 - P10008, 2012. DOI:10.1088/1748-0221/7/10/P10008

WOS-PHN-88 Deppner, I.; Herrmann, N.; Gonzalez-Diaz, D.; Ammosov, V.; Cheng, J.; Ciobanu, M.; Gapienko, V. ; Hildenbrand, K.D.; Kiseleva, A.; Kis, M.; Kresan, D.; Kotte, R.; Huangshan, C.; Leifels, Y. ; Fruehauf, J.; Li, C.; Li, Y.; Loizeau, P.-A. ; Naumann, L.; Petrovici, M.; Petris, M.; Semak, A.; Simion, V.; Stach, D.; Sun, Y.; Sviridov, Yu.; Tang, Z.; Usenko, E.; Wang, J.; Wang, Y. ; Wisniewski, K.; Wüstenfeld, J.; Xu, L.; Zaets, V.; Zhang, Y.; Zhu, X.: **The CBM time-of-flight wall.** *Nuclear instruments & methods in physics research / A* 661: S121 - S124, 2012. DOI:10.1016/j.nima.2010.09.165

WOS-PHN-89 Düllmann, Christoph Emanuel: **Superheavy elements at GSI: abroad research program with element 114 in the focus of physics and chemistry.** *Radiochimica acta* 100: 67-74, 2012. DOI:10.1524/ract.2011.1842

WOS-PHN-90 Egorova, I. A.; Charity, R. J.; Grigorenko, L. V.; Chajecki, Z.; Coupland, D.; Elson, J. M.; Ghosh, T. K.; Howard, M. E.; Iwasaki, H.; Kilburn, M.; Lee, Jenny; Lynch, W. G.; Manfredi, J.; Marley, S. T.; Sanetullaev, A.; Shane, R.; Shetty, D. V.; Sobotka, L. G.; Tsang, M. B.; Winkelbauer, J.; Wuosmaa, A. H.; Youngs, M.; Zhukov, M. V.: **Democratic Decay of ^{6}Be Exposed by Correlations.** *Physical review letters* 109: 202502, 2012. DOI:10.1103/PhysRevLett.109.202502

WOS-PHN-91 Eichmann, G.; Nicmorus, D.: **Nucleon to delta electromagnetic transition in the Dyson-Schwinger approach.** *Physical review / D* 85: 093004, 2012. DOI:10.1103/PhysRevD.85.093004

WOS-PHN-92 Even, Julia; Yakushev, Alexander; Düllmann, Christoph E.; Dvorak, Jan; Eichler, Robert; Gothe, Oliver; Hild, Daniel; Jäger, Egon; Khuyagbaatar, Jadambaa; Kratz, Jens V.; Krier, Jörg; Niewisch, Lorenz; Nitsche, Heino; Pysmenetska, Inna; Schädel, Matthias; Schausten, Brigitta; Türler, Andreas; Wiehl, Norbert; Wittwer, David: **Rapid Synthesis of Radioactive Transition-Metal Carbonyl Complexes at Ambient Conditions.** *Inorganic chemistry* 51: 6431 - 6433, 2012. DOI:10.1021/ic300305m

WOS-PHN-93 Filinov, V. S.; Bonitz, M.; Ivanov, Y.B.; Levashov, P.R.; Fortov, V.E.: **Quantum Monte Carlo Simulations of Strongly Coupled Quark-Gluon Plasma.** *Contributions to plasma physics* 52: 135 - 139, 2012. DOI:10.1002/ctpp.201100084

WOS-PHN-94 Filinov, V. S.; Ivanov, Yu. B.; Bonitz, M.; Levashov, P. R.; Fortov, V. E.: **Quantum simulations of strongly coupled quark-gluon plasma.** *Physics of atomic nuclei* 75: 693 - 697, 2012. DOI:10.1134/S1063778812060130

WOS-PHN-95 Fischer, T.; Blaschke, D.; Hempel, M.; Klähn, T.; astowiecki, R.; Liebendörfer, M.; Martinez-Pinedo, G.; Pagliara, G.; Sagert, I.; Sandin, F.; Schaffner-Bielich, J.; Typel, S.: **Core collapse supernovae in the QCD phase diagram.** *Physics of atomic nuclei* 75: 613 - 620, 2012. DOI:10.1134/S1063778812050067

WOS-PHN-96 Folkerts, Sarah; Litim, Daniel F.; Pawlowski, Jan M.: **Asymptotic freedom of YangMills theory with gravity.** *Physics letters / B* 709: 234 - 241, 2012. DOI:10.1016/j.physletb.2012.02.002

WOS-PHN-97 Fortov, Vladimir E; Sharkov, Boris Yu; Stöcker, Horst: **European Facility for Antiproton and Ion Research (FAIR): the new international center for fundamental physics and its research program.** *Physics / Uspekhi* 55: 582 - 602, 2012. DOI:10.3367/UFNe.0182.201206c.0621

WOS-PHN-98 Franchetti, G.; Zimmermann, F.: **New Approach to Resonance Crossing.** *Physical review letters* 109: 234102, 2012. DOI:10.1103/PhysRevLett.109.234102

WOS-PHN-99 Friese, Volker: **The CBM experimenta sta-**

tus report. *Physics of atomic nuclei* 75: 585 - 588, 2012. DOI:10.1134/S1063778812050079

WOS-PHN-100 Fritzsche, Stephan: **Relativistic many-body theory: A new field-theoretical approach.** *International journal of quantum chemistry* 112: 2688 - 2689, 2012. DOI:10.1002/qua.23291

WOS-PHN-101 Föhl, K; Düren, M; Koch, P; Zühlsdorf, M: **The WASA focussing light guide disc DIRC.** *Journal of Instrumentation* 7: C01002 - C01002, 2012. DOI:10.1088/1748-0221/7/01/C01002

WOS-PHN-102 Galatyuk, Tetyana; Lorenz, Manuel: **Investigating the microscopic properties of strongly interacting matter with HADES.** *Central European journal of physics* 10: 1295 - 1301, 2012. DOI:10.2478/s11534-012-0075-2

WOS-PHN-103 Gil, A.; Blanco, A.; Castro, E.; Diaz, J.; Garzon, J.A.; Gonzalez Diaz, Diego; Fouedjio, L.; Kolb, B.W.; Palka, M.; Traxler, Michael; Trebacz, R.; Zumbruch, Peter: **The slow control system of the HADES RPC wall.** *Nuclear instruments & methods in physics research / A* 661: S118 - S120, 2012. DOI:10.1016/j.nima.2010.08.033

WOS-PHN-104 Goecke, T.; Fischer, C.S.; Williams, R.: **Hadronic contribution to the muon : A DysonSchwinger perspective.** *Progress in particle and nuclear physics* 67: 563 - 568, 2012. DOI:10.1016/j.ppnp.2012.01.029

WOS-PHN-105 Gonzalez Diaz, Diego: **Simulation of resistive plate chambers with multi-strip readout.** *Nuclear instruments & methods in physics research / A* 661: S172S176, 2012. DOI:10.1016/j.nima.2010.09.067

WOS-PHN-106 Guo, ChenChen; Wang, YongJia; Li, QingFeng; Trautmann, W.; Liu, Ling; Wu, LiJuan: **Influence of the symmetry energy on the balance energy of the directed flow.** *Science China / Physics, mechanics & astronomy* 55: 252 - 259, 2012. DOI:10.1007/s11433-011-4616-2

WOS-PHN-107 Gutlich, Eiko; Forck, Peter; Ensinger, Wolfgang; Walasek-Hohne, Beata: **Scintillation Screen Studies for High-Dose Ion Beam Applications.** *IEEE transactions on nuclear science* 59: 2354 - 2359, 2012. DOI:10.1109/TNS.2012.2191797

WOS-PHN-108 Hartnack, Christoph; Oeschler, Helmut; Leifels, Yvonne; Bratkovskaya, Elena L.; Aichelin, Jörg: **Strangeness production close to the threshold in protonnucleus and heavy-ion collisions.** *Physics reports* 510: 119 - 200, 2012. DOI:10.1016/j.physrep.2011.08.004

WOS-PHN-109 Heckmann, K.; Buballa, M.; Wambach, J.: **Chiral restoration effects on the shear viscosity of a pion gas.** *The European physical journal / A* 48: 142, 2012. DOI:10.1140/epja/i2012-12142-2

WOS-PHN-110 Hempel, M.; Fischer, T.; Schaffner-Bielich, J.; Liebendörfer, M.: **New equations of state in simulations of core-collapse supernovae.** *The astrophysical journal / 1* 748: 70 -, 2012. DOI:10.1088/0004-637X/748/1/70

WOS-PHN-111 Henske, M.; Klein, M.; Köhli, M.; Lennert, P.; Modzel, G.; Schmidt, C.J.; Schmidt, U.: **The 10B based Jalousie neutron detector An alternative for ^3He filled position sensitive counter tubes.** *Nuclear instruments & methods in physics research / A* 686: 151 - 155, 2012. DOI:10.1016/j.nima.2012.05.075

WOS-PHN-112 Heupel, Walter; Eichmann, Gernot; Fischer, Christian S.: **Tetraquark bound states in a Bethe-Salpeter approach.** *Physics letters / B* 718: 545 - 549, 2012. DOI:10.1016/j.physletb.2012.11.009

WOS-PHN-113 Hofmann, Ingo; Meyer-ter-Vehn, Jürgen; Yan, Xueqing; Al-Omari, Husam: **Chromatic energy filter and characterization of laser-accelerated proton beams for particle therapy.** *Nuclear instruments & methods in physics research / A* 681: 44 - 54, 2012. DOI:10.1016/j.nima.2012.04.022

WOS-PHN-114 Holt, Jason D; Otsuka, Takaharu; Schwenk, Achim; Suzuki, Toshio: **Three-body forces and shell structure in calcium isotopes.** *Journal of physics / G* 39: 085111, 2012. DOI:10.1088/0954-3899/39/8/085111

WOS-PHN-115 Hudan, S.; McIntosh, A. B.; de Souza, R. T.; Bianchin, S.; Black, J.; Chbihi, A.; Famiano, M. ; Fregeau, M. O.; Gauthier, J.; Mercier, D.; Moisan, J.; Metelko, C. J.; Roy, R.; Schwarz, Carsten; Trautmann, Wolfgang; Yanez, R.: **Tracking saddle-to-scission dynamics using N/Z in projectile breakup reactions.** *Physical review / C* 86: 021603, 2012. DOI:10.1103/PhysRevC.86.021603

WOS-PHN-116 Ivanov, Yu. B.: **Baryon stopping as a signal of the mixed-phase onset.** *Physics of atomic nuclei* 75: 621 - 626, 2012. DOI:10.1134/S1063778812050110

WOS-PHN-117 Koivisto, H.; Suominen, P.; Tarvainen, O.; Spädtke, P.: **The electron cyclotron resonance ion source with arc-shaped coils concept (invited).** *Review of scientific instruments* 83: 02A312 -, 2012. DOI:10.1063/1.3662474

WOS-PHN-118 Kornilov, Vladimir; Boine-Frankenheim, Oliver: **Transverse decoherence and coherent spectra in long bunches with space charge.** *Physical review / Special topics / Accelerators and beams* 15: 114201, 2012. DOI:10.1103/PhysRevSTAB.15.114201

WOS-PHN-119 Kornilov, Vladimir; Boine-Frankenheim, Oliver: **Transverse decoherence and coherent spectra in long bunches with space charge.** *Physical review / Special topics / Accelerators and beams* 15: 114201, 2012. DOI:10.1103/PhysRevSTAB.15.114201

WOS-PHN-120 Korobkin, O.; Rosswog, S.; Arcones, A.; Winteler, C.: **On the astrophysical robustness of the neutron star merger r-process.** *Monthly notices of the Royal Astronomical Society* 426: 1940 - 1949, 2012. DOI:10.1111/j.1365-2966.2012.21859.x

WOS-PHN-121 Kreider, M.; Bär, R.; Beck, D.; Terpstra, W.; Davies, J.; Grout, V.; Lewis, J.; Serrano, J.; Wlostowski, T.: **Open borders for system-on-a-chip buses: A wire format for connecting large physics controls.** *Physical review /*

Special topics / Accelerators and beams 15: 082801, 2012. DOI:10.1103/PhysRevSTAB.15.082801

WOS-PHN-122 Käppeler, F.; Wiescher, M.; Langanke, K.: **Critical Reactions in Contemporary Nuclear Astrophysics.** 50: 165-210, 2012. DOI:10.1146/annurev-astro-081811-125543

WOS-PHN-123 Lapidus, K.; Agakishiev, G.; Balanda, A.; Bassini, R.; Behnke, C.; Belyaev, A.; Blanco, A.; Böhmer, M.; Cabanelas, P.; Carolino, N.; Chen, J. C.; Chernenko, S.; Diaz, J.; Dybczak, A.; Epple, E.; Fabbietti, L.; Fateev, O.; Finocchiaro, P.; Fonte, P.; Friese, J.; Fröhlich, I.; Galatyuk, T.; Garzon, J. A.; Gernhäuser, R.; Gil, A.; Göbel, K.; Golubeva, M.; Gonzalez-Diaz, D. ; Guber, F.; Gumberidze, M.; Harabasz, S.; Heidel, K.; Heinz, T.; Hennino, T.; Holzmann, R. ; Huck, P.; Hutsch, J.; Ierusalimov, A.; Iori, I. ; Ivashkin, A.; Jurkovic, M.; Kämpfer, B.; Kajetanowicz, M.; Karavicheva, T.; Koenig, I.; Koenig, W.; Kolb, B. W.; Korcyl, G.; Kornakov, G. ; Kotte, R.; Kozuch, A.; Krebs, E.; Krücken, R. ; Kuc, H.; Kühn, W.; Kugler, A.; Kurepin, A.; Kurilkin, A.; Kurilkin, P.; Ladygin, V.; Lalik, R. ; Lange, J. S.; Liu, M.; Liu, T.; Lopes, L.; Lorenz, M.; Lykasov, G.; Maier, L.; Malakhov, A. ; Mangiarotti, A.; Markert, J.; Metag, V.; Michalska, B.; Michel, J.; Müntz, C.; Münzer, R. ; Naumann, L.; Palka, M.; Parpottas, Y.; Pechenov, V.; Pechenova, O.; Pereira, A.; Pietraszko, J.; Przygoda, W.; Ramstein, B.; Rehnisch, C.; Reshetin, A.; Rosier, P.; Rustamov, A.; Sadovsky, A.; Salabura, P.; Scheib, T.; Schmah, A.; Schuldes, H.; Schwab, E.; Siebenson, J. ; Smolyankin, V.; Sobiella, M.; Sobolev, Yu. G.; Spataro, S.; Spruck, B.; Ströbele, H.; Stroth, J. ; Sturm, C.; Tarantola, A.; Teilab, K.; Tiflov, V.; Tlusty, P.; Traxler, M.; Trebacz, R.; Troyan, A.; Tsertos, H.; Usenko, E.; Vasiliev, T. ; Visotski, S.; Wagner, V.; Weber, M.; Wendisch, C.; Wüstenfeld, J.; Yurevich, S.; Zanevsky, Y.: **The HADES-at-FAIR project.** *Physics of atomic nuclei* 75: 589 - 593, 2012. DOI:10.1134/S1063778812050146

WOS-PHN-124 Leder, Markus; Reinhardt, Hugo; Weber, Axel; Pawlowski, Jan M.: **Color Coulomb potential in Yang-Mills theory from Hamiltonian flows.** *Physical review / D* 86: 107702, 2012. DOI:10.1103/PhysRevD.86.107702

WOS-PHN-125 Lesinski, T; Hebeler, K; Duguet, T; Schwenk, A: **Chiral three-nucleon forces and pairing in nuclei.** *Journal of physics / G* 39: 015108 -, 2012. DOI:10.1088/0954-3899/39/1/015108

WOS-PHN-126 Li, Z. J.; Toyoshima, A.; Asai, M.; Tsukada, K.; Sato, T. K.; Sato, N.; Kikuchi, T.; Nagame, Y. ; Schädel, M.; Pershina-Naegele, V.; Liang, X. H. ; Kasamatsu, Y.; Komori, Y.; Ooe, K.; Shinohara, A.; Goto, S.; Murajama, H.; Murakami, M.; Kudo, H.; Haba, H.; Takeda, Y.; Nishikawa, M.; Yokoyama, A.; Ikarashi, S.; Sueki, K.; Akiyama, K. ; Kratz, J. V.: **Sulfate complexation of element 104, Rf, in H_2SO_4/HNO_3 mixed solution.** *Radiochimica acta* 100: 157-164, 2012. WOS-PHN-127 Lippmann, Christian: **Particle identification.** *Nuclear instruments & methods in physics research / A* 666: 148 - 172, 2012. DOI:10.1016/j.nima.2011.03.009

WOS-PHN-128 Litvinova, Elena: **Quasiparticle-vibration coupling in a relativistic framework: Shell structure of Z=120 isotopes.** *Physical review / C* 85: 021303, 2012. DOI:10.1103/PhysRevC.85.021303

WOS-PHN-129 Loens, H. P.; Langanke, K.; Martinez-Pinedo, G.; Sieja, K.: **M1 strength functions from large-scale shell-model calculations and their effect on astrophysical neutron capture cross-sections.** *The European physical journal / A* 48: 34, 2012. DOI:10.1140/epja/i2012-12034-5

WOS-PHN-130 Luecker, Jan; Fischer, Christian S.: **Two-flavor QCD at finite temperature and chemical potential in a functional approach.** *Progress in particle and nuclear physics* 67: 200 - 205, 2012. DOI:10.1016/j.ppnp.2011.12.018

WOS-PHN-131 Lutz, M. F. M.; Semke, A.: **On the consistency of recent QCD lattice data of the baryon ground-state masses.** *Physical review / D* 86: 091502, 2012. DOI:10.1103/PhysRevD.86.091502

WOS-PHN-132 Lutz, M. F. M.; Vidana, I.: **On kinematical constraints in boson-boson systems.** *The European physical journal / A* 48: 124, 2012. DOI:10.1140/epja/i2012-12124-4

WOS-PHN-133 Ma, L. Z.; Zhang, X. Y.; Ni, D. S.; Wu, W.; Han, S. F.; Yao, Q. G.; Yuan, P.; Leibrock, H.; Xiang, Y.; Floch, E.: **The Cold Test of Super-FRS Superconducting Dipole Prototype for FAIR Project.** *IEEE transactions on applied superconductivity* 22: 9502104 - 9502104, 2012. DOI:10.1109/TASC.2012.2188371

WOS-PHN-134 Maas, Axel; Pawlowski, Jan M.; von Smekal, Lorenz; Spielmann, Daniel: **Gluon propagator close to criticality.** *Physical review / D* 85: 034037, 2012. DOI:10.1103/PhysRevD.85.034037

WOS-PHN-135 Maimone, F.; Tinschert, K.; Celona, L.; Lang, R.; Mäder, J.; Roßbach, J.; Spädtke, P.: **Operation of the CAPRICE electron cyclotron resonance ion source applying frequency tuning and double frequency heating.** *Review of scientific instruments* 83: 02A304 -, 2012. DOI:10.1063/1.3660252

WOS-PHN-136 Marketin, T.; Litvinova, E.; Vretenar, D.; Ring, P.: **Fragmentation of spin-dipole strength in ^{90}Zr and ^{208}Pb.** *Physics letters / B* 706: 477 - 481, 2012. DOI:10.1016/j.physletb.2011.11.050

WOS-PHN-137 Marketin, T.; Martinez-Pinedo, G.; Paar, N.; Vretenar, D.: **Role of momentum transfer in the quenching of Gamow-Teller strength.** *Physical review / C* 85: 054313, 2012. DOI:10.1103/PhysRevC.85.054313

WOS-PHN-138 Martinez-Pinedo, G.; Fischer, T.; Lohs, A.; Huther, L.: **Charged-Current Weak Interaction Processes in Hot and Dense Matter and its Impact on the Spectra of Neutrinos Emitted from Protoneutron Star Cooling.** *Physical review letters* 109: 251104, 2012. DOI:10.1103/PhysRevLett.109.251104

WOS-PHN-139 Meghna, K K; Banerjee, A; Biswas, S; Bhattacharya, S; Bose, S; Chattopadhyay, S; Das, G; Marick, C ; Saha, S; Viyogi, Y P: **Measurement of electrical properties of electrode materials for the bakelite Resistive Plate Chambers.** *Journal of Instrumentation* 7: P10003 - P10003, 2012. DOI:10.1088/1748-0221/7/10/P10003

WOS-PHN-140 Melkumov, G. L.; Anticic, T.; Baatar, B.; Barna, D.; Bartke, J.; Beck, H.; Betev, L.; Bialkowska, H.; Blume, C.; Bogusz, M.; Boimska, B. ; Book, J.; Botje, M.; Buncic, P.; Cetner, T. ; Christakoglou, P.; Chung, P.; Chvala, O.; Cramer, J. G.; Eckardt, V.; Fodor, Z.; Foka, Panagiota; Friese, Volker; Gadzicki, M.; Grebieszkow, K.; Höhne, C.; Kadija, K.; Karev, A. ; Kolesnikov, V. I.; Kolleger, T.; Kowalski, M.; Kresan, Dmytro; Laszlo, A.; Lacey, R.; Leeuwen, M. ; Mackowiak, M.; Makariev, M.; Malakhov, A. I.; Mateev, M.; Mitrovski, M.; Mrowczynski, St.; Nicolic, N.; Palla, G.; Planagiotou, A. D.; Peryt, W.; Pluta, J.; Prindle, D.; Pühlhofer, F.; Renfordt, R.; Roland, C.; Roland, G.; Rybczynski, M.; Rybicki, A.; Sandoval, A.; Schmitz, N.; Schuster, T.; Seyboth, P.; Sikler, F.; Skrzypczak, E.; Slodkowski, M.; Stefanek, G.; Stock, R.; Ströbele, H.; Susa, T.; Szuba, M.; Utvic, M.; Varga, D.; Vassiliou, M.; Veres, G. I.; Vestergombi, G.; Vranic, D.; Wlodarczyk, Z.; Wojtaszek-Szwarc, A.: **Evidence for the onset of deconfinement and quest for the critical point by NA49 at the CERN SPS.** *Physics of atomic nuclei* 75: 556 - 566, 2012. DOI:10.1134/S1063778812050158

WOS-PHN-141 Menendez, J.; Gazit, D.; Schwenk, A.: **Spin-dependent WIMP scattering off nuclei.** *Physical review / D* 86: 103511, 2012. DOI:10.1103/PhysRevD.86.103511

WOS-PHN-142 Morita, Kenji; Lee, Su Houng: **Charmonium mass in hot and dense hadronic matter.** *Physical review / C* 85: 044917, 2012. DOI:10.1103/PhysRevC.85.044917

WOS-PHN-143 Mota, Ph.; Kodama, T.; Derradi de Souza, R.; Takahashi, J.: **Coarse-graining scale and effectiveness of hydrodynamic modeling.** *The European physical journal / A* 48: 165, 2012. DOI:10.1140/epja/i2012-12165-7

WOS-PHN-144 Mühle, Carsten; Gurov, D.; Khavin, N.; Kolokolnikov, Y.; Moritz, G.; Utkin, A.; Vobly, P. ; Will, Christina; Winkler, Martin: **Radiation Resistant Prototype Dipole for the First Stage of Super-FRS.** *IEEE transactions on applied superconductivity* 22: 4003304 - 4003304, 2012. DOI:10.1109/TASC.2011.2175691

WOS-PHN-145 Müller, Hans; Mühle, Carsten; Pyka, Niels; Shim, Seong Yeub; Will, Christina: **Design Studies for the Extraction Septa of FAIR's SIS100 Synchrotron.** *IEEE transactions on applied superconductivity* 22: 4001304 - 4001304, 2012. DOI:10.1109/TASC.2011.2174949

WOS-PHN-146 Nakano, Eiji; Skokov, Vladimir; Friman, Bengt: **Transport coefficients of O(N) scalar field theories close to the critical point.** *Physical review / D* 85: 096007, 2012. DOI:10.1103/PhysRevD.85.096007

WOS-PHN-147 Ni, DongDong; Ren, ZhongZhou; Zhi, QiJun: **Calculations of β-decay half-lives of proton-rich nuclei.** *Science China / Physics, mechanics & astronomy* 55: 2397 - 2406, 2012. DOI:10.1007/s11433-012-4928-x

WOS-PHN-148 Nishimura, Nobuya; Fischer, Tobias; Thielemann, Friedrich-Karl; Fröhlich, Carla; Hempel, Matthias; Käppeli, Roger; Martinez-Pinedo, Gabriel; Rauscher, Thomas; Sagert, Irina; Winteler, Christian: **Nucleosynthesis in core-collapse supernova explosions triggered by a quark-hadron phase transition.** *The astrophysical journal / 1* 758: 9 -, 2012. DOI:10.1088/0004-637X/758/1/9

WOS-PHN-149 Nishimura, Nobuya; Kajino, Toshitaka; Mathews, Grant J.; Nishimura, Shunji; Suzuki, Toshio: **Impact of new β-decay half-lives on r-process nucleosynthesis.** *Physical review / C* 85: 048801, 2012. DOI:10.1103/PhysRevC.85.048801

WOS-PHN-150 Otwinowski, Jacek: **HIGH-pT PROCESSES MEASURED WITH ALICE AT THE LHC.** *Acta physica Polonica / B* 43: 713 -720, 2012. DOI:10.5506/APhysPolB.43.713

WOS-PHN-151 Pangon, V.: **Structure of the broken phase of the Sine-Gordon model using functional renormalization.** *International journal of modern physics / A* 27: 1250014, 2012. DOI:10.1142/S0217751X12500145

WOS-PHN-152 Papenbrock, T.; Reimann, S. M.; Kavoulakis, G. M.: **Condensates of p-Wave Pairs Are Exact Solutions for Rotating Two-Component Bose Gases.** *Physical review letters* 108: 075304, 2012. DOI:10.1103/PhysRevLett.108.075304

WOS-PHN-153 Pawlowski, P.; Brzychczyk, J.; Leifels, Yvonne; Trautmann, Wolfgang; Adrich, P.; Aumann, Thomas; Bacri, C.O.; Barczyk, T.; Bassini, R.; Bianchin, S. ; Boiano, C.; Boretzky, Konstanze; Boudard, A.; Chbihi, A.; Cibor, J.; Czech, B.; De Napoli, M.; Ducret, J.-E.; Emling, Hans; Frankland, J.D.; Gorbinet, T.; Hellström, M.; Henzlova, D.; Hlavac, S.; Imme, J.; Iori, I.; Johansson, H.; Kezzar, K.; Kupny, S.; Lafriakh, A.; Le Fevre, Arnaud; Le Gentil, E.; Leray, S.; Lukasik, J.; Lühning, Jost; Lynch, W.G.; Lynen, U.; Majka, Zbigniew; Mocko, M.; Müller, W.F.J.; Mykulyak, A.; Orth, Herbert; Otte, A.N.; Palit, R.; Panebianco, S.; Pullia, A.; Raciti, G.; Rapisarda, E.; Rossi, Dominic Michel; Salsac, M.-D.; Sann, H.; Schwarz, Carsten; Simon, Haik; Sfienti, C.; Sümmerer, K. ; Tsang, M.B.; Verde, G.; Veselsky, M.; Volant, C.; Wallace, M.; Weick, Helmut; Wiechula, Jens; Wieloch, A.; Zwieglinski, B.: **Neutron recognition in the LAND detector for large neutron multiplicity.** *Nuclear instruments & methods in physics research / A* 694: 47 - 54, 2012. DOI:10.1016/j.nima.2012.07.019

WOS-PHN-154 Petermann, I.; Langanke, K.; Martinez-Pinedo, G.; Panov, I. V.; Reinhard, P. -G.; Thielemann, F. -K.: **Have superheavy elements been produced in nature?.** *The European physical journal / A* 48: 122, 2012. DOI:10.1140/epja/i2012-12122-6

WOS-PHN-155 Petrovici, M; Petri, M; Simion, V; Barto, D; Caragheorgheopol, G; Constantin, F; Radulescu, L ; Adamczewski-Musch, J; Deppner, I; Doroud, K; Herrmann, N; Linev, S; Loizeau, P; Williams, M C S: **High counting rate, two-dimensional position sensitive timing RPC.** *Journal of Instrumentation* 7: P11003 - P11003, 2012. DOI:10.1088/1748-0221/7/11/P11003

WOS-PHN-156 Pleskac, Radek; Abou-Haidar, Z.; Agodi, C.; Alvarez, M.A.G.; Aumann, Thomas; Battistoni, G.; Bocci, A.; Böhlen, T.T.; Boudard, A.; Brunetti, A. ; Carpinelli, M.; Cirrone, G.A.P.; Cortes-Giraldo, M.A.; Cuttone, G.; De Napoli, M.; Durante, Marco ; Fernandez-Garcia, J.P.; Finck, C.; Golosio, B. ; Gallardo, M.I.; Iarocci, E.; Iazzi, F.; Ickert, Günter; Introzzi, R.; Juliani, D.; Krimmer, J.; Kurz, Nikolaus; Labalme, M.;

Leifels, Yvonne; Le Fevre, Arnaud; Leray, S.; Marchetto, F.; Monaco, V. ; Morone, M.C.; Oliva, P.; Paoloni, A.; Piersanti, Luca; Quesada, J.M.; Raciti, G.; Randazzo, N.; Romano, F.; Rossi, Dominic Michel; Rousseau, M.; Sacchi, R.; Sala, P.; Sarti, A.; Scheidenberger, Christoph; Schuy, Christoph; Sciubba, A.; Sfienti, C.; Simon, Haik; Sipala, V.; Spiriti, E.; Stuttge, L.; Tropea, S.; Younis, H. ; Patera, V.: **The FIRST experiment at GSI.** *Nuclear instruments & methods in physics research / A* 678: 130 - 138, 2012. DOI:10.1016/j.nima.2012.02.020

WOS-PHN-157 Pramanik, U. Datta; Chakraborty, S.; Basu, P.; Basu, J.; Banerjee, P.; Bemmerer, D.; Bose, S.; Chatterjee, S.; Elekes, Z.; Kempe, M.; Leifels, Y. ; Panja, J.; Mukherjee, A.; Rahaman, A.; Roy, S. ; Simon, H.; Sobiella, M.; Stach, D.; Wagner, A. ; Yakorev, D.: **Development of MMRPC prototype for the NeuLAND detector of the R3B collaboration.** *Nuclear instruments & methods in physics research / A* 661: S149 - S152, 2012. DOI:10.1016/j.nima.2010.10.055

WOS-PHN-158 Rau, Philip; Steinheimer, Jan; Schramm, Stefan; Stöcker, Horst: **Baryon resonances in a chiral hadronic model for the QCD equation of state.** *Physical review / C* 85: 025204, 2012. DOI:10.1103/PhysRevC.85.025204

WOS-PHN-159 Rau, Philip; Steinheimer, Jan; Schramm, Stefan; Stöcker, Horst: **Resonance states in an effective chiral hadronic model.** *Central European journal of physics* 10: 1302 - 1305, 2012. DOI:10.2478/s11534-012-0039-6

WOS-PHN-160 Redlich, Krzysztof: **Probing the QCD chiral cross-over transition in heavy ion collisions.** *Central European journal of physics* 10: 1254 - 1257, 2012. DOI:10.2478/s11534-012-0105-0

WOS-PHN-161 Reed, M. W.; Walker, P. M.; Cullen, I. J.; Litvinov, Yu. A.; Shubina, D.; Dracoulis, G. D.; Blaum, K.; Bosch, F.; Brandau, C.; Carroll, J. J. ; Cullen, D. M.; Deo, A. Y.; Detwiler, B.; Dimopoulou, C.; Dong, G. X.; Farinon, F.; Geissel, H.; Haettner, E.; Heil, M.; Kempley, R. S.; Knöbel, R.; Kozhuharov, C.; Kurcewicz, J.; Kuzminchuk, N.; Litvinov, S.; Liu, Z.; Mao, R.; Nociforo, C.; Nolden, F.; PlaßW. R.; Podolyak, Zs.; Prochazka, A.; Scheidenberger, C.; Steck, M. ; Stöhlker, Th.; Sun, B.; Swan, T. P. D.; Trees, G.; Weick, H.; Winckler, N.; Winkler, M.; Woods, P. J.; Xu, F. R.; Yamaguchi, T.: **Long-lived isomers in neutron-rich Z=7276 nuclides.** *Physical review / C* 86: 054321, 2012. DOI:10.1103/PhysRevC.86.054321

WOS-PHN-162 Reisdorf, W.; Leifels, Y.; Andronic, A.; Averbeck, R.; Barret, V.; Basrak, Z.; Bastid, N.; Benabderrahmane, M.L.; Caplar, R.; Crochet, P.; Dupieux, P.; Dzelalija, M.; Fodor, Z.; Gasik, P. ; Grishkin, Y.; Hartmann, O.N.; Herrmann, N.; Hildenbrand, K.D.; Hong, B.; Kang, T.I.; Kecskemeti, J.; Kim, Y.J.; Kirejczyk, M.; Kis, M. ; Koczon, P.; Korolija, M.; Kotte, R.; Kress, T. ; Lebedev, A.; Lopez, X.; Matulewicz, T.; Merschmeyer, M.; Neubert, W.; Petrovici, M.; Piasecki, K.; Rami, F.; Ryu, M.S.; Schüttauf, A. ; Seres, Z.; Sikora, B.; Sim, K.S.; Simion, V. ; Siwek-Wilczynska, K.; Smolyankin, V.; Stockmeier, M.; Stoicea, G.; Tyminski, Z.; Winiewski, K.; Wohlfarth, D.; Xiao, Z.G.; Xu, H.S.; Yushmanov, I. ; Zhilin, A.: **Systematics of azimuthal asymmetries in heavy ion collisions in the regime.** *Nuclear physics / A* 876: 1 - 60, 2012. DOI:10.1016/j.nuclphysa.2011.12.006

WOS-PHN-163 Renuka, Krishnakumar; Becker, Frank; Ensinger, Wolfgang; Forck, Peter; Haseitl, Rainer; Walasek-Hohne, Beata: **Imaging Properties of Scintillation Screens for High Energetic Ion Beams.** *IEEE transactions on nuclear science* 59: 2301 - 2306, 2012. DOI:10.1109/TNS.2012.2197417

WOS-PHN-164 Rodriguez, Tomas R.; Martinez-Pinedo, Gabriel: **Calculation of nuclear matrix elements in neutrinoless double electron capture.** *Physical review / C* 85: 044310, 2012. DOI:10.1103/PhysRevC.85.044310

WOS-PHN-165 Rossi, Dominic Michel; Adrich, P; Aksouh, F; Alvarez-Pol, H; Aumann, T; Benlliure, J; Bohmer, M ; Boretzky, K; Casarejos, E; Chartier, M; Chatillon, A; Cortina-Gil, D; Pramanik, UD; Emling, H; Ershova, O; Fernando-Dominguez, B; Geissel, H ; Gorska, M; Heil, M; Johansson, H; Junghans, AR ; Kiselev, O; Klimkiewicz, A; Kratz, JV; Kurz, N ; Labiche, M; Le Bleis, T; Lemmon, R; Litvinov, YA; Mahata, K; Maierbeck, P; Movsesyan, A; Nilsson, T; Nociforo, C; Palit, R; Paschalis, S; Plag, R; Reifarth, R; Simon, H; Sümmerer, K.; Wagner, A; Walus, W; Weick, H; Winkler, M: **Investigation of the Dipole Response in Exotic Nuclei-Experiments at the LAND-(RB)-B-3 Setup.** *Progress of theoretical physics / Supplement* 196: 465 - 470, 2012. WOS-PHN-166 Rustamov, A.: **Dilepton and strangeness production probed with HADES.** *Physics of atomic nuclei* 75: 576 - 579, 2012. DOI:10.1134/S1063778812050213

WOS-PHN-167 Sagert, I.; Fischer, T.; Pagliara, G.; Hempel, M.; Schaffner-Bielich, J.: **Strange Matter in Core-collapse Supernovae.** *Acta physica Polonica / B* 43: 741 -, 2012. DOI:10.5506/APhysPolB.43.741

WOS-PHN-168 Sagert, Irina; Tolos, Laura; Chatterjee, Debarati; Schaffner-Bielich, Jürgen; Sturm, Christian: **Soft nuclear equation-of-state from heavy-ion data and implications for compact stars.** *Physical review / C* 86: 045802, 2012. DOI:10.1103/PhysRevC.86.045802

WOS-PHN-169 Saito, T.R.; Nakajima, D.; Rappold, C.; Bianchin, S.; Borodina, O.; Bozkurt, V.; Göküzüm, B.; Kavatsyuk, M.; Kim, E.; Ma, Y.; Maas, F.; Minami, S.; Özel-Tashenov, B.; Achenbach, P.; Ajimura, S.; Aumann, T.; Gayoso, C. Ayerbe; Bhang, H.C.; Caesar, C.; Erturk, S.; Fukuda, T.; Guliev, E.; Hayashi, Y.; Hiraiwa, T.; Hoffmann, J. ; Ickert, G.; Ketenci, Z.S.; Khaneft, D.; Kim, M. ; Kim, S.; Koch, K.; Kurz, N.; Le Fevre, A.; Mizoi, Y.; Moritsu, M.; Nagae, T.; Nungesser, L. ; Okamura, A.; Ott, W.; Pochodzalla, J.; Sakaguchi, A.; Sako, M.; Schmidt, C.J.; Sekimoto, M.; Simon, H.; Sugimura, H.; Takahashi, T.; Tambave, G.J.; Tamura, H.; Trautmann, W.; Voltz, S. ; Yokota, N.; Yoon, C.J.; Yoshida, K.: **Production of hypernuclei in peripheral HI collisions: The HypHI project at GSI.** *Nuclear physics / A* 881: 218 - 227, 2012. DOI:10.1016/j.nuclphysa.2012.02.011

WOS-PHN-170 Saviano, Ninetta; Chakraborty, Sovan; Fischer, Tobias; Mirizzi, Alessandro: **Stability analysis of collective neutrino oscillations in the supernova accretion phase with realistic energy and angle distributions.** *Physical review / D* 85: 113002, 2012. DOI:10.1103/PhysRevD.85.113002

WOS-PHN-171 Schepers, Georg: **PANDA at FAIR.** *Hyperfine interactions* 213: 1 - 12, 2012. DOI:10.1007/s10751-011-0380-y

WOS-PHN-172 Schlüter, F.; Endres, J.; Zilges, A.; Savran, D.; Fritzsche, M.: **The Pygmy Dipole Resonance in ^{124}Sn.** *Acta physica Polonica / B* 43: 333 -, 2012. DOI:10.5506/APhysPolB.43.333

WOS-PHN-173 Schnizer, P.; Schnizer, B.; Akishin, P.; Mierau, A.; Fischer, E.: **SIS100 Dipole Magnet Optimization and Local Toroidal Multipoles.** *IEEE transactions on applied superconductivity* 22: 4001505 - 4001505, 2012. DOI:10.1109/TASC.2011.2177049

WOS-PHN-174 Schwarz, C; Britting, A; Bühler, P; Cowie, E; Dodokhov, V Kh; Düren, M; Eyrich, W; Föhl, K; Gruber, L; Hayrapetyan, A; Hoek, M; Hohler, R; Kalicy, G; Keri, T; Koch, P; Kröck, B; Lehmann, A; Lehmann, D; Lewandowski, B; Marton, J; Merle, O; Montgomery, R; Patsyuk, M; Peters, K; Rosner, G; Schepers, G; Schmitt, L; Schwiening, J; Seitz, B; Sfienti, C; Suzuki, K; Uhlig, F; Vodopianov, A S; Widmann, E: **The Barrel DIRC of PANDA.** *Journal of Instrumentation* 7: C02008 - C02008, 2012. DOI:10.1088/1748-0221/7/02/C02008

WOS-PHN-175 Schädel, Matthias: **Chemistry of superheavy elements.** *Radiochimica acta* 100: 579-604, 2012. DOI:10.1524/ract.2012.1965

WOS-PHN-176 Schädel, Matthias: **Chemistry of superheavy elements.** *Radiochimica acta* 100: 579 - 604, 2012. DOI:10.1524/ract.2012.1965

WOS-PHN-177 Selyuzhenkov, Ilya: **Anisotropic Flow and Other Collective Phenomena Measured in Pb-Pb Collisions with ALICE at the LHC.** *Progress of theoretical physics / Supplement* -: 153 - 158, 2012. WOS-PHN-178 Semke, A.; Lutz, M. F. M.: **Quark-mass dependence of the baryon ground-state masses.** *Physical review / D* 85: 034001, 2012. DOI:10.1103/PhysRevD.85.034001

WOS-PHN-179 Semke, A.; Lutz, M.F.M.: **Strangeness in the baryon ground states.** *Physics letters / B* 717: 242 - 247, 2012. DOI:10.1016/j.physletb.2012.09.008

WOS-PHN-180 Senger, Peter: **The compressed baryonic matter experiment at FAIR.** *Central European journal of physics* 10: 1289 - 1294, 2012. DOI:10.2478/s11534-012-0048-5

WOS-PHN-181 Serpico, Pasquale D.; Chakraborty, Sovan; Fischer, Tobias; Hüdepohl, Lorenz; Janka, Hans-Thomas; Mirizzi, Alessandro: **Probing the neutrino mass hierarchy with the rise time of a supernova burst.** *Physical review / D* 85: 085031, 2012. DOI:10.1103/PhysRevD.85.085031

WOS-PHN-182 Shahinur Rahman, Md.; Evangelou, E. K.; Konofaos, N.; Dimoulas, A.: **Gate stack dielectric degradation of rare-earth oxides grown on high mobility Ge substrates.** *Journal of applied physics* 112: 094501, 2012. DOI:10.1063/1.4763478

WOS-PHN-183 Shimbara, Y.; Fujita, Y.; Adachi, T.; Berg, G. P. A.; Fujimura, H.; Fujita, H.; Fujita, K.; Hara, K.; Hara, K. Y.; Hatanaka, K.; Kamiya, J.; Katori, K.; Kawabata, T.; Nakanishi, K.; Martnez-Pinedo, G.; Sakamoto, N.; Sakemi, Y.; Shimizu, Y.; Tameshige, Y.; Uchida, M.; Yoshifuku, M.; Yosoi, M.: **High-resolution study of Gamow-Teller transitions with the $^{37}Cl(^3He,t)^{37}Ar$ reaction.** *Physical review / C* 86: 024312, 2012. DOI:10.1103/PhysRevC.86.024312

WOS-PHN-184 Skokov, V.; Friman, B.; Redlich, K.: **Non-perturbative dynamics and charge fluctuations in effective chiral models.** *Physics letters / B* 708: 179 - 185, 2012. DOI:10.1016/j.physletb.2012.01.022

WOS-PHN-185 Soltveit, H.K.; Stachel, J.; Braun-Munzinger, P.; Musa, L.; Gustafsson, H.A.; Bonnes, U.; Oeschler, H.; Osterman, L.; Lang, S.: **The PreAmplifier ShAper for the ALICE TPC detector.** *Nuclear instruments & methods in physics research / A* 676: 106 - 119, 2012. DOI:10.1016/j.nima.2012.02.012

WOS-PHN-186 Spädtke, P.; Lang, R.; Mäder, J.; Maimone, F.; Roßbach, J.; Tinschert, K.: **Investigations on the structure of the extracted ion beam from an electron cyclotron resonance ion source.** *Review of scientific instruments* 83: 02B720 -, 2012. DOI:10.1063/1.3673633

WOS-PHN-187 Stafiniak, A.; Siemko, A.: **Towards Better Quality Assurance of the Electrical Integrity of Superconducting Accelerator Magnets.** *IEEE transactions on applied superconductivity* 22: 9000704 - 9000704, 2012. DOI:10.1109/TASC.2011.2174588

WOS-PHN-188 Steinheimer, J.; Botvina, A.; Gudima, K.; Mishustin, I.; Schramm, S.; Bleicher, M.; Stöcker, H.: **From FAIR to RHIC, hyper clusters and an effective strange EoS for QCD.** *Acta physica Polonica / B* 43: 619-626, 2012. DOI:10.5506/APhysPolB.43.619

WOS-PHN-189 Steinheimer, J.; Botvina, A.; Gudima, K.; Mishustin, I.; Schramm, S.; Stöcker, Horst: **From FAIR to RHIC, Hyper Clusters and an Effective Strange EoS for QCD.** *Acta physica Polonica / B* 43: 619 -, 2012. DOI:10.5506/APhysPolB.43.619

WOS-PHN-190 Steinheimer, J.; Gudima, K.; Botvina, A.; Mishustin, I.; Bleicher, M.; Stöcker, Horst: **Hypernuclei, dibaryon and antinuclei production in high energy heavy ion collisions: Thermal production vs. coalescence.** *Physics letters / B* 714: 85 - 91, 2012. DOI:10.1016/j.physletb.2012.06.069

WOS-PHN-191 Strasik, Ivan; Chetvertkova, V.; Mustafin, Edil; Pavlovic, M.; Belousov, Anton: **Depth profiling of residual activity of ^{237}U fragments as a range verification technique for ^{238}U primary ion beam.** *Physical review / Special topics / Accelerators and beams* 15: 071001, 2012. DOI:10.1103/PhysRevSTAB.15.071001

WOS-PHN-192 Strauss, Stefan; Fischer, Christian S.; Kellermann, Christian: **Analytic structure of Landau gauge ghost and gluon propagators.** *Progress in particle and nuclear physics* 67: 239 - 244, 2012. DOI:10.1016/j.ppnp.2011.12.025

WOS-PHN-193 Strasik, I.; Chetvertkova, V.; Mustafin, E.; Pavlovic, M.; Belousov, A.: **Depth profiling of residual activity of ^{237}U fragments as a range verification technique for ^{238}U primary ion beam.** *Physical review /*

Special topics / Accelerators and beams 15: 071001, 2012. DOI:10.1103/PhysRevSTAB.15.071001

WOS-PHN-194 Sugita, Kei: **Novel Concept of Truncated Iron-Yoked Cosine Theta Magnets and Design Studies for FAIR Septum Magnets.** *IEEE transactions on applied superconductivity* 22: 4902204 - 4902204, 2012. DOI:10.1109/TASC.2011.2174953

WOS-PHN-195 Tinschert, K.; Lang, R.; Mäder, J.; Roßbach, J.; Spädtke, P.; Komorowski, P.; Meyer-Reumers, M. ; Krischel, D.; Fischer, B.; Ciavola, G.; Gammino, S.; Celona, L.: **Design and investigations of the superconducting magnet system for the multipurpose superconducting electron cyclotron resonance ion source.** *Review of scientific instruments* 83: 02A319 -, 2012. DOI:10.1063/1.3666912

WOS-PHN-196 Trautmann, Wolfgang; WOLTER, H. H.: **Elliptic flow and the symmetry at supra-saturation density.** *International journal of modern physics / E* 21: 1230003-1 - 17, 2012. DOI:10.1142/s0218301312300032

WOS-PHN-197 Ugliano, Marcella; Janka, Hans-Thomas; Marek, Andreas; Arcones, Almudena: **Progenitor-explosion connection and remnant birth masses for neutrino-driven supernovae of iron-core progenitors.** *The astrophysical journal / 1* 757: 69 -, 2012. DOI:10.1088/0004-637X/757/1/69

WOS-PHN-198 Ugur, C; Bayer, E; Kurz, N; Traxler, M: **A 16 channel high resolution ($<$ 11 ps RMS) Time-to-Digital Converter in a Field Programmable Gate Array.** *Journal of Instrumentation* 7: C02004 - C02004, 2012. DOI:10.1088/1748-0221/7/02/C02004

WOS-PHN-199 Uhlig, F.; Britting, A.; Eyrich, W.; Lehmann, A.; Schwarz, C.; Schwiening, J.: **Performance studies of microchannel plate PMTs.** *Nuclear instruments & methods in physics research / A* 695: 68 - 70, 2012. DOI:10.1016/j.nima.2011.12.062

WOS-PHN-200 Voskresenskaya, M.D.; Typel, S.: **Constraining mean-field models of the nuclear matter equation of state at low densities.** *Nuclear physics / A* 887: 42 - 76, 2012. DOI:10.1016/j.nuclphysa.2012.05.006

WOS-PHN-201 Voskresensky, D. N.; Skokov, V. V.: **Viscosity and thermal conductivity effects at first-order phase transitions in heavy-ion collisions.** *Physics of atomic nuclei* 75: 770 - 775, 2012. DOI:10.1134/S1063778812050286

WOS-PHN-202 Walasek-Hohne, B.; Andre, C.; Forck, P.; Gutlich, E.; Kube, G.; Lecoq, P.; Reiter, A.: **Scintillating Screen Applications in Accelerator Beam Diagnostics.** *IEEE transactions on nuclear science* 59: 2307 - 2312, 2012. DOI:10.1109/TNS.2012.2200696

WOS-PHN-203 Wang, J; Wang, Y; Gonzalez Diaz, Diego; Chen, H; Fan, X; Linev, Sergey; Cheng, J: **A realistic design of the CBM-TOF wall based on modules commissioned in-beam.** *Journal of Instrumentation* 7: P10004 - P10004, 2012. DOI:10.1088/1748-0221/7/10/P10004

WOS-PHN-204 Wang, M.; Audi, G.; Wapstra, A.H.; Kondev, F.G.; MacCormick, M.; Xu, X.; Pfeiffer, B.: **The Ame2012 atomic mass evaluation.** *Chinese physics / C* 36: 1603 - 2014, 2012. DOI:10.1088/1674-1137/36/12/003

WOS-PHN-205 Wilfert, St.; Edelmann, Chr.: **Field emitter-based vacuum sensors.** *Vacuum* 86: 556 - 571, 2012. DOI:10.1016/j.vacuum.2011.08.008

WOS-PHN-206 Winkel, Mathias; Speck, Robert; Hübner, Helge; Arnold, Lukas; Krause, Rolf; Gibbon, Paul: **A massively parallel, multi-disciplinary BarnesHut tree code for extreme-scale N-body simulations.** *Computer physics communications* 183: 880 - 889, 2012. DOI:10.1016/j.cpc.2011.12.013

WOS-PHN-207 Winteler, C.; Käppeli, R.; Perego, A.; Arcones, A.; Vasset, N.; Nishimura, N.; Liebendörfer, M. ; Thielemann, F.-K.: **Magnetorotationally driven supernovae as the origin of early galaxy r-provess elements?.** *The astrophysical journal / 2* 750: L22 -, 2012. DOI:10.1088/2041-8205/750/1/L22

WOS publications to the programme Large-scale facilities for research with photons, neutrons and ions published in 2012

WOS-PNI-1 Afra, B.; Rodriguez, M.D.; Lang, M.; Ewing, R.C.; Kirby, N.; Trautmann, C.; Kluth, P.: **SAXS study of ion tracks in San Carlos olivine and Durango apatite.** *Nuclear instruments & methods in physics research / B* 286: 243 - 246, 2012. DOI:10.1016/j.nimb.2012.03.007

WOS-PNI-2 Alber, Ina; Sigle, Wilfried; Demming-Janssen, Frank; Neumann, Reinhard; Trautmann, Christina; van Aken, Peter A.; Toimil Molares, Maria Eugenia: **Multipole Surface Plasmon Resonances in Conductively Coupled Metal Nanowire Dimers.** *ACS nano* 6: 9711 - 9717, 2012. DOI:10.1021/nn303149p

WOS-PNI-3 Alencar, I.; Guedes, S.; Jonckheere, R.; Trautmann, C.; Soares, C.J.; Moreira, P.A.F.P.; Curvo, E.A.C.; Tello, C.A.; Nakasuga, W.M.; Dias, A.N.C.; Hadler, J.C.: **Projected length annealing of etched ^{152}Sm ion tracks in apatite.** *Nuclear instruments & methods in physics research / B* 288: 48 - 52, 2012. DOI:10.1016/j.nimb.2012.07.004

WOS-PNI-4 Ali, Mubarak; Nasir, Saima; Ramirez, Patricio; Ahmed, Ishtiaq; Nguyen, Quoc Hung; Fruk, Ljiljana; Mafe, Salvador; Ensinger, W.: **Optical Gating of Photosensitive Synthetic Ion Channels.** *Advanced functional materials* 22: 390 - 396, 2012. DOI:10.1002/adfm.201102146

WOS-PNI-5 Ali, Mubarak; Nasir, Saima; Ramirez, Patricio; Cervera, Javier; Mafe, Salvador; Ensinger, W.: **Calcium Binding and Ionic Conduction in Single Conical Nanopores with Polyacid Chains: Model and Experiments.** *ACS nano* 6: 9247 - 9257, 2012. DOI:10.1021/nn303669g

WOS-PNI-6 Ali, Mubarak; Ramirez, Patricio; Nguyen, Hung Quoc; Nasir, Saima; Cervera, Javier; Mafe, Salvador; Ensinger, W.: **Single Cigar-Shaped Nanopores Functionalized with Amphoteric Amino Acid Chains: Experimental and Theoretical Characterization.** *ACS nano* 6: 3631 - 3640, 2012. DOI:10.1021/nn3010119

WOS-PNI-7 Almomani, A.; Droba, M.; Ratzinger, U.; Hofmann, I.: **Matching the laser generated p bunch into a crossbar-H drift tube linac.** *Physical review / Special topics / Accelerators and beams* 15: 051302, 2012. DOI:10.1103/PhysRevSTAB.15.051302

WOS-PNI-8 Amaro, P.; Fratini, F.; Fritzsche, S.; Indelicato, P.; Santos, J. P.; Surzhykov, A.: **Parametrization of the angular correlation and degree of linear polarization in two-photon decays of hydrogenlike ions.** *Physical review / A* 86: 042509, 2012. DOI:10.1103/PhysRevA.86.042509

WOS-PNI-9 Amaro, Pedro; Schlesser, Sophie; Guerra, Mauro; Le Bigot, Eric-Olivier; Isac, Jean-Michel; Travers, Pascal; Santos, Jose Paulo; Szabo, Csilla I.; Gumberidze, Alexandre; Indelicato, Paul: **Absolute Measurement of the Relativistic Magnetic Dipole Transition Energy in Heliumlike Argon.** *Physical review letters* 109: 043005, 2012. DOI:10.1103/PhysRevLett.109.043005

WOS-PNI-10 Artemyev, A. N.; Jentschura, U. D.; Serbo, V. G.; Surzhykov, A.: **Boundfree pair production in ultrarelativistic ion collisions at the LHC collider: analytic approach to the total and differential cross sections.** *The European physical journal / C* 72: 1935, 2012. DOI:10.1140/epjc/s10052-012-1935-z

WOS-PNI-11 Atanasov, D. R.; Winckler, Nicolas; Balabanski, D.; Batist, L.; Bosch, Fritz; Boutin, D.; Brandau, Carsten; Dimopoulou, Christina; Essel, H. G.; Faestermann, T.; Geissel, Hans; Hachiuma, I.; Hess, S.; Izumikawa, T.; Kienle, Paul; Knöbel, Ronja; Kozhuharov, Christophor; Kurcewicz, Jan; Kuzminchuk, N.; Litvinov, S. A.; Litvinov, Yury; Mao, R. S.; Märtin, Renate; Mazzocco, M.; Münzenberg, G.; Namihira, K.; Nolden, Fritz; Ohtsubo, T.; Patyk, Z. ; Reuschl, R.; Sanjari, Mohammad Shahab; Scheidenberger, Christoph; Shubina, Daria; Spillmann, Uwe; Steck, Markus; Stöhlker, Thomas; Sun, B.; Suzuki, T.; Trassinelli, M.; Tupitsyn, I. I.; Weick, Helmut; Winkler, Martin; Winters, D. F. A.; Yamaguchi, T.: **Half-life measurements of stored fully ionized and hydrogen-like ^{122}I ions.** *The European physical journal / A* 48: 22, 2012. DOI:10.1140/epja/i2012-12022-9

WOS-PNI-12 Aurand, B.; Rödel, C.; Zhao, H.; Kuschel, S.; Wünsche, M.; Jäckel, O.; Heyer, M.; Wunderlich, F.; Kaluza, M. C.; Paulus, G. G.; Kuehl, T.: **Gain lifetime measurement of a Ni-like Ag soft X-ray laser.** *Review of scientific instruments* 83: 036104, 2012. DOI:10.1063/1.3694659

WOS-PNI-13 Baumgartl, M.; Orta, B.; Limpert, J.; Tünnermann, A.: **Impact of dispersion on pulse dynamics in chirped-pulse fiber lasers.** *Applied physics / B* 107: 263 - 274, 2012. DOI:10.1007/s00340-012-5010-0

WOS-PNI-14 Baumgartl, Martin; Chemnitz, Mario; Jauregui, Cesar; Meyer, Tobias; Dietzek, Benjamin; Popp, Jürgen ; Limpert, Jens; Tünnermann, Andreas: **All-fiber laser source for CARS microscopy based on fiber optical parametric frequency conversion.** *Optics express* 20: 4484 -, 2012. DOI:10.1364/OE.20.004484

WOS-PNI-15 Baumgartl, Martin; Lecaplain, Caroline; Hideur, Ammar; Limpert, Jens; Tünnermann, Andreas: **66 W average power from a microjoule-class sub-100 fs fiber oscillator.** *Optics letters* 37: 1640 -, 2012. DOI:10.1364/OL.37.001640

WOS-PNI-16 Bergues, Boris; Kübel, Matthias; Johnson, Nora G.; Fischer, Bettina; Camus, Nicolas; Betsch, Kelsie J.; Herrwerth, Oliver; Senftleben, Arne; Sayler, A. Max; Rathje, Tim; Pfeifer, Thomas; Ben-Itzhak, Itzik; Jones, Robert R.; Paulus, Gerhard G.; Krausz, Ferenc; Moshammer, Robert; Ullrich,

Joachim ; Kling, Matthias F.: **Attosecond tracing of correlated electron-emission in non-sequential double ionization.** *Nature Communications* 3: 813 -, 2012. DOI:10.1038/ncomms1807

WOS-PNI-17 Bernitt, S.; Brown, G. V.; Rudolph, J. K.; Steinbrügge, R.; Graf, A.; Leutenegger, M.; Epp, S. W.; Eberle, S.; Kubicek, K.; Mäckel, V.; Simon, M. C.; Träbert, E.; Magee, E. W.; Beilmann, C.; Hell, N.; Schippers, S.; Müller, A.; Kahn, S. M.; Surzhykov, A.; Harman, Z.; Keitel, C. H.; Clementson, J.; Porter, F. S.; Schlotter, W.; Turner, J. J.; Ullrich, J.; Beiersdorfer, P.; Lopez-Urrutia, J. R. Crespo: **An unexpectedly low oscillator strength as the origin of the Fexvii emission problem.** *Nature* 492: 225 - 228, 2012. DOI:10.1038/nature11627

WOS-PNI-18 Betsch, K. J.; Johnson, Nora G.; Bergues, B.; Kübel, M.; Herrwerth, O.; Senftleben, A.; Ben-Itzhak, I.; Paulus, G. G.; Moshammer, R.; Ullrich, J.; Kling, M. F.; Jones, R. R.: **Controlled directional ion emission from several fragmentation channels of CO driven by a few-cycle laser field.** *Physical review / A* 86: 063403, 2012. DOI:10.1103/PhysRevA.86.063403

WOS-PNI-19 Bharadia, S.; Vogel, M.; Segal, D. M.; Thompson, R. C.: **Dynamics of laser-cooled Ca^+ ions in a Penning trap with a rotating wall.** *Applied physics / B* 107: 1105 - 1115, 2012. DOI:10.1007/s00340-012-4871-6

WOS-PNI-20 Bierbach, J; Rödel, C; Yeung, M; Dromey, B; Hahn, T; Pour, A Galestian; Fuchs, S; Paz, A E; Herzer, S; Kuschel, S; Jäckel, Oliver; Kaluza, M C ; Pretzler, G; Zepf, M; Paulus, G G: **Generation of 10 μ W relativistic surface high-harmonic radiation at a repetition rate of 10 Hz.** *New journal of physics* 14: 065005 -, 2012. DOI:10.1088/1367-2630/14/6/065005

WOS-PNI-21 Boehme, Mario; Ionescu, Emanuel; Fu, Ganhua; Ensinger, Wolfgang: **Room temperature synthesis of samarium oxide nanotubes using cost-effective electroless deposition method.** *Journal of experimental nanoscience* 7: 344 - 353, 2012. DOI:10.1080/17458080.2010.533295

WOS-PNI-22 Breitkopf, Sven; Klenke, Arno; Gottschall, Thomas; Otto, Hans-Jürgen; Jauregui, Cesar; Limpert, Jens; Tünnermann, Andreas: **58mJ burst comprising ultrashort pulses with homogenous energy level from an Yb-doped fiber amplifier.** *Optics letters* 37: 5169 -, 2012. DOI:10.1364/OL.37.005169

WOS-PNI-23 Bret, A.; Piriz, A. R.; Tahir, N.: **Harmonic analysis of irradiation asymmetry for cylindrical implosions driven by high-frequency rotating ion beams.** *Physical review / E* 85: 036402, 2012. DOI:10.1103/PhysRevE.85.036402

WOS-PNI-24 Börner, M.; Fils, J.; Frank, Alexander; Blazevic, A.; Hessling, T.; Pelka, A.; Schaumann, G.; Schökel, A.; Schumacher, D; Basko, M. M.; Maruhn, J.; Tauschwitz, An.; Roth, M.: **Development of a Nomarski-type multi-frame interferometer as a time and space resolving diagnostics for the free electron density of laser-generated plasma.** *Review of scientific instruments* 83: 043501, 2012. DOI:10.1063/1.3701366

WOS-PNI-25 Cheal, B.; Cocolios, T. E.; Fritzsche, S.: **Laser spectroscopy of radioactive isotopes: Role and limitations of accurate isotope-shift calculations.** *Physical review / A* 86: 042501, 2012. DOI:10.1103/PhysRevA.86.042501

WOS-PNI-26 Chen, L.; PlaßW.R.; Geissel, Hans; Knöbel, Ronja; Kozhuharov, Christophor; Litvinov, Yu.A.; Patyk, Z.; Scheidenberger, Christoph; Siegien-Iwaniuk, K.; Sun, B.; Weick, Helmut; Beckert, K.; Beller, P.; Bosch, Fritz; Boutin, D. ; Caceres, L.; Carroll, J.J.; Cullen, D.M.; Cullen, I.J.; Franzke, B.; Gerl, Jürgen; Gorska, Magdalena; Jones, G.A.; Kishada, A.; Kurcewicz, Jan ; Litvinov, S.A.; Liu, Z.; Mandal, S.; Montes, F. ; Münzenberg, G.; Nolden, Fritz; Ohtsubo, T.; Podolyak, Zs.; Propri, R.; Rigby, S.; Saito, Nami ; Saito, Takehiko; Shindo, M.; Steck, Markus; Walker, P.M.; Williams, S.; Winkler, Martin; Wollersheim, Hans-Jürgen; Yamaguchi, T.: **New results on mass measurements of stored neutron-rich nuclides in the element range from Pt to U with the FRS-ESR facility at.** *Nuclear physics / A* 882: 71 - 89, 2012. DOI:10.1016/j.nuclphysa.2012.03.002

WOS-PNI-27 Claverie, Alain; Iwase, Akihiro; Mattei, Giovanni; Nordlund, Kai; Trautmann, Christina; Wiss, Thierry; Zinkle, Steve: **Basic research on ionic-covalent materials for nuclear applications [Guest Editorial].** *Nuclear instruments & methods in physics research / B* 277: v, 2012. DOI:10.1016/j.nimb.2012.02.026

WOS-PNI-28 Delgado, A.O.; Rizzutto, M.A.; Severin, D.; Seidl, T.; Neumann, R.; Trautmann, C.: **Latent track radius of PTFE irradiated with high energy ion beam.** *Nuclear instruments & methods in physics research / B* 273: 55 - 57, 2012. DOI:10.1016/j.nimb.2011.07.037

WOS-PNI-29 Droese, C.; Blaum, K.; Block, M.; Eliseev, S.; Herfurth, F.; Minaya Ramirez, E.; Novikov, Yu.N.; Schweikhard, L.; Shabaev, V.M.; Tupitsyn, I.I.; Wycech, S.; Zuber, K.; Zubova, N.A.: **Probing the nuclide 180W for neutrinoless double-electron capture exploration.** *Nuclear physics / A* 875: 1 - 7, 2012. DOI:10.1016/j.nuclphysa.2011.11.008

WOS-PNI-30 Dromey, B.; Rykovanov, S.; Yeung, M.; Hörlein, R.; Jung, D.; Gautier, D. C.; Dzelzainis, T.; Kiefer, D.; Palaniyppan, S.; Shah, R.; Schreiber, J.; Ruhl, H.; Fernandez, J. C.; Lewis, C. L. S.; Zepf, M.; Hegelich, B. M.: **Coherent synchrotron emission from electron nanobunches formed in relativistic laserplasma interactions.** *Nature physics* 8: 804 - 808, 2012. DOI:10.1038/nphys2439

WOS-PNI-31 Döbrich, Babette; Eichhorn, Astrid: **Can we see quantum gravity? Photons in the asymptotic-safety scenario.** *Journal of high energy physics* 2012: 156, 2012. DOI:10.1007/JHEP06(2012)156

WOS-PNI-32 Döbrich, Babette; Gies, Holger; Neitz, Norman; Karbstein, Felix: **Magnetically Amplified Tunneling of the Third Kind as a Probe of Minicharged Particles.** *Physical review letters* 109: 131802, 2012. DOI:10.1103/PhysRevLett.109.131802

WOS-PNI-33 Ecker, B.; Oliva, E.; Aurand, B.; Hochhaus, D. C.; Neumayer, P.; Zhao, H.; Zielbauer, B.; Cassou, K.; Daboussi, S.; Guilbaud, O.; Kazamias, S.; Le, T. T. T.; Ros, D.; Kühl, Thomas; Zeitoun, P.: **Gain lifetime measurement of a Ni-like Ag soft X-ray laser.** *Optics express* 20: 25391, 2012.

DOI:10.1364/OE.20.025391

WOS-PNI-34 Eichhorn, Astrid; Gies, Holger; Roscher, Dietrich: **Renormalization flow of axion electrodynamics.** *Physical review / D* 86: 125014, 2012. DOI:10.1103/PhysRevD.86.125014

WOS-PNI-35 Faik, Steffen; Basko, Mikhail M.; Tauschwitz, Anna; Iosilevskiy, Igor; Maruhn, Joachim A.: **Dynamics of volumetrically heated matter passing through the liquidvapor metastable states.** *High energy density physics* 8: 349 - 359, 2012. DOI:10.1016/j.hedp.2012.08.003

WOS-PNI-36 Fink, D.; Barea, J.; Beck, D.; Blaum, K.; Böhm, Ch.; Borgmann, Ch.; Breitenfeldt, M.; Herfurth, F.; Herlert, A.; Kotila, J.; Kowalska, M. ; Kreim, S.; Lunney, D.; Naimi, S.; Rosenbusch, M.; Schwarz, S.; Schweikhard, L.; Simkovic, F.; Stanja, J.; Zuber, K.: **Q Value and Half-Lives for the Double-β-Decay Nuclide ^{110}Pd.** *Physical review letters* 108: 062502, 2012. DOI:10.1103/PhysRevLett.108.062502

WOS-PNI-37 Fischer, D.; Globig, D.; Goullon, J.; Grieser, M.; Hubele, R.; de Jesus, V. L. B.; Kelkar, A.; LaForge, A.; Lindenblatt, H.; Misra, D.; Najjari, B.; Schneider, K.; Schulz, M.; Sell, M.; Wang, X.: **Ion-Lithium Collision Dynamics Studied with a Laser-Cooled In-Ring Target.** *Physical review letters* 109: 113202, 2012. DOI:10.1103/PhysRevLett.109.113202

WOS-PNI-38 Fraga, R. A. Costa; Kalinin, A.; Kühnel, M.; Hochhaus, D. C.; Schottelius, A.; Polz, J.; Kaluza, M. C.; Neumayer, Paul; Grisenti, R. E.: **Compact cryogenic source of periodic hydrogen and argon droplet beams for relativistic laser-plasma generation.** *Review of scientific instruments* 83: 025102 -, 2012. DOI:10.1063/1.3681940

WOS-PNI-39 Frantz, C.; Stein, N.; Zhang, Y.; Bouzy, E.; Picht, O.; Toimil Molares, Maria Eugenia; Boulanger, C.: **Electrodeposition of bismuth telluride nanowires with controlled composition in polycarbonate membranes.** *Electrochimica acta* 69: 30 - 37, 2012. DOI:10.1016/j.electacta.2012.01.040

WOS-PNI-40 Fritzsche, S; Surzhykov, A; Gumberidze, A; Stöhlker, Th: **Electron emission from highly charged ions: signatures of magnetic interactions and retardation in strong fields.** *New journal of physics* 14: 083018 -, 2012. DOI:10.1088/1367-2630/14/8/083018

WOS-PNI-41 Fritzsche, Stephan: **The Ratip program for relativistic calculations of atomic transition, ionization and recombination properties.** *Computer physics communications* 183: 1525 - 1559, 2012. DOI:10.1016/j.cpc.2012.02.016

WOS-PNI-42 Fuchs, S.; Blinne, A.; Rödel, C.; Zastrau, U.; Hilbert, V.; Wünsche, M.; Bierbach, J.; Frumker, E.; Förster, E.; Paulus, G. G.: **Optical coherence tomography using broad-bandwidth XUV and soft X-ray radiation.** *Applied physics / B* 106: 789 - 795, 2012. DOI:10.1007/s00340-012-4934-8

WOS-PNI-43 Gopal, A; May, T; Herzer, S; Reinhard, A; Minardi, S; Schubert, M; Dillner, U; Pradarutti, B ; Polz, J; Gaumnitz, T; Kaluza, M C; Jäckel, Oliver; Riehemann, S; Ziegler, W; Gemuend, H-P; Meyer, H-G; Paulus, G G: **Observation of energetic terahertz pulses from relativistic solid density plasmas.** *New journal of physics* 14: 083012 -, 2012. DOI:10.1088/1367-2630/14/8/083012

WOS-PNI-44 Gottschall, Thomas; Baumgartl, Martin; Sagnier, Aude; Rothhardt, Jan; Jauregui, Cesar; Limpert, Jens; Tünnermann, Andreas: **Fiber-based source for multiplex-CARS microscopy based on degenerate four-wave mixing.** *Optics express* 20: 12004 -, 2012. DOI:10.1364/OE.20.012004

WOS-PNI-45 Grieser, M.; Litvinov, Yu. A.; Raabe, R.; Blaum, K.; Blumenfeld, Y.; Butler, P. A.; Wenander, F.; Woods, P. J.; Aliotta, M.; Andreyev, A.; Artemyev, A. N.; Atanasov, Dinko; Aumann, Thomas; Balabanski, D.; Barzakh, A.; Batist, L.; Bernardes, A. -P.; Bernhardt, D.; Billowes, J.; Bishop, S.; Borge, M. ; Borzov, I.; Bosch, Fritz; Boston, A. J.; Brandau, Carsten; Catford, W.; Catherall, R.; Cederkäll, J.; Cullen, D.; Davinson, T.; Dillmann, Iris; Dimopoulou, Christina; Dracoulis, G.; Düllmann, Christoph Emanuel; Egelhof, Peter; Estrade, Alfredo; Fischer, D.; Flanagan, K.; Fraile, L.; Fraser, M. A.; Freeman, S. J.; Geissel, Hans; Gerl, Jürgen; Greenlees, P.; Grisenti, R. E.; Habs, D. ; Hahn, R.; Hagmann, Siegbert; Hausmann, M.; He, J. J.; Heil, Michael; Huyse, M.; Jenkins, D.; Jokinen, A.; Jonson, B.; Joss, D. T.; Kadi, Y.; Kalantar-Nayestanaki, N.; Kay, B. P.; Kiselev, Oleg ; Kluge, Heinz-Jürgen; Kowalska, M.; Kozhuharov, Christophor; Kreim, S.; Kröll, T.; Kurcewicz, J. ; Labiche, M.; Lemmon, R. C.; Lestinsky, Michael; Lotay, G.; Ma, X. W.; Marta, Michele; Meng, J.; Mücher, D.; Mukha, Ivan; Müller, Sonja; Murphy, A. St J.; Neyens, G.; Nilsson, T.; Nociforo, Chiara ; Nörtershäuser, W.; Page, R. D.; Pasini, M.; Petridis, N.; Pietralla, N.; Pfützner, M.; Podolyak, Z.; Regan, P.; Reed, M. W.; Reifarth, Rene; Reiter, P.; Repnow, R.; Riisager, K.; Rubio, B.; Sanjari, Mohammad Shahab; Savin, D. W.; Scheidenberger, Christoph; Schippers, S.; Schneider, Dieter; Schuch, R.; Schwalm, D.; Schweikhard, L. ; Shubina, Daria; Siesling, E.; Simon, Haik; Simpson, J.; Smith, J.; Sonnabend, Kerstin; Steck, Markus; Stora, T.; Stöhlker, Thomas; Sun, B.; Surzhykov, A.; Suzaki, F.; Tarasov, O.; Trotsenko, Sergiy; Tu, X. L.; Duppen, P.; Volpe, C.; Voulot, D.; Walker, P. M.; Wildner, E.; Winckler, N.; Winters, D. F. A.; Wolf, A.; Xu, H. S.; Yakushev, Alexander; Yamaguchi, T.; Yuan, Y. J.; Zhang, Y. H.; Zuber, K.: **Storage ring at HIE-ISOLDE.** *European physical journal special topics* 207: 1 - 117, 2012. DOI:10.1140/epjst/e2012-01599-9

WOS-PNI-46 Hahn, M.; Becker, A.; Grieser, M.; Krantz, C.; Lestinsky, Michael; Müller, A.; Novotny, O.; Repnow, R.; Schippers, S.; Spruck, K.; Wolf, A.; Savin, D. W.: **Storage ring coss-section measurements for electron impact single and double ionization of Fe^{9+} and single ionozation of Fe^{10+}.** *The astrophysical journal / 1* 760: 80 -, 2012. DOI:10.1088/0004-637X/760/1/80

WOS-PNI-47 Hahn, M.; Bernhardt, D.; Grieser, M.; Krantz, C.; Lestinsky, M.; Müller, A.; Novotny, O.; Repnow, R.; Schippers, S.; Wolf, A.; Savin, D. W.: **Electron-impact-ionization measurements using hyperfine-assisted state preparation of ground-state berylliumlike sulfur.** *Physical review / A* 85: 042713, 2012. DOI:10.1103/PhysRevA.85.042713

WOS-PNI-48 Hahn, M.; Grieser, M.; Krantz, C.; Lestinsky, Michael; Müller, A.; Novotny, O.; Repnow, R.; Schippers, S.; Wolf, A.; Savin, D. W.: **ADDENDUM: "Storage ring cross-section measurements for electron impact ionization of**

Fe^{12+} **forming** Fe^{13+} **and** Fe^{14+}**" (2011, ApJ, 735, 105).** *The astrophysical journal / 1* 761: 79 -, 2012. DOI:10.1088/0004-637X/761/1/79

WOS-PNI-49 Harmand, M; Murphy, C D; Brown, C R D; Cammarata, M; Döppner, T; Düsterer, S; Fritz, D; Förster, E; Galtier, E; Gaudin, J; Glenzer, S H ; Göde, S; Gregori, G; Hilbert, V; Hochhaus, D ; Laarmann, T; Lee, H J; Lemke, H; Meiwes-Broer, K -H; Moinard, A; Neumayer, P; Przystawik, A; Redlin, H; Schulz, M; Skruszewicz, S; Tavella, F ; Tschentscher, T; White, T; Zastrau, U; Toleikis, S: **Plasma switch as a temporal overlap tool for pump-probe experiments at FEL facilities.** *Journal of Instrumentation* 7: P08007 - P08007, 2012. DOI:10.1088/1748-0221/7/08/P08007

WOS-PNI-50 Hinke, C. B.; Böhmer, M.; Boutachkov, Plamen; Faestermann, T.; Geissel, Hans; Gerl, Jürgen; Gernhäuser, R.; Gorska, Magdalena; Gottardo, A.; Grawe, H.; Grbosz, J. L.; Krücken, R.; Kurz, Nikolaus; Liu, Z.; Maier, M.; Nowacki, F.; Pietri, Stephane; Podolyak, Zs.; Sieja, K.; Steiger, K.; Straub, K.; Weick, Helmut; Wollersheim, Hans-Jürgen; Woods, P. J.; Al-Dahan, N. ; Alkhomashi, N.; Ata, A.; Blazhev, A.; Braun, N. F.; Celikovic, I. T.; Davinson, T.; Dillmann, Iris; Domingo-Pardo, C.; Doornenbal, P. C.; de France, G.; Farrelly, G. F.; Farinon, Fabio; Goel, Namita; Habermann, T. C.; Hoischen, Robert; Janik, R.; Karny, M.; Kaka, A.; Kojouharov, I. M.; Kröll, Th.; Litvinov, Sergey; Myalski, S.; Nebel, F.; Nishimura, S.; Nociforo, Chiara; Nyberg, J.; Parikh, A. R.; Prochazka, Andrej; Regan, P. H.; Rigollet, C.; Schaffner, Henning; Scheidenberger, Christoph; Schwertel, S.; Söderström, P.-A.; Steer, S. J.; Stolz, A.; Strmen, P.: **Superallowed GamowTeller decay of the doubly magic nucleus** ^{100}Sn**.** *Nature* 486: 341 - 345, 2012. DOI:10.1038/nature11116

WOS-PNI-51 Hädrich, S.; Rothhardt, Jan; Krebs, M.; Demmler, S.; Limpert, J.; Tünnermann, A.: **Improving carrier-envelope phase stability in optical parametric chirped-pulse amplifiers by control of timing jitter.** *Optics letters* 37: 4910 -, 2012. DOI:10.1364/OL.37.004910

WOS-PNI-52 Jansen, Florian; Stutzki, Fabian; Jauregui, Cesar; Limpert, Jens; Tünnermann, Andreas: **High-power very large mode-area thulium-doped fiber laser.** *Optics letters* 37: 4546 -, 2012. DOI:10.1364/OL.37.004546

WOS-PNI-53 Jansen, Florian; Stutzki, Fabian; Otto, Hans-Jürgen; Eidam, Tino; Liem, Andreas; Jauregui, Cesar; Limpert, Jens; Tünnermann, Andreas: **Thermally induced waveguide changes in active fibers.** *Optics express* 20: 3997 -, 2012. DOI:10.1364/OE.20.003997

WOS-PNI-54 Jansen, Karl; Karbstein, Felix; Nagy, Attila; Wagner, Marc: $\Lambda_{\overline{MS}}$ **from the static potential for QCD with** n_f **=2 dynamical quark flavors.** *Journal of high energy physics* 2012: 25, 2012. DOI:10.1007/JHEP01(2012)025

WOS-PNI-55 Jauregui, Cesar; Eidam, Tino; Otto, Hans-Jürgen; Stutzki, Fabian; Jansen, Florian; Limpert, Jens; Tünnermann, Andreas: **Physical origin of mode instabilities in high-power fiber laser systems.** *Optics express* 20: 12912 -, 2012. DOI:10.1364/OE.20.012912

WOS-PNI-56 Jauregui, Cesar; Eidam, Tino; Otto, Hans-Jürgen; Stutzki, Fabian; Jansen, Florian; Limpert, Jens; Tünnermann, Andreas: **Temperature-induced index gratings and their impact on mode instabilities in high-power fiber laser systems.** *Optics express* 20: 440 -, 2012. DOI:10.1364/OE.20.000440

WOS-PNI-57 Jauregui, Cesar; Steinmetz, Alexander; Limpert, Jens; Tünnermann, Andreas: **High-power efficient generation of visible and mid-infrared radiation exploiting four-wave-mixing in optical fibers.** *Optics express* 20: 24957 -, 2012. DOI:10.1364/OE.20.024957

WOS-PNI-58 Jocher, Christoph; Eidam, Tino; Hädrich, Steffen; Limpert, Jens; Tünnermann, Andreas: **Sub 25fs pulses from solid-core nonlinear compression stage at 250W of average power.** *Optics letters* 37: 4407 -, 2012. DOI:10.1364/OL.37.004407

WOS-PNI-59 Jöhren, R; Berendes, R; Buglak, W; Hampf, D; Hannen, V; Mäder, J; Nörtershäuser, Wilfried; Sanchez Alarcon, Rodolfo Marcelo; Weinheimer, C: **APDs as single-photon detectors for visible and near-infrared wavelengths down to Hz rates.** *Journal of Instrumentation* 7: P02015 - P02015, 2012. DOI:10.1088/1748-0221/7/02/P02015

WOS-PNI-60 Kankainen, A.; Novikov, Yu. N.; Oinonen, M.; Batist, L.; Elomaa, V. -V.; Eronen, T.; Hakala, J. ; Jokinen, A.; Karvonen, P.; Reponen, M.; Rissanen, J.; Saastamoinen, A.; Vorobjev, G.; Weber, C.; Äystö J.: **Isomer and decay studies for the rp process at IGISOL.** *The European physical journal / A* 48: 49, 2012. DOI:10.1140/epja/i2012-12049-x

WOS-PNI-61 Kar, S.; Kakolee, K. F.; Qiao, B.; Macchi, A.; Cerchez, M.; Doria, D.; Geissler, M.; McKenna, P. ; Neely, D.; Osterholz, J.; Prasad, R.; Quinn, K. ; Ramakrishna, B.; Sarri, G.; Willi, O.; Yuan, X. Y.; Zepf, M.; Borghesi, M.: **Ion Acceleration in Multispecies Targets Driven by Intense Laser Radiation Pressure.** *Physical review letters* 109: 185006, 2012. DOI:10.1103/PhysRevLett.109.185006

WOS-PNI-62 Keppler, S.; Hornung, M.; Bödefeld, R.; Kahle, M.; Hein, J.; Kaluza, M. C.: **All-reflective, highly accurate polarization rotator for high-power short-pulse laser systems.** *Optics express* 20: 20742 -, 2012. DOI:10.1364/OE.20.020742

WOS-PNI-63 Khalfaoui, N.; Stoquert, J.P.; Haas, F.; Trautmann, Christina; Meftah, A.; Toulemonde, M.: **Damage creation threshold of** Al_2O_3 **under swift heavy ion irradiation.** *Nuclear instruments & methods in physics research / B* 286: 247 - 253, 2012. DOI:10.1016/j.nimb.2011.11.047

WOS-PNI-64 King, B.; Gies, H.; Di Piazza, A.: **Pair production in a plane wave by thermal background photons.** *Physical review / D* 86: 125007, 2012. DOI:10.1103/PhysRevD.86.125007

WOS-PNI-65 Klose, A.; Minamisono, K.; Geppert, Christopher; Frömmgen, N.; Hammen, M.; Krämer, J.; Krieger, A. ; Levy, C.D.P.; Mantica, P.F.; Nörtershäuser, Wilfried; Vinnikova, S.: **Tests of atomic charge-exchange cells for collinear laser spectroscopy.** *Nuclear instruments & methods in physics research / A* 678: 114 - 121, 2012. DOI:10.1016/j.nima.2012.03.006

WOS-PNI-66 Koerner, Joerg; Vorholt, Christian; Liebetrau, Hartmut; Kahle, Martin; Kloepfel, Diethard; Seifert, Reinhard; Hein, Joachim; Kaluza, Malte C.: **Measurement of temperature-dependent absorption and emission spectra of Yb:YAG, Yb:LuAG, and Yb:CaF_2 between 20C and 200C and predictions on their influence on laser performance.** *Journal of the Optical Society of America / B* 29: 2493 -, 2012. DOI:10.1364/JOSAB.29.002493

WOS-PNI-67 Kowalska, M.; Naimi, S.; Agramunt, J.; Algora, A.; Beck, D.; Blank, B.; Blaum, K.; Böhm, Ch.; Borgmann, Ch.; Breitenfeldt, M.; Fraile, L.M.; George, S.; Herfurth, F.; Herlert, A.; Kreim, S. ; Lunney, D.; Minaya-Ramirez, E.; Neidherr, D.; Rosenbusch, M.; Rubio, B.; Schweikhard, L.; Stanja, J.; Zuber, K.: **Trap-assisted decay spectroscopy with ISOLTRAP.** *Nuclear instruments & methods in physics research / A* 689: 102 - 107, 2012. DOI:10.1016/j.nima.2012.04.059

WOS-PNI-68 Kraus, D.; Otten, A.; Frank, A.; Bagnoud, V.; Blazevic, A.; Gericke, D.O.; Gregori, G.; Ortner, A.; Schaumann, G.; Schumacher, D.; Vorberger, J. ; Wagner, F.; Wünsch, K.; Roth, M.: **X-ray Thomson scattering on shocked graphite.** *High energy density physics* 8: 46 - 49, 2012. DOI:10.1016/j.hedp.2011.11.011

WOS-PNI-69 Krauser, J.; Nix, A.-K.; Gehrke, H.-G.; Hofsäss, H.; Trautmann, C.; Weidinger, A.: **Conductivity enhancement of ion tracks in tetrahedral amorphous carbon by doping with N, B, Cu and Fe.** *Nuclear instruments & methods in physics research / B* 272: 280 - 283, 2012. DOI:10.1016/j.nimb.2011.01.083

WOS-PNI-70 Krieger, A.; Blaum, K.; Bissell, M. L.; Frömmgen, N.; Geppert, Ch.; Hammen, M.; Kreim, K.; Kowalska, M.; Krämer, J.; Neff, T.; Neugart, R. ; Neyens, G.; Nörtershäuser, W.; Novotny, Ch.; Sanchez, R.; Yordanov, D. T.: **Nuclear Charge Radius of ^{12}Be.** *Physical review letters* 108: 142501, 2012. DOI:10.1103/PhysRevLett.108.142501

WOS-PNI-71 Kugland, N. L.; Aurand, B.; Brown, C. G.; Constantin, C. G.; Everson, E. T.; Glenzer, S. H.; Schaeffer, D. B.; Tauschwitz, A.; Niemann, C.: **Demonstration of a low electromagnetic pulse laser-driven argon gas jet x-ray source.** *Applied physics letters* 101: 024102, 2012. DOI:10.1063/1.4734506

WOS-PNI-72 Kurcewicz, J.; Farinon, F.; Geissel, H.; Pietri, S.; Nociforo, C.; Prochazka, A.; Weick, H.; Winfield, J.S.; Estrade, A.; Allegro, P.R.P.; Bail, A.; Belier, G.; Benlliure, J.; Benzoni, G. ; Bunce, M.; Bowry, M.; Caballero-Folch, R.; Dillmann, I.; Evdokimov, A.; Gerl, J.; Gottardo, A. ; Gregor, E.; Janik, R.; Kelic-Heil, A.; Knöbel, R.; Kubo, T.; Litvinov, Yu.A.; Merchan, E. ; Mukha, I.; Naqvi, F.; Pfützner, M.; Pomorski, M.; Podolyak, Zs.; Regan, P.H.; Riese, B.; Ricciardi, M.V.; Scheidenberger, C.; Sitar, B.; Spiller, P.; Stadlmann, J.; Strmen, P.; Sun, B.; Szarka, I.; Taeb, J.; Terashima, S.; Valiente-Dobon, J.J.; Winkler, M.; Woods, Ph.: **Discovery and cross-section measurement of neutron-rich isotopes in the element range from neodymium to platinum with the FRS.** *Physics letters / B* 717: 371 - 375, 2012. DOI:10.1016/j.physletb.2012.09.021

WOS-PNI-73 Kübel, M; Betsch, K J; Johnson, Nora G; Kleineberg, U; Moshammer, R; Ullrich, J; Paulus, G G; Kling, M F; Bergues, B: **Carrier-envelope-phase tagging in measurements with long acquisition times.** *New journal of physics* 14: 093027 -, 2012. DOI:10.1088/1367-2630/14/9/093027

WOS-PNI-74 LITVINOV, YU. A.; SOBICZEWSKI, A.; PARKHOMENKO, A.; CHEREPANOV, E. A.: **Description of heavy-nuclei masses by macroscopic-models.** *International journal of modern physics / A* E21: 1250038, 2012. DOI:10.1142/S0218301312500383

WOS-PNI-75 Lang, Maik; Zhang, Fuxiang; Li, Weixing; Severin, Daniel; Bender, Markus; Klaumünzer, Siegfried; Trautmann, Christina; Ewing, Rodney C.: **Swift heavy ion-induced amorphization of $CaZrO_3$ perovskite.** *Nuclear instruments & methods in physics research / B* 286: 271 - 276, 2012. DOI:10.1016/j.nimb.2011.12.028

WOS-PNI-76 Lestinsky, Michael; Badnell, N. R.; Bernhardt, D.; Bing, D.; Grieser, M.; Hahn, M.; Hoffmann, J.; Jordon-Thaden, B.; Krantz, C.; Novotny, O.; Orlov, D. A.; Repnow, R.; Shornikov, A.; Müller, A.; Schippers, S.; Wolf, A.; Savin, D. W.: **Electon-ion recombination of Mg^{6+} forming Mg^{5+} and of Mg^{7+} forming Mg^{6+}: Laboratory measurements and theoretical calculations.** *The astrophysical journal / 1* 758: 40 -, 2012. DOI:10.1088/0004-637X/758/1/40

WOS-PNI-77 Li, Jiguang; Naze, Cedric; Godefroid, Michel; Fritzsche, Stephan; Gaigalas, Gediminas; Indelicato, Paul; Jönsson, Per: **Mass- and field-shift isotope parameters for the 2s-2p resonance doublet of lithiumlike ions.** *Physical review / A* 86: 022518, 2012. DOI:10.1103/PhysRevA.86.022518

WOS-PNI-78 Linusson, P.; Fritzsche, S.; Hedin, L.; Eland, J. H. D.; Karlsson, L.; Rubensson, J.-E.; Feifel, R. ; Andersson,: **Formation of Kr^{3+} via core-valence doubly ionized intermediate states.** *Physical review / A* 85: 032502, 2012. DOI:10.1103/PhysRevA.85.032502

WOS-PNI-79 Loetzsch, R.; Jäckel, Oliver; Höfer, S.; Kämpfer, Tino; Polz, J.; Uschmann, I.; Kaluza, M. C.; Förster, E.; Stambulchik, E.; Kroupp, E.; Maron, Y.: **K-shell spectroscopy of silicon ions as diagnostic for high electric fields.** *Review of scientific instruments* 83: 113507 -, 2012. DOI:10.1063/1.4767452

WOS-PNI-80 Loetzsch, Robert; Uschmann, Ingo; Förster, Eckhard: **Spatially resolved twin domain distribution and lattice parameter variations in the near-surface region of $SrTiO_3$ single crystals.** *Applied physics / A* 106: 563 - 566, 2012. DOI:10.1007/s00339-011-6674-8

WOS-PNI-81 Lu, Fengyuan; Huang, Mengbing; Yaqoob, Faisal; Lang, Maik; Namavar, Fereydoon; Trautmann, Christina ; Sun, Hongtao; Ewing, Rodney C.; Lian, Jie: **Displacive radiation-induced structural contraction in nanocrystalline ZrN.** *Applied physics letters* 101: 041904 -, 2012. DOI:10.1063/1.4738772

WOS-PNI-82 Lu, Fengyuan; Lang, Maik; Huang, Mengbing; Namavar, Fereydoon; Trautmann, Christina; Ewing, Rodney C.; Lian, Jie: **ZrSi formation at ZrN/Si interface induced by ballistic and ionizing radiations.** *Nuclear instruments*

& methods in physics research / B 286: 266 - 270, 2012. DOI:10.1016/j.nimb.2012.01.023

WOS-PNI-83 Lu, Fengyuan; Wang, Jianwei; Lang, Maik; Toulemonde, Marcel; Namavar, Fereydoon; Trautmann, Christina; Zhang, Jiaming; Ewing, Rodney C.; Lian, Jie: **Amorphization of nanocrystalline monoclinic ZrO_2 by swift heavy ion irradiation.** *Physical chemistry, chemical physics* 14: 12295 -, 2012. DOI:10.1039/c2cp41553d

WOS-PNI-84 Lushchik, A.; Kärner, T.; Lushchik, Ch.; Schwartz, K.; Savikhin, F.; Shablonin, E.; Shugai, A.; Vasilchenko, E.: **Electronic excitations and defect creation in wide-gap MgO and $Lu_3Al_5O_{12}$ crystals irradiated with swift heavy ions.** *Nuclear instruments & methods in physics research / B* 286: 200 - 208, 2012. DOI:10.1016/j.nimb.2011.11.016

WOS-PNI-85 Lushchik, A.; Lushchik, Ch.; Schwartz, K.; Savikhin, F.; Shablonin, E.; Shugai, A.; Vasilchenko, E.: **Creation and clustering of Frenkel defects at high density of electronic excitations in wide-gap materials.** *Nuclear instruments & methods in physics research / B* 277: 40 - 44, 2012. DOI:10.1016/j.nimb.2011.12.051

WOS-PNI-86 Maero, G.; Herfurth, F.; Kluge, H.-J.; Schwarz, S.; Zwicknagel, G.: **Numerical investigations on resistive cooling of trapped highly charged ions.** *Applied physics / B* 107: 1087 - 1096, 2012. DOI:10.1007/s00340-011-4808-5

WOS-PNI-87 Maiorova, A. V.; Surzhykov, A.; Tashenov, S.; Shabaev, V. M.; Stöhlker, Th.: **Production and diagnostics of spin-polarized heavy ions in sequential two-electron radiative recombination.** *Physical review / A* 86: 032701, 2012. DOI:10.1103/PhysRevA.86.032701

WOS-PNI-88 Maiorova, A. V.; Telnov, D. A.; Shabaev, V. M.; Zaitsev, V. A.; Tupitsyn, I. I.; Plunien, G.; Stöhlker, T.: **The coulomb glory effect in collisions of antiprotons with heavy ions.** *Russian journal of physical chemistry / B* 6: 218 - 223, 2012. DOI:10.1134/S1990793112020200

WOS-PNI-89 Manika, I.; Maniks, J.; Zabels, R.; Gabrusenoks, J.; Krause, M.; Tomut, Marilena; Schwartz, Kurt: **Nanoindentation and Raman Spectroscopic Study of Graphite Irradiated with Swift ^{238}U Ions.** *Fullerenes, nanotubes & carbon nanostructures* 20: 548 - 552, 2012. DOI:10.1080/1536383X.2012.656064

WOS-PNI-90 Maniks, J.; Manika, I.; Zabels, R.; Grants, R.; Tamanis, E.; Schwartz, K.: **Nanostructuring and strengthening of LiF crystals by swift heavy ions: AFM, XRD and nanoindentation study.** *Nuclear instruments & methods in physics research / B* 282: 81 - 84, 2012. DOI:10.1016/j.nimb.2011.08.042

WOS-PNI-91 Matula, O; Fritzsche, S; Surzhykov, A: **Polarization correlations in radiative cascades following dielectronic recombination of high- Z ions.** *Journal of physics / B* 45: 215004, 2012. DOI:10.1088/0953-4075/45/21/215004

WOS-PNI-92 McConnell, S. R.; Artemyev, A. N.; Mai, M.; Surzhykov, A.: **Solution of the two-center time-dependent Dirac equation in spherical coordinates: Application of the multipole expansion of the electron-nuclei interaction.** *Physical review / A* 86: 052705, 2012. DOI:10.1103/PhysRevA.86.052705

WOS-PNI-93 Mukha, I.; Grigorenko, L.; Acosta, L.; Alvarez, M. A. G.; Casarejos, E.; Chatillon, A.; Cortina-Gil, D.; Espino, J. M.; Fomichev, A.; Garcia-Ramos, J. E.; Geissel, H.; Gomez-Camacho, J.; Hofmann, J. ; Kiselev, O.; Korsheninnikov, A.; Kurz, N.; Litvinov, Yu. A.; Martel, I.; Nociforo, C.; Ott, W. ; Pfützner, M.; Rodriguez-Tajes, C.; Roeckl, E. ; Scheidenberger, C.; Stanoiu, M.; Sümmerer, K.; Weick, H.; Woods, P. J.: **New states in ^{18}Na and ^{19}Mg observed in the two-proton decay of ^{19}Mg.** *Physical review / C* 85: 044325, 2012. DOI:10.1103/PhysRevC.85.044325

WOS-PNI-94 Märtin, R.; Weber, G.; Barday, R.; Fritzsche, Y.; Spillmann, U.; Chen, W.; DuBois, R. D.; Enders, J.; Hegewald, M.; Hess, S.; Surzhykov, A.; Thorn, D. B.; Trotsenko, S.; Wagner, M.; Winters, D. F. A.; Yerokhin, V. A.; Stöhlker, Th.: **Polarization Transfer of Bremsstrahlung Arising from Spin-Polarized Electrons.** *Physical review letters* 108: 264801, 2012. DOI:10.1103/PhysRevLett.108.264801

WOS-PNI-95 Möller, Max; Cheng, Yan; Khan, Sabih D.; Zhao, Baozhen; Zhao, Kun; Chini, Michael; Paulus, Gerhard G.; Chang, Zenghu: **Dependence of high-order-harmonic-generation yield on driving-laser ellipticity.** *Physical review / A* 86: 011401, 2012. DOI:10.1103/PhysRevA.86.011401

WOS-PNI-96 Müller, Sven; Schötz, Christian; Picht, Oliver; Sigle, Wilfried; Kopold, Peter; Rauber, Markus; Alber, Ina; Neumann, Reinhard; Toimil Molares, Maria Eugenia: **Electrochemical Synthesis of $Bi_{1x}Sb_x$ Nanowires with Simultaneous Control on Size, Composition, and Surface Roughness.** *Crystal growth & design* 12: 615 - 621, 2012. DOI:10.1021/cg200685c

WOS-PNI-97 Naimi, S.; Audi, G.; Beck, D.; Blaum, K.; Böhm, Ch.; Borgmann, Ch.; Breitenfeldt, M.; George, S.; Herfurth, F.; Herlert, A.; Kellerbauer, A.; Kowalska, M.; Lunney, D.; Minaya Ramirez, E. ; Neidherr, D.; Rosenbusch, M.; Schweikhard, L.; Wolf, R. N.; Zuber, K.: **Surveying the N=40 island of inversion with new manganese masses.** *Physical review / C* 86: 014325, 2012. DOI:10.1103/PhysRevC.86.014325

WOS-PNI-98 Nasir, Saima; Ali, Mubarak; Ensinger, Wolfgang: **Thermally controlled permeation of ionic molecules through synthetic nanopores functionalized with amine-terminated polymer brushes.** *Nanotechnology* 23: 225502 -, 2012. DOI:10.1088/0957-4484/23/22/225502

WOS-PNI-99 Nesterenko, D. A.; Blaum, K.; Block, Michael; Droese, C.; Eliseev, S.; Herfurth, Frank; Minaya Ramirez, E.; Novikov, Yu. N.; Schweikhard, L.; Shabaev, V. M.; Smirnov, M. V.; Tupitsyn, I. I.; Zuber, K.; Zubova, N. A.: **Double-β transformations in isobaric triplets with mass numbers A=124, 130, and 136.** *Physical review / C* 86: 044313, 2012. DOI:10.1103/PhysRevC.86.044313

WOS-PNI-100 Neumayer, P.; Aurand, B.; Costa Fraga, R. A.; Ecker, B.; Grisenti, R. E.; Gumberidze, A.; Hochhaus, D. C.; Kalinin, A.; Kaluza, M. C.; Kühl, T.; Polz, J.; Reuschl, R.; Stöhlker, T.; Winters, D.; Winters, N.; Yin, Z.: **Evi-**

dence for ultra-fast heating in intense-laser irradiated reduced-mass targets. *Physics of plasmas* 19: 122708, 2012. DOI:10.1063/1.4772773

WOS-PNI-101 Nguyen, Quoc Hung; Ali, Mubarak; Neumann, Reinhard; Ensinger, Wolfgang: **Saccharide/glycoprotein recognition inside synthetic ion channels modified with boronic acid.** *Sensors and actuators / B* 162: 216 - 222, 2012. DOI:10.1016/j.snb.2011.12.070

WOS-PNI-102 Niemann, C; Constantin, C G; Schaeffer, D B; Tauschwitz, A; Weiland, T; Lucky, Z; Gekelman, W ; Everson, E T; Winske, D: **High-energy Nd:glass laser facility for collisionless laboratory astrophysics.** *Journal of Instrumentation* 7: P03010 - P03010, 2012. DOI:10.1088/1748-0221/7/03/P03010

WOS-PNI-103 Nociforo, C; Farinon, F; Musumarra, A; Bosch, F; Boutin, D; Del Zoppo, A; Figuera, P; Fisichella, M; Geissel, H; Knöbel, R; Kojouharov, I; Kozhuharov, C; Kuboki, T; Kurcewicz, J; Litvinov, Yu A; Mazzocco, M; Motizuki, Y; Nolden, F ; Ohstubo, T; Ohkuma, Y; Patyk, Z; Pellegriti, M G; Pietri, S; Podolyak, Z; Prochazka, A; Sanjari, M S; Scheidenberger, C; Scuderi, V; Sun, B ; Suzuki, T; Torresi, D; Weick, H; Winfield, J S ; Winckler, N; Winkler, M; Wollersheim, H J; Yamaguchi, T: **Measurements of -decay half-lives at GSI.** *Physica scripta* T150: 014028, 2012. DOI:10.1088/0031-8949/2012/T150/014028

WOS-PNI-104 Nociforo, Chiara; Prochazka, Andrej; Kanungo, R.; Aumann, Thomas; Boutin, D.; Cortina-Gil, D.; Davids, B.; Diakaki, M.; Farinon, Fabio; Geissel, Hans; Gernhäuser, R.; Janik, R.; Jonson, B.; Kindler, Birgit; Knöbel, Ronja; Krücken, R.; Kurz, Nikolaus; Lantz, M.; Lenske, H.; Litvinov, Yu. A.; Lommel, Bettina; Mahata, K.; Maierbeck, P. ; Musumarra, A.; Nilsson, T.; Perro, C.; Scheidenberger, Christoph; Sitar, B.; Strmen, P.; Sun, B.; Szarka, I.; Tanihata, I.; Weick, Helmut ; Winkler, Martin: **One-neutron removal reactions on Al isotopes around the N=20 shell closure.** *Physical review / C* 85: 044312, 2012. DOI:10.1103/PhysRevC.85.044312

WOS-PNI-105 Novikov, Yu. N.; Vasiliev, A. A.; Gusev, Yu. I.; Nesterenko, D. A.; Popov, A. V.; Seliverstov, D. M. ; Seliverstov, M. D.; Khusainov, A. Kh.; Blaum, K. ; Eliseev, S. A.; Herfurth, F.; Block, M.; Vorobjev, G. K.; Jokinen, A.; Rodriguez, D.; Yavor, M. I.: **High-precision method of measuring short-lived nuclides by means of developed systems of ion traps for high-charge ions (MATS project).** *Atomic energy* 112: 139 - 146, 2012. DOI:10.1007/s10512-012-9535-4

WOS-PNI-106 Novotny, O.; Badnell, N. R.; Bernhardt, D.; Grieser, M.; Hahn, M.; Krantz, C.; Lestinsky, M. ; Müller, A.; Repnow, R.; Schippers, S.; Wolf, A.; Savin, D. W.: **ELECTRON-ION RECOMBINATION OF Fe XII FORMING Fe XI: LABORATORY MEASUREMENTS AND THEORETICAL CALCULATIONS.** *The astrophysical journal / 1* 753: 57 -, 2012. DOI:10.1088/0004-637X/753/1/57

WOS-PNI-107 Otto, Hans-Jürgen; Stutzki, Fabian; Jansen, Florian; Eidam, Tino; Jauregui, Cesar; Limpert, Jens; Tünnermann, Andreas: **Temporal dynamics of mode instabilities in high-power fiber lasers and amplifiers.** *Optics express* 20: 15710 -, 2012. DOI:10.1364/OE.20.015710

WOS-PNI-108 Paul, Amitesh; Pauly, C.; Trautmann, Christina; Mattauch, S.; Jutimoosik, Jaru; Yimnirun, Rattikorn ; Rujirawat, Saroj; Höpfner, Britta; Lauermann, Iver; Lux-Steiner, M.; Böni, P.: **Direct manipulation of the uncompensated antiferromagnetic spins in exchange coupled system by GeV ion irradiation.** *Applied physics letters* 100: 253102 -, 2012. DOI:10.1063/1.4729472

WOS-PNI-109 Paz Gandiaga, Nerea; Kuschel, S; Rödel, C; Schnell, M.; Jäckel, Oliver; Kaluza, M C; Paulus, G G: **Thomson backscattering from laser-generated, relativistically moving high-density electron layers.** *New journal of physics* 14: 093018 -, 2012. DOI:10.1088/1367-2630/14/9/093018

WOS-PNI-110 Pevarnik, Matthew; Healy, Ken; Toimil-Molares, Maria Eugenia; Morrison, Alan; Letant, Sonia E.; Siwy, Zuzanna S.: **Polystyrene Particles Reveal Pore Substructure As They Translocate.** *ACS nano* 6: 7295 - 7302, 2012. DOI:10.1021/nn302413u

WOS-PNI-111 Picht, Oliver; Müller, Sven; Alber, Ina; Rauber, Markus; Lensch-Falk, Jessica; Medlin, Douglas L.; Neumann, Reinhard; Toimil Molares, Maria Eugenia: **Tuning the Geometrical and Crystallographic Characteristics of Bi_2Te_3 Nanowires by Electrodeposition in Ion-Track Membranes.** *The journal of physical chemistry / C* 116: 5367 - 5375, 2012. DOI:10.1021/jp210491g

WOS-PNI-112 Plateau, G. R.; Geddes, C. G. R.; Thorn, D. B.; Chen, M.; Benedetti, C.; Esarey, E.; Gonsalves, A. J.; Matlis, N. H.; Nakamura, K.; Schroeder, C. B. ; Shiraishi, S.; Sokollik, T.; van Tilborg, J.; Toth, Cs.; Trotsenko, Sergiy; Kim, T. S.; Battaglia, M.; Stöhlker, Th.; Leemans, W. P.: **Low-Emittance Electron Bunches from a Laser-Plasma Accelerator Measured using Single-Shot X-Ray Spectroscopy.** *Physical review letters* 109: 064802, 2012. DOI:10.1103/PhysRevLett.109.064802

WOS-PNI-113 Povarnitsyn, M. E.; Andreev, N. E.; Levashov, P. R.; Khishchenko, K. V.; Rosmej, Olga: **Dynamics of thin metal foils irradiated by moderate-contrast high-intensity laser beams.** *Physics of plasmas* 19: 023110 -, 2012. DOI:10.1063/1.3683687

WOS-PNI-114 Preda, N.; Enculescu, M.; Gherendi, F.; Matei, E.; Toimil-Molares, M.E.; Enculescu, I.: **Synthesis of CdS nanostructures using template-assisted ammonia-free chemical bath deposition.** *Journal of physics and chemistry of solids* 73: 1082 - 1089, 2012. DOI:10.1016/j.jpcs.2012.05.003

WOS-PNI-115 Procter, T. J.; Billowes, J.; Bissell, M. L.; Blaum, K.; Charlwood, F. C.; Cheal, B.; Flanagan, K. T.; Forest, D. H.; Fritzsche, Stephan; Geppert, Ch.; Heylen, H.; Kowalska, M.; Kreim, K.; Krieger, A.; Krämer, J.; Lynch, K. M.; Mane, E. ; Moore, I. D.; Neugart, R.; Neyens, G.; Nörtershäuser, Wilfried; Papuga, J.; Rajabali, M. M. ; Stroke, H. H.; Vingerhoets, P.; Yordanov, D. T. ; akova, M.: **Nuclear mean-square charge radii of ^{63,64,66,6882}Ga nuclei: No anomalous behavior at N=32.** *Physical review / C* 86: 034329, 2012. DOI:10.1103/PhysRevC.86.034329

WOS-PNI-116 Przystawik, A.; Kickermann, A.; Al-Shemmary, A.; Düsterer, S.; Ellis, A. M.; von Haeften, K.; Harmand, M.; Ramakrishna, S.; Redlin, H.; Schroedter, L.; Schulz, M.; Seideman, T.; Stojanovic, N.; Szekely, J.; Tavella, F.; Toleikis, S.; Laarmann, T.: **Generation of the simplest rotational wave packet in a diatomic molecule: Tracing a two-level superposition in the time domain.** *Physical review / A* 85: 052503, 2012. DOI:10.1103/PhysRevA.85.052503

WOS-PNI-117 Ramirez, Patricio; Ali, Mubarak; Ensinger, Wolfgang; Mafe, Salvador: **Information processing with a single multifunctional nanofluidic diode.** *Applied physics letters* 101: 133108 -, 2012. DOI:10.1063/1.4754845

WOS-PNI-118 Rathje, T; Johnson, Nora G; Möller, M; Süßmann, F; Adolph, D; Kübel, M; Kienberger, R; Kling, M F; Paulus, G G; Sayler, A M: **Review of attosecond resolved measurement and control via carrierenvelope phase tagging with above-threshold ionization.** *Journal of physics / B* 45: 074003, 2012. DOI:10.1088/0953-4075/45/7/074003

WOS-PNI-119 Rauber, M; Muench, F; Toimil-Molares, M E; Ensinger, W.: **Thermal stability of electrodeposited platinum nanowires and morphological transformations at elevated temperatures.** *Nanotechnology* 23: 475710 -, 2012. DOI:10.1088/0957-4484/23/47/475710

WOS-PNI-120 Renisch, D.; Beyer, T.; Blaum, K.; Block, Michael; Düllmann, Ch.E.; Eberhardt, K.; Eibach, M.; Nagy, Sz.; Neidherr, Dennis; Nörtershäuser, Wilfried ; Smorra, C.: **Targets on superhydrophobic surfaces for laser ablation ion sources.** *Nuclear instruments & methods in physics research / A* 676: 84 - 89, 2012. DOI:10.1016/j.nima.2012.02.024

WOS-PNI-121 Repp, J.; Böhm, Christoph; Crespo Lopez-Urrutia, J. R.; Dörr, A.; Eliseev, S.; George, S.; Goncharov, M.; Novikov, Y. N.; Roux, C.; Sturm, S. ; Ulmer, S.; Blaum, K.: **PENTATRAP: a novel cryogenic multi-Penning-trap experiment for high-precision mass measurements on highly charged ions.** *Applied physics / B* 107: 983 - 996, 2012. DOI:10.1007/s00340-011-4823-6

WOS-PNI-122 Rodegheri, C C; Blaum, K; Kracke, H; Kreim, S; Mooser, A; Quint, Wolfgang; Ulmer, S; Walz, J: **An experiment for the direct determination of the g -factor of a single proton in a Penning trap.** *New journal of physics* 14: 063011 -, 2012. DOI:10.1088/1367-2630/14/6/063011

WOS-PNI-123 Rodriguez, M.D.; Afra, B.; Trautmann, C.; Toulemonde, M.; Bierschenk, T.; Leslie, J.; Giulian, R.; Kirby, N.; Kluth, P.: **Morphology of swift heavy ion tracks in metallic glasses.** *Journal of non-crystalline solids* 358: 571 - 576, 2012. DOI:10.1016/j.jnoncrysol.2011.10.028

WOS-PNI-124 Rothhardt, Jan; Demmler, Stefan; Hädrich, Steffen; Limpert, Jens; Tünnermann, Andreas: **Octave-spanning OPCPA system delivering CEP-stable few-cycle pulses and 22 W of average power at 1 MHz repetition rate.** *Optics express* 20: 10870 -, 2012. DOI:10.1364/OE.20.010870

WOS-PNI-125 Rothhardt, Jan; Heidt, Alexander M.; Hädrich, Steffen; Demmler, Stefan; Limpert, Jens; Tünnermann, Andreas: **High stability soliton frequency-shifting mechanisms for laser synchronization applications.** *Journal of the Optical Society of America / B* 29: 1257 -, 2012. DOI:10.1364/JOSAB.29.001257

WOS-PNI-126 Roux, C.; Böhm, Christoph; Dörr, A.; Eliseev, S.; George, S.; Goncharov, M.; Novikov, Y. N.; Repp, J.; Sturm, S.; Ulmer, S.; Blaum, K.: **The trap design of PENTATRAP.** *Applied physics / B* 107: 997 - 1005, 2012. DOI:10.1007/s00340-011-4825-4

WOS-PNI-127 Rödel, C.; an der Brügge, D.; Bierbach, J.; Yeung, M.; Hahn, T.; Dromey, B.; Herzer, S.; Fuchs, S.; Pour, A. Galestian; Eckner, E.; Behmke, M.; Cerchez, M.; Jäckel, Oliver; Hemmers, D.; Toncian, T.; Kaluza, M. C.; Belyanin, A.; Pretzler, G.; Willi, O.; Pukhov, A.; Zepf, M.; Paulus, G. G.: **Harmonic Generation from Relativistic Plasma Surfaces in Ultrasteep Plasma Density Gradients.** *Physical review letters* 109: 125002, 2012. DOI:10.1103/PhysRevLett.109.125002

WOS-PNI-128 Safari, L.; Amaro, P.; Fritzsche, S.; Santos, J. P.; Fratini, F.: **Relativistic total cross section and angular distribution for Rayleigh scattering by atomic hydrogen.** *Physical review / A* 85: 043406, 2012. DOI:10.1103/PhysRevA.85.043406

WOS-PNI-129 Safari, L.; Amaro, P.; Fritzsche, S.; Santos, J. P.; Tashenov, S.; Fratini, F.: **Relativistic polarization analysis of Rayleigh scattering by atomic hydrogen.** *Physical review / A* 86: 043405, 2012. DOI:10.1103/PhysRevA.86.043405

WOS-PNI-130 Schabinger, B.; Sturm, S.; Wagner, A.; Alonso, J.; Quint, W.; Werth, G.; Blaum, K.: **Experimental g factor of hydrogenlike silicon-28.** *The European physical journal / D* 66: 71, 2012. DOI:10.1140/epjd/e2012-20610-y

WOS-PNI-131 Schippers, S.; Bernhardt, D.; Müller, A.; Lestinsky, M.; Hahn, M.; Novotny, O.; Savin, D. W. ; Grieser, M.; Krantz, C.; Repnow, R.; Wolf, A.: **Storage-ring measurement of the hyperfine-induced $2s2p^3P_0 \rightarrow 2s^2 {}^1S_0$ transition rate in berylliumlike sulfur.** *Physical review / A* 85: 012513, 2012. DOI:10.1103/PhysRevA.85.012513

WOS-PNI-132 Schlegel, Theodor; Tikhonchuk, Vladimir T: **Classical radiation effects on relativistic electrons in ultraintense laser fields with circular polarization.** *New journal of physics* 14: 073034 -, 2012. DOI:10.1088/1367-2630/14/7/073034

WOS-PNI-133 Schmidt, Maximilian; Erne, Sebastian; Nowak, Boris; Sexty, Denes; Gasenzer, Thomas: **Non-thermal fixed points and solitons in a one-dimensional Bose gas.** *New journal of physics* 14: 075005 -, 2012. DOI:10.1088/1367-2630/14/7/075005

WOS-PNI-134 Schnell, Michael; Sävert, Alexander; Landgraf, Björn; Reuter, Maria; Nicolai, Maria; Jäckel, Oliver; Peth, Christian; Thiele, Tobias; Jansen, Oliver; Pukhov, Alexander; Willi, Oswald; Kaluza, Malte C.; Spielmann, Christian: **Deducing the Electron-Beam Diameter in a Laser-Plasma Accelerator Using X-Ray Betatron Radiation.** *Physical review letters* 108: 075001, 2012. DOI:10.1103/PhysRevLett.108.075001

WOS-PNI-135 Schole, Jan; Nowak, Boris; Gasenzer, Thomas:

Critical dynamics of a two-dimensional superfluid near a nonthermal fixed point. *Physical review / A* 86: 013624, 2012. DOI:10.1103/PhysRevA.86.013624

WOS-PNI-136 Schulz, M.; Riedel, R.; Willner, A.; Düsterer, S.; Prandolini, M. J.; Feldhaus, J.; Faatz, B.; Rossbach, J.; Drescher, M.; Tavella, F.: **Pulsed operation of a high average power Yb:YAG thin-disk multipass amplifier.** *Optics express* 20: 5038 -, 2012. DOI:10.1364/OE.20.005038

WOS-PNI-137 Schulz, M.; Wang, X.; Gundmundsson, M.; Schneider, K.; Kelkar, A.; Voitkiv, A. B.; Najjari, B.; Schöffler, M.; Schmidt, L. Ph. H.; Dörner, R.; Ullrich, J.; Moshammer, R.; Fischer, D.: **Strongly Enhanced Backward Emission of Electrons in Transfer and Ionization.** *Physical review letters* 108: 043202, 2012. DOI:10.1103/PhysRevLett.108.043202

WOS-PNI-138 Schuster, Beatrice; Fujara, F.; Merk, B.; Neumann, R.; Seidl, T.; Trautmann, C.: **Response behavior of ZrO_2 under swift heavy ion irradiation with and without external pressure.** *Nuclear instruments & methods in physics research / B* 277: 45 - 52, 2012. DOI:10.1016/j.nimb.2011.12.060

WOS-PNI-139 Schwen, D.; Bringa, E.; Krauser, J.; Weidinger, A.; Trautmann, C.; Hofsäss, H.: **Nano-hillock formation in diamond-like carbon induced by swift heavy projectiles in the electronic stopping regime: Experiments and atomistic simulations.** *Applied physics letters* 101: 113115, 2012. DOI:10.1063/1.4752455

WOS-PNI-140 Seidl, T.; Baake, O.; Hossain, U.H.; Bender, M.; Severin, D.; Trautmann, C.; Ensinger,: **In-situ investigation of polyvinyl formal irradiated with GeV Au ions.** *Nuclear instruments & methods in physics research / B* 272: 400 - 404, 2012. DOI:10.1016/j.nimb.2011.01.110

WOS-PNI-141 Seidl, Tim; Plotnikov, A.; Mustafin, Edil; Lopez, R.; Severin, Daniel; Floch, Eric; Trautmann, Christina; Golubev, A.; Smolyakov, A.; Tommasini, D.; Ensinger, W.: **Influence of swift heavy ion beams and protons on the dielectric strength ofpolyimide.** *Polymer degradation and stability* 97: 2396 - 2402, 2012. DOI:10.1016/j.polymdegradstab.2012.07.025

WOS-PNI-142 Serbun, P.; Jordan, F.; Navitski, A.; Müller, G.; Alber, I.; Toimil-Molares, M.E.; Trautmann, C.: **Copper nanocones grown in polymer ion-track membranes as field emitters.** *The European physical journal / Applied physics* 58: 10402 -, 2012. DOI:10.1051/epjap/2012110473

WOS-PNI-143 Seres, Enikoe; Seres, Jozsef; Spielmann, Christian: **Extreme ultraviolet light source based on intracavity high harmonic generation in a mode locked Ti:sapphire oscillator with 94 MHz repetition rate.** *Optics express* 20: 6185 -, 2012. DOI:10.1364/OE.20.006185

WOS-PNI-144 Seres, J.; Seres, E.; Spielmann, C.: **Classical model of strong-field parametric amplification of soft x rays.** *Physical review / A* 86: 013822, 2012. DOI:10.1103/PhysRevA.86.013822

WOS-PNI-145 Siminos, E.; Grech, M.; Skupin, S.; Schlegel, T.; Tikhonchuk, V. T.: **Effect of electron heating on self-induced transparency in relativistic-intensity laser-plasma interactions.** *Physical review / E* 86: 056404, 2012. DOI:10.1103/PhysRevE.86.056404

WOS-PNI-146 Smorra, C.; Beyer, T.; Blaum, K.; Block, Michael; Düllmann, Ch. E.; Eberhardt, K.; Eibach, M.; Eliseev, S.; Nagy, Sz.; Nörtershäuser, Wilfried; Renisch, D.: **Direct mass measurements of cadmium and palladium isotopes and their double-β transition Q values.** *Physical review / C* 85: 027601, 2012. DOI:10.1103/PhysRevC.85.027601

WOS-PNI-147 Smorra, C.; Rodriguez, T. R.; Beyer, T.; Blaum, K.; Block, Michael; Düllmann, Ch. E.; Eberhardt, K.; Eibach, M.; Eliseev, S.; Langanke, Karlheinz ; Martinez Pinedo, Gabriel; Nagy, Sz.; Nörtershäuser, Wilfried; Renisch, D.; Shabaev, V. M. ; Tupitsyn, I. I.; Zubova, N. A.: **Q value and half-life of double-electron capture in ^{184}Os.** *Physical review / C* 86: 044604, 2012. DOI:10.1103/PhysRevC.86.044604

WOS-PNI-148 Sorieul, S; Kerbiriou, X; Costantini, J-M; Gosmain, L; Calas, G; Trautmann, C: **Optical spectroscopy study of damage induced in 4H-SiC by swift heavy ion irradiation.** *Journal of physics / Condensed matter* 24: 125801, 2012. DOI:10.1088/0953-8984/24/12/125801

WOS-PNI-149 Sorokin, M.V.; Schwartz, K.; Voss, K.-O.; Rosmej, O.; Volkov, A.E.; Neumann, R.: **Color centers beyond the swift ion ranges in LiF crystals.** *Nuclear instruments & methods in physics research / B* 285: 24 - 29, 2012. DOI:10.1016/j.nimb.2012.05.012

WOS-PNI-150 Stutzki, Fabian; Jansen, Florian; Liem, Andreas; Jauregui, Cesar; Limpert, Jens; Tünnermann, Andreas: **26 mJ, 130 W Q-switched fiber-laser system with near-diffraction-limited beam quality.** *Optics letters* 37: 1073 -, 2012. DOI:10.1364/OL.37.001073

WOS-PNI-151 Tahir, N. A.; Sancho, J. Blanco; Shutov, A.; Schmidt, R.; Piriz, A. R.: **Impact of high energy high intensity proton beams on targets: Case studies for Super Proton Synchrotron and Large Hadron Collider.** *Physical review / Special topics / Accelerators and beams* 15: 051003, 2012. DOI:10.1103/PhysRevSTAB.15.051003

WOS-PNI-152 Tahir, N.A.; Kim, V.; Lamour, E.; Lomonosov, I.V.; Piriz, A.R.; Rozet, J.P.; Stöhlker, Thomas; Sultanov, V.; Vernhet, D.: **Two-dimensional thermal simulations of aluminum and carbon ion strippers for experiments at SPIRAL2 using the highest beam intensities.** *Nuclear instruments & methods in physics research / B* 290: 43 - 47, 2012. DOI:10.1016/j.nimb.2012.08.024

WOS-PNI-153 Tahir, N.A.; Kim, V.; Lamour, E.; Lomonosov, I.V.; Piriz, A.R.; Rozet, J.P.; Stöhlker, Thomas; Sultanov, V.; Vernhet, D.: **Two-dimensional thermal simulations of an aluminum beam stripper for experiments at SPIRAL2.** *Nuclear instruments & methods in physics research / B* 276: 66 - 69, 2012. DOI:10.1016/j.nimb.2012.01.040

WOS-PNI-154 Toimil Molares, Maria Eugenia: **Characterization and properties of micro- and nanowires of controlled size, composition, and geometry fabricated by electrodeposition**

and ion-track technology. *Beilstein journal of nanotechnology* 3: 860 - 883, 2012. DOI:10.3762/bjnano.3.97

WOS-PNI-155 Toimil-Molares, Maria Eugenia; Röntzsch, Lars; Sigle, Wilfried; Heinig, Karl-Heinz; Trautmann, Christina; Neumann, Reinhard: **Pipetting Nanowires: In Situ Visualization of Solid-State Nanowire-to-Nanoparticle Transformation Driven by Surface Diffusion-Mediated Capillarity.** *Advanced functional materials* 22: 695 - 701, 2012. DOI:10.1002/adfm.201102260

WOS-PNI-156 Toneev, V. D.; Voronyuk, V.: **The chiral magnetic effect: Beam-energy and system-size dependence.** *Physics of atomic nuclei* 75: 607 - 612, 2012. DOI:10.1134/S1063778812050274

WOS-PNI-157 Toulemonde, M.; Assmann, W.; Dufour, C.; Meftah, A.; Trautmann, C.: **Nanometric transformation of the matter by short and intense electronic excitation: Experimental data versus inelastic thermal spike model.** *Nuclear instruments & methods in physics research / B* 277: 28 - 39, 2012. DOI:10.1016/j.nimb.2011.12.045

WOS-PNI-158 Toulemonde, M.; Benyagoub, A.; Trautmann, C.; Khalfaoui, N.; Boccanfuso, M.; Dufour, C.; Gourbilleau, F.; Grob, J. J.; Stoquert, J. P.; Costantini, J. M.; Haas, F.; Jacquet, E.; Voss, K.-O.; Meftah, A.: **Dense and nanometric electronic excitations induced by swift heavy ions in an ionic CaF_2 crystal: Evidence for two thresholds of damage creation.** *Physical review / B* 85: 054112, 2012. DOI:10.1103/PhysRevB.85.054112

WOS-PNI-159 Trassinelli, M.; Prigent, C; Lamour, E; Mezdari, F; Merot, J; Reuschl, R; Rozet, J-P; Steydli, S ; Vernhet, D: **Investigation of slow collisions for (quasi) symmetric heavy systems: what can be extracted from high resolution x-ray spectra.** *Journal of physics / B* 45: 085202 -, 2012. DOI:10.1088/0953-4075/45/8/085202

WOS-PNI-160 Tupitsyn, I. I.; Kozhedub, Y. S.; Shabaev, V. M.; Bondarev, A. I.; Deyneka, G. B.; Maltsev, I. A.; Hagmann, Siegbert; Plunien, G.; Stöhlker, Th.: **Relativistic calculations of the K-K charge transfer and K-vacancy production probabilities in low-energy ion-atom collisions.** *Physical review / A* 85: 032712, 2012. DOI:10.1103/PhysRevA.85.032712

WOS-PNI-161 Vogel, Manuel; Quint, W.; Paulus, G.G.; Stöhlker, Th.: **A Penning trap for advanced studies with particles in extreme laser fields.** *Nuclear instruments & methods in physics research / B* 285: 65 - 71, 2012. DOI:10.1016/j.nimb.2012.05.001

WOS-PNI-162 Vorobjev, G.; Sokolov, A.; Thorn, A.; Herfurth, F.; Kester, O.; Quint, W.; Stöhlker, Thomas; Zschornack, G.: **Demonstration of charge breeding in a compact room temperature electron beam ion trap.** *Review of scientific instruments* 83: 053302 -, 2012. DOI:10.1063/1.4719668

WOS-PNI-163 Weber, Günter; Märtin, Renate; Surzhykov, A.; Yasuda, M.; Yerokhin, V. A.; Stöhlker, Th.: **PEBSI A Monte Carlo simulator for bremsstrahlung arising from electrons colliding with thin solid-state targets.** *Nuclear instruments & methods in physics research / B* 279: 155 - 159, 2012. DOI:10.1016/j.nimb.2011.10.048

WOS-PNI-164 Weber, U.; Bliedtner, J.; Schilling, M.; Iancu, G.; Trautmann, C.; Seidel, T; Engenhart-Cabillic, R. ; Zink, K.: **New Design and Manufacturing method for a Ripple filter in Ion Beam Therapy.** *Strahlentherapie und Onkologie* 188: 166-166, 2012. WOS-PNI-165 White, T. G.; Vorberger, J.; Brown, C. R. D.; Crowley, B. J. B.; Davis, P.; Glenzer, S. H.; Harris, J. W. O.; Hochhaus, D. C.; Le Pape, S.; Ma, T.; Murphy, C. D.; Neumayer, Paul; Pattison, L. K. ; Richardson, S.; Gericke, D. O.; Gregori, G.: **Observation of inhibited electron-ion coupling in strongly heated graphite.** *Scientific reports* 2: 1-5, 2012. DOI:10.1038/srep00889

WOS-PNI-166 Willner, A.; Hage, A.; Riedel, Robert; Grguras, I.; Simoncig, A.; Schulz, M.; Dzelzainis, T.; Höppner, H.; Huber, S.; Prandolini, M. J.; Dromey, B.; Zepf, M.; Cavalieri, A. L.; Tavella, Franz: **Coherent spectral enhancement of carrier-envelope-phase stable continua with dual-gas high harmonic generation.** *Optics letters* 37: 3672 -, 2012. DOI:10.1364/OL.37.003672

WOS-PNI-167 Wolf, R.N.; Beck, D.; Blaum, K.; Böhm, Ch.; Borgmann, Ch.; Breitenfeldt, M.; Herfurth, F.; Herlert, A.; Kowalska, M.; Kreim, S.; Lunney, D. ; Naimi, S.; Neidherr, D.; Rosenbusch, M.; Schweikhard, L.; Stanja, J.; Wienholtz, F.; Zuber, K.: **On-line separation of short-lived nuclei by a multi-reflection time-of-flight device.** *Nuclear instruments & methods in physics research / A* 686: 82 - 90, 2012. DOI:10.1016/j.nima.2012.05.067

WOS-PNI-168 Wurm, Michael; Beacom, John F.; Bezrukov, Leonid B.; Bick, Daniel; Blümer, Johannes; Choubey, Sandhya ; Ciemniak, Christian; DAngelo, Davide; Dasgupta, Basudeb; Derbin, Alexander; Dighe, Amol; Domogatsky, Grigorij; Dye, Steve; Eliseev, Sergey; Enqvist, Timo; Erykalov, Alexey; von Feilitzsch, Franz ; Fiorentini, Gianni; Fischer, Tobias; Göger-Neff, Marianne; Grabmayr, Peter; Hagner, Caren; Hellgartner, Dominikus; Hissa, Johannes; Horiuchi, Shunsaku; Janka, Hans-Thomas; Jaupart, Claude; Jochum, Josef; Kalliokoski, Tuomo; Kayunov, Alexei; Kuusiniemi, Pasi; Lachenmaier, Tobias; Lazanu, Ionel ; Learned, John G.; Lewke, Timo; Lombardi, Paolo; Lorenz, Sebastian; Lubsandorzhiev, Bayarto; Ludhova, Livia; Loo, Kai; Maalampi, Jukka; Mantovani, Fabio ; Marafini, Michela; Maricic, Jelena; Marrodan Undagoitia, Teresa; McDonough, William F.; Miramonti, Lino; Mirizzi, Alessandro; Meindl, Quirin; Mena, Olga; Möllenberg, Randolph; Muratova, Valentina; Nahnhauer, Rolf; Nesterenko, Dmitry; Novikov, Yuri N. ; Nuijten, Guido; Oberauer, Lothar; Pakvasa, Sandip ; Palomares-Ruiz, Sergio; Pallavicini, Marco; Pascoli, Silvia; Patzak, Thomas; Peltoniemi, Juha; Potzel, Walter; Räihä Tomi; Raffelt, Georg G.; Ranucci, Gioacchino; Razzaque, Soebur; Rummukainen, Kari; Sarkamo, Juho; Sinev, Valerij; Spiering, Christian; Stahl, Achim; Thorne, Felicitas; Tippmann, Marc; Tonazzo, Alessandra; Trzaska, Wladyslaw H.; Vergados, John D.; Wiebusch, Christopher ; Winter, Jürgen: **The next-generation liquid-scintillator neutrino observatory LENA.** *Astroparticle physics* 35: 685 - 732, 2012. DOI:10.1016/j.astropartphys.2012.02.011

WOS-PNI-169 Xie, Xinhua; Doblhoff-Dier, Katharina; Roither, Stefan; Schöffler, Markus S.; Kartashov, Daniil; Xu, Huailiang; Rathje, Tim; Paulus, Gerhard G.; Baltuska,

Andrius; Gräfe, Stefanie; Kitzler, Markus: **Attosecond-Recollision-Controlled Selective Fragmentation of Polyatomic Molecules.** *Physical review letters* 109: 243001, 2012. DOI:10.1103/PhysRevLett.109.243001

WOS-PNI-170 Yerokhin, V. A.; Pachucki, K.; Harman, Z.; Keitel, C. H.: **QED calculation of the nuclear magnetic shielding for hydrogenlike ions.** *Physical review / A* 85: 022512, 2012. DOI:10.1103/PhysRevA.85.022512

WOS-PNI-171 Yerokhin, V. A.; Surzhykov, A.; Märtin, R.; Tashenov, S.; Weber, G.: **Comparative study of the electron-atom and positron-atom bremsstrahlung.** *Physical review / A* 86: 032708, 2012. DOI:10.1103/PhysRevA.86.032708

WOS-PNI-172 Yerokhin, V. A.; Surzhykov, A.: **Relativistic configuration-interaction calculation of energy levels of core-excited states in lithiumlike ions: Argon through krypton.** *Physical review / A* 86: 042507, 2012. DOI:10.1103/PhysRevA.86.042507

WOS-PNI-173 Yordanov, D. T.; Bissell, M. L.; Blaum, K.; De Rydt, M.; Geppert, Ch.; Kowalska, M.; Krämer, J. ; Kreim, K.; Krieger, A.; Lievens, P.; Neff, T. ; Neugart, R.; Neyens, G.; Nörtershäuser, W.; Sanchez, R.; Vingerhoets, P.: **Nuclear Charge Radii of $^{21-32}$Mg.** *Physical review letters* 108: 042504, 2012. DOI:10.1103/PhysRevLett.108.042504

WOS-PNI-174 Yu Apel, Pavel; Blonskaya, Irina V; Orelovitch, Oleg L; Sartowska, Bozena A; Spohr, Reimar: **Asymmetric ion track nanopores for sensor technology. Reconstruction of pore profile from conductometric measurements.** *Nanotechnology* 23: 225503, 2012. DOI:10.1088/0957-4484/23/22/225503

WOS-PNI-175 Zastrau, U; Brown, C R D; Döppner, T; Glenzer, S H; Gregori, G; Lee, H J; Marschner, H; Toleikis, S; Wehrhan, O; Förster, E: **Focal aberrations of large-aperture HOPG von-Hamos x-ray spectrometers.** *Journal of Instrumentation* 7: P09015 - P09015, 2012. DOI:10.1088/1748-0221/7/09/P09015

WOS-PNI-176 Zastrau, U.; Burian, T.; Chalupsky, J.; Döppner, T.; Dzelzainis, T.W.J.; Fäustlin, R.R.; Fortmann, C.; Galtier, E.; Glenzer, S.H.; Gregori, G.; Juha, L.; Lee, H.J.; Lee, R.W.; Lewis, C.L.S.; Medvedev, N.; Nagler, B.; Nelson, A.J.; Riley, D. ; Rosmej, F.B.; Toleikis, S.; Tschentscher, T.; Uschmann, I.; Vinko, S.M.; Wark, J.S.; Whitcher, T. ; Förster, E.: **XUV spectroscopic characterization of warm dense aluminum plasmas generated by the free-electron-laser FLASH.** *Laser and particle beams* 30: 45 - 56, 2012. DOI:10.1017/S026303461100067X

WOS-PNI-177 Zhang, H.-Q.; Akram, N.; Skog, P.; Soroka, I. L.; Trautmann, C.; Schuch, R.: **Tailoring of keV-Ion Beams by Image Charge when Transmitting through Rhombic and Rectangular Shaped Nanocapillaries.** *Physical review letters* 108: 193202, 2012. DOI:10.1103/PhysRevLett.108.193202

WOS-PNI-178 Zhang, HQ.; Akram, N.; Soroka, I. L.; Trautmann, C.; Schuch, R.: **Transmission of highly charged ions through mica nanocapillaries of rhombic cross section.** *Physical review / A* 86: 022901, 2012. DOI:10.1103/PhysRevA.86.022901

WOS-PNI-179 Zhang, Y. H.; Xu, H. S.; Litvinov, Yu. A.; Tu, X. L.; Yan, X. L.; Typel, Stefan; Blaum, K.; Wang, M.; Zhou, X. H.; Sun, Y.; Brown, B. A.; Yuan, Y. J.; Xia, J. W.; Yang, J. C.; Audi, G.; Chen, X. C.; Jia, G. B.; Hu, Z. G.; Ma, X. W.; Mao, R. S. ; Mei, B.; Shuai, P.; Sun, Z. Y.; Wang, S. T.; Xiao, G. Q.; Xu, X.; Yamaguchi, T.; Yamaguchi, Y. ; Zang, Y. D.; Zhao, H. W.; Zhao, T. C.; Zhang, W.; Zhan, W. L.: **Mass Measurements of the Neutron-Deficient ^{41}Ti, ^{45}Cr, ^{49}Fe, and ^{53}Ni Nuclides: First Test of the Isobaric Multiplet Mass Equation in fp-Shell Nuclei.** *Physical review letters* 109: 102501, 2012. DOI:10.1103/PhysRevLett.109.102501

WOS-PNI-180 Zherebtsov, S; Süßmann, F; Peltz, C; Plenge, J; Betsch, K J; Znakovskaya, I; Alnaser, A S; Johnson, N G; Kübel, M; Horn, A; Mondes, V; Graf, C; Trushin, S A; Azzeer, A; Vrakking, M J J ; Paulus, G G; Krausz, F; Rühl, E; Fennel, T; Kling, M F: **Carrierenvelope phase-tagged imaging of the controlled electron acceleration from SiO 2 nanospheres in intense few-cycle laser fields.** *New journal of physics* 14: 075010 -, 2012. DOI:10.1088/1367-2630/14/7/075010

WOS publications to the programme Health published in 2012

WOS-HEALTH-1 Bleicher, Marcus; Burigo, Lucas; Durante, Marco; Herrlitz, Maren; Krämer, Michael; Mishustin, Igor; Müller, Iris; Natale, Francesco; Pshenichnov, Igor ; Schramm, Stefan; Taucher-Scholz, Gisela; Wälzlein, Cathrin: **Nanolesions induced by heavy ions in human tissues: Experimental and theoretical studies.** *Beilstein journal of nanotechnology* 3: 556 - 563, 2012. DOI:10.3762/bjnano.3.64

WOS-HEALTH-2 Pignalosa, Diana; Durante, Marco: **Overcoming resistance of cancer stem cells.** *The lancet / Oncology* 13: e187 - e188, 2012. DOI:10.1016/S1470-2045(12)70196-1

Further publications to the programme Physics of hadrons and nuclei published in 2012

NR-PHN-1 Adamczewski-Musch, J; Kurz, N; Linev, S; Zumbruch, P: **Data acquisition and online monitoring software for CBM test beams.** *Journal of physics / Conference Series* 396: 012001 -, 2012. DOI:10.1088/1742-6596/396/1/012001

NR-PHN-2 Al-Turany, Mohammad; Bertini, Denis; Karabowicz, Radoslaw; Kresan, Dmytro; Malzacher, Peter; Stockmanns, T.; Uhlig, Florian: **The FairRoot framework.** *Journal of physics / Conference Series* 396: 022001, 2012. DOI:10.1088/1742-6596/396/2/022001

NR-PHN-3 Geyer, S; Kester, O: **A transverse electron target for FAIR.** *Journal of physics / Conference Series* 388: 062001 -, 2012. DOI:10.1088/1742-6596/388/6/062001

NR-PHN-4 Göringer, Horst; Feyerabend, M; Sedykh, S: **High Performance Experiment Data Archiving with gStore.** *Journal of physics / Conference Series* 396: 042023 -, 2012. DOI:10.1088/1742-6596/396/4/042023

NR-PHN-5 Jung, C; Petzold, A; Pfeiler, C-E; Schwarz, Kilian: **ALICE Grid Computing at the GridKa Tier-1 Center.** *Journal of physics / Conference Series* 396: 042032 -, 2012. DOI:10.1088/1742-6596/396/4/042032

NR-PHN-6 Langanke, Karlheinz: **Supernova Dynamics and Explosive Nucleosynthesis.** *Journal of physics / Conference Series* 381: 012016 -, 2012. DOI:10.1088/1742-6596/381/1/012016

NR-PHN-7 Schwarz, Kilian; Uhlig, Florian; Karabowicz, Radoslaw; Montiel-Gonzalez, Almudena; Zynovyev, Mykhaylo; PreußCarsten: **Grid Computing at GSI for ALICE and FAIR - present and future.** *Journal of physics / Conference Series* 396: 032097 -, 2012. DOI:10.1088/1742-6596/396/3/032097

NR-PHN-8 Steinheimer, J; Xu, Z; Gudima, K; Botvina, A; Mishustin, I; Bleicher, M; Stöcker, Horst: **Anti- and Hypermatter Research at the Facility for Antiproton and Ion Research FAIR.** *Journal of physics / Conference Series* 389: 012022 -, 2012. DOI:10.1088/1742-6596/389/1/012022

Further publications to the programme Large-scale facilities for research with photons, neutrons and ions published in 2012

NR-PNI-1 Artemyev, A N; Surzhykov, A; Indelicato, P; Plunien, G; Stöhlker, Th: **Novel approach to theoretical investigation of heavy quasi-molecules.** *Journal of physics / Conference Series* 388: 092006 -, 2012. DOI:10.1088/1742-6596/388/9/092006

NR-PNI-2 Bana, D; Beyer, H F; Bosch, Fritz; Brandau, Carsten; Böhm, S; Chatterjee, S; Czarnota, M; Dousse, J -Cl; Gumberidze, Alexandre; Hagmann, Siegbert; Kozhuharov, Christophor; Liesen, Heinz-Dieter; Mokler, P H; Müller, A; Kumar, A; Pajek, M; Reuschl, R; Schmidt, E W; Sierpowski, D ; Spillmann, Uwe; Surzhykov, A; Stöhlker, Thomas ; Szlachetko, J; Tashenov, S; Trotsenko, Sergiy; Verma, P.; Warczak, A: **Enhanced radiative recombination of ^{92+}U ions with cooling electrons for the K-shell.** *Journal of physics / Conference Series* 388: 062044, 2012. DOI:10.1088/1742-6596/388/6/062044

NR-PNI-3 Bernhardt, D; Brandau, Carsten; Kozhuharov, Christophor; Müller, A; Schippers, S; Böhm, S; Bosch, Fritz; Jacobi, J; Kieslich, S; Knopp, H; Mokler, P H; Nolden, Fritz; Shi, W; Stachura, Z; Steck, Markus; Stöhlker, Thomas: **Dielectronic recombination of metastable berylliumlike xenon ions.** *Journal of physics / Conference Series* 388: 062036 -, 2012. DOI:10.1088/1742-6596/388/6/062036

NR-PNI-4 Bernhardt, D; Brandau, Carsten; Kozhuharov, Christophor; Müller, A; Schippers, S; Böhm, S; Bosch, Fritz; Jacobi, J; Kieslich, S; Knopp, H; Mokler, P H; Nolden, Fritz; Shi, W; Stachura, Z; Steck, Markus; Stöhlker, Thomas: **Towards a measurement of the $2s2p^3P_0$ - $2s^2{}^1S_0$ E1M1 two photon transition rate in Be-like xenon ions.** *Journal of physics / Conference Series* 388: 012007 -, 2012. DOI:10.1088/1742-6596/388/1/012007

NR-PNI-5 Blaum, Klaus; Eliseev, Sergey; Eronen, Tommi; Litvinov, Yuri: **Precision mass measurements for nuclear astro- and neutrino physics.** *Journal of physics / Conference Series* 381: 012013, 2012. DOI:10.1088/1742-6596/381/1/012013

NR-PNI-6 Brandau, C; Kozhuharov, C; Litvinov, Yu A; Müller, A; Bernhardt, D; Bernstein, L A; Bosch, F ; Currell, F J; Dimopoulou, C; Gumberidze, A; Heil, M; Nolden, F; Reifarth, R; Schippers, S; Schneider, D; Simon, H; Spillmann, U; Stachura, Z ; Steck, M; Stöhlker, Th; Wiedeking, M; Winckler, N; Winters, D F A: **Dielectronic recombination of in-flight synthesized exotic isotopes.** *Journal of physics / Conference Series* 388: 062042 -, 2012. DOI:10.1088/1742-6596/388/6/062042

NR-PNI-7 Bräuning-Demian, A; Ananyevna, A; Azuma, T; Bräuning, H; Dauvergne, D; Kanai, Y; Nakano, Y; Shindo, T; Suda, S; Yamazaki, Y: **Resonant coherent excitation of 191.1 MeV/u U^{89+} ions planar-channeled in a silicon crystal.** *Journal of physics / Conference Series* 388: 082036 -, 2012. DOI:10.1088/1742-6596/388/8/082036

NR-PNI-8 Cheal, B; Billowes, J; Bissell, M L; Blaum, K; Charlwood, F C; Flanagan, K T; Forest, D H; Geppert, Ch; Kowalska, M; Kreim, K; Krieger, A; Krämer, J; Lynch, K M; Mane, E; Moore, I D; Neugart, R; Neyens, G; Nörtershäuser, W; Papuga, J; Procter, T J; Rajabali, M M; Stroke, H H; Vingerhoets, P; Yordanov, D T; akova, M: **Laser spectroscopy of gallium isotopes beyond N = 50.** *Journal of physics / Conference Series* 381: 012071 -, 2012. DOI:10.1088/1742-6596/381/1/012071

NR-PNI-9 Cocolios, T E; Andreyev, A N; Antalic, S; Barzakh, A E; Bastin, B; Büscher, J; Darby, I G; Dexters, W; Fedorov, D V; Fedosseev, V N; Flanagan, K T; Franchoo, S; Fritzsche, S; Huber, G; Huyse, M; Keupers, M; Köster, U; Kudryavtsev, Yu; Mane, E; Marsh, B A; Molkanov, P L; Page, R D; Seliverstov, M D; Sjödin, A M; Stefan, I; Walle, J Van de; Duppen, P Van; Venhart, M; Zemlyanoy, S G: **Early onset of deformation in the neutron-deficient polonium isotopes.** *Journal of physics / Conference Series* 381: 012072 -, 2012. DOI:10.1088/1742-6596/381/1/012072

NR-PNI-10 Fratini, F; Surzhykov, A; Jahrsetz, T; Tichy, M; Buchleitner, A; Fritzsche, S: **Quantum correlations in the two-photon decay of few-electron ions.** *Journal of physics / Conference Series* 388: 082034 -, 2012. DOI:10.1088/1742-6596/388/8/082034

NR-PNI-11 Fritzsche, S; Grum-Grzhimailo, A N; Gryzlova, E V; Kabachnik, N M: **Angular correlations in the sequential two-photon double ionisation of atomic xenon.** *Journal of physics / Conference Series* 388: 032006 -, 2012. DOI:10.1088/1742-6596/388/3/032006

NR-PNI-12 Gryzlova, E V; Grum-Grzhimailo, A N; Fritzsche, S; Kabachnik, N M: **Angular distributions and correlations in sequential three-photon triple atomic ionization.** *Journal of physics / Conference Series* 388: 032040 -, 2012. DOI:10.1088/1742-6596/388/3/032040

NR-PNI-13 Gumberidze, A; Thorn, D B; Trotsenko, S; Bana, D; Beyer, H; Chen, W; DuBois, R D; Geyer, S; Grisenti, R; Hagmann, S; Hegewald, M; Hess, S; Indelicato, P; Kozhuharov, C; Märtin, R; Orban, I ; Petridis, N; Reuschl, R; Simon, A; Spillmann, U ; Surzhykov, A; Trassinelli, M; Weber, G; Winters, D F A; Winters, N; Yu, D; Stöhlker, Th: **Electron- and Proton-Impact Excitation in Stored Hydrogenlike Uranium Ions.** *Journal of physics / Conference Series* 388: 082035 -, 2012. DOI:10.1088/1742-6596/388/8/082035

NR-PNI-14 Hahn, M; Bernhardt, D; Grieser, M; Krantz, C; Lestinsky, M; Müller, A; Novotny, O; Repnow, R ; Schippers, S; Wolf, A; Savin, D W: **Electron impact ionization measurements at the Heidelberg heavy ion storage ring TSR.** *Journal of physics / Conference Series* 388: 062021 -, 2012. DOI:10.1088/1742-6596/388/6/062021

NR-PNI-15 Herfurth, Frank; Barth, Winfried; Clemente,

Gianluigi; Dahl, L A; Gerhard, P; Kaiser, Michael; Kester, Oliver; Kluge, Heinz-Jürgen; Krantz, C; Kotovskiy, Nikita; Kozhuharov, Christophor; Maier, Michael; Pfister, Jochen; Quint, Wolfgang; Ratzinger, U; Sokolov, Alexey; Stöhlker, Thomas; Vormann, Hartmut ; Vorobjev, G.; Wolf, A; Yaramishev, S; Schempp, A: **HITRAP Heavy, highly charged Ions at Rest: Status and experimental Opportunities.** *Journal of physics / Conference Series* 388: 142009, 2012. DOI:10.1088/1742-6596/388/14/142009

NR-PNI-16 Kellerbauer, Alban; Fritzsche, Stephan: **High-resolution optical spectroscopy of Os with a view to laser cooling of atomic anions.** *Journal of physics / Conference Series* 388: 012023 -, 2012. DOI:10.1088/1742-6596/388/1/012023

NR-PNI-17 McConnell, Sean; Artemyev, Anton; Surzhykov, Andrey: **Alignment of atomic inner-shell vacancies following nuclear decay.** *Journal of physics / Conference Series* 388: 082047 -, 2012. DOI:10.1088/1742-6596/388/8/082047

NR-PNI-18 Märtin, R; Barday, R; Enders, J; Poltoratska, Y; Spillmann, U; Weber, G; Stöhlker, Th: **Linear Polarization of the High-Energy End of Bremsstrahlung in Electron-Atom Collisions.** *Journal of physics / Conference Series* 388: 042027 -, 2012. DOI:10.1088/1742-6596/388/4/042027

NR-PNI-19 Novo, S Beceiro; Sümmerer, K; Cortina-Gil, D; Wimmer, C; Plag, R; Alvarez-Pol, H; Aumann, T; Behr, K; Boretzky, K; Casarejos, E; Chatillon, A ; Datta-Pramanik, U; Elekes, Z; Fulop, Z; Galaviz, D; Geissel, H; Giron, S; Greife, U; Hammache, F; Heil, M; Hoffman, J; Johansson, H; Karagiannis, C; Kiselev, O; Kurz, N; Larsson, K; Bleis, T Le; Litvinov, Y; Mahata, K; Muentz, C; Nociforo, C; Ott, W; Paschalis, S; Prokopowicz, W ; Rodriguez-Tajes, C; Rossi, D; Simon, H; Stanoiu, M; Stroth, J; Typel, S; Wagner, A; Wamers, F; Weick, H: **Coulomb Dissociation of ^{27}P.** *Journal of physics / Conference Series* 381: 012115 -, 2012. DOI:10.1088/1742-6596/381/1/012115

NR-PNI-20 Pajek, M; Bana, D; Brandau, C; Gumberidze, A; Jagodzinski, P; Kozhuharov, Ch; Surzhykov, A; Stöhlker, Th: **Radiative recombination of ions with electrons in cold magnetized plasma.** *Journal of physics / Conference Series* 388: 062045 -, 2012. DOI:10.1088/1742-6596/388/6/062045

NR-PNI-21 Reed, M W; Walker, P M; Cullen, I J; Litvinov, Yu A; Blaum, K; Bosch, Fritz; Brandau, Carsten; Carroll, J J; Cullen, D M; Deo, A Y; Detwiler, B ; Dimopoulou, Christina; Dracoulis, G D; Farinon, Fabio; Geissel, Hans; Haettner, E; Heil, Michael ; Kempley, R S; Knöbel, Ronja; Kozhuharov, Christophor; Kurcewicz, Jan; Kuzminchuk, N; Litvinov, Sergey; Liu, Z; Mao, R; Nociforo, Chiara ; Nolden, Fritz; PlaßW R; Prochazka, Andrej; Scheidenberger, Christoph; Shubina, Daria; Steck, Markus; Stöhlker, Thomas; Sun, B; Swan, T P D; Trees, G; Weick, Helmut; Winckler, Nicolas; Winkler, Martin; Woods, P J; Yamaguchi, T: **Technique for Resolving Low-lying Isomers in the Experimental Storage Ring (ESR) and the Occurrence of an Isomeric State in ^{192}Re.** *Journal of physics / Conference Series* 381: 012058 -, 2012. DOI:10.1088/1742-6596/381/1/012058

NR-PNI-22 Schippers, S; Bernhardt, D; Krantz, C; Lestinsky, M; Novotny, O; Miiller, A; Wolf, A: **Towards a storage-ring measurement of the hyperfine induced $2s2p^3P_0 \rightarrow$ 2s$^21S_0$ transition rate in berylliumlike sulfur.** *Journal of physics / Conference Series* 388: 152004 -, 2012. DOI:10.1088/1742-6596/388/15/152004

NR-PNI-23 Schippers, S; Bernhardt, D; Müller, A; Krantz, C; Grieser, M; Repnow, R; Wolf, A; Lestinsky, M ; Hahn, M; Novotny, O; Savin, D W: **Dielectronic recombination of xenonlike tungsten ions.** *Journal of physics / Conference Series* 388: 062028 -, 2012. DOI:10.1088/1742-6596/388/6/062028

NR-PNI-24 Schippers, S; Bernhardt, D; Müller, A; Krantz, C; Wolf, A; Lestinsky, M; Hahn, M; Novotny, O; Savin, D W: **Storage ring meets astrophysics: Dielectronic recombination of L-shell and M-shell iron ions.** *Journal of physics / Conference Series* 388: 062029 -, 2012. DOI:10.1088/1742-6596/388/6/062029

NR-PNI-25 Spillmann, U; Blumenhagen, K-H; Bräuning, H; Weber, G; Stöhlker, Th: **Planar position sensitive Ge(i)- and Si(Li)-detector systems for Compton Polarimetry in Atomic Physics with Highly Charged Ions.** *Journal of physics / Conference Series* 388: 142023 -, 2012. DOI:10.1088/1742-6596/388/14/142023

NR-PNI-26 Stolterfoht, N; Bodewits, Erwin; Hellhammer, Rolf; Juhasz, Zoltan; Sulik, Bela; Bayer, Veronika; Trautmann, Christine; Hoekstra, Ronnie: **Dynamics of ion guiding through nanocapillaries in insulating polymers.** *Journal of physics / Conference Series* 388: 012049, 2012. DOI:10.1088/1742-6596/388/1/012049

NR-PNI-27 Trotsenko, S; Kumar, A; Bana, D; Volotka, A V; Gumberidze, A; Kozhuharov, C; Thorn, D B; Beyer, H F; Fritzsche, S; Hagmann, S; Hess, S; Jagodzinski, P; Reuschl, R; Salem, S; Simon, A; Spillmann, U; Trassinelli, M; Tribedi, L C; Weber, G; Winters, D; Stöhlker, T: **Novel approach for studying two-photon transitions in heavy HCI.** *Journal of physics / Conference Series* 388: 082001 -, 2012. DOI:10.1088/1742-6596/388/8/082001

NR-PNI-28 Verma, P; Mokler, P H; Bräuning-Demian, A; Kozhuharov, C; Bräuning, H; Bosch, F; Hagmann, S ; Liesen, D; Stachura, Z; Wahab, M A: **Shell-differential electron capture in heavy ion-atom collisions at moderate collision velocities.** *Journal of physics / Conference Series* 388: 082008 -, 2012. DOI:10.1088/1742-6596/388/8/082008

NR-PNI-29 Vogel, Manuel; Birkl, Gerhard; Lindenfels, David von; Quint, Wolfgang: **Magnetic moments of bound electrons and nuclei by double resonance spectroscopy of highly charged ions in a Penning trap.** *Journal of physics / Conference Series* 388: 022065 -, 2012. DOI:10.1088/1742-6596/388/2/022065

NR-PNI-30 Voitkiv, A B; Najjari, B; Fischer, D; Artemyev, A N; Surzhykov, A: **Young-type interference in projectile-electron loss in energetic ion-molecule collisions.** *Journal of physics / Conference Series* 388: 102047 -, 2012. DOI:10.1088/1742-6596/388/10/102047

NR-PNI-31 Wang, Q M; Li, J G; Fritzsche, S; Godefroid,

M; Chang, Z W; Dong, C Z: **Theoretical study of hyperfine structure constants of Ga isotopes.** *Journal of physics / Conference Series* 388: 152009 -, 2012. DOI:10.1088/1742-6596/388/15/152009

NR-PNI-32 Weber, G; Bräuning, H; Surzhykov, A; Fritzsche, S; Märtin, R; Reuschl, R; Spillmann, U; Winters, D F A; Stöhlker, Th: **Direct Determination of the Magnetic Quadrupole Contribution to the Lyman-$_1$ Transition in U^{91+}.** *Journal of physics / Conference Series* 388: 082029 -, 2012. DOI:10.1088/1742-6596/388/8/082029

NR-PNI-33 Winters, D F A; Kühl, Th; Nörtershäuser, W; Stöhlker, Th: **Laser spectroscopy at the experimental storage ring - an overview.** *Journal of physics / Conference Series* 388: 152022, 2012. DOI:10.1088/1742-6596/388/15/152022

NR-PNI-34 Zhang, S F; Ma, X; Fischer, D; Moshammer, R; Voitkiv, A; Suske, J; Kühnel, K U; Hagmann, S; Krauss, A; Zhang, R T; Guo, D L; Ullrich, J: **Young-type interference in ionizing collisions between helium and hydrogen molecular ions.** *Journal of physics / Conference Series* 388: 102038 -, 2012. DOI:10.1088/1742-6596/388/10/102038

Further publications to the programme Health published in 2012

NR-HEALTH-1 Durante, M; Stöcker, H: **Relativistic protons for image-guided stereotactic radiosurgery.** *Journal of physics / Conference Series* 373: 012016 -, 2012. DOI:10.1088/1742-6596/373/1/012016

NR-HEALTH-2 Krämer, M; Scifoni, E; Wälzlein, C; Durante, M: **Ion beams in radiotherapy - from tracks to treatment planning.** *Journal of physics / Conference Series* 373: 012017 -, 2012. DOI:10.1088/1742-6596/373/1/012017

Doctoral theses 2012 supported by GSI

Programme Physics of hadrons and nuclei

beginsmall Alikhani, Babak: **Aufbau und Inbetriebnahme des DAGATA-Polarimeters.** Technische Universität Frankfurt, 2012.

Almomani, Ali: **RF acceleration of intense laser generated proton bunches.** Johann Wolfgang Goethe-Universität Frankfurt am Main, 2012.

Amar-Youcef, Samir: **Design and performance studies of the Micro-Vertex-Detector for the CBM experiment at FAIR.** Johann Wolfgang Goethe Universtität Frankfurt am Main, 2012.

Boucher, Jerome: **Feasibility studies of the $\overline{p}p- > pi^0e^+e^-$ electromagnetic channel at PANDA.** Johannes Gutenberg Universität Mainz, 2012.

Bozyk, Lars: **Entwicklung und Test eines Kryokollimator-Prototypen zur Kontrolle des dynamischen Vakuums im SIS100.** Technische Universität Darmstadt, 2012.

Castillo Hernandez, Juan Francisco: **Charged particle multiplicity studies in proton-proton collisions at a centre-of-mass energy of 10 TeV with the ALICE detector.** TU Darmstadt, 2012.

Comas Lijachev, Victor Fernandovich: **Experiments on multi-nucleon transfer reactions with the systems $^{58,64}Ni +^{207} Pb$ at SHIP.** Justus-Liebig-Universität Gießen, 2012.

Denicol, Gabriel: **Microscopic foundations of relativistic dissipative fluid dynamics.** Johann Wolfgang Goethe-Universität Frankfurt am Main, 2012.

Farinon, Fabio: **Unambiguous identification and investigation of uranium projectile fragments $\&$ discovery of 63 new neutron-rich isotopes in the element range $61 \leq Z \leq 78$ at the FRS.** Justus-Liebig-Universität Gießen, 2012.

Fasel, Markus: **Single-electron analysis and open charm cross section in proton-proton collisions at $\sqrt{}$s = 7 TeV.** Technische Universität Darmstadt, 2012.

Göcke, Tobias,: **Hadronic Contributions to the anomalous Magnetic Moment of the Muon.** Justus-Liebig-Universität Gießen, 2012.

Heredia Cardona, Julio Antonio: **Production and decay properties of neutron deficient isotopes with $N < 126$ and $74 \leq Z \leq 92$ at SHIP.** Johann Wolfgang Goethe-Universität Frankfurt am Main, 2012.

Kalweit, Alexander: **Production of light flavor hadrons and anti-nuclei at the LHC.** Technische Universität Darmstadt, 2012.

Kellermann, Christian,: **Glueball properties from the Bethe-Salpeter equation.** Technische Universität Darmstadt, 2012.

Kuzminchuk, Natalia: **Performance studies and improvements of a Time-of-Flight detector for isochronous mass measurements at the FRS-ESR facility.** Justus-Liebig-Universität Gießen, 2012.

Langer, Christoph: **Coulomb dissociation of ^{31}Cl and ^{32}Ar - constraining the rp process.** Johann Wolfgang Goethe-Universität Frankfurt am Main, 2012.

Leon Vargas, Hermes: **Jet fragmentation properties in proton-proton and Pb-Pb collisions with ALICE at the LHC.** Johann Wolfgang Universität Frankfurt am Main, 2012.

Lorenz, Manuel: **Vector meson production in p+Nb reactions and statistical particle production in Ar+KCl collisions.** Johann Wolfgang Goethe-Universität Frankfurt am Main, 2012.

Michel, Jan: **Development and implementation of a new Trigger and data Acquisition system for the HADES detector.** Johann Wolfgang Goethe-Universität Frankfurt, 2012.

Michler, Frank: **Finite lifetime effects on the photon emission from a quark-gluon plasma.** Johann Wolfgang Goethe-Universität Frankfurt am Main, 2012.

Panin, Valerii: **Fully exclusive measurements of quasi-free single-nucleon knockout reactions in inverse kinematics..** Technische Universität Darmstadt, 2012.

Puppel, Patrick: **Orts- und zeitaufgelöste Simulation strahlinduzierter dynamischer Vakuumeffekte in Schwerionensynchrotrons / von Patrick Puppel.** Johann Wolfgang Goethe-Universität Frankfurt am Main, 2012.

Seddiki, Selim: **Contribution to the development of the Micro-Vertex Detector of the CBM experiment and feasibility study of open charm elliptic flow measurements.** Johann Wolfgang Goethe-Universität Frankfurt am Main, 2012.

Weber, Dennis: **Effective realistic interactions for low momentum Hilbert spaces.** Technische Universität Darmstadt, 2012.

Zynovyev, Mykhaylo: **Conceptual design of an ALICE Tier-2 centre integrated into a multi-purpose computing facility.** Johann Wolfgang Goethe-Universität Frankfurt am Main, 2012.

Programme Large-scale facilities for research with photons, neutrons and ions

Alber, Ina,: **Synthesis and characterization of metal and semiconductor nanowires.** Heidelberg, 2012.

Andelkovic, Zoran: **Setup of a Penning trap for precision laser spectroscopy at HITRAP.** Johannes Gutenberg Universität Mainz, 2012.

Aurand, Bastian: **Untersuchungen zu Mechanismen der Laser-Teilchenbeschleunigung.** Johannes Gutenberg Universität Mainz, 2012.

Botermann, Benjamin: **Test der Speziellen Relativitätstheorie mittels Laserspektroskopie an relativistischen 7 Li +-Ionen am ESR.** Johannes Gutenberg Universität Mainz, 2012.

Brantjes, Nicolaas Petrus Marcus: **The g-Factor of Hydrogen-Like Heavy Ions as a Test for QED.** Ruprecht-Karls-Universität Heidelberg, 2012.

Carignano, Stefano: **Inhomogeneous chiral symmetry breaking phases.** Technische Universität Darmstadt, 2012.

Cazan, Radu Mircea: **Login to HeiDOK Preparation of cold Mg + ion clouds for sympathetic cooling of highly charged ions at SPECTRAP.** Johannes Gutenberg Universität Mainz, 2012.

El, Andrej: **Investigation of transition between kinetic theory and dissipative hydrodynamic formalisms.** Johann Wolfgang Goethe-Universität Frankfurt am Main, 2012.

Hochhaus, Daniel,: **X-ray diagnostics on isochorically heated warm dense matter.** Johann Wolfgang Goethe-Universität Frankfurt am Main, 2012.

Kramer, Frederick,: **J/ψ Production in $\sqrt{}$s=7 TeV pp Collisions.** Johann Wolfgang Goethe Universität Frankfurt am Main, 2012.

Kraus, Dominik: **Characterization of phase transitions in warm dense matter with X-ray scattering.** Technische Universität Darmstadt, 2012.

Krieger, Andreas: **Laser systems for collinear spectroscopy and the charge radius of ^{12}Be.** Universität Mainz, 2012.

Müller, Sven: **Morphological, Structural, and Compositional Characterization of Electrodeposited Bi(1-x)Sb(x) Nanowires.** Ruprecht-Karls-Universität Heidelberg, 2012.

Pitz, Nora: **Gas system, gas quality monitor and detector control of the ALICE Transition Radiation Detector and studies for a pre-trigger data read-out system.** Johann Wolfgang Goethe Universität Frankfurt am Main, 2012.

Schumacher, Dennis: **Untersuchung laserinduzierter Hohlraumstrahlung und Energieverlust von Schwerionen in indirekt geheizten Plasmen.** Technische Universität Darmstadt, 2012.

Schuster, Tim: **Hadron ratio fluctuations in heavy-ion collisions.** Johann Wolfgang Goethe-Universität Frankfurt am Main, 2012.

Shubina, Daria: **Schottky Mass Measurements of Heavy Neutron-Rich Nuclides in the Element Range $70 \leq Z \leq 79$ at the ESR.** Ruprecht-Karls-Universität Heidelberg, 2012.

Zhang, Tian: **Study of QCD-like theories at nonzero temperatures and densities.** Johann Wolfgang Universität Frankfurt am Main, 2012.

Programme Healths

Klinger, Jonas: **Entzündungshemmende Effekte von ionisierender Strahlung, untersucht in Co-Kultur Systemen humaner Endothelzellen und Leukozyten.** Technische Universität Darmstadt, 2012.

Lüchtenborg, Robert: **Real-time dose compensation methods for scanned ion beam therapy of moving tumors [12.12.2011].** GSI Diss 2012-01. TU Darmstadt, 2012.

Meyer, Barbara: **Kernweite H2AX-Phosphorylierung nach Schwerionenbestrahlung.** Technische Universität Darmstadt, 2012.

Richter, Daniel: **Treatment planning for tumors with residual motion in scanned ion beam therapy.** Technische Universität Darmstadt, 2012.

Tobias, Frank: **Analyse von schnellen dynamischen Prozessen und Proteininteraktionen nach dicht ionisierender Bestrahlung.** Technische Universität Darmstadt, 2012.

Experiments performed at the GSI accelerators in 2012

Compiled by Burkhard Kolb, beam time coordinator 2012

In all tables 1 shift represents 8 hours of beam delivered to an experiment including necessary accelerator tuning time.

Exp	Short title	Spokesperson	Area	Ion	Shifts main	Shifts parasitic
U207	Laser spectroscopy of Nobelium	Backe/Block	Y7	^{48}Ca		14
U252	Energy loss in laser generated plasma	Roth	Z6	^{12}C		7
U258	Synthesis of new elements at TASCA	Düllmann	X8	^{50}Ti, ^{48}Ca	399	
U261	SHE X-ray Fingerprinting With TASIspec	Rudolph	X8	^{48}Ca	51	
U267	Z = 120	Hofmann	Y7	^{50}Ti	5	
U272	Combined PHELIX-laser-UNILAC	Rosmej	Z6	^{50}Ti		16
U274	Ion energy loss in laser generated plasma	Roth/Blazevic	Z6	^{12}C, ^{48}Ca		20
U275	Theta Pinch Plasma Stripper	Jacoby	Z6	^{48}Ca		10
U276	LIGHT	Roth/Blazevic	Z6	^{48}Ca		5
U277	Study of shell effects in the system U+U	Heinz	Z7	U		33
U278	Decay properties of Db-258	Andersson	Y7	Ti		14
UBIO	Radiobiology	Scholz/Friedrich	X6, M-branch	Au,Ti, Pb, U		34
UMAT	Material science	Trautmann, Severin, Bender	X0, M1, M2, M3	Ti, Au, Pb, U	39	125

E039	Precision X-Ray Spectroscopy	Beyer	ESR	Au	67	
E075	HITRAP Decelerator Commissioning	Herfurth	ESR	^{50}Ti	28	
E087	Breakout of the hot CNO cycle	Woods	ESR	^{20}Ne	18	
E089	Laser cooling of C3+ ions at the ESR	Bussmann	ESR	^{12}C	22	
E090	Bremsstrahlung	Hagmann	ESR	^{238}U	40	
E105	Start of the EXL physics program with 56Ni	Kalantar	ESR	^{58}Ni	42	
E110	An Atomic Physics Method to Study High-Z Long-Lived Isomers	Brandau	ESR	^{238}U	17	
E113	Charge-changing cross sections many-electron, heavy ions	Dubois	ESR	U	2	

Exp	Short title	Spokesperson	Area	Ion	Shifts main	Shifts parasitic
S333	HADES commissioning	Pietraszko	HAD	^{208}Pb		2
S339	pi induced reactions/GEM-TPC tracking	Hartmann/ Leifels	HTB	^{2}H, ^{58}Ni		5
S370	Lifetime 3P0 He-like uranium	Reuschl	HTA	^{238}U		10
S388	Search for 30Ar	Mukha	FRS	^{36}Ar	15	
S401	CBM-detector tests	Heuser/Kis	HTB	^{84}Kr, ^{58}Ni		3
S406	Characterization of NeuLAND prototypes and the LAND detector	Boretzky	HTC	^{2}H	13	
S407	HADES Au+Au	Salabura	HAD	Au, ^{58}Ni	73	11
S411	Commissioning cryogenic stopping cell	Dendooven	FRS	^{238}U	18	
S412	Giant and Pygmy resonances in Sn nuclei	Aumann	HTC	^{136}Xe	43	1
S415	R&D on advanced detection techniques for isotopic identification	Taieb	FRS/HTC	^{238}U, ^{208}Pb	7	10
S417	FRS Tests	Nociforo	FRS, HTD	Ti/Au, ^{238}U		4
S424	AGATA-PRESPEC Commissioning	Korten	FRS	Ti, ^{80}Kr	23	2
S426	AGATA 85Br	Pietralla	HFS	^{86}Kr	6	
S428	AGATA Zr	Pietri	HFS	^{238}U	8	
S429	Quadrantic	Rudolph	HFS	^{208}Pb	17	4
S430	Pygmy 64Ni	Wieland	HFS	^{86}Kr	8	
S431	132Sn	Boutachkov	HFS	^{238}U	9	
S433	52Fe	Gadea	HFS	^{58}Ni	15	
SBIO	Radiobiology and Therapy-related experiments	Scholz/Bert/ Graeff	HTA, HTM	^{12}C, ^{48}Ca, ^{238}U	44	4
SESA	Space related radiation biophysics	Scholz	HTA	Ti, ^{58}Ni	19	6
SMAT	Material science	Trautmann/ Schuster	HTA, HTM	Au, ^{238}U	3	11

Statutory organs and scientific advisory committees of GSI (2012)

Compiled by K. Füssel

Supervisory Board / Aufsichtsrat (AR):

Dr. B. Vierkorn-Rudolf [chair],
Bundesministerium für Bildung und Forschung, Bonn/Berlin (Germany),
as representative of the Federal Republic of Germany

Ministerialrätin O. Keppler,
Bundesministerium für Bildung und Forschung, Bonn/Berlin (Germany),
as representative of the Federal Republic of Germany

Ministerialdirigent Dr. R. Bernhardt,
Hessisches Ministerium für Wissenschaft und Kunst, Wiesbaden (Germany),
as representative of the State of Hesse in Germany

Ministerialrätin I. Schäfer,
Ministerium für Bildung, Wissenschaft, Weiterbildung und Kultur, Mainz (Germany),
as representative of the State of Rhineland-Palatinate in Germany

Ministerialrat D. Klein,
Thüringer Kultusministerium, Erfurt (Germany),
as representative of the State of Thuringia in Germany

Prof. Dr. K.-H. Kampert,
Bergische Universität Wuppertal (Germany),
as representative of the Scientific Council of GSI

Dr. U. Steigenberger,
ISIS Rutherford Appleton Laboratory, Oxfordshire (United Kingdom),
as representatives from the fields of science and economy

Prof. Dr. R.-D. Heuer,
European Organization for Nuclear Research CERN, Geneva (Switzerland),
as representatives from the fields of science and economy

Dr. B. Lommel,
GSI Helmholtzzentrum für Schwerionenforschung,
ex officio as spokesperson of the Scientific-Technical Council of GSI

Directors' Board / Geschäftsführung (GF):

Prof. Dr. H. Stöcker, P. Hassenbach
Prof. Dr. K. Langanke (assoc.), Prof. Dr. O. Kester (assoc.)

Divisions / Bereiche:

Controlling / Organization: *N.N.*
FAIR@GSI: O. *Kester*
Finance / Procurement / Admin-IT: *F. Forster*
Personnel / Legal Matters / Patents: *A. Lambert*
Research: *K. Langanke*
Technical Infrastructure: *G. Walter*

Project Areas / Projektbereiche:

Project Coordination: *U. Weinrich*
Common Systems: *H. Reich-Sprenger*
Engineering: *R. Fuchs*
Primary Beams: *P. Spiller*
Stored Beams: *M. Steck*
Rare Isotopes Beams: *H. Simon*
Linac and Operations: *W. Barth*

Project Divisions / Projektabteilungen:

Accelerator Operations: *U. Scheeler*
Antiproton Separator: *K. Knie*
Beam Cooling: *C. Dimopoulou*
Beam Instrumentation: *M. Schwickert*
Beam Physics: *O. Boine-Frankenheim*
CBM Detectors: *C. Sturm*
Collector Ring: *O. Dolinskyy*
Configuration Management: *B. Schönfelder*
Control Systems: *R. Bär*
Cryogenics: *H. Kollmus*
Decelerator: *F. Herfurth*
Detector Laboratory: *C. J. Schmidt*
Electric Power Systems: *H. Ramakers*
Electronics: *E. Badura*
ESR: *F. Nolden*
Ion Sources: *R. Hollinger*
Linac: *L. Groening*
Linac RF: *G. Schreiber*
Mechanical Design: *R. Lotz*
Mechanical Integration: *C. Will*
NC Magnets and Alignment: *C. Mühle*
PANDA Detectors: *J. Schwiening*
Plasmaphysics Detectors: *A. Blazevic*
Processes and Communication: *N.N.*
Project Control: *G. Hickler*
Quality Assurance: *N.N.*
Ring RF: *H. Klingbeil*
SC Magnets and Testing: *E. Fischer*
SPARC Detectors: *Y. Litvinov*
Super-FRS: *M. Winkler*
System Planning: *D. Ondreka*
Target Laboratory: *B. Lommel*
Technology Laboratory: *N.N.*
Transportation and Installation: *M. Bevcic*
Vacuum Systems: *A. Krämer*

Research Areas / Forschungsschwerpunkte:

APPA / PNI: *T. Stöhlker*
Biophysics: *M. Durante*
CBM / NQM: J. *Stroth*
NuSTAR / ENNA: C. *Scheidenberger*
PANDA / HSD: K. *Peters*
IT: V. *Lindenstruth*

Research Divisions / Forschungsabteilungen:

ALICE: *S. Mascciochi*
Atomic Physics: *T. Stöhlker*
CBM: *P. Senger*
Core-IT: *K. Miers*
FOPI: *Y. Leifels*
FRS/SFRS: *H. Geissel*
Gamma-Spectroscopy: *J. Gerl / N. Pietralla*
HADES: *J. Stroth*
Hadron Physics I: *K. Peters*
Hadron Physics II: *F. Maas*
High Performance Computing: *W. Schön*
Library and Documentation: *K. Große*
Materials Research: *C. Trautmann*
Nuclear Reactions: *T. Aumann*
Plasma Physics and PHELIX: *T. Stöhlker (provisional)*
Scientific Computing: P. *Malzacher*
SHE-Chemistry: *C. E. Düllmann*
SHE-Physics: *F.-P. Hessberger*
Theory: *H. Feldmeier, C. Greiner, H. Stöcker, J. Wambach*

Scientific Council / Wissenschaftlicher Beirat (WBR):

https://www.gsi.de/work/organisation/wissenschaftliche_gremien/wr.htm

K.-H. Kampert [chair], Bergische Universität Wuppertal (Germany);
A. Bracco, University of Milano (Italy); *P. Chomaz*, CEA/Saclay, Gif-sur-Yvette (France); *R. Hayano*, University of Tokyo (Japan); *R. Heuer*, European Organization of Nuclear Research CERN, Geneva (Switzerland); *B. Jacak*, Stony Brook University, Stony Brook, New York (USA); *S. Jacquemot*, LULI, Palaiseau (France); *S. Myers*, European Organization of Nuclear Research CERN, Geneva (Switzerland); *T. Roser*, BNL, Upton (USA); *E. Tomasi-Gustafsson*, CEA/Saclay, IRFU/SPhN, IN2P3/IPN Orsay (France); *D. Vernhet*, Université Paris (France); *A. Warczak*, Jagiellonian University, Warsaw (Poland); *M. C. Wiescher*, University of Notre Dame, Notre Dame, Indiana (USA).
Secretary: K.-D. Groß

Scientific-Technical Council / Wissenschaftlich-Technischer Rat (WTR):

Bettina Lommel (Spokesperson); *Christina Trautmann; Peter Malzacher; Ralph Bär; Yvonne Leifels* (Vice-Spokesperson); *Dieter Ackermann; Yuri Litvinov; Angela Bräuning-Demian; Marcus Schwickert; Peter Senger; Jens Stadlmann; David Ondreka; Wolfgang Bayer; Magda Gorska; Frank Herfurth; Lars Schmitt;*

Scientific Advisory Committees of GSI

https://www.gsi.de/start/forschung/wissenschaftliche_gremien/pac.htm

General Program Advisory Committee G-PAC:

P. Giubellino[chair], INFN Turin, Turin (Italy);
B. Blank, CEN Bordeaux-Gradignan, Gradignan (France); *Y. Blumenfeld*, CERN, Geneva (Switzerland); *W. Catford*, University of Physics, Guilford (UK); *R. Hoekstra*, KVI Groningen, Groningen (The Netherlands); *S. Leupold*, Uppsala University, Uppsala (Sweden);

N. Pietralla, Technische Universität Darmstadt, Darmstadt (Germany); *H. Schatz*, Michigan State University, East Leasing (USA); *R. Schuch*, Stockholm University, Stockholm (Sweden); *A. Türler*, Paul Scherer Institut, Villigen (Switzerland); *M. Wada*, RIKEN, Saitama (Japan); *M. Weidemüller*, Ruprecht-Karls-Universität Heidelberg, Heidelberg (Germany).

PHELIX Committee:

V. Fortov [chair], JIHT, RAS, Moscow (Russia);
D. Gericke, University of Warwick, Coventry (UK); *A. Golubev*, ITEP, Moscow (Russia); *D. Schneider [vice-chair]*, LLNL-PAT/NIF, Livermore, California (USA); V. *Tikhonchuk*, University of Bordeaux 1, Talence (France); *O. Willi*, Heinrich Heine Universität, Düsseldorf (Germany).

Biophysics & Radio-Biology Program Advisory Committee (Bio-PAC):

G. Reitz [chair], Deutsches Zentrum für Luft- und Raumfahrt (DLR), Cologne (Germany); *F. A. Cucinotta*, NASA Johnson Space Center, Houston, Texas (USA); D. *Goodhead*, Emeritus Director of the Med. Res. Council Rad. and Genome Stability Unit, Oxford (United Kingdom); *T. Haberer*, HIT Betriebs GmbH am Universitätsklinikum Heidelberg, Heidelberg (Germany); *A. Kronenberg*, Lawrence Berkeley National Laboratory, Berkeley, California (USA); *L. Sabatier*, Institute of Cell. & Mol. Radiation Biology, Fonteney-aux-Roses (France).

Materials Research Program Advisory Committee (Mat-PAC):

P. Apel, JINR, Dubna (Russia); *S. Bouffard*, CEA-CNRS-ENSICAEN, Caen (France); *K. Hjort*, University of Uppsala, Uppsala (Sweden); *W. Wesch*, Friedrich-Schiller-Universität Jena, Jena (Germany).

Program Advisory Committee for FAIR-Related Beam Time Proposals (F-PAC):

J. Stadlmann [chair], GSI; L. Schmitt, GSI; W. Müller, GSI; C. Trautmann, GSI; H. Weick, GSI.

GSI Users' Group Executive Committee (UEC):

http://www-alt.gsi.de/forschung/usersgroup/index.html
Nuclear Structure:
T. Faestermann (Germany); M. Pfutzner (Poland); D. Cortina (Spain); A. Jungclaus (Spain); P. Regan [past chair], (UK)
Nuclear Collision:
P. Salabura (Poland); T. Matulewicz (Poland); Nicole Bastid (France)
Atomic Physics:
D. Dauvergne (France); A. Müller (Germany)
Plasma Physics:
J. Jacoby (Germany); T. Kühl (Germany)
Heavy Elements:
J. Kratz (Germany); A. Türler (Germany)
Theory:
W. Cassing (Germany)
Biophysics:
M. Löbrich (Germany)
Materials Research:
W. Ensinger [chair], (Germany)
Students:
B. Schuster (Germany)

Scientific Coordination:

Dr. K.-D. Groß

GSI Helmholtzzentrum für Schwerionenforschung GmbH

Organigramm

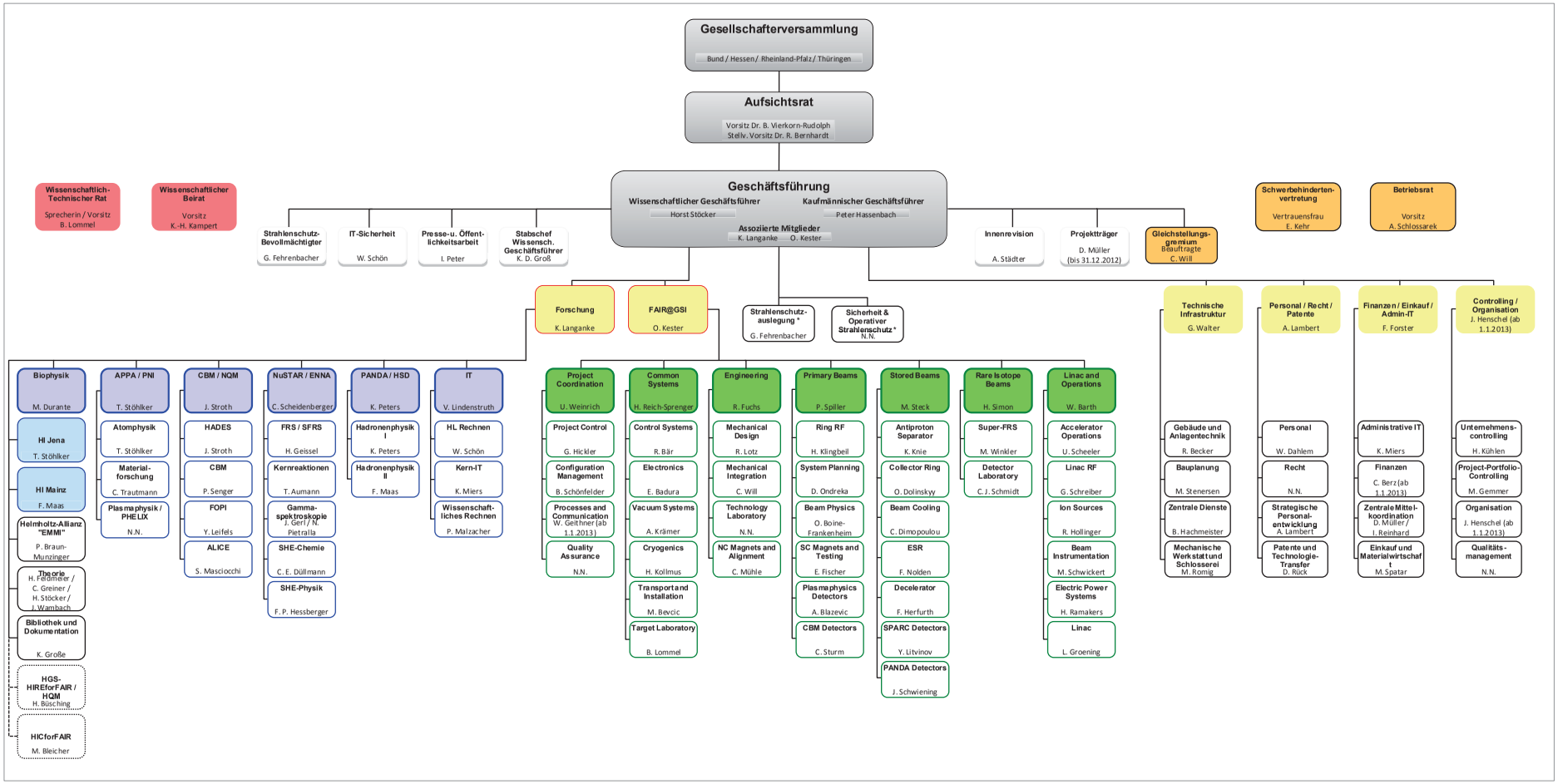

Legende:

Gesellschafts-rechtliches Organ der GSI	Gremium laut Satzung	Geschäfts-bereich	Projekt-bereich	GSI Forschungs-schwerpunkt	Helmholtz-Institut GSI	* Änderungen ausstehend
Stabs-abteilung	Gremium	Abteilung	Projekt-abteilung	Forschungs-abteilung	Kooperations-programm mit GSI-Beteiligung	

Stand: 14.12.2012

List of Authors